frontiers | Research Topics

Interaction between human activities and geo-environment for sustainable development

Edited by
Xuanmei Fan, Xiaoyan Zhao, Xiangjun Pei, Filippo Catani and Yunhui Zhang

Published in
Frontiers in Earth Science



FRONTIERS EBOOK COPYRIGHT STATEMENT

The copyright in the text of individual articles in this ebook is the property of their respective authors or their respective institutions or funders. The copyright in graphics and images within each article may be subject to copyright of other parties. In both cases this is subject to a license granted to Frontiers.

The compilation of articles constituting this ebook is the property of Frontiers.

Each article within this ebook, and the ebook itself, are published under the most recent version of the Creative Commons CC-BY licence. The version current at the date of publication of this ebook is CC-BY 4.0. If the CC-BY licence is updated, the licence granted by Frontiers is automatically updated to the new version.

When exercising any right under the CC-BY licence, Frontiers must be attributed as the original publisher of the article or ebook, as applicable.

Authors have the responsibility of ensuring that any graphics or other materials which are the property of others may be included in the CC-BY licence, but this should be checked before relying on the CC-BY licence to reproduce those materials. Any copyright notices relating to those materials must be complied with.

Copyright and source acknowledgement notices may not be removed and must be displayed in any copy, derivative work or partial copy which includes the elements in question.

All copyright, and all rights therein, are protected by national and international copyright laws. The above represents a summary only. For further information please read Frontiers' Conditions for Website Use and Copyright Statement, and the applicable CC-BY licence.

ISSN 1664-8714
ISBN 978-2-83251-661-4
DOI 10.3389/978-2-83251-661-4

About Frontiers

Frontiers is more than just an open access publisher of scholarly articles: it is a pioneering approach to the world of academia, radically improving the way scholarly research is managed. The grand vision of Frontiers is a world where all people have an equal opportunity to seek, share and generate knowledge. Frontiers provides immediate and permanent online open access to all its publications, but this alone is not enough to realize our grand goals.

Frontiers journal series

The Frontiers journal series is a multi-tier and interdisciplinary set of open-access, online journals, promising a paradigm shift from the current review, selection and dissemination processes in academic publishing. All Frontiers journals are driven by researchers for researchers; therefore, they constitute a service to the scholarly community. At the same time, the *Frontiers journal series* operates on a revolutionary invention, the tiered publishing system, initially addressing specific communities of scholars, and gradually climbing up to broader public understanding, thus serving the interests of the lay society, too.

Dedication to quality

Each Frontiers article is a landmark of the highest quality, thanks to genuinely collaborative interactions between authors and review editors, who include some of the world's best academicians. Research must be certified by peers before entering a stream of knowledge that may eventually reach the public - and shape society; therefore, Frontiers only applies the most rigorous and unbiased reviews. Frontiers revolutionizes research publishing by freely delivering the most outstanding research, evaluated with no bias from both the academic and social point of view. By applying the most advanced information technologies, Frontiers is catapulting scholarly publishing into a new generation.

What are Frontiers Research Topics?

Frontiers Research Topics are very popular trademarks of the *Frontiers journals series*: they are collections of at least ten articles, all centered on a particular subject. With their unique mix of varied contributions from Original Research to Review Articles, Frontiers Research Topics unify the most influential researchers, the latest key findings and historical advances in a hot research area.

Find out more on how to host your own Frontiers Research Topic or contribute to one as an author by contacting the Frontiers editorial office: frontiersin.org/about/contact

Interaction between human activities and geo-environment for sustainable development

Topic editors

Xuanmei Fan — Chengdu University of Technology, China
Xiaoyan Zhao — Southwest Jiaotong University, China
Xiangjun Pei — Chengdu University of Technology, China
Filippo Catani — University of Florence, Italy
Yunhui Zhang — Southwest Jiaotong University, China

Citation

Fan, X., Zhao, X., Pei, X., Catani, F., Zhang, Y., eds. (2023). *Interaction between human activities and geo-environment for sustainable development*. Lausanne: Frontiers Media SA. doi: 10.3389/978-2-83251-661-4

Table of contents

06 Interval Prediction of the Permeability of Granite Bodies in a High-Level Radioactive Waste Disposal Site Using LSTM-RNNs and Probability Distribution
Nisong Pei, Yong Wu, Rui Su, Xueling Li, Zhenghao Wu, Renhai Li and Heng Yin

19 Influence of Inter-Particle Friction and Damping on the Dynamics of Spherical Projectile Impacting Onto a Soil Bed
Weigang Shen, Tao Zhao, Giovanni B. Crosta, Feng Dai and Giuseppe Dattola

30 Pore-Water Pressure Model for Carbonate Fault Materials Based on Cyclic Triaxial Tests
Ling Zhu, Qingwen Yang, Luguang Luo and Shenghua Cui

42 Quantitative Evaluation of Coseismic Deformations Induced by Seismogenic Faulting in Mining Exploration Area During the 2018 Xingwen and 2019 Changning Earthquakes, Sichuan, China
Chunwei Sun, Sixiang Ling, Siyuan Zhao, Hong Wen and Sen Wang

54 Engineering Application of Landslide Susceptibility Mapping in Linear Engineering Optimization
Jinchang Shi

63 Geochemical Characteristics and Quality Appraisal of Groundwater From Huatugou of the Qaidam Basin on the Tibetan Plateau
Shengbin Wang, Zhan Xie, Fenglin Wang, Yuqing Zhang, Wanping Wang, Kui Liu, Zexue Qi, Fengyun Zhao, Guoqiang Zhang and Yong Xiao

76 Investigation on Deformation Mechanism and Treatment Effect of a Scattered Slope Based on Continuum–Discontinuum Element Method and Finite Difference Method
Meiben Gao, Hua Zhang, Shenghua Cui, Zhongteng Wu, Ji Liu, Lixia Feng, Feng Zeng, Ning Li, Fujiang Chen, Tianbin Li and Yan Zhang

87 Preliminary Study on Post-Peak Behavior and Fracture Characteristics of Hard Rock Under True Triaxial Stress
Feng Zeng, Meiben Gao, Fujiang Chen, Yongyi Yang and Yan Zhang

97 Washing Reagents for Remediating Heavy-Metal-Contaminated Soil: A Review
Heng Zhang, Yongxin Xu, Thokozani Kanyerere, Yang-shuang Wang and Minhui Sun

117 Interaction Between Brackish Water Intermittent Infiltration and Cultivated Soil Environment: A Case Study From Arid Piedmont Plain of Northwest China
Guo Leilei and Wang Zaimin

128 Structural Characteristics and Deformation Evolution of an Intra-Continental Fold-Thrust Belt in Eastern Sichuan: Insights Into Analogue Sandbox Models
Yang-Shuang Wang, Mo Xu, Yan-Na Yang, Qiang Xia, Bing Jiang, Chang Yang and Heng Zhang

151 Study on Mechanical Characteristics and Construction Control of the Railway Overlapping Tunnels
Yuan Fengjie, Liu Yang, Xu Qianwei, Zheng Yuanlin, Hu Lisheng, Zhao Ping and Cui Yuebang

162 Fracture Characteristics of Sliding Crack in Brittle Rock: Analysis Based on an Improved Equivalent Crack Model
Yin Zhang, Shenghua Cui, Zhibing Yu and Jianlong Cheng

175 DFT Study on the Compatibility Between Bentonite Clay Mineral and Hydration Products With the Polycarboxylate Water Reducer in the Cement Hydration Process
Huang Teng, Zhihao He, Gao Meiben and Jiaxing Zhang

184 Numerical Simulation of Wind-Driven Rain Based on the Eulerian Model
Hongyu Chen and Bo Zhou

191 Distribution Characteristics and Geogenic Mechanisms of Riverbed Overburden in Southwest China
Zongping Yan, Mo Xu, Xiaobing Kang, Leilei Guo and Shishu Zhang

210 Features and Formation Mechanism of the Jiaopenba Landslide, Southwestern Sichuan Province, China
Tong Shen, Yunsheng Wang, Xun Zhao, Heng Liu, Xuyang Wu, Yapei Chu, Panpan Zhai and Yang Han

228 The effect of seepage flow on movable solid materials research in debris flow experiments
Shun Yang, Meiben Gao, Jiaxua Jiao, Tao She and Kun Chen

239 Lithology-Based 3D Modeling of Urban Geological Attributes and Their Engineering Application: A Case Study of Guang'an City, SW China
Fang Zhou, Minghui Li, Congjun Huang, Hong Liang, Yujie Liu, Jianlong Zhang, Baodi Wang and Ming Hao

250 Combining river replenishment and restrictions on groundwater pumping to achieve groundwater balance in the Juma River Plain, North China Plain
Weizhe Cui, Qichen Hao, Yong Xiao, Yuchen Zhu, Jianfeng Li and Yuanjing Zhang

262 How do Geohazards Affect Household Consumption: Evidence From China
Luman Zhao and Boyi Zhu

271 Time-Varying Effect of Ductile Flexural Toppling Failure on Antidip Layered Rock Slope
Junchao Cai, Da Zheng, Nengpan Ju, Jue Wang, Xin Zhou and Da Li

279 Study on the genetic mechanism of high-temperature geothermal system and its engineering impact in the Woka graben, Tibet
Wen Zhang, Mo Xu and Sen Wu

292 Experimental study of the particle agglomeration on its mechanical properties of collapsible loess
Meng Zhao, Hong-Gang Wu, Wei Guo, Bo-Ren Tan, Cheng Hu, Rui Deng and Li-Yi Chen

305 Numerical investigation of groundwater flow systems and their evolution due to climate change in the arid Golmud river watershed on the Tibetan Plateau
Yong Xiao, Kui Liu, Yuqing Zhang, Hongjie Yang, Shengbin Wang, Zexue Qi, Qichen Hao, Liwei Wang, Yinfei Luo and Shiyang Yin

318 An empirical model for the travel distance prediction of deflection-type rock avalanches in the wenchuan earthquake area
Hailong Yang, Zuan Pei, Zhihao He, Jin Lei and Xiaotian Xia

332 The structure of a magnitude-frequency relation for debris flows conditioned by earthquake shock
Mei Han, Stephen G. Evans, Kun He, Hao Sun and Zhigang Ma

frontiers in Earth Science

ORIGINAL RESEARCH
published: 01 February 2022
doi: 10.3389/feart.2022.835308

Interval Prediction of the Permeability of Granite Bodies in a High-Level Radioactive Waste Disposal Site Using LSTM-RNNs and Probability Distribution

Nisong Pei[1,2], Yong Wu[1], Rui Su[3], Xueling Li[1], Zhenghao Wu[1], Renhai Li[2] and Heng Yin[1,2]*

[1]College of Environment and Civil Engineering, Chengdu University of Technology, Chengdu, China, [2]Sichuan Academy of Safety Science and Technology, Chengdu, China, [3]Beijing Research Institute of Uranium Geology, Beijing, China

During long-term geological tectonic processes, multiple fractures are often developed in the rock mass of high-level radioactive waste disposal sites, which provide channels for release of radioactive material or radionuclides. Studies on the permeability of fractured rock masses are essential for the selection and evaluation of geological disposal sites. With traditional methods, observation and operation of fractured rock mass penetration is time-consuming and costly. However, it is possible to improve the process using new methods. Based on the penetration characteristics of fractured rock mass, and using machine learning techniques, this study has created a prediction model of the fractured rock mass permeability based on select physical and mechanical parameters. Using the correlation coefficients developed by Pearson, Spearman, and Kendall, the proposed framework was first used to analyze the correlation between the physical and mechanical parameters and permeability and determine the model input parameters. Then, a comparison model was created for permeability prediction using four different machine-learning algorithms. The algorithm hyper-parameters are determined by a ten-fold cross-validation. Finally, the permeability interval prediction values are obtained by comparing and selecting the prediction results and probability distribution density function. Overall, the computational results indicate the framework proposed in this paper outperforms the other benchmarking machine learning algorithms through case studies in Beishan District, Gansu, China.

Keywords: high-level waste disposal, fractured rock mass permeability, machine learning, interval prediction, probability distribution

OPEN ACCESS

Edited by:
Yunhui Zhang,
Southwest Jiaotong University, China

Reviewed by:
Yusen He,
Grinnell College, United States
Jiahao Deng,
DePaul University, United States

***Correspondence:**
Yong Wu
ywu@cdut.edu.cn

Specialty section:
This article was submitted to Geohazards and Georisks, a section of the journal Frontiers in Earth Science

Received: *14 December 2021*
Accepted: *05 January 2022*
Published: *01 February 2022*

Citation:
Pei N, Wu Y, Su R, Li X, Wu Z, Li R and Yin H (2022) Interval Prediction of the Permeability of Granite Bodies in a High-Level Radioactive Waste Disposal Site Using LSTM-RNNs and Probability Distribution. Front. Earth Sci. 10:835308. doi: 10.3389/feart.2022.835308

INTRODUCTION

During long-term geological tectonic processes, multiple fractures of variable sizes often develop in high-level radioactive waste disposal site rock masses (Li et al., 2014). The fractured rock mass consists of irregular fractured structures and bedrock, which may be discontinuous, anisotropic, and heterogeneous. High-level radioactive waste often has strong radioactivity, high heat generation, high toxicity, and a long half-life. If the engineering barriers of the repository fail, the radionuclides will migrate via groundwater to human living environments along the cracks in the rock (Chapman and

Hooper, 2012). Generally, the multibarrier principle also ensures that in case of loss of one safety function of barrier, there are another barrier providing safety function. Nevertheless, the water flowing through interconnected fractures are preferential transport pathway for radionuclides. Release of radioactive material or radionuclides will not only cause environmental pollution, but also endanger human health and even cause lasting adverse effects on future generations. Release of radioactive material or radionuclides will not only cause environmental pollution, but also endanger human health and even cause lasting adverse effects on future generations (Zhang et al., 2021a; Zhang et al., 2021b).

Previous study of fractured rock mass permeability was mainly carried out through theoretical analysis and experimental observations (Zhou et al., 2006). Theoretical research has focused on the construction of mathematical models and numerical analyses. The current medium models of a fractured rock mass include three types: equivalent continuum (Hadgu et al., 2017), discontinuous (Ning et al., 2011), and mixed models combining both continuum and discontinuous models (Cao and Lin 2017). The equivalent continuum model ignores the fracture position and hydraulic characteristics calibration; therefore, it is difficult to guarantee calculation accuracy. The discontinuous medium model simulates the real leakage state, and its calculation results are highly reliable, but the calculation requirement is extremely large. The mixed model analyzes the characteristics of the internal rock mass fracture differences and uses different models to simulate the structural plane condition, which can consider the calculation results and the calculation difficulty; however, the discontinuous model is difficult to construct. The fractured rock mass consists of irregular fractured structures and bedrock, which may be discontinuous, anisotropic, and heterogeneous. (Zhang et al., 2018).

In experimental studies, the methods have included the steady-state, non-steady-state, capillary equilibrium, and plate model methods. For example, by using terrestrial laser scanning and ground-penetrating radar measurements, Longoni et al. (2012) described the discontinuities inside the rock mass and analyzed the characteristics of the rock slope fracture network. Based on the linear elastic fracture mechanics (LEFM) method and Perkins-Kern-Nordgren (PKN) models, Yao (2012) predicted the hydraulic fracturing performance of a three-layer water injection well, and then proposed an effective fracture toughness method considering the influence of the fracture process on fractures in ductile rock. Using the steady-state method, Jiang et al. (2014) proposed a parabolic variational inequality to solve the problem of transient free-surface seepage in a fractured network. Using the hydraulic geometric anisotropy coefficient and considering the direction, length, spacing, and hydraulic aperture characteristics of discrete fracture networks, Ren et al. (2015) performed a numerical simulation of the pipe network method for both connecting and directional pipes, and then verified the correlation between the hydraulic geometric anisotropy of the fracture network and the permeability anisotropy. By combining the extended finite element method with the equivalent continuum model, Khoei et al. (2016) established a two-phase fluid flow model in multiscale fractured porous media, and then analyzed the influence of crack direction, capillary pressure function, solid skeleton deformation, and the presence of short cracks on the fluid flow mode. Based on the unsteady flow mechanism in a single fracture and the finite element method, Lai et al. (2017) simulated the intrusion process of tight non-aqueous liquid in sand and mudstone cracks. Using numerical simulation methods combined with the temperature field information near cracks, Patterson et al. (2018) studied the details of convective penetration in a deep vertical fault zone.

TABLE 1 | Parameter selection range in the training process of machine learning algorithms.

Algorithm	Parameter	Notes
ANN	Number of hidden layer neurons	5,10, . . . , 50
	Number of hidden layers	1,2, . . . ,6
SVM	Capacity factor	1, 10, 100, 1,000
	Γ	0.001, 0.01, 0.1, 1
ELM	Number of hidden layer neurons	5, 10, . . . , 80
LSTM-RNN	Forgetting rate	0.1,0.2,0.3,0.4,0.5
	Number of iterations	20,30,40,50,60
	Stacked layers	2,3,4,5,6

All of the aforementioned methods require long-term continuous observation and testing, which need to have good control of the pressure difference measurement, flow control, and waterproof sealing, and are often costly. In addition, the internal rock mass structure is complex, and the observation results will inevitably form blind spots, which could lead to unreliable testing results.

With the rapid development of system mathematics and nonlinear technology, data mining methods are increasingly often used to solve quantitative analysis problems (He et al., 2017; Esteves et al., 2019; Gessulat et al., 2019; Li et al., 2021a). The principle of data mining methods is to use algorithms to analyze data and then learn how to understand the data behavior, to use it to predict new situations. In practice, this method has been widely applied to many different fields and has achieved effective results. For example, Deo (2015) summarized some successful case studies by applying data mining methods to the medical field in recent years. Ouyang et al. (2019) used the deep belief network and copula function to build a forecasting model with a short-term power load, which alleviates the impact of power consumption ramp-up to a certain extent. He and Kusiak (2018) applied a data mining method to build a wind turbine performance evaluation model for wind farms, which can effectively identify turbine failures. Xu et al. (2019) selected seven mainstream machine learning algorithms to construct a loess landslide sliding distance prediction model and extracted the threshold value of the landslide hazard range, which provides a reference for regional division of landslide hazard risk areas.

Compared with traditional methods for analyzing the fractured rock mass permeability, data mining methods have the advantages of simple operation, easy data acquisition (Li et al., 2020; Li et al., 2021b). However, there are currently few related studies, so much research needs to be carried out.

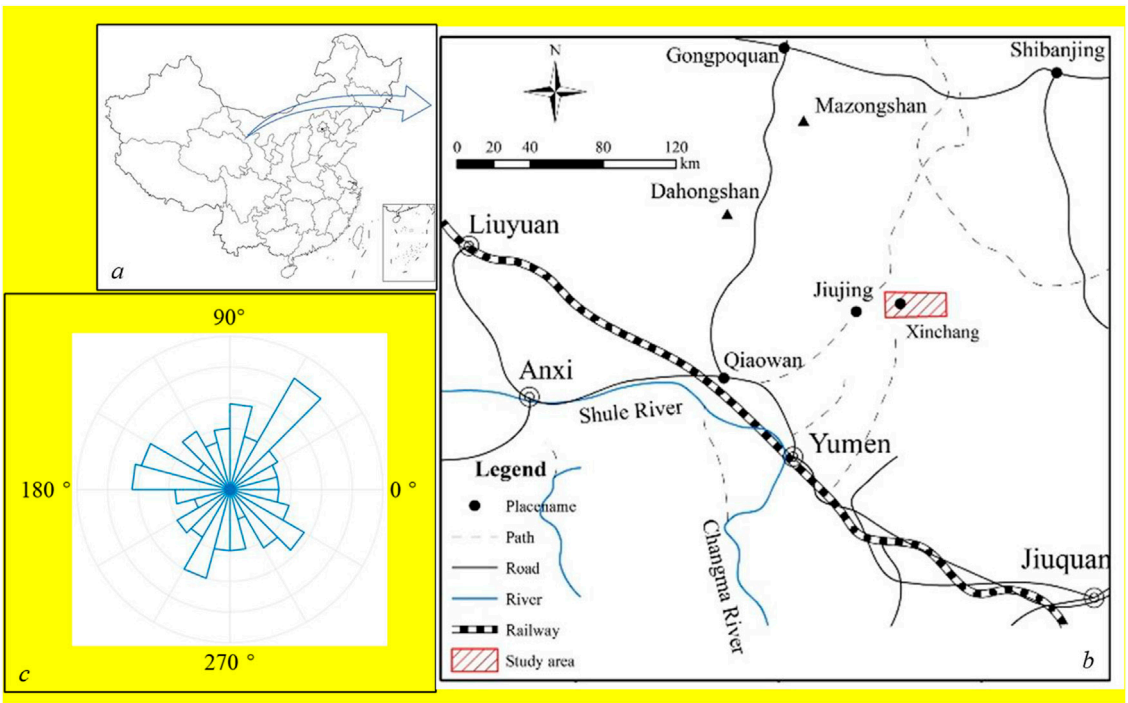


FIGURE 1 | Location map of the case study area. **(A,B)**: Location description of study area; **(C)**: The rose diagram of the joins trend.

In this paper, we proposed a data-driven framework based on LSTM-RNNs and probability distribution for Interval prediction of the permeability of granite bodies in a high-level radioactive waste disposal site. In order to improve prediction performance, the inputs are selected by the correlation analysis. To confirm the reliability of the prediction results of permeability, an interval evaluation is conducted by probability distribution function.

METHODOLOGY

In this paper, an interval prediction framework based on LSTM-RNNs and probability distribution is proposed for the fractured rock mass permeability for a high-level radioactive waste disposal site. First, rock sample data are obtained, including the physical and mechanical parameters, crack geometry, and permeability, which are based on laboratory tests. Then, a data correlation analysis is performed to obtain the correlation coefficient between the permeability and other parameters. In the second step, based on the four mainstream machine learning algorithms of artificial neural network (ANN), support vector machine (SVM), extreme learning machine (ELM), and long short-term memory recurrent neural network (LSTM-RNN), more relevant parameters and other model input parameters are selected; the permeability is used as the output to establish a simulation prediction model. The third step is to compare the mean absolute error (MAE), mean absolute percentage error (MAPE), root mean square error (RMSE) and maximum error rate (MER) returned by the four algorithms and compare and select the method that obtains the best simulation results. The fourth step is to analyze the error returned by the optimal algorithm for the simulation effect, obtain its probability distribution, and finally derive the permeability interval value based on the error distribution threshold.

Correlation Analysis

In this study, three major statistical correlation coefficients were selected for correlation analysis: Pearson, Spearman, and Kendall. All correlation coefficients reflect the variation trends and degrees between the two variables. Their magnitudes fluctuate in the range [−1,1], where 0 means that the two variables are independent of each other, and the closer the value is to ±1, the greater the correlation between the variables. The three correlation coefficient formulas were as follows:

$$\rho_{X,Y} = \frac{cov(X,Y)}{\sigma X \cdot \sigma Y} \tag{1}$$

$$r_s = 1 - \frac{6\sum_{i=1}^{n} d_i^2}{n^3 - n} \tag{2}$$

$$r_k = \frac{2}{n(n-1)} \sum_{i<j} sgn\left(x_i - x_j\right) sgn\left(y_i - y_j\right) \tag{3}$$

where $\rho_{X,Y}$ is the Pearson correlation coefficient; $cov(X,Y)$ is the covariance between variables ; σX is the standard deviation of the variables ; r_s is the Spearman correlation coefficient ; d_i refers to the order difference of the corresponding elements in the variable, namely $d_i = rank(X) - rank(Y)$; n is the number of samples ; r_k



FIGURE 2 | Typical fractured rock mass in the study area.

TABLE 2 | Modeling data.

Rock core no	Original density (g*cm^{-3})	Water content of 24 h saturation test	Mean crack width (mm)	Average roughness height of fracture surface (mm)	Fracture surface density (number/cm^2)	Compressive strength (MPa)	Peak axial strain /mm	Permeability (mD)
BS43-01	2.7105	0.69%	1.2	0.2201	0.0510	96.5014	1.0271	6.7866
BS43-03	2.5759	0.57%	0.6	0.2417	0.1338	39.7098	1.5914	9.8608
BSQ05-01	2.4637	1.10%	0.1	0.2537	0.0764	160.0309	1.1581	1.9145
BSQ05-02	2.4434	0.26%	0.2	0.2195	0.0191	26.5801	0.4441	4.2556
BSQ05-03	2.4592	1.11%	0.1	0.2678	0.0637	91.0825	1.0848	1.2678
BSQ05-04	2.4566	1.19%	0.1	0.2760	0.0701	85.1950	1.0510	2.1221
BSQ05-05	2.3430	1.10%	0.4	0.2489	0.0892	80.0817	1.0712	1.9311
BSQ08-01	2.5291	0.61%	0.1	0.2463	0.0764	98.8289	0.6426	2.6294
BSQ08-02	2.5422	0.74%	0.1	0.2524	0.0510	92.2946	1.0905	2.6300
BSQ08-03	2.4066	2.18%	1.9	0.2316	0.0318	10.3031	0.5780	2.5058
BSQ08-04	2.5193	1.19%	0.6	0.2284	0.0382	79.4756	0.8812	2.3218
BSQ08-05	2.4318	0.87%	0.1	0.1754	0.1019	60.0256	0.6051	2.7468
BSQ08-06	2.4033	0.51%	1.1	0.2468	0.0510	72.3811	0.6227	6.4057
BSQ08-07	2.5092	0.70%	1.2	0.2291	0.0637	42.8420	0.6642	3.6431
BSQ08-08	2.5171	0.66%	0.6	0.2656	0.0382	53.6849	0.5568	2.2796
BSQ11-01	2.4750	0.74%	0.1	0.2502	0.0892	160.0309	1.1581	1.4034
BSQ11-02	2.4738	0.18%	2.8	0.2051	0.0064	26.5801	0.4441	3.5128
BSQ11-03	2.5530	0.96%	0.6	0.2485	0.0064	91.0825	1.0848	3.3306
BSQ11-04	2.5770	1.12%	0.1	0.2731	0.0637	85.1950	1.0510	1.3990
BSQ11-05	2.5506	1.08%	1.3	0.2610	0.0382	80.0817	1.0712	2.0188

is the Kendall correlation coefficient; and $sgn(\cdot)$ is the sign function (see **Eq. 4** for details).

$$sgn(z) = \begin{cases} 1, z > 0 \\ 0, z = 0 \\ -1, z < 0 \end{cases} \tag{4}$$

Prediction Method

Based on the correlation analysis results, the parameters that are more relevant to the permeability are selected as the input to the machine learning algorithm and then used to predict the permeability. In this study, four algorithms, which are widely used in many fields, were selected to build: ANN, SVM, ELM, and LSTM-RNN. The algorithm principle (**Table 1**) and operation steps are as follows:

1) ANN

An ANN is a network composed of several neurons, which can process system information by simulating the structure and operating mechanism of the human brain (Das et al., 2014). This algorithm has strong nonlinear approximation ability and fault tolerance and is often used to deal with regression and clustering problems.

The excitation function of the neural network model for permeability prediction constructed in this study selects the sigmoid equation, which is shown in **Eq. 5**. The model loss function is the mean square error equation, as shown in **Eq. 6**.

$$S = \frac{1}{1 + e^{-t}} \tag{5}$$

$$C(w, b) \equiv \frac{1}{2n} \sum_x ||\bar{y} - y^2|| \tag{6}$$

where y is the real permeability, $\bar{y}$ is the permeability generated by the ANN, and w and b are the weights and biases of the algorithm's hidden layer. In the model training process, the number of hidden layers was set to 1, 2... 6, and the number of neurons was set to 5, 10... 50. The optimal number of hidden layers and the number of neurons in the algorithm were verified using 10-fold cross-validation to determine the best performance.

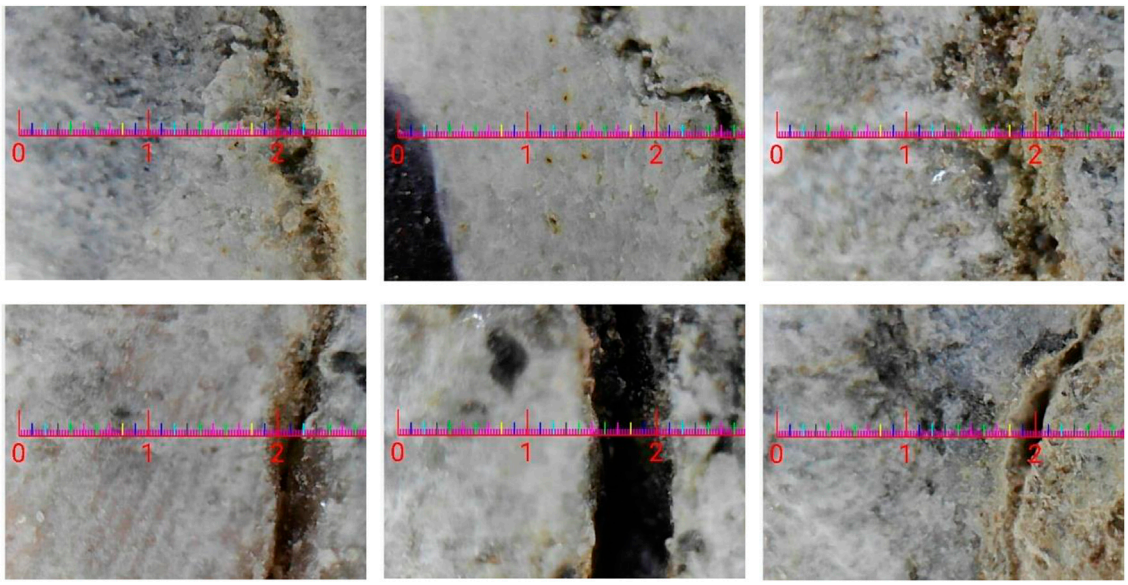


FIGURE 3 | Width measurement map of partial rock samples (units: mm).

TABLE 3 | Correspondence between variable data and symbols.

Variable name	Symbol
Original density	x1
Water content of 24 h Saturation test	x2
Mean crack width	x3
Average rough height of Fracture surface	x4
Fracture surface density	x5
Compressive strength	x6
Peak axial strain	x7
Permeability	y

2) SVM

The purpose of SVM modeling is to find a hyperplane based on the principle of maximum spacing, divide all samples, and simplify the solution to a convex quadratic programming problem. Since the advent of this algorithm (Cortes and Vapnik, 1995), it has shown strong performance in text classification and high-dimensional data processing, which makes it the most widely used machine learning algorithm in many fields (Abdi and Giveki, 2013; Ouyang et al., 2017; Ouyang et al., 2018). The kernel function of the SVM selects the Gaussian radial basis equation:

$$K\left(X, X'\right) = \exp\left(\frac{||-X-X'||}{2\sigma^2}\right) \tag{7}$$

where X is the input data vector, and σ is the standard deviation of the input data. During model training, the algorithm capacity coefficient C is set to 1, 10, 100, and 1,000, and the parameter $\gamma = \frac{1}{2\sigma^2}$ is set to 0.001,001, 0.1, and 1, and then the optimal parameter combination is determined by 10-fold cross-validation. The model loss function is the mean square error **Eq.6**.

3) ELM

ELM is a type of single hidden layer feedforward neural network (SLFN). During model training, the algorithm can eliminate the iterative optimization of the input layer weights to the hidden layer and only randomly assign values (Huang et al., 2004; Huang et al., 2006). Therefore, the algorithm has the advantages of a simple mathematical model, fast learning speed, strong generalization ability, and global optimal solutions. At present, the algorithm has been widely used in many fields and has achieved good application results (Li et al., 2018). The solving function of ELM is expressed as follows:

$$f(X) = \sum_1^L \beta_l G(a, b, X) \tag{8}$$

where L is the number of hidden layers of the extreme training machine, a and b are hidden layer node parameters , β_l is the hidden layer outer weight parameter, and G(·) is the algorithm excitation function, as shown in **Eq. 8**. During ELM training, only the number of neurons in the hidden layer must be determined. This parameter was set to 5,10, . . . ,80, and the optimal parameter was determined by 10-fold cross-validation. The model loss function is the mean square error **Eq. 6**.

4) LSTM-RNN

LSTM-RNN is a time recursive algorithm based on a recurrent neural network (RNN). Through an in-depth understanding of the

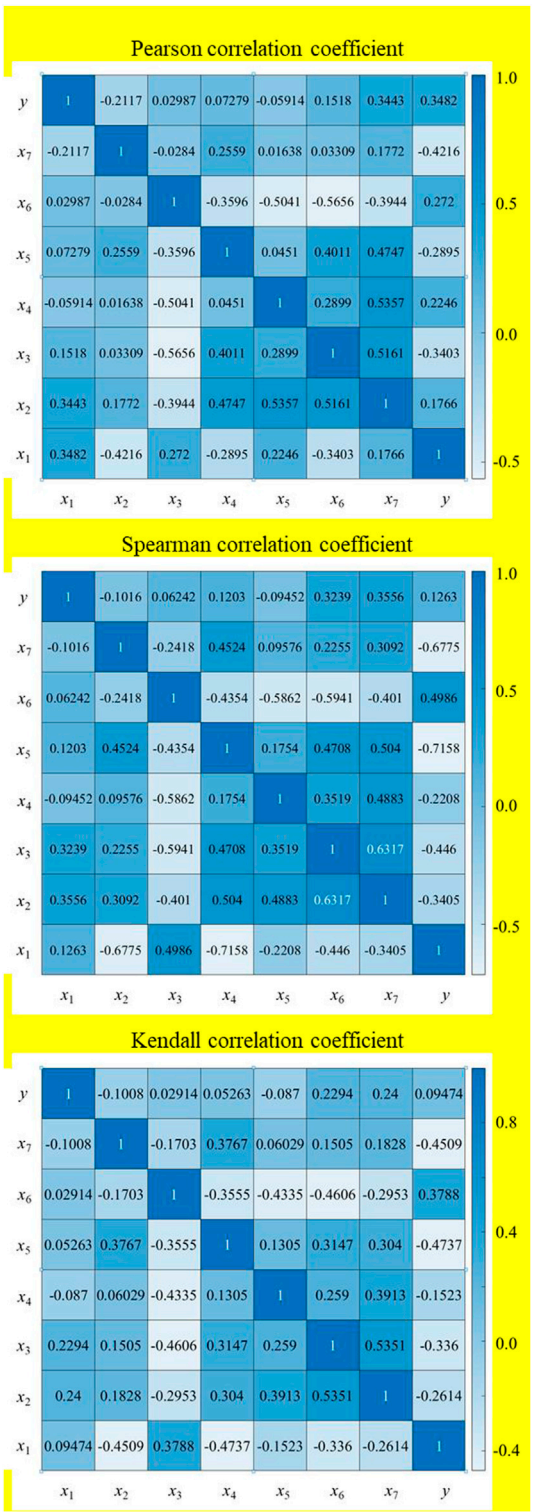


FIGURE 4 | Correlation coefficient results.

global characteristics of the data, it provides the algorithm with more powerful generalization capabilities than other models. Compared with RNN, this algorithm adds a structure of information availability

TABLE 4 | Combination of input and output parameters.

Group	Input parameters	Target parameters
Group 1	x1, x2, x3, x4, x5, x6, x7	Y
Group 2	x2, x3, x4, x5, x6, x7	Y
Group 3	x1, x2, x3, x4, x6, x7	y
Group 4	x2, x3, x4, x6, x7	y

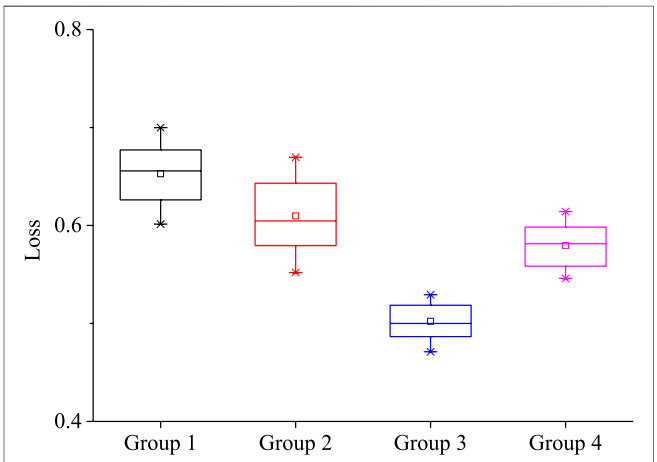


FIGURE 5 | Fitting performance of different input parameters.

judgment in the training process: the LSTM network (Hochreiter and Schmidhuber, 1997), which consists of input, forgetting, and output gates. When the information flow enters the algorithm network, the redundant information that does not meet the algorithm rules is placed in the forget gate and removed (Li et al., 2021c). In practice, the LSTM-RNN algorithm can be expressed by **Eqs 9–13** (Irie et al., 2018):

$$i_t = \sigma(W_{xi}x_t + W_{hi}h_{t-1} + W_{ci}c_{t-1} + b_i) \quad (9)$$

$$f_t = s\left(W_{xf}x_t + W_{hf}h_{t-1} + W_{cf}c_{t-1} + b_f\right) \quad (10)$$

$$c_t = f_t c_{t-1} + i_t \tanh(W_{xc}x_t + W_{hc}h_{t-1} + b_c) \quad (11)$$

$$o_t = s(W_{xo}x_t + W_{ho}h_{t-1} + W_{co}c_{t-1} + b_o) \quad (12)$$

$$\bar{y}_t = o_t \tanh(c_t) \quad (13)$$

where Wxi, Whi, Wci, Wxf, Whf, Wcf, Wxc, Whc, Wxo, Who, and Wco are the weight parameters of the algorithm excitation function; i_t, f_t, c_t, and o_t are the input gates, forgetting gates, and information judgment status, respectively; and s(·) is the sigmoid excitation function. In the algorithm training process, the forgetting rate parameter was set to 0.1, 0.2, 0.3, 0.4, and 0.5; the number of iterations parameter was set to 20, 30, 40, 50, 60; and the number of stacking layers was set to 2, 3, 4, 5, and 6. The optimal parameter combination was determined by 10-fold cross-validation. The model loss function is the mean square error **Eq. 6**.

Error Evaluation Function

To quantitatively evaluate the simulation of the permeability by the selected machine learning algorithm, it is important to

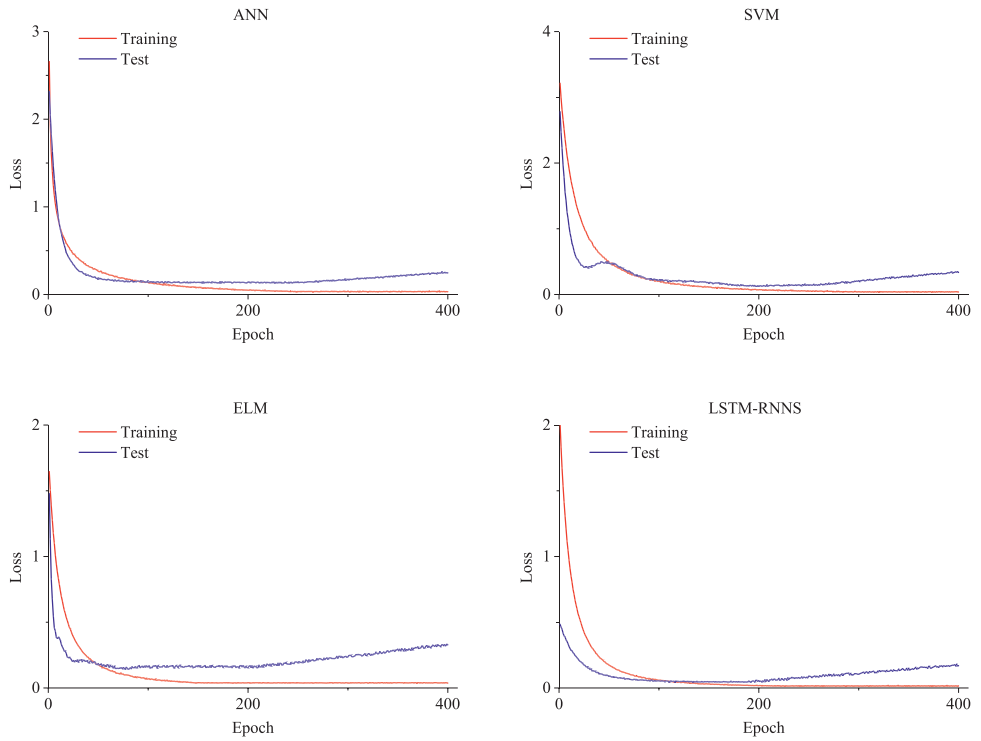


FIGURE 6 | Calculation results of four algorithm loss curves.

TABLE 5 | Evaluation of the calculation effect of the selected algorithm.

Algorithm	MAE	MAPE (%)	RMSE	MER (%)
ANN	0.3337	11.79	0.3986	28.19
SVM	0.2962	12.64	0.3718	39.82
ELM	0.3511	14.30	0.4427	34.36
LSTM-RNNs	0.1695	6.70	0.2102	13.37

analyze the model to predict its performance. Four evaluation functions were chosen in this study: MAE (mean absolute error), MAPE (mean absolute percentage error), RMSE (root mean square error), and MER (max error rate). The evaluation function equations are as follows:

$$MAE = \frac{1}{n}\sum_{t=1}^{n}\left|\bar{y}_t - y_t\right| \tag{14}$$

$$MAPE = \frac{1}{n}\sum_{t=1}^{n}\left|\frac{\bar{y}_t - y_t}{y_t}\right| \tag{15}$$

$$RMSE = \sqrt{\frac{1}{n}\sum_{t=1}^{n}\left(\bar{y}_t - y_t\right)^2} \tag{16}$$

$$MER = \frac{\max\left(\bar{y}_t - y_t\right)}{y_{MER}} \tag{17}$$

where y_t is the real permeability data, $\bar{y}_t$ is the calculated permeability data, and y_{MER} is the real permeability data where the maximum error occurs.

By analyzing the four evaluation function equations, MAE can reflect the actual deviation between the real permeability and the calculated value, which can evaluate the dispersion of the algorithm error. MAPE reflects the ratio between the real data and the calculated value, which can evaluate the percentage accuracy of the algorithm, because of the square term. RMSE is more sensitive to large algorithm errors than other evaluations functions. Finally, MER reflects the maximum error ratio, which can be used to evaluate the ability of the algorithm to control the maximum error. It can be seen that the four types of evaluation indicators can evaluate the overall algorithm performance.

Interval Prediction of Permeability

To make the calculated results of permeability prediction more reliable, this study introduces the concept of interval prediction. Interval prediction can reflect the inherent prediction uncertainty and has a high fault-tolerance rate **Table 1**. The interval prediction in this study is divided into the following three steps.

1) Obtain the absolute value of the true error returned by the optimal algorithm based on the prediction results of the machine learning algorithm.
2) Determine the most suitable probability distribution function type for the error dataset using probability analysis methods.
3) Obtain prediction intervals with different reliabilities based on the point prediction results and probability density function.

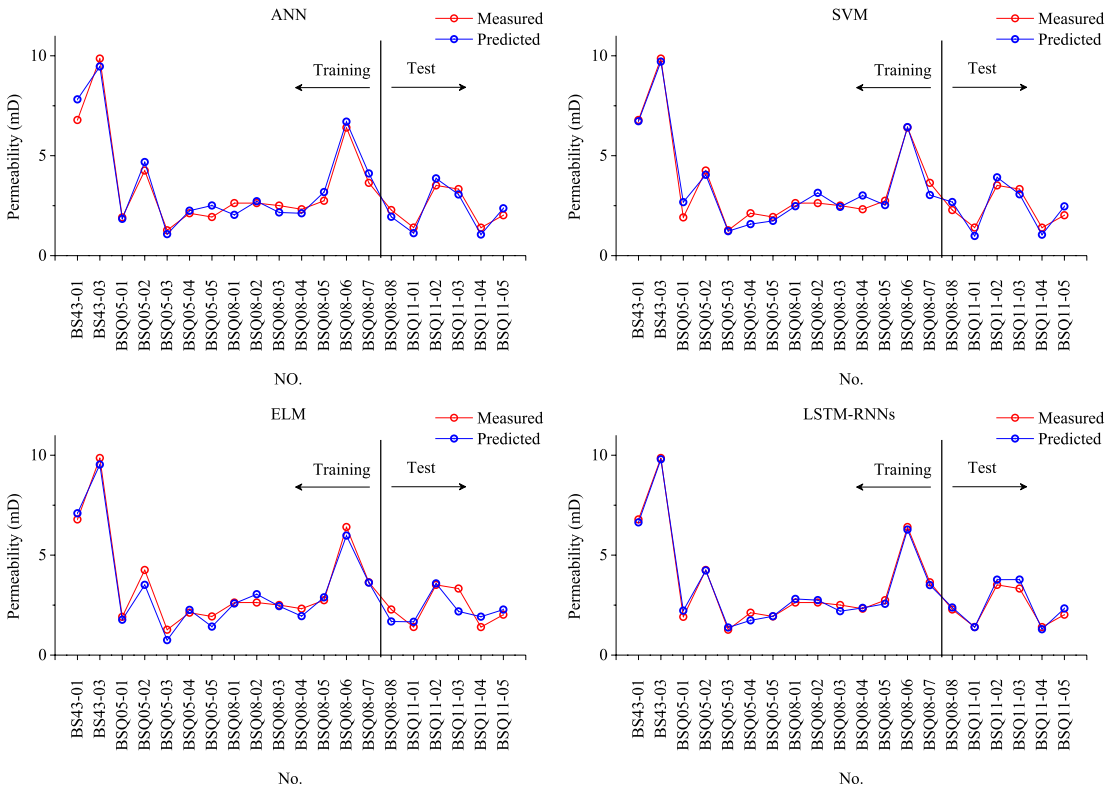


FIGURE 7 | Summary of calculation results of the four algorithms.

Because the permeability error data set is a vector, the process of determining its probability distribution function can be simplified to a fitting problem, in which the data set is substituted into different probability distribution functions, the log likelihood estimation test is used to quantitatively evaluate the fitting effect, and then the fitting function is obtained. In this study, four classical parameter distribution functions were selected: gamma (**Eq. 18**), lognormal (**Eq. 19**), exponential (**Eq. 20**), and Weibull (**Eq. 21**). Their equations are as follows:

$$f(\mathrm{x}) = \frac{(x/\theta)^{\alpha} e^{-x/\theta}}{x\tau(\alpha)} \tag{18}$$

$$f(\mathrm{x}) = \frac{1}{x\sigma\sqrt{2\pi}} \exp\left(-z^2/2\right) \tag{19}$$

$$f(\mathrm{x}) = \frac{e^{-x/\theta}}{\theta} \tag{20}$$

$$f(\mathrm{x}) = \frac{\tau(x/\theta)^{\tau} e^{-(x/\theta^{\tau})}}{x} \tag{21}$$

where α and θ are the fitting parameters of the gamma distribution, z and σ are the fitting parameters of the lognormal distribution, θ is the fitting parameter of the exponential distribution, and τ and θ are the fitting parameters of the Weibull distribution. Selecting the reliability p to obtain the prediction result of the permeability interval, the equation is as follows:

$$\bar{y} \in \left[\mathrm{y} - VaR_P(y), \mathrm{y} + VaR_P(y)\right] \tag{22}$$

$$VaR_P(X) = F_X^{-1}(p) \tag{23}$$

where $F_X^{-1}(p)$ is the inverse of the cumulative distribution function (CDF) of the probability distribution function and VaR is the threshold corresponding to the distribution function.

DATA COLLECTION

The rock sample was from an actual radioactive waste disposal site in Beishan District, Gansu Province (**Figures 1A,B**), with no perennial rivers on the surface of the study area, no permanent surface water, and all surface waters formed by seasonal valley flows following intermittent floods. The study area is located in the middle section of the Liuyuan–Tiancang fold belt in the northern Tianshan–Yinshan zonal structural system, which belongs to the Erdaojing–Xiananluzi–Jiusidun north fault fold belt (**Figure 2**). The chemical composition of major dissolved components of the groundwater in the area is mainly composed of Na-Cl·SO_4, and the groundwater is divided into three main types: bedrock fissure water, basin pore-fissure water, and valley depression fissure-pore water. The lithology of the strata in the area is mainly magmatic rock, mostly granite, which is dominated by medium-fine grained granodiorite, medium-fine grained monzonitic granite, and biotite diorite, all the rockmass are

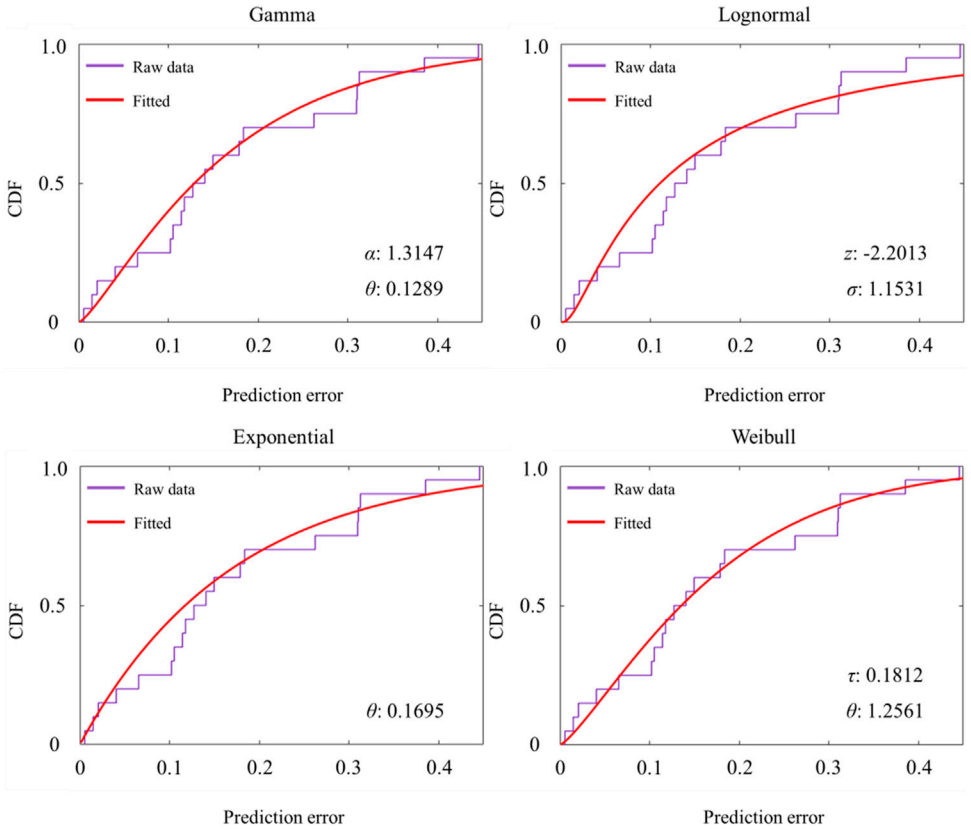


FIGURE 8 | Fitting result of forecast error probability distribution.

TABLE 6 | Fitting effect evaluation.

Distribution	Log likelihood	Fitting mean	Fitting variance
Gamma	15.9286	0.1695	0.0218
Lognormal	13.2983	0.2151	0.1286
Exponential	15.5004	0.1695	0.0287
Weibull	16.1979	0.1686	0.0182

TABLE 7 | Threshold calculation result.

p-value	VaR
0.90	0.2426
0.95	0.3520
0.99	0.4340

joint developed (**Figure 3**). As illustrated in **Figure 1C**, the trend of joints in the study area is mostly northeast to southwest.

Through on-site sampling, three-dimensional laser scanning, and indoor physical and mechanical tests, the modeling data were obtained, including the original density of the rock sample, average fracture width, average fracture surface roughness height, fracture surface density (the number of cracks per unit area), water content of 24 h saturation test, compressive strength, peak axial strain, and rock sample permeability (**Table 2**). Additionally, the sample is a standard cylinder with a bottom circle diameter of 50 mm and a height of 100 mm.

COMPUTATIONAL RESULTS

Correlation Analysis Results

To determine the internal correlation between the case data, it is necessary to obtain the optimal input parameters of the simulation model. First, we performed a correlation analysis on the selected data. To facilitate the description, the variable data were assigned mathematical symbols, and the corresponding relationship is shown in **Table 3**.

Then, the following parameters were calculated separately: permeability (y), original density (x1), water content of a 24 h water tent saturation test (x2), mean crack width (x3), average rough height of fracture surface (x4), fracture surface density (x5), Pearson correlation coefficient between compressive strength (x6) and peak axial strain (x7), Spearman correlation coefficient, and Kendall correlation coefficient. Among them, the correlation coefficient between permeability and other parameters is used to evaluate the correlation closeness, and the correlation coefficient between other parameters (excluding permeability data) is to

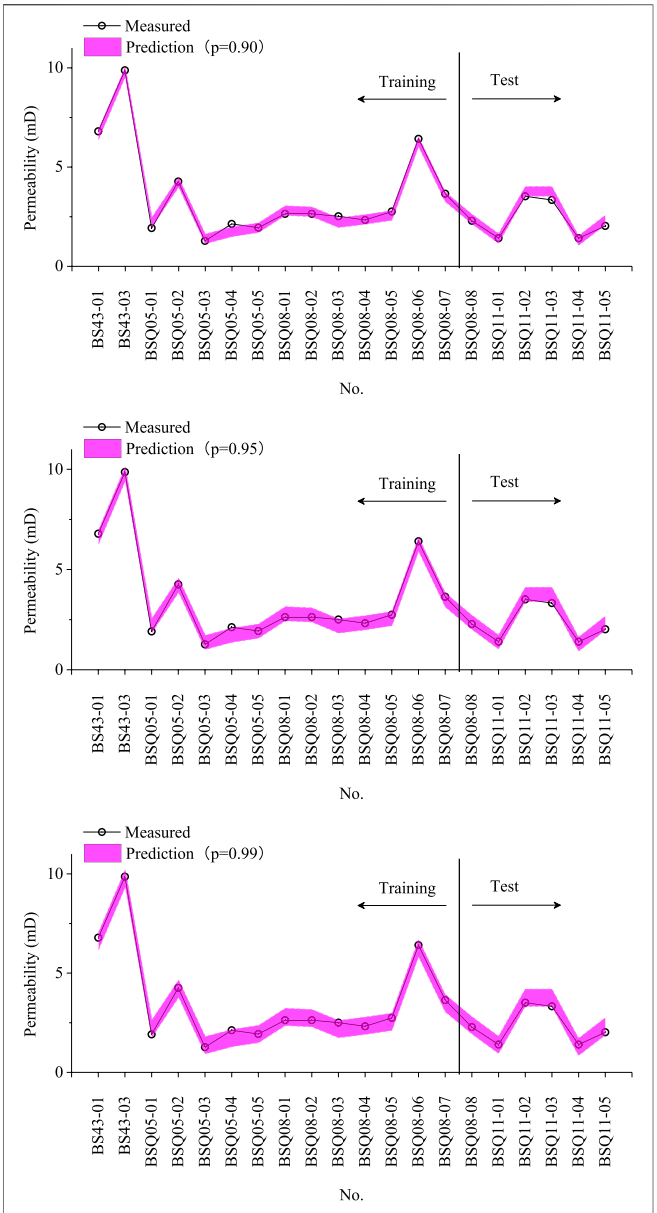


FIGURE 9 | Simulation results of permeability interval prediction.

eliminate redundant input to simplify the calculation. The results are presented in **Figure 4**.

It can be seen from **Figure 4** that the permeability has the strongest correlation with the water content of the 24 h saturation test, with correlation coefficients of -0.4216, −0.6775, and −0.4509, respectively, which shows the weakest correlation with the original density and the fracture surface density, with correlation coefficients between permeability and original density of 0.3482, 0.1263, and 0.0947, respectively. The ratios of the correlation coefficients between the permeability and fracture surface density were 0.2246, −0.22208, and −0.1523, respectively. Four sets of input parameters were selected to construct the permeability simulation model to reflect the influence of the input parameters scientifically and quantitatively on the simulation results. The parameter combination details are presented in **Table 4**.

Prediction Results

Before building the simulation model, a simple neural network was used to test the fitting performance of the four combinations. The hidden layer of this simple neural network was set to two layers, with twenty neurons in each layer. The obtained data were divided into a training set and a test set according to the ratio of 70 and 30%, and then simulation experiments were conducted on the four combinations, respectively, finally obtaining the loss value when the different combinations converged. To clearly compare the algorithm fitment under different input conditions, this study grouped the loss values once the operation stabilized, and then drew a box diagram, as shown in **Figure 5**.

Figure 5 shows the returned loss value when the algorithm is stable under different combinations. Among them, the loss value obtained by Group 1 was (0.6001, 0.6969), Group 2 was (0.5534, 0.6697), Group 3 was (0.4705, 0.5282), and Group 4 was (0.5479, 0.6149). The loss value obtained in Group 2 had the largest fluctuation range, up to 0.1166. The loss value obtained in Group 1 was the largest, as its fitting was the worst, while the obtained value in Group 3 was the smallest, and the fluctuation range is also the smallest, only 0.0585. Thus, when Group 3 was used as the input, the fitting effect was the best.

Subsequently, using Group 3 as the input, four methods were selected, including ANN, SVM, ELM, and LSTM-RNN, to construct a simulation model for permeability prediction. In the calculation, the hyper-parameters of all algorithms were adjusted and optimized by cross-validation. Therefore, the relevant connections in the dataset were better investigated. In the training process, the training data set was used to establish the connection between the input and target parameters, and then the test data were used to verify the connection. **Figure 6** shows the computational performance of the four algorithms.

It can be seen from **Figure 6** that during training, the algorithm loss decreases as the number of iterations increases. When the number of iterations reached 220, the loss of the ANN algorithm began to converge; for SVM, it was 200 times, for ELM, it was 150 times, and for LSTM-RNN, it was approximately 140 times. Observing the test process, the number of convergence iterations of the four algorithms was less than that of the training process. However, as the number of iterations increased, the training process loss tended to increase slightly. The analysis shows that there was an over-fitting situation at this time. To prevent errors caused by overfitting, this study chose the number of iterations corresponding to the smallest loss value during the test as the final model. That is, when the number of ANN iterations was 256, the loss value of 0.1334 was the smallest. When the number of SVM iterations was 221, its loss reached a minimum of 0.1276. For ELM, when the number of iterations was 191, the loss value was 0.1537. The results are similar for LSTM-RNNs; when the number of iterations was

158, the loss value was only 0.0453. **Table 5** summarizes the evaluation indicators of all the algorithm test sets, and **Figure 7** shows the final calculation results.

According to **Table 5**, based on the calculated data, the MAE value obtained by the LSTM-RNN algorithm was only 0.1695, which is smaller than the 0.3337, 0.2962, and 0.3511 for ANN, SVM, and ELM. The MAPE values of the four algorithms were 11.79, 12.64, 14.30, and 6.70%, respectively; the RMSE values were 0.3986, 0.3718, 0.4427, and 0.2102, respectively; and the MER values were 28.19, 39.82, 34.36, and 13.37%, respectively. Thus, the simulation effect of the LSTM-RNN algorithm was the best, and its MAE, MAPE, and RMSE values were only half of those of the other algorithms. Most importantly, the LSTM-RNN algorithm was only 13.37% in the indicator of the largest error in the evaluation of the MER. This means that the difference between the simulated data and real data did not exceed 15%, which reflects the powerful stability and generalizability of the algorithm.

Interval Prediction Results

Based on the comparison calculation, the permeability simulation result was obtained based on the LSTM-RNN algorithm, and the calculation error was also obtained. To make the simulation results more reliable, this study introduced the concept of interval prediction, which increases the fault tolerance of the calculation results. To ensure the generalizability of the interval prediction model, this study first calculated the model training data error, analyzed the probability distribution type of the error generated during the training process, and then extracted the tail thresholds corresponding to different *p*-values. Finally, the prediction interval was obtained based on this threshold.

First, it was assumed that the error data in the training phase was normally distributed, and the K-S test was performed (Alexandrowicz and Gula, 2020); however, the calculation result negated this assumption. Subsequently, this study selected four types of widely used non-normal distribution functions to perform the fitting: gamma, lognormal, exponential, and Weibull distributions. The calculation results are shown in **Figure 8**. Log likelihood (Staude, 2001) was selected as the evaluation index of the fitting situation, which shows that the larger the value, the better the fitting effect. The evaluation results are presented in **Table 6**.

Figure 8 shows the fitting results of the four probability density functions. Combining **Eqs 18–21**, the fitting parameters of the gamma, lognormal, exponential, and Weibull distributions were 1.3147 and 0.1289, −2.113 and 1.1531, 0.1695, and 0.1812 and 1.2561, respectively. The four probability distribution functions had the best fitting effect under a combination of the above parameters.

Table 6 shows the fitting conditions of the four probability density functions, and the evaluation indicators log likelihood were 15.9286, 13.2983, 15.5004, and 16.1979, respectively. By comparison, it was found that the evaluation index of the Weibull distribution was greater than that of the other three probability density functions, so it can be concluded that the prediction error of permeability is most consistent with the Weibull distribution.

Subsequently, based on the Weibull distribution probability density function and **Eq. 23**, the VaR values at *p*-values of 0.90, 0.95, and 0.99 were obtained. The calculation results are presented in **Table 7**. Finally, the interval simulation results of permeability were obtained based on the simulation results and thresholds of the LSTM-RNNs. The calculation results are shown in **Figure 9**.

It can be seen from **Figure 9** that, regardless of the interval simulation under the threshold value, the reliability of the calculation result is better than that of the point value simulation, which gives the algorithm a stronger reliability. When the *p*-value was 0.90, the interval value was the smallest. As the value of *p* increased, the simulation interval increased. In summary, when *p* is 0.90, there are still five points that do not fall within the interval; when *p* is 0.95, only two points are outside the interval; when *p* is 0.99, all points fall into the interval, and the reliability reaches up to 100% at this time.

CONCLUSION

Considering the low-permeability granite body in the study area as the disposal site for high-level radioactive waste, this study focuses on the simulation method of its permeability. To improve the efficiency of permeability acquisition, this study proposed a model structure based on comparing and selecting different machine learning methods, which is different from traditional methods. This method simplifies the acquisition of basic data, optimizes the permeability data calculation steps, and strengthens the reliability of the permeability calculation results. Based on case studies, the main conclusions of this paper are as follows.

1) Based on the correlation analysis, it can be seen that the granite permeability in the case site has the strongest correlation with the water content of the 24 h saturation test, but the weakest correlation with the original density and fracture surface density. Based on this knowledge and machine learning pre-calculation, the input parameters of the permeability simulation model were selected as the original density, saturated water 24 h water content, average crack width, average roughness height of fracture surfaces, compressive strength, and peak axial strain.
2) Based on the ten-fold cross-validation, the computing power of the four machine learning algorithms was optimized, and the respective final calculation results were obtained. The comparison shows that the LSTM-RNN algorithm has the best computational performance, followed by SVM, and then ANN, while ELM has the worst computational performance. Finally, the calculation results of the LSTM-RNN were chosen to perform the interval prediction.
3) Based on the training error of LSTM-RNNs, the probability density function is fitted, and the Weibull distribution fitting effect is concluded to be the best. Therefore, thresholds with p-values of 0.90, 0.95, and 0.99, and the corresponding prediction intervals were obtained. Compared with point value prediction, interval prediction is more reliable.

DATA AVAILABILITY STATEMENT

The original contributions presented in the study are included in the article/Supplementary Material, further inquiries can be directed to the corresponding author.

AUTHOR CONTRIBUTIONS

NP conceptualized the study, contributed to the study methodology, and wrote the original draft. YW contributed to the study methodology, data curation and investigation. RS and XL contributed to data analysis and investigation. NP and ZW contributed to software and formal analysis. RL and HY contributed to investigation and writing-original draft. All authors have read and agreed to the published version of the manuscript.

FUNDING

This research is supported by the key program of Sichuan Province (2018JY0425; 2018SZ0290).

REFERENCES

Abdi, M. J., and Giveki, D. (2013). Automatic Detection of Erythemato-Squamous Diseases Using PSO-SVM Based on Association Rules. *Eng. Appl. Artif. Intell.* 26 (1), 603–608. doi:10.1016/j.engappai.2012.01.017

Alexandrowicz, R. W., and Gula, B. (2020). Comparing Eight Parameter Estimation Methods for the Ratcliff Diffusion Model Using Free Software. *Front. Psychol.* 11, 484737. doi:10.3389/fpsyg.2020.484737

Cao, R.-h., and Lin, H. (2017). Experimental and Numerical Study of Failure Behavior and Energy Mechanics of Rock-like Materials Containing Multiple Joints. *Adv. Mater. Sci. Eng.* 2017, 1–17. doi:10.1155/2017/6460150

Chapman, N., and Hooper, A. (2012). The Disposal of Radioactive Wastes Underground. *Proc. Geologists' Assoc.* 123 (1), 46–63. doi:10.1016/j.pgeola.2011.10.001

Cortes, C., and Vapnik, V. (1995). Support-vector Networks. *Mach Learn.* 20 (3), 273–297. doi:10.1007/bf00994018

Das, G., Pattnaik, P. K., and Padhy, S. K. (2014). Artificial Neural Network Trained by Particle Swarm Optimization for Non-linear Channel Equalization. *Expert Syst. Appl.* 41 (7), 3491–3496. doi:10.1016/j.eswa.2013.10.053

Deo, R. C. (2015). Machine Learning in Medicine. *Circulation* 132 (20), 1920–1930. doi:10.1161/circulationaha.115.001593

Esteves, J. T., de Souza Rolim, G., and Ferraudo, A. S. (2019). Rainfall Prediction Methodology with Binary Multilayer Perceptron Neural Networks. *Clim. Dyn.* 52 (3-4), 2319–2331. doi:10.1007/s00382-018-4252-x

Gessulat, S., Schmidt, T., Zolg, D. P., Samaras, P., Schnatbaum, K., Zerweck, J., et al. (2019). Prosit: Proteome-wide Prediction of Peptide Tandem Mass Spectra by Deep Learning. *Nat. Methods* 16 (6), 509–518. doi:10.1038/s41592-019-0426-7

Hadgu, T., Karra, S., Kalinina, E., Makedonska, N., Hyman, J. D., Klise, K., et al. (2017). A Comparative Study of Discrete Fracture Network and Equivalent Continuum Models for Simulating Flow and Transport in the Far Field of a Hypothetical Nuclear Waste Repository in Crystalline Host Rock. *J. Hydrol.* 553, 59–70. doi:10.1016/j.jhydrol.2017.07.046

He, Y., and Kusiak, A. (2018). Performance Assessment of Wind Turbines: Data-Derived Quantitative Metrics. *IEEE Trans. Sustain. Energ.* 9 (1), 65–73. doi:10.1109/tste.2017.2715061

He, Y., Kusiak, A., Ouyang, T., and Teng, W. (2017). Data-driven Modeling of Truck Engine Exhaust Valve Failures: A Case Study. *J. Mech. Sci. Technol.* 31 (6), 2747–2757. doi:10.1007/s12206-017-0518-1

Hochreiter, S., and Schmidhuber, J. (1997). Long Short-Term Memory. *Neural Comput.* 9 (8), 1735–1780. doi:10.1162/neco.1997.9.8.1735

Huang, G. B., Zhu, Q. Y., and Siew, C. K. (2004). Extreme Learning Machine: a New Learning Scheme of Feedforward Neural Networks. *Neural Networks* 2, 985–990. doi:10.1109/IJCNN.2004.1380068

Huang, G. B., Zhu, Q. Y., and Siew, C. K. (2006). Extreme Learning Machine: Theory and Applications. *Neurocomputing* 70 (1-3), 489–501. doi:10.1016/j.neucom.2005.12.126

Irie, K., Lei, Z., Schlüter, R., and Ney, H. (2018). "Prediction of LSTM-RNN Full Context States as a Subtask for N-Gram Feedforward Language Models," in 2018 IEEE International Conference on Acoustics, Speech and Signal Processing (ICASSP), Calgary, AB, April 15–20, 2018 (IEEE), 6104–6108.

Jiang, Q., Ye, Z., and Zhou, C. (2014). A Numerical Procedure for Transient Free Surface Seepage through Fracture Networks. *J. Hydrol.* 519, 881–891. doi:10.1016/j.jhydrol.2014.07.066

Khoei, A. R., Hosseini, N., and Mohammadnejad, T. (2016). Numerical Modeling of Two-phase Fluid Flow in Deformable Fractured Porous media Using the Extended Finite Element Method and an Equivalent Continuum Model. *Adv. Water Resour.* 94, 510–528. doi:10.1016/j.advwatres.2016.02.017

Lai, J., Wang, G., Fan, Z., Chen, J., Qin, Z., Xiao, C., et al. (2017). Three-dimensional Quantitative Fracture Analysis of Tight Gas Sandstones Using Industrial Computed Tomography. *Sci. Rep.* 7 (1), 1825. doi:10.1038/s41598-017-01996-7

Li, B., Wong, R. C. K., and Milnes, T. (2014). Anisotropy in Capillary Invasion and Fluid Flow through Induced sandstone and Shale Fractures. *Int. J. Rock Mech. Mining Sci.* 65, 129–140. doi:10.1016/j.ijrmms.2013.10.004

Li, H., Xu, Q., He, Y., and Deng, J. (2018). Prediction of Landslide Displacement with an Ensemble-Based Extreme Learning Machine and Copula Models. *Landslides* 15 (10), 2047–2059. doi:10.1007/s10346-018-1020-2

Li, H., Xu, Q., He, Y., Fan, X., and Li, S. (2020). Modeling and Predicting Reservoir Landslide Displacement with Deep Belief Network and EWMA Control Charts: a Case Study in Three Gorges Reservoir. *Landslides* 17 (3), 693–707. doi:10.1007/s10346-019-01312-6

Li, H., Deng, J., Feng, P., Pu, C., Arachchige, D. D. K., and Cheng, Q. (2021a). Short-Term Nacelle Orientation Forecasting Using Bilinear Transformation and ICEEMDAN Framework. *Front. Energ. Res.* 9, 780928. doi:10.3389/fenrg.2021.780928

Li, H., Deng, J., Yuan, S., Feng, P., and Arachchige, D. D. K. (2021b). Monitoring and Identifying Wind Turbine Generator Bearing Faults Using Deep Belief Network and EWMA Control Charts. *Front. Energ. Res.* 9, 799039. doi:10.3389/fenrg.2021.799039

Li, H., Xu, Q., He, Y., Fan, X., Yang, H., and Li, S. (2021c). Temporal Detection of Sharp Landslide Deformation with Ensemble-Based LSTM-RNNs and Hurst Exponent. *Geomatics, Nat. Hazards Risk* 12 (1), 3089–3113. doi:10.1080/19475705.2021.1994474

Longoni, L., Arosio, D., Scaioni, M., Papini, M., Zanzi, L., Roncella, R., et al. (2012). Surface and Subsurface Non-invasive Investigations to Improve the Characterization of a Fractured Rock Mass. *J. Geophys. Eng.* 9 (5), 461–472. doi:10.1088/1742-2132/9/5/461

Ning, Y., Yang, J., An, X., and Ma, G. (2011). Modelling Rock Fracturing and Blast-Induced Rock Mass Failure via Advanced Discretisation within the Discontinuous Deformation Analysis Framework. *Comput. Geotechn.* 38 (1), 40–49. doi:10.1016/j.compgeo.2010.09.003

Ouyang, T., Kusiak, A., and He, Y. (2017). Predictive Model of Yaw Error in a Wind Turbine. *Energy* 123, 119–130. doi:10.1016/j.energy.2017.01.150

Ouyang, T., He, Y., and Huang, H. (2018). Monitoring Wind Turbines' Unhealthy Status: a Data-Driven Approach. *IEEE Trans. Emerging Top. Comput. Intell.* 3 (2), 163–172. doi:10.1109/TETCI.2018.2872036

Ouyang, T., He, Y., Li, H., Sun, Z., and Baek, S. (2019). Modeling and Forecasting Short-Term Power Load with Copula Model and Deep Belief Network. *IEEE Trans. Emerg. Top. Comput. Intell.* 3 (2), 127–136. doi:10.1109/tetci.2018.2880511

Patterson, J. W., Driesner, T., Matthai, S., and Tomlinson, R. (2018). Heat and Fluid Transport Induced by Convective Fluid Circulation within a Fracture or Fault. *J. Geophys. Res. Solid Earth* 123 (4), 2658–2673. doi:10.1002/2017jb015363

Ren, F., Ma, G., Fu, G., and Zhang, K. (2015). Investigation of the Permeability Anisotropy of 2d Fractured Rock Masses. *Eng. Geol.* 196, 171–182. doi:10.1016/j.enggeo.2015.07.021

Staude, G. H. (2001). Precise Onset Detection of Human Motor Responses Using a Whitening Filter and the Log-Likelihood-Ratio Test. *IEEE Trans. Biomed. Eng.* 48 (11), 1292–1305. doi:10.1109/10.959325

Xu, Q., Li, H., He, Y., Liu, F., and Peng, D. (2019). Comparison of Data-Driven Models of Loess Landslide Runout Distance Estimation. *Bull. Eng. Geol. Environ.* 78 (2), 1281–1294. doi:10.1007/s10064-017-1176-3

Yao, Y. (2012). Linear Elastic and Cohesive Fracture Analysis to Model Hydraulic Fracture in Brittle and Ductile Rocks. *Rock Mech. Rock Eng.* 45 (3), 375–387. doi:10.1007/s00603-011-0211-0

Zhang, Y., Xu, M., Li, X., Qi, J., Zhang, Q., Guo, J., et al. (2018). Hydrochemical Characteristics and Multivariate Statistical Analysis of Natural Water System: A Case Study in Kangding County, Southwestern China. *Water* 10 (1), 80. doi:10.3390/w10010080

Zhang, Y., Dai, Y., Wang, Y., HuangXiao, X. Y., Xiao, Y., and Pei, Q. (2021a). Hydrochemistry, Quality and Potential Health Risk Appraisal of Nitrate Enriched Groundwater in the Nanchong Area, Southwestern China. *Sci. Total Environ.* 784, 147186. doi:10.1016/j.scitotenv.2021.147186

Zhang, Y., He, Z., Tian, H., Huang, X., Zhang, Z., Liu, Y., et al. (2021b). Hydrochemistry Appraisal, Quality Assessment and Health Risk Evaluation of Shallow Groundwater in the Mianyang Area of Sichuan Basin, Southwestern China. *Environ. Earth Sci.* 80 (17), 576. doi:10.1007/s12665-021-09894-y

Zhou, Q., Salve, R., Liu, H. H., Wang, J. S., and Hudson, D. (2006). Analysis of a Mesoscale Infiltration and Water Seepage Test in Unsaturated Fractured Rock: Spatial Variabilities and Discrete Fracture Patterns. *J. Contam. Hydrol.* 87 (1-2), 96–122. doi:10.1016/j.jconhyd.2006.05.001

Conflict of Interest: The authors declare that the research was conducted in the absence of any commercial or financial relationships that could be construed as a potential conflict of interest.

Publisher's Note: All claims expressed in this article are solely those of the authors and do not necessarily represent those of their affiliated organizations, or those of the publisher, the editors, and the reviewers. Any product that may be evaluated in this article, or claim that may be made by its manufacturer, is not guaranteed or endorsed by the publisher.

Copyright © 2022 Pei, Wu, Su, Li, Wu, Li and Yin. This is an open-access article distributed under the terms of the Creative Commons Attribution License (CC BY). The use, distribution or reproduction in other forums is permitted, provided the original author(s) and the copyright owner(s) are credited and that the original publication in this journal is cited, in accordance with accepted academic practice. No use, distribution or reproduction is permitted which does not comply with these terms.

frontiers in Earth Science

ORIGINAL RESEARCH
published: 09 March 2022
doi: 10.3389/feart.2022.835271

Influence of Inter-Particle Friction and Damping on the Dynamics of Spherical Projectile Impacting Onto a Soil Bed

Weigang Shen[1,2], *Tao Zhao*[3]*, *Giovanni B. Crosta*[4], *Feng Dai*[2] *and Giuseppe Dattola*[4]

[1]*Faculty of Geosciences and Environmental Engineering, Southwest Jiaotong University, Chengdu, China,* [2]*State Key Laboratory of Hydraulics and Mountain River Engineering, College of Water Resource and Hydropower, Sichuan University, Chengdu, China,* [3]*Department of Civil and Environmental Engineering, Brunel University London, London, United Kingdom,* [4]*Department of Earth and Environmental Sciences, Università degli Studi di Milano Bicocca, Milan, Italy*

This study investigates the dynamics of a spherical projectile impact onto a granular bed via numerical simulations by discrete element method (DEM). The granular bed is modeled as an assembly of polydisperse spherical particles and the projectile is represented by a rigid sphere. The DEM model is used to investigate the cratering process, including the dynamics of the projectile and energy transformation and dissipation. The cratering process is illustrated by tracking the motion of the projectile and granular particles in the bed. The numerical results show that the dynamics of the projectile follows the generalized Poncelet law that the final penetration depth is a power-law function of the falling height. The numerical results can match well the experimental data reported in the literature, demonstrating the reliability of the DEM model in analyzing the impact of a spherical projectile on a granular bed. Further analyses illustrate that the impact process consists of three main stages, namely the impact, penetration and collapse, as characterized by the evolution of projective velocity, strong force chains and crater shape. The initial kinetic and potential energy of the projectile is dissipated mainly by inter-particle friction which governs the projectile dynamics. The stopping time of projectile decreases as the initial impact velocity increases. The final penetration depth scales as one-third the power of total falling height and is inversely proportional to the macroscopic granular friction coefficient.

Keywords: discrete element method, projectile impact, granular bed, catering, particle friction

OPEN ACCESS

Edited by:
Filippo Catani,
University of Florence, Italy

Reviewed by:
Meng Zhao,
Chengdu University, China
Ge Gao,
McGill University, Canada

****Correspondence:***
Tao Zhao
tao.zhao@brunel.ac.uk

Specialty section:
This article was submitted to Geohazards and Georisks, a section of the journal Frontiers in Earth Science

Received: *14 December 2021*
Accepted: *18 January 2022*
Published: *09 March 2022*

Citation:
Shen W, Zhao T, Crosta GB, Dai F and Dattola G (2022) Influence of Inter-Particle Friction and Damping on the Dynamics of Spherical Projectile Impacting Onto a Soil Bed. Front. Earth Sci. 10:835271. doi: 10.3389/feart.2022.835271

INTRODUCTION

The impact of projectiles on granular media are widespread phenomena in nature, such as asteroids colliding onto planetary surfaces (Senft and Stewart, 2009), raindrops falling into soil (Marston et al., 2010), people walking on sand beaches (Uehara et al., 2003) and rockfalls impacting onto soil buffering layers (Wang and Cavers, 2008; Calvetti and di Prisco, 2012; Su et al., 2018; Shen et al., 2019). The related research contributes to a better understanding of the formation of impact craters and the design of efficient shock absorbers. Though it has been studied via experiments, numerical simulations and analytical theories (Newhall and Durian, 2003; Wada et al., 2006; Crassous et al., 2007; Katsuragi and Durian, 2007; Clark et al., 2015; Li et al., 2016; Ye et al., 2016; Horabik et al., 2018; Ye et al., 2018; Zhang et al., 2021) in the past several decades, the understanding of impact

process is still limited owing to the complexities of such events (Wada et al., 2006; Tiwari et al., 2014; Horabik et al., 2018).

The dynamic interaction between projectiles and granular media is complex because it depends on the kinematics of the projectile (e.g. size, density, velocity and shape) and the mechanical properties of the granular media (e.g. bulk density, inter-particle friction, inter-particle damping and particle size). A part of these factors have been systematically analyzed by a series of experimental tests (Newhall and Durian, 2003; Uehara et al., 2003; Katsuragi and Durian, 2013). The focus of these tests is on the ejection process, the crater morphology and the penetration dynamics, aiming to find a scaling law for crater size and penetration depth. For a spherical projectile impacting onto granular media, it is well established that the crater diameter scales with the power of 1/4 the kinetic energy of the projectile and the final penetration depth scales with the power of 1/3 the falling height (Uehara et al., 2003). The observed deceleration of the impacting sphere can be interpreted by the generalized Poncelet force law (Uehara et al., 2003). The stopping time of a spherical projectile has also been studied in different experiments (Ciamarra et al., 2004; Katsuragi and Durian, 2007). It was found to be a decreasing function of the impact velocity with an asymptotic plateau at high impact velocities. Newhall and Durian (2003) investigated the effect of projectile shape on the penetration of a projectile into a granular layer. Their results indicate that for low velocity impacts, the projectile shape plays a crucial role such that the sharper/elongated objects can penetrate more deeply. Recently, with the help of photo-elastic particles and high speed camera, the microscopic inter-particle force networks in the granular media have been clearly identified by Clark et al. (2012). Based on the obtained results of force networks, the propagation and topology of the force networks were investigated (Clark et al., 2015; Takahashi et al., 2018). However, researchers are still far from a comprehensive understanding of the cratering mechanisms and the mechanical responses of the granular media (Wada et al., 2006; Tiwari et al., 2014), because it is difficult to control some physical parameters without changing other crucial parameters during the experiments. In particular, the influence of inter-particle friction and damping on the dynamics of projectile has not been investigated (Clark et al., 2015).

The aforementioned micro- and macro-mechanical responses of granular media can also be addressed by the discrete element method (DEM) (Cundall and Strack, 1979), especially for their loose and discontinuous natures (Wada et al., 2006; Li et al., 2016; Shen et al., 2018). With careful calibrations, the DEM modeling allows researchers to quantitatively analyze some physical processes that are nearly impossible to obtain in experiments (Utili et al., 2015; Zhang et al., 2015; Gao G. and Meguid M., 2018; Gao G. and Meguid M. A., 2018; Shen et al., 2021a), e.g. force wave propagation, energy evolution. In addition, the DEM allows a parametric analysis on one factor without altering other factors (Seguin et al., 2009). In the literature, both two- and three-dimensional (i.e., 2D and 3D) DEM models have been employed to study the projectile impacts on granular media (Tanaka et al., 2002; Ciamarra et al., 2004; Wada et al., 2006; Seguin et al., 2009; Kondic et al., 2012; Tiwari et al., 2014; Li et al., 2016; Horabik et al., 2018). Bourrier et al. (2010) and Zhang et al. (2017) investigated the impact-induced force chain evolution and its relation to the global mechanical response of granular media by 2D DEM. Wada et al. (2006) and Li et al. (2016) investigated the impact cratering processes of granular materials by 3D DEM models, reproducing the total mass and the velocity distribution of the impact-induced ejecta. The above studies show that the DEM is an effective and efficient method to investigate the impact of projectiles onto granular media. It is worth to note that the inter-particle friction and damping can be changed easily but not change the geometrical and mechanical properties of granular particles by using DEM.

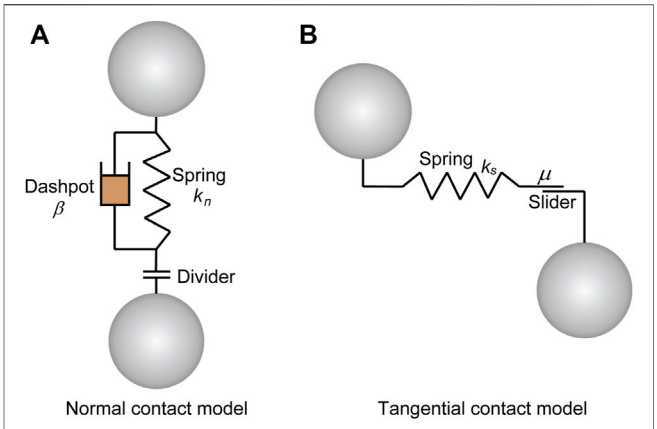


FIGURE 1 | The DEM contact model between two contacting particles. **(A)** Normal contact model, **(B)** Tangential contact model.

The present study employs a 3D DEM model to investigate the dynamics of projectile impact onto granular media, with detailed parametric analyses of inter-particle friction and material damping. The paper is organized as follows: **Section 2** presents a brief introduction of the DEM theory and the numerical model configurations. **Section 3** summarizes the numerical results and discusses the dynamics of projectile and the energy transformation and dissipation during the impact process. Finally, conclusions on the projectile impact process are provided in **Section 4**.

METHODOLOGY AND NUMERICAL MODEL CONFIGURATIONS

Discrete Element Method Theory

The open-source DEM code ESyS-Particle (Wang and Mora, 2009; Weatherley et al., 2014) is employed to run all simulations presented herein. This code has been widely employed to study the mechanical behavior of soil and rock (Utili et al., 2015; Zhao

et al., 2017; Shen et al., 2018; Zhao et al., 2018; Shen et al., 2021b; Gao and Meguid, 2021). In DEM, the granular material is mimicked as an assembly of closely packed rigid spherical particles. The translational and rotational motions of each particle are governed by the Newton's second law of motion as expressed in **Eqs 1, 2**.

$$\boldsymbol{F_i} = m_i \frac{d^2}{dt^2}\boldsymbol{r_i} \tag{1}$$

$$\boldsymbol{T_i} = I_i \frac{d\boldsymbol{\omega_i}}{dt} \tag{2}$$

where $\boldsymbol{F_i}$ is the resultant force acting on particle i; $\boldsymbol{r_i}$ is the position of its centroid; m_i is the particle mass; $\boldsymbol{T_i}$ is the resultant moment acting on the particle; $\boldsymbol{\omega_i}$ is the angular velocity and I_i is the moment of inertia.

In DEM, the inter-particle interactions are computed by the cohesionless frictional model. This employs a linear elastic-spring model to calculate the normal and tangential contact forces (**Figure 1**). In order to replicate the energy dissipation by particle asperities being sheared off and the plastic deformations at contacts, a linear viscous damping model (dashpot model) is employed in the normal direction. Thus, the normal contact force (F_n) is calculated as,

$$F_\mathbf{n} = k_\mathbf{n} u_\mathbf{n} + F_\mathbf{n}^\mathbf{d} \tag{3}$$

where u_n is the overlapping length between two particles in the normal contact direction; k_n is the normal contact stiffness and F_n^d is the normal damping force. The stiffness of particle normal contact is defined as $k_\mathrm{n} = \pi E(R_\mathrm{A} + R_\mathrm{B})/4$ with E being the Young's modulus of particles, R_A and R_B being the radii of the two contacting particles, respectively.

The damping force (F_n^d) is calculated as

$$F_\mathbf{n}^\mathbf{d} = -2\beta\sqrt{0.5(m_\mathrm{A} + m_\mathrm{B})k_\mathbf{n}}v_\mathbf{n} \tag{4}$$

where β is the damping ratio; m_A and m_B are the mass of the two contacting particles, and v_n is the relative velocity between the particles in the normal direction.

The shear force at the current time step (F_s^n) is calculated incrementally as,

$$F_s^n = F_s^{n-1} + (\Delta F_{s1} + \Delta F_{s2}) \tag{5}$$

where F_s^{n-1} is the shear force at the previous iteration time step. ΔF_{s1} is calculated as $\triangle u_s k_s$ with k_s being the shear contact stiffness and $\triangle u_s$ being the incremental shear displacement. The shear stiffness is calculated as $k_s = \pi E(R_A + R_B)/(8(1+\upsilon))$ with υ being the particle Poisson's ratio. ΔF_{s2} is the shear force related to the rotation of particle contact plane. A detailed description of these two shear force terms can be found in Wang and Mora (2009).

The magnitude of the shear force is limited by the Coulomb's friction law as,

$$|F_\mathbf{s}| \le \mu |F_\mathbf{n}| \tag{6}$$

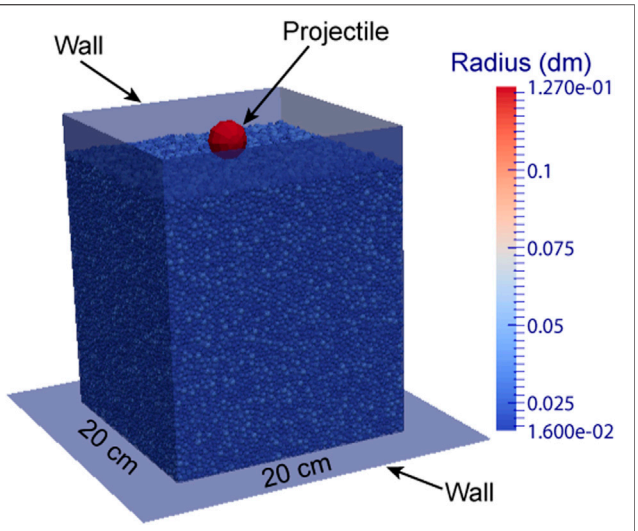


FIGURE 2 | Numerical model configurations. Particles are colored on the basis of their radii.

where μ is the friction coefficient of particle.

The shear induced moment is computed as:

$$M = F_s \boldsymbol{r_i} \tag{7}$$

Numerical Model Configurations

The numerical model configuration of a projectile colliding onto a granular bed is shown in **Figure 2**. The projectile is modeled as a rigid sphere of diameter (D) 2.54 cm. The granular bed is represented by an assembly of rigid spherical particles with radius uniformly ranging from 1.6 to 3.0 mm. It is prepared by randomly generating a loose packing of spherical particles in a cubic container space confined by rigid boundary walls. These particles are then released to settle downward under gravity until the kinetic energy of the system becomes nil. The acceleration due to gravity (g) is equal to 9.81 m/s^2. After the gravitational deposition, the granular bed has dimensions of 22.1 cm in thickness (T), 20.0 cm in length (L) and width (W). The solid volume fraction is 0.58 and the bulk density (ρ_g) is 1.54 g/cm^3. Consequently, it can be calculated T/D = 8.7, L/D = 7.9 and W/D = 7.9. According to Seguin et al. (2008), the influence of model size on granular penetration can be neglected if $T/D > 2.6$, $L/D > 5.0$ and $W/D > 5.0$. Hence, the boundary conditions employed in the present study are acceptable.

The input parameters of the DEM model are listed in **Table 1**. The material properties of the projectile and particles in the granular bed are chosen according to the well-documented experimental data reported in Katsuragi and Durian (Katsuragi and Durian, 2007; Katsuragi and Durian, 2013). For the granular particles, the inter-particle friction coefficient (μ) is obtained by measuring the material angle of repose (θ_r) in the DEM to match approximately that of glass beads commonly used in experiments (≈22°). For the projectile, the

TABLE 1 | Input parameters used in the DEM simulations.

DEM parameter	Value	DEM parameter	Value
Bed particle radius (mm)	1.6–3.0	Poisson's ratio of projectile, υ_p	0.25
Projectile diameter, D (cm)	2.54	Damping ratio of bed particles, β_b	0.01
Bed particle density, ρ_b (kg/m^3)	2,650	Damping ratio of projectile, β_p	0.0
Projectile density, ρ_p (kg/m^3)	8,070	Friction coefficient of bed particle, μ_b	0.6
Young's modulus of bed particles, E_b (Pa)	1×10^9	Friction coefficient of projectile, μ_p	0.6
Young's modulus of projectile, E_p (Pa)	1×10^9	Gravitational acceleration, g (m/s^2)	9.81
Poisson's ratio of bed particles, υ_b	0.25	Time step size, Δt (s)	1×10^{-6}

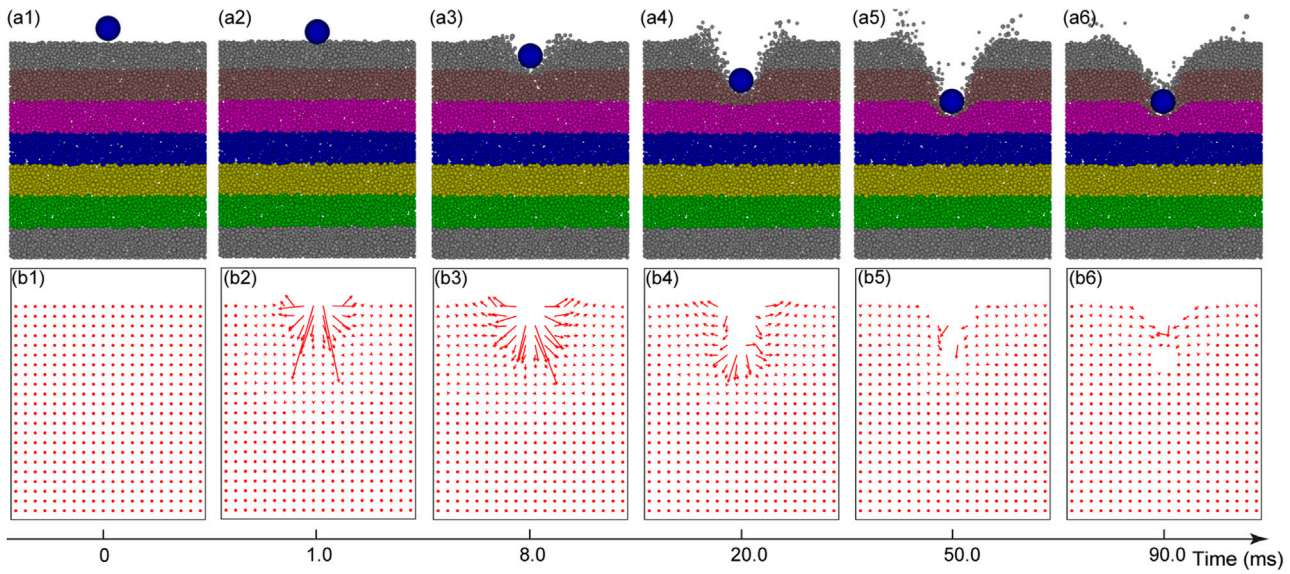


FIGURE 3 | Snapshots of a projectile colliding into a granular bed from t = 0–90 ms (v_0 = 5.0 m/s). The series **(a1–a6)** are snapshots of a 1 cm thick vertical slice of the model through the axisymmetric center of the granular bed. The series **(b1–b6)** are the corresponding velocity fields. The length of the arrow is scaled by the velocity magnitude. The velocities smaller than 0.01 m/s are plotted as dots.

Young's modulus and friction angle are set the same as those of the bed particles. The density of the projectile is set the same as that of a steel ball. During simulations, the projectile is positioned in the middle and just above the granular bed with an initial downward velocity (v_0). Each simulation lasts around 20 h on a standard desktop computer (Intel® Core™ i7 CPU, 4.00 GHz × 8, and 16 GB RAM).

RESULTS

The DEM model has been employed to investigate the dynamic response of the projectile and granular bed during the impact process. A series of simulations are computed under conditions of various initial impact velocities (v_0). The obtained numerical results are compared with the well-documented experimental and numerical data reported in the literature (Uehara et al., 2003; Katsuragi and Durian, 2007; Tiwari et al., 2014), in terms of the formation of crater, the dynamics of projectile, the penetration depth and the stopping time of projectile. In addition, the energy transformation and dissipation during the impact are analyzed quantitatively.

Formation of Crater

Figure 3 illustrates the dynamic cratering process of the projectile colliding on and penetrating into the granular bed for test with v_0 = 5.0 m/s. For visualization purpose, the granular bed has been divided into seven equal-sized sub-layers with distinct colors at t = 0 (**Figure 3**). To plot the velocity field, the bed has been divided into 20 × 21 equal-sized grid cells along a vertical plane and then the average velocity of all the particles in each grid cell can be obtained. From **Figure 3**, it can be observed that after t = 0, the projectile gradually penetrates the granular bed. The granular particles around the projectile are significantly disturbed. In the meantime, the deformation of granular bed is still small, and no obvious crater can be observed. As the simulation continues, particles beneath the projectile move downward and the side particles move laterally, forming a bowl-shaped crater. After a few milliseconds, the projectile enters the granular bed completely (**Figure 3**). Meanwhile, the particles above the projectile continually move laterally and the diameter of the crater increases gradually (**Figure 3**). After the projectile penetrates into the granular bed, the top and lateral particles are still in dynamic motion with relatively small velocities (**Figure 3**). At

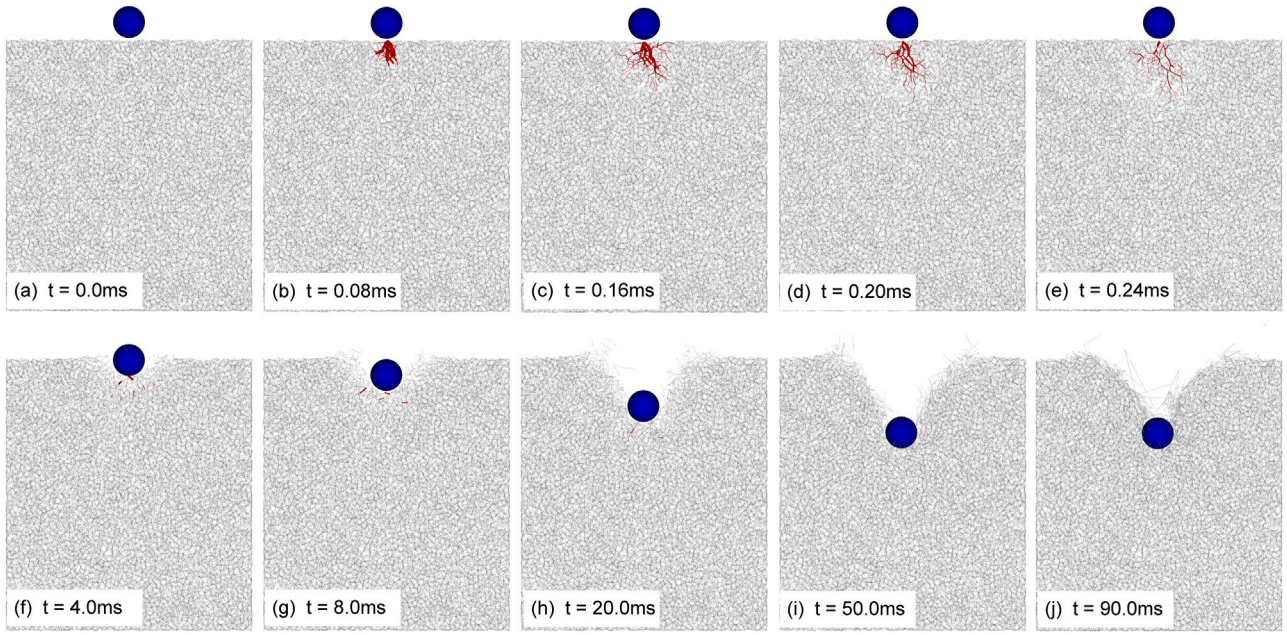


FIGURE 4 | Evolutions of contact force chains during the impact process (v_0 = 5.0 m/s). The thickness of force chains is proportional to the force magnitude, and red if force is larger than 0.6 N, otherwise gray. Note that the threshold value (0.6 N) is the largest contact force at t = 0.0 s. **(A)** t = 0.0 ms, **(B)** t = 0.08 ms, **(C)** t = 0.16 ms, **(D)** t = 0.20 ms, **(E)** t = 0.24 ms, **(F)** t = 4.0 ms, **(G)** t = 8.0 ms, **(H)** t = 20.0 ms, **(I)** t = 50.0 ms. **(J)** t = 90.0 ms.

50 ms, the projectile stops moving, and an instantaneous deep crater is formed (**Figure 3**). Then, this transient crater begins to collapse. The collapsed particles gradually bury the projectile, forming a final stable crater (**Figure 3**). The numerical observations of the cratering process reveal three distinct stages: impact, penetration and side collapse. The impact stage is featured by the initial collision of a projectile onto the granular medium with very small bed deformation (e.g., **Figure 3**). The penetration stage is characterized by the rapid downward movement of the projectile in the granular media and the gradual expansion of the crater size (e.g., **Figures 3a3–a5**). The collapse stage involves the toppling of the transient crater and the formation of a final stable crater (e.g. **Figures 3a6, b6**). These observations agree with some well-documented experimental and numerical results reported in the literature (Ciamarra et al., 2004; Wada et al., 2006; Li et al., 2016).

The corresponding compressive force wave propagation within the impacted granular bed can be represented by the evolution of force chains, as shown in **Figure 4**. Here, the force chain is defined as a network of straight lines connecting the centers of contacting particles. The thickness of these lines is proportional to the magnitude of normal contact force. According to Bourrier et al. (2008), the propagation of force chains within an assembly of granular materials can be used to analyze the propagation of compressive stress waves. From **Figure 4**, it can be observed that before impact, the force chains are uniformly distributed within the granular bed, as determined by the gravity force (**Figure 4A**). At impact, large contact forces occur immediately beneath the projectile and small contact forces distribute in the propagation front (**Figure 4B**), indicating the propagation of compressive wave. Over time, a clear and intact force chain network is formed in the granular bed (**Figure 4C**). After a certain time, the force chains stop propagating and begin to destruct (**Figures 4D, E**). As the projectile penetrates into the granular bed, the force chain beneath the projectile is almost totally broken, but a small number of force chains still exist at the bottom edge of the projectile (**Figures 4F–H**). During the collapse stage, the large contact force chains (red lines) totally disappear (**Figures 4I, J**).

Projectile Dynamics

Figures 5A, B show the evolution of velocity (v) and penetration depth (y) of the projectile during the cratering process, respectively, for simulations of different initial velocities. The positive directions of the position and velocity are defined vertically down. Once the projectile impacts on the granular bed, the velocity firstly exhibits a rapid decrease and then slows down gradually to zero. According to Tiwari et al. (2014), the rapid decrease of the projectile velocity is due to the formation of strong force chain network in the granular bed. During the impact, the projectile must overcome the resistant force exerted by the bed materials (i.e. the force chain network), resulting in the rapid decrease of its velocity. In general, the time at which the projectile stops moving is defined as the stopping time (t_s). The stopping time decreases with the initial impact velocity. An impact at a high velocity exhibits a short stopping time. This phenomenon has also been observed by some experimental and numerical studies (Katsuragi and Durian, 2007; Seguin et al., 2009). For the evolution of projectile penetration depth (**Figure 5B**), it increases gradually to the final penetration

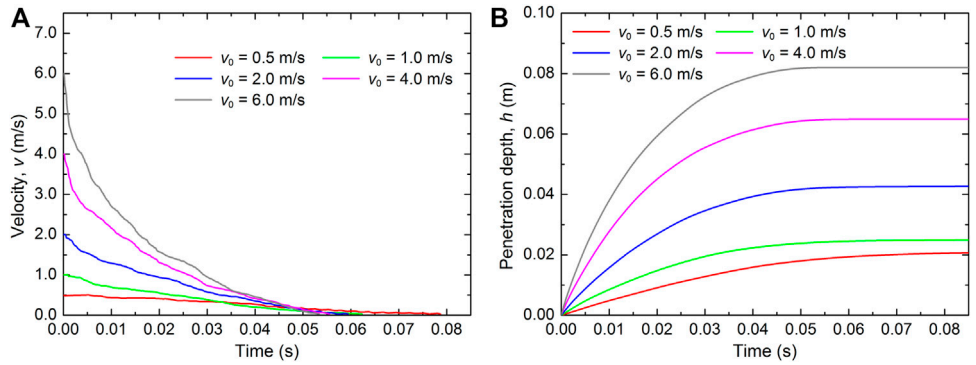


FIGURE 5 | Evolutions of the **(A)** velocity (v) and **(B)** penetration depth (h) of projectiles for the numerical tests with different impact velocities. $y = 0$ corresponds to the position at which the projectile just contacts with the granular bed.

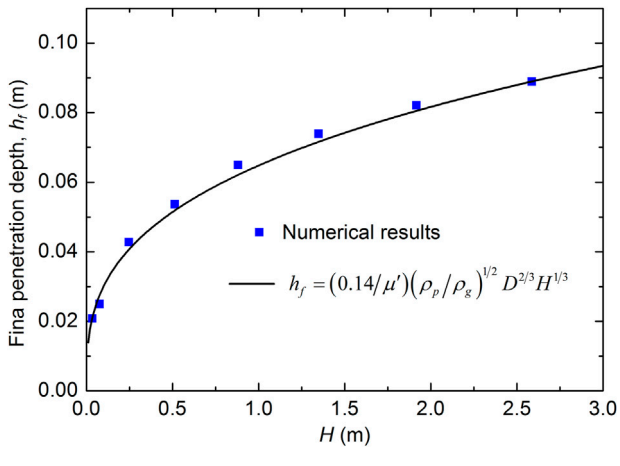


FIGURE 6 | Relationship between the final penetration depth (h_f) and the total falling height ($H = h_f + v_0^2/2g$). The black line corresponds to the empirical equation obtained by Uehara et al. (3) in their experimental studies.

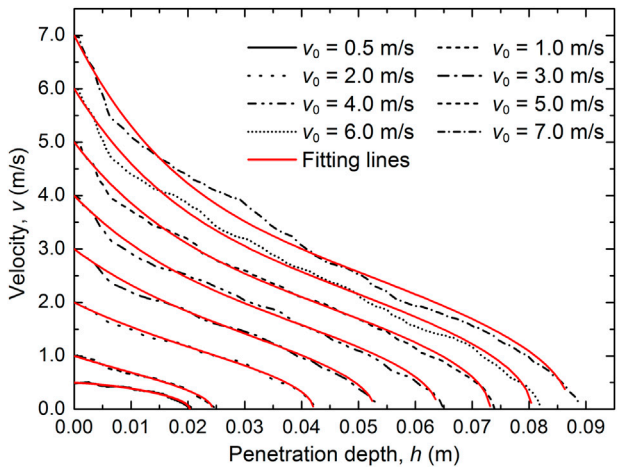


FIGURE 7 | Relationships between the velocity and penetration depth of projectiles for the numerical tests of different impact velocities. The black curves represent the numerical results and the red curves are obtained by fitting the numerical results using **Eq. 9**.

depth (h_f). As expected, it increases with the impact velocity. The impact at low velocity can lead to a relatively shallow crater, and specifically, the final penetration depth may be less than the projectile diameter (i.e. 0.0254 m). By contrast, the projectile with a relatively high speed can be entirely submerged in the granular bed, as implied in **Figure 5B**.

According to Uehara et al. (2003), the final penetration depth of a projectile can be estimated by an empirical formula $h_f = (0.14/\mu')(\rho_p/\rho_g)^{1/2} D^{2/3} H^{1/3}$ with μ' being the macroscopic friction coefficient of bed particles and H being the falling height. μ' is calculated as the tangent of the repose angle (θ_r). H is representative falling height calculated as the sum of the final penetration depth and the free fall height ($H = h_f + v_0^2/2g$). **Figure 6** shows the relationship between the final penetration depth and the total falling height from the current DEM simulations. The black curve shows the analytical results predicted by the empirical formula by Uehara et al. (2003). As shown in this figure, the numerical results can match well the empirical formula, demonstrating the accuracy of the empirical formula.

In the literature, several studies reported that the dynamics of a projectile can be assumed to follow the generalized Poncelet law (Katsuragi and Durian, 2007; Seguin et al., 2009),

$$m\ddot{h} = mg - mv^2/d_1 - kh \tag{8}$$

where h is the penetration depth of the projectile, m is the projectile mass; g is the gravity acceleration of value 9.8 m/s^2; d_1 is the material parameter of unit length; k is the elastic constant of contact. The solution of this equation shows the relationship between the velocity and penetration depth, as:

$$\frac{v^2}{v_0^2} = e^{-\frac{2h}{d_1}} - \frac{kd_1 h}{mv_0^2} + \left(\frac{gd_1}{v_0^2} + \frac{kd_1^2}{2mv_0^2}\right)\left(1 - e^{-\frac{2h}{d_1}}\right) \tag{9}$$

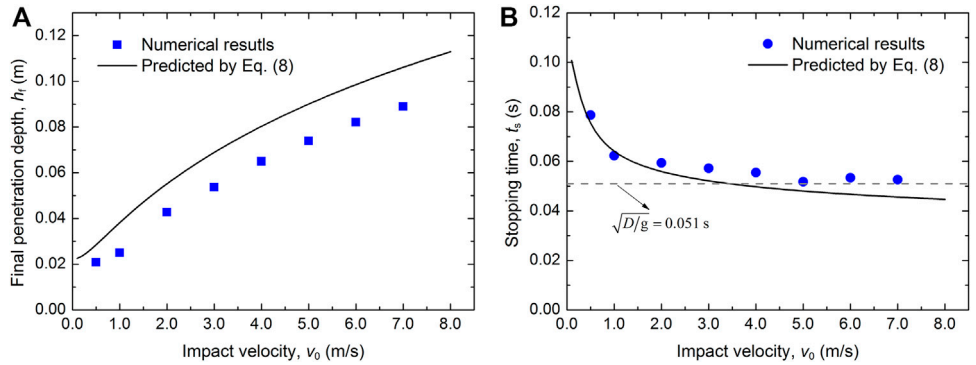


FIGURE 8 | Dependences of **(A)** the final penetration depth and **(B)** the stopping time on the impact velocity. The black curves show the final penetration depth and stopping time predicted by **Eq. 8** using the parameters d_1 and k calculated from **Eqs 10, 11**.

Figure 7 illustrates the relationships between the velocity and penetration depth for numerical simulations with different impact velocities. These curves exhibit the trend of a progressive change from a concave-down to a convex-up shape. Generally, there is a rapid decrease of velocity to zero at the end of penetration stage. These behaviors have also been observed in experiments by Katsuragi and Durian (2013) and DEM simulations by Tiwari et al. (2014). In addition, as shown in **Figure 7**, the numerical results can be well fitted by **Eq. 9**. This indicates that the dynamics of projectile in the present DEM study obeys well the generalized Poncelet law.

According to Katsuragi and Durian (2013), the fitting parameters d_1 and k in **Eq. 8** can be approximately calculated as

$$d_1 = D\left(0.25/\mu'\right)\left(\rho_p/\rho_g\right) \tag{10}$$

$$k = 12mgD^{-1}\mu'\left(\rho_g/\rho_p\right)^{1/2} \tag{11}$$

Thus, d_1 and k are estimated as 0.0831 m and 56.049 N/m, respectively. By substituting these values into **Eq. 8**, the final penetration depth and stopping time of the projectiles with different impact velocities can be predicted and compared with the numerical results (**Figure 8**). It can be seen that the final penetration depths predicted by **Eq. 8** using the parameters d_1 and k calculated from **Eqs 10, 11** are larger than the numerical results. However, the increasing trend of the data obtained in numerical modeling is in accordance with the prediction of **Eq. 8**. The stopping time firstly shows a rapid decrease as the impact velocity increases from 0 to 1.0 m/s, and then it gradually approaches a stable value. For low impact velocities ($v_0 < 1.0$ m/s), the stopping time can be well predicted by **Eq. 8**, while for higher impact velocities, **Eq. 8** would underestimate the stopping time. However, the general decreasing trend of the stopping time matches well the prediction of **Eq. 8**. In addition, according to Katsuragi and Durian (2007), the ultimate stopping time can be estimated using $\sqrt{D/g}$. This theoretical estimation is plotted as a gray dashed line in **Figure 8B**.

Energy Transformation and Dissipation

Analyses of the energy evolution, transformation and dissipation are important for a comprehensive understanding of the interaction process between the projectile and granular bed. The analyses also allow a quantitative evaluation of the role of inter-particle friction and damping on the projectile dynamics. The total energy (E_T) of the granular system consists of potential energy (E_P), kinetic energy (E_K), elastic strain energy (E_S) and the energy loss due to inter-particle friction (E_F) and local contact viscous damping (E_D). The method to calculate these energy components in the context of DEM has been detailed in (Shen et al., 2018). In this study, all these energy components were recorded during the simulations and subsequently analyzed regarding the energy evolution, transformation and dissipation, as shown in **Figure 9**. The kinetic energy of the projectile (E_K^p) and the granular bed (E_K^g), the potential energy of the projectile (E_P^p), the energy dissipated by friction between the projectile and granular bed (E_F^p), the energy dissipated by damping (E_D^g) and friction (E_F^g) are recorded separately. The potential energy (E_P^p) is defined with respect to the bottom of the granular bed. The strain energy (E_S) is not plotted because its value is negligibly small. All these energy components

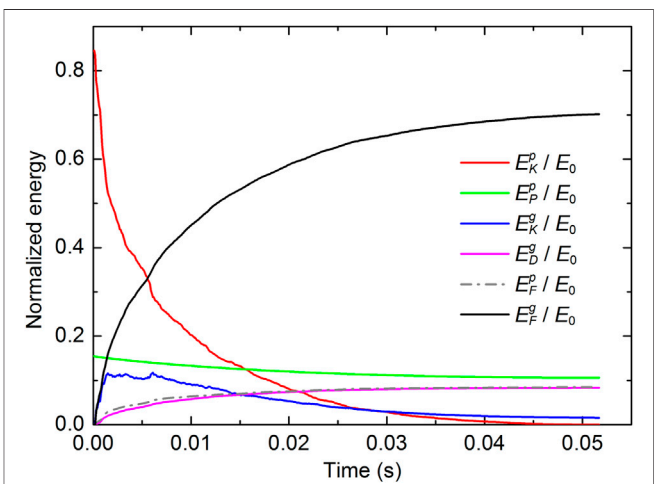


FIGURE 9 | Evolution and transformation of energy components during a simulation of $v_0 = 5.0$ m/s. All the energy components are normalized by the initial mechanical energy (kinetic energy plus potential energy) of the projectile (E_0).

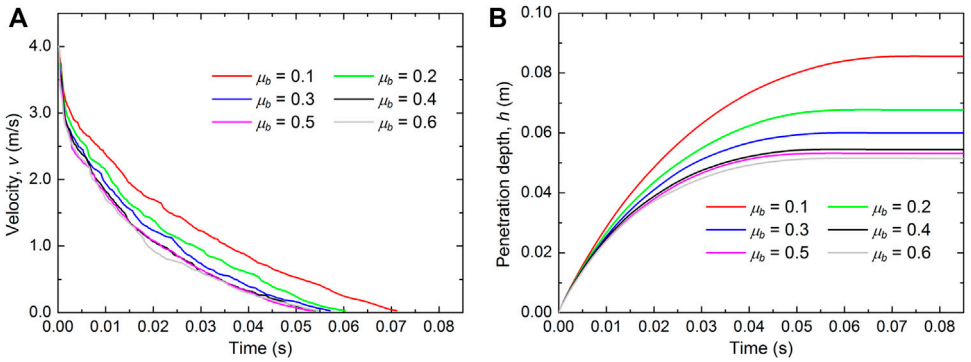


FIGURE 10 | Evolutions of **(A)** velocity and **(B)** penetration depth of projectiles for the numerical tests of various friction coefficients of bed particles (under the condition of v_0 = 4.0 m/s).

are normalized by the initial mechanical energy of the projectile (E_0: the initial kinetic energy plus potential energy). As illustrated in **Figure 9**, the whole system involves a cascade of energy evolution which begins when the projectile impacts onto the granular bed. After the collision occurs (t = 0), the kinetic energy of the projectile decreases rapidly, while that of the granular bed increases rapidly to the peak value at t = 1.5 ms. During this period, only a small amount of energy is dissipated by inter-particle friction and damping. After t = 1.5 ms, the kinetic energy of both the projectile and granular bed decreases slowly. However, the decreasing rate of kinetic energy of the granular bed is smaller than that of the projectile. This is because during the penetration stage of the projectile, a certain portion of projectile kinetic energy can still be transferred to the granular bed. To limit the computation time, the calculation is terminated when the projectile stops. Hence, at t = 51.8 ms, the kinetic energy of the projectile vanishes, while the granular bed still has a little of kinetic energy. From **Figure 9**, it also can be seen that nearly 70% of the mechanical energy of the projectile is dissipated by the inter-particle friction in the granular bed. The energy consumed by the friction of projectile and the damping of granular bed is less than 10% of E_0. Thus, from the perspective of energy consumption, it can be speculated that compared with the particle damping, the inter-particle friction plays a dominant role in the mechanical response of granular bed against the projectile impact. However, in addition to the energy consumption, it is also necessary to study the influences of inter-particle friction and damping on the projectile dynamics.

Influence of Inter-Particle Friction on Projectile Dynamics

To investigate the influence of inter-particle friction (μ_b), a series of impact tests are performed with the bed particle friction coefficient (μ_b) ranging from 0.1 to 0.6. In these numerical tests, the granular bed is also generated by gravitational deposition as described in **Section 2.2**. Since the porosity of the granular bed depends on the inter-particle friction, the value of μ_b is set as 0.1 during the gravitational deposition, such that the inter-particle friction can be varied to investigate its influence on the projectile dynamics without changing the initial stable state and especially the porosity of the granular bed. After the gravitational deposition, the volume fraction and bulk density (ρ_g) of the granular bed are 0.61 and 1.61 g/cm^3, respectively.

Figure 10 shows the evolutions of velocities and penetration depths of the projectiles for the numerical tests with various inter-particle friction coefficients. Generally, the velocity first shows a rapid decrease at the initial impact and then decreases gradually to zero. As the inter-particle friction increases, the stopping time of projectile decreases. For $\mu_b \geq 0.4$, the evolutions of velocities are almost identical and the projectiles stop at the same time. As for the penetration depth, it increases gradually to a peak value after the collision is initiated. The final penetration depth decreases as the inter-particle friction increases. For the tests with $\mu_b \geq 0.4$, the evolution of the projectile penetration depth is nearly identical and the projectiles almost stop at the same position. These results indicate that the inter-particle friction indeed has a significant influence on the projectile dynamics. However, it has a relatively negligible influence on the velocity and penetrating depth of the projectile after the inter-particle friction is beyond 0.4. The dependence of the final penetration depth and stopping time on the friction coefficient of particles are illustrated in **Figures 11A, B**, respectively. It can be seen that both the final penetration depth and stopping time decrease as the inter-particle friction increases. After the inter-particle friction increases to 0.4, both the final penetration depth and stopping time become relatively stable. This is in accord with the general trend of the prediction by **Eq. 8**. Actually, such a phenomenon is related to the dependence of the macroscopic friction coefficient of the granular bed (μ') on the microscopic inter-particle friction. For spherical particles, if particle rotation is allowed, the macroscopic friction (μ') increases with the inter-particle friction (μ_b) and reaches the peak value after μ_b increases to 0.45 (Suiker and Fleck, 2004). According to **Eqs 10, 11**, d_1 and k tend to be constant values when the macroscopic friction coefficient reaches its limit. Thus, the dynamics of projectile is not sensitive to μ_b when it increases beyond 0.45.

Influence of Particle Damping on Projectile Dynamics

In this study, the linear dashpot model **Eq. (4)** is used in DEM to simulate the energy dissipation due to elastic wave propagation through a solid particle. This kind of model has been widely

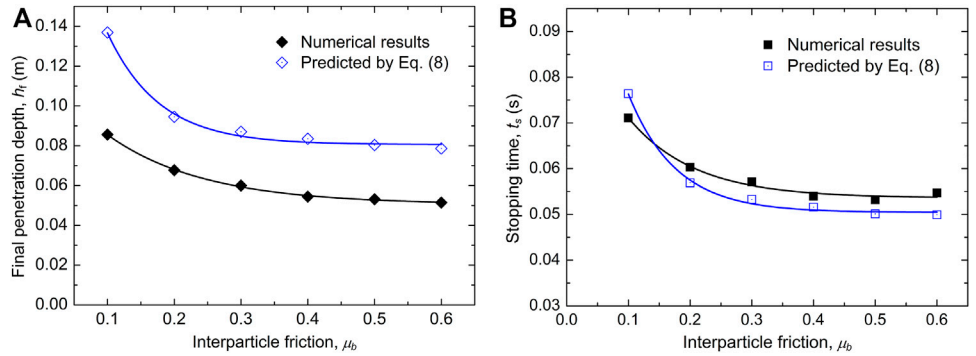


FIGURE 11 | Dependences of **(A)** final penetration depth and **(B)** stopping time of projectile on the friction coefficient of particles in granular bed.

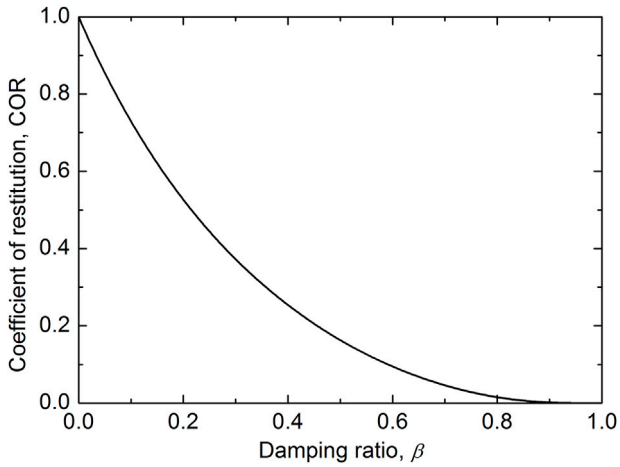


FIGURE 12 | Relationship between the coefficient of restitution (COR) and the damping ratio (β).

applied to numerical simulations of granular materials (Mao et al., 2004; Zhou et al., 2016; Gao G. and Meguid M. A., 2018; Li and Zhao, 2018; Shen et al., 2018). The damping ratio (β) in this model quantifies the plastic properties of particles. In the laboratory, the coefficient of restitution (COR) is commonly used as an index of this plastic property of solid materials. It can be measured in the laboratory from a series of drop tests (Imre et al., 2008). The relationship between the COR and the damping ratio (β) is depicted in **Figure 12**. The derivation of this equation can be found in (Gao G. and Meguid M., 2018). Thus, by varying the damping ratio, the influence of material damping of the granular bed on the projectile dynamics can be investigated. **Figure 13** gives the evolution of velocity and penetration depth of the projectiles for the numerical tests at various damping ratios (i.e. 0.01, 0.1, 0.2 and 0.3). The corresponding COR values are 0.97, 0.73, 0.53 and 0.37, respectively. From **Figure 13A**, it can be observed that the damping ratio has little influence on the projectile velocity. For the tests with different damping ratios, the evolutions of velocity of the projectiles are nearly the same and the projectiles nearly stop at the same time. From **Figure 13B**, it can be observed that in the cases of $\beta < 0.2$, the final penetration depth decreases with the increase of the damping ratio. However, an increase of β from 0.01 to 0.2 leads to only 7.3% decrease of the final penetration depth. In addition, for the cases of $\beta \geq 0.2$, the evolution of penetration depth of is nearly the same. Thus, it can be concluded that the main factor determining the dynamics of projectile is the inter-particle friction rather than the particle damping of a granular material.

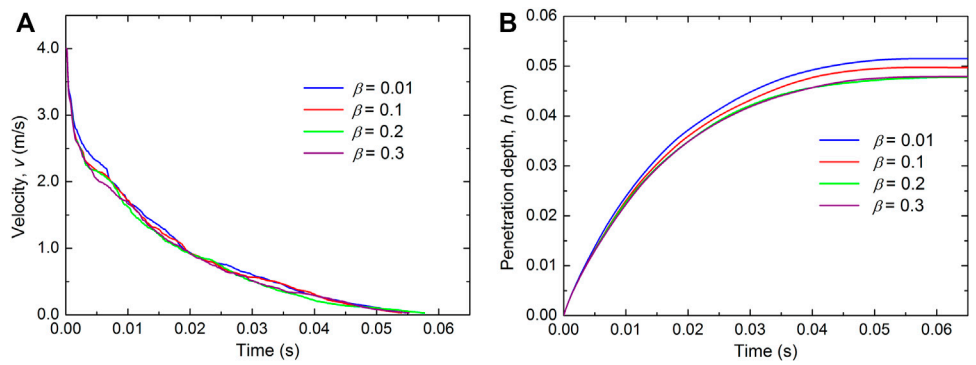


FIGURE 13 | Evolutions of **(A)** velocity and **(B)** penetration depth of projectiles for the numerical tests of various damping ratios (under the condition of $v_0 = 4.0$ m/s).

CONCLUSIONS

The impact of a spherical projectile into a granular bed is analyzed *via* three-dimensional numerical modeling by the discrete element method. This model is validated by comparing the numerical and experimental results reported in the literature. The validated model is then used to investigate the influence of inter-particle friction and material damping on the dynamics of projectile. The main conclusions of this study are as follows:

1. Based on the numerical modeling, three key interaction stages, namely the impact, penetration and collapse, are identified. The impact stage is characterized by the initial collision of projectile onto the granular bed, the rapid decrease of projectile velocity and the formation of strong force chain networks. The penetration stage is featured by the movement of the projectile inside the granular bed and the crater expansion. The collapse stage involves the toppling of the deepest transient crater and the formation of a final static crater.
2. During the whole impact process, the initial kinetic and potential energy of the projectile is dissipated mainly by inter-particle friction, while only a small part of energy loss is induced by projectile-particle friction and inter-particle damping.
3. The parametric study on the inter-particle friction and damping shows that the inter-particle friction is the main factor determining the projectile dynamics.

DATA AVAILABILITY STATEMENT

The raw data supporting the conclusion of this article will be made available by the authors, without undue reservation.

AUTHOR CONTRIBUTIONS

TZ, GC, and FD contributed to conception and design of the study. WS performed the numerical simulations and organized the database. WS wrote the first draft of the manuscript. TZ, WS, GC, FD, and GD contributed to manuscript revision, read, and approved the submitted version.

FUNDING

This research was supported, in whole or in part, by the National Natural Science Foundation of China (No. 42107155), the Royal Society, Sino-British Fellowship Trust International Exchanges Award (No. IES\R2\202023), the Fundamental Research Funds for the Central Universities (No. 2682021CX061), the National Key R&D Program of China (No. 2017YFC1502500).

REFERENCES

Bourrier, F., Nicot, F., and Darve, F. (2010). Evolution of the Micromechanical Properties of Impacted Granular Materials. *Comptes Rendus Mécanique* 338, 639–647. doi:10.1016/j.crme.2010.09.007

Bourrier, F., Nicot, F., and Darve, F. (2008). Physical Processes within a 2D Granular Layer during an Impact. *Granular Matter* 10 (6), 415–437. doi:10.1007/s10035-008-0108-0

Calvetti, F., and di Prisco, C. (2012). Rockfall Impacts on Sheltering Tunnels: Real-Scale Experiments. *Géotechnique* 62 (10), 865–876. doi:10.1680/geot.9.p.036

Clark, A. H., Kondic, L., and Behringer, R. P. (2012). Particle Scale Dynamics in Granular Impact. *Phys. Rev. Lett.* 109 (23), 238302. doi:10.1103/physrevlett.109.238302

Clark, A. H., Petersen, A. J., Kondic, L., and Behringer, R. P. (2015). Nonlinear Force Propagation during Granular Impact. *Phys. Rev. Lett.* 114 (14), 144502. doi:10.1103/physrevlett.114.144502

Crassous, J., Beladjine, D., and Valance, A. (2007). Impact of a Projectile on a Granular Medium Described by a Collision Model. *Phys. Rev. Lett.* 99 (24), 248001. doi:10.1103/physrevlett.99.248001

Cundall, P. A., and Strack, O. D. L. (1979). A Discrete Numerical Model for Granular Assemblies. *Géotechnique* 29 (1), 47–65. doi:10.1680/geot.1979.29.1.47

Gao, G., and Meguid, M. A. (2021). On the Role of Joint Roughness on the Micromechanics of Rock Fracturing Process: a Numerical Study. *Acta Geotech*. doi:10.1007/s11440-021-01401-8

Gao, G., and Meguid, M. A. (2018b). On the Role of Sphericity of Falling Rock Clusters-Insights from Experimental and Numerical Investigations. *Landslides* 15 (2), 219–232. doi:10.1007/s10346-017-0874-z

Gao, G., and Meguid, M. (2018a). Modeling the Impact of a Falling Rock Cluster on Rigid Structures. *Int. J. Geomech.* 18 (2), 1–15. doi:10.1061/(asce)gm.1943-5622.0001045

Horabik, J., Sochan, A., Beczek, M., Mazur, R., Ryżak, M., Parafiniuk, P., et al. (2018). Discrete Element Method Simulations and Experimental Study of Interactions in 3D Granular Bedding during Low-Velocity Impact. *Powder Tech.* 340, 52–67. doi:10.1016/j.powtec.2018.09.004

Imre, B., Räbsamen, S., and Springman, S. M. (2008). A Coefficient of Restitution of Rock Materials. *Comput. Geosciences* 34 (4), 339–350. doi:10.1016/j.cageo.2007.04.004

Katsuragi, H., and Durian, D. J. (2013). Drag Force Scaling for Penetration into Granular media. *Phys. Rev. E Stat. Nonlin Soft Matter Phys.* 87 (5), 052208. doi:10.1103/PhysRevE.87.052208

Katsuragi, H., and Durian, D. J. (2007). Unified Force Law for Granular Impact Cratering. *Nat. Phys* 3 (6), 420–423. doi:10.1038/nphys583

Kondic, L., Fang, X., Losert, W., O'Hern, C. S., and Behringer, R. P. (2012). Microstructure Evolution during Impact on Granular Matter. *Phys. Rev. E Stat. Nonlin Soft Matter Phys.* 85 (1), 011305. doi:10.1103/PhysRevE.85.011305

Li, X., and Zhao, J. (2018). Dam-break of Mixtures Consisting of Non-newtonian Liquids and Granular Particles. *Powder Tech.* 338, 493–505. doi:10.1016/j.powtec.2018.07.021

Li, Y., Dove, A., Curtis, J. S., and Colwell, J. E. (2016). 3D DEM Simulations and Experiments Exploring Low-Velocity Projectile Impacts into a Granular Bed. *Powder Tech.* 288, 303–314. doi:10.1016/j.powtec.2015.11.022

Mao, K., Wang, M. Y., Xu, Z., and Chen, T. (2004). DEM Simulation of Particle Damping. *Powder Technol.* 142 (2), 154–165. doi:10.1016/j.powtec.2004.04.031

Marston, J. O., Thoroddsen, S. T., Ng, W. K., and Tan, R. B. H. (2010). Experimental Study of Liquid Drop Impact onto a Powder Surface. *Powder Tech.* 203 (2), 223–236. doi:10.1016/j.powtec.2010.05.012

Newhall, K. A., and Durian, D. J. (2003). Projectile-shape Dependence of Impact Craters in Loose Granular media. *Phys. Rev. E Stat. Nonlin Soft Matter Phys.* 68 (6), 060301. doi:10.1103/PhysRevE.68.060301

Pica Ciamarra, M., Lara, A. H., Lee, A. T., Goldman, D. I., Vishik, I., and Swinney, H. L. (2004). Dynamics of Drag and Force Distributions for Projectile Impact in a Granular Medium. *Phys. Rev. Lett.* 92 (19), 194301. doi:10.1103/physrevlett.92.194301

Seguin, A., Bertho, Y., and Gondret, P. (2008). Influence of Confinement on Granular Penetration by Impact. *Phys. Rev. E Stat. Nonlin Soft Matter Phys.* 78 (1), 010301. doi:10.1103/PhysRevE.78.010301

Seguin, A., Bertho, Y., Gondret, P., and Crassous, J. (2009). Sphere Penetration by Impact in a Granular Medium: a Collisional Process. *Europhys. Lett.* 88, 44002. doi:10.1209/0295-5075/88/44002

Senft, L. E., and Stewart, S. T. (2009). Dynamic Fault Weakening and the Formation of Large Impact Craters. *Earth Planet. Sci. Lett.* 287 (3), 471–482. doi:10.1016/j.epsl.2009.08.033

Shen, W., Luo, G., and Zhao, X. (2021a). On the Impact of Dry Granular Flow against a Rigid Barrier with Basal Clearance via Discrete Element Method. *Landslides*. doi:10.1007/s10346-021-01805-3

Shen, W., Zhao, T., and Dai, F. (2021b). Influence of Particle Size on the Buffering Efficiency of Soil Cushion Layer against rockfall Impact. *Nat. Hazards* 108 (2), 1469–1488. doi:10.1007/s11069-021-04741-6

Shen, W., Zhao, T., Dai, F., Jiang, M., and Zhou, G. G. D. (2019). DEM Analyses of Rock Block Shape Effect on the Response of rockfall Impact against a Soil Buffering Layer. *Eng. Geology*. 249, 60–70. doi:10.1016/j.enggeo.2018.12.011

Shen, W., Zhao, T., Zhao, J., Dai, F., and Zhou, G. G. D. (2018). Quantifying the Impact of Dry Debris Flow against a Rigid Barrier by DEM Analyses. *Eng. Geology*. 241, 86–96. doi:10.1016/j.enggeo.2018.05.011

Su, Y., Cui, Y., Ng, C. W. W., Choi, C. E., and Kwan, J. S. H. (2018). Effects of Particle Size and Cushioning Thickness on the Performance of Rock-Filled Gabions Used in protection against boulder Impact. *Can. Geotech. J.* 56 (2), 198–207. doi:10.1139/cgj-2017-0370

Suiker, A. S. J., and Fleck, N. A. (2004). Frictional Collapse of Granular Assemblies. *J. Appl. Mech.* 71 (3), 350–358. doi:10.1115/1.1753266

Takahashi, T., Clark, A. H., Majmudar, T., and Kondic, L. (2018). Granular Response to Impact: Topology of the Force Networks. *Phys. Rev. E* 97 (1), 012906. doi:10.1103/PhysRevE.97.012906

Tanaka, K., Nishida, M., Kunimochi, T., and Takagi, T. (2002). Discrete Element Simulation and experiment for Dynamic Response of Two-Dimensional Granular Matter to the Impact of a Spherical Projectile. *Powder Technol.* 124 (1), 160–173. doi:10.1016/s0032-5910(01)00489-2

Tiwari, M., Mohan, T. R., and Sen, S. (2014). Drag-force Regimes in Granular Impact. *Phys. Rev. E Stat. Nonlin Soft Matter Phys.* 90 (6), 062202. doi:10.1103/PhysRevE.90.062202

Uehara, J. S., Ambroso, M. A., Ojha, R. P., and Durian, D. J. (2003). Low-speed Impact Craters in Loose Granular media. *Phys. Rev. Lett.* 90 (19), 194301. doi:10.1103/physrevlett.90.194301

Utili, S., Zhao, T., and Houlsby, G. T. (2015). 3D DEM Investigation of Granular Column Collapse: Evaluation of Debris Motion and its Destructive Power. *Eng. Geology*. 186, 3–16. doi:10.1016/j.enggeo.2014.08.018

Wada, K., Senshu, H., and Matsui, T. (2006). Numerical Simulation of Impact Cratering on Granular Material. *Icarus* 180 (2), 528–545. doi:10.1016/j.icarus.2005.10.002

Wang, B., and Cavers, D. S. (2008). A Simplified Approach for rockfall Ground Penetration and Impact Stress Calculations. *Landslides* 5 (3), 305–310. doi:10.1007/s10346-008-0123-6

Wang, Y., and Mora, P. (2009). "The ESyS_Particle: A New 3-D Discrete Element Model with Single Particle Rotation," in *Advances in Geocomputing*. Editor H. Xing (Berlin, Heidelberg: Springer Berlin Heidelberg), 183–228. doi:10.1007/978-3-540-85879-9_6

Weatherley, D., Hancock, W., and Boris, V. (2014). "ESyS-Particle Tutorial and User's Guide Version 2.1," in *Earth Systems Science Computational Centre* (Brisbane, Australia: The University of Queensland).

Ye, X., Wang, D., and Zheng, X. (2016). Criticality of post-impact Motions of a Projectile Obliquely Impacting a Granular Medium. *Powder Tech.* 301, 1044–1053. doi:10.1016/j.powtec.2016.07.043

Ye, X., Wang, D., and Zheng, X. (2018). Effect of Packing Fraction on Dynamic Characteristics of Granular Materials under Oblique Impact. *Powder Tech.* 339, 211–222. doi:10.1016/j.powtec.2018.07.099

Zhang, G., Tang, H., Xiang, X., Karakus, M., and Wu, J. (2015). Theoretical Study of rockfall Impacts Based on Logistic Curves. *Int. J. Rock Mech. Min. Sci.* 78, 133–143. doi:10.1016/j.ijrmms.2015.06.001

Zhang, L., Nguyen, N. G. H., Lambert, S., Nicot, F., Prunier, F., and Djeran-Maigre, I. (2017). The Role of Force Chains in Granular Materials: from Statics to Dynamics. *Eur. J. Environ. Civ. En.* 21 (7-8), 874–895. doi:10.1080/19648189.2016.1194332

Zhao, T., Crosta, G. B., Utili, S., and De Blasio, F. V. (2017). Investigation of Rock Fragmentation during Rockfalls and Rock Avalanches via 3-D Discrete Element Analyses. *J. Geophys. Res. Earth Surf.* 122 (3), 678–695. doi:10.1002/2016jf004060

Zhang, Y., Dai, Y., Wang, Y., Huang, X., Xiao, Y., and Pei, Q. (2021). Hydrochemistry, Quality and Potential Health Risk Appraisal of Nitrate Enriched Groundwater in the Nanchong area, Southwestern China. *Sci. Total Environ.* 784, 147186. doi:10.1016/j.scitotenv.2021.147186

Zhao, T., Crosta, G., Dattola, G., and Utili, S. (2018). Dynamic Fragmentation of Jointed Rock Blocks during Rockslide-Avalanches: Insights from Discrete Element Analyses. *J. Geophys. Res. Sol.Ea.* 123, 1–20. doi:10.1002/2017jb015210

Zhou, W., Ma, X., Ng, T.-T., Ma, G., and Li, S.-L. (2016). Numerical and Experimental Verification of a Damping Model Used in DEM. *Granular Matter* 18 (1), 1. doi:10.1007/s10035-015-0597-6

Conflict of Interest: The authors declare that the research was conducted in the absence of any commercial or financial relationships that could be construed as a potential conflict of interest.

Publisher's Note: All claims expressed in this article are solely those of the authors and do not necessarily represent those of their affiliated organizations, or those of the publisher, the editors and the reviewers. Any product that may be evaluated in this article, or claim that may be made by its manufacturer, is not guaranteed or endorsed by the publisher.

Copyright © 2022 Shen, Zhao, Crosta, Dai and Dattola. This is an open-access article distributed under the terms of the Creative Commons Attribution License (CC BY). The use, distribution or reproduction in other forums is permitted, provided the original author(s) and the copyright owner(s) are credited and that the original publication in this journal is cited, in accordance with accepted academic practice. No use, distribution or reproduction is permitted which does not comply with these terms.

frontiers in Earth Science

ORIGINAL RESEARCH
published: 15 March 2022
doi: 10.3389/feart.2022.842765

Pore-Water Pressure Model for Carbonate Fault Materials Based on Cyclic Triaxial Tests

Ling Zhu[1], *Qingwen Yang*[1]*, *Luguang Luo*[1,2] *and Shenghua Cui*[1]

[1]State Key Laboratory of Geohazard Prevention and Geoenvironment Protection, Chengdu University of Technology, Chengdu, China, [2]Faculty of Geo-Information Science and Earth Observation (ITC), University of Twente, Enschede, Netherlands

Pore-water pressure generation in the saturated carbonate fault zone plays a key role in the initiation of the Daguangbao landslide, which is the largest landslide triggered by the 2008 Wenchuan earthquake in China. This paper examines the pore-water pressure behavior and the influence of cyclic stress and initial stress state, and establishes a pore-water pressure model of carbonate fault materials. A series of cyclic triaxial tests of saturated carbonate fault materials were carried out, covering a broad range of frequencies, cyclic shear stress ratios and confining pressures. The test results show that the pore-water pressure in the materials increases rapidly under cyclic loading, revealing a significant liquefaction potential. The generation of pore-water pressure is barely affected by frequency. The higher cyclic shear stress ratio accelerates the generation of the pore-water pressure, while the higher confining pressure increases liquefaction resistance. Furthermore, an energy method is proposed to evaluate the development behavior of the pore-water pressure. An energy-based pore-water pressure model that accounts for the effects of frequency, cyclic shear stress ratio and confining pressure is established. The generation of the pore-water pressure is attributed to the grain crushing in the special fault materials with low-strength calcareous cementation. This work provides a novel model and some innovative observations for better understanding the pore-water pressure behavior of carbonate fault materials under seismic loading.

Keywords: carbonate fault materials, pore-water pressure, cyclic stress, initial stress state, model

OPEN ACCESS

Edited by:
Yunhui Zhang,
Southwest Jiaotong University, China

Reviewed by:
Cong Zhang,
Hohai University, China
Zhilu Chang,
Nanchang University, China

***Correspondence:**
Qingwen Yang
yangqingwen1991@outlook.com

Specialty section:
This article was submitted to Geohazards and Georisks, a section of the journal Frontiers in Earth Science

Received: *24 December 2021*
Accepted: *20 January 2022*
Published: *15 March 2022*

Citation:
Zhu L, Yang Q, Luo L and Cui S (2022) Pore-Water Pressure Model for Carbonate Fault Materials Based on Cyclic Triaxial Tests. Front. Earth Sci. 10:842765. doi: 10.3389/feart.2022.842765

HIGHLIGHTS

- The pore-water pressure behavior of the saturated carbonate fault materials was investigated.
- The influences of cyclic stress and initial stress state on the pore-water pressure generation and dissipated energy were revealed.
- An energy-based pore-water pressure model was established.

INTRODUCTION

During the long-term tectonic activities, the bedding fault was formed and developed (Wang, 2009). The strength of bedding fault materials is very low. The bedding fault is widely distributed in the mountains, and the strength degradation of bedding faults often determine the slope stability. It has been previously reported that some large landslides initiated along the bedding fault, such as the

Chiu-fen-erh-shan landslide (Wang et al., 2003), Daguangbao (DGB) landslide (Cui et al., 2018; Cui et al., 2020), and Qiyangou landslide (Fan et al., 2019), etc. In addition, the generation of pore-water pressure under seismic loading resulted in the strength degradation in the sliding zone, which was the key factor for the initiation and movement of landslide. Wang

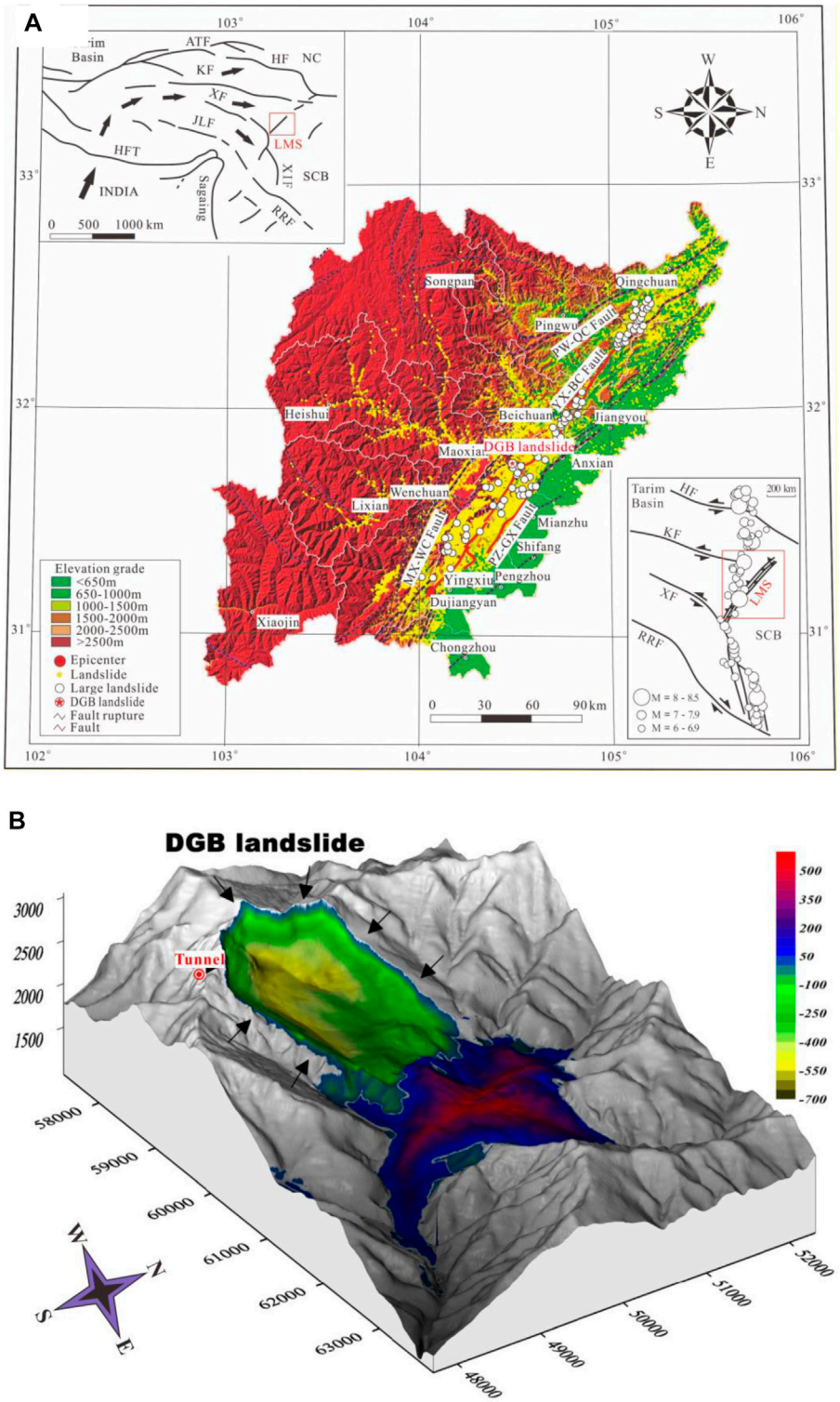


FIGURE 1 | The location **(A)** and 3D topography **(B)** of the DGB landslide.

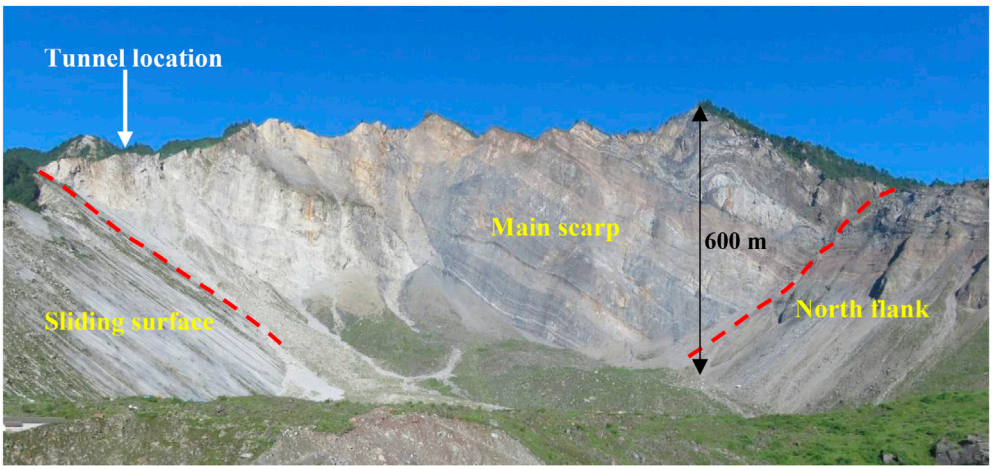


FIGURE 2 | The source area of the DGB landslide.

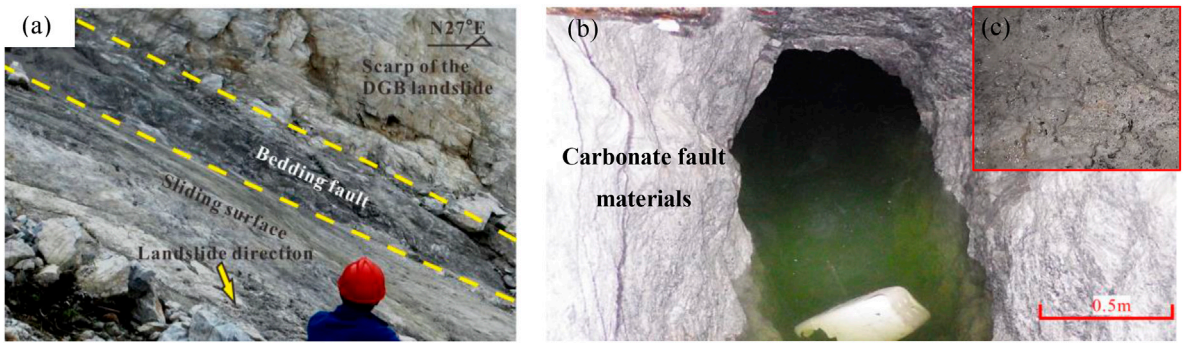


FIGURE 3 | Bedding fault characteristic **(A)**, groundwater in the tunnel **(B)** and saturated carbonate fault materials **(C)**.

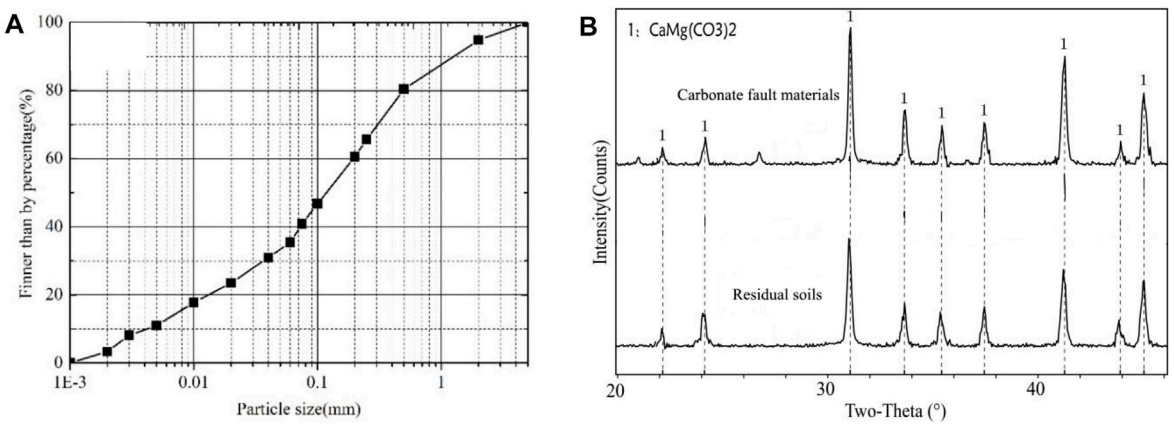


FIGURE 4 | (A) Particle size distributions and **(B)** the XRD results of carbonate fault materials and residual soils on the sliding surface.

et al. (2014) proposed that liquefaction of the runout path material enhanced the mobility of the Donghekou landslide through the ring shear test. Pei et al. (2017) reported that the steady-state strength of the sliding zone was close to 0 due to the generation of pore-water pressure, which was the reason for the long-distance and fluidized movement of the Shibeiyuan landslide.

TABLE 1 | Test scheme.

Sample No	ρ_d (g/cm^3)	*w* (%)	CSR	*f* (Hz)	σ_3 (kPa)	N_L
S1	1.8	11.23	0.325	1	100	91
S2	1.8	11.31	0.325	2	100	198
S3	1.8	11.27	0.325	3	100	264
S4	1.8	11.29	0.238	1	100	257
S5	1.8	11.3	0.411	1	100	44
S6	1.8	11.31	0.325	1	150	70
S7	1.8	11.33	0.325	1	200	58

Note:ρ_d, *dry density;* w, *water content;* CSR, *cyclic shear stress ratio;* f, *frequency;* σ_3, *consolidation pressure;* N_L, *the number of loading cycles leading to sample failure.*

Zhu et al. (2022) proposed that the sliding surface liquefaction caused complex surface landforms and long-runout movement of the LSB landslide. Therefore, it is crucial to investigate the pore-water pressure behavior of the sliding zone and establish a pore-water pressure model to evaluate the slope stability.

For a long time, the generation law of pore-water pressure and the pore-water pressure model under cyclic loading have been studied based on the results of field measurement and laboratory tests. Seed et al. (1976) first proposed the pore-water pressure development model of sand under cyclic loading based on isobaric consolidation undrained test. Polito et al. (2013) established an energy-based pore pressure generation model for use in predicting *in situ* pore pressures in soils subjected to nonsinusoidal loadings. Wang et al. (2013) proposed a formula to characterize the relationship between the peak axial strain and the peak pore-water pressure after 1,000 cycles. Chen et al. (2013) effectively evaluated the field liquefaction potential during the 1999 Chi-Chi earthquake by means of hysteresis loop energy and the proposed neural network. Liu et al. (2015) presented a fluid coupled-DEM model to investigate the generation mechanism of pore-water pressure. Azeiteiro et al. (2017) suggested that standard cyclic triaxial tests using uniform loads could be used for realistic energy-based assessment of in-situ liquefaction

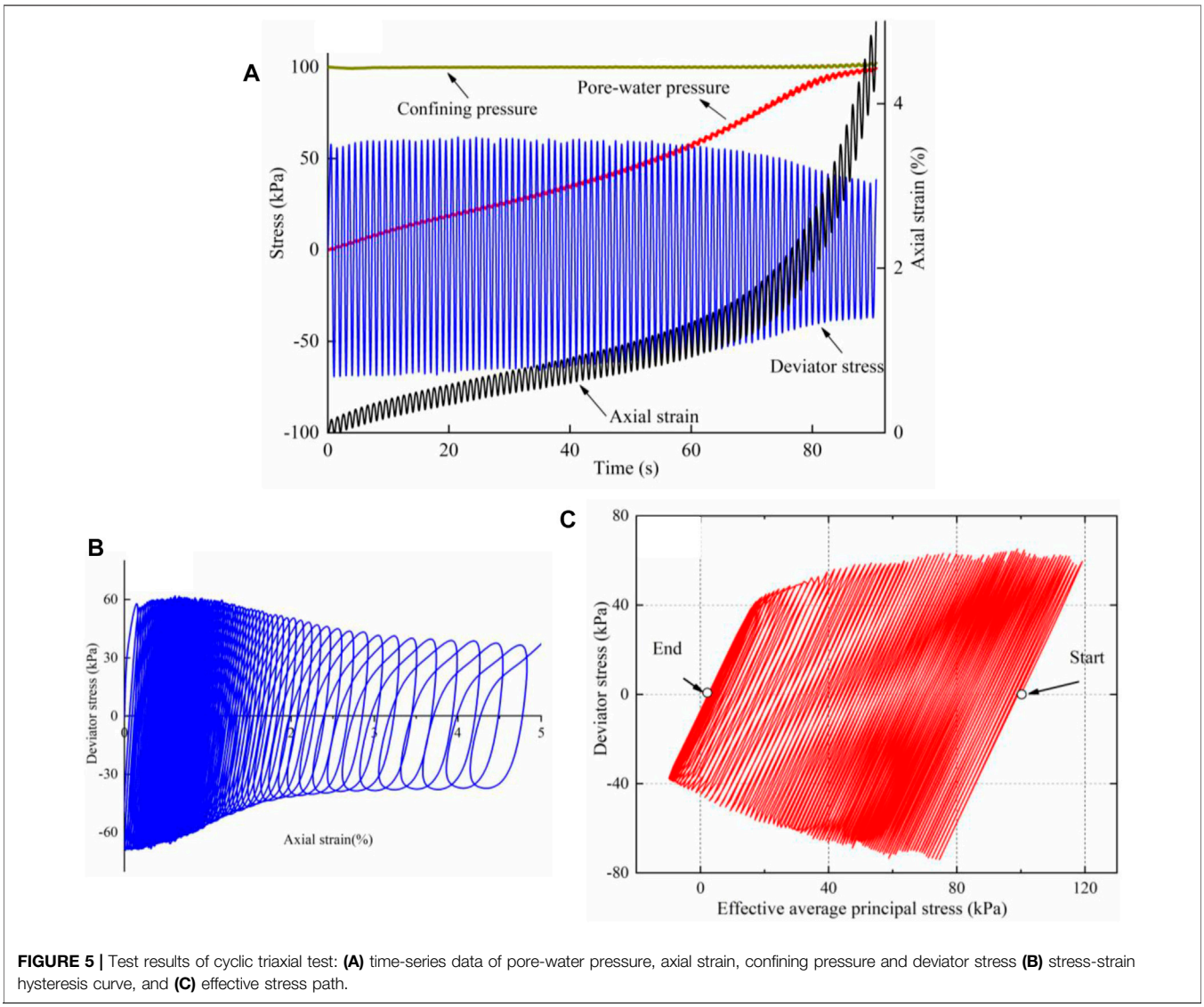


FIGURE 5 | Test results of cyclic triaxial test: **(A)** time-series data of pore-water pressure, axial strain, confining pressure and deviator stress **(B)** stress-strain hysteresis curve, and **(C)** effective stress path.

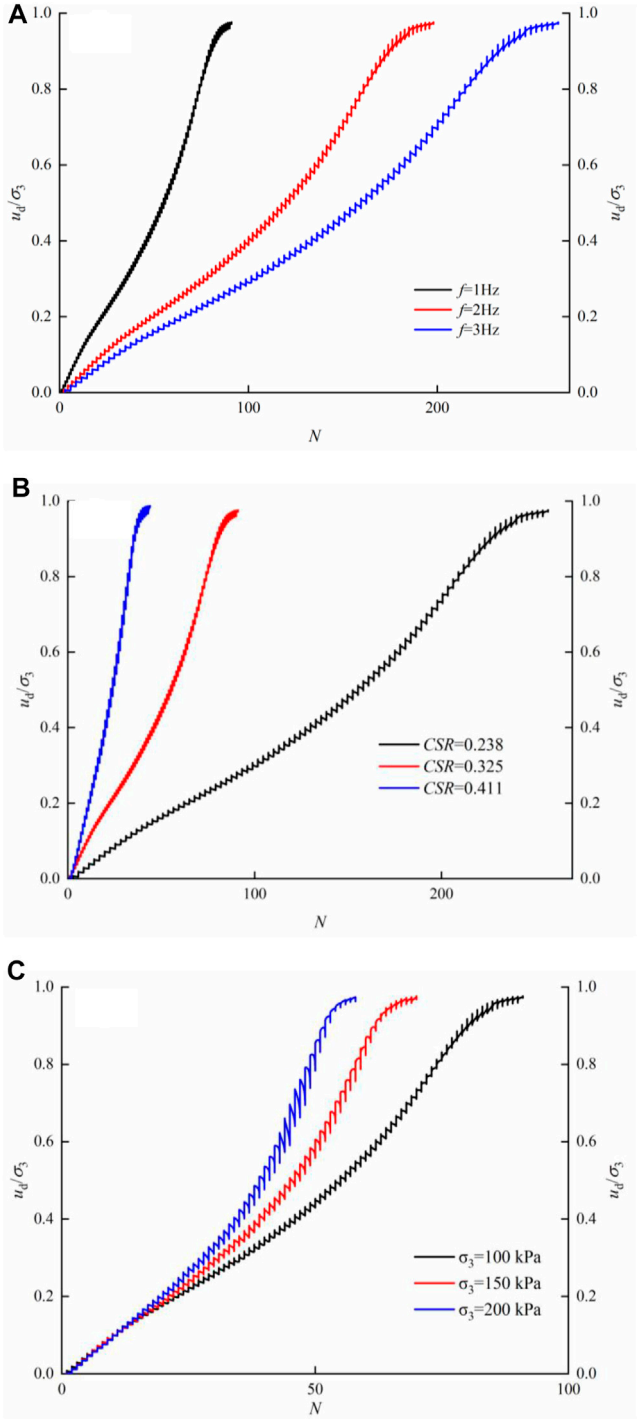


FIGURE 6 | Relations between u_d/σ_3 and N under different frequencies **(A)**, cyclic shear stress ratios **(B)** and confining pressures **(C)**.

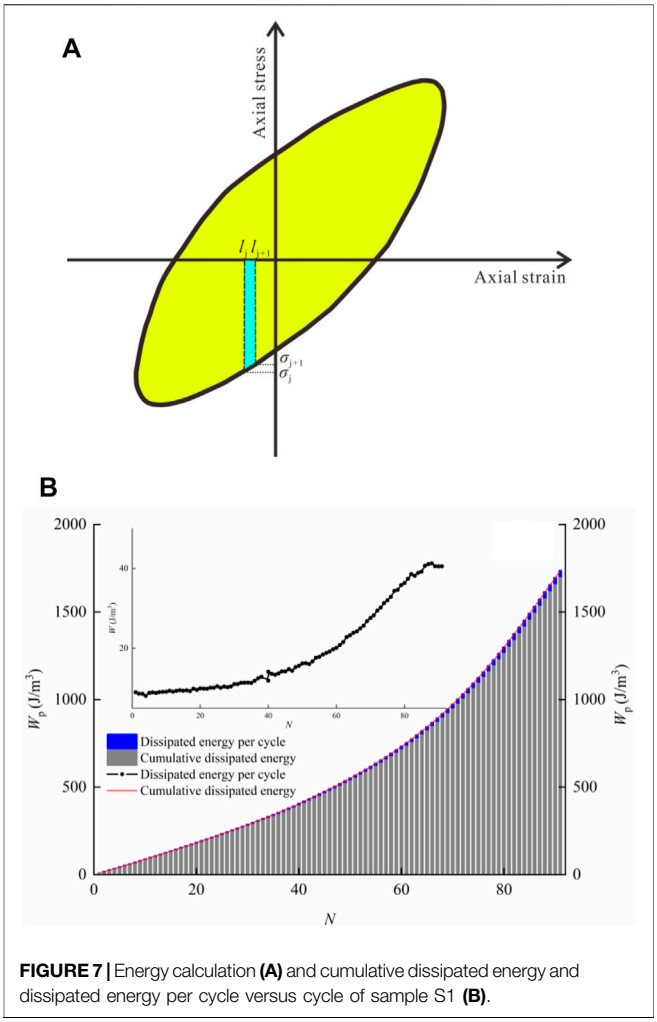


FIGURE 7 | Energy calculation **(A)** and cumulative dissipated energy and dissipated energy per cycle versus cycle of sample S1 **(B)**.

potential. Javdanian et al. (2017) derived an NF-GMDH-based model based on laboratory results that can be successfully used for strain energy-based estimation of liquefaction potential. Amini and Noorzad (2018) proposed an energy-based method to evaluate the liquefaction potential of fiber-reinforced sands. Yang and Pan (2018) investigated a unique relationship between the residual pore pressure and dissipated energy for isotropic and anisotropic consolidated sand with different densities and cyclic stress amplitudes. Chen et al. (2019) proposed a new strain-based model to assess the residual excess pore-water pressure generation in fully saturated sands. Javdanian (2019) proposed a strain energy-based method to accurately predict the energy required for liquefaction of sandy soil and silty sand samples in cyclic triaxial tests. Shan et al. (2020) reported that the dynamic strength of artificial marine clays with different mineral compositions was illustrated by VEDR cyclic strength from the perspective of energy dissipation. Ni et al. (2020) evaluated the effects of the initial deviatoric stress and cyclic stress amplitude on the liquefaction potential based on the energy-based method. Pan and Yang (2020) proposed an energy approach based on the energy density concept for liquefaction assessment, which could better capture the effect of loading randomness on sand liquefaction behavior. Zhang et al. (2020) established a three-parameter pore-water pressure model of fiber-reinforced sands that accounts for the effects of fiber content, fiber length, relative density, cyclic stress ratio, and sand particle diameter.

The pore-water pressure generation law of different materials under cyclic loading has been extensively investigated (Chang et al.,

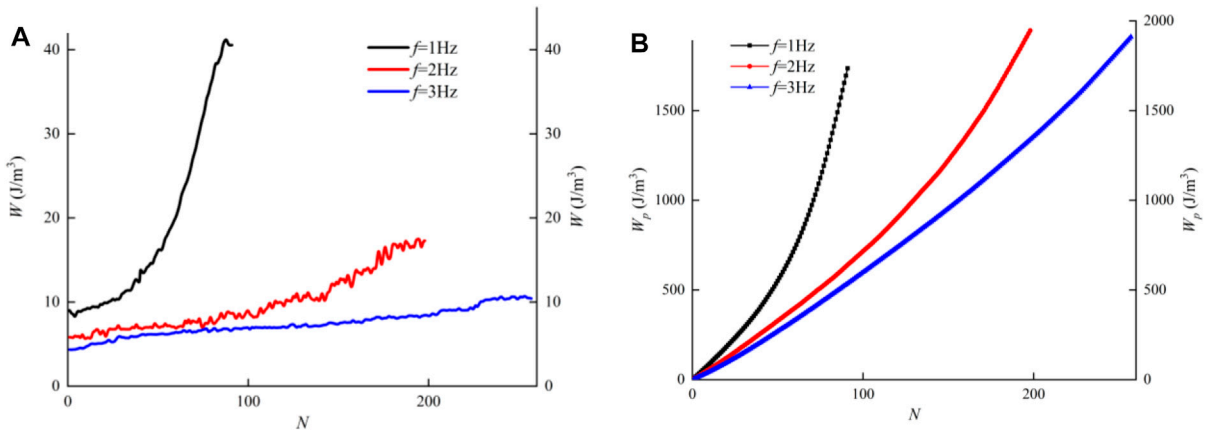


FIGURE 8 | Evolution characteristics of dissipated energy under different frequencies: **(A)** dissipated energy per cycle and **(B)** cumulative dissipated energy.

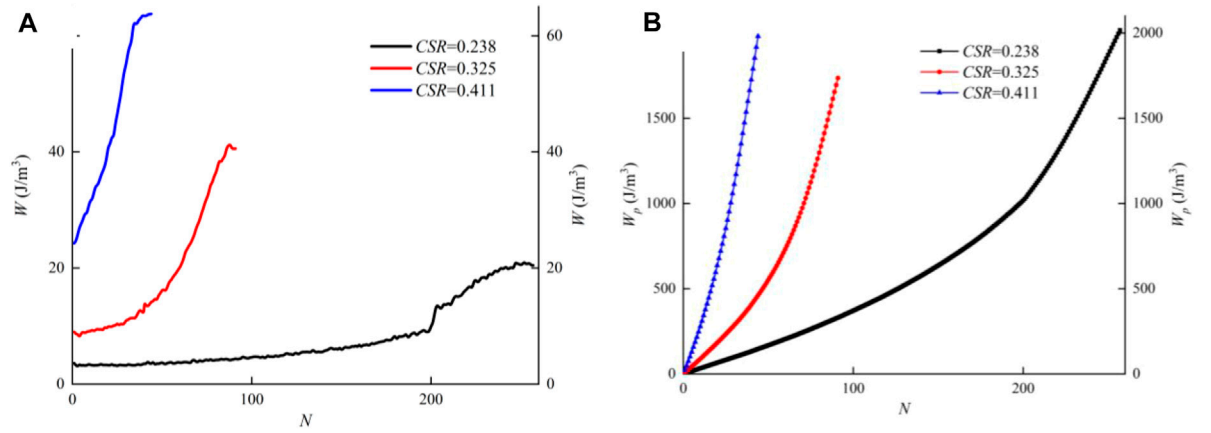


FIGURE 9 | Evolution characteristics of dissipated energy under different cyclic shear stress ratios: **(A)** dissipated energy per cycle and **(B)** cumulative dissipated energy.

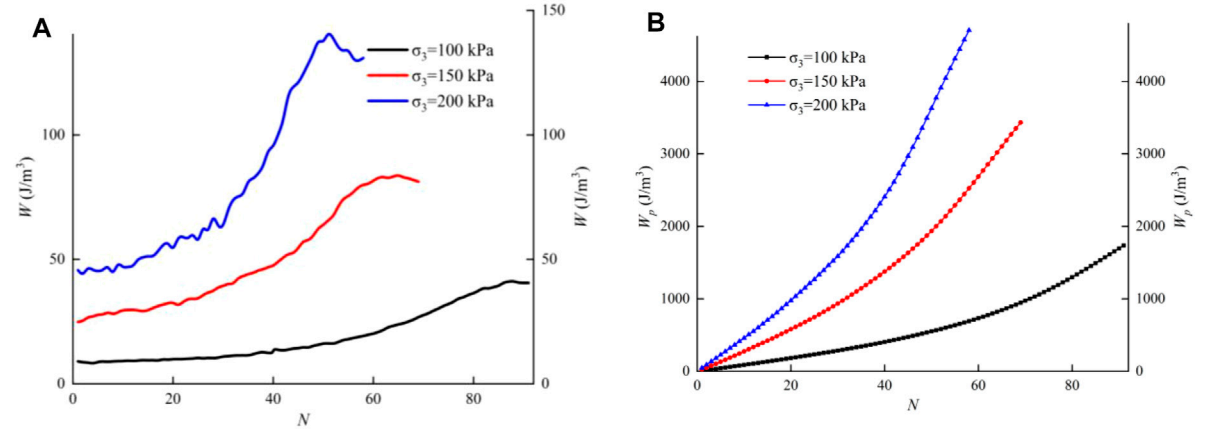


FIGURE 10 | Evolution characteristics of dissipated energy under different confining pressures: **(A)** dissipated energy per cycle and **(B)** cumulative dissipated energy.

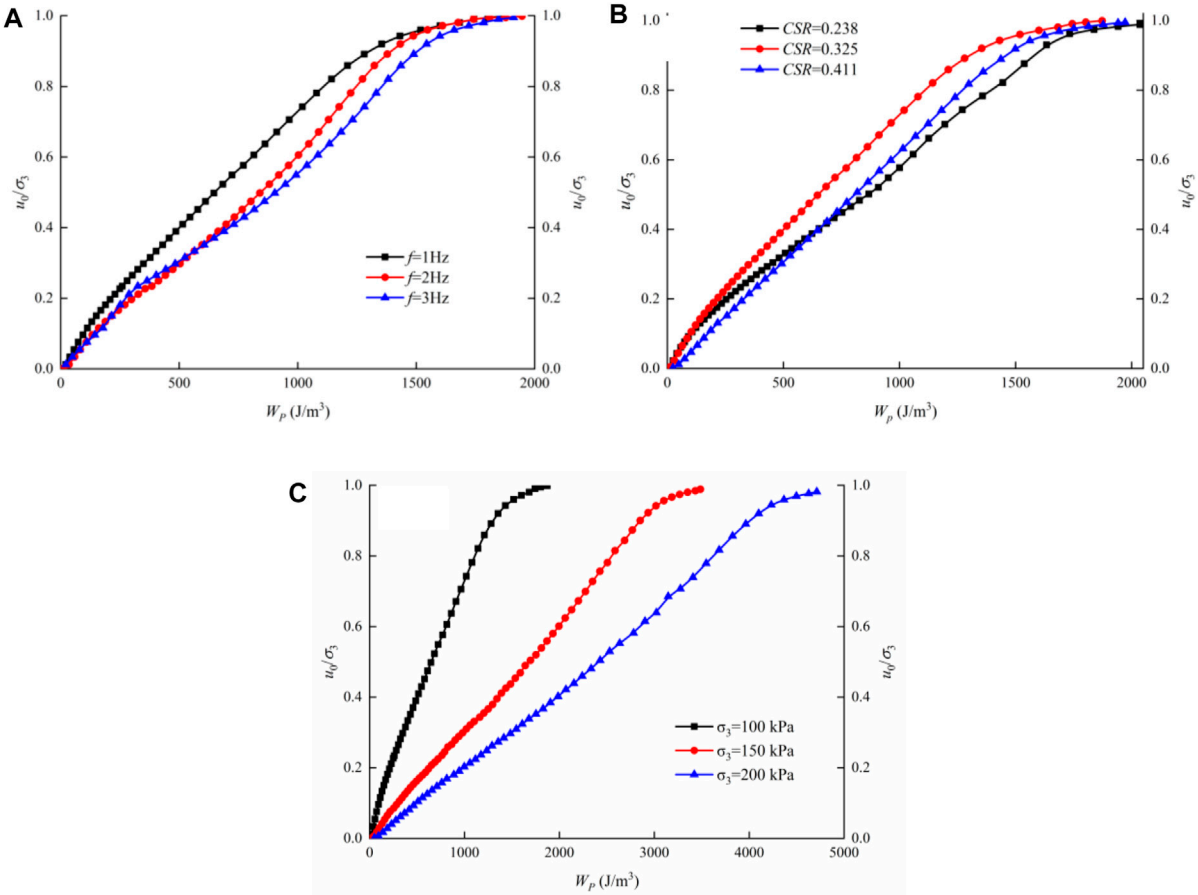


FIGURE 11 | Relation between pore-water pressure ratio and cumulative dissipated energy under different frequencies **(A)**, cyclic shear stress ratios **(B)** and confining pressures **(C)**.

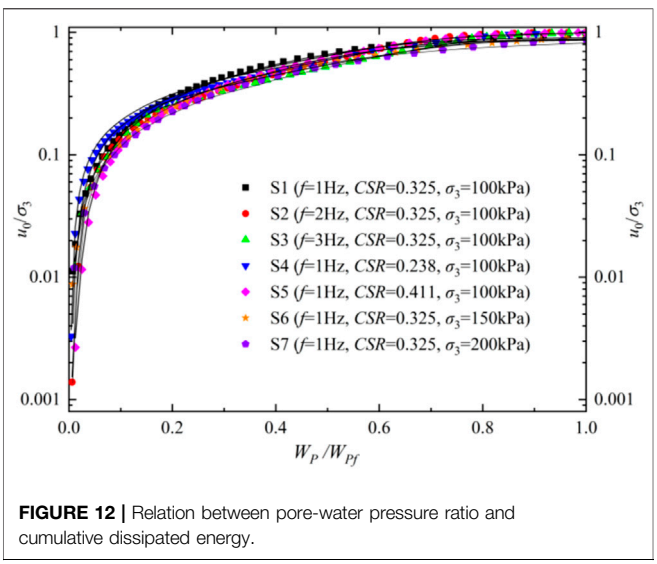


FIGURE 12 | Relation between pore-water pressure ratio and cumulative dissipated energy.

1983; Mitchell and Dubin 1986; Charlie et al., 1989; Sitharam and Govindaraju 2007; Polito et al., 2008; Hazirbaba and Rathje, 2009; Wang et al., 2010; Pan and Yang 2018; Balreddy et al., 2019; Zhang et al., 2020). However, energy is a scalar and can be directly iterated to reflect the generation process of pore-water pressure under complex stress paths, thus the energy-based pore-water pressure model is more reliable than the other pore-water pressure models. In addition, most studies only focus on some ideal materials, which is quite different from the real site situation. In this paper, a detailed field investigation and a series of saturated triaxial tests of carbonate fault materials were carried out. The pore-water pressure behavior in the materials was investigated. An energy-based pore-water pressure model is established considering the effect of frequencies, cyclic shear stress ratios, and confining pressures. The generation mechanism of pore-water pressure was investigated. This study is beneficial to evaluate the stability variability of the DGB landslide during the 2008 Wenchuan earthquake.

CHARACTERISTICS OF CARBONATE FAULT MATERIALS

Geological Background

The 2008 Wenchuan earthquake triggered 112 large landslides with an area of more than 50,000 m^2 (Xu et al., 2011), of which

the DGB landslide with a volume of about 1.2×109 m^3 is located in Gaochuan Township, Mianyang City, and it is the largest landslide triggered by the 2008 Wenchuan earthquake (**Figure 1A**). The maximum thickness of the landslide mass is 570 m (Huang et al., 2012). The source area of DGB landslide is composed of a main scarp and two lateral flanks (**Figure 2**). A sliding surface with a length of 1.8 km is exposed in the southern flank. The exposed rocks in the sliding surface were highly weathered and extensively fractured. A bedding fault was found at the intersection of the main scarp and the sliding surface in the southern flank (**Figure 3A**). To investigate its formation mechanism, a tunnel was excavated along the sliding surface at the back of the mountain (**Figure 1B**).

As shown in **Figures 3A,B** 3~5 m thick bedding fault was found in the tunnel, indicating that the sliding surface was formed within the pre-existing bedding fault. The zone is mainly composed of carbonate fault materials. In addition, the bedding fault is below the groundwater level (Pei et al., 2018; Cui et al., 2021), and there is abundant groundwater in the tunnel. Due to long-term tectonic compression and shear, the materials in the bedding fault are seriously fragmented, similar to soil. Moreover, the groundwater seepage on the section of the bedding fault can be seen. The natural water content of the materials reaches 11.94% (**Figure 3C**). The carbonate fault materials mainly consisted of 5.68% breccia, 53.98% sand, 29.8% silt, and 10.54% clay. The non-uniform coefficient and curvature coefficient were 57.34 and 1.92, respectively. The plastic limit and liquid limit were 7.41 and 11.87, respectively. The plastic index and permeation coefficient were 4.46 and 8.1×10^{-5}, respectively. The tested materials were obtained in the tunnel, and it is not disturbed by the landslide movement. Therefore, it is appropriate to investigate the generation law of pore-water pressure in the bedding fault under seismic loading.

Test Sample and Scheme

A cylindrical sample with a diameter of 50 mm and a height of 100 mm is used in this test. Due to the limitation of test conditions, particles larger than 5 mm are removed, and the sample is mainly composed of sand particles (0.075–2 mm), accounting for about 56% of the total mass. The content of breccia (>5 mm) in the materials is less than 10%. According to Kuenza et al. (2004), the mechanical behavior of the samples was mainly controlled by the matrix material when the content of particles larger than 5 mm in the material is less than 40%. The pore-water pressure behavior may not be influenced by the removed breccias. Therefore, this test result can reflect the generation characteristic of pore-water pressure in the bedding fault. **Figure 4A** shows the particle size distribution of the sample. The composition of the carbonate fault materials is similar to the residual soils on the sliding surface, which is mainly composed of dolomite. This result further demonstrates that the DGB landslide triggered along the bedding fault, which was mainly composed of carbonate fault materials. **Figure 4B** illustrates the X-ray diffraction (XRD) results.

The materials with an initial water content of 5% were allowed to stand in a closed surroundings for 24 h. The initial density of the sample with a diameter of 50 mm and a height of 100 mm is 1.8 kg/m^3. The samples were saturated by de-aired water with the assistance of carbon dioxide. The degree of saturation was checked by B_D, which is the ratio between the increment of excess pore water pressure (Δu) and the increment of confining pressure ($\Delta\sigma_3$) under undrained conditions ($B_D = \Delta u/\Delta\sigma_3$) (Skempton 1954; Tokimatsu et al., 1990). When this parameter is greater than 0.95, the sample is considered to be saturated. After saturation, consolidation pressures of 100, 150, and 200 kPa were separately applied in both lateral and axial directions. Due to the limitation of the cyclic triaxial test apparatus, it is impossible to apply the real 2008 Wenchuan earthquake loading, Cui et al. (2017) reported that the dominated seismic wave frequencies during the Wenchuan earthquake were 2–3 Hz. The sinusoidal loadings with different frequencies of 1, 2 and 3 Hz and cyclic shear stress ratios of 0.238, 0.325, and 0.411 were separately implemented. The sample is failed when the axial strain reaches 5%. The test scheme is shown in **Table 1**.

TABLE 2 | Fitting results.

Sample No	a	R^2
S1	4.5	0.9977
S2	3	0.9965
S3	3	0.9872
S4	3.1	0.9988
S5	3.3	0.9912
S6	3.4	0.9968
S7	3.1	0.9979

TEST RESULTS

Figure 5A shows the time-series records of the pore-water pressure, axial strain, deviator stress under the confining pressure of 100 kPa. it can be seen from **Figure 5A** that the pore-water pressure increases rapidly at the initial stage, and pore-water pressure reaches 20 kPa at ~20 s. Gradually, the generation rate of pore-water pressure slows down slightly, and the pore-water pressure is about 35 kPa at 40 s. The generation rate of pore-water pressure gradually increases after that and the pore-water pressure reaches 90 kPa at 80 s. Finally, the pore-water pressure is approximately equal to confining pressure when the axial strain reaches 5%. The axial strain increases slowly at 0–70 s, only reaching 1.5%. After the pore-water pressure ratio exceeded 0.7, the axial strain increases rapidly and reaches 5% in a very short time. In addition, the cyclic deviator stress is stable at 0–60 s, then decreases slightly. The peak deviator stress decreases to only 40 kPa at 90 s. The hysteresis curve widens gradually with increasing cycles, as presented in **Figure 5B**. **Figure 5C** shows the effective stress path. Effective average principal stress ($p' = 1/3(\sigma_1+2\sigma_3)$) decreases continuously. The effective stress path reaches the original point at the end of the test. As a result, the materials show high liquefaction potential.

Figure 6A indicates the pore-water pressure ratio (u_d/σ_3) versus cycles (N) curve under various frequencies. From **Figure 6A**, the generation law of the u_d/σ_3 is similar under

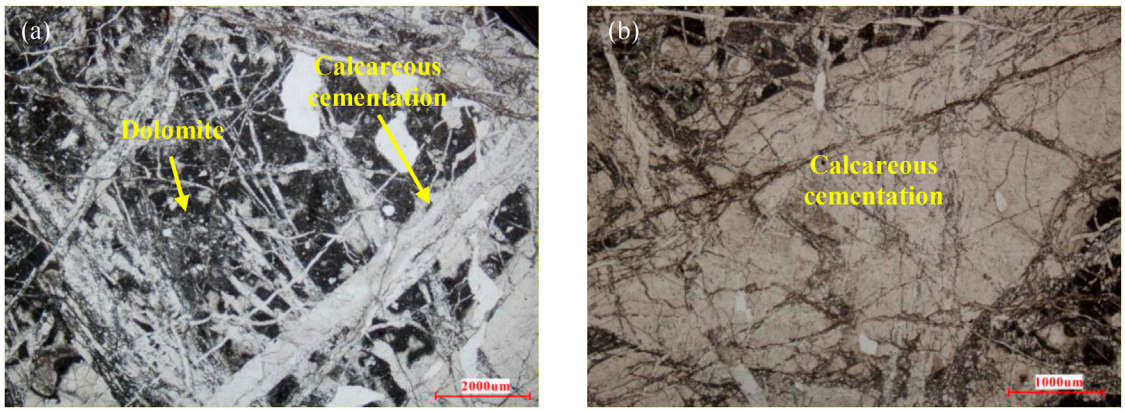


FIGURE 13 | Carbonate fault materials with low-strength cementation from microscope. 2 × 10 **(A)**, 4 × 10 **(B)**.

different frequencies, and the u_d/σ_3 increases rapidly. Finally, the u_d/σ_3 is approximately equal to 1 and liquefaction occurs. To achieve 5% axial strain, 91, 198, and 264 cycles are required at frequencies of 1, 2 and 3 Hz, respectively. It can be found that the time required for liquefaction (~90 s) is almost the same, indicating that the frequency has little impact on the generation rate of the pore-water pressure. **Figure 6B** shows the u_d/σ_3 versus N curves under a variety of cyclic shear stress ratios (CSR = 0.238, 0.325, and 0.411). From **Figure 6B**, the pore-water pressure increases rapidly under different cyclic shear stress ratios. The u_d/σ_3 is greater than 0.95 when the axial strain reaches 5%. All samples exhibit the same pattern. However, the greater cyclic shear stress ratio accelerates the generation of the pore-water pressure, and fewer cycles are required for liquefaction. As shown in **Figure 6B**, for the cyclic shear stress ratios of 0.238, 0.325, and 0.411, the number of cycles required to cause sample liquefaction are correspondingly 257, 91, and 44, respectively. This result reveals that the cyclic shear stress ratios change the generation rate of pore-water pressure. In addition, the u_d/σ_3 versus N curves under different confining pressures (σ_3 = 100, 150, and 200 kPa) are shown in **Figure 6C**. The u_d/σ_3 increases rapidly in the initial stage, and then the u_d/σ_3 slows down slightly. The generation rate of u_d/σ_3 gradually accelerates with increasing cycles. The samples can be liquefied under different confining pressures.

PORE-WATER PRESSURE GENERATION MODEL

The applied cyclic loading causes the generation of pore-water pressure in the sample, and an amount of energy is dissipated in this process. It can be summarized as input energy (E_i), output energy (E_0) and dissipated energy (W) (He and Cao, 1990). The formula is expressed as $E_i = E_0 + W$. Saturated soil is composed of soil particles and pore water. During the cyclic loading, the dissipated energy is an important index to reveal the generation process of pore-water pressure. Therefore, in this paper, an energy analysis method is used to evaluate the generation of pore-water pressure in carbonate fault materials, and an energy-based pore-water pressure model is established.

Dissipated Energy

The area of the hysteresis curve can properly represent the dissipated energy of single cycle. Most previous studies simplified the hysteresis curve into an ellipse, and the dissipated energy was obtained by calculating the area of the ellipse. However, due to the hysteresis curve is not a standard ellipse, this calculation method has significant shortcomings. Therefore, a new method is proposed here to accurately calculate the area of the hysteresis curve. The hysteresis curve is divided into several tiny polygons by the stress and strain of adjacent data. The sum of all polygon areas is the area of the hysteretic curve (**Figure 7A**).

To precisely calculate the hysteresis curve area, 40 group stress-strain data in a cycle are obtained. The calculation formula of hysteresis curve area is as $W_i = S_i = \sum_{j=1}^{39} \frac{1}{2}(\sigma_j + \sigma_{j+1})(l_{j+1} - l_j)$. Where W_i is the dissipated energy of the ith cycle, S_i is the hysteresis curve area of the ith cycle, σ_j and l_j are the axial stress and axial strain of the jth cycle. Therefore, the cumulative dissipated energy (W_{pi}) is the sum of the hysteresis curve area from 1st to ith cycles, and the cumulative dissipated energy is obtained by $W_{pi} = \sum_1^i W_i$. We introduce the average pore-water pressure (u_0), defined as the average of the maximum and minimum pore-water pressures per cycle, to clearly illustrate the generation behavior of pore-water pressure, and the formula is as $\mu_{0,i} = (\mu_{max,i} + \mu_{min,i})/2$. Where $u_{0,i}$ is the average pore-water pressure of the ith cycle, $u_{max,i}$ and $u_{min,i}$ are the maximum pore-water pressure and minimum pore-water pressure of the ith cycle, respectively.

Figure 7B shows the cumulative dissipated energy (W_{pi}), dissipated energy per cycle (W_i) versus cycle (N) of sample S1. As shown in **Figure 7B**, the dissipated energy per cycle gradually increases with growing cycles. However, it is noted that the dissipated energy per cycle is basically the same (about 9.15 J/m^3) in the first 30 cycles. After that, the dissipated energy per cycle increases, and the dissipated energy per cycle is basically stable towards the end of the test, about 40.55 J/m^3. The

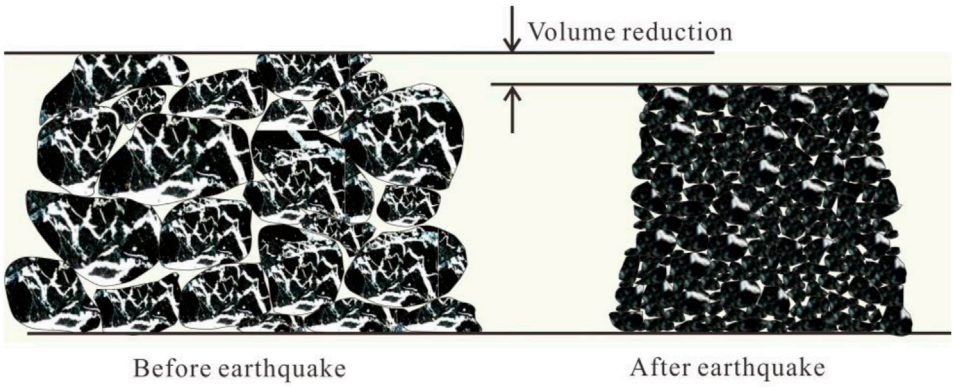


FIGURE 14 | Schematic diagram of liquefaction mechanism.

cumulative dissipated energy throughout the cyclic loading process demonstrates an accelerated generation trend.

Figure 8 shows the dissipated energy per cycle and cumulative dissipated energy versus cycle under different frequencies. From **Figure 8A**, the dissipated energy per cycle is lower at higher frequencies, and the increased rate of dissipated energy per cycle with increasing cycles is faster at low frequencies. However, the frequency has little effect on the total dissipated energy required to trigger liquefaction, as shown in **Figure 8B**. **Figure 9** shows the dissipated energy per cycle and cumulative dissipated energy versus cycle under different cyclic shear stress ratios. Under the condition of a larger cyclic shear stress ratio, the cyclic loading causes greater dissipated energy per cycle (**Figure 9A**). However, the cumulative dissipated energy required to trigger liquefaction is essentially the same for different cyclic shear stress ratios (**Figure 9B**). **Figure 10** shows the dissipated energy per cycle and cumulative dissipated energy versus cycle under different confining pressures. The dissipated energy per cycle is great at large confining pressure (**Figure 10A**). The increase of the confining pressure leads to a rise in the cumulative dissipated energy required to liquefy (**Figure 10B**). Based on the above test results, it is noted that the dissipated energy per cycle increases with increasing cycles for all samples, with the maximum dissipated energy per cycle near the time of sample liquefaction, after which it remains stable or decreases slightly. In addition, frequency and cyclic shear stress ratio have little effect on the total dissipated energy required to trigger liquefaction, while the confining pressure has a significant effect.

Relationship Between Pore-water Pressure Ratio and Cumulative Dissipated Energy

The pore-water pressure ratio versus cumulative dissipated energy curves under different frequencies and cyclic shear stress ratios show the same development characteristic, as shown in **Figures 11A,B**. The pore-water pressure ratio increases with increasing cumulative dissipated energy. According to the generation characteristics of pore-water pressure, the curve can be divided into two stages. Before the pore-water pressure ratio is 0.9, the pore-water pressure ratio and cumulative dissipated energy increase rapidly, and the slope of the curve is large. After that, the cumulative dissipated energy continuously increases while the pore-water pressure ratio remains stable. **Figure 11C** shows the pore-water pressure ratio versus cumulative dissipated energy curves under different confining pressures. It can be seen that the pore-water pressure ratio shows the same development characteristic. The pore-water pressure increases rapidly in the initial stage, and then tends to be stable. However, the contribution of cumulative dissipated energy to pore-water pressure generation is significantly influenced by the confining pressure, and the greater dissipated energy is required to trigger liquefaction in the higher confining pressure.

Normalized Model of Pore-water Pressure Ratio and Cumulative Dissipated Energy

To establish an energy-based pore-water pressure model considering the effect of frequency, cyclic shear stress ratio and confining pressure. The cumulative dissipated energy and cycles are normalized. The normalization results are shown in **Figure 12**. From **Figure 12**, the pore-water pressure ratio versus cumulative dissipated energy ratio (W_p/W_{pf}) are properly fitted by the exponential function,

$$\log\left(\mu_d/\sigma_3\right) = 1 - e^{\left(1-a\left(W_p/W_{pf}\right)\right)} \quad (1)$$

where W_{pf} is the cumulative dissipated energy trigger sample liquefaction, a is the test parameter. The fitting results are shown in **Table. 2**.

DISCUSSION

Previous studies have attributed the soils liquefaction to the movement and rearrangement of grains (Lade and Yamamuro, 1997; Ovando-Shelley and Perez, 1997; Yamamuro and Covert, 2001). Afterwards, it is recognized that for loose sandy soils, the generation of pore-water pressure is mainly caused by the movement and rearrangement of grains, while in medium to dense sandy soils, and the generation of pore-water pressure is mainly due to grain crushing (Wang and Sassa, 2000; Wang and

Sassa, 2002; Fukuoka et al., 2007). In addition, grain crushing susceptibility varies significantly for different materials. Under shear loading, siliceous sands exhibit shear dilatancy behavior due to low grain crushing susceptibility. Weathered granite sand with short transport distance exhibits a high susceptibility to grain crushing. Thus weathered dense granite sand properties under shear loading undergo three stages, 1) initial negative dilatancy due to grain movement and rearrangement, 2) dilatancy, and 3) negative dilatancy due to grain crushing (Wang and Sassa, 2000). The bedding fault of the DGB landslide is composed of special geological materials, which is formed by dolomite subjected to long-term tectonic shear and compression, so its structure is poor (Cui et al., 2021). In addition, the material grains are filled with a large amount of calcareous and argillaceous cementations, and the strength of these cementations is lower than the dolomite (Zhu et al., 2019) (**Figures 13A,B**). Therefore, for these special materials, it is noted that a special liquefaction mechanism of the bedding fault materials under cyclic loading, that is, liquefaction caused by cementation breakage. Under cyclic loading, when the cyclic loading exceeds the strength of the cementation, the grain crushing occurs, resulting in a reduction of the volume, so that the load originally borne by the particle skeleton is borne by the pore water, resulting in a rise in the pore-water pressure, and as illustrated in **Figure 14**. The low-strength calcareous and argillaceous cementations are easily broken by cyclic loading, thus this special material is more prone to occur in grain crushing than conventional soil. The pore-water pressure rise in the bedding fault caused by grain crushing plays a major role due to the high grain crushing susceptibility.

CONCLUSION

The tests on bedding fault material shows that the pore-water pressure increases rapidly during cyclic loading, and the carbonate fault materials have a high liquefaction potential. Frequency has little effect on the generation of the pore-water pressure. The higher cyclic shear stress ratio accelerates the generation of the pore-water pressure, while the higher confining pressure increases liquefaction resistance. Frequency and cyclic shear stress ratio have little effect on the total dissipated energy required to trigger liquefaction, while the confining pressure has a significant effect. We establish an energy-based pore-water pressure model of carbonate fault materials considering the effect of frequency, cyclic shear stress ratio and confining pressure.

DATA AVAILABILITY STATEMENT

The original contributions presented in the study are included in the article/Supplementary Material, further inquiries can be directed to the corresponding authors.

AUTHOR CONTRIBUTIONS

LZ designed the conceptualization, methodology, data curation, and original draft preparation. QY performed data curation and formal analysis. LL was responsible for data curation and Language. SC designed the methodology.

FUNDING

This study was financially sponsored by the National Natural Science Foundation of China (Grant Nos. 41931296), the National Key R&D Program of China (No. 2017YFC1501002) and the National Nature Science Foundation of China (Grant Nos. 41907254 and 41521002).

REFERENCES

Azeiteiro, R. J. N., Coelho, P. A. L. F., Taborda, D. M. G., and Grazina, J. C. D. (2017). Energy-based Evaluation of Liquefaction Potential under Non-uniform Cyclic Loading. *Soil Dyn. Earthquake Eng.* 92, 650–665. doi:10.1016/j.soildyn.2016.11.005

Balreddy, M. S., Dinesh, S. V., and Sitharam, T. G. (2019). "Effect of Fines on Pore Pressure Development during Cyclic Loading," in *Soil Dynamics and Earthquake Geotechnical Engineering* (Singapore: Springer), 83–90. doi:10.1007/978-981-13-0562-7_10

Chang, C. S., Kuo, C. L., and Selig, E. T. (1983). Pore Pressure Development during Cyclic Loading. *J. Geotechnical Eng.* 109 (1), 103–107. doi:10.1061/(asce)0733-9410(1983)109:1(103)

Charlie, W. A., Veyera, G. E., and Doehring, D. O. (1989). Dilatational-wave-induced Pore-Water Pressure in Soil. *Exp. Mech.* 29 (4), 437–442. doi:10.1007/bf02323864

Chen, G., Zhao, D., Chen, W., and Juang, C. H. (2019). Excess Pore-Water Pressure Generation in Cyclic Undrained Testing. *J. Geotech. Geoenviron. Eng.* 145 (7), 04019022. doi:10.1061/(asce)gt.1943-5606.0002057

Chen, Y.-R., Chen, J.-W., Hsieh, S.-C., and Chang, Y.-T. (2013). Evaluation of Soil Liquefaction Potential Based on the Nonlinear Energy Dissipation Principles. *J. Earthquake Eng.* 17 (1), 54–72. doi:10.1080/13632469.2012.691256

Cui, S., Pei, X., and Huang, R. (2018). Effects of Geological and Tectonic Characteristics on the Earthquake-Triggered Daguangbao Landslide, China. *Landslides* 15 (4), 649–667. doi:10.1007/s10346-017-0899-3

Cui, S., Pei, X., Jiang, Y., Wang, G., Fan, X., Yang, Q., et al. (2021). Liquefaction within a Bedding Fault: Understanding the Initiation and Movement of the Daguangbao Landslide Triggered by the 2008 Wenchuan Earthquake (Ms = 8.0). *Eng. Geology* 295, 106455. doi:10.1016/j.enggeo.2021.106455

Cui, S., Wang, G., Pei, X., Huang, R., and Kamai, T. (2017). On the Initiation and Movement Mechanisms of a Catastrophic Landslide Triggered by the 2008 Wenchuan (Ms 8.0) Earthquake in the Epicenter Area. *Landslides* 14 (3), 805–819. doi:10.1007/s10346-016-0754-y

Cui, S., Yang, Q., Pei, X., Huang, R., Guo, B., and Zhang, W. (2020). Geological and Morphological Study of the Daguangbao Landslide Triggered by the Ms. 8.0 Wenchuan Earthquake, China. *Geomorphology* 370, 107394. doi:10.1016/j.geomorph.2020.107394

Fan, W., Lv, J., Cao, Y., Shen, M., Deng, L., and Wei, Y. (2019). Characteristics and Block Kinematics of a Fault-Related Landslide in the Qinba Mountains, Western China. *Eng. Geology* 249, 162–171. doi:10.1016/j.enggeo.2018.12.019

Fardad Amini, P., and Noorzad, R. (2018). Energy-based Evaluation of Liquefaction of Fiber-Reinforced Sand Using Cyclic Triaxial Testing. *Soil Dyn. Earthquake Eng.* 104, 45–53. doi:10.1016/j.soildyn.2017.09.026

Fukuoka, H., Sassa, K., and Wang, G. (2007). Influence of Shear Speed and normal Stress on the Shear Behavior and Shear Zone Structure of Granular Materials in

Naturally Drained Ring Shear Tests. *Landslides* 4 (1), 63–74. doi:10.1007/s10346-006-0053-0

Hazirbaba, K., and Rathje, E. M. (2009). Pore Pressure Generation of Silty Sands Due to Induced Cyclic Shear Strains. *J. Geotech. Geoenviron. Eng.* 135 (12), 1892–1905. doi:10.1061/(asce)gt.1943-5606.0000147

He, G., and Cao, Y. (1990). Fundamentals and Applications of the Energy Method in Soil Dynamics. *China Civil Eng. J.* 23 (3), 2–10. (In Chinese).

Huang, R., Pei, X., Fan, X., Zhang, W., Li, S., and Li, B. (2012). The Characteristics and Failure Mechanism of the Largest Landslide Triggered by the Wenchuan Earthquake, May 12, 2008, China. *Landslides* 9 (1), 131–142. doi:10.1007/s10346-011-0276-6

Javdanian, H. (2019). Evaluation of Soil Liquefaction Potential Using Energy Approach: Experimental and Statistical Investigation. *Bull. Eng. Geol. Environ.* 78 (3), 1697–1708. doi:10.1007/s10064-017-1201-6

Javdanian, H., Heidari, A., and Kamgar, R. (2017). Energy-based Estimation of Soil Liquefaction Potential Using GMDH Algorithm. *Iran J. Sci. Technol. Trans. Civ. Eng.* 41 (3), 283–295. doi:10.1007/s40996-017-0061-4

Kuenza, K., Towhata, I., Orense, R. P., and Wassan, T. H. (2004). Undrained Torsional Shear Tests on Gravelly Soils. *Landslides* 1 (3), 185–194. doi:10.1007/s10346-004-0023-3

Lade, P. V., and Yamamuro, J. A. (1997). Effects of Nonplastic Fines on Static Liquefaction of Sands. *Can. Geotech. J.* 34 (6), 918–928. doi:10.1139/t97-052

Liu, G., Rong, G., Peng, J., and Zhou, C. (2015). Numerical Simulation on Undrained Triaxial Behavior of Saturated Soil by a Fluid Coupled-DEM Model. *Eng. Geology* 193, 256–266. doi:10.1016/j.enggeo.2015.04.019

Mitchell, R. J., and Dubin, B. I. (1986). Pore Pressure Generation and Dissipation in Dense Sands under Cyclic Loading. *Can. Geotech. J.* 23 (3), 393–398. doi:10.1139/t86-055

Ni, X., Ye, B., Cheng, Z., and Ye, G. (2020). Evaluation of the Effects of Initial Deviatoric Stress and Cyclic Stress Amplitude on Liquefaction Potential of Loose and Medium-Dense Sands: An Energy-Based Method. *Soil Dyn. Earthquake Eng.* 136, 106236. doi:10.1016/j.soildyn.2020.106236

Ovando-Shelley, E., and Pérez, B. E. (1997). Undrained Behaviour of Clayey Sands in Load Controlled Triaxial Tests. *Géotechnique* 47 (1), 97–111. doi:10.1680/geot.1997.47.1.97

Pan, K., and Yang, Z. X. (2018). Effects of Initial Static Shear on Cyclic Resistance and Pore Pressure Generation of Saturated Sand. *Acta Geotechnica* 13 (2), 473–487.

Pan, K., and Yang, Z. X. (2020). Evaluation of the Liquefaction Potential of Sand under Random Loading Conditions: Equivalent Approach versus Energy-Based Method. *J. Earthquake Eng.* 24 (1), 59–83. doi:10.1080/13632469.2017.1398693

Pei, X. J., Cui, S. H., and Huang, R. Q. (2018). A Model of Initiation of Daguangbao Landslide: Dynamic Dilation and Water Hammer in Sliding Zone during strong Seismic Shaking. *Chin. J. Rock Mech. Eng.* 37 (2), 430–448. (In Chinese).

Pei, X., Zhang, X., Guo, B., Wang, G., and Zhang, F. (2017). Experimental Case Study of Seismically Induced Loess Liquefaction and Landslide. *Eng. Geology* 223, 23–30. doi:10.1016/j.enggeo.2017.03.016

Polito, C., Green, R. A., Dillon, E., and Sohn, C. (2013). Effect of Load Shape on Relationship between Dissipated Energy and Residual Excess Pore Pressure Generation in Cyclic Triaxial Tests. *Can. Geotech. J.* 50 (11), 1118–1128. doi:10.1139/cgj-2012-0379

Polito, C. P., Green, R. A., and Lee, J. (2008). Pore Pressure Generation Models for Sands and Silty Soils Subjected to Cyclic Loading. *J. Geotech. Geoenviron. Eng.* 134 (10), 1490–1500. doi:10.1061/(asce)1090-0241(2008)134:10(1490)

Seed, H. B., Martin, P. P., and Lysmer, J. (1976). Pore-water Pressure Changes during Soil Liquefaction. *J. Geotech. Engrg. Div.* 102 (4), 323–346. doi:10.1061/ajgeb6.0000258

Shan, Y., Meng, Q., Yu, S., Mo, H., and Li, Y. (2020). Energy Based Cyclic Strength for the Influence of mineral Composition on Artificial marine clay. *Eng. Geology* 274, 105713. doi:10.1016/j.enggeo.2020.105713

Sitharam, T. G., and Govindaraju, L. (2007). Pore Pressure Generation in Silty Sands during Cyclic Loading. *Geomechanics and Geoengineering* 2 (4), 295–306. doi:10.1080/17486020701670460

Skempton, A. W. (1954). The Pore-Pressure Coefficients A and B. *Géotechnique* 4 (4), 143–147. doi:10.1680/geot.1954.4.4.143

Tokimatsu, K., Yoshimi, Y., and Ariizumi, K. (1990). Evaluation of Liquefaction Resistance of Sand Improved by Deep Vibratory Compaction. *Soils and Foundations* 30 (3), 153–158. doi:10.3208/sandf1972.30.3_153

Wang, B., Chen, G., and Jin, D. (2010). Pore Water Pressure Increment Model for Saturated Nanjing fine Sand Subject to Cyclic Loading. *Earthq. Eng. Eng. Vib.* 9 (4), 569–576. doi:10.1007/s11803-010-0038-9

Wang, F., and Sassa, K. (2000). Relationship between Grain Crushing and Excess Pore Pressure Generation by sandy Soils in Ring-Shear Tests. *J. Nat. Disaster Sci.* 22 (2), 87–96. doi:10.2328/jnds.22.87

Wang, G., Huang, R., Lourenço, S. D. N., and Kamai, T. (2014). A Large Landslide Triggered by the 2008 Wenchuan (M8.0) Earthquake in Donghekou Area: Phenomena and Mechanisms. *Eng. Geology* 182, 148–157. doi:10.1016/j.enggeo.2014.07.013

Wang, G., and Sassa, K. (2002). Post-failure Mobility of Saturated Sands in Undrained Load-Controlled Ring Shear Tests. *Can. Geotech. J.* 39 (4), 821–837. doi:10.1139/t02-032

Wang, J., Guo, L., Cai, Y., Xu, C., and Gu, C. (2013). Strain and Pore Pressure Development on Soft marine clay in Triaxial Tests with a Large Number of Cycles. *Ocean Eng.* 74, 125–132. doi:10.1016/j.oceaneng.2013.10.005

Wang, S. (2009). Geological Nature of Rock and its Deduction for Rock Mechanics. *Chin. J. Rock Mech. Eng.* 28 (3), 433–450. (In Chinese).

Wang, W. N., Chigira, M., and Furuya, T. (2003). Geological and Geomorphological Precursors of the Chiu-Fen-Erh-Shan Landslide Triggered by the Chi-Chi Earthquake in central Taiwan. *Eng. Geology* 69 (1-2), 1–13. doi:10.1016/s0013-7952(02)00244-2

Xu, Q., Zhang, S., and Li, W. (2011). Spatial Distribution of Large-Scale Landslides Induced by the 5.12 Wenchuan Earthquake. *J. Mt. Sci.* 8 (2), 246–260. doi:10.1007/s11629-011-2105-8

Yamamuro, J. A., and Covert, K. M. (2001). Monotonic and Cyclic Liquefaction of Very Loose Sands with High silt Content. *J. Geotech. Geoenviron. Eng.* 127 (4), 314–324. doi:10.1061/(asce)1090-0241(2001)127:4(314)

Yang, Z. X., and Pan, K. (2018). Energy-based Approach to Quantify Cyclic Resistance and Pore Pressure Generation in Anisotropically Consolidated Sand. *J. Mater. Civ. Eng.* 30 (9), 04018203. doi:10.1061/(asce)mt.1943-5533.0002419

Zhang, H., Zhang, J., Zhang, Z., Zhang, M., and Cao, W. (2020). Variation Behavior of Pore-Water Pressure in Warm Frozen Soil under Load and its Relation to Deformation. *Acta Geotech.* 15 (3), 603–614. doi:10.1007/s11440-018-0736-4

Zhu, L., Cui, S., Pei, X., Zhang, X., Wang, H., He, S., et al. (2022). Investigation of the Characteristics and Long-Runout Movement Mechanisms of the Luanshibao Landslide on the Eastern Margin of the Qinghai-Tibet Plateau. *Soil Dyn. Earthquake Eng.* 153, 107094. doi:10.1016/j.soildyn.2021.107094

Zhu, L., Pei, X., Cui, S., Liang, Y., and Luo, L. (2019). Experimental Study on Dynamic Damage and Strength Characteristics of Rock with Vein Mass. *Chin. J. Rock Mech. Eng.* 38 (05), 900–911. (In Chinese).

Conflict of Interest: The authors declare that the research was conducted in the absence of any commercial or financial relationships that could be construed as a potential conflict of interest.

Publisher's Note: All claims expressed in this article are solely those of the authors and do not necessarily represent those of their affiliated organizations, or those of the publisher, the editors and the reviewers. Any product that may be evaluated in this article, or claim that may be made by its manufacturer, is not guaranteed or endorsed by the publisher.

Copyright © 2022 Zhu, Yang, Luo and Cui. This is an open-access article distributed under the terms of the Creative Commons Attribution License (CC BY). The use, distribution or reproduction in other forums is permitted, provided the original author(s) and the copyright owner(s) are credited and that the original publication in this journal is cited, in accordance with accepted academic practice. No use, distribution or reproduction is permitted which does not comply with these terms.

frontiers | Frontiers in Earth Science

ORIGINAL RESEARCH
published: 05 April 2022
doi: 10.3389/feart.2022.880692

Quantitative Evaluation of Coseismic Deformations Induced by Seismogenic Faulting in Mining Exploration Area During the 2018 Xingwen and 2019 Changning Earthquakes, Sichuan, China

Chunwei Sun[1], Sixiang Ling[1], Siyuan Zhao[2], Hong Wen[1] and Sen Wang[1]*

[1]Faculty of Geosciences and Environmental Engineering, Southwest Jiaotong University, Chengdu, China, [2]State Key Laboratory of Hydraulics and Mountain River Engineering, College of Water Resources and Hydropower, Sichuan University, Chengdu, China

OPEN ACCESS

Edited by:
Xiangjun Pei,
Chengdu University of Technology, China

Reviewed by:
Jing Luo,
Northwest Institute of Eco-Environment and Resources (CAS), China
Zain Maqsood,
National University of Sciences and Technology (NUST), Pakistan
Dao-Yuan Tan,
Hong Kong Polytechnic University, Hong Kong SAR, China

***Correspondence:**
Siyuan Zhao
zhaosiyuan@scu.edu.cn

Specialty section:
This article was submitted to Geohazards and Georisks, a section of the journal Frontiers in Earth Science

Received: *21 February 2022*
Accepted: *17 March 2022*
Published: *05 April 2022*

Citation:
Sun C, Ling S, Zhao S, Wen H and Wang S (2022) Quantitative Evaluation of Coseismic Deformations Induced by Seismogenic Faulting in Mining Exploration Area During the 2018 Xingwen and 2019 Changning Earthquakes, Sichuan, China. Front. Earth Sci. 10:880692. doi: 10.3389/feart.2022.880692

In the period between December 2018 and July 2019, a series of earthquakes (EQs), including the 16 December 2018 Ms 5.7 Xingwen mainshock and the 17 June 2019 Ms 6.0 Changning mainshock, struck the Changning shale gas exploration field in the southern margin of the Sichuan Basin. The Xingwen and Changning EQs both occurred on concealed faults, which led to hundreds of casualties, and affected a total of over 160 thousand people in southern Sichuan. The aftershock sequences following the Xingwen and Changning EQs were clustered in the vicinity of the Jianwu syncline and Changning anticline, respectively, and occurred mostly at depths of 3–7 km. In this study, coseismic surface deformation measurements obtained through differential interferometric synthetic aperture radar (D-InSAR) data were used to identify the faulting geometries and distributions. The coseismic deformation maps have maximum line-of-sight (LOS) displacements of ~4.53 cm on the northwest side of the Xingwen EQ source fault and ~7.84 cm on the southwest side of the Changning EQ source fault. The calculated static Coulomb stress changes indicated that most aftershocks occurred in increasing stress zones following the mainshock ruptures. From the InSAR deformation field, a complicated concealed seismogenic doublet fault was inferred, which predominately exhibited left-lateral strike-slip motion during the Xingwen and Changning EQs. The footwall ramp of the basement fault reactivated first, and resulted in the Xingwen EQ and concentrating stresses beneath the Changning anticline, which induced the Changning EQ half a year later. Compared with previous studies, we proposed that the fault network was lubricated by water that was injected during shale gas exploration, facilitating the occurrence of the Xingwen and Changning EQs. Such work evaluated the coseismic deformations of the Xingwen and Changning EQs, and derived the regional faulting distribution from aftershock sequences. It could provide useful information for monitoring and analyzing seismic activity around the hinge zones of folds in mining exploration areas, which contributes to effective risk assessment of disasters associated with seismic geo-environments.

Keywords: eathquake, coseismic deformation, mining exploration area, D-InSAR, seismogenic fault

INTRODUCTION

In the period between December 2018 and July 2019, two major earthquakes (EQs) with aftershocks, namely, the Xingwen and Changning EQs, struck southern Yibin city, Sichuan Province, where is situated in the southern margin of the Sichuan Basin (**Figure 1A**; **Table 1**). The magnitudes Ms of the mainshocks were 5.7 and 6.0, respectively. China Earthquake Networks Centre (https://data.earthquake.cn) recorded 10 Ms > 3 aftershocks (the largest is a Ms 5.3 event) followed the Xingwen EQ, and 68 Ms > 3 aftershocks (the largest is a Ms 5. 3 event) followed the Changning EQ. Preliminary teleseismic waveform analyses suggested that the rupture processes responsible for the Xingwen and Changning EQs occurred on concealed strike-slip faults (e.g., Yi et al., 2019; Yin et al., 2019; Liu and Zahradník, 2020). On the other hand, previous studies performed on the Changning-Gongxian region and around Yibin city have revealed earthquakes induced by water injection (e.g., Sun et al., 2017; Lei et al., 2017; Lei et al., 2019a), seismic hazards triggered by hydraulic fracturing (e.g.,

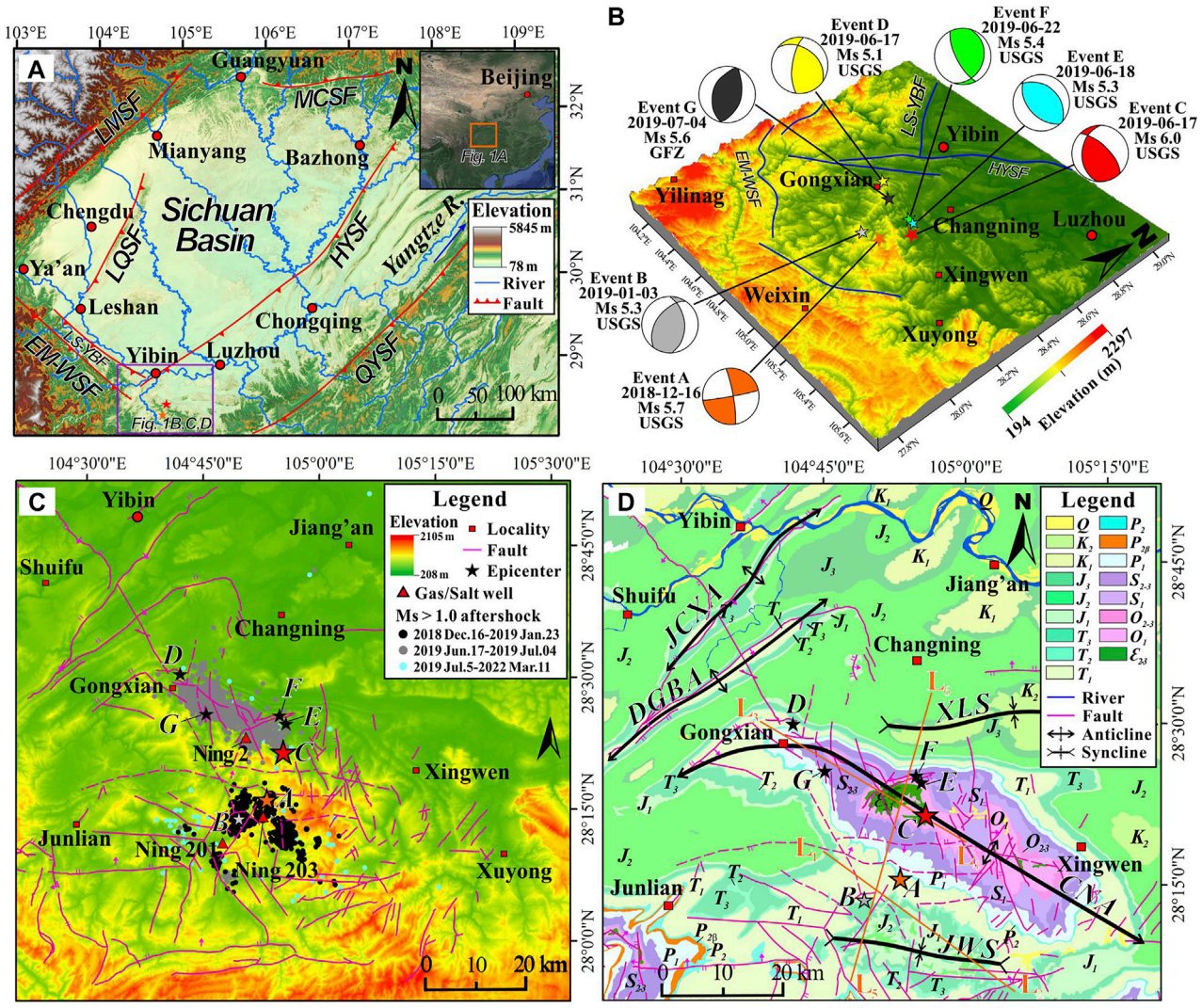


FIGURE 1 | (A) Simplified topographical and tectonic map of the Sichuan Basin. *MCSF*: Micangshan fault; *LMSF*: Longmenshan fault; *LQSF*: Longquanshan fault; *HYSF*: Huayingshan fault; *QYSF*: Qiyaoshan fault; *EM-WSF*: Emei-Washan fault; *LS-YBF*: Leshan-Yibin fault. **(B)** Topographic map and focal mechanism solutions of the Ms 5.7 Xingwen mainshock (Event A, orange star) with its largest aftershock (Event B, grey star) and the Ms 6.0 Changning mainshock (Event C, red star) with its Ms > 5.0 aftershocks (Events D-G, other stars). **(C)** Topography and EQ information with faults in the study area. Stars indicate the epicenters of Events A-G. The dark, gey, and light blue dots refer to the Ms > 1.0 aftershocks (Lei et al., 2019a; Hu et al., 2020; Long et al., 2020; CENC, 2022). Fault data are derived from a 1:200,000 geological map and Long et al. (2020). **(D)** Geological map. CNA, Changning anticline; DGBA, Dengganba anticline; JCXA, Jiacunxi anticline; JWS, Jianwu syncline; XLS, Xiangling syncline. Q, Quaternary; K_2, Upper Cretaceous; K_1, Lower Cretaceous; J_3, Upper Jurassic; J_2, Middle Jurassic; J_1, Lower Jurassic; T_3, Upper Triassic; T_2, Middle Triassic; T_1, Lower Triassic; P_2, Upper Permian; $P_{2\beta}$, Upper Permian Emeishan basalt; P_1, Lower Permian; $S_{2\text{-}3}$, Middle to Upper Silurian; S_1, Lower Silurian; $O_{2\text{-}3}$, Middle to Upper Ordovician; O_1, Lower Ordovician; $\epsilon_{2\text{-}3}$, Middle to Upper Cambrian. Profiles L_1–L_2 and L_3–L_4 are displayed in **Figure 6**, and Profile L_5–L_6 is displayed in **Figure 7**.

TABLE 1 | Earthquake parameters that were used in this study.

Event	EQ name	Ms	Shock	Date (yy-mm-dd)	Time (UTC+8)	Latitude (°)	Longitude (°)	Depth (km)
A	"12.16" Xingwen EQ	5.7	Mainshock	2018-12-16	12:46:07	N28.24	E104.92	12
B	"1.3" Gongxian EQ	5.3	Afterschock	2019-01-03	08:48:06	N28.20	E104.86	15
C	"6.17" Changning EQ	6.0	Mainshock	2019-06-17	22:55:43	N28.34	E104.96	10[a]
D	"6.17" Gongxian EQ	5.1	Afterschock	2019-06-17	23:36:01	N28.47	E104.72	11.5[a]
E	"6.18" Changning EQ	5.3	Afterschock	2019-06-18	07:34:33	N28.39	E104.95	10[a]
F	"6.22" Gongxian EQ	5.5	Afterschock	2019-06-22	22:29:56	N28.40	E104.94	10
G	"7.4" Gongxian EQ	5.6	Afterschock	2019-07-04	10:17:58	N28.40	E104.78	8

Note: The data are quoted from China Earthquake Networks Center (CENC, 2022).
[a]These depths are from German Research Centre for Geosciences (GFZ). Ms is the surface wave magnitude.

TABLE 2 | Focal mechanism solutions for "12.16" Xingwen and "6.17" Changning EQs.

EQs	Source	Magnitude	Depth (km)	Fault plane 1			Fault plane 2		
				Strike (°)	Dip (°)	Rake (°)	Strike (°)	Dip (°)	Rake (°)
Xingwen	USGS[a]	Mw 5.3	17.5	80	87	−173	349	83	−3
	GFZ[b]	Mw 5.3	26	246	70	−166	359	77	−21
	Yi[c]	Ms 5.7	3	80	85	−166	349	76	−5
Changning	USGS[a]	Mw 5.8	11.5	314	65	62	185	37	135
	GFZ[b]	Mw 5.8	10	315	61	53	192	46	137
	Yi[c]	Ms 6.0	3	131	51	36	16	63	135
	HU[d]	Mw 5.7	12	323	57	65	184	40	123

[a]USGS, United States Geological Survey
[b]GFZ, German Research Centre for Geosciences
[c]Yi = Yi et al. (2019)
[d]HU, Harvard University
Mw is the moment magnitude; Ms is the surface wave magnitude.

Hu et al., 2018; He et al., 2019) and the three-dimensional velocity structure and faulting styles (e.g., Lei et al., 2019b; Liu and Zahradník, 2020; Long et al., 2020). The focal mechanism solutions for the Xingwen and Changning EQs, each of which produced a series of Ms > 5.0 aftershocks (**Figure 1B**), were provided from the U.S. Geological Survey (abbr. USGS) and the German Research Centre for Geosciences (abbr. GFZ) (**Table 2**). However, the seismogenic faults responsible for these two major EQs have not been identified or studied in detail. Field investigations were carried out immediately after the Xingwen and Changning EQs, but no obvious surface ruptures were found. Owing to the complex topography and dense coverage of vegetation in the EQ-impacted source regions, it is difficult to determine the geometric and kinematic characteristics of the seismogenic faults, and their relationships with nearby active faults is unknow. These problems constitute great significance for understanding the tectonic activity and seismogenic trends in this region, which would be helpful for preventing and controlling coseismic geo-hazards in the southern margin of the Sichuan Basin.

Fortunately, the interferometric synthetic aperture radar (InSAR) deformation fields produced by the Xingwen and Changning EQs are highly beneficial for a better understanding the motions and properties of the seismogenic faults. The two major EQs with a series of Ms >5.0 aftershocks thereby provide a good opportunity to study the seismic activity of the region and the relationship between seismogenic fault and coseismic deformation in the southern margin of the Sichuan Basin. In this particular case, the InSAR analysis is highly helpful to obtain the coseismic displacement field, that will improve our understanding of faulting in the region. The InSAR technique has been extensively and successfully applied to determine the coseismic displacements of EQs, especially megathrust EQs (Simons et al., 2002; Biggs et al., 2006; Zuo et al., 2016; Wang et al., 2017; Zhao et al., 2018). Meanwhile, differential interferometric synthetic aperture radar (D-InSAR), based on radar satellite synthetic aperture radar (SAR) imagery, has emerged as an indispensable tool to measure the millimetre-scale deformation of the Earth's surface (Stramondo et al., 2011; Syahreza et al., 2018) produced by a wide variety of natural phenomena, such as earthquakes, volcanic eruptions, land subsidence (Bonì et al., 2017; Aguirre et al., 2018; Sarychikhina et al., 2018; Zhao et al., 2018; Su et al., 2019), ice sheet and glacier movements (Liao et al., 2018), and landslides (Raspini et al., 2017; Carlà et al., 2019). Regional-scale surface deformation can be measured by D-InSAR technique with a high

sensitivity, which is useful to detect coseismic deformation generated by concealed seismogenic faulting.

In this study, the ascending InSAR observations was used to provide robust constraints on the location of the seismogenic fault and coseismic deformation, from which we can deduce the mechanisms of seismogenic faults. We first described the regional faults, including the Mabian-Yanjian fault, the Zhaotong-Lianfeng fault, and the Huayingshan fault (**Figure 1A**), in the Yibin region. Then, two pairs of ascending orbit Sentinel-1A (S1A) SAR images covering the periods of Xingwen and Changning EQs occurrence were used for D-InSAR processing. The coseismic deformation and seismogenic faults were analyzed, and a geostructural model with an EQ sequence was proposed. This study aspires to achieve three objectives: 1) to explore the coseismic surface deformation generated by the Xingwen and Changning EQs, 2) to characterize the seismogenic faults for the two EQs, and 3) to reveal the regional kinematics of these seismogenic faults and their tectonic implications from the perspective of a geostructural model with an EQ sequence. The study region could present a case study of the seismogenic mechanism responsible for earthquakes with magnitudes less than 6.0 that frequently occur within the subparallel EW-trending Yunnan-Guizhou fold belt in the southern margin of the Sichuan Basin. This investigation could thereby provide information crucial for ascertaining that the Xingwen and Changning EQ sequences in the Jianwu syncline and the Changning anticline were probably caused by long-term hydraulic fracturing.

GEOLOGICAL AND EARTHQUAKE SETTINGS

Regional Geology

A concentrated series of earthquake events struck Changning, Gongxian, and Xingwen Counties, which are situated approximately 5–10 km SE of Yibin city, between December 2018 and July 2019 (**Figures 1A,B**; **Table 1**). Tectonically, the study area is situated in the transition zone (i.e., the junction) between the Sichuan Basin in the upper Yangtze quasi-Platform and the Yunnan-Guizhou fold belt, which is located in the southern margin of the Sichuan Basin (**Figure 1A**; Sun et al., 2017). Structurally, regional faults are well developed and are characterized by the dominant NE-trending Huayingshan fault zone, the NW-trending Emei-Washan fault zone, and the NW-trending Leshan-Yibin fault. In particular, the study area is located in the southern junction between the Huayingshan and Emei-Washan fault zones (**Figures 1A,B**).

The study region is nestled atop a tectonic alpine landform with an elevation ranging from 208 to 2,105 m above sea level (**Figure 1C**). This region is dominated by the Triassic and Cretaceous sedimentary rocks, with a few units from the Cambrian, Ordovician, Silurian, and Permian periods (**Figure 1D**). The Silurian, Jurassic and Cretaceous strata mainly consist of sandstone and siltstone interlayered with mudstone. The Triassic outcrops comprise sandstone with shale (T_3), limestone and dolomite (T_2), and siltstone, flysch layers of mudstone, shale and sandstone (T_1). The Cambrian, Ordovician, and Permian outcrops are composed mostly of limestone and dolomite interlayered with shale, sandstone, or siltstone, while the upper Permian stratum includes the Emeishan basalt ($P_{2\beta}$). The crystalline basement of the Sichuan Basin is roughly bounded by the Huayingshan fault zone (Li et al., 2015). The basement comprises rigid granite in the west at depths of 3–6 km and weakly metamorphosed rocks (which are relatively plastic) in the east at depths of 6–9 km (Zhou et al., 1997). The basement depth in the northeastern Yibin area ranges from 7.0 to 13.0 km, while that of southwestern Yibin is less than 5.0 km, reflecting a slope of the crystalline basement (Li et al., 2018; Wang et al., 2018b). The geological structures in the study area exhibits numerous anticlines (i.e., the Jiacunxi, Dengganba, and Changning anticlines) in addition to the Jianwu and Xiangling synclines (**Figure 1D**). The Changning anticline, which trends NW-SE, extends through Gongxian in the NW to the Xuyong area in the SE. The core of the Changning anticline exposes the Cambrian system, and the surrounding strata successively expose the Ordovician, Silurian, Permian, Triassic, and Jurassic; in the south, the Jianwu syncline is exposed with the Jurassic constituting its core strata (**Figure 1D**). The study area boasts abundant shale gas resources (e.g., Ning 201, Ning 203, shown in **Figure 1C**) in the Changning shale gas field and salt mine (e.g., Ning 2, shown in **Figure 1C**), and these resources are widely exploited by hydraulic fracturing through the water injection method (Sun et al., 2017; Lei et al., 2017, 2019).

Earthquake Setting

Two major EQs struck southern Yibin city between December 2018 and July 2019, resulting in a series of aftershocks (Ms > 5) that affected the entire study area (**Figures 1B,C**), as described in **Table 1**. The first mainshock occurred at 12:46 p.m. local time on 16 December 2018 with a magnitude of Ms 5.7, which resulted in a seismic intensity of VII on the Modified Mercalli scale (CENC, 2022). Its epicenter was located at 28.24°N, 104.92°E (Xingwen County) with a focal depth of 12 km; this event is known as the "12.16" Xingwen EQ (Event A, **Table 1**; **Figures 1B–D**). The "12.16" Xingwen EQ caused damage to more than 500 buildings and 17 injuries (CENC, 2022), and an aftershock occurred on 3 January 2019 with a magnitude of Ms 5.3 (Event B, **Table 1**; **Figures 1B–D**). The Xingwen EQ occurred on a fault located between the Changning anticline and Jianwu syncline, while the aftershocks were located primarily to the south of the Xingwen mainshock and around the Jianwu syncline (**Figures 1C,D**).

The second mainshock occurred at 22:53 p.m. local time on 17 June 2019 with a magnitude of Ms 6.0, which resulted in a seismic intensity of VIII on the Modified Mercalli scale (CENC, 2022). Its epicenter was located at 28.34°N, 104.96°E (Changning County) with a focal depth of 10 km; this event is known as the "6.17" Changning EQ (Event C, **Table 1**; **Figures 1B–D**). The "6.17" Changning EQ caused damage to more than 1,000 buildings, took the lives of 13 people, and injured 226 others (CENC, 2022). The epicenter of the "6.17" Changning mainshock was approximately 15 km from the mainshock of the "12.16" Ms 5.7 Xingwen EQ. Four of the aftershocks, which all had magnitudes greater than 5 (Ms 5.1, Ms 5.3, Ms 5.4, and Ms 5.6 in chronological order),

TABLE 3 | Parameters of the Sentinel-1A pairs that were used in this study (A is ascending orbit).

No.	Acquisition time	Path No.	Azi. angle	Perp.B(m)	Incidence (°)	EQ event
Xingwen EQ	20181204-20181216	128 (A)	−168.13	10	43.92	A
Channing EQ	20190609-20190621	55 (A)	−167.44	11	33.90	C/D/E

occurred from 17 June to 4 July 2019 (Events D, E, F and G, respectively, **Table 1**; **Figures 1B–D**). The epicenter of the Changning EQ mainshock and its aftershocks were located mostly within the Changning anticline (**Figure 1D**).

MATERIALS AND METHODS

InSAR Data

The coseismic deformation field is fundamental for analyzing the intensity and seismogenic mechanism of an earthquake. However, the low number of ground GPS stations deployed in the Yibin area has heretofore made it difficult to measure the coseismic deformation field by conventional crustal deformation observation techniques (e.g., Simons et al., 2002; Anzidi et al., 2009). Therefore, SAR images have become important data for deriving the coseismic deformation field. To isolate the coseismic surface deformation induced by a series of EQs in the Yibin area, we used SAR data acquired before and after the two events by the Sentinel-1A (S1A) satellite. S1A carries a C-band microwave sensor that runs in Terrain Observation by Progressive Scans (TOPS) mode and boasts a large spatial coverage (i.e., 250 km) with a repeat time of 12 days (Attema et al., 2008; Geudtner et al., 2014). S1A SAR data have been extensively applied to monitor coseismic deformation fields with a short revisit period, a high orbit accuracy, and high-altitude interferograms in vegetation-covered areas (e.g., Zuo et al., 2016; Zhao et al., 2018; Kovács et al., 2019). We downloaded S1A SAR images covering the entire study area acquired before and after the EQs for the analysis. Field investigations suggested that the rupture did not break the surface, and descending orbit data are characterized by low-quality observations; thus ascending data are more suitable for this task (e.g., Zhao et al., 2018). Therefore, two pairs of ascending orbit S1A single look complex (SLC) images were employed to constrain the coseismic deformation of the Xingwen and Changning EQs. The detailed parameters of the S1A data were described in **Table 3**. The SLC images were all produced in Interferometric Wide (IW) swath mode. The pixel spacing in the slant range and azimuth directions are 2.33 and 13.93 m, respectively.

Interferogram Processing

The traditional two-pass differential interferometric method with the burst-by-burst processing approach was used to process the S1A SAR images before and after each EQ, from which the interferometric phase could be obtained (e.g., Hanssen, 2001). First, SLC bursts were co-registered using precise orbit data in conjunction with 30-m resolution digital elevation model (DEM) data taken from the Advanced Land Observing Satellite digital surface model (ALOS DSM) AW3D30 (https://www.eorc.jaxa.jp/ALOS/en/aw3d30). Using the same DEM covering the study area to remove the residual topographic component, D-InSAR interferograms were calculated for each burst with multilook factors of 2.33 and 13.93 m pixels in the azimuth and range directions, respectively. Third, using the enhanced spectral diversity method, which is often applied for along-track interferometry in regions where successive bursts overlap in the azimuth direction, the residual azimuth phase ramp (attributable to possible azimuth mis-registration) was compensated. Finally, we projected the unwrapped 30-m-resolution data from the satellite azimuth, and calculated the deformation values for the investigated areas, with the range coordinate converted into Universal Transverse Mercator (UTM) coordinates (e.g., He et al., 2018). In addition, to obtain a better deformation phase, the phase effects caused by errors due to thermal and atmospheric noise and orbit errors were removed (e.g., Goldstein and Werner, 1998; Hanssen, 2001; Liu et al., 2016).

Coulomb Failure Stress Calculation

The static Coulomb failure stress (CFS) change induced by an EQ was used to assess the potential of future seismicity after the Xingwen and Changning EQs. The dislocation model combined with the CFS model (Okada, 1985) was used to evaluate the static CFS changes in the surrounding regions following the Xingwen and Changning EQs. The CFS change is estimated from the earthquake source model using the Coulomb failure stress criterion, as described as follows:

$$\Delta CFS = \Delta\tau_s + \mu'\Delta\sigma_n$$

where ΔCFS denotes the CFS change along the receiver fault, $\Delta\tau_s$ is the change in the shear stress in the fault slip direction, μ' denotes the effective friction coefficient of the receiver fault, and $\Delta\sigma_n$ is the change in the normal stress on the receiving fault plane.

In the following calculations, changes in the shear stress $\Delta\tau_s$ on a receiver fault are positive, and $\Delta\sigma_n$ is positive for an increasing clamping normal stress, where pressure is defined as positive value. According to previous studies (e.g., Lin and Stein, 2004; Toda et al., 2005, 2011), μ' varies from 0.1 to 0.4 for faults with considerable cumulative slip or high pore pressure, and varies from 0.4 to 0.8 for faults with little cumulative slip. In this study, an effective friction coefficient of 0.4 was adopted for the analysis, which is the mean value within the range suitable for continental strike-slip faults (Toda et al., 2005). Young's modulus and Poisson's ratio were set to 8×10^5 bar and 0.25, respectively. The Coulomb 3.3 software, developed by the USGS (Toda et al.,

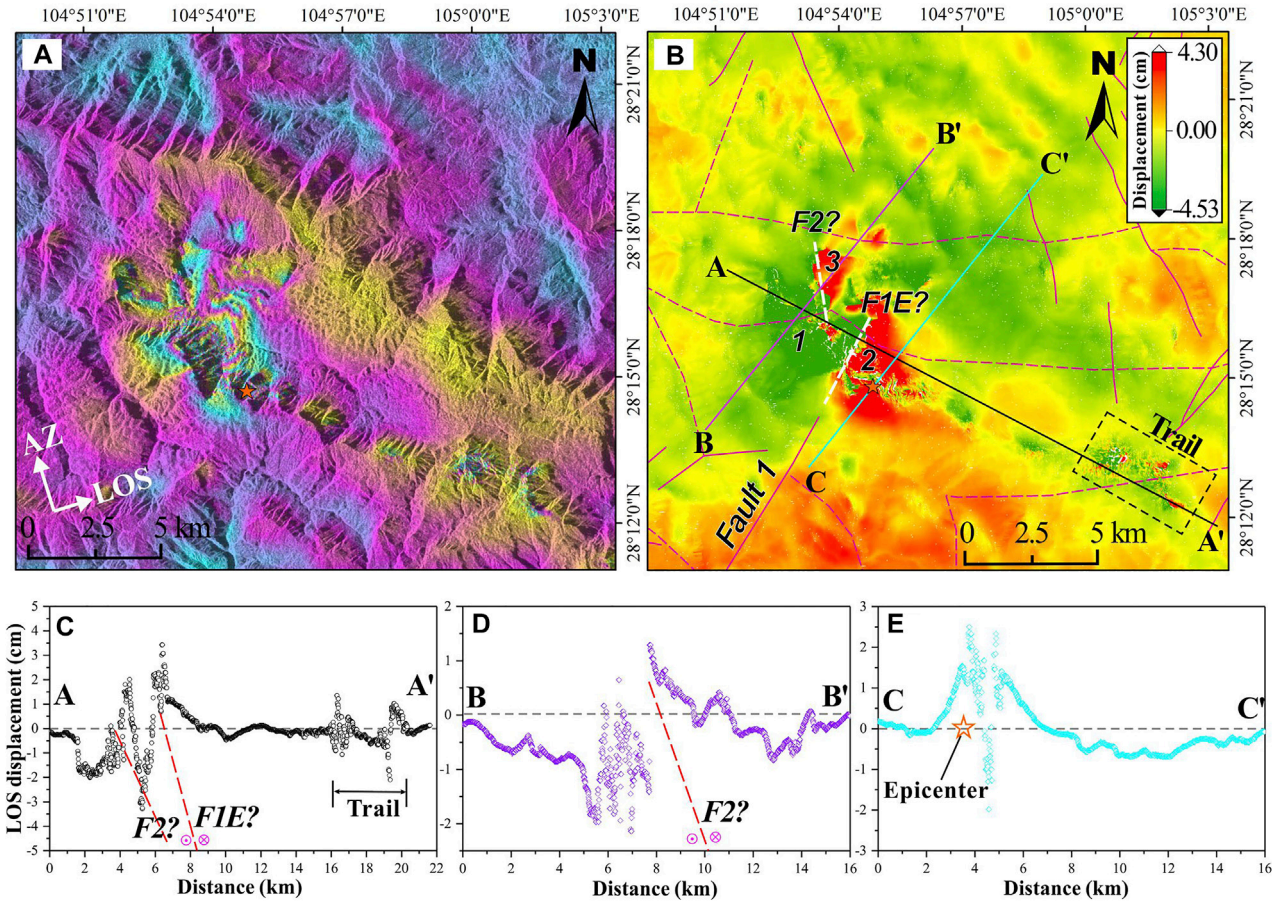


FIGURE 2 | Coseismic deformation field of the "12.16" Ms 5.7 Xingwen earthquake. **(A)** Sentinel-1A ascending interferograms. **(B)** Coseismic displacement field from Sentinel-1A ascending oribit InSAR data. The maximum positive and negative LOS displacements are 4.30 and 4.53cm, respectively. **(C**,**D**,**E)** Line-of-sight (LOS) displacements in the ascending InSAR measurements along Profile A–A′ **(C)**, Profile B–B′ **(D)**, and Profile C–C′ **(E)** in **(B)**. The orange star represents the epicenter of the Ms 5.7 Xingwen earthquake. F1 and F2: Faults 1 and 2, respectively; F1E: Extension of Fault 1.

2005, 2011), was applied to calculate the CFS changes. The results of CFS changes denote the average changes adjacent to the fault.

RESULTS

The D-InSAR ascending orbit interferograms and coseismic deformation maps revealed clear interferometric fringes caused by the Xingwen and Changning EQs (**Figures 2–4**). The high coherence was mainly attributable to the sparse vegetation coverage, whereas the low coherence was primarily caused by atmospheric errors. Meanwhile, the low coherence was also influenced by the temporal and geometrical distortions in the areas of steep terrain and dense vegetation. The total displacement along the line-of-sight (LOS) direction of an InSAR interferogram largely depended on the contributions of the east-west and up-down components, which was constructively or destructively interfered on the two sides of a seismogenic fault. As shown in these figures, the Xingwen and Changning EQs caused subsidence, which was accompanied by some horizontal deformation.

Coseismic Deformation by the "12.16" Xingwen EQ

The D-InSAR interferograms and deformation maps of the "12.16" Xingwen EQ (**Figure 2**) showed some incoherent regions in the near-field region of the seismogenic fault but clear interferometric fringes. The whole displacement field, which covered an area of approximately 10 × 10 km^2, exhibited periodicity with a butterfly-shaped fringe distribution (**Figure 2A**). Moreover, a "trail" was observed ~8 km to the SE of the Xingwen EQ epicenter (**Figures 2A,B**). The LOS deformation in the ascending deformation map ranged from −4.53 to 4.30 cm. We also plotted three profiles (oriented NW, NE, and NE) across the main coseismic deformation field (**Figures 2C–E**). The epicenter, located along the southeastern boundary of the coseismic deformation field, exhibited a small and generally negligible displacement (nearly 0 cm, **Figure 2C**). Profiles A–A′ and B–B′ (NW- and NE-trending cross-sections, respectively, across the inferred seismogenic fault)

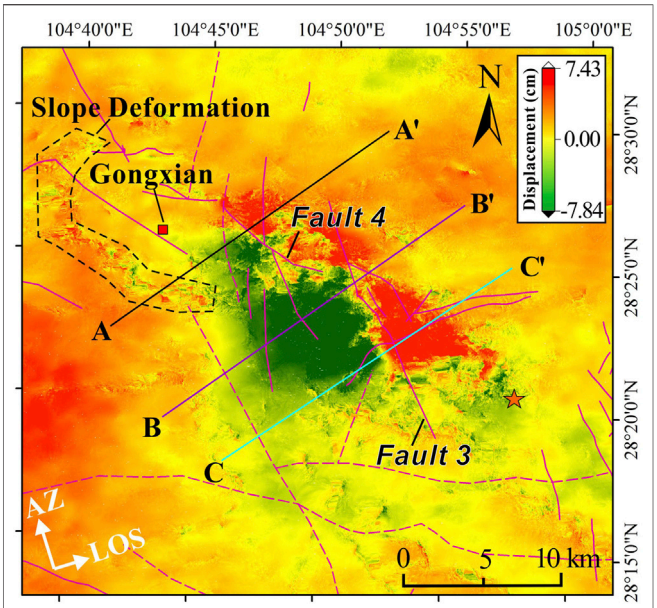


FIGURE 3 | Coseismic displacement field caused by the "6.17" Ms 6.0 Changning earthquake from Sentinel-1A ascending orbit InSAR data. The maximum positive and negative LOS displacements are 7.43 and 7.84 cm, respectively.

displayed LOS displacement curves with maximum differential displacements of ~8 and ~3.5 cm, respectively (**Figures 2C,D,E**). Additionally, the abovementioned trail of displacement had a range of ~2 cm along the ridge (**Figure 2C**). We speculated that this deformation occurred near ridges, which probably resulted from the amplification of displacement by seismic waves (e.g., Havenith et al., 2003; Meunier et al., 2008; Li et al., 2019). Profile C–C′ displayed a positive displacement (**Figure 2E**), indicating uplift of the east wall.

The LOS deformation field displayed an anomaly with two dissociated positive displacement zones (Zones 2 and 3). We inferred that this anomaly resulted from two major concealed faults (Faults 1 and 2) that ruptured during the Xingwen EQ (**Figure 2B**). Although negative displacement fields were distributed to the west and northeast of Zones 2 and 3, they were clustered mainly in Zone 1 (**Figure 2B**). Therefore, the fringes and displacements were asymmetric across the source fault striking subparallel to the north, implying two concealed rupture faults (Faults 1 and 2) in a direction subparallel to the north across the coseismic displacement field. Negative displacements were presented in the ascending deformation map for the west wall of the fault, while positive displacements were observed for the east wall of the fault, constituting the left-lateral strike-slip motion. This discovery was consistent with previous knowledge from the focal mechanism solution of the mainshock (**Figure 1B**; **Table 2**), which indicated that the "12.16" Xingwen EQ predominantly demonstrated strike-slip motion. However, these D-InSAR measurements revealed two major rupture processes (along Faults 1 and

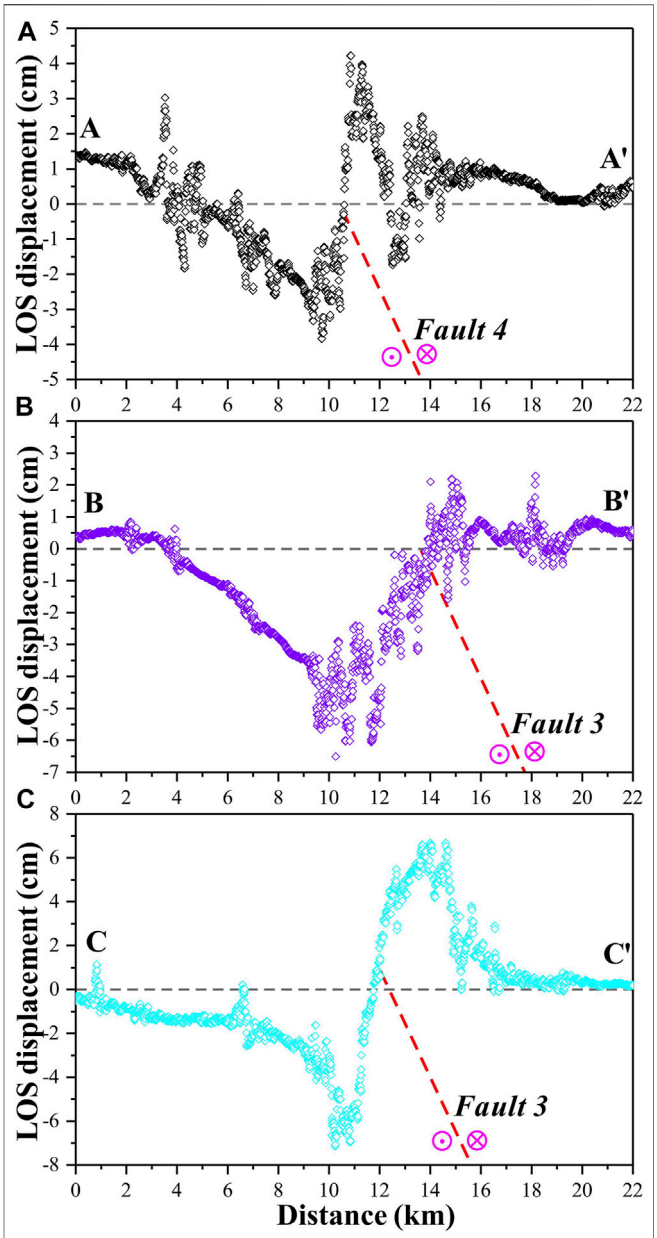


FIGURE 4 | Line-of-sight (LOS) displacements in the ascending InSAR measurements along multiple profiles. **(A)** LOS displacements along Profile A–A′. **(B)** LOS displacements along Profile B–B′. **(C)** LOS displacements along Profile C–C′. The locations of Profiles A–A′, B–B′, and C–C′ are shown in **Figure 3**.

2) during the Xingwen EQ. According to the geological structural feature (**Figures 1C,D**), it could be deduced that the coseismic deformation fields of the Xingwen EQ were primarily generated from the rupture of Fault 1, and were also contributed from the displacement of Fault 2 that was driven by the former Fault 1. It suggested that left-lateral strike-slip deformation was induced by complicated seismogenic structures, as was also reported by Gong et al. (2019).

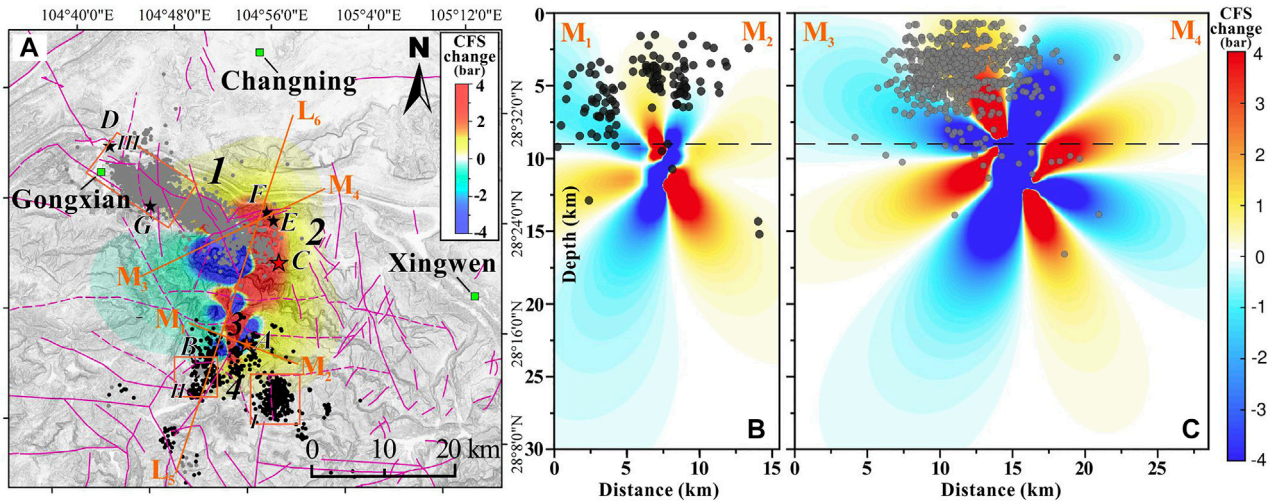


FIGURE 5 | Coulomb failure stress (CFS) changes in the study area. **(A)** CFS change at a depth of 9 km. **(B,C)** CFS changes on Profiles M_1–M_2 and M_3–M_4, which are labeled in **(A)**. Stars denote the epicenters of the Ms > 5 aftershocks. Dark and grey dots represent the epicenters of the Ms > 1 aftershocks of the Xingwen and Changning earthquakes, respectively. The cross-section of Profile L_5–L_6 is presented in **Figure 7**.

Coseismic Deformation by the "6.17" Changning EQ

The coseismic deformation maps of the "6.17" Changning EQ from the D-InSAR measurements are shown in **Figure 3**. The whole coseismic displacement field, which covered an area of approximately 20 × 15 km^2, displayed a rectangular distribution with a NW-trending long side. The LOS displacements in the ascending deformation map ranged from -7.84 to 7.43 cm. The epicenter, located along the southeastern margin of the coseismic deformation field, featured a small, negligible displacement (approximately 0 cm). The maximum difference between the maximum positive and negative displacements was approximately 15 cm, which is located near the speculated seismogenic fault approximately 4 km NW of the epicenter. The northwest direction of epicentre, there has a clear signal, which probably caused by the topographic and remained atmospheric errors (**Figure 3**).

The clear deformation fields were asymmetric across the source fault striking along the NW, implying a NW-trending seismogenic fault bisecting the coseismic displacement field (**Figure 3**). Three NE-trending profiles were constructed across the northern, middle, and southern portions of the inferred seismogenic fault (**Figure 4**). The maximum displacements reached ~4.5 cm, ~6.5 cm, and ~7 cm on Profiles A–A′, B–B′, and C–C′, respectively (**Figures 4A–C**). All three components of the fault displaced an analogous tangential curve along the cross-sections, resulting in negative displacements on the southwestern sides of Faults 3 and 4. Meanwhile, positive displacements were discovered in the ascending deformation map for the east wall of the fault, while corresponding negative displacements were found for the west wall, constituting left-lateral strike-slip movement. Therefore, Fault 3 was identified as the inferred seismogenic fault from the coseismic displacement field established by the InSAR data. This hypothesis was in agreement with previous focal mechanism solutions. The focal mechanism solution of the mainshock revealed that the "6.17" Changning EQ displayed left-lateral strike-slip movement with a minor component of over-thrusting motion (**Figure 1B**; **Table 2**), which is also supported by Yi et al. (2019). However, coseismic displacements also clearly occurred along Fault 4. Hence, we proposed that Fault 4 have simultaneously ruptured with Fault 3, which accorded with the concealed seismogenic doublet that formed during the Changning EQ reported by Liu and Zahradník (2020).

Changes in the Coulomb Failure Stress

The Coulomb failure stress changes (ΔCFS) on the surrounding faults after a mainshock play an important role in triggering subsequent earthquakes within seismic zones (e.g., Freed, 2005; Wang et al., 2018a; Zhao et al., 2018; Cui et al., 2021). Here we combined the Xingwen and Changning EQs to illustrate the CFS changes in **Figure 5**. The ΔCFS at a depth of 9 km was calculated (**Figure 5A**) for the receiver faults: a strike of 349°, dip of 83° and rake of -3° for the Xingwen EQ, and a strike of 314°, dip of 65° and rake of 62° for the Changning EQ. **Figure 5A** shows that there are four positive (stress increase) ΔCFS areas marked as Zones 1, 2, 3, and 4. Large ΔCFS increases were mostly concentrated around the inferred seismogenic faults. Evidently, most aftershocks correlated very well with increases in the ΔCFS. Moreover, ~80% of the aftershocks following the Changning EQ occurred to the NW of the Changning mainshock with increasing ΔCFS in Zone 1 (**Figure 5A**), whereas ~60% of the Xingwen aftershocks were clustered to the SW and SE of the Xingwen mainshock with increasing ΔCFS in Zone 4 (**Figure 5A**). Furthermore, we constructed three

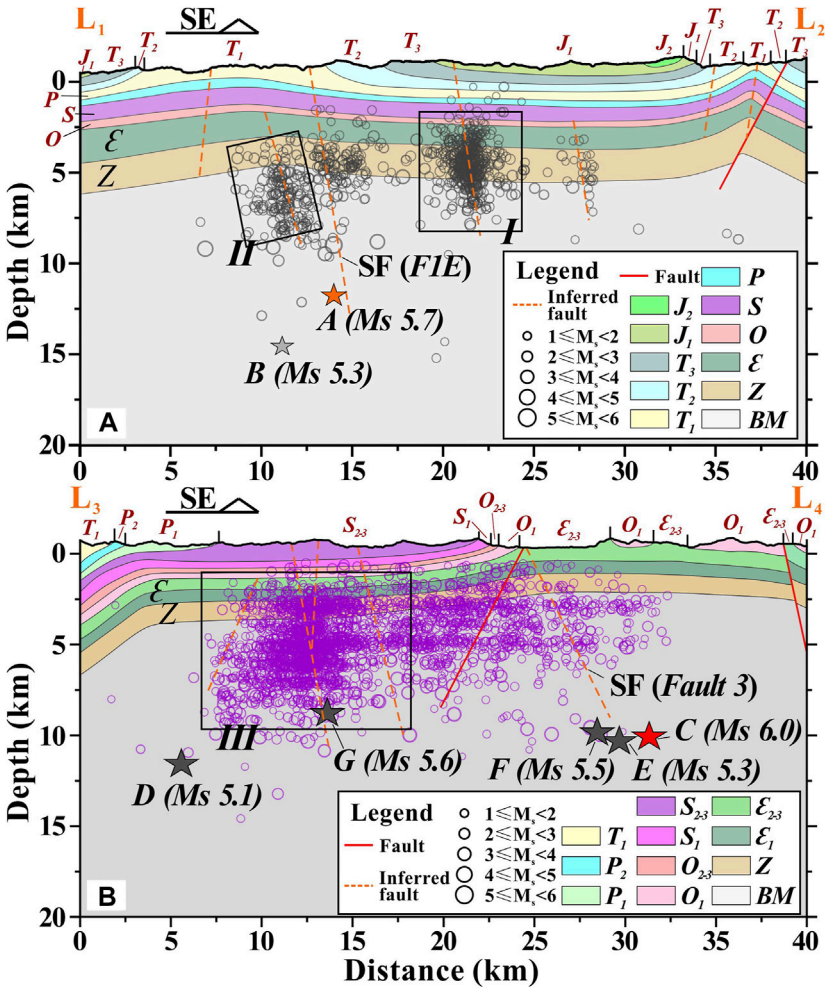


FIGURE 6 | Geological sections with faults laid atop the projected earthquakes within 5 km of Profiles L_1–L_2 and L_3–L_4 in **Figure 1D**. The geological sections were drawn based on a 1:200,000 geological map. SF: Seismogenic fault; BM: Proterozoic and Archaeozoic basement.

cross-sections across the inferred seismogenic fault segment, as shown in **Figure 5A**. Three negative ΔCFS lobes were recognized on Profile M_1–M_2 as a result of the Xingwen EQ, and more than ~60% of the aftershocks occurred in these decreasing ΔCFS zones (**Figure 5B**). However, four positive ΔCFS lobes were identified across the inferred seismogenic fault as a result of the Changning EQ, and ~70% of the corresponding aftershocks were clustered in increasing ΔCFS zones (**Figure 5C**). The cross-sections in **Figures 5B,C** demonstrated that the aftershocks were clustered at depths of 2–7 km, which were shallower than the fault plane responsible for the mainshock. These ΔCFS calculations indicated that the Xingwen and Changning mainshocks induced stresses and promoted seismicity on the surrounding fault network. Hence, ~80% of the Xingwen aftershocks occurred on the surrounding faults, which were clustered in the SE (Zone I) and SW (Zone II), ~70% of the aftershocks following the Changning EQ occurred on the NW fault network in Zone III (**Figure 5A**).

DISCUSSION

The velocity structure and fault network of the study area have been partly identified by Long et al. (2020), but many faults have yet to be found or verified within this complicated fault network. The concealed seismogenic faults responsible for the Xingwen and Changning EQs was in proximity to many surrounding faults, which raised essential questions about the relationship and interaction among these faults. Nevertheless, the relationship and interaction between the seismogenic faults and the surrounding fault network in the investigated area remain unknown. Our findings indicated that the seismogenic faults responsible for the Xingwen and Changning EQs are concealed strike-slip faults. We identified the seismogenic fault of the Xingwen EQ as the NE extension of the northern segment of Fault 1, because the InSAR-derived surface trace of the seismogenic fault and the aftershock distribution were consistent with this interpretation (**Figure 2B**). Moreover, the rupture of Fault 1 resulted in the deformation of a secondary fault

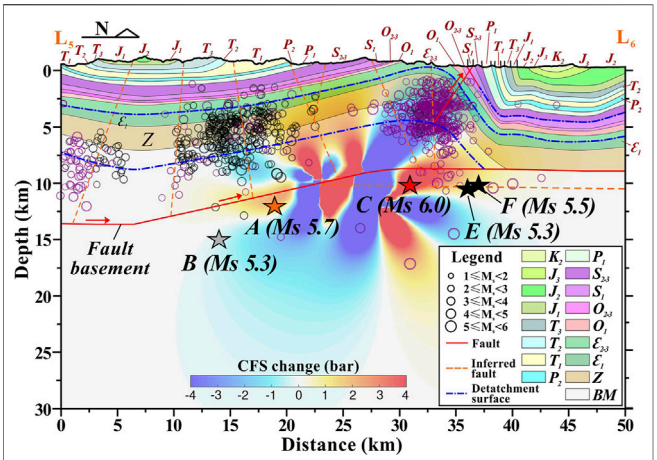


FIGURE 7 | Tectonic geological sections (Profile L_5–L_6 in **Figures 1D**, **5A**) with projected earthquakes within 5 km laid atop the Coulomb failure stress changes along Profile L_5–L_6. The geological sections were drawn based on a 1:200,000 geological map and He et al. (2019). BM: Proterozoic and Archaeozoic basement.

of Fault 2, which led to the coseismic surface deformation on both sides of Fault 2. The seismogenic fault responsible for the Changning EQ was identified as Fault 3 by the coseismic displacement changes around its southwestern and northeastern sides (**Figure 3A**). Although many aftershocks were clustered around the extensions of Faults 1 and 3, many aftershocks were also concentrated in Zones I and II during the Xingwen EQ and in Zone III during the Changning EQ (**Figure 5A**).

The source depth and distribution characteristics can be implied by projecting the aftershock locations. The aftershock projections onto the geological sections of Profiles L_1–L_2, L_3–L_4, and L_5–L_6 are illustrated in **Figures 6**, **7**. The hypocentres of the aftershocks following the Xingwen and Changning EQs were distributed mostly at depths of 2–10 km. We identified the inferred concealed faults from the sequences of hypocentres; clusters could be clearly distinguished in Zones I and II during the Xingwen EQ, and a vague cluster can be detected in Zone III during the Changning EQ (**Figures 5A**, **6**). The structural model in **Figure 7** depicted the tectonic setting that facilitated the occurrence of earthquakes across the Jianwu syncline and the Changning anticline. The Xingwen and Changning mainshocks were projected onto the break in the basement fault ramp, indicating that most of the aftershocks were shallower than the two mainshocks. Furthermore, the hypocentres of the aftershocks following the Xingwen and Changning EQs were relatively concentrated within the hinge zones of the Jianwu syncline and the Changning anticline, respectively (**Figure 7**). The earthquake cluster locations reflected the shear behavior between the strata layer and the shear failure of the faulted basement, which resulted in the Xingwen and Changning EQs. The calculated ΔCFS values also reflected shear failure of the faulted basement, and the crustal stress was also concentrated along the axes of the Jianwu syncline and Changning anticline.

We propose an interpretation where the fault basement was initially reactivated as a result of shear failure due to the Xingwen EQ located between the Jianwu syncline and the Changning anticline, which resulted in the concentration of stress under the Changning anticline. Thereafter the fault basement fractured along the hinge zone of the Changning anticline, which subsequently led to the Changning EQ half a year following the Xingwen EQ. According to previous studies (e.g., Sun et al., 2017; Lei et al., 2019a, 2019b), the increase in seismic activity (mostly Ms < 5.0) over the last ~10 years was induced by hydraulic fracturing in the Changning gas exploration field, where the hypocentres were concentrated mostly at depths of 3–7 km. The hypocentres of the Xingwen and Changning aftershocks were also likely facilitated by elevated pore pressures due to the injection of water over the past ~10 years into gas wells and salt mine wells (e.g., Ning 201, Ning 203 and Ning 2, **Figure 1C**). In other words, the fault network was lubricated by water that was injected during shale gas exploration. Then, crustal stresses became concentrated within the hinge zones of the Jianwu syncline and Changning anticline, which resulted in the Xingwen EQ near the Jianwu syncline and the Changning EQ beneath the Changning anticline. Meanwhile, the injection of water also led to clusters of seismic activity in Zones I and II in the Jianwu syncline and Zone III NW of the Changning anticline (**Figures 5A**, **6**).

CONCLUSION

We investigated the coseismic deformation associated with the 2018 Xingwen and 2019 Changning EQs using S1A data. Evident coseismic displacements were identified on both sides of the seismogenic faults responsible for the Xingwen EQ (December 2018) and the Changning EQ (June 2019) according to the InSAR imagery. The InSAR observations demonstrated the concealed seismogenic doublet with left-lateral strike-slip motion for the Xingwen and Changning EQs and an apparent thrust-slip component for the Changning EQ. The aftershock hypocentres were mostly shallower than 10 km; the Xingwen aftershocks were predominantly clustered in the Jianwu syncline, whereas the Changning aftershocks were mostly clustered in the Changning anticline. The faulted basement was first sheared along a ramp, resulting in the Xingwen EQ; then, the crustal stresses became concentrated in the basement beneath the Changning anticline, resulting in the Changning EQ half a year later. The Xingwen and Changning EQs probably resulted from long-term hydraulic fracturing during shale gas exploration; consequently, the clusters of seismic activity in the hinge zones of the abovementioned folds need to be further monitored and analyzed in the future. The D-InSAR analysis on seismic deformations produced by seismogenic faulting could arouse the understanding of seismic geo-environment in similar mining exploration areas, which is helpful for assessing disaster risks associated with earthquakes.

DATA AVAILABILITY STATEMENT

The original contributions presented in the study are included in the article/Supplementary Material, further inquiries can be directed to the corresponding author.

AUTHOR CONTRIBUTIONS

SZ and SL conceptualized the research, and contributed to data analysis and investigation. CS contributed to the study methodology and the writing of the original draft. HW and SW contributed the field surveys and draft modification. All authors have agreed the publication of the manuscript.

FUNDING

This study is financially supported by the National Natural Science Foundations of China (Nos 41907228; 42007248), the Second Tibetan Plateau Scientific Expedition and Research Program (No. 2019QZKK0905), the Sichuan Science and Technology Program (No. 2020YFS0297), and the Sichuan Science and Technology Innovation and Seeding Cultivation (No. 2021086).

ACKNOWLEDGMENTS

We would like to thank the European Space Agency (ESA) for providing the satellite data used in this paper. We also thank Xiaohui Hu from the Institute of Disaster Prevention, Feng Long from Seismological Bureau of Sichuan Province, and Xinlin Lei from Geological Survey of Japan share the aftershock location data.

REFERENCES

Aguirre, P., Vásquez, J., de la Llera, J. C., González, J., and González, G. (2018). Earthquake Damage Assessment for Deterministic Scenarios in Iquique, Chile. *Nat. Hazards* 92, 1433–1461. doi:10.1007/s11069-018-3258-3

Anzidei, M., Boschi, E., Cannelli, V., Devoti, R., Esposito, A., Galvani, A., et al. (2009). Coseismic Deformation of the Destructive April 6, 2009 L'Aquila Earthquake (central Italy) from GPS Data. *Geophys. Res. Lett.* 36, L17307. doi:10.1029/2009GL039145

Attema, E., Davidson, M., Floury, N., and Levrini, G. (2008). "Sentinel-1 ESA's New European Radar Observatory," in *European Conference on Synthetic Aperture Radar VDE*. Friedrichshafen, Germany: VDE, 1–4.

Biggs, J., Bergman, E., Emmerson, B., Funning, G. J., Jackson, J., Parsons, B., et al. (2006). Fault Identification for Buried Strike-Slip Earthquakes Using InSAR: the 1994 and 2004 Al Hoceima, Morocco Earthquakes. *Geophys. J. Int.* 166, 1347–1362. doi:10.1111/j.1365-246X.2006.03071.x

Bonì, R., Meisina, C., Cigna, F., Herrera, G., Notti, D., Bricker, S., et al. (2017). Exploitation of Satellite A-DInSAR Time Series for Detection, Characterization and Modelling of Land Subsidence. *Geosciences* 7, 25. doi:10.3390/geosciences7020025

Carlà, T., Intrieri, E., Raspini, F., Bardi, F., Farina, P., Ferretti, A., et al. (2019). Perspectives on the Prediction of Catastrophic Slope Failures from Satellite InSAR. *Sci. Rep.* 9, 14137. doi:10.1038/s41598-019-50792-y

CENC (2022). China Earthquake Networks Center. Sichuan Earthquake Administration, China Earthquake Administration. Available at: http://www.eqsc.gov.cn.

Cui, S., Pei, X., Jiang, Y., Wang, G., Fan, X., Yang, Q., et al. (2021). Liquefaction within a Bedding Fault: Understanding the Initiation and Movement of the Daguangbao Landslide Triggered by the 2008 Wenchuan Earthquake (Ms = 8.0). *Eng. Geology*. 295, 106455. doi:10.1016/j.enggeo.2021.106455

Freed, A. M. (2005). Earthquake Triggering by Static, Dynamic, and Postseismic Stress Transfer. *Annu. Rev. Earth Planet. Sci.* 33, 335–367. doi:10.1146/annurev.earth.33.092203.122505

Geudtner, D., Torres, R., Snoeij, P., Davidson, M., and Rommen, B. (2014). Sentinel-1 System Capabilities and Applications. *IEEE Geosci. Remote Sensing Symp.* 2014, 1457–1460. doi:10.1109/IGARSS.2014.6946711

Goldstein, R. M., and Werner, C. L. (1998). Radar Interferogram Filtering for Geophysical Applications. *Geophys. Res. Lett.* 25, 4035–4038. doi:10.1029/1998GL900033

Gong, Y., Zhao, M., Long, F., and Fu, Y. (2019). Precise Relocation of Aftershock Sequence of Xingwen M5.7 Earthquakes on December 16, 2018. *Earthquake Res. Sichuan* 172, 1–5. (in Chinese with English Abstract). doi:10.13716/j.cnki.1001-8115.2019.03.001

Hanssen, R. F. (2001). *Radar Interferometry: Data Interpretation and Error Analysis (308pp)*. Netherlands: Kluwer Academic Publishers.

Havenith, H.-B., Vanini, M., Jongmans, D., and Faccioli, E. (2003). Initiation of Earthquake-Induced Slope Failure: Influence of Topographical and Other Site Specific Amplification Effects. *J. Seismology* 7, 397–412. doi:10.1023/a:1024534105559

He, D., Lu, R., Huang, H., Wang, X., Jiang, H., and Zhang, W. (2019). Tectonic and Geological Setting of the Earthquake Hazards in the Changning Shale Gas Development Zone, Sichuan Basin, SW China. *Pet. Exploration Development* 46, 1051–1064. doi:10.1016/S1876-3804(19)60262-4

He, P., Hetland, E. A., Niemi, N. A., Wang, Q., Wen, Y., and Ding, K. (2018). The 2016 Mw 6.5 Nura Earthquake in the Trans Alai Range, Northern Pamir: Possible Rupture on a Back-Thrust Fault Constrained by Sentinel-1A Radar Interferometry. *Tectonophysics* 749, 62–71. doi:10.1016/j.tecto.2018.10.025

Hu, J., Chen, J., Chen, Z., Cao, J., Wang, Q., Zhao, L., et al. (2018). Risk Assessment of Seismic Hazards in Hydraulic Fracturing Areas Based on Fuzzy Comprehensive Evaluation and AHP Method (FAHP): a Case Analysis of Shangluo Area in Yibin City, Sichuan Province, China. *J. Pet. Sci. Eng.* 170, 797–812. doi:10.1016/j.petrol.2018.06.066

Hu, X., Sheng, S., Wan, Y., Bu, Y., and Li, Z. (2020). Study on Focal Mechanism and post-seismic Tectonic Stress Field of the Changning, Sichuan, Earthquake Sequence on June 17th 2019. *Process Geophys. (in Chinese)* 35 (5), 1657–1681. doi:10.6038/pg2020DD0378

Kovács, I. P., Bugya, T., Czigány, S. z., Defilippi, M., Lóczy, D., Riccardi, P., et al. (2019). How to Avoid False Interpretations of Sentinel-1A TOPSAR Interferometric Data in Landslide Mapping? A Case Study: Recent Landslides in Transdanubi, Hungary. *Nat. Hazards* 96, 693–712. doi:10.1007/s11069-018-3564-9

Lei, X., Huang, D., Su, J., Jiang, G., Wang, X., Wang, H., et al. (2017). Fault Reactivation and Earthquakes with Magnitudes of up to Mw4.7 Induced by Shale-Gas Hydraulic Fracturing in Sichuan Basin, China. *Sci. Rep.* 7, 7971. doi:10.1038/s41598-017-08557-y

Lei, X., Wang, Z., and Su, J. (2019a). The December 2018 ML 5.7 and January 2019 ML 5.3 Earthquakes in South Sichuan Basin Induced by Shale Gas Hydraulic Fracturing. *Seismological Res. Lett.* 90, 1099–1110. doi:10.1785/0220190029

Lei, X., Wang, Z. W., Wang, Z., and Su, J. (2019b). Possible Link between Long-Term and Short-Term Water Injections and Earthquakes in Salt Mine and Shale Gas Site in Changning, South Sichuan Basin, China. *Earth Planet. Phys.* 3, 510–525. doi:10.26464/epp2019052

Li, B., Song, Y. B., Wang, Q., Wang, Z. B., Guo, L., Jiang, J. M., et al. (2018). Magnetic Field Characteristics and Geological Significance of Sichuan basin. *Geophys. Geochemical Exploration* 42, 937–945. (in Chinese with English Abstract). doi:10.11720/wtyht.2018.1527

Li, C., He, D., Sun, Y., He, J., and Jiang, Z. (2015). Structural Characteristic and Origin of Intra-continental Fold belt in the Eastern Sichuan basin, south China Block. *J. Asian Earth Sci.* 111, 206–221. doi:10.1016/j.jseaes.2015.07.027

Li, X.-n., Ling, S.-x., Sun, C.-w., Xu, J.-x., and Huang, T. (2019). Integrated rockfall hazard and Risk Assessment along Highways: an Example for Jiuzhaigou Area after the 2017 Ms 7.0 Jiuzhaigou Earthquake, China. *J. Mt. Sci.* 16, 1318–1335. doi:10.1007/s11629-018-5355-x

Liao, H., Meyer, F. J., Scheuchl, B., Mouginot, J., Joughin, I., and Rignot, E. (2018). Ionospheric Correction of InSAR Data for Accurate Ice Velocity Measurement at Polar Regions. *Remote Sensing Environ.* 209, 166–180. doi:10.1016/j.rse.2018.02.048

Lin, J., and Stein, R. S. (2004). Stress Triggering in Thrust and Subduction Earthquakes and Stress Interaction between the Southern San Andreas and

Nearby Thrust and Strike-Slip Faults. *J. Geophys. Res.* 109, B02303. doi:10.1029/2003JB002607

Liu, G., Song, R., Guo, H., Perski, Z., Yue, H., Han, C., et al. (2016). Filtering SAR Interferometric Phase Noise Using a Split-Window Model. *Remote Sensing Lett.* 7, 800–809. doi:10.1080/2150704x.2016.1187316

Liu, J., and Zahradník, J. (2020). The 2019 M W 5.7 Changning Earthquake, Sichuan Basin, China: A Shallow Doublet with Different Faulting Styles. *Geophys. Res. Lett.* 47, e2019GL085408. doi:10.1029/2019GL085408

Long, F., Zhang, Z. W., Zhang, Z., Qi, Y., Liang, M., Ruan, X., et al. (2020). Three Dimensional Velocity Structure and Accurate Earthquake Location in Changning-Gongxian Area of Southeast Sichuan. *Earth Planet. Phys.* 4, 1–15. doi:10.26464/epp2020022

Meunier, P., Hovius, N., and Haines, J. A. (2008). Topographic Site Effects and the Location of Earthquake Induced Landslides. *Earth Planet. Sci. Lett.* 275, 221–232. doi:10.1016/j.epsl.2008.07.020

Okada, Y. (1985). Surface Deformation Due to Shear and Tensile Faults in a Half-Space. *Bull. Seismological Soc. America* 75 (4), 1135–1154. doi:10.1785/bssa0750041135

Raspini, F., Bardi, F., Bianchini, S., Ciampalini, A., Del Ventisette, C., Farina, P., et al. (2017). The Contribution of Satellite SAR-Derived Displacement Measurements in Landslide Risk Management Practices. *Nat. Hazards* 86, 327–351. doi:10.1007/s11069-016-2691-4

Sarychikhina, O., Glowacka, E., and Robles, B. (2018). Multi-sensor DInSAR Applied to the Spatiotemporal Evolution Analysis of Ground Surface Deformation in Cerro Prieto basin, Baja California, Mexico, for the 1993-2014 Period. *Nat. Hazards* 92, 225–255. doi:10.1007/s11069-018-3206-2

Simons, M., Fialko, Y., and Rivera, L. (2002). Coseismic Deformation from the 1999 Mw 7.1 Hector Mine, California, Earthquake as Inferred from InSAR and GPS Observations. *Bull. Seismological Soc. America* 92, 1390–1402. doi:10.1785/0120000933

Stramondo, S., Chini, M., Bignami, C., Salvi, S., and Atzori, S. (2011). X-, C-, and L-Band DInSAR Investigation of the April 6, 2009, Abruzzi Earthquake. *IEEE Geosci. Remote Sensing Lett.* 8, 49–53. doi:10.1109/lgrs.2010.2051015

Su, Z., Yang, Y.-H., Li, Y.-S., Xu, X.-W., Zhang, J., Zhou, X., et al. (2019). Coseismic Displacement of the 5 April 2017 Mashhad Earthquake (Mw 6.1) in NE Iran through Sentinel-1A TOPS Data: New Implications for the Strain Partitioning in the Southern Binalud Mountains. *J. Asian Earth Sci.* 169, 244–256. doi:10.1016/j.jseaes.2018.08.010

Sun, X., Yang, P., and Zhang, Z. (2017). A Study of Earthquakes Induced by Water Injection in the Changning Salt Mine Area, SW China. *J. Asian Earth Sci.* 136, 102–109. doi:10.1016/j.jseaes.2017.01.030

Syahreza, S., Fadhli, A., Saepuloh, A., and Lateh, H. (2018). Combining the Sentinel-1A/B DinSAR Interferometry to Detect Deformation Associated with Pidie Jaya Earthquake. *J. Phys. Conf. Ser.* 1120, 012021. doi:10.1088/1742-6596/1120/1/012021

Toda, S., Stein, R. S., Richards-Dinger, K., and Bozkurt, S. B. (2005). Forecasting the Evolution of Seismicity in Southern California: Animations Built on Earthquake Stress Transfer. *J. Geophys. Res.* 110, B05S16. doi:10.1029/2004JB003415

Toda, S., Stein, R. S., Sevilgen, V., and Lin, J. (2011). "Coulomb 3.3 Graphic-Rich Deformation and Stress-Change Software for Earthquake, Tectonic, and Volcano Research and Teaching-User Guide," in *U.S. Geological Survey Open-File Report*, 63. 2011–1060, Available at: https://pubs.usgs.gov/of/2011/1060/, Accessed date: March 2018. doi:10.3133/ofr20111060

Wang, H., Liu-Zeng, J., Ng, A. H.-M., Ge, L., Javed, F., Long, F., et al. (2017). Sentinel-1 Observations of the 2016 Menyuan Earthquake: A Buried Reverse Event Linked to the Left-Lateral Haiyuan Fault. *Int. J. Appl. Earth Observation Geoinformation* 61, 14–21. doi:10.1016/j.jag.2017.04.011

Wang, L., Gao, H., Feng, G., and Xu, W. (2018a). Source Parameters and Triggering Links of the Earthquake Sequence in central Italy from 2009 to 2016 Analyzed with GPS and InSAR Data. *Tectonophysics* 744, 285–295. doi:10.1016/j.tecto.2018.07.013

Wang, Z. J., Wang, H. C., Dong, D., and Qin, J. (2018b). Review of Geophysical Results of Huayingshan Fault Zone. *Earthquake Res. Shichuan* 168, 6–12. (in Chinese with English abstract). doi:10.13716/j.cnki.1001-8115.2018.03.002

Yi, G. X., Long, F., Liang, M. J., Zhao, M., and Wang, S. W. (2019). Focal Mechanism Solutions and Seismogenic Structure of the 17 June 2019 Ms 6.0 Sichuan Changning Earthquake Sequence. *Chin. J. Geophys.* 62 (9), 3432–3447. (in Chinese with English Abstract). doi:10.6038/cjg2019N0297

Yin, X. X., Guo, A. N., Zhao, T., and Li, S. H. (2019). Characteristics of the Regional Tectonic Stress Field of the Changning Ms 6.0 Earthquake, Sichuan Province. *China Earthquake Eng. J.* 41 (5), 1215–1220. (in Chinese with English Abstract). doi:10.3969/j.issn.1000–0844.2019.05.1215

Zhao, D., Qu, C., Shan, X., Gong, W., Zhang, Y., and Zhang, G. (2018). InSAR and GPS Derived Coseismic Deformation and Fault Model of the 2017 Ms7.0 Jiuzhaigou Earthquake in the Northeast Bayanhar Block. *Tectonophysics* 726, 86–99. doi:10.1016/j.tecto.2018.01.026

Zhou, R. J., Tang, R. C., Qian, H., Wen, D. H., Ma, S. H., He, Y. L., et al. (1997). An Application of Seismotectonic Analogy to the Huyingshan Fault Zone in East Sichuan. *J. Seimological Res.* 20, 316–322. (in Chinese with English abstract).

Zuo, R., Qu, C., Shan, X., Zhang, G., and Song, X. (2016). Coseismic Deformation fields and a Fault Slip Model for the Mw7.8 Mainshock and Mw7.3 Aftershock of the Gorkha-Nepal 2015 Earthquake Derived from Sentinel-1A SAR Interferometry. *Tectonophysics* 686, 158–169. doi:10.1016/j.tecto.2016.07.032

Conflict of Interest: The authors declare that the research was conducted in the absence of any commercial or financial relationships that could be construed as a potential conflict of interest.

Publisher's Note: All claims expressed in this article are solely those of the authors and do not necessarily represent those of their affiliated organizations, or those of the publisher, the editors and the reviewers. Any product that may be evaluated in this article, or claim that may be made by its manufacturer, is not guaranteed or endorsed by the publisher.

Copyright © 2022 Sun, Ling, Zhao, Wen and Wang. This is an open-access article distributed under the terms of the Creative Commons Attribution License (CC BY). The use, distribution or reproduction in other forums is permitted, provided the original author(s) and the copyright owner(s) are credited and that the original publication in this journal is cited, in accordance with accepted academic practice. No use, distribution or reproduction is permitted which does not comply with these terms.

frontiers | Frontiers in Earth Science

ORIGINAL RESEARCH
published: 12 April 2022
doi: 10.3389/feart.2022.861057

Engineering Application of Landslide Susceptibility Mapping in Linear Engineering Optimization

*Jinchang Shi**

Shaanxi Institute of Engineering Prospecting, Xi'an, China

Regional landslide susceptibility mapping has an important role in guiding linear engineering optimization. Based on the geographic information system (GIS) platform and R language MaxEnt software, in this research, the China National Highway 109 New Line Expressway (Beijing Sixth Ring Road-City Boundary Section) was taken as an example. Using the maximum entropy (MaxEnt) model, with ten evaluation indicators, including the elevation, slope, aspect, relief, topographic wetness index (TWI), roughness, lithology, distance to road, normalized difference vegetation index (NDVI), and land use type, a landslide susceptibility mapping was completed to support linear engineering optimization. The ROC value of the prediction model was 82.1%, and the $\%LR_{class}$ was 2.25, which strongly demonstrated the reliability of the landslide susceptibility mapping results. Then, the percentages of two roads with different landslide probability levels were calculated. It was found that only 10% of the new line was in a very high class, which was much lower than 26% of the existing line. This study proved that the regional landslide susceptibility mapping can be used to support optimization of the construction plan of the new line and provided a broader basis for decision-making for similar linear projects in future engineering projections.

Keywords: landslide susceptibility mapping, MaxEnt (maximum entropy), landslide, highway, maximum entropy model

OPEN ACCESS

Edited by:
Xuanmei Fan,
Chengdu University of Technology, China

Reviewed by:
Milad Janalipour,
K. N. Toosi University of Technology, Iran
Gaetano Pecoraro,
University of Salerno, Italy

***Correspondence:**
Jinchang Shi
ShiJC007@163.com

Specialty section:
This article was submitted to Geohazards and Georisks, a section of the journal Frontiers in Earth Science

Received: *24 January 2022*
Accepted: *21 March 2022*
Published: *12 April 2022*

Citation:
Shi J (2022) Engineering Application of Landslide Susceptibility Mapping in Linear Engineering Optimization. Front. Earth Sci. 10:861057. doi: 10.3389/feart.2022.861057

INTRODUCTION

Landslides, one of the major types of geological hazards, are widely distributed all over the world. Landslides have caused severe damage to infrastructures and several casualties (Fan et al., 2018; Lin and Wang, 2018; Qu et al., 2020). It has been found that as a useful tool to support governments in making smart decisions, landslide susceptibility mapping has shown great effects for many aspects (He et al., 2020; Maharjan et al., 2021; Su et al., 2021; Zhao et al., 2021).

Currently, landslide susceptibility mapping is applied primarily in risk assessment, monitoring and early warning, urban planning, and land use (Reichenbach et al., 2018; Janalipour et al., 2021). For example, Remondo et al. (2005) took landslide susceptibility mapping as an indispensable layer to develop a map of the hazard potential of landslides and then combined this layer with the value of goals influenced by landslides to determine the landslide risk mapping to aid city risk management. Additionally, Huang et al. (2020) integrated the monitoring data from a synthetic aperture radar (SAR) satellite and landslide susceptibility mapping and produced a dynamic regional landslide monitoring model with consideration of the slope resistance and landslide activity. At the same time, many researchers (Intrieri et al., 2012; Keefer et al., 1987; Liu, 2004; Osanai et al., 2010; Baum and Godt 2010; He et al., 2020) coincidentally tried to find a novel model to combine the rainfall data

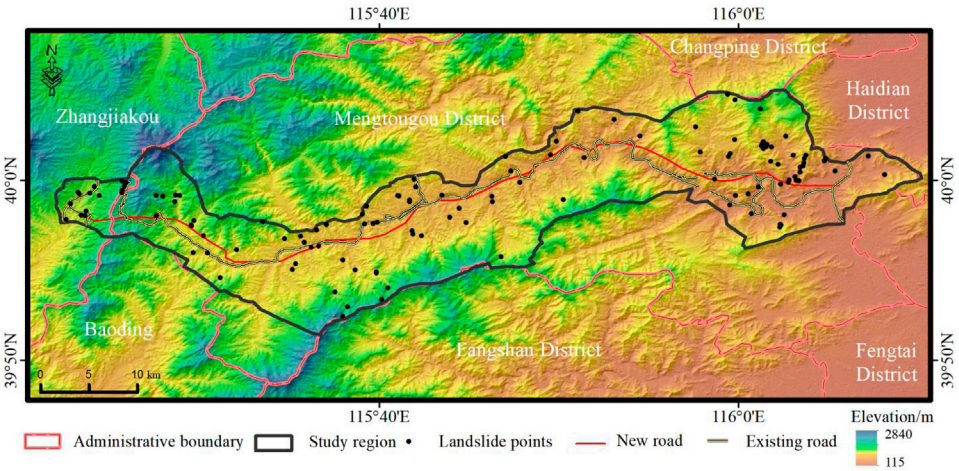


FIGURE 1 | Location of the study area and distribution of the landslides.

from satellites or rainfall recorders with landslide susceptibility mapping to produce a regional real-time landslide warning system. Furthermore, to guide urban planning work and land use, Yao et al. (2018) mixed landslide susceptibility mapping into the definition of urban affordability and then clearly showed the developed and undeveloped areas around the county of Suide, Shaanxi Province in China. Less work has been attempted for linear engineering, which is commonly called lifeline engineering.

Compared with other engineering projects, linear engineering projects such as gas lines, highways, and railways have a unique feature: one point of damage will cause failure for the entire system (Das et al., 2011). Highway work is always accompanied by large slope cutting engineering, which results in the occurrence of more landslides (Laimer 2017; Zhang and Zhang, 2014; Li et al., 2020). More importantly, Hakan (2022) monitored the evolution of a road network during an 11-year time-space in Arhavi and found that road extension works were associated with the large majority (90.1%) of mass movements in the area, which was similar to the possible effect of a theoretical earthquake, with a magnitude greater than Mw = 6.0. Therefore, road engineering has to face more threats from landslides, and route optimization must always be performed after a period of operation. Therefore, it is necessary to find a better method to easily support regional linear engineering optimization using proven useful tools such as landslide susceptibility mapping.

Considering the aforementioned aspects, in this research, the National Highway 109 New Line Expressway (Beijing Sixth Ring Road-City Boundary Section) project in China was taken as an example. The maximum entropy model of machine learning was used to evaluate the landslide susceptibility mapping function to perform a reasonable quantitative analysis of the existing highways and proposed new highways to support linear engineering optimization. First, all data, including digital elevation models (DEMs), landslide points, and other original data, were used as input into the open-source MaxEnt software program (https://biodiversityinformatics.amnh.org/open_source/maxent/) after preprocessing to export the landslide susceptibility value of each pixel. Second, the landslide susceptibility value in the ASCII format was opened on the QGIS platform and divided into five grades using the natural breakpoint method after the predictive accuracy was checked using the value of the area under the curve of the receiver operating curve (AUC–ROC) and $\%LR_{class}$. Third, the lengths of the new and existing roads in each susceptible class were calculated, and the rationality of the new route was analyzed.

Study Area

The China National Highway 109 New Line Expressway (Beijing Sixth Ring Road-City Boundary Section) (**Figure 1**), with a total length of 69.2 km, starts from the Beijing Sixth Ring Road to the east and ends at the Zhangjiajie city of Hebei Province. It serves the two cities and plays a vital role in communication and social development. To better include and assess the existing landslides and potentially related geohazard chain, the watersheds of the mountains on both sides of the line are taken as the research boundary. Compared with the equidistant expansion of 200 m along both sides in the traditional manner, it was helpful to take high-level disasters into account (Fan et al., 2019a).

The total study area of 628 km^2 was a typical mountainous landform with sandstone and basalt as the main strata, with only a few small inactive faults. According to remote sensing interpretation and the on-site investigation, 126 landslide disasters were found. All landslides were randomly distributed on two sides of the highway.

METHODOLOGY

Model Choice

Different assessment models have significant impact on the results of landslide susceptibility mapping. At present, the commonly used landslide susceptibility evaluation models can be divided into knowledge-driven, data-driven, and physical model-driven models (Reichenbach et al., 2018). The

TABLE 1 | Advantages and disadvantages of common machine learning modes in landslide susceptibility assessment.

Model	Difficulty	Advantages	Disadvantages
Decision trees	Easy–middle	Simple understanding and operation, visual decision tree, fewer data required	Unstable, greatly affected by data classification
Artificial neural networks	Easy–middle	Fit for multidimensional problems need fewer input data, the optimization model can be fitted in real time	Black box, the model parameters need to be manually selected, and the dimensions need to be pre-reduced
Maximum entropy model	Easy	Open-source independent software, easy to operate, just need point samples, the influence between each factor, and the target can be seen	The operation process is prone to fall for inconsistencies in data dimensions
Support vector machines	Easy–middle	Parameter dimension can be greater than the number of samples, a multi-class kernel function can be chosen	Easy to overfit, cannot provide probability estimates
Bayesian model	Middle	Fewer training samples are required, speed is fast, performance is good for the reduction of the dimension problem	Requires a sample independence test in advance, low precision

knowledge-driven type of model has greater subjectivity, while the physical model-driven type requires a large number of accurate mechanical parameters, which limits the application of these two methods. Practice has proven that data-driven models have higher accuracy than the other two types (Reichenbach et al., 2018; Chen and Li, 2020). With the development of artificial intelligence, the machine learning model has become the most popular model in data-driven models, and a large amount of work has proven that the evaluation result of the machine learning model is better than that of the traditional statistical model (Reichenbach et al., 2018; Chen et al., 2021; Zhao et al., 2021). The common machine learning models include the random forest model, decision tree model, support vector machine, Bayesian model, and god-level network model. Each model has its advantages and disadvantages (**Table 1**).

Recently, scientists have also begun to apply the maximum entropy model, which was originally used and is still popular in the field of species habitat suitability assessment (Merow et al., 2013), in the evaluation of landslide susceptibility. The evaluation results have been effective and better than models as support vector machines and artificial neural networks (Chen et al., 2017; Teimouri and Nalivan, 2020). At the same time, according to the basic theory of landslide assessment, future landslides will occur in similar areas where landslides have occurred in the past, which is consistent with the basic theory of species habitat suitability assessment (Reichenbach et al., 2018). Therefore, the choice of a maximum entropy model could achieve a better result to support linear engineering optimization and further verify the suitability of this interdisciplinary evaluation model for landslide assessment to enrich the optional model and guide actual production.

Theory of the Maximum Entropy Model

MaxEnt is a machine learning model that quantitatively calculates the probability of landslide occurrence in the evaluation area using the Bayesian rule based on the geological environment indicators of the training landslide (Rahmati et al., 2016). The specific calculation principle is that the study area is divided into a finite pixel set X, with the assumption that x represents each computing unit. Then, $x \in X$ in the study area and $\pi(x)$ represents the probability distribution value of landslide occurrence in each computing unit $0<P(x)<1$. The sum of the probability values of all computing units is 1. The landslide value of the calculation grid is taken as the response variable y, if the calculation unit has a landslide, $y = 1$, otherwise it is 0. Therefore, the probability of the landslide conditional distribution $P(y|x)$ can be expressed as follows:

$$P(y = 1|x) = \frac{P(x|y = 1)P(y = 1)}{P(x)}, \tag{1}$$

where $P(y = 1|x)$ is the probability of a landslide at a specific point x; $P(y|x = 1)$ is the probability of a landslide at a specific point x under the landslide distribution conditions, which is also $\pi(x)$; $P(y = 1)$ is the overall incidence of landslides; and $P(x)$ is the probability of landslide occurrence at any point x.

Since $P(x)$ indicates that any point x of all calculation units X in the study area is equal to $1/|x|$, the aforementioned formula can be transformed into the following equation:

$$P(y = 1|x) = \pi(x)P(y = 1)|X|. \tag{2}$$

Considering the probabilities of landslide occurrence and nonoccurrence are equal, namely $[P(y = 0) = P(y = 1) = 0.5]$, the equation can be further simplified as follows:

$$P(y = 1|x) = \frac{P(x|y = 1)}{P(x|y = 1) + P(x|y = 0)}. \tag{3}$$

The application of the MaxEnt model directly depends on the conditional probability $P(y = 1|x)$. The larger the conditional probability is, the greater the possibility of landslide occurrence will be. The event occurrence data $\pi(x)$ can be used for modeling, instead of directly estimating $P(y = 1|x)$. The value of $\pi(x)$ estimated with the principle of maximum entropy is equal to the Gibbs probability distribution represented by the exponent. If n features (f_i, $i = 1, 2, \ldots, n$) are considered, the Gibbs probability distribution can be defined as follows:

$$q_\lambda(X) = \frac{\exp\left(\sum_{i=1}^{n} \lambda_i f_i(x)\right)}{Z_\lambda}. \tag{4}$$

In the formula, Z_λ is a normalization constant to ensure that the sum of $q_\lambda(x)$ is 1. In the estimation of $q_\lambda(x)$, the model uses the

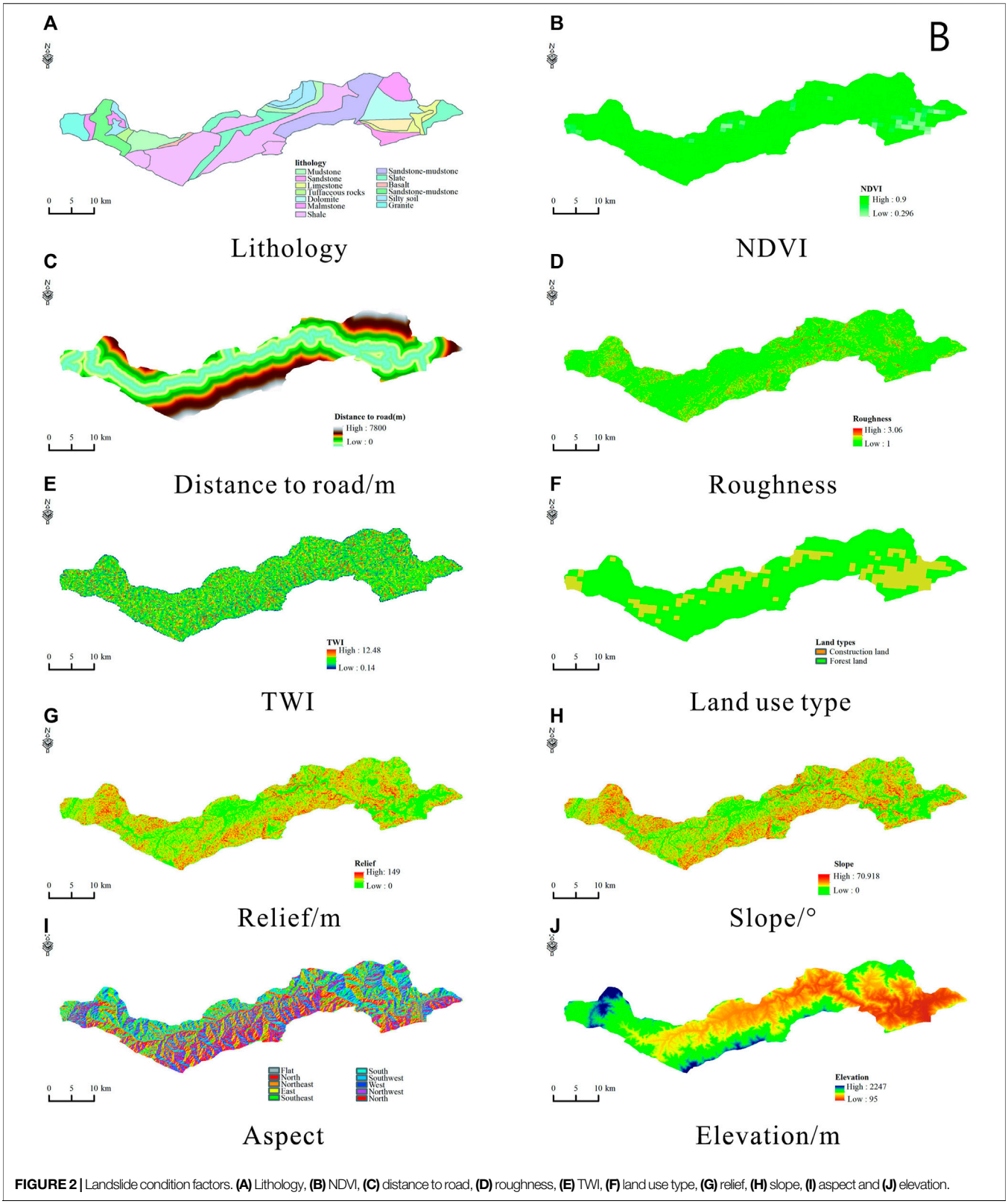


FIGURE 2 | Landslide condition factors. **(A)** Lithology, **(B)** NDVI, **(C)** distance to road, **(D)** roughness, **(E)** TWI, **(F)** land use type, **(G)** relief, **(H)** slope, **(I)** aspect and **(J)** elevation.

regularization I_2 to find the distribution closest to the constraints to avoid overfitting. Therefore, the MaxEnt model maximizes the processing of log-likelihood. If the event occurs m times within the study area, the difference between the log-likelihood and the regularization should be maximized, which is expressed as follows:

TABLE 2 | Data source.

Type	Source	Resolution/scale	Index
DEM	http://www.gscloud.cn/	30 m	Elevation, aspect, slope, TWI, roughness, relief
Geological map	http://geocloud.cgs.gov.cn/#/portal/home	1:500,000	Lithology
Remote sensing images	https://scihub.copernicus.eu/dhus/#/home	10 m	NDVI, distance to road
Land use type	http://www.resdc.cn/Default.aspx	30 m	Land use type

$$\frac{1}{m}\sum_{i=1}^{n}\mathrm{In}\left[q_{\lambda}\left(x_i\right)\right]-\sum_{j=1}^{n}\beta_j\left|\lambda_j\right|, \tag{5}$$

where β_j is the regularization parameter of the *jth* feature f_j. The maximum entropy model finds that the Gibbs distribution not only conforms to the existing data but also has good generalization significance.

Data Processing and Parameter Settings

The landslide susceptibility mapping based on the MaxEnt model mainly included the following steps.

1 Building an assessment index system: collecting landslide database elements, such as geological maps, digital elevation models, and other data, to determine the evaluation index system;
2 Data preprocessing in the QGIS platform: making the coordinate system of all evaluation indicators uniform, determining the type and size of the evaluation unit, and outputting it in an ASCII format;
3 Importing the MaxEnt software for calculation: importing the indicators obtained in the previous step and setting the training and verification ratio, and training times;
4 Landslide susceptibility classification and analysis: the calculation results were imported into the GIS platform, and the natural breakpoint method was used for susceptibility classification to achieve the landslide susceptibility mapping in the study area. The specific process is shown in **Figure 2**.

The data source of used indexes in this study is given in **Table 2**. All the layers are resampled to 30 m resolution on the pixel. All the indicators can be seen in **Figure 2**. The quantitative evaluation of the landslide susceptibility could be achieved by setting the distribution ratio of the training data and the verification data, the number of training times, and the output type recommended by Merow et al. (2013). The main parameters that needed to be set were the data split ratio and the training times. The rest of the parameters were related options such as whether to produce the ROC curve and the output type. According to the previous studies (Merow et al., 2013; Chen et al., 2017; Reichenbach et al., 2018), 80% of the landslide data of the 126 landslides, about 111 landslides, were used for the training of the model, and the remaining 20% landslide were used for the verification model. The number of training times for the model was 100. The calculation output type was a logical calculation, and the output format was the ASCII type. The line for jackknife analysis options was selected (**Figure 3**).

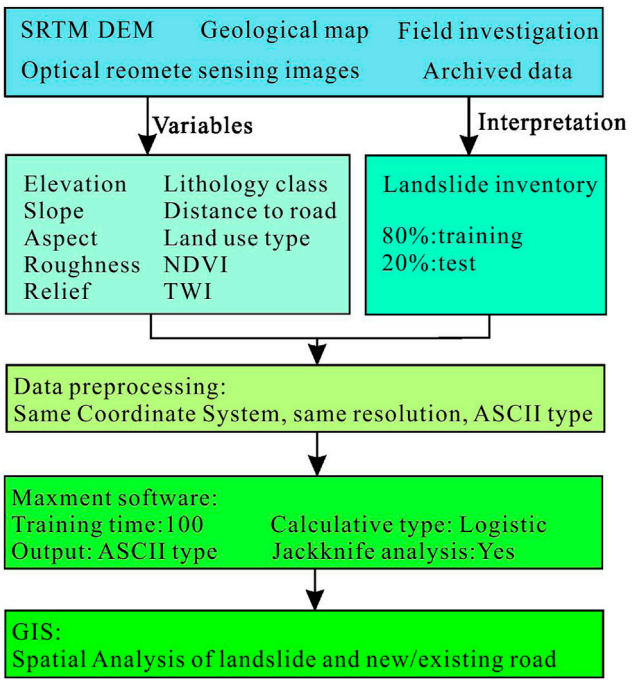


FIGURE 3 | Flowchart of landslide susceptibility mapping using the MaxEnt model.

RESULTS

Accuracy of Model Training and Testing

Using the receiver operating characteristic curve and the area under the curve, the model accuracy and the partition results were tested. As shown in **Figure 4**, the training model value reached 80.2%, and the verification accuracy reached 82.1%. According to the evaluation standard of the ROC–AUC value (Reichenbach et al., 2018), the value of the ROC–AUC was good when the value was calculated between 0.8 and 0.9. Therefore, both model training and verification achieved good prediction accuracy, and the results had a certain credibility.

Landslide Susceptibility Mapping

The calculated value of the MaxEnt model was in the range from 0 to 1. The larger the value was, the greater chance there was that the landslide was prone to happen. The results were divided into five categories using the natural breakpoints, namely, the very low-susceptibility area (0–0.144), low-susceptibility area (0.114–0.296), medium-susceptibility area

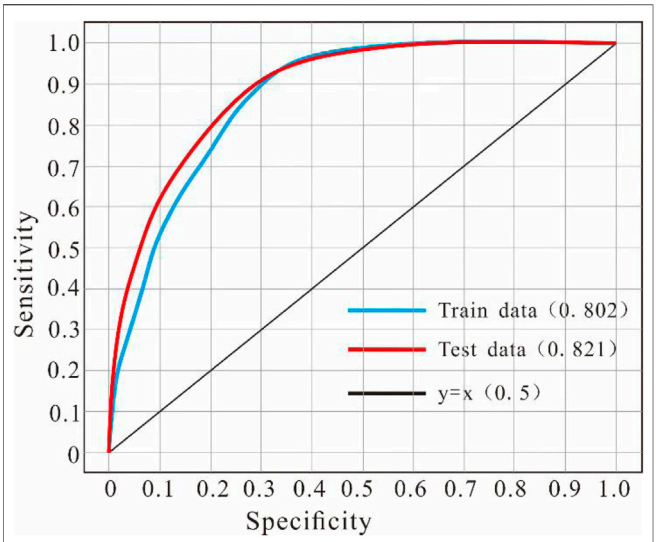


FIGURE 4 | Analysis of the ROC curves of the train and test data.

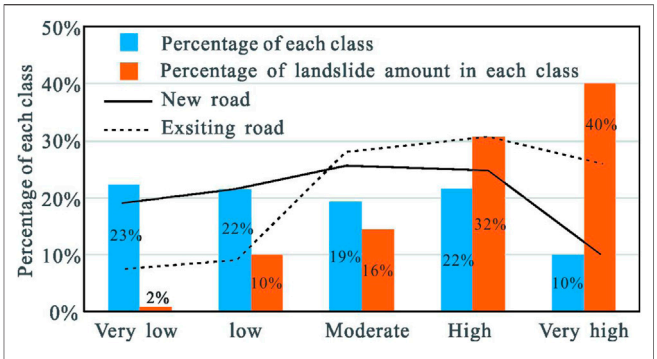


FIGURE 6 | Percentages of landslides and road lengths for each landslide susceptibility level.

(0.296–0.436), high-susceptibility area (0.436–0.584), and very high-susceptibility area (0.584–0.993). The spatial distribution of the landslide susceptibility grades is shown in **Figure 5**. It can be seen that very high-susceptibility areas of landslides were mainly distributed on two sides of the middle section of the newly built line, and the ends of the east and west sides near the cities experienced heavy human activity. The very low- and low-susceptibility areas were distributed in places without human influence or with few human influences.

With the help of grid statistical analysis tools on the GIS platform, the areas of different levels can be quantified. As shown in **Figure 6**, very low-susceptibility landslide-prone areas accounted for 2% of the total, the low-susceptibility landslide-prone areas accounted for 10%, the medium-susceptibility landslide-prone areas accounted for 16%, the high-susceptibility landslide-prone areas accounted for 32%, and the area of very high-susceptibility level accounted for 40%. In the results of the landslide susceptibility mapping, 90 (72%) of the 126 landslides were located in two categories: high-susceptibility area and very high-susceptibility area.

At the same time, to better evaluate the usefulness of the results, we used the $\%LR_{class}$ index to evaluate the prediction performance. The criterion of the $\%LR_{class}$ index was defined according to the area ratio of each grade predicted by the model and the proportion of predicted landslide points. The greater the value of $\%LR_{class}$ was, the better the prediction result of the model would be. This index $\%LR_{class} = S/A$, where S is the proportion of landslide sites in each stability grade and A is the area of each stability grade predicted by the model. After calculating the index to be 2.25, it was determined that the evaluation results had an excellent performance (Chen et al., 2017; Viet et al., 2018). Therefore, the assessment results were comprehensively evaluated in terms of the performance of the model from different aspects. All the results showed good directness, and they could be used to support linear engineering optimization.

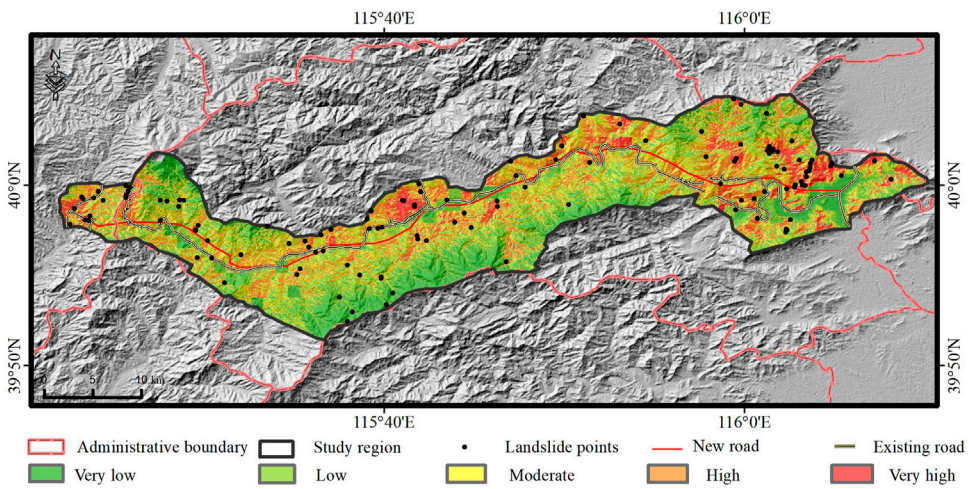


FIGURE 5 | Landslide susceptibility map.

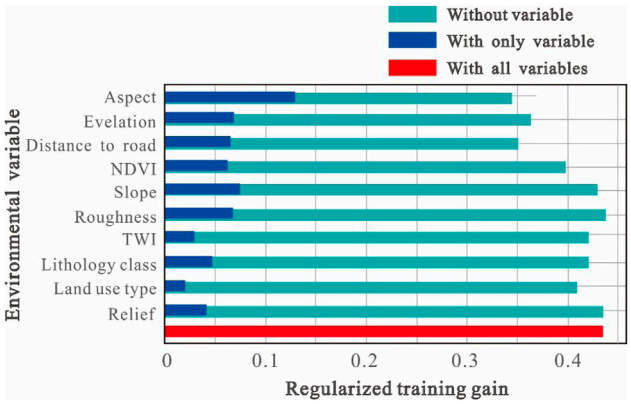


FIGURE 7 | Contribution of different indexes to landslide susceptibility results.

Quantitative Analysis of Susceptibility of New and Old Highways

Using the GIS extraction tool, the pixels of the different susceptibility levels of the new and old highways were passed through. It was found that for the new highway, as marked by a continuous dark line in **Figure 7**, only 10% was in the very high-susceptibility area, and the other four levels were distributed evenly, at about 20%. However, for the old highway, as marked by a dash dark line in **Figure 7**, 26% of the highway was in a very high level, 32% was in the high-susceptibility areas, 25% was in the medium-susceptibility areas, and the low- and very low-susceptibility areas together only made up 17%. Therefore, the newly built road faced fewer threats than the old road, especially in very high- and high-susceptibility regions, which had reduced threats of about 16% and 13%, separately, which also supported the necessity of building the proposed road and the rationality of the new route selection work.

DISCUSSION

Evaluation of the Contribution of Different Factors to the Model

Selecting the jackknife option in the MaxEnt model could reveal the impact of different evaluation indicators on the susceptibility evaluation results (Merow et al., 2013; Chen et al., 2017). After the calculation of the changing relationship between one index and the corresponding ROC value, the contribution rates of all the assessed indexes could be exported. As shown in **Figure 6**, all the indexes for the evaluation results were greater than zero, indicating that all of the indicators had certain roles for the model. Additionally, it could be seen that the six indexes, namely, the slope, aspect, distance from the road, NDVI, elevation, surface roughness, and land use type, had nearly a 90% impact on the landslide evaluation results in total, while the other indexes contributed less to the landslide rate.

The results of this analysis were consistent with field surveys and related experiences (Su et al., 2021). The slope aspect affected the weathering of the rock and soil, which in turn affected the internal mass movement after the infiltration of rainwater. The distance from the road reflected the negative effect of human activities on the local environment. The NDVI represented the ecological restoration after the occurrence of landslides (Tehraniand Janalipour, 2020). Sparser than the stable slope area, the corresponding NDVI value was also smaller, and it could thus be used to distinguish the landslide area and the non-landslide area (Tehrani et al., 2021). The elevation affected the *in situ* stress distribution, weathering, and other factors of the slope. The surface roughness indicated the difference between the landslide occurrence area and the non-landslide area after mass transport.

Earthquake and Road Construction

The facts determined by Hakan (2022) are interesting and remarkable. Compared with the study area in Arhavi and this research, it was clearly shown that the roads passed through different landforms and construction technology (Tanyas et al., 2020). The former road was mainly located on the mountainside, which caused two more types of damage to the upper and lower slopes, compared to the majority on the slope toe in the road for this research. At the same time, the road in this research was planned to have a low retaining wall at the foot of the slope influenced by cutting regions and vegetation recovery actions, rather than simply leaving the soil and rock exposed.

It should be noted that while humans have caused many deadly landslides for engineering projections, there have also been numerous conveniences for people's lives. However, compared with earthquake-induced landslides that have almost occurred during a short period, road-related landslides need a longer time to evolve to an unstable status. Hence, this provides more time and opportunities to prevent unfortunate events. Previously determined facts (Fan et al., 2019b; 2019c) have strongly proven that proper low-cost monitoring equipment can achieve successful landslide warnings before landslide failure to prevent property damage.

At the same time, as shown in **Figure 7**, the new road shows a better situation than the existing road from the aspect of length percentages in different susceptibility levels, but it should be noted that the situation may change from a low threat to a middle or high threat with new road and frequency of human activities involved.

CONCLUSION

Taking the China National Highway 109 New Line Expressway (Beijing Sixth Ring Road-City Boundary Section) project as an example, in this research, the watersheds on both sides of the non-traditional line were used as the evaluation boundary; the landslide susceptibility evaluation index of 10 evaluation indicators for 126 landslides was constructed. The system adopted the machine learning MaxEnt model to evaluate the susceptibility mapping of landslide geological hazards along the way. To support linear engineering optimization, the landslide susceptibility zoning of the old and the new roads was analyzed,

which provided a theoretical basis for route optimization and route selection. The main conclusions were as follows:

1) The MaxEnt models performed well for landslide susceptibility mapping. The training and verification accuracies of the landslide susceptibility mapping based on the GIS and MaxEnt models reached 80.2% and 82.1%, respectively. At the same time, the $\%LR_{class}$ index was used to verify the results, and the value was 2.25, which also proved the validity of the result. This further revealed that the MaxEnt model used for the spatial assessment of vegetation and animal analysis could also be applied to landslide susceptibility mapping across disciplines.
2) The use of the jackknife tool could reveal the different index contributions to landslide susceptibility mapping. In this research, the landslides were mainly affected by the slope, aspect, distance from road, NDVI, elevation, roughness, and land use type, and their cumulative contribution rate reached 90%.
3) Landslide susceptibility mapping could be used to support linear engineering optimization. After the completion of the susceptibility mapping, the relationships between the newly planned routes and the existing roads passing through the different landslide susceptibility levels were innovatively calculated. Overall, 24% of the newly built roads were located in the high-susceptibility area, and 10% were located in the very high-susceptibility area. Furthermore, 26% of the existing roads were in the very high-susceptibility area, and 32% were in the high-susceptibility area.

DATA AVAILABILITY STATEMENT

The raw data supporting the conclusion of this article will be made available by the authors, without undue reservation.

AUTHOR CONTRIBUTIONS

JS completed all the work.

ACKNOWLEDGMENTS

The author acknowledges LetPub (www.letpub.com) for linguistic assistance during the preparation of this manuscript.

REFERENCES

Baum, R. L., and Godt, J. W. (2010). Early Warning of Rainfall-Induced Shallow Landslides and Debris Flows in the USA. *Landslides* 7 (3), 259–272. doi:10.1007/s10346-009-0177-0

Chen, W., Chen, X., Peng, J., Panahi, M., and Lee, S. (2021). Landslide Susceptibility Modeling Based on ANFIS with Teaching-Learning-Based Optimization and Satin Bowerbird Optimizer. *Geosci. Front.* 12 (1), 93–107. doi:10.1016/j.gsf.2020.07.012

Chen, W., and Li, Y. (2020). GIS-based Evaluation of Landslide Susceptibility Using Hybrid Computational Intelligence Models. *Catena* 195, 104777. doi:10.1016/j.catena.2020.104777

Chen, W., Pourghasemi, H. R., Kornejady, A., and Zhang, N. (2017). Landslide Spatial Modeling: Introducing New Ensembles of Ann, Maxent, and Svm Machine Learning Techniques. *Geoderma* 305, 314–327. doi:10.1016/j.geoderma.2017.06.020

Das, I., Stein, A., Kerle, N., and Dadhwal, V. K. (2011). Probabilistic Landslide hazard Assessment Using Homogeneous Susceptible Units (Hsu) along a National Highway Corridor in the Northern Himalayas, india. *Landslides* 8 (3), 293–308. doi:10.1007/s10346-011-0257-9

Fan, X., Domènech, G., Scaringi, G., Huang, R., Xu, Q., Hales, T. C., et al. (2018). Spatio-temporal Evolution of Mass Wasting after the 2008 Mw 7.9 Wenchuan Earthquake Revealed by a Detailed Multi-Temporal Inventory. *Landslides* 15, 2325–2341. doi:10.1007/s10346-018-1054-5

Fan, X., Scaringi, G., Korup, O., West, A. J., Westen, C. J., Tanyas, H., et al. (2019a). Earthquake-Induced Chains of Geologic Hazards: Patterns, Mechanisms, and Impacts. *Rev. Geophys.* 57 (2), 421–503. doi:10.1029/2018rg000626

Fan, X., Xu, Q., Alonso-Rodriguez, A., Subramanian, S. S., Li, W., Zheng, G., et al. (2019b). Successive Landsliding and Damming of the Jinsha River in Eastern Tibet, china: Prime Investigation, Early Warning, and Emergency Response. *Landslides* 16, 1003–1020. doi:10.1007/s10346-019-01159-x

Fan, X., Xu, Q., Liu, J., Subramanian, S. S., He, C., Zhu, X., et al. (2019c). Successful Early Warning and Emergency Response of a Disastrous Rockslide in Guizhou Province, china. *Landslides* 16 (12), 2445–2457. doi:10.1007/s10346-019-01269-6

He, J. Y., Qiu, H. J., Qu, F. H., Hu, S., Yang, D., Shen, Y., et al. (2020). Prediction of Spatiotemporal Stability and Rainfall Threshold of Shallow Landslides Using the Trigrs and Scoops3d Models. *Catena* 197, 104999. doi:10.1016/j.catena.2020.104999

Huang, J., Mowen, X., and Atkinson, P. M. (2020). Dynamic Susceptibility Mapping of Slow-Moving Landslides Using Psinsar. *Int. J. Remote Sensing* 41 (19), 7509–7529. doi:10.1080/01431161.2020.1760398

Intrieri, E., Gigli, G., Mugnai, F., Fanti, R., and Casagli, N. (2012). Design and Implementation of a Landslide Early Warning System. *Eng. Geology*. 147-148, 124–136. doi:10.1016/j.enggeo.2012.07.017

Janalipour, M., Abbaszadeh Tehrani, N., Shafri, H. Z. M., Salehi, S., Mohammadzadeh, A., and Ghasemi, S. (2021). Satellite-based Monitoring of lake Urmia basin Health with Focus on its Ecosystem Regulating Services by Applying Total Ecosystem Health (TEH) Model. *Int. J. Environ. Sci. Technol* 18, 3427–3440. doi:10.1007/s13762-021-03786-1

Keefer, D. K., Wilson, R. C., Mark, R. K., Brabb, E. E., Brown, W. M., Ellen, S. D., et al. (1987). Real-Time Landslide Warning during Heavy Rainfall. *Science* 238 (4829), 921–925. doi:10.1126/science.238.4829.921

Laimer, H. J. (2017). Anthropogenically Induced Landslides - A challenge for Railway Infrastructure in Mountainous Regions. *Eng. Geology*. 222, 92–101. doi:10.1016/j.enggeo.2017.03.015

Li, Y., Wang, X., and Mao, H. (2020). Influence of Human Activity on Landslide Susceptibility Development in the Three Gorges Area. *Nat. Hazards* 104, 2115–2151. doi:10.1007/s11069-020-04264-6

Lin, Q., and Wang, Y. (2018). Spatial and Temporal Analysis of a Fatal Landslide Inventory in China from 1950 to 2016. *Landslides* 15 (12), 2357–2372. doi:10.1007/s10346-018-1037-6

Liu, C. (2004). Methods and Application of Early Warning of Geo-Hazards in China. *Geotechnical Eng. Word* 7 (7), 16–17.

Maharjan, S., Gnyawali, K. R., Tannant, D. D., Xu, C., and Lacroix, P. (2021). Rapid Terrain Assessment for Earthquake-Triggered Landslide Susceptibility with High-Resolution DEM and Critical Acceleration. *Front. Earth Sci.* 9, 689303. doi:10.3389/feart.2021.689303

Merow, C., Smith, M. J., and Silander, J. A. (2013). A Practical Guide to MaxEnt for Modeling Species' Distributions: what it Does, and Why Inputs and Settings Matter. *Ecography* 36, 1058–1069. doi:10.1111/j.1600-0587.2013.07872.x

Osanai, N., Shimizu, T., Kuramoto, K., Kojima, S., and Noro, T. (2010). Japanese Early-Warning for Debris Flows and Slope Failures Using Rainfall Indices with

Radial Basis Function Network. *Landslides* 7 (3), 325–338. doi:10.1007/s10346-010-0229-5

Qu, F., Qiu, H., Sun, H., and Tang, M. (2020). Post-failure Landslide Change Detection and Analysis Using Optical Satellite sentinel-2 Images. *Landslides* 18 (1), 447–455. doi:10.1007/s10346-020-01498-0

Rahmati, O., Pourghasemi, H. R., and Melessec, A. M. (2016). Application of Gis-Based Data Driven Random forest and Maximum Entropy Models for Groundwater Potential Mapping: a Case Study at Mehran Region, iran. *Catena* 137, 360–372. doi:10.1016/j.catena.2015.10.010

Reichenbach, P., Rossi, M., Malamud, B. D., Mihir, M., and Guzzetti, F. (2018). A Review of Statistically-Based Landslide Susceptibility Models. *Earth-Science Rev.* 180, 60–91. doi:10.1016/j.earscirev.2018.03.001

Remondo, J., Bonachea, J., and Cendrero, A. (2005). A Statistical Approach to Landslide Risk Modelling at basin Scale: from Landslide Susceptibility to Quantitative Risk Assessment. *Landslides* 2 (4), 321–328. doi:10.1007/s10346-005-0016-x

Su, Q., Tao, W., Mei, S., Zhang, X., Li, K., Su, X., et al. (2021). Landslide Susceptibility Zoning Using C5.0 Decision Tree, Random Forest, Support Vector Machine and Comparison of Their Performance in a Coal Mine Area. *Front. Earth Sci.* 9, 781472. doi:10.3389/feart.2021.781472

Tanyas, H., Gorum, T., Kirschbaum, D. B., and Lombardo, L. (2020). Could Road Constructions Be More Disastrous Than an Earthquake in Terms of Landsliding? *Earth's Future* 12, 127–143. doi:10.1002/essoar.10503922.1

Tehrani, N. A., and Janalipour, M. (20202020). Predicting Ecosystem Shift in a Salt Lake by Using Remote Sensing Indicators and Spatial Statistics Methods (Case Study: Lake Urmia basin). *Environ. Eng. Res.* 26 (4), 225. doi:10.4491/eer.2020.225

Tehrani, N. A., Shafri, H. Z. M., Salehi, S., Chanussot, J., and Janalipour, M. (2021). Remotely-Sensed Ecosystem Health Assessment (RSEHA) Model for Assessing the Changes of Ecosystem Health of Lake Urmia Basin. *Int. J. Image Data Fusion* 26 (26), 1–14. doi:10.1080/19479832.2021.1924880

Teimouri, M., and Nalivan, O. A. (2020). Susceptibility Zoning and Prioritization of the Factors Affecting Landslide Using MaxEnt, Geographic Information System and Remote Sensing Models (Case Study: Lorestan Province). *Hydrogeomorphology* 6 (21), 155–179. doi:10.22092/ijwmse.2020.126344.1658

Tran, T. V., Alvioli, M., Lee, G., and An, H. U. (2018). Three-dimensional, Time-dependent Modeling of Rainfall-Induced Landslides over a Digital Landscape: a Case Study. *Landslides* 15 (6), 1071–1084. doi:10.1007/s10346-017-0931-7

Wang, Y., Zhang, M.-s., Xue, Q., and Wu, S.-d. (2018). Risk-based Evaluation on Geological Environment Carrying Capacity of mountain city - A Case Study in Suide County, Shaanxi Province, China. *J. Mt. Sci.* 15 (12), 2730–2740. doi:10.1007/s11629-017-4798-9

Zhang, S., and Zhang, L. M. (2014). Human Vulnerability to Quick Shallow Landslides along Road: Fleeing Process and Modeling. *Landslides* 11 (6), 1115–1129. doi:10.1007/s10346-014-0468-y

Zhao, Z., Liu, Z. y., and Xu, C. (2021). Slope Unit-Based Landslide Susceptibility Mapping Using Certainty Factor, Support Vector Machine, Random Forest, CF-SVM and CF-RF Models. *Front. Earth Sci.* 9, 589630. doi:10.3389/feart.2021.589630

Conflict of Interest: The author declares that the research was conducted in the absence of any commercial or financial relationships that could be construed as a potential conflict of interest.

Publisher's Note: All claims expressed in this article are solely those of the authors and do not necessarily represent those of their affiliated organizations, or those of the publisher, the editors and the reviewers. Any product that may be evaluated in this article, or claim that may be made by its manufacturer, is not guaranteed or endorsed by the publisher.

Copyright © 2022 Shi. This is an open-access article distributed under the terms of the Creative Commons Attribution License (CC BY). The use, distribution or reproduction in other forums is permitted, provided the original author(s) and the copyright owner(s) are credited and that the original publication in this journal is cited, in accordance with accepted academic practice. No use, distribution or reproduction is permitted which does not comply with these terms.

frontiers | Frontiers in Earth Science

ORIGINAL RESEARCH
published: 05 May 2022
doi: 10.3389/feart.2022.874881

Geochemical Characteristics and Quality Appraisal of Groundwater From Huatugou of the Qaidam Basin on the Tibetan Plateau

Shengbin Wang[1,2], Zhan Xie[3], Fenglin Wang[1,2], Yuqing Zhang[3], Wanping Wang[1,2], Kui Liu[3], Zexue Qi[1,2], Fengyun Zhao[3], Guoqiang Zhang[1,2] and Yong Xiao[3]**

[1]Bureau of Qinghai Environmental Geological Prospecting, Xi'ning, China, [2]Key Lab of Geo-Environment of Qinghai Province, Xi'ning, China, [3]Faculty of Geosciences and Environmental Engineering, Southwest Jiaotong University, Chengdu, China

Groundwater is the foremost water resource for various purposes in arid regions. The extremely arid climate makes groundwater geochemistry there evolve faster in a short distance and water supply face higher pressure of poor geochemical quality. A hyper-arid watershed on the Tibetan Plateau was investigated to get insights into the geochemical signature, formation, and quality suitability of groundwater there. A total of 13 surface water samples and 32 phreatic groundwater samples were collected for hydrogeochemical analysis. The results showed groundwater had better hydrogeochemical quality than surface water and was more favorable for human society utilization. Groundwater was dominated by relatively fresh hydrochemical facies of HCO_3–Ca, mixed HCO_3–Na·Ca, and mixed Cl–Mg·Ca type with more than 93% of samples having the TDS below 1,000 mg/L. Most of the groundwaters were soft fresh water (84.38%) and had excellent to good quality (93%) for domestic purposes based on entropy-weighted water quality index evaluation. Groundwater was suitable for irrigation in terms of sodium and permeability hazard, but the potential salinity hazard should be concerned. The poor geochemical quality of groundwater was ascribed to the salinity caused by strong evaporation. Natural rock–water interactions including silicate weathering, carbonate dissolution, and cation exchange were still the predominated processes governing groundwater chemical composition. The influence of human activities was very limited. Groundwater resource exploitation and management should mainly consider the salinity and strong evaporation due to shallow water depth.

Keywords: hydrochemistry, salinity, groundwater quality, EWQI, arid region

OPEN ACCESS

Edited by:
Xiangjun Pei,
Chengdu University of Technology, China

Reviewed by:
Qian Sun,
Qilu University of Technology (Shandong Academy of Sciences), China
Yizhi Sheng,
Miami University, United States

****Correspondence:***
Zexue Qi
qzx13639722055@126.com
Yong Xiao
xiaoyong@swjtu.edu.cn

Specialty section:
This article was submitted to Geohazards and Georisks, a section of the journal Frontiers in Earth Science

Received: *13 February 2022*
Accepted: *04 April 2022*
Published: *05 May 2022*

Citation:
Wang S, Xie Z, Wang F, Zhang Y, Wang W, Liu K, Qi Z, Zhao F, Zhang G and Xiao Y (2022) Geochemical Characteristics and Quality Appraisal of Groundwater From Huatugou of the Qaidam Basin on the Tibetan Plateau. Front. Earth Sci. 10:874881. doi: 10.3389/feart.2022.874881

1 INTRODUCTION

Water resources are significantly important for the development of various aspects, such as human society, eco-environment, and agriculture, for a region (Gu et al., 2017b; Hao et al., 2018; Chaudhry and Sachdeva, 2020; Singh et al., 2020; Xiao et al., 2022b). Due to the scarce precipitation and surface water resource, arid and semiarid regions have more fragile eco-environment system and face greater challenges in balancing current development and sustainability when compared with humid regions (Zhang Q. et al., 2021; Li et al., 2021; Qu et al., 2021). Groundwater is essential for the development of diverse aspects of human society including domestic, irrigational, and industrial usages and also the

maintenance of the eco-environment in these water-scarce regions due to its widespread distribution, easy accessibility, and good stability (Xiao et al., 2018; Yousefi et al., 2018; Li et al., 2020; Yin et al., 2020). Thus, a comprehensive understanding of groundwater resources and their availability is crucial for the effective management of the precious water resources and sustainable development of the human community (Su et al., 2020; Dragon, 2021; Zhang J. et al., 2022).

In the past decades, research articles mainly focused on the water quantity (Hao et al., 2014; Havril et al., 2018; Omar et al., 2020). A large amount of studies were conducted to investigate the aquifer distribution and hydrogeological conditions, evaluate the quantity and sustainability of groundwater resources, and further make management policies and exploitation strategies (Gu et al., 2017b; Yin et al., 2017; Hao et al., 2018; Sun et al., 2019). In fact, groundwater availability is not only determined by the quantity but also constrained by the hydrochemical quality (Satheeskumar et al., 2020; Xiao et al., 2021b). The hydrochemical composition is the key factor determining the suitability of groundwater resources for domestic usage, industry, agriculture, and ecosystem development. Therefore, many scholars have conducted studies on groundwater chemistry regarding its status, genetic mechanisms, influencing factors, evolution, quality suitability, and so on and have made great contributions to the sustainable groundwater management worldwide (Huang et al., 2018; Yin et al., 2019; Banadkooki et al., 2020; Jiang et al., 2022).

In nature, the physicochemical composition of groundwater is governed by multiple factors including recharge water, aquifers' lithologies, residence time, and climatic conditions (Helena et al., 2000; Venkatramanan et al., 2017; Wu et al., 2020; Xiao et al., 2022a). Generally, groundwater chemistry evolves very slowly and keeps similar chemical composition (Zhang et al., 2021c), especially in humid regions. This is ascribed to the slow rock–water interaction and large recharge water quantity of humid regions. Thus, groundwater in humid regions usually presents in fresh, stable hydrogeochemical nature, and relatively good quality regionally (Zhang et al., 2021b). However, the extremely arid climatic conditions and strong evaporation in arid and hyper-arid regions make the hydrogeochemical evolution of groundwater there faster (Xiao et al., 2017; Yang et al., 2018; Zhao et al., 2018; Guo et al., 2019) and evolving from fresh water to hyper salt water even at a very short distance (Sheng et al., 2018; Luo et al., 2021). Recent drastic climate change forms new disturbance to groundwater chemistry and makes it more complex (Ma et al., 2019; Barbieri et al., 2021; Chen et al., 2021). In addition to the natural factors, groundwater chemistry has been facing the threats from human society (Guo et al., 2022). Groundwater chemistry genetic formation becomes more complex and unstable under the conditions of drastic natural climate change and great pressures of social development (Díaz-Alcaide and Martínez-Santos, 2019; Eslami et al., 2019; Yousefi et al., 2019; Zhang L. et al., 2022). Therefore, a comprehensive and deep understanding of groundwater chemistry is essential for the rational groundwater exploitation and sustainable management of groundwater resources in arid and semiarid regions.

The present study took a hyper-arid watershed in the Qaidam Basin on the Tibetan Plateau as an example to reveal the hydrogeochemical characteristics, quality, suitability, and genetic formation of groundwater in hyper-arid regions. The specific aims are to 1) illustrate and compare the hydrogeochemical signatures of surface water and groundwater, 2) understand why the groundwater resource is more suitable as the supplying water resource for arid regions, 3) assess groundwater quality for domestic and irrigation purposes, and 4) reveal the hydrogeochemical patterns of groundwater in hyper-arid regions. This research can provide scientific hydrogeochemical support for rational and sustainable utilizing groundwater in arid regions.

2 STUDY AREA

The present study area is a typical endorheic watershed located in the northwest of the Qaidam Basin on the Tibetan Plateau (**Figure 1**). It extends from 89°51′23″ to 90°47′44″ longitudes and 37°50′41″ to 38°22′4″ latitudes, and covers about 4,511 km^2 in total. This region is surrounded by the Qimantage Mountain in the south and Ahadi Mountain in the north. The Sibalik River is the main river running from the mountainous area in the southwest toward the northeast and then the east. The present study area belongs to the continental plateau climate and is characterized by strong evaporation and low rainfall. The annual average rainfall only approximates 55 mm, but the annual average evaporation can reach to about 2,850 mm. This climate feature makes the study area having scarce water resources, especially for surface water. Most water resources originate from the melting of snow and precipitation in the mountainous area.

The landform here involves the alluvial fan Gobi desert, overflow zone, and tail lake zone. Due to the shallow groundwater level, the overflow zone is presented as the desert oasis. The local resident settlements and farmlands are mainly located in this area. The lithology varies from a single thick layer of coarse-grained pebbly gravel and sand in the upper reaches area to multiple thin layers of fine sand, silt, and clay in the lower reach area (**Figure 2**). Groundwater in the basin is recharged mainly from the upper part of the alluvial fan by the Sibalik River, and flows from the southwest to the northwest and then to the east. Groundwater level depth varies from more than 100 m in the upper area to nearly 0 m in the downstream area. It discharges mainly through spring and evaporation.

3 MATERIAL AND METHODS

3.1 Sampling and Analysis

A total of 13 surface water samples and 32 groundwater samples were collected from the study area. The surface waters were mainly sampled from the rivers from the mountain pass to the Lake Gas Hure. Groundwater samples were concentrated in the middle reaches of the watershed where the human settlements and farmlands were located. All groundwaters were sampled from the phreatic aquifers. All samples were collected during the summer of 2020. The samples were collected in pre-washed

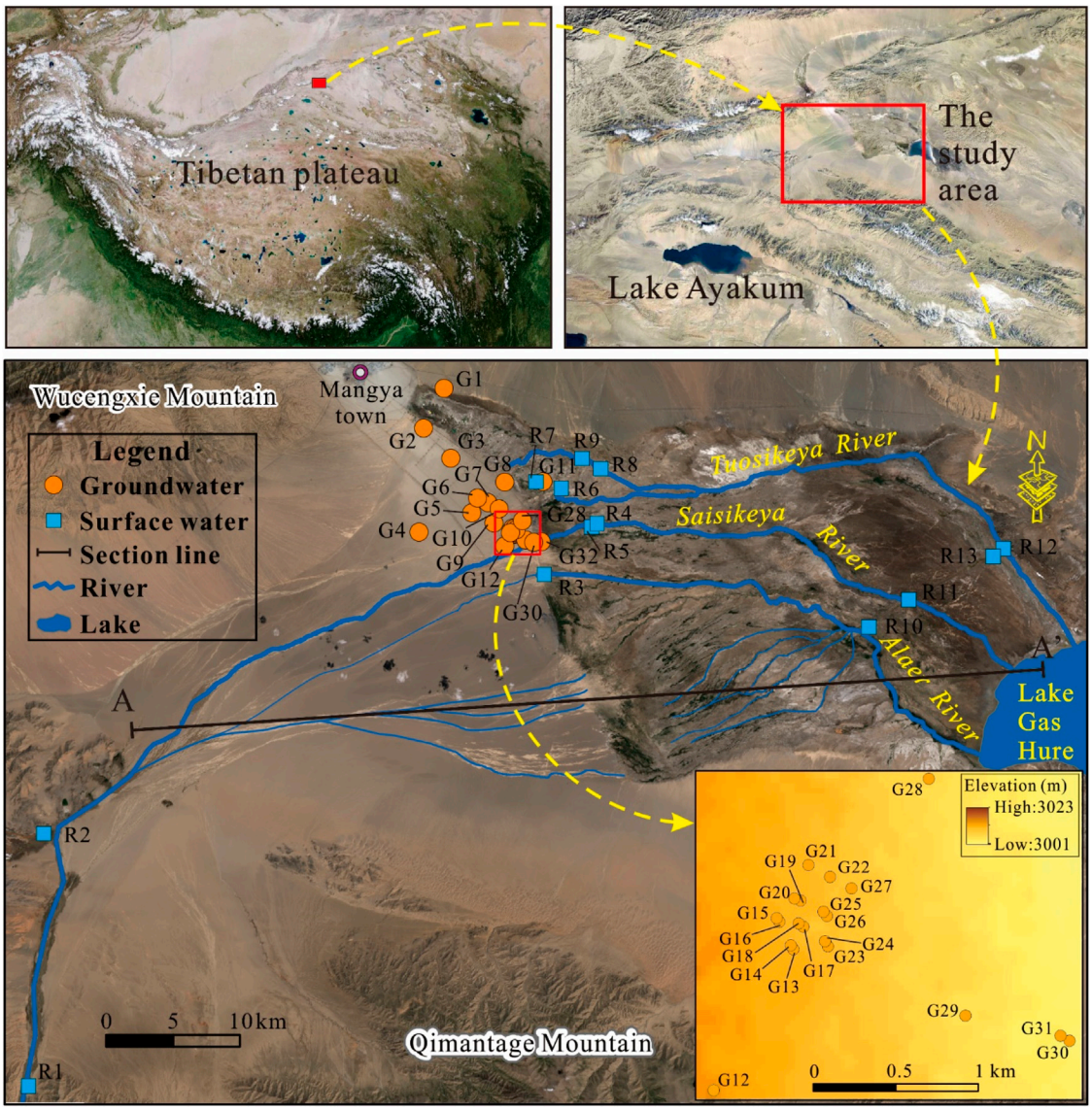


FIGURE 1 | Location map of the Hutugou watershed and groundwater sampling points.

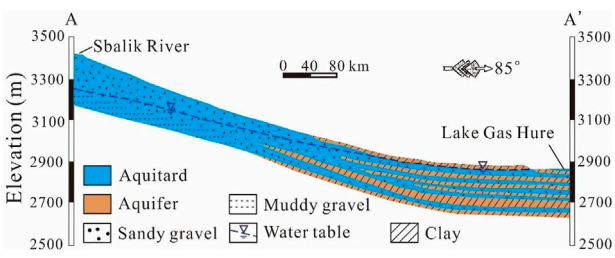


FIGURE 2 | Cross section presenting hydrogeological condition along the A-A'.

high-density polyethylene bottles with 1-L volume. Groundwater was sampled from boreholes and wells after pumping for more than 15 min. The samples were stored under 4°C and sent to the laboratory of groundwater sciences and engineering of the institute of hydrogeology and environmental geology, Chinese Academy of Geological Sciences for analysis within 24 h. Parameters including water temperature (T), pH, and electrical conductivity (EC) were measured *in situ* using a portable instrument (HANNA HI98130, Italy). Other parameters were determined in the laboratory. The HCO_3^- was determined using acid–base titration. Ions including Cl^-, SO_4^{2-}, NO_3^-, NO_2^-, NH_4^+, and F^- were measured with the aid of ion chromatography (Shimadzu LC-10ADvp, Kyoto, Japan). Major cations involving K^+, Na^+, Ca^{2+}, and Mg^{2+} were determined by the inductively coupled plasma spectrometry (Agilent 7500ce ICP-MS, Tokyo, Japan). Total dissolved solids (TDS) were obtained using the gravimetric method. The accuracy of laboratory analysis was checked with the aid of ionic charge

balance error percentage (**Eq. 1**) (Xiao et al., 2022c). All samples had the ionic charge balance error percentage between -5% and 5%, indicating reasonably good analytical accuracy.

$$\%ICBE = \frac{\sum_i^m ce_i^+ - \sum_i^m ce_i^-}{\sum_i^m ce_i^+ + \sum_i^m ce_i^-}, \quad (1)$$

where ce_i^+ represents the charge concentration of a specific cation and ce_i^- is the charge concentration of a specific anion. All of them have the unite of milliequivalent per liter.

3.2 Entropy-Weighted Water Quality Index

The entropy-weighted water quality index (EWQI) is an improved comprehensive approach based on the water quality index (WQI) which is widely used to assessing the suitability of groundwater quality for domestic purposes. The EWQI assessment can be performed as follows:

Step 1: obtaining the eigenvalue matrix Y (**Eq. 2**) with the normalized physicochemical data that can be obtained *via* **Eq. 3**.

$$Y = \begin{bmatrix} y_{11} & y_{12} & \cdots & y_{1n} \\ y_{21} & y_{22} & \cdots & y_{2n} \\ \vdots & & \ddots & \vdots \\ y_{m1} & y_{m2} & \cdots & y_{mn} \end{bmatrix}, \quad (2)$$

$$y_{ij} = \frac{x_{ij} - (x_{ij})_{min}}{(x_{ij})_{max} - (x_{ij})_{min}}, \quad (3)$$

where m and n are the number of sample and index, respectively, x_{ij} signifies the value of parameter j of sample i, and$(x_{ij})_{\max}$ and $(x_{ij})_{\min}$ present the maximum and minimum of samples' parameters, respectively.

Step 2: calculating the entropy weight of each parameter.

$$P_{ij} = \frac{y_{ij}}{\sum_{i=1}^m y_{ij}}, \quad (4)$$

$$e_j = -\frac{1}{lnm} \sum_{i=1}^m (P_{ij} \times lnP_{ij}), \quad (5)$$

$$w_j = \frac{1 - e_j}{\sum_{i=1}^n (1 - e_j)}, \quad (6)$$

where P_{ij} is the ratio of parameter j of sample I, e_j signifies the information entropy of parameter j, and w_j denotes the entropy weight of parameter j.

Step 3: obtaining the quality rating scale (q_j) of every sample.

$$q_j = 100 \times \frac{C_j}{S_j}, \quad (7)$$

where C_j signifies the parameter value of each sample and S_j is the permissible limit of each parameter recommended by the national standard or World Health Organization.

Step 4: computing the EWQI value.

$$EWQI = \sum_{j=1}^m (w_j \times q_j). \quad (8)$$

The chemical quality of water can be divided into five categories based on the aforementioned EWQI value, that is, excellent quality (EWQI ≤ 50), good quality (50 < EWQI ≤ 100), medium quality (100 < EWQI ≤ 150), poor quality (150 < EWQI ≤ 200), and extremely poor quality (EWQI > 200).

4 RESULTS AND DISCUSSION

4.1 Physicochemical Features of Surface Water and Groundwater

The physicochemical characteristics of sampled surface waters and groundwaters were statistically summarized in **Table 1**. The guidelines of drinking water recommended by the Chinese guideline (GAQS, 2017) and World Health Organization (WHO, 2017) were also involved in the Table for comparison.

Surface water in the study area showed a slightly alkaline feature with the pH value varying from 7.58 to 8.84, averaging at 8.27. The total dissolved solids (TDS) of sampled surface waters in the study area ranged from 503.20 mg/L to 7,669.06 mg/L, demonstrating a significant large salinity variation feature. It averaged at 2,568.73 mg/L, and approximately 53.85% of samples exceeded the drinking water guideline of 1,000 mg/L. Surface water demonstrated relatively fresh characteristics in the middle–upper stream area, but saline features in the middle–lower stream area. This coincides with the arid climate characteristics of the study area. All the major cations and anions also showed large variations in the concentration, suggesting fresh to extremely saline features for surface water from the mountain pass to the terminal lake. The concentrations of F^- and NO_2^- of sampled surface waters were all below the detected limits. The NO_3^- and NH_4^+ were in the range of 1.00–50.00 mg/L and 0.00–0.20 mg/L, respectively, with an average of 6.85 mg/L and 0.06 mg/L. These two ions were all within the drinking water guidelines for all sampled surface waters.

Groundwater sampled in the study area had the pH value in the range of 6.97–8.89 with a mean of 7.93, indicating a nearly neutral to slightly alkaline nature. The TDS value of groundwater varied from 368.32 mg/L to 5,838.14 mg/L with a mean of 822.70 mg/L. Groundwater also showed a large variation of salinity in the study area, but was much fresher than the surface water. Approximately 93.75% of sampled groundwaters were with the TDS value below the desirable limit of 1,000 mg/L, implying good quality for drinking purposes. The concentrations of major cations and anions in groundwater presented relatively small variations when compared with surface water. The concentration of Na^++K^+ ranged from 56.30 mg/L to 641.2 mg/L with an average of 127.57 mg/L. The Ca^{2+} and Mg^{2+} concentrations of groundwater were in the range of 16.03–350.70 mg/L and 23.08–856.58 mg/L, respectively. The contents of major anions were in the range of 74.45–1,538.53 mg/L for Cl^-, 38.42–768.48 mg/L for SO_4^{2-}, and 146.45–3,356.10 mg/L for HCO_3^-. Except for the sample collected at G31, all other sampled groundwaters in the study area had relatively low major ion concentrations, indicating fresh nature. F^-, NO_3^-, and NH_4^+ of groundwater were observed with the concentration in the range of 0.00–0.08 mg/L, 0.00–24.00 mg/L and 0.00–0.12 mg/L, respectively. All groundwater samples had these three ion content below the desirable limits for drinking purposes. The concentration of NO_2^- in sampled groundwaters

TABLE 1 | Statistical \summary of the physicochemical parameters of groundwater and related guideline for drinking water purpose.

	Index	Unit	Min	Max	Mean	SD[a]	Guideline	% of samples beyond the guideline
Surface water	T	°C	4.50	16.00	8.51	3.58	—	—
	pH	—	7.58	8.84	8.27	0.32	6.5–8.5[b]	23.08%
	TH	mg/L	275.22	1989.09	948.88	702.75	450[b]	53.85%
	TDS	mg/L	503.20	7,669.06	2,568.73	2,348.87	1,000[b]	53.85%
	Na^++K^+	mg/L	73.02	2,120.31	580.82	671.86	—	—
	Ca^{2+}	mg/L	60.12	350.70	129.34	95.33	75[c]	69.23%
	Mg^{2+}	mg/L	24.30	428.29	151.97	164.08	50[c]	46.15%
	Cl^-	mg/L	120.53	3,296.85	849.85	1,045.33	250[b]	38.46%
	SO_4^{2-}	mg/L	96.06	1,431.29	648.93	527.56	250[b]	61.54%
	HCO_3^-	mg/L	42.24	646.81	341.14	197.36	—	—
	F^-	mg/L	—	—	—	—	1.0[b]	—
	NO_3^-	mg/L	1.00	50.00	6.85	13.25	50.0[c]	0%
	NO_2^-	mg/L	—	—	—	—	0.02[b]	—
	NH_4^+	mg/L	0.00	0.20	0.06	0.06	0.2[b]	0%
Groundwater	T	°C	4.00	13.00	7.37	2.40	—	
	pH	—	6.97	8.89	7.93	0.33	6.5–8.5[b]	3.13%
	TH	mg/L	155.12	4,403.52	517.20	941.90	450[b]	6.25%
	TDS	mg/L	368.32	5,838.14	822.70	1,105.75	1,000[b]	6.25%
	Na^++K^+	mg/L	56.30	641.20	127.57	114.38	—	
	Ca^{2+}	mg/L	16.03	350.70	72.96	60.80	75[c]	12.5%
	Mg^{2+}	mg/L	23.08	856.58	83.29	192.87	50[c]	9.38%
	Cl^-	mg/L	74.45	1,538.53	182.46	295.16	250[b]	6.25%
	SO_4^{2-}	mg/L	38.42	768.48	151.82	163.90	250[b]	6.25%
	HCO_3^-	mg/L	146.45	3,356.10	451.17	718.23	—	
	F^-	mg/L	0.00	0.08	0.01	0.02	1.0[b]	0%
	NO_3^-	mg/L	0.00	24.00	4.28	4.22	50.0[c]	0%
	NO_2^-	mg/L	0.00	0.24	0.02	0.05	0.02[b]	9.38%
	NH_4^+	mg/L	0.00	0.12	0.02	0.04	0.2[b]	0%

[a]*Standard deviation.*
[b]*Chinese guideline (GAQS, 2017).*
[c]*WHO guideline (WHO, 2017).*

varied between 0.00 and 0.24 mg/L with a mean of 0.02 mg/L. About 9.38% of groundwater samples (0.08 mg/L for G23 and G25, 0.24 mg/L for G31) were found with the NO_2^- content exceeding the desirable limit of 0.02 mg/L.

4.2 Hydrogeochemical Facies of Surface Water and Groundwater

The hydrogeochemical composition and features of surface water and groundwater were demonstrated using the Piper trilinear diagram (**Figure 3**). The lower left and lower right triangular of the Piper trilinear diagram demonstrate the cations and anions composition, respectively, and the diamond field in the center presents the different hydrochemical facies that water samples may belong to (Gu et al., 2017a; Gu et al., 2019; Jiang et al., 2022; Xiao et al., 2022a).

The Piper diagram showed that almost all surface water samples were plotted in the [Na^+] type field of the lower-left triangular (**Figure 3A**), suggesting that surface water in the study area was dominated by Na^+ for the cations. This coincides with the arid climatic features of the study area. While for the major anions, although most of the surface water samples were observed situating in the [Cl^-] type field of the lower-right triangular (**Figure 3A**), some surface water samples were also found plotting in the [SO_4^{2-}] and [HCO_3^-] type field. This suggests that the surface water evolved from the fresh hydrochemical facie of HCO_3^- type to salty Cl^- type in the study area. It can be seen from the central diamond shape of the Piper diagram (**Figure 3A**), the hydrochemical facies of surface water evolved from the fresh type of HCO_3–Ca to salty Cl–Na. Surface water in the study area was dominated by salty mixed Cl–Ma·Ca type and Cl–Na type, followed by fresh HCO_3–Ca type and salty Cl–Ca type. As presented in **Table 1**, more than 53% of the sampled surface waters had the TDS beyond the drinking desirable limit of 1,000 mg/L, thus, were not suitable for drinking purposes in most locations of the study area.

As demonstrated in **Figure 3B**, most of the sampled groundwaters were plotted in the [Na^+] type field of the lower-left triangular and the [HCO_3^-] type field of the lower-right triangular of the Piper diagram, suggesting Na^+ and HCO_3^- were the dominant cation and anion for groundwater in the study area. It can be seen that some groundwater samples were situating in the [Ca^{2+}] type or [Mg^{2+}] field of the lower-left triangular and in the [SO_4^{2-}] type or [Cl^-] field of the lower-right triangular of the Piper

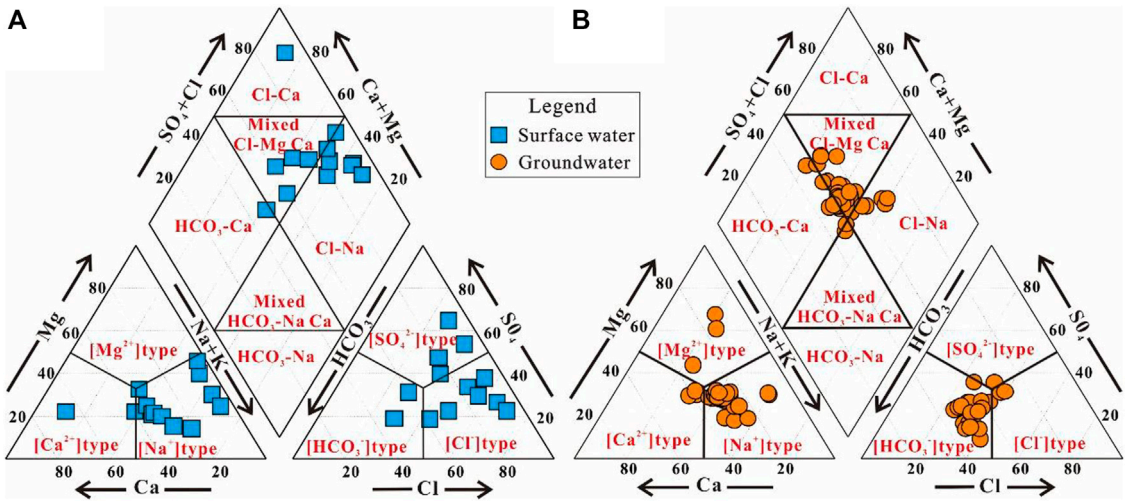


FIGURE 3 | Piper diagrams showing the hydrochemistry of **(A)** surface water and **(B)** groundwater in the study area.

diagram, illustrating that some groundwaters in the study area were dominated by Ca^{2+} or Mg^{2+} for the cations and SO_4^{2-} or Cl^- for the anions. The central diamond shape of the Piper diagram presented that the sampled groundwaters in the study area were in the hydrochemical facies of HCO_3–Ca, mixed HCO_3–Na·Ca, mixed Cl–Mg·Ca, and Cl–Na (**Figure 3B**). Most of the samples had relatively fresh hydrochemical facies, and about 15.63, 6.25, and 62.5% of the sampled groundwaters belonged to the HCO_3–Ca, mixed HCO_3–Na·Ca, and mixed Cl–Mg·Ca types, respectively. In addition, approximately 15.63% of groundwater samples were classified as the relatively salty hydrochemical facies of Cl–Na (**Figure 3B**). Groundwater in the study area also presented an evolution from a very fresh hydrochemical feature to salty hydrochemical feature. This coincides with the surface water evolution. Groundwater showed a slow evolving rate from fresh water to the salty water, and presents fresher features in the middle–upper area when compared with surface water at the same location. The statistical summary of groundwater chemical composition (**Table 1**) also suggested the sampled groundwaters had a relatively good quality in terms of the salinity. More than 93% of the sampled groundwaters were with the TDS within the drinking desirable limit of 1,000 mg/L. Thus, groundwater is the prior water resource for various purposes of the local development.

4.3 Groundwater Quality Assessment

As described previously, groundwater in the study area has fresher quality than surface water and is more favorable for various usages, thus, more attentions are paid to groundwater in the present study.

4.3.1 Domestic Purpose

The sampled groundwaters were plotted in the integrated water quality diagram of the total hardness (TH) versus the total dissolved solids (TDS) (**Figure 4**). It can be clearly seen that most of the sampled groundwaters belonged to the moderately hard fresh category (9.38%) and the soft fresh category (84.38%). Only two groundwater samples (6.25%) were observed situating in the poor quality category, and all of these two groundwater samples belonged to the very hard brackish category. Overall, groundwater in the study area had relatively good quality in terms of TH and TDS.

To further illustrate the quality of groundwater for drinking purposes, the entropy-weighted water quality index (EWQI) approach was introduced in the present study. Parameters except for water temperature (T) were all involved in the EWQI assessment. The results demonstrated that groundwater in the study area had a relatively large variation of EWQI values ranging from 22 to 461 (**Figure 5**). Most of the groundwater samples (90.63%) were with the

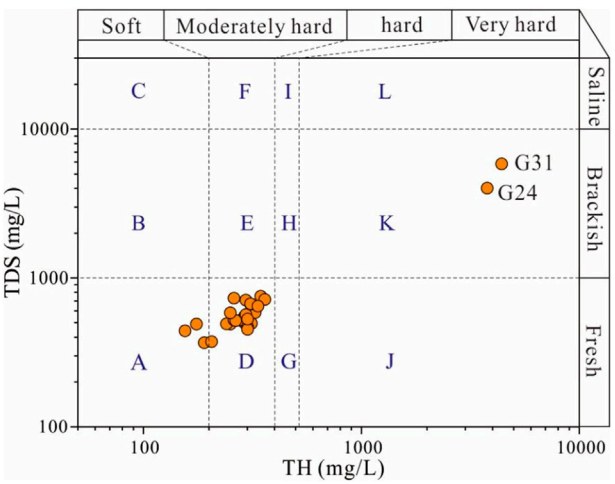


FIGURE 4 | Plots of total hardness (TH) versus total dissolved solids (TDS) of groundwater.

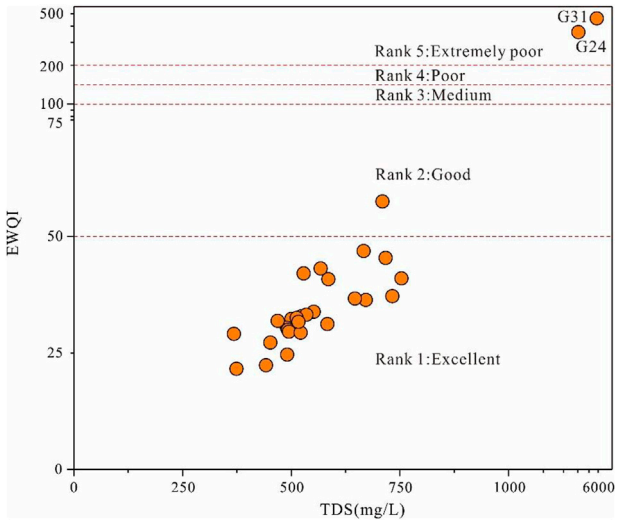


FIGURE 5 | Plots of total dissolved solids (TDS) versus EWQI value of groundwater.

EWQI value below 50, implying excellent water quality (Rank 1). In addition, one groundwater sample (3.13%) had the EWQI value in the range of 50–100 (Rank 2), indicating good water quality. All the groundwaters of these two categories were quite suitable for drinking purposes. The other two sampled groundwaters (i.e., G24 and G31) (6.25%) had a relatively high EWQI value of 357 and 461, respectively, and belonged to the extremely poor quality category (Rank 5), implying groundwater at these two sites were not suitable for direct drinking purposes. This result coincides with the aforementioned results of the integrated water quality diagram (**Figure 4**). Overall, most groundwater in the study area had relatively good quality and suitable for domestic purpose.

In particular, the EWQI value of groundwater sampled at G24 was dominantly contributed by Mg^{2+}, TH, HCO_3^-, Cl^-, SO_4^{2-}, and TDS, Ca^{2+} with the contribution percentage of 33, 17, 12, 7, 7, 7, and 5%, respectively. The groundwater sampled at G31 was predominantly contributed by Mg^{2+}, TH, NO_2^-, HCO_3^-, Cl^-, TDS, SO_4^{2-}, and Ca^{2+} with the contribution percentage of 28, 15, 13, 11, 8, 7, 6, and 6%, respectively. Therefore, the relatively poor overall quality of groundwater in the study area is predominantly ascribed to the high salinity. The high nitrite concentration is also responsible for the high EWQI value, that is , the poor quality of groundwater G31.

4.3.2 Irrigational Purpose

The high concentration of ions in irrigation water could pose irreversible harms to soil structure. Special attention should be paid to the arid and semiarid regions due to the potential high salinity of water caused by strong evaporation (Luo et al., 2021).

The sodium adsorption ratio (SAR) is an effective approach to reveal the possible soil structure damage caused by the replacement of the Ca^{2+} and Mg^{2+} on soil mediums to Na^+ in irrigation water (Xiao et al., 2021a). It is commonly coupled with the EC value to illustrate the potential sodium and salinity hazard when used for long-term irrigation. As demonstrated in **Figure 6**, except for the groundwater sampled at G31, other samples belonged to the S1 category of sodium hazard assessment, suggesting a low sodium hazard for water used for long-term irrigation usage. For groundwater sample G31, it is located in the S2 category, indicating a medium sodium hazard. For the salinity hazard, the sampled groundwaters were observed plotted in three categories including C2, C3, and C4. Groundwater samples were dominantly plotted in the C3 category (84.38%), and a small portion was situated in the C2 (6.25%) and C4 (6.25%), implying a high salinity hazard for groundwaters at most sampling sites (84.38%), and a medium hazard and very high hazard for groundwaters at a small portion of sampling sites (6.25% for medium hazard, and 6.25% very high hazard).

Percentage sodium (%Na) is a robust tool to reveal the possible hazard of Na^+ posed to the structure of soils (Xiao et al., 2020). It has been widely combined with the EC to construct the Wilcox diagram to assess the suitability of water for agricultural irrigation. As shown in **Figure 7**, most sampled groundwaters were situated in the categories of excellent to good (6.25%), good to permissible (84.38%), and permissible to suitable (3.13%), demonstrating suitable quality for agricultural irrigation. Meanwhile, two groundwater samples (G24 and G31) were found with a high sodium hazard risk if used for long-term irrigation, thus not suitable for agricultural usage.

The permeability index (PI) is a useful parameter for revealing the permeability effect posed by irrigation water and has been widely used worldwide (Xiao et al., 2020; Luo et al., 2021). The Doneen diagram, which coupled PI with the total concentration, groups the irrigation water quality into three categories, that is, class-I, class-II, and class-III (Gu et al., 2018; Xiao et al., 2021a). The class-I category indicates irrigation water would make the soil 100% maximum permeability and is suitable for long-term agricultural irrigation. The class-II and class-III categories demonstrate 75% maximum permeability and 25% maximum permeability, respectively, and are slightly appropriate and not

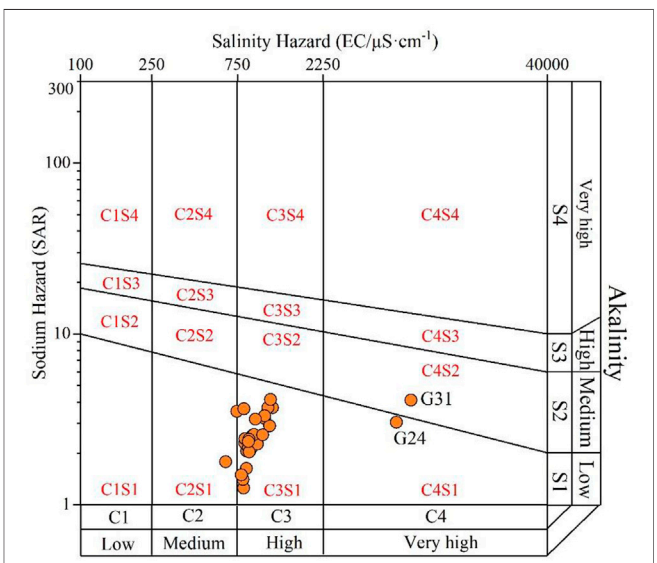


FIGURE 6 | Irrigation quality of groundwater in relation to sodium and salinity hazard.

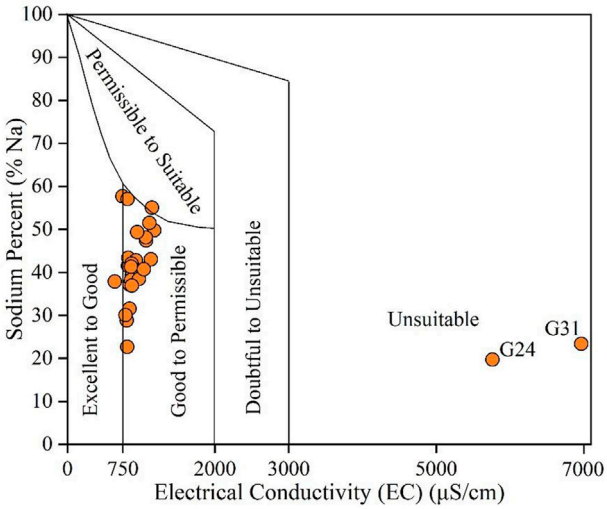


FIGURE 7 | Wilcox diagram presenting the suitability of groundwater quality for irrigation.

suitable for irrigation. The assessing results of the Doneen diagram are shown in **Figure 8**. It can be clearly seen that all sampled groundwaters had the PI value below 80, and 93.75 and 6.25% of samples belonged to class-I and class-II categories, respectively. This suggests that all groundwater sampled in the study area would not threaten the permeability of soil when used for long-term agricultural irrigation.

Overall, groundwaters sampled in the study area had nearly no sodium hazard and permeability hazard to soil structure. However, salinity hazards should be concerned as more than 93% of groundwater samples may pose high to very high salinity threats to soils if used for long-term irrigation. This mainly occurs in the lower reaches of the watershed where the groundwater level is relatively shallow.

4.4 Hydrogeochemical Patterns of Groundwater

Understanding the mechanisms governing groundwater chemical compositions is essential for rational groundwater resource exploitation and sustainable management (Hao et al., 2020).

In nature, groundwater chemistry is dominantly governed by three categories, that is, precipitation, rock–water interaction, and evaporation (Xiao et al., 2022a). These three main governing mechanisms can be visually revealed using the Gibbs diagrams that constructed by $Na^+/(Na^+{+}Ca^{2+})$ vs. TDS and $Cl^-/(Cl^- + HCO_3^-)$ vs. TDS (Hao et al., 2020). As shown in **Figure 9**, most of the groundwater samples (93.75%) were plotted in the rock dominance, illustrating that the sampled groundwaters in the study area were dominantly controlled by the rock–water interaction on the hydrochemical composition. In addition, two samples (G24 and G31) were observed plotting the evaporation dominance of the two sub-diagrams of Gibbs, suggesting that the hydrochemistry of groundwater at these two sites was mainly controlled by evaporation in nature. Thus, the poor water quality of groundwater for domestic and irrigational purposes was dominantly caused by the strong evaporation.

To further illustrate the specific rock–water interaction contributing to most of the groundwater samples, the end-member diagrams of Na^+-normalized Ca^{2+} versus HCO_3^- (Xiao et al., 2022b) of groundwater were introduced in the present study. As illustrated in **Figure 10**, groundwater samples collected in the study area were situated in the silicate dominance and toward the carbonates dominance, indicating the natural chemical components of groundwater in the study area dominantly originated from the silicate weathering (**Eq. 9**) and also carbonate dissolution. However, evaporative dissolution was not the main contributor of groundwater chemical composition.

$$2NaAlSi_3O_8{+}2CO_2{+}11H_2O{\rightarrow}Al_2Si_2O_5(OH)_4{+}4H_4SiO_4{+}2Na^+ {+}2HCO_3^-. \quad (9)$$

The bivariate plots of major chemical ions of groundwater were presented in **Figure 11**. As shown in **Figure 11A**, most of the groundwater samples were plotted away from the halite line (Na^+/Cl^- ratio of 1:1), suggesting that halite dissolution was not the main process contributing major ions to groundwater. In addition, it can be clearly seen from the **Figures 11B,C** that almost all groundwater samples were also observed situating away from the 1:1 line of Ca^{2+}/SO_4^{2-} and $(Ca^{2+}{+}Mg^{2+})/SO_4^{2-}$, indicating that the sulfate dissolution was not the main contributor of groundwater chemical composition. All the aforementioned facts confirmed the end-member results that groundwater chemistry was not controlled by evaporative dissolution. In the meantime, **Figure 11D** shows that most of the groundwater samples were plotted along the 1:1 line of $(Ca^{2+}{+}Mg^{2+})/(SO_4^{2-} + HCO_3^-)$,

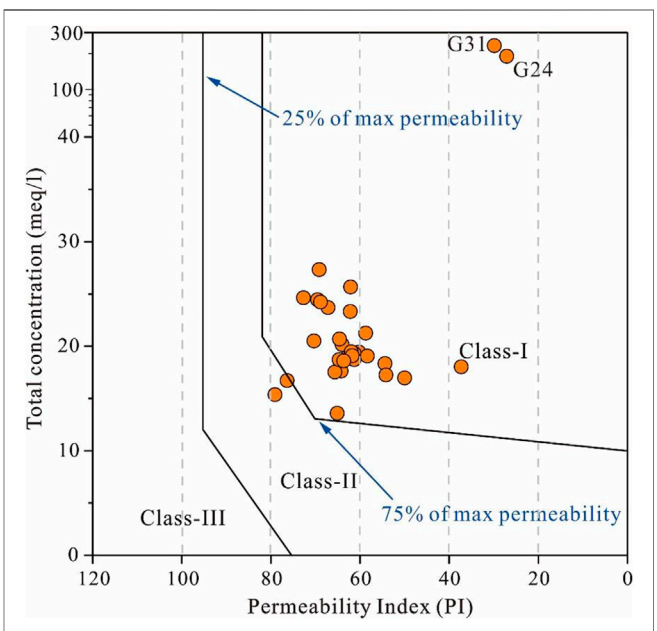


FIGURE 8 | Doneen diagram for assessing the suitability of groundwater quality for irrigation.

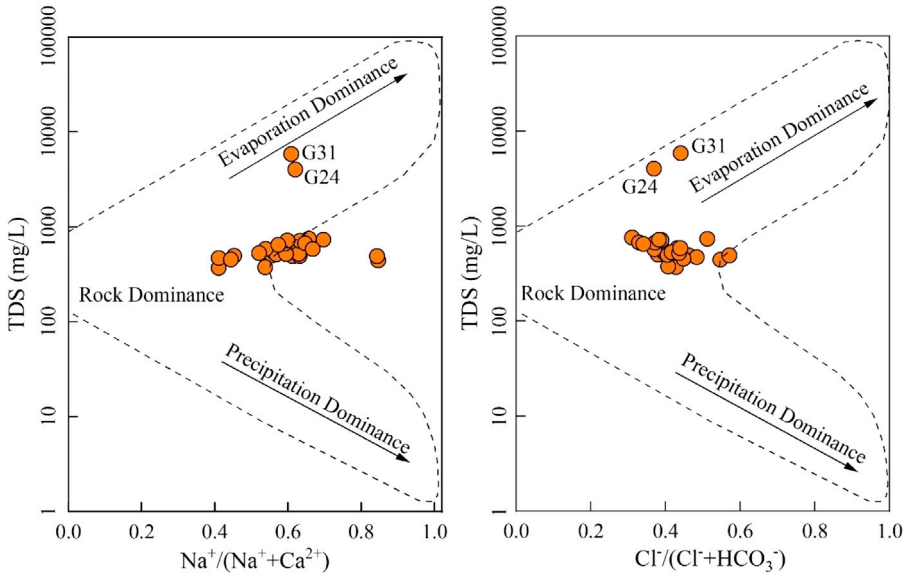


FIGURE 9 | Gibbs diagrams for groundwater samples in the study area.

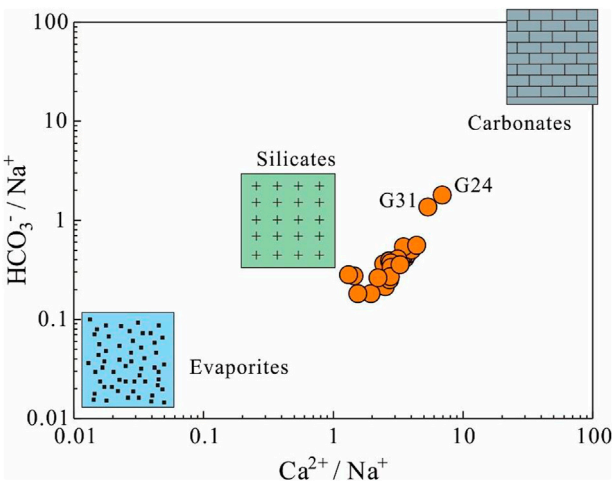


FIGURE 10 | Plots of Na-normalized Ca versus HCO_3 of groundwater in the study area.

implying sulfate dissolution or carbonate dissolution. However, as mentioned previously, the sulfate dissolution is not the main process; thus, carbonate dissolution is the process contributing to the major chemistry of groundwater in the study area. This coincides with the end-member diagram results.

In addition, ion exchange is also an important proces in the groundwater environment. Chloro-alkaline indices (CAI-1 and CAI-2) expressed in **Eqs 10** and **11** are useful tools to get insights into potential ion exchange interactions (Hao et al., 2020; Xiao et al., 2022b). As shown in the bivariate diagram of chloro-alkaline indices (**Figure 12**), most of the groundwater samples (84.38%) were with the negative CAI-1 and CAI-2, indicating the cation-exchange reaction (**Eq. 12**) is an important process contributing groundwater chemistry. This process dominantly occurs in the fresher groundwater in the upper part of the watershed. Meanwhile, about 15.63% of sampled groundwaters were observed to have positive values for both CAI-1 and CAI-2, implying the reverse cation-exchange reaction (**Eq. 13**). However, this process was dominantly situated in the lower parts of the watershed with relatively higher salinity.

$$\mathbf{CAI-1} = \frac{\boldsymbol{Cl^- - (Na^+ + K^+)}}{\boldsymbol{Cl^-}}, \tag{10}$$

$$\boldsymbol{CAI-2} = \frac{\boldsymbol{Cl^- - (Na^+ + K^+)}}{\boldsymbol{SO_4^{2-} + CO_3^{2-} + HCO_3^- + NO_3^-}}, \tag{11}$$

$$\mathrm{Ca^{2+}\ (or\ Mg^{2+})} + \mathrm{2NaX\ (solids)} \rightarrow \mathrm{2Na^+} + \mathrm{CaX_2\ (or\ MgX_2)\ (solids)}, \tag{12}$$

$$\mathrm{2Na^+ + CaX_2\ (or\ MgX_2)\ (solids)} \rightarrow \mathrm{Ca^{2+}\ (or\ Mg^{2+})} + \mathrm{2NaX\ (solids)}. \tag{13}$$

Anthropogenic inputs are found to be another important contribution to groundwater chemical composition in many regions worldwide and cannot be ignored. NO_3^- is an important indicator for anthropogenic inputs into the groundwater environment. Generally, the natural background limit of NO_3^- is 10 mg/L. Groundwater with NO_3^- concentration beyond this limit is usually considered as being influenced by anthropogenic pollution inputs. In the present study, only one collected groundwater sample (G24) was found with the NO_3^- concentration of 24 mg/L and beyond this natural limit. All other groundwater samples had the NO_3^- concentration within the natural threshold. Therefore, anthropogenic pollutant inputs were not a widespread process contributing to groundwater chemistry.

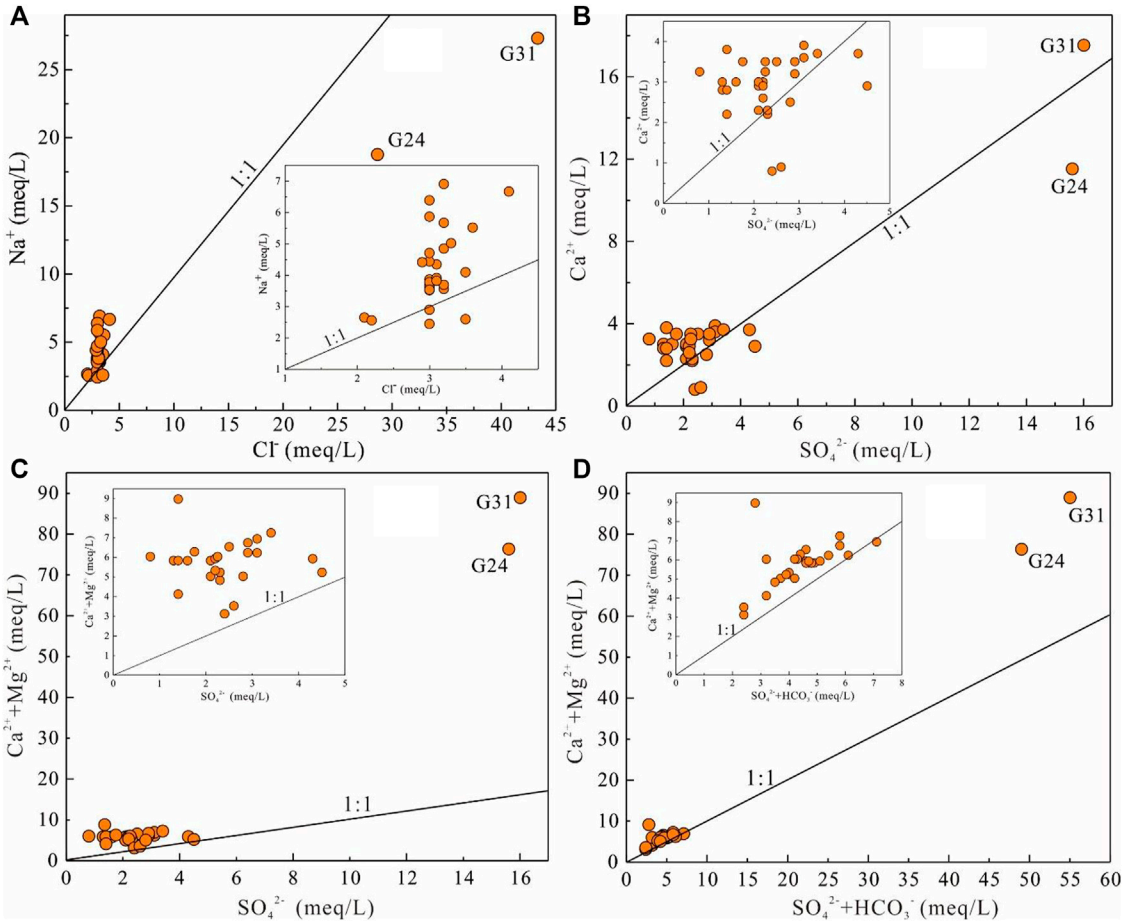


FIGURE 11 | Scatter plots of **(A)** Na^+ vs. Cl^-, **(B)** Ca^{2+} vs. SO_4^{2-}, **(C)** (Ca^{2+}+Mg^{2+}) vs. SO_4^{2-}, and **(D)** (Ca^{2+}+Mg^{2+}) vs. (SO_4^{2-} + HCO_3^-) of groundwater in the study area.

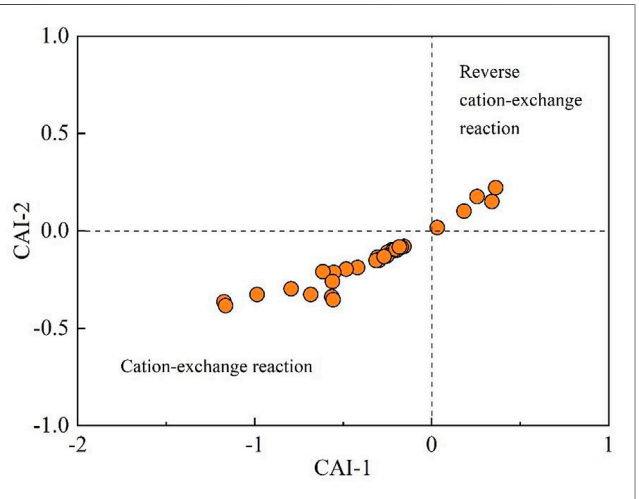


FIGURE 12 | Scatter plots of chloro-alkaline indices illustrating ion exchange reaction.

Groundwater at the local site (G24) should be concerned for the anthropogenic pollution. In addition, three sites were found with the NO_2^- concentration exceeding the drinking water desirable limit, and also implied anthropogenic influence. Fortunately, these two ions were not observed to have the significant relationships with other major ions according to the Pearson correlation coefficient results. Thus, although anthropogenic pollution inputs had elevated the content of nitrogen, the major chemistry of groundwater was not affected by anthropogenic activities. Therefore, salinity caused by strong evaporation is the main threat to groundwater quality in the study area.

5 CONCLUSION

A hyper-arid watershed in the Qaidam Basin on the Tibetan Plateau was investigated concerning its groundwater geochemical characteristics, genesis, and quality suitability. The main findings are as follows:

The present research indicated groundwater and surface water in the study area had a slightly alkaline nature and their hydrochemistry was characterized by arid climatic features. Both groundwater and surface water had a large variation of salinity and evolved from fresh water to salty water in the watershed. Surface water was dominated by salty mixed Cl–Ma·Ca type and Cl–Na type, and more than 53% of the sampled surface waters had the TDS beyond the drinking desirable limit of 1,000 mg/L. Most of the sampled groundwaters belonged to the relatively fresh hydrochemical facies of HCO_3–Ca, mixed HCO_3–Na·Ca, mixed Cl–Mg·Ca type, and less than 7% of samples had the TDS exceeding the drinking desirable limit. Groundwater had relatively good quality in terms of the salinity when compared with surface water, and was the prior water resource for the local water supply.

Groundwater in the study area was mainly soft fresh water (84.38%), followed by moderately hard fresh water (9.38%) and very hard brackish water (6.25%). The sampled groundwaters had the EWQI value ranging from 22 to 461, and more than 93% of groundwater was excellent to good quality (EWQI < 100). The poor quality of groundwater was dominantly ascribed to the salinity, and also contributed by the nitrite locally. Most of the sampled groundwaters were suitable for irrigation and would not pose a sodium hazard and permeability hazard, but the salinity hazard should be concerned.

The geochemical composition of groundwater in the study area was dominantly governed by the natural rock–water interaction. The poor quality of groundwater at local sites was ascribed to the relatively high salinity caused by strong evaporation rather than anthropogenic influence. Groundwater chemical components mainly originated from silicate weathering, carbonate dissolution, and cation exchange. Anthropogenic pollution only elevated some local nitrogen concentration, but was not responsible for the high salinity. Groundwater salinity caused by strong evaporation should be considered in groundwater exploitation and management in arid regions like the present study area.

DATA AVAILABILITY STATEMENT

The raw data supporting the conclusion of this article will be made available by the authors, without undue reservation.

AUTHOR CONTRIBUTIONS

Conceptualization: SW, YX, and FW; methodology: SW, ZX, and YZ; formal analysis: SW, WW, ZQ, KL, GZ, and FZ; investigation: SW, ZQ, KL, and GZ; data curation: SW, ZX, ZQ, GZ, and FZ; software: ZX, YZ, KL, and FZ; writing—original draft: SW; writing—review and editing: YX; and supervision: FW, WW, and YX.

FUNDING

This research was funded by the Natural Science Foundation of China (Grant Number 42007183), the Fundamental Research Funds for the Central Universities (Grant Number 2682021ZTPY063), the Key Lab of Geo-Environment of Qinghai Province (Grant Number 2021KJ011, 2021KJ00102), the Student Research Training Program of Southwest Jiaotong University (Grant Number 210815), and the Research Project on Teaching Reform of Southwest Jiaotong University (Grant Number 20201023-04).

ACKNOWLEDGMENTS

The authors appreciate the editors and reviewers for their critical comments and suggestions which greatly helped them to improve the present manuscript.

REFERENCES

Banadkooki, F. B., Ehteram, M., Panahi, F., Sh. Sammen, S. S., Othman, F. B., and El-Shafie, A. (2020). Estimation of Total Dissolved Solids (TDS) Using New Hybrid Machine Learning Models. *J. Hydrol.* 587, 124989. doi:10.1016/j.jhydrol.2020.124989

Barbieri, M., Barberio, M. D., Banzato, F., Billi, A., Boschetti, T., Franchini, S., et al. (2021). Climate Change and its Effect on Groundwater Quality. *Environ. Geochem. Health*. doi:10.1007/s10653-021-01140-5

Chaudhry, A. K., and Sachdeva, P. (2020). Groundwater Quality and Non-carcinogenic Health Risk Assessment of Nitrate in the Semi-arid Region of Punjab, India. *J. Water Health* 18 (6), 1073–1083. doi:10.2166/wh.2020.121

Chen, J., Kuang, X., Lancia, M., Yao, Y., and Zheng, C. (2021). Analysis of the Groundwater Flow System in a High-Altitude Headwater Region under Rapid Climate Warming: Lhasa River Basin, Tibetan Plateau. *J. Hydrol. Reg. Stud.* 36, 100871. doi:10.1016/j.ejrh.2021.100871

Díaz-Alcaide, S., and Martínez-Santos, P. (2019). Review: Advances in Groundwater Potential Mapping. *Hydrogeology J.* 27 (7), 2307–2324. doi:10.1111/j.1753-318X.2009.01025.x

Dragon, K. (2021). Identification of Groundwater Conditions in the Recharge Zone of Regionally Extended Aquifer System with Use of Water Chemistry and Isotopes (Lwowek Region, Poland). *J. Hydrol. Reg. Stud.* 34, 100787. doi:10.1016/j.ejrh.2021.100787

Eslami, F., Yaghmaeian, K., Mohammadi, A., Salari, M., and Faraji, M. (2019). An Integrated Evaluation of Groundwater Quality Using Drinking Water Quality Indices and Hydrochemical Characteristics: a Case Study in Jiroft, Iran. *Environ. Earth Sci.* 78 (10), 314. doi:10.1007/s12665-019-8321-1

GAQS (2017). *Standards for Groundwater Quality (GB/T 14848-2017)*. Beijing: General Administration of Quality Supervision.

Gu, X., Xiao, Y., Yin, S., Hao, Q., Liu, H., Hao, Z., et al. (2018). Hydrogeochemical Characterization and Quality Assessment of Groundwater in a Long-Term Reclaimed Water Irrigation Area, North China Plain. *Water* 10 (9), 1209. doi:10.3390/w10091209

Gu, X., Xiao, Y., Yin, S., Liu, H., Men, B., Hao, Z., et al. (2019). Impact of Long-Term Reclaimed Water Irrigation on the Distribution of Potentially Toxic Elements in Soil: An *In-Situ* Experiment Study in the North China Plain. *Ijerph* 16 (4), 649. doi:10.3390/ijerph16040649

Gu, X., Xiao, Y., Yin, S., Pan, X., Niu, Y., Shao, J., et al. (2017a). Natural and Anthropogenic Factors Affecting the Shallow Groundwater Quality in a Typical Irrigation Area with Reclaimed Water, North China Plain. *Environ. Monit. Assess.* 189 (10). doi:10.1007/s10661-017-6229-3

Gu, X., Xiao, Y., Yin, S., Shao, J., Pan, X., Niu, Y., et al. (2017b). Groundwater Level Response to Hydrogeological Factors in a Semi-arid basin of Beijing, China. *J. Water Supply Res. Tec* 66 (4), 266–278. doi:10.2166/aqua.2017.093

Guo, L., Wang, G., Sheng, Y., Shi, Z., and Sun, X. (2019). Groundwater Microbial Communities and Their Connection to Hydrochemical Environment in

Golmud, Northwest China. *Sci. Total Environ.* 695, 133848. doi:10.1016/j.scitotenv.2019.133848

Guo, Y., Li, P., He, X., and Wang, L. (2022). Groundwater Quality in and Around a Landfill in Northwest China: Characteristic Pollutant Identification, Health Risk Assessment, and Controlling Factor Analysis. *Expo. Health*. doi:10.1007/s12403-022-00464-6

Hao, Q., Lu, C., Zhu, Y., Xiao, Y., and Gu, X. (2018). Numerical Investigation into the Evolution of Groundwater Flow and Solute Transport in the Eastern Qaidam Basin since the Last Glacial Period.*Geofluids* 2018. 1–12. doi:10.1155/2018/9260604

Hao, Q., Shao, J., Cui, Y., and Xie, Z. (2014). Applicability of Artificial Recharge of Groundwater in the Yongding River Alluvial Fan in Beijing through Numerical Simulation. *J. Earth Sci.* 25 (3), 575–586. doi:10.1007/s12583-014-0442-6

Hao, Q., Xiao, Y., Chen, K., Zhu, Y., and Li, J. (2020). Comprehensive Understanding of Groundwater Geochemistry and Suitability for Sustainable Drinking Purposes in Confined Aquifers of the Wuyi Region, Central North China Plain. *Water* 12 (11), 3052. doi:10.3390/w12113052

Havril, T., Tóth, Á., Molson, J. W., Galsa, A., and Mádl-Szőnyi, J. (2018). Impacts of Predicted Climate Change on Groundwater Flow Systems: Can Wetlands Disappear Due to Recharge Reduction? *J. Hydrol.* 563, 1169–1180. doi:10.1016/j.jhydrol.2017.09.020

Helena, B., Pardo, R., Vega, M., Barrado, E., Fernandez, J. M., and Fernandez, L. (2000). Temporal Evolution of Groundwater Composition in an Alluvial Aquifer (Pisuerga River, Spain) by Principal Component Analysis. *Water Res.* 34 (3), 807–816. doi:10.1016/s0043-1354(99)00225-0

Huang, L., Wang, L., Zhang, Y., Xing, L., Hao, Q., Xiao, Y., et al. (2018). Identification of Groundwater Pollution Sources by a SCE-UA Algorithm-Based Simulation/Optimization Model. *Water* 10 (2), 193. doi:10.3390/w10020193

Jiang, W., Liu, H., Sheng, Y., Ma, Z., Zhang, J., Liu, F., et al. (2022). Distribution, Source Apportionment, and Health Risk Assessment of Heavy Metals in Groundwater in a Multi-mineral Resource Area, North China. *Expo. Health*. doi:10.1007/s12403-021-00455-z

Li, C., Gao, X., Li, S., and Bundschuh, J. (2020). A Review of the Distribution, Sources, Genesis, and Environmental Concerns of Salinity in Groundwater. *Environ. Sci. Pollut. Res.* 27 (33), 41157–41174. doi:10.1007/s11356-020-10354-6

Li, P., Karunanidhi, D., Subramani, T., and Srinivasamoorthy, K. (2021). Sources and Consequences of Groundwater Contamination. *Arch. Environ. Contam. Toxicol.* 80 (1), 1–10. doi:10.1007/s00244-020-00805-z

Luo, Y., Xiao, Y., Hao, Q., Zhang, Y., Zhao, Z., Wang, S., et al. (2021). Groundwater Geochemical Signatures and Implication for Sustainable Development in a Typical Endorheic Watershed on Tibetan Plateau. *Environ. Sci. Pollut. Res.* 28 (35), 48312–48329. doi:10.1007/s11356-021-14018-x

Ma, R., Zhang, B., and Zhou, X. (2019). The Effects of Climate Change and Groundwater Exploitation on the Spatial and Temporal Variations of Heavy Metal Content in maize in the Luan River Catchment of China. *Environ. Sci. Pollut. Res.* 27 (1), 1035–1052. doi:10.1007/s11356-019-07012-x

Omar, P. J., Gaur, S., Dwivedi, S. B., and Dikshit, P. K. S. (2020). A Modular Three-Dimensional Scenario-Based Numerical Modelling of Groundwater Flow. *Water Resour. Manage.* 34 (6), 1913–1932. doi:10.1007/s11269-020-02538-z

Qu, S., Shi, Z., Liang, X., Wang, G., and Jin, X. (2021). Origin and Controlling Factors of Groundwater Chemistry and Quality in the Zhiluo Aquifer System of Northern Ordos Basin, China. *Environ. Earth Sci.* 80 (12), 439. doi:10.1007/s12665-021-09735-y

Satheeskumar, V., Subramani, T., Lakshumanan, C., Roy, P. D., and Karunanidhi, D. (2020). Groundwater Chemistry and Demarcation of Seawater Intrusion Zones in the Thamirabarani delta of South India Based on Geochemical Signatures. *Environ. Geochem. Health* 43, 757–770. doi:10.1007/s10653-020-00536-z

Sheng, Y., Wang, G., Zhao, D., Hao, C., Liu, C., Cui, L., et al. (2018). Groundwater Microbial Communities along a Generalized Flowpath in Nomhon Area, Qaidam Basin, China. *Groundwater* 56 (5), 719–731. doi:10.1111/gwat.12615

Singh, K. K., Tewari, G., and Kumar, S. (2020). Evaluation of Groundwater Quality for Suitability of Irrigation Purposes: A Case Study in the Udham Singh Nagar, Uttarakhand. *J. Chem.* 2020, 1–15. doi:10.1155/2020/6924026

Su, H., Geng, D., Zhang, Z., Luo, Q., and Wang, J. (2020). Assessment of the Impact of Natural and Anthropogenic Activities on the Groundwater Chemistry in Baotou City (North China) Using Geochemical Equilibrium and Multivariate Statistical Techniques. *Environ. Sci. Pollut. Res.* 27 (22), 27651–27662. doi:10.1007/s11356-020-09117-0

Sun, Q., Shao, J., Wang, Y., and Ma, T. (2019). Research on Appropriate Borehole Density for Establishing Reliable Geological Model Based on Quantitative Uncertainty Analysis. *Arab J. Geosci.* 12 (13), 410. doi:10.1007/s12517-019-4533-7

Venkatramanan, S., Chung, S. Y., Selvam, S., Lee, S. Y., and Elzain, H. E. (2017). Factors Controlling Groundwater Quality in the Yeonjegu District of Busan City, Korea, Using the Hydrogeochemical Processes and Fuzzy GIS. *Environ. Sci. Pollut. Res.* 24 (30), 23679–23693. doi:10.1007/s11356-017-9990-5

WHO (2017). *Guidelines for Drinking-Water Quality Fourth Edition Incorporating the First Addendum*. Geneva, Switzerland: World Health Organization.

Wu, X., Zhang, L., Hu, B. X., Wang, Y., and Xu, Z. (2020). Isotopic and Hydrochemical Evidence for the Salinity Origin in the Coastal Aquifers of the Pearl River Delta, Guangzhou, China. *J. Contaminant Hydrol.* 235, 103732. doi:10.1016/j.jconhyd.2020.103732

Xiao, Y., Hao, Q., Zhang, Y., Zhu, Y., Yin, S., Qin, L., et al. (2022a). Investigating Sources, Driving Forces and Potential Health Risks of Nitrate and Fluoride in Groundwater of a Typical Alluvial Fan plain. *Sci. Total Environ.* 802, 149909. doi:10.1016/j.scitotenv.2021.149909

Xiao, Y., Liu, K., Hao, Q., Li, Y., Xiao, D., and Zhang, Y. (2022b). Occurrence, Controlling Factors and Health Hazards of Fluoride-Enriched Groundwater in the Lower Flood plain of Yellow River, Northern China. *Expo. Health* 14, 2. doi:10.1007/s12403-021-00452-2

Xiao, Y., Liu, K., Hao, Q., Xiao, D., Zhu, Y., Yin, S., et al. (2022c). Hydrogeochemical Insights into the Signatures, Genesis and Sustainable Perspective of Nitrate Enriched Groundwater in the piedmont of Hutuo Watershed, China. *CATENA* 212, 106020. doi:10.1016/j.catena.2022.106020

Xiao, Y., Liu, K., Yan, H., Zhou, B., Huang, X., Hao, Q., et al. (2021a). Hydrogeochemical Constraints on Groundwater Resource Sustainable Development in the Arid Golmud Alluvial Fan plain on Tibetan Plateau. *Environ. Earth Sci.* 80 (22), 750. doi:10.1007/s12665-021-10076-z

Xiao, Y., Shao, J., Cui, Y., Zhang, G., and Zhang, Q. (2017). Groundwater Circulation and Hydrogeochemical Evolution in Nomhon of Qaidam Basin, Northwest China. *J. Earth Syst. Sci.* 126 (2), 8. doi:10.1007/s12040-017-0800-8

Xiao, Y., Shao, J., Frape, S. K., Cui, Y., Dang, X., Wang, S., et al. (2018). Groundwater Origin, Flow Regime and Geochemical Evolution in Arid Endorheic Watersheds: a Case Study from the Qaidam Basin, Northwestern China. *Hydrol. Earth Syst. Sci.* 22 (8), 4381–4400. doi:10.5194/hess-22-4381-2018

Xiao, Y., Xiao, D., Hao, Q., Liu, K., Wang, R., Huang, X., et al. (2021b). Accessible Phreatic Groundwater Resources in the Central Shijiazhuang of North China Plain: Perspective from the Hydrogeochemical Constraints. *Front. Environ. Sci.* 9. doi:10.3389/fenvs.2021.747097

Xiao, Y., Yin, S., Hao, Q., Gu, X., Pei, Q., and Zhang, Y. (2020). Hydrogeochemical Appraisal of Groundwater Quality and Health Risk in a Near-Suburb Area of North China. *J. Water Supply: Res. Technology-Aqua* 69 (1), 55–69. doi:10.2166/aqua.2019.101

Yang, N., Wang, G., Shi, Z., Zhao, D., Jiang, W., Guo, L., et al. (2018). Application of Multiple Approaches to Investigate the Hydrochemistry Evolution of Groundwater in an Arid Region: Nomhon, Northwestern China. *Water* 10 (11), 1667. doi:10.3390/w10111667

Yin, S., Gu, X., Xiao, Y., Wu, W., Pan, X., Shao, J., et al. (2017). Geostatistics-based Spatial Variation Characteristics of Groundwater Levels in a Wastewater Irrigation Area, Northern China. *Water Supply* 17 (5), 1479–1489. doi:10.2166/ws.2017.052

Yin, S., Xiao, Y., Gu, X., Hao, Q., Liu, H., Hao, Z., et al. (2019). Geostatistical Analysis of Hydrochemical Variations and Nitrate Pollution Causes of Groundwater in an Alluvial Fan plain. *Acta Geophys.* 67 (4), 1191–1203. doi:10.1007/s11600-019-00302-5

Yin, S., Xiao, Y., Han, P., Hao, Q., Gu, X., Men, B., et al. (2020). Investigation of Groundwater Contamination and Health Implications in a Typical Semiarid Basin of North China. *Water* 12 (4), 1137. doi:10.3390/w12041137

Yousefi, M., Asghari, F., Zuccarello, P., Oliveri Conti, G., Ejlali, A., Mohammadi, A., et al. (2019). Spatial Distribution Variation and Probabilistic Risk Assessment of Exposure to Fluoride in Ground Water Supplies: A Case

Study in an Endemic Fluorosis Region of Northwest Iran. *Ijerph* 16 (4), 564. doi:10.3390/ijerph16040564

Yousefi, M., Ghoochani, M., and Hossein Mahvi, A. (2018). Health Risk Assessment to Fluoride in Drinking Water of Rural Residents Living in the Poldasht City, Northwest of Iran. *Ecotoxicology Environ. Saf.* 148, 426–430. doi:10.1016/j.ecoenv.2017.10.057

Zhang, J., Jing, H., Dong, K., Jin, Z., and Ma, J. (2022a). The Effect of Drip Irrigation under Mulch on Groundwater Infiltration and Recharge in a Semi-arid Agricultural Region in China. *Water Supply*. doi:10.2166/ws.2022.033

Zhang, L., Li, P., and He, X. (2022b). Interactions between Surface Water and Groundwater in Selected Tributaries of the Wei River (China) Revealed by Hydrochemistry and Stable Isotopes. *Hum. Ecol. Risk Assess. Int. J.* 28 (1), 1–21. doi:10.1080/10807039.2021.2016054

Zhang, Q., Xu, P., Chen, J., Qian, H., Qu, W., and Liu, R. (2021a). Evaluation of Groundwater Quality Using an Integrated Approach of Set Pair Analysis and Variable Fuzzy Improved Model with Binary Semantic Analysis: A Case Study in Jiaokou Irrigation District, East of Guanzhong Basin, China. *Sci. Total Environ.* 767, 145247. doi:10.1016/j.scitotenv.2021.145247

Zhang, Y., Dai, Y., Wang, Y., Huang, X., Xiao, Y., and Pei, Q. (2021b). Hydrochemistry, Quality and Potential Health Risk Appraisal of Nitrate Enriched Groundwater in the Nanchong Area, Southwestern China. *Sci. Total Environ.* 784, 147186. doi:10.1016/j.scitotenv.2021.147186

Zhang, Y., He, Z., Tian, H., Huang, X., Zhang, Z., Liu, Y., et al. (2021c). Hydrochemistry Appraisal, Quality Assessment and Health Risk Evaluation of Shallow Groundwater in the Mianyang Area of Sichuan Basin, Southwestern China. *Environ. Earth Sci.* 80 (17), 576. doi:10.1007/s12665-021-09894-y

Zhao, D., Wang, G., Liao, F., Yang, N., Jiang, W., Guo, L., et al. (2018). Groundwater-surface Water Interactions Derived by Hydrochemical and Isotopic (222Rn, Deuterium, Oxygen-18) Tracers in the Nomhon Area, Qaidam Basin, NW China. *J. Hydrol.* 565, 650–661. doi:10.1016/j.jhydrol.2018.08.066

Conflict of Interest: The authors declare that the research was conducted in the absence of any commercial or financial relationships that could be construed as a potential conflict of interest.

Publisher's Note: All claims expressed in this article are solely those of the authors and do not necessarily represent those of their affiliated organizations, or those of the publisher, the editors, and the reviewers. Any product that may be evaluated in this article, or claim that may be made by its manufacturer, is not guaranteed or endorsed by the publisher.

Copyright © 2022 Wang, Xie, Wang, Zhang, Wang, Liu, Qi, Zhao, Zhang and Xiao. This is an open-access article distributed under the terms of the Creative Commons Attribution License (CC BY). The use, distribution or reproduction in other forums is permitted, provided the original author(s) and the copyright owner(s) are credited and that the original publication in this journal is cited, in accordance with accepted academic practice. No use, distribution or reproduction is permitted which does not comply with these terms.

frontiers | Frontiers in Earth Science

ORIGINAL RESEARCH
published: 13 May 2022
doi: 10.3389/feart.2022.894923

Investigation on Deformation Mechanism and Treatment Effect of a Scattered Slope Based on Continuum–Discontinuum Element Method and Finite Difference Method

Meiben Gao[1,2,3,4], Hua Zhang[1], Shenghua Cui[4], Zhongteng Wu[2,3], Ji Liu[4], Lixia Feng[1], Feng Zeng[1], Ning Li[1], Fujiang Chen[1], Tianbin Li[4] and Yan Zhang[4]**

[1]School of Emergency Management, Xihua University, Chengdu, China, [2]Key Laboratory of Geohazard Prevention of Hilly Mountains, Ministry of Natural Resources, Fuzhou, China, [3]Fujian Key Laboratory of Geohazard Prevention, Fuzhou, China, [4]State Key Laboratory of Geohazard Prevention and Geoenvironment Protection, Chengdu University of Technology, Chengdu, China

OPEN ACCESS

Edited by:
Yunhui Zhang,
Southwest Jiaotong University, China

Reviewed by:
Meng Zhao,
Chengdu University, China
Tong Shen,
Henan University of Urban Construction, China
Dongsheng Wu,
Jinan University, China

***Correspondence:**
Meiben Gao
gaomb@mail.xhu.edu.cn
Yan Zhang
zhylr1988@126.com

Specialty section:
This article was submitted to Geohazards and Georisks, a section of the journal Frontiers in Earth Science

Received: 12 March 2022
Accepted: 13 April 2022
Published: 13 May 2022

Citation:
Gao M, Zhang H, Cui S, Wu Z, Liu J, Feng L, Zeng F, Li N, Chen F, Li T and Zhang Y (2022) Investigation on Deformation Mechanism and Treatment Effect of a Scattered Slope Based on Continuum–Discontinuum Element Method and Finite Difference Method. Front. Earth Sci. 10:894923. doi: 10.3389/feart.2022.894923

Slope deformation and failure is an inevitable engineering problem in highway construction and operation in mountainous areas. Its essence is a continuous–discontinuous gradual failure process of slope under the action of unbalanced force. Slope deformation and failure mechanism is the basis and key content of its emergency treatment and comprehensive treatment. In this study, the continuous–discontinuous element method (CDEM) and finite difference method are used to analyze the deformation mechanism and support the effect of a scattered slope in the Biwei Expressway. The results showed that the change in the local geological environment caused by roadbed excavation leads to slope slippage along the surface and then pulls the upper rock mass gradually to produce slippage failure, resulting in the stability gradually decreasing. The mechanism is traction sliding–tensile cracking. The continuous–discontinuous element method can effectively simulate the formation process of the main and sub sliding planes during excavation and can better display the phenomenon of slope failure and gradual disintegration. The emergency disposal of the gravity anti-sliding retaining wall in front of the slope can effectively control further deformation and ensure temporary stability. In comprehensive treatment, step-type slope excavation, gravity anti-sliding retaining wall, and anchor frame beam are adopted to control the deformation and failure of slope and ensure long-term stability. The numerical simulation results are consistent with the actual results, which effectively explains the rationality of this study. The research results of this study can provide some reference for the emergency treatment and comprehensive treatment of slopes in mountainous areas and for the construction and operation of highways and other infrastructure in mountainous areas.

Keywords: slope, deformation mechanism, CDEM, excavation, sliding-tensile cracking

HIGHLIGHTS

1. The essence of slope instability is a continuous–discontinuous progressive deformation and failure process of slope under unbalanced mechanical conditions.
2. The slope has experienced a process of excavation–front part sliding–traction–back part sliding–gradual disintegration.
3. The novel CDEM method can effectively simulate the process of slope deformation, failure, and even disintegration.
4. The instability mechanism of the scattered slope in the LK0+063-LK0+400 section of the Biwei Expressway is traction sliding–tensile cracking.

INTRODUCTION

High and steep slopes are common along mountain highways due to subgrade excavation. Progressive slope movement or catastrophic slope failure of highway slopes could potentially cause severe safety problems to the construction workers and damages to the adjacent property with associated fatalities (Uribe-Etxebarria et al., 2005; Pantelidis, 2011; Shen et al., 2019a). Slope instability and its related hazards have always been the major issue that highway construction and management departments must face (Liang and Pensomboon, 2010; Zhang et al., 2021). Therefore, ensuring the stability of the slope is of vital significance to the safe construction and operation of highways in mountainous areas (Ju et al., 2011; Xue et al., 2015).

Some studies have systematically summarized the characteristics, influence factors, classification, failure mechanism, and mechanical model of slope based on a large number of slope engineering cases (Huang, 2009; Shen et al., 2019b; Zhang et al., 2019; Cui et al., 2021). Slope stability evaluation methods are also proposed (Griffiths and Lane, 1999; Zheng, et al., 2005; Kang et al., 2009). Huang (2009) investigated geological conditions, triggering factors, and mechanisms of some typical large-scale landslides in southwest China. Xue et al. (2018) analyzed the failure mechanism and stabilization of a basalt rock slide with weak layers. Wei et al. (2009) analyzed slope stability by the strength reduction and limit equilibrium methods. Li and Xu (2015) proposed a slope stability probability classification (SSPC) method to assess the stability of rock slopes in the Yunnan province of China. Marques and Lukiantchuki (2017) evaluated highway slope stability by numerical modeling. Before slope excavation or treatment, the deformation characteristics and failure mechanism should be evaluated (Ma et al., 2018; Xue et al., 2018; Zhao et al., 2019), while the stability and sliding force are usually first analyzed and calculated and then followed by the design of corresponding supporting measures (Singh et al., 2008; Zhao and Wu, 2014). Zhao and Wu (2014) designed bolt support for slope reinforcement based on the geographic information system. Yuan-cheng et al. (2019) adopted a two-stage support to the high fill slope. For complex slopes, the combined support system of the gravity anti-sliding retaining wall and anchor frame beam is widely used in mountainous slope treatment (Wei et al., 2012; Duan et al., 2014; Su et al., 2015), and there are many successful cases (Dong et al., 2010; Lin et al., 2020). The abovementioned research results have important reference significance for the further study of slope mechanism, emergency treatment, and comprehensive treatment. In fact, the essence of slope instability is a continuous–discontinuous process of gradual deformation and even disintegration of the slope under the condition of unbalanced mechanics (Li et al., 2009). It is advisable to study its deformation and failure mechanism from the perspective of continuous and discontinuous so as to provide a theoretical basis for its treatment.

The Biwei Expressway is located in the mountainous area of Southwest China, with a total length of about 125.5 km. The expressway is designed with a width of 21.5 m, a speed of 80 km/h, and four lanes in both directions. Due to the mountainous terrain and complex geological conditions along the route, during the excavation of subgrade in the LK0+063-LK0+400 section, the right-side high slope is deformed and partially collapsed, accompanied by many cracks. The internal structure is very loose, which may cause large-scale landslides at any time. The slope has undergone deformation and sliding several times and is now in a scattered state. A scattered slope is a slope undergoing a deformation–fracture–fragmentation process with a scattered structure. Its failure is a continuous–discontinuous process, which is the main difference from a normal landslide. However, there are few research studies on scattered landslides (Lai et al., 2005), especially the simulation and mechanism of the deformation–fracture–fragmentation process. In this study, combined with the actual slope, a continuous–discontinuous element method is used to analyze the deformation mechanism and the emergency response effect of the gravity-retaining wall and finally explore the comprehensive treatment effect by finite difference numerical simulation methods.

OVERVIEW OF STUDIED SLOPE ENGINEERING

Geological Conditions

The project area is situated in the Yunnan-Guizhou Plateau with a typical warm–humid monsoon climate. The precipitation in the region ranges from 793.1–984.5 mm, with an average annual precipitation of 851.6 mm. The subgrade slope is located in the northern slope of the Miaoling Mountains, with an elevation of 2000–2060 m, a height difference of about 60 m, and a slope angle of 20–25°. Surface water is generally developed with only streams. Groundwater mainly contains bedrock fissure water existing in the basalt structural plane and pore water in the Quaternary loose accumulation layer, and both of them are supplied by atmospheric precipitation. The landform type belongs to dissolution hills. Shrubs on the slope surface are well-developed. The rock strata in the area mainly consist of basalt and shale, dipping gently with little topographic relief. The Quaternary loose overburden is distributed in gentle slopes and valleys, which mainly comprise clay, silty clay, and gravel. The Luozhou–Hezhang anticline and Yadu faults are mainly geological structures in the area, and the Yadu faults are inactive nowadays. Seismic intensity is VI degree.

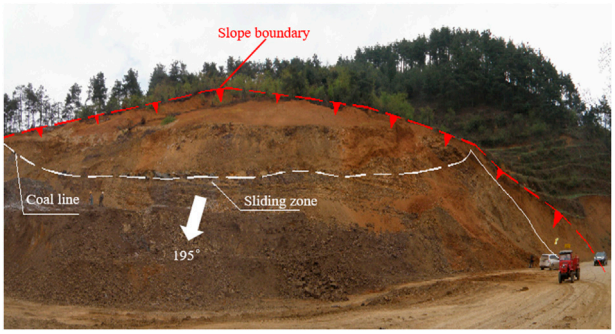


FIGURE 1 | Panoramic view of the slope in the section between chainages LK0+063LK0+400.

Deformation Characteristics of Slope

The umbrella pattern soil landslide is formed during subgrade excavation with a height of 13 m (See **Figure 1**). The high shear notch is developed on the front edge of the slope due to subgrade excavation. Under continuous creep, the soil in the shear notch area is squeezed out, slumped along the slope, and accumulated at the foot of the slope. Two sliding planes are developed in the slope, which is a step-shaped landslide. The main sliding body is 75 m long, 106 m wide, 4,654 m^2 in area, 10 m in average thickness, and 5.1 × 10^4 m^3 in volume. The sliding direction is 195°, and the sliding angle is 25°. The shear outlet in front of the slope is at the elevation of 2015 m and the upper edge sliding wall at the elevation of 2051 m, resulting in a relative height difference of 36 m (See **Figure 2**). The sub-sliding body is located at the front of the slope, with an angle of 45°.

The upper edge deformation of the slope is serious, the overall dislocation is 3–4 m (**Figure 2B**), and the tensile crack width is 2–3 m, forming the main sliding body (**Figure 2**). There is a secondary sliding body in the front part of the main sliding body. The angle of the secondary sliding plane is 45°. The sliding distance of the sub sliding body is 7–8 m, which is higher than that of the main sliding body (3–4 m).

The excavation profile has shown that the upper part of the slope is the Permian Longtan Formation comprising clay rock mixed with coal line and residual slope clay. The residual slope clay is in a plastic-soft to plastic state with a thickness of 7–8m, and the clay rock is completely weathered with a thickness of 1–10 m. The lower part of the slope is strongly weathered basalt, which is cut by bedding or crossing structural planes with a thickness of 5–10 cm, and the rock mass structure is very broken and fragmented (**Figure 2C**). The upper layer is seriously mixed with mud, mainly comprising fully weathered basalt mixed with soft plastic clay.

Moreover, according to the interpretation results of high-density electrical profiles and drilling data, the characteristics of the sliding body, sliding zone, and sliding bed are obtained.

(1) The sliding body mainly comprises cohesive soil with a small amount of gravel. Since, the slope mainly slides along the interface between clay and basalt, the upper part mainly contains clay with a loose structure. The lower part slides along the fully weathered basaltic weak zone, so the sliding body at the lower part of the east side is sandwiched with 3–5 m thick heavily weathered basalt. The rock mass has not been disturbed, and the original structural characteristics were kept to a certain extent. According to the

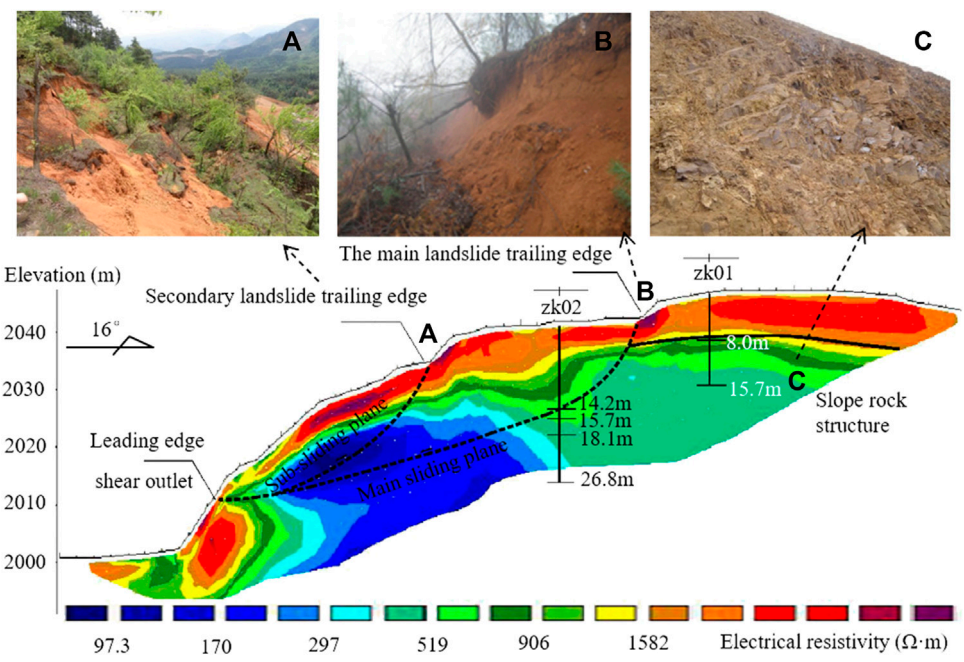


FIGURE 2 | Interpretation results of the Werner section and deformation characteristics. **(A)**: Secondary landslide trailing edge, **(B)**: The main landslide trailing edge, **(C)**: Slope rock structure.

interpretation of high-density electrical profiles, the apparent resistivity of this section is high (**Figure 2**), indicating loose sliding soil with low water content.

(2) The front edge of the sliding zone is buried 5–6 m deep and 0.5–2 cm thick, which is gray–white and gray–yellow soft plastic clay with good toughness. According to the core characteristics of the borehole (zk02), it is considered that the sliding zone is located 14.2 m underground, with a thickness of about 10 cm, and its composition is grayish–yellow clay. The west sliding zone is a black coal line with high water content, while the east sliding zone is a weak zone of fully weathered basalt with a thickness of 10 cm and very low water content. According to the interpretation of high-density electrical profiles, the water content along the sliding zone is high, especially near the shear outlet of the leading edge, and the apparent resistivity is quite different. The apparent resistivity isoline at the sliding zone displays a convex form (**Figure 2**).

(3) The sliding bed comprises grayish–yellow–grayish–black carbonaceous shale and strongly weathered basalt, cut by structural planes, and the rock mass is fractured. According to the interpretation of high-density electrical profiles, the apparent resistivity of the sliding bed is generally low, which indicates that the rock mass integrity of the sliding bed is poor and fractures are well-developed (**Figure 2**).

FORMATION MECHANISM

Internal Factors: Rock and Soil Structure

According to the excavation results, the lower part of the slope is strongly weathered basalt with cataclastic structure, and the weak structural plane with a thickness of 5–10 cm is developed inside, with locally condensed calcareous basalt. Therefore, the overall performance of the rock property is poor. The upper part is claystone and carbonaceous shale with a coal line, dipping 150° with an angle of 16°. First, the inclination of the rock layer is opposite to the inclination of the slope, which is not conducive to its stability. Furthermore, the carbon shale belongs to soft rock, and the underlying strongly weathered basalt structure is broken, so their physical and mechanical properties are poor, and their contact interface is a weak structural plane. Under the action of groundwater and *in situ* stress field, the contact zone is muddy, which further reduces and weakens their physical and mechanical properties and will become a potential sliding surface under the long-term continuous creep. This unfavorable combination of structural planes and the underlying rock soil structure with weak structural planes are the internal causes of its instability.

Inducing Factors: Slope Instability Induced by Subgrade Excavation

In the early stage, subgrade excavation was carried out according to the slope ratio of 1:0.75–1:1, resulting in the height of leading-edge free space reaching 13 m and forming a favorable free space condition and high and steep slope. Moreover, the front edge of the slope belongs to the anti-sliding section, and excavation will seriously weaken the anti-sliding ability of the slope itself. Therefore, the excavation first provides a good free space condition for its sliding and second reduces the anti-sliding resistance, inducing the sliding deformation of the slope along the carbonaceous shale, tuffaceous basalt layer, and the interlayer dislocation zone and finally shearing out from the leading edge.

Simulation Analysis of Slope Mechanism Based on the CDEM

In fact, the essence of slope instability is a continuous–discontinuous deformation and failure process of the geological body under unbalanced mechanical conditions. The continuum–discontinuum element method (CDEM), proposed by Professor Li Shihai, is an explicit numerical method for solving highly fused meshes and particles based on the basic framework of generalized Lagrange equations. In this method, the continuum algorithm and discontinued algorithm are coupled, and the progressive failure process of the material is simulated through the fracture of the block boundary and inside the block. The numerical calculation model in the CDEM-BlockdyNA consists blocks and interfaces between blocks (**Figure 3**). Most of the finite element calculations involved appear in blocks. Blocks can comprise single or multiple finite elements, which are used to represent continuous physical characteristics of materials such as elasticity and plasticity. The common boundary between arbitrary blocks is called an interface. The calculation of the interface is mainly based on discrete elements, which is being used to express the discontinuous physical characteristics of materials such as displacement and impact. This method can not only simulate the elastic, plastic, damage, and fracture process of materials under static and dynamic loads but also simulate the movement, collision, flow, and accumulation process of broken granular materials, especially suitable for the whole process simulation of progressive instability and failure of slope deformation–fracture–fragmentation. Therefore, in this study, the CDEM method is used to simulate the whole process of scattered slope in the LK0+063-LK0+400 section of the Biwei Expressway to discuss its instability mechanism. The Mohr–Coulomb criterion and maximum tensile stress criterion were adopted for numerical calculation, and the calculation parameters are shown in **Table 1**.

Figure 4 shows the displacement nephogram of slope deformation and failure process at different time steps. According to **Figure 4A**, the excavation causes the front edge of the slope to form a good airport condition and begin to slide in the lower part of the slope, forming a sliding plane. Without support, the sliding plane gradually extends backward and cracks occur in the middle of the slope (**Figure 4B**). With the development of the sliding plane inside and on the upper part of the slope and the downward expansion of the crack in the middle of the slope, the sub-sliding plane is gradually formed (**Figure 4C**). The initial sliding plane develops further toward the rear edge and top of the slope, and the main slip surface gradually forms (**Figure 4D**). The numerical simulation results are consistent with the actual slope, indicating that the numerical

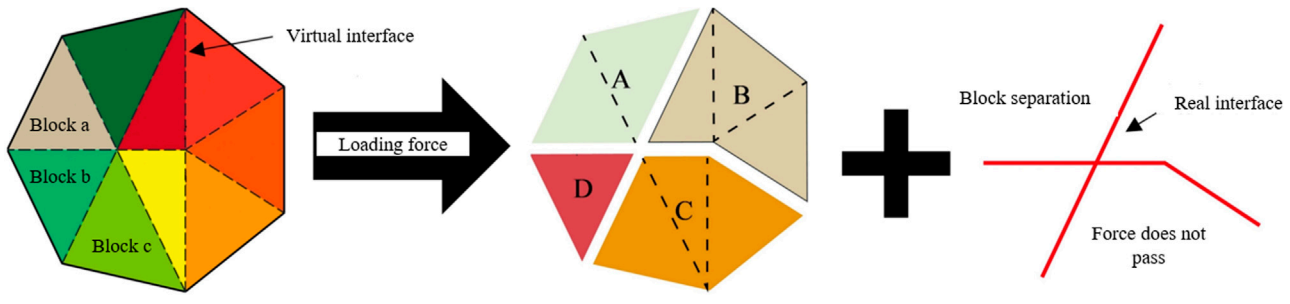


FIGURE 3 | Block and interface diagram of the CDEM (modified from Feng et al., 2017).

TABLE 1 | Numerical modeling parameters.

Stratum	Natural density γ (kN/m^3)	Elastic modulus E (kPa)	Poisson's ratio μ	Internal friction angle φ (°)	Cohesive strength C (kPa)
Clay mixed with gravel	19.0	10	0.33	15.5	20
shale	22.0	1,200	0.265	35	30
Strongly weathered basalt	23.0	900	0.25	40	15
Porphyry basalt	26.0	36,000	0.21	50	220

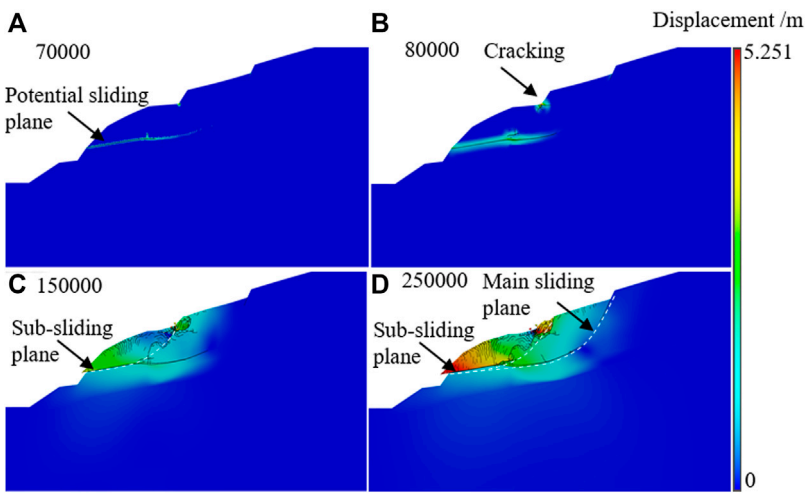


FIGURE 4 | Displacement nephogram of slope (unit:m). **(A)**: t = 70,000 steps, **(B)**: t = 80,000 steps, **(C)**: t = 1,50,000 steps, **(D)**: t = 2,50,000 steps.

simulation results can effectively reflect the formation process of the main sliding and sub-sliding plane during the excavation of the slope.

Figure 5 shows the maximum principal stress nephogram of slope deformation and failure process at different time steps. According to **Figure 5A**, the maximum principal stress of the slope gradually increases from top to bottom, which is generally controlled by the stress field of the slope. The principal stress direction near the surface is approximately vertical to the slope surface and gradually turns downward to the vertical direction. As the CDEM method is adopted, when the deformation between element meshes is too large and failure occurs, the block changes from a continuous state to a discontinuous state, and the related calculation units will disintegrate (as shown in the white area in **Figure 5B**). When the internal cracks of the slope are gradually formed, the related rock and soil bodies inside the slope are destroyed and disintegrated. Numerical calculation shows some white spots or areas, and connecting these white areas is the

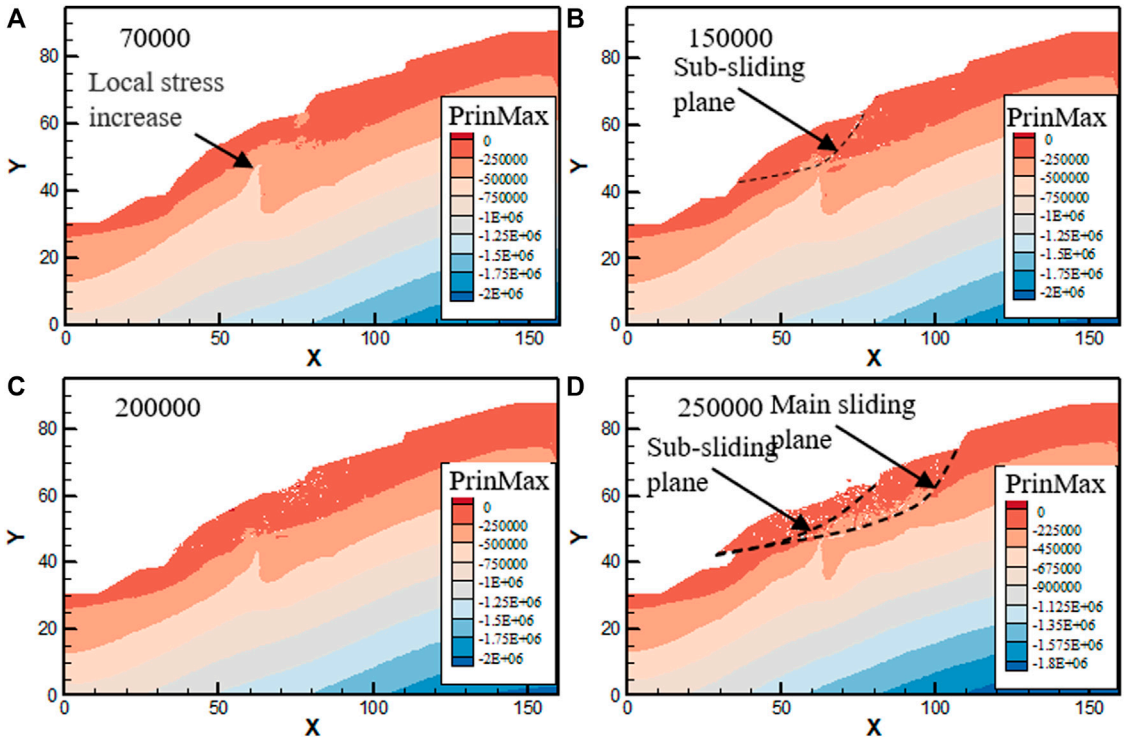


FIGURE 5 | Maximum principal stress nephoram (unit:Pa). **(A)**: t = 70,000 steps, **(B)**: t = 1,50,000 steps, **(C)**: t = 2,00,000 steps, **(D)**: t = 2,50,000 steps.

sliding plane of the slope (**Figure 5B**). Without support, the slope is further deformed and disintegrated, and finally, two sliding planes are formed (Fig. 5cd). At the same time, according to **Figure 5D**, there are many white areas in the sliding body, indicating that many cracks are developed in the sliding body. The sloping structure is very loose and broken, close to the state of granular, which is consistent with the actual situation.

The excavation formed an exposed surface with a height of 13m, which destroyed the original equilibrium state of the slope and led to a sharp adjustment of the stress state of the slope. The lower rock and soil mass produced plastic yield, strain accumulation and unloading looseness, and slippage along the open surface. The sliding of the lower slope rock mass produces traction, which causes the upper rock mass to gradually slip and destroy, and the stability gradually decreases. When the tensile or shear plastic zone is extended to complete penetration, the slope will lose stability. The softening and lubrication of groundwater promote the occurrence and development of sliding. In conclusion, the mechanism of slope instability is the excavation process that weakens its anti-sliding force and induces the generation of continuous creep along the internal weak structural plane and the final shear out along the leading edge. The mechanism is traction sliding–tensile cracking.

SLOPE EMERGENCY TREATMENT

The emergency disposal technology of slope (landslide) is mainly a quick and effective disposal technology for sliding body, which is a temporary disposal technology to prevent slope instability or further deformation of slope body and gain time for personnel evacuation and emergency deployment. It is an important step in the emergency disposal process of landslide geological disasters. Emergency rescue and disposal of landslide geological disasters is usually carried out on the basis of experience and in-site mapping without detailed investigation data, mainly including emergency rescue and disposal of dangerous situations and disasters, which is characterized by temporary rapidity, small disturbance, strong pertinence, and conservative scheme. At present, the slope of the K0+063~ LK0+400 section of the Biwei Expressway is in constant creep deformation, and the rock and soil mass at the front shear outlet is extruded and collapsed, which is in an unstable state in the natural state. In case of adverse working conditions such as earthquakes and heavy rainfall, the landslide may lose its stability as a whole, endangering the construction and traffic safety of the National Way 326. In order to ensure the normal operation of roads and other infrastructure in the affected area and the normal construction of the Biwei Expressway and further provide time and space for comprehensive treatment of these slopes, this study discusses the effect of adopting mortar block stone gravity anti-slide retaining wall as an emergency disposal measure. The anti-sliding retaining wall has the characteristics of small disturbance and fast construction and can be used as a part of subsequent treatment projects. The top width of the retaining wall is 2 m, the wall height is 10 m, and the back slope is 1:0.25. The specific effect analysis is as follows:

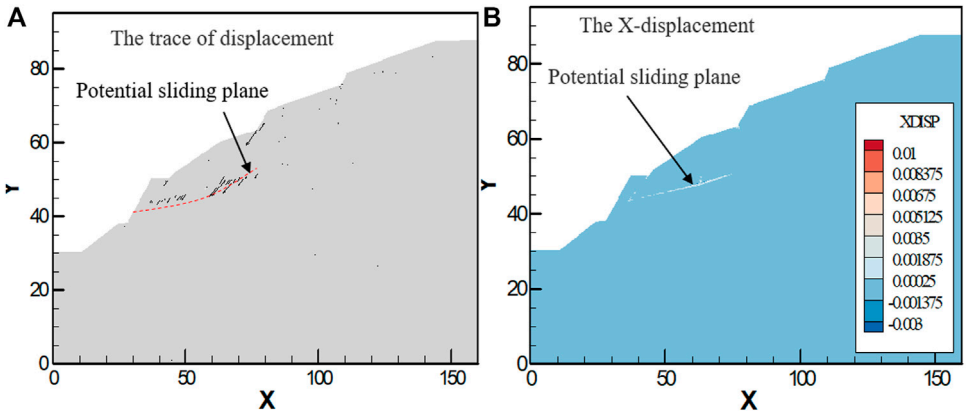


FIGURE 6 | Displacement trace and *X*-direction displacement diagram after the retaining wall is applied. **(A)**: The trace of displacement, **(B)**: X-displacement.

Figure 6 shows the displacement trace and *X*-direction displacement diagram after the retaining wall is applied. According to **Figure 6**, after the retaining wall is applied, the slope still has a sliding trend toward the surface, but the displacement trace distribution is mainly concentrated on the potential sliding plane. Meanwhile, the sliding surface is not connected, indicating that the retaining wall as an emergency treatment measure can effectively restrain the further deformation of the slope and ensure temporary stability.

In order to compare and analyze the deformation characteristics of the slope before and after the retaining wall was applied, 10 displacement monitored points were set on the sliding plane (see **Figure 7** for specific layout) to monitor the displacement characteristics of the sliding plane under two situations. According to **Figure 8A**, before the retaining wall is applied, the general characteristic of the displacement of the measured points is that the displacement of the measured points at the front edge of the slope is larger than that at the rear edge, specifically M1> M2> M3> M4> M5> M6> M7> M8> M10 > M9. The monitoring results once again verify that the instability mechanism of the slope is traction sliding–tensile cracking. The displacement of the measured point M1 is the largest, with a magnitude of up to 4.5 m. The displacement of measured points M9 and M10 is the smallest, about 0.5 m. According to **Figure 8B**, after the emergency measures of the retaining wall are applied, the displacement of measured points on the sliding plane is generally controlled, and there is no large displacement measured point; especially the displacement of measured points M1, M2, and M3 on the front edge of landslide is effectively controlled. Among the ten measured points, the displacement of the measured point M4 is the largest, with a value of about 0.0014m, which is related to the development of the sub sliding plane. The measured point M4 is located at the junction of the main sliding plane and the sub sliding plane. In addition, there is a certain distance between M4 and the retaining wall, so its suppression effect has a certain loss, resulting in the displacement of measured point M4 being larger than that of other points. The comparative

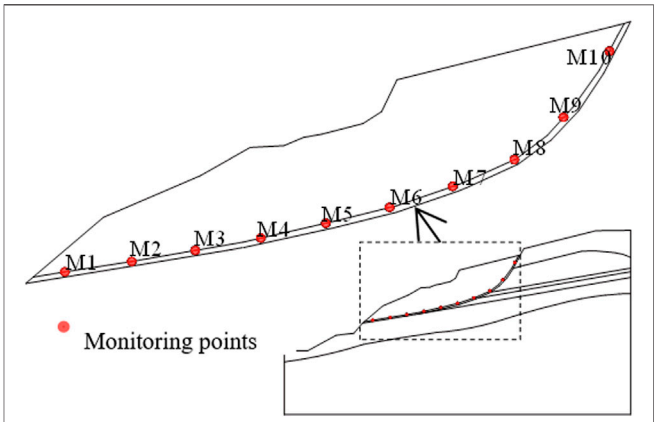


FIGURE 7 | Layout of monitoring points.

results show that the retaining wall can effectively control the further deformation of the slope, ensure the temporary stability of the slope, ensure the normal construction and passage of related roads, and then provide time and space for the comprehensive treatment of the slope, which is a good emergency treatment measure.

SLOPE COMPREHENSIVE TREATMENT AND EFFECT ANALYSIS

Slope Treatment Measures

Before treatment, the slope was in an unstable state. If the foot of the slope is further excavated according to the previous slope ratio (1:0.75–1:1), or there is heavy rainfall, the slope may be deformed and further destroyed, causing widespread instability.

Combined with the current situation of the slope and related construction conditions, the slope is re-excavated. The final excavation height of the slope is 57.55 m. The re-excavation is divided into six levels, and the first five levels are carried out according to the height of 10 m per level. The detailed treatment

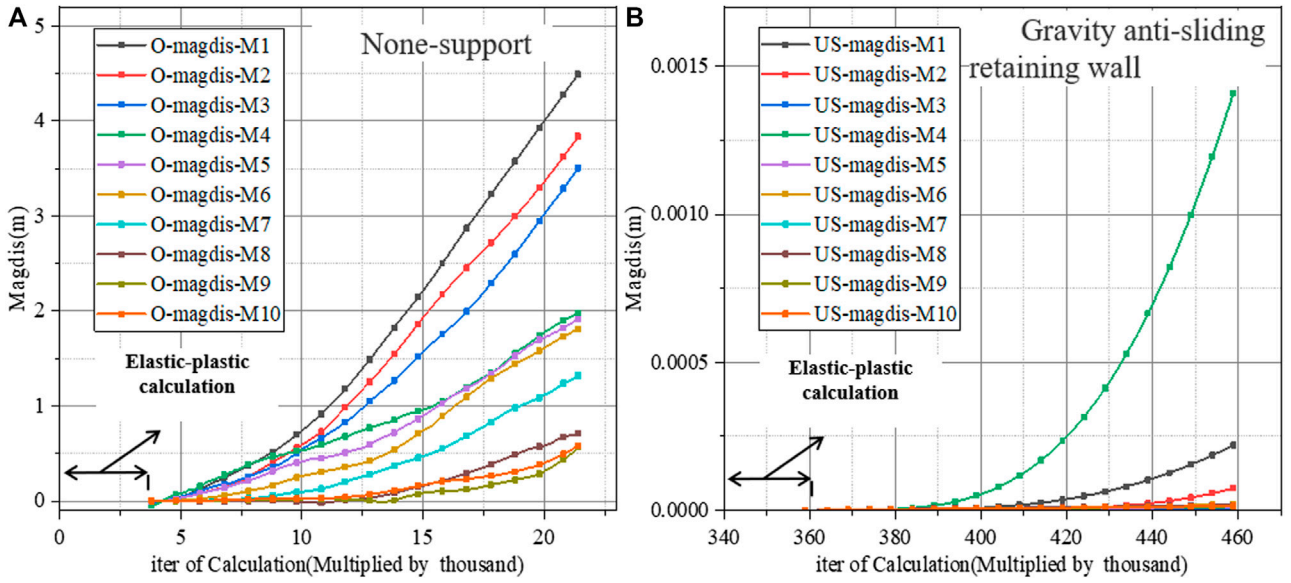


FIGURE 8 | Monitoring diagram of displacement of measuring points before and after applying the retaining wall. (O stands for the original state without supports, and the US stands for under support by gravity anti-sliding retaining well.). **(A)**: None-support, **(B)**: Gravity anti-sliding retaining wall supporting.

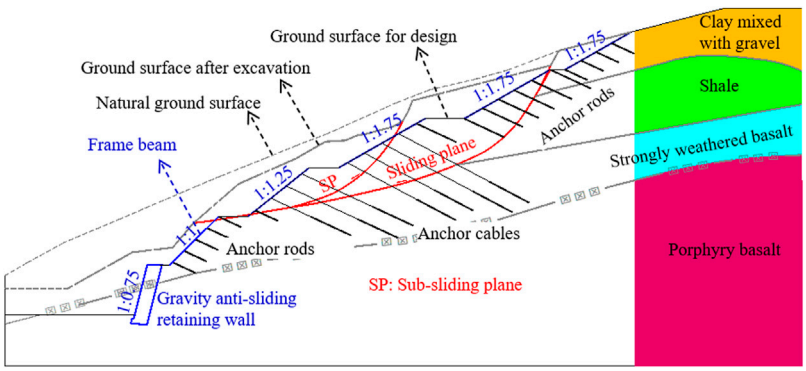


FIGURE 9 | Treatment profile for the slope.

for each level is as follows: the slope cutting and gravity retaining wall are used for the first level, with a slope ratio of 1:0.75. The slope cutting and anchor frame beam are used for the second level, with a slope ratio of 1:1 and an anchor length of 5 m (spacing 3 m × 3 m). The slope cutting and an anchor cable frame beam are used for the third level, with a slope ratio of 1:1.25 and an anchor cable length of 18–25 m (spacing 4 m × 4 m). The slope cutting and anchor cable frame beam are used for the fourth level, with a slope ratio of 1:1.75 and an anchor cable length of 25–30 m (spacing 4 m × 4 m). The 5th–6th level slopes are cut at a ratio of 1:1.75 and supported by anchor frame beams with a length of 5–9 m (spacing 3 m × 3 m). For the anchor frame beam, the anchor rod adopts a φ25 ribbed steel bar, and the frame beam is 0.3 m × 0.3 m in size, and C25 concrete is used for cast-in-place construction. For the anchor cable frame beam, the anchor cable comprises six strands with φ15.2. The frame beam is 0.6 m × 0.6 m in size, and C25 concrete is used for cast-in-place construction. At the same time, intercepting drains are set at the outer edge of the slope and the load shedding platforms at all levels. The slope treatment profile is shown in **Figure 9**.

Effect Analysis

Based on the abovementioned analysis, the slope deformation can be effectively controlled by using the anti-sliding retaining wall as emergency support. In this case, with comprehensive support, the subsequent deformation of the slope and the deformation of the supporting structure belong to plastic failure. Fast Lagrangian Analysis of Continua 3D (FLAC3D) adopts an explicit Lagrangian algorithm and mixed-discrete partition technology, which can accurately simulate the plastic failure and flow of

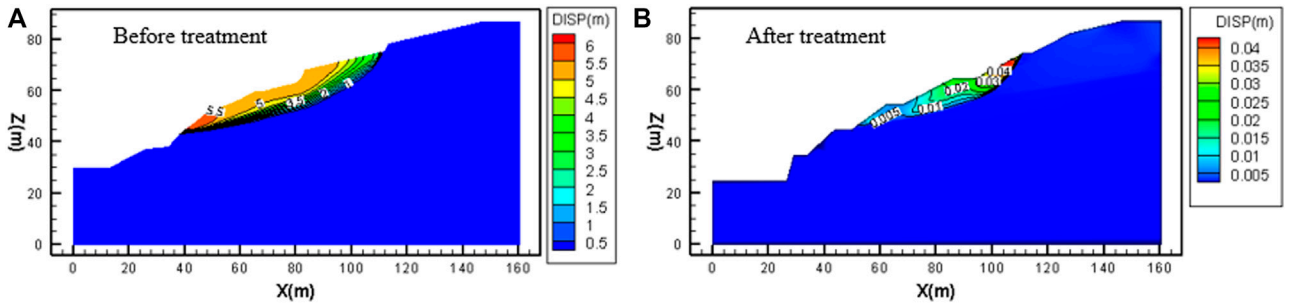


FIGURE 10 | Slope displacement nephogram before and after treatment. **(A)**: Before treatment, **(B)**: After treatment.

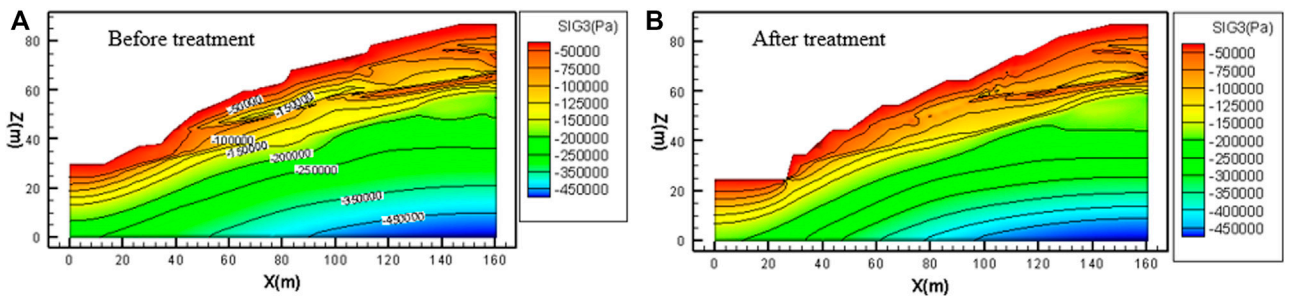


FIGURE 11 | Minimum principal stress nephogram before and after treatment. **(A)**: Before treatment, **(B)**: After treatment.

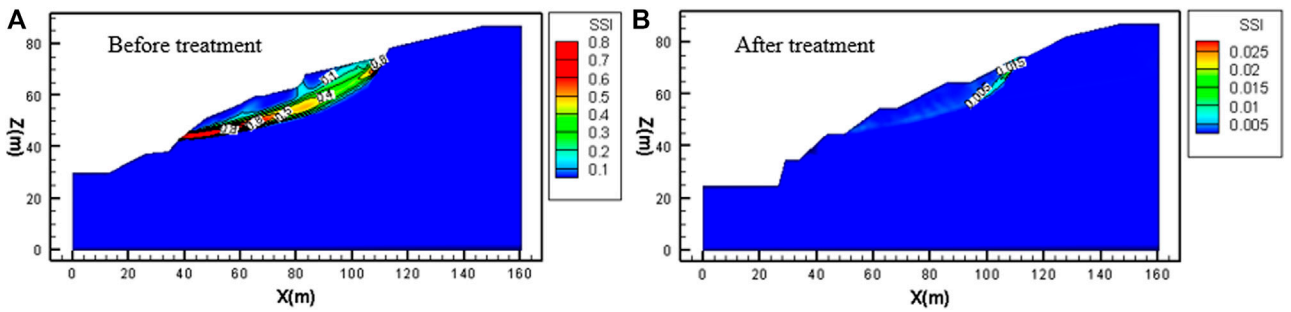


FIGURE 12 | Maximum shear strain increment nephogram before and after treatment. **(A)**: Before treatment, **(B)**: After treatment.

materials. It can simulate three-dimensional structural mechanical properties and plastic flow of soil, rock, and other materials. At the same time, the FLAC3D program also provides structural elements (such as anchor rods, anchor cables, etc.) to simulate slope reinforcement, making it easy to evaluate the support effect. Therefore, the FLAC3D program is selected to analyze the comprehensive support effect of the slope. Based on the existing deformation and failure characteristics of the slope, the slope model before and after treatment is established using the numerical software FLAC3D. Rock and soil mass is considered elastoplastic materials in PLAC3D, and the failure of material follows the Mohr–Coulomb yield criterion. At the same time, constraints are imposed on the model. Horizontal displacement constraints in the *X* direction are imposed on both sides of the model. Only vertical displacement is allowed, but horizontal displacement is not allowed. The upper surface is free, and the lower surface is fixed. Concerning the parameters in **Table 1**, numerical modeling is carried out for the slope before and after treatment. The modeling results are shown in **Figures 10–12**.

The deformation of the slope does not converge before treatment (**Figure 10A**). Under the condition of sliding and squeezing at the trailing edge of the sliding body, the leading edge of the sliding body deforms most, forming a shear outlet, which will lead to sliding instability. If the treatment is carried out according to the changed design, there will be a small deformation at the upper part of the slope, with a value of

4 cm (**Figure 10B**), which can be effectively controlled. The comparison between the two conditions shows that slope deformation can be effectively controlled under the treatment.

Deformation and failure of the slope will lead to the change of principal stress in the slope. The soil stress concentration near the potential sliding plane at the bottom of the slope body is obvious before treatment (**Figure 11A**). After treatment according to the design change, the stress concentration at the bottom of the slope is eliminated, and the stress distribution is relatively uniform (**Figure 11B**).

The sliding plane or potential sliding plane of the slope can be reflected by the maximum shear strain increment. An obvious shear strain increment zone is formed at the bottom of the slope before treatment, that is, the sliding plane runs through the trailing edge of the slope from the leading edge, and the shear strain increment near the shear outlet of the leading edge and the trailing edge is the largest (**Figure 12A**). The sliding plane can be divided into the main sliding plane and secondary sliding plane along the shear strain increment zone. The main sliding plane runs through the bottom of the whole sliding body, and the secondary sliding plane is from the middle step to the front edge of the sliding body. After treatment, only the rear edge of the slope has a shear strain increment zone, and there is no obvious shear strain increment zone in the middle and lower part of the slope, which proves that the sliding plane is not completely penetrated (**Figure 12B**). The analysis of shear strain increment shows that the treatment can inhibit the formation of a slope sliding plane and ensure that the slope will not form through the sliding plane. The treatment effect is obvious.

In summary, numerical modeling results show that the slope was unstable before treatment and will slide after further deformation. After the comprehensive treatment mentioned above, the analysis of slope deformation, stress, and potential sliding plane shows that the slope deformation is effectively controlled. The stress is relatively uniform, and the formation of the sliding plane is restrained, indicating that the treatment effect is obvious. The slope will be in a stable state after treatment.

CONCLUSION

(1) The slope has experienced a process of excavation–front part sliding–traction–back part sliding– gradual disintegration. At present, the internal cracks of the slope are developed, making its structure very loose and broken in a scattered state. There are two sliding planes on the slope, and its current condition is unstable. If it is not been treated in time, further deformation will lead to its overall instability.
(2) The numerical simulation results of the CDEM reappear in the formation process of the main sliding plane and sub-sliding plane during the excavation of the slope, and the sub-sliding plane is formed earlier than the main sliding plane, revealing the instability mechanism of the slope is traction sliding–tensile cracking. It also shows that the CDEM is suitable for the whole process simulation of progressive instability and failure of slope deformation–fracture–fragmentation.
(3) Retaining the wall as an emergency treatment measure can effectively restrain the further deformation of the slope and ensure temporary stability.
(4) The comprehensive treatment with the gravity anti-sliding retaining wall + anchor cable (rod) frame beam can effectively control the deformation of the slope and ensure its long-term stability. In addition, it has the characteristics of flexible setting, cost-saving, and reliable technology and is widely used in slope prevention and control along with mountainous areas.

DATA AVAILABILITY STATEMENT

The original contributions presented in the study are included in the article/Supplementary Material, further inquiries can be directed to the corresponding authors.

AUTHOR CONTRIBUTIONS

MG and HZ were responsible for writing. JL provided engineering data and geophysical analysis of the slope. SC, ZW, and LF analyzed the deformation and failure characteristics of the slope. YZ, FZ, and NL conducted numerical simulation analysis, TL and FC were responsible for review and proofreading.

FUNDING

This research was supported by the National Natural Science Foundation of China (Nos. 42130719 and U19A20111), the Opening Foundation of Key Laboratory of Geohazard Prevention of Hilly Mountains, Ministry of Natural Resources (Fujian Key Laboratory of Geohazard Prevention) (Grant No. FJKLGH 2022K005), the National and Regional Research Center for The Belt and Road Initiative, National Ethnic Affairs Commission of China-Japan Emergency Management Research Center (RBYJ 2021–005), and the On-campus Talent Introduction Project at Xihua University (No. Z201055 & Z201125).

REFERENCES

Cui, S., Pei, X., Jiang, Y., Wang, G., Fan, X., Yang, Q., et al. (2021). Liquefaction within a Bedding Fault: Understanding the Initiation and Movement of the Daguangbao Landslide Triggered by the 2008 Wenchuan Earthquake (Ms = 8.0). *Eng. Geol.* 295, 106455. 1-20. doi:10.1016/j.enggeo.2021.106455

Dong, J., Zhu, Y., Zhou, Y., and Ma, W. (2010). Dynamic Calculation Model and Seismic Response for Frame Supporting Structure with Prestressed Anchors. *Sci. China Technol. Sci.* 53 (7), 1957–1966. doi:10.1007/s11431-010-3241-z

Duan, J., Yan, Z.-x., Guo, R.-j., and Ren, Z.-h. (2014). Response Analysis of Frame Supporting Structure of Slope under Harmonic Vibration. *Math. Problems Eng.* 2014, 1–13. doi:10.1155/2014/603863

Feng, C., Li, S. H., Hao, W. H., and Ge, W. (2017). Numerical Simulation for Penetrating and Blasting Process of EPW Based on CDEM. *J. Vib. Shock* 36 (13), 11–18. 26(In Chinese with English abstract). doi:10.13465/j.cnki.jvs.2017.13.002

Griffiths, D. V., and Lane, P. A. (1999). Slope Stability Analysis by Finite Elements. *Géotechnique* 49 (3), 387–403. doi:10.1680/geot.1999.49.3.387

Ju, N., Zhao, J., Huang, R., and Duan, H. (2011). Dynamic Design and Construction of Highway Cut Slopes in Huangshan Area, China. *J. Mt. Sci.* 8 (2), 154–165. doi:10.1007/s11629-011-2113-8

Kang, G.-C., Song, Y.-S., and Kim, T.-H. (2009). Behavior and Stability of a Large-Scale Cut Slope Considering Reinforcement Stages. *Landslides* 6 (3), 263–272. doi:10.1007/s10346-009-0164-5

Lai, Z. S., Wu, J. Y., and Ma, J. X. (2005). Study on Excavation Parameters for High Rock Slope of Scattered Structure. *Chin. J. Rock Mech. Eng.* 24 (12), 2183–2187. (In Chinese with English abstract). doi:10.3321/j.issn:1000-6915.2005.12.030

Li, S. H., Liu, T. P., and Liu, X. Y. (2009). Analysis Method for Landslide Stability. *Chin. J. Rock Mech. Eng.* 28 (s2), 3309–3324. (In Chinese with English abstract). doi:10.3321/j.issn:1000-6915.2009.z2.004

Li, X. Z., and Xu, Q. (2015). Application of the SSPC Method in the Stability Assessment of Highway Rock Slopes in the Yunnan Province of China. *Bull. Eng. Geol. Environ.* 75 (2), 551–562. doi:10.1007/s10064-015-0792-z

Liang, R., and Pensomboon, G. (2010). Multicriteria Decision-Making Approach for Highway Slope Hazard Management. *J. Infrastruct. Syst.* 16 (1), 50–57. doi:10.1061/(asce)1076-0342(2010)16:1(50)

Lin, Y.-l., Li, Y.-x., Zhao, L.-h., and Yang, T. Y. (2020). Investigation on Seismic Response of a Three-Stage Soil Slope Supported by Anchor Frame Structure. *J. Cent. South Univ.* 27 (4), 1290–1305. doi:10.1007/s11771-020-4367-1

Ma, G., Hu, X., Yin, Y., Luo, G., and Pan, Y. (2018). Failure Mechanisms and Development of Catastrophic Rockslides Triggered by Precipitation and Open-Pit Mining in Emei, Sichuan, China. *Landslides* 15 (7), 1401–1414. doi:10.1007/s10346-018-0981-5

Marques, G. S., and Lukiantchuki, J. A. (2017). Evaluation of the Stability of a Highway Slope through Numerical Modeling. *DYNA* 84 (200), 121–128. doi:10.15446/dyna.v84n200.53850

Pantelidis, L. (2011). A Critical Review of Highway Slope Instability Risk Assessment Systems. *Bull. Eng. Geol. Environ.* 70 (3), 395–400. doi:10.1007/s10064-010-0328-5

Runqiu, H. (2009). Some Catastrophic Landslides since the Twentieth Century in the Southwest of China. *Landslides* 6 (1), 69–81. doi:10.1007/s10346-009-0142-y

Shen, T., Wang, Y.-s., Luo, Y.-h., Xin, C.-c., Liu, Y., and He, J.-x. (2019b). Seismic Response of Cracking Features in Jubao Mountain during the Aftershocks of Jiuzhaigou Ms7.0 Earthquake. *J. Mt. Sci.* 16 (11), 2532–2547. doi:10.1007/s11629-019-5570-0

Shen, T., Wang, Y., Huang, Z., Li, J., Zhang, X., Cao, W., et al. (2019a). Formation Mechanism and Movement Processes of the Aizigou Paleolandslide, Jinsha River, China. *Landslides* 16 (2), 409–424. doi:10.1007/s10346-018-1082-1

Singh, T. N., Gulati, A., Dontha, L., and Bhardwaj, V. (2008). Evaluating Cut Slope Failure by Numerical Analysis-A Case Study. *Nat. Hazards* 47 (2), 263–279. doi:10.1007/s11069-008-9219-5

Su, H., Hu, J., and Yang, M. (2015). Evaluation Method for Slope Stability under Multianchor Support. *Nat. Hazards Rev.* 16 (4), 04014034. doi:10.1061/(ASCE)NH.1527-6996.0000171

Uribe-Etxebarria, G., Morales, T., Uriarte, J. A., and Ibarra, V. (2005). Rock Cut Stability Assessment in Mountainous Regions. *Environ. Geol.* 48 (8), 1002–1013. doi:10.1007/s00254-005-1323-1

Wei, W. B., Cheng, Y. M., and Li, L. (2009). Three-dimensional Slope Failure Analysis by the Strength Reduction and Limit Equilibrium Methods. *Comput. Geotechnics* 36 (1-2), 70–80. doi:10.1016/j.compgeo.2008.03.003

Wei, Z., Yin, G., Wang, J. G., Wan, L., and Jin, L. (2012). Stability Analysis and Supporting System Design of a High-Steep Cut Soil Slope on an Ancient Landslide during Highway Construction of Tehran-Chalus. *Environ. Earth Sci.* 67 (6), 1651–1662. doi:10.1007/s12665-012-1606-2

Xue, D., Li, T., Wei, Y., and Gao, M. (2015). Mechanism of Reactivated Badu Landslide in the Badu Mountain Area, Southwest China. *Environ. Earth Sci.* 73 (8), 4305–4312. doi:10.1007/s12665-014-3714-7

Xue, D., Li, T., Zhang, S., Ma, C., Gao, M., and Liu, J. (2018). Failure Mechanism and Stabilization of a Basalt Rock Slide with Weak Layers. *Eng. Geol.* 233, 213–224. doi:10.1016/j.enggeo.2017.12.005

Yuan-cheng, G., Hao, D., Yun-hua, L., Qing, Q., and Jun-wei, J. (2019). Stability Analysis and Application of Two-Stage Support on the High Fill Slope. *J. Phys. Conf. Ser.* 1168, 022064. doi:10.1088/1742-6596/1168/2/022064

Zhang, Y.-h., Wang, Y.-s., Wang, W.-s., Liu, J., and Yuan, L.-l. (2019). Zircon U-Pb-Hf Isotopes and Mineral Chemistry of Early Cretaceous Granodiorite in the Lunggar Iron Deposit in Central Lhasa, Tibet Y, China. *J. Cent. South Univ.* 26 (12), 3457–3469. doi:10.1007/s11771-019-4266-5

Zhang, Y., He, Z., Tian, H., Huang, X., Zhang, Z., Liu, Y., et al. (2021). Hydrochemistry Appraisal, Quality Assessment and Health Risk Evaluation of Shallow Groundwater in the Mianyang Area of Sichuan Basin, Southwestern China. *Environ. Earth Sci.* 80 (17576), 1–16. doi:10.1007/s12665-021-09894-y

Zhao, J., and Wu, H. (2014). Study on the Slope Bolt Support Design Based on GIS. *Tociej* 8 (1), 458–462. doi:10.2174/1874149501408010458

Zhao, L., Li, D., Tan, H., Cheng, X., and Zuo, S. (2019). Characteristics of Failure Area and Failure Mechanism of a Bedding Rockslide in Libo County, Guizhou, China. *Landslides* 16, 1367–1374. doi:10.1007/s10346-019-01188-6

Zheng, H., Liu, D. F., and Li, C. G. (2005). Slope Stability Analysis Based on Elasto-Plastic Finite Element Method. *Int. J. Numer. Meth. Engng* 64 (14), 1871–1888. doi:10.1002/nme.1406

Conflict of Interest: The authors declare that the research was conducted in the absence of any commercial or financial relationships that could be construed as a potential conflict of interest.

Publisher's Note: All claims expressed in this article are solely those of the authors and do not necessarily represent those of their affiliated organizations, or those of the publisher, the editors, and the reviewers. Any product that may be evaluated in this article, or claim that may be made by its manufacturer, is not guaranteed or endorsed by the publisher.

Copyright © 2022 Gao, Zhang, Cui, Wu, Liu, Feng, Zeng, Li, Chen, Li and Zhang. This is an open-access article distributed under the terms of the Creative Commons Attribution License (CC BY). The use, distribution or reproduction in other forums is permitted, provided the original author(s) and the copyright owner(s) are credited and that the original publication in this journal is cited, in accordance with accepted academic practice. No use, distribution or reproduction is permitted which does not comply with these terms.

frontiers | Frontiers in Earth Science

ORIGINAL RESEARCH
published: 23 May 2022
doi: 10.3389/feart.2022.897921

Preliminary Study on Post-Peak Behavior and Fracture Characteristics of Hard Rock Under True Triaxial Stress

Feng Zeng[1,2,3]*, *Meiben Gao*[1,2,3,4], *Fujiang Chen*[1,2,3], *Yongyi Yang*[1,5] and *Yan Zhang*[4]*

[1]School of Emergency Science, Xihua University, Chengdu, China, [2]Key Laboratory of Geohazard Prevention of Hilly Mountains, Ministry of Natural Resources, Fuzhou, China, [3]Fujian Key Laboratory of Geohazard Prevention, Fuzhou, China, [4]State Key Laboratory of Geohazard Prevention and Geoenvironment Protection, Chengdu University of Technology, Chengdu, China, [5]The Center of National Railway Intelligent Transportation System Engineering and Technology, China Academy of Railway Sciences Corporation Limited, Beijing, China

The post-peak behavior and fracture characteristics of hard rock are correlated with the stability and bearing capacity of engineering rock mass. However, there are relatively few research studies on the post-peak mechanical behavior and fracture characteristics of hard rock under true triaxial stress. Therefore, this study carried out relevant true triaxial compression tests and acoustic emission (AE) monitoring. It is concluded that under a true triaxial condition, the number of post-peak steps increases first and then decreases with the increasing σ_2, which implies that the rock failure evolves from shear failure to a more complex tension–shear mixed failure and finally evolves into a failure mode dominated by tensile failure. The overall level of the rock fracture angle (θ) at low σ_3 is higher than that at high σ_3. In the range of stress level in this study, when σ_3 is high, the fracture angle of granite increases with increasing σ_2, and its regularity is obvious, while when σ_3 is low, the regularity of the fracture angle increases with the increasing σ_2 is not obvious. It is found that there are three different types of cracking processes in granite. Meanwhile, the expansion rates of three different racking types are calculated by simplified treatment, which are about the order of 10^{-5}–10^{-4} m/s. The research results of this study could supply a useful reference for the understanding of deep hard rock fracture behavior.

Keywords: post-peak behavior, acoustic emission, hard rocks, failure mode, expansion rate

OPEN ACCESS

Edited by:
Yunhui Zhang,
Southwest Jiaotong University, China

Reviewed by:
Zhaofeng Wang,
Institute of Rock and Soil Mechanics (CAS), China
Hong Xu,
Changsha University of Science and Technology, China

***Correspondence:**
Feng Zeng
zengfeng2522@163.com
Yan Zhang
zhangyan2020@cdut.edu.cn

Specialty section:
This article was submitted to Geohazards and Georisks, a section of the journal Frontiers in Earth Science

Received: *16 March 2022*
Accepted: *13 April 2022*
Published: *23 May 2022*

Citation:
Zeng F, Gao M, Chen F, Yang Y and Zhang Y (2022) Preliminary Study on Post-Peak Behavior and Fracture Characteristics of Hard Rock Under True Triaxial Stress. Front. Earth Sci. 10:897921. doi: 10.3389/feart.2022.897921

1 INTRODUCTION

With the increasing excavation depth of deep underground engineering in the world, the influence of high ground stress and complex geological environments on deep rock mass is increasing. Geological disasters such as spalling and rock burst occur frequently, which seriously restrict the development of deep underground engineering in the world (Martin et al., 1999; Feng, 2011; Li et al., 2017; Gong et al., 2019; Gao et al., 2021). The study of the failure and instability of deep rock mass through true triaxial tests is helpful to study the occurrence and mechanism of engineering rock mass disasters such as spalling and rock burst (Haimson and Chang, 2000; He et al., 2010; Li et al., 2015; Feng et al., 2016; Lu et al., 2020; Feng et al., 2021). Therefore, it is of great significance to research the mechanics and fracture behavior of hard rock under a true triaxial stress condition deep underground by the true triaxial test.

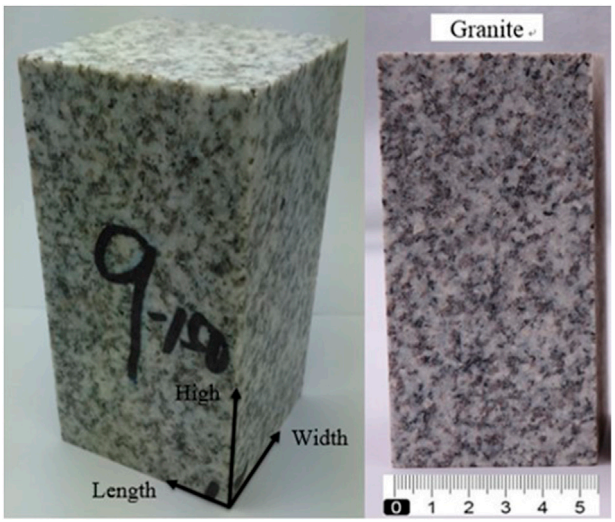


FIGURE 1 | Granite tested in the true triaxial compression experiment.

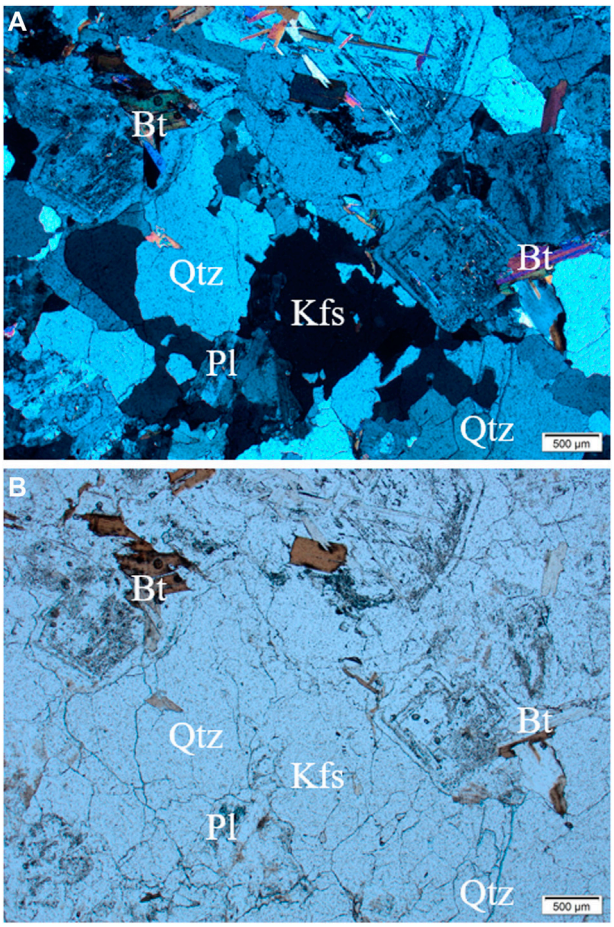


FIGURE 2 | Optical micrograph of tested granite. **(A)** Crossed polars **(B)**, plane polarized light [quartz (Qtz), K-feldspar (Kfs), plagioclase (Pl), and biotite (Bt)].

The mechanical properties of rocks are usually influenced by many factors such as lithology, stress state, loading mode and loading rate, water pressure, and temperature. Generally, when the rock object to be studied is selected, the stress state is the most important factor affecting the mechanical behavior of rock. At the moment, the rock's mechanical properties are mostly carried out by the uniaxial test and the conventional triaxial test. Generally, when the studied rock is in the shallow strata, the conventional triaxial test or even uniaxial test can be used to simulate the stress state of this shallow part. However, when in deep strata, uniaxial or conventional triaxial tests cannot simulate the high true three-dimensional stress state of the deep strata, so the deep rock mechanics research based on the true triaxial test is the trend of rock mechanics development in the future.

Acoustic emission (AE) is the phenomenon of a transient elastic wave which is produced by the energy released during the evolution of a microcrack when rock failure occurs (Lockner, 1993). The evolution process of crack initiation, propagation, and coalescence can be analyzed by AE signals generated in different deformation and failure periods of rock (Tuncay and Ulusay, 2008; Fortin et al., 2011; Rück et al., 2017). Real-time AE monitoring based on the rock cracking process can realize the quantitative study of the rock fracture process.

At present, there are few studies on AE of rocks under the true triaxial stress state. Combining the AE source location results with actual failure morphology, the cracking evolution of rock under the true triaxial stress state can be realized. The research derived from the AE location results can achieve the research on spatial shape, propagation rate and direction, and the evolution process of the cracks (Ohtsu, 1991; Lei et al., 2000; Thompson et al., 2005). Therefore, the study of rock mechanical behavior and AE characteristics under true triaxial stress state can help us understand the cracking characteristics and mechanical properties of deep rock mass and lay a solid study foundation for the research of disaster-causing processes and mechanisms of deep rock mass.

2 TRUE TRIAXIAL COMPRESSION TEST AND ACOUSTIC EMISSION MONITORING METHODS

2.1 Sample Preparation

As shown in **Figure 1**, the granite selected in this experiment is monzogranite from Gansu Province, China (Zhang et al., 2019; Zhang, 2020). According to the testing average value of a group of rock samples, the density of granite is 2.61 g/cm^3, the average P-wave velocity is 3,590 m/s, the uniaxial compressive strength (UCS) is 141 MPa, Poisson's ratio is about 0.27, and Young's modulus is about 54 GPa.

As shown in **Figure 2**, it is observed by an optical microscope that the rock is granular mosaic, consisting mainly of about 40% plagioclase, 33% quartz, 17% K-feldspar, and 10% other substances.

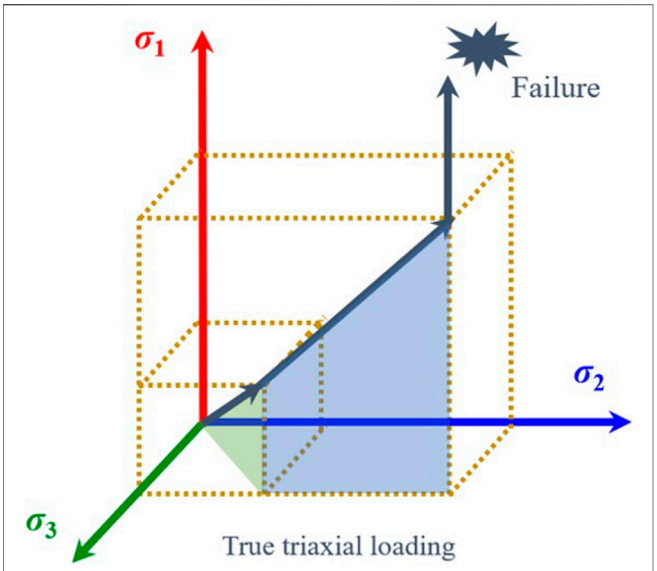


FIGURE 3 | Adopted true triaxial loading stress paths of tested rocks.

2.2 Testing Apparatus

The main experimental apparatus used in this study includes a true triaxial test system (Feng et al., 2016) and AE system (Zhang et al., 2019). The true triaxial testing machine can achieve the whole stress–strain curve of rock under loading or unloading stress paths. It can accommodate a 50 × 50 × 100-mm^3 cuboid sample. The maximum principal stress (σ_1) and intermediate principal stress (σ_2) are exerted by a hydraulic driving piston, and the minimum principal stress (σ_3) is exerted by hydraulic oil in the true triaxial chamber. The maximum output stresses σ_1, σ_2, and σ_3 can reach 1,200 MPa, 1,200 MPa, and 100 MPa, respectively.

The AE monitoring threshold value is set to be 40–50 dB in the experiment of this study. In this experiment, eight high-frequency AE sensors are encapsulated in a small anti-hydraulic protective shell and are fixed on the surface of the rock sample by a sealant to carry out AE data monitoring and acquisition. During the test, the AE monitoring is matched with the recording time of the stress–strain curve, and the rock fracture information is monitored in the whole process.

2.3 Testing Plan and Adopted Stress Path

Through a large number of statistical analyses of the research literature on *in situ* stress in the study area, within the range of 700 m underground, the maximum horizontal ground stress σ_H is about 4.5–27.0 MPa, the minimum horizontal ground stress σ_h is about 2.6–13.1 MPa, and the vertical crustal stress σ_V is about 0–27.0 MPa.

In order to better analyze the mechanical behavior of the tested rock under different depths and different ground stress conditions, the true triaxial stress level of this study is determined by considering the relevant engineering background and the characteristics of the true triaxial test as follows:

The minimum principal stress σ_3 is 5, 10, 20, and 30 MPa, respectively. When σ_3 is 5 MPa, the corresponding σ_2 is 5, 20, 50, 75, and 100 MPa, respectively. When σ_3 is 10 MPa, the corresponding σ_2 is 10 MPa, 20 MPa, 50 MPa, 75, and 100 MPa, respectively. When σ_3 is 20 MPa, the corresponding σ_2 is 20, 50, 75, and 100 MPa, respectively; when σ_3 is 30 MPa, the corresponding σ_2 is 30, 50, 75, and 100 MPa, respectively. Meanwhile, some supplementary experiments are carried out according to the actual situation.

The stress path taken in this study is shown in **Figure 3**:

(1) Load simultaneously in each stress direction to the σ_3 level with a loading rate of 0.5 MPa/s ($\sigma_1 = \sigma_2 = \sigma_3$).
(2) σ_3 remains unchanged, σ_1 and σ_2 are simultaneously loaded to the set σ_2 level with a loading rate of 0.5 MPa/s ($\sigma_1 = \sigma_2$).
(3) σ_2 and σ_3 remain unchanged, and σ_1 is loaded with a loading rate of 0.5 MPa/s. When σ_1 comes near the rock crack damage stress σ_{cd}, the control method is varied from stress control to strain control to achieve the rock post-peak curve, and the rate of ε_1 strain control is 0.015 mm/min.

3 POST-PEAK CHARACTERISTICS OF HARD ROCK UNDER TRUE TRIAXIAL COMPRESSION TEST

The post-peak stress drop is a phenomenon where the bearing capacity of a rock drops rapidly and then rises slightly after reaching the peak value. It is shown in the curve shape that the stress–strain curve drops rapidly and then rises and then falls again. Based on the stress–strain curve of the granite rock under the true triaxial compression condition, this section analyzes variation law of the post-peak steps and brittle stress drop characteristics. It is concluded that when σ_3 is small (σ_3 = 5 MPa) or large (σ_3 = 30 MPa), the number of post-peak steps of granite increases first and then decreases with increasing σ_2. With the increase in σ_2, the post-peak curve shape tends to become a type II curve, and its brittle failure characteristics are more obvious with the increase in σ_2.

It can be seen from **Figure 4** that when σ_3 is 5 MPa and σ_2 is 5, 20, 50, and 100 MPa, the post-peak step numbers during the whole stress–strain curve of the granite is 0, 2, 3, and 1, respectively. **Figure 5** shows that when σ_3 is 30 MPa and σ_2 is 5, 20, 50, and 100 MPa, the number of the post-peak steps during the complete stress–strain curve of the granite is 1, 1, 2, and 0, respectively. Obviously, with increasing σ_2, the number of post-peak steps of granite increases first and then decreases, the shape of post-peak curve tends to be a type II curve, and the brittle failure characteristics of the rock are more obvious.

The periodic post-peak stress drop, that is, the brittle stress drop of the rock's post-peak curve, is related to the alternating interaction between the tensile failure and the shear failure during the post-peak failure. It is generally believed that brittle stress drop is caused by tensile failure, and the post-peak curve steps are a process of shear failure. Therefore, the number of post-peak steps increases first and then decreases with the increasing σ_2, which means that the post-peak failure process of the rock is more

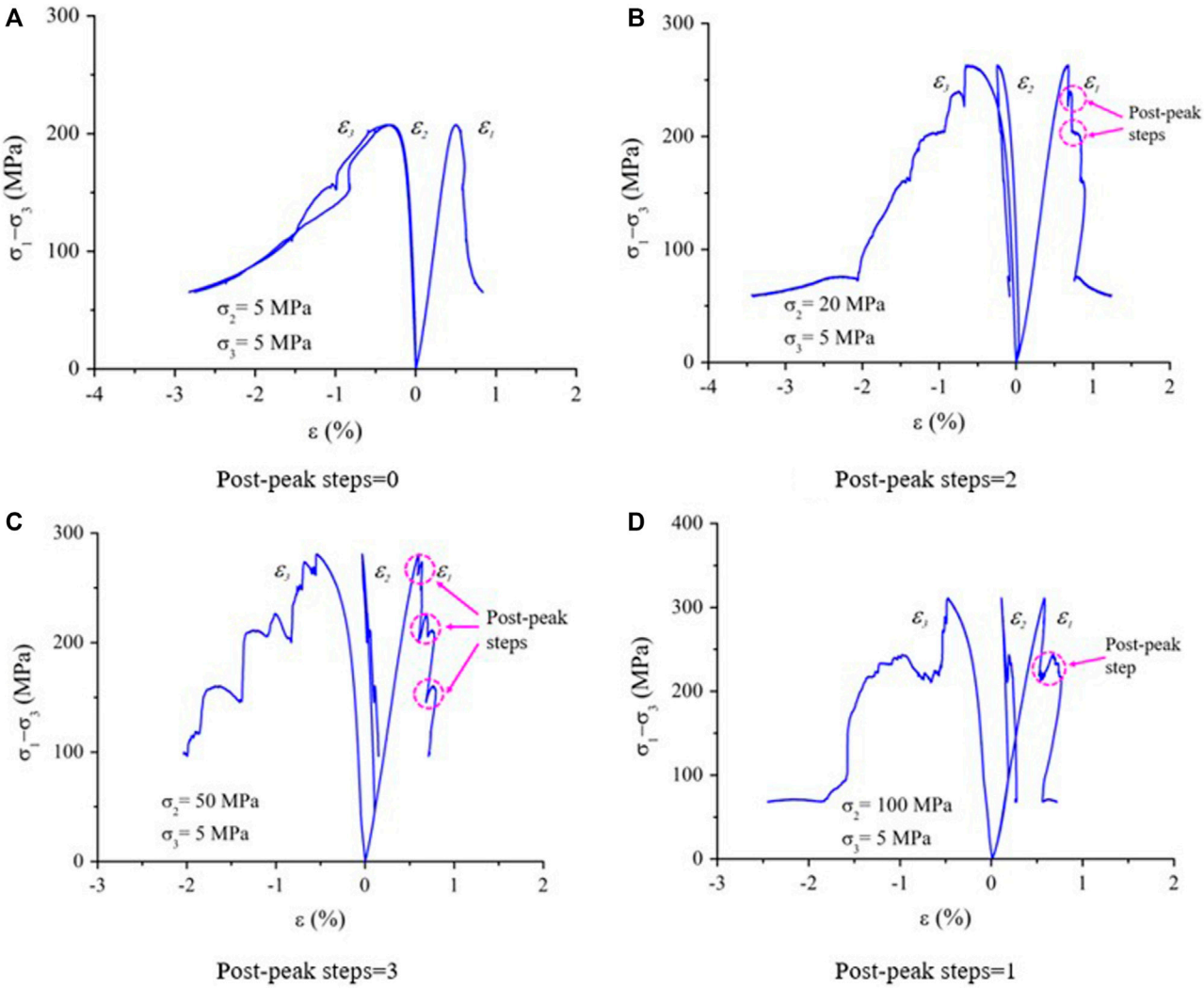


FIGURE 4 | Step number at post-peak increases first and then decreases with the increase in σ_2 (σ_2 = 5 MPa). The post-peak steps is indicated by a dotted circle in the figure.

complex with the increase in σ_2. From the evolution process of post-peak curves of **Figures 4**, **5**, it indicates that with the increasing σ_2, the internal failure of the rock changes from shear failure to a more complex tensile–shear mixed failure, and eventually evolves into a failure mode dominated by tensile failure (Zhang, 2020).

4 FAILURE MODE OF HARD ROCK UNDER TRUE TRIAXIAL COMPRESSION TEST

Figures 6–9 are the diagrams of the failure mode of granite rock under true triaxial compression changing with σ_2 under different σ_3 (Zhang, 2020). **Figure 10** is the diagram and statistics of the fracture angle of granite under true triaxial compression. At the same time, the example of a typical rock sample in **Figure 10** shows the definition of the fracture angle under true triaxial compression: the actual failure of the rock samples in true triaxial test forms a failure surface intersected with σ_1–σ_2 plane, perpendicular or approximately perpendicular to the σ_1–σ_3 plane (Mogi, 1971; Haimson, 2006; Mogi, 2007). In practice, the angle of failure surface (θ) can be expressed by the angle between the macroscopic main crack and the loading direction of σ_3, that is, the fracture angle (θ).

Since the actual failure of rock samples under true triaxial compression forms a failure surface perpendicular or approximately perpendicular to the σ_1–σ_3 plane, although **Figures 6–9** show only the failure situation of the σ_1–σ_3 plane of the rock samples, it is considered that it can represent the failure situation and characteristics of rock samples in space. As shown in **Figures 6–9**, the macroscopic main cracks of most granite rocks pass through the corner of the sample and penetrate the whole sample.

Combined with **Figures 6–10**, it is found that the failure mode of granite is more inclined to tensile failure when σ_3 is lower (σ_3 = 5 MPa) than that when σ_3 is higher, and the overall level of

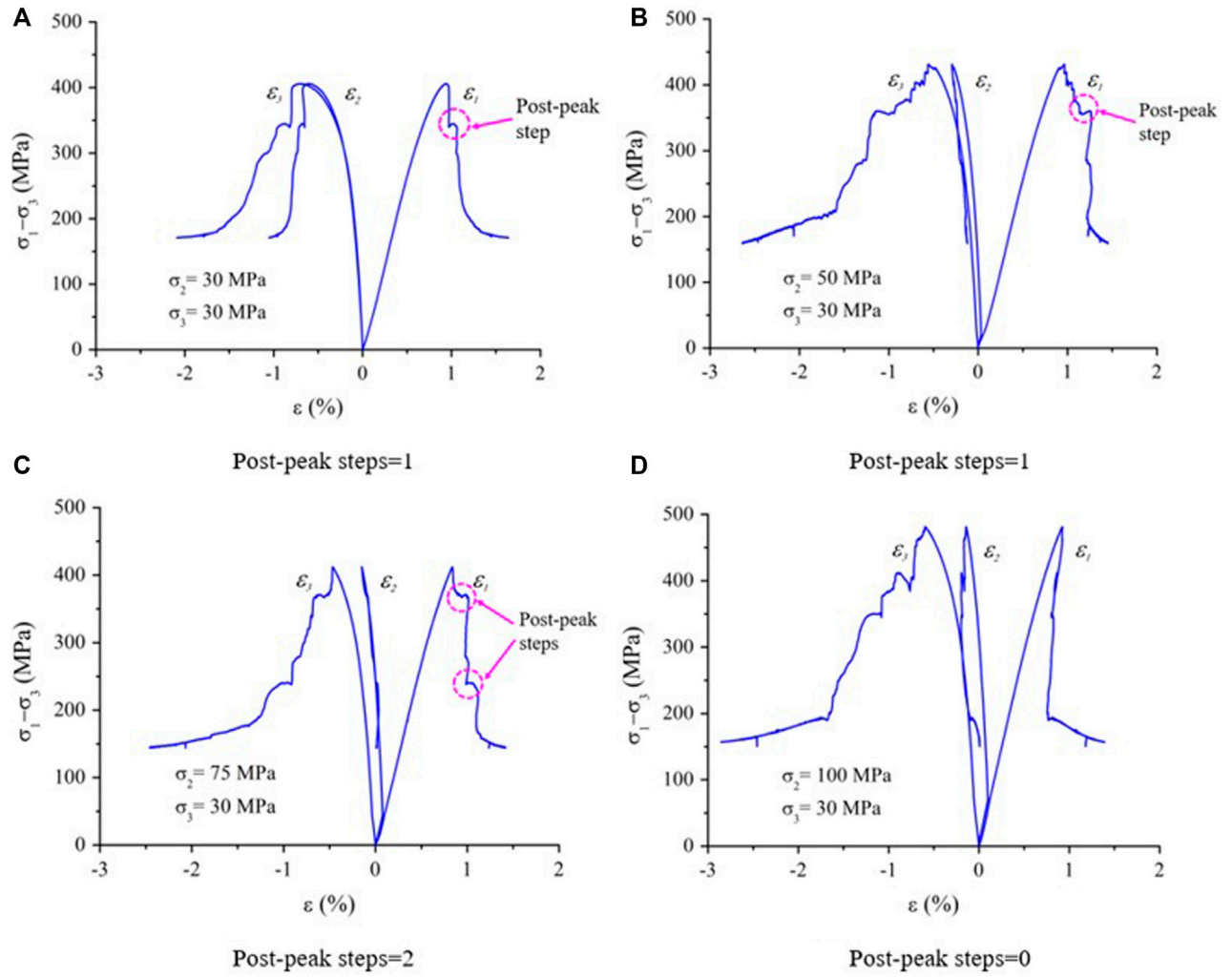


FIGURE 5 | Step number at the post-peak increases first and then decreases with the increase in σ_2 (σ_2 = 30 MPa). The post-peak steps is indicated by a dotted circle in the figure.

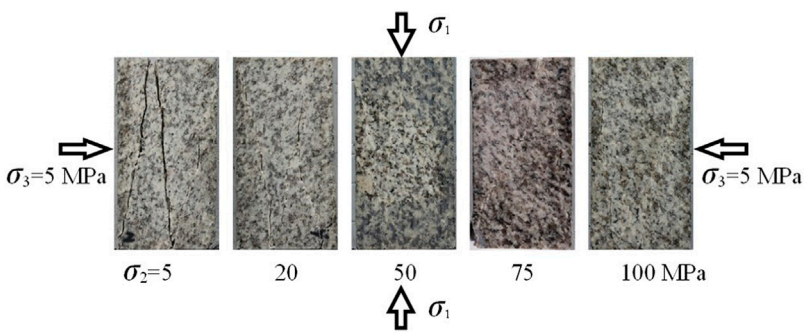


FIGURE 6 | Failure modes of tested granite change with σ_2 when σ_3 is 5 MPa.

fracture angle (θ) value is higher than that of other σ_3 stress levels, and the number of macroscopic cracks in the σ_1–σ_3 plane is relatively large. When σ_3 is high (σ_3 = 20 MPa, 30 MPa), most samples have only one macroscopic main crack and the fracture angle (θ) is generally low. When σ_3 is 10 MPa, the fracture angle fluctuation of rock samples increases and is irregular, which may be because σ_3 = 10 MPa is the critical value range of granite failure mode from tensile failure to shear failure.

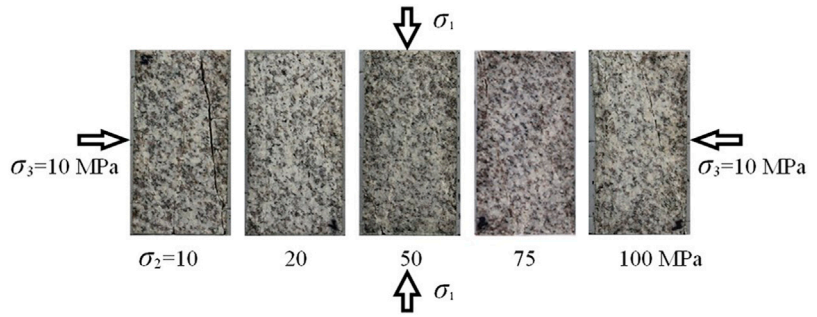


FIGURE 7 | Failure modes of tested granite change with σ_2 when σ_3 is 10 MPa.

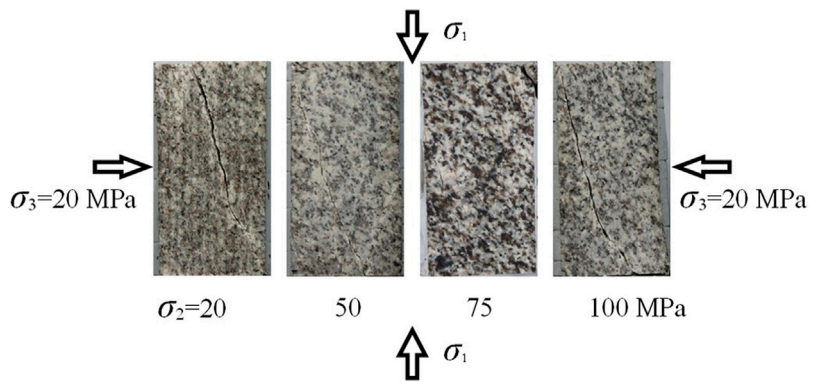


FIGURE 8 | Failure modes of tested granite change with σ_2 when σ_3 is 20 MPa.

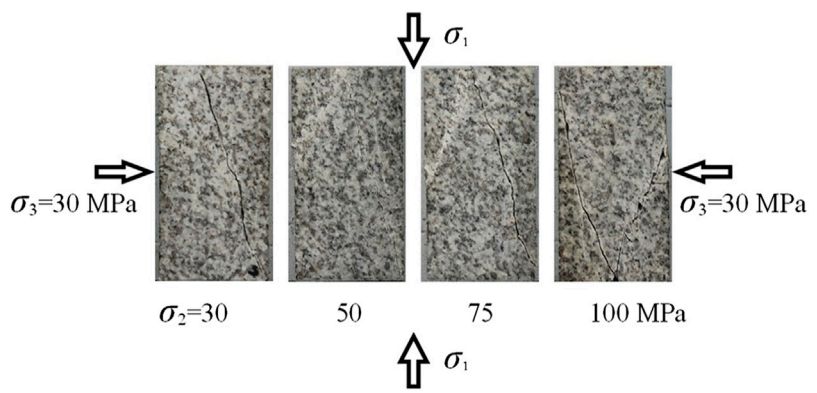


FIGURE 9 | Failure modes of tested granite change with σ_2 when σ_3 is 30 MPa.

Many previous studies have been done on the variation of rock fracture angle with σ_2. Haimson and Chang (2000) believed that fracture angle of Westerly granite monotonically increases with the increasing σ_2 under the condition that σ_3 is constant. Ma and Haimson (2016) found that when σ_2 increases to σ_2 greater than σ_3, the failure plane angles of Coconino and Bentheim sandstones also increased. Moreover, some other studies have the same view (Mogi, 1971; Chang and Haimson, 2012). Feng et al. (2016) believed that the fracture angle of the rock under true triaxial stress would first increase and then decrease with the increasing σ_2.

The variation of granite rock fracture angle with σ_2 in this article is shown in **Figure 10**. In the range of the stress level in this article, when σ_3 is high (σ_3 = 20 MPa, 30 MPa), the fracture angle of granite increases with the increasing σ_2, and the regularity is obvious. When σ_3 is low (σ_3 = 5 MPa, 10 MPa), the regularity of the fracture angle increasing with σ_2 is not obvious.

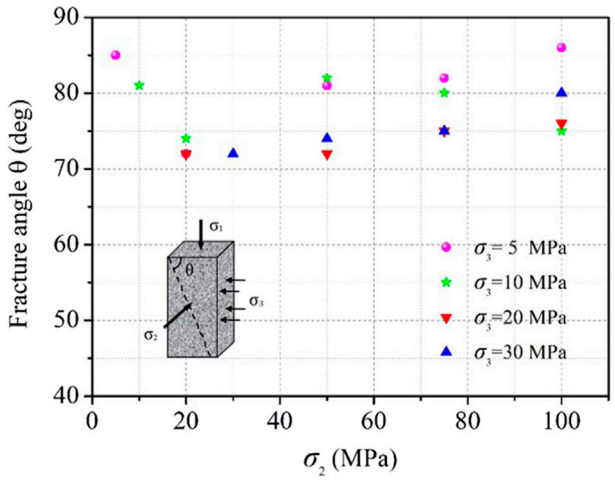


FIGURE 10 | Fracture angles of tested granite change with σ_2 under different σ_3 stress states.

5 ESTIMATION OF ROCK CRACK PROPAGATION RATE BASED ON ACOUSTIC EMISSION LOCATION

The AE source localization technology can be applied to research the spatial distribution and development characteristics of cracks during rock failure. **Figures 11**, **12** show the AE source location and the actual failure process of granite samples under true triaxial condition (σ_2 = 75 MPa, σ_3 = 20 MPa). By comparing the actual crack distribution of the rock sample in **Figure 11** with corresponding AE source location results, it is found that they are in good agreement with each other, which shows that AE source location results can basically indicate the morphological characteristics and cracking evolution process of the rock sample during the final failure.

The different colors corresponding to the elliptical area in **Figure 12** represent the formation process of different rock samples in the test monitoring. Comprehensively considering the temporal and spatial distribution characteristics of macro and micro cracks during the final rock failure, and according to the differences of crack propagation time and formation process of rock samples, the cracks in the four elliptical areas in the figure are divided into three different types, and the elliptical areas are distinguished by three different colors of red, blue, and green, respectively. This part attempts to estimate the cracking surface expansion rates of these three different fracture forms, and further analyzes the differences in the formation process of three typically different cracking processes of rock from the perspective of fracture surface expansion rates.

Figure 12 shows the two-dimensional and three-dimensional displays of the shape and size of the rock cracking surface, where the cracks on the plane ABCD and plane A`B`C`D` are shown in the X-Y plane through the perspective map from the negative direction of the *Z* axis.

For the cracks shown in the blue elliptical region on the X-Y plane in **Figure 12B**, the cracks in the region above the right corner of the sample are selected for calculation. **Figure 12A** shows the spatial morphology of the crack. After accurate measurement, the lengths of the cracking surface on the plane ABCD and plane A`B`C`D` are 28 and 30 mm, respectively. For convenient calculation, the average value of 29 mm is taken to

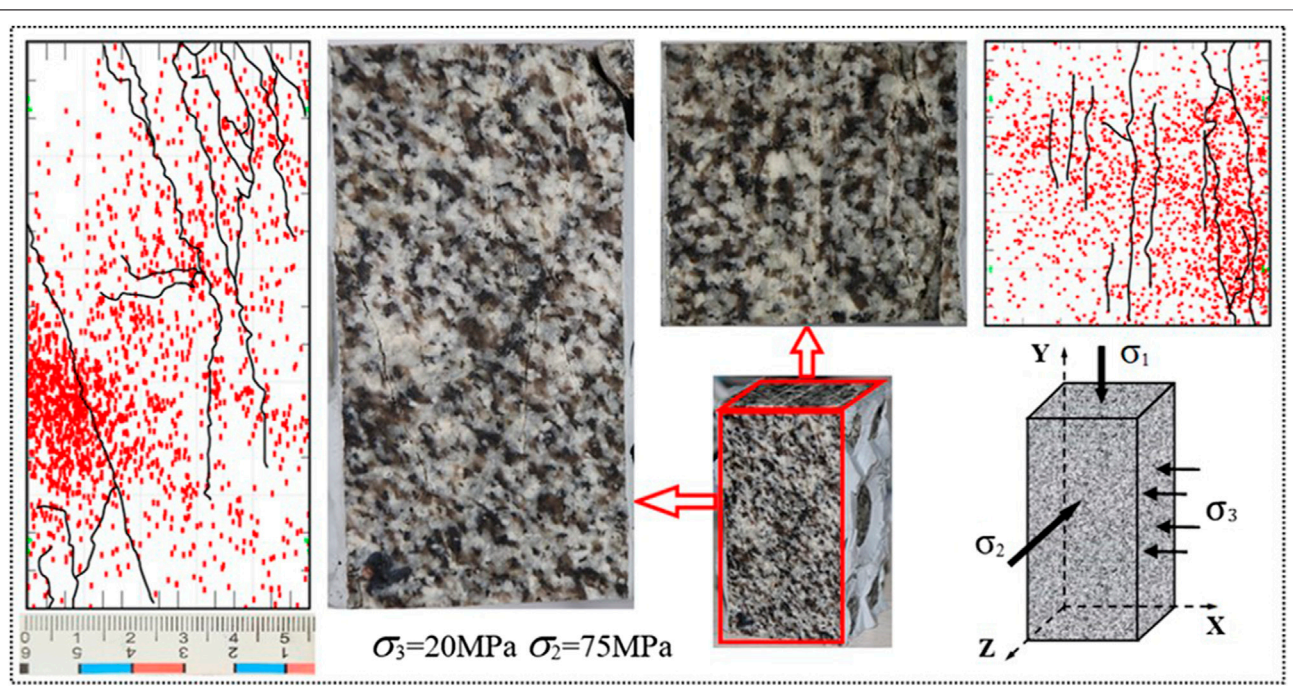


FIGURE 11 | Comparison diagram of final failure mode, acoustic emission source location results, and crack sketch of tested granite under the true triaxial stress state.

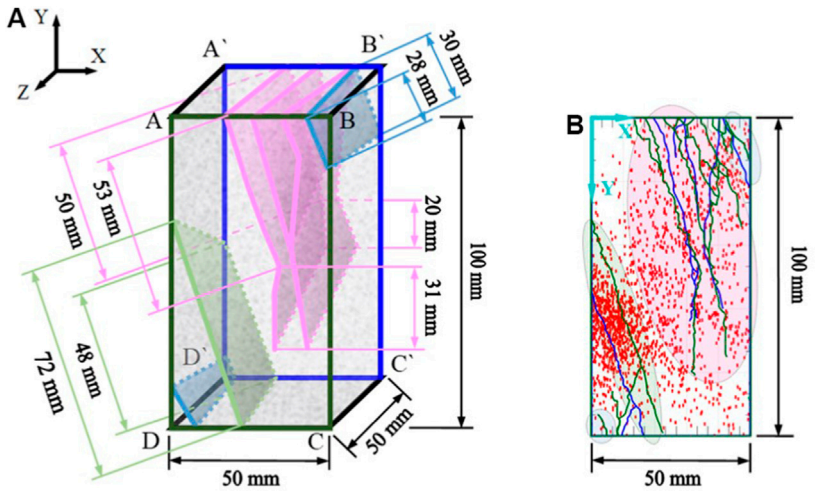


FIGURE 12 | Display of the three-dimensional crack failure morphology of tested granite under true triaxial stress state. **(A)** 3-dimensional failure morphology and **(B)** 2-dimensional failure morphology.

represent the propagation length of the cracking surface. Based on the AE localization results, the initial time of the crack is 1,250 s, and the final formation time of the crack is 1,625 s, with a time difference of 375 s. It can be considered that the extension time of the cracking surface is 375 s. Therefore, the expansion rate of the cracking surface can be estimated to be 77.3 μm/s.

Similarly, for the broken zone composed of multiple macro and micro cracks in the red elliptical region in **Figure 12B**, due to the complex evolution process of rock micro cracks in this progressive failure process, different micro cracks interact and connect with each other, and the distribution range is relatively wide.

Therefore, in order to estimate the cracking surface expansion rate, reasonable assumptions are needed to simplify the analysis process. It is considered that the main macroscopic cracking surfaces in the region are formed at the same time as shown in **Figure 12A**, and one of the longest cracking surfaces is selected for calculation. The lengths of the cracking surface on the plane ABCD and plane A`B`C`D` are 84 and 70 mm, respectively, with an average of 77 mm. At the same time, the test monitoring shows that the progressive cracking process of the cracks runs through the whole test process and the period is long. Therefore, 365 and 3,348 s corresponding to the time before and after the cracking formation are selected as the starting and ending points for calculating the propagation time of the cracking surface, and the difference between the two is 2,983 s. The calculated expansion rate of the cracking surface is about 25.8 μm/s.

For the single macroscopic cracking surface formed in the green elliptical region in **Figure 12B**, the lengths of the cracking surface on the plane ABCD and plane A`B`C`D` are 72 and 48 mm, respectively, with an average of 60 mm. By using the AE localization analysis, it is found that the cracking process extends from one end to the other end of the macroscopic cracking surface. The experimental monitoring shows that the starting and ending points of the macroscopic cracking surface expansion time are 365 and 1,625 s, respectively, and the difference is 1,260 s. Therefore, the expansion rate of the cracking surface can be estimated to be 47.6 μm/s.

6 DISCUSSION

It should be pointed out that the crack morphology is very different in practice, the evolution process of crack propagation is very complex, and the propagation process of the cracking surface in three-dimensional space is more complex. It is very difficult to accurately measure the expansion rate of the cracking surface. Therefore, this article determines the length of macro cracks by forming a two-dimensional spatial cracking surface and calculating the average value. At the same time, due to the continuous evolution process of rock cracks, it is subjective to determine the initiation and termination time of the rock cracking surface, which will lead to errors in calculation of the cracking surface expansion time. In addition, the expansion of the spatial cracking surface does not necessarily develop from one end to the other, but may simultaneously propagate and connect with each other from multiple locations inside the rock to form a macroscopic cracking surface. Therefore, the expansion rate of the cracking surface in this article is only a ratio of the average projection length of the final macroscopic cracking surface on the two-dimensional plane and its expansion time, and does not pay attention to the specific expansion form and process of the cracking surface. In this article, the expansion rates of three typical cracking surfaces are 77.3 μm/s, 25.8 μm/s, and 47.6 μm/s, respectively. Therefore, it can be considered that the cracking expansion rate of granite within the scope of this study is about the magnitude of 10^{-5}–10^{-4} m/s.

7 CONCLUSION

(1) Under true triaxial condition, the number of post-peak steps increases first and then decreases with increasing

σ_2. It is generally believed that the brittle stress drop is caused by tensile failure, and the post-peak steps are caused by shear failure. This means that the post-peak failure of the rock becomes more complex with the increase in σ_2, indicating that with increasing σ_2, the rock failure evolves from shear failure to a more complex tension–shear mixed failure and finally evolves into a failure mode dominated by tensile failure.

(2) The overall level of the fracture angle (θ) of granite at low σ_3 is higher than that at high σ_3, and the number of macroscopic cracks is relatively large in the σ_1–σ_3 plane. When σ_3 is high, most samples have only one macroscopic main crack, and the fracture angle (θ) is generally low. In the range of the stress level in this article, when σ_3 is high, the fracture angle of granite increases with increasing σ_2, and the regularity is obvious, while when σ_3 is low, the regularity of the fracture angle increases with increasing σ_2 is not obvious.

(3) According to the difference of crack propagation time and formation process, it is found that there are three different types of cracking processes in granite. At the same time, the expansion rates of the three different racking types are calculated by a simplified treatment, which are about the order of 10^{-5}–10^{-4} m/s.

DATA AVAILABILITY STATEMENT

The raw data supporting the conclusion of this article will be made available by the authors, without undue reservation.

AUTHOR CONTRIBUTIONS

All authors listed have made a substantial, direct, and intellectual contribution to the work and approved it for publication.

FUNDING

This research was supported by the Science and technology project fund for Returned Students of Sichuan Province in 2021 (No. 212603), Japan Emergency Management Research Center of Xihua University (Nos. RBYJ 2021-008 and RBYJ 2021-005), the Opening Foundation of Key Laboratory of Geohazard Prevention of Hilly Mountains, Ministry of Natural Resources (Fujian Key Laboratory of Geohazard Prevention) (Grant No. FJKLGH 2022K005), the On-campus Talent Introduction Project of Xihua University (Nos. Z212015 and Z201055), the National Natural Science Foundation of China (Grant No. 42107211), and the Center of National Railway Intelligent Transportation System Engineering and Technology (Contract No. RITS2021KF04), China Academy of Railway Sciences Corporation Limited.

The funder was not involved in the study design, collection, analysis, interpretation of data, the writing of this article or the decision to submit it for publication.

ACKNOWLEDGMENTS

The authors sincerely acknowledge the support from Key Laboratory of Ministry of Education on Safe Mining of Deep Metal Mines, Northeastern University.

REFERENCES

Chang, C., and Haimson, B. (2012). A Failure Criterion for Rocks Based on True Triaxial Testing. *Rock Mech. Rock Eng.* 45, 1007–1010. doi:10.1007/s00603-012-0280-8

Feng, X.-T., Zhang, X., Kong, R., and Wang, G. (2016). A Novel Mogi Type True Triaxial Testing Apparatus and its Use to Obtain Complete Stress-Strain Curves of Hard Rocks. *Rock Mech. Rock Eng.* 49 (5), 1649–1662. doi:10.1007/s00603-015-0875-y

Feng, X. T. (2011). *Rockburst Mechanisms, Monitoring, Warning, and Mitigation*. Oxford: CRC Press.

Feng, X. T., Wang, Z. F., Zhou, Y. Y., Yang, C. X., Pan, P. Z., and Kong, R. (2021). Modelling Three-Dimensional Stress-dependent Failure of Hard Rocks[J]. *Acta Geotech.* 16 (11–12), 1–31. doi:10.1007/s11440-020-01110-8

Fortin, J., Stanchits, S., Vinciguerra, S., and Guéguen, Y. (2011). Influence of Thermal and Mechanical Cracks on Permeability and Elastic Wave Velocities in a Basalt from Mt. Etna Volcano Subjected to Elevated Pressure[J]. *Tectonophysics* 503 (1), 60–74. doi:10.1016/j.tecto.2010.09.028

Gao, Y. H., Wang, K. Z., and Zhou, C. (2021). A Numerical Study on True Triaxial Strength and Failure Characteristics of Jointed Marble. *Acta Geotech*. doi:10.1007/s11440-021-01300-y

Gong, F.-q., Si, X.-f., Li, X.-b., and Wang, S.-y. (2019). Experimental Investigation of Strain Rockburst in Circular Caverns under Deep Three-Dimensional High-Stress Conditions. *Rock Mech. Rock Eng.* 52, 1459–1474. doi:10.1007/s00603-018-1660-5

Haimson, B., and Chang, C. (2000). A New True Triaxial Cell for Testing Mechanical Properties of Rock, and its Use to Determine Rock Strength and Deformability of Westerly Granite. *Int. J. Rock Mech. Min. Sci.* 37, 285–296. doi:10.1016/s1365-1609(99)00106-9

Haimson, B. (2006). True Triaxial Stresses and the Brittle Fracture of Rock. *Pure Appl. Geophys.* 163, 1101–1130. doi:10.1007/s00024-006-0065-7

He, M. C., Miao, J. L., and Feng, J. L. (2010). Rock Burst Process of Limestone and its Acoustic Emission Characteristics under True-Triaxial Unloading Conditions. *Int. J. Rock Mech. Min. Sci.* 47, 286–298. doi:10.1016/j.ijrmms.2009.09.003

Lei, X. L., Nishizawa, O., Kusunose, K., Cho, A., Satoh, T., and Nishizawa, O. (2000). Compressive Failure of Mudstone Samples Containing Quartz Veins Using Rapid AE Monitoring: the Role of Asperities[J]. *Tectonophysics* 328 (3), 329–340. doi:10.1016/s0040-1951(00)00215-8

Li, X., Du, K., and Li, D. (2015). True Triaxial Strength and Failure Modes of Cubic Rock Specimens with Unloading the Minor Principal Stress. *Rock Mech. Rock Eng.* 48 (6), 2185–2196. doi:10.1007/s00603-014-0701-y

Li, X., Tao, M., Wu, C., Du, K., and Wu, Q. (2017). Spalling Strength of Rock under Different Static Pre-confining Pressures. *Int. J. Impact Eng.* 99, 69–74. doi:10.1016/j.ijimpeng.2016.10.001

Lockner, D. (1993). The Role of Acoustic Emission in the Study of Rock Fracture. *Int. J. Rock Mech. Min. Sci. Geomech. Abstr.* 30 (7), 883–899. doi:10.1016/0148-9062(93)90041-b

Lu, J., Yin, G., Zhang, D., Gao, H., Li, C., and Li, M. (2020). True Triaxial Strength and Failure Characteristics of Cubic Coal and Sandstone under Different Loading Paths. *Int. J. Rock Mech. Min. Sci.* 135, 104439. doi:10.1016/j.ijrmms.2020.104439

Ma, X., and Haimson, B. C. (2016). Failure Characteristics of Two Porous Sandstones Subjected to True Triaxial Stresses. *J. Geophys. Res. Solid Earth* 121, 6477–6498. doi:10.1002/2016jb012979

Martin, C. D., Kaiser, P. K., and Mccreath, D. R. (1999). Hoek-Brown Parameters for Predicting the Depth of Brittle Failure Around Tunnels. *Can. Geotech. J.* 36 (1), 136–151. doi:10.1139/t98-072

Mogi, K. (2007). *Experimental Rock Mechanics*. London: CRC Press.

Mogi, K. (1971). Fracture and Flow of Rocks under High Triaxial Compression. *J. Geophys. Res.* 76, 1255–1269. doi:10.1029/jb076i005p01255

Ohtsu, M. (1991). Simplified Moment Tensor Analysis and Unified Decomposition of Acoustic Emission Source: Application to *In Situ* Hydrofracturing Test. *J. Geophys. Res.* 96 (B4), 6211–6221. doi:10.1029/90jb02689

Rück, M., Rahner, R., Sone, H., and Dresen, G. (2017). Initiation and Propagation of Mixed Mode Fractures in Granite and Sandstone[J]. *Tectonophysics* 717, 270–283. doi:10.1016/j.tecto.2017.08.004

Thompson, B. D., Young, R. P., and Lockner, D. A. (2005). Observations of Premonitory Acoustic Emission and Slip Nucleation during a Stick Slip Experiment in Smooth Faulted Westerly Granite. *Geophys. Res. Lett.* 32, L10304. doi:10.1029/2005gl022750

Tuncay, E., and Ulusay, R. (2008). Relation between Kaiser Effect Levels and Pre-stresses Applied in the Laboratory. *Int. J. Rock Mech. Min. Sci.* 45 (4), 524–537. doi:10.1016/j.ijrmms.2007.07.013

Zhang, Y., Feng, X.-T., Yang, C., Zhang, X., Sharifzadeh, M., and Wang, Z. (2019). Fracturing Evolution Analysis of Beishan Granite under True Triaxial Compression Based on Acoustic Emission and Strain Energy. *Int. J. Rock Mech. Min. Sci.* 117, 150–161. doi:10.1016/j.ijrmms.2019.03.029

Zhang, Y. (2020). *Energy Evolution Mechanism of Failure Process of Deep Hard Rock and Discrimination of Typical Hazard Types of Deep Tunnel*. Shengyang: Northeastern University

Conflict of Interest: YY was employed by the China Academy of Railway Sciences Corporation Limited.

The remaining authors declare that the research was conducted in the absence of any commercial or financial relationships that could be construed as a potential conflict of interest.

Publisher's Note: All claims expressed in this article are solely those of the authors and do not necessarily represent those of their affiliated organizations, or those of the publisher, the editors, and the reviewers. Any product that may be evaluated in this article, or claim that may be made by its manufacturer, is not guaranteed or endorsed by the publisher.

Copyright © 2022 Zeng, Gao, Chen, Yang and Zhang. This is an open-access article distributed under the terms of the Creative Commons Attribution License (CC BY). The use, distribution or reproduction in other forums is permitted, provided the original author(s) and the copyright owner(s) are credited and that the original publication in this journal is cited, in accordance with accepted academic practice. No use, distribution or reproduction is permitted which does not comply with these terms.

frontiers | Frontiers in Earth Science

REVIEW
published: 01 June 2022
doi: 10.3389/feart.2022.901570

Washing Reagents for Remediating Heavy-Metal-Contaminated Soil: A Review

Heng Zhang[1,2]*, *Yongxin Xu*[2], *Thokozani Kanyerere*[2], *Yang-shuang Wang*[3] and *Minhui Sun*[1]

[1]Sichuan Metallurgical Geological Survey and Design Group Co. Ltd, Chengdu, China, [2]Department of Earth Sciences, University of the Western Cape, Cape Town, South Africa, [3]College of Environment and Civil Engineering, Chengdu University of Technology, Chengdu, China

Heavy-metal pollution of soils has become a major environmental concern around the world presently. Soil washing provides an effective measure of removing contaminants from soil permanently, of which washing reagent plays a vital role in the process. This article reviews the current knowledge acquired on the main aspects concerning washing reagents of soil washing for remediation of heavy-metal-contaminated soil based on more than 150 published studies over a period from 1990 to 2021. The review identifies and discusses the types of washing reagents with their associated characteristics. Based on the factors influencing washing remediation, multi-criteria decision-analysis, together with an integrated four-step procedure, is put forward to manage the selection and prioritizing of washing reagents. It crops out from the literature survey that the selection of the washing reagents is a balanced process by considering washing effect, environmental impact, and cost-effectiveness. On the basis of such observation and evaluation, it is recommended that further study should be focused on developing new washing reagents or compound washing reagents that possess the advantage over heavy-metal removal ability, eco-friendliness, and cost-effectiveness as well. Selecting washing agents that are capable of being recovered from waste such as dissolved organic matter would be a promising trend in washing remediation. Artificial intelligence is expected to assist in the selection of washing reagents.

Keywords: soil washing, heavy metals, affecting factors, multi-criteria decision analysis, selection procedure

OPEN ACCESS

Edited by:
Yunhui Zhang,
Southwest Jiaotong University, China

Reviewed by:
Gang Yang,
Sichuan Agricultural University, China
Liu Shengyu,
Chengdu University of Information Technology, China

***Correspondence:**
Heng Zhang
hengz1982@163.com
3772858@myuwc.ac.za

Specialty section:
This article was submitted to Geohazards and Georisks, a section of the journal Frontiers in Earth Science

Received: *22 March 2022*
Accepted: *20 April 2022*
Published: *01 June 2022*

Citation:
Zhang H, Xu Y, Kanyerere T, Wang Y-s and Sun M (2022) Washing Reagents for Remediating Heavy-Metal-Contaminated Soil: A Review. Front. Earth Sci. 10:901570. doi: 10.3389/feart.2022.901570

1 INTRODUCTION

Heavy-metal pollution of water and soils has become a major environmental concern around the world for the last few decades due to anthropogenic activities that lead to pollution, such as mining, smelting, electroplating, and wastewater irrigating (Jez and Lestan, 2016; Wang et al., 2020; Zhang et al., 2021a; Zhang et al., 2021b). Globally, there are over five million sites covering 20 million ha of land in which the soils are contaminated by various heavy metals (He et al., 2015; Liu et al., 2018). Soil contamination with heavy metals poses serious environmental hazards owing to the fact that heavy metals are non-biodegradable and they can accumulate in living organisms and cause long term harmful effects to human health. Therefore, there is an urgent need to remediate heavy-metal contaminated soils and protect environmental integrity of soils.

Various remediation techniques based on physical, chemical, and even biological processes have been proposed to remove heavy metals from contaminated soils. Among these techniques,

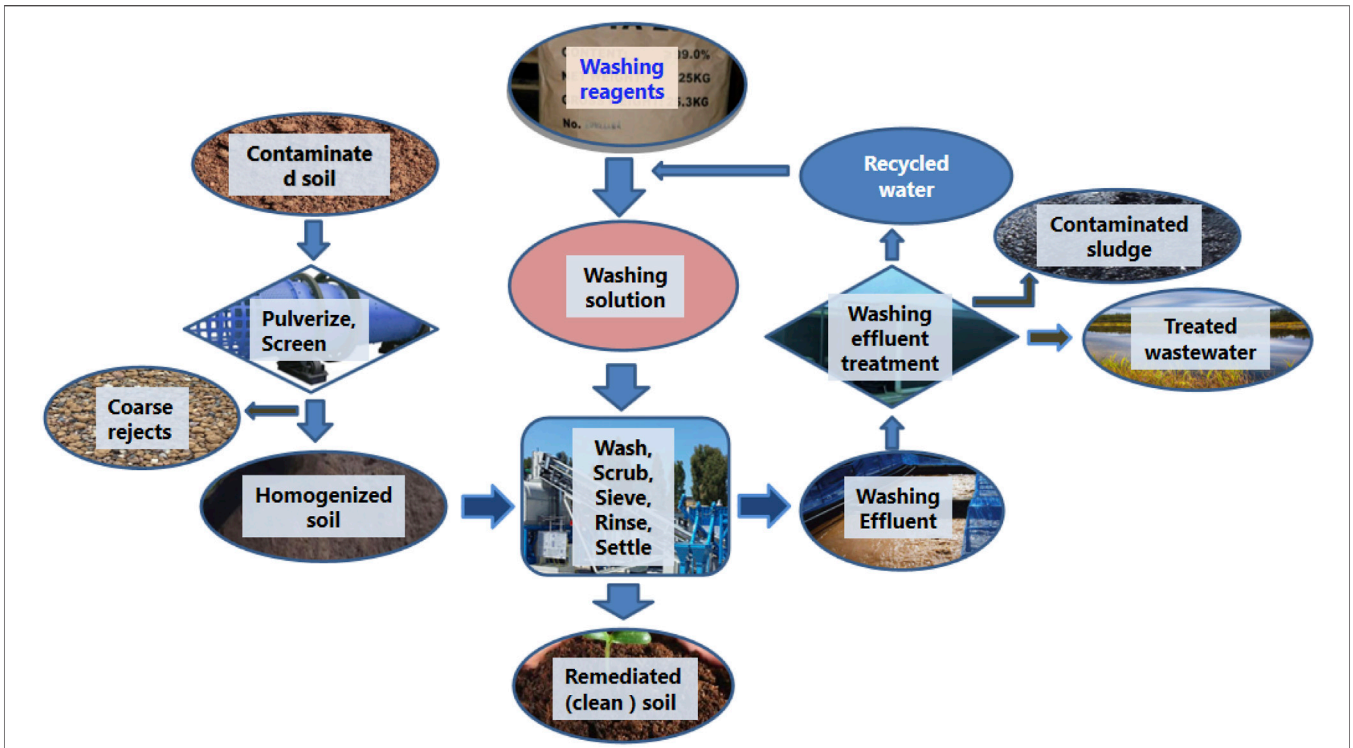


FIGURE 1 | Typical technological process of soil washing (after Liu L et al., 2018).

soil washing is considered an effective measure that can permanently remove heavy metals from soil with high-remediation efficiency despite the concern of losing some nutrients and causing secondary pollution (Wei et al., 2016; Feng et al., 2020). Soil washing employs physical processes to separate the most contaminated soil particles (**Figure 1**), which in turn undergo chemical extraction with specific washing reagents to transfer heavy metals from the soil to solution (Saponaro et al., 2002; Dermont et al., 2008). The remediation effectiveness of soil washing is closely related to the extracting reagents. Several studies in Superfund programmes of the United States have shown that a wrong selection of washing reagents may lead to the failure of washing remediation (USEPA, 2004; 2005). Thus, the research on washing reagents is a hot button of washing remediation.

Due to the extremely important role of washing reagents in soil washing remediation, an array of chemicals has been tested to formulate effective washing solutions (Moutsatsou et al., 2005; Bilgin and Tulun, 2015). Nevertheless, most of these washing extracts are developed on a case-by-case basis depending on the specific contaminant type at a particular site. Different washing reagents exhibit different effects and mechanisms under varying conditions (Liu et al., 2021). To the authors' knowledge, there are few systematic studies on washing reagents of soil washing. The objective of the present article was to review current knowledge acquired on the main aspects concerning washing reagents of soil washing for remediation of heavy metals, which help to provide a significant reference for the study of soil washing. The review covered a brief description on washing reagents' types with their associated characteristics. It also discussed factors that influence washing remediation and summarized the selection and prioritizing method of washing reagents. Finally, based on the current challenges, perspectives on washing reagents were provided for future research.

2 TYPES AND CHARACTERISTICS OF WASHING REAGENTS

Most chemicals have been investigated as washing reagents for remediating the heavy-metal contaminated soils (Yang et al., 2009; Fedje et al., 2013; Alghanmi et al., 2015). These washing reagents are generally divided into four categories, namely inorganic reagents, chelating reagents, surfactants, and compound chemical reagents.

2.1 Inorganic Reagents

The commonly used inorganic solutions include water, inorganic acids, alkali, inorganic compounds, and reducing or oxidizing (redox) reagents. The mechanism of soil washing with inorganic reagents is mainly to destroy the functional groups of the soil surface and form complex formation with heavy metals through washing, acidolysis, and complexation or ion exchange, thus exchanging and desorbing the heavy metals from the soil to the leachates (Ke, et al., 2004).

2.1.1 Water

Water, which is economic and easy to access, is able to flush away contaminants that are of soluble state. In a pilot study, which was

carried out by Xiong et al. (2016), deionized water was reported to remove over 70% of hexavalent chromium. However, heavy metals are sparingly soluble and predominantly in the sorbed state; thus, washing the soils with water alone would not be expected to remove significant amount of heavy metals (Dikinya and Arela, 2010).

2.1.2 Acids

The most commonly reported acids used as washing reagents include hydrochloric acid (HCl), sulfuric acid (H_2SO_4), nitric acid (HNO_3), and phosphoric acid (H_3PO_4). Oh et al. (2015) conducted a risk assessment of two different heavy-metal-contaminated soils that were collected from a former refinery site in Korea. As a result, it was found that 1 M HCl and 1 M HNO_3 were effective for the removal of all heavy metals including Cd, Pb, Cu, Zn, Ni, and As, but HNO_3 was considered the most efficient extract for Pb because the maximum removal efficiency of which reached 96.9%. Lin et al. (2012) performed laboratory- and pilot-scale washing of soils contaminated with Cr, Cu, Ni, and Zn using HCl, H_2SO_4, EDTA, and citric acid. H_2SO_4 with the concentrations between 0.3 M and 1 M was reported to have the best performance, and the removal efficiencies achieved 41%–42%, 38%–68%, 23%–25%, 47%–53%, and 42%–55%, respectively, when targeting Cr, Cu, Ni, Zn, and the total metal content.

Acids generally remove heavy metals from the soil relying on ion exchange and dissolution of soil components/discrete metal compounds, and the removal efficiency of inorganic acids varied in different studies. However, the high removal efficiency of heavy metals is usually achieved at the acid concentration of >1 mol/L, whereas a high concentration of acids causes a high increase in acidity of the treated soil, thus resulting in massive nutrient loss, soil structure change, and causing harm to microorganisms. Kwak et al. (2019) assessed the soil before and after washing remediation with sulfuric acid and phosphoric acid and found that the adverse effects observed in soil algae and earthworms after remediation were related to changes in soil pH, EC, total nitrogen, and total phosphorus. Owing to the changes in physical and chemical properties of soil, treated soil might need time to recover from the remediation before habitat quality and function are restored. Furthermore, wastewater and treated soils need to be neutralized, and the strong acidic conditions also have high requirements on treatment equipment.

2.1.3 Alkali

Alkali used as a washing reagent is not as popular as acids. The commonly used alkali for soil washing is sodium hydroxide. Yang et al. (2013) made use of 0.05 M H_2SO_4 and 0.05 M NaOH to wash soil contaminated by As and Pb. The result showed that sodium hydroxide solution had better performance on the removal of As than sulfuric acid. Sodium hydroxide is, especially effective in removing arsenic from soils, which is due to the ligand displacement reaction of hydroxyl ions with arsenic species and high pH conditions that can prevent reabsorption of arsenic. Similar to strong acids, alkali also causes serious damage to the physical and chemical properties of soil.

2.1.4 Inorganic Salts

The use of salt solutions may be an effective alternative to acid or alkali washing since these inorganic salt reagents have less damage to the physical and chemical properties of treated soils. Chloride salt solutions are the most investigated because metal ions can form soluble metal-Cl complexes with chloride, which is conducive to metal ions to dissolve into the solution (Dermont et al., 2008; Wahla and Kirkham, 2008). Ferric trichloride was reported to be effective in the removal of heavy metals, including Cd, Pb, Zn, and Cu (Zhai et al., 2018; Guo et al., 2019). Elements Fe and Cl are important constituents of soils; however, the research of Chen and Wu (2018) indicated that $FeCl_3$ would also acidify the soil. Furthermore, the high concentration of $FeCl_3$ can make the solution sticky, and therefore it is hard for the heavy-metal ions to spread in the solution, which can affect the extraction efficiency (Guo et al., 2016). ferric trichloride, according to Nedwed and Clifford (2000), the acidified NaCl and $CaCl_2$ solutions were comparable and efficient with conventional extractants (EDTA and HCl) in removing Pb from fine-grained soils but with minimized destruction of soils' physico-chemistry and microbiology. Alam et al. (2001) tried to apply several salts (including potassium phosphate, potassium chloride, potassium nitrate, potassium sulfate, or sodium perchlorate) to extract arsenic from a modeled soil and found that potassium phosphate was the most effective in the pH range of 6–8 (more than 40% extraction).

2.1.5 Reducing or Oxidizing (Redox) Reagents

Reducing and oxidizing reagents provide another option to enhance solubilization of heavy metals since chemical oxidation/reduction can convert metals to more soluble or less toxic forms through valence change. The United States Environmental Protection Agency (USEPA) has conducted laboratory research on Pb extraction involving redox manipulations and valence changes to promote the removal of various Pb compounds from synthetic contaminated soils since the 1990s (USEPA, 1994). Wang et al. (2014) investigated the removal of Cr (VI) from contaminated soil using sodium carboxymethyl cellulose stabilized nanoscale zero-valent iron that was prepared from steel pickling waste liquor and found that 80% of the loaded Cr (VI) was reduced to less toxic Cr (III) when the soil was treated with 0.3 g/L of Fe nanoparticles for 72 h. Several oxidant reagents have also been used to enhance the removal of heavy metals. Lin et al. (2001) used sodium hypochlorite as an oxidizer reagent in the chloride-based leaching process (2 M NaCl at pH 2) to extract metallic Pb-particles (smaller than 0.15 mm) and other Pb-species from highly contaminated soils. Based on the removal mechanism, the use of reducing or oxidizing reagents is usually limited to the heavy metals, which are varied in solubility and toxicity under different valences.

2.2 Chelating Reagents

Chelating reagents are capable of forming stable water-soluble complexes with a variety of metal ions through chelating and

desorption, thus creating favorable conditions for soil washing. Various chelating reagents have been tested for soil washing, and their roles are becoming increasingly important. There are generally two kinds of chelating reagents that are commonly used in the study and practice, namely aminopolycarboxylic acids (also called synthetic chelating reagents) and natural low molecular organic acids (NLMOAs).

2.2.1 Aminopolycarboxylic Acids

Aminopolycarboxylic acids such as ethylenediamine tetraacetic acid (EDTA), diethylenetriamine five acetic acid (DTPA), hydroxyethyl ethylenediamine triacetate (HEDTA), ethylene glycol double tetraacetic acid (EGTA), nitrilotriacetic acid (NTA), N-(2-acetamide) iminodiacetic acid (ADA), ethylenediaminedisuccinic acid (EDDS), and iminodisuccinic acid (IDSA), have strong ability to activate metals and thus are commonly utilized in the soil washing processes due to their ability to interact with the majority of heavy metals (Leõstan et al., 2008).

EDTA and its homologs form stable complexes with several heavy metals over a wide pH range, consequently becoming one of the most commonly investigated chelating reagents. Voglar and Lestan (2012) washed garden soil from a chemical extraction plant with 0.06 M EDTA on a pilot-scale and on average removed 79%, 38%, 70%, and 80% of Pb, Zn, Cd, and As, respectively. Jez and Lestan (2016) used H_4EDTA, Na_2H_2EDTA, and $CaNa_2$EDTA to wash twenty soil samples from Pb-contaminated areas in Slovenia, Austria, Czech Republic, in Pribram and United States, and removed more than 70% of Pb from the contaminated soils. EDTA is recognized as the most effective synthetic chelating reagent (especially for Pb, Cd, and Cu) because: 1) EDTA has a strong chelating ability for cationic heavy metals; 2) EDTA can treat a broad range of soil types; and 3) EDTA is recoverable and reusable owing to its low biodegradability. Compared to extraction with acids that changes the soil matrix, EDTA largely preserves soil property as a plant substrate. However, EDTA also presents two main disadvantages: 1) the price of EDTA products is high, and EDTA is a non-selective extracting reagent that are able to form a strong complex with a variety of metals, including both target toxic heavy metals and alkaline-earth cations such as Al^{3+}, Ca^{2+}, Fe^{2+}, and Mg^{2+}, and thus extracts large quantities of soil nutrients and meanwhile increases the cost; 2) EDTA may pose an ecological threat if it is not recycled or destroyed in the washing process because EDTA is resistant to chemical and biological degradation and thus has the potential for remobilizing heavy metals in the environment. The research conducted by Jez and Lestan (2016) showed that 15% and up to 64% of applied EDTA was retained in acidic soils after remediation, while in average 1% and up to 22% of EDTA was retained in calcareous soils.

Since EDTA has poor biodegradability and high persistence in the soil environment, which may result in deterioration of soil functions and groundwater pollution, biodegradable chelators such as ethylenediaminedisuccinic acid (EDDS), iminodisuccinic acid (IDSA), methylglycinediacetic acid (MGDA), iminodisuccinic acid (ISA), glutamate-N,N-diacetic acid (GLDA), glucomonocarbonic acid (GCA), 3-hydroxy-2,2′-iminodisuccinic acid (HIDS), and polyaspartic acid (PASP), have been suggested as alternatives to EDTA (Luo et al., 2015; Satyro, et al., 2016; Yoo et al., 2018). Begum et al. (2012) conducted lab-scale washing treatments of samples from metal-contaminated soils for the removal of the toxic metal ions using EDDS, MGDA, IDSA, GLDA, and HIDS, and as a result, GLDA showed relatively higher removal efficiencies for Cd, Cu, Ni, Pb, and Zn at pH 7 but tended to remove less soil organic matter, total and plant available ammonium, and exchangeable K, Na, Ca, and Mg which support the revitalization of the treated soils. Wang et al. (2018; 2020) also conducted batch washing to evaluate the potential for several biodegradable chelators for removing Cd, Pb, and Zn from polluted soils and found that GLDA, IDSA and ISA were appealing alternatives to EDTA.

Compared to extraction with acids that changes the soil matrix, aminopolycarboxylate chelating reagents largely preserve soil properties as a plant substrate. However, the eco-environmental consequences due to the release of aminopolycarboxylate acids into the surroundings become an issue of concern (Rahman et al., 2010). The lethal exposure resulting from some of the aminopolycarboxylate acids is likely to persist for a long period because of their poor photo-, chemo- and biodegradability, and in most cases, an increase in the threshold values for toxic effects may be observed with metal complexation. Thus, an increasing interest is focused on the development and use of the eco-friendly chelating reagent having better biodegradability and less environmental toxicity. According to the study by Begum et al. (2012) and Wang et al. (2018), GLDA appears to possess the greatest potential to rehabilitate polluted soils with limited toxicity remaining. However, Kaurin et al. (2020) designed a pilot-scale experiment using EDTA and biodegradable GLDA, EDDS, and IDS as chelators and argued about the advantage of EDTA over tested biodegradable chelators in process and remediation efficiency and environmental safety under realistic conditions.

2.2.2 Natural Low-Molecular Organic Acids

Natural low-molecular organic acids including acetic, citric, oxalic, tartaric, formic, malic, lactic, succinic, and fumaric acids are natural products of root exudates and microbial secretions as well as plant and animal residue decomposition in soils. These natural organic acids are considered biodegradable and eco-friendly chelating reagents, which are able to promote the dissolution and transformation of heavy metals from soils by forming complexes. Consequently, a large number of studies are conducted using varied NLMOAs. Acetic acid was used to leach Pb in field demonstrations at Fort Polk in Leesville, LO, but the nuisance of odors and its relative low removal efficiency limited its application (ITRC, 2003). Xiao et al. (2019) also studied the washing remediation of Cd and Zn using NLMOAs including acetic, oxalic, citric, and tartaric acids and concluded that in view of heavy-metal removal efficiencies and less disturbing on soil fertilities and plant growth, NLMOAs, especially citric acid, were more suitable than HCl, EDTA, and NTA.

The washing mechanism of using NLMOAs includes 1) the desorption of soil minerals by organic acids and the displacement

of hydrogen ions; 2) organic acids complex with heavy metals to form positively charged metal complexes and exchange ions with soil; 3) after adsorption of organic acids on the soil surface, their functional groups complex with heavy metals to form ternary complexes; 4) coordination occurs between organic acids and heavy metals, and the complexes produced are not adsorbed to the soil, thus reducing the adsorption (Zhou et al., 2002; Zhou et al., 2016). The NLMOAs vary in ligand form, dissociation constant (pKa), and function group, which resulted in different removal efficiency of heavy metals (Li et al., 2011). Usually, the removal ability of the NLMOAs has a positive correlation with its dissociation constant and the number of carboxyl groups (-COOH). Although the NLMOAs are less effective in removing heavy metals from soils than aminopolycarboxylic acids because they are reported only effective to dislodge the exchangeable, carbonate, and reducible fractions of heavy metals (Peters, 1999; Wuana et al., 2010), they are more eco-friendly to the environment.

2.3 Surfactants

Surfactants are surface-active compounds which are able to change the interface state of the solution system significantly. Since surfactants are capable of assisting the solubilization, dispersal, and desorption of hydrophobic compounds and heavy metals due to their hydrophobic and hydrophilic portions, they are considered promising washing solutions to remediate heavy-metal-contaminated soils (Liu et al., 2019). Surfactants with different structures and properties can serve for different decontamination purposes. Generally, surfactants are classified into four categories: anionic (negatively charged), cationic (positively charged), nonionic (uncharged), and amphoteric (presents both positive and negative charges at an intermediate pH). Cationic surfactants are mainly nitrogen-containing organic amine derivatives which can dissociate cations in water. Since cationic surfactants make the surface of the matrix hydrophobic and easily cause secondary pollution in soil by adsorption, consequently, they are rarely used in soil washing. Anionic surfactants are the most productive and most widely used surfactants, which are classified into sulfonate and sulfate salts according to their structure of hydrophilic groups. Nonionic surfactants can be used in combination with other surfactants due to the good compatibility because the main hydrophilic group of nonionic surfactants is an undissociated ether group in an aqueous solution. Therefore, anionic and nonionic surfactants are widely used in soil remediation. The surfactant molecules are found either in nature or as products of laboratory synthesis, corresponding with the natural and synthetic origin; consequently, the current surfactants reviewed in soil remediation research and practice are usually classified into biosurfactants and chemical surfactants. The heavy-metal removal mechanism is that surfactant first adsorbed on the soil surface and interacted with the organic molecules and heavy-metal ions, causing the heavy-metal ions to leave the soil particle surface *via* ionic exchange and surfactant-associated complexation, and then a complex micelle forms, which would prevent the adsorption of heavy-metal ions to the soil (**Figure 2**).

2.3.1 Chemical Surfactants

The commonly used chemical surfactants include sodium dodecyl benzene sulfonate (SDBS), sodium dodecyl sulfate (SDS), cetyl trimethyl ammonium bromide (CTAB), Tween, TritonX, and polyoxyethylene laurel ether (Brij-35). Chen and Fu (2012) studied the heavy-metal removal effects of SDBS, SDS, and Tween-80 and found that the removal rates of chromium and cadmium by Tween-80 achieved 37.06% and 61.2%, respectively. Sun et al. (2011) compared the removal effects of SDS, CTAB, and Tween-80 in heavy metals contaminated soils through lab-scale experiments. The result indicated that these three surfactants showed poor performance on the clay soils but good extraction ability for sandy soils, and the removal ability was in the order of SDS > CTAB > Tween-80. Although several studies are conducted on the heavy-metal removal ability of chemical surfactants, the use of chemical surfactants to wash heavy-metal contaminated soils is still unpopular due to the following reasons: 1) the removal efficiency is limited because the polluted soils have a strong adsorption effect on the surfactants, thus causing adverse effect of removing heavy metals from the soil; and 2) the use dosage of surfactants and cost would be high. Therefore, chemical surfactants are always accompanied by other washing reagents to increase the heavy-metal removal ability.

2.3.2 Biosurfactants

Biosurfactants are bio-available surface-active compounds that are mainly generated in the vital movement of bacteria, fungi, and yeast as well as the metabolites of plants and animals (Paria, 2008; Liu et al., 2019). The commonly investigated surfactin, rhamnolipids, cyclodextrin, and sophorolipids are produced by microorganisms, while saponin and tannic acid are produced by plants. Owing to different produced microorganisms, raw matter, and process conditions, biosurfactants have many different types of structures and chemical compositions (e.g., fatty acids, glycolipids, lipopeptides, lipopolysaccharides, and lipoproteins).

Biosurfactants are beneficial for improving the interaction between microorganisms and contaminants in soil and have little negative impact on soil structure and microbial growth; thus, in recent years, biosurfactants have attracted wide attention in soil remediation (Maity et al., 2013; Kholghi et al., 2020). Gusiatin et al. (2019) applied saponin, tannic acid, and rhamnolipids to remove multi-metals from soils. The removal efficiency order of Cu, Ni, and Zn was saponin > tannic acid > rhamnolipids, whereas saponin and tannic acid were the least effective for Pb removal (18%–31% and 11%–35%, respectively). These three biosurfactants effectively removed the heavy metals of the exchangeable and acid soluble fraction and partially removed them from the reducible and oxidizable fraction. A new trend in soil washing with biosurfactants is the use of plant extracts containing saponins instead of commercial powder products. Saponins extracted from soapberry (*Sapindus mukorossi* L) and soapnut fruit pericarp have a better potential for the removal of heavy metals (Ni, Cr, and Mn) from the soil than commercial saponin (Maity et al., 2013; Wang et al., 2015; Ye et al., 2015). Furthermore, with plant extracts, the operational

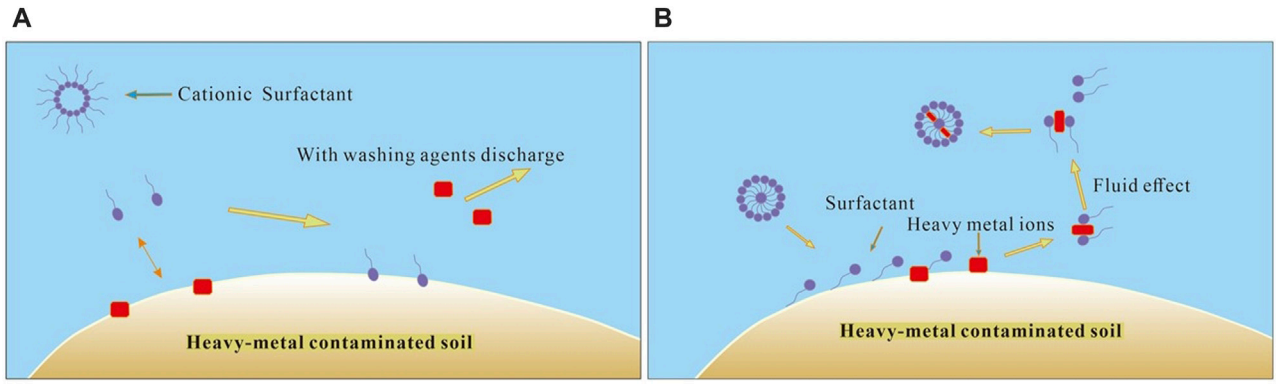


FIGURE 2 | Mechanisms of soil washing with surfactants [**(A)** mechanism of washing with cationic surfactants; **(B)** mechanism of washing with anionic surfactants and biosurfactants].

costs of soil remediation are substantially lower than those with commercial biosurfactants.

Compared to other washing reagents, biosurfactants are important reagents in soil remediation because they are biodegradable, hypotoxic, easily available, and have high selectivity to metal removal. However, concerns on the application of biosurfactants exist in the following aspects: 1) the cost is usually relatively high; 2) there is a risk of secondary pollution caused by the recycle process of leaching waste as well as the parts of toxic reagent; 3) several biosurfactants may be required to remedy the multiple-metal-contaminated soils due to the diverse affinities of biosurfactants to different heavy metals.

2.4 Compound Chemical Reagents

Various metals often coexist at contaminated sites. These coexisting metals, together with the need of soil protection, present difficulties to soil washing due to their dissimilar chemical properties. Under this situation, a single reagent may be insufficient to achieve the remediation goal. For instance, Na2EDTA is recognized as the most effective chelating reagent to remove cationic metals but not in anionic metals (Udovic and Lestan, 2010). By contrast, NLMOAs (e.g., oxalic acid, citric acid, and tartaric acid) and some inorganic acids (e.g., phosphoric acid and nitric acid) attain much higher anionic metal extraction from soils, sediments, and mine wastes (Drahota et al., 2014). Consequently, using multiple solutions as compound chemical reagents to improve the removal efficiency has become a new favorite method in recent years. There are mainly two kinds of compound chemical reagents: 1) mixed reagents that are composed of several solutions; and 2) dissolved organic matter from various wastes or composts.

2.4.1 Mixed Reagents

Since the heavy-metal removal abilities from soils vary among different washing reagents, there is the possibility of enhancing the washing effect by combining different reagents. Plenty of studies were conducted on the development of mixed reagents recently, and most of the studies showed that the combination of multiple reagents achieved higher removal efficiencies than a single reagent did (**Table 1**).

As can be seen from **Table 1**, nearly all kinds of common reagents are involved in the combination of mixed reagents: aminopolycarboxylic acids–NLMOAs, aminopolycarboxylic acids–chemical surfactants, aminopolycarboxylic acids–biosurfactants, aminopolycarboxylic acids–inorganic salts, and NLMOAs–biosurfactants. In addition to these commonly used mixed washing reagents, novel combinations of solutions such as combination of EDTA, NLMOAs, saponin, and nanoscale zero-valent iron, deep eutectic solvents were reported to remove heavy metals from contaminated soils (Wang et al., 2014; Mukhopadhyay et al., 2016; Mehrabi et al., 2020; Huang et al., 2021). Mixed reagents were developed due to the following advantages: 1) increase the removal efficiency of target heavy metals when a single reagent is insufficient; 2) decrease the dosage of an expensive reagent and thus decrease the cost; and 3) decrease the dosage of a toxic reagent and thus protect soil from damage. However, not all the combinations of mixed reagents can be expected to have better performance. For instance, Li et al. (2011) reported that the combination of "Citric acid + SDBS + EDTA" got a worse leaching efficiency of chromium than using citric acid alone. Furthermore, despite the aforementioned advantages of mixed reagents, there is still a risk of increasing secondary pollution to the environment which is caused by the combination of different reagents.

2.4.2 Dissolved Organic Matter

Washing reagents should be compounds which have a high number of functional groups that are capable of forming complexes with metal ions and removing them from soil to the washing solution. Such reagents can be dissolved organic matter (DOM) of different origins, for e.g., wastewater treatment, food processing, or wine processing (Klik et al., 2021). DOM possesses multiple binding sites and thus has the ability to form highly stable and soluble organo-metallic complexes with heavy metals, which is a desirable characteristic of washing reagents that can be used in soil washing technology.

TABLE 1 | Study on mixed reagents of washing remediation to soils contaminated with heavy metals.

Mixed reagent	Heavy metal	Removal efficiency	Optimum condition	Reference
H_2SO_4 + Na_2SO_4	Cr	Total Cr (70.35%) and Cr^{6+} (71.56%)	Solution concentration: 0.4 M for both, soil-to-solution ratio 1:20, 6 h, room temperature	Xu et al. (2016)
CA + $CaCl_2$, CA + $FeCl_3$, and CA + $CaCl_2$ + $FeCl_3$	Cd	86.31%–89.61%	CA + $FeCl_3$ (3:1)	Zhou et al. (2017)
NaCl + HCl, $CaCl_2$ + HCl, and $FeCl_3$ + HCl	Cd	78.9%	0.1 M HCl and 0.4 M $FeCl_3$, soil-to-solution ratio 1:2, 3 h, wash twice	Chen et al. (2014)
CA + SDBS, CA + EDTA, and CA + SDBS + EDTA	Cr	Removal efficiency of Cr was decreased when using the combination of SDBS, EDTA, and CA	0.5 M CA alone, soil-to-solution ratio 1:20, 24 h, wash twice	Li et al. (2011)
Saponin + EDDS and EDTA + TX-100	Pb and Cu	Pb (99.8%) and Cu (85.7%)	10 mM EDDS and 3,000 mg/L saponin	Cao et al. (2013)
EDTA + CA + SDBS	Pb, Zn, Cr, Cu, and Ni	Pb (99.7%), Zn (99.4%), Cr (49.2%), Cu (99.7%), and Ni (98.4%)	pH = 2, EDTA: CA = 0.66: 1, 0.1% SDBS	Cui et al. (2013)
EDDS + EDTA	Cu, Zn, and Pb	Equivalent extraction efficiency of the target metals as EDTA, but reduction in the dosage of EDTA	EDDS: EDTA = 1:1, step-gradient chelant washing is good for the removal of Pb; 24-h continuous washing is better for the removal of Cu	Beiyuan et al. (2018)
HCl + NaOH	As	Arsenic-containing flocs lower than the Korean standard test	0.2 M HCl followed by 1 M HCl (second step) and 1 M NaOH solution (third step)	Jang et al. (2007)
$FeCl_3$ + NLMOAs (CA, MA, and TA)	Cd and Pb	Cd (72.15%), Pb (30.26%)	10 mM $FeCl_3$ and 20 mM organic acid	Liu et al., 2018
Na_2EDTA + OA + H_3PO_4	As and Cd	As (41.9%) and Cd (89.6%)	Na_2EDTA (0.075 M), OA (0.075 M), and H_3PO_4 (0.05 M). Washing sequence: H_3PO_4, OA, and Na_2EDTA; the soil-to-solution ratio is 1:15, room temperature	Wei et al. (2016)
HCl + rhamnolipid	Cd	86.78%	HCl (1 M): rhamnolipid (2%) = 2:1, soil-to-solution ratio is 1:8, 24 h	Guo et al. (2019)
CA + saponin	Zn, Pb, and Cu	Zn (67.2%), Pb (68.8%), and Cu (37.7%)	CA (40 mM) and saponin 3%; volume ratio of CA to saponin solution is 1:5 for the removal of Zn and Pb, while 1:1 for Cu	Xu et al. (2014)
NLMOAs + nanoscale zero-valent iron (nZVI)	Pb	Mine (64%) and farmland soil (83%)	0.2 M CA and 2.0 g/L nZVI	Wang et al. (2014)
Deep eutectic solvents (DESs) + saponin	Pb	72%	40% fructose-based DESs and 1% saponin or 10% DESs and 2% saponin	Mukhopadhyay et al. (2016)
Choline-based DESs + EDTA-2Na	Pb	95.79%	0.02 M EDTA-2Na, DES/water = 2, molar ratio of choline chloride–ethylene glycol is 0.75, 2 h	Huang et al. (2021)

The DOM in the forms of soluble humic substances and volatile fatty acids have a high potential to be used as washing reagents to remove heavy metals (Hartley et al., 2014; Kulikowska et al., 2015; Dong et al., 2021). Soluble humic substances are composed of humic acids and fulvic acids, which show good surface-active properties, such as decreasing the surface tension of water, and in this regard, they are similar to plant biosurfactants. The interaction of humic acids with metal ions results in the formation of strong metal–humate complexes. Fulvic acids have a poorly developed aromatic nucleus and numerous side chains with oxygen-containing functional groups (Stevenson, 1994), and they contain more carboxylic groups than humic acids. The lower molecular weight of fulvic acids, due to their low degree of polymerization and their higher content of functional groups, favor the formation of more soluble, bioavailable, and mobile complexes with heavy metals. Volatile fatty acids are also effective in the removal of heavy metals. Zou et al. (2019) applied volatile fatty acids, which were derived from food waste, as soil washing reagent to treat contaminated soil and attained removal rates of 57.09% and 23.55% of extractable fractions of vanadium and chromium, respectively.

In addition to the aforementioned humic substances and volatile fatty acids, there are other sources of DOM. Distillery sludge and alkaline substances, including NaOH, KOH, $Ca(OH)_2$, and $Mg(OH)_2$, were employed to prepare DOM solution to treat Cd-contaminated soil through soil washing. Approximately 80% of Cd was removed from the soil, while other indices of soil fertility were improved after soil washing (Liu and Chen, 2013). Can et al. (2018) employed four wastes including pineapple peel, soybean straw, broad bean straw, and tea residue to remove Cd, Pb, and Zn in contaminated soils and found that pineapple peel has the highest removals for Cd (90.1%), Pb (18.6%), and Zn (15.2%). The relatively high metal removal was mainly attributed to the effective removal of the exchangeable and acid soluble fractions due to the fact that hydroxyl, carboxyl, amine, carbonyl, and amide groups were involved in the interaction with metal ions by complexation or ion exchange. Some liquid waste can be used directly to treat soil without the need of extracting DOM. For example, Zhang et al. (2017) employed a citric acid fermentation broth to wash heavy-metal polluted soil. This solution contained a variety of microbial metabolites that were derived from three carboxylic acid cycles along with other components in the form of organic acids and surface-active

TABLE 2 | Classification and characteristics of washing reagents.

Classification	Sub-type	Commonly used washing reagent	Washing mechanism	Advantage	Disadvantage
Inorganic reagents	Water, acids, alkali, salts, and reducing or oxidizing reagents	Water, HCl, HNO_3, NaOH, $FeCl_3$, Na_2SO_3, NaClO, and $KMnO_4$	Ion exchange, dissolution of metal compounds, complexation, and valence change	Removal efficiency is usually good; acids and salts have a wide range of applications; cheap	Acid or alkali strongly affects the pH of the soils and causes damage to the soil structure and loss of important nutrient substance
Chelating reagents	Aminopolycarboxylic acids important natural low-molecular organic acids	EDTA, DTPA, EDDS, GLDA, IDSA, NTA, OA, CA, TA, AA, MA, and FA	Desorb heavy metals from the surface of soil particles and form stable chelates with heavy metal ions in soil solution	EDTA is effective on all kinds of heavy metals over a wide pH range; EDDS, IDSA, and GLDA are biodegradable; NLMOAs are biodegradable and eco-friendly	EDTA and DTPA have low biodegradability; NTA is poisonous; expensive
Surfactants	Chemical surfactants and biosurfactants	SDBS, SDS, Tween, TritonX; surfactin, rhamnolipids, cyclodextrin, sophorolipid, saponin, and tannic acid	Change soil surface properties, enhance the solubility of organic ligands in water, or transfer the contaminants from the solid phase to the liquid phase through ion exchange	Chemical surfactants improve the heavy-metal removal ability with other washing reagents; biosurfactants are effective to remove heavy metals and are also biodegradable and eco-friendly	Chemical surfactants alone are always ineffective, and they are poor in biodegradability; removal efficiency of biosurfactants is usually not very high; usually expensive
Compound chemical reagents	Mixed reagents and dissolved organic matter	H_2SO_4 + Na_2SO_4, CA + $FeCl_3$, CA + EDTA, EDDS + EDTA, HCl + rhamnolipid, soluble humic substances, volatile fatty acids, and citric acid fermentation broth	Compound washing mechanism depends on the component reagents	Usually higher removal efficiency of heavy metals, more eco-friendly, and more cost-efficient	Not always get ideal results

substances. Preliminary investigations showed that this type of washing solution was highly applicable for the removal of Cd, Cr, Cu, and Pb from the soil, and the removal efficiency was higher than that of the citric acid solution but had only a small effect on the mineral composition of the soil.

Compared to other commercial washing reagents, DOM costs very low because it can be derived from various wastes or composts. Furthermore, composts and various kinds of wastes are rich not only in soluble organics but also in nutrients, which indicates that DOM as a washing reagent can both remove heavy metals and fertilize the treated soil by increasing the content of organic matter and nutrients. Therefore, the use of DOM as a washing reagent is a recent improvement in soil washing.

2.5 Characteristics of Washing Reagents

Based on the aforementioned, each type of washing reagent has both advantages and limitations (**Table 2**). Generally, the inorganic acids HCl, H_2SO_4, HNO_3, and H_3PO_4 are effective in removing heavy metals. Alkali was reported to be especially effective in the removal of As. However, acid or alkali washing strongly affects the pH of the soils, thus causing damage to the soil structure as well as important loss of soil mineral substances and organic matter. Inorganic salts and reducing or oxidizing reagents are reported to have a good performance in the removal of heavy metals, but they are generally less effective in comparison with inorganic acids.

EDTA is reported to be effective in extracting most kinds of heavy metals from soils, but it has poor biodegradability and thus is worried by some researchers to cause secondary pollution to soil and groundwater. EDDS, IDSA, GLDA, and NTA are biodegradable; accordingly, they are usually considered substitutes of EDTA. GLDA appears to possess the greatest potential to rehabilitate polluted soils with limited toxicity remaining among these reagents. However, opinions are divided on this point. EDTA is tested to have better performance on remediation efficiency and environmental safety over the aforementioned biodegradable chelators in a recent pilot-scale study. Another important limitation is that these aminopolycarboxylic acids are too expensive to be widely used. Natural low-molecular organic acids such as citric acid, oxalic acid, tartaric acid, and acetic acid are reported to be less effective for the removal of the heavy metals in comparison with EDTA, but they are biodegradable and thus are considered to be more eco-friendly to the environment. Citric acid is reported to be the most effective washing reagent among these NLMOAs.

Chemical surfactants are seldom reported to have good ability on heavy metal extraction from contaminated soils, but they are able to improve the removal ability of heavy metals when used together with other washing agents. Compared with the chemical surfactants, biosurfactants are much effective in the removal of heavy metals although the removal efficiency is generally not as good as strong acids and EDTA, and the difference is obvious in extracting rates of biosurfactants to different heavy metals. Moreover, biosurfactants are biodegradable and easy to be available. However, the cost of chemical surfactants and biosurfactants is usually high.

Compound chemical reagents are mixed reagents or compounds that have a high number of functional groups

which are capable of forming complexes with metal ions and removing them from soil. Compared to single washing reagents, compound chemical reagents usually have a good performance in the removal of heavy metals. DOM is eco-friendly and cost-efficient, thus becoming a promising washing reagent in recent improvements in soil washing.

3 SELECTION OF WASHING REAGENTS FOR THE REMEDIATION OF HEAVY-METAL-CONTAMINATED SOILS

3.1 Affecting Factors of the Selection of Washing Reagents

Although plenty of washing reagents are employed to treat the heavy-metal-contaminated soil, it is important to mention that the selection of the most suitable reagents depends highly on the affecting factors. Therefore, understanding of the affecting factors is fundamental to the choice of reagents for washing remediation. There are various factors that affect the application of washing remediation; however, geochemistry of the soil, metal characteristics, washing reagents together with the processing conditions, and treatment and reuse of the washing effluent influence the environment, and the cost and available budget are considered the primary affecting factors.

3.1.1 Geochemistry of the Contaminated Soil

Soil is a dynamic system, which is a heterogeneous mixture of organic and mineral components with differences in pH values, redox conditions, moisture content, and undergoing gradual alterations in response to changes in the environment. The sub-factors of soil geochemistry that affect the applicability and effectiveness of washing include soil texture, organic matter content, cation exchange capacity, and buffering capacity.

3.1.1.1 Soil Texture

Research works have shown that the solubilization/exchange/extraction of heavy metals by washing differs considerably for different soil types. For example, the extraction of lead using hydrochloric acid differs greatly in the allophanic soil and the smectitic soil (Isoyama and Wada, 2007). Furthermore, particle size plays an important role in soil washing. Fine particles have high surface areas for retaining strongly inorganic contaminants and further partially consist of recalcitrant minerals; thus, contaminants can be enriched in fine particles (Ko et al., 2005). Consequently, it is easier to remove heavy metals from larger size particles than very fine particles such as silt and clay since less molecular attraction is exited between heavy metals and large soil particles than fine particles. Furthermore, heavy metals could readily be readsorbed by iron-manganese oxides that are located on the surface of fine particles than larger size particles, and the combination is too strong to make the metals migrate to the solution (Xia et al., 2009). There is a generally held opinion that soil washing is only effective for sandy and granular soils where the clay and silt content (particles less than 0.063 mm) is less than 25% of the soil because the clay-rich soils pose problems such as difficulties with materials handling, solid-liquid separation, longer contact time, and even reduced extraction efficiency (Tampouris et al., 2001; Wuana and Okieimen, 2011). Recently, Yang et al. (2016) and Rui et al. (2018) reported effective washing processes that have treated soils with high clay/silt content (>50%) using compound chemical reagents.

3.1.1.2 Organic Matter Content

The carboxyl groups (adsorption sites) on organic matter or humic substances have a high affinity for heavy metals; therefore, organic matter usually has strong absorption to the washing reagents. Based on the study of Morin et al. (1999), inner-sphere adsorption complexes are directly observed in soils contaminated with Pb; thus, high rates of Pb removal seldom occur from organic matter and metal oxides. Furthermore, the strong absorption between the organic matter and washing reagents not only reduces the concentration of solution so as to inhibit metal extraction but also has a toxic effect on microorganisms in the soil if a large amount of the reagent is adsorbed for a long time.

3.1.1.3 Cation Exchange Capacity

The exchangeable cations of major elements such as Fe, Ca, and Mg may interfere with the washing process owing to the competition between exchangeable cations and the target heavy metals. For example, the low selectivity of EDTA causes a great consumption of this reagent due to the potential chelation of all the exchangeable cations presented in soil, such as Ca^{2+}, Fe^{3+} (Palma and Ferrantelli, 2005).

3.1.1.4 Buffering Capacity of Soils

Calcite in the contaminated soil forms the buffering capacity of heavy metal removal through soil washing, especially acid leaching. The high calcite content or high buffering capacity may decrease the acid-leaching efficiency; thus, acid leaching may be ineffective in soils that have a high buffering capacity, such as calcareous soils (Tejowulan and Hendershot, 1998). This adverse effect of buffering capacity of soils to heavy-metal removal would also be supported by the fact that the addition of calcium carbonate to soil would strongly reduce metal scavenging by the solution from all soil fractions (Ash et al., 2015).

Based on the aforementioned, sub-factors from the soil geochemistry aspect that may limit the applicability and effectiveness of soil washing include 1) high clay/silt content; 2) high organic matter content; 3) high content of Fe and Ca element; and 4) high calcite content or high buffering capacity.

3.1.2 Characteristics of Metal Contaminants

Toxic metals are present in various chemical forms in soils, which exhibit different physical and chemical behaviors in terms of chemical interactions, mobility, biological availability, and potential toxicity. Consequently, the removal efficiency of various heavy metals differs considerably owing to the varied characteristics of metal contaminants which include metal type, concentration, valence, speciation (distribution of chemical species), and fractionation (fractions according to bonding with specific soil substrates) of heavy metals (Maity et al.,

2013; Zhai et al., 2018). For example, chromium exists either as the species of trivalent chromium Cr (III) or as hexavalent chromium Cr (VI). Cr (VI) can be easily reduced to Cr (III), and meanwhile, it can also be transformed from Cr (III) to Cr (VI) by manganese oxide in the soil. Washing with hydrochloric acid is relatively efficient for chromate (CrO_4^{2-}) removal from non-allophanic soils, but it is inefficient for the removal of trivalent chromium Cr^{3+}, particularly from soil that has high cation exchange capacity (Isoyama and Wada, 2007).

Chemical speciation plays a vital role in the solubility, thus influencing the removal of metals from soils; however, the metal speciation analysis can be complicated (especially when the soil is contaminated with a complex mixture of metal compounds); thus, the metal fraction according to soil substrates is often applied. The partitioning of metals according to their association with the soil substrates is usually determined by the sequential extraction procedure, the methods of which are widely used, include the Tessier procedure and BCR sequential extraction procedure (Fernández et al., 2004). A total of five fractions are involved in the extraction procedure by Tessier et al. (1979), including F1) exchangeable, F2) acid soluble/carbonate bound, F3) reducible/Fe-Mn bound, F4) oxidizable/organic matter and sulfide bound, and F5) residual. BCR procedure is largely similar to that produced by Tessier with the chief difference in the first fraction of the procedure. Instead of evaluating the exchangeable and carbonate bound separately, the BCR procedure combines both in the first fraction (Zimmerman and Weindorf, 2010). The fractionation of heavy metals in soil is closely related to soil geochemistry. The exchangeable fraction is mostly adsorbed on humus and clay which is easy to remove; the carbonate bond is most sensitive to pH value; the Fe-Mn oxide bond is to be released when the redox potential decreases; the organic bound is released under strong oxidation conditions; however, the residue fraction is the most stable. Therefore, the fractions most amenable to removal by chemical washing are 1) exchangeable, 2) associated with carbonates, and 3) associated with reducible Fe-Mn oxides of soils (Peters, 1999), while metals associated with the residual soil fraction, imbedded in the mineral lattices or discrete particle forms, are difficult to be removed. Meanwhile, the extraction of heavy metals that are bound to exchangeable and carbonate fractions is faster compared to the fraction of Fe-Mn oxides (Wasay et al., 2001). Nevertheless, the metal fractionation data does not always clearly explain metal removal efficiency because removal efficiency also depends on other factors such as metal concentration and soil geochemistry. Meanwhile, the research of Ash et al. (2015) indicated that there would be a fraction of redistribution during the washing process.

Metal fractionation is important for the choice consideration of washing reagents. Generally, heavy metals in the water-soluble state can be removed by water; while heavy metals in exchangeable, carbonate and Fe-Mn bound can be removed by ion exchange through salt solutions or through chelating and complexing of chelating agents and surfactants; and the removal of organic matter and sulfide bound as well as residual generally requires high concentration of acids and chelating reagents with strong chelating ability.

3.1.3 Washing Reagents and the Processing Condition

Washing reagents are generally the solutions with the functions of ion exchange, chelation, and complexation, and the removal ability of heavy metals differs considerably among the extracting reagents. The effects of the washing reagents, together with their processing conditions on removing heavy metals from contaminated soil, should be carefully considered in both *in situ* leaching and *ex situ* washing despite the fact that quantities of studies have been conducted. Moon et al. (2012) studied the removal effect of Zn using several washing reagents, including inorganic acids, alkali, and NLMOAs. The results showed that using HCl at 3 M achieved the highest removal efficiency of Zn, while the removal effect of residence time (1 h or 2 h) and soil to solution ratio (from 1:10 to 1: 20) was not obvious. However, the research of Zhu et al. (2013) indicated that EDTA was the most effective for the removal of Cd and Pb, and the optimal processing conditions were: 0.1 M EDTA, soil-to-solution ratio 1:6, residence time 3 h, and washing two times. Sun et al. (2011) studied the optimum processing condition of removing heavy metals in the sandy and clay soils using surfactants (SDS, CTAB, and Tween 80). The removal efficiency order in sandy soils was SDS > CTAB > Tween 80, and the highest removal rate of heavy metals Cu, Zn, Pb, Ni, and Cd was achieved under the condition: soil-to-solution ratio 1:50, moral ratio (surfactants/heavy metal) 15:1, and pH 4. These case studies reflect that type and dosage of the washing reagent, pH value, temperature, residence time, soil-to-solution ratio, washing times, and the order of sequential washing are important sub-factors of washing reagents that affect the removal of heavy metals.

Generally, washing reagents with a strong chelating ability or strong acidity have a good heavy-metal removal effect on soil (**Table 2**); however, strong chelating ability and strong acidity may cause adverse effects on the environment. Usually, the higher the concentration of the washing agent, the better the removal ability; however, high concentrations of washing reagents can lead to the loss of large numbers of ions.

The pH of the washing solution plays a significant role in the extractability of heavy metals from soils. The extractability of most cationic heavy metals (e.g., Cd, Cu, Pb, and Zn) increases when the solution pH decreases. At low pH, the protons (H^+) added can react with soil surface sites (layer silicate minerals and/or surface functional groups, including Al-OH, Fe-OH, and COOH groups) and enhance the desorption of metal cations, which are transferred into the washing fluid (Isoyama and Wada, 2007). However, for the arsenic-contaminated soil, good removal ability is achieved under both strong acid and strong alkali conditions.

The residence time, which is also called washing time or contact time, is one of the main sub-factors affecting the removal efficiency. It is necessary to ensure that the washing solution is in full contact with the soil particles so as to leach out heavy metals. The residence time is directly related to the consumption of the washing reagent, thus increasing the cost. There is usually an optimal residence time for the washing process, within which the removal efficiency of the heavy metals increases sharply with the increase of the residence time. However, after the optimum residence time, the continued consumption of the washing reagent could not

significantly improve the removal efficiency. In general, the residence time of inorganic washing reagents is relatively short, while that of organic reagents is relatively longer so as to ensure a sufficient reaction between reagents and heavy metals in soil (Wang, 2013). Under inorganic acid washing condition, the extraction of exchangeable and residual fractions was less variable above more than 15 min, while in the case of Fe/Mn oxide and organic/sulfides fractions, there are possibly a gradual extraction of As and Zn by an increase of reaction time (Ko et al., 2005).

The soil-to-solution ratio refers to the ratio of the mass or volume of the soil to the washing reagent. The removal efficiency of heavy metals usually increases with the decrease of the soil to solution ratio because the reduction of the soil to solution ratio means an increase in the amount of washing reagent added to the contaminated soil. The choice of soil to solution ratio should be appropriate because it is not conducive to stirring if the ratio is too large (e.g., bigger than 1:2), while too small of the ratio (e.g., smaller than 1:20) will increase the load of the equipment as well as the consumption of washing reagent and waste effluent, thus increasing the cost of treatment.

During the washing process, the number of washing times reflects the change of soil to solution ratio. The study of the washing times can better reflect the removal effect of different washing batches on heavy metals so as to maximize the heavy-metal removal efficiency of the washing reagent.

The optimum processing conditions vary among studies owing to the differences in soil geochemistry, metal contaminants, and washing reagents. However, these sub-factors in terms of washing reagents are related to each other. The times of washing reflect the change of soil to solution ratio, while the soil to solution ratio and concentration reflect the different ratios of the dosage of washing reagent and the amount of soil to some extent.

3.1.4 Influence on Soil and the Environment

Before the implementation of soil washing, the influences of remediation on the soil and environment should be considered carefully because some of the extracting reagents can persist in the environment at unacceptable levels, which may cause adverse influence on surrounding residents, microbial communities, and other organisms in the soil. For example, EDTA is low in degradation; thus, there is a potential to contaminate soil and groundwater. EDDS is considered a degradable chelating reagent; however, in the case of being taken as the only source of carbon and nitrogen, Cr (III)-EDDS, Fe (III)-EDDS, Pb-EDDS, Al-EDDS, and Cd-EDDS have degraded, while Cu-EDDS, Ni-EDDS, and Hg-EDDS have not degraded yet (Vandevivere et al., 2001). Citric acid and tartaric acid are usually considered eco-friendly chelating agents; however, they are also reported to cause an 80% loss of the elements (Wasay et al., 1988).

3.1.5 Treatment and Reuse of the Washing Effluent

The remediation process produces a final effluent which contains washing reagents and extracted metals at concentrations higher than discharge limits; therefore, an important factor in connection with the application of washing reagents to full scale remains; however, the subsequent treatment of the washing effluent before it can be safely discharged into the aquatic environment so as to avoid of secondary pollution or be reused to reduce remediation cost.

Several strategies are proposed for the treatment of the washing effluent. The treatment of soil acidification and effluent caused by washing with inorganic acids is neutralization and precipitation. The commonly used effluent treatment techniques for chelating reagents include trans-complexation, ion exchange, reverse osmosis, advanced oxidation processes, and electrochemical method (Pociecha and Lestan, 2010; Sun et al., 2015; Satyro et al., 2017). Kim and Ong (1999) introduced the trans-complexation method: the Pb in the EDTA complex was replaced with Fe^{3+} at low pH, and the Pb was subsequently removed using NaOH as a precipitating agent. This process was relatively expensive and proved difficult if the EDTA was complexed with more than one metal. Lim and Kim (2013) used alkaline chemicals to precipitate arsenic and heavy metals in the effluent containing oxalic acid and then reused the decontaminated effluent for the soil washing. Juang and Wang (2000) proposed electrolytic recovery of Pb and Cu from a solution containing EDTA using sensitive and expensive cation-exchange membranes, but the process of which was technically quite complicated. Di Palma et al. (2003) proposed reverse osmosis for the separation of EDTA complexes from the washing solution, while the soil colloidal particles tend to clog the membranes. Finzgar and Lestan (2000) proposed oxidative decomposition of EDTA complexes in washing solution using advanced oxidation processes, which was much less effective when the washing solution was either turbid or colored. The treatment of electrochemical-advanced oxidation processes was more robust but consumed a significant amount of electricity and used an expensive boron-doped diamond anode (Pociecha and Lestan, 2009). Pociecha and Lestan (2010) used electrocoagulation with an Al sacrificial anode to separate the Pb, Zn and Cd from a washing solution. Satyro et al. (2016) applied the combined TiO^{2-} photocatalytic processes to decontaminate the effluents which were produced in the washing process of polluted soil using EDDS as an organic chelate. Despite the fact that various techniques have been studied, the difficulty and high cost of effluent treatment make it an obstacle to the full scale application and commercialization of soil washing technologies.

3.1.6 Cost and Available Budget

The price of the washing reagents and the available budget are key constraints that affect the implementation of soil washing. For example, EDDS is an eco-friendly chelating agent with good heavy-metal removal efficiency, but the relatively high price limits its application (Hong and Jiang, 2005). Zhou et al. (2016) compared the costs of different remediation techniques and concluded that the cost of soil washing is up to seven times more expensive than other available remediation techniques. Due to the high costs, several cases of soil washing in the Superfund program of the United States (**Table 3**) failed implementation

TABLE 3 | Examples of deselected soil-washing projects in the Superfund Program (data extracted from Dermont et al., 2008).

Site location and description	Media	Metal	Reasons of soil washing failure	Alternative selected technology
Sacramento Army Depot, oxidation lagoons, OU4, CA	Soil	Cr and Pb	Costs	Solidification/stabilization; off-site disposal
Zanesville Well Field, OH	Soil	As, Cr, Hg, and Pb	Soil volume was much smaller than originally projected	Off-site disposal
United Scrap Lead/SIA, OH (lead battery recycling)	Soil/ sediments	As and Pb	Costs	Soil disposed off-site if Pb levels above 1,550 μg/g; containment of the soil below this level

(Dermont et al., 2008). Therefore, soil washing is practical only when the cost and available budget are balanced, and the low cost of the washing reagent is an eternal pursuit in the practice of soil washing.

The aforementioned affecting factors have internal relationships among themselves, which interact with each other and work together to determine the removal of heavy metals from soils.

3.2 Preliminary Choice of Washing Reagents Based on the Affecting Factors

The inorganic acids, chloride salts, chelating reagents, and biosurfactants are generally reported effective in the removal of heavy metals (**Supplementary Table S1**). However, each kind of washing reagent has both advantages and limitations. Strong inorganic acids have strong heavy-metal removal ability and low price, but they strongly affect the pH of the soil. Alkali has strong removal ability to As and medium removal ability to Zn and Hg, which is cheap in price but poor in eco-friendliness. The heavy-metal removal ability, eco-friendliness, and cost-effectiveness of chloride salts are at a medium level. Aminopolycarboxylic acids are poor in cost-effectiveness; EDTA has strong heavy-metal removal ability and is medium in eco-friendliness. Other degradable aminopolycarboxylic acids are medium in heavy-metal removal ability and good in eco-friendliness. Natural low molecular organic acids, which a have medium level of heavy-metal removal ability, are good in eco-friendliness and cost-effectiveness. Synthetic surfactants are poor in heavy-metal removal ability, eco-friendliness, and cost-effectiveness. Biosurfactants which have medium heavy-metal removal ability are eco-friendly but poor in cost-effectiveness. Dissolved organic matters present medium heavy-metal removal ability, but they are good in eco-friendliness and cost-effectiveness. During the preliminary choice process of washing reagents for the common heavy metals, washing effect, environmental impact, and cost-effectiveness should be balanced to get the suitable options. Under the condition of ensuring the removal effect, the impact on the environment and cost should be reduced as far as possible.

Due to technical issues of uncertainties in different soil and contaminant characteristics, together with the relationship of the affecting factors, it is difficult to make decisions on the selection of suitable washing reagents. Moreover, remediation practices are unique (Hou et al., 2014) in that they involve multiple local stakeholders in the decision-making process (Lehigh et al., 2020). To come to a consensus on such complex interdisciplinary problems, different multi-criteria decision-analysis (MCDA) tools, adopted for choosing an optimum site-specific remediation method, have been developed (Hou et al., 2018). A promising MCDA method that is able to assist the choice of washing reagents is the analytical hierarchy process (AHP) (Saaty, 1980), which can be used to combine all the representative criteria into a "criteria tree", with different levels of priorities accordingly. The application of AHP involves the decomposition of the ultimate goal into a three-level hierarchy consisting of subcriteria of the goal. A suitable washing reagent means that it is able to remove the metals to meet safety standards, meanwhile preserving the natural soil properties to the maximum extent within a reasonable budget. Accordingly, the top of the hierarchy is the goal of the analysis, relating to the "choice of washing reagent"; the middle level contains more specific criteria with regard to the objective, relating to "heavy-metal removal efficiency," "influence on soil and environment," and "cost and available budget," which can take a reference as **Supplementary Table S1**; and the bottom level refers to the most specific criteria related to the main criteria in the middle level: 1) "types of washing reagents" is chosen to support the "influence on soil and environment," 2) "soil geochemistry," "metal characteristics," and "washing reagents and the processing conditions" are taken into account to support "heavy-metal removal efficiency," and 3) "price of washing reagents" and "treatment and reuse of washing effluent" are considered to support "cost and available budget". The AHP hierarchy structure of affecting factors in the choice of washing reagents is shown in **Figure 3**.

Each subcriterion in the criteria tree is represented by a value supporting the criterion of upper level through pair comparison. Then, the weights reflecting the relative importance order of criterion at each level are assigned based on the opinions of experts or the objective judgment of the decision-maker. The values of supporting objective and relative weights for all levels are calculated and then sorted. The preliminary choice of washing reagents is based on the following principle: highly suitable washing reagents obtain high values, while less suitable reagents obtain lower values.

$$SI = \sum_{i=1}^{n} v_i w_i, \tag{1}$$

where SI is the suitability index of washing reagent; n is the total number of subcriteria; v_i is the value for subcriterion i; and w_i is the weight assigned to subcriterion i.

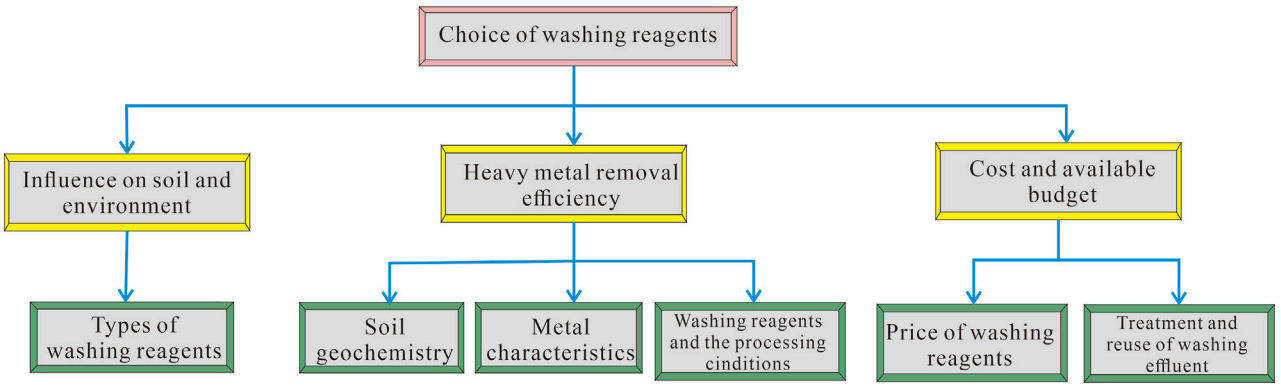


FIGURE 3 | AHP hierarchy structure of the preliminary choice of washing reagents.

Since criteria interaction in decision-making problems is complex, therefore, another MCDA method named INfluence-based deciSIon guiDE (INSIDE) which combines the Decision Making Trial and Evaluation Laboratory and Analytic Network Process (ANP) techniques, is introduced as a methodology to prioritize between remediation methods for a contaminated groundwater aquifer (Naseri-Rad et al., 2020). Therefore, taking criteria interaction into account, INSIDE is also useful for the preliminary choice of washing reagents.

3.3 Integrated Procedure of Selecting Washing Reagents

The selection of washing reagents is aimed at assisting the removal of heavy metals but preserving the natural soil properties within reasonable budget limits, which is also considered a balanced process of washing effect, environmental impact, and cost-effectiveness. Therefore, during the process of choosing washing reagents, the main affecting factors of the reagents for washing remediation should be taken into account comprehensively. Four steps are included in the procedure of choosing washing reagents (**Figure 4**).

First, a feasibility analysis of soil washing should be conducted based on the learning of soil geochemistry, the characteristics of heavy-metal contaminates, and the remediation goal which are available through the environmental investigation and risk assessment of contaminated sites. Soil washing is usually supported by limited clay content (usually less than 25%) and low content of humic, as well as low content of Fe, and Ca elements, and calcite from the soil geochemistry aspect. Metal speciation is another important factor that affects soil washing from the aspect of heavy metal characteristics. The fractions most amenable to the removal of metals by washing are associated with exchangeable carbonates and reducible Fe-Mn oxides of soils, while metals associated with organic matter and sulfide bond and residual fractions are difficult to be removed. If the factors of soil geochemistry and heavy-metal characteristics show great negative influence on soil washing, the determination of remediation through washing and the choice of reagents should be cautious. Either auxiliary ways such as heating, ultrasonic, microwave, and electrokinetics are needed to enhance the removal of heavy metals or other remediation techniques should be taken into account to achieve the remediation goal (Zhang et al., 2016; Chang et al., 2020; Choi et al., 2021).

Second, the preliminary choice of washing reagents should be conducted once the washing remediation is determined. During this process, the factors of washing effect, eco-environment impact, and cost are required to be considered a whole to get the suitable options. Multi-criteria decision-analysis (MCDA) based on AHP or ANP can be adopted to assist the preliminary choice of washing reagents.

Third, laboratory studies are required to testify the remediation effect of initially screened reagents, as well as to get the optimum processing conditions such as reagent dosage, temperature, pH, residence time, soil-to-solution ratio, washing times, and washing sequences. Batch tests are usually beneficial to soil washing, while column tests are helpful to soil leaching.

Fourth, a pilot study is necessary so as to optimize the processing conditions which are obtained through laboratory studies before the implementation of soil washing in full scale. Once the washing reagents and the processing conditions are finally determined, soil washing can be implemented to achieve the remediation goals.

To sum up, the selection of washing reagents for the remediation of heavy-metal-contaminated soils is concluded as shown in **Figure 5**.

4 SUMMARY AND RECOMMENDATIONS

Soil washing, which is considered an effective technology that can be used to permanently remove heavy metals from soil, is particularly relevant for the remediation of heavy-metal-contaminated soils. The

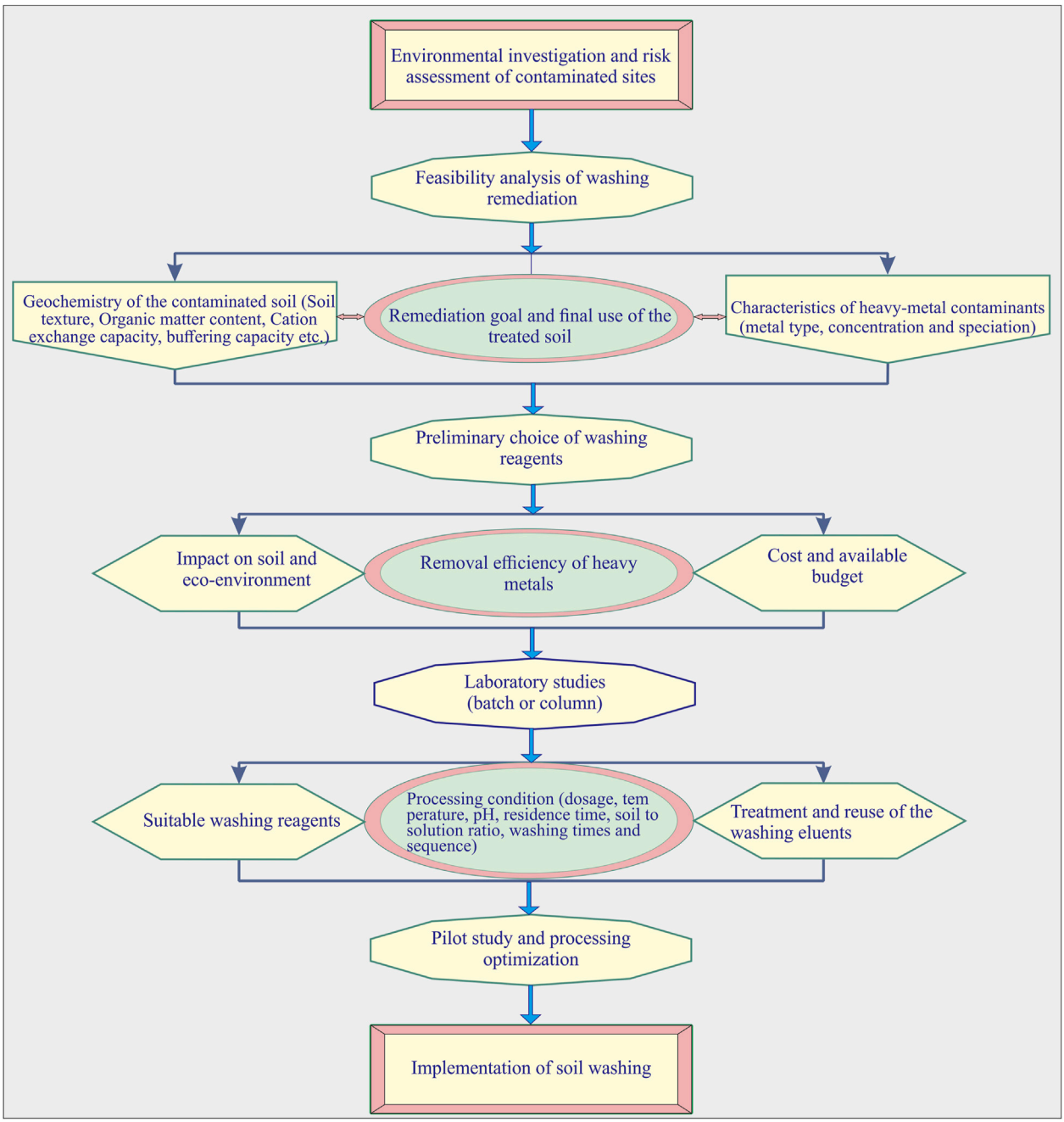


FIGURE 4 | Procedure of choosing washing reagents in soil remediation (four steps are included: 1) feasibility analysis of washing remediation; 2) preliminary choice of washing reagents; 3) laboratory study; 4) pilot study and processing optimization).

key point to the success of washing remediation technology is that appropriate washing reagents can be selected. This article identified and discussed the types of washing reagents with their associated characteristics and focused on the selection of washing reagents for extracting heavy metals from soils. The commonly used washing reagents include inorganic reagents, chelating reagents, surfactants, and compound chemical reagents. It is noted that each kind of washing reagent has both advantages and limitations. The review also showed that heavy-metal removal of washing remediation is generally related to the geochemistry of the contaminated soil, metals characteristics, and washing reagents together with the processing conditions, treatment and reuse of the washing effluent, and influence on the environment as well as the cost and available budget. The selection and prioritizing of washing reagents is a balanced process that considers washing effect, environmental impact, and cost-effectiveness. Therefore, the multi-criteria decision-analysis method

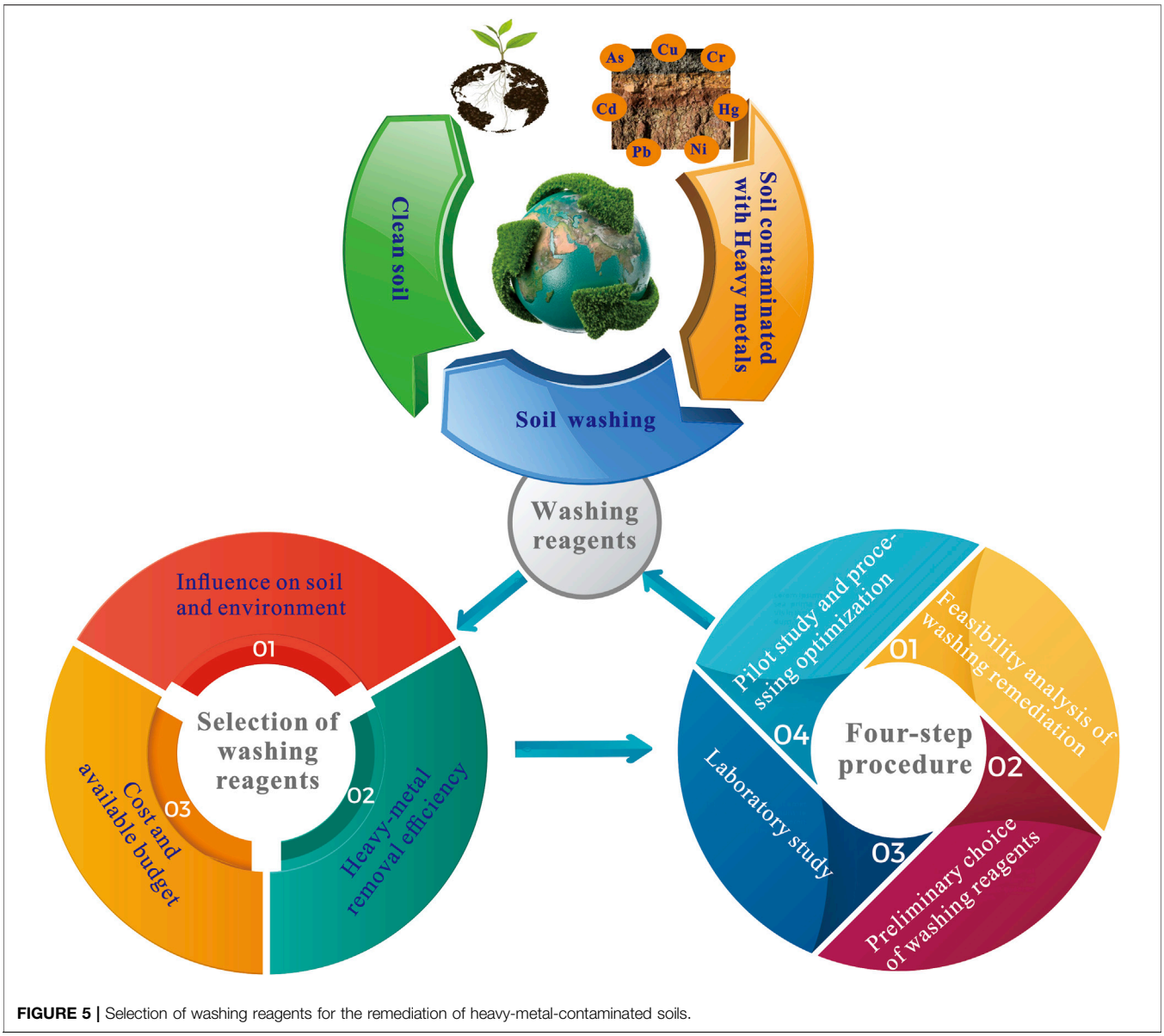


FIGURE 5 | Selection of washing reagents for the remediation of heavy-metal-contaminated soils.

is suggested to assist the preliminary choice analysis of washing reagents. Furthermore, an integrated four-step procedure for the selection of washing reagents is put forward:

1) Feasibility analysis of soil washing is carried out based on the learning of soil geochemistry, heavy-metal contaminates, and the remediation goal;
2) Preliminary screening of washing reagents is conducted based on the analysis of washing effect, environmental impact, and cost-effectiveness through the MCDA method;
3) Laboratory studies are required to testify the remediation effect of initially selected reagents, as well as to get the optimum processing conditions;
4) A pilot study is necessary so as to optimize the processing conditions before the implementation of soil washing in full scale. Soil washing can then be successfully implemented.

Based on the review, soil washing technology for the removal of heavy metals continues to progress toward using washing reagents that possess the advantage over heavy-metal removal, eco-friendliness, and cost-effectiveness. The perspectives of washing reagents are foreseen as follows:

1) Developing new washing reagents or compound washing reagents which are highly effective on heavy-metal removal but low risk of environmental pollution and low cost. Searching for washing reagents that are capable of being recovered from waste (e.g., dissolved organic matter) would be a promising trend.
2) Research on the improvement of removal ability of the heavy-metal residual fraction is needed since it is difficult to remove the residual fraction from a technical aspect. The research on the combination of washing reagents with other auxiliary ways

or other remediation technologies (e.g., bioremediation) may be a solution.
3) Study on the treatment and recycling of washing effluent so as to manage the cost-effectiveness as well as the risk of secondary pollution that might be induced.
4) Artificial intelligence is expected to be applied to assist in the selection of washing reagents and the survey of *in situ* remediation environments.

AUTHOR CONTRIBUTIONS

HZ: investigation, data curation, and writing—original draft. YX: conceptualization and writing—review and editing. TK: data curation and methodology. Y-W: software. MS: methodology.

ACKNOWLEDGMENTS

The authors wish to thank Sichuan Provincial Bureau of Metallurgical Geological Exploration, China, for the financial support (No. [2018]158). The contributions of all references cited in this article are also acknowledged.

SUPPLEMENTARY MATERIAL

The Supplementary Material for this article can be found online at: https://www.frontiersin.org/articles/10.3389/feart.2022.901570/full#supplementary-material

Supplementary Table S1 | Laboratory and field investigations on washing remediation of commonly used washing reagents, together with the recommendation index of heavy-metal removal ability, eco-friendliness, and cost-effectiveness.

REFERENCES

Alam, M. G. M., Tokunaga, S., and Maekawa, T. (2001). Extraction of Arsenic in a Synthetic Arsenic-Contaminated Soil Using Phosphate. *Chemosphere* 43, 1035–1041. doi:10.1016/S0045-6535(00)00205-8

Alghanmi, S. I., Al Sulami, A. F., El-Zayat, T. A., Alhogbi, B. G., and Abdel Salam, M. (2015). Acid Leaching of Heavy Metals from Contaminated Soil Collected from Jeddah, Saudi Arabia: Kinetic and Thermodynamics Studies. *Int. Soil Water Conservation Res.* 3 (3), 196–208. doi:10.1016/j.iswcr.2015.08.002

Arab, F., and Mulligan, C. N. (2018). An Eco-Friendly Method for Heavy Metal Removal from Mine Tailings. *Environ. Sci. Pollut. Res.* 25, 16202–16216. doi:10.1007/s11356-018-1770-3

Ash, C., Tejnecký, V., Šebek, O., Houška, J., Chala, A. T., Drahota, P., et al. (2015). Redistribution of Cadmium and Lead Fractions in Contaminated Soil Samples Due to Experimental Leaching. *Geoderma* 241-242, 126–135. doi:10.1016/j.geoderma.2014.11.022

Begum, Z. A., Rahman, I. M. M., Tate, Y., Sawai, H., Maki, T., and Hasegawa, H. (2012). Remediation of Toxic Metal Contaminated Soil by Washing with Biodegradable Aminopolycarboxylate Chelants. *Chemosphere* 87 (10), 1161–1170. doi:10.1016/j.chemosphere.2012.02.032

Beiyuan, J., Tsang, D. C. W., Valix, M., Baek, K., Ok, Y. S., Zhang, W., et al. (2018). Combined Application of EDDS and EDTA for Removal of Potentially Toxic Elements under Multiple Soil Washing Schemes. *Chemosphere* 205 (AUG), 178–187. doi:10.1016/j.chemosphere.2018.04.081

Bilgin, M., and Tulun, Ş. (2015). Biodrying for Municipal Solid Waste: Volume and Weight Reduction. *Environ. Technol.* 36, 1691–1697. doi:10.1080/09593330.2015.1006262

Cao, M., Hu, Y., Sun, Q., Wang, L., Chen, J., and Lu, X. (2013). Enhanced Desorption of PCB and Trace Metal Elements (Pb and Cu) from Contaminated Soils by Saponin and EDDS Mixed Solution. *Environ. Pollut.* 174, 93–99. doi:10.1016/j.envpol.2012.11.015

Chang, J.-H., Dong, C.-D., Huang, S.-H., and Shen, S.-Y. (20202020). The Study on Lead Desorption from the Real-Field Contaminated Soil by Circulation-Enhanced Electrokinetics (CEEK) with EDTA. *J. Hazard. Mater.* 383, 121194. doi:10.1016/j.jhazmat.2019.121194

Chen, C., Wang, G., and Wang, J. (2014). Study on the Leaching Effect of HCl and Three Neutral Salt. *J. Saf. Environ.* (05), 211–216.

Chen, F., and Fu, M. (2012). Study on Remediation of Soils Polluted by Heavy Metals Using Surfactants. *Sichuan Environ.* 31 (4), 61–64.

Chen, W., Qu, Y., Xu, Z., He, F., Chen, Z., Huang, S., et al. (2017). Heavy Metal (Cu, Cd, Pb, Cr) Washing from River Sediment Using Biosurfactant Rhamnolipid. *Environ. Sci. Pollut. Res. Int.* 24 (6), 16344–16350. doi:10.1007/s11356-017-9272-2

Chen, X., and Wu, Y. (2018). Remediation Mechanism of Multi-Heavy Metal Contaminated Soil by Using Different Chemical Washing Reagents. *Chin. J. Environ. Eng.* 12 (10), 2845–2854. doi:10.12030/j.cjee.201804192

Choi, J., Lee, D., and Son, Y. (2021). Ultrasound-assisted Soil Washing Processes for the Remediation of Heavy Metals Contaminated Soils: The Mechanism of the Ultrasonic Desorption. *Ultrason. Sonochemistry* 74 (2021), 105574. doi:10.1016/j.ultsonch.2021.105574

Cui, J., Xue, W., Yan, Z., Liu, S., and Wang, N. (2013). Repairing of Heavy Metals Contaminated Soil with Different Surfactants. *J. Dalian Dalian Polytech. Univ.* 32 (04), 279–282. doi:10.19670/j.cnki.dlgydxxb.2013.04.013

Dermont, G., Bergeron, M., Mercier, G., and Richer-Laflèche, M. (2008). Soil Washing for Metal Removal: A Review of Physical/chemical Technologies and Field Applications. *J. Hazard. Mater.* 152, 1–31. doi:10.1016/j.jhazmat.2007.10.043

Di Palma, L., Ferrantelli, P., Merli, C., and Petrucci, E. (2003). Treatment of the Solution Extracted from Metal Contaminated Soils by Reverse Osmosis and Chemical Precipitation. *Ann. Chim.* 93, 1005–1011. doi:10.2116/analsci.19.1687

Dikinya, O., and Areola, O. (2010). Comparative Analysis of Heavy Metal Concentration in Secondary Treated Wastewater Irrigated Soils Cultivated by Different Crops. *Int. J. Environ. Sci. Technol.* 7 (2), 337–346. doi:10.1007/bf03326143

Dong, Y., Lin, H., Zhao, Y., and Gueret Yadiberet Menzembere, E. R. (20212021). Remediation of Vanadium-Contaminated Soils by the Combination of Natural Clay Mineral and Humic Acid. *J. Clean. Prod.* 279, 123874. doi:10.1016/j.jclepro.2020.123874

Drahota, P., Grösslová, Z., and Kindlová, H. (2014). Selectivity Assessment of an Arsenic Sequential Extraction Procedure for Evaluating Mobility in Mine Wastes. *Anal. Chim. Acta* 839, 34–43. doi:10.1016/j.aca.2014.06.022

Fedje, K. K., Yillin, L., and Strömvall, A.-M. (2013). Remediation of Metal Polluted Hotspot Areas through Enhanced Soil Washing - Evaluation of Leaching Methods. *J. Environ. Manag.* 128, 489–496. doi:10.1016/j.jenvman.2013.05.056

Feng, C., Zhang, S., Li, L., Wang, G., Xu, X., Li, T., et al. (2018). Feasibility of Four Wastes to Remove Heavy Metals from Contaminated Soils. *J. Environ. Manage* 212, 258–265. doi:10.1016/j.jenvman.2018.01.030

Feng, W., Zhang, S., Zhong, Q., Wang, G., Pan, X., Xu, X., et al. (2020). Soil Washing Remediation of Heavy Metal from Contaminated Soil with EDTMP and PAA: Properties, Optimization, and Risk Assessment. *J. Hazard. Mater.* 381, 120997. doi:10.1016/j.jhazmat.2019.120997

Fernández, E., Jiménez, R., Lallena, A. M., and Aguilar, J. (2004). Evaluation of the Bcr Sequential Extraction Procedure Applied for Two Unpolluted Spanish Soils. *Environ. Pollut.* 131 (3), 355–364. doi:10.1016/j.envpol.2004.03.013

Finzgar, N., and Lestan, D. (2000). Heap Leaching of Pb and Zn Contaminated Soil Using Ozone/UV Treatment of EDTA Extractants. *Chemosphere* 63, 1736–1743. doi:10.1016/j.chemosphere.2005.09.015

Gan, W., He, Y., Zhang, X., Shan, Y., Zheng, L., and Lin, Y. (2012). Speciation Analysis of Heavy Metals in Soils Polluted by Electroplating and Effect of Washing to the Removal of the Pollutants. *J. Ecol. Rural Environ.* 28 (1), 82–87. doi:10.3969/j.issn.1673-4831.2012.01.014

Gitipour, S., Ahmadi, S., Madadian, E., and Ardestani, M. (2016). Soil Washing of Chromium- and Cadmium-Contaminated Sludge Using Acids and

Ethylenediaminetetra Acetic Acid Chelating Agent. *Environ. Technol.* 37 (1), 145–151. doi:10.1080/09593330.2011.597784

Guo, W., Zhang, H., Yin, X., Wang, L., and Wang, Z. (2019). Cadmium Removal from Contaminated Soil inside Non-ferrous Metal Smelter by Washing. *Chin. J. Environ. Eng.* 13 (2), 389–395. doi:10.1080/15320383.2019.1689919

Guo, X., Wei, Z., Wu, Q., Li, C., Qian, T., and Zheng, W. (2016). Effect of Soil Washing with Only Chelators or Combining with Ferric Chloride on Soil Heavy Metal Removal and Phytoavailability: Field Experiments. *Chemosphere* 147, 412–419. doi:10.1016/j.chemosphere.2015.12.087

Gusiatin, Z. M., Klik, B., and Kulikowska, D. (2017). Tannic Acid for Remediation of Historically Arsenic-Contaminated Soils. *Environ. Technol.* 40 (8), 1050–1061. doi:10.1080/09593330.2017.1417490

Gusiatin, Z. M., Radziemska, M., and Żochowska, A. (2019). Sequential Soil Washing with Mixed Biosurfactants Is Suitable for Simultaneous Removal of Multi-Metals from Soils with Different Properties, Pollution Levels and Ages. *Environ. Earth Sci.* 78, 529. doi:10.1007/s12665-019-8542-3

Gusiatin, Z. M. (2014). Tannic Acid and Saponin for Removing Arsenic from Brownfield Soils: Mobilization, Distribution and Speciation. *J. Environ. Sci.* 26 (4), 855–864. doi:10.1016/s1001-0742(13)60534-3

Gzar, H. A., Abdul-Hameed, A. S., and Yahya, A. Y. (2014). Extraction of Lead, Cadmium and Nickel from Contaminated Soil Using Acetic Acid. *Open J. Soil Sci.* 04 (6), 207–214. doi:10.4236/ojss.2014.46023

Hartley, N. R., Tsang, D. C. W., Olds, W. E., and Weber, P. A. (2014). Soil Washing Enhanced by Humic Substances and Biodegradable Chelating Agents. *Soil Sediment Contam. Int. J.* 23 (6), 599–613. doi:10.1080/15320383.2014.852511

He, J., Tang, J., Liu, T., and Xin, X. (2017). Removal of Heavy Metals in the Presence of the Biodegradable Biosurfactant of Sophorolipid from the Municipal Dewatered Sludge. *dwt* 89, 225–232. doi:10.5004/dwt.2017.21353

He, Z., Shentu, J., Yang, X., Baligar, V. C., Zhang, T., and Stoffella, P. J. (2015). Heavy Metal Contamination of Soils: Sources, Indicators, and Assessment. *J. Environ. Indic.* 9, 17–18.

Hong, P. K. A., and Jiang, W. (2005). "Factors in the Selection of Chelating Agents for Extraction of Lead from Contaminated Soil: Effectiveness, Selectivity, and Recoverability," in *Biologechemistry of Chelating Agents*. Editors B Nowack and JM Vanbriesen (Washington DC: American Chemical Society), 421–432. doi:10.1021/bk-2005-0910.ch025

Hou, D., Al-tabbaa, A., Chen, H., and Mamic, I. (2014). Factor Analysis and Structural Equation Modelling of Sustainable Behaviour in Contaminated Land Remediation. *J. Clean. Prod.* 84, 439–449. doi:10.1016/j.jclepro.2014.01.054

Hou, D., Ding, Z., Li, G., Wu, L., Hu, P., Guo, G., et al. (2018). A Sustainability Assessment Framework for Agricultural Land Remediation in China. *Land Degrad. Dev.* 29, 1005–1018. doi:10.1002/ldr.2748

Huang, K., Shen, Y., Wang, X., Song, X., Yuan, W., Xie, J., et al. (20212021). Choline-based Deep Eutectic Solvent Combined with EDTA-2Na as Novel Soil Washing Agent for Lead Removal in Contaminated Soil. *Chemosphere* 279, 130568. doi:10.1016/j.chemosphere.2021.130568

Interstate Technology and Regulatory Council (2003). *Characterization and Remediation of Soils at Closed Small Arms Firing Ranges*. Washington, DC: Technical/Regulatory Guidelines.

Isoyama, M., and Wada, S. (2007). Remediation of Pb-Contaminated Soils by Washing with Hydrochloric Acid and Subsequent Immobilization with Calcite and Allophanic Soil. *J. Hazard. Mater.* 143, 636–642. doi:10.1016/j.jhazmat.2007.01.008

Jang, M., Hwang, J. S., Choi, S. I., and Park, J. K. (2005). Remediation of Arsenic-Contaminated Soils and Washing Effluents. *Chemosphere* 60 (3), 344–354. doi:10.1016/j.chemosphere.2004.12.018

Jang, M., Hwang, J. S., and Choi, S. I. (2007). Sequential Soil Washing Techniques Using Hydrochloric Acid and Sodium Hydroxide for Remediating Arsenic-Contaminated Soils in Abandoned Iron-Ore Mines. *Chemosphere* 66 (1), 8–17. doi:10.1016/j.chemosphere.2006.05.056

Jez, E., and Lestan, D. (2016). EDTA Retention and Emissions from Remediated Soil. *Chemosphere* 151, 202–209. doi:10.1016/j.chemosphere.2016.02.088

Jia, J., Huang, Y., Liu, F., Shi, W., Hou, C., and Teng, Y. (2018). Washing Remediation of Mercury Contaminated Soil from Mercury Mining Area. *Environ. Prot. Chem. Industry* 38 (2), 231–235. doi:10.3969/j.issn.1006-1878.2018.02.020

Jiang, X., Li, X., Zhang, J., Lu, J., Chang, J., and Cui, D. (2012). Study of Citric Acid Extraction and Washing from Different Soil Polluted by Cr. *Chin. Agric. Sci. Bull.* 28 (02), 278–281. doi:10.1007/s11783-011-0280-z

Jiao, W. (2017). *New Biodegradable Chelator GLDA Leaching Restoration of Heavy Metal Contaminated Soil*. Changchun: Jilin University.

Juang, R., and Wang, S. W. (2000). Electrolytic Recovery of Binary Metals and EDTA from Strong Complexed Solutions. *Water Res.* 34, 3179–3185. doi:10.1016/s0043-1354(00)00061-0

Juwarkar, A. A., Nair, A., Dubey, K. V., Singh, S. K., and Devotta, S. (2007). Biosurfactant Technology for Remediation of Cadmium and Lead Contaminated Soils. *Chemosphere* 68 (10), 1996–2002. doi:10.1016/j.chemosphere.2007.02.027

Kaurin, A., Gluhar, S., Tilikj, N., and Lestan, D. (2020). Soil Washing with Biodegradable Chelating Agents and Edta: Effect on Soil Properties and Plant Growth. *Chemosphere* 260, 127673. doi:10.1016/j.chemosphere.2020.127673

Ke, X., Li, P., Gong, Z., Yin, W., and Su, D. (2004). Advances in Flushing Agents Used for Remediation of Heavy Metal-Contaminated Soil. *Chin. J. Ecol.* 23 (5), 145–149. doi:10.13292/J.1000-4890.2004.0171

Kholghi, N., Amani, H., Malekmahmoodi, S., and Amiri, A. (2020). Investigation on Heavy Metal Removal from a Crude Oil Contaminated Soil Using Rhamnolipid Biosurfactant as a New Eco-Friendly Method. *Tenside Surfactants Deterg.* 57 (6), 515–520. doi:10.3139/113.110710

Kim, C., and Ong, S. K. (1999). Recycling of Lead-Contaminated EDTA Wastewater. *J. Hazard. Mat.* 69, 273–286. doi:10.1016/s0304-3894(99)00115-6

Klik, B., Gusiatin, Z. M., and Kulikowska, D. (2021). Quality of Heavy Metal-Contaminated Soil before and after Column Flushing with Washing Agents Derived from Municipal Sewage Sludge. *Sci. Rep.* 11 (1), 15773. doi:10.1038/s41598-021-95441-5

Ko, I., Lee, C. H., Lee, K. P., Lee, S. W., and Kim, K. W. (2005). Remediation of Soil Contaminated with Arsenic, Zinc, and Nickel by Pilot-Scale Soil Washing. *Environ. Prog.* 25 (1), 39–48. doi:10.1002/ep.10101

Kulikowska, D., Gusiatin, Z. M., Bułkowska, K., and Klik, B. (2015). Feasibility of Using Humic Substances from Compost to Remove Heavy Metals (Cd, Cu, Ni, Pb, Zn) from Contaminated Soil Aged for Different Periods of Time. *J. Hazard. Mater.* 300, 882–891. doi:10.1016/j.jhazmat.2015.08.022

Kwak, J. I., Nam, S.-H., Kim, S. W., Bajagain, R., Jeong, S.-W., and An, Y.-J. (2019). Changes in Soil Properties after Remediation Influence the Performance and Survival of Soil Algae and Earthworm. *Ecotoxicol. Environ. Saf.* 174, 189–196. doi:10.1016/j.ecoenv.2019.02.079

Lee, J.-C., Kim, E. J., and Baek, K. (2017). Synergistic Effects of the Combination of Oxalate and Ascorbate on Arsenic Extraction from Contaminated Soils. *Chemosphere* 168, 1439–1446. doi:10.1016/j.chemosphere.2016.11.155

Lehigh, G. R., Wells, E. C., and Diaz, D. (2020). Evidence-informed Strategies for Promoting Equitability in Brownfields Redevelopment. *J. Environ. Manag.* 261, 110150. doi:10.1016/j.jenvman.2020.110150

Leõstan, D., Luo, C., and Li, X. (2008). The Use of Chelating Agents in the Remediation of Metal-Contaminated Soils: A Review. *Environ. Pollut.* 153, 3–13. doi:10.1016/j.envpol.2007.11.015

Li, D., Hao, X., Zhou, D., and Zhan, X. (2011). Remediation of Chromium Residue Contaminated Soil Using a Washing Technology. *J. Agro-Environment Sci.* 30 (12), 2451–2457.

Li, H., and Pan, G. (2015). Simultaneous Removal of Harmful Algal Blooms and Microcystins Using Microorganism- and Chitosan-Modified Local Soil. *Environ. Sci. Technol.* 49 (10), 6249–6256. doi:10.1021/acs.est.5b00840

Lim, M., and Kim, M.-J. (2013). Reuse of Washing Effluent Containing Oxalic Acid by a Combined Precipitation-Acidification Process. *Chemosphere* 90, 1526–1532. doi:10.1016/j.chemosphere.2012.08.047

Lin, H. K., Man, X. D., and Walsh, D. E. (20012001). Lead Removal via Soil Washing and Leaching. *Jom* 53, 22–25. doi:10.1007/s11837-001-0007-x

Lin, K. (2009). *Research on the Leaching Characteristics of Mercury and its Remediation by Washing of Serious Polluted Soil, a Case in Qingzhen, Guizhou Province* (Guiyang, China: Guizhou University). Doctoral dissertation.

Lin, Y.-T., Chien, Y.-C., and Liang, C. (2012). A Laboratory Treatability Study for Pilot-Scale Soil Washing of Cr, Cu, Ni, and Zn Contaminated Soils. *Environ. Prog. Sustain. Energy* 31 (3), 351–360. doi:10.1002/ep.10555

Liu, C.-C., and Chen, G.-B. (2013). Reclamation of Cadmium-Contaminated Soil Using Dissolved Organic Matter Solution Originating from Wine-Processing Waste Sludge. *J. Hazard. Mater.* 244-245, 645–653. doi:10.1016/j.jhazmat.2012.10.060

Liu, G. H., Ren, J., Gang, H. U., Qin, S., and Fan, C. W. (2018). Effects of Low Molecular Organic Acids on the Removing of pb,cd in Calcareous Soils. *Hubei Agricultural Sciences* 057 (006), 43–47.

Liu, J., Xue, J., and Wei, X. (2019). Research Progress of Surfactant Washing for Remediation of Heavy Metal Pollution in Soil. *Chin. J. Soil Sci.* 50 (1), 240–245.

Liu, J., Zhao, L., Liu, Q., Li, J., Qiao, Z., Sun, P., et al. (2021). A Critical Review on Soil Washing during Soil Remediation for Heavy Metals and Organic Pollutants. *Int. J. Environ. Sci. Technol.* 19, 601–624. doi:10.1007/s13762-021-03144-1

Liu, L., Hu, S. P., Chen, Y. X., and Li, H. (2010). Feasibility of Washing as a Remediation Technology for the Heavy Metals-Polluted Soils Left by Chemical Plant. *Ying Yong Sheng Tai Xue Bao* 21 (6), 1537–1541.

Liu, L., Li, W., Song, W., and Guo, M. (2018). Remediation Techniques for Heavy Metal-Contaminated Soils: Principles and Applicability. *Sci. Total Environ.* 633, 206–219. doi:10.1016/j.scitotenv.2018.03.161

Liu, P. Y., Liu, H., Li, Y. J., and Dong, C. X. (2014). Remediation of Arsenic Contaminated Soils and Treatment of Washing Effluent Using Calcined Mn-Fe Layered Double Hydroxide. *Amr* 955-959, 2014–2021. doi:10.4028/www.scientific.net/amr.955-959.2014

Liu, R., Liu, J., Zhang, J., Yan, X., and Yuan, C. (2018). Two Carboxylic Ligands Controlled Coordination Polymers Based on Cd II Ion. *J. Mol. Struct.* 1164 (6), 45–49. doi:10.1016/j.molstruc.2018.03.036

Luo, C., Wang, S., Wang, Y., Yang, R., Zhang, G., and Shen, Z. (2015). Effects of EDDS and Plant-Growth-Promoting Bacteria on Plant Uptake of Trace Metals and PCBs from E-Waste-Contaminated Soil. *J. Hazard. Mater.* 286, 379–385. doi:10.1016/j.jhazmat.2015.01.010

Maity, J. P., Huang, Y. M., Hsu, C.-M., Wu, C.-I., Chen, C.-C., Li, C.-Y., et al. (2013). Removal of Cu, Pb and Zn by Foam Fractionation and a Soil Washing Process from Contaminated Industrial Soils Using Soapberry-Derived Saponin: a Comparative Effectiveness Assessment. *Chemosphere* 92 (10), 1286–1293. doi:10.1016/j.chemosphere.2013.04.060

Makino, T., Sugahara, K., Sakurai, Y., Takano, H., Kamiya, T., Sasaki, K., et al. (2006). Remediation of Cadmium Contamination in Paddy Soils by Washing with Chemicals: Selection of Washing Chemicals. *Environ. Pollut.* 144 (1), 2–10. doi:10.1016/j.envpol.2006.01.017

Mehrabi, N., Abdul Haq, U. F., Reza, M. T., and Aich, N. (2020). Application of Deep Eutectic Solvent for Conjugation of Magnetic Nanoparticles onto Graphene Oxide for Lead(II) and Methylene Blue Removal. *J. Environ. Chem. Eng.* 8 (2020), 104222. doi:10.1016/j.jece.2020.104222

Mohamed, M. A., Efligenir, A., Husson, J., Persello, J., Fievet, P., and Fatin-Rouge, N. (2013). Extraction of Heavy Metals from a Contaminated Soil by Reusing Chelating Agent Solutions. *J. Environ. Chem. Eng.* 1 (3), 363–368. doi:10.1016/j.jece.2013.05.015

Moon, D. H., Lee, J.-R., Wazne, M., and Park, J.-H. (2012). Assessment of Soil Washing for Zn Contaminated Soils Using Various Washing Solutions. *J. Industrial Eng. Chem.* 18 (2), 822–825. doi:10.1016/j.jiec.2011.11.137

Morin, G., Ostergren, J. D., Juillot, F., Ildefonse, P., Calas, G., and Brown, G. E., Jr. (1999). XAFS Determination of the Chemical Form of Lead in Smelter-Contaminated Soils and Mine Tailings; Importance of Adsorption Processes. *Am. Mineralogist* 84, 420–434. doi:10.2138/am-1999-0327

Moutsatsou, A., Gregou, M., Matsas, D., and Protonotarios, V. (2005). Washing as a Remediation Technology Applicable in Soils Heavily Polluted by Mining-Metallurgical Activities. *Chemosphere* 63 (10), 1632–1640. doi:10.1016/j.chemosphere.2005.10.015

Mukhopadhyay, S., Mukherjee, S., Adnan, N. F., Hayyan, A., Hayyan, M., Hashim, M. A., et al. (2016). Ammonium-based Deep Eutectic Solvents as Novel Soil Washing Agent for Lead Removal. *Chem. Eng. J.* 294, 316–322. doi:10.1016/j.cej.2016.02.030

Naseri-Rad, M., Berndtsson, R., Persson, K. M., and Nakagawa, K. (2020). INSIDE: An Efficient Guide for Sustainable Remediation Practice in Addressing Contaminated Soil and Groundwater. *Sci. Total Environ.* 740 (2020), 139879. doi:10.1016/j.scitotenv.2020.139879

Nedwed, T., and Clifford, D. A. (2000). Feasibility of Extracting Lead from Lead Battery Recycling Site Soil Using High-Concentration Chloride Solutions. *Environ. Prog.* 19, 197–206. doi:10.1002/ep.670190312

Neilson, J. W., Artiola, J. F., and Maier, R. M. (2003). Characterization of Lead Removal from Contaminated Soils by Nontoxic Soil-Washing Agents. *J. Environ. Qual.* 32 (3), 899–908. doi:10.2134/jeq2003.8990

Oh, S., Bade, R., Lee, H., Choi, J., and Shin, W. S. (2015). Risk Assessment of Metal(loid)-Contaminated Soils before and after Soil Washing. *Environ. Earth Sci.* 74 (1), 703–713. doi:10.1007/s12665-015-4075-6

Palma, L. D., and Ferrantelli, P. (2005). Copper Leaching from a Sandy Soil: Mechanism and Parameters affecting EDTA Extraction. *J. Hazard. Mater.* 122 (1-2), 85–90. doi:10.1016/j.jhazmat.2005.03.010

Paria, S. (2008). Surfactant-enhanced Remediation of Organic Contaminated Soil and Water. *Adv. Colloid Interface Sci.* 138, 24–58. doi:10.1016/j.cis.2007.11.001

Peters, R. W. (1999). Chelant Extraction of Heavy Metals from Contaminated Soils. *J. Hazard. Mater.* 66, 151–210. doi:10.1016/s0304-3894(99)00010-2

Pociecha, M., and Lestan, D. (2010). Using Electrocoagulation for Metal and Chelant Separation from Washing Solution after Edta Leaching of Pb, Zn and Cd Contaminated Soil. *J. Hazard. Mat.* 174 (1-3), 670–678. doi:10.1016/j.jhazmat.2009.09.103

Pociecha, M., and Lestan, D. (2009). EDTA Leaching of Cu Contaminated Soil Using Electrochemical Treatment of the Washing Solution. *J. Hazard. Mater.* 165, 533–539. doi:10.1016/j.jhazmat.2008.10.006

Qi, X., Xu, X., Zhong, C., Jiang, T., Wei, W., and Song, X. (2018). Removal of Cadmium and Lead from Contaminated Soils Using Sophorolipids from Fermentation Culture of Starmerella Bombicola Cgmcc 1576 Fermentation. *Int. J. Environ. Res. Public Health* 15 (11), 2334. doi:10.3390/ijerph15112334

Rahman, I. M. M., Hossain, M. M., Begum, Z. A., Rahman, M. A., and Hasegawa, H. (2010). "Eco-environmental Consequences Associated with Chelant-Assisted Phyto-Remediation of Metal-Contaminated Soil," in *Handbook of Phytoremediation*. Editor I. A. Golubev (New York: Nova Science Publishers), 709–722.

Ramamurthy, A., and Schalchian, H. (2013). Surfactant Assisted Removal of Cu(II), Cd(II) and Pb(II) from Contaminated Soils. *Environ. Prot. Eng.* 39 (3), 87–99. doi:10.37190/epe130307

Rashad, M., Assaad, F. F., and Shalaby, E. A. (2013). Effect of Dissolved Organic Matter Derived from Waste Amendments on the Mobility of Inorganic Arsenic (Iii) in the Egyptian Alluvial Soil. *Int. J. Energy & Environ.* 4 (4), 677–686.

Reddy, K. R., Danda, S., Yukselen-Aksoy, Y., and Al-Hamdan, A. Z. (2010). Sequestration of Heavy Metals in Soils from Two Polluted Industrial Sites: Implications for Remediation. *Land Contam. Reclam.* 18 (1), 13–23. doi:10.2462/09670513.909

Rui, D., Wu, Z., Wu, Y., Chen, X., Liu, J., and Ding, J. (2018). Synergistic Remediation of Heavy Metal Cd and Pb Contaminated Clay by Freeze-Thaw and Chemical Washing. *Trans. Chin. Soc. Agric. Eng. Trans. CSAE)* 34 (23), 199–205. doi:10.11975/j.issn.1002-6819.2018.23.025

Saaty, T. L. (1980). *The Analytical Hierarchy Process*. New York, NY, USA: McGraw-Hill.

Saponaro, S., Bonomo, L., Barbafieri, M., and Petruzzelli, G. (2002). Soil Washing Feasibility at a Manufacturing Gas Plant Site. *Soil Sediment Contam. An Int. J.* 11 (5), 751–767. doi:10.1080/20025891107078

Satyro, S., Race, M., Di Natale, F., Erto, A., Guida, M., and Marotta, R. (2016). Simultaneous Removal of Heavy Metals from Field-Polluted Soils and Treatment of Soil Washing Effluents through Combined Adsorption and Artificial Sunlight-Driven Photocatalytic Processes. *Chem. Eng. J.* 283, 1484–1493. doi:10.1016/j.cej.2015.08.039

Satyro, S., Race, M., Marotta, R., Dezotti, M., Guida, M., and Clarizia, L. (2017). Photocatalytic Processes Assisted by Artificial Solar Light for Soil Washing Effluent Treatment. *Environ. Sci. Pollut. Res.* 24, 6353–6360. doi:10.1007/s11356-016-6431-9

Singh, A. K., and Cameotra, S. S. (2013). Efficiency of Lipopeptide Biosurfactants in Removal of Petroleum Hydrocarbons and Heavy Metals from Contaminated Soil. *Environ. Sci. Pollut. Res.* 20 (10), 7367–7376. doi:10.1007/s11356-013-1752-4

Stevenson, F. J. (1994). *Humus Chemistry, Genesis, Composition, Reactions*. 2nd edn. Canada, USA: John Wiley & Sons, 512.

Subirés-Muñoz, J. D., García-Rubio, A., Vereda-Alonso, C., Gómez-Lahoz, C., Rodríguez-Maroto, J. M., García-Herruzo, F., et al. (2011). Feasibility Study of the Use of Different Extractant Agents in the Remediation of a Mercury Contaminated Soil from Almaden. *Sep. Purif. Technol.* 79, 151–156. doi:10.1016/j.seppur.2011.01.032

Sun, H., Wang, H., Qi, J., Shen, L., and Lian, X. (2011). "Study on Surfactants Remediation in Heavy Metals Contaminated Soils," in *2011 International*

Symposium on Water Resource and Environmental Protection (Xi'an: IEEE), 1862–1865. doi:10.1109/iswrep.2011.5893616

Sun, T., Lu, K., and Wang, H. (2015). Advance in Washing Technology for Remediation of Heavy Contaminated Soils: Effect of Eluants and Washing Conditions. *J. Zhejiang A F Univ.* 32 (1), 140–149. doi:10.11833/j.issn.2095-0756.2015.01.021

Tampouris, S., Papassiopi, N., and Paspaliaris, I. (2001). Removal of Contaminant Metals from Fine Grained Soils, Using Agglomeration, Chloride Solutions and Pile Leaching Techniques. *J. Hazard. Mater.* 84, 297–319. doi:10.1016/s0304-3894(01)00233-3

Tao, Y. (2013). *The Selection of Washing Reagents for Soils Polluted by Cadmium and Chromium*. Changsha: Central South University.

Tejowulan, R. S., and Hendershot, W. H. (1998). Removal of Trace Metals from Contaminated Soils Using EDTA Incorporating Resin Trapping Techniques. *Environ. Pollut.* 103, 135–142. doi:10.1016/S0269-7491(98)00080-3

Tessier, A., Campbell, P. G. C., and Bisson, M. (1979). Sequential Extraction Procedure for the Speciation of Particulate Trace Metals. *Anal. Chem.* 51, 844–851. doi:10.1021/ac50043a017

Udovic, M., and Lestan, D. (2010). Redistribution of Residual Pb, Zn, and Cd in Soil Remediated with Edta Leaching and Exposed to Earthworms (eisenia Fetida). *Environ. Technol.* 31 (6), 655–669. doi:10.1080/09593331003610907

USEPA (19941994). *A Literature Review Summary of Metals Extraction Processes Used to Remove Lead from Soils, Project Summary*. Cincinnati, OH: Office of Research and Development. *EPA/600/SR-94/006*.

USEPA (2004). *Summary of Status Report Updates, Changes, and Deletions, Appendix D of Treatment Technologies for Site Clean up: Annual Status Report*. 11th ed. Washington, DC: Office of Solid Waste and Emergency Response. *EPA 542-R-03-009*.

USEPA (2005). *Superfund Programs' Proposed Plan, Myers Property Site*. New York, NY: USEPA. Region II. July, 2005.

Vandevivere, P. C., Saveyn, H., and Verstraete, W. (2001). Biodegradation of metal–[s,s]-edds complexes. *Environ. Sci. Technol.*

Voglar, D., and Lestan, D. (2012). Pilot-scale Washing of Metal Contaminated Garden Soil Using EDTA. *J. Hazard. Mater.* 215-216, 32–39. doi:10.1016/j.jhazmat.2012.02.022

Wahla, I. H., and Kirkham, M. B. (2008). Heavy Metal Displacement in Salt-Water-Irrigated Soil during Phytoremediation. *Environ. Pollut.* 155 (2), 271–283. doi:10.1016/j.envpol.2007.11.020

Wang, G., Pan, X., Zhang, S., Zhong, Q., Zhou, W., Zhang, X., et al. (2020). Remediation of Heavy Metal Contaminated Soil by Biodegradable Chelator-Induced Washing: Efficiencies and Mechanisms. *Environ. Res.* 186, 109554. doi:10.1016/j.envres.2020.109554

Wang, G., Zhang, S., Xu, X., Zhong, Q., Zhang, C., Jia, Y., et al. (2016). Heavy Metal Removal by GLDA Washing: Optimization, Redistribution, Recycling, and Changes in Soil Fertility. *Sci. Total Environ.* 569-570, 557–568. doi:10.1016/j.scitotenv.2016.06.155

Wang, G., Zhang, S., Zhong, Q., Xu, X., Li, T., Jia, Y., et al. (2018). Effect of Soil Washing with Biodegradable Chelators on the Toxicity of Residual Metals and Soil Biological Properties. *Sci. Total Environ.* 625, 1021–1029. doi:10.1016/j.scitotenv.2018.01.019

Wang, Q., Liu, X., Wang, C., Zhang, X., Li, H., Chen, T., et al. (2015). Solubilization Effect of Surfactants on Morphological Transformation of Cadmium and Pyrene in Cocontaminated Soils. *Water Air Soil Pollut.* 226, 1–9. doi:10.1007/s11270-015-2409-3

Wang, S., and Mulligan, C. N. (2004). Rhamnolipid Foam Enhanced Remediation of Cadmium and Nickel Contaminated Soil. *Water Air & Soil Pollut.* 157 (1-4), 315–330. doi:10.1023/b:wate.0000038904.91977.f0

Wang, W. (2013). *Study on Leaching Technology of Zn, Pb, Cu Contaminated Soils*. Changsha: Central South University.

Wang, Y., Fang, Z., Liang, B., and Tsang, E. P. (2014). Remediation of Hexavalent Chromium Contaminated Soil by Stabilized Nanoscale Zero-Valent Iron Prepared from Steel Pickling Waste Liquor. *Chem. Eng. J.* 247, 283–290. doi:10.1016/j.cej.2014.03.011

Wasay, S. A., Barrington, S., and Tokunaga, S. (2001). Organic Acids for the *In Situ* Remediation of Soils Polluted by Heavy Metals: Soil Flushing in Columns. *Water, Air, & Soil Pollut.* 127, 301–314. doi:10.1023/a:1005251915165

Wasay, S. A., Barrington, S., and Tokunaga, S. (1988). Remediation of Soils Polluted by Heavy Metals Using Salts of Organic Acids and Chelating Agents. *Environ. Technol.* 19, 369–380.

Wei, M., Chen, J., and Wang, X. (2016). Removal of Arsenic and Cadmium with Sequential Soil Washing Techniques Using Na2EDTA, Oxalic and Phosphoric Acid: Optimization Conditions, Removal Effectiveness and Ecological Risks. *Chemosphere* 156, 252–261. doi:10.1016/j.chemosphere.2016.04.106

Wu, L., Xian, S., Kong, D., Ou, M., and Deng, Q. (2016). Remediation of Cd Polluted Soil by Co-leaching of Tannic Acid and Citric Acid. *Environ. Eng.* (08), 178–181. doi:10.13205/j.hjgc.201608037

Wuana, R. A., and Okieimen, F. E. (2011). Heavy Metals in Contaminated Soils: A Review of Sources, Chemistry, Risks and Best Available Strategies for Remediation. *ISRN Ecol.* 2011, 1–20. doi:10.5402/2011/402647

Wuana, R. A., Okieimen, F. E., and Imborvungu, J. A. (2010). Removal of Heavy Metals from a Contaminated Soil Using Organic Chelating Acids. *Int. J. Environ. Sci. Technol.* 7 (3), 485–496. doi:10.1007/bf03326158

Xia, W., Li, X., Gao, H., Huang, B., Zhang, H., Liu, Y., et al. (2009). Influence Factors Analysis of Removing Heavy Metals from Multiple Metal-Contaminated Soils with Different Extractants. *J. Cent. South Univ. Technol.* 16 (01), 108–111. doi:10.1007/s11771-009-0018-2

Xiao, R., Ali, A., Wang, P., Li, R., Tian, X., and Zhang, Z. (2019). Comparison of the Feasibility of Different Washing Solutions for Combined Soil Washing and Phytoremediation for the Detoxification of Cadmium (Cd) and Zinc (Zn) in Contaminated Soil. *Chemosphere* 230, 510–518. doi:10.1016/j.chemosphere.2019.05.121

Xiong, H., Wang, X., Ma, J., Xia, F., Han, C., Pei, Y., et al. (2016). Discussion on Available Condition of *Ex-Situ* Soil Washing for Remediation of Chromiun-Contaminated Soil. *Environ. Eng.* 34 (11), 155–161. doi:10.13205/j.hjgc.201611033

Xu, F., Liu, N., Liu, J., Liu, H., and Chen, T. (2016). Chromium Leaching by Sulfuric Acid/sodium Sulfate Composite Eluent from Chromium Slag. *Environ. Eng.* 34 (9), 155–159. doi:10.13205/j.hjgc.201609034

Xu, Z., Xu, D., Guo, S., Qiu, X., and Li, F. (2014). Combined Leaching of Heavy Metals in Soil by Citric Acid and Saponin. *J. Agro-Environment Sci.* 33 (8), 1519–1525. doi:10.11654/jaes.2014.08.008

Yan, J., Mo, C., Wang, D., and Xie, Y. (2015). Removal of Chromium from Soil by Saponin. *J. Guangxi Univ. (Nat Sci Ed)* 40 (3), 558–564. doi:10.13624/j.cnki.issn.1001-7445.2015.0558

Yang, J.-S., Hwang, J.-M., Baek, K., and Kwon, M. J. (2013). Soil Washing and Effluent Treatment for Contaminated Soil with Toxic Metals. *Korean Chem. Eng. Res.* 51 (6), 745–754. doi:10.9713/kcer.2013.51.6.745

Yang, J.-S., Lee, J. Y., Baek, K., Kwon, T.-S., and Choi, J. (2009). Extraction Behavior of as, Pb, and Zn from Mine Tailings with Acid and Base Solutions. *J. Hazard. Mater.* 171, 443–451. doi:10.1016/j.jhazmat.2009.06.021

Yang, J., and Mosby, D. (2006). Field Assessment of Treatment Efficacy by Three Methods of Phosphoric Acid Application in Lead-Contaminated Urban Soil. *Sci. Total Environ.* 366 (1), 136–142. doi:10.1016/j.scitotenv.2005.09.050

Yang, J., Wang, J., Li, J., and Li, H. (2016). Discussion on Heavy Metals Removal Efficiency in Clay by Soil Washing. *Environ. Sci. Technol.* 39 (S2), 294–298.

Yang, X., Bai, L., Deng, L., Chen, T., Pan, C., and Fan, H. (2014). Research on Drip Washing and Rehabilitation of Soil in Polluted Areas of Electroplate. *China Environ. Prot. Ind.* (9), 50–52. doi:10.3969/j.issn.1006-5377.2014.09.010

Ye, M., Sun, M., Wan, J., Fang, G., Li, H., Hu, F., et al. (2015). Evaluation of Enhanced Soil Washing Process with Tea Saponin in a Peanut Oil-Water Solvent System for the Extraction of PBDEs/PCBs/PAHs and Heavy Metals from an Electronic Waste Site Followed by Vetiver Grass Phytoremediation. *J. Chem. Technol. Biotechnol.* 90 (11), 2027–2035. doi:10.1002/jctb.4512

Yoo, J. C., Beiyuan, J., Wang, L., Tsang, D. C. W., Baek, K., Bolan, N. S., et al. (2018). A Combination of Ferric nitrate/EDDS-Enhanced Washing and Sludge-Derived Biochar Stabilization of Metal-Contaminated Soils. *Sci. Total Environ.* 616-617, 572–582. doi:10.1016/j.scitotenv.2017.10.310

Zhai, X., Li, Z., Huang, B., Luo, N., Huang, M., Zhang, Q., et al. (2018). Remediation of Multiple Heavy Metal-Contaminated Soil through the Combination of Soil Washing and *In Situ* Immobilization. *Sci. Total Environ.* 635, 92–99. doi:10.1016/j.scitotenv.2018.04.119

Zhan, H., Jiang, Y., Wang, B., Zhu, K., and Zhao, B. (2012). Study on Removal Efficiencies and Mechanism of Heavy Metal from Sewage Irrigated Soils by

Saponin Compared with Commonly Used Washing Agents. *Int. J. Sci. Eng. Res.* 3, 1–9.

Zhang, H., Gao, Y., and Xiong, H. (2017). Removal of Heavy Metals from Polluted Soil Using the Citric Acid Fermentation Broth: a Promising Washing Agent. *Environ. Sci. Pollut. Res.* 24 (10), 9506–9514. doi:10.1007/s11356-017-8660-y

Zhang, S. (2013). *Study on Washing Remediation of Cadmium, Lead Contaminated Calcareous Soil* (Changsha, China: Central South University). Doctoral dissertation.

Zhang, S., Wen, J., Hu, Y., Fang, Y., Zhang, H., Xing, L., et al. (2019). Humic Substances from Green Waste Compost: an Effective Washing Agent for Heavy Metal (Cd, Ni) Removal from Contaminated Sediments. *J. Hazard. Mater.* 366, 210–218. doi:10.1016/j.jhazmat.2018.11.103

Zhang, W., Xu, F., Yang, Y., Huang, H., Jiang, W., Tian, L., et al. (2016). Process Analysis and Design Suggestion on *Ex-Situ* Washing Technology for Heavy Metal Contaminated Soil. *Environ. Eng.* 34 (12), 177–182. doi:10.13205/j.hjgc.201612037

Zhang, Y., Dai, Y., Wang, Y., Huang, X., Xiao, Y., and Pei, Q. (2021a). Hydrochemistry, Quality and Potential Health Risk Appraisal of Nitrate Enriched Groundwater in the Nanchong Area, Southwestern China. *Sci. Total Environ.* 784, 147186. doi:10.1016/j.scitotenv.2021.147186

Zhang, Y., He, Z., Tian, H., Huang, X., Zhang, Z., Liu, Y., et al. (2021b). Hydrochemistry Appraisal, Quality Assessment and Health Risk Evaluation of Shallow Groundwater in the Mianyang Area of Sichuan Basin, Southwestern China. *Environ. Earth Sci.* 80 (17), 576. doi:10.1007/s12665-021-09894-y

Zhou, D., Zheng, C., and Chen, H. (2002). Interaction of Cadmium and Citric Acid, Edta in Several Kinds of Soil. *Acta Pedol. Sin.* 39 (1), 29–36. doi:10.11766/trxb200004040105

Zhou, F., Zhong, L., and Yang, S. (2017). Leaching Effects of Compound Eluent on Cadmium Contaminated Soil. *J. Anhui Agric. Sci.* 45 (23), 52–54. doi:10.3969/j.issn.0517-6611.2017.23.018

Zhou, J., Liang, Z., Cai, X., Mao, Y., and Zhou, M. (2016). Chemical Leaching Remediation of Soil Contaminated by Heavy Metals: a Review. *Environ. Prot. Technol.* 22 (4), 54–57.

Zhu, G. X., Guo, Q. J., Yang, J. X., Zhang, H. Z., Wei, R. F., Wang, C. Y., et al. (2013). Research on the Effect and Technique of Remediation for Multi-Metal Contaminated Tailing Soils. *Huan Jing Ke Xue* 34 (9), 3690–3696.

Zhu, Q., Shao, C., Zhang, Z., and Wen, X. (2010). Saponin Biosurfactant-Enhanced Flushing for the Removal of Heavy Metals from Soils. *Acta Sci. Circumstantiae* 30 (12), 2491–2498. doi:10.1631/jzus.A1000244

Zimmerman, A. J., and Weindorf, D. C. (2010). Heavy Metal and Trace Metal Analysis in Soil by Sequential Extraction: a Review of Procedures. *Int. J. Anal. Chem.* 2010 (3-4), 387803. doi:10.1155/2010/387803

Zou, Q., Xiang, H., Jiang, J., Li, D., Aihemaiti, A., Yan, F., et al. (2019). Vanadium and Chromium-Contaminated Soil Remediation Using VFAs Derived from Food Waste as Soil Washing Agents: a Case Study. *J. Environ. Manag.* 232, 895–901. doi:10.1016/j.jenvman.2018.11.129

Conflict of Interest: HZ and MS are employed by Sichuan Metallurgical Geological Survey and Design Group Co. Ltd.

The remaining authors declare that the research was conducted in the absence of any commercial or financial relationships that could be construed as a potential conflict of interest.

Publisher's Note: All claims expressed in this article are solely those of the authors and do not necessarily represent those of their affiliated organizations, or those of the publisher, the editors, and the reviewers. Any product that may be evaluated in this article, or claim that may be made by its manufacturer, is not guaranteed or endorsed by the publisher.

Copyright © 2022 Zhang, Xu, Kanyerere, Wang and Sun. This is an open-access article distributed under the terms of the Creative Commons Attribution License (CC BY). The use, distribution or reproduction in other forums is permitted, provided the original author(s) and the copyright owner(s) are credited and that the original publication in this journal is cited, in accordance with accepted academic practice. No use, distribution or reproduction is permitted which does not comply with these terms.

frontiers | Frontiers in Earth Science

ORIGINAL RESEARCH
published: 02 June 2022
doi: 10.3389/feart.2022.894033

Interaction Between Brackish Water Intermittent Infiltration and Cultivated Soil Environment: A Case Study From Arid Piedmont Plain of Northwest China

Guo Leilei[1] *and Wang Zaimin*[2]*

[1]Department of Resources and Environmental Engineering, Sichuan Water Conservancy College, Chengdu, China, [2]College of Environment and Civil Engineering, Chengdu University of Technology, Chengdu, China

Brackish groundwater was widely used in arid areas which may cause soil salinization and groundwater environmental declines. To ensure the sustainable development of agriculture in arid areas, brackish water intermittent infiltration experiments were conducted in Southern Xinjiang, Northwest China between June to September 2018, and Hydrus-2D numerical simulation was used to analyze the underground pipe drainage systems. The field experiments were carried out during cotton growth stages after the first freshwater flood infiltration and salt washing. Two control experiments were, respectively, designed as freshwater (0.68 g/L) and brackish water (1.66 g/L) with water amount of 1.0 Q = 572 mm. Other eight groups (1.05–1.40 Q) were compared to analyze the effect of soil salt leaching by increasing the brackish water amount. The results showed that the soil moisture content was almost less than the field capacity of 0.203 at depth of 0–60 cm before each infiltration due to roots water uptake, and the soil water holding capacity rate was lower than 0.2 after 5 days under 1.20–1.40 Q brackish water treatments. Variation of $EC_{1:5}$ at depth of 0–30 cm was less than 0.5 dS/m. Salt mainly accumulated at the depth of 40–60 cm whether the water amount was excessive or insufficient even under the fresh water infiltration. The optimal brackish water amount was 1.15 Q = 657.8 mm, and the soil total salinity was less than 0.55 dS/m ($EC_{1:5}$) and reached mild salinization degree. Numerical simulations were used based on the 2018 field experimental results and extended by another 10 years. The soil salt accumulated to 1.10–2.99 dS/m ($EC_{1:5}$) at the depth of 40–60 cm during 0–30 days. The no salinization area expanded to depth of 40–45 cm after 120 days and reduced during non-infiltration period due to evaporation effect. The soil salt was gradually leached and less than 0.55 dS/m ($EC_{1:5}$) after 10 years. The optimized leaching–drainage system could not only provide a low salinity soil condition for cotton growth and realize sustainable cultivation but also greatly protect the soil and groundwater environment.

Keywords: brackish water intermittent infiltration, arid area, salt accumulation, numerical simulations, leaching-drainage system, Hydrus-2D

OPEN ACCESS

Edited by:
Yunhui Zhang,
Southwest Jiaotong University, China

Reviewed by:
Xianwen Li,
Northwest A&F University, China
Yujiang He,
Chinese Academy of Geological Sciences, China

***Correspondence:**
Wang Zaimin
wangzaimin13@cdut.cn

Specialty section:
This article was submitted to Geohazards and Georisks, a section of the journal Frontiers in Earth Science

Received: *11 March 2022*
Accepted: *25 April 2022*
Published: *02 June 2022*

Citation:
Leilei G and Zaimin W (2022) Interaction Between Brackish Water Intermittent Infiltration and Cultivated Soil Environment: A Case Study From Arid Piedmont Plain of Northwest China. Front. Earth Sci. 10:894033. doi: 10.3389/feart.2022.894033

1 INTRODUCTION

Due to rapid population growth and significant industrial development, freshwater scarcity has been an urgent problem to be addressed around the world (Zhang et al., 2021a; Zhang et al., 2021b; Li et al., 2021). Brackish groundwater as an alternative source was used to solve the shortage of fresh water and has been widely used in cotton fields in Southern Xinjiang, Northwest China (Qi et al., 2018; Hu et al., 2020). Brackish water under mulched was intermittently infiltrated into the soil to irrigate salt-tolerant crops, which could increase soil nutrients, and the total salts would not be excessively accumulated (Wang et al., 2014; Li et al., 2018; Chen et al., 2018; Wu et al., 2021; Wang Z. et al., 2022). However, long-term salt supply leads to salt accumulation in soil, which not only threatens the cotton growth but also threaten the groundwater environment (Wang H. et al., 2022; Wang J. et al., 2022; Cao et al., 2022). Therefore, it is necessary to develop an optimized leaching–drainage system to effectively improve the soil salinization, ensure the sustainable development of agriculture in arid areas, and protect the groundwater environment.

Many scholars had studied the leaching requirement, influencing factors, and calculation models of different infiltration ways and crops (Šimůnek et al., 2016; Jia et al., 2021; Feng et al., 2022; Ochege et al., 2022). Salt and fresh water rotation infiltration, deficit infiltration, and intermittent infiltration were indicated to be superior (Zeng et al., 2014; Peng et al., 2016; Chen et al., 2022). The effect of intermittent infiltration on leaching salt was better than that of flood infiltration at the depth of 10–30 cm and had little difference at the depth of 30–60 cm. Intermittent point source infiltration could leach salt below 50 cm of soil some years later (Zhang et al., 2010). The leaching fraction (LF) was small in the shallow groundwater table field and more effective near the infiltration tapes (Hanson et al., 2009). Additional brackish water also was considered to leach excess soil salt to avoid soil salinization (Li et al., 2014). So, it is necessary to scientifically determine the infiltration water amount, quality, and frequency based on the salt-tolerant of crops and leaching requirement (Maas and Hoffman 1977; Beltrán 1999; Chu et al., 2016; Min et al., 2017).

The salt leaching effect of the drainage system depended on the local groundwater table. In the shallow water table areas, brackish water infiltration may lead to soil secondary salinization, which was suggested to control the water table through drainage canals or shafts to desalinate and improve soil quality (Sun et al., 2015). Groundwater evaporation had little impact on the salt accumulation content in the vadose zone when the water table was about 3.0 m in sandy regions and 5.0 m in loam regions (Li et al., 2014). An underground pipe drainage system was more suitable for deep water table areas (Sallam 2017; Inosako et al., 2019), which could effectively improve soil salinization and increase crop yield (Heng et al., 2018; Tian et al., 2018). In our experimental field, the water table ranged from 7.0 to 8.0 m in 2018 and had 1.8 m deep drainage channels.

To optimize the intermittent infiltration regimes of the brackish water leaching–drainage system, field leaching experiments were conducted in Southern Xinjiang based on soil physical properties and salt leaching requirements. Specific objectives of the research were to 1) analyze the effect of different leaching fractions (LF) on salt accumulation and cotton yield and determined the optimal infiltration water amount; 2) calibrate the HYDRUS-2D simulations using the experimental data; and 3) use the model to calculate the effects on desalting of underground pipe drainage system for 10 years.

2 MATERIALS AND METHODS

2.1 Experimental Site

The leaching experiments were carried out in the Tarim Basin of southern Xinjiang, Northwest China, between June to September 2018 in the cotton field. The experimental site was located 901 m above mean sea level (**Figure 1**). The field belongs to continental desert climate with less rain and strong evaporation. The annual precipitation was 53.3–62.7 mm, and the annual evaporation was 2,273–2,788 mm. Compared with evaporation and crop transpiration, the supply of atmospheric rainfall was very little. The fresh water (FW) was taken from the Peacock River with an average total dissolved solids (TDS) of 0.62–0.72 g/L, and the brackish water (BW) was taken from a well located in the test field with TDS of 1.61–1.71 g/L (**Table 1**). The sodium adsorption ratio (SAR) of infiltration water ranged from 10 to 14 of FW and 8–9 of BW. The main soil type was loamy sand (**Table 2**). The electrical conductivity of soil was less than 1.0 dS/m with no salinization (Slavich and Petterson 1993; Chen et al., 2018). The field water capacity was 0.2.

2.2 Infiltration Scheme

The leaching experiments were conducted in 10 randomly selected field plots, each having a size of 225 m^2 (**Figure 2**). There were set as 17 infiltration lines with the mode of "one mulch, two infiltration lines, and four rows". In total, 2 infiltration lines were installed for every four rows of cotton. The distance between the infiltration lines was 55 cm and that between two cotton rows was 20 cm. Infiltration points along each line were spaced 30 cm apart, while the non-mulched area of bare soil was 40-cm wide. Before sowing, flood infiltration of fresh water was conducted to leach salt and preserve soil water on 20 April, with amount of 57.3 mm. Then, cotton seeds were sown and mulched with degradable plastic sheeting. Brackish water was conducted one time per 5 days, for totally 14 times. The emitter flow was 2.2 L/h. The amount of applied infiltration water during the growing stages followed traditional irrigation patterns of cotton (**Table 3**). In total, 2 groups of control experiments were designed for fresh water of 0.68 g/L and brackish water of 1.66 g/L with 1.0 Q = 572 mm. Other eight groups of MDI experiments leached soil salt by increasing the amount of brackish water with 1.05–1.40 Q.

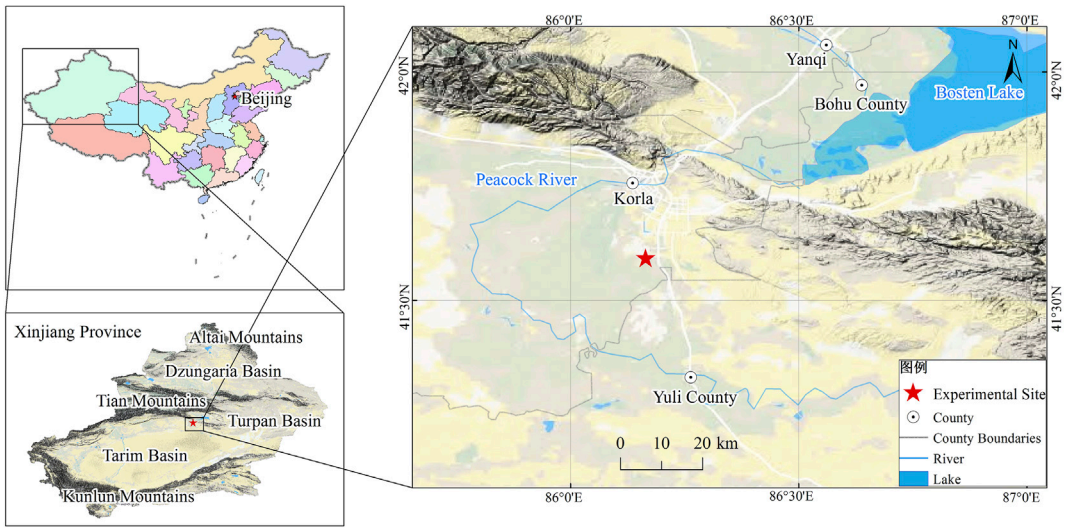


FIGURE 1 | Location of the experimental site.

TABLE 1 | TDS of infiltration water in 2018.

Infiltration water		TDS (g/L)	EC (dS/m)	Hydrochemical type
FW	Average	0.68	1.14	$MgSO_4$
	Standard deviation	0.041	0.04	
BW	Average	1.66	2.79	$MgSO_4$
	Standard deviation	0.04	0.04	

FW: fresh water; BW: brackish water; TDS: total dissolved solids; EC: electrical conductivity

TABLE 2 | Soil properties of the soil.

Depth (cm)	Sand (%) (50–2000 μm)	Silt (%) (2–50 μm)	Clay (%) (<2 μm)	Bulk density (g/cm^3)	Soil type	$EC_{1:5}$ of soil (dS/m)
0~5	52.12	40.06	7.82	1.51	Loamy sand	0.12
5~35	43.69	50.8	6.51	1.58		0.11
35~40	40.40	51.13	8.47	1.56		0.33
40~45	46.27	47.22	6.51	1.63		3.54
45~65	51.48	41.36	7.16	1.70		16.44
65–100	52.70	39.20	7.10	1.74		3.63

2.3 Monitoring

The soil samples were drilled at 8:00 p.m. before each infiltration for gravimetric water content and $EC_{1:5}$ analysis. The sampling interval of each sample was 10 s at a depth of 0–60 cm and 20 s at depth of 60–100 cm. The soil water content was measured by the drying method. The $EC_{1:5}$ was referred to the *EC* of 1–5 soil/water suspensions using a conductivity meter (DDS-307, INESA Scientific Instrument Co., Ltd., Shanghai, China).

2.4 Numerical Model

A 600 × 100 m section was to present the water–salt transport–based 2D conceptual model (**Figure 3**). The infiltration point was simplified as line water supply. Under the intermittent infiltration of brackish water, soil salt mainly accumulated in 40–60 cm (Chen et al., 2018; Li et al., 2018; Hu et al., 2020), and the soil was less affected by evaporation below 1.2 m (Heng et al., 2018). The pipe was theoretically suggested to install underground 1.6m, vertical to infiltration line (**Figure 3**).

The numerical simulation of soil water–salt transport was conducted using HYDRUS (Šimůnek et al., 2016; Katarina et al., 2019). The ground pipe was set as the free drainage boundary, the bare area was the atmospheric boundary, and the dipper was the variable flow boundary ($Var.Fl_1$). The water quantity data of the infiltration point

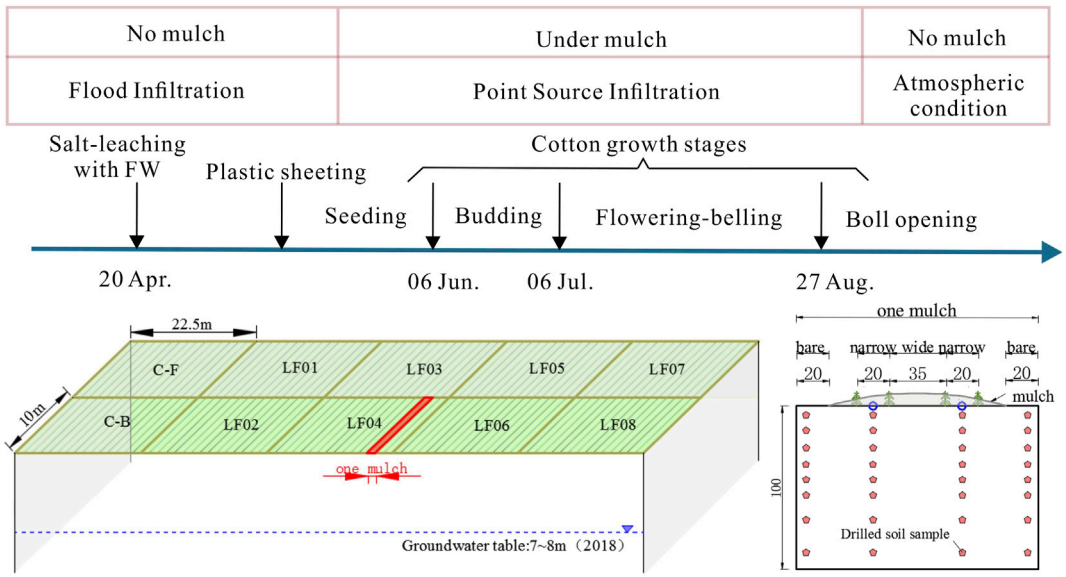


FIGURE 2 | Distribution of field plots and the intermittent infiltration mode.

TABLE 3 | Amount of intermittent infiltration water applied at different growth stages.

Infiltration order		1	2	3	4–10	11–13	14	Total water quantity (mm)
Actual dates		June 27	July 2	July 7	July 13, 18, 22, 28 August 1, 7, 12	August 17, 22, 28	September 2	
Control experiment	C-F-1.0Q	14.10	18.50	41.00	46.60	46.50	32.70	572.00
	C-B-1.0Q	14.10	18.50	41.00	46.60	46.50	32.70	572.00
Leaching experiment	LF01–1.05Q	14.81	19.43	43.05	48.93	48.83	34.34	600.60
	LF02–1.10Q	15.51	20.35	45.10	51.26	51.15	35.97	629.20
	LF03–1.15 Q	16.22	21.28	47.15	53.59	53.48	37.61	657.80
	LF04–1.20Q	16.92	22.20	49.20	55.92	55.80	39.24	686.40
	LF05–1.25Q	17.63	23.13	51.25	58.25	58.13	40.88	715.00
	LF06–1.30Q	18.33	24.05	53.30	60.58	60.45	42.51	743.60
	LF07–1.35Q	19.04	24.98	55.35	62.91	62.78	44.15	772.20
	LF08–1.40Q	19.74	25.90	57.40	65.24	65.10	45.78	800.80

was assigned by **Table 3**. There was no flow in the Y direction of the model and under the mulch except infiltration points (Var.Fl_2).

Flow boundary condition:

Lateral boundaries:

$$q_y = 0. \tag{1}$$

Atmospheric boundaries:

$$-K(h)\left(\frac{\partial h}{\partial z}+1\right) = q_a(t)\ (0 \le y \le 20, 60 \le y \le 90, 130 \le y \le 170, 280 \le y \le 320, 430 \le y \le 470, 580 \le y \le 600, \quad Z = 160). \tag{2}$$

Var.Fl_1:

$$-K(h)\left(\frac{\partial h}{\partial z}+1\right) = q_d(t)\ (50 \le y \le 60, 90 \le y \le 100, 200 \le y \le 210, 240 \le y \le 250, 350 \le y \le 360, 390 \le y \le 400, 500 \le y \le 510, 540 \le y \le 550, \quad Z = 160). \tag{3}$$

Var.Fl_2:

$$-K(h)\left(\frac{\partial h}{\partial z}+1\right) = 0\ (20 \le y \le 50, 60 \le y \le 90, 100 \le y \le 130, 170 \le y \le 200, 210 \le y \le 240, 250 \le y \le 280, 320 \le y \le 350, 360 \le y \le 390, 400 \le y \le 430, 470 \le y \le 500, 510 \le y \le 540, 550 \le y \le 580, \quad Z = 160). \tag{4}$$

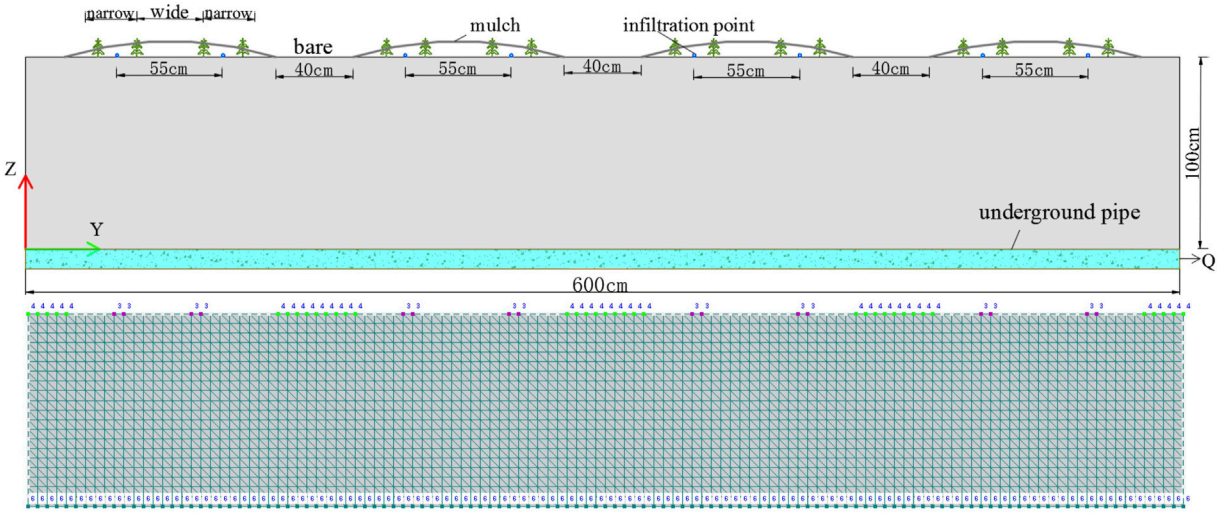


FIGURE 3 | Conceptual model of the 2D soil water flow under mulched intermittent infiltration.

TABLE 4 | Soil hydraulic parameters for the simulations.

	Depth (cm)	θ_r	θ_s	α (1/cm)	n	K_s (cm/day)	l	D_L (cm)	D_T (cm)
Initial parameters	0–5	0.0353	0.3502	0.0198	1.4308	28	0.5	20	20
	5–35	0.0323	0.3247	0.0159	1.4479	21	0.5	20	20
	35–40	0.0369	0.3348	0.0124	1.4706	18	0.5	20	20
	40–45	0.0313	0.319	0.0213	1.3842	18	0.5	20	20
	45–65	0.0302	0.31	0.0324	1.3227	15	0.5	20	20
	65–100	0.0302	0.3053	0.0393	1.2877	13	0.5	20	20
Final parameters	0–5	0.0257	0.302	0.0198	1.4308	38	0.5	25	21
	5–35	0.0243	0.308	0.0159	1.4479	32	0.5	30	25
	35–40	0.0270	0.319	0.0124	1.4706	31	0.5	23	18
	40–45	0.0221	0.328	0.0213	1.3842	30	0.5	21	15
	45–65	0.0203	0.341	0.0324	1.3227	32	0.5	20	16
	65–100	0.0222	0.35	0.0393	1.2877	33	0.5	24	20

Solute boundary conditions:

$$-\theta\left(D_{yz}\frac{\partial c}{\partial y}+D_{zz}\frac{\partial c}{\partial z}\right)+qc=q_d c_d\,(50\le y\le 60, 90\le y\le 100, 200\le y\le 210, 240\le y\le 250, 350\le y\le 360, 390\le y\le 400, 500\le y\le 510, 540\le y\le 550, \quad Z=160), \tag{5}$$

where h is the water pressure head, cm; θ is the volumetric water content, cm^3/cm^3; c is the salinity of the soil water, g/L; t is time, day; x and z are the spatial coordinates, cm; K is the unsaturated hydraulic conductivity, cm/d; D was the dispersion coefficient, cm^2/d; q_y, q_d, and q_a are the water flux of lateral boundaries, infiltration points, bare soil surface, cm/day; c_a was the salinity of the infiltration water, g/L.

The soil hydraulic properties were described using the standard equations of Van Genuchten (1980). The estimated hydraulic parameters were listed in **Table 4**. The initial longitudinal dispersion coefficient (D_L) and transverse dispersion coefficient (D_T) were defined by previous literature (Wang et al., 2014; Singh et al., 2019). The final diffusion coefficient was set to 1.58 cm^2/day after verification and adjustment based on the experimental values (Wang et al., 2017; Ranjbar et al., 2019). The linear isotherm adsorption coefficient K_d was set as 0.28 $cm^3\ g^{-1}$ (Kadyampakeni et al., 2018).

3 RESULTS AND DISCUSSION

3.1 HYDRUS Model Calibration

We simulated the spatial distributions of soil water and salt in the two-direction under mulched intermittent infiltration. Furthermore, the model values of HYDRUS-2D were

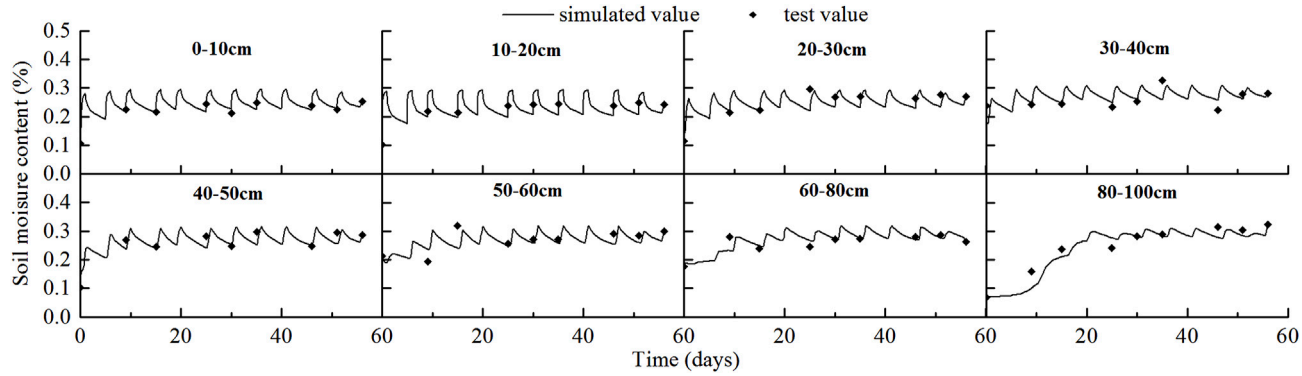


FIGURE 4 | Comparison of measured and simulated value of SMC in 0–100 cm depth.

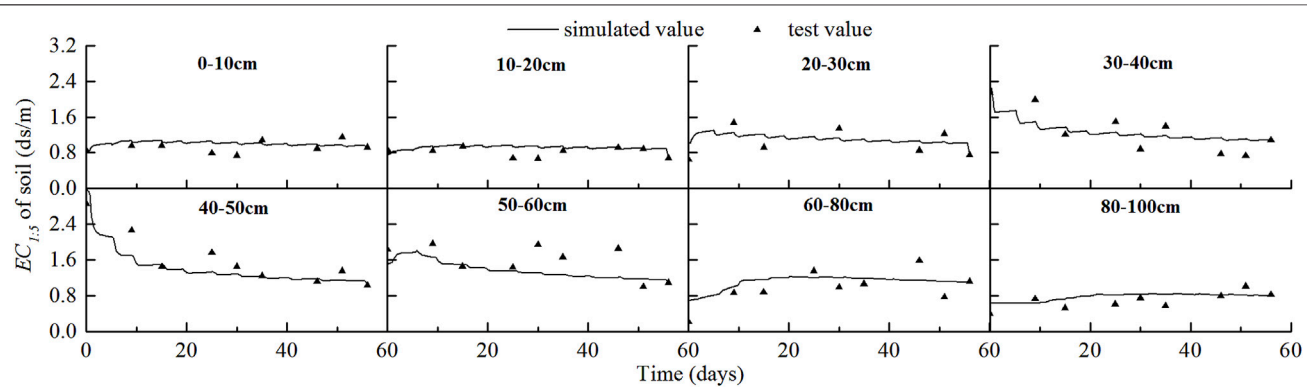


FIGURE 5 | Comparison of measured and simulated value of $EC_{1:5}$ in 0–100 cm depth.

TABLE 5 | Results in *t* test of simulated and observed values.

	N	Mean deviation	Std. deviation	Std. error mean	t	df	P	Sig. (2-tailed)
SMC	72	0.013	0.026	0.003	−4.151	71	0.870	0.001
$EC_{1:5}$	72	0.327	2.455	0.289	−1.121	71	0.129	0.262

TABLE 6 | Standards for different soil salinization grades.

Degree of soil salinization	No salinization	Mild	Moderate	Severe	Extreme severe
ECe (dS/m)	<2	2–4	4–8	8–15	>15
$EC_{1:5}$ (dS/m)	<0.55	0.55–1.10	1.10–2.20	2.20–4.12	>3.0
Total salinity of soil (mg/cm^3)	<2.46	2.46–4.92	4.92–9.84	9.84–18.46	>18.46

compared with actual observed values (**Figures 4**,**5**). The model could display the dynamic variation of soil moisture and salinity better with infiltration events. A *t*-test was carried out between the measured and simulated values, and the results showed that the significance level of $p > 0.05$, indicating that the simulation results of the solute transport model were verified successfully (**Table 5**).

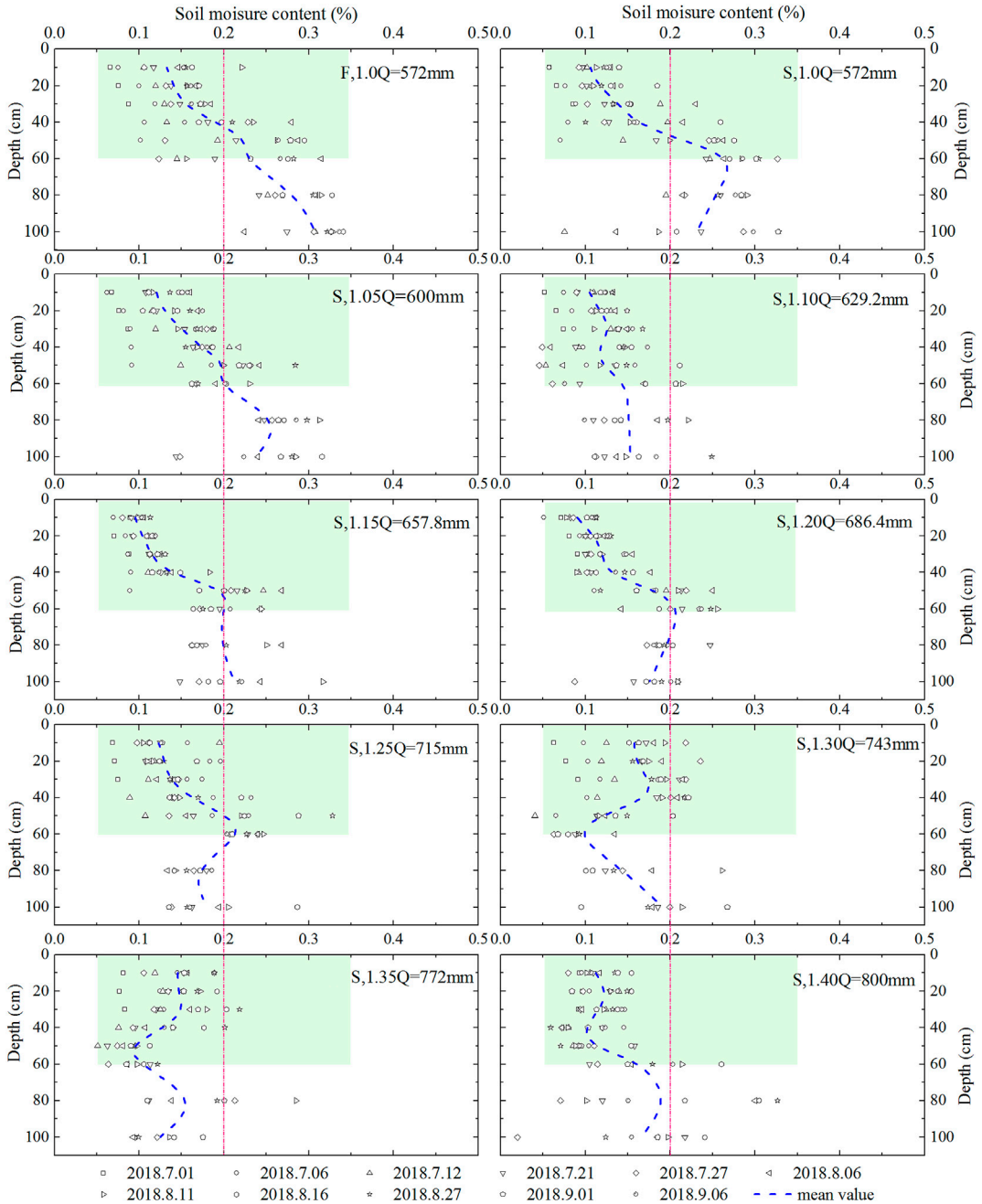


FIGURE 6 | Variation of soil water at different depths in the field.

3.2 Soil Water and Salinization Variation

Soil samples were collected the day before infiltration treatment and obtained soil moisture dates, which could better reflect the water holding capacity of the soil (**Figure 6**). Within a single infiltration interval of 5 days, the migration distance of soil water in unsaturated zone was more than 40 cm. Due to the water uptake by plant roots, the soil moisture content was almost less than the field capacity of 0.203 at depth of 0–60 cm before each infiltration, and the water mainly existed at the depth of 60–100 cm. Compared two control experiment schemes, the soil water migrated faster under fresh water treatment and the soil reached saturation at the depth of 100 cm with moisture content of 0.35. Brackish water changed the soil structure and reduced the soil permeability because of high sodium ion content and large sodium adsorption ratio. The soil water holding capacity rate was lower than 0.2 after 5 days with 1.20Q–1.40Q brackish water treatments.

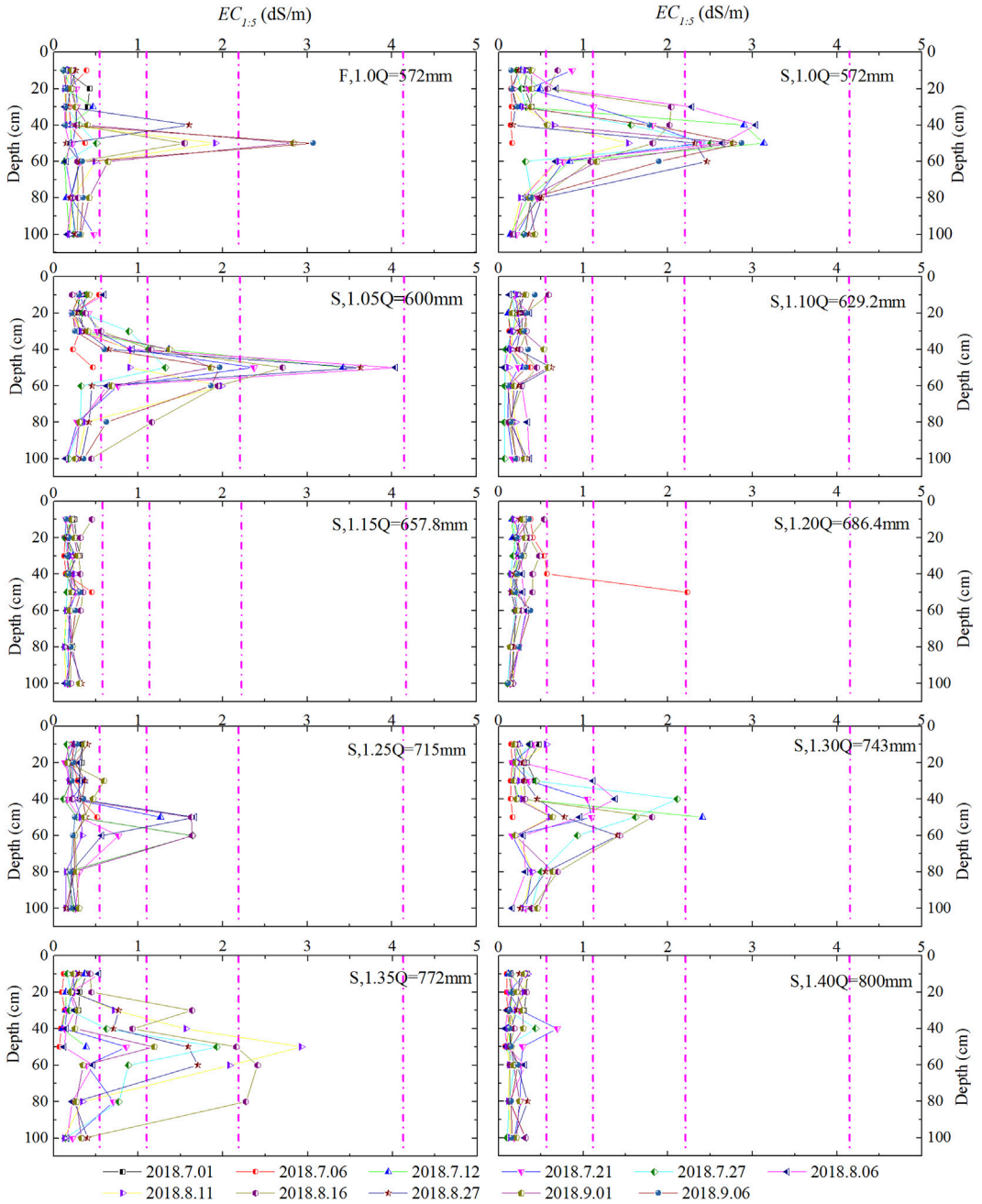


FIGURE 7 | Variation of soil salinization at different depths in the field.

The soil salt accumulation at the depth of 0–30 cm was lower under water leaching in the whole growth period (**Figure 7**). The $EC_{1:5}$ of soil in the root zone was basically less than 0.55 dS/m, which was no salinized (**Table 6**). There was massive salt accumulation at the depth of 30–60 cm. The average salinity of the 10 experimental groups was 0.539 ds/m, 0.979 dS/m and 0.684 ds/m respectively at the depth of 30–40, 40–50, 50–60 cm. The maximum salinity was accumulated at the depth of 40–50 cm. When the groundwater level was greater than the limit evaporation depth, the soil in the root zone formed a "low salt zone" at the depth of 0–30 cm. The cumulative increase of soil salt at the depth of 30–50 cm reached largest, and decreased below 50 cm.

3.3 Soil Environmental Effect Analysis

Comparing the soil salinity of each infiltration event to the first leaching salt by fresh water (20 April) showed that the variation of $EC_{1:5}$ at depth of 0–30 cm was less than 0.5 dS/m (**Figure 8**). The root distribution was measured and time-variable through plant growth which could be accounted for by modifying the ratio

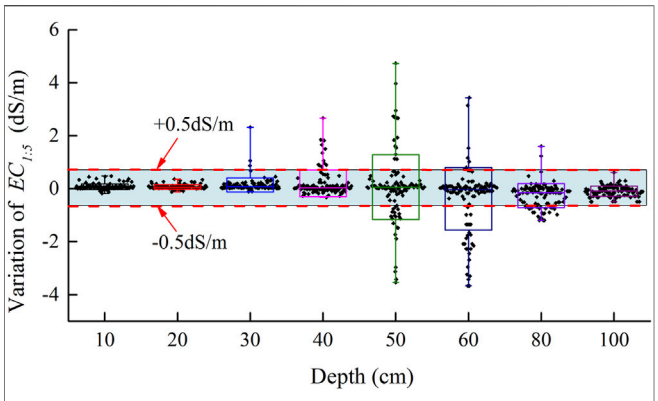


FIGURE 8 | Variation of soil EC1:5 compared to initial time after leaching salt by fresh water (20 April) at different depths.

between evaporation and transpiration (Wang et al., 2014). Soil salinization mainly occurs in 30–60 cm, and the variation of $EC_{1:5}$ exceed 4.0 dS/m. Root uptake as a key way to transport soil water into atmosphere contributed mainly to soil salinization. The average variation of $EC_{1:5}$ showed that the soil salt little changed before and after brackish water infiltration. The brackish water intermittent infiltration under plastic mulch could effectively improve soil salinization and protect the cultivated environment.

Soil salinity was evaluated using the electric conductivity of the saturation extract as EC_e, which could be calculated from measured values of $EC_{1:5}$ using EC_e = 3.64 $EC_{1:5}$ (Slavich and Petterson 1993; Wang et al., 2014). We evaluated the salinization degree of soil based on **Table 6** (Fitzpatrick 1980; Akça et al., 2020).

The maximum salinity of 10 experimental treatments at depth of 40–50 cm was 3.07, 2.46, 1.99, 0.274, 0.32, 0.38, 1.64, 1.43, 2.41, 0.31 dS/m respectively. Fresh water infiltration would still lead to soil moderate salinization. The soil salinity decreased first and then increased with increasing infiltration water amount of 1.0–1.35Q under brackish water infiltration. The total salt of soil was the lowest with water treatment of 1.15 Q = 657.8 mm. The $EC_{1:5}$ of soil was less than 0.55 dS/m, reaching the degree of no salinization. Whether the amount of water was too large or too small, it would lead to salt accumulation. The leaching intensity was not enough with low water amount, resulting in the accumulation of salt in the topsoil. Numerous ions were input into the soil through large amount of water, which could not be absorbed by plants and lead to root salt stress. The optimization of soil environment achieved the best effect with 1.15 Q water treatment.

3.4 Long-Term Simulations of Leaching-Drainage System

Long-term infiltration causes the salt of topsoil to penetrate into the deep soil layer and then salinize the groundwater. At present, the drainage channel with the depth of 1.8 m in the experimental field could not meet the salt discharge requirement. Therefore, underground pipe drainage system should be adopted to receive the upper leaching water and salt, collect and recycle it, desalinate soil, and protect groundwater. We simulate water–salt of soil under a leaching–drainage system for 10 years with 1.15 Q = 657.8 mm treatment (**Figure 9**).

Soil water gradually pushed downward under brackish water intermittent infiltration, and soil salinity is gradually concentrated to the edge of the wetting front. Under the leaching of multiple infiltration points, the wetting front overlaps with each other to make the salt migrate downward, forming a "low salination soil layer". The salt mainly accumulated to 1.10–2.99 dS/m at the depth of 40–60 cm during 0–30 days, and the soil salinity under mulch area was lower than 0.55 dS/m

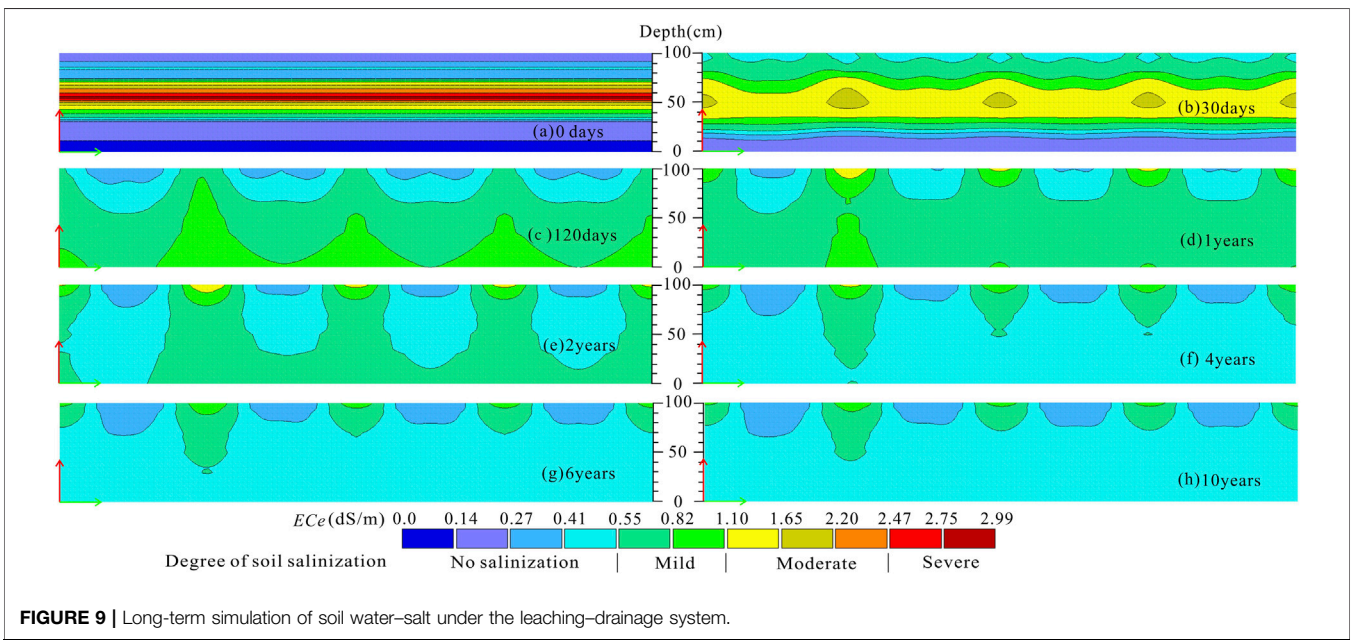


FIGURE 9 | Long-term simulation of soil water–salt under the leaching–drainage system.

at depth of 0–10 cm. After 120 days, no salinization soil area expanded to depth of 40–45 cm. During non-infiltration period (121–365 days), the soil salt moved upward under evaporation effect, and the no salinization area was reduced and showed mild salinization. Figures 7E–H showed the prediction results of 2–10 years. The salt was gradually leached and discharged through underground pipe. The soil total salt under mulch was less than 0.55 dS/m, which could not only provide a low salt area for cotton growth but also control soil salt accumulation and protect soil as well as groundwater environment.

4 CONCLUSION

Combined field leaching experiments under the brackish water intermittent infiltration in 2018 and the Hydrus-2D soil water transport numerical model under the leaching-drainage system, we analyzed the optimal leaching water amount and predicted the soil salinization degree after 10 years. The main conclusions of this paper are as follows.

Within a single infiltration interval of 5 days, soil water transported to below 40 cm in unsaturated zone, and soil moisture content was almost less than the field capacity of 0.203 at depth of 0–60 cm due to the root water uptake. Soil water holding capacity rate was lower than 0.2 under 1.20Q–1.40Q brackish water treatments. The field leaching experiments showed that whatever the higher or lower amount of infiltration water, the salt all accumulated at depth of 40–50 cm. We recommend that the optimum amount of brackish water for leaching was 1.15 Q = 600 mm, and the soil salinity in the soil was less than 2.0 dS/m as no salinization. The LF = 1.15 could ensure the no salinization environment of soil and realize the sustainable cultivation of cotton.

To prevent the accumulation of salt in the deep soil layer, the salt in the root zone should be drained during the intermittent infiltration period. The 10-year simulation results of the leaching–drainage system showed that salt mainly accumulated to 1.10–2.99 dS/m at the depth of 40–60 cm during 0–30 days. No salinization area expanded to depth 40–45 cm after 120 days and reduced under evaporation effect during non-infiltration period. The soil salt was gradually leached and discharged through underground pipe and was less than 0.55 dS/m after 10 years, which could provide a theoretical basis for the protecting soil and groundwater environment.

DATA AVAILABILITY STATEMENT

The raw data supporting the conclusions of this article will be made available by the authors, without undue reservation.

AUTHOR CONTRIBUTIONS

LG contributed to field experiments, testing, data analysis, and article writing. ZW contributed to fund support, field experiments, data analysis, and article polishing.

FUNDING

This work was supported by the National Natural Science Foundation of China [Grant No.41702259] and Doctoral research start up fund of Technological Innovation R & D project [2021SCSZYD-03].

REFERENCES

Akça, E., Aydin, M., Kapur, S., Kume, T., Nagano, T., Watanabe, T., et al. (2020). Long-term Monitoring of Soil Salinity in a Semi-arid Environment of Turkey. *Catena* 193, 104614. doi:10.1016/j.catena.2020.104614

Beltrán, J. M. (1999). Irrigation with Saline Water: Benefits and Environmental Impact. *Agric. Water Manage.* 40 (2), 183–194.

Cao, Y., Cai, H., Sun, S., Gu, X., Mu, Q., Duan, W., et al. (2022). Effects of Drip Irrigation Methods on Yield and Water Productivity of Maize in Northwest China. *Agric. Water Manag.* 259, 107227. doi:10.1016/j.agwat.2021.107227

Chen, F., Cui, N., Jiang, S., Li, H., Wang, Y., Gong, D., et al. (2022). Effects of Water Deficit at Different Growth Stages under Drip Irrigation on Fruit Quality of Citrus in the Humid Areas of South China. *Agric. Water Manag.* 262, 107407. doi:10.1016/j.agwat.2021.107407

Chen, W., Jin, M., Ferré, T. P. A., Liu, Y., Xian, Y., Shan, T., et al. (2018). Spatial Distribution of Soil Moisture, Soil Salinity, and Root Density beneath a Cotton Field under Mulched Drip Irrigation with Brackish and Fresh Water. *Field Crops Res.* 215, 207–221. doi:10.1016/j.fcr.2017.10.019

Chu, L.-l., Kang, Y.-h., and Wan, S.-q. (2016). Effect of Different Water Application Intensity and Irrigation Amount Treatments of Microirrigation on Soil-Leaching Coastal Saline Soils of North China. *J. Integr. Agric.* 15 (9), 2123–2131. doi:10.1016/s2095-3119(15)61263-1

Feng, D., Li, G., Wang, D., Wulazibieke, M., Cai, M., Kang, J., et al. (2022). Evaluation of AquaCrop Model Performance under Mulched Drip Irrigation for Maize in Northeast China. *Agric. Water Manag.* 261, 107372. doi:10.1016/j.agwat.2021.107372

Fitzpatrick, E. A. (1980). *Soil*. London: The Pitman Press.

Hanson, B. R., May, D. E., Simünek, J., Hopmans, J. W., and Hutmacher, R. B. (2009). Drip Irrigation Provides the Salinity Control Needed for Profitable Irrigation of Tomatoes in the San Joaquin Valley. *Cal. Ag.* 63 (3), 131–136. doi:10.3733/ca.v063n03p131

Heng, T. H., Liao, R. K., Wang, Z. H., and Wu, W. Y. (2018). Effects of Combined Drip Irrigation and Sub-surface Pipe Drainage on Water and Salt Transport of Saline-Alkali Soil in Xinjiang, China[J]. *J. Arid Land* 10 (06), 932–945. doi:10.1007/s40333-018-0061-7

Hu, Y., Li, X., Jin, M., Wang, R., Chen, J., and Guo, S. (2020). Reduced Co-occurrence and Ion-specific Preferences of Soil Microbial Hub Species after Ten Years of Irrigation with Brackish Water. *Soil Tillage Res.* 199, 104599. doi:10.1016/j.still.2020.104599

Inosako, K., Saito, T., and Omachi, K. (2019). Analysis by Numerical Experiments of Desalinization of a Salt-Affected Paddy Field Using a Rice Husk Underdrainage System. *Paddy Water Environ.* 17, 211–219. doi:10.1007/s10333-019-00713-6

Jia, Q., Shi, H., Li, R., Miao, Q., Feng, Y., Wang, N., et al. (2021). Evaporation of Maize Crop under Mulch Film and Soil Covered Drip Irrigation: Field Assessment and Modelling on West Liaohe Plain, China. *Agric. Water Manag.* 253, 106894. doi:10.1016/j.agwat.2021.106894

Kadyampakeni, D. M., Morgan, K. T., Nkedi-Kizza, P., Schumann, A. W., and Jawitz, J. W. (2018). Modeling Water and Nutrient Movement in Sandy Soils

Using HYDRUS-2D. *J. Environ. Qual.* 47 (6), 1546–1553. doi:10.2134/jeq2018.02.0056

Katarina, L. G., de Miranda, J. H., Silveira, L. K., and van Genuchtenbc, M. T. (2019). HYDRUS-2D Simulations of Water and Potassium Movement in Drip Irrigated Tropical Soil Container Cultivated with Sugarcane. *Agric. Water Manag.* 221, 334–347. doi:10.1016/j.agwat.2019.05.010

Li, S., Luo, W., Jia, Z. H., and Pan, Y. X. (2014). Impact of Water Table Depth and Shallow Groundwater Use on Salt Leaching Cycle in Irrigated Areas. *J. Hydraulic Eng.* 45 (8), 950–957. (in Chinese). doi:10.13243/j.cnki.slxb.2014.08.008

Li, X., Huang, X., and Zhang, Y. (2021). Spatio-temporal Analysis of Groundwater Chemistry, Quality and Potential Human Health Risks in the Pinggu Basin of North China Plain: Evidence from High-Resolution Monitoring Dataset of 2015-2017. *Sci. Total Environ.* 800, 149568. doi:10.1016/j.scitotenv.2021.149568

Li, X., Jin, M., Zhou, N., Jiang, S., and Hu, Y. (2018). Inter-dripper Variation of Soil Water and Salt in a Mulched Drip Irrigated Cotton Field: Advantages of 3-D Modelling. *Soil Tillage Res.* 184, 186–194. doi:10.1016/j.still.2018.07.016

Maas, E. V., and Hoffman, G. J. (1977). Crop Salt Tolerance-Current Assessment. *J. Irrig. Drain. Div.* 103 (2), 115–134. doi:10.1061/jrcea4.0001137

Min, W., Guo, H. J., and Hu, Z. Q. (2017). Cotton Growth and the Fate of N Fertilizer as Affected by Saline Water Irrigation and N Fertigation in a Drip-Irrigated Field. *Acta Agric. Scand. Sect. B-Soil Plant Sci.* 67 (8), 712–722. doi:10.1080/09064710.2017.1338309

Ochege, F. U., Luo, G., Yuan, X., Owusu, G., Li, C., and Justine, F. M. (2022). Simulated Effects of Plastic Film-Mulched Soil on Surface Energy Fluxes Based on Optimized TSEB Model in a Drip-Irrigated Cotton Field. *Agric. Water Manag.* 262, 107394. doi:10.1016/j.agwat.2021.107394

Peng, Z. Y., Wu, J. W., and Huang, J. S. (2016). Feasibility of Applying Intermittent Irrigation on Solute Leaching. *Adv. Water Sci.* 27 (1), 31–39. (in Chinese). doi:10.14042/j.cnki.32.1309.2016.01.004

Qi, Z., Feng, H., Zhao, Y., Zhang, T., Yang, A., and Zhang, Z. (2018). Spatial Distribution and Simulation of Soil Moisture and Salinity under Mulched Drip Irrigation Combined with Tillage in an Arid Saline Irrigation District, Northwest China. *Agric. Water Manag.* 201, 219–231. doi:10.1016/j.agwat.2017.12.032

Ranjbar, A., Rahimikhoob, A., Ebrahimian, H., and Varavipour, M. (2019). Simulation of Nitrogen Uptake and Distribution under Furrows and Ridges during the Maize Growth Period Using HYDRUS-2D. *Irrig. Sci.* 37 (4), 495–509. doi:10.1007/s00271-019-00627-5

Sallam, G. A. H. (2017). "The Assessment of Egypt's Subsurface Drainage System," in *The Handbook of Environmental Chemistry* (Berlin, Heidelberg: Springer), 1–32.

Šimůnek, J., Van Genuchten, M. Th., and Sejna, M. (2016). The HYDRUS Software Package for Simulating Two and Three Dimensional Movement of Water, Heat, and Multiple Solutes in Variably-Saturated Porous Media. Technical Manual 2.

Singh, S., Coppi, L., Wang, Z., Tenuta, M., and Holländer, H. M. (2019). Regionalisation of Nitrate Leaching on Pasture Land in Southern Manitoba. *Agric. Water Manag.* 222, 286–300. doi:10.1016/j.agwat.2019.05.016

Slavich, P., and Petterson, G. (1993). Estimating the Electrical Conductivity of Saturated Paste Extracts from 1:5 Soil, Water Suspensions and Texture. *Soil Res.* 31, 73. doi:10.1071/sr9930073

Sun, Z. Z., Yue, C. F., and Shi, K. B. (2015). Analysis of Drainage Measures in Xinjiang Water-Saving Irrigation Area. *Water Sav. Irrig.* 5, 20–25. (in Chinese). doi:10.3969/j.issn.1007-4929.2015.05.006

Tian, F. Q., Wen, J., Hu, H. C., and Ni, G. (2018). Review on Water and Salt Transport and Regulation in Drip Irrigated Fields in Arid Regions. *J. Hydraulic Eng.* 49 (01), 126–135. (in Chinese). doi:10.13243/j.cnki.slxb.20170909

van Genuchten, M. T. (1980). A Closed-form Equation for Predicting the Hydraulic Conductivity of Unsaturated Soils. *Soil Sci. Soc. Am. J.* 44, 892–898. doi:10.2136/sssaj1980.03615995004400050002x

Wang, H., Feng, D., Zhang, A. Q., et al. (2022). Effects of Saline Water Mulched Drip Irrigation on Cotton Yield and Soil Quality in the North China Plain. *Agric. Water Manag.* 262, 107405. doi:10.1016/j.agwat.2021.107405

Wang, J. W., Du, Y. D., Niu, W. Q., et al. (2022). Drip Irrigation Mode Affects Tomato Yield by Regulating Root-Soil-Microbe Interactions. *Agric. Water Manag.* 260, 107188. doi:10.1016/j.agwat.2021.107188

Wang, J. J., Huang, Y. F., Long, H. Y., et al. (2017). Simulations of Water Movement and Solute Transport through Different Soil Texture Configurations under Negative-pressure Irrigation. *Hydrol. Process.* 31 (14), 2599–2612. doi:10.1002/hyp.11209

Wang, Z. M., Li, Z. F., and Zhan, H. B. (2022). Effect of Long-Term Saline Mulched Drip Irrigation on Soil-Groundwater Environment in Arid Northwest China. *Sci. Total Environ.* 820, 153222. doi:10.1016/j.scitotenv.2022.153222

Wang, Z. M., Jin, M. G., Šimůnek, J., et al. (2014). Evaluation of Mulched Drip Irrigation for Cotton in Arid Northwest China. *Irrig. Sci.* 32, 15–27. doi:10.1007/s00271-013-0409-x

Wu, Y., Bian, S.-f., Liu, Z.-m., Wang, L.-c., Wang, Y.-j., Xu, W.-h., et al. (2021). Drip Irrigation Incorporating Water Conservation Measures: Effects on Soil Water-Nitrogen Utilization, Root Traits and Grain Production of Spring Maize in Semi-arid Areas. *J. Integr. Agric.* 20 (12), 3127–3142. doi:10.1016/s2095-3119(20)63314-7

Zeng, W., Xu, C., Wu, J., and Huang, J. (2014). Soil Salt Leaching under Different Irrigation Regimes: HYDRUS-1D Modelling and Analysis. *J. Arid. Land* 6 (1), 44–58. doi:10.1007/s40333-013-0176-9

Zhang, P., Zhao, X. F., Zhang, T., Zhang, G., Li, B., Xu, H., et al. (2010). Leaching Salinity Effect of Drip Irrigation on Soil of Oasis Shelter Forests in Arid Area. *Trans. CSAE* 26 (10), 25–30. (in Chinese). doi:10.3969/j.issn.1002-6819.2011.05.005

Zhang, Y., Dai, Y., Wang, Y., Huang, X., Xiao, Y., and Pei, Q. (2021a). Hydrochemistry, Quality and Potential Health Risk Appraisal of Nitrate Enriched Groundwater in the Nanchong Area, Southwestern China. *Sci. Total Environ.* 784, 147186. doi:10.1016/j.scitotenv.2021.147186

Zhang, Y., He, Z., Tian, H., Huang, X., Zhang, Z., Liu, Y., et al. (2021b). Hydrochemistry Appraisal, Quality Assessment and Health Risk Evaluation of Shallow Groundwater in the Mianyang Area of Sichuan Basin, Southwestern China. *Environ. Earth Sci.* 80 (17), 576. doi:10.1007/s12665-021-09894-y

Conflict of Interest: The authors declare that the research was conducted in the absence of any commercial or financial relationships that could be construed as a potential conflict of interest.

Publisher's Note: All claims expressed in this article are solely those of the authors and do not necessarily represent those of their affiliated organizations, or those of the publisher, the editors, and the reviewers. Any product that may be evaluated in this article, or claim that may be made by its manufacturer, is not guaranteed or endorsed by the publisher.

Copyright © 2022 Leilei and Zaimin. This is an open-access article distributed under the terms of the Creative Commons Attribution License (CC BY). The use, distribution or reproduction in other forums is permitted, provided the original author(s) and the copyright owner(s) are credited and that the original publication in this journal is cited, in accordance with accepted academic practice. No use, distribution or reproduction is permitted which does not comply with these terms.

frontiers | Frontiers in Earth Science

ORIGINAL RESEARCH
published: 03 June 2022
doi: 10.3389/feart.2022.897882

Structural Characteristics and Deformation Evolution of an Intra-Continental Fold-Thrust Belt in Eastern Sichuan: Insights Into Analogue Sandbox Models

Yang-Shuang Wang[1], *Mo Xu*[1]*, *Yan-Na Yang*[1], *Qiang Xia*[1], *Bing Jiang*[1], *Chang Yang*[2] *and Heng Zhang*[3]

[1]State Key Laboratory of Geohazard Prevention and Geoenvironment Protection, College of Environment and Civil Engineering, Chengdu University of Technology, Chengdu, China, [2]Chongqing Institute of Geology and Mineral Resources, Chongqing, China, [3]Sichuan Metallurgical Geological Survey and Design Group Co. Ltd, Chengdu, China

OPEN ACCESS

Edited by:
Xiaoyan Zhao,
Southwest Jiaotong University, China

Reviewed by:
Hua-Wen Cao,
China Geological Survey, China
Deng Mingzhe,
SINOPEC Petroleum Exploration and Production Research Institute, China

***Correspondence:**
Mo Xu
xm@cdut.edu.cn

Specialty section:
This article was submitted to Geohazards and Georisks, a section of the journal Frontiers in Earth Science

Received: *16 March 2022*
Accepted: *22 April 2022*
Published: *03 June 2022*

Citation:
Wang Y-S, Xu M, Yang Y-N, Xia Q, Jiang B, Yang C and Zhang H (2022) Structural Characteristics and Deformation Evolution of an Intra-Continental Fold-Thrust Belt in Eastern Sichuan: Insights Into Analogue Sandbox Models. Front. Earth Sci. 10:897882. doi: 10.3389/feart.2022.897882

The Eastern Sichuan area is a typical fold-and-impulse zone. It is bounded by the Qiyue Mountain fault, with septal folds on the east and on the west. Based on previous geological mapping and surface geological structure research as well as the fault-related folding theory, in this study, tectonophysical simulation experiments were conducted to investigate the tectonic geometry and kinematics of the Eastern Sichuan fold-impulse zone. The experiments were conducted by selecting different experimental materials and changing the physical properties of the cover, the friction between the cover and the basement, the number of slip layers, the burial depth, and other factors. Finally, the similarity of the results to the morphological characteristics of the real geological structure was assessed. The results show that the deformation style is influenced to some extent by the brittle shear strength and the ductile shear strength of the basement, and the different interlayer cohesions between the competent and incompetent layers, the high rheology, and the burial depth of the slickensides played crucial roles in the formation of the final evolution of the Eastern Sichuan fold fault zone. The step-like system, composed of a lower crustal crystalline basement detachment surface, regional boundary fractures, and the overlying Cambrian and Triassic synclines, is a necessary condition for the formation of the Eastern Sichuan fold and fault zone and controls the overall evolution of the zone. Under the action of multiple phases of tectonic activity with different main stress orientations, the geological phenomenon of multiple superimposed phases of folding in different directions observed at present in the Eastern Sichuan area was formed. The well-developed karst features are not conducive to the construction of a project tunnel in the area where tightly closed back-slope, fissures, and normal faults have developed in the Eastern Sichuan fold and fault zone.

Keywords: Eastern Sichuan, physical simulation, slippage, folded-splash zones, tectonic geometry, and kinematics, engineering influence

1 INTRODUCTION

The concept of a fold and thrust belt was introduced by Rich (1934) for the first time. Since then, many scholars have conducted relevant research on this topic. In general, the terms "thick-skinned" and "thin-skinned" tectonics are widely used when describing the structural geometry of fold and thrust belts (Pfiffner 2006). Thick-skinned tectonics involves thrust faults that reach down into the crystalline basement. In some cases, the thrust faults run parallel to the basement cover contact a few kilometers beneath this contact. In contrast, thin-skinned tectonics relates to thrust sheets where the sedimentary cover is detached from its crystalline substratum along a detachment layer that consists of mechanically weak rocks. The thickness of the detached cover sediments is typically in the order of 1–10 km (Adrian 2017). Understanding the styles of deformation processes and the mechanisms of faulting and folding is crucial, all of which are active in variable proportions throughout the entire evolution of a fold and thrust belt (Jamison 1992; Woodward 1999). Understanding both the interactions and the relationship between the macroscopic fold and thrust processes and the mesoscopic and microscopic fabric-forming processes is necessary to reconstruct the tectonic evolution.

As one of the typical tectonic styles of fold and thrust belts in the foreland region of a collisional zone, the Eastern Sichuan fold-thrust belt (ESFTB) is situated in the eastern margin of the middle and upper Yangtze blocks in the South China Craton (Charvet 2013; Lu et al., 2014; Zhang et al., 2013) (**Figure 1**). It is bordered by the Dabashan arcuate thrust belt to the northeast, the Youjiang fold-thrust belt to the south, the Xuefeng–Dayong fold-thrust belt to the east, and the Huayingshan fault to the west (Tang and Cui 2012; Zhao et al., 2017). In a similar way, the ESFTB consists of two deformation domains with significantly different deformation styles and characteristics (Li et al., 2015). The Western Hunan–Hubei thick-skinned tectonic zone located between the Qiyueshan and Dayong faults is characterized by trough-like folds, while the Eastern Sichuan thin-skinned tectonic zone located between the Qiyueshan and Huayingshan faults is characterized by a high-steep anticline (**Figure 2**). Therefore, the ESFTB is an ideal area to study Jura-type folds.

Recent research and geological exploration have confirmed that in such systems, a weak basal layer (e.g., gypsum and shale) serves as the main décollement, which has been recognized as a key factor controlling the deformation of the sedimentary sequences during shortening (Davis and Terry 1985; Oner and Dilek 2013; Mount 2014; Boutoux et al., 2016). Two or multiple layer detachments have been reported in many folds and thrust belts worldwide, such as the Jura fold-thrust belt in Switzerland (Rameil 2008; Malz et al., 2016), the Apennines in Italy (Massoli et al., 2006; Tavani and Cifelli 2010), the southeast Zagros in Iran (Ghazian and Buiter 2014), and the Western Gibraltar Arc between the Mediterranean and the Atlantic (Expósito et al., 2012). Based on the statistics of drilling holes, field investigations, and seismic dates, the ESFTB was mainly controlled by two ductile décollements: 1) one in the gypsum and shale of the Lower–Middle Cambrian Longwangmiao Formation and Gaotai Formation and 2) the other in the dark gray gypsum-bearing dolomite of the Lower Triassic Jialingjiang Formation. However, although previous research has consistently concluded that these detachments played an important role in the development and deformation progress of the ESFTB (Chu et al., 2012a; Tang and Cui 2012; Li et al., 2015), few studies have been conducted on the relationship between the deformation processes, the mechanisms of the folding and thrusting, and the mechanical properties, relative thickness, depth, and vertical and horizontal distribution of the multiple décollements (Brogi 2008; Hayes and Hanks 2008). Furthermore, the structural characteristics and geodynamic origin of the ESFTB are still debated, and the proposed tectonic interpretations vary (Li et al., 2002; Yan et al., 2003; Shen et al., 2009; Li 2015; Zou et al., 2015).

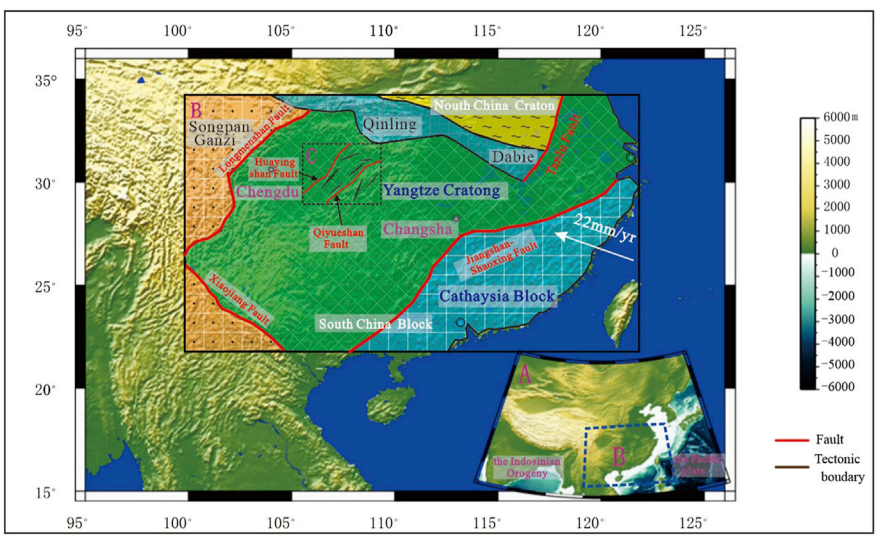


FIGURE 1 | Tectonic map of South China (modified after Deng et al., 2014).

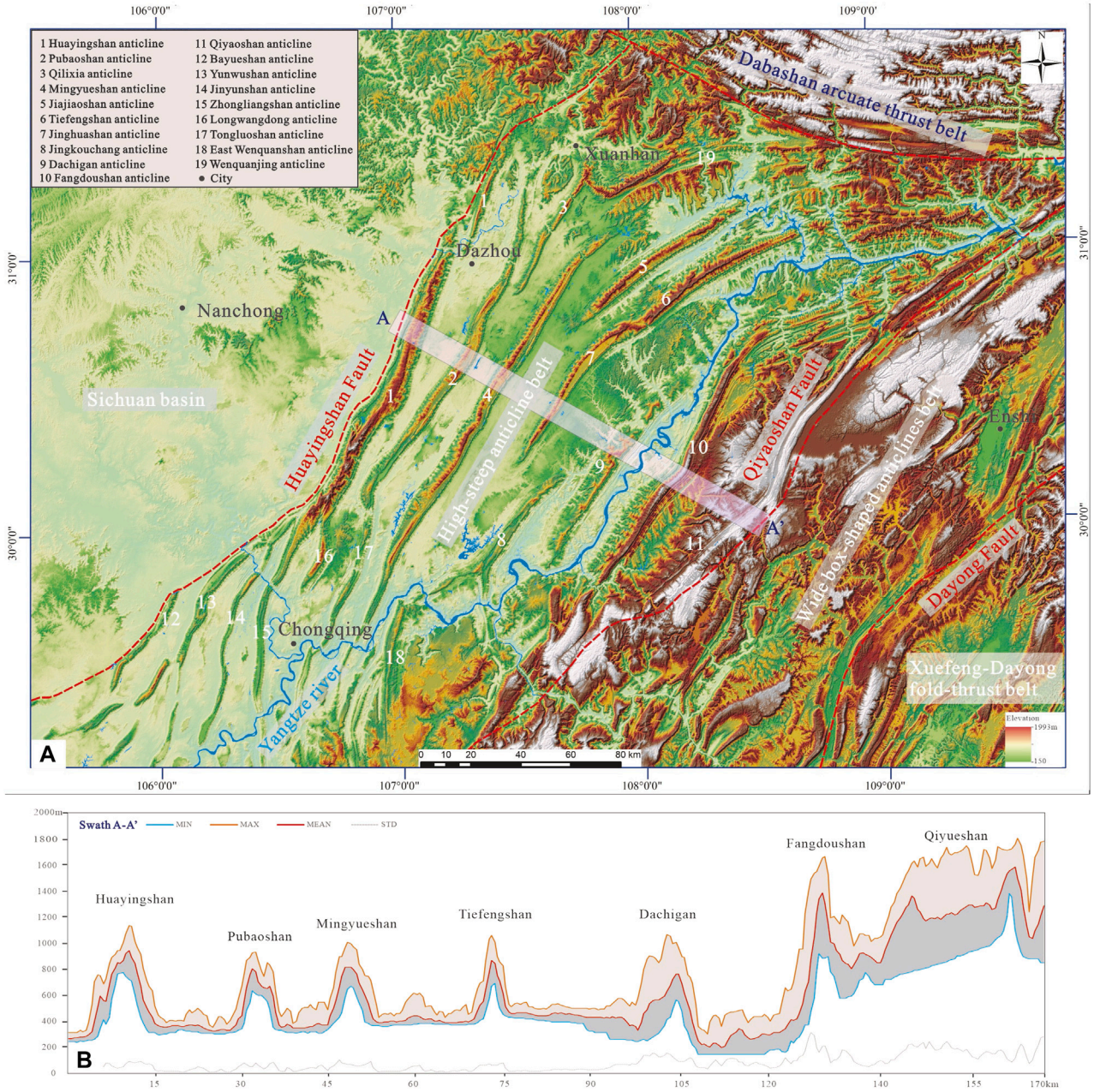


FIGURE 2 | Location and digital elevation map of the study area. **(A)** Digital elevation map of the Eastern Sichuan basin (on **Figure 1** for location). **(B)** Cross section of the digital elevation map of the Eastern Sichuan basin (See A–A′ on **(A)** for location).

Physical analog modeling has been proven to be an effective tool for studying the deformation processes and mechanisms of fold and thrust belts (Zanon and Janette Souza Gomes 2019; Meng and Hodgetts 2019; Graveleau et al., 2012; Santolaria et al., 2015; Santolaria et al., 2015). Previous studies have revealed that many factors play important roles in the analog modeling of fold and thrust belts, such as the physical properties of the materials, the rate of shortening, the thickness ratio of the brittle overburden to the basal décollement, and the geometry and dip of the boundaries (Rossetti et al., 2000; Bonini et al., 2012; Reiter et al., 2011). In this study, six sets of analog modeling experiments were conducted to systematically investigate the geometry and timing of the deformation progress, as well as how and where the shortening was accommodated. Each experiment was analyzed based on detailed monitoring, field geological surveys, digital elevation model (DEM) measurements, and seismic sections. Finally, based on existing research results and the results of this study, the structural

deformation was comprehensively analyzed, providing new robust insights into the tectonic evolution of the ESFTB.

2 GEOLOGIC SETTING AND PETROGRAPHY

2.1 Background Geology of the Yangtze Block in the South China Craton

The ESFTB was controlled by the evolution of the middle and upper Yangtze blocks in the South China Craton (SCC), which have experienced a complex tectonic evolution since the early Neoproterozoic (**Figure 1A**) (Charvet 2013; Lu et al., 2014; Deng et al., 2014). The basement of the Yangtze Block to the northwest and that of the Cathaysia Block to the southeast were conjoined by the Neoproterozoic collision that formed the SCC (Li et al., 2009; Wang P. et al., 2012). It is surrounded by the Philippine Plate and the paleo-Pacific subduction systems to the southeast and the India–China Block to the southwest. To the north, it is welded to the North China Craton by the Qinling–Dabie orogenic belt, and this amalgamation ended in the Late Jurassic (**Figure 1B**) (Zhang 1997; Faure et al., 2001; Faure et al., 2008). The subduction of the Pacific Plate began to play a significant role in the evolution of the SCC from the Mesozoic to Cenozoic (Chu et al., 2012b; Li et al., 2009; Zhang et al., 2019a, 2019b). The Early Mesozoic event in the central part of the SCC is referred to as the Indosinian Orogeny, and it was characterized by well-developed thrust faults, folds, and pervasive cleavage of the sedimentary cover as well as ductile syn-metamorphic deformation in the decollement layer and basement rocks. Some scholars have concluded that the NE–SW trending structures in the ESFTB are related to this Early Mesozoic event (Li et al., 2009; Shu et al., 2009).

2.2 Regional Geology of the Eastern Sichuan Fold-Thrust Belt

The ESFTB, located in the eastern margin of the Yangtze Block in the SCC, is recognized as a famous NNE–SSW-trending intracontinental orogeny and covers an area about 200 km wide and nearly 400 km long. The sedimentary strata are nearly continuous from the Precambrian to Cenozoic (with a total thickness of ~10 km), with several important unconformities (**Figure 3**). It is composed of two main lithological units: the Sinian to Middle Triassic marine sequence and the Upper Triassic to Late Jurassic–Early Cretaceous terrestrial sequence (Li, 2007; Li et al., 2015; Zhang et al., 2021a, 2021b, 2021c). The Neoproterozoic Banxi Group and its equivalents have generally been recognized as the folded basement of the Yangtze Block (Yan et al., 2003; Li et al., 2015). The Cambrian strata commonly consist of massive dolomite, gypsum, mudstone, and gray shale. The Ordovician strata consist of limestone interlayered with dolostone and argillaceous siltstone. The Silurian strata are composed of celadon shale and sandstone. The Carboniferous strata mainly consist of dolomite interlayered with clastic rocks and limestone. The Permian strata mainly consist of carbonate-rich rocks, whereas the Lower and Middle Triassic strata consist of limestone and dolomite layers interbedded with shale, mudstone, or sandstone. From the Upper Triassic to Cretaceous, the sedimentary series mainly occur in the Eastern Sichuan domain and are entirely continental facies sequences with red terrestrial clastic rocks (Yan et al., 2003; Wang et al., 2005; Shu et al., 2009). Based on the field exploration and seismic data, we found that most of the sedimentary stratigraphy was involved in the structural deformation system, which originated from the Lower–Middle Cambrian Longwangmiao–Gaotai regional detachment or the Lower Triassic Jialingjiang regional detachment within the core of the anticline (**Figure 4**).

From west to east, the structural style in the ESFTB varies from the Eastern Sichuan high-steep anticline belt to the Western Hunan–Hubei wide box-shaped anticline belt formed by the northeast-striking Qiyaoshan thrust fault. From north to south, in plane view, we discovered that there are distinct differences along strike based on a digital elevation map of the ESFTB (**Figure 2A**), and it can be divided into three sub-regions: 1) the northern E–W arcuate structural belt, 2) the middle NE–SW parallel structural belt, and 3) the southern N–S broom-shaped structural belt.

Due to the influence of the Dabashan Arc, the thrust structures in the northern E-W arcuate structural belt exhibit a tight arcuate geometry. The thrust belt is composed of a series of several subparallel ENE–WSW-striking anticlines. The Yunanchang, Longjuba, and Qiyaoshan anticlines and the northernmost part of the Fangdoushan anticline (**Figure 2A**) are characterized by intense folding and thrusting, and the arc-like structural belt buckles toward the NW direction in the plane. The middle NE-SW parallel structural belt is mainly composed of the Huayingshan, Tongluoshan, Mingyueshan, Jinghuashan, Fangdoushan, and Qiyaoshan anticlines (**Figure 2A**). The structure of the belt is characterized by high-steep dip angle anticlines; compared with the northern and the southern structural belts, the middle structural belt is more continuous and stable, with a parallel axis striking about N30°E. Based on the topographic profile A-A' (**Figure 2B**) and geological cross-section B-B' (**Figure 3B**), from west to east, the structural deformation system changes from trough-like folds and box folds to Jura-type folds. The southern N–S trending broom-shaped structural belt is composed of the Bayueshan, Yunwushan, Jinyunshan, Zhongliangshan, and Longwangdong anticlines from west to east (**Figure 2A**). These anticlines are branch structures of the Huayingshan anticline, and the orientations of their axes are not parallel and change from N30°E to N40°E in the west to S–N in the east.

3 EXPERIMENTAL PROCEDURE AND ANALYTICAL TECHNIQUES

The physical tectonics simulation experiments were mainly conducted to study the geological structural deformation; using the experimental model simulation method, the formation process of the orthogonal tectonic phenomena in the field was investigated, and the morphological characteristics during each stage of the deformation process

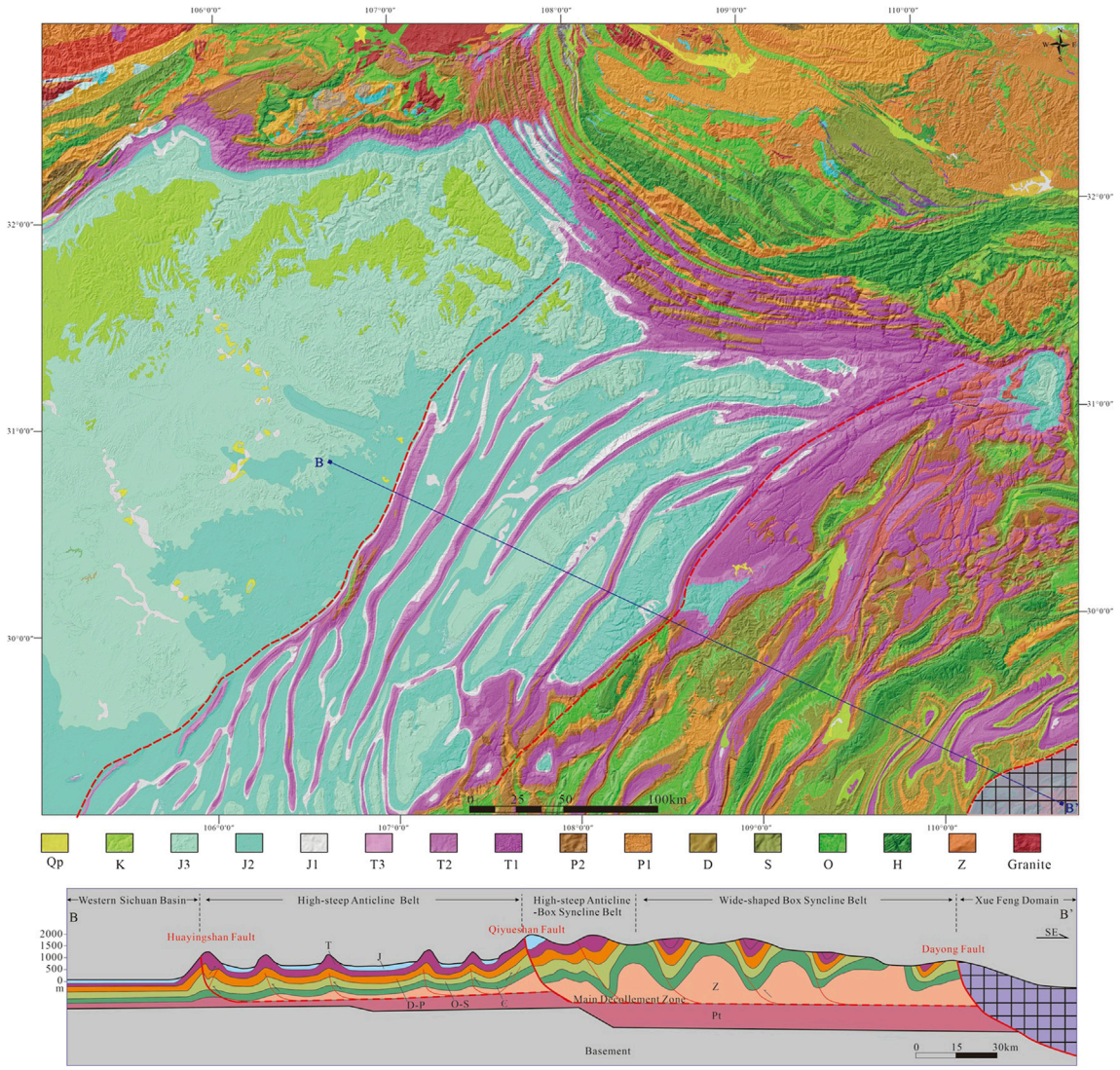


FIGURE 3 | Simplified geological sketch map and cross section of the Eastern Sichuan basin.

were observed. This is one of the most effective methods of studying the forced deformation of laminated materials (Buchanan and Mc Clay 1991; Zhou et al., 2007; Yan et al., 2016).

3.1 Modeling Strategy

The experimental setup used for the physical simulation experiments in this article was obtained from the tectonophysical simulation laboratory of the Key Laboratory of Tectonogenesis and Metallogenesis, Ministry of Land and Resources, Chengdu University of Technology (**Figure 5A**). The size of the experimental sandbox was 100 cm × 60 cm × 40 cm, and the experimental device used a hydraulic system to provide the required stress. The system can be used to conduct simulation experiments involving extrusion, tension, augmentation, bottom incision, shearing, and bottom shearing. The steps of the experimental process, according to the experimental model, included laying the experimental materials, opening the experimental control system, setting the speed and running distance of the pusher, and running the pusher to conduct the experiment. During the experiment, a digital camera was used to monitor the side and upper surfaces of the experimental model in real time and to collect the experimental data.

As was discussed by Hubbert (1937), our methodology is based on the geometry, material, dynamic, time, and boundary similarity principles, which focus on the validity of the tectonic analog experiments. Simulation experiments conducted on this basis can reflect natural processes more scientifically (Bonini et al., 2012; Yan et al., 2016).

3.2 Material Properties and Model Scaling

To produce a fold-thrust belt in our physical models, appropriate analog materials were used to simulate the upper crust. These materials were characterized by their elastic-frictional plastic behavior. We employed quartz sand, which is a granular

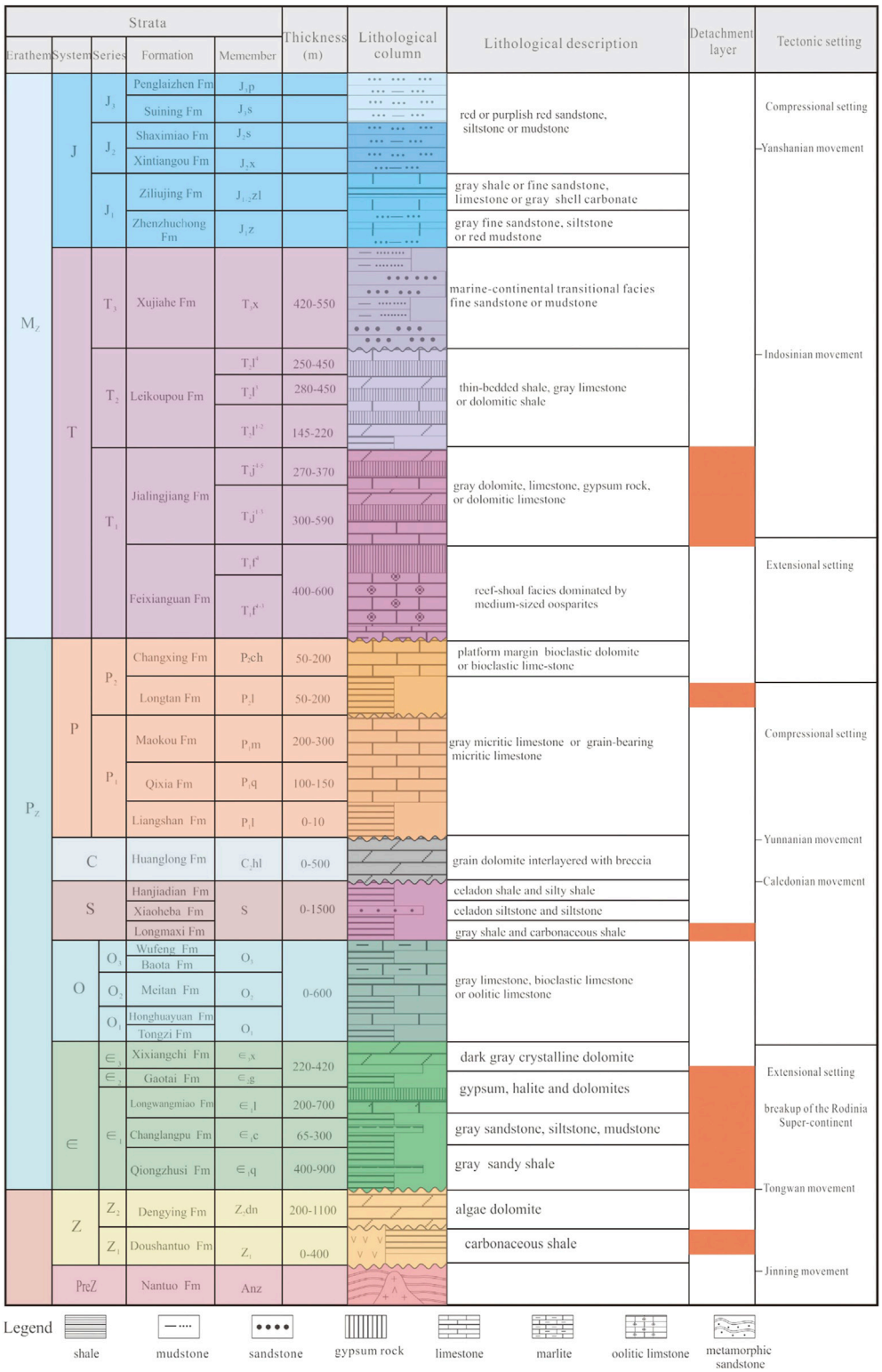


FIGURE 4 | Stratigraphic column of the Eastern Sichuan fold-thrust belt with the location of potential décollement zones (modified after Li 2015).

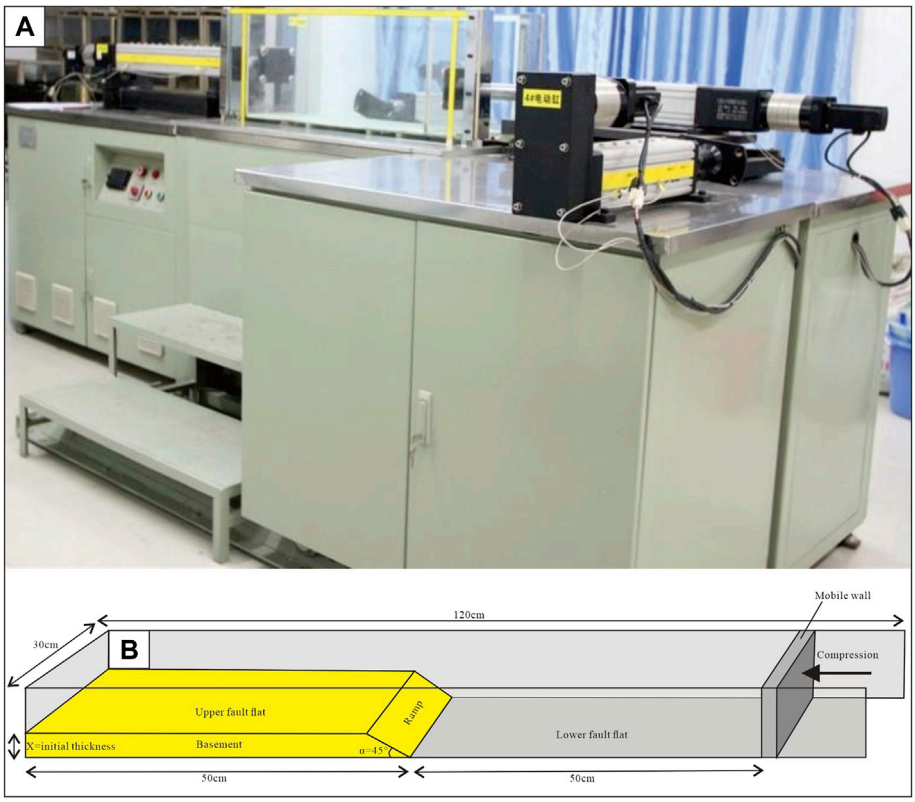


FIGURE 5 | (A) Key Laboratory of Tectonics, College of Earth Sciences, Chengdu University of Technology. **(B)** Experimental apparatus with model dimensions and details of all experiments.

material used in nearly every simulation of brittle deformation due to its potential to generate kink folds (Mulugeta and Koyi 1992). Because of its low cohesive force, quartz sand is ideal for simulating brittle deformation of the upper crust. Furthermore, we used glass microbeads, which have a lower cohesion strength than quartz sand and are therefore weaker (Panien et al., 2006) The diameter of the microglass beads used was about 0.3 mm, and the internal friction angle was about 25° (Mulugeta and Koyi, 2006). Researchers have suggested that these beads can be used to simulate relatively weak competent rocks such as carbonates, mudstone, and shale. A silica gel is an ideal material for simulating the slippage layer in the cap layer in physical simulation experiments. Silicone with a viscosity of less than 5×10^4 Pa-s has Newtonian fluid properties at low strain rates (Graveleau and Dominguez, 2008). In the experimental model, a silica gel was mainly used to simulate the paste saltstone slip layer in the septal-folded cover. Green quartz sand was used as a marker layer in the experiment, and its physical properties were the same as those of the undyed quartz sand.

The boundary conditions of the formation, thickness of the brittle/ductile layer, extrusion velocity, differential stress, basal shear stress, ductile layer shear stress, brittle/ductile ratio, shear strain rate, and geometric features of the brittle and ductile layers were focused on according to the physical simulation similarity principle (**Table 1**) in order to meet the requirements of the experimental study (Hubbert 1937). The experimental model was initially 100 cm long, 60 cm wide, and 30 cm high. A large amount of low-temperature thermochronological data indicate that the main formation age of the Eastern Sichuan fold belt is 165–75 Ma (Mei et al., 2010; Li et al., 2011; Wang W. et al., 2012). Based on equilibrium section data, previous scholars have determined that the Eastern Sichuan fold belt was shortened by a total of about 140 km during the Late Jurassic–Late Cretaceous, with a total shortening of about 32%, including 72.5 km on the southeast side of the Qiyue Mountains and 67.5 km on the northwest side of the Qiyue Mountains (Mei et al., 2010; Wu et al., 2019). Therefore, in the model, the squeezing pressure was applied from the right side to push the right active end toward the left, and the total shortening was 320 mm, with the same shortening rate of 32%. In order to reveal the maximum possibility and the most complex deformation characteristics of the sandbox model and the geological processes in the most effective timeframe, the choice of a low speed and reasonable effective extrusion speed was crucial for the mechanism of the sandbox model simulation (Zhao 2017). In the simulation test, the speed of the pushing plate was set to 0.01 mm/s so that we could successively observe a clear and comprehensive deformation process of the sandbox wedge and the construction style. In the experiment, the kinetic similarity between the physical model and the prototype is as follows:

TABLE 1 | Scaling parameters between models and nature.

Parameter	Model	Nature	Model/nature ratio (*)
Particle size (mm)			
-Dry quartz sands	0.2	-	-
-Glass microbeads	0.3	-	-
Ductile-layer viscosity	8.3 × 103 Pa s	1 × 1,018 Pa s	η^*≈8.3 × 10–15
Internal friction	0.65	0.60–0.85	u^* = 0.76~1.08
Density (g/cm3)			
-Dry quartz sands	1.3[a]	-Brittle layer 2.4–2.8[b]	ρ^* ≈0.5
-Glass microbeads	1.4[c]	-Ductile layer 2.4–2.8[b]	ρ^* ≈0.5
-Silicon putty	0.83	-Detachment layer 2.2	ρ^* = 0.38
Gravity acceleration	9.8 m/s^2	9.8 m/s^2	g^* = 1
Length, l	1 m	200 km	L^* = 5 × 10–6
Stress, σ			
-Dry quartz sands	100–150pa[b,d]	40–60 MPa 12 MPa	σ^* = ρ^*×g^*×L^* = 2.5*10–6
-Glass microbeads	30pa[b,e]	-	-

[a]*Wang et al. (2016)*
[b]*Gomes (2013)*
[c]*Panien et al. (2006)*
[d]*Eisenstadt and Sims (2005)*
[e]*Krantz (1991)*

$$\sigma^* = \rho^* \times g^* \times L^*, \quad (1)$$

where σ^* is the stress ratio between the model and the prototype; ρ^* is the density ratio; and g^* and L^* are the gravitational acceleration and length ratios, respectively. The experiments were conducted in a normal gravity field; so, the ratio of the gravitational acceleration was $g^* = 1$. The density ratio was $\rho^* \approx 0.5$, i.e., the density of the experimental material was approximately equal to half the density of the stratum.

In the experiment, the 1000-mm model represented about 200 km of the geology in Eastern Sichuan; so, the similarity coefficient was about

$L^* = 5 \times 10^{-6}$ and 1 cm = 2 km in the model.

The viscosity of the stratum was about 1×10^{18} Pa·s. The viscosity of the silicone was 8.3×10^3 Pa·s. The viscosity similarity factor was $\eta^* \approx 8.3 \times 10^{-15}$.

$$\eta^* = \sigma^* \times t^*. \quad (2)$$

Based on **Eqs 1**, **2**, $t^* \approx 3.3 \times 10^{-9}$, i.e., 1 h of simulated time was equal to 3.5×10^4 a of geological time.

3.3 Experimental Setup and Method

It is better to design multiple groups of comparison tests for the experimental design because through comparison of multiple groups of experiments, the influence of each variable in the model on the experiment can be analyzed and the influences of the experiment-related elements on the experiment can be clarified. According to the specific geological formations in the study area, the model size and the running rate of the pusher were calculated according to the similarity ratio principle, and the experimental model was finally designed. We conducted six experiments in a 100 cm (length) × 30 cm (width) × 30 cm (height) deformation box (**Figure 5B**). The box was composed of a flat, horizontal base plate bounded by two fixed lateral glass walls and two vertical plastic walls, one of which was mobile (the backstop) and the other was fixed. The model deformation was accomplished by moving the mobile wall using a screw-jack controlled by a stepper motor. All of the model devices are shown in **Figure 6**. In sandbox analog models, the friction along the glass walls is not negligible, but the impact of the lateral friction is even greater in models with basal friction (Vendeville 2007; Soulouniac et al., 2012). However, these negative factors can be totally avoided if a thin silicone coating is applied to the lateral walls (Costa and Vendeville, 2002; 2004; Koyi and Cotton, 2004). We reduced the influence of the lateral friction between the sand and the glass sidewalls by lubricating the glass walls with a viscous coating, thus minimizing the lateral friction that could affect the kinematics during the experiments.

The tectonic shortening rate in the Eastern Sichuan area in the Mesozoic (165–75 Ma) was about 32%. The Qiyue Mountain Fault was an important pivot for the transition from septal to septal folding and was a product of the northwest migration of the shallow part of a pre-existing high-angle fracture. The dip angle of the Huaying Mountains Rift controlled the wavelength of the septal folds, and a steeper dip angle (45°) was more favorable for the development of typical septal folds (Wu et al., 2019).

The sandbox simulation experiments were divided into six groups (**Figure 6**), and the specifications of the layout of the materials in the model were 1000 × 300 × 30 mm (length × width × height). In experiment 1, only quartz sand was used as the experimental material to simulate rigid ground. There was a 10-mm basement step at the fixed end above the extrusion end, and the step surface had a dip angle of 45°. Half of the 250–750-mm high and low step surfaces were laid at each side. In experiment 2, as a comparison experiment to experiment 1, the other conditions were the same, but the quartz sand was replaced by microglass beads (**Figure 6B**). In experiment 3, the

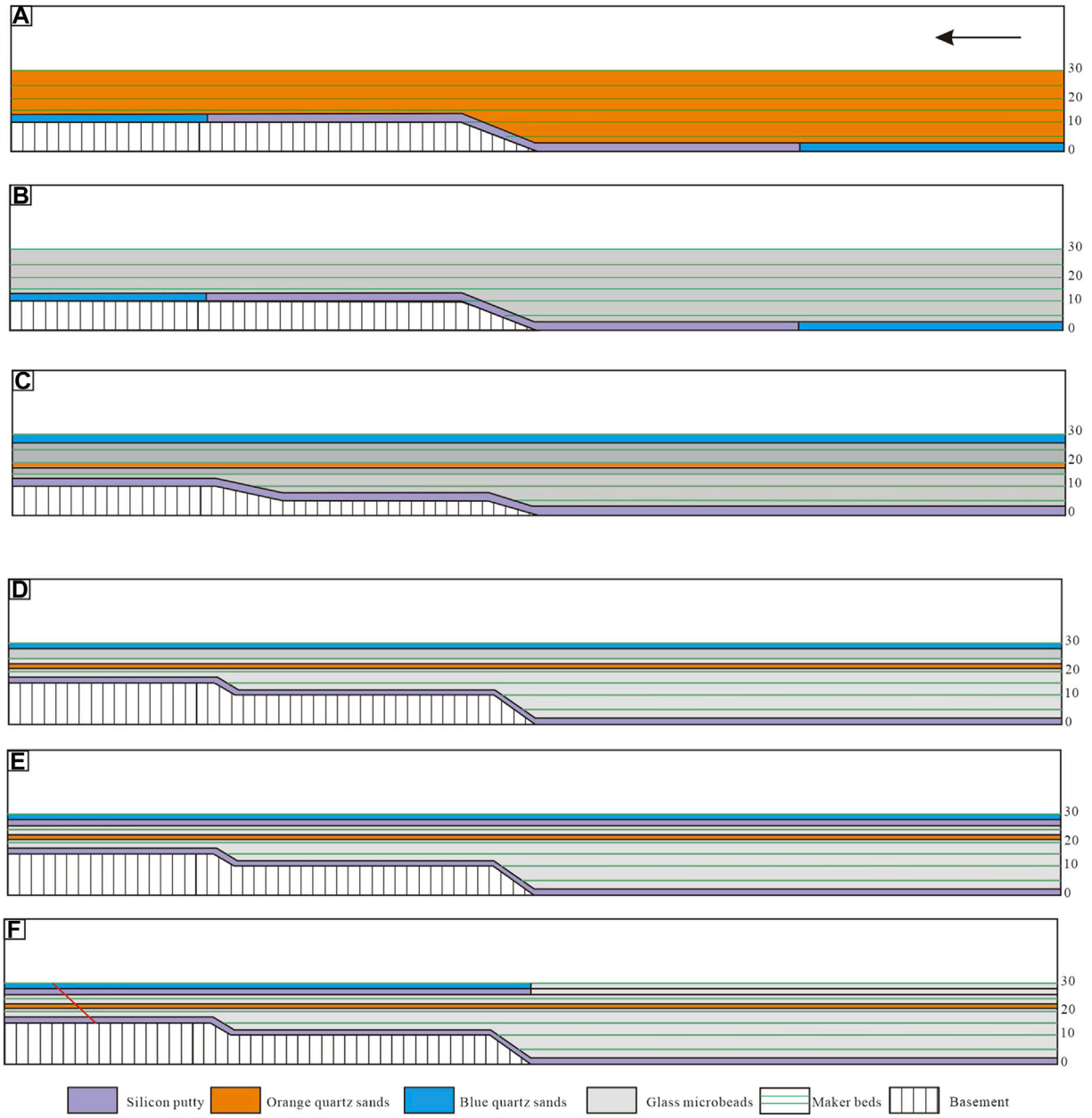


FIGURE 6 | Sketch showing the model configurations.

substrate step was set to a two-step substrate rising state. One step of 500 mm at the substrate, followed by another 750-mm step, constituting a step above the level of 5 and 10 mm rigid substrate (**Figure 6C**). The micro-glass beads were used to form the basal layer, and 2.5-mm quartz sand was used to form the middle and top layers to simulate a rigid ground sandwich and a cover layer, respectively. In addition, 3 mm of silicone was uniformly spread across the bottom of the model. In experiment 4, as a comparison experiment to experiment 3, the materials used were the same, but the heights of the two steps were changed. The steps for experiment 5 were the same as those for experiment 4, but a 2-mm-thick layer of silicone resin was added to simulate double-layer slip tectonic deformation (**Figure 6E**). Experiment 6 was based on experiment 5, but only the second layer of silicone resin was laid on the elevated part of the basement, and the silicone resin and quartz sand cover were replaced by microglass beads in the unelevated area of the basement, which is consistent with the regional geological map. This is in general agreement with the fact that the Triassic and Jurassic strata in the intertrench area have been almost stripped away, and a metal baffle with an inclination of about 45° was added at

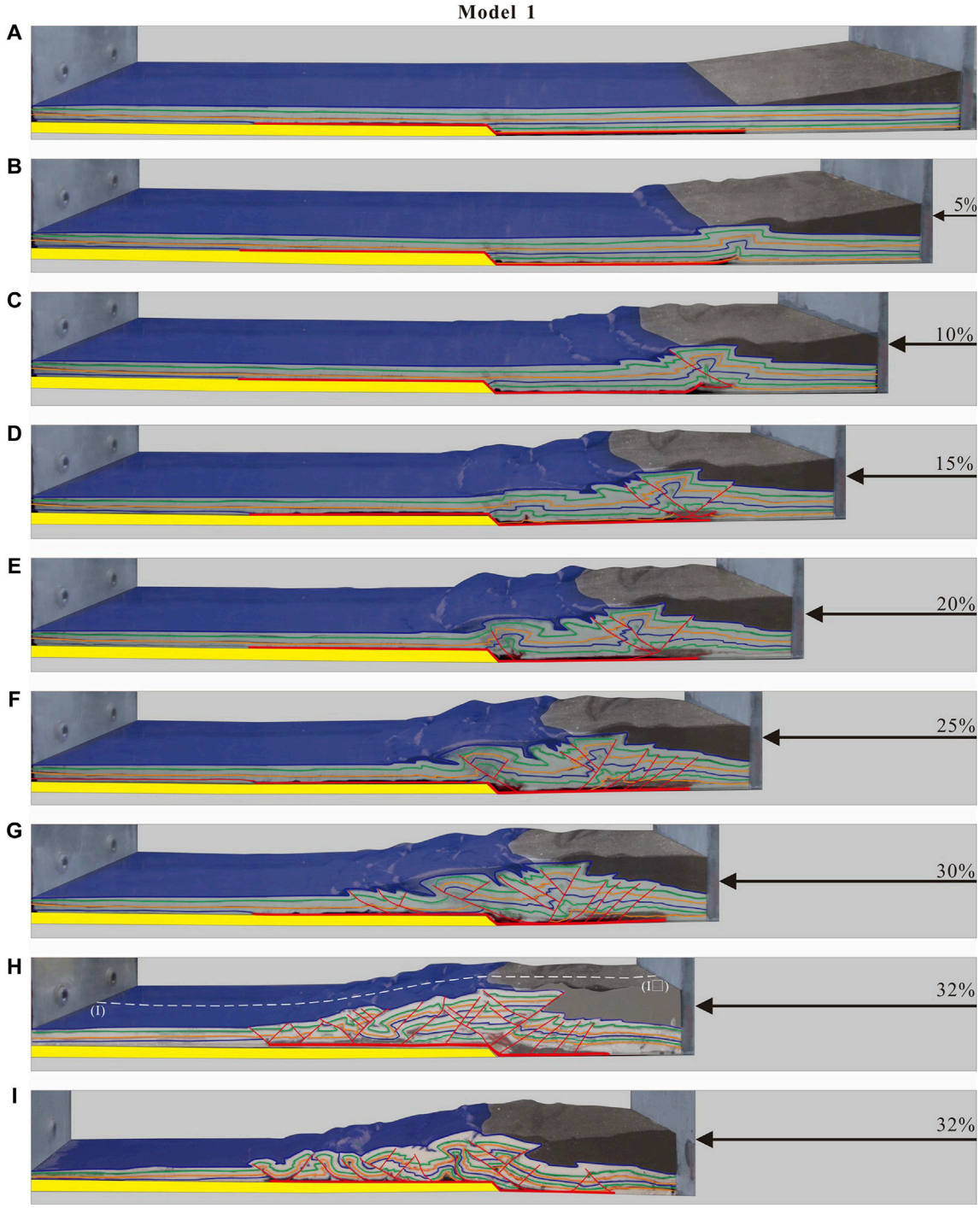


FIGURE 7 | Sequential deformation features of model-1.

the fixed end of the model to simulate the pre-existing polished fracture (**Figure 6F**).

3.4 Experimental Limitations

The complexity of natural tectonic deformation, such as multi-phase superimposed deformation, syn-tectonic deposition, and the influence of denudation on staged-growth deformation, was not considered; so, the model did not fully compensate for the control of the deformation due to denudation. The model starts with the main controlling factors and simplifies the influence of the microscopic heterogeneity according to the composition of the stratigraphic rocks. This is

an idealization and simplification of the geological prototype, especially because there are multiple sets of slip layers in the area, while the model uses a maximum of two slip layers. It should be noted that deep geophysical data such as the seismic reflection profile and magnetotelluric profile were analyzed (Zou 2011; Deng et al., 2014). There are some limitations in the distribution of the gypsum layer in Eastern Sichuan, and the heterogeneity of the slippage layer could not be fully reflected in the experiments. Thus, the control of the influence of the slip layers on the cover in the experimental model was not ideal, and it is necessary to further explore the influence of complex factors, such as multi-layer slip layers plus the basement morphology, on the folded and alluvial zones in East Sichuan.

4 RESULTS

4.1 Group 1

Figure 8 illustrates the seven deformation stages in experiment 1. In the shortening stage of the extrusion, a low amplitude slip knee fold was formed at the junction of the silicone-layered bottom plate and the non-silicone-layered bottom plate, and this knee fold further developed into a box fold (**Figure 7A**). As the compression rate increased, a tile-like recoil wedge formed in front of the movable baffle, and the undeformed sand body kept proliferating into the wedge to form a new recoil fault. The size of the wedge increased continuously. When the compression rate was 15%, the first recoil fault was formed, which only absorbed a very small part of the displacement, after which it soon ceased to be active. At a shortening rate of 20–32%, the previously formed fault rotated, and the fault yield changed as the deformation was continuously transmitted. The recoil fault yield became more gentle, and conversely, the recoil fault yield became steeper, leading to gravitational slip collapse, causing the upper plate of the fault to slide downward along the fault surface, thus causing the fault slip distance to gradually decrease as well.

From the cross-section (**Figure 7I**), it can be seen that the new rebound faults were developed under the old ones, and they extended in a sequential manner toward the foreland, i.e., in a foreshortened manner. Then, the other tectonic units were formed one by one in the foreland in the same way (**Figures 7E–H**), and some small recoil faults began to develop in the upper and middle tectonic layers, slightly deforming the strata.

4.2 Group 2

In experiment 2, the quartz sand in experiment 1 was replaced with microglass beads, and at first, the initial horizontal stratum began to slide and form the first fold (d = 5%) along the silica-lined and nonsilica-lined locations under the compression applied by the right movable baffle (**Figure 8B**). At d = 10%, small fault propagation folds began to develop and the model became active at the basement uplift site and was the first to form a second fold (**Figure 8C**). As the extrusion continued, the fault propagation folds led to the uplift of the overlying strata. The front flank of the fold became steeper, while the back flank became shallower, and inverted folds (d = 15–20%) were gradually formed (**Figures 8C, D**). At this point, the basement tectonic layer had a tendency to thicken, but the overall deformation was not obvious, and the model deformation in this stage did not occur sequentially from right to left. Then, slight uplift (d = 25%) occurred and shifted successively forward on the elevated basement surface (**Figure 8F**). When the shortening rate was d = 30–32%, the slip effect propagated farther, and three more tightly closed back-slope folds and three wide slow oblique style folds were formed in turn at intervals (**Figures 8G, H**). At this time, the model results were closer to the slot-blocking transition zone tectonic morphology. At this point, the model results were closer to the tectonic pattern of a channel-blocking transition zone.

4.3 Group 3

Figure 9 shows the overall simulation process of experiment 3. In this experiment, in order to explore the influence of the basement uplift height and the combined morphology of energetic and non-energetic strata on the experimental simulation results, the basement steps were set at two step-like basement uplifts; and silicone, microglass beads, and quartz sand were used to represent the actual stratigraphic slippage (e.g., paste salt rock and shale), non-ergodic layers (e.g., thin-slabbed tuff and dolomite), and andergodic layers (e.g., thick layers, massive tuff, and sandstone) in the East Sichuan area, respectively. The stages of the entire evolutionary process are explained later in detail.

At d = 5%, the basal tectonic layer started to shorten locally under the compression applied by the right movable baffle, leading to folded uplift of the overlying strata (**Figure 9B**). Unlike in experiment 2, the central tectonic layer and the upper tectonic layer in experiment 3 did not change uniformly, with thickening or thinning anomalies between the layers, forming a fold deformation pattern with thick top and thin flanks. When d = 10–15%, the basement tectonic layer gradually developed basement retrograde faults (three at this time) (**Figures 9C, D**). These basement retrograde faults together formed the double basement structure, which led to the thickening of the strata in the vertical direction. However, the actual increase in the stratigraphic thickness was not significant because the angle of the retrograde faults at this point was not high and the break distance was small. As the baffle continued to move to the left, at a shortening of d = 20%, plastic flow occurred on the first elevated step, i.e., there was local deformation at the leading edge, resulting in a small amount of uplift of the overlying strata (**Figure 9E**). The occurrence of deformation indicates that the stress was no longer confined to the double structure at this point, and it begins to be transmitted forward. When d = 25–32% (**Figures 9F–H**), the number of basement retrograde faults on the first-stage bench increased again, and all of the faults broke through the upper tectonic layer, allowing more fold patterns to develop on the leading edge of the retrograde region. The final section morphology of this experiment is shown in **Figure 9I**. The second-stage terrace experienced

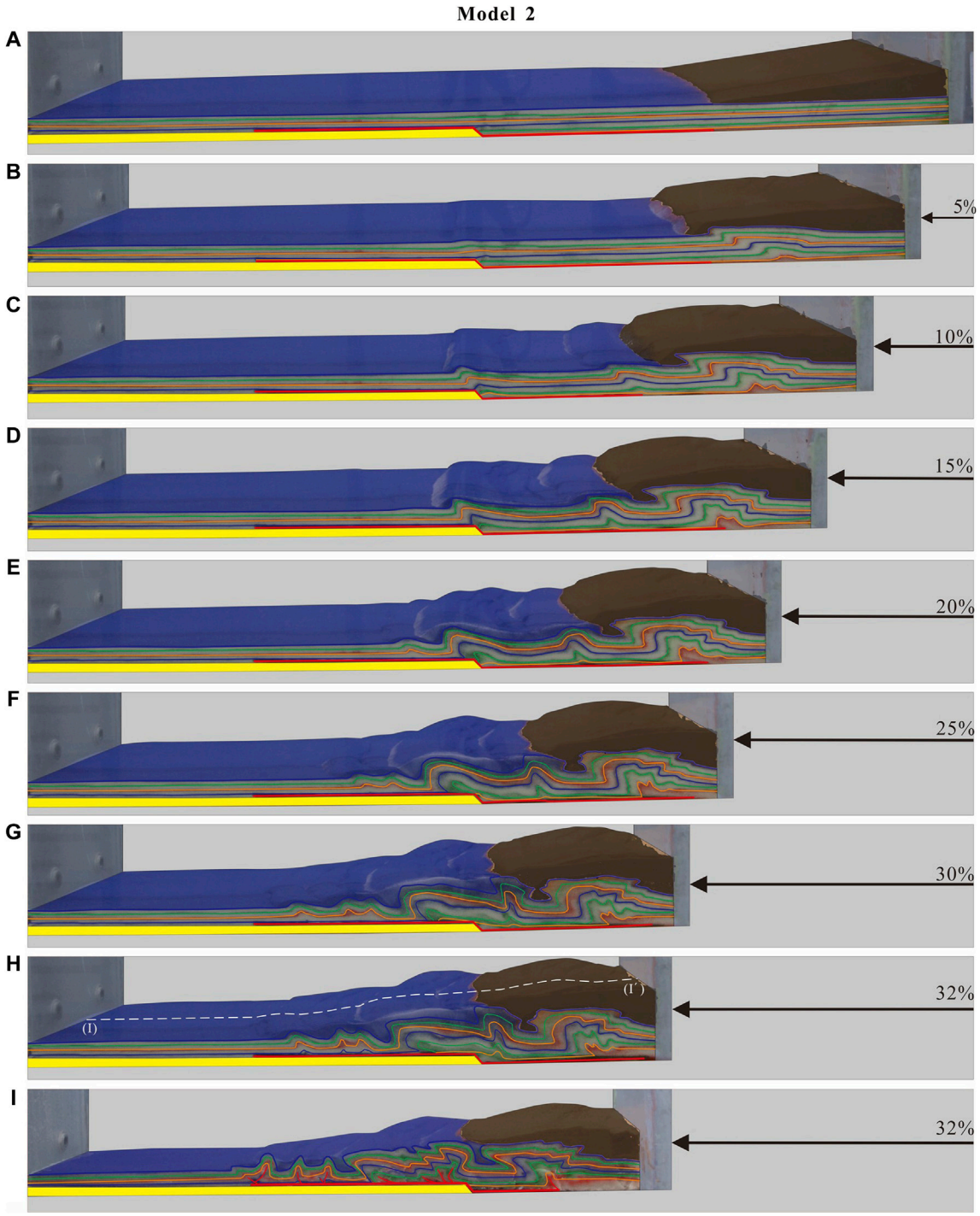


FIGURE 8 | Sequential deformation features of model-2.

almost no transfer deformation, and a box-like backslope with an oblique style with wavelengths of nearly 1:1 in the frontal zone of the first-stage terrace was formed, with steeper production on both flanks and flatter and wider turning ends. This is different from the high steep and tightly closed backslope morphology in the Eastern Sichuan area.

4.4 Group 4

Considering that the final deformation of experiment 3 did not propagate above the second step surface even when its shortening rate reached the maximum, in order to discuss the effect of increasing the height of the basal uplift and thinning the thickness of the cover on the propagation distance, in experiment 4, the

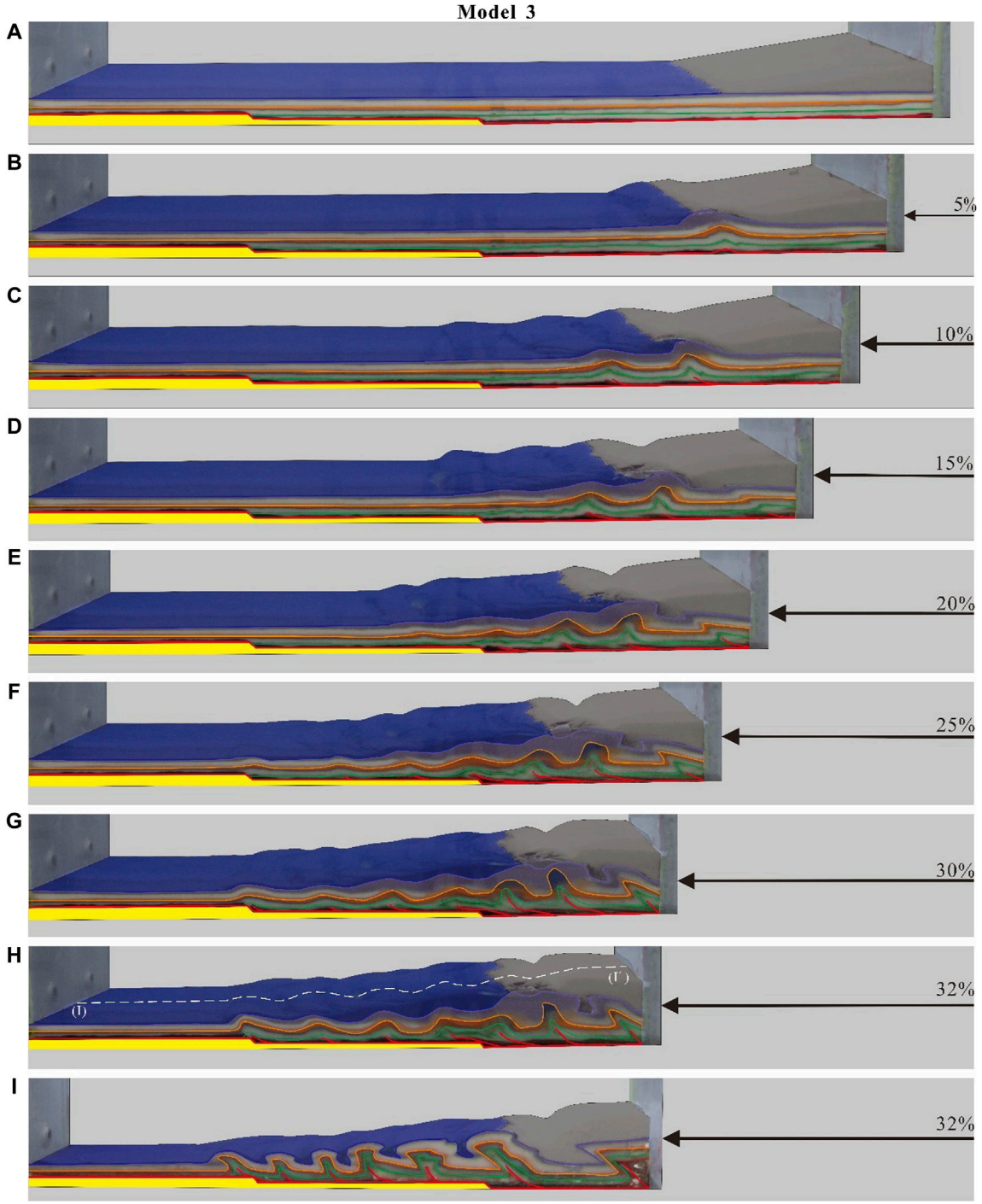


FIGURE 9 | Sequential deformation features of model-3.

heights of the two steps were increased by 5 mm based on the setup of experiment 3 (**Figure 7D**).

When the shortening rate was d = 5%, a box-like slip fold first developed near the extrusion end (**Figure 10B**); and at the same time, a slight bulge developed in the first step elevation area due to the blocking effect of the rigid base plate. As the extrusion proceeded, when d = 10%, a foreshortening fault developed on each of the two front flanks of the first two box folds, and the faulting also made the original single-fold pattern more complex (**Figure 10C**). When d = 15%, a third fold formed between the first two, and the backslope pattern was steep on the front flanks and shallow on the back

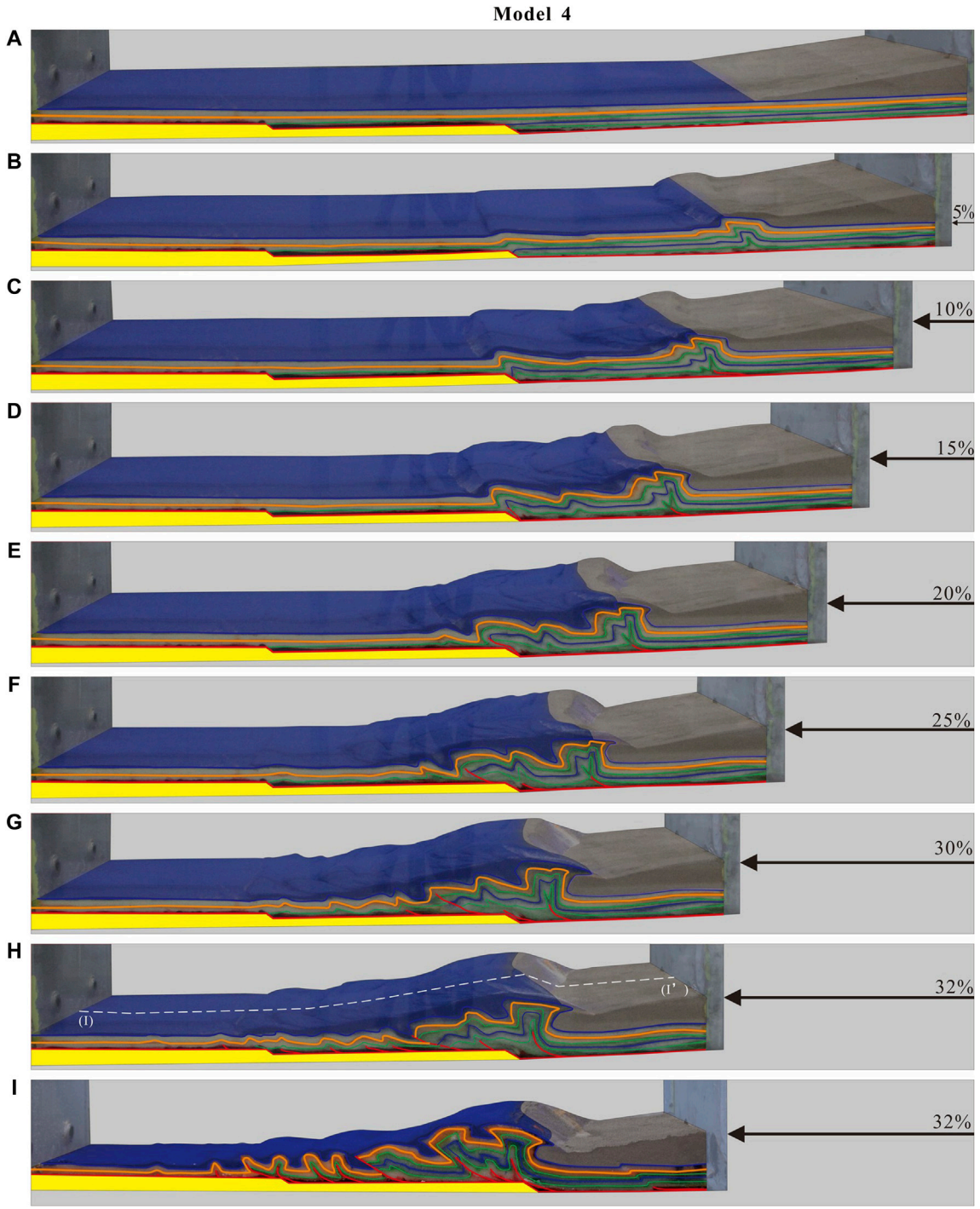


FIGURE 10 | Sequential deformation features of model-4.

flanks at this time (**Figure 10D**). As the shortening rate increased (d = 20–25%), the fold wavelengths in the trailing edge tectonic zone were compressed and shortened. At this time, the oblique was tightly closed, while the dorsal slope was wide and shallow, and the model exhibited a septal groove fold style (**Figure 10F**). It can be clearly seen from the cross section that when d = 32% (**Figure 10I**), the tectonic units were produced successively on the three platforms (high, middle, and low) formed by the two-step height change sites. Both experiment 4 and experiment 3 had the same total shortening rate, but model 4 developed significantly more tectonic units than model 3; so, the elevation of the base ahead

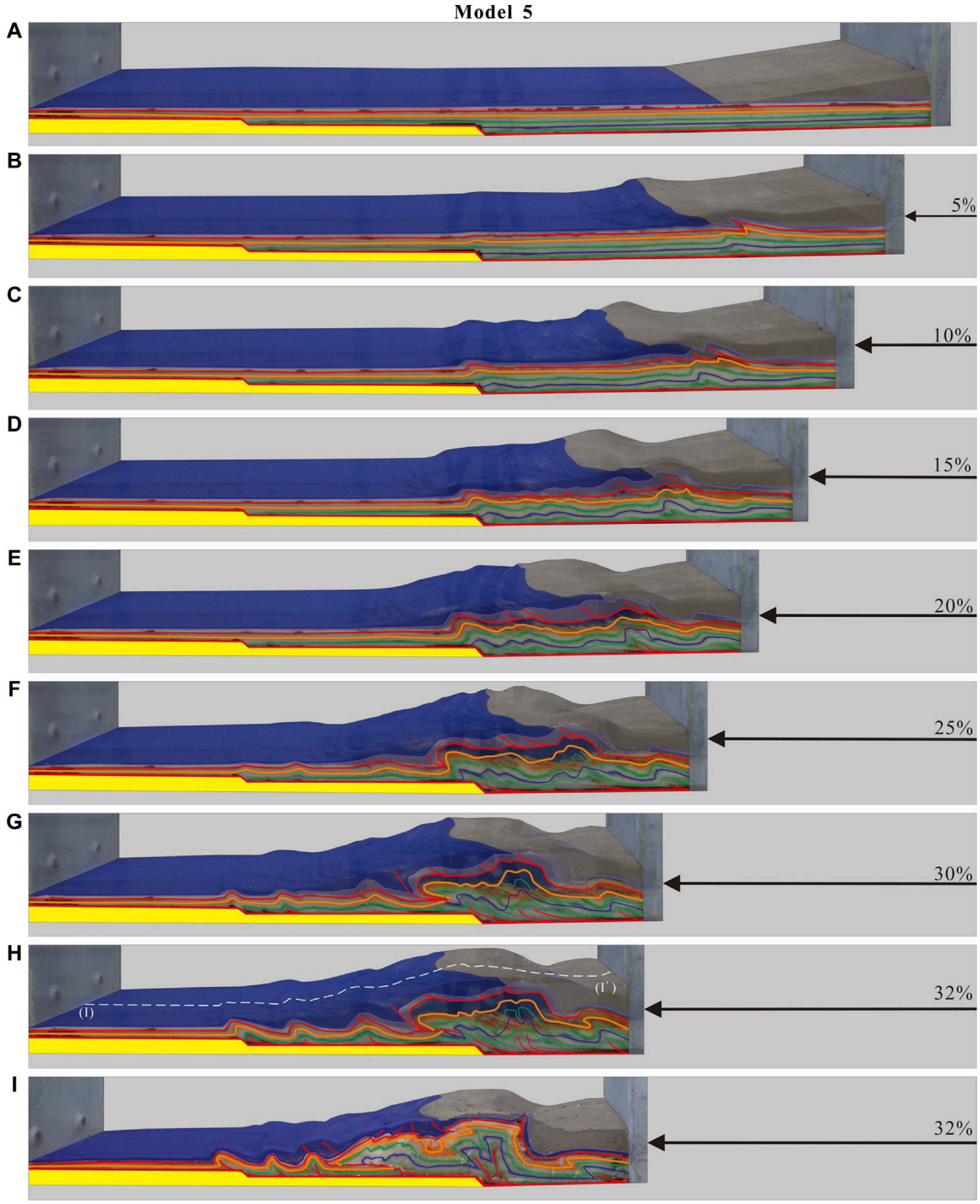


FIGURE 11 | Sequential deformation features of model-5.

of the extrusion and the thinning of the cover thickness obviously caused the slip action to propagate further. The folds developed on the highest terrace were characterized by narrow dorsal and wide diagonal folds, and the model's tectonic frontal zone contained the beginning of a Jurassic-style fold pattern.

4.5 Group 5

In experiment 5, we set up two sets of slip layers in the model to study the overall kinematic evolution of the fold punch-off system, and the bottom layer of silicone was used to simulate the gypsum and shale of the Lower–Middle Cambrian Longwangmiao Formation and Gaotai Formation. The upper

silicone layer was used to simulate the dark gray gypsum-bearing dolomite of the Lower Triassic Jialingjiang Formation.

Figure 11 shows the deformation process of model 5 with increasing shortening. When the compression was d = 5%, model 5 was also the first model in which the upper tectonic layer was the first to appear in the antecedent direction of the retrograde fault. The bottom of the upper plate of the fault thickened, the thickness of the top layer remained basically unchanged, the level bent, and a fault propagation fold was formed. The deformation was weaker in the lower tectonic layer than in the upper tectonic layer. Subsequently, the second and third faults, which rushed to the foreland in the direction of the first fault, formed in succession, and their development process was similar. The upper plate of the fault formed fault propagation folds (d = 10–15%). As the shortening increased, the thickness of the upper layer basically remained unchanged, the fault no longer developed, and the level continued to bend under the influence of the change in the fault production. The lower tectonic layer deformed relatively strongly, forming fault propagation folds, and the fold pattern was mainly compound (d = 20–25%). Under continued compression to 32%, i.e., to the final form of the model, due to the action of the double-layered slip layer, the model underwent layered deformation. Finally, the model's morphology became very complex near the root zone near the extrusion end, while the frontal zone transitioned from the compartmentalized groove zone fold style to the compartmentalized fold style. It should be noted that the propagation distance of model 5 was shorter than that of model 4, and the deformation propagation did not reach the highest step surface. This may have been caused by the formation of more foreshortening fault displacement in the upper slip-off tectonic layer during the extrusion process, which absorbed a considerable proportion of the energy.

4.6 Group 6

Based on the information gained from the results of experiment 5, we simulated the actual geological conditions of the ESFTB. We made the following changes to the setup of experiment 6: first, we kept the double-layer slip system composed of the upper and lower silica resin layers at the fixed end, and since the tectonic layers above the Jialingjiang Formation in the western part of Xiangjiang have basically experienced denudation, the upper slip layer on the mobile side was eliminated, and all of the silica resin and quartz sand on this side of the model were replaced with microglass beads. Second, considering that the low-temperature thermochronological data show that the polished backslip formed earlier than the adjacent backslip to the east (Richardson et al., 2008; Wang P. et al., 2012), a metal sheet with an inclination of 45° was added to the highest step plane at the fixed end of the model to simulate the pre-existing polished fracture (**Figure 7F**).

The seven stages of the deformation of model 6 are shown in **Figure 12**. When d = 5%, the extrusion end and the first basement height uplift site were the locations of the stress concentration, and two boxed backslopes were formed first, with the axial surface tending to slope toward the extrusion end (**Figure 12B**). When d = 10%, the sequence of formation of the tectonic units did not develop one by one toward the front edge, and the stratum began to uplift between the two backslopes. When d = 15% compression, two vectors and three backslopes were formed at the back edge (**Figure 12C**). As the compression continued to increase (d = 20–25%), the backslope became wider and shallower, while the diagonal became increasingly more tightly closed, forming a typical septal fold (**Figure 12D**). During this stage, fault slip folds started to form on the first uplift plane and at the second uplift site. It can be seen from the model that the main slip layer controlling the deformation at this time was the lower slip layer (**Figure 12E**). In contrast to the previous experimental model, when d = 25–30%, the deformation of the physical model propagated quickly to the left, and folds began to rumble both on the third step plane and at the location where the metal sheet was buried, forming three tightly closed backslopes. The model cross section at d = 32% shows that the overall tectonic style of the section was dominated by the development of an extrusion-formed stacked tile structure (**Figure 12I**), and the main tectonic deformation occurred between the upper and lower silicone layers, with strong stratigraphic deformation between the silicone layers and the development of multiple backlash fractures and fault-related folds. The model's trailing edge zone exhibited a typical septal groove style of folding, and the leading edge zone exhibited a typical septal block style of folding.

5 DISCUSSION

5.1 Controls on Modeled Structural Styles

Model 1 was capped by quartz sand, and the capping deformation was dominated by faults. However, folds were difficult to form, and even when they were formed, they were quickly destroyed via fault modification. In model 2, the quartz sand was replaced with microglass beads. The structural style formed was dominated by folds, and the fracture did not damage the fold flanks to a large extent. Therefore, the folding-impulse fault zone deformation style was influenced by the brittle shear strength and basal ductile shear strength to a certain extent. Moreover, the lithology of the cover layer in the folding area should not be that hard or soft in the deformation stage; otherwise, a series of foreshortening stacked tile-like recoil pushover structures and recoil fault structures will form.

Model 2 deformed significantly in the layer above the silicone layer, while the non-silicone layer was not deformed or was insignificantly deformed, indicating that the silicone slip layer effectively reduced the friction at the bottom of the model. In addition, the slip layer was necessary for the formation of slip faults and fault-related folds, and it controlled the overall evolutionary process of the ESFTB. From the deformation propagation process, the lower burial depth of the slip layer and the thicker cover layer in models 1–3 compared to models 4–6 limited the effective propagation distance. The formation sequence of the tectonic units did not develop from the extrusion end to the leading edge one by one. The units developed earlier at the basement uplift site or near the basement friction change zone, and the tectonic units at these locations entered the active state earlier, thus increasing the transmission distance of the slip layer in the leading edge direction. It should be noted that the

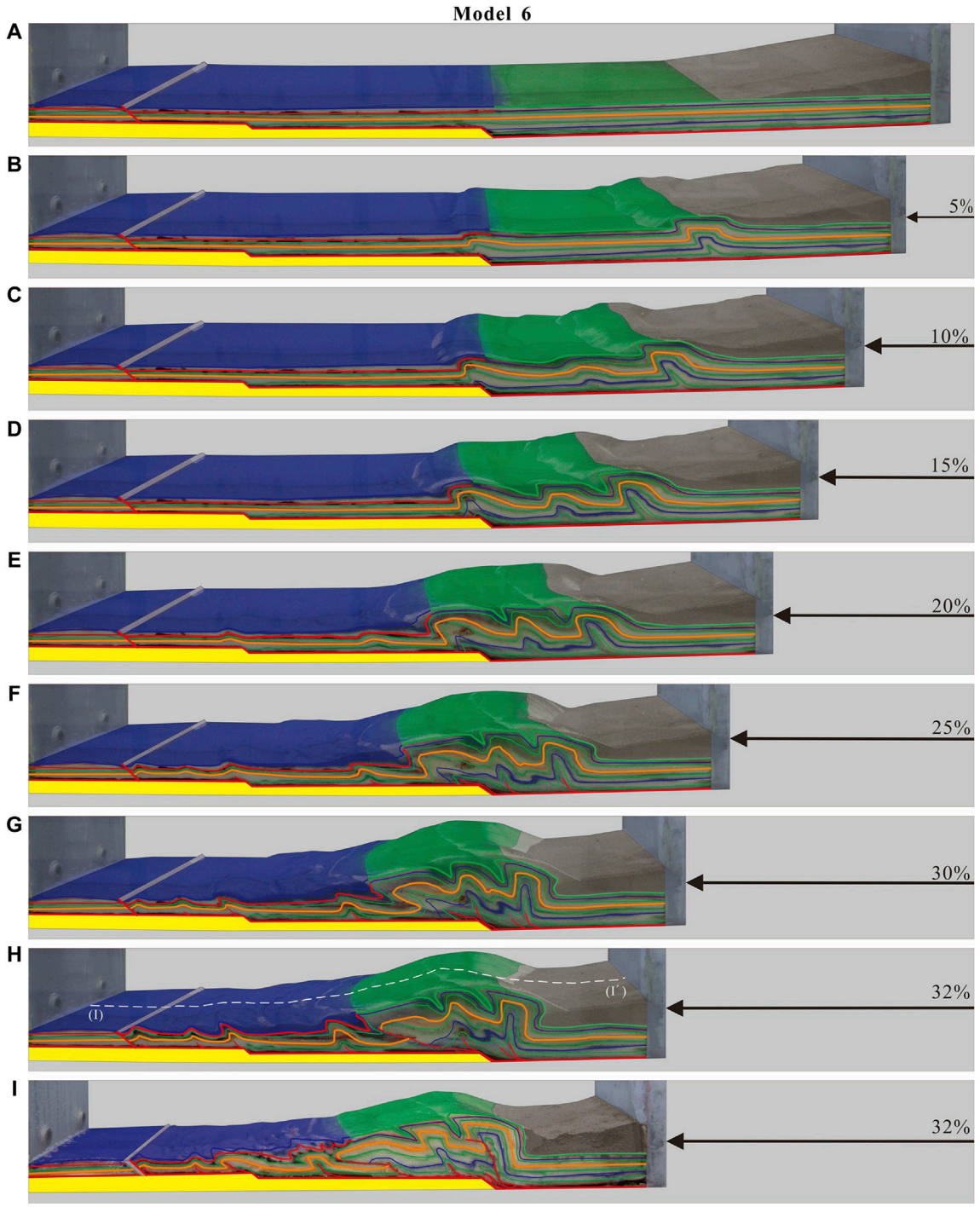


FIGURE 12 | Sequential deformation features of model-6.

upper slip fault in the trailing edge tectonic zone in model 5 absorbed more of the displacement, which may be the main reason for its shorter transmission distance compared with that in model 4. In the model containing two sets of slip layers, the positive retrograde fault propagating upward from the bottom slip layer was the main deformation mode, and its propagation mode was forward spreading. The fault broke through the quartz sand layer without breaking through the upper slip layer; so, the rock layer was mostly a retrograde fault under the upper slip layer, while it bent above to form back-slip folds.

Based on the deformation pattern of models 3–6, the folding of the microglass bead layer (non-ergodic layer) was mainly

controlled by bending flow deformation, and the material between the layers appeared to thicken or thin abnormally, forming two types of folding deformation patterns: 1) thin top and thick flank and 2) thick top and thin flank. When the quartz sand layer (dry layer) was subjected to extrusion fold deformation, it exhibited a bending and sliding fold pattern, and the thicknesses of the vertical layers were basically equal, i.e., the layers of the folds were basically in line with the concentric fold law. However, by changing the elevation height of the basement in the model, the cover layer with a larger thickness above the slip layer easily formed a septate fold. The ESFTB is controlled by boundary fractures, the crystalline basement in the lower crust, and the overlying Cambrian and Triassic slip layers. The foreshortening fault developed at the foremost edge of the model is similar in nature to the Huaying Mountain fault, and the location of the depth change of the slip layer in the model is comparable to that of the Qiyue Mountain fault and Dayong fault. When the model's shortening rate reached 25%, the deformation of the physical model began to accelerate. This stage corresponds to the tectonic deformation stage in the Yanshan period. This is consistent with the low-temperature thermal chronology data obtained in previous studies and the equilibrium section evidence, which indicate that during the Mesozoic, the strata in the study area experienced a rapid expansion of faults and a rapid increase in the fold amplitude (Mei et al., 2010; Li et al., 2011). The shortening rate of the Eastern Sichuan fold zone at the end of the experiment was about 32%, and the total shortening was about 140 km. The ESFTB developed from southeast to northwest in the order of snow peak uplift, slotted tectonic zone, slot-file transition zone, and Middle Sichuan weak deformation zone. By changing the boundary conditions of model 6, simulation results that were in general agreement with the geological prototype were finally obtained (**Figure 3B**). Similar to the natural geological structures, model 6 shows that the Western Hunan–Hubei domain is dominated by trough-like folds, while the Eastern Sichuan domain is dominated by high-steep anticlines.

5.2 Structural Characteristics of the Fold and Thrust Belt

The tectonic style of the study area is a typical folded-alluvial belt style, and the geomorphological features are extremely complex, which makes analyzing the tectonic style very difficult. The uplift of the landforms in western Hunan–Europe was large, while the landforms in Eastern Sichuan are low overall but are locally high and steep (**Figure 2D**). The tectonic style of the study area varies significantly from one tectonic unit to another. A large number of previous studies have shown that the overall tectonic characteristics are that the cover layer slipped and deformed above the basement. A large number of reverse faults were developing, and the cover fold slipping surface was mostly located in the Cambrian system above the Aurora system. The top interface of the basement was the deepest slip boundary, and the cover layer and the basement constituted a significant tectonic incompatibility. The main deformation was concentrated in the central tectonic layer (S-T), and the regional stress field and basement fracture control influenced the style of the deep and shallow tectonic assemblages in the study area, resulting in a certain degree of differences from east to west (Liu 1995; Ding et al., 2005; Mei et al., 2010). The tectonic zone in western Hunan–Europe is strongly deformed, and the basal Paleozoic strata have been uplifted up to the surface, forming a series of folds with a wide backward slope and a tight backward slope. The tectonic style is a typical basal-involved septal fold structure. The tectonic zone in Eastern Sichuan is steep and complex, but the stratigraphic deformation is weaker than that in western Hunan–Europe. Regarding the surface deposition in the Triassic and Jurassic systems, on the plane, the tectonic style is a septal fold structure with a wide and slow oblique and tight backward slope.

From the available seismic analysis results (**Figure 13**), the study area was influenced by the basement slip fault, which caused significant uplift and deformation of the tectonic layers, and the large pushover fault that developed at the back edge of the deformation allowed coordinated deformation. It cuts through all the tectonic layers and makes a certain degree of connection between them; so, the deformation characteristics of each tectonic layer tend to be consistent, while the deformation of the layers is different (Zhang 2019). In the vertical direction, the seismic profile exhibits obvious tectonic differentiation, and the general rule is that the upper tectonic layers are concentric equal-thickness folds, which are tectonically complete, tightly closed, high, steep, and large in scale. The fractures in the wings of the energetic rock folds in the central tectonic layers are very well developed, and the non-energetic layers located above and below them often underwent plastic flow and formed uncoordinated folds with thick wings and thin tops or thick tops and thin wings. The lower tectonic layer still experienced concentric and equal-thickness folding, and the structure is nearly symmetrical, gradually becoming shallower downward. In addition, the two flanking dip-axis faults often form a Y-shape and then disappear at the bottom of the crystalline basement (Li 2015).

Based on the results of the physical simulation experiments, it was concluded that large thrust faults developed at the deformed trailing edge of the study area only when there was a basement slip layer, and the slip layer underwent multiple transgressive uplift events from southeast to northwest. In the location where the basal slip layer was uplifted, rebound faults and anticlinal faults were more likely to develop, the formation mechanism of which was lateral and vertical upward flow of the basal slip layer under the extrusion stress. During the extrusion process, recoil faults easily formed between the adjacent slip layers in the vertical direction, leading to stepwise uplift of the basal slip layers, and the middle-superior tectonic layers were further developed on this basis. This phenomenon was also confirmed during the physical simulation experiments.

5.3 Deformation Evolution and Mechanisms

Regarding the analysis of the kinematic extension process of the East Sichuan fold-splash belt, considerable research has been carried out on this topic, and various models of the deformation extension genesis have been proposed (Liu 1995; Li et al., 2002; Yan et al., 2003; Hu et al., 2009; Ding et al., 2005; Ding et al., 2005;

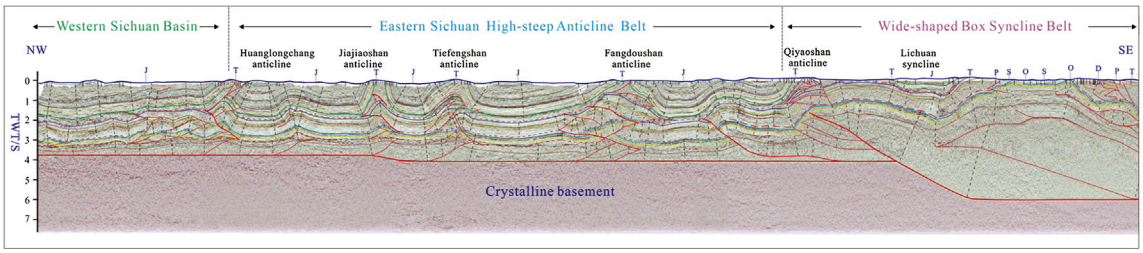


FIGURE 13 | Interpreted seismic section across the ESFB (modified after Zhang 2019).

Ding et al., 2008; Mei et al., 2010; Li et al., 2015; Yan et al., 2016; Gu et al., 2021). The genesis of the Eastern Sichuan fold-fault zone has been described by previous authors, and their results can be summarized as the following four main approaches: 1) the two backs and one break theory (Li et al., 2002); 2) the fault traction fold theory (Yan et al., 2003); 3) the external stress theory (Liu 1995); and 4) the cohesive difference and overburden pressure theory (Zhang 1997). According to Li et al. (2002), the study area has undergone a tectonic evolution process of early septal fold assemblage, a middle two backs and one break tectonic pattern, and finally late septal folding. When the rock layer was displaced upward along the bottom slip layer, an initial backslope with a sharp-edged tectonic style was formed due to traction. As the extrusion continued, the backslope further expanded to form a septal fold when the rock layers overlapped significantly at the fault slope. According to Zhang et al. (2019a), when the strata were buried at shallow depths, the interstratigraphic cohesion difference played a major role in controlling the folding. When the interstratigraphic cohesion difference was small, sagging folds formed. When the strata were buried deeper, the overlying stratigraphic pressure was the main controlling factor, and only septal folds formed.

To analyze the geodynamic origin of the arcuate belts, the following three main factors should be taken into consideration: first, the lithologic combination of the strata is indispensable in understanding the deformation of the geological structure. From the Aurignacian to the Middle Triassic, the study area developed and evolved into a passive continental margin basin due to intermittent intra-land rifting. From the Late Triassic to the Jurassic, the study area entered the foreland basin evolutionary stage due to the influence of the circumferential collisional orogeny, and the Sujiahe Formation was deposited in the Sichuan Basin (Li et al., 2002). During this period, more than 10,000 m of carbonate, paste rocks, sandstone, and mudstone were deposited in the Eastern Sichuan area. The soft and hard stratigraphic sequences were deposited in the Eastern Sichuan area (**Figure 4**). The difference in the interstratigraphic cohesion between the competent and non-competent layers and the high rheology of the slippage layers supplied the necessary stratigraphy and lithology for the formation of the Eastern Sichuan fold fault zone.

Second, the boundary conditions were also an important factor. The boundary geometry was an important controlling factor in the generation of the tectonic deformation style, and the results of this study show that the high, steep folded fault zone in Eastern Sichuan was affected by the pre-existing regional faults (the arc-shaped high-angle Qiyue Mountain Fault and Huaying Mountain Fault in the SW projection) (He and Zhou 2018; Wu et al., 2019), together with the step-like system composed of the slickensides and basement detachment surface. When the burial depth of the slip layer is shallow, the stratum forms a septal fold; when the burial depth of the slip layer increases, the stratum forms a septal groove fold.

Finally, the formation of the Eastern Sichuan fold-fault zone was inextricably linked to the evolution of the tectonic stress fields in the different geological periods. The complex structural style observed on the plane and in the profiles in the study area and the variable kinematic indicators are the result of the superposition of multiple periods of tectonic activity. 1) During the Garidonian–Haixi period, a series of cryptic fractures formed in Eastern Sichuan, which are basically consistent with the fold axis, and mainly underwent differential lifting and lowering movements in a tensional environment, forming a relatively gentle fold-combination style paleotectonic pattern of compartmentalized tectonics. 2) In the early stage of the Indo-Chinese movement, the fracturing activity strengthened, and the extrusion between the Pacific Plate and the Asian Plate along the western Pacific Ocean caused step-like differential uplift of the strata in Eastern Sichuan. At this time, the cover layer was deformed by extensional slip, with the weak Cambrian rock layer acting as the main slip layer, forming the prototype of the extrusion folding. 3) Entering the Yanshan period, further extrusion in the NW–SE direction caused the Mesozoic strata to expand and fold with increasing amplitude. 4) In the Xishan period, the Indian Ocean Plate collided with the Asian–European Plate and transformed the pre-existing NE-oriented fold belt into NNE-oriented spacer folds, and the inherited structures were transformed during this period. With the further strengthening of the extrusion stress of the circumferential massif, the regional differential uplift and denudation were strong, with an early uplift time, large uplift amplitude, and high denudation degree in the western Hunan–European region, exposing septal fold type folds. In Eastern Sichuan, the uplift occurred later, the uplift amplitude was smaller, and shallow separate folds were exposed.

5.4 Effects on the Construction of Karst Tunnels

The geological conditions in the study area are complex, and the construction of mountain tunnels often encounters

disadvantageous karst geological phenomena, especially karst surge water, which can affect the progress of the project in minor cases and cause loss of life and property in extreme cases (Xu, 2018). The constructed tunnel becomes a new groundwater drainage obstruction, changing the groundwater circulation path and causing a significant drop in the groundwater level, which destroys the equilibrium state of the groundwater environment and has negative effects on the geological environment, such as surface water point leakage, reservoir drought, and surface karst collapse (Gong 2010; Liu et al., 2015; Zhong 2018). Identifying the karst engineering hydrogeological conditions in the high steep backslope in Eastern Sichuan and the traffic corridor that can be passed through the planned tunnel is beneficial to achieving sustainable development of the economy and ecological environment in Eastern Sichuan.

The unique tectonic background and stratigraphic assemblage in the high and steep back-slope area in Eastern Sichuan control the direction of the groundwater runoff and the karst development. The development of karst landforms is closely related to the nature of the rocks, geological structures, and alternating conditions of the water circulation, which causes the karst landform assemblage to exhibit obvious spatial variation. In this study, we focused on two points: fold and fracture tectonics.

1) The karst development characteristics and distribution range of the folds are related to the sequence of the rock layers, the thickness of the soluble rocks, the degree of rock bending, the characteristics of the joint fracture development, and the water catchment. Under the special geological and tectonic background, the soluble rocks and non-soluble rocks in the study area are alternately exposed in the near-core part of the backslope in the form of strips. Usually, the tighter the axis of the backslope, the larger the scale of the accompanying longitudinal fissures, and the phenomenon of interlayer deficiency can even occur, which is conducive to the infiltration and flow of groundwater and the concentration of groundwater into the deep circulation. Thus, the karst development is, especially strong, and the surface is mostly developed along the longitudinal structural surface of the large-scale karst depressions in the form of beads; for example, the scale of the karst depressions in the northern Yangtze River region in the Guanyinxia backslope is more than 0.2 km^2. In contrast, the karst depressions developed in the core of the box-shaped backslope are dense but small in scale, and the groundwater circulation and dissolution are more dispersed. Thus, the scale of the karst depressions developed on the surface is smaller, such as the depressions developed in the north section of the Yulin River in the Mingyue Mountain backslope, but their areas are small, mostly <0.1 km^2. Regarding the asymmetric high steep backslope, the slow flanks usually have weak interlayer fissure development, and they often form small-scale troughs or bead-like karst depressions. The longitudinal fissures in the steeper flank are more developed, and the longitudinal fissures are conducive to the concentrated circulation and dissolution of the surface and groundwater. They often form a cascading dark river pipeline in this flank (e.g., the Zhongliang Mountain Dry Weantang Reservoir-Qingliangan Dark River Pipeline), and the transverse fissures provide a convenient way for the karst pipeline to break through the restriction imposed by the non-soluble rocks in the vertical direction. For example, the Huaying Mountain Green Water Cave Dark River connects the Feixianguan Formation with the karst groundwater of both the Feixianguan and Jialingjiang Formations, which makes the karst development characteristics and karst hydrogeological conditions complicated. Therefore, the steep flanks mostly develop long, continuous, large-scale karst troughs and valleys.
2) In general, the karst development in the fault zone decreases gradually as the tensor faults transition to compressional faults. Under the strong tectonic compressional effect, the associated faults are mainly compressional-torsional faults, and the fault zones are mostly closed and are characterized by vesiculation and water isolation. However, the influence of the compressional-torsional faults with developed joints and fissures increases as the fragmentation of the rock body, the water-richness, and the degree of karst development increase. For example, the 260-m burial depth of the Zhongliang Mountain Sheima Tunnel intersects the Baimiaozi reverse fault at a large angle on the western flank of the back-slope, and the fault fragmentation zone and influence zone have well-developed joint fissures and broken rock masses. After the excavation, water gushed into the entire section in the form of rain and fissure strands, and wide dissolution and pores were intensively developed. The fault fragmentation zone of the tensor fault had a large degree of fracturing, a high fissure rate, and a strong water-richness, and the karst activity mostly occurred along the fault zone. Under the effect of differential dissolution, many karst pipes and dark rivers were formed, such as the large-scale pearl-shaped waterfall caves developed along the N-S orthogonal fault in the Cataract Gorge on the north side of the Yangtze River on the backslope of the Guanyin Gorge. The influence of fault development on the groundwater distribution and karst development is manifested in the width of the different tectonic fault zones and structural surface development characteristics, and fracture displacement is another important factor affecting karst development. For example, the activity on the Baimiaozi reverse fault has led to the direct contact between the third section of the Feixianguan Group tuff and the Jialingjiang Group tuff, which are divided by the fourth section of the Feixianguan Group shale, and the originally relatively independent karst aquifers have established a unified hydraulic connection. This led to serious leakage of shallow karst water from the three sections of tuffs in the Feixianguan Group when the tunnel excavation process reached the tuffs of the Jialingjiang Group.
3) The high steep back-slope mountains are natural barriers to the east-west traffic corridors in the Eastern Sichuan area, seriously hindering the economic development of urban areas. Tunnels can be used to quickly traverse folded mountainous

areas, but the impact of trans-ridge tunnel construction on regional groundwater levels often induces serious geological disasters such as karst collapse, underground aquifer destruction, and surface water evacuation and drying, threatening the safe construction of tunnels and the local ecological and geological environment. For example, 300 karst collapses and about 110 drained wellsprings have occurred in the Zhongliang Mountain area (Wu et al., 2021). The karst collapses have mainly been concentrated in the low-lying karst trough valleys or karst depressions on the steeper backslope flank. Because the tension fissures are more developed, these zones are more conducive to the pooling of surface water and groundwater, and the alternating cycle of the groundwater level is more intense. The precondition for a collapse to occur is the existence of a karst fissure or cave system in the surface layer of bedrock at a certain depth below the ground. Targeted blocking and prevention measures can improve the prevention and control of karst collapse disasters and achieve better economic and social effects.

6 CONCLUSION

From the preceding analysis and the analog model experiments conducted in this study, we drew the following major conclusions:

1) The physical simulation experiments revealed that the lithology of the cover layer in the fold formation area should not be too soft or too hard in the deformation stage; otherwise, a series of foreshortening stacked tile recoil thrusting structures and recoil fault structures will form.
2) The different interstratigraphic cohesion between the competent and non-competent layers and the high rheology of the slip layers provide the necessary stratigraphic lithology for the formation of the Eastern Sichuan fold-fault zone. The multi-layered detachment slip structure is the fundamental reason for the formation of the fault-fold tectonic style in the study area.
3) The area where the basal detachment surface or the lower slip layer is uplifted is the location of the tectonic stress concentration, which is more likely to develop recoil faults.
4) The deformation of the ESFTB was controlled by a step-like system composed of the lower crustal crystalline basement detachment surface, regional boundary fractures, and the overlying Cambrian and Triassic slickensides. When the burial depth of the slip layer is shallow, the stratum forms septal folds.
5) The regional tectonic pattern generally exhibits the forward-spreading retrogradational thrusting and overlapping thin-skin structure style, with a complex structural style in the plane and profiles and variable kinematic indicators, which were caused by the superposition of multiple phases of tectonic activity.
6) The developed karst features are not conducive to the construction of the project tunnel in the area with a tightly closed backslope, fissures, and normal faults in the Eastern Sichuan fold and fault zone.

DATA AVAILABILITY STATEMENT

The raw data supporting the conclusion of this article will be made available by the authors, without undue reservation.

AUTHOR CONTRIBUTIONS

Y-SW, MX, and Y-NY contributed to the conception and design of the study. QX organized the database. CY performed the statistical analysis. Y-SW wrote the first draft of the manuscript. QX, BJ, CY, and HZ wrote sections of the manuscript. All authors contributed to manuscript revision and read and approved the submitted version.

FUNDING

This study was supported by the Natural Science Foundation of China's project under No. 42072283.

ACKNOWLEDGMENTS

We thank Professor Li Zhongquan from the School of Earth Sciences, Chengdu University of Technology, for the physical simulation experiment of the Key Laboratory of Tectonic Mineralization and Accumulation of the Ministry of Natural Resources. Dr. Ding Xiao's assistance during the experiment is appreciated. LetPub (www.letpub.com) is appreciated for its linguistic assistance during the preparation of this manuscript.

REFERENCES

Adrian, P. O. (2017). 'Thick-Skinned and Thin-Skinned Tectonics: A Global Perspective. *Geosciences* 7, 71. doi:10.3390/geosciences7030071

Bonini, M., Sani, F., and Antonielli, B. (2012). Basin Inversion and Contractional Reactivation of Inherited Normal Faults: A Review Based on Previous and New Experimental Models. *Tectonophysics* 522-523 (3), 55–88. doi:10.1016/j.tecto.2011.11.014

Boutoux, A., Bellahsen, N., Nanni, U., Pik, R., Verlaguet, A., Rolland, Y., et al. (2016). Thermal and Structural Evolution of the External Western Alps: Insights from (U-Th-Sm)/He Thermochronology and RSCM Thermometry in the Aiguilles Rouges/Mont Blanc Massifs. *Tectonophysics* 683, 109–123. doi:10.1016/j.tecto.2016.06.010

Brogi, A. (2008). Kinematics and Geometry of Miocene Low-Angle Detachments and Exhumation of the Metamorphic Units in the Hinterland of the Northern Apennines (Italy). *J. Struct. Geol.* 30, 2–20. doi:10.1016/j.jsg.2007.09.012

Buchanan, P. G., and Mcclay, K. R. (1991). Sandbox Experiments of Inverted Listric and Planar Fault Systems. *Tectonophysics* 188 (1–2), 97–115. doi:10.1016/0040-1951(91)90317-l

Charvet, J. (2013). The Neoproterozoic-Early Paleozoic Tectonic Evolution of the South China Block: An Overview. *J. Asian Earth Sci.* 74, 198–209. doi:10.1016/j.jseaes.2013.02.015

Chu, Y., Faure, M., Lin, W., and Wang, Q. (2012a). Early Mesozoic Tectonics of the South China Block: Insights from the Xuefengshan Intracontinental Orogen. *J. Asian Earth Sci.* 61, 199–220. doi:10.1016/j.jseaes.2012.09.029

Chu, Y., Lin, W., Faure, M., Wang, Q., and Ji, W. (2012b). Phanerozoic Tectonothermal Events of the Xuefengshan Belt, Central South China: Implications from UPb Age and LuHf Determinations of Granites. *Lithos* 150, 243–255. doi:10.1016/j.lithos.2012.04.005

Costa, E., and Vendeville, B. C. (2002). Experimental Insights on the Geometry and Kinematics of Fold-And-Thrust Belts above Weak, Viscous Evaporitic Décollement. *J. Struct. Geol.* 24, 1729–1739. doi:10.1016/s0191-8141(01)00169-9

Davis, D. M., and Engelder, T. (1985). The Role of Salt in Fold-And-Thrust Belts. *Tectonophysics* 119, 67–88. doi:10.1016/0040-1951(85)90033-2

Deng, Y., Zhang, Z., Badal, J., and Fan, W. (2014). 3-D Density Structure under South China Constrained by Seismic Velocity and Gravity Data. *Tectonophysics* 627, 159–170. doi:10.1016/j.tecto.2013.07.032

Ding, D., Guo, T., and Zhai, C. (2005). Knee-fold Structure in the Western Ezhou-Yudong Region[J]. *Pet. Exp. Geol.* 27 (03), 205–210. (In Chinese and English Abstract). doi:10.3969/j.issn.1001-6112.2005.03.001

Dong, Y., Zha, X., Fu, M., Zhang, Q., Yang, Z., and Zhang, Y. (2008). Characteristics of the Dabashan fold Thrust Nappe Structure at the Southern Margin of the Qinling,China. *Geol. Bull. China* 27 (9), 1493–1508. (In Chinese and English Abstract). doi:10.3969/j.issn.1671-2552.2008.09.011

Eisenstadt, G., and Sims, D. (2005). Evaluating Sand and Clay Models: Do Rheological Differences Matter? *J. Struct. Geol.* 27, 1399–1412.

Expósito, I., Balanyá, J. C., Crespo-Blanc, A., Díaz-Azpiroz, M., and Luján, M. (2012). Overthrust Shear Folding and Contrasting Deformation Styles in a Multiple Decollement Setting, Gibraltar Arc External Wedge. *Tectonophysics* 576-577, 86–98. doi:10.1016/j.tecto.2012.04.018

Faure, M., Lin, W., and Le Breton, N. (2001). Where Is the North China-South China Block Boundary in Eastern China? *Geol* 29, 119–122. doi:10.1130/0091-7613(2001)029<0119:witncs>2.0.co;2

Faure, M., Lin, W., Monié, P., and Meffre, S. (2008). Palaeozoic Collision between the North and South China Blocks, Triassic Intracontinental Tectonics, and the Problem of the Ultrahigh-Pressure Metamorphism. *Comptes Rendus Geosci.* 340, 139–150. doi:10.1016/j.crte.2007.10.007

Ghazian, R. K., and Buiter, S. J. H. (2014). Numerical Modelling of the Role of Salt in Continental Collision: An Application to the Southeast Zagros Fold-And-Thrust Belt. *Tectonophysics* 632, 96–110. doi:10.1016/j.tecto.2014.06.006

Gomes, C. J. S. (2013). Investigating New Materials in the Context of Analog-Physical Models. *J. Struct. Geol.* 46, 158–166.

Gong, R. (2010). Study on the Impact of Tunnel Construction on the Groundwater Environment of Septic Karst-Rich Backslope. *Environ. Sci. Pollut. Res. Int.* 28, 40203–40216. doi:10.1007/s11356-021-13919-1

Graveleau, F., and Dominguez, S. (2008). Analogue Modelling of the Interaction Between Tectonics, Erosion and Sedimentation in Foreland Thrust Belts. *Geoscience* 340, 324–333. doi:10.1016/j.crte.2008.01.005

Graveleau, F., Malavieille, J., and Dominguez, S. (2012). Experimental Modelling of Orogenic Wedges: A Review. *Tectonophysics* 538-540, 1–66. doi:10.1016/j.tecto.2012.01.027

Gu, Z., Wang, X., Nunns, A., Zhang, B., Jiang, H., Fu, L., et al. (2021). Structural Styles and Evolution of a Thin-Skinned Fold-And-Thrust Belt with Multiple Detachments in the Eastern Sichuan Basin, South China. *J. Struct. Geol.* 142, 104191. doi:10.1016/j.jsg.2020.104191

Hayes, M., and Hanks, C. L. (2008). Evolving Mechanical Stratigraphy during Detachment Folding. *J. Struct. Geol.* 30, 548–564. doi:10.1016/j.jsg.2008.01.006

He, W., and Zhou, J. (2018). 'Physical Simulation of the Characteristics and Formation Mechanism of the Southeast Sichuan Horsetail Fold Belt. *Earth Sci.* 43, 2133–2148. doi:10.3799/dqkx.2020.202

Hu, S., Zhu, G., and Liu, G. (2009). The Folding Time of the Eastern Sichuan Jura-Type Fold Belt: Evidence From Unconformity. *Geol. Rev.* 55 (1), 32–42. (In Chinese and English Abstract)

Huang, H., He, D., and Li, Y. (2019). Determination and Formation Mechanism of the Luzhou Paleo Southeatern Sichuan Basin. *Earth Sci. Front.* 26 (1), 102–120. doi:10.1016/j.ngib.2021.08.003

Hubbert, M. K. (1937). Theory of Scale Models as Applied to the Study of Geologic Structures. *Geol. Soc. Am. Bull.* 48, 1459–1520. doi:10.1130/gsab-48-1459

Jamison, W. R. (1992). Stress Spaces and Stress Paths. *J. Struct. Geol.* 14, 1111–1120. doi:10.1016/0191-8141(92)90063-3

Koyi, H. A., and Cotton, J. (2004). Experimental Insights on the Geometry and Kinematics of Fold-And-Thrust Belts above Weak, Viscous Evaporitic Décollement; a Discussion. *J. Struct. Geol.* 26, 2139–2141. doi:10.1016/j.jsg.2004.04.001

Krantz, R. W. (1991). Measurements of Friction Coefficients and Cohesion for Faulting and Fault Reactivation in Laboratory Models Using Sand and Sand Mixtures. *Tectonophys.* 188, 203–207.

Li, C., He, D., Sun, Y., He, J., and Jiang, Z. (2015). Structural Characteristic and Origin of Intra-continental Fold Belt in the Eastern Sichuan Basin, South China Block. *J. Asian Earth Sci.* 111, 206–221. doi:10.1016/j.jseaes.2015.07.027

Li, F. (2015). *Study on the Seismic Hazard of Isolated Back-Slope Structures in Chongqing*. China: Ph.D., Institute of Geology.

Li, X.-H., Li, W.-X., Li, Z.-X., Lo, C.-H., Wang, J., Ye, M.-F., et al. (2009). Amalgamation between the Yangtze and Cathaysia Blocks in South China: Constraints from SHRIMP U-Pb Zircon Ages, Geochemistry and Nd-Hf Isotopes of the Shuangxiwu Volcanic Rocks. *Precambrian Res.* 174, 117–128. doi:10.1016/j.precamres.2009.07.004

Li, Z., Ran, L., Chen, Z., Lu, Z., and Duan, X. (2002). 'Geological Model and Gas-Bearing Analysis of High Steep Tectonic Genesis in East Sichuan. *J. Chengdu Inst. Technol.* 1, 605–609. doi:10.1016/j.engeos.2020.06.005

Li, Z. X. (2007). Formation of the 1300-km-wide Intracontinental Orogen and Postorogenic Magmatic Province in Mesozoic South China: A Flat-Slab Subduction Model. *Geology*, 35 179–182. doi:10.1130/G23193A.1

Li, S., Li, J., and Zhou, Y. (2011). Evidence of Fission Traces for the Middle Cenozoic Tectonic Uplift in the Southeastern Margin of the Sichuan Basin. *J. Petrology Mineralogy* 30 (2), 225–233. (In Chinese and English Abstract). doi:10.3969/j.issn.1000-6524.2011.02.007

Liu, D., Yang, L. Z., and Yu, S. U. J. (2015). Ecological and Environmental Problems and Effects of Drainage in the Huayin Mountain Tunnel [J]. *J. Southwest Jiaot. Univ.* 36 (3), 308–313. (In Chinese and English Abstract). doi:10.3969/j.issn.0258-2724.2001.03.021

Liu, S. (1995). The Thin-Skinned Tectonic Model of Eastern Sichuan[J]. *Sichuan J. Geol.* 15 (4), 264–267. (In Chinese and English Abstract).

Lu, G., Zhao, L., Zheng, T., Kaus, B. J. P., and Kaus, P. (2014). Strong Intracontinental Lithospheric Deformation in South China: Implications from Seismic Observations and Geodynamic Modeling. *J. Asian Earth Sci.* 86, 106–116. doi:10.1016/j.jseaes.2013.08.020

Malz, A., Madritsch, H., Meier, B., and Kley, J. (2016). An Unusual Triangle Zone in the External Northern Alpine Foreland (Switzerland): Structural Inheritance, Kinematics and Implications for the Development of the Adjacent Jura Fold-And-Thrust Belt. *Tectonophysics* 670, 127–143. doi:10.1016/j.tecto.2015.12.025

Massoli, D., Koyi, H. A., and Barchi, M. R. (2006). Structural Evolution of a Fold and Thrust Belt Generated by Multiple Décollements: Analogue Models and Natural Examples from the Northern Apennines (Italy). *J. Struct. Geol.* 28, 185–199. doi:10.1016/j.jsg.2005.11.002

Mei, L., Liu, Z., and Tang, J. (2010). Progressive Intra-terranean Extensional Deformation in the Xiang-Exi-Eastern Sichuan Mesozoic: Evidence from Fission Traces and Equilibrium Profiles. *Earth Sci.* 35 (2), 161–174. (In Chinese and English Abstract).

Meng, Q., and Hodgetts, D. (2019). Structural Styles and Decoupling in Stratigraphic Sequences with Double Décollements during Thin-Skinned Contractional Tectonics: Insights from Numerical Modelling. *J. Struct. Geol.* 127, 103862. doi:10.1016/j.jsg.2019.103862

Mount, V. S. (2014). Structural Style of the Appalachian Plateau Fold Belt, North-Central Pennsylvania. *J. Struct. Geol.* 69, 284–303. doi:10.1016/j.jsg.2014.04.005

Mulugeta, G., and Koyi, H. (1992). Episodic Accretion and Strain Partitioning in a Model Sand Wedge. *Tectonophysics* 202, 319–333. doi:10.1016/0040-1951(92)90117-o

Oner, Z., and Dilek, Y. (2013). Fault Kinematics in Supradetachment Basin Formation, Menderes Core Complex of Western Turkey. *Tectonophysics* 608, 1394–1412. doi:10.1016/j.tecto.2013.06.003

Panien, M., Schreurs, G., and Pfiffner, A. A. (2006). Mechanical Behaviour of Granular Materials Used in Analogue Modelling: Insights from Grain Characterisation, Ring-Shear Tests and Analogue Experiments. *J. Struct. Geol.* 28, 1710–1724. doi:10.1016/j.jsg.2006.05.004

Rameil, N. (2008). Early Diagenetic Dolomitization and Dedolomitization of Late Jurassic and Earliest Cretaceous Platform Carbonates: A Case Study from the

Jura Mountains (NW Switzerland, E France). *Sediment. Geol.* 212, 70–85. doi:10.1016/j.sedgeo.2008.10.004

Reiter, K., Kukowski, N., and Ratschbacher, L. (2011). The Interaction of Two Indenters Inanalogue Experiments and Implications for Curved Fold-and-Thrust Belts. *Earth Planet. Sci. Lett.* 302, 132–146. doi:10.1016/j.epsl.2010.12.002

Rich, J. L. (1934). 'Mechanics of Low-Angle Overthrust Faulting as Illustrated by Cumberland Thrust Block, Virginia, Kentucky, and Tennessee. *AAPG Bull.* 18, 1584–1596. doi:10.1306/3d932c94-16b1-11d7-8645000102c1865d

Richardson, N. J., Densmore, A. L., and Seward, D. (2008). Extraordinary Denudation in the Sichuan Basin: Insights from Low-Temperature Thermochronology Adjacent to the Eastern Margin of the Tibetan Plateau. *J. Geophys. Res.* 113 (B4), 1–23. doi:10.1029/2006JB004739

Rossetti, F., Faccenna, C., Ranalli, G., and Storti, F. (2000). 'Convergence Rate-dependent Growth of Experimental Viscous Orogenic Wedges. *Earth Planet. Sci. Lett.* 178, 367–372. doi:10.1016/S0012-821X(00)00082-0

Santolaria, P., Vendeville, B. C., Graveleau, F., Soto, R., and Casas-Sainz, A. (2015). Double Evaporitic Décollements: Influence of Pinch-Out Overlapping in Experimental Thrust Wedges. *J. Struct. Geol.* 76, 35–51. doi:10.1016/j.jsg.2015.04.002

Shen, C. B., Mei, L. F., and Xu, S. H. (2009). 'Fission Track Dating of Mesozoic Sandstones and its Tectonic Significance in the Eastern Sichuan Basin, China. *Radiat. Meas.* 44, 945–949. doi:10.1016/j.radmeas.2009.10.001

Shu, L. S., Zhou, X. M., Deng, P., Wang, B., Jiang, S. Y., Yu, J. H., et al. (2009). 'Mesozoic Tectonic Evolution of the Southeast China Block: New Insights from Basin Analysis. *J. Asian Earth Sci.* 34, 376–391. doi:10.1016/j.jseaes.2008.06.004

Souloumiac, P., Maillot, B., and Leroy, Y. M. (2012). Bias Due to Side Wall Friction in Sand Box Experiments. *J. Struct. Geol.* 35, 90–101. doi:10.1016/j.jsg.2011.11.002

Tang, L., and Cui, M. (2012). Structural Deformation and Fluid Flow from East Sichuan to the Northwestern Periphery of the Xuefeng Uplift, China. *Petroleum Sci.* 9, 429–435. doi:10.1007/s12182-012-0226-5

Tavani, S., and Cifelli, F. (2010). Deformation Pattern Analysis and Tectonic Implications of a Décollement Level within the Central Apennines (Italy). *Geol. J.* 45, 582–596. doi:10.1002/gj.1198

Vendeville, B. C. (2007). "The 3-D Nature of Stress Fields in Physical Experiments and its Impact on Models Overall Evolution," in *European Geosciences Union General Assembly, 15e20 April 2007* (Vienna, Austria: EGU2007-A-02960).

Wang, P., Liu, S., and Gao, X. (2012a). AFT Record of Three-Dimensional Tectonic Extension in the Eastern Sichuan Arc. *J. Geophys.* 55 (5), 1662–1673. (In Chinese and English Abstract). doi:10.6038/j.issn.0001-5733.2012.05.023

Wang, W., Zhou, M. F., Yan, D. P., and Li, J. W. (2012b). Depositional Age, Provenance, and Tectonic Setting of the Neoproterozoic Sibao Group, Southeastern Yangtze Block, South China. *Precambrian Res.* 192-195, 107–124. doi:10.1016/j.precamres.2011.10.010

Wang, C. Y., Cheng, X. G., Chen, H. L., Ding, W. W., Lin, X. B., Wu, L., et al. (2016). The Effect of Foreland Palaeo-Up Lift on Deformation Mechanism in the Wupoer Fold and Thrust Belt, NE Pamir: Constraints From Analogue Modelling. *J. Geodyn.* 100, 115–129.

Wang, Y., Zhang, Y., Fan, W., and Peng, T. (2005). Structural Signatures and 40Ar/39Ar Geochronology of the Indosinian Xuefengshan Tectonic Belt, South China Block. *J. Struct. Geol.* 27, 985–998. doi:10.1016/j.jsg.2005.04.004

Woodward, N. B. (1999). Competitive Macroscopic Deformation Processes. *J. Struct. Geol.* 21, 1209–1218.

Wu, H., Qiu, N., Chang, J., Zhang, J., and Wang, Y. (2019). 'Physical Simulation of the Formation of Multiple Sets of Slip-Layer Folded Tectonic Zones in East Sichuan. *Earth Sci.* 44, 784–797. (In Chinese and English Abstract). doi:10.3799/dqkx.2018.109

Wu, Y. B., Yin, R. C., Lei, M. T., Dai, J. L., Jia, L., Pan, Z. Y., et al. (2021). Triggering Factors and Prevention-Control Countermeasures of Karst Collapses Caused by Tunnel Construction in the Zhongliangshan Area, Chongqing. China. *CARSOLOGICA Sin.* 40 (2), 246–252. doi:10.11932/karst20210204

Xu, Z. (2018). *Complex Karst Tunnel Surge Water Evolution Mechanism and Comprehensive Disaster Prevention and Control Research*. Chengdu University of Technology.

Yan, D., Xu, Y., and Dong, Z. (2016). Fault-related Fold Styles and Progressions in Fold-thrust Belts: Insights from Sandbox Modeling. *J. Geophys. Res. Solid Earth* 121 (3), 2086–2111. doi:10.1002/2015JB012397

Yan, D., Zhou, M., and Song, H. (2003). Origin and Tectonic Significance of a Mesozoic Multi-Layer Over-thrust System within the Yangtze Block (South China). *Tectonophysics*, 361, 239–254. doi:10.1016/S0040-1951(02)00646-7

Zanon, M. L., and Janette Souza Gomes, C. (2019). Sandbox Models of Fault-Bend Folding: A New Investigation with a Pre-existing Fault Ramp. *J. Struct. Geol.* 127, 103864. doi:10.1016/j.jsg.2019.103864

Zhang, K. J. (1997). North and South China Collision along the Eastern and Southern North China Margins. *Tectonophysics* 270, 145–156.

Zhang, X., Shan, Y., Nie, C., and Ni, Y. (2013). 'Numerical Simulation of the Mesozoic East Sichuan Fold Belt: Influence of Slip Zone Depth on Platform Cover Fold Patterns. *Geotect. Metallogeny* 37, 622–632. (In Chinese and English Abstract). doi:10.16539/j.ddgzyckx.2013.04.014

Zhang, X. L. (2019). *Tectonic Evolution and Genesis Mechanism of the West-East Eurasian Region*. Beijing: China University of Geosciences.

Zhang, Y. H., Cao, H. W., Hollis, S. P., Tang, L., Xu, M., Jiang, J. S., et al. (2019a). Geochronology, Geochemistry and Sr-Nd-Pb-Hf Isotopes of the Early Paleogene Gabbro and Granite from Central Lhasa, Southern Tibet: Petrogenesis and Tectonic Implications. *Int. Geol. Rev.* 61 (7), 868–894. doi:10.1080/00206814.2018.1476187

Zhang, Y. H., Dai, Y. S., Wang, Y., Huang, X. Y., and Pei, Q. M. (2021a). Hydrochemistry, Quality and Potential Health Risk Appraisal of Nitrate Enriched Groundwater in the Nanchong Area, Southwestern China. *Sci. Total Environ.* 784, 147186. doi:10.1016/j.scitotenv.2021.147186

Zhang, Y. H., He, Z. H., Tian, H. H., Huang, X., Zhang, Z. X., Liu, Y., et al. (2021b). Hydrochemistry Appraisal, Quality Assessment and Health Risk Evaluation of Shallow Groundwater in the Mianyang Area of Sichuan Basin, Southwestern China. *Environ. Earth Sci.* 80 (17), 576. doi:10.1007/s12665-021-09894-y

Zhang, Y. H., Li, X., Luo, M., Wei, C. L., Huang, X., Xiao, Y., et al. (2021c). Hydrochemistry and Entropy-Based Groundwater Quality Assessment in the Suining Area, Southwestern China. *J. Chem.* 559, 1–11. doi:10.1155/2021/5591892

Zhang, Y. H., Wang, Y. S., Wang, W. S., Liu, J., and Yuan, L. L. (2019b). Zircon U-Pb-Hf Isotopes and Mineral Chemistry of Early Cretaceous Granodiorite in the Lunggar Iron Deposit in Central Lhasa, Tibet Y, China. *J. Central South Univ.* 12, 3457–3469. doi:10.1007/s11771-019-4266-5

Zhao, D. (2017). *Tectonic Geometry and Kinematics of the Eastern Margin of the Sichuan Basin*. Beijing: China University of Geosciences.

Zhong, L. (2018). *'Study on the Spatial Differentiation Characteristics of Karst and the Construction of Evaluation System in the High Steep Backslope Area of East Sichuan*. Ph. D., Chengdu: Chengdu University of Technology.

Zhou, J., Xu, F., and Chunguang, W. (2007). Shortening of Analogue Models with Contractive Substrata: Insights into the Origin of Purely Landward-Vergent Thrusting Wedge along the Cascadia Subduction Zone and the Deformation Evolution of Himalayan-Tibetan Orogen. *Earth Planet. Sci. Lett.* 260 (1), 313–327. doi:10.1016/j.epsl.2007.05.048

Zou, H. (2011). *Characteristics of the Cambrian Gypsum-salt Rocks in Sichuan Basin*. MA: Chengdu University of Technology.

Zou, Y., Duan, J., Zhao, Y., Zhang, X., and Li, Z. (2015). 'Tectonic Features and Their Evolution in the High Steep Fault Zone of East Sichuan. *J. Geol.*, 558 2046–2052. doi:10.1007/s13202-016-0305-z

Conflict of Interest: Author HZ was employed by Sichuan Metallurgical Geological Survey and Design Group Co. Ltd.

The remaining authors declare that the research was conducted in the absence of any commercial or financial relationships that could be construed as a potential conflict of interest.

Publisher's Note: All claims expressed in this article are solely those of the authors and do not necessarily represent those of their affiliated organizations, or those of the publisher, the editors, and the reviewers. Any product that may be evaluated in this article, or claim that may be made by its manufacturer, is not guaranteed or endorsed by the publisher.

Copyright © 2022 Wang, Xu, Yang, Xia, Jiang, Yang and Zhang. This is an open-access article distributed under the terms of the Creative Commons Attribution License (CC BY). The use, distribution or reproduction in other forums is permitted, provided the original author(s) and the copyright owner(s) are credited and that the original publication in this journal is cited, in accordance with accepted academic practice. No use, distribution or reproduction is permitted which does not comply with these terms.

frontiers | Frontiers in Earth Science

ORIGINAL RESEARCH
published: 08 June 2022
doi: 10.3389/feart.2022.857172

Study on Mechanical Characteristics and Construction Control of the Railway Overlapping Tunnels

Yuan Fengjie[1], Liu Yang[2], Xu Qianwei[3], Zheng Yuanlin[4], Hu Lisheng[5], Zhao Ping[1] and Cui Yuebang[3]*

[1]The Fifth Engineering Company of CREGC, Chengdu, China, [2]Chongqing Survey Institute, Chongqing, China, [3]School of Transportation Engineering, Tongji University, Shanghai, China, [4]Chongqing Urban Construction Investment (Group) Co.Ltd, Chongqing, China, [5]China Railway No.2 Engineering Group Co., Ltd, Chengdu, China

In tunnel engineering, newly built tunnels will disturb the surrounding strata and close-to-existing tunnels, which may cause secondary lining cracking and overall damage to existing tunnels. In this paper, combined with the engineering problem of longitudinal cracks in the secondary lining of the lower tunnel caused by the super-close construction of a new tunnel in Chongqing, China, the deformation laws of the tunnel vault, inverted arch, and transverse brace during the construction of an overlapping tunnel are studied by using the finite element method. According to the distribution characteristics of stratum shear stress and plastic zone, the stratum and tunnel disturbance are analyzed. At the same time, combined with the field records, the causes and distribution laws of longitudinal cracks in the lower tunnel lining are explored. The research results show that the main reason for the cracking of the secondary lining is the bias effect of the post-excavation tunnel construction on the lower tunnel. When the tunnel spacing is small, the stratum maximum shear stress is concentrated, the penetration of the plastic deformation zone is more connected, and the settlement of the vault, horizontal convergence, and the deformation of the upper part of the arch waist of the lower tunnel are more intensified. This short-distance bias action causes the deformation of the stratum and the tunnel and eventually cracks in the lining.

Keywords: overlapping tunnels, lining crack, numerical simulation, proximity construction impact, construction control

OPEN ACCESS

Edited by:
Yunhui Zhang,
Southwest Jiaotong University, China

Reviewed by:
Xiantang Zhang,
Shandong University of Science and Technology, China
Weigang Shen,
Southwest Jiaotong University, China

****Correspondence:***
Xu Qianwei
xuqianwei@tongji.edu.cn

Specialty section:
This article was submitted to Geohazards and Georisks, a section of the journal Frontiers in Earth Science

Received: *18 January 2022*
Accepted: *14 April 2022*
Published: *08 June 2022*

Citation:
Fengjie Y, Yang L, Qianwei X, Yuanlin Z, Lisheng H, Ping Z and Yuebang C (2022) Study on Mechanical Characteristics and Construction Control of the Railway Overlapping Tunnels. Front. Earth Sci. 10:857172. doi: 10.3389/feart.2022.857172

1 INTRODUCTION

With the continuous development of tunnel construction, it is inevitable to encounter the problem of imminent disturbance caused by the construction of new tunnels in super-close disturbance parallel to the existing lower tunnel. Designers and engineers must analyze the mechanics and deformation behavior of the stratum and the tunnel caused by the excavation of the upper and lower overlapped tunnels, especially the impact of the post-excavation tunnel on the first excavated tunnel and stratum, which will help the safe construction and operation of the upper and lower overlapping tunnels.

Many scholars have conducted relevant research on the construction mechanics effects of tunnels adjacent to existing structures.

On the one hand, the excavation of tunnels close to building structures (foundation pits or tunnels) could have an impact. Based on the engineering example of a newly built shield tunnel

that traverses an existing tunnel underneath, Li (Peng et al., 2014) studied vertical displacement and longitudinal stress changes of existing tunnels on the effects of new tunnels. Do et al. (2015) investigated the structural mechanical properties and deformation characteristics of the existing tunnel under the condition of the change in the distance between the tunnels. Yun et al. (2014) developed an application program that can use actual field monitoring based on the principal component analysis method (PCA), which can be used to monitor the behavior of the tunnel structure and prevent large deformations and even cracking. Based on the engineering example of a new tunnel under the double tunnel, Cooper et al. (2001) constructed an empirical equation through theoretical analysis to predict the settlement and suggested using it as a preliminary forecasting tool. In addition, the data of three parallel tunnels were combined for verification and analysis, and it was proposed that the loss of ground stiffness would lead to the volume loss of the existing tunnels. Zhang and Huang (2014) studied the ground and structural disturbances caused by the interaction mechanics of multi-line overlapping tunnels in China. Through numerical simulation and on-site monitoring, Standing et al. (2015) analyzed the dynamic response of the upper tunnel lining structure's cast iron segment joints to the new lower tunnel. Liang et al. (2013) studied the dynamic response of the blasting vibration of the new railway tunnel to the adjacent existing railway tunnel and analyzed the influence of the existing tunnel lining structure before and after the blasting vibration, which was of reference significance for analyzing and controlling cracks in the secondary lining. Zhao et al. (2016) carried out experimental and numerical simulation studies on the influence of blasting vibration of adjacent tunnels on existing tunnels and analyzed the axial and radial mechanical responses of existing tunnels. Hage Chehade and Shahrour (2008) established a two-dimensional model to analyze the mechanical response of tunnel construction under the different relative positions. Addenbrooke and Potts (2001) analyzed the ground deformation caused by the construction of the double tunnel and the mechanical behavior of the tunnel lining. Asano et al. (2003) put forward the observation and excavation control measures for the nearby existing mountain tunnels through the combination of the investigation results from the fault zone and simulation results from finite element analysis. Byun et al. (2006) conducted a scaled model test to study the mechanical behavior of the stratum and tunnel caused by the new upper-level tunnel and analyzed the longitudinal arch effect and stress flow disturbance of the lower tunnel caused by the upper tunnel.

On the other hand, the construction of building structures adjacent to the tunnel could have an impact. Zheng and Wei (2008) used a two-dimensional model to study the response of the existing tunnel caused by the excavation of the overlying soil. Schroeder et al. (2004) used numerical simulation to predict the impact of pile group load on existing tunnels to ensure the acceptance and deformation

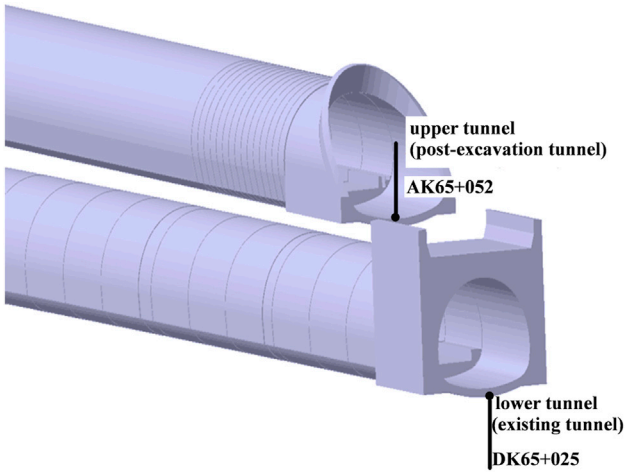


FIGURE 1 | Schematic diagram of the spatial location of the Bajiaogou overlapping tunnels

safety of the tunnel structure. Beyabanaki and Gall (2017) studied the mechanical response and deformation characteristics of foundation pit excavation to the existing tunnel underneath and analyzed the internal force and deformation stability of the lower tunnel lining. Shin et al. (2011) simulated and analyzed soft rock tunnels through the establishment of a dynamic simulation model. By establishing the finite element model, Liu et al. (2011) carried out research on the disturbance effects and control measures of the construction of the new open-cut tunnel. Park et al. (2018) analyzed the influence of the excavation damage zone caused by blasting on the overall stability of the tunnel. Dolezalova (Marta, 2001) analyzed the deformation and stress changes of a group of subway tunnels in an open-air excavation environment. Hu et al. (2003) and Jia (2006) studied the effects of different tunnel excavation methods and construction control measures based on field measurements. Sharma et al. (2001) investigated the construction deformation disturbance of two parallel tunnels using on-site monitoring results and found that there was a significant coupling effect between the two.

Moreover, there has been related research work on tunnel lining cracks. Dong et al. (2019) and others established a model that integrates basic SegNet and focal loss functions through deep learning (DL) technology, which improves the distribution prediction ability of small cracks and overlapping damage in tunnel linings. Huang et al. (2018) proposed a new image recognition algorithm based on deep learning for visual inspection of tunnel cracks and leakage defects. Qu (Zhong et al., 2016) researched the detection and repair methods of concrete tunnel lining surface cracks. An improved seepage detection algorithm aims at the detection of concrete tunnel lining surface cracks.

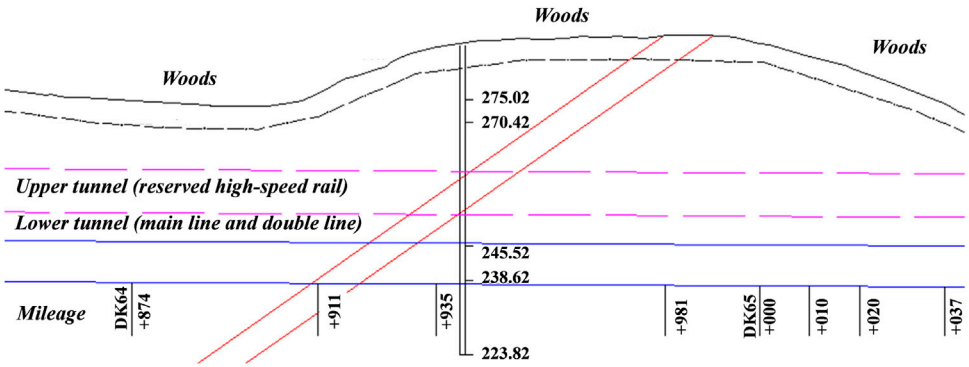


FIGURE 2 | Longitudinal relationship diagram of the upper and lower tunnels.

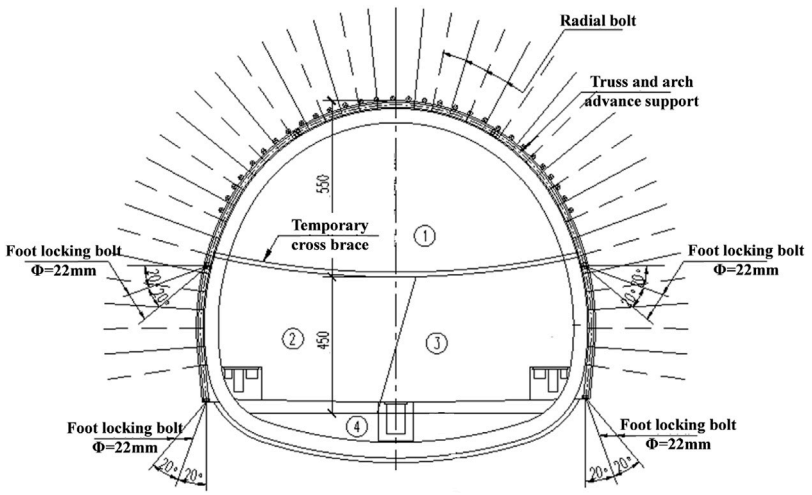


FIGURE 3 | Construction process of a double-track tunnel step method with temporary transverse bracing.

In summary, there have been a large number of studies on the interaction between the construction of a tunnel and close-to-existing buildings or structures (including tunnels). However, so far, there have been few studies on the construction disturbance effect of the upper and lower overlapped tunnels. In this paper, the stress and deformation behavior of the stratum and tunnel during the construction of overlapping tunnels are studied. The cause and distribution of the longitudinal cracks in the secondary lining of the lower tunnel are analyzed.

2 PROJECT OVERVIEW

2.1 Design Overview

The upper and lower adjacent overlapping tunnels in this study are shown in **Figure 1**. The maximum buried depths of the vault of the upper and lower tunnels are 130 and 149 m, respectively, and the longitudinal position relationship is shown in **Figure 2**. The tunnel area is mainly woodland with an elevation of 217.9–302.3 m. The minimum height difference between the upper and lower tunnel track surfaces in the tunnel mileage section of this study is about 14.3 m, and the minimum net rock layer is about 2.5 m. The entire section is located on a straight line, and a single-sided slope with a longitudinal slope of 3% is designed.

The tunnel is excavated by the mining method and supported in advance by the large pipe shed. In general, the construction is carried out from the bottom to the top, and after the construction of the lower tunnel is completed, the construction of the upper tunnel will be carried out. **Figure 3** shows the construction diagram of the upper and lower tunnels, which are constructed by the two-step temporary inverted arch method, with temporary cross bracing. The initial support of the upper and lower tunnels is C25 shotcrete with a thickness of 30 and 27 cm, respectively, and

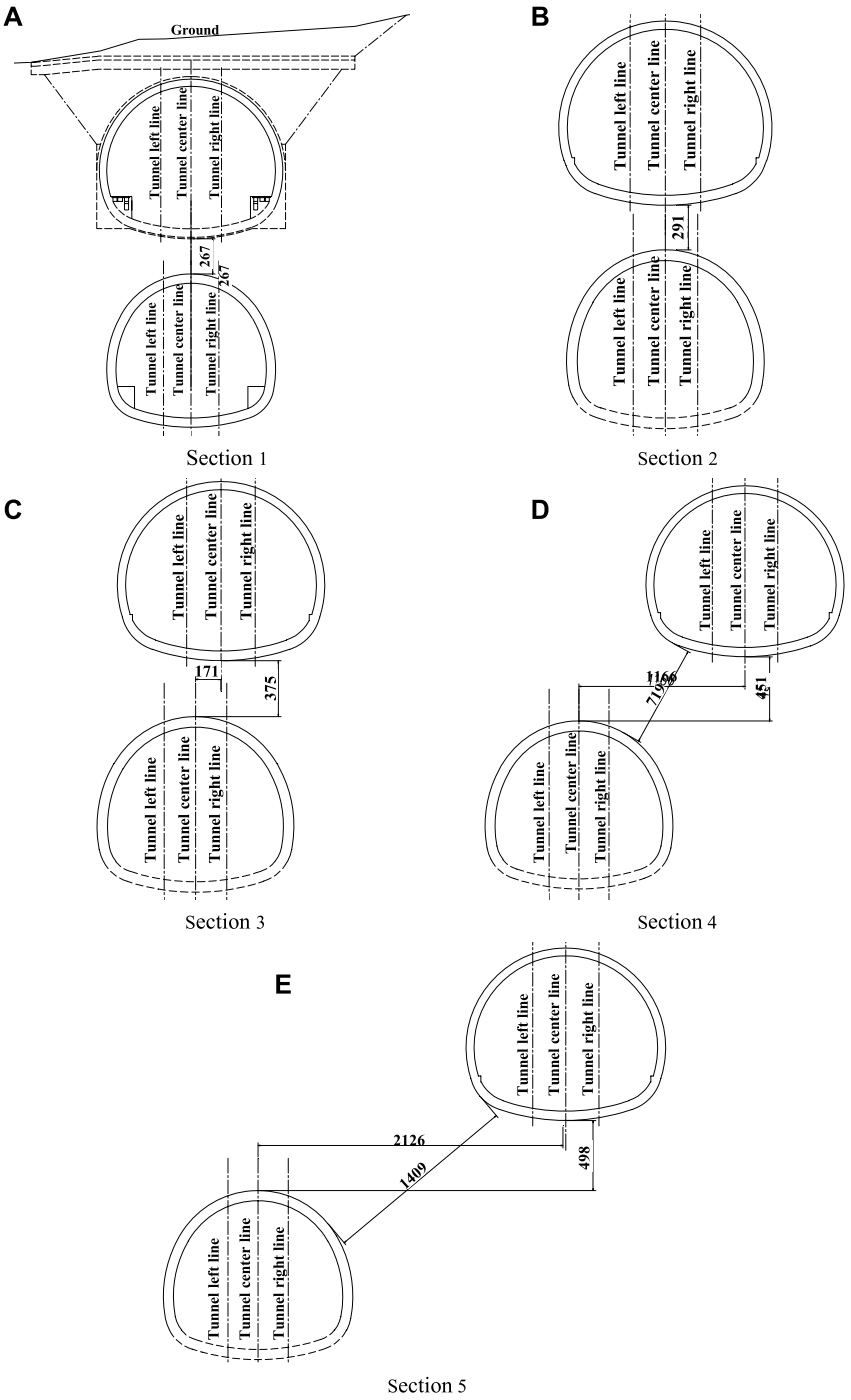


FIGURE 4 | Typical cross section of the overlapped tunnels (unit: mm).

the lining is C35 reinforced concrete with a thickness of 55 and 70 cm, respectively.

2.2 Engineering Geology

The stratum in the tunnel area is a monoclinic structure with a complex geological structure and poor geological development, mainly including accumulations, coal seam gas, soft rock, and trench soft soil. The overall surrounding rock of the tunnel is relatively soft, the joint fissures are relatively developed, and it is covered with artificially filled soil, silty clay, and silty clay. The surface water in the site area is mainly gully water, which is recharged by atmospheric rainfall, while the groundwater is mainly poured water and fissure water, which is mainly recharged by infiltration such as atmospheric rainfall. It has little impact on concrete and tunnel construction.

TABLE 1 | Information table of each section.

Section	Tunnel depth/m	Tunnel vertical clear distance/m	Horizontal distance between tunnels/m
Section 1	2.7	2.7	0
Section 2	10.4	2.9	0
Section 3	31.3	3.8	1.7
Section 4	49.4	4.5	11.7
Section 5	74.7	4.9	21.5

TABLE 2 | Physical and mechanical parameters of model materials.

Material name	Weight/kN·m^{-3}	Poisson's ratio	Cohesion(c)/kPa	Angle of internal friction (φ)/°	Deformation modulus (Es)/GPa
Stratum surrounding rock	26	0.42	160	24.5	1.65
Bolt reinforcement area	28.6	0.42	176.0	27.0	1.8
C25 concrete	25	0.2	—	—	28
C35 concrete	25	0.2	—	—	31.5
Steel	78.5	0.25	—	—	200

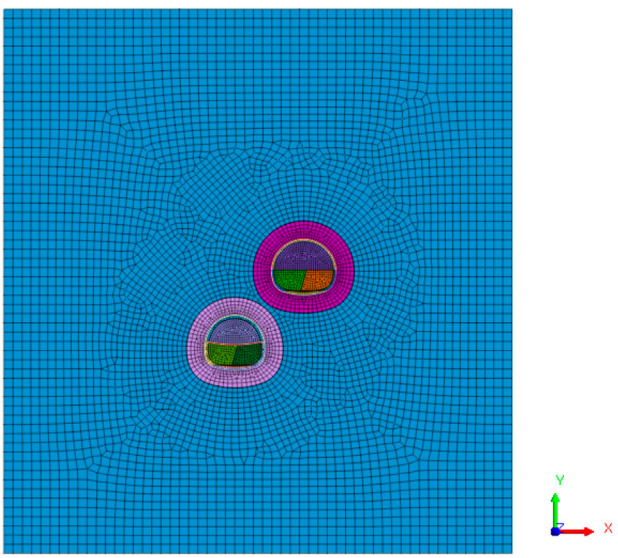


FIGURE 5 | Two-dimensional finite element calculation model.

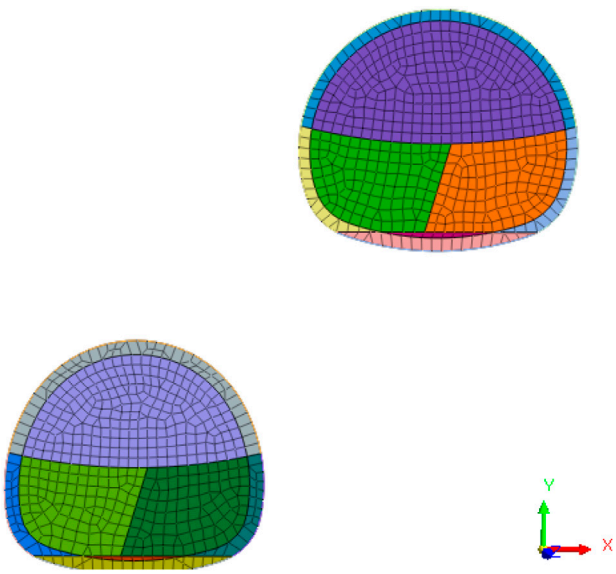


FIGURE 6 | Anchor rod equivalent reinforcement area and secondary lining model.

3 NUMERICAL SIMULATION ESTABLISHMENT OF OVERLAPPING TUNNELS

3.1 Typical Cross Sections of Upper and Lower Overlap Tunnels

The vertical spacing between the upper and lower tunnels is about 2~5 m, the horizontal spacing is about 0–22 m, and the buried depth of the upper tunnels gradually increases from 3 to 75 m. Five typical sections in the study section are selected for research. The relative position relationship between the upper and lower tunnels is shown in **Figure 4**, and the corresponding buried depth and spacing are shown in **Table 1**.

3.2 Numerical Simulation of Overlapping Tunnels

The interaction between the stratum and the structure is analyzed and studied by finite element numerical simulation. Taking into account the range of interaction between the research object and the surrounding soil, select the influence range of tunnel excavation (3–5 times the tunnel radius). According to the relevant design data,

TABLE 3 | A brief description of the construction steps of the sequential construction method.

Construction sequence	Content	Remark
Step 1	Initial stress	Apply boundary conditions, gravity loads
Step 2	Displacement clear	Check "Displacement reset"
Step 3	Lower tunnel construction	Excavation of cavern ①, spray mixing, application of anchor rods, and temporary horizontal bracing
Step 4	Lower tunnel construction	Excavation of cavern ②, spraying, and application of anchor rod
Step 5	Lower tunnel construction	Excavation of cavern ③, spraying, and application of bolts
Step 6	Lower tunnel construction	Excavation of cavern ④, spraying, and application of bolts
Step 7	Lower tunnel construction	Construct secondary lining and remove the temporary cross brace
Step 8	Upper tunnel construction	Excavation of cavern ①, spray mixing, application of anchor rods, and temporary horizontal bracing
Step 9	Upper tunnel construction	Excavation of cavern ②, spraying, and application of anchor rod
Step 10	Upper tunnel construction	Excavation of cavern ③, spraying, and application of bolts
Step 11	Upper tunnel construction	Excavation of cavern ④, spraying, and application of bolts
Step 12	Upper tunnel construction	Construct secondary lining and remove the temporary cross brace

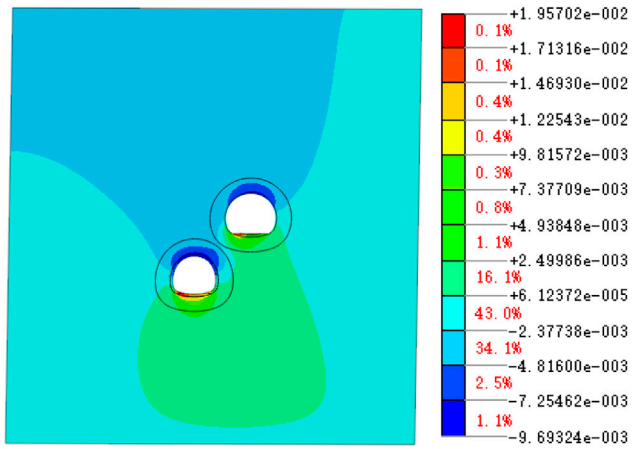


FIGURE 7 | Vertical displacement after excavation of the upper tunnel (unit: m).

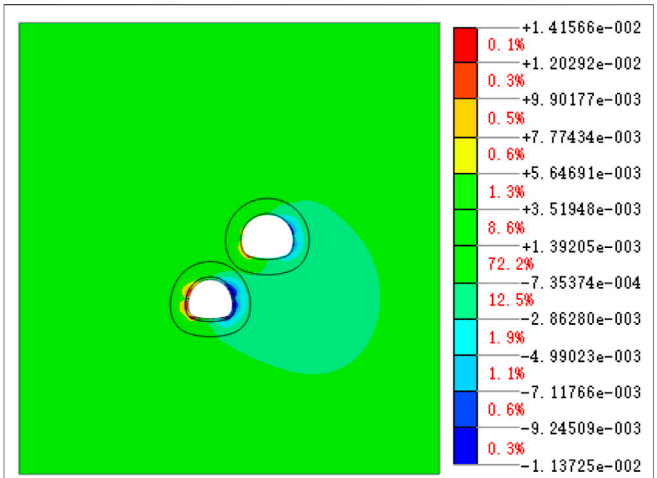


FIGURE 8 | Horizontal displacement after excavation of the upper tunnel (unit: m).

the mechanical parameters of the rock mass around the tunnel section are selected. In the calculation model, the surrounding rock is simulated by the two-dimensional elements of the Mohr-Coulomb constitutive model. The secondary lining is simulated by linear elastic constitutive two-dimensional elements. One-dimensional beam elements with an elastic constitutive model are adopted for concrete and temporary cross braces. In some cases, bolt support can be equivalent to soil reinforcement in numerical simulation. The detailed values of the material parameters of the model are shown in **Table 2**.

Set the normal displacement constraint boundary on the side and bottom of the model, and the boundary on the top of the model is a free surface. As shown in **Figure 5**, take **Section 4** as an example to illustrate the numerical simulation grid division of the model. The model is 110 m long and 118 m high. The upper and lower tunnel excavation zones and the secondary lining model are shown in **Figure 6**.

3.3 Simulation of Excavation Conditions

According to the actual working conditions, the lower tunnel is first excavated, and then the upper tunnel is excavated. The construction sequence of the two tunnels is shown in **Table 3**. According to the overlap, the tunnel construction process is divided into 12 construction stages according to the simulation of key steps.

4 MODEL RESULT ANALYSIS

4.1 Vertical Displacement

Take **Section 4** as an example to present the simulation results and analyze them. **Figure 7** shows the vertical displacement cloud image caused by the completion of Step12. During the excavation of tunnels, arch crown settlement and arch bottom uplift will occur. After the construction of the upper tunnel, the vault settlement of the lower tunnel increased from 8.9 to 9.7 mm, an increase of 9%, compared with the results of step 7. And the distribution of stratum settlement is asymmetric, and the settlement trend is inclined below the joint action of the upper and lower tunnels.

4.2 Horizontal Displacement

Figure 8 shows the horizontal displacement cloud diagram caused by the completion of Step12. During the excavation of the tunnel, the

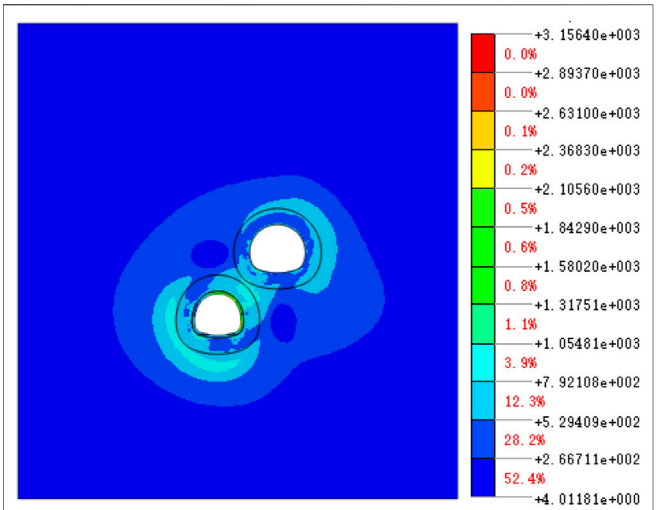


FIGURE 9 | Maximum shear stress after excavation of the upper tunnel (unit: kPa).

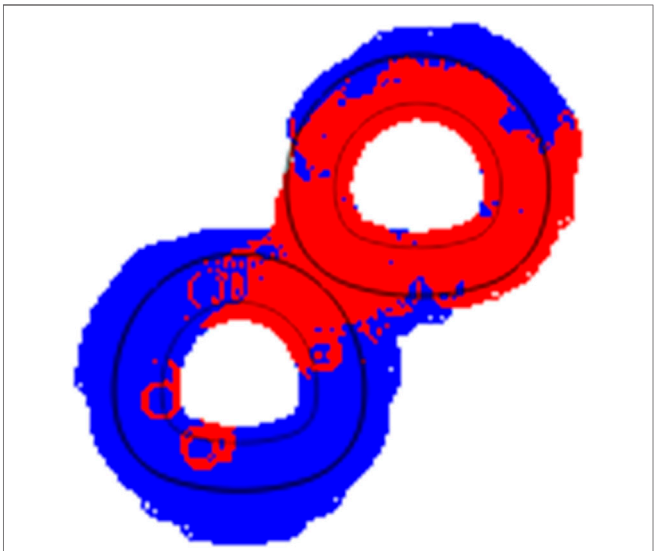


FIGURE 10 | Distribution of the plastic zone after excavation of the upper tunnel (red: plastic or failure; blue: unloading or reloading).

arch waist and the area above it will produce horizontal deformation, which can increase the potential factors of the secondary lining tension cracking. After the construction of the upper tunnel, the horizontal deformation of the arch waist and above the lower tunnel increased from 10.7 to 11.3 mm, an increase of 6%, and the horizontal convergence increased from 23.2 to 25.6 mm, an increase of 10%, compared with the results of step 7. It can be seen that the horizontal convergence deformation of the arch waist and the area above increased due to the construction of the upper tunnel.

4.3 Maximum Formation Shear Stress

Figure 9 shows the maximum stress cloud image caused by the completion of Step12. During the excavation of the tunnel, there is a

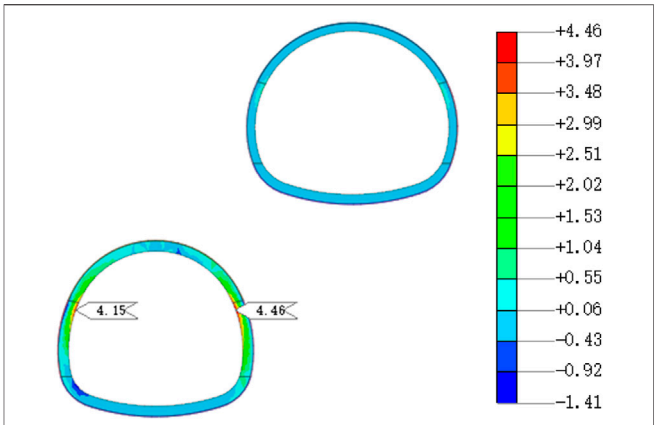


FIGURE 11 | *Y*-direction stress of the secondary lining structure of the lower tunnel (unit: MPa).

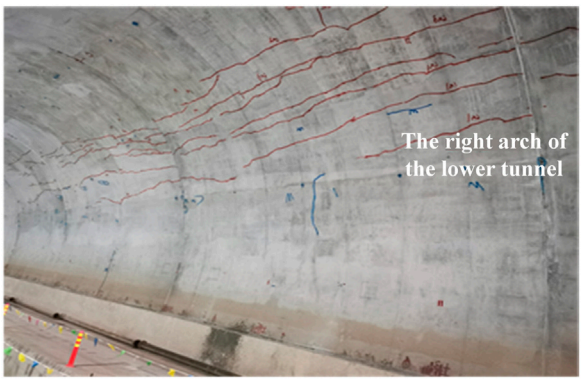


FIGURE 12 | Site photo of the partial longitudinal crack on the right side of the lower tunnel.



FIGURE 13 | Site photos of longitudinal cracks on the left and right sides of the lower tunnel.

TABLE 4 | Crack situation table

Crack number	Location	Crack length/m	Crack width/mm	Crack width depth/cm	Crack type
Crack 1#	Arch right	12	0.3	11.8	Vertical
Crack 2#	Arch right	12	0.2	7.7	Vertical
Crack 3#	Arch right	12	0.3	9	Vertical
Crack 4#	Arch right	12	0.3	10.9	Vertical
Crack 5#	Arch right	12	0.4	11.9	Vertical
Crack 6#	Arch right	12	0.2	12.5	Vertical
Crack 7#	Arch right	12	0.3	11.2	Vertical
Crack 8#	Right wall	2	0.3	7.8	Hoop
Crack 9#	Arch right	12	0.3	8.4	Vertical

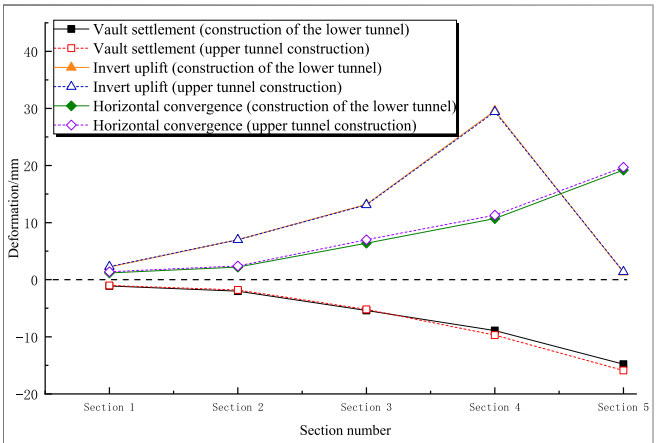


FIGURE 14 | Displacement result analysis at different cross-sections

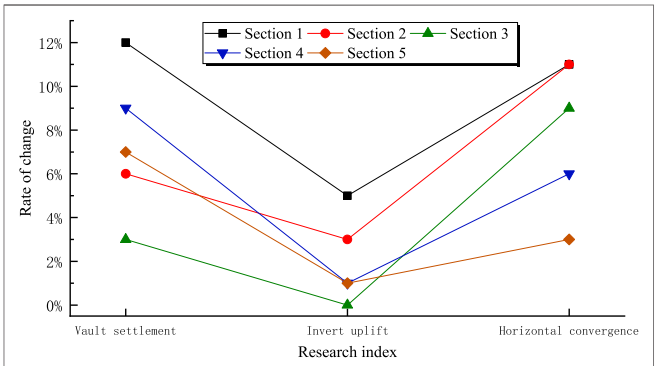


FIGURE 15 | Displacement result analysis at different cross-sections

concentration of shear stress around the tunnel, which is mainly concentrated in the range of 3–8 m around the tunnel, that is, around the end of the anchor rod. Therefore, in actual construction, the quality of the anchor rod should be ensured, especially the depth of the anchor rod and the stability of the soil near the tunnel. At the same time, the shear stress concentration area at the stratum connection part is significantly higher than that of the surrounding stratum, which means that the stratum soil in this area will be damaged first, and it should be properly reinforced during construction. In addition, the shear stress concentration of the lower tunnel is mainly concentrated above the arch waist, which is close to the secondary lining crack found on site.

4.4 Plastic Zone Distribution

Figure 10 shows the distribution cloud map of the formation plastic zone caused by the completion of Step12. Part of the plastic zone appears around the tunnel excavation area, and it is easy to form a penetrating plastic zone between the upper and lower tunnels. Moreover, the plastic zone of the lower tunnel is mainly located above the arch waist on both sides, which is also consistent with the location of the shear stress concentration. The plastic zone reflects the distribution of rock mass instability and failure, especially at the stratum connection. The distribution of the plastic zone is relatively obvious, and there is serious penetration. Therefore, in the actual construction, one needs to pay attention to the proper reinforcement of the rock mass at the connection between the upper and lower tunnels to avoid the penetration of the plastic zone.

4.5 Secondary Lining Stress

Figure 11 shows the vertical stress distribution cloud diagram of the secondary lining caused by the completion of Step 12. It can be seen that the tensile stress of the secondary lining of the lower tunnel appears to stress concentration near the left and right arch waists, and the maximum tensile stress in the *Y* direction is 4.15 and 4.46 mpa, respectively. The tensile stress distribution of the left and right arch waist is significant.

5 ANALYSIS OF THE CRACKS IN THE LINING STRUCTURE OF THE LOWER TUNNEL

5.1 Actual Lining Cracks

According to the actual measurement on site, after the construction of the upper tunnel (post-excavation tunnel) was completed, longitudinal cracks appeared in some areas of the lower tunnel (existing tunnel). As shown in **Figure 12**, the cracks occurred mainly at the right waist of the lower tunnel, which was adjacent to the upper tunnel. As shown in **Figure 13**, cracks appeared in both the left and right arches of the lower tunnel.

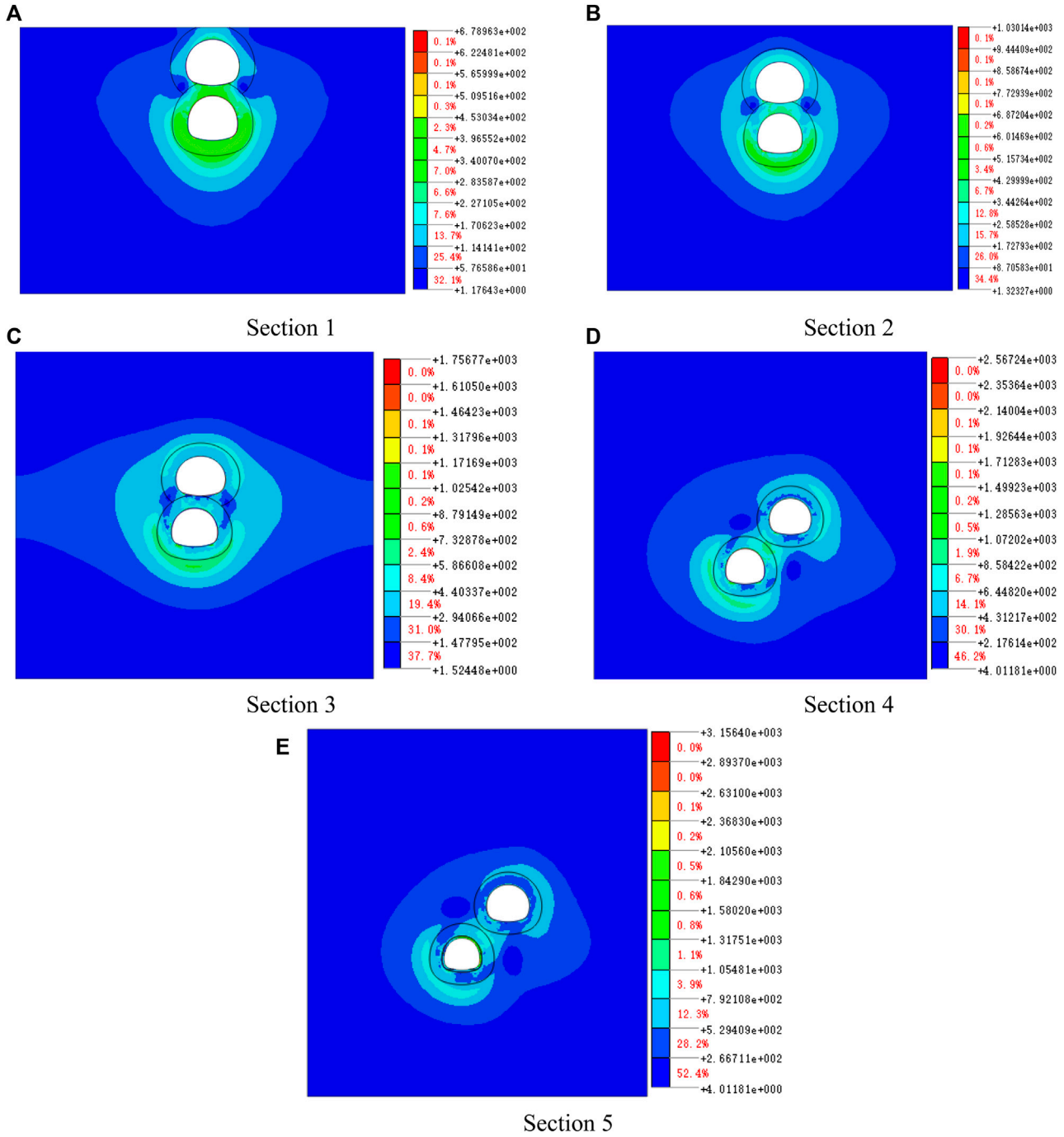


FIGURE 16 | Maximum shear stress cloud diagram of displacement at different cross-sections (unit: kPa).

Table 4 has given the specific conditions of the cracks. It can be found that the crack length is 12 m, the crack width is 0.2~0.4 mm, and the crack depth is 7.7~12.5 cm.

5.2 Analysis of the Causes of Cracks

When comparing the tensile stress calculation result of the obvious tensile area of the secondary lining of the lower tunnel caused by the construction of the upper tunnel with the standard value of the tensile strength of C35 concrete of 2.2 MPa, it can be found that the maximum tensile stress of the secondary lining of the lower tunnel obtained by the cross-section simulation calculation is greater than 2.2 MPa, so cracks extending along the *Z* direction in the XY plane will occur, which appear as longitudinal cracks.

Although the above is a quantitative judgment, to further analyze the development law of tunnel cracks caused by

construction mechanical properties, it is necessary to analyze the cause and law of the secondary lining cracks of the lower tunnel based on the characteristics of stratum deformation and the distribution law of stratum shear stress and plastic zone.

Figure 14 shows the tunnel displacement curve of each section after the completion of step 12, and **Figure 15** shows the absolute change rate of the influence of the upper tunnel on the lower tunnel, in which the tunnel buried depth, tunnel vertical clear distance, and tunnel horizontal distance from **Section 1** to **Section 5** gradually increase. According to **Figures 14**, **15**, in terms of vault settlement, when the buried depth is shallow and the tunnel distance is close, the construction of the upper tunnel will rebound the vault settlement of the lower tunnel to a certain extent, in which **Section 1** rebounds by 12%. With the increase in the distance between the two tunnels, it will gradually increase the vault settlement of the lower tunnel, in which **Section 5** settlement increases by 7%. In terms of invert displacement, the influence of the upper tunnel construction on the invert of the lower tunnel uplift is relatively small, of which **Section 1** has the largest change rate, and the uplift is only increased by 5%. In terms of horizontal convergence, the construction of the upper tunnel will lead to an increase in the horizontal displacement of the lower tunnel. The greater the distance between the two tunnels, the greater the increase and the maximum increase is 11%. It can be seen that the vault settlement and horizontal convergence of the lower tunnel at different sections are mainly affected, while the inverted arch has little effect. Considering the vertical deformation of the arch crown and the horizontal deformation of the arch waist, greater oblique deformation above the arch waist will be obtained. The deformation law of the upper part of the arch waist reflects the causes of the cracks in the lower tunnel.

Figure 16 shows the maximum shear stress distribution of different sections after step 12. It can be seen that the shear stress is mainly concentrated in the range of 3~8 m around the tunnel. In this range, the overlapped tunnel arrangement has the greatest influence, and the most significant part is still in the upper part of the lower arch. As the upper and lower tunnels are gradually staggered on the plane, this influence gradually weakens, and as the distance increases and staggers, the maximum shear stress is gradually distributed in the area between the two tunnels, and the influence of the right arch of the lower tunnel is more obvious than that of the left arch.

5.3 Crack Distribution Law

1) The characteristics of tunnel displacement and the distribution of shear stress indicate that there is a greater risk of cracks near the left and right arch waists of the lower tunnel, which not only reflects the location of the cracks, but also explains the reasons for the changes in the cracks.
2) The distribution trend of the maximum shear stress shows that the bias effect of the upper tunnel on the lower tunnel increases with the decrease in the distance between the tunnels. The bias effect decreases with the increase of distance, and the lining cracks of the lower tunnel appear gradually.
3) The change rate of the deformation influence of the lower tunnel decreases with the increase in the distance between the two tunnels. Under the large lining deformation, the lower tunnel is easy to crack in the arch's waist and upper part.

6 CONCLUSION

In this paper, aiming at the longitudinal cracks in the secondary lining of the tunnel, numerical simulation is used to analyze the mechanical response of the construction of the upper and lower overlapping tunnels. The causes and distribution laws of longitudinal cracks in the lower tunnel lining are explored. The following conclusions are drawn:

1) The vault settlement and horizontal convergence are the main influences of the upper tunnel on the lower tunnel are. The deformation law of the upper part of the larger arch waist constitutes the cause of the cracks in the lower tunnel, and the arch waist on the side close to the tunnel is easily cracked. Therefore, the construction should focus on the deformation of the vault and arch waist.
2) As the distance between overlapping tunnels increases from near to far, the influence of the upper tunnel construction on the lower tunnel is that the horizontal convergence deformation increases gradually, and the vertical deformation changes from the rebound to intensified settlement.
3) The maximum shear stress and plastic deformation area have similar distribution laws. If the distance between the tunnels is too small, it will produce obvious shear stress concentration and increase the penetration degree of the plastic zone, resulting in high stress on the lower tunnel lining, reflecting the corresponding relationship between the maximum shear stress distribution area, the plastic area and the crack distribution of the lower tunnel.
4) The stress and deformation characteristics of the stratum and lining structure reflect that the post-excavation tunnel has a biasing effect on the existing tunnel, which constitutes the cause of tunnel cracks. Measures should be taken in time to weaken this effect during construction to avoid tunnel cracks.

DATA AVAILABILITY STATEMENT

The original contributions presented in the study are included in the article/Supplementary Material, further inquiries can be directed to the corresponding author.

AUTHOR CONTRIBUTIONS

YF and LY: Georisjk analysis; XQ: numerical simulation; ZY: georisk analysis; HL: crack analysis; ZP: construction control; and CY: numerical simulation.

REFERENCES

Addenbrooke, T. I., and Potts, D. M. (2001). Twin Tunnel Interaction: Surface and Subsurface Effects. *Int. J. Geomech.* 1 (2), 249–271. doi:10.1061/(asce)1532-3641(2001)1:2(249)

Asano, T, Ishihara, M., Kiyota, Y., Kurosawa, H., and Ebisu, S. (2003). An Observational Excavation Control Method for Adjacent Mountain Tunnels [J]. *Tunn. Undergr. Space Technol.* 18 (2-3), 291–301. doi:10.1016/s0886-7798(03)00043-9

Beyabanaki, A.R., and Gall, V. (2017). 3D Numerical Parametric Study of the Influence of Open-Pit Mining Sequence on Existing Tunnels [J]. *Int. J. Min. Sci. Technol.* 27 (03), 459–466.

Byun, G., Kim, D., and Lee, S. (2006). Behavior of the Ground in Rectangularly Crossed Area Due to Tunnel Excavation under the Existing Tunnel[J]. *Tunn. Undergr. Space Technol.* 21 (3-4), 361–367. doi:10.1016/j.tust.2005.12.178

Cooper, M.L., Chapman, D.N., and Rogers, C.D.F. (2001). Prediction of Settlement in Existing Tunnel Caused by the Second of Twin Tunnels[J]. *Transp. Res. Rec.* 1814 (1), 103–111. doi:10.3141/1814-12

Do, N.-A., Dias, D., and Oreste, P. (2015). 3D Numerical Investigation on the Interaction between Mechanized Twin Tunnels in Soft Ground. *Environ. Earth Sci.* 73 (5), 2101–2113. doi:10.1007/s12665-014-3561-6

Dong, Y., Wang, J., Wang, Z., Zhang, X., Gao, Y., Sui, Q., et al. (2019). A Deep-Learning-Based Multiple Defect Detection Method for Tunnel Lining Damages. *IEEE Access* 7, 182643–182657. doi:10.1109/access.2019.2931074

Hage Chehade, F., and Shahrour, I. (2008). Numerical Analysis of the Interaction between Twin-Tunnels: Influence of the Relative Position and Construction Procedure. *Tunn. Undergr. Space Technol.* 23 (2), 210–214. doi:10.1016/j.tust.2007.03.004

Hu, Z. F., Yue, Z. Q., Zhou, J., and Tham, L. G. (2003). Design and Construction of a Deep Excavation in Soft Soils Adjacent to the Shanghai Metro Tunnels. *Can. Geotech. J.* 40 (5), 933–948. doi:10.1139/t03-041

Huang, H.-w., Li, Q.-t., and Zhang, D.-m. (2018). Deep Learning Based Image Recognition for Crack and Leakage Defects of Metro Shield Tunnel. *Tunn. Undergr. Space Technol.* 77, 166–176. doi:10.1016/j.tust.2018.04.002

Jia, J. (2006). Study of Controlling Measures on the Deflection of Metro Tunnels Due to Overlying Excavation[J]. *Undergr. Constr. Ground Mov.* 26 (s), 158–163. doi:10.1061/40867(199)18

Liang, Q., Li, J., Li, D., and Ou, E. (2013). Effect of Blast-Induced Vibration from New Railway Tunnel on Existing Adjacent Railway Tunnel in Xinjiang, China. *Rock Mech. Rock Eng.* 46 (1), 19–39. doi:10.1007/s00603-012-0259-5

Liu, H., Li, P., and Liu, J. (2011). Numerical Investigation of Underlying Tunnel Heave during a New Tunnel Construction. *Tunn. Undergr. Space Technol.* 26 (2), 276–283. doi:10.1016/j.tust.2010.10.002

Marta, D. O. L. E. Z. A. L. O. V. A. (2001). Tunnel Complex Unloaded by a Deep Excavation[J]. *Comput. Geotechnics* 28 (3), 69–493. doi:10.1016/S0266-352X(01)00005-2

Park, S., Kim, J.-S., and Kwon, S. (2018). Investigation of the Development of an Excavation Damaged Zone and its Influence on the Mechanical Behaviors of a Blasted Tunnel. *Geosystem Eng.* 21 (3), 165–181. doi:10.1080/12269328.2018.1461139

Peng, L., Du, S., Ma, Xi., Yin, Z., and Shen, S. (2014). Centrifuge Investigation into the Effect of New Shield Tunnelling on an Existing Underlying Large-Diameter Tunnel. *Tunn. Undergr. Space Technol.* 42, 59–66. doi:10.1016/j.tust.2014.02.004

Schroeder, F. C., Potts, D. M., and Addenbrooke, T. I. (2004). The Influence of Pile Group Loading on Existing Tunnels. *Géotechnique* 54 (6), 351–362. doi:10.1680/geot.2004.54.6.351

Sharma, J. S., Hefny, A. M., Zhao, J., and Chan, C. W. (2001). Effect of Large Excavation on Deformation of Adjacent MRT Tunnels. *Tunn. Undergr. Space Technol.* 16 (2), 93–98. doi:10.1016/s0886-7798(01)00033-5

Shin, J.-H., Moon, H.-G., and Chae, S.-E. (2011). Effect of Blast-Induced Vibration on Existing Tunnels in Soft Rocks. *Tunn. Undergr. Space Technol.* 26 (1), 51–61. doi:10.1016/j.tust.2010.05.004

Standing, J. R., Potts, D. M., Vollum, R., Burland, J. B., and Avgerinos, V. (2015). Research into the Effect of Tunneling on Existing Tunnels[J]. *Infrastructure* 2 (59), 301–312. doi:10.1680/ecsmge.60678

Yun, H.-B., Park, S.-H., Mehdawi, N., Mokhtari, S., Chopra, M., Reddi, L. N., et al. (2014). Monitoring for Close Proximity Tunneling Effects on an Existing Tunnel Using Principal Component Analysis Technique with Limited Sensor Data. *Tunn. Undergr. Space Technol.* 43 (7), 398–412. doi:10.1016/j.tust.2014.06.003

Zhang, Z., and Huang, M. (2014). Geotechnical Influence on Existing Subway Tunnels Induced by Multiline Tunneling in Shanghai Soft Soil. *Comput. Geotechnics* 56 (3), 121–132. doi:10.1016/j.compgeo.2013.11.008

Zhao, H.-b., Long, Y., Li, X.-h., and Lu, L. (2016). Experimental and Numerical Investigation of the Effect of Blast-Induced Vibration from Adjacent Tunnel on Existing Tunnel. *KSCE J. Civ. Eng.* 20 (1), 431–439. doi:10.1007/s12205-015-0130-9

Zheng, G., and Wei, S. (2008). Numerical Analyses of Influence of Overlying Pit Excavation on Existing Tunnels[J]. *J. Cent. South Univ. Technol.* 15 (s2), 69–75. doi:10.1007/s11771-008-0438-4

Zhong, Q., Bai, L., An, S., Ju, F., and Liu, L. (2016). Lining Seam Elimination Algorithm and Surface Crack Detection in Concrete Tunnel Lining[J]. *J. Electron. Imaging* 25 (6).063004. doi:10.1117/1.JEI.25.6.063004

Conflict of Interest: Authors YF and ZP were employed by The Fifth Engineering Company of CREGC; author ZY was employed by Chongqing Urban Construction Investment (Group) Co., Ltd.; and author HL was employed by China Railway No. 2 Engineering Group Co., Ltd.

The remaining authors declare that the research was conducted in the absence of any commercial or financial relationships that could be construed as a potential conflict of interest.

Publisher's Note: All claims expressed in this article are solely those of the authors and do not necessarily represent those of their affiliated organizations, or those of the publisher, the editors, and the reviewers. Any product that may be evaluated in this article, or claim that may be made by its manufacturer, is not guaranteed or endorsed by the publisher.

Copyright © 2022 Fengjie, Yang, Qianwei, Yuanlin, Lisheng, Ping and Yuebang. This is an open-access article distributed under the terms of the Creative Commons Attribution License (CC BY). The use, distribution or reproduction in other forums is permitted, provided the original author(s) and the copyright owner(s) are credited and that the original publication in this journal is cited, in accordance with accepted academic practice. No use, distribution or reproduction is permitted which does not comply with these terms.

frontiers | Frontiers in Earth Science

ORIGINAL RESEARCH
published: 08 June 2022
doi: 10.3389/feart.2022.893549

Fracture Characteristics of Sliding Crack in Brittle Rock: Analysis Based on an Improved Equivalent Crack Model

Yin Zhang[1,2]*, *Shenghua Cui*[1]*, *Zhibing Yu*[2] *and Jianlong Cheng*[1]

[1]State Key Laboratory of Geohazard Prevention and Geoenvironment Protection, Chengdu University of Technology, Chengdu, China, [2]Sichuan Road and Bridge (Group) Co., Ltd., Chengdu, China

Under low confinement axial compression, the failure of brittle rock is mainly caused by tensile fracture. Many scholars adopt the sliding crack as an idealized model to present the intrinsic mechanism of the tensile failure but due to the complex configuration of sliding crack, its stress intensity factor (SIF) calculation has always been a difficult problem. In this study, an improved model of sliding crack is proposed; in the context of linear elastic fracture mechanics (LEFM) and weight function method, the expression of stress intensity factor (SIF) has been derived. The propagation manners of sliding crack under axial loading and lateral unloading conditions have been further analyzed. The extended finite element method (XFEM) is employed to verify the correctness of the theoretical SIF formulation and its inferences. The formula of SIF shows that a sliding crack is highly sensitive to the change of the lateral stress, which theoretically explains compressive failure characteristics of brittle rock as follows: 1) under the condition of axial compression, increasing the lateral stress has a very strong no-linear impact on the strength of brittle rock; 2) under the condition of lateral unloading, the destruction of rock is more abrupt and ferocious than that of the loading case. In order to confirm that micro-fractures in rocks are notably influenced by confining pressure, as the former theoretical fracture analysis predicted, the tri-axial compression test combined with the acoustic emission monitoring technique has been conducted on basalt samples. According to the acoustic waveform parameter method, it shows that increasing the confining pressure will greatly reduce the proportion of tension-type fractures, which indirectly proves the correctness of the sliding crack hypothesis and fracture analysis.

Keywords: crack, LEFM, SIF, brittle rock, micro-fracture, acoustic emission

OPEN ACCESS

Edited by:
Yunhui Zhang,
Southwest Jiaotong University, China

Reviewed by:
Peifeng Han,
Southwest University of Science and Technology, China
Zizheng Guo,
Hebei University of Technology, China

***Correspondence:**
Yin Zhang
zhangyin0503@gmail.com
Shenghua Cui
cuishenghua18@cdut.edu.cn

Specialty section:
This article was submitted to Geohazards and Georisks, a section of the journal Frontiers in Earth Science

Received: *10 March 2022*
Accepted: *30 March 2022*
Published: *08 June 2022*

Citation:
Zhang Y, Cui S, Yu Z and Cheng J (2022) Fracture Characteristics of Sliding Crack in Brittle Rock: Analysis Based on an Improved Equivalent Crack Model. Front. Earth Sci. 10:893549. doi: 10.3389/feart.2022.893549

1 INTRODUCTION

It is well known that the destruction mechanism of most materials under compressive stress is shearing failure; however, for brittle rocks, tensile fracture (i.e., splitting, spalling) is a common failure pattern, even in prevailing overall compressive stresses (Nemat-Nasser and Horii, 1982; Renshaw and Schulson, 2001; Wong and Baud, 2012; Huang et al., 2019). The tensile cracks caused by compressive load make the rocks exhibit a variety of complex and nonlinear behaviors, which has been intensively studied by scholars of rock mechanics (Horii and Nemat-Nasser, 1985; Zuo et al., 2008; Wang et al., 2012; Clayton and Knap, 2014).

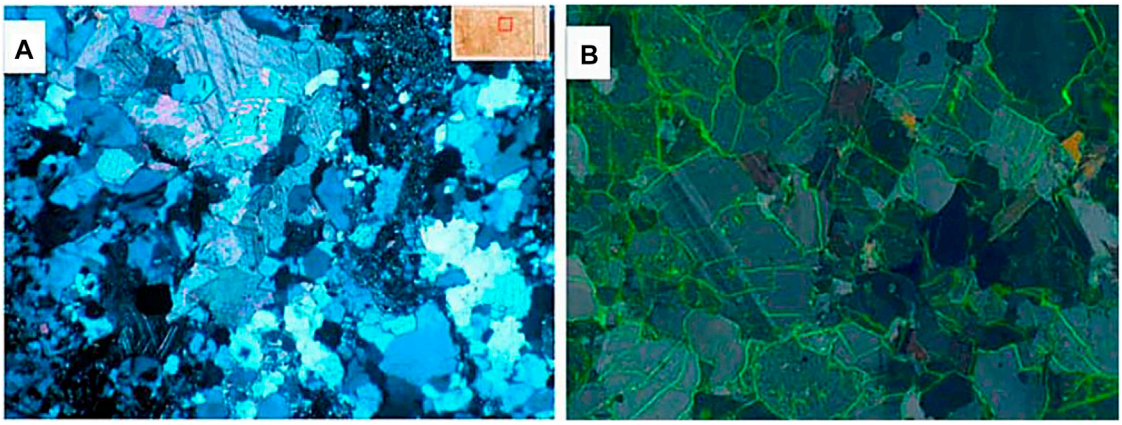


FIGURE 1 | Example of the meso-structures observed in polarized light thin section. **(A)** Diorite and **(B)** granite (Lan et al., 2010).

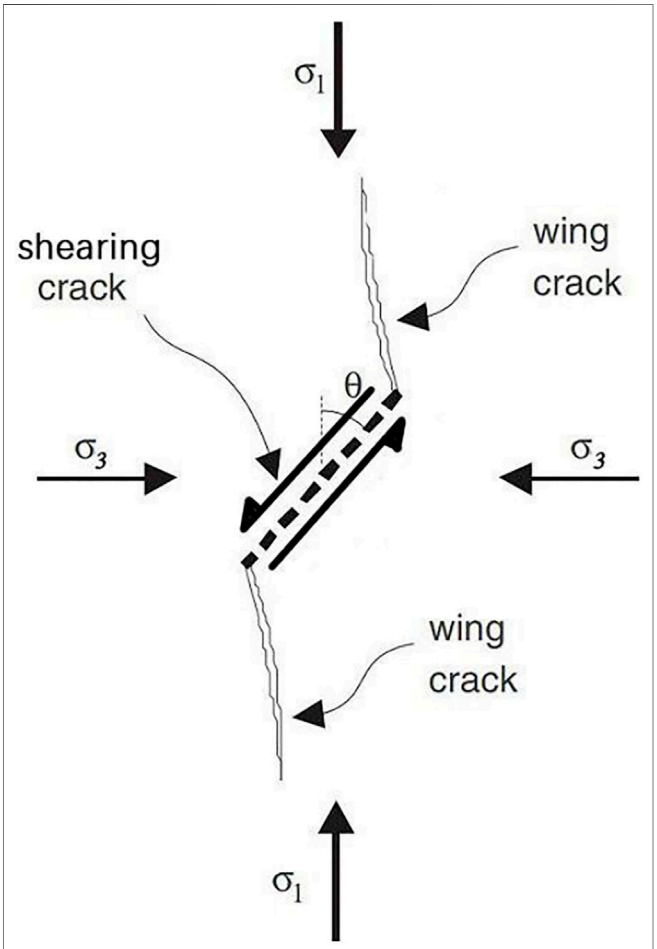


FIGURE 2 | Schematic diagram of the sliding crack model (Yuan S. C., 2006).

The traditional mechanics of homogeneous materials cannot explain how tensile cracks emerge in an overall compressive environment, so the mesoscopic structure needs to be taken into consideration (Yuan and Harrison, 2006). The rock material contains a plenty of mesoscopic defects, such as cracks, cavities, soft or hard inclusions, and material crystal boundaries **Figure 1** (Jing, 2003; Read, 2004; Cui et al., 2021). When the rock body is subjected to far-field compressive stress, the defects would cause local distortion to the stress field and tensile stress concentration. As load increases, tensile fractures emerge in succession, then crack growth and coalescence would lead to instability and final failure of the rock body in consequence (Dragon et al., 2000).

Although the geometrical shapes of defects in rocks are various, the main fracture mechanism could be summarized as a tensile crack caused by insufficient shearing resistance of defects (Olsson and Peng, 1976; Wong, 1982). Therefore, many scholars adopt sliding crack as an idealized model to describe the compressive tensile fracture. The sliding crack model is first proposed by Brace and Bombolakis, (1963), and great progress has been made later (Ashby and Hallan, 1986; Nemat-Nasser and Obata, 1988; Renshaw and Schulson, 2001). The sliding crack starts from a pre-existing inclined crack subjected to shear force. Due to insufficient shearing resistance of the inclined crack, tensile cracks nucleation on the two ends of the pre-existing sliding crack, and these tension cracks then continue to grow in a stable manner with increasing axial compression curving toward the direction of maximum principal stress (Nemat-Nasser and Horii, 1982), as shown in **Figure 2**. The newly formed tensile cracks are called wing cracks.

For low-porosity brittle rocks, the sliding crack model is proved capable of explaining general rock mechanical behavior observed both in the laboratory and on the field (Basista and Gross, 1998; Eberhardt et al., 1999; Shao and Rudnicki, 2000).

1) Strong influence of confining pressures on the strength and failure modes;
2) Non-linearity in the stress–strain relation and degradation of the elastic constants;
3) Volumetric dilatancy after complete unloading due to opening of tensile cracks;

4) Hysteresis loops observed in the stress–strain curves in cyclic load;
5) Load-induced anisotropy ensuing from a directional process of micro-crack evolution;
6) Pronounced permanent lateral strain after complete unloading; little permanent strain in the direction of maximum compression;
7) Strongly path-dependent stress–strain relations.

Since the sliding crack model has a significant theoretical value in brittle material mechanics, efforts have been taken for decades to investigate its fracture process by theoretical analysis, model experimental illustration, and numerical simulation.

Bieniawski (1967) discussed the fracture process of brittle fracture of rock theoretically, and experimental verification has been conducted on the mechanism for rock tested under compressive stress conditions. Nemat-nasser and Horii (1982) analyzed the sliding crack model by LEFM and a series of qualitative experiments have been performed on thin plates of Columbia Resin CR 39, and analytical results have been accepted. Janeiro and Einstein, (2010) experimentally studied the cracking behavior of brittle heterogeneous materials. Without restraint, uniaxial compression tests are conducted on prismatic gypsum specimens containing one or two pre-cracks. Kari Kolari (2017) studied the 3D sliding crack model subject to uniaxial compressive and tensile loading, with crack opening displacements derived from Castigliano's second theorem, and completely agreed with the results of numerical simulations. Xun et al.,(2020) used the XFEM with the non-local stress field calculation to simulate the crack initiation and propagation of sliding cracks.

The concept of the stress intensity factor (SIF) is the central idea of fracture analysis, but due to the complex morphology of the sliding crack model, SIF cannot be derived directly. Therefore, the sliding crack is usually modeled as an equivalent straight crack, in which the wedging force on the pre-crack area opens the crack. The first model was proposed by Fairhurst and Cook (1966). Later, more and more equivalent crack models for SIF of sliding crack are proposed, and some of these models are summarized as follows:

Steif (1984) assumed that the wing cracks were straight, and the influence of the initial crack on the growth of wing cracks could be represented by a wedging slip displacement. Horii and Nemat-Nasser (1986) developed a single rectilinear crack inclined to the direction of the maximum stress and concluded that the rectilinear crack is driven by a pair of point forces collinear with the direction of the initial crack. Ashby and Hallam (1986) assumed that wing cracks had a fixed orientation, parallel to the major principal stress, and crack extension was driven by the normal and shear stresses along with the initial crack faces. Kemeny and Cook (1987) proposed a model in which a symmetrically opposite center force drove a crack oriented in the maximum stress direction. Lehner and Kachanov (2001) suggested that the wing crack could be represented by both wedge displacement-driven and stress-driven systems and then proposed a SIF model by equating the wedge displacement and acting stress effects in driving the wing crack growth.

Among the SIF solutions obtained from these simplified models, some lack accuracy because the models are too simplified, some are only capable of uniaxial loading, and some are too complicated to explain the physical meaning clearly.

In the present research study, the equivalent crack model of sliding crack has been improved. In this model, the fracture-driving force on the shear crack is no longer simplified to a point force, and the distributed stress on the wing cracks is also taken into consideration, so the model has higher accuracy and is suitable for various stress states and stress paths. By using the weight function, a more accurate SIF formulation is obtained based on the improved crack model, and the nonlinear fracture characteristics of sliding crack are discussed. According to the SIF formulation, the length of wing cracks under axial loading and lateral unloading are analyzed, which has explained the non-linearity of lateral stress on rock strength and the rock's sensitivity to lateral stress changes. Finally, the tri-axial compression tests are carried out on Emei basalt, and the waveform parameter method is used to classify the mode (shearing or tensile) of micro-fracture events. The test results have verified the inferences of fracture analysis and indirectly proved that the sliding crack is the main fracture mechanism behind the deformation and failure of brittle rock.

2 FRACTURE ANALYSIS ON SLIDING CRACK

Linear elastic fracture mechanics (LEFM) originated from the elastic solutions of straight cracks, it is difficult to deal with kinked and curved cracks. Therefore, an equivalent straight crack model has been established, with the configuration and fracture mode similar to that of sliding crack. In this way, an approximate expression of SIF is derived.

2.1 Modified Sliding Crack Model

Consider that an infinite body is deformed by a plane strain subjected to uniform compressive stress at infinity, maximum principal stress σ_1 is aligned to the Cartesian coordinate axis y, and minimum principal stress σ_3 is aligned to axis x. The body contains a pre-existing shearing crack PP′, and two symmetry wing cracks initiate at its tips and propagate in a slightly curved path toward the direction of the maximum compressive stress, as shown in **Figure 3A**. The length of PP′ is $2a$, at an angle of θ (termed as *crack angle*) with respect to axis y. The matrix is assumed to be isotropic and linear elastic with Young's modulus E and Poisson's ratio ν. The shearing crack PP' is tightly closed, and the friction resistance between the crack surfaces obeys Coulomb's law.

2.1.1 Driving Force and Fracture Initiation Criteria

As axial load increases or lateral confinement decreases, the shearing stress σ_t acting on the shearing crack (PP′) increases. When the friction resistance τ_f of shearing crack is surpassed by σ_t, stress concentrated at the crack tips plays the role of compensating the absence of friction resistance. Since shearing cracks are pre-existing and there is no cohesion on crack surfaces,

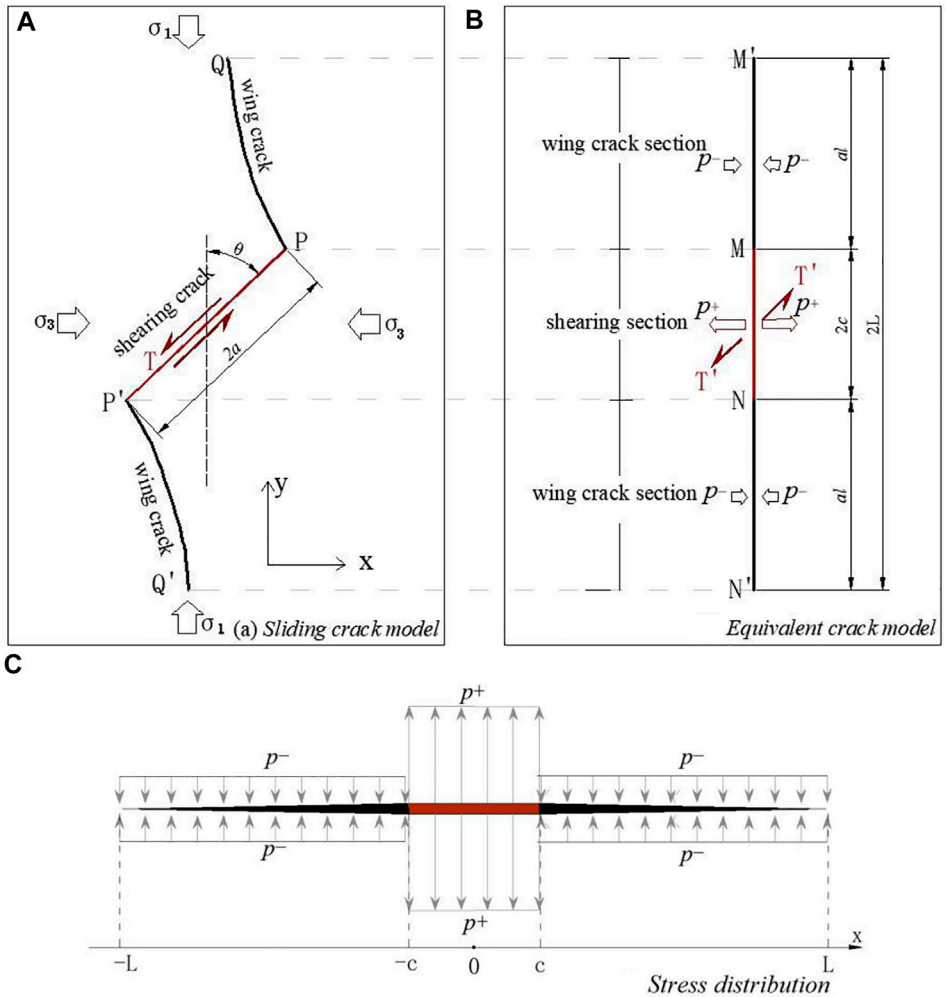


FIGURE 3 | Analytical model of a sliding crack. **(A)** Sliding crack model and **(B)** equivalent crack model. **(C)** Stress distribution on the equivalent crack model.

Coulomb's law is used to describe the shear resistance of shearing cracks. The difference between σ_t and τ_f is the fracture driving force T, which leads to nucleation and growth of wing cracks.

$$T = \sigma_t - \tau_f = D_1\sigma_1 - D_3\sigma_3, \tag{1}$$

where
$D_1 = \sin\theta(\cos\theta - \mu_f \sin\theta)$, $D_3 = \cos\theta(\sin\theta + \mu_f \cos\theta)$, and
μ_f is the fiction coefficient of the crack surfaces.

Before initiation of wing-cracks, the crack (PP′) is a typical model II fracture, according to the basic solutions of LEFM. The fracture initiation criterion is:

$$T\sqrt{\pi a} = K_{IIc} = \frac{\sqrt{3}}{2}K_{Ic}, \tag{2}$$

where K_{IIc} is model II fracture toughness and K_{Ic} is model I fracture toughness.

After substituting **Equation 1** for **Equation 2**, a new equation is obtained as follows:

$$D_1\sigma_1 - D_3\sigma_3 = \frac{\sqrt{3}}{2\sqrt{\pi a}}K_{Ic}. \tag{3}$$

As shown previously, the fracture initiation criterion is a linear function of principal stress.

2.1.2 Equivalent Straight Crack and Force

Wing cracks are tension cracks propagating in a stable manner, gradually turning their direction to the direction of max-principal stress. To make the kinked and curved crack tractable, it is decided to simplify the sliding crack into an equivalent straight crack, which is the projection of the sliding crack to axial y, as shown in **Figure 3B**. With the total length of the equivalent crack is $2L$, the shearing crack section is $2c$, and the wing crack section is L_w, c and L_w can be expressed as follows:

$$c = a\cos\theta \quad L_w = al, \tag{4}$$

where a is the half-length of pre-existing crack, and l is the dimensionless length of wing crack (in the following study, l is

more often used to represent wing crack length rather than L_w itself.).

The fracture driving force T is to PP′ and T' is to MN. In order to ensure that the load condition is basically equivalent to the sliding crack model, T' and T are in the same directions, and the resultant forces are identical, the relationship between T' and T satisfy is verified as follows:

$$Ta = T'c \Rightarrow T' = T\sec\theta. \tag{5}$$

For linear elastic materials, individual components of stress, strain, and displacement are additive. Based on the superposition concept, it is applicable to replace stress on the boundary with traction force on the crack faces. In addition, wing cracks are tensile cracks, and only normal traction force that causes mode I fracture needs to be taken into consideration. It is seen from the equivalent model that there are two main forces affecting the extension of wing cracks.

1) Crack-opening force: the component of T' perpendicular to the crack on shearing crack (MN), noted by p^+.

$$p^+ = T'\sin\theta = T\tan\theta = (D_1\sigma_1 - D_3\sigma_3)\tan\theta. \tag{6}$$

2) Crack closure force: the traction force on wing cracks (MM′ and NN′), approximate to σ_3, noted by p^-.

$$p^- = \sigma_3. \tag{7}$$

2.2 SIF and Its Nonlinear Features

2.2.1 Analytical Formulation of SIF

As set forth, an equivalent straight crack model is proposed by projecting a sliding crack to axis y, and the forces (p^+ and p^-) that cause crack propagation are obtained. Now, SIF could be figured out by a LEFM technique known as the weight function. The weight function is a SIF calculation method proposed by Buckner (1970) and Rice (1972) based on Green's formula, by which many SIF problems under complex load conditions could be solved.

For the convenience of description, a local coordinate system of the equivalent crack is established, as shown in **Figure 3C**. Axis x is parallel to the crack line, and the coordinate origin is located at the center of the crack. In this coordinate system, the force on the crack could be represented by the sectional function $p(x)$.

$$p(x) = \begin{cases} p^+ = (D_1\sigma_1 - D_3\sigma_3)\tan\theta, [-c, c] \\ p^- = \sigma_3, \ [-L, -c) \cup (c, L] \end{cases}. \tag{8}$$

According to weight function method, the SIF of a straight line crack is given by the following equation:

$$K_I = \int_{-L}^{L} p(x)w(x)dx, \tag{9}$$

where, $w(x)$ is the weight function, representing the SIF caused by an unit load on Point x.

$$w(x) = \frac{1}{\sqrt{\pi L}}\sqrt{\frac{L-x}{L+x}}. \tag{10}$$

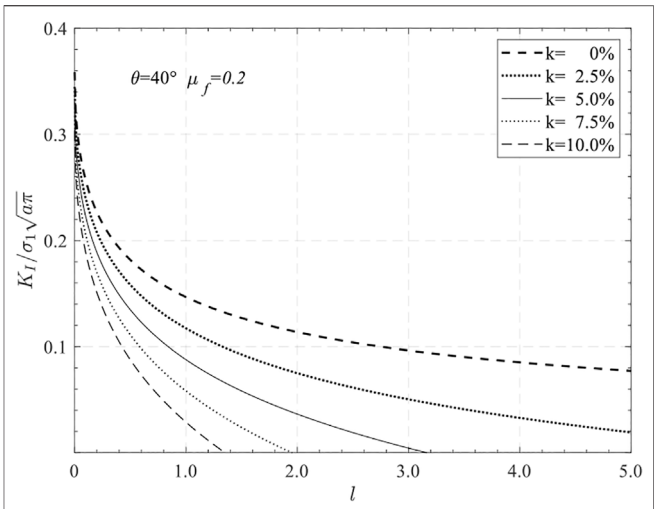


FIGURE 4 | SIF as a function of l and k ($\mu_f = 0.2, \theta = 50^\circ$, $k = \sigma_3/\sigma_1$).

Substituting **Eqs 8**, **10** for **Eq. 9**, the following equation is obtained:

$$\begin{aligned} K_I &= \int_{-L}^{L} p(x)w(x)dx \\ &= p^+\int_{-c}^{c} w(x)dx + p^-\int_{-L}^{-c} w(x)dx + p^-\int_{c}^{L} w(x)dx. \end{aligned} \tag{11}$$

By integrating the aforementioned equations and making an arrangement again, the equation of SIF is obtained as follows:

$$K_I = \sqrt{\pi c}[h_1 D_1\tan\theta\sigma_1 - (h_1 D_3\tan\theta + h_2)\sigma_3], \tag{12}$$

where $h_1(n) = \frac{2\sqrt{n}}{\pi}\arctan\frac{1}{\sqrt{n^2-1}}$; $\quad h_2(n) = \sqrt{n} - h_1(n)$;
$n = L/c = 1 + l/\cos\theta$.

It is known from **Equation 11** that K_I is influenced by n, and n is a function of variable l. Therefore, the value of SIF is decided by l when σ_1 and σ_3 are determined.

2.2.2 Nonlinear Features of SIF to *l*

According to **Equation 11**, the relationship between K_I and l is complex, and the curve graph of K_I varying with l is shown in **Figure 4**.

By comparing the curve lines of SIF and l, two main conclusions are drawn as follows:

1) *Wing cracks are highly stable.* K_I and l are negatively correlated, and the stress intensity factor decreases rapidly with the increase of crack length (especially at the beginning of crack extension), which means the larger the σ_3, the faster the dropping rate of K_I. Due to the stability of wing cracks, a larger external force is required to make the cracks go on expanding, which indirectly provides a fracture mechanical basis for the stable crack propagation stage of the rock deformation theory.
2) *Minimum principal stress has a strong controlling effect on long wing cracks.* When the wing crack is short, the SIF of the corresponding σ_3 changes little; when the crack is long, the

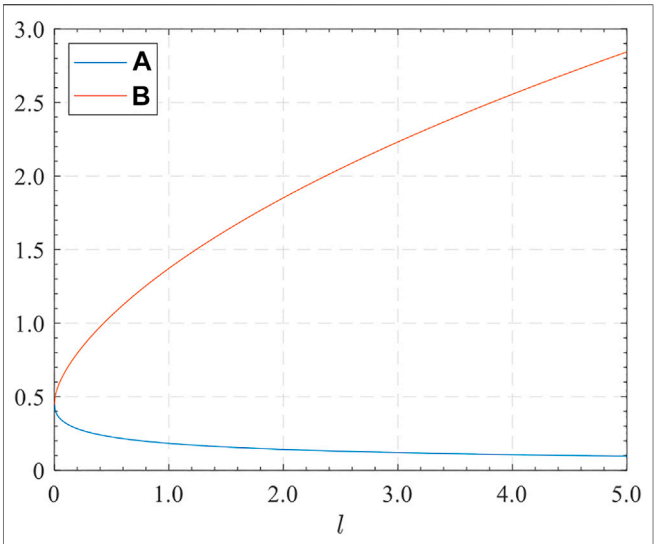


FIGURE 5 | Stress coefficients (A and B) versus *l*.

SIF of the corresponding σ_3 changes a lot. Therefore, when σ_3 is high, it is hard to form long wing cracks. This is why tensile micro-fractures are suppressed in the high confining pressure compression test of brittle rock. Compared with tensile failure, σ_3 has a relatively small effect on shear cracks. If confining pressure increases, the rock failure shifts to the shearing mode.

2.2.3 Influence Coefficients of σ_1 and σ_3

The shearing mode (taking the classical Mohr–Coulomb theory as an example) is controlled by the shearing force, and the magnitude of the shearing force is independent of the length of the shearing zone. So, based on the shearing hypothesis, the deformation and failure of the rock are in a linear relationship with respect to σ_1 and σ_3. However, the sliding crack model is controlled by the SIF, and the effects of σ_1 and σ_3 on the SIF vary with the wing crack growth (l); thus, based on the sliding crack hypothesis, the deformation failure of the rock is of a strong non-linear feature.

In order to discuss the contributions of σ_1 and σ_3 to the SIF, **Eq. 13** is obtained as follows:

$$K_1 = \sqrt{\pi c}[A(l)\sigma_1 - B(l)\sigma_3], \quad (13)$$
$$A(l) = h_1 D_1 \tan\theta \quad B(l) = h_1 D_3 \tan\theta + h_2.$$

From **Figure 5**, it is known that A gradually descends with the increase of l, meanwhile B ascends rapidly. It indicates that the crack-opening effect of σ_1 gradually decreases with the wing crack growth, while the crack closure effect of σ_3 increases. It also suggests that σ_3 has a strong controlling effect on long wing cracks.

Nonlinear characteristics of A and B could be explained as follows: since σ_1 is only included in p^+, which only acts on the middle of the crack (shearing section), the effect of σ_1 on the crack tip is weakened, while the action range between

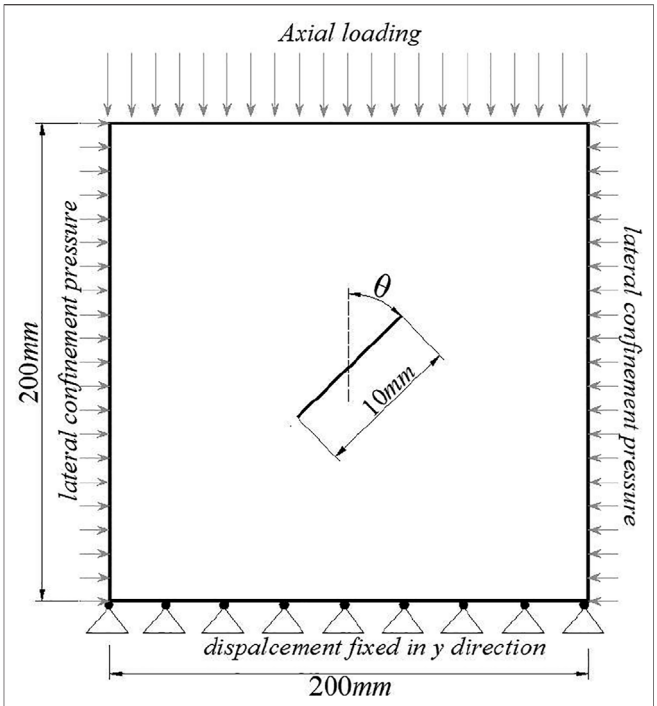


FIGURE 6 | XFEM model of an inclined crack in a rectangular plane.

TABLE 1 | Material parameters of the XFEM model.

E (GPa)	*v*	σ_y (MPa)	γ_n (J/mm)	γ_t (J/mm)	μ_f
50	0.2	70	0.2	0.2	0.2

The material parameters are not corresponding to any specific rock material and only serve as a theoretical analysis instead.

σ_1 and crack tip gets large with crack extension. However, σ_3 acts on the entire wing cracks; it is obvious that as the crack extends, more traction forces will be incurred to the crack, so a greater stress concentration effect is developed as expected.

3 XFEM FRACTURE SIMULATION

In order to verify the correctness of the SIF theoretical formula (**Eq. 12**), the propagation process of a single crack in a plane subject to compressive loading is simulated by an extended finite element method (XFEM).

3.1 XFEM Fracture Model

Geometric model. As shown in **Figure 6**, a closed inclined crack ($\theta = 45^\circ$ and $2a = 10$ mm) is set in the middle of the rectangular plane. In order to weaken the boundary effect, the size of the rectangular plane (120 × 200 mm) is much larger than that of the crack length.

Material model and parameter. 1) XFEM element: the XFEM element material obeys the linear elastic law (elastic modulus E;

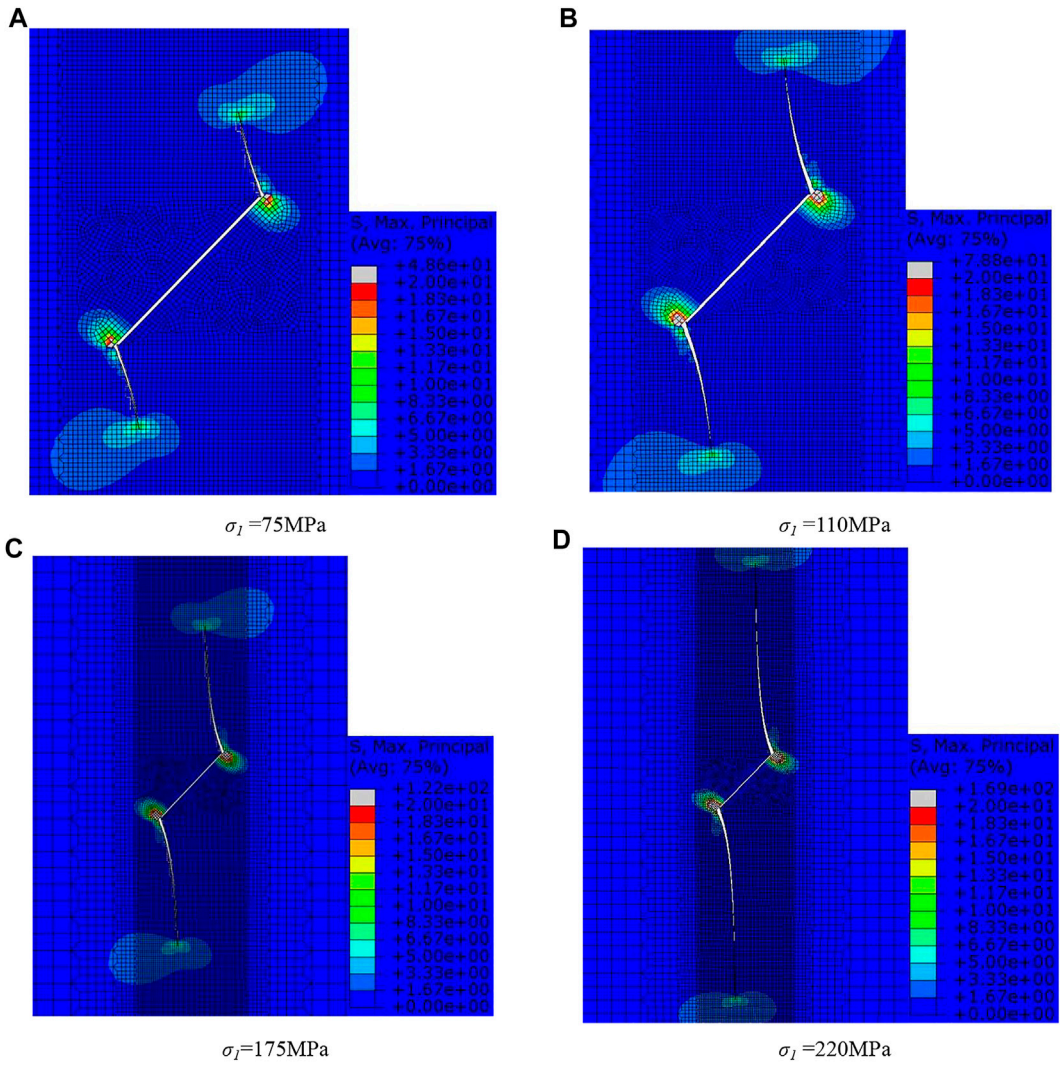


FIGURE 7 | Maximum principal stress and crack propagation of the XFEM model. **(A)** σ_1 = 75 MPa, **(B)** σ_1 = 110 MPa, **(C)** σ_1 = 175 MPa, and **(D)** σ_1 = 220 MPa.

Poisson ratio v) before yielding. The maximum principal stress criterion (yielding strength σ_y) is selected as the yield criterion. After yielding, the XFEM element obeys the linear damage law based on fracture energy. When the specified fracture energy is reached (normal fracture energy γ_n or tangential fracture energy γ_t), the XFEM element separates from each other and re-combine into a crack. 2) Contact model of the closed crack surfaces: the normal contact relation of the crack surfaces is rigid, and the tangential contact behavior obeys coulomb's law of fiction, in which the shear strength is proportional to the normal stress. The material parameters are shown in **Table 1**.

Loading method. Four sets of loading tests with different lateral confinement pressures (0, 5, 10, and 20 MPa) and the axial loading are limited by displacement. In addition, in order to simulate a rigid closed shearing crack, the normal displacement of the shearing crack is fixed, so that it can only slip in the tangential direction.

3.2 Fracture Propagation and SIF

The fracture propagation process and the maximum principal stress contour are shown in **Figure 7**. At the beginning of crack extension, the angle between the wing crack and the pre-crack is about 70° (**Figure 7A**). As the wing crack expands, the crack bends and gradually approaches the direction of the maximum principal stress (**Figure 7D**). The crack trajectory is completely consistent with the theoretical 2D sliding crack model. The dynamic fracture process of a sliding crack could be well simulated by XFEM.

Although the XFEM could be used to simulate the natural propagation path of the crack, it cannot obtain the SIF directly at the crack tip. Therefore, in this study, the coordinates of the crack trajectory are obtained by the XFEM, based on which a static crack model is established, so the SIF can be calculated by the traditional contour integral method. In this way, it could be guaranteed that the crack numerical model is identical to the real crack path, and thus a more accurate SIF of sliding crack could be obtained. SIF values

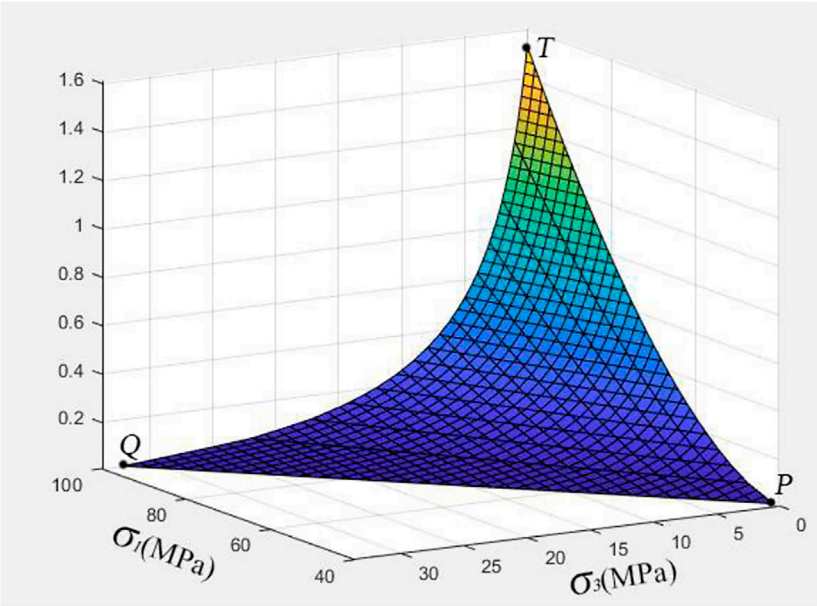


FIGURE 8 | Shape of function l (σ_1, σ_3) (K_{IC} = 6 MP·m$^{0.5}$, a = 0.01 m, θ = 40°, and μ_f = 0.2).

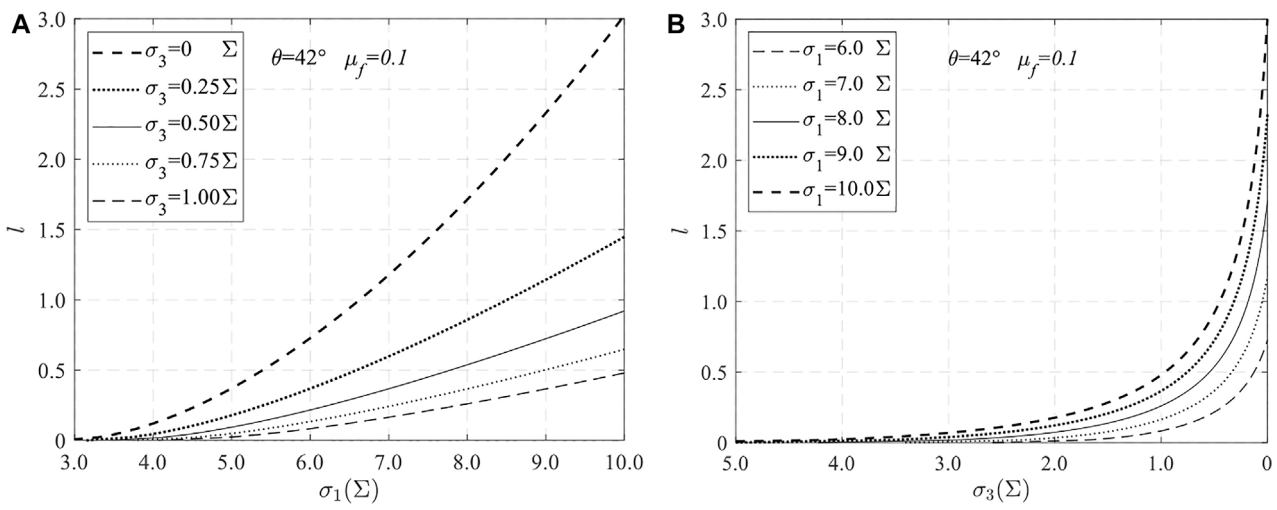


FIGURE 9 | (A) l as a function of σ_1 with σ_3 fixed. **(B)** l as a function of σ_3 with σ_1 fixed (K_{IC} = 2 MP·m$^{0.5}$ and a = 0.01 m).

corresponding to different crack lengths are listed in **Table 2**, the axial stress σ_1 = 200MPa, and lateral stress σ_3 = 0, 5.0, 10.0, and 20.0 MPa.

The differences between the theoretical results (**Eq. 11**) and the numerical simulation results are controlled within 5.0%, which indicates that both the equivalent model (**Figure 5**) and calculating method are reasonable. However, if the wing crack length is long, the theoretical result tends to be larger. The larger the confining pressure, the larger the error. Therefore, the theoretical formula is suitable for the case in which the confining pressure is small and the wing cracks are relatively short.

4 LENGTH OF WING CRACK

4.1 Implicit Function of l (σ_1, σ_3)

Previously, the nonlinear features of SIF varying with l had been analyzed, but in a practical situation, the crack propagates when the SIF reaches the fracture toughness of the material under the effect of external force and the length of the crack is limited by the far-field stress (σ_1, σ_3); therefore, the way that l varies with stress is practically more important. By replacing K_I with K_{IC} (fracture toughness of mode I) in **Eq. 13**, the functional relationship between l and principal stresses (σ_1 and σ_3) is obtained.

TABLE 2 | Numerical simulation and theoretical calculation results of SIF.

σ_3 (MPa)	L_w (mm)	SIF(MPa·m$^{0.5}$)		Error (%)
		Numerical value	Theoretical value	
0	5.0	114.9	109.9	−4.36
	10.0	91.1	93.2	2.27
	15.0	72.9	75.3	3.28
	20.0	67.4	70.2	4.22
5.0	5.0	91.9	89.9	−2.20
	10.0	63.4	64.1	1.11
	15.0	42.0	43.9	4.52
	20.0	33.3	35.1	5.46
10.0	5.0	65.8	63.6	−3.31
	10.0	27.7	27.3	−1.57
	15.0	6.3	6.6	4.11
	20.0	−11.5	−10.9	−5.14
20.0	5.0	7.9	7.2	−9.14
	10.0	−35.7	−33.3	−6.62
	15.0	−67.4	−62.3	−7.51
	20.0	−99.1	−91.4	−7.73

$$K_{IC} = \sqrt{\pi c}[A(l)\sigma_1 - B(l)\sigma_3]. \quad (14)$$

The function l (σ_1, σ_3) cannot be written out in an explicit form, but it can be plotted numerically as follows:

As shown in **Figure 8**, the function of l (σ_1, σ_3) is highly nonlinear. The shape of l (σ_1,σ_3) is a concave surface, which indicates that both axial loading and lateral unloading lead to an increase of the wing crack, and the growth rate would also increase. The curve line PT is a loading path with σ_3 = 100MPa, the curve line QT is a lateral unloading path with σ_1 = 100MPa; the intersection line of the function surface and the plane σ_1−σ_3 is the crack initiation criterion functions (**Eq. 3**).

4.2 Axial Loading and Lateral Unloading

For the convenience of plotting, the fracture strength K_{IC} of the material is taken as a reference, and the stress unit is defined as:

$$\Sigma = \frac{K_{IC}}{\sqrt{\pi a}}. \quad (15)$$

The growth curve of l corresponding to axial monotonic loading is shown in **Figure 10A**, and the growth curve of l corresponding to lateral monotonic unloading is shown in **Figure 10B**. Under the conditions of axial loading and lateral unloading, the propagation characteristics of wing cracks have big differences. The major ones are summarized as follows:

1) The crack length curve sees a linear feature under the condition of axial loading: the crack length l increases monotonically with the increase of σ_1, and the growth rate is relatively low at the beginning. After a short and slight decline, the growth rate of the crack length rises and soon remains almost unchanged, exhibiting a linear growing trend. The result shows that the larger the σ_3, the smaller the slope of the curve, which indicates that σ_3 greatly constrains the crack propagation under the condition of the σ_1 monotonic increase shown in **Figure 9A**.

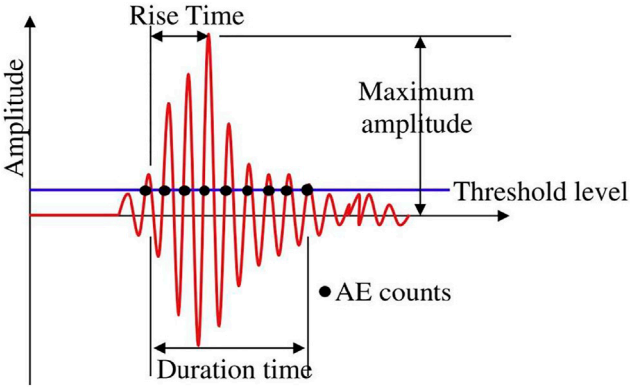


FIGURE 10 | AE parameters in an AE hit (Ohno K., 2010).

2) Under the condition of lateral unloading, the crack length grows exponentially: the crack length l increases monotonically with the decrease of σ_3, and the growth rate of the crack is very low at first; when σ_3 is close to zero, the growth rate shoots up exponentially. It indicates that when the brittle rock is under low-confined compression, a small disturbance of σ_3 will cause a large crack expansion. Therefore, the brittle rock failure is abrupt and violent under the unloading condition shown in **Figure 9B**.

5 CRACK CLASSIFICATION BASED ON ACOUSTIC EMISSION

Assuming that the micro-fracture mechanism of brittle rock under low-confined compression is sliding crack, σ_3 has a more significant controlling effect on tensile fracture (wing crack) than shear fracture (pre-exist shearing crack) according to the previous analysis results. That is to say that increasing the confining pressure improves the resistance of rock against axial pressure, and more sliding cracks would be formed before the rock failure, of which wing cracks are much shorter.

It can be inferred that with increasing confining pressure, the risk of micro-tensile fracture events decreases, while the risk of shearing fracture events increases. In the following parts, the correctness of this inference will be verified by the tri-axial test combined with the waveform parameter method.

5.1 Waveform Parameter Method

The fracturing behavior of materials can be nondestructively monitored by the acoustic emission (AE) technique, using sensors that detect the transient elastic waves after any crack propagation event (Aggelis, D. G., 2012). Micro-fracture failure in rock may cause local elastic energy release and transmit into elastic waves. The elastic waves caused by different fracture events are various in waveforms. Theoretically, the mechanism of micro-fractures could be analyzed by waveform. AF (average frequency) and RA (rise time over the maximum Amplitude) are important parameters for judging the fracture mechanism for the waveform parameter method (Ohno K., 2010).

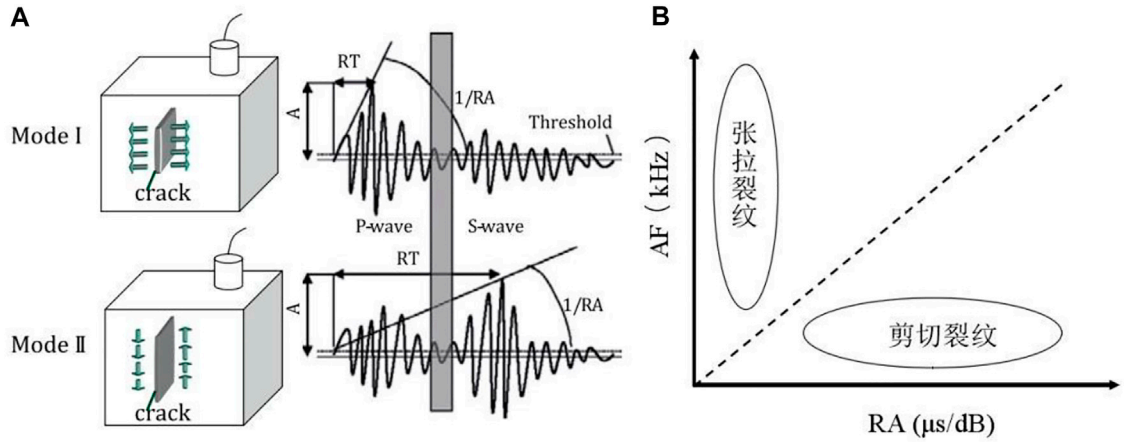


FIGURE 11 | Schematic diagram of identifying fracture mode by the waveform parameter method. **(A)** Fracture mode and AE waveform (D. G. Aggelis et al., 2012); **(B)** relationship between the *AF* and *RA* value (Ohno K., 2010).

$$RA = RT/A, \quad AF = RC/DT, \tag{16}$$

where *RT* is rise time, *A* is maximum amplitude, *RC* is ring-down count, and *DT* is duration time. The meaning of each waveform parameter is shown in **Figure 10**.

In the case of a tensile fracture (model I) that occurs, most of the elastic energy appears in the form of a longitudinal wave, which is characterized by high AF and low RA. In the case of a shear fracture (model II), most of the elastic energy transforms into a transverse wave, which is featured with low *AF* and high *RA*, as shown in **Figure 11A**.

Each acoustic emission signal could be represented as a point in the *RA-AF* plane, which is called the wave characteristics point (WCP). According to the characteristics of longitudinal and transverse waves, the WCP of tensile fracture will be located in the upper left part of the *RA-AF* plane, and the WCP of shearing fracture will be located in the lower right part of the plane, as shown in **Figure 11B**.

According to the waveform characteristics of tensile fracture and shearing fracture discussed previously, an FMI (fracture mode index) is proposed to represent a fracture mode.

$$FMI = AF/RA. \tag{17}$$

It could be seen from **Figure 11B** that when the value of FMI is high, the fracture event tends to be a tensile fracture; otherwise, it tends to be a shear fracture.

5.2 Micro-Crack Classification of Brittle Rock

In order to analyze the influence of confining pressure on micro-fractures, tri-axial tests combined with acoustic emission monitoring were carried out on Emei basalt. The rock cores are taken from the cavern buried at a depth of 460 m underground at the Baihetan hydropower station, and the standard rock sample (with a diameter of 50 mm and a height of 100 mm) is made of a homogenous and flawless core.

Four groups of tri-axial tests with different confining pressures (0, 10, 20, and 30 MPa) are conducted, and each group has four samples. The confining pressure is loaded to the specified value first, and then the axial pressure is applied by the displacement control method (0.05 mm/min); meanwhile, the acoustic emission events of the rock are monitored until the failure of the sample. Under different confining pressures, the stress–strain curve and corresponding AE ringing times are shown in the following figure.

According to the stage theory of rock deformation (Cai and Kaiser, 2004), at the beginning of compression, the AE events are mainly caused by the closure of cracks or cavities. Also, near the peak strength, the AE events are mainly caused by the coalescence of cracks. Therefore, it is assumed that the AE events in the middle of the loading process are mainly caused by sliding cracks. Thus, the AE events in the middle of the loading process are selected for waveform parameter analysis, and the images of WCP in the AF-RA plane are drawn as follows:

It could be seen from **Figure 12** that increasing of confining pressure makes the WCP shift to the lower right corner. It suggests that increasing confining pressure has a significant effect on the tensile crack and increases the proportion of shearing crack, which is consistent with the prediction result of the sliding crack model (**Section 3.2**).

The WCP is scattered in a wild range. Although the distribution of WCPs can be seen intuitively, the WCPs cannot be described quantitatively. Therefore, a single parameter ($\overline{FMI}$) is proposed to represent a bunch of WCPs. First, it is necessary to find a feature point that represents all WCPs. Suppose that there are n (*1,2... n*) WCPs and the *i*th WCP is represented by coordinates (x_i, y_i), the coordinates of the feature point are (X, Y), which are calculated by the following formulas:

$$X = \frac{1}{n}\sum_{1}^{n} x_i, \quad Y = \frac{1}{n}\sum_{1}^{n} y_i, \tag{18}$$

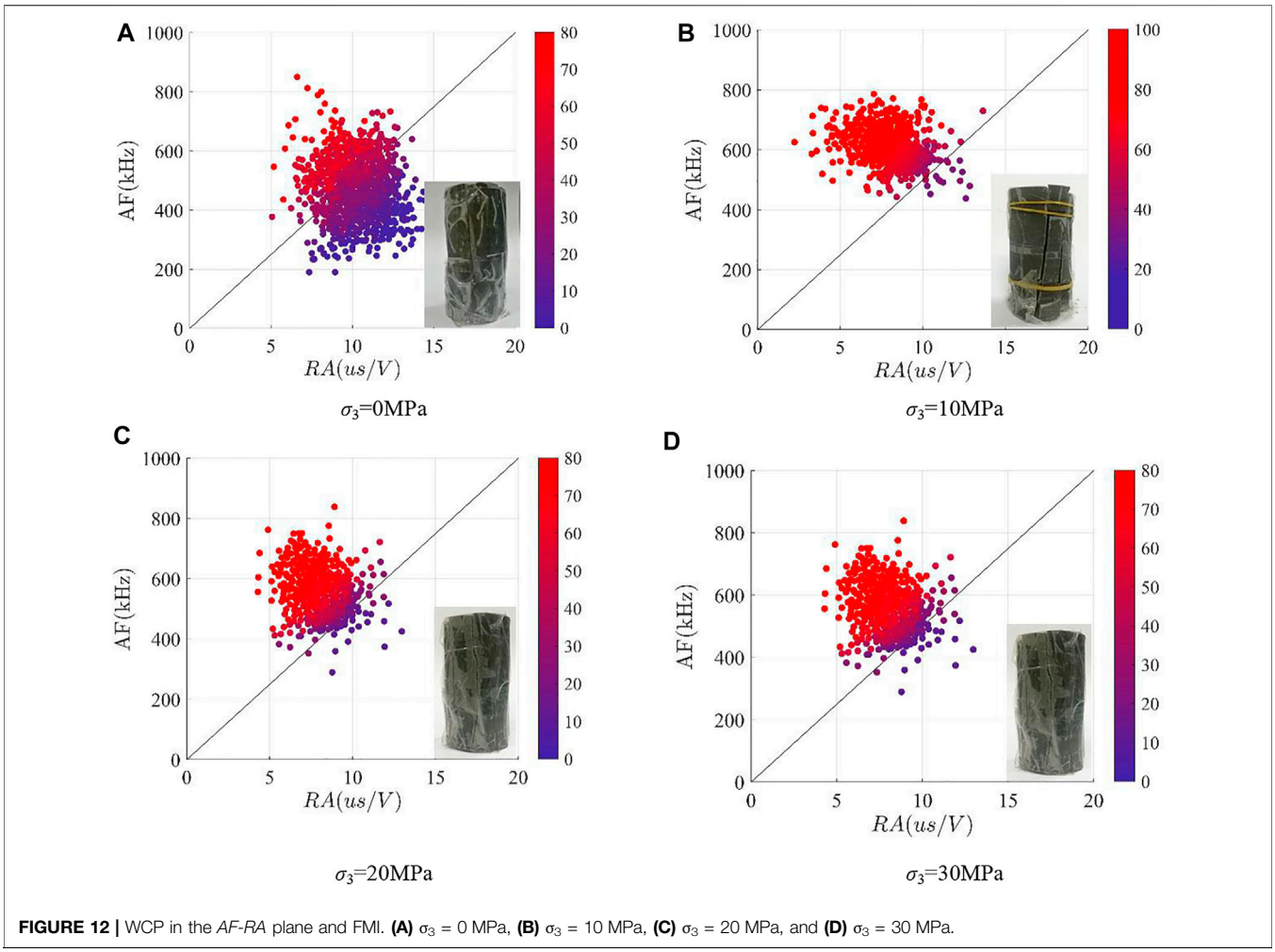


FIGURE 12 | WCP in the *AF-RA* plane and FMI. **(A)** σ_3 = 0 MPa, **(B)** σ_3 = 10 MPa, **(C)** σ_3 = 20 MPa, and **(D)** σ_3 = 30 MPa.

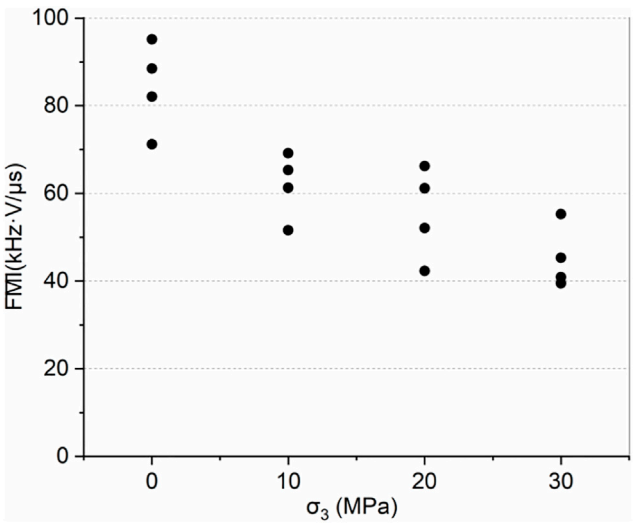


FIGURE 13 | Experimental results of $\overline{FMI}$ under different confining pressures.

$$\overline{FMI} = X/Y. \tag{19}$$

Then, the FMI of the feature point, noted by $\overline{FMI}$, represents the fracture tendency of all WCPs. $\overline{FMI}$ of all samples is shown in the **Figure 13**.

It could be seen from **Figure 13** that increasing of confining pressure leads to a smaller value of $\overline{FMI}$, especially when the confining pressure increases from 0 to 10 Mpa, $\overline{FMI}$ decreases significantly, but when the confining pressure increases from 20 to 30 MPa, the decrease gets slower. It indicates that when the confining pressure is low, confining pressure of tensile fracture increases significantly, which is consistent with the conclusion of the previous theoretical analysis.

6 CONCLUSION

In this study, the theoretical formula of SIF is deduced by the equivalent straight crack model and verified by XFEM. On the basis of the SIF formula, the crack lengths under different loading conditions have been analyzed. Finally, tri-axial tests are carried

out on Emei basalt, and the micro-fracture is analyzed by the waveform parameter method, which indirectly proves the correctness of the theoretical analysis. The conclusions are drawn as follows:

1) A new equivalent model of sliding crack is proposed, and the calculation formula of SIF at the wing crack tip is deduced by the weight function method. The calculation method is simple and has a clear physical meaning. By XFEM numerical simulation and contour integration, it is shown that the theoretical formula has high precision, and the error is about 5%.
2) Minimum principal stress has a strong controlling effect on long wing cracks. In other words, it is hard to form long wing cracks when σ_3 is high. This is the reason why tensile fractures are suppressed in the high confining pressure compression test of brittle rock.
3) Under the condition of axial loading, the wing crack increases in an almost linear way, and the growth rate is negatively correlated with σ_3. It indicates that under low confined compressive conditions, increasing confining pressure could greatly improve the strength of brittle rock.
4) Under the condition of lateral unloading, the growth rate of the crack is very low at first; when σ_3 is close to zero, the growth rate shoots up exponentially. It indicates that a small disturbance of σ_3 will cause a large crack expansion in brittle rock. Therefore, the brittle rock failure is abrupt and violent under the unloading condition.
5) Tri-axial compression tests are carried out on Emei basalt, and the rock micro-fracture events are analyzed by the waveform parameter method. The test results show that increasing of confining pressure could greatly reduce the tensile fracture tendency of micro-fractures but increase the shear tendency. Confining pressure has a significant effect on tensile cracks, which indirectly proves the correctness of the theoretical analysis of fracture.

DATA AVAILABILITY STATEMENT

The raw data supporting the conclusion of this article will be made available by the authors, without undue reservation.

AUTHOR CONTRIBUTIONS

YZ: fracture analysis and XFEM simulation. SC: fracture analysis and tri-axial test. JC: experimental data analysis.

FUNDING

The study is partially supported by the National Science Foundation of China (Nos. 41907254 and 41931296), National Key R&D Program of China (No. 2017YFC1501002), and Funds for Creative Research Groups of China (Grant No. 41521002). YZ was financially supported by the State Key Laboratory of Geohazard Prevention and Geoenvironment Protection (SKLGP) and Chengdu University of Technology.

REFERENCES

Aggelis, D. G., Mpalaskas, A. C., Ntalakas, D., and Matikas, T. E. (2012). Effect of Wave Distortion on Acoustic Emission Characterization of Cementitious Materials. *Construction Building Mater.* 35, 183–190. doi:10.1016/j.conbuildmat.2012.03.013

Ashby, M. F., and Hallam, S. D. (1986). The Failure of Brittle Solids Containing Small Cracks under Compressive Stress States. *Acta Metallurgica* 34 (3), 497–510. doi:10.1016/0001-6160(86)90086-6

Basista, M., and Gross, D. (1998). The Sliding Crack Model of Brittle Deformation: an Internal Variable Approach. *Int. J. Sol. Structures* 35 (5-6), 487–509. doi:10.1016/s0020-7683(97)00031-0

Bieniawski, Z. T. (1967). Mechanism of Brittle Fracture of Rock. *Int. J. Rock Mech. Mining Sci. Geomechanics Abstr.* 4 (4), 395–406. doi:10.1016/0148-9062(67)90030-7

Brace, W. F., and Bombolakis, E. G. (1963). A Note on Brittle Crack Growth in Compression. *J. Geophys. Res.* 68 (12), 3709–3713. doi:10.1029/jz068i012p03709

Bueckner, H. F. (1970). A Novel Principle for the Computation of Stress Intensity Factors. *Z. fürAngewandte Mathematik Mechanik* 50, 529–545.

Cai, M., and Kaiser, P. K. (2004). Generalized Crack Initiation and Crack Damage Stress Thresholds of Brittle Rock Masses Near Underground Excavations. *Int. J. Rock Mech. Mining Sci.* 41 (5), 834–847. doi:10.1016/j.ijrmms.2004.02.001

Clayton, J. D., and Knap, J. (2014). A Geometrically Nonlinear Phase Field Theory of Brittle Fracture. *Int. J. Fract* 189 (2), 139–148. doi:10.1007/s10704-014-9965-1

Cui, S., Pei, X., Jiang, Y., Wang, G., Fan, X., Yang, Q., et al. (2021). Liquefaction within a Bedding Fault: Understanding the Initiation and Movement of the Daguangbao Landslide Triggered by the 2008 Wenchuan Earthquake (Ms = 8.0). *Eng. Geology.* 295, 106455. doi:10.1016/j.enggeo.2021.106455

Dragon, A., Halm, D., and Desover, T. (2000). Anisotropic Damage in Quasi-Brittle Solids: Modeling, Computational Issues and Applications. *Comp. Methods Appl. Mech. Eng.* 183 (3–4), 331–352. doi:10.1016/s0045-7825(99)00225-x

Eberhardt, E., Stead, D., and Stimpson, B. (1999). Quantifying Progressive Pre-peak Brittle Fracture Damage in Rock during Uniaxial Compression. *Int. J. Rock Mech. Mining Sci.* 36, 361–380. doi:10.1016/s0148-9062(99)00019-4

Fairhurst, C., and Cook, N. G. W. (1966). The Phenomenon of Rock Splitting Parallel to the Direction of Maximum Compression in the Neighborhood of a Surface. *Proc. 1st Int. Congress Rock Mech.* 25, 697–692.

Horii, H., and Nemat-Nasser, S. (1986). Brittle Failure in Compression: Splitting, Faulting and Brittle-Ductile Transition. *Phil. Trans. R. Soc. Lond. Ser. A, Math. Phys. Sci.* 319 (1549), 337–374.

Horii, H., and Nemat-Nasser, S. (1985). Compression-induced Microcrack Growth in Brittle Solids: Axial Splitting and Shear Failure. *J. Geophys. Res.* 90 (B4), 3105–3125. doi:10.1029/jb090ib04p03105

Huang, C., Yang, W., Duan, K., Fang, L., Wang, L., and Bo, C. (2019). Mechanical Behaviors of the Brittle Rock-like Specimens with Multi-Non-Persistent Joints under Uniaxial Compression. *Construction Building Mater.* 220, 426–443. doi:10.1016/j.conbuildmat.2019.05.159

Janeiro, R. P., and Einstein, H. H. (2010). Experimental Study of the Cracking Behavior of Specimens Containing Inclusions (Under Uniaxial Compression). *Int. J. Fract* 164 (1), 83–102. doi:10.1007/s10704-010-9457-x

Jing, L. (2003). A Review of Techniques, Advances and Outstanding Issues in Numerical Modelling for Rock Mechanics and Rock Engineering. *Int. J. Rock Mech. Mining Sci.* 40 (3), 283–353. doi:10.1016/s1365-1609(03)00013-3

Kemeny, J. M., and Cook, N. G. W. (1987). Crack Models for the Failure of Rock under Compression. *Proc. 2nd Int. Conf. Constitutive Laws Eng. Mat* 2, 879–887.

Kolari, K. (2017). A Complete Three-Dimensional Continuum Model of wing-crack Growth in Granular Brittle Solids. *Int. J. Sol. structures* 115-116, 27–42. doi:10.1016/j.ijsolstr.2017.02.012

Lan, H., MartinC, D., and Hu, B. (2010). Effect of Heterogeneity of Brittle Rock on Micromechanical Extensile Behavior during Compression Loading. *J. Geophys. Res.* 115 (B1). doi:10.1029/2009jb006496

Lehner, F., and Kachanov, M. (2001). "On Modelling of "Winged" Cracks Forming under Compression," in *Physical Aspects of Fracture*, 73–75. doi:10.1007/978-94-010-0656-9_6

Nemat-Nasser, S., and Obata, M. (1988). A Microcrack Model of Dilatancy in Brittle Materials. *J. Appl. Mech.* 55 (1), 24–35. doi:10.1115/1.3173647

Nemat-Nasser, S., and Horii, H. (1982). Compression-induced Nonplanar Crack Extension with Application to Splitting, Exfoliation, and Rockburst. *J. Geophys. Res. Solid Earth* 87 (B8), 6805–6821.

Ohno, K., and Ohtsu, M. (2010). Crack Classification in concrete Based on Acoustic Emission. *Construction Building Mater.* 24 (12), 2339–2346. doi:10.1016/j.conbuildmat.2010.05.004

Olsson, W. A., and Peng, S. S. (1976)., 13. Pergamon, 53–59. doi:10.1016/0148-9062(76)90704-xMicrocrack Nucleation in marble*Int. J. Rock Mech. Mining Sci. Geomechanics Abstr.*2

Read, R. S. (2004). 20 Years of Excavation Response Studies at AECL's Underground Research Laboratory. *Int. J. Rock Mech. Mining Sci.* 41 (5), 1251–1275. doi:10.1016/j.ijrmms.2004.09.012

Renshaw, C. E., and Schulson, E. M. (2001). Universal Behaviour in Compressive Failure of Brittle Materials. *Nature* 412 (6850), 897–900. doi:10.1038/35091045

Rice, J. R. (1972). Some Remarks on Elastic Crack-Tip Stress Fields. *Int. J. Sol. Structures* 8 (6), 751–758. doi:10.1016/0020-7683(72)90040-6

Steif, P. S. (1984). Crack Extension under Compressive Loading. *Eng. Fracture Mech.* 20 (3), 463–473. doi:10.1016/0013-7944(84)90051-1

Wang, Y. X., Cao, P., Huang, Y. H., Chen, R., and Li, J. T. (2012). Nonlinear Damage and Failure Behavior of Brittle Rock Subjected to Impact Loading. *Int. J. Nonlinear Sci. Numer. Simulation* 13 (1), 61–68. doi:10.1515/ijnsns-2011-104

Wong, T.-f., and Baud, P. (2012). The Brittle-Ductile Transition in Porous Rock: A Review. *J. Struct. Geology.* 44, 25–53. doi:10.1016/j.jsg.2012.07.010

Wong, T.-F. (1982). Effects of Temperature and Pressure on Failure and post-failure Behavior of Westerly Granite. *Mech. Mater.* 1 (1), 3–17. doi:10.1016/0167-6636(82)90020-5

Xun, Xi., Wu, X., Guo, Q., and Cai, M. (2020). Experimental Investigation and Numerical Simulation on the Crack Initiation and Propagation of Rock with Pre-existing Cracks. *Ieee Access* 8, 129636–129644.

Yuan, S. C., and Harrison, J. P. (2006). A Review of the State of the Art in Modelling Progressive Mechanical Breakdown and Associated Fluid Flow in Intact Heterogeneous Rocks. *Int. J. Rock Mech. Mining Sci.* 43 (7), 1001–1022. doi:10.1016/j.ijrmms.2006.03.004

Zuo, J.-p., Li, H.-t., Xie, H.-p., Ju, Y., and Peng, S.-p. (2008). A Nonlinear Strength Criterion for Rock-like Materials Based on Fracture Mechanics. *Int. J. Rock Mech. Mining Sci.* 45 (4), 594–599. doi:10.1016/j.ijrmms.2007.05.010

Conflict of Interest: YZ and ZY were employed by the company Sichuan Road and Bridge (Group) Co., Ltd.

The remaining authors declare that the research was conducted in the absence of any commercial or financial relationships that could be construed as a potential conflict of interest.

Publisher's Note: All claims expressed in this article are solely those of the authors and do not necessarily represent those of their affiliated organizations, or those of the publisher, the editors, and the reviewers. Any product that may be evaluated in this article, or claim that may be made by its manufacturer, is not guaranteed or endorsed by the publisher.

Copyright © 2022 Zhang, Cui, Yu and Cheng. This is an open-access article distributed under the terms of the Creative Commons Attribution License (CC BY). The use, distribution or reproduction in other forums is permitted, provided the original author(s) and the copyright owner(s) are credited and that the original publication in this journal is cited, in accordance with accepted academic practice. No use, distribution or reproduction is permitted which does not comply with these terms.

frontiers | Frontiers in Earth Science

ORIGINAL RESEARCH
published: 16 June 2022
doi: 10.3389/feart.2022.890968

DFT Study on the Compatibility Between Bentonite Clay Mineral and Hydration Products With the Polycarboxylate Water Reducer in the Cement Hydration Process

Huang Teng[1,2], *Zhihao He*[3,4,5]*, *Gao Meiben*[5] and *Jiaxing Zhang*[3,4]

[1]Key Laboratory of Solid Waste Treatment and Resource Recycle Ministry of Education, Southwest University of Science and Technology, Mianyang, China, [2]School of Environment and Resource, Southwest University of Science and Technology, Mianyang, China, [3]State Key Laboratory of Geohazard Prevention and Geoenvironment Protection, Chengdu University of Technology, Chengdu, China, [4]College of Environmental and Civil Engineering, Chengdu University of Technology, Chengdu, China, [5]School of Emergency Management, Xihua University, Chengdu, China

As one of the most used grouting materials, cement has the characteristics of low price and a wide resource of raw material. With the in-depth research and application of cement admixture, the compatibility between different water-reducing agents and clay has become one of the critical factors that affects the cement hydration process. Due to the adsorption of clay on cement additives, the dispersion efficiency of the water reducer will be reduced, also the strength and impermeability of hydration products will be adversely affected. This paper studies the adsorption characteristics of different PCE superplasticizers on bentonite clay minerals and hydration products using a molecular simulation technique. Results showed that there is competitive adsorption between the clay and hydration products when the admixture participates in the hydration reaction, the additives are likely to adsorb on the CH rather than the clay minerals, while the adsorption energy of the hydration product C-S-H is the highest, thus the preferential adsorption order and compatibility between clay minerals and hydration products on admixtures could also be obtained. PDOS (partial density of states) analysis concluded that some new characteristic peaks and rearrangement of the bonding orbitals may appear after the adsorption, with the peak value of the minerals higher than that of jennite, which is also consistent with the adsorption energy. This study aims to reveal the interaction mechanism and compatibility between the hydration product and clay minerals, hoping to fully utilize the advantages of both clay minerals and admixtures in the cement hydration process.

Keywords: geological disasters, grouting material, cement hydration, bentonite, compatibility, DFT

OPEN ACCESS

Edited by:
Yunhui Zhang,
Southwest Jiaotong University, China

Reviewed by:
Gang Li,
The University of Melbourne, Australia
Nian Xu,
Chengdu University of Information Technology, China

***Correspondence:**
Zhihao He
hezhihaohao@163.com

Specialty section:
This article was submitted to Geohazards and Georisks, a section of the journal Frontiers in Earth Science

Received: *07 March 2022*
Accepted: *03 May 2022*
Published: *16 June 2022*

Citation:
Teng H, He Z, Meiben G and Zhang J (2022) DFT Study on the Compatibility Between Bentonite Clay Mineral and Hydration Products With the Polycarboxylate Water Reducer in the Cement Hydration Process. Front. Earth Sci. 10:890968. doi: 10.3389/feart.2022.890968

1 INTRODUCTION

With the rapid development of various engineering construction methods, unfavorable geological conditions, such as joints and fracture zones with dense fissures and water-saturated fissures, are often exposed in engineering activities, resulting in geological disasters such as instability and damage of the slope and surrounding rock, threatening engineering construction and safe operation.

For the prevention and control of the above rock mass cracks and water inrush disasters, the grouting method is usually used for plugging and reinforcement. As one of the most used grouting materials, cement has the characteristics of low price and a wide resource of raw material. Due to the environmental pollution caused by the production process, there is an urgent need to seek similar environmentally friendly substitute materials. Adding a certain amount of clay minerals into the cement slurry may be conducive to improve the stone strength and injectability of the slurry (Jae et al., 2014; Sharma et al., 2021), while admixtures in cement hydration could also effectively adjust or improve the hydration time and mechanical properties, which may possess advantages of small dosage and low cost (Wang, 2013).

With the in-depth research and application of cement hydration admixtures, the compatibility between additives, such as the polycarboxylate superplasticizer, and clay minerals has also become a key factor in the performance of cement slurry (Tregger et al., 2010; Nathan et al., 2010; Jae et al., 2014). As clay will compete with cement to adsorb the polycarboxylate superplasticizer at the same time, there may be an adverse effect on the strength, wearability, and pourability of the hydration products (Norvell et al., 2007; Pardal et al., 2009; Ng and Plank, 2012). Wang et al. (2013) studied that the adsorption capacity of montmorillonite on the polycarboxylate superplasticizer is much greater than that of the cement, so the dispersion ability on the polycarboxylate superplasticizer may decrease obviously. Lei et al. (2012) also studied the interaction between sodium bentonite and the polycarboxylate superplasticizer, and found that the adsorption form in clay minerals varied with the difference of admixture concentration. When the concentration of admixture is relatively large, the polycarboxylate superplasticizer will mainly adsorb between the layers of clay minerals.

Most of the existing studies mainly focus on macroscopic experiments with different polycarboxylate superplasticizers (Hu, 2013; Roig-Flores et al., 2021; Wang, 2013). By characterizing the TOC (total organic carbon) value of the water reducer before and after adsorption, the adsorption capacity of clay minerals will be further estimated. While research on the interaction mechanism between clay minerals and polycarboxylate superplasticizers is limited, the influential rule of different mineral compositions on the performance of a water reducer still lacks recognition. With the rapid development of computer technology, the research of molecular simulation in the performance and structural design of cement also shows unique advantages, which could obtain various physical and chemical properties of the molecular system, and can also explore the chemical reaction path, transition state, and reaction mechanism from the electronic level. Jingming et al. (2009) investigated the molecular environment and the alkyl chain arrangement in the interlayer of cation surfactant-modified montmorillonite using the molecular simulation technique, and the influence caused by water content in organic montmorillonite with different surfactant loading concentrations was also studied. By building the adsorption model using the molecular simulation, our team's previous studies found that the adsorption energy of hydration product $Ca(OH)_2$(CH) with different functional groups will be varied, the order of the adsorption energy is sulfonic group > carboxyl group > amide group > benzene ring; the ratio of hydroxyl group and carboxyl group will also affect the adsorption energy on CH (Zhang et al., 2021a; He, 2022).

So based on our previous studies, bentonite clay mineral has been taken as the research object in the text. Combined with the cognition on the adsorption characteristic between the mineral composition of bentonite and different water reducers, we will then further reveal the discrepancy of adsorption energy and the interaction mechanism on different hydration products, so the preferential adsorption order and compatibility in cement hydration will be explored (Li et al., 2005; Chen et al., 2017; Zhang J et al., 2017).

2 MODELS AND CALCULATION METHODS

As an important material in cement hydration products, calcium silicate hydrate (C-S-H) typically accounts for 60%–70% of the whole hydration product. For the complexity and amorphism of the C-S-H structure, Taylor considered that C-S-H gel is a highly deformed tobermorite/jennite-like structure. Bonaccorsi et al. (2004) also studied the crystal structures of tobermorite and summarized the molecular models with three different layer spacing: 9, 11, and 14 Å. In many cases, tobermorite, and jennite crystals are used to replace C-S-H gel (Muralidharan et al., 2005; Jeffrey et al., 2011; Vidmer et al., 2014; Yan, 2017). In order to simplify the calculation in this article, we will then take the jennite as the model of cement hydration product C-S-H, with the molecular formula $Ca_9Si_6O_{18}(OH)_6{\cdot}8(H_2O)$ (Churakov, 2008; Muralidharan et al., 2005).

2.1 Calculation Methods and Parameter Design

Molecular simulation methods mainly contain quantum mechanics (QM) and classical mechanics methods. As a method of quantum mechanics, density functional theory (DFT) has been widely used in material synthesis and surface adsorption. The chemical reaction usually occurs when different molecules collide with each other, and are then adsorbed on the surface. Therefore, the complexity and possibility of the reaction can be further judged through the structure models and calculations of the adsorption energy (Chen and Ye, 2010; Wu et al., 2018). In this study, the surface models of the clay minerals, hydration products, and the adsorption behavior were established based on the DFT method, while the calculation was carried out by $Dmol^3$ modules in Material Studio (MS). The equilibrium configuration at the lowest energy was determined by geometry optimization using the Becke-Perdew (BP) correction approximation under the generalized gradient approximation (GGA), which can further investigate the variation rules of the adsorption energy and surface charge distribution. The calculation accuracy was set as fine, unless otherwise specified, and the smearing value was set as 0.005 (Wu, et al., 2018; Babaei, et al., 2020; Orazi, et al., 2020; Xing et al., 2020).

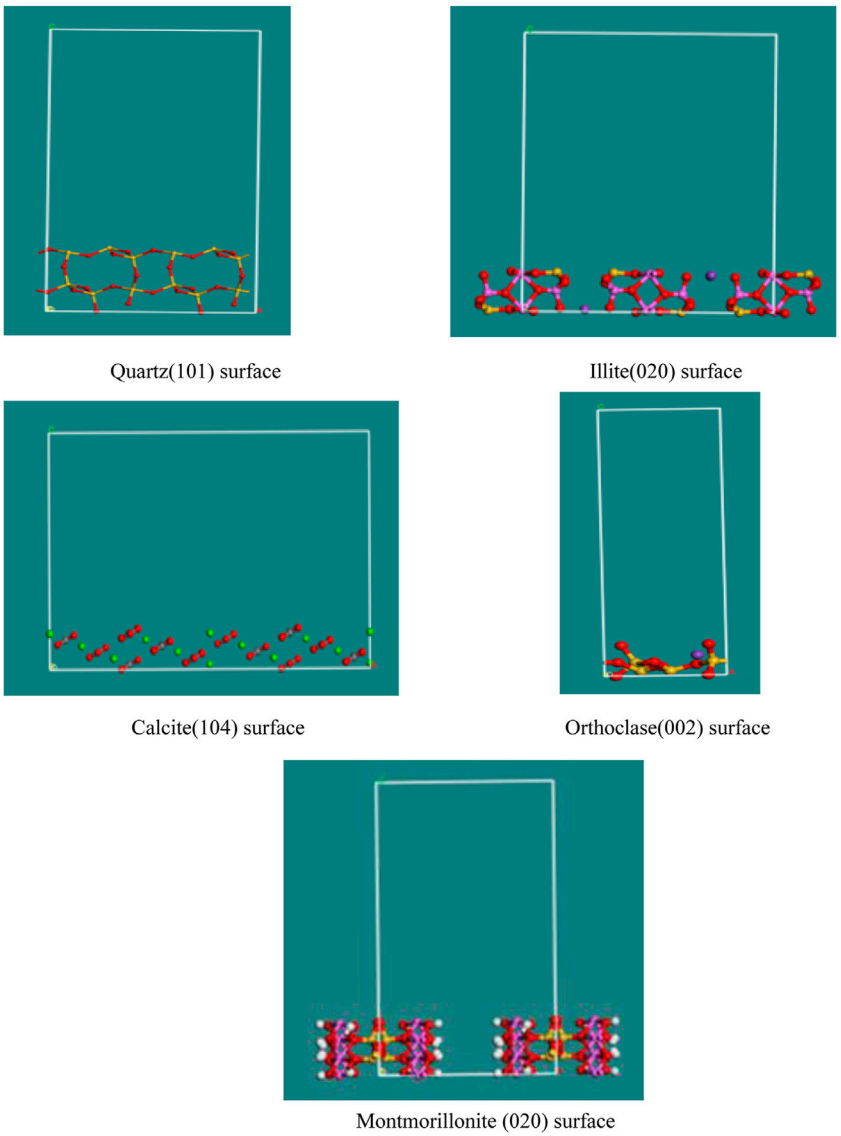


FIGURE 1 | Models of the different crystal planes for the clay minerals adopted in the text.

The adsorption energies between the admixtures and clay minerals or the hydration products were calculated as:

$$E_{ads} = E_{total\,(admistures\,on\,clay)} - E_{admixtures} - E_{clay} \quad (1)$$

$$E_{ads} = E_{total\,(admixtures\,on\,hydration\,products)} - E_{admixtures} - E_{hydration\,products} \quad (2)$$

where E_{ads} is the adsorption energy, $E_{\text{admixtures } on\ clay}$ and $E_{\text{admixtures } on\ hydration\ products}$ are the total energy after surface adsorption on the clay minerals or the hydration products, $E_{\text{admixtures}}$, E_{clay}, and $E_{hydration\ products}$ are the energies of different admixtures and the minerals before the adsorption. For cases with low adsorption energy, the absorbability is more likely to occur (Zhang S et al., 2017; Bao et al., 2018).

2.2 Calculation Models

Montmorillonite is the main mineral composition of bentonite, and due to the different origins of natural bentonite, the types and content of impurities, such as quartz, calcite, and illite, may be varied. So this study will then focus on the competitive adsorption of the additives between the bentonite clay minerals and the hydration products (Wang et al., 2014; Ko and Kang, 2016; Han et al., 2019).

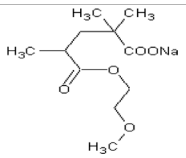
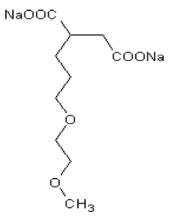
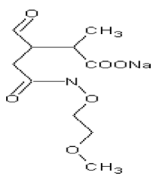
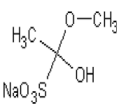
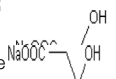
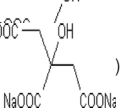
Molecular structure models of different minerals were adopted as shown in **Figure 1**.

According to our previous studies, taking the crystal plane corresponding to the maximum XRD diffraction peak of the single mineral, the crystal planes will also be geometrically optimized by Dmol^3 modules (He, 2022). The energy of

TABLE 1 | Calculation results for the total energy of different minerals after geometry optimization.

Composition	Total energy after geometric optimization/*Ha*
Quartz (101) surface	–5282.5567855
Illite (020) surface	–6105.745843
Calcite (104) surface	–11300.8164968
Orthoclase (002) surface	–4872.0182861
Montmorillonite (020) surface	–6826.1044255

TABLE 2 | Typical functional groups and molecular structures adopted in the text.

	Typical functional group	Molecular structure
(a)	-COOMe, $-CH_2-O-CH_2-$	
(b)	-COOMe, $-CH_2-O-CH_2-$	
(c)	-COOMe, $-CONH_2$, $-CH_2-O-CH_2-$	
(d)	$-SO_3Me$	
(e)	-OH, -COOH,	Sodium tartrate 
(f)	-OH, -COOH,	Sodium citrate ()

different lattice planes after geometric optimization is shown in **Table 1**.

Admixtures could improve the flow characteristics in the process of cement hydration by dispersion and lubrication. The adsorptive action of the polycarboxylate superplasticizer is mainly due to functional groups such as the hydroxyl group (-OH), carboxyl group ($-COO^-$), sulfonic acid group ($-SO_3^-$), etc., while the length and the density of the side chain could also directly affect the dispersing effect (Yan et al., 2017; Yinwen et al., 2014; Zhang et al., 2021b). Based on our previous studies, taking the functional groups or structural composition of different admixtures as shown in **Table 2**, the adsorption characteristics between the admixtures and the clay minerals will then be explored. For the polycarboxylate superplasticizer involved in this paper, we took a polymerization degree of $n = 1$ as an example (He, 2022).

3 RESULTS AND DISCUSSION

3.1 Adsorption Models of Different Minerals on the Bentonite

3.1.1 Comparison of Adsorption Energy

Clay minerals often contain different impurities, which may reflect the difference in the impact of the hydration process and the properties of hydration products. The adsorption energy of different hydration admixtures on the hydration product CH has been calculated from our previous research, among which sodium tartrate is the lowest (He, 2022). So for sodium tartrate, the comparison of the adsorption energy of different bentonite minerals is presented in **Table 3**.

The adsorption energy is −11.36 eV in montmorillonite, lower than that in other minerals, so the admixtures may be easier to adsorb on the montmorillonite, while the adsorption sequence of different minerals is as follows: montmorillonite > illite > calcite > orthoclase > quartz, which may illustrate that there is competitive adsorption between the clay minerals and hydration products when the admixture sodium tartrate participates in the hydration reaction.

3.1.2 PDOS of Different Minerals Before and After the Adsorption

Based on the molecular dynamics simulation, the total density of states (TDOS) and partial density of states (PDOS) could conduce to obtain more interaction properties and mechanisms of the system, such as electronic structures, tunneling spectroscopy, etc. (Babaei et al., 2020; Xing et al., 2020; Zhang et al., 2015).

Comparison of illite before and after the adsorption with sodium tartrate is presented in **Figure 2**, the sum of the bonding orbital was mainly attributed to the *s* or *p* orbitals, while the *d* and *f* orbitals had little effect on the bond formation. Specifically, the bonding orbital was mainly provided by the *s*

TABLE 3 | Calculation results of the adsorption energy between different minerals of bentonite and sodium tartrate (1 Ha = 27.2114 eV).

	Sodium tartrate	E_{total} (Ha)	E_{ads} (Ha)	E_{ads} (eV)
Compositions	Quartz (101) surface	–6213.5326	–0.0657	–1.7873
	Illite (020) surface	–7037.0253	–0.3693	–10.0494
	Calcite (104) surface	–12232.0567	–0.3300	–8.9808
	Orthoclase (002) surface	–5803.2234	–0.2950	–8.0271
	Montmorillonite (020) surface	**–7757.4321**	**–0.4175**	**–11.3613**

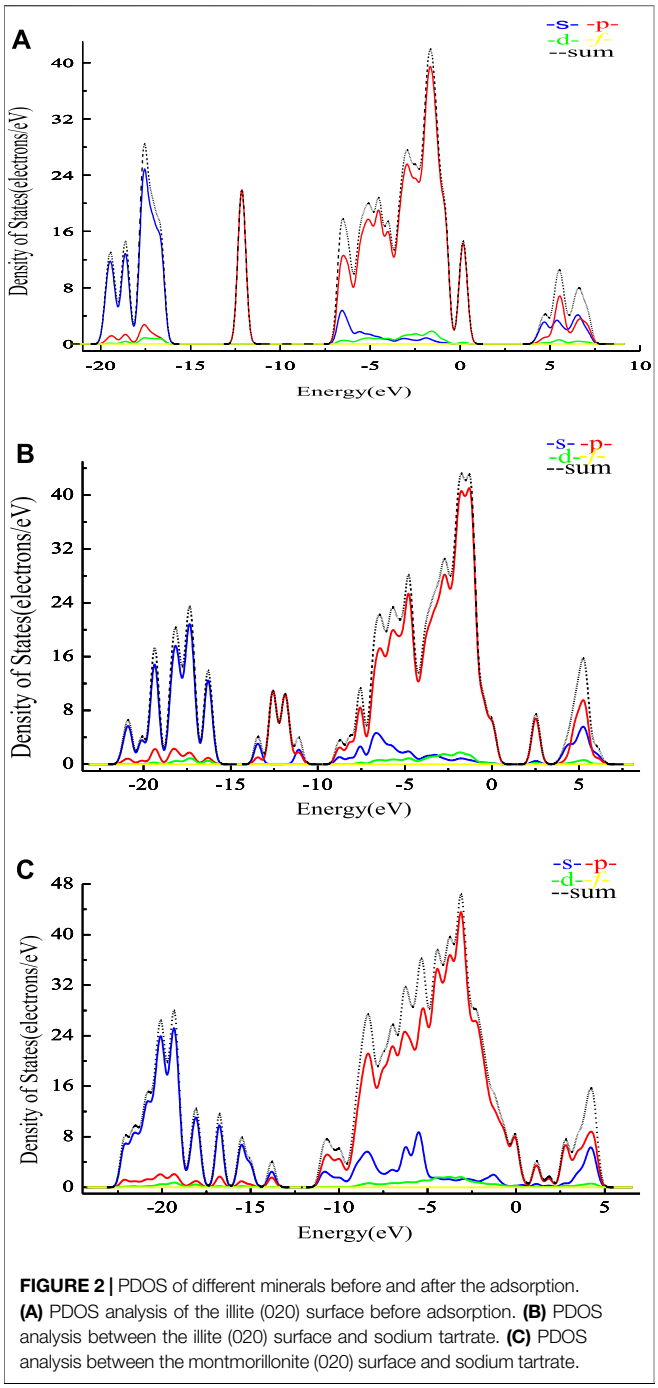
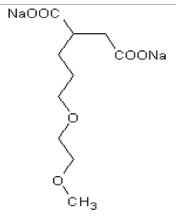
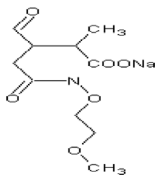
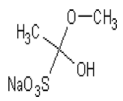
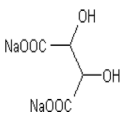
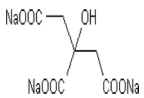


FIGURE 2 | PDOS of different minerals before and after the adsorption. **(A)** PDOS analysis of the illite (020) surface before adsorption. **(B)** PDOS analysis between the illite (020) surface and sodium tartrate. **(C)** PDOS analysis between the montmorillonite (020) surface and sodium tartrate.

orbital at approximately −20 to −16 eV, while the *p* orbitals were mainly attributed to the bonding atomic orbitals at nearly −12 and −7.5 to 0 eV, etc., with the peak value of 41.9 electrons/eV for the density of states before adsorption.

As shown in **Figures 2B,C** some new characteristic peaks of the *p* orbital were present at nearly −12.5 eV. Also rearrangement of the density for the *s* and *p* orbitals, with the peak value (43.2 electrons/eV), was higher than that before the adsorption, which may confirm the chemical bonding and interaction between illite and sodium tartrate. The peak value of montmorillonite (46.5

TABLE 4 | Calculations of the adsorption energy between the different additives and montmorillonite.

	Functional group	Montmorillonite (020) surface	
		E_{ads}/Ha	E_{ads}/eV
(a)		0.2219	6.0383
(b)		−0.1438	−3.9126
(c)		0.2345	6.3801
(d)		**−0.4175**	**−11.3613**
(e)		−0.2467	−6.7133

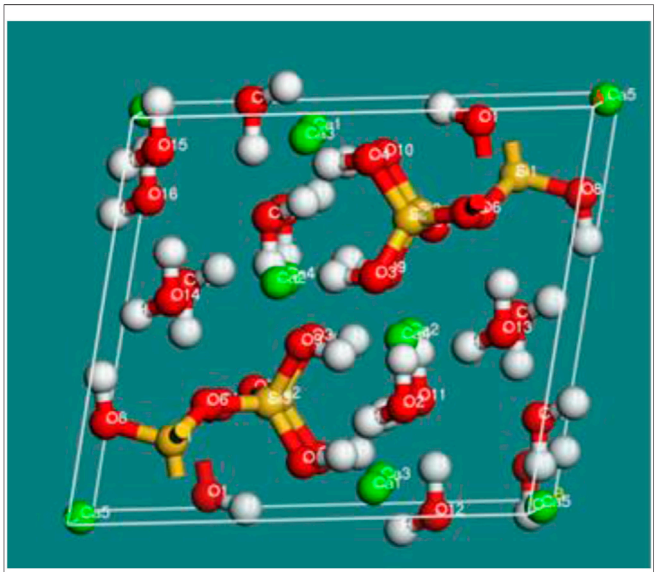
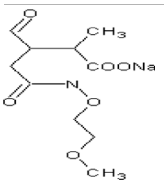
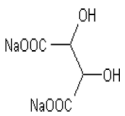
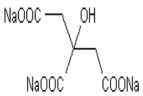


FIGURE 3 | Model of the jennite structure.

TABLE 5 | Calculation results for the total energy of jennite after geometry optimization.

Composition	Total energy after geometric optimization/Ha
Jennite (020) surface	−4,796.2470029
Jennite (001) surface	−10,270.6417208
Jennite (010) surface	−10,270.3770792

TABLE 6 | Calculations of the adsorption energy between the different admixtures and jennite.

Functional group	E_{ads}/eV	
	Jennite (001) surface	2.6964
	Jennite (010) surface	−0.3711
	Jennite (020) surface	0.01614
	Jennite (001) surface	**0.6498**
	Jennite (010) surface	**−8.5237**
	Jennite (020) surface	**−7.6280**
	Jennite (001) surface	4.1260
	Jennite (010) surface	−3.8899
	Jennite (020) surface	−4.6673

electrons/eV) is also higher than that of illite, which is consistent with the adsorption energy calculated before.

3.2 Adsorption Models of Different Admixtures on Montmorillonite

Based on our previous studies, as montmorillonite has the lowest adsorption energy when compared with the other minerals in bentonite, we will then further compare the adsorption energy between montmorillonite and other typical functional groups shown in **Table 2**, and the calculation result of the adsorption energy is presented in **Table 4**.

There was a large discrepancy in the adsorption energy between different admixtures and montmorillonite. For functional groups such as carboxyl ($-COO^-$) (**Table 4a**) and sulfonic acid groups ($-SO_3^-$) (**Table 4c**), the adsorption energy has a positive value, suggesting that adsorption for montmorillonite may be rather difficult on additives. The adsorption energy in sodium tartrate is the least among all additives, followed by sodium citrate, indicating that such additives could be easier adsorbed with clay minerals, thus may be more liable to reduce the dispersion of the water reducer in the hydration process. Compared with our previous findings, the adsorption energy of admixtures on montmorillonite clay was usually higher than that on hydration product CH, which demonstrates that admixtures may be more prone to be adsorbed on CH than clay minerals (He, 2022).

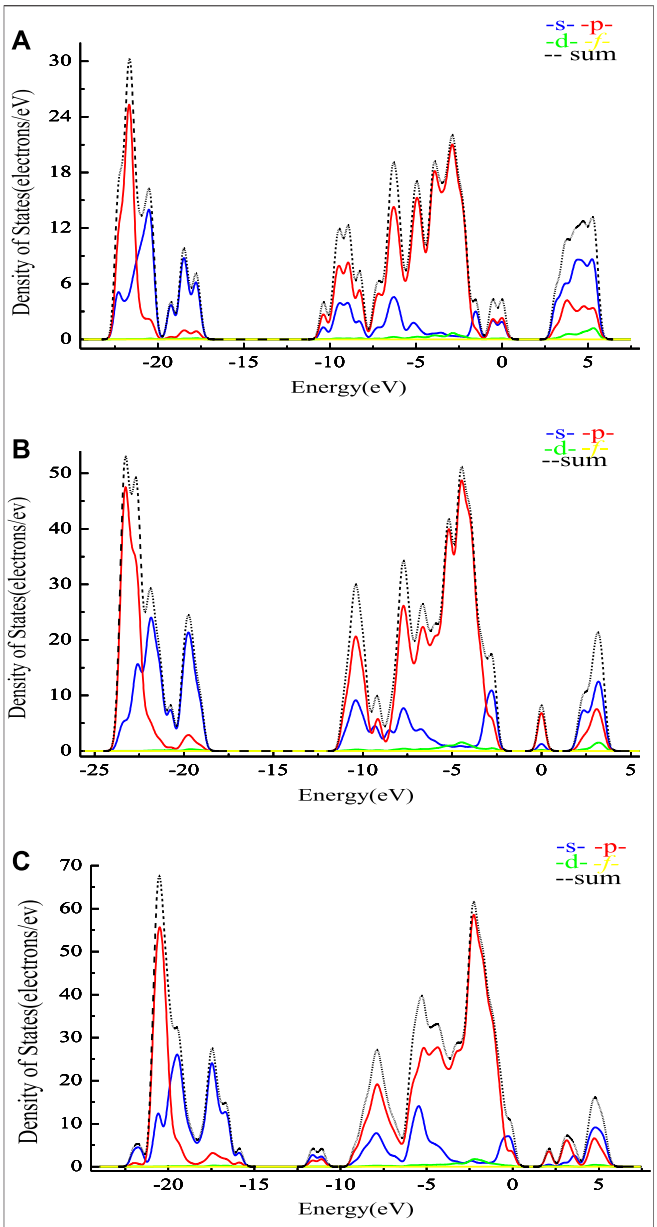


FIGURE 4 | PDOS analysis of jennite before and after the adsorption with sodium tartrate. **(A)** PDOS analysis of the jennite (020) surface before adsorption. **(B)** PDOS analysis of the jennite (010) surface before adsorption. **(C)** PDOS analysis between the jennite (010) and sodium tartrate.

3.3 Adsorption Models Between the C-S-H and Additives

3.3.1 Calculation of Adsorption Energy on C-S-H

Calcium silicate hydrate (C-S-H) may account for a large proportion of all hydration products. As discussed above, we will then take the defined crystal structure of jennite (**Figure 3**) to simulate the C-S-H structure in this text. The calculation results

TABLE 7 | The comparison of Mulliken charge populations for sodium tartrate before and after adsorption.

Atomic layer of sodium tartrate (with atom number)	Mulliken charge populations	
	Before adsorption	After adsorption on the jennite (010) surface
C (1)	0.072	0.084
C (2)	0.353	0.307
C (3)	0.072	−0.285
C (4)	0.353	0.402
O (5)	−0.667	−0.672
O (6)	−0.390	−0.347
O (7)	−0.667	−0.470
O (8)	−0.390	−0.558
O (9)	−0.447	−0.498
O (10)	−0.447	−0.991
H (11)	0.077	0.115
H (12)	0.077	0.178
H (13)	0.245	0.278
H (14)	0.245	0.315
Na (15)	0.707	0.650
Na (16)	0.707	0.647

for the total energy after geometry optimization are shown in **Table 5**.

For the discrepancy of the total energy in different planes of jennite, we will then further build the adsorption models between C-S-H and the above admixtures. The calculation of the adsorption energy is shown in **Table 6**.

The adsorption energy between the jennite (001) surface and different admixtures has positive values, indicating that the adsorption is rather difficult that surface. Jennite (010) and (020) surfaces present a lower adsorption energy in sodium tartrate, indicating that sodium tartrate may be easier to adsorb on the hydration product C-S-H, with a more significant delayed coagulation effect on the hydration reaction. Comparing the adsorption energy of sodium tartrate in clay minerals and hydration products, the adsorption energy of sodium tartrate on hydration product CH is the lowest, followed by montmorillonite, while the adsorption energy of the hydration product C-S-H is the highest (Bonaccorsi et al., 2004; Babaei et al., 2020; Xing et al., 2020).

Combined with the calculation results of adsorption energy between the clay minerals and the hydration products on the admixtures, the binding capacity of bentonite with the admixtures varies due to the difference of mineral composition and the content. The higher the content of montmorillonite, the easier the combination with additives. Also, as the content of CH and C-S-H is not always consistent in different stages of the hydration process, the adsorption energy of admixtures on hydration products would change accordingly. This could also further reflect the preferential adsorption order and compatibility between clay minerals and hydration products on the admixtures.

3.3.2 PDOS of Jennite Before and After the Adsorption

As presented in **Figure 4**, the horizontal axis of the energy for jennite (010) may tend to the lower state when compared with jennite (020). Unlike the minerals as shown in **Figure 2**, the bonding orbital at approximately −22, −10 ~ −7.5, and 5 eV, etc. may consist of both the *s* and *p* orbitals, while the other peaks of the bonding orbital were mainly provided by a single orbital. The peak value of density of states for jennite (010) (53 electrons/eV) is much higher than that of jennite (020). With higher density of states, the total energy could be higher, which may be positively associated with the total energy of different planes as shown in **Table 4**.

Comparing PDOS before and after adsorption with sodium tartrate, with a higher peak value after adsorption (67.7 electrons/eV), some new characteristic peaks may also occur near −11 and 3 eV. While the extent of change is not so fierce when compared with the minerals as shown in **Figure 2**, which could mean the interaction between jennite is weaker than that of minerals, further confirming the adsorption energy as calculated before.

3.3.3 Mulliken Population Analysis

The distribution of charge between each component atom could be calculated by Mulliken charge populations, which can further provide proof for the bonding and interaction between atoms. Mulliken population analysis for sodium tartrate is presented in **Table 7**.

The charge of the component atoms for sodium tartrate will be varied when adsorbed on jennite, as for the C (3) atom, the Mulliken charge population could change from 0.072 to −0.285, also some of the atoms such as O (7),O (8),O (10), and H (12) would have variable changes. With the variation and redistribution of the electrical charges, we can further intuitively understand the interplay between the additives and hydration product C-S-H.

4 CONCLUSION

This paper mainly analyzes the adsorption characteristic between the hydration product and bentonite clay mineral with additives in the cement hydration process. Combined with the calculation of the adsorption energy and the state density, the competitive adsorption and the compatibility between the hydration product and the clay minerals was further revealed, the conclusions are as follows:

(1) There is competitive adsorption between clay and hydration products when the admixture participates in the hydration reaction. The adsorption sequence of different minerals is as follows: montmorillonite > illite > calcite > orthoclase > quartz. The adsorption energy between the additives and hydration product CH is the lowest, followed by montmorillonite, while the adsorption energy of hydration product C-S-H is the highest.
(2) The binding capacity of bentonite with the admixtures varies due to the difference of mineral composition and the content. The higher the content of montmorillonite, the easier the combination with additives. While the proportions of CH and C-S-H in different stages of the hydration process could also reflect the preferential adsorption order and

compatibility between clay minerals and hydration products on the admixtures.

(3) Comparing PDOS between the minerals and hydration products with different admixtures can also conclude that there are some new characteristic peaks of the *p* orbital and rearrangement of the density for the *s* and *p* orbitals after the adsorption. The peak value of density of states shows a rising trend after adsorption, while the extent of change in jennite is not so fierce when compared with the minerals, which could further verify that the interaction between jennite is weaker than that of minerals.

DATA AVAILABILITY STATEMENT

The datasets presented in this study can be found in online repositories. The names of the repository/repositories and accession number(s) can be found in the article/supplementary material.

AUTHOR CONTRIBUTIONS

HT contributed for theoretical calculation and thesis writing; ZH and GM contributed for the overall idea and thinking of the manuscript, also the thesis modification; JZ contributed for the processing of data and thesis modification.

ACKNOWLEDGMENTS

Thanks to the Opening fund of State Key Laboratory of Geohazard Prevention and Geoenvironment Protection (Chengdu University of Technology) SKLGP 2022K011 and Sichuan Science and Technology Plan Project (Key R&D project) 2021YFQ0066. We also appreciate the Foundation 17zx7140 of Southwest University of Science and Technology and the supercomputing support of Chengdu University of Technology and National Supercomputing Beijing & Shenzhen Center.

REFERENCES

Babaei, Z., Najafi Chermahini, A., Dinari, M., and Dinari, M. (2020). Glycerol Adsorption and Mechanism of Dehydration to Acrolein over TiO2 Surface: A Density Functional Theory Study. *J. Colloid Interface Sci.* 563, 1–7. doi:10.1016/j.jcis.2019.12.051

Bao, Li., Liu, S., Guo, J., and Zhang, L. (2018). Interaction Between Low Rank Coal and Kaolinite Particles: A DFT Simulation. *Appl. Surf. Sci.* 456, 215–220. doi:10.1016/j.apsusc.2018.06.121

Bonaccorsi, E., Merlino, S., and Taylor, H. F. W. (2004). The Crystal Structure of Jennite, $Ca_9Si_6O_{18}(OH)_6{\cdot}8H2O$. *Cem. Concr. Res.* 34, 1481–1488. doi:10.1016/j.cemconres.2003.12.033

Chen, J., and Ye, C. (2010). A First-Principle Study of the Effect of Vacancy Defects and Impurity on Adsorption of O_2 on Sphalerite Surface. *Colloids Surf. A:Physiochem Eng. Aspects* 363 (1/3), 56–63. doi:10.1016/j.colsurfa.2010.04.013

Chen, H., Koopal, L. K., Xiong, J., Avena, M., and Tan, W. (2017). Mechanisms of Soil Humic Acid Adsorption onto Montmorillonite and Kaolinite. *J. Colloid Interface Sci.* 504, 457–467. doi:10.1016/j.jcis.2017.05.078

Churakov, S. V. (2008). Hydrogen Bond Connectivity in Jennite from Ab Initio Simulations. *Cem. Concr. Res.* 38, 1359–1364. doi:10.1016/j.cemconres.2008.08.004

Han, H., Rafiq, M. K., Zhou, T., Xu, R., Mašek, O., and Li, X. (2019). A Critical Review of Clay-Based Composites with Enhanced Adsorption Performance for Metal and Organic Pollutants. *J. Hazard. Mater.* 369, 780–796. doi:10.1016/j.jhazmat.2019.02.003

He, Z. (2022). *Study on the Characteristics of Time-Varying Viscosity Grouting Material and its Blocking Mechanism of Tunnel Water Inrush- Take Mira Mountain Section of Linla Highway as an Example*. Chengdu: Chengdu University of Technology. (in Chinese).

Hu, Q. (2013). *Effects of Microfines on the Dispersibility of Polycarboxylate Superplasticizer*. Chongqing: Chongqing University. (in Chinese).

Jae, E. O., Y B, J., and Jeong, Y. (2014). Characterization of Geopolymers from Compositionally and Physically Different Class F Fly Ashes. *Cem. Concr. Compos.* 50, 16–26. doi:10.1016/j.cemconcomp.2013.10.019

Jeffrey, W. B., Hamlin, M. J., and Richard, A. L. (2011). Mechanism of Cement Hydration. *Cem. Concr. Res.* 41, 1208–1223. doi:10.1016/j.cemconres.2010.09.011

Jingming, W., Yang, H., Zhu, J., and Shen, W. (2009). Molecular Dynamic Simulation on Interlayer Micro-structure in Organic Montmorilionite. *J. Mineral. Pet.* 29 (1), 33–37. (in Chinese). doi:10.19719/j.cnki.1001-6872.2009.01.006

Ko, Y. C., and Kang, B. (2016). The Effect of the Mineralogical Composition of Various Bentonites on CEC Values Determined by Three Different Analytical Methods. *Appl. Clay Sci.* 126, 153–159. doi:10.1016/j.clay.2016.03.010

Lei, L., and Plank, J. (2012). Synthesis, Working Mechanism and Effectiveness of a Novel Cycloaliphatic Superplasticizer for Concrete. *Cem. Concr. Res.* 42 (1), 118–123. doi:10.1016/j.cemconres.2011.09.003

Li, C.-Z., Feng, N.-Q., Li, Y.-D., and Chen, R.-J. (2005). Effects of Polyethlene Oxide Chains on the Performance of Polycarboxylate-Type Water-Reducers. *Cem. Concr. Res.* 35 (5), 867–873. doi:10.1016/j.cemconres.2004.04.031

Muralidharan, K., Simmons, J. H., Deymier, P. A., and Runge, K. (2005). Molecular Dynamics Studies of Brittle Fracture in Vitreous Silica: Review and Recent Progress. *J. Non-Crystalline Solids* 351, 1532–1542. doi:10.1016/j.jnoncrysol.2005.03.026

Nathan, A., Tregger, M. E., and Pakula Surendra, P. S. (2010). Influence of Clays on the Rheology of Cement Pastes. *Cem. Concr. Res.* 40, 384–391. doi:10.1016/j.cemconres.2009.11.001

Ng, S., and Plank, J. (2012). Interaction Mechanisms between Na Montmorillonite Clay and MPEG-Based Polycarboxylate Superplasticizers. *Cem. Concr. Res.* 42 (6), 847–854. doi:10.1016/j.cemconres.2012.03.005

Norvell, J. K., Stewart, J. G., Juenger, M. C., and Fowler, D. W. (2007). Influence of Clays and Clay-Sized Particles on Concrete Performance. *J. Mat. Civ. Eng.* 19 (12), 1053–1059. doi:10.1061/(asce)0899-1561(2007)19:12(1053)

Orazi, V., Juan, A., González, E. A., Marchetti, J. M., and Jasen, P. V. (2020). DFT Study of Ethanol Adsorption on CaO(0 0 1) Surface. *Appl. Surf. Sci.* 500, 144254. doi:10.1016/j.apsusc.2019.144254

Pardal, X., Pochard, I., and Nonat, A. (2009). Experimental Study of Si-Al Substitution in Calcium-Silicate-Hydrate (C-S-H) Prepared under Equilibrium Conditions. *Cem. Concr. Res.* 39, 637–643. doi:10.1016/j.cemconres.2009.05.001

Roig-Flores, M., Lucio-Martin, T., Alonso, M. C., and Guerreiro, L. (2021). Evolution of Thermo-Mechanical Properties of Concrete with Calcium Aluminate Cement and Special Aggregates for Energy Storage. *Cem. Concr. Res.* 141, 106323. doi:10.1016/j.cemconres.2020.106323

Sharma, M., Bishnoi, S., Martirena, F., and Scrivener, K. (2021). Limestone Calcined Clay Cement and Concrete: A State-Of-The-Art Review. *Cem. Concr. Res.* 149, 106564. doi:10.1016/j.cemconres.2021.106564

Vidmer, A., Sclauzero, G., and Pasquarello, A. (2014). Infrared Spectra of Jennite and Tobermorite from First-Principles. *Cem. Concr. Res.* 60, 11–23. doi:10.1016/j.cemconres.2014.03.004

Wang, Z., Hu, Q., Wang, Y., Wang, L., and Zhang, L. (2013). Interlayer Absorption Characteristics of Montmorillonite to Polycarboxylate Superplasticizer. *J. Chin. Ceram. Soc.* 41 (8), 1100–1104. (in Chinese). doi:10.7521/j.issn.0454-5648.2013.08.12

Wang, J., Ma, H., Yuan, W., He, W., Wang, S., and You, J. (2014). Synthesis and Characterization of an Inorganic/organic-Modified Bentonite and its Application in Methyl Orange Water Treatment. *Desalination Water Treat.* 52 (40/41/42), 7660–7662. doi:10.1080/19443994.2013.830690

Wang, L. (2013). *Effect of Clay Minerals on the Performance of Polycarboxylate Superplasticizer and Mechanism Research*. Beijing: China University of Mining & Technology. (in Chinese).

Wu, Y., Zhang, L., Liu, Y., and Qu, Y. (2018). Adsorption Mechanisms of Metal Ions on the Potassium Dihydrogen Phosphate (1 0 0) Surface: A Density Functional Theory-Based Investigation. *J. Colloid Interface Sci.* 522, 256–263. doi:10.1016/j.jcis.2018.03.073

Xing, J., Wang, C., Zou, C., and Zhang, Y. (2020). DFT Study of Se and SeO_2 Adsorbed on CaO (0 0 1) Surface: Role of Oxygen. *Appl. Surf. Sci.* 510, 145488. doi:10.1016/j.apsusc.2020.145488

Yan, Y. (2017). *Atomic Simulation and Performance Design of the Calcium Silicate Hydrates*. Nanjing: Southeast University. (in Chinese).

Yinwen, L., Chaolong, Y., Yunfei, Z., Jian, Z., Huilong, G., and Mangeng, L. (2014). Study on Dispersion, Adsorption and Flow Retaining Behaviors of Cement Mortars with TPEG-type Polyether Kind Polycarboxylate Superplasticizers. *Construction and Build. Mater.* 64, 324–332. doi:10.1016/j.conbuildmat.2014.04.050

Zhang, J., Pei, X., Wang, W., and He, Z. (2017). Hydration Process and Rheological Properties of Cementitious Grouting Material. *Constr. Build. Mater.* 139, 221–231. doi:10.1016/j.conbuildmat.2017.01.111

Zhang, S., Liu, Q., Gao, F., Li, X., Liu, C., Li, H., et al. (2017). Mechanism Associated with Kaolinite Intercalation with Urea: Combination of Infrared Spectroscopy and Molecular Dynamics Simulation Studies. *J. Phys. Chem. C.* 121 (1), 402–409. doi:10.1021/acs.jpcc.6b10533

Zhang, Y, Kong, X, Lu, Z, and Hou, S (2015). Effects of the Charge Characteristics of Polycarboxylate Superplasticizers on the Adsorption and the Retardation in Cement Pastes. *Cement and Concrete Res.* 67, 184–196. doi:10.1016/j.cemconres.2014.10.004

Zhang, Y., He, Z., Tian, H., Huang, X., Zhang, Z., Liu, Y., et al. (2021a). Hydrochemistry Appraisal, Quality Assessment and Health Risk Evaluation of Shallow Groundwater in the Mianyang Area of Sichuan Basin, Southwestern China. *Environ. Earth Sci.* 80 (17), 576. doi:10.1007/s12665-021-09894-y

Zhang, Y., Dai, Y., Wang, Y., HuangXiao, X. Y., Xiao, Y., and Pei, Q. (2021b). Hydrochemistry, Quality and Potential Health Risk Appraisal of Nitrate Enriched Groundwater in the Nanchong Area, Southwestern China. *Sci. Total Environ.* 784, 147186. doi:10.1016/j.scitotenv.2021.147186

Conflict of Interest: The authors declare that the research was conducted in the absence of any commercial or financial relationships that could be construed as a potential conflict of interest.

Publisher's Note: All claims expressed in this article are solely those of the authors and do not necessarily represent those of their affiliated organizations, or those of the publisher, the editors and the reviewers. Any product that may be evaluated in this article, or claim that may be made by its manufacturer, is not guaranteed or endorsed by the publisher.

Copyright © 2022 Teng, He, Meiben and Zhang. This is an open-access article distributed under the terms of the Creative Commons Attribution License (CC BY). The use, distribution or reproduction in other forums is permitted, provided the original author(s) and the copyright owner(s) are credited and that the original publication in this journal is cited, in accordance with accepted academic practice. No use, distribution or reproduction is permitted which does not comply with these terms.

frontiers | Frontiers in Earth Science

ORIGINAL RESEARCH
published: 20 June 2022
doi: 10.3389/feart.2022.917514

Numerical Simulation of Wind-Driven Rain Based on the Eulerian Model

*Hongyu Chen and Bo Zhou**

College of Architecture and Environment, Sichuan University, Chengdu, China

The wind-driven rain model based on the Eulerian multiphase model is the most widely used in engineering applications of green buildings. In this study, a real-world case of wind-driven rain was simulated using a wind-driven rain solver based on the Eulerian multiphase model developed by OpenFOAM. Separation of flow was observed at the front edges of the top of the building in the numerical simulation results, and the separated flow lines reconnected in the middle region of the roof. This type of corner flow with separation produces an accelerated horizontal airflow and increases the catch ratio; hence, there is often a larger catch ratio at the windward facades near the roof. The simulation results show that the Eulerian model used in this study possesses adequate capability and accuracy for wind-driven rain simulation.

Keywords: building design, building facades, wind-driven rain, numerical simulation, catch ratio

OPEN ACCESS

Edited by:
Yunhui Zhang,
Southwest Jiaotong University, China

Reviewed by:
Qili Hu,
Chengdu University of Technology, China
Liting Hao,
Beijing University of Civil Engineering and Architecture, China

***Correspondence:**
Bo Zhou
zxt001@163.com

Specialty section:
This article was submitted to Geohazards and Georisks, a section of the journal Frontiers in Earth Science

Received: *11 April 2022*
Accepted: *30 May 2022*
Published: *20 June 2022*

Citation:
Chen H and Zhou B (2022) Numerical Simulation of Wind-Driven Rain Based on the Eulerian Model. Front. Earth Sci. 10:917514. doi: 10.3389/feart.2022.917514

INTRODUCTION

Sustainable utilization of water resource has been a urgent topic around world (Zhang et al., 2021a; Zhang et al., 2021b). Wind-driven rain is a natural phenomenon in which raindrops fall with a nonzero horizontal velocity due to the influence of the wind field to form oblique rain. This oblique rain affects the water and heat exchange properties and material durability of building facades when acting on buildings and is a significant source of moisture for building facades. Its destructive consequences can take many forms, including moisture accumulation in porous materials leading to water seepage, frost damage, moisture-induced salt migration, weathering and discoloration, and cracking of structures due to thermal and moisture gradients. Runoff following wind-driven rain is also a contributing factor to the appearance of surface contamination patterns on facades. Moreover, it has been noted in the literature that the combination of wind and rain has a non-negligible effect on the load effect on the building structure as additional rain loads are generated by raindrops striking building facades (Blocken et al., 2013). Therefore, the study of the wind-driven rain phenomenon is of great significance to the performance design of buildings. Raindrops are constantly in a state of non-equilibrium motion due to gravity and viscous drag during their descent as well as the variation of wind speed, resulting in uncertainty in the velocity of raindrops; this is one of the complexities of the wind-driven rain problem.

Early wind-driven rain studies were based on a semi-empirical approach combining a theoretically derived form with field measurements (Lacy, 1971; Rydock, et al., 2005). The standard meteorological data measured at weather stations were wind speed, wind direction, and horizontal rainfall, and wind-driven rainfall was not usually measured. Therefore, researchers have established semi-empirical relationships between wind-driven rain loads and meteorological parameters (wind speed, wind direction, and horizontal rainfall). The development of the relationships has been guided by experimental observations in which both free wind-driven rain and wind-driven rain on buildings increase in approximate proportion to wind speed and horizontal rainfall. These formulae are semi-empirical in that there is a theoretical basis for their form, but free

parameters are chosen to fit the experimental data. The many limitations of this approach, including the difficulties in fully revealing the intrinsic complexity of the wind-driven rain problem associated with using experimental and semi-empirical methods, have led to the increased use of numerical methods in recent research efforts.

Choi (1993) introduced the first Euler–Lagrange method to solve the raindrop trajectory and conducted a wind-driven rain study on two-dimensional and three-dimensional buildings. He proposed a numerical method to simulate wind-driven rain around buildings. This model is made up of two components. The flow around the building is calculated by solving $k-\varepsilon$ of the two-equation turbulence model. The motion of the raindrops in the wind field is calculated by considering the forces acting on the droplets, then deriving the raindrop trajectories by solving the equations of motion. Wind-driven rain around rectangular buildings with different aspect ratios was investigated. The raindrop trajectories for various sizes of droplets were determined, and their velocities and directions when they struck the buildings at different locations were calculated. The amount of rainfall that fell on different parts of building facades and the corresponding intensities were obtained. The effects of wind speed, rainfall intensity, and building geometry on wind-driven rain were also investigated. In a subsequent study, Choi (1999) proposed another method to calculate the impact of wind-driven rain on building facades. This method enables the quantitative numerical simulation of wind-driven rain. Blocken and Carmeliet (2000a) and Blocken and Carmeliet (2000b) further developed the work of Choi by examining the transient variation of wind-driven rain over time and space during rainfall while considering meteorological conditions that could vary at any time. They incorporated numerical techniques for wind-driven rain simulation into a method for estimating wind-driven rain loads on a practical new building envelope based on buildings, which yields accurate estimates of spatial and temporal distribution, as well as meteorological data for the building site. This numerical method was also applied to several arithmetic sequences from a validated low-level test. The calculated results showed that the local distribution of driven rain loads on the building envelope can be accurately predicted with this numerical method. Ooi et al. (2020) used Lagrangian particle tracking methods to assess the effectiveness of different mitigation methods under the wind-driven rain. The research showed that the effectiveness of horizontal and vertical barriers was dependent on the size of the raindrops, with vertical barriers being more effective for smaller sized raindrops and horizontal barriers being more effective for larger sized raindrops.

The discrete model in the Euler–Lagrangian system proposed by previous scholars was once the main method for wind-driven rain studies. However, the disadvantages of this method are obvious: only the relative values at the physical level can be obtained, various field maps such as velocity and pressure fields of low buildings in continuous phase wind fields cannot be obtained similarly, and the pre-processing calculation and post-processing work of the simulation are time-consuming.

Huang and Li (2010) conducted the first numerical simulation study of buildings under the coupling effect of wind and rain using a multiphase model in the Eulerian–Eulerian system. They proposed a new numerical simulation method for wind-driven rain based on the Eulerian multiphase model and verified its accuracy for wind-driven rain coupled with the measured data of windward facades of isolated low-rise buildings reported by Blocken et al. (2013). This model divides the raindrops into several different phases according to their particle size, and, when combined with the wind phase, flow control equations can be established for each phase in the model. The coupling effect of the interacting forces between wind and rain and the gravitational effect of raindrops are incorporated into the model in the form of a term at the right end of the equation, thereby simplifying the setting of the model's boundary conditions. Kubilay et al. (2013) simulated the wind-driven rain field of a high-rise tower based on the Eulerian multiphase model, then compared and analyzed the calculated results with the field measured data to validate the model, and found that the calculation time required by the Eulerian multiphase model was reduced about 10 times compared with that of the earlier Lagrangian model. Compared with the earlier Eulerian–Lagrangian method, the biggest advantage of wind-driven rain simulation using the Eulerian multiphase model is that the setting of rain phase boundary conditions is simplified; only the volume fraction and the corresponding velocity components of the rain phase are required to be set at the boundary, and the wind-driven rain parameters are relatively easier to obtain (Kubilay et al., 2015a; Kubilay et al., 2015b; Pettersson, 2016). This model also has better method robustness, and the computational time can be reduced significantly. Wang et al. (2020) analyzed the wind-driven rain distribution characteristics of low-rise buildings under typhoons using the Eulerian multiphase model and field measurement, verifying the reliability of the model and the important effects of wind speed, wind direction, and horizontal rainfall intensity. He also found that the wind-driven rain effect received by the windward facade of the building under extreme meteorological conditions is higher than that of the building roof. In recent years, the numerical simulation method based on the Eulerian multiphase model has become extensively used in the field of wind-driven rain research.

In this study, the wind-driven rain solver based on the Eulerian multiphase model developed by OpenFOAM was used to analyze the model solution process and applied to the simulation of a wind-driven rain instance. The numerical results were then compared with experimentally measured results to verify the accuracy and effectiveness of the model and to lay the foundation for future research and development.

CONTROL EQUATIONS FOR WIND-DRIVEN RAIN

In this study, the three-dimensional steady-state Reynolds-averaged Navier–Stokes (RANS) equations were used for the wind field control equations, and the renormalization group (RNG) $k-\varepsilon$ model was used for the turbulence model (Yakhot et al., 1992). In the Eulerian multiphase model, the rain phase is simulated based on the continuum assumption, and the wind and rain phases are considered to be unidirectionally coupled, i.e., only the effect of the wind phase

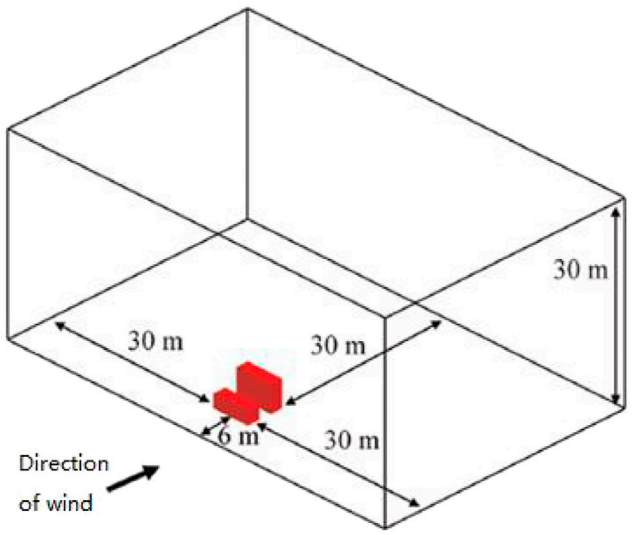


FIGURE 1 | Diagram of the computational domain.

on the rain phase is accounted for; the effect of the rain phase on the wind phase is ignored. Every rain phase corresponds to a certain range of raindrop sizes within which the raindrops have similar wind-driven rain behavior. For each rain phase, its continuity equation and corresponding momentum equation are as follows:

$$\frac{\partial \alpha_d}{\partial t} + \frac{\partial \alpha_d \bar{u}_{d,j}}{\partial x_j} = 0 \tag{1}$$

$$\frac{\partial \alpha_d \bar{u}_{d,j}}{\partial t} + \frac{\partial \alpha_d \bar{u}_{d,i} \bar{u}_{d,j}}{\partial x_j} + \frac{\partial \alpha_d \overline{u'_{d,i} u'_{d,j}}}{\partial x_j} = \alpha_d g + \alpha_d \frac{3\mu_a}{\rho_w d^2} \frac{C_d \mathrm{Re}_R}{4} \left(\bar{u}_i - \bar{u}_{d,i}\right) \tag{2}$$

where d is the diameter of the raindrop, α_d is the volume fraction of the rain phase d, $\bar{u}_{d,j}$ is the velocity component of the rain phase d in the j direction, $\bar{u}_i$ is the wind speed component in the i direction, ρ_w is the density of water, μ_a is the dynamic viscosity of air, g is the acceleration due to gravity, C_d is the drag coefficient of the raindrop, and Re_R is the relative Reynolds value calculated based on the relative velocities of the wind and rain phases. A horizontal line on a variable indicates that Reynolds averaging is performed for this variable.

CHARACTERIZATION PARAMETERS OF WIND-DRIVEN RAIN

The intensity of wind-driven rain is usually expressed in terms of the specific catch ratio $\eta_d(d)$ for horizontal rainfall intensity and the catch ratio η. Specific catch ratio $\eta_d(d)$ is related to a specific rain phase d, whereas catch ratio η is related to the sum of the rain phases corresponding to all droplet sizes in the entire raindrop spectrum. The specific catch ratio $\eta_d(d)$ and the catch ratio η can be determined using the following equations:

$$\eta_d(d) = \frac{R_{wdr}(d)}{R_h(d)} = \frac{\alpha_d |V_n(d)|}{R_h f_h(R_h, d)} \tag{3}$$

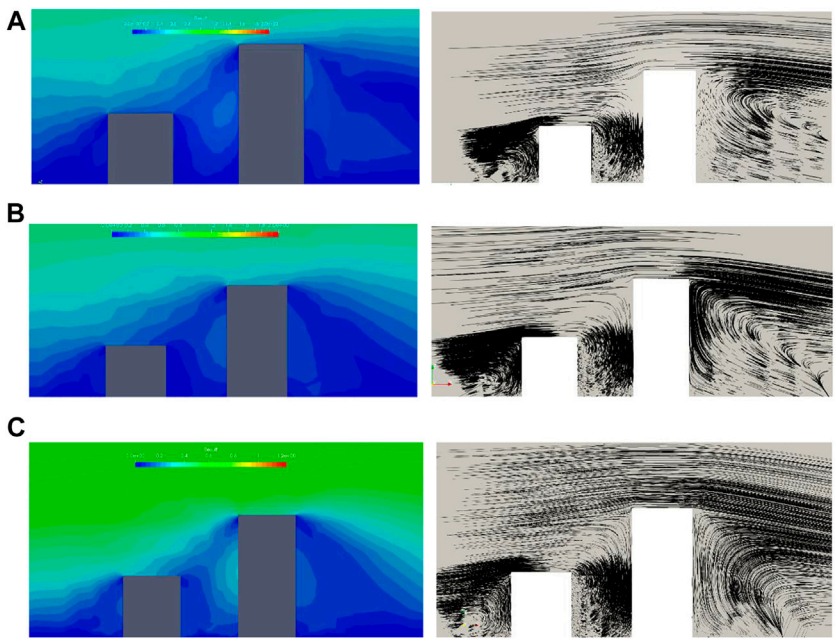


FIGURE 2 | Normalized velocity (U/U_{ref}) distribution and flow line distribution of wind field at different reference velocities: **(A)** U_{ref} = 1m/s, **(B)** U_{ref} = 3m/s, and **(C)** U_{ref} = 5m/s.

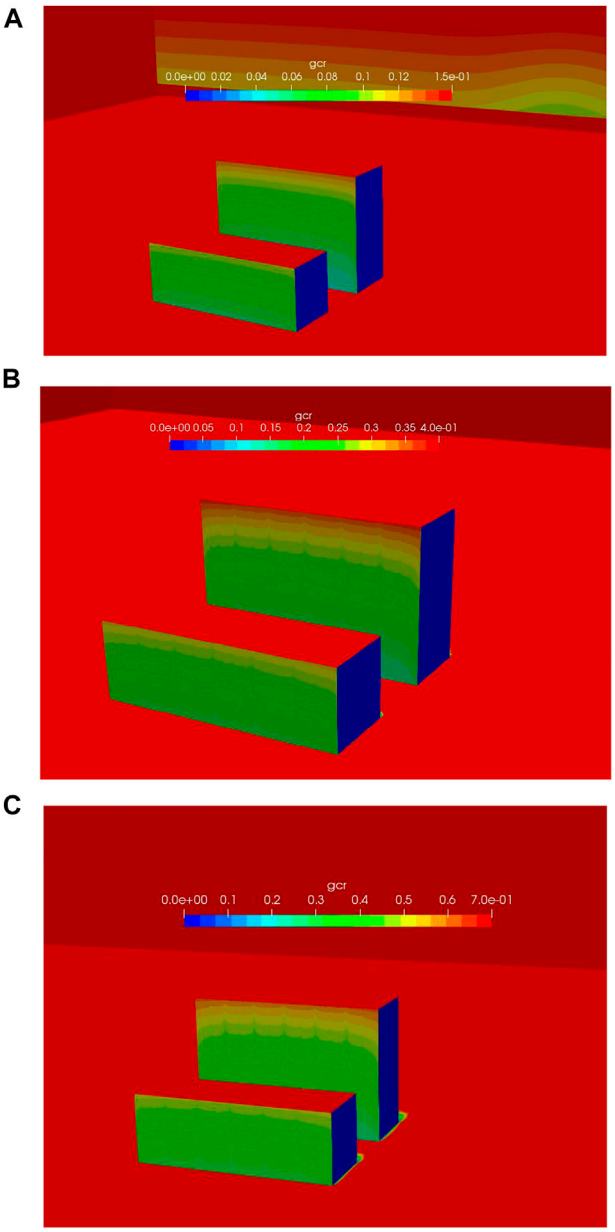


FIGURE 3 | Catch ratio distribution of building facades at different reference velocities: **(A)** U_{ref} = 1m/s, **(B)** U_{ref} = 3m/s, and **(C)** U_{ref} = 5m/s.

$$\eta_G = \int_d f_h(d)\eta_d(d)\mathrm{d}d \tag{4}$$

where R_{wdr} is the wind-driven rain intensity; R_h is the horizontal rainfall intensity (R_h = 10mm/h in the calculations of this study); $f_h(R_h, d)$ is the size distribution of raindrops that pass through the horizontal plane, which is simulated in this study based on the raindrop distribution spectrum given by Best (1950) and $|V_n(d)|$ is the size of the rain phase velocity perpendicular to the building facade.

BOUNDARY CONDITIONS

The velocity profile of the wind speed at the entrance boundary is determined according to the logarithmic law using the following equation:

$$U(z) = \frac{u^*_{ABL}}{\kappa}\ln\left(\frac{z+z_0}{z_0}\right) \tag{5}$$

where $U(z)$ is the average wind speed at height z; u^*_{ABL} is the frictional velocity of the atmospheric boundary layer; κ is the von Karman constant, which usually takes the value of 0.42; and z_0 is the aerodynamic roughness length (z_0 = 0.49m in the calculations of this study). In this study, $u^*_{ABL} = 0.24U_{\mathrm{ref}}$, where U_{ref} is the reference wind speed at a height of z_0. The profiles of turbulent kinetic energy k and turbulent dissipation rate ε at the entrance boundary are determined using the following equations:

$$k(z) = (I_u U(z))^2 \tag{6}$$

$$\varepsilon(z) = \frac{u^{*3}_{ABL}}{k(z+z_0)} \tag{7}$$

where I_u is the turbulence intensity along the flow lines.

As for the solid wall boundary, the standard wall function (Launder and Spalding, 1983) is used for the simulation, and the wall roughness is corrected by the gravel roughness (Cebeci and Bradshaw, 1977). The relationship between the gravel roughness height k_s and the roughness constant C_s is determined using the following equation (Blocken et al., 2007):

$$k_s = \frac{Ez_0}{C_s} \tag{8}$$

where E is the empirical constant and takes the value of 9.793.

The rain phase boundary conditions of the Eulerian model are simpler to set than those of the Lagrangian method, requiring only the volume fraction and initial velocity of the raindrops at the entrance boundary and top boundary. The horizontal velocity of the raindrops is assumed to be equal to the wind speed at the entrance boundary and top boundary; therefore, the relative horizontal velocity of the wind phase and the rain phase at the entrance boundary are zero. The vertical velocity of the rain phase is the vertical landing terminal velocity $V_t(d)$ of the raindrops, which can be determined using Stokes' law, and the phase volume fraction of the raindrops is determined using the following equation:

$$\alpha_d = \frac{R_h f_h(R_h, d)}{V_t(d)} \tag{9}$$

The two sides of the computational domain are set as symmetric boundaries, and the exit boundary is set as the pressure exit boundary.

MATERIALS AND METHODS

A real-world case of wind-driven rain was simulated using a wind-driven rain solver based on the Eulerian multiphase model

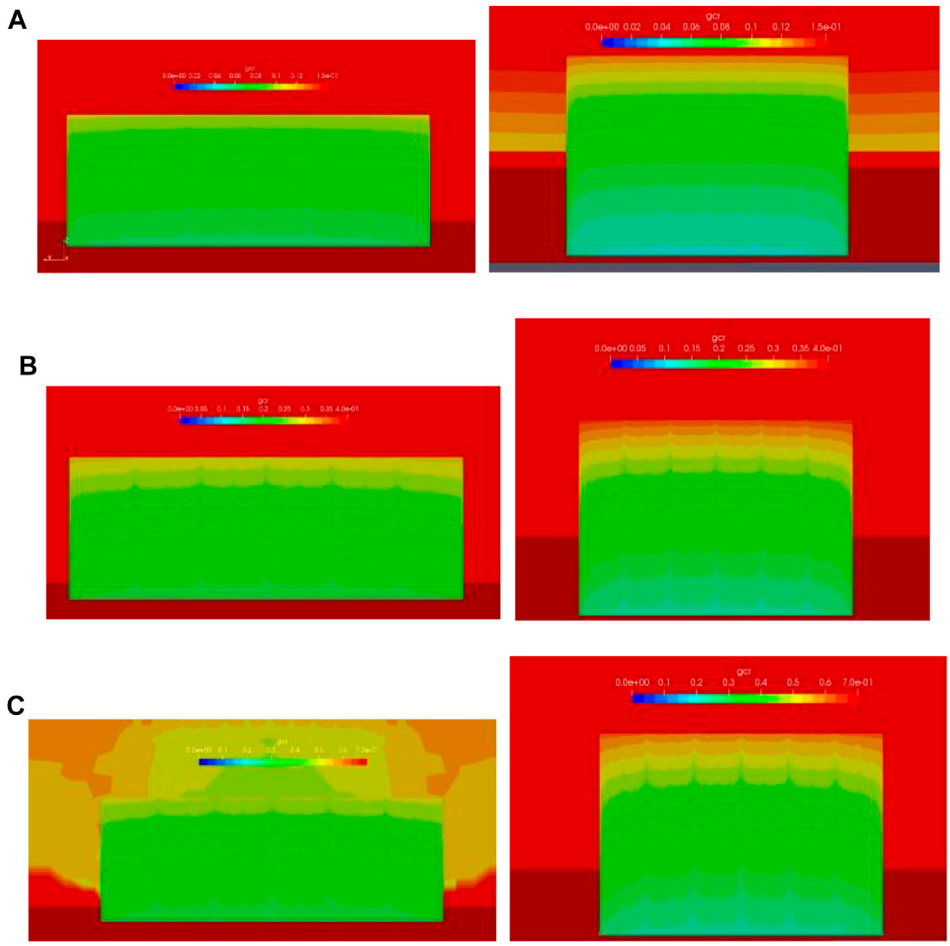


FIGURE 4 | Catch ratio distribution of windward building facades at different reference velocities: **(A)** U_{ref} = 1m/s, **(B)** U_{ref} = 3m/s, and **(C)** U_{ref} = 5m/s.

developed by OpenFOAM (Kubilay et al., 2015a; Kubilay et al., 2015b). The geometric shape of the calculations was as shown in **Figure 1**. There were two rectangular buildings of 6 m in length and 2 m in width within the computational domain. The height of the upstream building was 2.17 m, the height of the downstream building was 4.29 m, and the distance between the two buildings was 2 m. To obtain calculation results with adequate accuracy, a locally scaled grid was used. The grid was placed on both the top and sides of the windward facades of the building, with a minimum grid size of 0.004 m and a total grid size of about three million.

The constant wind phase flow field around the building was the first to be simulated in the numerical simulation. A coupled pressure–velocity approach was used for the wind field simulation with the SIMPLE algorithm as the solution algorithm, and the second-order discrete format was used for both the convective and viscous terms in the wind field control equations. In this study, three different inflow velocity conditions were simulated, corresponding to wind speeds of U_{ref} = 1, 3, and 5 m/s, respectively. After obtaining the constant solution for the wind phase flow field, it was used as an input condition for solving the rain phase field. The criterion for assessing convergence when solving for the wind and rain-phase fields was that the residual values were less than 10^{-5}. In the rain phase field, a total of 17 rain phases with different diameters (diameters of 0.3, 0.4, 0.5, 0.6, 0.7, 0.8, 0.9, 1.0, 1.2, 1.4, 1.6, 1.8, 2.0, 3.0, 4.0, 5.0, and 6.0 mm) were simulated. The specific catch ratio of each rain phase was determined individually using **Eq. 3**, and then the catch ratio was determined using **Eq. 4**.

RESULTS AND DISCUSSION

The normalized velocity distribution and flow line distribution of the wind field at different reference velocities were as shown in **Figure 2**. It can be seen that the normalized velocity at the various locations of the wind field was affected by the reference velocity. The greater the reference velocity, the greater the normalized velocity at the corresponding location of the wind field. The reason for this is that the parameter used here for the normalized velocity is the reference velocity U_{ref} with a corresponding height of z_0 = 0.49m. Therefore, it is obvious that the velocities at most of the locations, especially those higher than z_0, were greater than the reference velocity U_{ref}. As a result, the normalized velocity

increased with the reference velocity U_{ref}. On the other hand, flow separation was observed at the front edges of the top of both buildings in all three working conditions, as seen in the velocity and flow line diagrams (**Figure 2**), and the separated flow lines reconnected in the middle region of the roof. The main structures of the flow fields were very similar: there was a vortex with a scale comparable to the width of the building before the upstream building; there was also a vortex with a scale comparable to the width of the building between the two buildings; and there was another vortex of a larger scale after the downstream building due to flow separation. It is evident from the results that different reference velocities had little effect on the vortex structure of the flow field regardless of the size or location of the vortex.

Figure 3 shows the catch ratio distribution of the building facades at different reference velocities. It can be seen for all wind velocity cases that the catch ratio of the upstream and downstream building facades at the same height was smaller than that of the upstream building at the same location, and the reason for this can be identified by analyzing the flow characteristics of the wind field and rain phase field. It can be seen from the velocity cloud diagrams and flow line diagrams in **Figure 2** that the vortex generated in the area between the two buildings extended mainly in the vertical direction, whereas the vortex before the upstream building extended mainly in the horizontal direction. For this reason, the catch ratio of the windward facades of the downstream building was smaller than that of the upstream building at the same height.

Figure 4 shows the catch ratio distributions of the windward building facades at different reference velocities. It can be seen that all of the catch ratio distributions were high at the top and low at the bottom. This is mainly because the airflow was accelerated near the roof, where corner flow is formed, resulting in greater horizontal velocity and a greater catch ratio, whereas further down the building, the horizontal wind speed became smaller due to obstruction by the building, giving a smaller catch ratio.

The wind-driven rain model developed based on OpenFOAM provided numerical simulation results that model the case study well. Separation of flow was observed at the front edges of the top of the building, and the separated flow lines reconnected in the middle region of the roof. This type of corner flow with separation produces an accelerated horizontal airflow and increases the catch ratio; hence, there is often a larger catch ratio at the windward facades near the roof. Compared with previous work, our work simplified the rain-phase boundary conditions, made it easier to obtain the wind-driven rain parameters, and significantly reduced the computational time. In addition, our simulation results can be a guide for the design of buildings. There was also some limitation in our numerical models. As with most numerical models, our work involves simplifying boundary conditions and material properties during the analysis process, which ignores some factors that may affect the accuracy of the results.

CONCLUSION

In this study, a numerical simulation of a specific case was performed using a wind-driven rain model developed based on OpenFOAM. The main conclusions are as follows:

1) Separation of flow was observed at the front edges of the top of the two buildings, and the separated flow lines reconnected in the middle region of the roof. Different reference velocities had little effect on the vortex structure of the flow field regardless of the size or location of the vortex.
2) The vortex generated in the area between the two buildings extended mainly in the vertical direction, whereas the vortex before the upstream building extended mainly in the horizontal direction. As a result, the catch ratio of the windward facade of the downstream building is smaller than that of the upstream building at the same height.
3) The airflow was accelerated near the roof, where corner flow was formed, resulting in greater horizontal velocity and a greater catch ratio, whereas further down the building, the horizontal wind speed became smaller due to obstruction by the building, giving a smaller catch ratio.
4) The simulation results suggest that the Eulerian model utilized in this study is capable and accurate enough to simulate wind-driven rain.

DATA AVAILABILITY STATEMENT

The raw data supporting the conclusion of this article will be made available by the authors, without undue reservation.

AUTHOR CONTRIBUTIONS

HC: Investigation, Methodology, Writing-Original draft preparation. BZ: Validation, Supervision.

REFERENCES

Best, A. C. (1950). The Size Distribution of Raindrops. *Q.J R. Met. Soc.* 76 (327), 16–36. doi:10.1002/qj.49707632704

Blocken, B., and Carmeliet, J. (2000a). Driving Rain on Building Envelopes I. Numerical Estimation and Full-Scale Experimental Verification. *J. Therm. Envel. Build. Sci.* 24 (1), 61–85. doi:10.1106/UJ12-PFHK-VQFP-8GAL

Blocken, B., and Carmeliet, J. (2000b). Driving Rain on Building Envelopes- II. Representative Experimental Data for Driving Rain Estimation. *J. Therm. Envelope Build. Sci.* 24 (2), 89–110. doi:10.1106/EGXC-T4CL-E8VN-9JRL

Blocken, B., Stathopoulos, T., and Carmeliet, J. (2007). CFD Simulation of the Atmospheric Boundary Layer: Wall Function Problems. *Atmos. Environ.* 41 (2), 238–252. doi:10.1016/j.atmosenv.2006.08.019

Blocken, B., Derome, D., and Carmeliet, J. (2013). Rainwater Runoff from Building Facades: A Review. *Build. Environ.* 60 (1), 339–361. doi:10.1016/j.buildenv.2012.10.008

Cebeci, T., and Bradshaw, P. (1977). *Momentum Transfer in Boundary Layers*. Washington, DC: Hemisphere.

Choi, E. C. C. (1993). Simulation of Wind-Driven-Rain Around a Building. *J. Wind Eng. Ind. Aerodyn.* 46, 721–729. doi:10.1016/b978-0-444-81688-7.50080-2

Choi, E. C. C. (1999). Wind-driven Rain on Building Faces and the Driving-Rain Index. *J. Wind Eng. Ind. Aerodyn.* 79 (1), 105–122. doi:10.1016/S0167-6105(97)00296-1

Huang, S. H., and Li, Q. S. (2010). Numerical Simulations of Wind-Driven Rain on Building Envelopes Based on Eulerian Multiphase Model. *J. Wind Eng. Industrial Aerodynamics* 98 (12), 843–857. doi:10.1016/j.jweia.2010.08.003

Kubilay, A., Derome, D., Blocken, B., and Carmeliet, J. (2013). CFD Simulation and Validation of Wind-Driven Rain on a Building Facade with an Eulerian Multiphase Model. *Build. Environ.* 61 (1), 69–81. doi:10.1016/j.buildenv.2012.12.005

Kubilay, A., Derome, D., Blocken, B., and Carmeliet, J. (2015a). Numerical Modeling of Turbulent Dispersion for Wind-Driven Rain on Building Facades. *Environ. Fluid Mech.* 15 (1), 109–133. doi:10.1007/s10652-014-9363-2

Kubilay, A., Derome, D., Blocken, B., and Carmeliet, J. (2015b). Wind-driven Rain on Two Parallel Wide Buildings: Field Measurements and CFD Simulations. *J. Wind Eng. Industrial Aerodynamics* 146, 11–28. doi:10.1016/j.jweia.2015.07.006

Lacy, R. E. (1971). "An Index of Exposure to Driving Rain," in *Services and Environmental Engineering. Essential Information from the Building Research Establishment* (Garston: Construction Press), 232–239.

Launder, B. E., and Spalding, D. B. (1983). "The Numerical Computation of Turbulent Flows," in *Numerical Prediction of Flow, Heat Transfer, Turbulence and Combustion* (Pergamon), 96–116. doi:10.1016/b978-0-08-030937-8.50016-7

Ooi, C., Ge, Z., Poh, H. J., and Xu, G. (2020). Assessing Effectiveness of Physical Barriers against Wind-Driven Rain for Different Raindrop Sizes. *Eng. Analysis Bound. Elem.* 111, 186–194. doi:10.1016/j.enganabound.2019.11.007

Pettersson, K., Krajnovic, S., Kalagasidis, A. S., and Johansson, P. (2016). Simulating Wind-Driven Rain on Building Facades Using Eulerian Multiphase with Rain Phase Turbulence Model. *Build. Environ.* 106, 1–9. doi:10.1016/j.buildenv.2016.06.012

Rydock, J. P., Lisø, K. R., Førland, E. J., Nore, K., and Thue, J. V. (2005). A Driving Rain Exposure Index for Norway. *Build. Environ.* 40 (11), 1450–1458. doi:10.1016/j.buildenv.2004.11.018

Wang, X. J., Li, Q. S., and Li, J. C. (2020). Field Measurements and Numerical Simulations of Wind-Driven Rain on a Low-Rise Building during Typhoons. *J. Wind Eng. Industrial Aerodynamics* 204, 104274. doi:10.1016/j.jweia.2020.104274

Yakhot, V., Orszag, S. A., Thangam, S., Gatski, T. B., and Speziale, C. G. (1992). Development of Turbulence Models for Shear Flows by a Double Expansion Technique. *Phys. Fluids A Fluid Dyn.* 4 (7), 1510–1520. doi:10.1063/1.858424

Zhang, Y., Dai, Y., Wang, Y., Huang, X., Xiao, Y., and Pei, Q. (2021a). Hydrochemistry, Quality and Potential Health Risk Appraisal of Nitrate Enriched Groundwater in the Nanchong Area, Southwestern China. *Sci. Total Environ.* 784, 147186. doi:10.1016/J.Scitotenv.2021.147186

Zhang, Y., He, Z., Tian, H., Huang, X., Zhang, Z., Liu, Y., et al. (2021b). Hydrochemistry Appraisal, Quality Assessment and Health Risk Evaluation of Shallow Groundwater in the Mianyang Area of Sichuan Basin, Southwestern China. *Environ. Earth Sci.* 80 (17), 576–592. doi:10.1007/S12665-021-09894-Y

Conflict of Interest: The authors declare that the research was conducted in the absence of any commercial or financial relationships that could be construed as a potential conflict of interest.

Publisher's Note: All claims expressed in this article are solely those of the authors and do not necessarily represent those of their affiliated organizations, or those of the publisher, the editors and the reviewers. Any product that may be evaluated in this article, or claim that may be made by its manufacturer, is not guaranteed or endorsed by the publisher.

Copyright © 2022 Chen and Zhou. This is an open-access article distributed under the terms of the Creative Commons Attribution License (CC BY). The use, distribution or reproduction in other forums is permitted, provided the original author(s) and the copyright owner(s) are credited and that the original publication in this journal is cited, in accordance with accepted academic practice. No use, distribution or reproduction is permitted which does not comply with these terms.

frontiers | Frontiers in Earth Science

ORIGINAL RESEARCH
published: 23 June 2022
doi: 10.3389/feart.2022.895769

Distribution Characteristics and Geogenic Mechanisms of Riverbed Overburden in Southwest China

Zongping Yan[1,2], *Mo Xu*[1]*, *Xiaobing Kang*[1], *Leilei Guo*[2] *and Shishu Zhang*[3]

[1]State Key Laboratory of Geohazard Prevention and Geoenvironment Protection, Chengdu University of Technology, Chengdu, China, [2]Sichuan Water Conservancy Vocational College, Chengdu, China, [3]Power China Chengdu Engineering Corporation Limited, Chengdu, China

The distribution, scale, and engineering geological characteristics of riverbed overburden have become one of the key issues in the construction of water conservancy and hydropower engineering projects in southwest China. In this study, we summarize and discuss the (variation of thickness) distribution and the geogenic (formation) mechanisms of riverbed overburden in the associated rivers. This was done by compiling thickness data from constructed and planned dams. The results show that the overburden thickness is generally shallower in the upper Tibetan Plateau region, it is thickest in the marginal mountain region in the middle reaches, and shallower in the lower reaches of the mountain regions that are in contact with the Yunnan-Guizhou Plateau or Sichuan Basin. This holds true with the shallow-thick-shallow Distribution Law. Additionally, the river overburden has the characteristic of thickening gradually from the basin edge to the plateau slope. Through the genesis, source, and distribution of the aggradation deposits in the riverbed, the geogenic (formation) mechanisms of the river overburden layer is explored, and the coupling effect of tectonic-climatic-fluvial sedimentation processes on the variation of overburden thickness and spatial distribution is proposed. Finally, the geological problems encountered when engineering dams in thick overburden are analyzed, and common engineering measures are put forward. The results provide basic data support for water resources exploitation and further development of river engineering in Southwest China.

Keywords: southwest China, river, overburden, distribution, geogenic mechanisms

OPEN ACCESS

Edited by:
Xiaoyan Zhao,
Southwest Jiaotong University, China

Reviewed by:
Chengcheng Li,
China University of Geosciences Wuhan, China
Jianping Chen,
Jilin University, China

***Correspondence:**
Mo Xu
xm@cdut.edu.cn

Specialty section:
This article was submitted to Geohazards and Georisks, a section of the journal Frontiers in Earth Science

Received: *14 March 2022*
Accepted: *04 May 2022*
Published: *23 June 2022*

Citation:
Yan Z, Xu M, Kang X, Guo L and Zhang S (2022) Distribution Characteristics and Geogenic Mechanisms of Riverbed Overburden in Southwest China. Front. Earth Sci. 10:895769. doi: 10.3389/feart.2022.895769

1 INTRODUCTION

The thickness of riverbed overburden poses great challenges to the construction of hydropower projects in river basins, thus it is of great theoretical value and engineering significance to study the distribution law and the geogenic (formation) mechanisms of riverbed overburden layer thickness. As is well known, rivers transport soil from the hillside to tributaries, to the main stem, and then from the main stem to the lowland, especially in mountainous areas (Fabrizio et al., 2018). The riverbeds formed are a variety of loose deposits closely related to the topography and geomorphology, parent rock lithology, geological structure, neotectonic movement, and climate environments. The formation types are complicated and its lithofacies and thickness vary greatly.

Many researchers have analyzed the exploration and experimental data of dam sites, and used numerical simulations and physical models to study riverbed overburden from the aspects of the formation mechanisms, distribution law, engineering characteristics, exploration, anti-seepage

technology, and related engineering geological problems (foundation bearing capacity, seepage deformation, uneven settlement, sand liquefaction, etc.) (Hedayati Talouki et al., 2015; Michael, 2018; Luo and Huang, 2020; Yu and Shao, 2020; Zhang et al., 2021). The thickness variation of riverbed overburden has the obvious characteristics of basin and region, and there are many new achievements in the study of riverbed overburden from the dam site areas, especially in the section of the riverbed engineering area to the main stem and tributaries of rivers (Shi, 1986; Wang Y. S. et al., 2007; Xu et al., 2008; Wang, 2009; Xu et al., 2010; Yu and Shao, 2020; Yu and Shao, 2020).According to borehole data from construction sites of hydropower stations, the thickness variation of riverbed overburden from the top of Tiger Leaping Gorge to Xiakou is thinner in the upper and lower reaches of the Jinsha River, and deepest in the middle reaches (Hongyan Dam site thickness of 250 m) (Wang., 2009). The deposit layer in the Yalong river bed is often over 30 m thick and can be up to 51 m thick (Wang L. S. et al., 2007).The thickness of the riverbed overburden increases from the lower reaches to the upper reaches of the Dadu River, and suddenly decreases in the Dagangshan area of the middle reaches, and the longitudinal section of the main stem bed cover forms a "W" shape (Xu et al., 2010).The riverbed overburden of the Minjiang River appears thick in the upper reaches and thin in the lower reaches (Wang et al., 2005).Research on the distribution and geogenic mechanisms of riverbed overburden in southwest China is mainly focused on a single dam site or individual river sections, meanwhile there is less systematic research on the thickness variation of riverbed overburden in the primary rivers of Southwest China. These rivers include the Jinsha, Tsangpo, Lancang, Nujiang, etc.

Parts of the previously mentioned rivers are in the slope zone transition from the Qinghai-Tibet Plateau to the Yunnan-Guizhou Plateau and the Sichuan Basin. This is one of the regions with the most abundant water resources and also the most developed deep riverbed overburden. As for the origins of the overburden, there are many opinions, but no agreement has been reached yet. Xu et al. (2010) proposed that global climate change and eustacy (sea level rise and fall) cause the thick overburden of river valleys. Wang et al. (2005) proposed that earthquakes, heavy rains, and other disasters induce mountain collapse, landslide and debris flow, resulting in river blockage and other phenomena where the landslide front is directly deposited on the early overburden, resulting in local accumulation of deep overburden. Wang et al. (2006) proposed that during the interglacial period of the last glacial max, the river valley was strongly eroded and cut into the basal layer below the present riverbed, and then rapidly backfilled to form the deep overburdenlayer. Ding et al. (2021) investigated the 26.5 m-thick lakebed profile at the bottom of Tongzilin Dam in the Yalong River and proposed that the formation of the overburden was the result of the combined action of climate fluctuations and strong tectonic activity (local tectonic subsidence). Bridgland (2000) and Maddy et al. (2001) proposed that the reasons affecting the development of fluvial geomorphology (including riverbed cover) can be summarized as dynamic changes within the fluvial system and non-fluvial origins which are based on the geological records of the river terraces of the Thames River in the United Kingdom during the Middle Pleistocene. By considering ice dynamics, bedrock erosion, and sediment transport processes, Delaney and Adhikari (2020) simulated the sediment discharge of alpine glaciers that experienced 100 years of accelerated glacier melting, and found that during the glacier retreat sediment emissions are likely to increase significantly, and depending on the amount of sediment stored under the ice, there are additional effects based on the different glacial topography and bed roughness. Alexey et al. (2019) studied riverbed deposition of rivers in the Russian Far East under extreme rainfall conditions and found that the upper reaches of secondary tributaries and part of the estuaries of large tributaries were areas with increased deposition. Syvitski et al. (2022) reviewed that Global warming is also substantially affecting the global sediment cycle through temperature impacts (sediment production and transport, sea ice cover, glacial ice ablation and loss of permafrost), precipitation changes, desertification and wind intensities, forest fire extent and intensity, and acceleration of sea-level rise. Humans have transformed the mobilization, transport and sequestration of sediment, to the point where human action now dominates these fluxes at the global scale as seen in data from 1950 to 2010. Summarizing previous studies, it is shown that the formation of the riverbed overburden is related to several factors, such as tectonic movement, climate change, sedimentary law, geological environment, and geological disasters. However, the origin of the regional deep overburden in the primary rivers of southwest China may be more complex and diverse.

As for the classification of overburden thickness, most researchers demarcate 30 m as the boundary of thick overburden. The code for engineering geological investigation of water resources and hydropower in China (GB50487-2008) stipulates that the thickness greater than 40 m of overburden layer of is considered thick. This study adopts three categories according to the specification, namely the shallow layer (< 40 m), a deep overburden layer (40–100 m), and giant-thick overburden layer (> 100 m). For clarity the terms "thick and thin" or "thickness" is used when regarding the vertical height of the overburden layer(s) and the above terms are used when distinguishing the impact on hydrological engineering projects as shown in **Table 1**.

Based on previous work, this paper systematically summarizes and explores the distribution characteristics and geogenic mechanism of riverbed overburden in major rivers of Southwest China by grading and analyzing many of the boreholes related to already built or planned dams (sluices). This will provide engineering experience, reference, and basic data support for the hydropower cascade planning, development, and site selection of river channel projects in Southwest China.

2 RIVERBED OVERBURDEN DEPTH DISTRIBUTION CHARACTERISTICS

By summarizing the overburden thickness and composition data of 632 dams (sluices) that have been built or planned in Southwest China, the thickness variation of overburden in

TABLE 1 | The riverbed overburden thickness characteristic table in the upper Reaches of the Yangtze River.

River	Maximum thickness/m	Corresponding position	General characteristics of overburden thickness			
			Mainstem			Tributary
			Giant-thick Overburden (>100 m)	Deep overburden(40–100 m)	shallow layer (<40 m)	
Jinsha River	250	Hongyan dam site	The main riverbed overburden is"bead-like", the middle and upper reaches of Tiger Leaping Gorge reach the thickest, the middle reaches are thinner, and the lower reaches are generally thicker, The section from Xinshizhen to Yibin city presents a belt-like distribution of deep layers			Except for Yalong River, the overburden thickness of the Jinsha River tributaries is generally less than 40 m, but the overburden thickness of the middle and lower reaches of the Jinsha River tributaries is relatively thicker, for example, the overburden thickness of the Shuiluo River basin is relatively thicker, that is, it is thicker in the upstream and thinner in the lower reaches. The Chongjiang River in the Shigu water source area has a deep overburden, with a maximum thickness of 132.80 m. In addition, the tributaries are thick in local sections and near the confluence, but the overall thickness is irregular
			①Qizong- Longpan section	①Lawa-Qizong section. ②Longpan-Xiaxiakou section. ③Panzhihua-yibin city section	①Above the Lawa dam site. ②Xiaxiakou-panzhihua section	
Yalong River	109.2	Jiangbian dam site	The main stem is bound by the Lenggu dam site, and the thickness of overburden in the lower reach is 30–50 m, while the thickness of overburden in the upper reach is less than 30 m			The upper Yalong River tributaries have shallow overburden, such as in the Xianshui River Basin where the overburden is less than 40 m. The overburden of the middle and lower reaches of tributaries is generally thicker, for example, the overburden of the Jiulong River Basin is generally thicker, of which the Jiangbian dam site is 109.2 m. However, the xigeda formation exists in many dam sites in the Anning River Basin. The bedrock has not been explored in many dam sites, and the thickness is difficult to be determined
				The river section below Lenggu dam site	The river section above Lenggu dam site	
Dadu River	>420	yele dam site	The overburden in the headwater area above the Shuangjiangkou dam site of the main stem is shallower, and the riverbed overburden of the lower reach is in a continuous and stable distribution of "strip", and the overall thickness increases from the downstream to the upstream			The distribution of deep overburden in the tributaries of Dadu River is also relatively common, for example, the Nanya River and Tianwan River have giant-thick overburden, but there are fluctuations
			①Daoban- Danba section. ②Yeba-Yingliangbao section	①Shuangjiangkou-Daoban section. ②Danba- Yeba section. ③Reach below Yingliangbao (except for Dagangshan and Angu Dam site)	①Above the Shuangjiangkou dam site. ②Dagangshan dam site. ③Angu dam site	
Minjiang River	101.5	Shiziping dam site	The riverbed overburden in the upper reaches of Minjiang River isthicker from the lower to upper reaches, while the riverbed overburden in the middle and lower reaches is shallower			The deep overburden of the tributaries of the upper Minjiang River is widely distributed. For example,
				Diexi to Xuankou town	The river below Xuankou	

(Continued on following page)

TABLE 1 | (*Continued*) The riverbed overburden thickness characteristic table in the upper Reaches of the Yangtze River.

River	Maximum thickness/m	Corresponding position	General characteristics of overburden thickness			
			Mainstem			Tributary
			Giant-thick Overburden (>100 m)	Deep overburden(40–100 m)	shallow layer (<40 m)	
Qingyi River	104.46	Maotan dam site	The overburden distribution of the mainstem of the Qingyi River is thicker in the upper and lower reaches and shallower in the middle ①Maotan dam site	①Qiaoqi-Xiaoguanzi dam site	①Below the Xiaoguanzi dam site (except Maotan dam site)	the overburden of the Zagunao River, Heishui River and Erhe River basins is generally about 40–80 m, and the overburden at the Shiziping dam site of Zagunao River is 101.5 m The distribution of tributary overburden is irregular, and its thickness fluctuates greatly
Tuojiang River	49.9	Guankou dam site	The Tuojiang main stem overburden is shallower			The riverbed overburden of the tributaries in the upper reaches Tuojiang River is thick and irregular
Fujiang River	107	Yinping dam site	The riverbed overburden in the main stem of Fujiang River is relatively shallow, and the thickness is less than 40 m			The riverbed overburden of the tributary Huoxi River is relatively thick, but there are fluctuations
Jialing River	73	Xianyaba dam site	The deposit layer of the main stem of Jialing River is 10–25 m. In the upper reaches of Jialing River, the overburden is shallower, while in the middle reaches, the overburden is thicker, and the lower reaches to the Yangtze River, the overburden is shallower			The riverbed overburden in the upper tributaries of the Jialing River is relatively thick. Among them, the Bailongjiang riverbed overburden is thicker in the middle reaches and relatively thin in the upper and lower reaches. The majority of the deposit layer of the Baishui River basin is 40 m thick or more. The middle and lower reaches of the Jialing River tributaries have a shallower overburden

each major river basin is as follows: the Yellow River (Reach above Lanzhou) (61), the Jialing River (69), the Fujiang River (28), and the Tuojiang River (6), the Minjiang River (56), the Qingyi River (22), the Dadu River (75), the Yalong River (89), the Jinsha River (104), the Lancang River (29), the Nujiang River (36), the Lixian River (9), the Irrawaddy River (9), the Nanpan River (9) and the Yuanjiang River (4), the Yarlung Tsangpo river (26), etc. The distribution is shown in **Figure 2**.

2.1 Main Riverbed Overburden Thickness Variation Characteristics

2.1.1 The Upper Reaches of the Yangtze River

The upper reaches of the Yangtze River at the Jinsha River and its important tributaries such as the Yalong, Dadu, and Min Rivers have deep riverbed overburden (**Figure 1**), with diverse lithofacies and complex structures. In the upper reaches of the Yangtze River (from Yibin to Chongqing) and its tributaries, such as the Tuojiang and Jialing Rivers, the riverbed overburden is mainly composed of a single sand and gravel layer of small thickness (**Table 1**).

2.1.2 Nujiang River

The riverbed overburden in the Nujiang River Basin is relatively shallow. It is generally 20–40 m thick. However, the thickness of the riverbed overburden at the Songta dam site is 58–70 m. Above the Songta dam site the riverbed overburden thickness is 10–15 m. In some cases however (between the upper and lower reaches) there are almost no deposits, and the riverbed is bedrock. From the Songta dam site to the Saige dam site, the

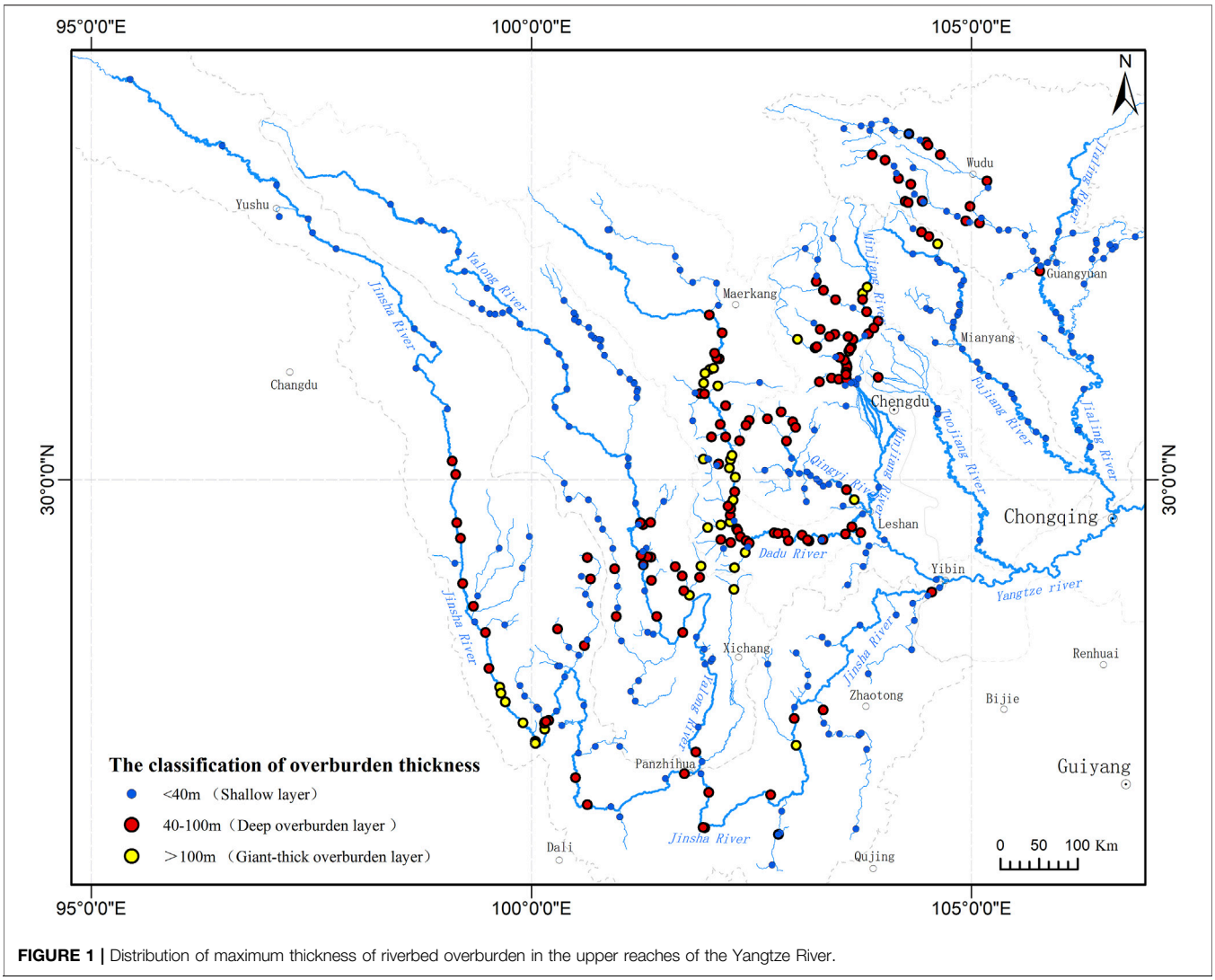


FIGURE 1 | Distribution of maximum thickness of riverbed overburden in the upper reaches of the Yangtze River.

overburden layer is 25–40 m. Downstream of the Songta dam the overburden is 10–15 m. The overall thickness is shallow in the upstream and downstream portions and deep in the middle (**Figure 2**).

2.1.3 Lancang River

The overburden in the main stem of the Lancang River between the upper and lower reaches has a consistent thickness of between 20 and 30 m. Analyzing the overburden thicknesses based on longitudinal distribution; the upstream is thinner, the middle is thicker, and the downstream is thinner. The tributaries to the Lancang have relatively thin overburden layers (**Figure 2**).

2.1.4 Yellow River (Above Lanzhou)

The Yellow River basin (above Lanzhou) has a relatively thin overburden thickness. The main stem riverbed overburden is 2–26 m thick and mainly composed of pebbles and gravel. The overburden of the tributary Tao and Huangshui Rivers are less than 40 m, except at the Jiudianxia dam site in the Tao River where it is 56 m. The overburden of the Tao River is thicker in the upper reaches and shallower in the middle and lower reaches.

2.1.5 Yarlung Tsangpo River

The thickness of the overburden in the middle and upper reaches of the Yarlung Tsangpo River can reach more than 120 m while the wide valley area in the lower reaches may reach hundreds of meters. The maximum thickness of the overburden in the Niyang and Lhasa Rivers is more than 100 and 400 m respectively. At the Qushui Bridge location on the Yarlung Zangbo (Tsangpo?) River in Zedang, the thickness of riverbed overburden is more than 50 m, and in the Lhasa area, the thickness of riverbed overburden is 123 m. The maximum thickness of the sand and gravel layers in the adjacent ancient riverbed as measured by electromagnetic exploration is 600 m (Yu and Shao, 2020).

2.1.6 Other River(s)

For other river basins, such as the Lixianjiang, Irrawaddy, Nanpanjiang, Yuanjiang, and others on the Yunnan-Guizhou Plateau, the overburden of the riverbeds are predominately

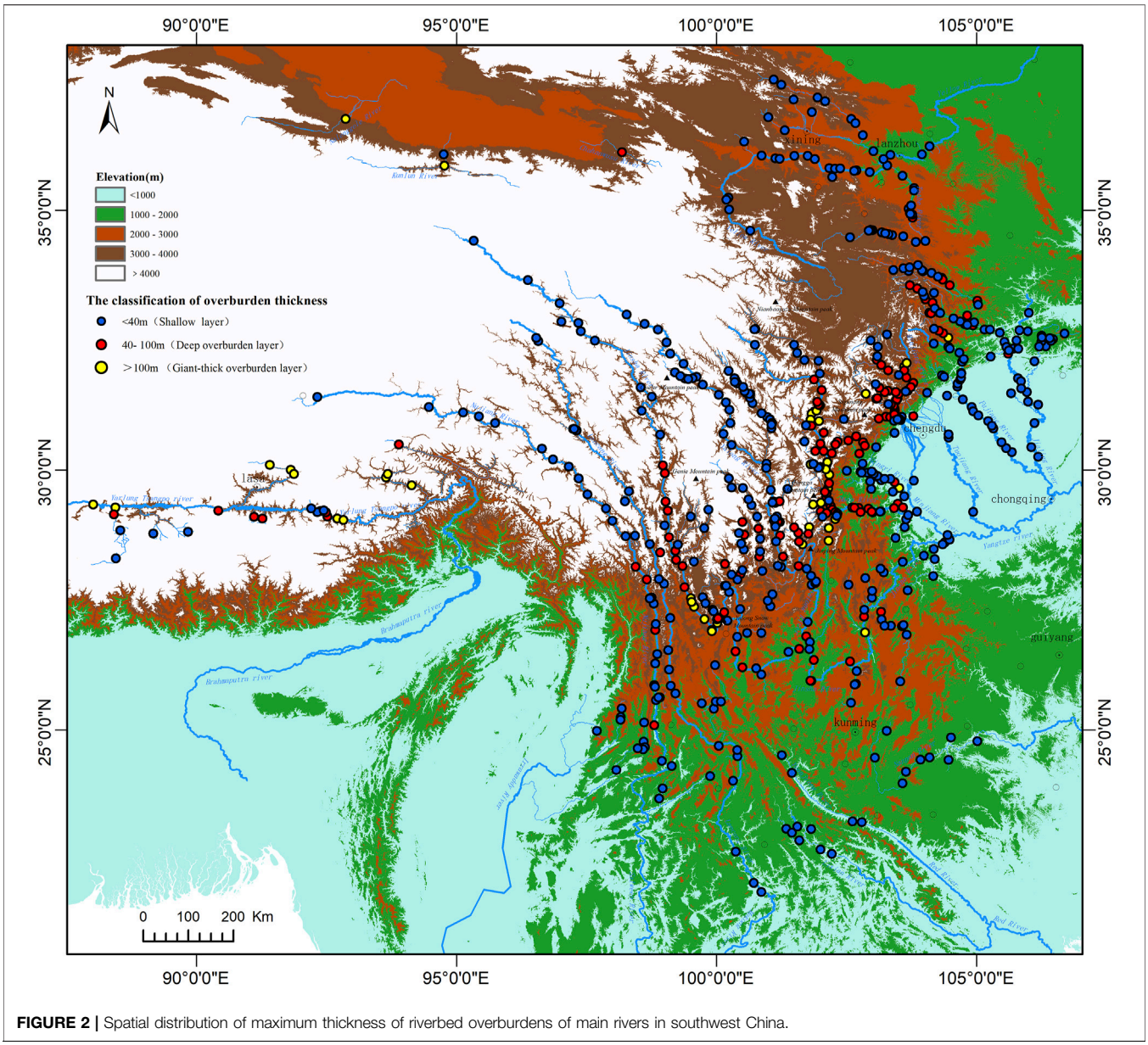


FIGURE 2 | Spatial distribution of maximum thickness of riverbed overburdens of main rivers in southwest China.

considered shallow (<40 m). More specifically the relative overburden of the Lixianjiang and Irrawaddy are shallow, while the Nanpanjiang and Yuanjiang are thicker in comparison.

2.2 Regional Thickness Variation Characteristics

Summarizing the exploration data related to riverbed overburden; the results show that the distribution of deep riverbed overburden presents regional characteristics. According to the characteristics of topography, terrain, and the climate of the basin, they can be roughly divided into the Tibetan plateau area, marginal alpine valley area, Piedmont or marginal mountainous plain area, Yunnan-Guizhou Plateau area, and the Sichuan Basin area.

The riverbed overburden is the thickest in the alpine valley areas at the margin of the Tibetan Plateau, namely the Longmen and Hengduan Mountain areas, and it is of a consistent thickness along the following mountain ranges: Xuebaoding—Siguniang Mountain—Gongga Mountain—Jinping Mountain—Yulong Snow Mountain—Meili Snow Mountain. The contact zone between the mountains and the Yunnan-Guizhou Plateau, and the Piedmont area of the contact zone between the mountains and the Sichuan Basin has an overburden that is thicker than the mountain range in the previous example, however, the thickness of the overburden is greater in the upper river valley than in the lower river valley where it runs into the basin. The Jialing, the Tuojiang, the Fujiang, the upper reaches of the Minjiang, and the Qingyi Rivers all show the thickest overburden in the Longmenshan section. The overburden becomes thinner after

it enters the Sichuan Basin. The riverbed overburden in the Yunnan-Guizhou Plateau and Sichuan basins is relatively shallow. When the Jialing, Fujiang, Tuojiang, Minjiang and other associated rivers enter the Sichuan Basin the overburden becomes thinner. Additionally, the riverbed overburden of the Li, Yuan, and Nanpan Rivers in the Yunnan-Guizhou Plateau is generally less than 40 m. For example, the thickness of the riverbed overburden of the Nanpan River is 15–25 m. After the Nujiang, Irrawaddy, and Lancang Rivers flow into Myanmar and Laos, the riverbed overburdens are generally thinner. Finally, the riverbed overburden is not uniform across the inner part of the Tibetan Plateau, but it is thinnest when it reaches the periphery. For example, the eastern margin of the Tibetan Plateau is the headwaters area of the Nujiang, Lancang, Jinsha, and other major rivers and the thickness of the riverbed overburden is predominantly less than 20 m. Additionally the riverbed overburden in the basins above Lanzhou on the Yellow River is shallower. However, the main stem of the Yarlung Tsangpo River and its tributaries, the Lhasa, and Nianchu Rivers all have a riverbed overburden that is more than 100 m in most areas. Interestingly the overburden tends to decrease near the Himalayan mountains.

In summary, the main rivers in Southwest China generally have deep riverbed overburden, where the thickness is generally between 10 and 100—m, local sections can reach into the hundreds of meters. Generally, the thickness of riverbed overburden is shallower in the upper reaches of the Tibetan Plateau, thickest in the marginal mountain areas of the middle reaches, and shallower in the contact areas of the lower reaches. The Yunnan-Guizhou Plateau and Sichuan Basin show a shallow-thick-shallow distribution pattern. Overall, it has the characteristics of thickening gradually from the basin edge to the plateau slope, and the river overburden also has the characteristics of thickening from the downstream to the upstream (**Figure 2**).

3 PRELIMINARY STUDY ON FORMATION MECHANISMS OF RIVERBED OVERBURDEN

The formation types of riverbed overburden are complex. Different rivers, different sections of the same river, and even different time periods of the same river section may have different causes (Luo, 1995). Based on the engineering geological data, this paper explores the distribution characteristics of the existing riverbed overburden, and then analyzes the formation mechanisms of the riverbed overburden in the primary rivers of Southwest China.

3.1 Characteristics of Overburden Material Composition

The main sources of riverbed overburden in Southwest China are mainly alluvial-proluvial deposits, glacial (glaciofluvial, moraine) deposits, dammed lake deposition, and landslide and collapse deposits.

3.1.1 Alluvial-Proluvial Deposits

The alluvial-proluvial sediments in riverbeds in Southwest China can be classified as coarse as boulders or fine to sand (and loess?). The dominant species is gravel that is mainly composed of drift pebbles intercalated with sand, others are gravelly sand and sandy structure with good sorting and roundness. In addition, the sand is usually lenticular in the horizontal or has an oblique laminar distribution. The bed of the mountain river is narrow, the lateral swing is limited, the floodplain is not developed, and downcutting is obvious. The normal thickness of alluvial-proluvial deposits is generally less than 30 m (Xu et al., 2008).

Alluvial-proluvial deposits are mainly distributed in the upper and lower portions of the deep and huge thick overburden reaches. The bottom layer is partially cemented and generally unable to move. The deposits are widely distributed in riverbeds and terraces.

3.1.2 Glacial Deposits

(1) Characteristics

Glacial deposits are one of the most important quaternary deposits in northwest Yunnan, Western Sichuan, and Tibet. Glacial moraines and glaciofluvial deposits are the major contributors to the overburden layers. The glacial deposits in China almost all belong to giant-grained or boulder soil and crushed stone soil. The glacial deposits lack intermediate grain size (or discontinuous deposits), and the lithology mainly depends on the lithology of local parent rocks (Zhang et al., 2009).

(2) Distribution range

Glacial deposits mainly exist in riverbank slopes and terrace zones. With the development of hydropower and accurate drilling data of the riverbed, there is a range of glacial deposits differing in thickness at the bottom of some riverbeds.

The glacial deposits found in the studied riverbeds are distributed into separate layers. This distribution varies from the central Longmen mountains to the Hengduan mountains. Specifically, the glacial deposits were distributed in different periods in the mountains between Minshan to Mangkang and the Yunling river tributaries, and around the Yulong Mountains, Haba Mountains, White snow Mountains, Gongga Mountains, Siguniang mountains and other high mountains. The deposits are oriented around the river tributaries of the riverbeds and valley terraces. For example, there are several glacial deposits in the Minjiang and Qingyi rivers around Siguniang Mountain. The glacial deposits in the Minjiang River are mainly distributed in the upper reaches of the main stem, the tributary Erhe River, and the upper reaches of the Zagunao River. This is especially noted in the northeast and east slopes of Siguniang Mountain. Glacial deposits in the Qingyi River are distributed in the upper east river basin, in the southwest slope of Siguniang Mountain and the southeast slope of Jiajinshan Mountain.

Glacial deposits in the Dadu River around the Gongga Mountains are distributed in the middle and upper reaches of the river. The main stem is mainly distributed in the reaches between the Qionglai Mountains and the Daxueshan Mountains.

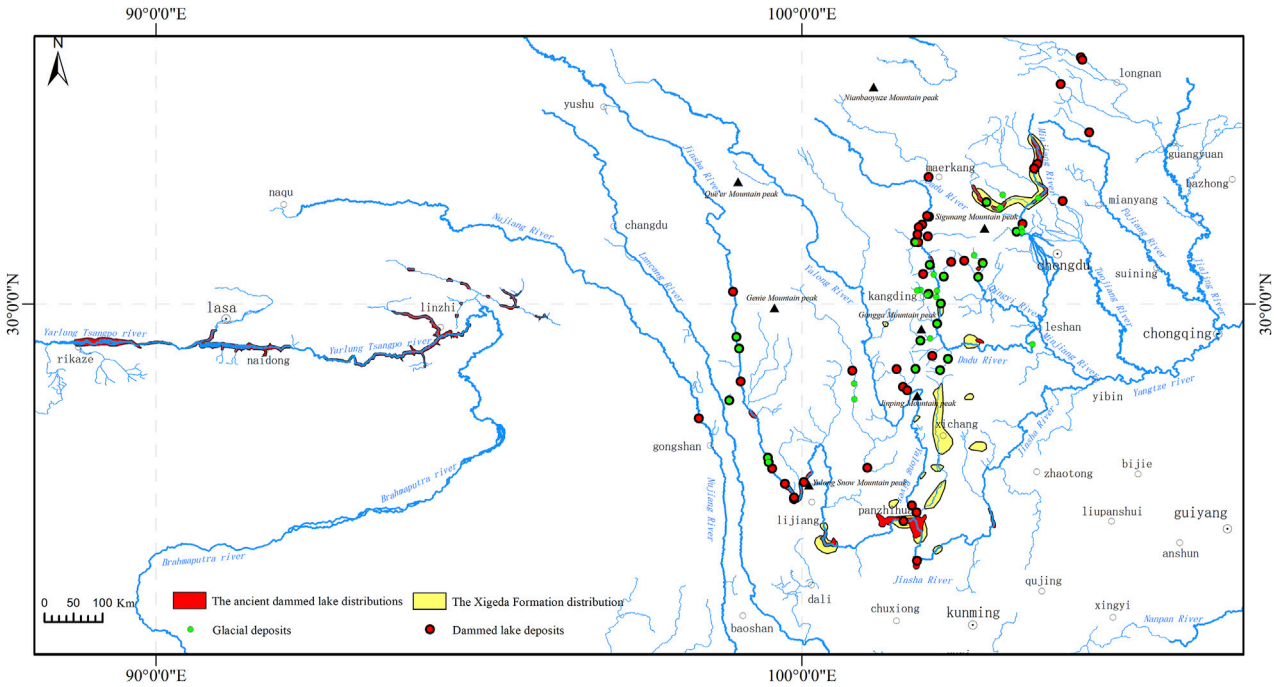


FIGURE 3 | Distribution of Main Causes of RiverBed Overburden in Southwest China (Distribution of ancient dammed lakes, according to Wang Y. S. et al., 2007; Li et al., 2010; Zhang et al., 2020; Wang et al., 2021.Distribution of Xigeda Formation, according to Xu and Liu, 2011).

Glacial deposits in the tributaries are mainly distributed in the upper reaches of the Nanya River, the upper reaches of the Tianwan River, the lower reaches of the Yanzigou River, the whole basin of the Wasihe River and the Geshizahe River, etc.

Glacial deposits in the Yalong River around Saneiri are distributed in the Litang River section on the eastern slope of the Shaluli Mountains. The glacial deposits of the Jinsha River near the Yulong Mountains are distributed in the upper reaches between the Shaluli Mountains and the Mangkang-Yunling Mountains and the Qizong-Tacheng section of the Tiger Leaping Gorge.

The sequence of distribution of glacial deposits is given in the following examples. Along the margins of the Tibetan Plateau and in mountain canyon valleys glacial deposits are primarily distributed at the bottom and middle layers of the riverbed. At the contact zone between the mountains and the Yunnan-Guizhou Plateau and the Sichuan Basin, the deposits are primarily distributed on the river terraces. In the Jinsha River, for example, glacial deposits are located at the bottom of the riverbed in the upper reaches. Near Shigu, they are in the middle layer of the riverbed mixed with other deposits. In the lower reaches they are above the river terraces. Essentially, the lower altitude of the Sichuan Basin accounts for the higher distribution of glacial deposits. For example, the shaft overburden on the left and right sides of the Xiluodu dam site is mainly composed of glacial and glaciofluvial deposits with a thickness of 42–59 m (He and You, 2013). At the same time, the middle and lower layers of the Yarlung Tsangpo riverbed are mostly glacial deposits (**Figure 3**).

Analyzing longitudinal distributions between Hengduan Mountain and Longmen Mountain, no glacial deposits were found in the riverbed of the Jialing and Yellow Rivers in the north, or from the Nujiang and Lancang Rivers in the south, however glacial deposits were found on the terraces of the river valleys. In the middle area of the previously mentioned river sections, glacial deposits are found in the riverbed. In addition, there are large accumulations in the valleys of the Hengduan Mountains, many of which are of single or mixed glacial origins. Tu et al. (2008) found that since the Quaternary, which was influenced by glacier movement, a layer of glaciofluvial and moraine deposits has been widely accumulated along the middle reaches of the Dadu River at an altitude of 700–1500 m, with a maximum thickness of more than 100 m and the thinnest point is just a few meters.

(3) Geogenic (Formation) Mechanism(s)

The eastern part of the Tibetan Plateau is divided into three glacial periods: the last glacial period, the penultimate glacial period, and the antepenultimate glacial period. There were no quaternary ice sheets, but some intermittent distribution of ice caps and mountain glacial centers formed by high mountains, planation surfaces, and high-level basins (Li et al., 1991). The high mountains in the Hengduan Mountain range have experienced several glacial periods. As the glaciers melted, the water carried a large amount of moraine debris along the way that finally collected in the river valleys and basins. In the middle and upper reaches of the Dadu River, Gongga Mountain is the

most concentrated and developed area of glaciers in the Hengduan Mountains. The moraines of the last glacial period (Dali Glaciation of late Pleistocene) are distributed below 2000 m, and the ancient glacial erosion and accumulation remains are distributed in bands from the center to the periphery downstream of these mountains. The lower limit of the distribution ranges from about 2000 m above sea level on the edge of the plateau to more than 5,000 m above sea level in the interior of the plateau (Shi and Zheng, 1995).

3.1.3 Dammed Lake Deposits

(1) Characteristics

Dammed lake deposition is primarily composed of interbedded silty clay and silty fine sand. It is typically of uniform grain size in thick layers ~ huge thick layers with obvious horizontal bedding, and few other fossils except spores and pollen (Zhang et al., 2020).

(2) Distribution range

The dammed lake depositions are primarily found as a mix with other deposits or as a formation of separate layers generally found in riverbed overburden (**Figure 2**). These deposits are consistent with those of dammed paleolakes. For example, the ancient Shigu Lake retains thick lacustrine sediments in the middle of the riverbed of the Tiger Leaping Gorge section, the Jinsha-Longjie section of the ancient Longjie Lake, as well as the riverbeds of Zhaizicun, Xuelongbu, Temi, Qiaojia Lake, Xigda Lake, Taoyuan Lake, Daju Lake, Shigu Lake, Jintang and other dammed paleolakes have thick lacustrine sediments.

The dammed paleolakes existed in Diexi and downstream in the Minjiang River Basin, as well as in the Zagunao River, a tributary of the Minjiang River (Wang L. S. et al., 2007). These have layers of dammed lake deposits in the Futang and Diexi sections of the main stem of the Minjiang River, Shiziping in the tributary of the Zagunao River, and the Yuzixi II in the tributary of the Erhe River.

The Tongzilin dammed paleolake in the Yalong River is mainly distributed in the Tongzilin-Ertan section. The Lingguan River dammed paleolake (Li et al., 2010) in the upper reaches of the Qingyi River has a thick layer of dammed lake depositions in the riverbed segments such as Xiaoguanzi, Minzhi, and Zuijugou.

Dammed lake depositions are widely distributed in the middle and upper reaches of the main stem of the Dadu River, and dammed paleolakes (deposits?) such as Kairaocun and Jiajun have been discovered (Zhong and Ji, 2012).

Since the late Pleistocene, several river-blocking events have occurred in the south-north river system in Southwest China, forming several dammed lake deposits (Li et al., 2010). The dammed lake depositions are roughly distributed along the Gongga Mountain-Yulong Mountain line and extend along the Jinsha and Dadu River valleys to the Tibetan plateau. The specific distribution area is in the intersection of the Tibetan Plateau, Yunnan Plateau, and Sichuan Basin where there is an abrupt change in elevation.

(3) Formation Mechanism

Dammed lake deposits are from lakes formed by dammed or regional subsidence (fault depression or depression) due to the river flowing through the area. For example, the Xuelongnang and Temi dammed paleolakes in the upper reaches of the Jinsha River were probably formed by large landslides triggered by seismic activity in the area (Chen and Cui, 2015; Chen J. et al., 2021). The dammed paleolakes in the Benzilan-Qiaojia section of the Jinsha River are mostly formed by landslides or glacial deposits blocking the Jinsha River (Zhang et al., 2020).

Due to the continuous uplifting process of the Tibetan plateau, the increased erosion of the river has resulted in a large number of dammed lake deposits being distributed downstream. There may be multiple dammed river events in the same river section, many of which are preserved in the formation of terraces. For example, Zhang et al. (2007) studied the lacustrine lamellar clay layer and its formation by landslide debris flow blocking the river in the early to middle of the late Pleistocene as found under the fourth terrace on both sides of the valley in the Benzilan area of the Jinsha River. Some researchers have also found landslide dammed paleolakes in the Lancang and Nujiang River basins, mainly preserved on river terraces. Additionally, the Gushui paleo-lake in the Lancang River in the Gushui area of Deqin County, Yunnan Province, was formed in the late last interglacial period of the early Pleistocene and the early interglacial period of the last Pleistocene, it was found at the base of the third and fourth terraces (Zhang and Zhao, 2008). A further example is the sand-layer of a barrier lake formation that is about 100 m thick in the ninth terrace of the Nujiang River valley in the Daojie-Huitongqiao section which was formed during the middle and late Pliocene between 4.2 and 2.6 Ma (Zhao et al., 2012).

Based on the current dating of the riverbed overburden, it has been concluded that the dammed lake depositions have formed starting from the Late Pleistocene and Holocene eras and continued to the present. The upper age limit of dammed lake depositions in the Benzilan-Qiaojia section of the Jinsha River is from the late Pleistocene, and the lower age limit is from the late to the early Pleistocene (Zhang et al., 2020). The dammed lake depositions in the middle reaches of the Dadu River were formed from 18 Ka to 11 Ka (Li C. Z. et al., 2015). The lacustrine deposit at the Tongzilin dam site in the Yalong River started at 25 Ka and lasted to ~10 Ka (Ding et al., 2021). The dammed lake depositions in Dixi, from Dixi to the lower reaches of the Minjiang River and its tributary the Zagunao River, were dated to about 20 Ka BP (Wang Y. S. et al., 2007). This period from the late Pleistocene to Holocene, is also the period of accelerated rise of the Tibetan plateau (Li et al., 1979).

There are also some lacustrine sediments widely distributed in Southwest China, mainly preserved in terrace form, such as the lacustrine sediments of the Xigda Formation, which are 4.2–3.3 or 2.6–1.8 Ma BP in the middle and late Pliocene or to the early Pleistocene (Zhao et al., 2008). The Longjie silts along the valley of the Jinsha River from Sanduizi of Panzhihua City to Baimakou of Wuding County belong to the late Pleistocene (Li H. L. et al., 2015).

3.1.4 Geological Hazard Deposits

(1) Characteristics

Colluvial deposits are a primary source of riverbed overburden in Southwest China. The colluvial deposits are a loose, non-cohesive soil containing rock fragments. The particle size composition of landslide deposits varies greatly, and the particle size distribution range is very wide. Debris flow deposits are mainly composed of gravel, sand, silt, and clay, and the grain gradation varies significantly.

(2) Distribution range

The deposits formed by geological disasters, such as hillside collapse, landslide and debris flow, are primarily distributed in mountain rivers where the riverbed has a large gradient. These deposits have a short transient time in the river and are usually found in small, isolated pockets dotted in the longitudinal direction of the river. Examples of this are in the Wudong section of the Jinsha River and the Xiaoguanzi section or the Qingyi River. The sediments are seldom distributed in bands, instead they are mixed with other sediments to form layers during river cutting. This can be seen in the Tiger Leaping Gorge section of the Jinsha River and the Danba to Luding section of the Dadu River. Large landslides and debris flows are typical mechanisms in blocking a river. Once the dam breaks, the depositions will form a long strip-shaped distribution pattern downstream. As the Tibetan plateau continues to rise, the capacity for river erosion is increased. Consequently, the remains of the disaster sediment are eroded, leaving little residual sediment in the riverbed. However, a large quantity of sediment is retained in the valley terrace and bank slopes. For example, the Xuenongnang dammed paleolake on the upper reaches of the Jinsha River was formed by an earthquake-induced landslide. After the dam broke, the depositions were distributed within a range of 3.5 km from the downstream side (Chen and Cui, 2015). Additionally, disaster deposits exist in the form of accumulation predominantly along riverbanks as a result of the deep river cutting.

(3) Formation Mechanism(s)

The formation mechanisms for geological hazard deposits are heavily influenced by external factors such as earthquakes and rainstorms, this may also be coupled with rapid uplift and deep river cutting. This is a result of the very active internal and external geodynamic processes in the eastern margin of the Qinghai-Tibet Plateau. Both large and giant landslides, hillside collapses and debris flows occur frequently in mountain canyon valleys, forming deep accumulations in local areas. The concentrated occurrence time of paleo-landslides in mountain canyon valleys of the Dadu River basin and the upper reaches of the Minjiang River basin is 20–30 Ka, and the highest frequency of the paleo-landslides in the Dadu River is 15–25 Ka, speculated to have occurred in the late Pleistocene. The strong tectonic activity of the Dadu River Basin resulted in frequent large-scale landslides, consequently a large volume of paleo-landslide deposits remains in the Dadu River basin today (Zhang et al., 2021). The Xuelongnang and Temi dammed paleolakes in the upper reaches of the Jinsha River were probably formed by large-scale landslides triggered and blocked by paleo-seismic activity in this area (Chen and Cui, 2015; Chen Y. et al., 2021). The age of the existing geological disaster deposits is mainly in the 20–30 Ka range, which is in the glacial peak of the last glacial period.

3.2 Geogenic Mechanisms

3.2.1 Overburden Formation Mechanisms in Primary Rivers

The riverbed overburden thickness of the main rivers in Southwest China presents a shallow layer with a single origin that is primarily alluvium or alluvial-pluvial. The formation of deep or huge thick riverbed overburden is the result of multiple genesis. The controlling factors vary in different reaches of each river. According to the material characteristics of current riverbed overburden, the genesis of main river overburden is discussed.

(1) Minjiang River

The riverbed overburden in the Minjiang River basin was formed by dammed lake deposition, glacial sediments and alluvial-proluvial deposits. From the regional distribution data, there are dammed lake deposits of differing thickness in the riverbed of the main and tributary rivers in the upper reaches of the Minjiang River, especially in the Diexi section. The bottom of the overburden layer of the main stem and the left bank tributaries of the Minjiang River in the east slope of Siguiniang Mountain is mostly glaciofluvial sediments.

The deep riverbed overburden in the upper reaches of the Minjiang River is mainly distributed in the middle portion of the Longmen Mountains. During the uplifting process of the Tibetan plateau, the main peaks of Qionglai and Sionglai Mountains, formed from the surrounding highlands and above the snow line, becoming the local center of quaternary glaciation. During the glacial period, glaciers developed on Qionglai Mountain, During the interglacial period, the glaciers melted anddeep river cutting occurred carrying a large amount of the glacial moraine deposits into the Minjiang River which was subsequently deposited in the Minjiang River valley. During the uplift of Longmen Mountain, seismic activity resulted in the river also uplifting causing the deep valley to form, the result of which was increased erosion deposits blocking the river. Wang L. S. et al. (2007) studied landslide derived and other small-scale ancient barrier lakes in Dixi, Maoxian, Wenzhen, Mianyang, Guogou, and Lixian in the upper reaches of the Minjiang River. Thi indicated that earthquakes and rainstorms lead to (hillside) collapse, landslide and debris flows blocking the river, or the landslide front is deposited directly on the early overburden, which resulted in local accumulation of deep overburden.

(2) Qingyi River

The deep riverbed overburden is mainly deposited in the upper reaches of the Qingyi River. The origin of the overburden in the main source Baoxing River basin is complex. The riverbed overburden in the East River showed

that the bottom of the river is ice-water sediment, and the middle layer is alluvial-pluvial, debris flow accumulation, colluvial and barrier deposits, and the surface layer is the modern river alluvium. The riverbed of the Xihe River has a deep overburden. The bottom of the riverbed overburden is an alluvial-proluvial layer, the middle is a dammed lake deposition layer, and the surface is a modern river alluvial layer. These are typical at the Chujugou Power Station sluice site.

The source of the Qingyi River is the Qionglai and Jiajinshan Mountains, both of which are areas with intense crustal uplift occurring from the late to recent periods. The local climate characteristics, leading to frequent geological disasters such as debris flow and river blocking events, and forming dammed lake deposition in the riverbed are primary sources. The thickness of the river deposits at the Xiaoguanzi dam site area reaches a maximum depth of 87 m and has 10 distinct layers according to its origin. The sixth and eighth layers are dammed lake deposits and the fifth and seventh layers are debris flow deposits; it was found that the left bank of the Baoxing River was blocked by two extra-large debris flows in Guangou (Peng, 1996). In addition, the Donghe River basin is located on the southeast slope of Siguniang Mountain. The glaciation of Siguniang Mountain led to the existence of glacial deposits at the bottom of the riverbed.

(3) Dadu River

The deep overburden in the Dadu River basin is distributed continuously and stably in "bands" and has the characteristics of a continuous regional development in spatial distribution. According to the material origin of the overburden, the Dajinchuan Section (above Danba County reach) is composed of dammed lacustrine and alluvial-pluvial deposits. The middle and upper reaches of the Dadu River (above Dagangshan) are mainly composed of glaciofluvial, dammed lake, and alluvial-diluvial deposits. The lower reaches of Dagang Mountain are mainly composed of alluvial-pluvial deposits.

Tectonic movement controlled the development of the Dadu River valley. Based on the north-south structure control the Dadu River valley above Shimian county was an "L" shape. Below Shimian county, due to the east-west uplift block of Shimian-Ebian, the river turns sharply to the east. Under the action of neotectonic movement, the broad valley basins of the Jinchuan intermountain depression, the Jiajun tectonic adaptive basin, the Hanyuan fault depression basin, and other wide valley basins were formed.

During the late Pleistocene Dali glacial period, moraines piled up in the middle and upper reaches of the Dadu River valley forming weir dams. Meanwhile, the terminal moraine of the tributary also blocked the Dadu River valley forming barrier lakes allowing lacustrine sediments to be deposited in the riverbed. As the climate warmed in the postglacial period, the melting of the glaciers and the increased flowing water broke the dam. The glacier descending height was higher in the Dajinchuan section increasing the strength of the erosion. The glacier descending height was lower in the upper part of Dagang Mountain, the weir dam was taller, the lake deposits were thicker, the river erosion had not cut through the moraine, and the glacier accretion overburden was developed before the current riverbed. The moraines in the lower reaches of Dagang Mountain are mainly preserved on the river terraces (Shi, 1986).

The deep overburden of the Dadu River is the result of the composite accumulation of tectonic subsidence and glaciation (Shi, 1986). The Dajinchuan reach is a tectonic multilayer accretion, and the middle and upper reaches of the Dadu River are the products of the last glacial period (Dali Glaciation of late Pleistocene) and tectonic-controlled adaptive valley basins (such as Jiajun). Areas below Dagangshan are mainly the result of tectonic control, such as faulted basins (e.g. Hanyuan basins).

(4) Yalong River

The riverbed overburden in the upper reaches of the Yalong River is relatively shallow, generally less than 40m, primarily located in the eastern margin of the Tibetan plateau, and the river erosion rate is relatively high. The deep overburden of the Yalong River is mainly distributed in the middle and lower reaches. The deposit layer can be divided into three parts along the depth, the upper layer is modern river deposit; the middle layer is composed of alluvial, pluvial, barrier lacustrine, and is comparatively thick; the bottom layer is alluvial and colluvial deposits (Wang et al., 2006; Wang Y. S. et al., 2007). The overburden of the lower reaches of the Yalong River is composed of the middle layer attributed to deposits originating from the Tongzilin dammed lake. The dam site of the Tongzilin Hydropower Station has developed a 51 m thick deposit profile, which is generally composed of a lower alluvial layer (10 m thick), middle lacustrine layer (26 m thick) and upper alluvial layer (15 m thick) (Ding et al., 2021).

The origin of overburden of the Upper-Yalong River is dominated by deposits that are caused by blocking, while the middle and upper Yalong River sections are dominated by deposits typically associated with a composite origin. The deep overburden is caused by the second layer accretion sequence, and the dating of the accretion layer are 10–20 Ka bp (Wang Y. S. et al., 2007). This period was during the last glacial maximum when glaciers were widely developed. The decreased river flow coupled with the low potential energy and increased glacial debris resulted in the river filling and damming, forming a thick multi-geogenic accretion overburden. During the post-glacial period, the rivers incised rapidly, but did not cut through the accretion layer. Therefore, the deep overburden in the Yalong River is a climatic geogenic model formed during the last glacial maximum (Wang L. S. et al., 2007).

(5) Jinsha River

The riverbed overburden in the Jinsha River can be roughly divided into four sections according to the thickness: the source area (above the Lawa dam site) (<40 m), the lawa dam site to Daju section (>40 m), the Daju to Panzhihua city (<40 m), and the section below Panzhihua city (>40 m). Among them, the riverbed overburden in the source area and Daju to Panzhihua city is thinner, with a predominant alluvial layer, the cause of which

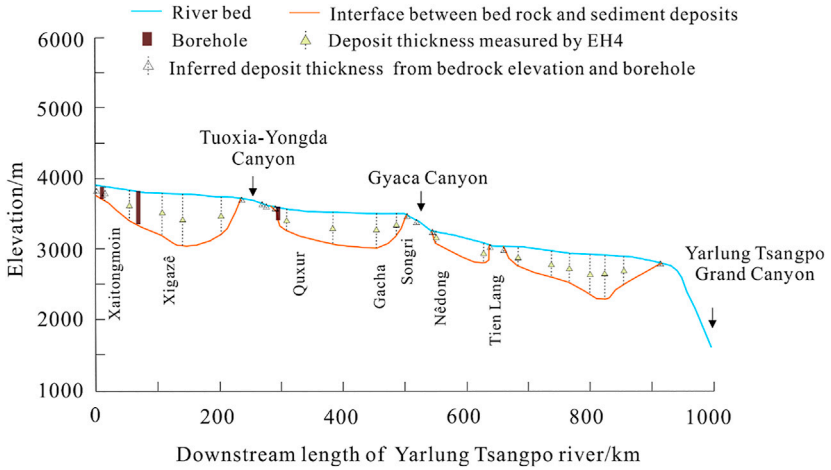


FIGURE 4 | Longitudinal profiles of interface between bed rock and sediment deposits along the Yalu Tsangpo River Valley (Wang et al., 2014, modification).

may be mainly tectonic. The source area is in the Tibetan Plateau, which has been in the process of continuous uplift, and therefore the river erosion capacity is greater than the accumulation rate. The main reason for the thin riverbed overburden from Daju to Panzhihua city may be that it is in the same tectonic region, the Yangtze platform, so the uplift and subsidence of the crust and river erosion are at roughly the same level.

The separate layers of overburden from the Lawa dam site to the Daju section are composed of dammed lake deposits, glacial deposits, and deposits of geological hazards. Wang (2009) proposed that the thick riverbed overburden in this reach was formed by the ancient Gulongpan fault basin under the influence of neo-tectonic movement.

The Jinsha River overburden from Panzhihua city to Yibin city are primarily composed of alluvial-proluvial sediments in the top and bottom layers, and dammed lake deposits or mixed sediments in the middle layers. Ge et al. (2006) studied the Jinsha River from Tuoding to Yibin city and proposed that climate change directly affected the precipitation conditions of the Jinsha River basin. During the rainy period, the river channels were strongly incised, developing deep grooves, and included mass wasting of the bank slopes. During dry periods, the Jinsha River cuts down slowly, and the river channels form large deposits.

(6) Yarlung Tsangpo River

According to the available geological data, the riverbed overburden of the main Yarlung Tsangpo River and its tributaries, such as the Lhasa and Nianchu Rivers, has a large burial depth, mainly affected by glaciation and tectonic factors. The stratigraphic structure of the longitudinal riverbed overburden in the Yarlung Tsangpo River is basically a binary structure, with the upper layer being a modern alluvial-pluvial layer and the middle and lower layers primarily consisting of glacial moraine deposits.

The main stem of Yarlung Tsangpo River is characterized by a narrow and wide valley and thick river and lake deposits. Wang et al. (2014) studied the riverbed thickness from Xetongmen to the Yalu Tsangpo Canyon and found that, due to the variation in uplift rates of different river sections, the uplift rates of the canyon section were high, while the uplift rates of the wide valley section were low, the bedrock surface of the canyon river channel were several hundred meters higher than the sediment-bedrock interface of the broad valley river section in its upper reaches. The result was the formation of a huge "sediment reservoir." Over the past million years, the pebble sediment had been filling this sediment reservoir forming a thick layer. At the same time, it also caused the valley floor to rise and widen, turning the v-shaped valley into a u-shaped valley (**Figure 4**).

Lacustrine sediments of dammed paleolakes are widely distributed along the valley of the Yarlung Tsangpo River basin across the southeastern Tibetan Plateau. There are several ancient dammed lakes in the middle and lower reaches of the Yarlung Tsangpo River, such as Dazhuka, Jiedexiu, Gega, Yigong, Zhongyu, Talu, Guxiang, Songzong, Yupu, Dongjiu, Lulang and others. The spatial distribution of these paleolakes may be controlled by the north-south normal fault system or follow active fault lines such as the Jiali fault. The paleolakeshad developed since the last glacial period, mainly during the last glacial maximum and the early Holocene, lasting for thousands to tens of thousands of years (Wang et al., 2021).

(7) Other river(s)

The deep riverbed overburden in the Jialing and Tuojiang River basins are mainly distributed in the Longmen Mountain area. Among them are the Jialing River tributaries; the Bailong River, the Baishui River, and the Fujiang branch of the Liuhuo River have developed deep overburden with zonal distribution. These deep overburden layers are mainly composed of alluvial or alluvial-proluvial deposits. Additionally, there are collapse

deposits on the side of the river and dammed lake deposits in some sections of the river.

The deep riverbed overburden of the Nujiang, Yellow, and Lancang Rivers are mainly distributed and are similar in having a point-type distribution, where its origin is mainly formed by collapse, landslides, and debris flow.

3.2.2 Discussion on the Geogenic Mechanisms of Thick Riverbed Overburden in Southwest China

According to existing and ongoing research achievements the formation of deep overburden is very complicated with a deposit composition of fluvial and non-fluvial origins.

The change of dynamic conditions in the river system can only control the self-organization process of low-level streams (Yi et a1., 2021). It can cause the river to accumulate and cut down, but the influence is generally limited to a certain reach of a river, the time scale of the influence is short (10–1000 a), and the overburden is shallow (<40 m) (Maddy et a1., 2001).

There are many non-fluvial factors (contributing to the geogenic mechanisms), including erosion base level change, tectonic movement, climate change and so on (Bridgland, 2000; Alexey et al., 2019; Delaney and Adhikari, 2020); Xu et al. (2008) proposed that the existence of deep riverbed overburden in Southwest China was directly related to the increase and decrease in sea level since the Quaternary. However, some studies found that the influence of sea level rise and fall on river geomorphology development was only limited to the reach near the estuary (mainly downstream). It has little impact on the middle and upper reaches of inland rivers (Merritts et a1., 1994).

Tectonic movement and climate change are two important factors controlling the riverbed overburden thickness. However, the coupling of tectonic movement and climate change in the evolution of riverbed overburden is of primary concern.

Tectonic movement is a major contributor to the formation and evolution of rivers. Macroscopically, the Tibetan Plateau controls the sedimentary and biogeochemical exchange between mountains and oceans, and there are dynamic linkages and coevolution between tectonic plates and river systems, the macro-structure of the river system in the eastern Tibetan Plateau is controlled by tectonic movement (Yi et a1., 2021) A large number of low-temperature thermochronology studies have revealed the rapid exhumation of the southeastern margin of the plateau in Cenozoic stages at about 60–40 Ma BP, 30–20 Ma BP and 20–0 Ma BP (Clift and Sun, 2006; Liu et al., 2018). The South Slope of the Western Kunlun Mountains Plateau is the highest, and the southeast part of the Qinghai-Xizang Plateau, which flows east to the north of Tibet and is the source of the Yangtze and Yellow rivers, is the lowest, and descends by a steep slope (fault) to the mountains on the border of western Sichuan and the Yunnan-Guizhou Plateau. This general tilt from northwest to southeast is undoubtedly an important factor in controlling the flow of rivers like the Jinsha River, the Salween River, and the Lancang River (Li et al., 1979). On a smaller scale, the integral block uplift of the Tibetan plateau also has local differences. From the point of view of the specific river reach, the river spans different tectonic units, and the ascending and the up-and-down movement between tectonic units further contribute to river erosion and accumulation change, forming the riverbed overburden aggradation layer (Xu et al., 2008). For example, the longitudinal profile of the Dadu riverbed from the upper to the lower reaches shows a gentle-steep-gentle fold shape. The thickness of the valley deposits on the steep slope is different, the thin part is about 20 m, and the steep slope is in the Sichuan-Yunnan south-north tectonic belt, which is obviously related to the continuous uplift of neotectonics (Luo, 1995).

The variation in topography caused by tectonic movement not only affects slope stability, but also affects climate. The uplift on the eastern margin of the Tibetan Plateau, increases the potential energy of flowing water to carry out strong erosion and river cutting. There are various types of gravity based physical and geological processes active on these slopes. At the same time, in the middle-lower reaches of many rivers in Southwest China, the longitudinal gradient of the riverbed becomes steeper as it moves down the valley. As the steepness increases river erosion and cutting are also increased, and the physical and geological effects such as valley slope collapse, landslide and debris flow also increases, and these in turn form dammed lakes and colluvium deposits. The periodic uplift of the Tibetan Plateau and the resulting water and heat conditions, combined with global climate changes, have caused four alternating glacial and interglacial periods to occur on the plateau (Li et al., 1979). Some mountains in the eastern margin of the Tibetan Plateau formed glaciers when the mountains uplifted above the height of the snow line during the last glacial period. Some mountains at higher altitudes developed quaternary glacial periods, such as Mt. Gongga and Mt. Yulong, etc., but at least 12 relatively low-lying mountains between 4,200 m and 4,500 m only developed during the last glacial period. These mountains were strongly uplifted by about 1000 m due to the Gonghe Movement in the late Pleistocene causing them to move above the snow line and thus were only affected by the last glacial period (Cui et al., 2011). During the late Pleistocene, the glaciers advanced along these river valleys (Li et al., 1979). As a result of intense erosion of the upper source of the glacier, the longitudinal slope of the bedrock valley floor is shallower than that of the modern riverbed, and the overburden of the valley floor gradually thickens from the marginal mountain mouth of the basin to the upper reaches, forming deep deposits (e.g., Minjiang River valley) (Luo, 1995). At the same time, the strong rise of the Tibetan Plateau changed the atmospheric circulation, the monsoon had become dominant, and impacted the occurrence and development of quaternary sediments of different geogenic types in the valley (An et al., 2006).

As the climate warms (the glacial-interglacial transition), glacier melting accelerates in the alpine valley region, and river flow velocity and flux increase. According to model simulations, river sediment discharge increases 3–19 times after 100 years of accelerated glacial retreat (Delaney and Adhikari, 2020). Such high-speed sediment discharge leads to a reduction in the sedimentation of the riverbed, and only thinner sediments can be formed on the original overburden of the river valley. During the transition from the interglacial period to the glacial period, the climate gradually becomes colder and more unstable, which may lead to higher

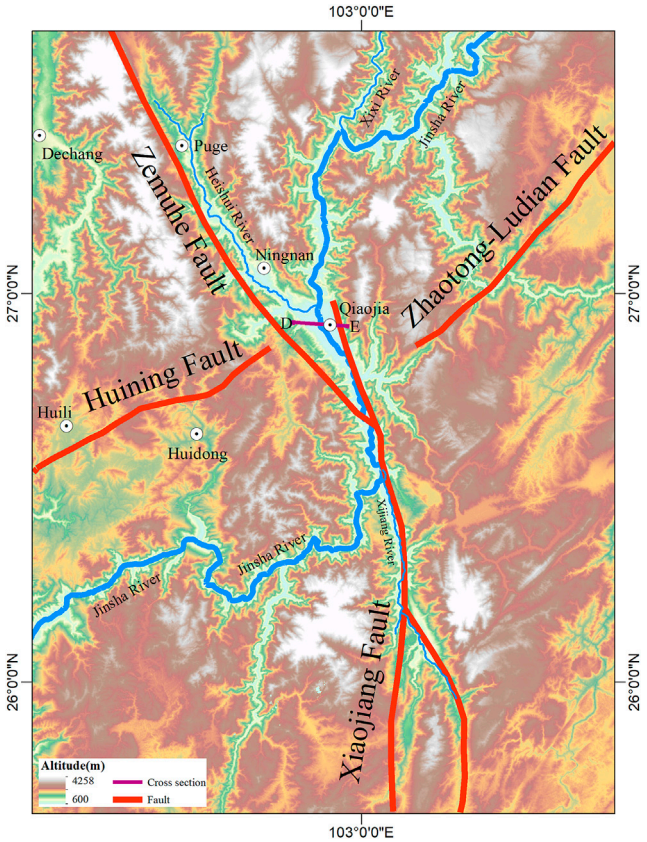


FIGURE 5 | Tectonic setting of the Qiaojia Basin (Shan et al., 2021, modification).

flood frequency and intensity, causing rivers to undercut. As the climate begins to cool, vegetation coverage decreases or even disappears, and as the average temperature continues to decrease, the vegetation coverage also decreases or even disappears. This cooling combined with the increased freeze-thaw action, more sediments enter the river, and the combination of higher sediment flux and lower stream flow cause the increased deposition of river overburden (Bridgland, 2000; Maddy et al., 2001; Liu et al., 2006) studied the four sets of lake terraces and lacustrine sediments of the Yarlung Tsangpo Grand Canyon and its tributary the Niyang River, using 14C dating found that during glacial advances the growth of the Zelunglung glacier on Mt. Namche Barwa formed ice dams and barrier lakes in the Yarlung Zangbo River, and developed corresponding lacustrine deposits. During the interglacial period the ice dam broke, the lake water was released and the lacustrine sediments decreased. In addition, according to the study, the rapid melting of plateau glaciers during the interglacial period was the trigger for earthquakes. During the last deglacial period, the rapid melting and erosion of mountain glaciers (or ice caps) unloading in the Tibetan Plateau might have induced frequent seismic activity in this area (Zhong et al., 2021).

The thickness of riverbed overburden is a geological phenomenon of the coupling effect of tectonic, climatic, and fluvial sedimentary processes during the Quaternary period. Take Qiaojia County section of the main stem of the Jinsha River as an example, the thickness of the overburden layer is nearly 900 m as revealed by wide-area electromagnetic resistivity sounding profile. Additionally, its lowest point is 100 m below sea level. According to the latest drilling data, the platform overburden thickness of Qiaojia County is more than 733 m (Shan et al., 2021; Cheng et al., 2022).

The formation of riverbed overburden in the Qiaojia section of the Jinsha River is mostly controlled by tectonic activity and fluvial sedimentation. Initially, the deposition process is controlled by these two processes (**Figures 5**, **6**). The Qiaojia County section is mainly controlled by Xiaojiang fault and Zemuhe fault, forming a nearly elliptical pull-apart Basin that formed 1.1 ma ago and ended at about 34 ka (Li et al., 2016; Shan et al., 2021). According to the 14C dating data, the relative subsidence time of the basin stopped at about 34 ka, and its average subsidence rate was about 1–2 mm/year, slightly higher than the erosion rate of 0.4 mm/year in the Qiaojia section of the Jinsha River (Huang et al., 2010; Shan et al., 2021), indicating that it was the river accumulation stage.

At the same time, the tectonic and fluvial processes affected the evolution of drainage catchment and backflow, and then affected the sediment. Before the Jinsha River was connected, there was a south-flow paleo-drainage system extending along the Xiaojiang fault zone in the Qiaojia section. The upper reaches of the Xixi River flowed into the ancient Honghe River system after passing the Paleo-Xiaojiang River. According to the heavy mineral analysis of paleo-fluvial sediments in the overburden of this section, the provenance area is close to Qiaojia basin, which is inferred to be the product of the Paleo-Jinsha River flowing south. There are three main layers of paleo-fluvial alluvial facies, accounting for about 50% of the total thickness (**Table 2**). The late Quaternary uplift of the Yunnan Plateau blocked the Xixihe-Baihetan-Qiaojia paleo-drainage from flowing south, capturing the upstream erosion process of the ancient Duiping River (one of the branches of the Niulanjiang paleo-drainage). This resulted in the reversed flow of the Qiaojia River segment to the north, through the Jinsha River (Li et al., 2009; Cheng et al., 2022).

The effects of climate change should now also be considered as an important factor in the formation of overburden. Luoji Mountain in the upper reaches of Zemu River on the north side of Qiaojia Basin still retains well-preserved Quaternary moraines of Penultimate Glaciation (MIS 6) early stages of the last Glaciation(MIS 4) and late stage of the Last Glaciation (MIS 2) (Tang et al., 2021) Since the last glacial period, the sedimentary climate in this region was dry and cold, with less precipitation, and the sediments were mainly from physical weathering. According to stratigraphic sporopollen analysis, the overburden in this section transitioned through a dry-cold grassland environment, mild-humid environment, warm-humid environment, and a modern dry-hot climate. The sporopollen assemblage reveals that the environmental evolution cycle was consistent with the sedimentary cycle. Each sedimentary layer of the overburden in this section is composed of multiple cyclic deposits with a coarse-fine grain size change (Shan et al., 2021).

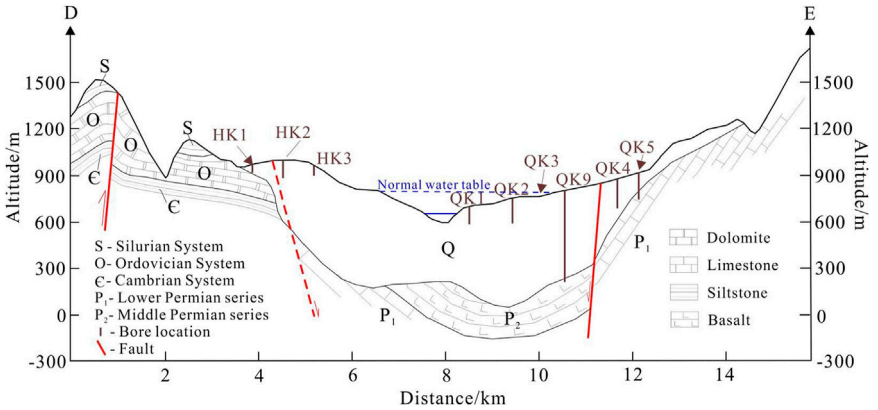


FIGURE 6 | Geological model of the Qiaojia Basin (Shan et al., 2021, modification).

TABLE 2 | Sedimentary sequence revealed by boreholesin Qiaojia Basin(Cheng et al., 2022, modification).

Stratigraphic position	Sedimentary facies type	Top boundary altitude/m	Core depth/m	Single layer thickness/m
Quaternary Strata	⑪Slope-pluvial facies	834.13	0.00	160.80
		673.33	160.80	
	⑩alluvial- Pluvial facies	665.04	169.09	8.29
	⑨Lacustrine facies	613.73	220.40	51.31
	⑧alluvial- Pluvial facies	560.13	274.00	53.6
	⑦Fluvial facies	523.83	310.30	36.3
	⑥alluvial- Pluvial facies	500.04	334.09	23.79
	⑤Fluvial facies	472.79	361.34	27.25
	④Lacustrine facies	445.23	388.90	27.56
	③alluvial- Pluvial facies	436.59	397.54	8.64
	②Fluvial facies	128.75	705.38	307.84
	①alluvial- Pluvial facies	105.93	728.20	22.82
	Bedrock section			

Finally, the coupling effect of the three factors is conclusive. Both tectonic activity and climate change lead to frequent landslides, floods and debris flows in this section, which then affect the river geological processes. The overburden in this section can be traced to lacustrine sediments, debris flow alluvium and slope-alluvium, accounting for about 50% of the total thickness (Cheng et al., 2022). Among them, the evidence suggests that the lacustrine sediments are from dammed lake deposits. There are many ancient landslide bodies near Qiaojia basin, and there is a huge ancient landslide residue about 3 km away from the lower boundary of the Qiaojia Basin, which certainly blocked the Jinsha River and formed a large barrier lake, providing conditions for the static water deposition (Li et al., 2016).

4 HYDROENGINEERING GEOLOGICAL PROBLEMS AND TREATMENT OF DEEP OVERBURDEN

The spatial distribution of hydropower resources in China are uneven as they are affected by topography and climate conditions. The hydropower resources in major rivers such as the Jinsha River in Southwest China are very rich, thus, it has become the center of hydroengineering construction in China. Flood control and hydroelectric are two of the main engineering activities in Southwest China. The construction of dams often encounters thick overburden. The diverse genesis of deep overburden restricts the site and dam type for hydroelectric power stations, These are often based on differences in lithology, sediment grading, structure, particle shape, density, and degree of cementation. Altogether it increases the complexity of the dam junction layout and adds further complexity to the foundation design.

Faced with complex and thick overburden and the general risk of dam construction, there are two main treatment methods for overburden: excavate all the overburden layers, or alternately, partial excavation of the overburden layers.

4.1 Excavation of all the Overburden

When the overburden layer is relatively thin and its removal will not add further technical problems and will not increase the amount of engineering and investment too great, the overburden layer can be removed completely and treated according to the conventional damming technology on bedrock.

For example, the thickness of the riverbed overburden at the Wudongde Hydropower Station on the Jinsha River is 52–73 m. After all the overburden was excavated, a hyperbolic thin arch dam was built on the limestone bedrock. The dam has a maximum height of 265 m. For the Shuangjiangkou Hydropower Station on the Dadu River, the riverbed overburden depth is 48–57 m (partial 67.8 m). The decision was made to excavate all the overburden layer at the bottom of the core wall, build the core wall directly on granite, and construct a 314 m high rockfill dam with a gravel-soil vertical core (Liu, 2015). In both cases the removal of the relatively thin overburden did not add unnecessary complexity and additional financial burden onto the project allowing the dam to be built on bedrock.

4.2 Partial Excavation of Overburden

When the thickness of the overburden is very large, the cost of excavation may be too high and overall construction becomes more difficult. It may be decided to retain part of the overburden and build the dam directly on the overburden layer, but the engineering characteristics of the thick overburden often result in three major problems: dam foundation deformation, dam foundation seepage, and/or sand liquefaction. These three problems are directly related to the safety and financial investment of the project.

(1) Dam foundation deformation

The riverbed overburden layer of the dam foundation may have different geogenic types, a complex structure, differing thicknesses of each layer, and different physical and mechanical properties, each of which adversely affect the stress distribution and overall deformation of the dam body, core, and anti-seepage walls. Therefore, based on the specific situation of the project it is necessary to reinforce the overburden layer within a certain range of the dam foundation, this increases the strength and stability of the foundation and reduces the uneven deformation of the dam body. the reinforcement measures such as the excavation and replacement, consolidation grouting, vibro-replacement stone columns and Jet Grouting are often adopted.

The Pubugou Hydropower station dam in the main stem of the Dadu River is located on a deep overburden with a depth of 78 m. The uneven deformation of the dam's foundation is the key to dam foundation treatment. All soils above 670 m of the originally designed foundation surface should have been excavated. During construction, the soft soil and soil layers which are susceptible to liquefaction were found in the dam foundation. The result was the final foundation surface was excavated to a depth of 667 m, and a backfill measure was adopted to 670 m of the dam foundation design height. At the same time, 10 m deep consolidation grouting was carried out under the dam foundation. The results show that the overburden after grouting meets the design requirements of foundation bearing capacity and deformation modulus, and the continued operation of the reservoir indicates that these measures were successful (Xue et al., 2012).

The original design of the composite geomembrane inclined-wall rockfill dam of the Renzonghai Hydropower Station was to excavate all the silt loam layers within 20 m of the dam foundation. Two additional problems presented themselves in this plan, first because it is difficult to excavate silt loam and second, the resulting pile up after excavation which may cause soil erosion and pollution of the river channel, it was decided to reinforce the foundation by vibro-replacement stone columns in the project implementation stage (Fan and Wang, 2012).

(2) Dam Foundation Seepage

Due to the nature of riverbed overburden and its variable sedimentary makeup there is a strong tendency for dam foundation seepage. The specific reasons for foundation seepage are that the overburden has coarse grain, boulders, low permeability resistance, strong permeability, and the more common local overhead. More specifically seepage deformation failure forms, such as contact scouring and soil piping resulting from glacial deposits, alluvial-proluvial deposits, and colluvial-sliding deposits add to foundation seepage. Engineering measures must necessarily be taken to prevent seepage and premature dam failure. Curtain grouting of the dam foundation or the construction of a concrete anti-seepage wall to cut off the seepage path and reduce hydraulic gradient are common methods (Hedayati Talouki et a1., 2015; Luo and Huang, 2020). The seepage control measures mainly include the vertical cutoff technique, the horizontal anti-seepage technique, and joint seepage control. In China, the concrete cut-off wall or the combination of cut-off wall and curtain grouting are the most common for the construction of high earth-rock dams on a deep overburden layer. This is mainly due to their mature technology and their highly effective ability to protect against permeability. Horizontal anti-seepage techniques are more suitable for dam foundations with weak permeability. When the overburden is thick and the vertical anti-seepage conditions are unfavorable or are too cost intensive, the horizontal anti-seepage scheme should be studied and adopted, but the effect of the Horizontal anti-seepage technique is limited. For tall and medium height dams, complex strata and projects with large anti-seepage requirements, the final technique should be carefully selected.

A typical example is the Tarbela Dam in Pakistan, this high dam of 147 m was built on a 230 m thick overburden layer. Using horizontal seepage prevention measures, the dam used a length of 1,432 m of clay paving seepage prevention. The result was that after initial water filling the dam foundation permeability was unacceptably high. During water storage in 1974, there were more than 100 collapse pits, in 1978 after a dumping soil treatment, the overall seepage and the seepage of the dam foundation has tended to be stable (Dang and Fang, 2011).

(3) Sand Liquefaction

Loose sand layers are typical in thick riverbed overburden and are susceptible to liquefaction. In particular, the sand lens interlayers are mostly distributed in the nearshore along the

river. The thickness is generally less than 2 m, and the maximum thickness is about 13 m. The liquefaction of sand layers often occurs during earthquakes. Sand liquefaction has several harmful effects, such as sand-boils and waterspouts, ground subsidence, inducing high-speed landslides, creating foundation instability, etc. Sand liquefaction results when the pore water pressure increases, the effective stress of the soil skeleton decreases, and the soil is transformed from solid to liquid.

Chen et al. (2013) has reviewed the site liquefaction phenomenon during earthquakes over the past 20 years and concluded that the depth of soil liquefaction can reach 20 m, however, below 20 m sand liquefaction becomes more difficult. For a sand layer that is in the location of the dam foundation where it is judged to be possible for liquefaction, the measures of excavating or changing the soil should be taken. When excavation is difficult or uneconomical, artificial infill measures may be taken, or concrete diaphragm wall or other methods can be used to enclose the liquefiable layer under the foundation. The possible liquefied sand layer of the dam foundation of the Huangjinping Hydropower Station on the Dadu River was treated using basic excavation and setting the pressure on the slope downstream of the dam. The foundation of Jinping Hydropower station in the Yalong River prevents the liquefaction of the Sand Lens body through the technique of consolidation irrigation.

5 CONCLUSION

Based on the analysis of the exploration data of riverbed overburden in the primary river basins of Southwest China, the results show that:

(1) The riverbed overburden in Southwest China shows a certain regularity. The riverbed overburden in the Tibetan Plateau is shallower in the headstream area, it is thickest in the middle reaches along the mountain canyon valleys, and entering the plain area, and into the piedmont slope areas and the Yunnan Plateau, the overburden is shallower.
(2) The deep overburden in most river reaches can be vertically divided into three layers. The middle layer is a sequence of aggradation of multi-genesis deposits, mainly consisting of glacial deposits, damming lake deposits, and landslide and debris flow caused by geological disasters. The Glacial deposits are mainly distributed in the valley belt around the mountain which is above the snow line. Dammed lake deposits and geological disaster deposits are widely distributed, mainly in mountain canyon valleys where the riverbed gradient is large. Typically, the upper layers are modern river deposits, while the bottom layers are made up of paleo-riverbed deposits.
(3) The combination of regional tectonic movement, climate change, and river system development are major contributing factors to the origin of the aggradation resulting in the deep overburden of major rivers in Southwest China, this includes the Jinsha, Dadu, Yalong, Qingyi, Min, and Yarlung Tsangpo Rivers. However, the overburden of each river is the result of a complex action of multiple auxiliary sources guided by the effects of these main controlling factors. Due to the specific topography and geomorphology, geological environment, drainage evolution, and the local differential ascending and descending movement, there are clearly differences in the genesis of each river basin. However, no matter what factor or multiple factors are at work, the coupling of tectonic-climatic-fluvial sedimentation processes always affects the thickness variation and spatial distribution of riverbed overburden in Southwest China.
(4) In hydroengineering projects over thick overburden of riverbeds, two primary treatment methods are adopted: to remove the overburden completely or to remove it partially. When the dam foundation is placed on the overburden layer, there are three primary engineering problems that need to be addressed: dam foundation deformation, dam foundation seepage, and sand liquefaction.

DATA AVAILABILITY STATEMENT

The raw data supporting the conclusion of this article will be made available by the authors, without undue reservation.

AUTHOR CONTRIBUTIONS

ZY contributed to the data acquisition, investigation and wrote the original draft. MX and XK contributed to the data acquisition, the conception and design of the study. LG and SZ contributed to the data acquisition and graphic editing. The authors would like to thank Joshua Schmidt for his help on the English editing of the manuscript. All authors have read and agreed to the published version of the manuscript.

FUNDING

This research is supported by the State Key Laboratory of Geohazard Prevention and Geoenvironment Protection at Chengdu University of Technology (SKLGP2018Z018);Power China Chengdu Engineering Corporation Limited (P238-2014);The College Science Foundation of Sichuan Water Conservancy Vocational College (KY2021-07).

SUPPLEMENTARY MATERIAL

The Supplementary Material for this article can be found online at: https://www.frontiersin.org/articles/10.3389/feart.2022.895769/full#supplementary-material

REFERENCES

An, Z. S., Zhang, P. Z., Wang, E. Q., Wang, S. M., Qiang, X. K., Li, L., et al. (2006). Changes of the Monsoon-Arid Environment in China and Growth of the Tibetan Plateau since the Miocene. *Quat. Sci.* 26 (5), 678–693.

Bridgland, D. R. (2000). River Terrace Systems in North-West Europe: an Archive of Environmental Change, Uplift and Early Human Occupation. *Quat. Sci. Rev.* 19, 1293–1303. doi:10.1016/S0277-3791(99)00095-5

Chen, G. X., Jin, D. D., Chang, X. D., Li, X. J., and Zhou, G. L. (2013). Review of Soil Liquefaction Characteristics during Major Earthquakes in Recent Twenty Years and Liquefaction Susceptibility Criteria for Soils. *Rock Soil Mech.* 34 (10), 2737–2755+2795. doi:10.16285/j.rsm.2013.10.005

Chen, J., Cui, Z. J., Chen, R. C., and zheng, X. X. (2021a). The Origin and Evlution of Temi Paleolandslide-Dammed Lake in the Upper Jinsha River. *Earth Sci. Front.* 28 (2), 085–093. doi:10.13745/j.esf.sf.2020.9.9

Chen, J., and Cui, Z. J. (2015). Discevery of Outhurst Deposits Induced by the Xuelongnang Paleolandslide-Dammed Lake in the Upper Jinsha River,China and its Environmental and Hazard Significance. *Acta Sedimentol. Sin.* 33 (02), 275–284. doi:10.14027/j.cnki.cjxb.2015.02.007

Chen, Y., Wu, B., Xiong, Z., Zan, J., Zhang, B., Zhang, R., et al. (2021b). Evolution of Eastern Tibetan River Systems Is Driven by the Indentation of India. *Commun. Earth Environ.* 2, 256. doi:10.1038/s43247-021-00330-4

Cheng, W. Q., Tai, Z. H., Xiang, F., Huang, H. X., Zhou, Y. H., Song, L., et al. (2022). The Characteristics of Fluvial Deposition and Heavy Minerals in Qiaojia Basin: Indication for the Transfixion of Jinsha River, Southwestern China. *J. Chenghu Univ. Technol. Sci. Technol. Ed.* 49 (1), 84–93+103.

Clift, P. D., and Sun, Z. (2006). The Sedimentary and Tectonic Evolution of the Yinggehai-Song Hong Basin and the Southern Hainan Margin, South China Sea: Implications for Tibetan Uplift and Monsoon Intensification. *J. Geophys. Res.* 111 (B6), a–n. doi:10.1029/2005JB004048

Cui, Z. J., Chen, Y. X., Zhang, W., Zhou, S. Z., Zhou, L. P., Zhang, M., et al. (2011). Research History, Glacial Chronology and Origins of Quaternary Glaciations in China. *Quat. Sci.* 31 (5), 749–763.

Dang, L. C., and Fang, G. D. (2011). Major Technical Problems of Constructing Dam on Deep Overburden. *Water Power* 37 (2), 24–28+45.

Delaney, I., and Adhikari, S. (2020). Increased Subglacial Sediment Discharge in a Warming Climate: Consideration of Ice Dynamics, Glacial Erosion, and Fluvial Sediment Transport. *Geophys. Res. Lett.* 47. doi:10.1029/2019GL085672

Ding, Y., Zhang, X., He, Z., Lu, C., and Bao, S. (2021). Sedimentary Environment of a Dammed Lake Buried in the Modern Riverbed of the Yalong River During the Last Glacial Maximum and its Implication for Fluvial Geomorphic Evolution. *Geomorphology* 378, 107588. doi:10.1016/j.geomorph.2020.107588

Fan, Y., and Wang, L. H. (2012). Application of Vibro Replacement Stone Column in Renzonghai Weak Dam Foundation Reinforcement Treatment. *China Water Power & Electrification* 93 (11), 55–60.

Ge, Z. S., Liu, Q. Y., Xu, Q. M., Li, H. Z., Xue, G. F., Mei, Y. T., et al. (2006). The Geomorphic Evolution and Characteristics of the River Bed Lower Reaches of Jinshajiang River. *Quat. Sci.* 26 (03), 421–428.

He, W. Z., and You, F. (2013). *Shaft Construction in the Deep Overburden Layer Segment of Xiluodu Hydropower Station Hydropower and New Energy*, 30 32–35. doi:10.13622/j.cnki.cn42-1800/tv.2013.05.011

Hedayati Talouki, H., Lashkaripour, G. R., Ghafoori, M., and Saba, A. A. (2015). Assessment and Presentation of a Treatment Method to Seepage Problems of the Alluvial Foundation of Ghordanloo Dam, NE Iran. *J. Geol. Soc. India* 85, 377–384. doi:10.1007/s12594-015-0227-2

Huang, D., Yang, d. Y., Li, l. P., Shi, C. A., Lu, F., Ge, Z. S., et al. (2010). Incision Rates of the Baihetan Section of the Jinsha River. *Quat. Sci.* 30 (5), 872–876.

Li, C. Z., Wang, S. B., Fu, J. L., and Jiang, F. C. (2015a). Sedimentary Environment Evolutionary Characteristics of Longjie Silt Layer in the Middle Reaches of the Jinsha River,Yunnan. *Geol. Bull. China* 34 (1), 113–120.

Li, H. L., Zhang, Y. Q., and Li, J. H. (2010). Meridional River Systems and Ancient Dammed Lakes on the East Margin of the Tibetan Plateau. *Quat. Sci.* 30 (4), 812–824.

Li, H. L., Zhang, Y. Q., Qiao, Y. S., Zhu, F. S., and Li, J. H. (2015b). A Study of the Sediments in the Middle Reaches of the Dadu River on the Eastern Margin of the Tibetan Plateau and its Seismogeological Implications. *Geol. Bull. China* 34 (1), 104–112.

Li, J. J., Wen, S. X., Zhang, Q. S., Wang, F. B., Zheng, B. X., and Li, B. Y. (1979). Discussion on the Timing, Magnitude and Style of Uplift of the Tibetan Plateau. *Sci. Sin.* (6), 608–616.

Li, J. J., Zhou, S. Z., and Pan, B. T. (1991). The Problems of Quaternary Glaciations in the Eastern Part of Qinghai-Xizang Plateau. *Quat. Sci.* (3), 193–203.

Li, L. P., Yang, D. Y., Huang, D., Ge, Z. S., Xu, Q. M., and Wang, X. Y. (2009). Drainage Evolution of QiaoJia-XinShiZhen Section of Jinsha River. *Quat. Sci.* 29 (2), 327–333.

Li, T.-t., Pei, X.-j., Huang, R.-q., and Jin, L.-d. (2016). The Formation and Evolution of the Qiaojia Pull-Apart Basin, North Xiaojiang Fault Zone, Southwest China. *J. Mt. Sci.* 13 (6), 1096–1106. doi:10.1007/S11629-015-3778-1

Liu, S. H. (2015). Safety Assessment of Hydraulic Structures Built on Overburden Layer. *Dam Saf.* (1), 46–63.

Liu, Y. P., Montgomery, D. R., Hallet, B., Tang, W. Q., Zhang, J. L., and Zhang, X. Y. (2006). Quaternary Glacier Blocking Events at the Entrance of Yarlungzangbo Great Canyon, Southeast Tibet. *Quat. Sci.* 26 (1), 52–62.

Liu-Zeng, J., Zhang, J., McPhillips, D., Reiners, P., Wang, W., Pik, R., et al. (2018). Multiple Episodes of Fast Exhumation since Cretaceous in Southeast Tibet, Revealed by Low-Temperature Thermochronology. *Earth Planet. Sci. Lett.* 490, 62–76. doi:10.1016/j.epsl.2018.03.011

Luo, S. C. (1995). Cognition of Geological Problems of Thick Overburden Layer. *Hydroelectr. Power* (4), 21–24+58.

Luo, Y., and Huang, Y. (2020). Effect of Open-Framework Gravel on Suffusion in Sandy Gravel Alluvium. *Acta Geotech.* 15 (9), 2649–2664. doi:10.1007/s11440-020-00933-9

Maddy, D., Bridgland, D., and Westaway, R. (2001). Uplift-driven Valley Incision and Climate-Controlled River Terrace Development in the Thames Valley, UK. *Quat. Int.* 79, 23–36. doi:10.1016/S1040-6182(00)00120-8

Mahinov, A., Shevtsov, M., and Tkachenko, A. (2019). The Influence of Disastrous Floods on Riverbeds Processes in the Far East of Russia. *MATEC Web Conf.* 265, 06004. doi:10.1051/matecconf/201926506004

Marra, F., Motta, L., Brock, A. L., Macrì, P., Florindo, F., Sadori, L., et al. (2018). Rome in its Setting. Post-glacial Aggradation History of the Tiber River Alluvial Deposits and Tectonic Origin of the Tiber Island. *PLos One* 13 (3), e0194838–24. doi:10.1371/journal.pone.0194838

Merritts, D. J., Vincent, K. R., and Wohl, E. E. (1994). Long River Profiles, Tectonism, and Eustasy: A Guide to Interpreting Fluvial Terraces. *J. Geophys. Res.* 99 (B7), 14031–14050. doi:10.1029/94JB00857

Nield, M. C. (2018). Grout Curtain Construction at Bolivar Dam, Ohio. *Environ. Eng. Geoscience* 24, 121–136. doi:10.2113/gseegeosci.24.1.121

Peng, S. X. (1996). Preliminary Study on Lacustrine Deposit under Sluicegate at Xiaoguanzi Hydroelectric Power Station. *J. Geol. Hazards Environ. Preserv.* 7 (4), 34–36. doi:10.1007/bf02652053

Shan, Z. G., Cheng, W. Q., Wang, P., Wang, Y. S., Li, D. Z., and Chen, J. P. (2021). Sedimentary Construction and Mechanism of QiaoJia Basin in JinSha River-Evidence from Driling and Geophysical Exploration. Proceedings of 2021 national engineering geology Academic Annual Conference. 230–239.

Shi, J. L. (1986). Study on the Riverbed Thick Overburden Layer and Engineering Geological Problems of Dadu River. *Sichuan Water Power* 9 (3), 10–15.

Shi, Y. F., and Zheng, B. X. (1995). Studies on Altitude Climatic Environment in the Middle and East Parts of Tibetan Plateau during Quaternary Maximum Glaciation. *J. Glaciol. Geocryol.* 17 (2), 97–112.

Syvitski, J., Ángel, J. R., Saito, Y., Overeem, I., Vörösmarty, C. J., Wang, H., et al. (2022). Earth's Sediment Cycle during the Anthropocene. *Nat. Rev. Earth Environ.* 3, 179–196. doi:10.1038/s43017-021-00253-w

Tang, Q. Y., Zhang, W., Liu, L., Chai, L., Li, Y. P., Zhang, L. Q., et al. (2021). Glacier Scale and Paleoclimate Reconstruction since Penultimate Glaciation in the Qingshui Valley, Luoji Mountain, Western Sichuan. *J. Glaciol. Geocryol.* 43 (6), 1869–1877.

Tu, G. X., Huang, R. Q., and Deng, H. (2008). Deformation and Failure Mechanism of an Outwash Deposit under Scouring of River Water. *J. Eng. Geol.* 14 (5), 598–604.

Wang, L. S., Wang, X. Q., Xu, X. N., and Cui, J. (2007b). What Happened on the Upstream of Minjiang River in Sichuan Province 20, 000 Years Ago. *Earth Sci. Front.* 14 (4), 189–196.

Wang, L. S., Yang, L. Z., Wang, X. Q., and Duan, L. P. (2005). Discovery of Huge Ancient Dammed Lake on Upstream of Minjiang River in Sichuan, China. *J. Chenghu Univ. Technol. Sci. Technol. Ed.* 32 (1), 1–11.

Wang, P., Wang, H. Y., Hu, G., Qin, J. T., and Li, C. P. (2021). A Preliminary Study on the Development of Dammed Paleolakes in the Yarlung Tsangpo River Basin,southeastern Tibet. *Earth Sci. Front.* 28 (2), 035–045. doi:10.13745/j.esf.sf.2020.9.18

Wang, Q. G. (2009). Causes of Riverbed Deep Cover and Engineering Significance of Tiger Leaping Gorge Reach of Jinsha River. *Chin. J. Rock Mech. Eng.* 28 (7), 1455–1466.

Wang, Y. S., Huang, R. Q., Duan, H. P., and Wei, M. (2006). An Intensive Erosion in the Last Glaciation in the West of China. *J. Chenghu Univ. Technol. Sci. Technol. Ed.* 33 (1), 73–76.

Wang, Y. S., Luo, Y. H., Tang, X. J., and Sun, Y. M. (2007a). Characteristics of the Thick Deposit Layer Underlain with Unloaded Bedrock Forming the River Bed of Yalong River and Their Implications in Dam Construction. *J. Eng. Geol.* 15 (2), 164–168.

Wang, Z. Y., Yu, G. A., Wang, X. Z., and Liu, L. (2014). Impact of Techtonic Motion on Sediment Storage and Morphology of Yalu Tsangpo Valley. *J. Sediment Res.* (2), 1–7. doi:10.16239/j.cnki.0468-155x.2014.02.001

Xu, Q., Chen, W., Jin, H., and Zhang, Z. Y. (2010). Characteristics and Distribution of Thick Overburdens along the Dadu River Valley. *Quat. Sci.* 30 (1), 30–36.

Xu, Q., Chen, W., and Zhang, Z. Y. (2008). New View on Forming Mechanism of Deep Overburden on Riverbed in Southwest China. *Adv. Earth Sci.* 23 (5), 448–456.

Xu, Z. M., and Liu, W. L. (2011). Some Problems in the Study of the Genesis of Xigeda Formation. *Earth Sci. Front.* 18 (5), 256–270.

Xue, S. D., Lu, J. M., and Pang, B. (2012). Treatment of Deep Thick Cover Layer of Dam Foundation of Pubugou Hydropower Station. *Yangtze River* 43 (04), 35–38. doi:10.16232/j.cnki.1001-4179.2012.04.024

Yu, T., and Shao, L. (2020). Study on the Dynamic Characteristics of Dam Foundation on Deep Riverbed Overburden with Soft Soil Layer. *Rock Soil Mech.* 41 (1), 267–277. doi:10.16285/j.rsm.2019.0407

Zhang, X. B., Liu, Y., Hu, K. H., Hu, C. H., Dai, B., and Liu, W. M. (2020). Geological Implication of the Jinsha River Flowing Eastward,Ancient Dammed Lake Deposition,and Quaternary River Evolution in China. *Mt. Res.* 38 (6), 805–815. doi:10.16089/j.cnki.1008-2786.000557

Zhang, Y. S., Liu, X. Y., Wu, R. A., Guo, C. B., and Ren, S. S. (2021). Cognization, Characteristics, Age and Evolution of the Ancient Landslides along the Deep-Cut Valleys on the Eastern Tibetan Plateau,China. *Earth Sci. Front.* 28 (2), 94–105. doi:10.13745/j.esf.sf.2020.9.10

Zhang, Y. S., Qu, Y. X., Wang, X. L., Yao, X., and Guo, C. B. (2009). On the Engineering Geological Classification of Quaternary Glacial Deposits Is Southwestern Mountain Area of China. *J. Eng. Geol.* 17 (5), 581–589.

Zhang, Y. S., Zhao, X. T., and Hu, D. G. (2007). An Ancient Landslide-Dammed Lake Found in the Jinsha River Valley Near Benzilan, Dêqên, Yunnan and its Significance. *Geol. Bull. China* 26 (8), 970–975.

Zhang, Y. S., and Zhao, X. T. (2008). Sedimentary Characteristics of the Quaternary Damed Lake in the Lancang River Near the Dêqên Guoshui Area, Yunnan and its Significance. *Acta Geol. Sin.* 82 (2), 262–268+296.

Zhao, X. T., Hu, D. G., and Zhang, Y. S. (2008). Genesis and Age of the Gravels Underlying the Xigeda Formation of Panzhihua,Sichuan,China,and Valley Development of the Ancient Jinsha River. *Acta Geosci. Sin.* 29 (1), 1–12.

Zhao, X. T., Tong, Y. B., Wu, Z. H., Ye, P. S., and Hu, D. G. (2012). Buried Gravels and Dammed-Lake Sediments of the Pliocene Nujiang River Discovered in the Daojie Basin,western Yunnan Province and Their Magneto-Stratigraphic Evidence. *Geol. Bull. China* 31 (2/3), 227–234.

Zhong, H. P., and Ji, F. (2012). Preliminary Study on Sedimentary Characteristics and Evolution Process of Jiajun Ancient Dammed Lake in Dadu River. *China Water Transp.* 12 (4), 182–184.

Zhong, N., Jiang, H. C., Li, H. B., Xu, H. Y., and Liang, L. J. (2021). The Impact of Climate Transition on Seismic Activities on the Eastern Margin of the Tibetan Plateau during the Last Deglaciation. *Acta Geosci. Sin.* 42 (1), 21–31.

Conflict of Interest: SZ was employed by Power China Chengdu Engineering Corporation Ltd.

The remaining authors declare that the research was conducted in the absence of any commercial or financial relationships that could be construed as a potential conflict of interest.

Publisher's Note: All claims expressed in this article are solely those of the authors and do not necessarily represent those of their affiliated organizations, or those of the publisher, the editors and the reviewers. Any product that may be evaluated in this article, or claim that may be made by its manufacturer, is not guaranteed or endorsed by the publisher.

Copyright © 2022 Yan, Xu, Kang, Guo and Zhang. This is an open-access article distributed under the terms of the Creative Commons Attribution License (CC BY). The use, distribution or reproduction in other forums is permitted, provided the original author(s) and the copyright owner(s) are credited and that the original publication in this journal is cited, in accordance with accepted academic practice. No use, distribution or reproduction is permitted which does not comply with these terms.

frontiers | Frontiers in Earth Science

ORIGINAL RESEARCH
published: 08 July 2022
doi: 10.3389/feart.2022.919268

Features and Formation Mechanism of the Jiaopenba Landslide, Southwestern Sichuan Province, China

Tong Shen[1,2]*, *Yunsheng Wang*[2]*, *Xun Zhao*[2], *Heng Liu*[1], *Xuyang Wu*[1], *Yapei Chu*[1], *Panpan Zhai*[1] and *Yang Han*[1]

[1]Henan University of Urban Construction, School of Civil Engineering, Pingdingshan, China, [2]State Key Laboratory of Geohazard Prevention and Geoenvironment Protection, Chengdu University of Technology, Chengdu, China

The Jiaopenba landslide, which represents a typical large basalt high-speed remote landslide, is located in Emeishan City, southwestern Sichuan province, China. Based on the field investigation, the characteristics of the Jiaopenba landslide have been revealed. The Jiaopenba landslide occurred on the steep Mount Emei. Landslide materials with a volume of approximately 6.75×10^8 m^3 slid down from a high position, forming a large-scale high-speed remote debris flow, with the farthest sliding distance of about 7.5 km. The landslide area is located in the west wing of the Emeishan anticline, which is cut by faults to form a monoclinal fault-block mountain. Although the shear outlet of the landslide is near the slope toe and does not have good free conditions, there are faults passing through the slope toe of the bedding slope of the fault hanging wall, the landslide is affected by the fault activity, and the integrity of the layered slope is poor. When the foot of the slope is empty, the fault zone is compressed and plastic extrusion, which leads to bedding slip of the slope rock mass and greatly weakens the interlayer bonding force. When coupled with long structural planes on both sides to form side crack planes, a large-scale inclined plate structure is formed. Under the action of a strong earthquake and other external forces, the rock mass near the fault can be damaged by tension, and a large-scale high-position landslide can be formed by the mode of compression-slip-tension fracture.

Keywords: Jiaopenba landslide, Emeishan basalt, earthquake-induced paleolandslide, high-speed remote landslide, formation mechanism

OPEN ACCESS

Edited by:
Xiaoyan Zhao,
Southwest Jiaotong University, China

Reviewed by:
Shuo Zhang,
North China University of Water Conservancy and Electric Power, China
Qiang Gao,
Shandong Agricultural University, China

***Correspondence:**
Tong Shen
20201001@hncj.edu.cn
Yunsheng Wang
wangys60@163.com

Specialty section:
This article was submitted to Geohazards and Georisks, a section of the journal Frontiers in Earth Science

Received: *13 April 2022*
Accepted: *30 May 2022*
Published: *08 July 2022*

Citation:
Shen T, Wang Y, Zhao X, Liu H, Wu X, Chu Y, Zhai P and Han Y (2022) Features and Formation Mechanism of the Jiaopenba Landslide, Southwestern Sichuan Province, China. Front. Earth Sci. 10:919268. doi: 10.3389/feart.2022.919268

HIGHLIGHTS

1 The Jiaopenba landslide occurred on the steep Mount Emei, with a volume of approximately 6.75×10^8 m^3 slid down from a high position along a surface formed by weak intercalation of volcanic agglomerate and breccia, and the farthest sliding distance reached about 7.5 km.
2 Due to the accumulation of landslide materials and the erosion and undercutting of rivers in the later stage, the platform terrain separated by the river valley formed the fifth level planation plane in the study area (elevation: 900–1,000 m). Through the comparative analysis of regional plantation levels and combined with the research results of Valley evolution in Dadu River Basin, it can be judged that the landslide was roughly formed in the Middle Pleistocene.

3 The occurrence of landslide needs to go through three stages: deformation accumulation stage, triggering instability stage, and sliding failure stage.
4 Jiaopenba landslide developed in the hanging wall of the fault. The landslide is affected by fault activity, and the integrity of the layered slope is poor. When the foot of the slope was empty, the fault zone was compressed and plastically extruded, which led to bedding slip of the slope rock mass and greatly weakened the interlayer bonding force. When coupled with long structural planes on both sides to form side crack planes, a large-scale inclined plate structure was formed. Under the action of a strong earthquake, the rock mass near the fault can undergo tensile failure, forming a large high-position landslide in the mode of compression-slip-tension fracture.
5 The investigation shows that the Emeishan basalt debris flow is mainly composed of coarse-grained rocks. In the process of motion, large particles often collide with each other, with obvious momentum transfer. In addition, the basalt debris particles with a higher degree of fracture have better particle sphericity, and particles with good sphericity are prone to bounce and roll during movement. Under this movement mode, the effective friction coefficient between particles and the sliding surface is lower and has a momentum transfer effect during the movement. The combination of factors makes the landslide debris flow maintain a higher speed and a longer distance.

INTRODUCTION

Widely distributed Permian-age basalts throughout Southwest China are often selected as ideal sites for large hydropower projects because of their huge thick layer structure, high strength, and formation of a canyon landform (Wei, 2007; Han, 2015; Shen et al., 2019a). Another remarkable feature of Emeishan basalt is that they are composed of multiple overflow cycles with weak intercalations such as tuff, volcanic agglomerate, and breccia (Xu, 2010; Sun, 2011). Although Emeishan basalt has high strength and a huge thick layer structure, the slope rock mass is generally stable. However, basalt has special lithologic characteristics and mechanical properties of the rock mass. Once the high-level basaltic rock mass with huge potential energy loses stability, it can develop into a high-speed and long-runout giant landslide disaster (Xu, 2010; Tian, 2015; Wei, 2016; Yang, 2017; Wen, 2021). Related studies have shown that Emeishan basalt is a special rock series that can breed large-scale high-position and long-distance landslide disasters (Shen, 2019). In history, such landslides have caused a lot of casualties, property losses, and far-reaching environmental effects. For example, on 23 November 1965, one such basalt landslide occurred in Lannigou, Yunnan province: five villages were buried and caused 444 deaths. Another basalt landslide struck Touzhai, in Zhaotong City, Yunnan province, on 23 September 1991, and 216 people were killed. On 27 July 2010, a large basalt landslide near Ermanshan, Hanyuan city in Sichuan province: buried 20 people, damaged 97 houses, and forced 1,500 people to be transferred.

Why do so many catastrophic landslides occur along basalt slopes, and what is the formation mechanism of these landslides? This study aims to solve these problems. Jiaopenba landslide is a typical large basalt high-speed remote landslide event. Based on the detailed geological survey, combined with remote sensing interpretation data, laboratory test, the characteristics, failure mechanism, and movement processes of the landslide are studied.

REGIONAL GEOLOGICAL SETTING

The landslide area is located in the west wing of the Emeishan anticline in the Daeshan fault block cut by the Emeishan, Xinkaisi, Wanniansi, and Maziba faults (**Figure 1**). Granites of the Pre-Sinian System constitute the core of the Emeishan anticline, and the Sinian, Cambrian, Ordovician, Permian, and Triassic strata respectively constitute the two wings of the anticline.

Since the Middle Pleistocene, affected by the tectonic stress in the west, the Emeishan area has been strongly uplifted many times, accompanied by strong and frequent seismicity (Wang et al., 2013). The seismic intensity of the study area is degree VII.

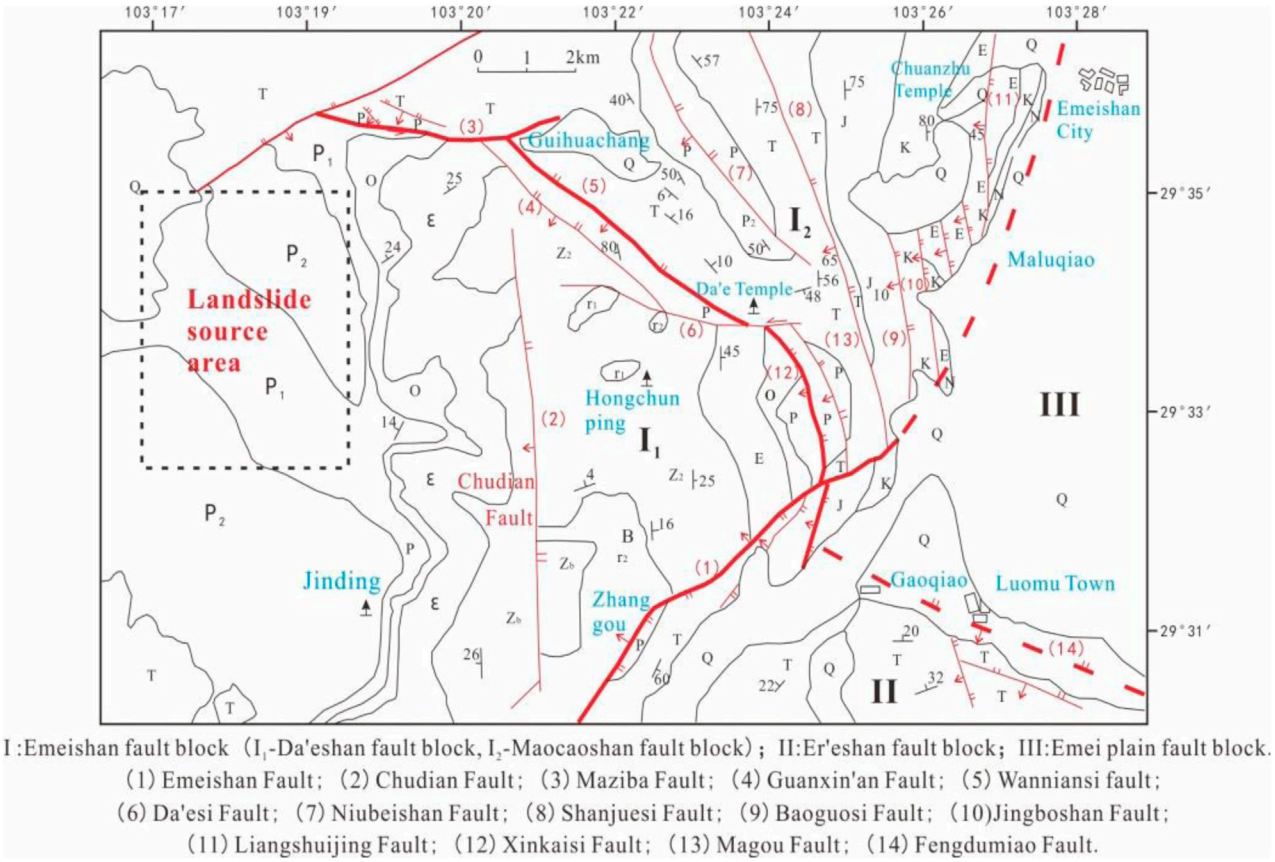
The landslide is located in the Jiaopenba area, Emeishan City, Sichuan province, China, which is generally distributed as a strip in the northwest direction (**Figure 2**). The back edge of the landslide area is located in Leidongping (elevation: 2,340 m), and the front edge of the landslide area is distributed in Nanmuping (elevation: 830 m). The height difference between the back and front edges of the landslide area is 1,510 m.

According to the integrated geological investigation, there are faults (**Figure 3**) passing through the shearing surface of the landslide (the elevation distribution of the faults is mainly exposed in the range of 1,320–1,350 m), and the landslide is located at the hanging wall of the fault. The fault strike extends toward the northeast, and the fracture surface leans to the southeast, with a dip angle of 60°–70°, which belongs to the branch fault of the Maziba fault. The fault is mainly translational and also shows the nature of the reverse fault. The west segment of the fault is covered by Quaternary materials.

Shihe River flows from the south to the north through the front edge of the landslide source area (**Figures 2**, **3**). It originates from the Wanfoding and Jieyindian areas of Emei Mountain. Due to the continuous undercutting and erosion of the slope toe by the river, an open valley landform is formed in the front of the slope. The exposed strata in the study area are mainly basalts of the Upper Permian Emeishan Formation ($P_2\beta$), which formed the landslide source (**Figure 3**). The basalts are underlain by limestone of the Lower Permian Yangxin Formation (P_1Y) and overlain by sandstones of the Lower Triassic Feixianguan Formation (T_1f), which primarily are exposed along both banks of the Shihe Valley.

CHARACTERISTICS OF THE LANDSLIDE

Based on field investigation, combined with the movement evolution process, the material composition, and structural



I :Emeishan fault block (I$_1$-Da'eshan fault block, I$_2$-Maocaoshan fault block); II:Er'eshan fault block; III:Emei plain fault block.

FIGURE 1 | The tectonic setting of the study region.

characteristics of the landslide, the landslide area was subdivided into a conflux area (I), source area (II), transportation area (III), and accumulation area (IV).

Conflux Area

The conflux area of the landslide is distributed in the upper part of the landslide source area, with an elevation range of 2,350–3,099 m. Because the upper part of the rear edge of the landslide is a flat planation surface, the stratigraphic dip angle in the Jinding area is 10°–20°, which can form a large catchment section. The area has abundant precipitation, developed bedrock fissures, and good penetration. With rainfall, snow infiltration, and groundwater runoff along the layer, the water continuously converges at the trailing edge of the landslide (**Figures 2**, **3**).

Layered fissures and columnar joints are developed in Emeishan Basaltic rock mass, which provides channels for the seepage of atmospheric precipitation and surface water. Groundwater is mostly active in rock strata with pore structure and columnar joints. The tuff interlayer in basalt has poor water permeability and becomes a relatively impermeable layer, forming a bedrock fissure aquifer. Field investigation reveals that spring water is exposed near Leidongping (elevation 2,340 m) below the confluence area (**Figure 4**), and obvious corrosion can be seen in the bedrock exposed near the spring.

Landslide Source Area

The landslide source area is located in the west wing of the Emeishan anticline, which is cut by faults to form a monoclinal bedding slope. In terms of overall topography, the middle and lower parts of the slope are relatively steep due to the influence of fold structure, the slope is moderately inclined (the stratum dip angle is 30°–35°), and the elevation at the foot of the mountain is 1,300 m. The slope tends to be gentle toward the upper part, the elevation of the trailing edge of the landslide source area is 2,500 m, and the height difference between the top and the foot of the mountain in the source area is 1,200 m (**Figure 5**).

After the landslide occurrence, a huge groove topography was formed in the source area (**Figures 2**, **5**). A large area of smooth bedding plane of limestone of Lower Permian Yangxin Formation (P_1y) is exposed in the landslide source area, parts of the unslided Emeishan Basaltic Rocks still exist at the trailing edge of the source area (**Figure 3**), which have strong weathering and unloading, and joint fissures are developed. The bedrock attitude in the source area is 306° ∠35°, which generally shows a medium dip bedding slope. The original slope of the rock mass

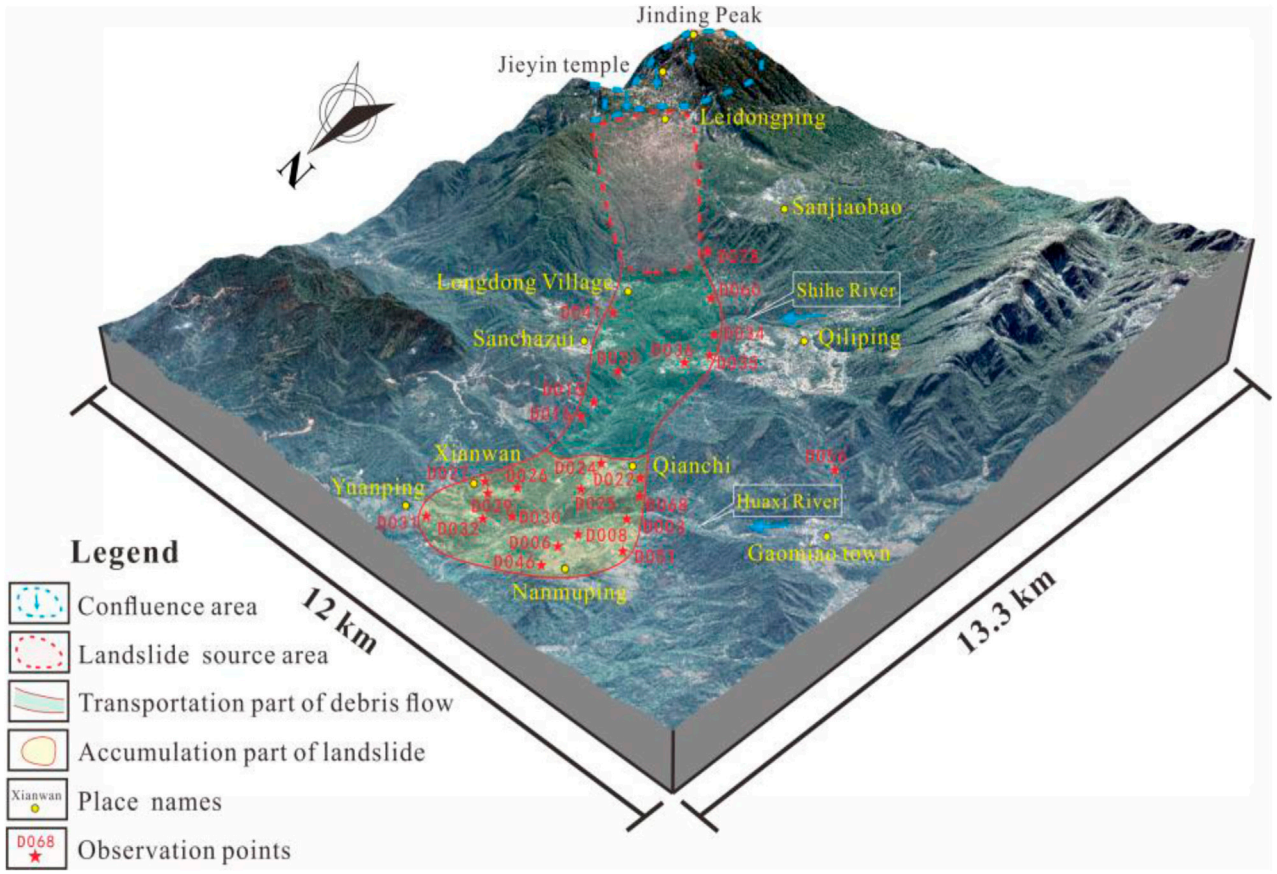


FIGURE 2 | Remote sensing image of the Jiaopenba paleolandslide (image from Google Earth).

is about 40°, the overall sliding direction is 319°, and the sliding volume is about 6.75×10^8 m^3.

Transportation Area

After the landslide slid out of the shear outlet, a large amount of landslide materials moved rapidly along the Shihe valley toward the NW direction, forming a high-speed remote debris flow with rapid disintegration (**Figure 2**).

The sliding range of the circulation area is about 5 km. The elevation of the rear edge of the circulation area is about 1,400 m, the front edge is about 900 m, and the height difference is 500 m. The terrain of the circulation area is relatively gentle, with a gradient of about 10°–15°, and there are two-stage scarps (**Figure 2**). In the process of high-speed movement, the debris flow strongly scraped the loose materials on the surface of the main ditch bed. Due to the energy consumption caused by gentle terrain change and scraping, some landslide materials scattered and accumulated in the ditch and both sides of the ditch, whereas those with greater energy continued to move with the scraped materials.

A large number of fractured stones and boulders, mostly basalt mixed with sandstone, are widely distributed throughout this area (**Figure 2**). The particle size is generally 2–20 cm, and clasts are mostly angular; the basaltic gravels are highly weathered, and some show severe argillization. The basaltic stones were mainly amygdaloidal and massive, and a large amount of sandstone was also mixed into the deposits, proving that the landslide materials scraped and collided with the mountain, after which massive bedrock materials were carried within the flow. Some larger basaltic boulders with a generally amygdaloidal structure, with maximum dimensions of $7 \times 5 \times 3$ m^3 (**Figure 6**), were distributed along this area (observation points D060, D041, D034, D033, D016, and D036).

The accumulation body distributed in the landslide transportation area has the accumulation characteristics of inverse grading structure: the upper part of the landslide accumulation body contains more large-sized boulders, whereas the lower part contains fewer boulders, mainly small particles such as gravel and breccia (**Figure 7**). Bedrock is exposed near survey point D015 (4 km away from the landslide source area) (**Figure 7**), and the lithology is sandstones of the Upper Triassic Xujiahe Formation (T_3x). Scratches can be seen on the rock mass surface, formed by scraping the bedrock with landslide materials (**Figure 7**). The scratches point downstream along the valley, indicating the movement direction of landslide materials (320°).

Accumulation Areas

After a long distance of landslide material movement, it gradually entered the accumulation stage due to the change of terrain and the

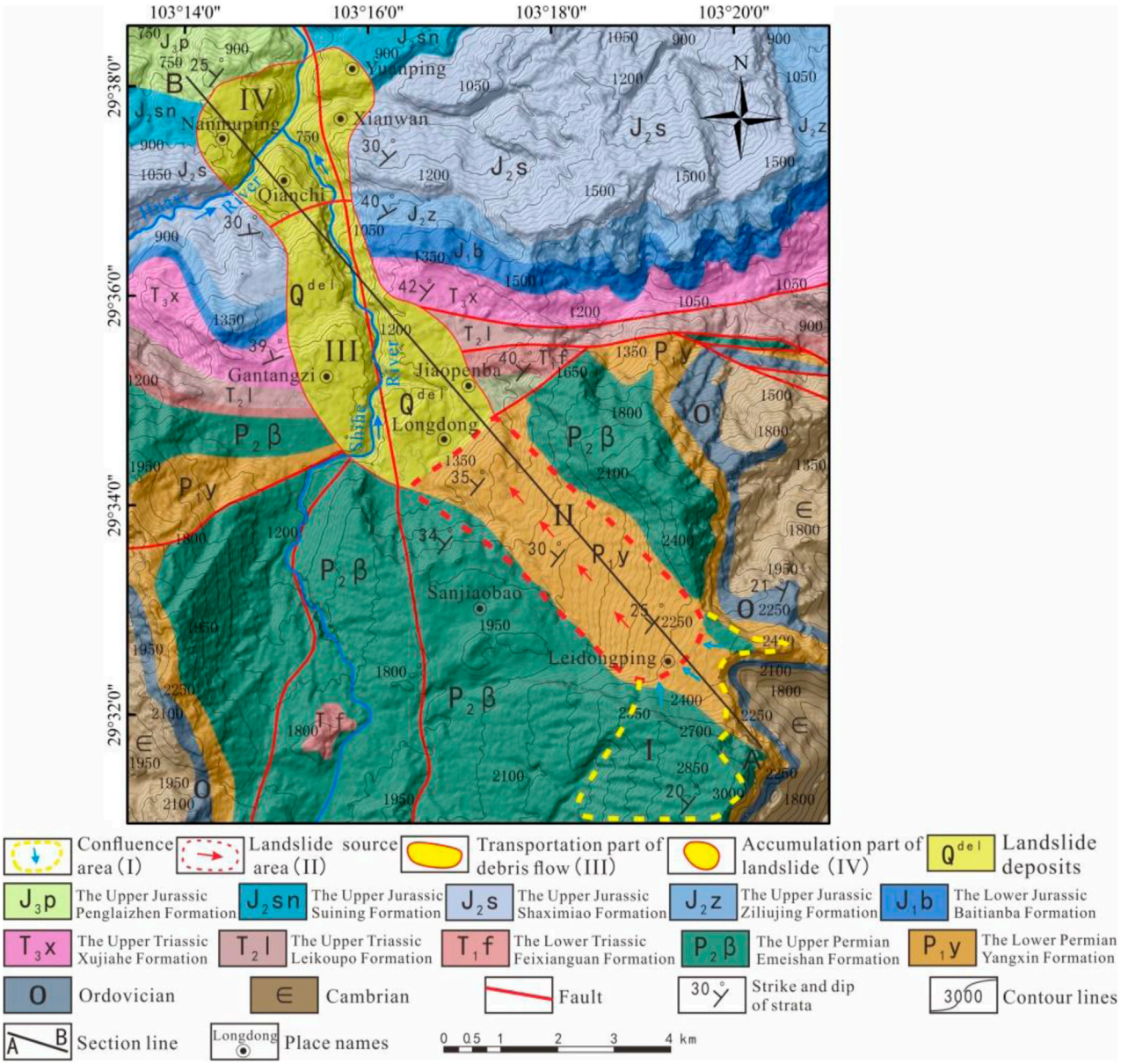


FIGURE 3 | Geomorphological sketch map of the Jiaopenba paleolandslide area.

gradual dissipation of energy. The accumulation area is mainly distributed in the areas of Qianchi (**Figure 8**), Xianwan, Yuanping, and Nanmuping. Because of the accumulation of landslide materials and the erosion of the river in the later stage, the platform terrain separated by the river valley formed in the accumulation area (**Figures 2**, **3**). Due to the long-term erosion and undercutting of the landslide accumulation by the river, a good section that can reveal the internal structure and material composition of the accumulation can be displayed.

This area is covered with landslide deposits mainly composed of soil with massive gravel- and boulder-sized clasts. The gravels were highly weathered with mostly sub-angular clasts with a particle size of 0.5–10 cm and a maximum diameter of 20 cm; their structure was disordered and dense, with mainly argillaceous and some calcareous cementation and some show severe argillization. Most of the gravels are basalt mixed with sandstone and dolomite (**Figures 8**, **9**), proving that the landslide materials scraped and collided with the mountain, after which massive bedrock materials were carried within the flow. Some larger basaltic boulders with a generally amygdaloidal structure, with volumes up to 10 m^3, were distributed along this area (**Figures 8**, **9**).

A good profile of landslide deposits (**Figure 9**), 76 m high, at observation point D032 (elevation: 770 m), exposes the internal structure of the debris deposit. The landslide deposits here are mainly composed of soil with massive basalt gravels and boulders. These gravels, which have mostly 0.2–5 cm angular clasts (18 cm



FIGURE 4 | Spring is exposed near Leidongping below the confluence area **(A)** The distant view. (**(B)** Dissolution grooves are developed in limestone).

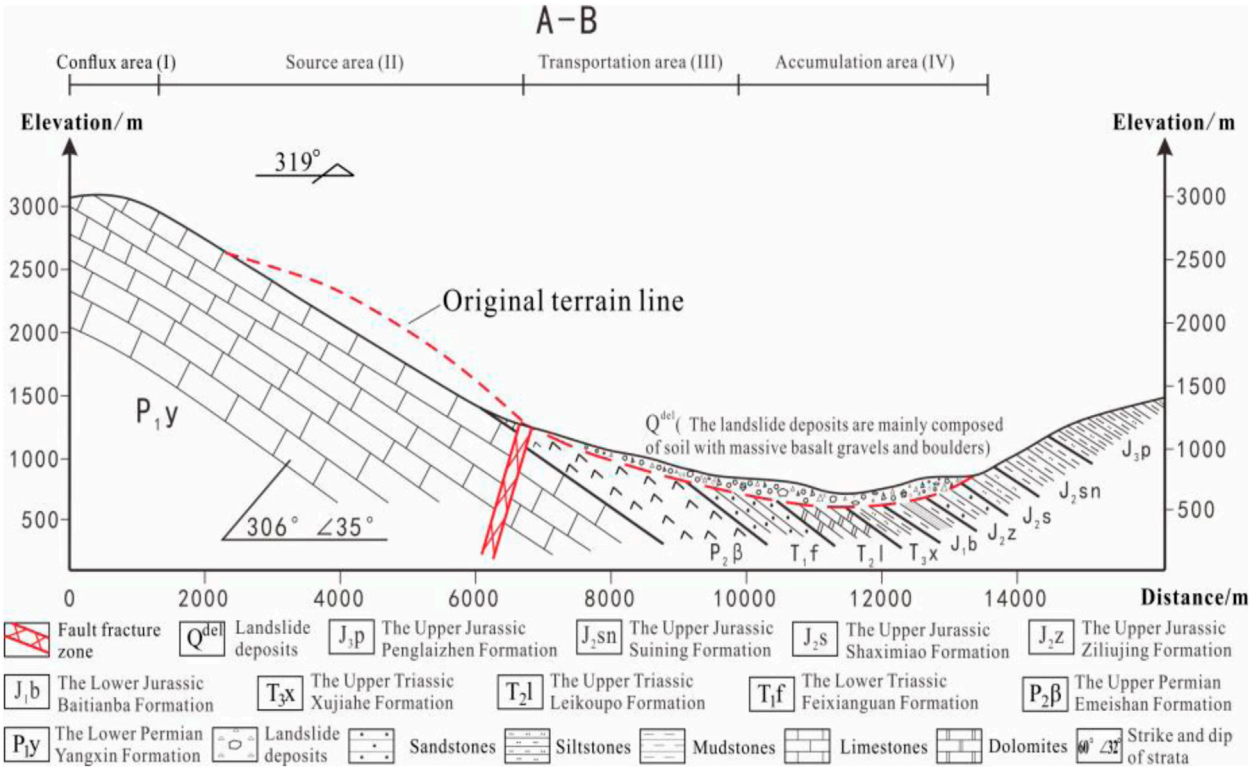


FIGURE 5 | The geological cross section profile of the Jiaopenba paleolandslide.

maximum diameter) of amygdaloidal and massive basalt, mixed with sandstone and dolomite, are chaotically arranged with compact cementation, and some show severe argillization. At different heights of the vertical section, the internal structure of the debris deposit also has the accumulation characteristics of an inverse grading structure.

Observation point D051 (elevation: 770 m) is located on the platform of Nanmuping village and belongs to the front edge of landslide accumulation. There is a good profile of landslide deposits exposed here (**Figure 10**), and the landslide materials were mainly composed of soil with massive basaltic gravel- and boulder-sized clasts (**Figure 10**). The gravels were highly weathered with mostly sub-angular clasts with a particle size of 0.2–10 cm and a maximum diameter of 20 cm; their structure was disordered and dense, with mainly argillaceous and some calcareous cementation. The basaltic stones were mainly



FIGURE 6 | Basalt boulders widely distributed in the landslide transportation area. **(A,B,C,D,E)** Basalt boulders distributed at observation points D060, D041, D034, D033, and D016, respectively. **(G,I)** Basalt boulders buried on the surface can be seen at observation point D035 (seriously weathered and show severe argillization). **(F,H,J)** Massive basalt boulders and gravels exposed at the observation point D036.

amygdaloidal and massive, and a large amount of dolomites were also mixed into the deposits, proving that the front of landslide debris flow scraped and collided with the mountain and carried the Dolomites of the Triassic Leikoupo Formation along the way. In addition, basaltic boulders are distributed around the survey site, and some show severe argillization. The saprolite crusts from chemical weathering occurring along discontinuity surfaces and enclosing the inner fresher core stone made the rock mass evolve into the structure of soil sandwiching rock (**Figure 10**). This "soil sandwiching rock" structure is more common in the seriously weathered basalt (Xu, 2005; Wang, 2013; Zhang, 2017).

The landslide finally blocked the Shihe River and formed a landslide dam. The upper parts of Nanmuping, Yuanping, Xianwan, and Qianchi are platform topography, forming a complete ancient landslide dam body, which were cut by rivers and separated from each other so that the material composition inside the accumulation body can be shown. According to the investigation results of the distribution of landslide deposits and the interface deposits front base cover, it is inferred that the accumulation thickness of the ancient landslide dam is about 150 m, and the total volume of landslide accumulation is about 3.7×10^8 m^3. In addition, through the on-site investigation of the



FIGURE 7 | The deposits and the bedrock after scraping are distributed in the landslide transportation area. **(B)** Landslide deposits at observation point D033. **(A,C)** There are many larger basaltic boulders in the upper part of landslide accumulation. **(E)** The material composition of the lower part of the landslide accumulation body is mainly composed of fine particles such as gravel and breccia. **(D,F)** The basaltic stones were mainly amygdaloidal and some show severe argillization. **(H)** Bedrock is exposed near survey point D015. **(G,I)** Scratches can be seen on the rock mass surface.

internal material composition of landslide accumulation at different locations, the debris deposit has the accumulation characteristics of inverse grading structure at different heights in the vertical profile of the landslide deposits. According to the research findings of scholars at home and abroad, many large-scale, high-speed, long-distance landslide debris flows show the accumulation characteristics of inverse grading structure in kinematics (Paola, 2000; Evans, 2006; Fan, 2019; Chen, 2021; Wu et al., 2021).

FORMATION MECHANISM OF THE JIAOPENBA LANDSLIDE

Landslide occurrence needs to go through three stages: deformation accumulation, triggering instability, and sliding failure.

Deformation Accumulation Process of Emeishan Basaltic Rock Mass

(1) Lithologic Composition Feature of Hard Rock and Intercalated Soft Rock

A large area of smooth bedding plane of limestone of Lower Permian Yangxin Formation (P_1Y) is exposed in the landslide source area, and parts of the unslided Emeishan Basaltic Rocks still exist at the trailing edge of the source area (**Figure 3**). Furthermore, according to the field investigation, most accumulations are composed of basalt blocks, and there exists no limestone component. It can be inferred that the sliding surface of the landslide is controlled by the weak intercalation of volcanic agglomerate and breccia at the bottom of Emeishan basalt (**Figure 11**).

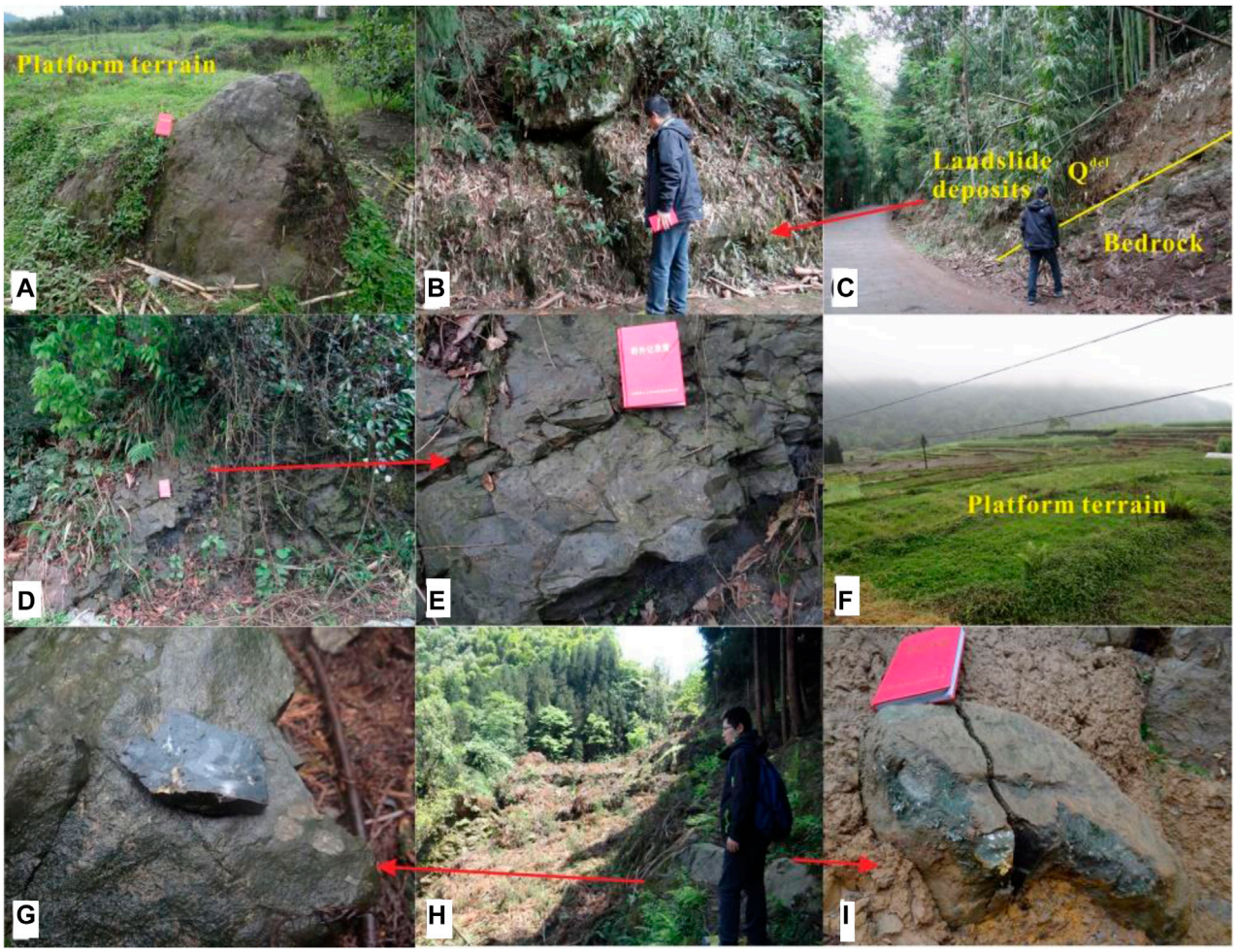


FIGURE 8 | Landslide deposits distributed around Qianchi Village. **(A)** Large basaltic boulders distributed at observation point D024. **(C)** The bedrock cover interface exposed at observation point D022. **(B)** Landslide deposits at the east side of the bedrock cover interface. **(D,E)** Large basaltic boulders distributed at observation point D025. **(F)** Landslide accumulation platform in Qianchi Village. **(G,H,I)** Landslide deposits at observation point D068.

During the condensation process of karst flow, primary columnar joints and layered joints parallel to the rock flow surface and perpendicular to the columnar joints are widely developed in Emeishan basalt (mainly including lithologic interface and eruption discontinuity formed by volcanic agglomerate, breccia layer, and tuff layer). The extensive development of layered joints makes basalt show a layered structure similar to sedimentary rock, which can often breed large-scale deformation and failure. In particular, volcanic agglomerates and breccias of the eruption discontinuity are mainly distributed at the bottom of each eruption cycle, with more pores, loose structure, and weak strength. These intercalations readily disintegrated and softened when wet, weakening the interlayer bonding within the rock mass, resulting in very low shear strength in the dip direction along the slope (**Figure 12A**).

(2) The Influence of Tectonic Reconstruction, Superficial and Epigene-Action

Although the shear outlet of the landslide is near the slope toe and does not have good free conditions, there are faults passing through the slope toe of the bedding slope of the fault hanging wall. The landslide is affected by the fault activity, and the integrity of the layered slope is poor (**Figure 13**). When the slope toe is free due to the continuous erosion of the river, the fault zone is compressed and plastic extrusion, which leads to bedding slip of the slope rock mass and greatly weakens the interlayer bonding force. When coupled with long structural planes on both sides to form side crack planes, a large-scale inclined plate structure is formed (**Figure 12B**). Therefore, the development of faults at the foot of the slope in the landslide source area played a controlling role in the formation of the shear outlet and the instability of the slope.

The deformation accumulation process of the Emeishan Basaltic rock mass is accompanied by the whole rock mass evolution process: the unique primary structural plane of Emeishan basalt makes the basaltic rock mass have a series of transverse and longitudinal staggered weak planes at the

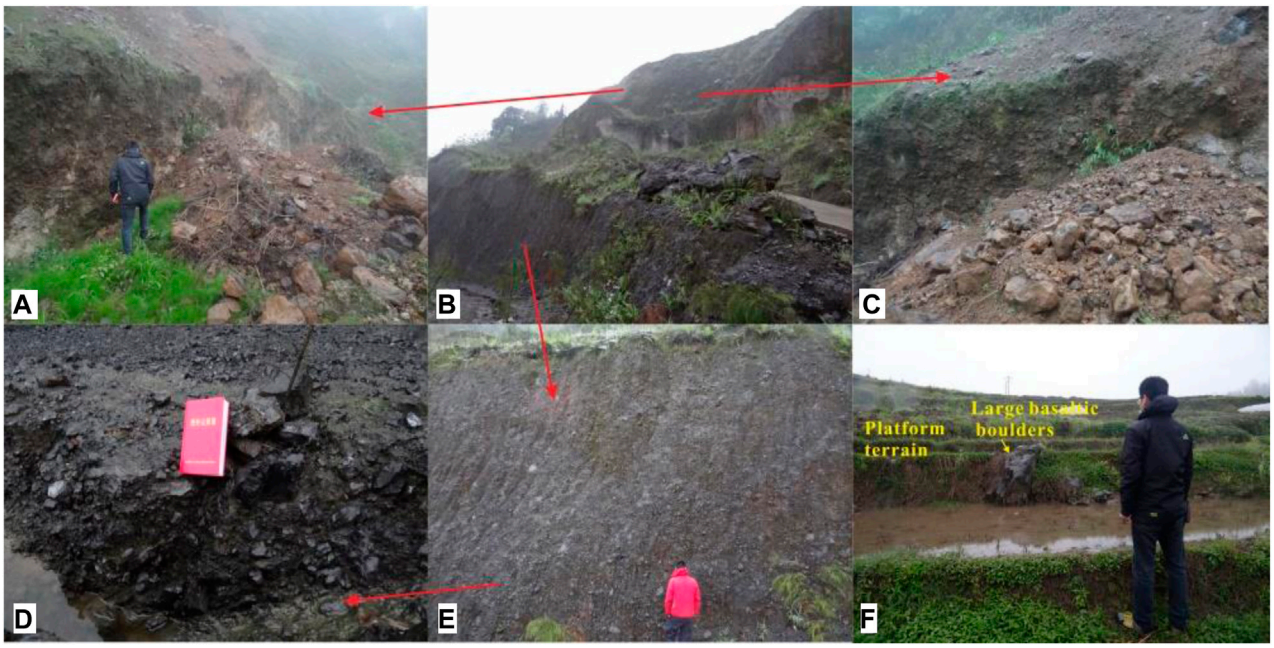


FIGURE 9 | Landslide deposits distributed around Yuanping Village. **(B)** Landslide deposits in excavation at observation point D032 show the typical accumulation characteristics of the inverse grading structure. **(A,C)** There are many large rocks and boulders in the upper part of the landslide accumulation. **(D,E)** The lower part of the landslide accumulation is mainly composed of fine particles such as gravel and breccia. **(F)** Large basaltic boulders distributed on a platform at observation point D031.

beginning of diagenesis, which provides a potential fracture surface for the development of rock mass fragmentation. In the later stage, the rock mass was affected by tectonism and shallow epigenetic transformation. On the basis of primary formation, the structural plane further deformed and developed, and new fractures were generated. The rock mass structure further tended to be broken and cracked, and the saprolite crusts from chemical weathering occurred along discontinuity surfaces. Most of its mineral components have been transformed into clay minerals, soluble components, and other residual minerals, and the mechanical strength is closer to the soil. After a long-term deformation accumulation process, the Emeishan Basaltic rock mass has gradually changed from the original thick layered structure to the inclined plate structure and became an unstable slope body.

Triggering Instability Process of Emeishan Basaltic Rock Mass

The landslide accumulation area is distributed in the areas of Qianchi, Xianwan, Yuanping, and Nanmuping. Due to the accumulation of landslide materials and the erosion and undercutting of rivers in the later stage, the platform terrain separated by the river valley formed the fifth level planation plane in the study area (elevation: 900–1,000 m). Through the comparative analysis of regional planation levels and combined with the research results of Valley evolution in Dadu River Basin (Wang et al., 2013), it can be judged that the landslide was roughly formed in the Middle Pleistocene.

The thickness of the basalt stratum in the landslide area reaches tens of meters or even hundreds of meters, characterized by an extremely thick layered bedding rock slope. It is almost impossible for heavy rainfall to trigger such a large-scale landslide event. Through the study of seismic landslides, strong earthquake events in high earthquake intensity areas can often induce large-scale rock landslide events (Fan, 2019; Valagussa, 2019; Cui, 2020; Zhao, 2021a). The landslide area is located in the VII earthquake intensity area. According to the above analysis, the landslide is triggered by a strong earthquake event in the Middle Pleistocene, and the strong earthquake is the key factor causing the final sliding instability of the landslide (**Figure 12C**).

According to the theory of stress-wave propagation (Shen et al., 2019b; Hidayat et al., 2020; Luo et al., 2020; Zhao et al., 2021b; Hazarika et al., 2021), a compressional seismic wave will be reflected into a tensile wave when it meets a structural defect during propagation; this could increase the acceleration across the defect. As a result, tensile fractures may have formed as the reflected waves and incident waves were superposed. The seismic waves thus would have been magnified by the structural defects when the earthquake occurred, resulting in further tensional failure of the rock mass and tensile cracks in the upper part of the slope (**Figure 12C**).

Jiaopenba landslide developed in the hanging wall of the fault (**Figures 5**, **12**, **13**). The landslide is affected by fault activity, and the integrity of the layered slope is poor. When the foot of the slope was empty, the fault zone was compressed and plastically extruded, which led to bedding slip of the slope rock mass and greatly weakened the interlayer bonding force.

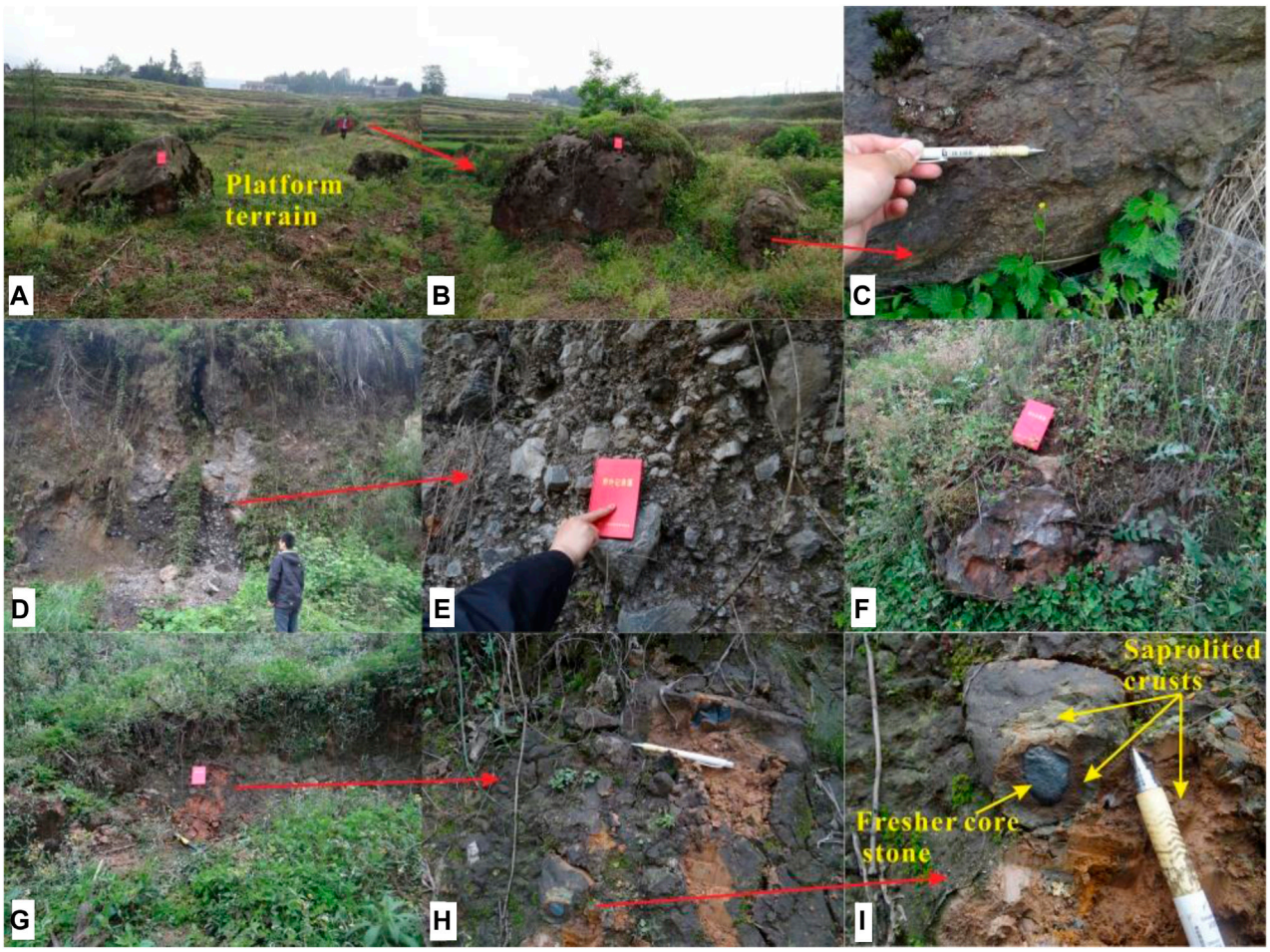


FIGURE 10 | Landslide deposits distributed around Nanmuping Village. **(A,B,C)** Large basaltic boulders distributed on a platform at observation point D046 (the basaltic blocks show severe argillization). **(D,E,F)** Landslide deposits at observation point D051. **(G,H,I)** Large basaltic boulders near observation point D051 are seriously weathered and present the structure of soil sandwiching rock.



FIGURE 11 | The weak intercalation of volcanic agglomerates and breccias form the contact surface between basalt and underlying limestone (the photographing orientation is 340°).

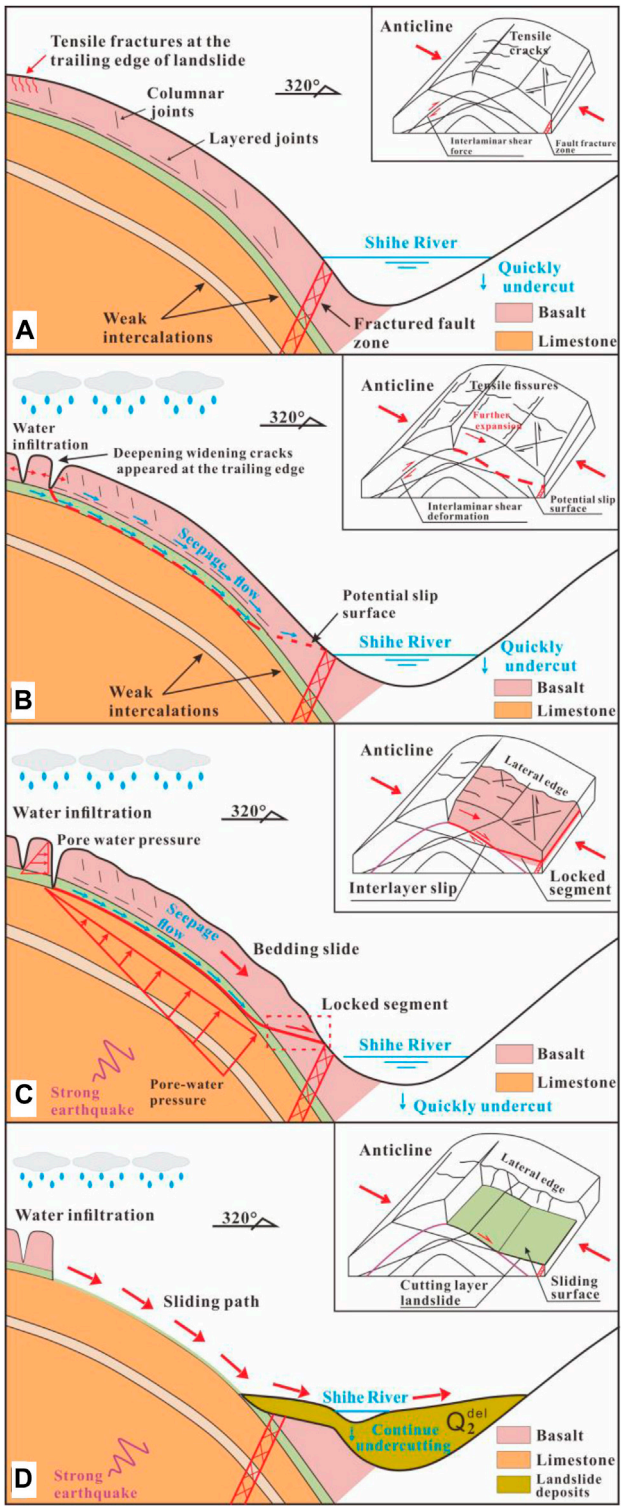


FIGURE 12 | Schematic diagram of deformation and instability mechanism of Jiaopenba landslide.

When coupled with long structural planes on both sides to form side crack planes, a large-scale inclined plate structure was formed. Under the action of a strong earthquake, the rock mass near the fault can undergo tensile failure, forming a large high-position landslide in the mode of compression-slip-tension fracture (**Figure 12D**).

Long-Distance Sliding Mechanism of Emeishan Basaltic Rock Mass

Three key conditions are needed for the Jiaopenba landslide to maintain long-distance sliding.

(1) The Landslide Body Is at a High Position and Has a High Potential Energy

The elevation difference between the back edge of the slip source area and the front edge of the landslide area is 1,510 m, the height difference is huge, and the landslide body is in the high position of the slope, providing the sliding body with tremendous potential energy when sliding out of the shear outlet (**Figures 2**, **5**).

(2) Basaltic Rock Mass in Landslide Source Area Has a High Degree of Fragmentation

The size of broken blocks in the source area, confined by structural planes at all levels, plays a controlling role in the composition of debris size of the landslide accumulation and has a profound impact on the movement and evolution of the landslide.

The investigation of the particle size composition of 36 basalt landslide deposits in Southwest China reveals that the landslide materials are mainly coarse-grained debris (particle size > 2 mm), whereas the content of fine-grained components (particle size < 2 mm) is relatively small, and the clay particles are almost missing (particle size < 0.005 mm) (**Figure 14**). Therefore, the investigation shows that the Emeishan basalt debris flow is mainly composed of coarse-grained rocks. In the process of motion, large particles often collide with each other, with obvious momentum transfer so that they can slide farther (Wang, 2018; Ahmadipur, 2019; Wang, 2021).

(3) The Friction Energy Dissipation Between Particles Is Weak After the Landslide Body Starts to Move, and It Can Keep High-Speed Movement for a Long Time

Due to the high degree of development and uniform distribution of structural planes of basaltic rock mass, the sphericity of clastic particles after crushing structural bodies surrounded by structural planes is often better. Sphericity refers to the similarity between the shape of debris particles and spheres. Sphericity reflects the shape of particles in three-

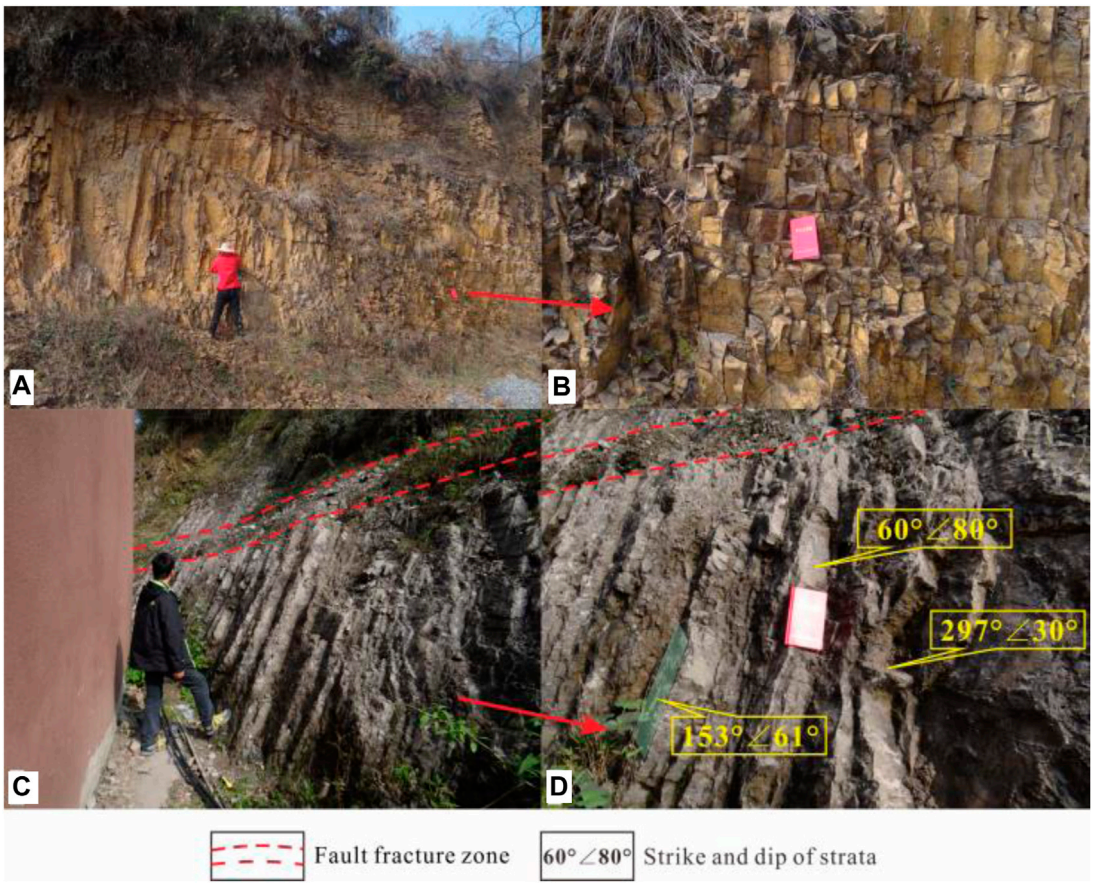


FIGURE 13 | Basaltic bedrock is exposed in the landslide source. **(A)** Columnar joints are developed in basaltic rocks. **(B)** The degree of rock fragmentation and cracking is high. **(C)** Fault fracture zone is exposed near the shear outlet of the landslide. **(D)** The attitude of bedrock in the source area.

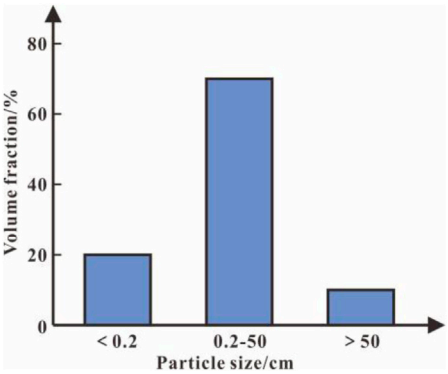


FIGURE 14 | Statistics of particle size composition of basalt landslide deposits in Southwest China.

dimensional space. Generally, the sphericity coefficient is calculated by the formula proposed by Krubin (1941):

$$\varnothing = \sqrt[3]{BC/A^2}, \quad (1)$$

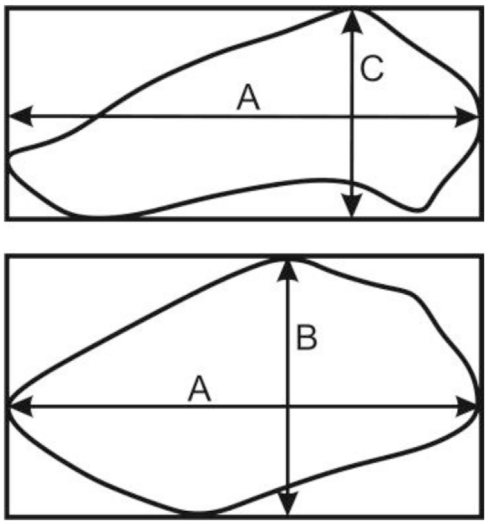


FIGURE 15 | Schematic diagram of the position of A, B, and C axes of debris particles (the upper part is the sectional view of debris particles, and the lower part is the plan view).

TABLE 1 | Sphericity investigation of basalt clastic particles.

Investigation points	Number	Particle diameter (cm)			Sphericity coefficient ∅	Proportion of particles with good sphericity (%)
		A	B	C		
D032	1	12.3	5.6	3.6	0.51	60
	2	5	4.5	3.7	0.87	
	3	11	5.1	2.6	0.48	
	4	4.8	4	3.2	0.82	
	5	6.4	4.8	2.5	0.66	
	6	5.2	3.9	2.5	0.71	
	7	3.1	2.6	1.2	0.69	
	8	2.7	2	1.6	0.76	
	9	3.8	3.5	3.2	0.92	
	10	4	2.6	1.1	0.56	
	11	2.2	1.5	0.8	0.63	
	12	7.5	2.4	1	0.35	
	13	8	5.1	3	0.62	
	14	8.6	6.1	3.6	0.67	
	15	5.5	2	0.9	0.39	
	16	2.8	1.5	0.7	0.51	
	17	2.3	1.6	1.3	0.73	
	18	5.8	2.9	1.3	0.48	
	19	3.6	2.3	1.9	0.7	
	20	12.2	5.8	5.1	0.58	
	21	8.3	6.8	5	0.79	
	22	1.9	0.8	1	0.61	
	23	6	1.9	0.8	0.35	
	24	2.5	2	1.7	0.81	
	25	10	7.9	5.2	0.74	
	26	5.1	1.2	0.7	0.32	
	27	7.6	7	5.6	0.88	
	28	3	1.5	1	0.55	
	29	9.2	7.2	6.9	0.84	
	30	6.7	3.3	1.5	0.48	
D033	1	8	6.7	4.1	0.75	67
	2	4.9	3	1.3	0.55	
	3	4.3	2.1	0.7	0.43	
	4	20.7	10.6	10.3	0.63	
	5	10.2	7.5	5	0.71	
	6	6.3	5.9	5.2	0.92	
	7	5.1	3.2	0.8	0.46	
	8	8.3	5.2	4.2	0.68	
	9	6.6	3.4	0.8	0.4	
	10	9.1	8.3	6.2	0.85	
	11	8.5	5.4	1.9	0.52	
	12	11.6	10.6	4.8	0.72	
	13	5.6	3.2	2.8	0.66	
	14	7.5	6.8	3.6	0.76	
	15	5	4.1	2	0.69	
	16	13.7	10.9	6.8	0.73	
	17	4	3.1	2.1	0.74	
	18	3.2	2	1	0.58	
	19	15.2	11.3	6.7	0.69	
	20	6.5	2.6	0.9	0.38	
	21	4.8	3	1.7	0.6	
	22	5	3.1	1.1	0.51	
	23	5.3	3.9	1.8	0.63	
	24	18.1	17.6	12.8	0.88	
	25	13.6	8.1	2	0.44	
	26	7.7	6	4.9	0.79	
	27	8.5	7.9	6.9	0.91	
	28	5.2	3.4	2.1	0.64	
	29	9.6	7.1	2.4	0.57	
	30	6.4	5.3	4.6	0.84	

(Continued on following page)

TABLE 1 | (*Continued*) Sphericity investigation of basalt clastic particles.

Investigation points	Number	Particle diameter (cm)			Sphericity coefficient ∅	Proportion of particles with good sphericity (%)
		A	B	C		
D051	1	4.1	1.5	0.5	0.35	53
	2	1.3	0.9	0.5	0.64	
	3	3.7	2.2	1.1	0.56	
	4	3	1.5	0.4	0.41	
	5	2.8	2.3	1.7	0.79	
	6	3.4	1.2	0.5	0.37	
	7	5.9	5.5	4.8	0.91	
	8	8.2	4.8	2.3	0.55	
	9	6.3	4.1	3.6	0.72	
	10	1.5	1.2	0.5	0.64	
	11	2.4	1.6	0.5	0.52	
	12	4.3	3.2	1.9	0.7	
	13	3.9	1.7	1	0.48	
	14	7.9	6.7	6.2	0.87	
	15	5.3	2.5	1.3	0.49	
	16	5.5	3.4	1.8	0.59	
	17	9.4	6.8	5.1	0.73	
	18	6	5	4.5	0.85	
	19	1.9	1.2	0.4	0.51	
	20	2.1	1.9	0.7	0.67	
	21	6	1.8	1.2	0.39	
	22	5.6	4.8	3.1	0.78	
	23	3.7	1.3	0.6	0.38	
	24	2.9	2.5	2.3	0.88	
	25	4.2	1.6	1.1	0.46	
	26	7.1	4.4	2.7	0.62	
	27	2.8	0.6	0.4	0.31	
	28	4.8	3.9	3	0.8	
	29	6.5	6.1	5.6	0.93	
	30	3.4	2.6	1.4	0.68	

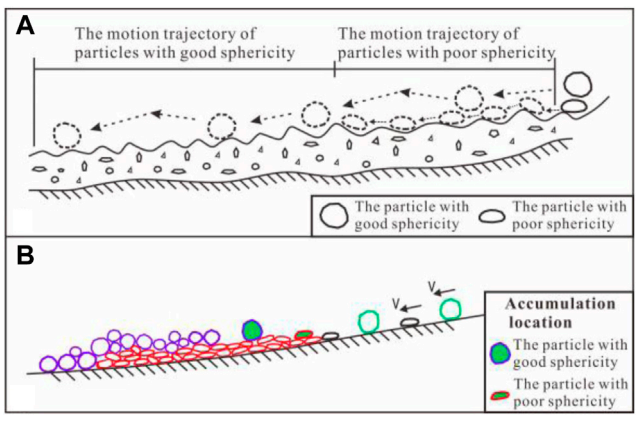


FIGURE 16 | Differential movement phenomenon and accumulation morphology of debris particles with different sphericity. **(A)** Schematic diagram of the motion trajectory of debris particles with different sphericity. **(B)** Schematic diagram of debris flow accumulation morphology.

where ∅ is the sphericity coefficient, *A* is the maximum diameter on the largest space plane of the particle, B is the maximum diameter perpendicular to axis *A* on the largest space plane, and *C* is the maximum diameter perpendicular to the largest space plane. The three axes *A*, *B*, and *C* are perpendicular to each other in space but do not necessarily intersect at one point (**Figure 15**).

The sphericity of debris particles was investigated at the Jiaopenba landslide accumulation area. The survey points were D032, D033, and D051 (the locations of the survey points are shown in **Figures 2**, **7**, **9**, **10**). At each survey site, a measurement area was randomly selected. According to the calculation formula of the Krubin sphericity coefficient, 30 debris particles were randomly selected in the measurement area to calculate their sphericity. Finally, the sphericity coefficients of each debris particle were statistically summarized (**Table 1**). Results indicate that the basalt debris particles with a higher degree of fracture have better particle sphericity (the proportion of debris particles with sphericity above 0.6 in the study area is about 60%), and particles with good sphericity are prone to bounce and roll during movement (**Figure 16**). Under this movement mode, the effective friction coefficient between particles and sliding surface is lower and has a momentum transfer effect during the movement, so that the basalt debris particles exhibit stronger mobility and thus can slide further distances, and then the scope of the landslide will be even greater.

After long-term weathering, the basaltic rock mass in the landslide source area becomes saprolite crusts with a layered structure. Most of its mineral components have been transformed

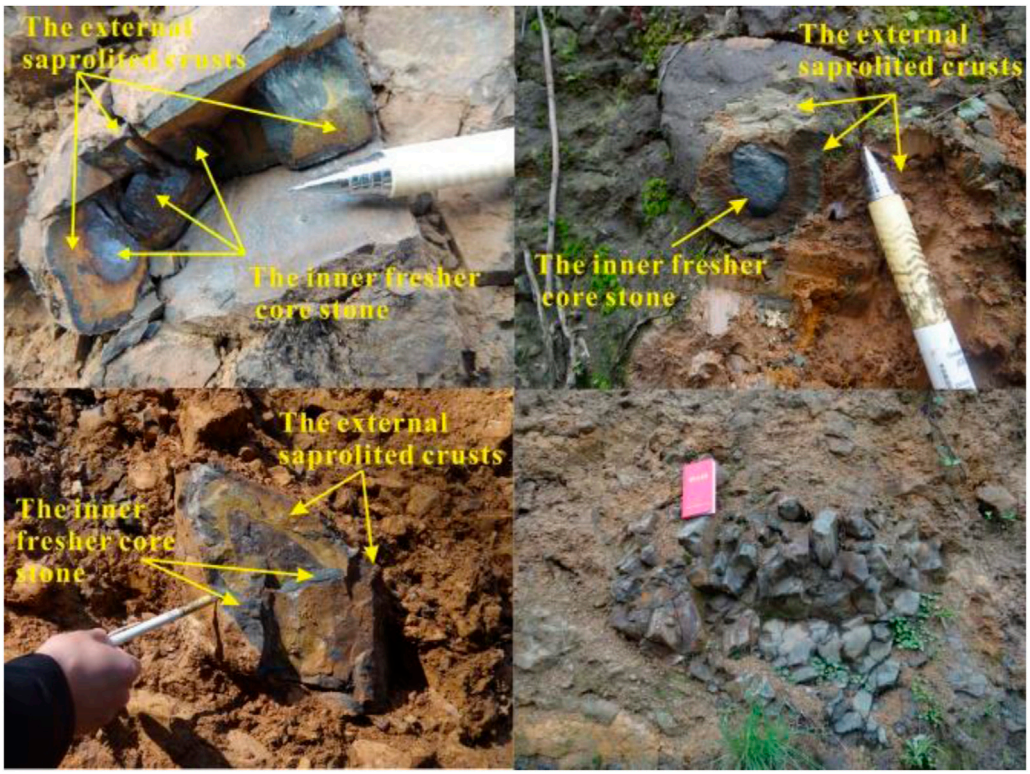


FIGURE 17 | Basaltic rocks present the structure the structure of soil sandwiching rock due to severe weathering.

TABLE 2 | Physical and hydraulic property indexes of weathered basalt (Wang, 2013).

Rock mass structure	Density (g/cm$^{3)}$	Porosity (%)	Permeability (×10^{-3}μm^2)
The external saprolite crusts	1.8816	32.82	301.5157
The inner fresher core stone	2.9434	0.24	0.0081

into clay minerals, soluble components, and other residual minerals. The external saprolite crusts crumble as soon as it is pinched, and their mechanical strength is almost lost (**Figure 17**, **Table 2**). Therefore, after the unstable sliding of the rock mass, the external saprolite crusts quickly break into fine particles, scatter around the inner fresher core stone, and act as a "lubricant."

Moreover, the landslide body passed through a far valley section in the process of sliding. Due to the existence of quaternary deposits with higher water content around Shihe River, it also plays a certain role in lubricating the movement of landslide materials. The comprehensive effect of the above factors makes the landslide debris flow maintain a higher speed and a longer distance.

CONCLUSION

The Jiaopenba landslide was a giant basalt high-speed landslide debris flow induced by a combination of factors, probably including strong earthquake ground shaking. The landslide occurred on the steep Mount Emei, with a volume of approximately 6.75×10^8 m^3 slid down from a high position along a surface formed by weak intercalation of volcanic agglomerate and breccia, and the farthest sliding distance reached about 7.5 km.

On the basis of primary formation, the basalt was affected by tectonism and shallow epigenetic transformation, and its structural plane further deformed and developed, resulting in new fractures. The saprolite crusts from chemical weathering developed along discontinuity surfaces, and most of the mineral components have been transformed into clay minerals, soluble components, and other residual minerals, and their strength is closer to the soil. After a long-term deformation accumulation process, the basaltic rock mass has gradually changed from the original thick layered structure to the inclined plate structure and became an unstable slope body.

Jiaopenba landslide developed in the hanging wall of the fault. When the slope toe was empty, the fault zone was compressed and plastically extruded, which led to bedding slip of the slope rock mass and greatly weakened the interlayer bonding force. When coupled with long structural planes on both sides to form side crack planes, a

large-scale inclined plate structure was formed. Under the action of a strong earthquake, the rock mass near the fault can undergo tensile failure, forming a large high-position landslide in the mode of compression-slip-tension fracture.

The basalt debris flow is mainly composed of coarse-grained rocks. In the process of motion, large particles often collide with each other, with an obvious momentum transfer effect. In addition, the basalt debris particles with a higher degree of fracture have better particle sphericity, which are prone to bounce and roll during movement. Under this movement mode, the effective friction coefficient between particles and the sliding surface is lower. The combination of factors makes the landslide debris flow maintain a higher speed and a longer distance.

DATA AVAILABILITY STATEMENT

The datasets presented in this study can be found in online repositories. The names of the repository/repositories and accession number(s) can be found in the article/supplementary material.

AUTHOR CONTRIBUTIONS

TS and YW were responsible for writing. XZ provided engineering data and geophysical analysis of the slope. HL, XW, and YC analyzed the deformation and failure characteristics of the slope. PZ and YH were responsible for review and proofreading.

FUNDING

This research was supported by the National Natural Science Foundation of China (Project no. 41877235) and the Funds for Creative Research Groups of China (Project no. 41521002). The authors express their gratitude for the financial assistance.

REFERENCES

Ahmadipur, A., Qiu, T., and Sheikh, B. (2019). Investigation of Basal Friction Effects on Impact Force from a Granular Sliding Mass to a Rigid Obstruction. *Landslides* 16 (6), 1089–1105. doi:10.1007/s10346-019-01156-0

Chen, J., Chen, R. C., and Cui, Z. J. (2021). Research Progress on the Morphology and Sedimentology of Long Runout Landslide. *Earth Sci. Front.* 28 (4), 349–360. doi:10.13745/j.esf.sf.2020.7.2

Cui, S., Yang, Q., Pei, X., Huang, R., Guo, B., and Zhang, W. (2020). Geological and Morphological Study of the Daguangbao Landslide Triggered by the Ms. 8.0 Wenchuan Earthquake, China. *Geomorphology* 370, 107394. doi:10.1016/j.geomorph.2020.107394

Evans, S. G., Mugnozza, G. S., Strom, A. L., Hermanns, R. L., Ischuk, A., and Vinnichenko, S. (2006). Landslides from Massive Rock Slope Failure and Associated Phenomena. *Landslides* 49, 03–52. doi:10.1007/978-1-4020-4037-5_1

Fan, X., Scaringi, G., Korup, O., West, A. J., Westen, C. J., Tanyas, H., et al. (2019). Earthquake-Induced Chains of Geologic Hazards: Patterns, Mechanisms, and Impacts. *Rev. Geophys.* 57 (2), 421–503. doi:10.1029/2018rg000626

Han, G. (2015). *A Type of Asymmetric Distributed Deep-Seated Crack Formation Mechanism: A Case Study of Baihetan Hydropower Station*. Chengdu: Doctoral Dissertation of Chengdu University of Technology. in Chinese.

Hazarika, H., Rohit, D., Pasha, S. M. K., Maeda, T., Masyhur, I., Arsyad, A., et al. (2021). Large Distance Flow-Slide at Jono-Oge Due to the 2018 Sulawesi Earthquake, Indonesia. *Soils Found.* 61 (1), 239–255. doi:10.1016/j.sandf.2020.10.007

Hidayat, R. F., Kiyota, T., Tada, N., Hayakawa, J., and Nawir, H. (2020). Reconnaissance on Liquefaction-Induced Flow Failure Caused by the 2018 Mw 7.5 Sulawesi Earthquake, Palu, Indonesia. *J. Eng. Technol. Sci.* 52 (1), 51–65. doi:10.5614/j.eng.technol.sci.2020.52.1.4

Luo, Y., Fan, X., Huang, R., Wang, Y., Yunus, A. P., and Havenith, H. B. (2020). Topographic and Near-Surface Stratigraphic Amplification of the Seismic Response of a Mountain Slope Revealed by Field Monitoring and Numerical Simulations. *Eng. Geol.* 271, 105607. doi:10.1016/j.enggeo.2020.105607

Paola, C. (2000). Sedimentology and Sedimentary Basins: from Turbulence to Tectonics. *Nature* 405, 171–197. doi:10.1038/35012122

Shen, T. (2019). *Formation Mechanism of Large-Scale High-Position and Long-Distance Landslide in Emeishan Basalt*. Chengdu: Doctoral Dissertation of Chengdu University of Technology. in Chinese.

Shen, T., Wang, Y., Huang, Z., Li, J., Zhang, X., Cao, W., et al. (2019a). Formation Mechanism and Movement Processes of the Aizigou Paleolandslide, Jinsha River, China. *Landslides* 16 (2), 409–424. doi:10.1007/s10346-018-1082-1

Shen, T., Wang, Y.-s., Luo, Y.-h., Xin, C.-c., Liu, Y., and He, J.-x. (2019b). Seismic Response of Cracking Features in Jubao Mountain during the Aftershocks of Jiuzhaigou Ms7.0 Earthquake. *J. Mt. Sci.* 16 (11), 2532–2547. doi:10.1007/s11629-019-5570-0

Sun, S. Q. (2011). *Study on the Types of Rock Mass Structural Planes and Engineering Effect in Emeishan Basalt*. Chengdu: Doctoral Dissertation of Chengdu University of Technology. in Chinese.

Tian, Y. Y., Xu, C., Xu, X. W., Wu, S. E., and Chen, J. (2015). Spatial Distribution Analysis of Coseismic and Pre-earthquake Landslides Triggered by the 2014 Ludian Ms 6.5 Earthquake. *Seismol. Geol.* 37 (1), 291–306. doi:10.3969/j.issn.0253-4967.2015.01.023

Valagussa, A., Marc, O., Frattini, P., and Crosta, G. B. (2019). Seismic and Geological Controls on Earthquake-Induced Landslide Size. *Earth Planet. Sci. Lett.* 506, 268–281. doi:10.1016/j.epsl.2018.11.005

Wang, P. (2013). *Fragmentation Mechanism of Original Rock Mass in Touzhai Landslide*. Kunming: Master's thesis of Kunming University of Science and Technology. in Chinese.

Wang, Y. S., Wang, D. P., Wang, J. Z., Fu, R. H., and Yang, Y. N. (2013). Study on the Formation of the Emei Faulty Bock Mountain. *South-to-North Water Transfers Water Sci. Technol.* 11 (1), 110–113. doi:10.3724/SP.J.1201.2013.01110

Wang, Y. F., Dong, J. J., and Cheng, Q. G. (2018). Normal Stress-dependent Frictional Weakening of Large Rock Avalanche Basal Facies: Implications for the Rock Avalanche Volume Effect. *J. Geophys. Res. Solid Earth* 123 (4), 3270–3282. doi:10.1002/2018JB015602

Wang, Y. F., Lin, Q. W., Li, K., Shi, A. W., Li, T. H., and Cheng, Q. G. (2021). Review on Rock Avalanche Dynamics. *J. Earth Sci. Environ.* 43 (1), 164–181. doi:10.19814/j.jese.2020.10001

Wei, Y. J., Chu, H. L., Zhuang, M. G., Wang, C. F., and Bai, Y. Y. (2016). Formation Mechanism of Wangshan-Zhuakousi Landslide in Emei City, Sichuan Province. *J. Eng. Geol.* 24 (3), 476–483. doi:10.13544/j.cnki.Jeg.2016.03.018

Wei, Y. J. (2007). *Study on Characteristics of Rock Mass Structure and Engineering Application of Emeishan Basalts in Project Site of Hydroelectric Power Station in Southwest China*. Chengdu: Doctoral Dissertation of Chengdu University of Technology. in Chinese.

Wen, B. P., and Wang, F. (2021). Precursors and Motion Characteristics of the 1965 Lannigou Rockslides and the Subsequent Evolution. *Hydrogeology Eng. Geol.* 48 (6), 72–80. doi:10.16030/j.cnki.issn.1000-3665.202108065

Wu, H., Pei, X. J., Cui, S. H., Huang, R. Q., and Song, C. (2021). Study of Topographic and Geological Controls on Landslide Development and Distribution within Mountainous Regions Influenced by Strong Earthquakes. *Chin. J. Rock Mech. Eng.* 40 (5), 972–986. doi:10.13722/j.cnki.jrme.2020.0944

Xu, Z. M., Huang, R. Q., and Tang, Z. G. (2005). Kinetics of Silicate Mineral Dissolution and its Implications for Landslide Studies. *Chin. J. Rock Mech. Eng.* 24 (09), 1479–1491. in Chinese.

Xu, Q., Dong, X. J., Deng, M. L., Chen, L., and Hu, Z. M. (2010). The Ermanshan Rock Slide-Debris Flow of July 27, 2010 in Hanyuan, Sichuan: Characteristics and Failure Mechanism. *J. Eng. Geol.* 18 (5), 609–622. in Chinese.

Yang, J.-q., Xu, Z.-m., Zhang, R., Chen, J.-p., Ren, Z., Luo, R.-z., et al. (2017). Formation and Evolution of Emeishan Basalt Saprolite in Vadose Zones of Touzhai Landslide Source Rockmass. *J. Mt. Sci.* 14 (6), 1174–1184. doi:10.1007/s11629-016-4169-y

Zhang, X. S. (2017). *Expansion Mechanism of Weathering Front of Rock Blocks with Low Permeability in Slope Unsaturated Zone*. Kunming: Master's thesis of Kunming University of Science and Technology. in Chinese.

Zhao, B., Su, L., Wang, Y., Ji, F., Li, W., and Tang, C. (2021a). Insights into the Mobility Characteristics of Seismic Earthflows Related to the Palu and Eastern Iburi Earthquakes. *Geomorphology* 391, 107886. doi:10.1016/j.geomorph.2021.107886

Zhao, B., Wang, Y., Wu, J., Su, L., Liu, J., and Jin, G. (2021b). The Mogangling Giant Landslide Triggered by the 1786 Moxi M 7.75 Earthquake, China. *Nat. Hazards* 106, 459–485. doi:10.1007/s11069-020-04471-1

Conflict of Interest: The authors declare that the research was conducted in the absence of any commercial or financial relationships that could be construed as a potential conflict of interest.

Publisher's Note: All claims expressed in this article are solely those of the authors and do not necessarily represent those of their affiliated organizations or those of the publisher, the editors, and the reviewers. Any product that may be evaluated in this article, or claim that may be made by its manufacturer, is not guaranteed or endorsed by the publisher.

Copyright © 2022 Shen, Wang, Zhao, Liu, Wu, Chu, Zhai and Han. This is an open-access article distributed under the terms of the Creative Commons Attribution License (CC BY). The use, distribution or reproduction in other forums is permitted, provided the original author(s) and the copyright owner(s) are credited and that the original publication in this journal is cited, in accordance with accepted academic practice. No use, distribution or reproduction is permitted which does not comply with these terms.

frontiers | Frontiers in Earth Science

TYPE Original Research
PUBLISHED 14 July 2022
DOI 10.3389/feart.2022.896897

Check for updates

OPEN ACCESS

EDITED BY
Yunhui Zhang,
Southwest Jiaotong University, China

REVIEWED BY
Dong Chen,
Xi'an Shaanxi, China
Lingfeng Gong,
Chengdu Geological Survey Center, China

*CORRESPONDENCE
Shun Yang,
yangshun09@foxmail.com

SPECIALTY SECTION
This article was submitted to Geohazards and Georisks, a section of the journal Frontiers in Earth Science

RECEIVED 15 March 2022
ACCEPTED 27 June 2022
PUBLISHED 14 July 2022

CITATION
Yang S, Gao M, Jiao J, She T and Chen K (2022), The effect of seepage flow on movable solid materials research in debris flow experiments.
Front. Earth Sci. 10:896897.
doi: 10.3389/feart.2022.896897

COPYRIGHT
© 2022 Yang, Gao, Jiao, She and Chen. This is an open-access article distributed under the terms of the Creative Commons Attribution License (CC BY). The use, distribution or reproduction in other forums is permitted, provided the original author(s) and the copyright owner(s) are credited and that the original publication in this journal is cited, in accordance with accepted academic practice. No use, distribution or reproduction is permitted which does not comply with these terms.

The effect of seepage flow on movable solid materials research in debris flow experiments

Shun Yang[1,2]*, Meiben Gao[1,3,4], Jiaxua Jiao[1,2], Tao She[5] and Kun Chen[1,2]

[1]School of Emergency Management, Xihua University, Chengdu, China, [2]Sichuan College of Emergency Management, Chengdu, China, [3]Key Laboratory of Geohazard Prevention of Hilly Mountains, Ministry of Natural Resources, Fuzhou, China, [4]Fujian Key Laboratory of Geohazard Prevention, Fuzhou, China, [5]Institute of Exploration Technology, CAGS, Chengdu, China

Debris flows is one of the most common natural disasters in mountainous areas, posing a seriously risk to local people's life and property. It is fundamental basis to study the criteria for movement of solid materials subjected to seepage flow and surface flow for the purpose of prevent this hazard. Therefore, mechanical analysis methods and laboratory experiments were used to study the effect of seepage flow on movable solid materials in debris flow. First, the definition of movable solid materials was proposed. Then, a geological model of debris flow is established considering saturated seepage flow. Finally, through mechanical analysis, formulas for dynamical force and resistance force are derived. The results show that the dynamical force and resistance force increase linearly with depth when the geologic model is homogenous and the seepage flow saturates the entire debris layer. It also indicated that pore-water pressure is one of the most important factors for causing debris flow, especially when the slope angle exceeds 12°. Through comparing the results of tests and theoretical analysis under saturated seepage flow, the discrepancy is only 1.3%–24.2%, showing that the formulas are fairly reliable. The motion of the solid materials should be described as a mechanical problem rather than a statistic qualitative description. The research contributes to the source volume calculation of small debris-flow watersheds and advances the study of the movable solid materials in complex dynamic conditions.

KEYWORDS

debris flow, seepage flow effect, solid materials, movable, experiment

Introduction

The interaction between natural geo-environment and human activities leads to a series of geological hazards, such as debris flow, landslide, groundwater deterioration etc. (Degetto et al., 2015; Hu et al., 2016; Li Q. et al., 2021, Li X. et al., 2021; Zhang et al., 2021a, 2021b). A debris flow consists of a sediment-water mixture driven by gravity and is related to factors such as geological tectonics, topographical conditions, hydrology, and human engineering (Xu, 2010). Debris flows have been reported in more than 70 countries globally and every year cause severe economic losses and human casualties, which seriously retard social and

economic development (Dahal et al., 2009; Liu et al., 2010; Cui et al., 2011; McCoy et al., 2012). Generally, three conditions are required for debris flows: a steep slope angle, abundant water, and sufficient loose solid materials. According to Takahashi (2007), the mechanical triggers of debris flows can be classified into three types, namely erosion by surface runoff, transformation from landslides, and collapse of debris dams. By studying the water content before the onset of debris flow, the thinner soil layer fails by rainfall infiltration, which increases the weight and thereby increases the matrix suction. Gravity and hydrodynamics are the main criteria for debris-flow formation (Chen et al., 2006). Numerous experiments and field surveys have found that the pore-water pressure increases as loose solid materials move with the surface water, which leads to liquefaction (Wang and Sassa, 2003; Iverson and Schaeffer, 2004). Based on laboratory experiments and field observations, Mao and Duan (2009) analyzed in detail saturated seepage in the soil layer to elucidate the relationship between buoyancy and the seepage force, they also concluded that water pressure at the soil surface can be transformed into seepage force on the soil.

Through experimentation and field observations, researchers found the landslide mass fails to move upon increasing of the pore-water pressure. Pore-water pressure plays a key role in the triggering of slope failures and enhancing the mobility of debris flows (Zhou, 2014). Through monitoring, the pore-water pressure at different points during soil failure, show the pore-water pressure rises quickly at the initial infiltration and decreases sharply before failure. Using a rotating ring shearing experiment, soil liquefied to form a debris flow because of a dramatic change in pore-water pressure (Sassa et al., 2004); this theory was also verified by other researchers (Emmanuel and Simon, 2006). The soil matrix suction of unsaturated soil is determined the landslide mass stability from. Through field surveys, experimentation, and theoretical analysis, Richard (2005) identified three processes by which slope failure forms a debris flow: Coulomb failure, liquefaction by high pore-water pressure, and energy dissipation. Stability against shallow mass sliding in saturated sandy slopes under seepage depends on the flow direction and hydraulic gradient, particularly near the ground surface (Hossein and Soheil, 2008). Although the liquefaction process is thought to reflect the flow, variations process still require further study. Slope materials is one of the important supplies of material for debris flows, the slope failures were not triggered by positive pore pressure but by a decrease in suction due to the wetting of the soil (Hu et al., 2015). Field observations have found that the slope failures across a slope are random and discontinuous (Guo et al., 2021). As for the catastrophic debris flow slides initiation, Carey explore the potential failure mechanisms in response to seismic loading and elevated pore-water pressures by the dynamic back-pressured shear box (Carey et al., 2019; Carey et al., 2021). It found that whilst looser coarse-grained fills display a ductile style of deformation in response to elevated pore water pressures, denser fine-grained fills display a brittle style of deformation and require higher levels of pore water pressure to initiate failure.

Loose solid materials are an essential condition of debris flow formation, previous research indicated that water infiltration induced the migration of fine particles within soil slopes and lead to the initiation of shallow failure and subsequent debris flows (Guo and Cui, 2020). Gravel soil is widely distributed in the source region, clay content can influence gravel soil mass failure and debris flow initiation significantly (Chen et al., 2010; Chen et al., 2018). Given the numerous solid materials distributed in a typical watershed, the question arises as to how much solid material is required to form a debris flow and how the debris flow moves. Currently, most volume calculations are based on statistical analyses. Numerous statistical studies have focused on debris flow volume calculations, such as the volume and distribution of loose solid materials or the traditional concept of effective solid materials (Tang et al., 2011; Qiao et al., 2012), even some researchers established novel approach to estimate the glacial moraine reserves in the Parlung Tsangpo basin (Wang et al., 2022). These studies have aided in debris flow prevention and reconstruction. However, most such methods are based on field surveys and statistics and lack physical or mechanical data. Thus, we analyze debris-flow formation by asking whether loose solid materials will move under given hydrodynamic conditions in a debris-flow source area given the dynamic force and resistance. This is a mechanical equilibrium problem rather than a broadly qualitative description, as is the problem of movable solid materials (Yang, 2014). In mountainous areas, the significant height differences of the topography satisfy the conditions for debris-flow initiation, whereas the surfaces of sloped gullies are relatively constant. A certain quantity of heavy rainfall, surface flow, and underground water could provide sufficient water. Abundant deposits due to rock avalanches, landslides, or gully deposits provide sufficient loose solid materials. The topographic conditions may be assumed to be constant because of the minimal changes over decades, or even hundreds of years, unless a natural catastrophe occurs. The water conditions due to rainfall and surface flow have been extensively researched in studies of hydrology and natural disasters and combined with the complexity of loose solid materials to constrain debris-flow initiation, forecasting, and prevention.

The current study is based on the mechanical equilibrium principle and begins by defining the movable solid material of a debris flow. Next, we develop a geological model of saturated seepage flow based on natural phenomena. A mechanical analysis leads to two equations: one for the driving force and one for the resistance force. Finally, the theoretical results are verified by comparison with the results of flume experiments. In addition, we discuss the difference between the traditional definitions of dynamic reserve, effective solid material, and movable solid material. This research thus provides a quantitative method to calculate the dynamics of loose solid material in debris flows upstream from source areas. The results of this research should contribute to designing prevention measures in small-debris-flow watersheds.

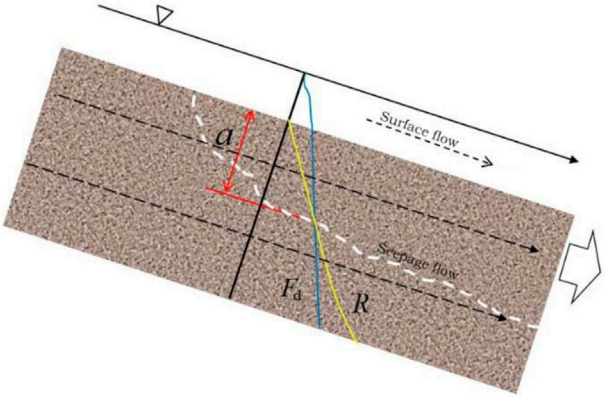


FIGURE 1
General diagram of movable solid materials.

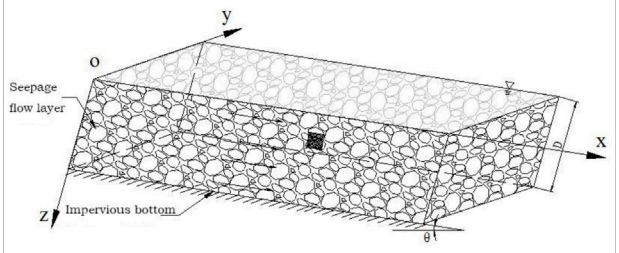


FIGURE 2
A general view of the geologic model under saturated seepage flow conditions.

Materials and methods

Definition

Currently, most calculations of the volume of solid material in small watersheds are based on statistics and estimations and can result in statistical errors ranging from 70% to 150%. For the design of debris-flow check dams, an unreasonable volume of loose solid material can lead to high costs or low preventability. Therefore, based on Yang's (2014) research, we propose herein the concept of "movable solid materials", which we define with the help of the critical depth a (see Figure 1), when the driving force exceed the resistance beneath the slope surface.

F_d is the driving force and the R is the resistance force in Figure 1. When $F_d < R$, the entire layer of loose solid material is stable. When $F_d = R$, the layer of loose solid materials is in the critical, or movable, state. While $F_d > R$, the loose solid materials within the critical depth fail, as shown below.

$$\text{Formulas for movable solid materials} \begin{cases} F_d < R & \textit{stable state} \\ F_d = R & \textit{critical state} \\ F_d > R & \textit{fail to move} \end{cases} \tag{1}$$

Thus, the movable solid materials are the solid materials within the critical depth when $F_d = R$, the critical depth can be represented as a.

Geological model of saturated seepage flow

The deposition mode and the amount of loose solid material in debris flow watershed affect the thickness of the loose solid material, the mechanical characteristics of the material, the slope angle, and various hydrodynamic characteristics. Generally, the motion of movable solid material is controlled by the relationships between slope angle, hydrodynamic conditions, gravity, and resistance. Given the definition, when the superposition of the hydrodynamic component and the gravity component exceeds the resistance, the solid material would lose failure and even initiate a debris flow.

Water is the essential ingredient in debris flows and mainly comes from rainfall, surface water flow, and groundwater flow. The water movement occurs in saturated seepage flow, unsaturated flow, and surface flow. Figure 2 shows the model of saturated seepage flow of loose solid materials. We assume that the particles are heterogeneous and anisotropic. The porosity of the detrital grain layer is n, the thickness is D, the slope angle is θ, and the thickness of the surface water layer is H ($H = 0$ means an absence of surface water). Finally, the bottom plate is impermeable, and the saturated seepage flow is distributed over the whole layer.

Mechanics analysis

When the slope angle is less than the natural angle of repose, the loose solid materials remain static. However, a certain hydrodynamic contribution of seepage flow and surface flow will disturb the equilibrium, allowing the loose solid material to move in a debris flow. The seepage force and the drag force generated by surface flow are the main hydrodynamic forces and are related by the following equations.

The seepage force F_1 depends on the hydraulic gradient, the equation described as follows.

$$F_1 = \gamma_w j V \tag{2}$$

where γ_w is the water density, $j = \Delta h / \Delta L$ is the hydraulic gradient, $\Delta h = \Delta z + \Delta p / \gamma_w + (\Delta u)^2 / 2g$ is water head difference or head loss, ΔL is the seepage path, Δz is the position head difference, $\Delta p / \gamma_w$ is the pressure head difference, and $(\Delta u^2 / 2g)$ is the flow velocity head difference.

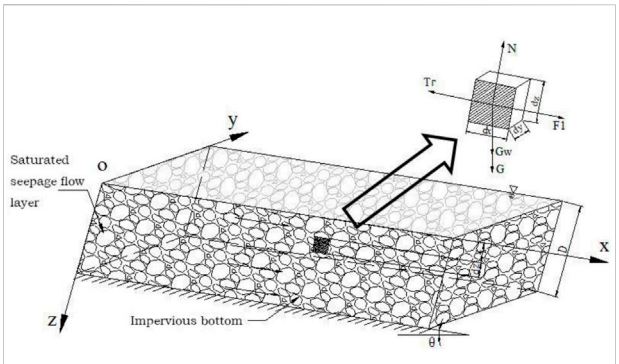


FIGURE 3
The mechanical analysis diagram of the solid materials unit under saturated seepage flow conditions.

For saturated seepage flow, we select a differential volume element $dxdydz$, along the slope incline direction at any depth to perform the mechanical analysis (see Figure 3). The volume element $dxdydz$ is subjected to gravity, seepage force, and shear resistance between the particles.

The differential force dG of gravity exerted on the soil and water is

$$dG = \gamma_{sat}\frac{z}{\cos\theta}dxdy \tag{3}$$

where γ_{sat} is the saturated density of the slope layer, $dxdy$ is the bottom area of the small element, and θ is the slope angle used in the geologic model.

Therefore, the differential force exerted on the saturated layer in the x direction is

$$dG_x = \gamma_{sat} z \tan\theta\, dxdy \tag{4}$$

The differential force in the z direction is

$$dG_z = \gamma_{sat} z\, dxdy \tag{5}$$

The differential force dG_w of gravity exerted on the volume element is

$$dG_w = \gamma_{sat} dV \tag{6}$$

where dV is the volume element, $dV = dxdydz$, and dz being the thickness of the volume element.

The differential force dG_{wx} of gravity exerted in the x direction on the volume element is

$$dG_{wx} = \gamma_{sat} \sin\theta dV \tag{7}$$

The differential force dG_{wz} of gravity exerted in the z direction on the volume element is

$$dG_{wz} = \gamma_{sat} \cos\theta dV \tag{8}$$

The differential seepage force dF_1 exerted in the x direction on the volume element is

$$dF_1 = \gamma_w j dV \tag{9}$$

Considering the low flow velocity in the saturated layer, we set the flow velocity head difference to a minimum ($\Delta u^2 = 0$). The volume element is taken to be parallel to the slope debris layer, and the water pressure on the upstream side is the same as that on the downstream side, so we can neglect the water pressure head. Therefore, Eq. 9 can be rewritten as follows.

$$dF_1 = \gamma_w \sin\theta dxdydz \tag{10}$$

During the seepage process, the particle framework prevents water flow in the pores between the particles. We assume dense debris so that the shear resistance $d\tau_r$ between the particles is

$$d\tau_r = (\gamma_s - \gamma_w)(1-n)\cos\theta dxdydz \tag{11}$$

where γ_s is the soil particle density, n is porosity, θ is the slope angle, $dV = dxdydz$ is the volume of the volume element, and dz is the thickness of the volume element.

The dynamic force along the slope direction includes the seepage force and the force of gravity, which can be expressed as following

$$dF_d = \gamma_w \sin\theta dxdydz + \gamma_{sat} z \tan\theta\, dxdy + \gamma_{sat} \sin\theta dxdydz \tag{12}$$

The force in the z direction is mainly composed of the gravity component $d\sigma$, which is expressed as

$$d\sigma = \gamma_{sat} z\, dxdy + \gamma_{sat} \cos\theta dxdydz \tag{13}$$

The pore-water pressure dp is given by the following

$$dp = \gamma_w z\, dxdy \tag{14}$$

Combined with the Mohr–Coulomb criterion, the differential resistance dR exerted in the x direction on the volume element is

$$dR = c + (d\sigma - dp)\tan\varphi + d\tau_r \tag{15}$$

Therefore, Eqs 12, 15 give the dynamic force and resistance exerted on the volume element, respectively, at the depth z and for saturated seepage flow. Eq. 12 consists of the seepage force dF_1, the force of gravity in the x direction dG_x, and the force of gravity exerted on the volume element dG_{wx}. Eq. 15 describes cohesion c, friction in the deposited layer, and shear resistance between the particles $d\tau_r$.

Eqs 12, 15 lead to an expression for the dynamic and resistance stress distribution vertical with respect to the slope direction for the volume element undergoing saturated seepage flow. Generally, the dynamic force and the resistance vary with slope angle, soil strength, and porosity of the layer. The depth z is the variable; the thickness of the volume element is dz, which we assume is the characteristic particle size d_{50} of the soil layer, and the bottom area of the volume element is $dA = dxdy = 1$, therefore, Eqs 12, 15 can be integrated to give as follows.

$$F_d = (\gamma_w + \gamma_{sat})\sin\theta d_{50} + \gamma_{sat} z \tan\theta \tag{16}$$

TABLE 1 The parameters of the deposit under saturated seepage flow conditions.

Layer	Slope angle	θ	°	12
Particles	Porosity	n	—	0.3
	Characteristic particle size	d_{50}	mm	3
	Cohesion	c	Pa	0
	Internal friction angle	φ	°	30
	Particle density	γ_s	kN/m^3	22.3
Saturated seepage flow	Water density	γ_w	kN/m^3	10
	Saturated density	γ_{sat}	kN/m^3	18.4

the aim of Italic symbols (Slope angle θ, Porosity n, Characteristic particle size d_{50}, Cohesion c,Internal friction angle φ, Particle density γs, Water density γw, Saturated density γsat) are distinguished primarily from traditional units characters.

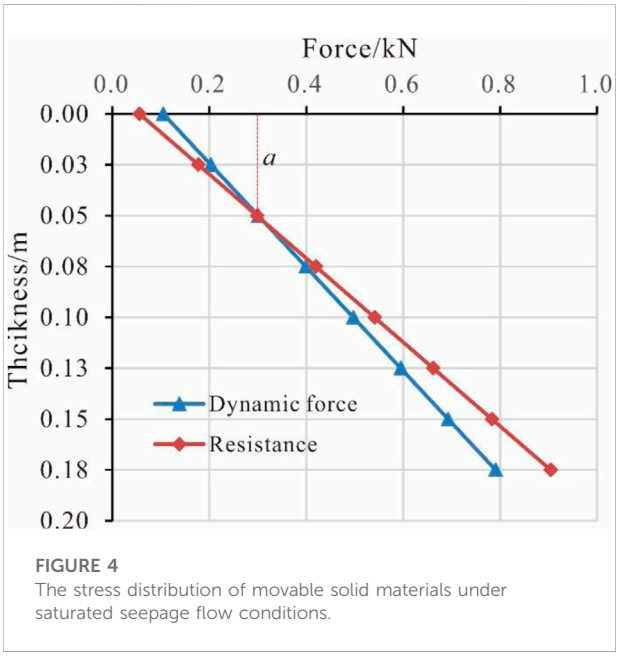


FIGURE 4
The stress distribution of movable solid materials under saturated seepage flow conditions.

$$R = c + [\gamma_{sat}\cos\theta\tan\varphi + (\gamma_s - \gamma_w)(1-n)\cos\theta]d_{50} + (\gamma_{sat} - \gamma_w)z\tan\varphi \quad (17)$$

Results

Stress distribution

The porosity and density are constant when the slope layer contains homogeneous and isotropic particles, so the dynamic force and the resistance vary linearly with depth (i.e., with z). When the slope material consists of heterogeneous particles, the density and the porosity vary with depth, so the dynamic force and the resistance are nonlinear in depth. We assume a slope angle $\theta = 12°$, homogeneous particles of fine sand of characteristic particle size $d_{50} = 3$ mm, porosity $n = 0.3$, cohesion $c = 0$ Pa, an inner friction angle $\varphi = 30°$, a particle layer density $\gamma_s = 22.3$ kN/m^3, and a water density γ_w and a saturated density γ_{sat} of 10.0 and 18.4 kN/m^3, respectively. Table 1 lists all the parameters and their values.

Using the parameters given in Table 1 produces the distribution of dynamic force and resistance along the z direction shown in Figure 4.

From Figure 4, it shows that the dynamic force and resistance of movable solid material under saturated seepage flow are linear in depth. The results show that the critical thickness a of the homogenous layers is approximately 5 cm for these fixed conditions. However, the soil layer composition in natural debris flow watersheds varies and includes soil types such as clay, silt soil, sand, and gravel. Thus, the distribution of the dynamic force and resistance force should increase nonlinearly with depth.

Experiment verification and analysis

We now verify the formulas derived above against experiments carried out in a laboratory using the apparatus shown in Figure 5. This apparatus includes a water tank, flume, circular water pond, and frame. The flume slope can be adjust in different angles, and the flow route of the experiment can be captured from side view of the flume glass; the water pump can provide a constant flow of water from water pond.

Two varieties of sand were used as the experimental materials for the geologic experiments. The parameters of these sands are listed in Table 2. The grain size distributions (1–2 and 2–5 mm) are isotropic. The water content of the sand is less than 3% in each experiment. The pore water pressure is recorded by sensors, the seepage flow discharge is fixed at 440 ml/s and the experimental slope angle is set as given in Table 3.

During the experiments, the sand starts to move as it undergoes seepage-flow infiltration. Each experiment can be stopped in two ways: when a section of sand collapses, or when the sand is stable for more than 5 min. All experiments were recorded by using a video camera.

The flow regime of experiments with different slope angles was recorded in side-view by the video camera, which shows that the sand layer evolves from stable to collapse upon saturation of the seepage flow infiltration (see Figure 6).

Figure 6 shows that, as the saturated seepage flow infiltrates into the sand layer, fine particles less than 2 mm in size move out through the outlet and large particles move after several seconds. Next, the whole layer collapses and the debris flow forms. This is especially apparent at the larger slope angles, such as 12°, 15°, 18°, and 20°. The pore-water sensors record the pore-water pressure. The red, blue, and green curves in Figure 7 show the results of sensors four to six, respectively.

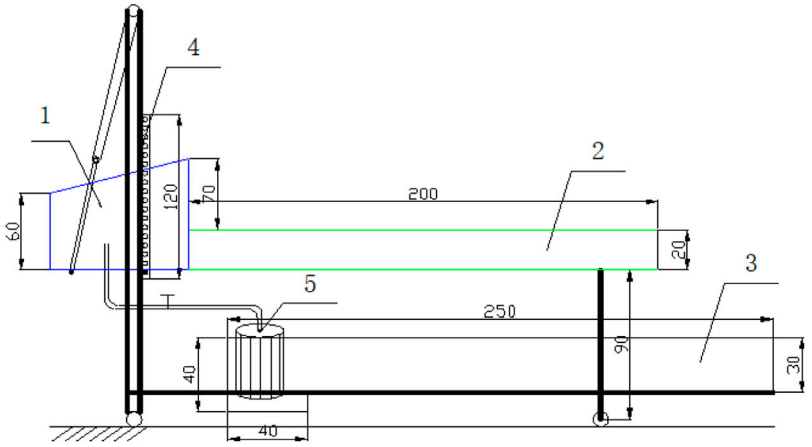


FIGURE 5
Schematic of the experimental setup (units in cm) one water tank, two experiment flume, three circular water pond, four frame, five water pump.

TABLE 2 The experimental sand materials.

Experiment materials	Grain size (mm)	Density (kg/m^3)	Seepage velocity (cm/s)	Friction angle (degree)	Friction angle in water (degree)
sand 1	2–5	2,230	1.0–5.0	13	10
sand 2	1–2	1744	0.0–1.0	15	11

TABLE 3 The experimental conditions.

Grain size (mm)	Discharge (ml/s)	Slope angle (degree)					
1–5	440	6	9	12	15	18	20

In the experiments, the water level in the sand layer rises rapidly and the sensors record significant variations in pore-water pressure with increasing water level, together with sand particle movements on the surface. When the slope angle is less than 12°, the pore-water pressure gradually stabilizes after the water level rises (see Figures 7A–C). The video data show that moving sand particles appear at 50 s and the thickness is less than 0.30 cm. When the slope angle exceeds 12°, sand particles move on the surface as the water level rises but stabilize quickly and then decrease slightly (see Figures 7D–F). In the video, the particle movement began after 30 s, and the thickness increases to over 2.90 cm.

Verification of dynamic expression

The experiment of water flow discharge was set to 440 ml/s and run with six different slope angles: 6°, 9°, 12°, 15°, 18°, and 20°. Since the sand particle size was 2–5 mm, each experimental layer was 0.80 m long by 0.20 m wide, and we assumed that the whole layer was isotropic. In addition, each seepage flow discharge was constant because the experimental conditions were the same. A geotechnical test gave a porosity $n = 0.32$, which was constant. In addition, the position of sand moving in this layer under different slopes was determined by visual interpretation of the experimental images. We then entered the data from the images into Eq. 16 and calculated the driving force under different conditions and compared the calculated results with the pore-water pressure recorded in each experiment. The parameters used in the formulas are given in Table 1, and the experimental and calculated results appear in Table 4. The parameters recorded in the table are the moving thickness for various slopes, the force of gravity exerted on the sand within the moving thickness, the pore-water pressure corresponding to sand motion during the test, and the dynamic theoretical pore-water pressure.

According to the flume experiment record and the calculation by Eq. 16, it can attain the comparison between those two values, seen Figure 8.

From Figure 8, it shows that, with increasing flume slope angle, the seepage force in the sand particles varies. When the slope angle is less (greater) than 15°, the calculated value is



FIGURE 6
The flow regime under different slope angles **(A)** 6°, **(B)** 9°, **(C)** 12°, **(D)** 15°, **(E)** 18°, and **(F)** 20°; the red dots indicate the sensor locations in the center longitudinal section.

smaller (greater) than the experimental value. For saturated seepage, the error analysis gives an error between the experimental and the calculated results from 1.3% to 24.2% percent, which shows that the theoretical results are consistent with the experimental results.

Discussion

Loose solid materials initiated by rainfall and surface flow have been widely researched (Takahashi 2007) and classified as either landslide-transforming type or water-erosion type. Based on hydraulic theory and assuming saturated seepage conditions, we derive dynamic force and resistance formulas that consider the force of gravity and pore-water pressure. Pore-water pressure depends on position and is difficult to measure because the position easily changes when the loose material layer fails. Thus, the model proposed in this work needs to be improved in future research.

Contrast between movable solid material and traditional solid material

The volume of loose solid materials is one of the most important parameters in the design of debris flow prevention (Ministry of Land and Resources of the People's Republic of China, 2006). Many researchers have focused on the solid material content of a debris flow and numerous studies have used the terms of loose solid material, dynamical reserve, and effective solid materials, but the research methods were based on quantitative descriptions, field surveys, and calculations based on experiments. The contrast between movable solid materials and the traditional concept is made evident in Table 5.

Solid material is a defined qualitative concept in traditional debris flow studies, but a definition of what kind of loose content will form a debris flow under specific hydrologic conditions has still not appeared in published research. In practical applications, most volume calculations of loose solid material are based on field survey estimates. The debris-flow dynamical reserve of the

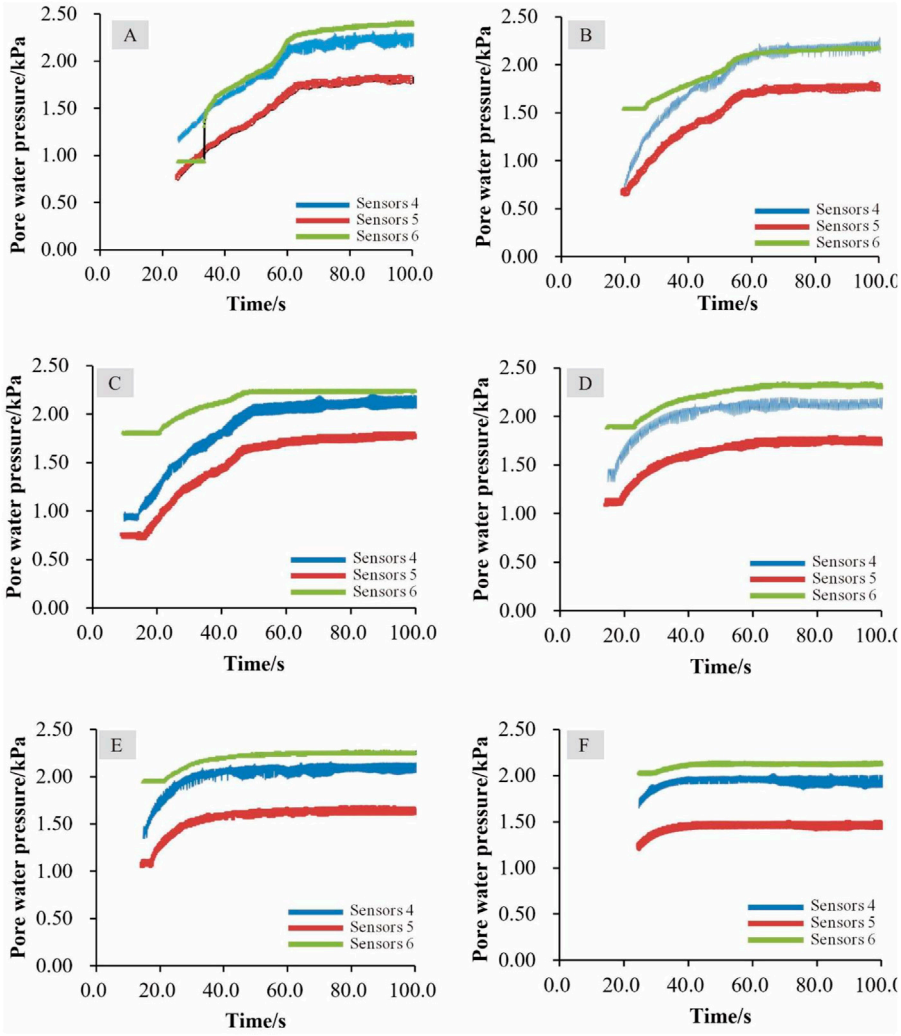


FIGURE 7
Pore-water pressure changes through the experimental process for various slope angles **(A)** 6°, **(B)** 9°, **(C)** 12°, **(D)** 15°, **(E)** 18°, and **(F)** 20°.

TABLE 4 Comparison of experiment value and calculation value under saturated seepage in 60 cm section.

Slope angle (degree)	Flume experiment			Eq. 16 (kPa)
	Thickness at 60 cm section (m)	Gravity component (kPa)	Pore-water pressure record at 60 cm (kPa)	③+④ (kPa)	
①	②	③	④	⑤	⑥
6	0.05	0.097	1.372	1.469	1.336
9	0.05	0.146	1.496	1.642	1.466
12	0.05	0.196	1.508	1.807	1.417
15	0.05	0.247	1.559	1.755	1.544
18	0.05	0.299	1.572	1.819	1.843
20	0.05	0.335	1.600	1.935	2.040

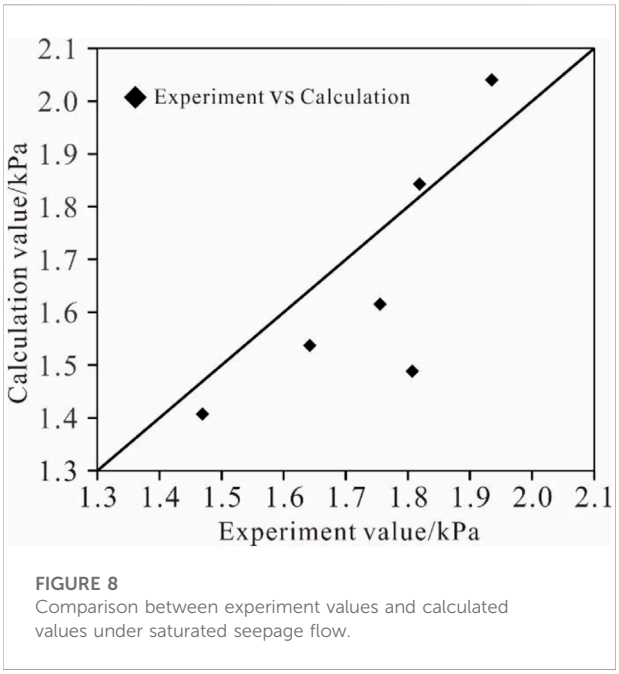


FIGURE 8
Comparison between experiment values and calculated values under saturated seepage flow.

loose solid material volume can be calculated by measuring the length, width, and estimated potential thickness. However, a problem with this approach is that the estimated thickness originated from investigating outside and there is no practical meaning. The thickness should be controlled by the mechanical properties of the solid materials. The effective solid materials concept is defined as the solid material that joins the debris flow because of water, but this concept does not apply in the current example.

The potential movement of loose solid materials down a sloped surface and the quantity of solid material that moves due to rainfall is a mechanical problem that should be treated by propulsion and resistance. As with the analysis above, the dynamic propulsion includes seepage flow, surface flow, and gravity components. The debris-flow dynamic propulsion contributed by rainfall can be calculated based on rainfall, runoff, and convergence for a certain frequency of rainfall. Resistance is due to cohesion, friction, and shear resistance between particles in the soil layer. The concept of a moving solid material is based on mechanical equilibrium, which has a clear physical meaning, in contrast with the traditional definition.

Dynamic characteristics of soil-mechanical and water-mechanical debris flow

Based on the diversity of dynamic characteristics, debris flows can be divided into soil-mechanical and water-mechanical debris flows. With the former, the debris flow moves over the slope, the driving force consists of gravity and the soil shearing force, and the loose soil materials are mainly generated by rock falls and landslides. With the latter, the slope over which the debris flows route is less than 15°, and the driving force comes from hydrodynamics and gravity, so the loose solid material is mainly deposited on the gully sides and at the slope toe in the form of rock avalanches and slope bodies. Currently, significant research has focused on debris-flow initiation in the source area, which is caused by rainfall and surface water, whereas few studies have focused on the characteristics of the loose solid materials of a debris flow area under seepage flow and surface flow. In the latter category, Takahashi (2007) systematically studied the debris flow initiation mechanism in a saturated soil layer with seepage and thin surface water flow.

Field surveys and experiments indicate that loose solid materials are distributed widely in the debris flow watershed, but the area and volume are distributed randomly. Specially, slope materials is one of the important supplies of material for debris flows, field survey show that the slope failures are random and discontinuous in each landslide (Guo et al., 2021). Heterogeneous characteristics are reflected in the wide range of grain sizes and particle densities that depend on the source rock. Anisotropy in porosity, strength, seepage, and rheology means that these parameters also depend on direction. In

TABLE 5 The contrast between movable solid materials and traditional loosen solid materials concept.

Terms	The movable solid materials	Loose solid material	Dynamical reserve	The effective solid materials
Concept	When the sum of the hydrological force and the gravity component are equal to the resistance, the solid is within the critical depth	Loose solid materials distributed in watershed widely	The potential solid materials to form a debris flow in the source area	Loose solid materials of the slope and gully bank fail to move by water saturation and scour, especially to join the next debris flow's solid materials
Volume calculation method	Calculation by mechanical model	Estimate the area and depth in the debris flow watershed	Investigate the area and depth of the potential debris flow watershed	Estimate the area and depth
Mechanical meaning	Mechanical equilibrium	none	none	none

addition, soil-water content and the changeable topographic surface also significantly affect the water confluence, seepage field, and runoff field.

There are two common particle types in loose solid materials: one is coarse particles that constitute the framework of the soil, and the other is fine particles that fill in the pore space of the framework. The stability of the slope is determined by the shear resistance of the coarse particles. Under seepage flow, the fine particles are carried away by the seepage force, which changes the viscosity of the seepage flow. With increasing loss of fine particles, the framework may be destroyed by the shear force. Thus, given abundant loose solid materials in the topography, the seepage force and surface flow mechanics control the layer's destruction form, and the movable thickness and the spatial distribution are determined by the gross volume of the loose solid materials.

Conclusion

Loose solid materials transform into debris flows under the seepage flow effect is one of the most common natural disasters in mountainous areas. The high frequency of debris flow events in the rainy season pose significant risk to local people's lives and properties and require rehabilitation and reconstruction scientifically.

Water and loose solid materials are essential components of a debris flow. Based on the principle of mechanical equilibrium, this work defines movable solid materials and expresses clearly the movable characteristics of a debris flow firstly. Movable solid materials become relevant when the dynamic force is greater than the resistance, which define with the critical depth.

Taking saturated seepage flow as an example, a geologic model is set up and a mechanical analysis is carried out. A dynamic force formula and a resistance formula are derived based on specific conditions. When the geologic model is homogenous and the seepage flow saturates the whole debris layer, the dynamic force and resistance increase linearly with depth for the given parameters.

Mechanical analysis and laboratory experiments show that fine sand particles are carried out of the layers by seepage water flow and that the pore-water pressure is a vital driving force, which confirms the results of previous research, especially when the slope angle exceeds 12°. Comparing the experimental results with the calculated results under saturated seepage flow reveals a discrepancy of 1.3%–24.2% for the assumed conditions, showing that the calculated results are suitably accurate.

By considering the concepts, calculations, and mechanics of traditional solid materials and movable solid materials, we conclude that the motion of loose solid materials due to hydrodynamic forces is a mechanical problem rather than the traditional problem of qualitative description and estimation. Thus, further study of movable solid materials in complex dynamic condition is required.

Data availability statement

The original contributions presented in the study are included in the article/supplementary material, further inquiries can be directed to the corresponding author.

Author contributions

SY carried out experiment design, data analysis and manuscript writing. MG taken the experiment, participated in the discussion and decision-making process. JJ taken out of the experiment and discussion in advance. TS writing reviewing. KC carried out the manuscript editing and supervision. All the authors participated and contributed to the final manuscript.

Funding

This research work was supported by the Talent Introduction Program of Xihua University (Grand No. Z211016), the Opening Foundation of Key Laboratory of Geohazard Prevention of Hilly Mountains, Ministry of Natural Resources (Grant No. FJKLGH 2022K005) and the National Natural Science Foundation of China (Grant No. 41502330).

Conflict of interest

The authors declare that the research was conducted in the absence of any commercial or financial relationships that could be construed as a potential conflict of interest.

Publisher's note

All claims expressed in this article are solely those of the authors and do not necessarily represent those of their affiliated organizations, or those of the publisher, the editors and the reviewers. Any product that may be evaluated in this article, or claim that may be made by its manufacturer, is not guaranteed or endorsed by the publisher.

Acknowledgments

The authors appreciate the editors and reviewers for their critical and valuable comments and suggestions that greatly helped us to improve the present manuscript. We would also like to thank Charlesworth Author Services [https://www.cwauthors.com.cn] for English language editing work.

References

Carey, J., Cosgrove, B., Norton, K., Massey, C. I., Petley, D. N., and Lyndsell, B. (2021). Debris flow-slide initiation mechanisms in fill slopes, Wellington, New Zealand. *Landslides* 18, 2061–2072. doi:10.1007/s10346-021-01624-6

Carey, J., Massey, C., Lyndsell, B., and Petley, D. (2019). Displacement mechanisms of slow-moving landslides in response to changes in pore water pressure and dynamic stress. *Earth Surf. Dynam.* 7 (3), 707–722. doi:10.5194/esurf-7-707-2019

Chen, H., Dadson, S., and Chi, Y.-Q. (2006). Recent rainfall-induced landslides and debris flow in northern Taiwan. *Geomorphology* 77, 112–125. doi:10.1016/j.geomorph.2006.01.002

Chen, N., Gao, Y., Yang, C., and Hu, G. s. (2018). Effect of clay content to the strength of gravel soil in the source region of debris flow. *J. Mt. Sci.* 15, 2320–2334. doi:10.1007/s11629-018-4911-8

Chen, N., Zhou, W., Yang, C., Hu, G., Gao, Y., Han, D., et al. (2010). The processes and mechanism of failure and debris flow initiation for gravel soil with different clay content. *Geomorphology* 121 (3-4), 222–230. doi:10.1016/j.geomorph.2010.04.017

Cui, P., Hu, K., Zhuang, J., Yang, Y., and Zhang, J. (2011). Prediction of debris flow danger area by combining hydrological and inundation simulation methods. *J. Mt. Sci.* 8 (1), 1–9. doi:10.1007/s11629-011-2040-8

Dahal, R., Hasegawa, S., Nonomura, A., Yamanaka, M., Masuda, T., Nishino, K., et al. (2009). Failure characteristics of rain fall-induced shallow landslides in granitic terrains of Shikoku Island of Japan. *Environ. Geol.* 56 (7), 1295–1310. doi:10.1007/s00254-008-1228-x

Degetto, M., Gregoretti, C., and Bernard, M.(2015). Comparative analysis of the differences between using LiDAR and contour-based DEMs for hydrological modeling of runoff generating debris flows in the Dolomites. *Front. Earth Sci.* 49 3, 21. doi:10.3389/feart.2015.00021

Emmanuel, J., and Simon, M. (2006). The mobilization of debris flows from shallow landslides. *Geomorphology* 74, 207–218. doi:10.1016/j.geomorph.2005.08.013

Guo, C., and Cui, Y. (2020). Pore structure characteristics of debris flow source material in the Wenchuan earthquake area. *Eng. Geol.* 267 (1), 105499. doi:10.1016/j.enggeo.2020.105499

Guo, X., Li, Y., Cui, P., Yan, Y., Wang, B., Zhang, J., et al. (2021). Spatiotemporal characteristics of discontinuous soil failures on debris flow source slopes. *Eng. Geol.* 295, 106438. doi:10.1016/j.enggeo.2021.106438

Hossein, G., and Soheil, G. (2008). Stability of sandy slopes under seepage conditions. *Landslides* 5, 397–406. doi:10.1007/s10346-008-0132-5

Hu, W., Dong, X., Wang, G., van Asch, T., and Hicher, P. (2016). Initiation processes for run-off generated debris flows in the Wenchuan earthquake area of China. *Geomorphology* 253, 468–477. doi:10.1016/j.geomorph.2015.10.024

Hu, W., Xu, Q., Wang, G., van Asch, T., and Hicher, P. (2015). Sensitivity of the initiation of debris flow to initial soil moisture. *Landslides* 12, 1139–1145. doi:10.1007/s10346-014-0529-2

Iverson, R., and Schaeffer, D. (2004). Regulation of landslide motion by dilatancy and pore-pressure feedback. AGU Fall Meeting, 273–280.

Li, Q., Huang, D., Pei, S., Qiao, J., and Wang, M. (2021). Using physical model experiments for hazards assessment of rainfall-induced debris landslides. *J. Earth Sci.* 32, 1113–1128. doi:10.1007/s12583-020-1398-3

Li, X., Huang, X., and Zhang, Y. H. (2021). Spatio-temporal analysis of groundwater chemistry, quality and potential human health risks in the Pinggu basin of North China Plain: Evidence from high-resolution monitoring dataset of 2015–2017. *Sci. Total Environ.* 800, 1495568. doi:10.1016/j.scitotenv.2021.149568

Liu, J., You, Y., Chen, X., and Fan, J. (2010). Identification of potential sites of debris flows in the upper Min River drainage, following environmental changes caused by the Wenchuan earthquake. *J. Mt. Sci.* 3, 255–263. doi:10.1007/s11629-010-2017-z

Mao, C., and Duan, X. (2009). On seepage forces and application. *Rock Soil Mech.* 30 (6), 1569–1574. (in Chinese). 10.00-7598(2009)06-1569-07.

McCoy, S., Kean, J., Coe, J., Tucker, G., Staley, D., Wasklewicz, T., et al. (2012). Sediment entrainment by debris flows: *In situ* measurements from the headwaters of a steep catchment. *J. Geophys. Res.* 117 (F3). doi:10.1029/2011jf002278

Ministry of Land and Resources of the People's Republic of China (2006). *Specification of geological investigation for debris flow stabilization*. DZ\T 0220. Beijing: Ministry of Land and Resources of the People's Republic of China. (in Chinese).

Qiao, J., Huang, D., and Yang, Z. (2012). Statistical method on dynamic reserve of debris flow's source materials in meizoseismal area of wenchuan earthquake region. *Chin. J. Geol. Hazard Control* 23 (02), 1–6. (in Chinese). doi:10.3969/j.issn.1003-8035.2012.02.001

Richard, M. (2005). Regulation of landslide motion by dilatancy and pore pressure feedback. *J. Geophys. Res.* 110 (F2), F02015. doi:10.1029/2004JF000268

Sassa, K., Fukuoka, H., Wang, G., and Ishikawa, N. (2004). Undrained dynamic-loading ring-shear apparatus and its application to landslide dynamics. *Landslides* 1 (1), 7–19. doi:10.1007/s10346-003-0004-y

Takahashi, T. (2007). *Debris flow: Mechanics, prediction and countermeasures*. London, UK: Taylor and Francis Group, 33–101.

Tang, C., Li, W., and Ding, J. (2011). Field investigation and research on giant debris flow on august 14, 2010 in yinxiu town, epicenter of wenchuan earthquake. *Earth Science-Journal China Univ. Geosciences* 36 (1), 172–180. (in Chinese). doi:10.3799/dqkx.2011.018

Wang, G., and Sassa, K. (2003). Pore-pressure generation and movement of rainfall-induced landslides: Effects of grain size and fine-particle content. *Eng. Geol.* 69, 109–125. doi:10.1016/S0013-7952(02)00268-5

Wang, J., Cui, P., Wang, H., Zhang, G., Zou, Q., Chen, X., et al. (2022). Novel approach to estimating glacial moraine reserves in the Parlung Tsangpo basin. *Front. Earth Sci.* 10, 853089. doi:10.3389/feart.2022.853089

Xu, Q. (2010). The 13 august 2010 catastrophic debris flows in sichuan province: Characteristics, genetic mechanism and suggestions. *J. Eng. Geol.* 18 (5), 576–608. (in Chinese). doi:10.04-9665/2010/18(5)-0596-13

Yang, S. (2014). *Study on the movable critical model of solid materials under hydro-dynamical condition in debris flow area*. Beijing: University of Chinese Academy of Sciences, 2–4. (in Chinese).

Zhang, Y. H., Dai, Y. S., Wang, Ying, Huang, X., Xiao, Y., Pei, Q. M., et al. (2021a). Hydrochemistry, quality and potential health risk appraisal of nitrate enriched groundwater in the Nanchong area, southwestern China. *Sci. Total Environ.* 2021, 784147186. doi:10.1016/j.scitotenv.2021.147186

Zhang, Y. H., He, Z. H., Tian, H. H., Huang, X., Zhang, Z. X., Liu, Y., et al. (2021b). Hydrochemistry appraisal, quality assessment and health risk evaluation of shallow groundwater in the Mianyang area of Sichuan Basin, southwestern China. *Environ. Earth Sci.* 80 (17), 576. doi:10.1007/s12665-021-09894-y

Zhou, G. (2014). Effect of pore water pressure on the triggering and mobilization of landslides. *Chin. J. Nat.* 36 (5), 11325–11335. (in Chinese). doi:10.3969/j.issn.0253-9608.2014.05.003

frontiers | Frontiers in Earth Science

METHODS
published: 15 July 2022
doi: 10.3389/feart.2022.918285

Lithology-Based 3D Modeling of Urban Geological Attributes and Their Engineering Application: A Case Study of Guang'an City, SW China

Fang Zhou[1], Minghui Li[1]*, Congjun Huang[1], Hong Liang[1], Yujie Liu[1], Jianlong Zhang[1], Baodi Wang[2] and Ming Hao[3]*

[1]Department of Geological Information, Chengdu Center, China Geological Survey, Chengdu, China, [2]Department of Fundamental Geological, Natural Resources Aerial Geophysical and Remote Sensing Center of China Geological Survey, Beijing, China, [3]Department of Geological Information, Research Center of Applied Geology of China Geological Survey, Chengdu, China

OPEN ACCESS

Edited by:
Yunhui Zhang,
Southwest Jiaotong University, China

Reviewed by:
Qiqiang Ren,
Chengdu University of Technology, China
Zhaoliang Li,
Natural Resources Aerial Geophysical Exploration and Remote Sensing Center of China Geological Survey, China
Wu Zhichun,
East China University of Technology, China

***Correspondence:**
Fang Zhou
791630163@qq.com
Minghui Li
Lmh680408@163.com

Specialty section:
This article was submitted to Geohazards and Georisks, a section of the journal Frontiers in Earth Science

Received: *12 April 2022*
Accepted: *30 May 2022*
Published: *15 July 2022*

Citation:
Zhou F, Li M, Huang C, Liang H, Liu Y, Zhang J, Wang B and Hao M (2022) Lithology-Based 3D Modeling of Urban Geological Attributes and Their Engineering Application: A Case Study of Guang'an City, SW China. Front. Earth Sci. 10:918285. doi: 10.3389/feart.2022.918285

Urban geological modeling (UGM) is a fundamental approach for the visualization of underground space and recognition of complex geological conditions of a city. Previous UGM studies, with the assumption of homogeneous geological characteristics, have resulted in deviated modeling properties due to the negligence of parameters with obviously different spatial distributions in lithologies. This study presents a case study of Guang'an city in SW China by using a sequential simulation interpolation (SSI) method that reflects geological heterogeneity by combining field surveys, topography, borehole data, geological profiles, and stratigraphic columns to establish a lithology distribution model in the study area. The geotechnical attribute model of the area of interest was established based on lithology to capture subtle variations in lithology due to obvious differences in geotechnical characteristics of clay, sand, mudstone, sandy mudstone, and shaly sandstone. This 3D model could provide a reference for the urban underground space master planning and future sustainable development of Guang'an city. In addition, this study also discusses the prospects and directions of urban geological modeling and provides a few suggestions for engineering in urban areas.

Keywords: urban geological modeling, urban underground space, sequential simulation interpolation, geotechnical attribute model, Guang'an city

INTRODUCTION

Urban areas are the priority place where people gather and anthropogenic activities occur. It is estimated that over 70% of the world's population will be living in urban areas by 2050 (Price et al., 2018; Zhang et al., 2021b). Rapid urbanization has put massive pressure on land use and environmental optimization and has brought enormous challenges to urban master planning and sustainable development. These are forcing urban designers and administrators to take action to alleviate environmental pressure caused by population explosion and to assess new suitable spaces for future development.

Abbreviations: AHP, analytic hierarchy process; DEM, digital elevation model; MUGM, most unfavorable grade method; SGS, sequential Gaussian simulation; SIS, sequential indicator simulation; SSI, sequential simulation interpolation; TIN, triangulated irregular network; UGM, urban geological modeling; UUS, urban underground space.

Urban underground space (UUS) is a potential space that can be adapted to surface architecture and conditions and has attracted increasing attention worldwide as a promising way to address human-land conflicts, big city diseases, and future sustainable development problems. Proper use of UUS could make most of the available space and mitigate the potential interactions between the existing and planned objects (Li et al., 2021).

Distinct from the urban surface, UUS is fragile and vulnerable to damage during the development and utilization due to its geological features (Zhu et al., 2016), which would experience permanent and irreversible changes once utilized. Also, irrational development often leads to irregular arrangement of underground structures, which could cause safety issues, such as geological hazards like collapse and seepage (Tan et al., 2021). Therefore, it is crucial to identify the urban geological features before the utilization of UUS (Liao et al., 2006).

The advancement of computer processing speed and visualization methodology has enabled geologists to reveal the geology of UUS in an easy-to-read format through two-dimensional (2D) mapping and three-dimensional (3D) visualization. 2D mapping based on the GIS platform is mainly used for surface and subsurface UUS surveys worldwide (Dai et al., 2001; Xiong et al., 2006; El May et al., 2010; Hou et al., 2016; Peng and Peng, 2018; Andriamamonjisoa and Hubert-Ferrari, 2019; Zhou et al., 2019; Li et al., 2020; Mao et al., 2020), which could integrate geological factors with groundwater, geothermal, and geological materials (Doyle, 2016; Andriamamonjisoa and Hubert-Ferrari, 2019; Zhou et al., 2019). Combined with evaluation methods such as the analytic hierarchy process (AHP) and the most unfavorable grade method (MUGM), a comprehensive multielement qualitative to semi-quantitative UUS assessment model could be constructed (Guan et al., 2008; Peng et al., 2010; Liu et al., 2011; Peng and Peng, 2018). 3D modeling is an advanced visualization of these factors in UUS survey (Thierry et al., 2009; Tame et al., 2013; Mielby and Sandersen, 2017; He et al., 2020). It is characterized by the reflection of survey depth on the z-axis and spatial coupling of geological bodies, which has become a popular technique, gradually replacing 2D mapping in UUS survey, although its direct use may come from derived 2D map outputs (Price et al., 2018). However, previous studies using this approach may have considered geological features to be homogenous rather than heterogeneous, which could produce deviations in the geotechnical properties. Therefore, when modeling the attributed characteristics of geotechnical properties, caution should be taken in the selection of the interpolation method, the recognition of geological heterogeneity, and variations of small-scale vertical lithology to minimize the possible modeling deviations.

This study introduced the concepts of geological modeling based on the workflow in the GOCAD (version 2017) platform and proposed the proper selection of the interpolation method for lithology and geotechnical properties based on the available 2D/3D datasets. Sequential indicator simulation (SIS) that depicts the lithological spatial distribution and provides a zonal basis for attribute parameter models was chosen to build the 3D lithology model. Accordingly, small-scale variations in lithology with the lengths of the cores were revealed by collecting lithology data from 38 nonprofit boreholes distributed in the study area (**Figure 1**).

The attribute model of geotechnical properties based on the zonation of lithology was constructed using the sequential Gaussian simulation (SGS) method, which reveals distribution characteristics of geological conditions. Furthermore, 2D information derived from 3D geological and geotechnical properties was presented for UUS optimization and urban master planning.

3D MODELING METHODOLOGY

Introduction to Geostatistics Interpolation

Geostatistics is a powerful technique to estimate unknown values in a specific field based on the available data by interpolation, which is the core of the system (Hou, 1996; Hou, 1997; Hu, 2007). A proper interpolation method could reduce the deviation of interpolation results when building 3D geological models and is thus crucial for geologists and modelers to get reliable results.

Kriging and SSI are the most commonly adopted interpolation tools in 2D mapping and 3D modeling, respectively. In particular, the application of Kriging has been widely used in the fields of geology, oil, mining, and atmosphere (Wycisk et al., 2009; Yan et al., 2011; Yu et al., 2013). Theoretically, kriging takes regionalized variables as the core variables and attempts to obtain the best, unbiased, and minimum variance interpolation results (Xin et al., 1997), which indicate deterministic mapping or modeling results. The interpolation is merely from the initial available data using correlation defined by variograms (or semi-variograms). Comparing SSI against Kriging, SSI transforms data to a standard normal distribution; a value is randomly drawn from the normal distribution, and then the value and original data are used to interpolate (Rahimi et al., 2018). After that, the simulated values are then back-transformed to the reference distribution to acquire the real value.

The differences between Kriging and SIS demonstrate distinct application scenarios. SSI highlights the potential to respond to the heterogeneity and uncertainty of rocks and soils that show different geotechnical properties varying with positions (Asghari et al., 2009). The interpolation results of SSI are less smooth than those of the kriging method due to the mathematical logic (Liu et al., 2018), which corresponds to the underground distribution of geological bodies.

Therefore, kriging is suitable for small-scale and data-rich situations, whereas SSI is a better stochastic approach for urban geological modeling (UGM), especially for regions with uneven data distribution and large-scale modeling. Modeling using SSI instead of the kriging method could minimize the deviations of modeling and maintain a better intensity of global spatial variation (Hu, 2007; Zhao et al., 2010).

Sequential Simulation Interpolation Parameter Settings

The semi-variogram model is crucial to SSI; thus, the parameter settings of the semi-variogram model affect the reliability of modeling results. There are two sections in the semi-variogram model that represent spatial correlation in

TABLE 1 | Empirical formulas in parameter settings.

Formula section	Variable	Key factor	Formula for key factors
Vertical	Average points of the well (ANPW)	Number of lags (NLV)	min (100, (ANPW)/2)
	Average height of the well (AH)	Lag distance (LD)	AH/(2* NLV)
Areal	Minimum x distance between wells (mXD)	Number of X columns (NXC)	min (MXD/mXD+1,100)
	Minimum y distance between wells (mYD)	Number of Y columns (NYC)	min (MYD/mYD+1,100)
	Maximum x distance between wells (MXD)	Number of lags (NLA)	Max (NXC,NYC)
	Maximum y distance between wells (MYD)	Lag distance (LD)	Max (MXD, MYD)/NLA

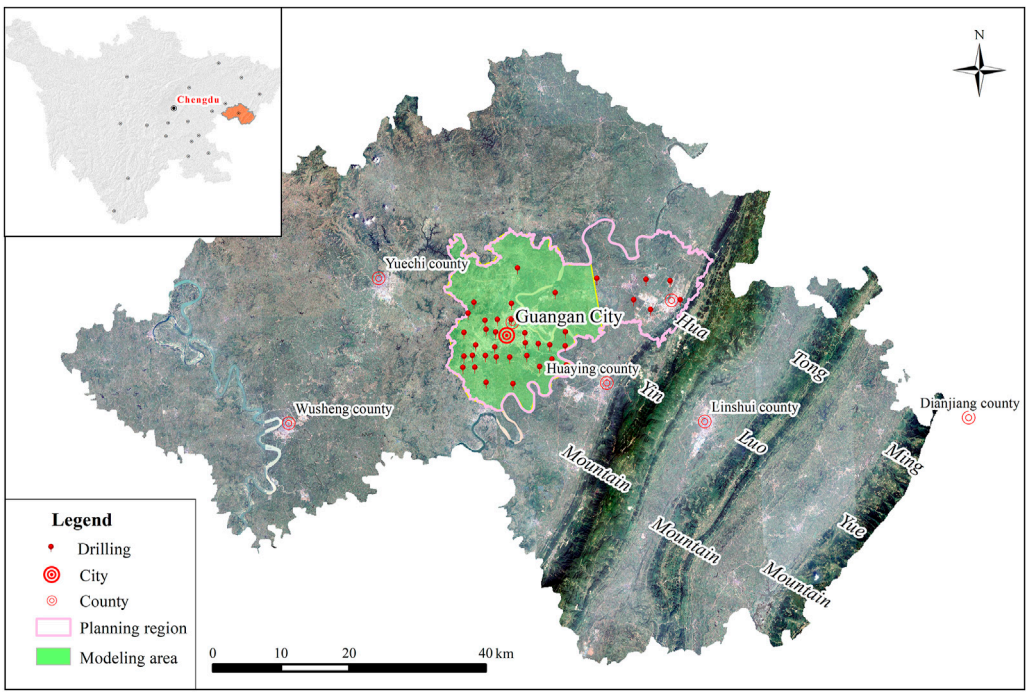


FIGURE 1 | Location of Guang'an city and the modeling area.

vertical and areal sectors, respectively. The key factors of the parameter setting consist of lag distance, number of lags, tolerance, bandwidth, direction, range, and sill. Lag distance and the number of lag computation based on data characteristics using empirical formulas are shown in **Table 1**. Tolerance and bandwidth are automatically calculated based on the lag distance and data characteristics. The direction, range, and sill are defined in the experiment by calculating the distance vs. semi-variance of data pairs which respond to the spatial correlation of input data. Direction and relevant range will be set when the semi-variance of data pairs sustains the longest distance in a particular direction. Sill is defined when the semi-variance of data pairs reaches a steady state in distance. **Figure 2** demonstrates the case of the sand lithology semi-variogram model. The major direction was set to 45°, and the minor direction was set to 135° because semi-variance of data pairs sustains the longest distance in 45°. The corresponding range is set to 3,400 and 3,000 m; the sill value is set to about 0.2 where the semi-variance roughly remains constant along distance.

3D Geological Modeling Workflow

The GOCAD platform, initially designed for reservoir modeling and sedimentary formation, is compatible with UGM and mining modeling to meet the increasing requirements of diverse modeling tasks. This package provides tools for geologists to construct UUS models with pure data or multifactor datasets, including borehole data, 2D boundaries, cross sections, and seismic data (Zhou et al., 2020). Furthermore, regardless of data density, this package is capable of establishing a desired model covering all available data in the workflow, which is characterized by streamlining steps.

In general, the modeling workflow includes four steps (**Figure 3**). First, the available datasets for the tasks are gathered, analyzed, and sorted out. Second, contact relationships of strata are classified into conformable, eroded, baselap, and unconformable. Third, all strata data are imported to

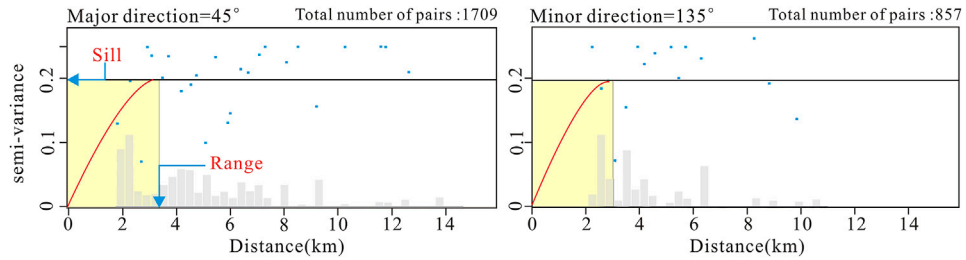


FIGURE 2 | Semi-variogram model of sand.

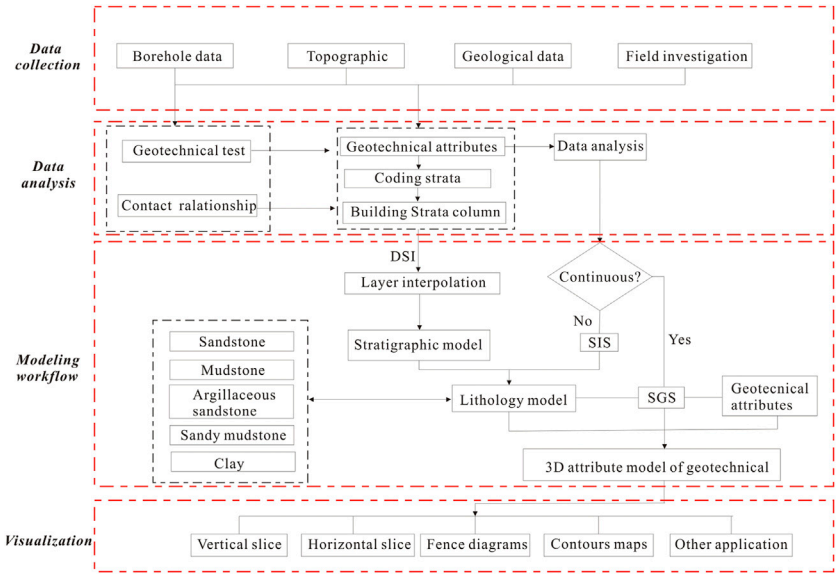


FIGURE 3 | Workflow of 3D geological modeling.

the workflow to produce a triangulated irregular network (TIN) surface of formations using the discrete smooth interpolation (DSI) method. Then, a fault framework is constructed, and contact relationships are revised based on the formation ages of faults. Finally, a specific grid size is set up, and a geological model is established by superposing strata and faults together.

Once the geological model is produced, the property model can be combined with the dataset through streamlining steps. First, properties from the borehole data are analyzed and classified, and thus, semi-variograms that reflect the spatial variability of different properties are built, respectively. Second, a lithology model is established based on the rock classification using SIS, an SSI method designed for a discrete dataset. Finally, a property model is constructed based on lithology zonation using SGS; an SSI method was designed for continuous datasets, such as porosity and permeability.

The workflow offered by GOCAD software not only improves the modeling speed but also ensures conflict-free processing of the multi-source datasets and precise modeling results.

3D MODELING AND RESULTS

Geological Setting

Guang'an city is situated at the junction of Sichuan province and Chongqing city and has lower elevations in the west than in the east (**Figure 1**) (Zhang et al., 2021a). It spans two different natural geographic regions, the red soil hilly area of Sichuan and the lower mountain area of the Huaying Mountain, and belongs to the Upper Yangtze platform and the Central Sichuan depression (Wei et al., 2017). The area is characterized by weak active fractures, with low magnitude seismic activity mainly in the eastern part. The Cambrian, Ordovician, Silurian, Carboniferous, Permian, Triassic, Jurassic, and Quaternary strata are exposed in the study area with gentle dip angles (1–5°). The most widely distributed Jurassic Shaximiao Formation (J_2s) of 400–500 m thickness shows moderate to strong weathering (**Figure 4**). Interlayered and lenticular sand and mudstone account for about 80% of the entire outcrop.

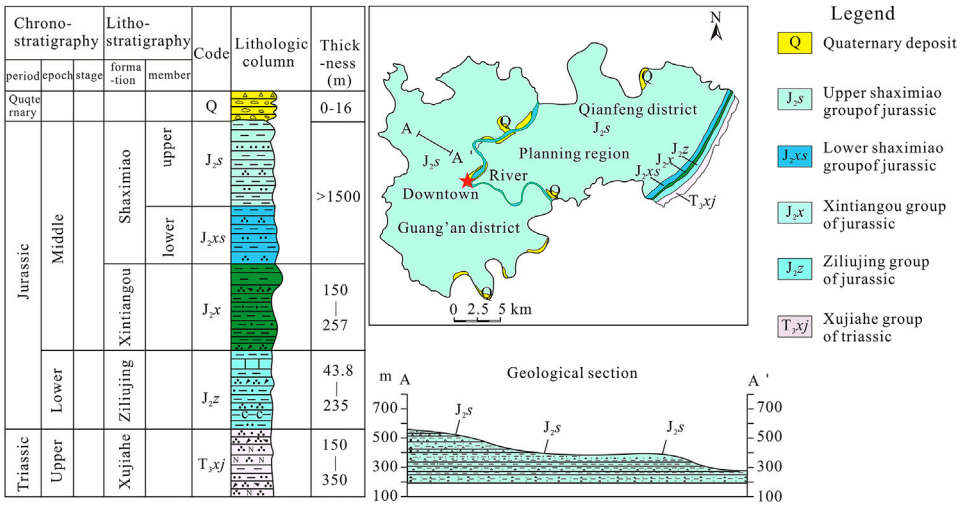


FIGURE 4 | Simplified geological map of the study area.



FIGURE 5 | Geotechnical unit classification of the Shaximiao Formation (J_2s) in the study area.

Introduction to Modeling Raw Data

The modeling raw data are composed of boreholes, DEM, and geological section in this study.

Boreholes could offer reality intrusive investigation data which are vital to construct a reliable geological model. The stratigraphic and attribute modeling data are primarily derived from 38 nonprofit boreholes distributed in the study area. Wells are scattered in the planning region of Guang'an city and primarily located in the west region. Altitude and depth vary from 409 to 236 m and from 120.4 to 50 m. All the wells were drilled vertically,

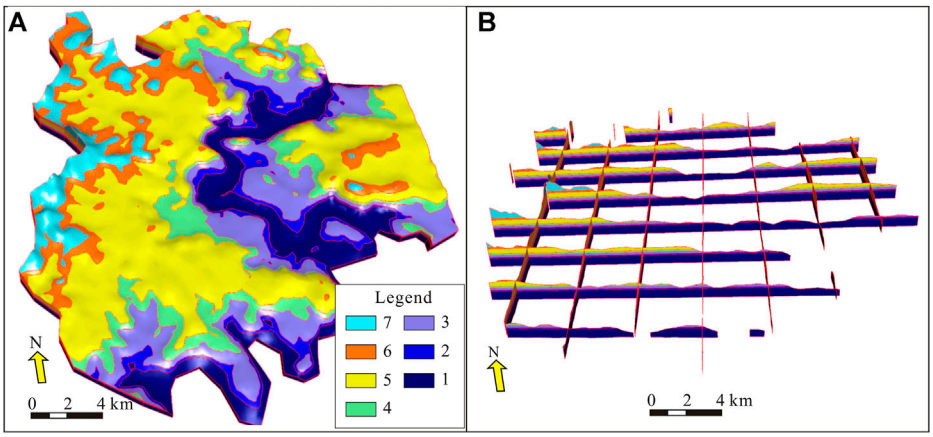


FIGURE 6 | 3D Geological model of Guang'an city **(A)** and fence diagram **(B)**.

and coring was performed along the whole well section. Lengths of coring are between 0.3 and 0.7 m. The mechanical experiment of coring was performed in two qualified companies located in Sichuan and Chongqing. Tensile strength and shear strength experiments were implemented by the southern construction engineering testing corporation in Chongqing, and other attribute experiments were accomplished by the geological engineering exploration institute corporation in Sichuan. Specific attribute experiments in one coring sample, which were carried out more than once, were averaged for attribute modeling, such as compression strength and tensile strength.

The geological section was adopted to provide a whole picture of the stratum to support stratigraphic stratification. In this study, a geological section was surveyed in the northwest area in the study area, (**Figure 4**) and it ranges from 510 to 253 m in altitude. The outcrops of the section only consist of the Shaximiao (J_2s) Formation. Therefore, stratigraphic stratification was implemented according to the proportion and rhythm of sand and mudstone in the outcrop.

DEM provides the surface shape of the model. DEM data were downloaded from the public Google earth map with 30 m resolution in the .tiff format, which covered the whole Guang'an city, and was converted to the .dat format for modeling in a GIS-based platform.

Stratigraphic Modeling

To perform stratigraphic modeling, the priority task is to stratify and construct a stratigraphic column. The Jurassic Shaximiao Formation (J_2s), as the primarily exposed formation in the study area, is dominated by sand and mudstone with insignificant stratigraphy, but lithostratigraphy offers a way to correlate and group similar geological layers, according to their assemblage, geotechnical properties, and geological evolution history. It is combined with the gentle occurrence and geological section survey of the strata. Stratigraphic stratification was rationale marked for the Shaximiao (J_2s) Formation. Thus, the Shaximiao (J_2s) Formation can be divided into seven geotechnical units and named from one to seven in altitude from 450 to 200 m (**Figure 5**). The stratigraphic column which constrains the vertical deposition sequence of the seven units was established. In the column, the contact relationship is set to be conformable due to the absence of sedimentary gaps between those units. The surface digital elevation model (DEM) obtained from Google Earth is used to represent surface to cover the available datasets, with the contact relationship with geotechnical units set to be eroded. Fracture is rare in the study area and was thus not included in the workflow.

On the basis of the abovementioned work, TIN surfaces of units were possible to construct. DSI was employed in the process to generate the TIN surfaces, and the stratigraphic mark was used as "hard" data to constrain the depth of the surfaces. A GIS-based outline of the modeling area was adopted to constrain the extension and shape of the model. The top and bottom of the stratigraphic model were set to 600 and 150 m in altitude, respectively, to include all the above-mentioned datasets. The resolution of the model was set distinctively to satisfy the data interpolation requirement. Horizontal grid cells were set to 200 m × 200 m to reduce the number of grids and processing time. Vertical grid cells set to 1 m for unit 7 to unit 2 and 5 m for unit 1. Since most borehole data were between unit 7 and unit 2, they require a higher resolution for further attribute interpolation than unit 1 (**Figure 6**).

The whole stratigraphic modeling process mentioned in this section is illustrated in **Figure 3**.

Lithology and Engineering Geological Modeling

Inferior lithology was ignored in the previous geological modeling. The dominant lithology in the units or layers was adopted to represent the units or layers, which skipped subtle vertical lithological changes. This study transformed the lithology to a logging curve format and classified them into five categories of clay, sand, mudstone, shaly sandstone, and sandy mudstone

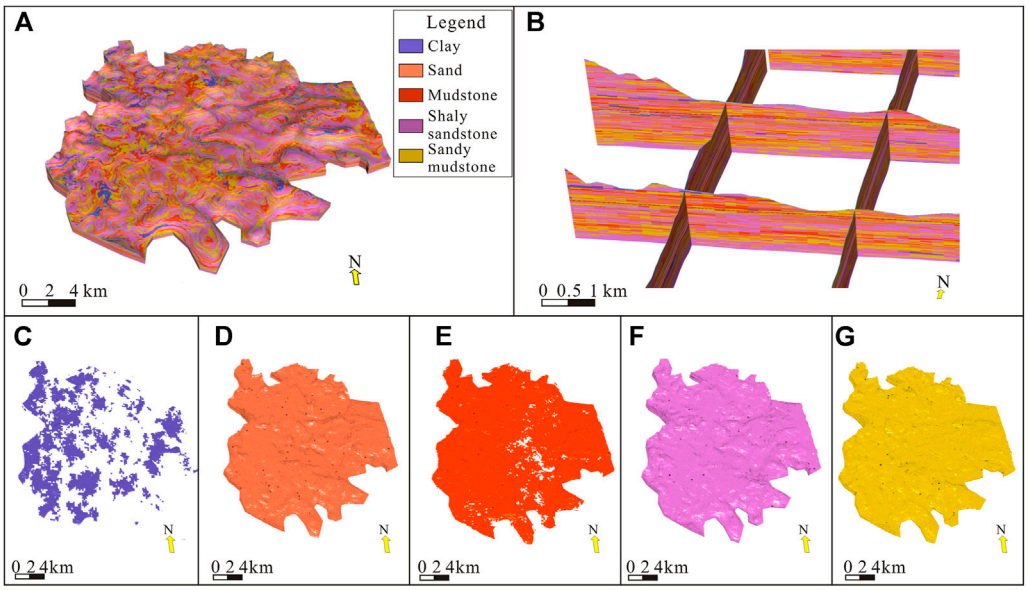


FIGURE 7 | Lithology model **(A)**, fence diagram **(B)**, and lithology distribution of the research area **(C,D,E,F, and G)**.

based on the coring length without neglecting small-scale lithological changes.

Furthermore, the lithology curves were upscaled to the high vertical resolution grids as mentioned earlier; combined with the SIS method and semi-variogram, the lithology model (**Figure 7**) could be established following the workflow introduced previously. This approach could capture subtle vertical changes in lithology and make full use of core data, effectively refining the lithology modeling.

After lithology modeling, it is possible to produce the attribute of geotechnical properties from the borehole records. In Guang'an city, each property, such as porosity, cohesion, and permeability, was established, respectively, due to the different geological characteristics between lithologies. The process of property modeling is similar to that of lithology modeling. Interpolation employed in property modeling (**Figure 8**) was SGS because geotechnical logging data were considered to be continuous rather than discrete.

DISCUSSION

Borehole and topographic data were adopted to produce the initial 3D urban geological model of Guang'an city. Based on the high-resolution urban geological model, lithologies of clay, sand, mudstone, shaly sandstone, and sandy mudstone and 12 geotechnical properties were modeled. Horizontal (**Figure 9**) and vertical slices of these models described previously were set to demonstrate the extension of geological bodies. The lithology and property variations with depth and the underground geology conditions were thus revealed. Importantly, the geotechnical model and derived 2D outputs provide the potential for the qualitative or quantitative assessment of UUS combined with the evaluation methods such as AHP or numerical simulation. More details of implication are discussed below:

Visualization

Visualization is the primary application of the 3D geological model. In contrast to the traditional GIS-based illustrations that are constrained in a fixed 2D-scene, the 3D geological model offers the ability to rotate the model in real 3D space from the surface to certain depth, which reveals the panorama of the study area. Meanwhile, fence diagrams, cross sections, and 2D slice extracts from the model present the extension and tendency of geobodies where investigation data are absent.

Furthermore, fence diagram, cross sections, 2D slices, and artificial construction could be coupled in the geological model to detect possible spatial distribution conflicts. Specifically, it is vital to underground artificial construction, such as tunnel construction. The model could provide measurable packages of hazardous geobodies (faults and gypsum) that have major effect on cost and safety in tunnel construction which could mitigate waste of space in tunnel construction by offering precise coordinates of these hazardous geobodies at the planning phase of tunnel construction.

Statistics and Simulation

The geological model is the visualization of numerals and data from multisource investigation. Therefore, it is essentially measurable and statistical of all the elements that are consisted in the geological model. Statistics of the geological model could offer the overall picture of features that interest the users of the model.

Mostly mentioned urban geological model statistics characteristics including area, volume, distance, and curvature could be accomplished by the statistic of stratigraphic structure

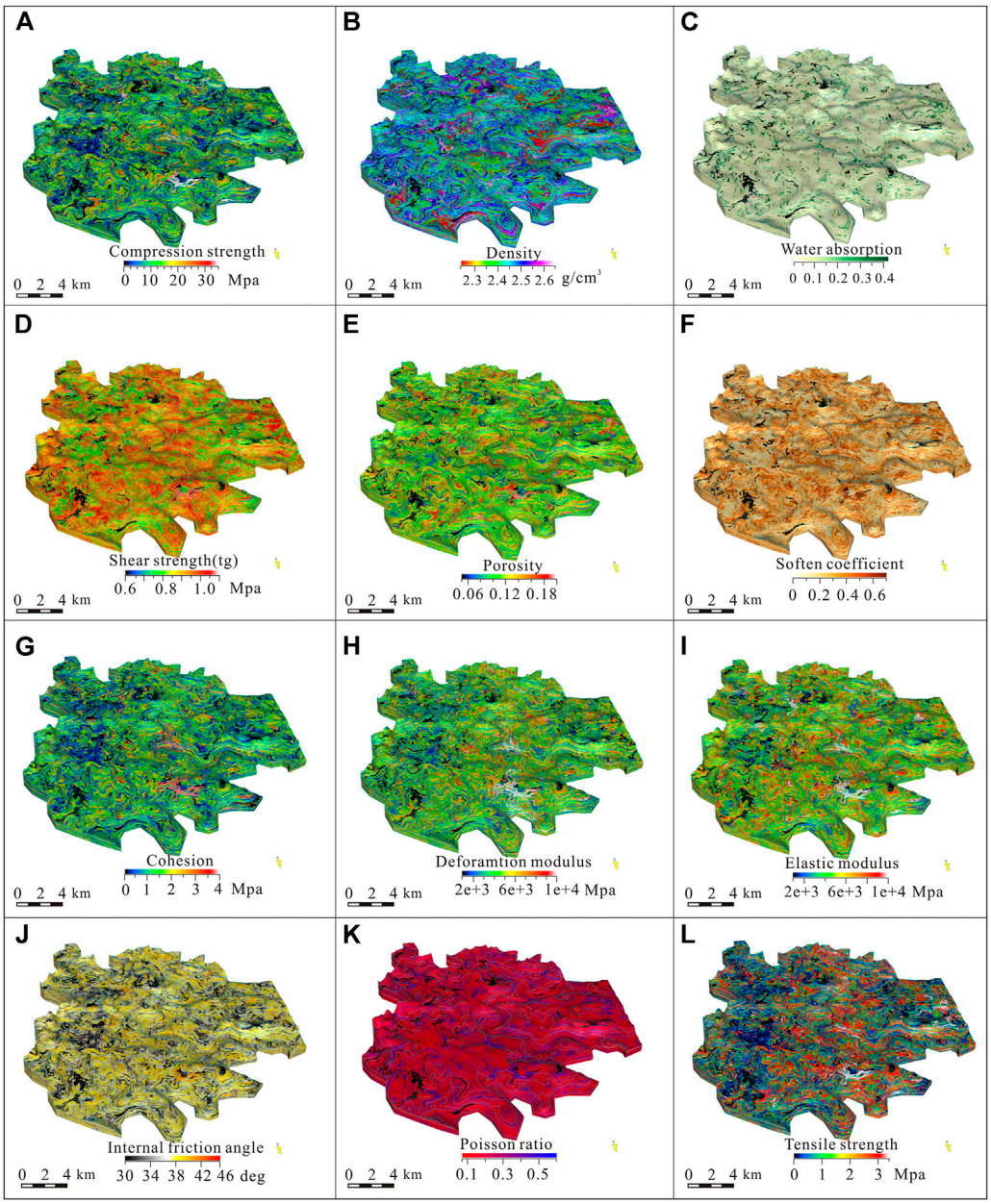


FIGURE 8 | Geotechnical attribute model of Guang'an city. **(A)** compression strength; **(B)** density; **(C)** water absorption; **(D)** shear strength (tg); **(E)** porosity; **(F)** soften coefficient; **(G)** cohesion; **(H)** deformation modulus; **(I)** elastic modulus; **(J)** internal friction angle; **(K)** Poisson's ratio; **(L)** tensile strength.

modeling. Additional information like properties or attributes is usually derived from the attribute or property model. Features of the corresponding properties could be revealed by generating visualization diagrams and charts of the properties such as histograms, cross-plots, and pie-charts. Furthermore, natural resource reserve computation or analysis is available through a combination of particular dimensional properties on the basis of previous statistics.

Simulation is a major application of the urban geological model and statistics. The differentiation between simulation and statistic is enormous. Simulation mainly focuses on the dynamic restoration of the geological process and illustrates the principle of the present phenomenon. Meanwhile, simulation provides predictions of geology evolution over time or under particular situations. However, statistics is merely the summary of the present phenomenon without restoring or predicting the function.

Generally, realization of the specific simulation purpose through the integrating geological model with simulation software packages, for instance, Flac3D and ANSYS, is commonly adopted to implement geomechanics simulation, and FEFLOW is employed to simulate underground water

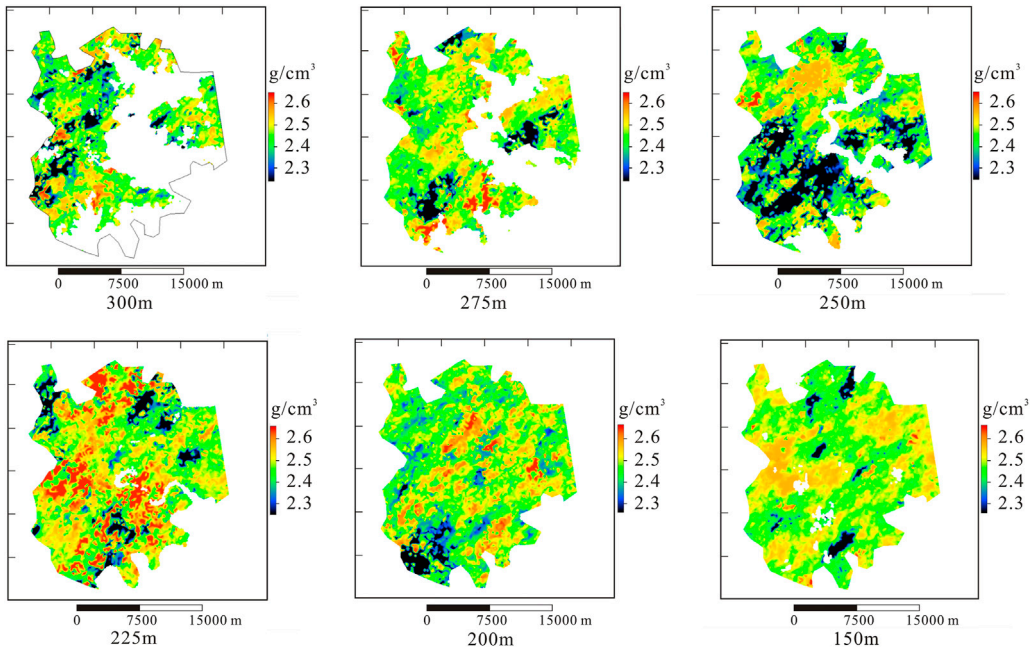


FIGURE 9 | Horizontal slices of the geotechnical model in different elevations (considering density as an example).

migration and preservation. However, caution should be taken to mitigate simulation deviation caused by tiny deformation while transferring the model to simulation software packages and parameter settings before simulation.

3D Assessment of the Geological Resource

Traditional assessments of urban geological resources are two-dimensional (x, y) based on the GIS platform. The urban geological model offers the ability to conduct the assessment in three dimensions (x, y, and z). Taking suitability evaluation of urban underground space exploitation as an example, the urban geological model offers a high-dimensional dataset from heterogeneous property/attribute modeling. Every cell that makes up the model is an independent unit for assessment. Quantities of properties/attributes are dimensional of the units. Even more, assessors could transfer two-dimensional properties or factors into 3D for the units by assigning the properties or factors to the units with the same plane coordinates. Furthermore, by coupling AHP, MUGM, or the unsupervised learning algorithm, a three-dimensional quantitative evaluation of urban underground space could be achieved.

Suggestions for Future Urban Underground Space Utilization

Although the modeling approach of UUS provides impressive results, a few questions still need to be discussed before its wide utilization in future projects. First of all, data quantity and density uncertainty could give outcomes that deviated from the actual situation. An additional intrusive investigation is a precise way to obtain underground geological conditions, but it is costly and time-consuming. Therefore, combining the region-scale geophysical methods, which could provide a framework of the area of interest, with the available borehole data as "hard" constraints can alleviate the uncertainty and improve the reliability in a shorter time frame and at a lower cost. Second, due to the different theoretical frameworks that software manufacturers employed, the format barriers of geological models reduce the communication between disciplines and hinder the share of results to a wider audience. Therefore, there is an urgent need for a universal format of the UUS model that could be applied in various modeling systems. Third, the popularity and application of UUS should be further explored. The UUS model is not only a tool to illustrate the spatial coupling of geological bodies, but more importantly, it provides primary and public data for other disciplines. In recent years, attempts have been made in the applications of UUS models in underground engineering, geothermal, and groundwater. However, multidisciplinary collaboration and applications still need to be deepened to facilitate the usability of geological models produced by geologists. Finally, artificial construction coupling with geological models needs further research, in particular platforms that can simultaneously display, modify, and analyze the construction and geological models.

Generally, 3D UGM describes UUS in a regional scale and cannot replace the site-specific intrusive investigation. It could provide a brief reference with a gradually precise reliability modeling approach before conducting a site-specific assessment. Integrated with geotechnical variability and semi-quantitative analysis, 3D UGM enables urban planners to assess potential application and conflicts of underground geological unit assets and to optimize the future development of the urban underground survey.

CONCLUSION

Stratigraphy, lithology, and 12 geotechnical properties were successfully modeled. Horizontal slices of the geotechnical model at various altitudes were set up for display and query based on the borehole data by GOCAD software. Given the possible heterogeneous and inadequate data display in this case study, a better method to model the lithology and properties is to adopt SIS and SGS as interpolation methods instead of kriging. These methods provide the ability to model and capture variations in geotechnical properties based on lithology zonation and the high-resolution grid in the core-length scale.

Although the results of geotechnical property modeling are likely to be influenced by insufficient information or lower data density, this modeling is still a vital approach to identify the underground geological conditions, guide the initial evaluation, and restrict the UUS design based on physical characteristics. This 3D UGM, thus, will lower the future risk and uncertainty of decision-making in the spatial planning of UUS in Guang'an city (Zhang et al., 2020).

DATA AVAILABILITY STATEMENT

The raw data supporting the conclusions of this article will be made available by the authors, without undue reservation.

AUTHOR CONTRIBUTIONS

FZ performed modeling and dataset cleaning and wrote the first draft of the manuscript. ML, YL, and CH contributed to field investigation and geotechnical unit classification. HL and MH contributed to data collection and organization. JZ and BW contributed to manuscript revision, read, and approved the submitted version.

FUNDING

This research was financially supported by the China Geological Survey projects "Comprehensive geological survey of resources and environment in Guang'an, Sichuan" (DD20190524), "Geological survey of multi-energy resources in important basins in southwest China" (DD20221661), and "Geological safety examination and risk assessment in economic circle of Chengdu-Chongqing" (DD20221733).

ACKNOWLEDGMENTS

The authors would like to appreciate the software technical support from Paradigm Inc. They also would like to express their gratitude for content's revised suggestions from reviewers and the editor.

REFERENCES

Andersen, T. R., Poulsen, S. E., Pagola, M. A., Medhus, A. B., and Vernoux, J. F. (2020). Geophysical Mapping and 3D Geological Modelling to Support Urban Planning: A Case Study from Vejle, Denmark. *J. Appl. Geophys.* 180 (1), 104130–104164. doi:10.1016/J.Jappgeo.2020.104130

Andriamamonjisoa, S. N., and Hubert-Ferrari, A. (2019). Combining Geology, Geomorphology and Geotechnical Data for a Safer Urban Extension: Application to the Antananarivo Capital City (Madagascar). *J. Afr. Earth Sci.* 151, 417–437. doi:10.1016/J.Jafrearsci.2018.12.003

Asghari, O., Soltni, F., and Amnieh, H. B. (2009). Comparison between Sequential Gaussian Simulation (SGS) of Choghart Ore Deposit and Geostatistical Estimation Through Ordinary Kriging. *Aust. J. Basic Appl. Sci.* 3 (1), 12.

Dai, F. C., Lee, C. F., and Zhang, X. H. (2001). GIS-based Geo-Environmental Evaluation for Urban Land-Use Planning: A Case Study. *Eng. Geol.* 61 (4), 257–271. doi:10.1016/S0013-7952(01)00028-X

Doyle, M. R. (2016). From Hydro/Geology to the Streetscape: Evaluating Urban Underground Resource Potential. *Tunn. Undergr. Space Technol.* 55, 83–95. doi:10.1016/J.Tust.2016.01.021

El May, M., Dlala, M., and Chenini, I. (2010). Urban Geological Mapping: Geotechnical Data Analysis for Rational Development Planning. *Eng. Geol.* 116 (1), 129–138. doi:10.1016/J.Enggeo.2010.08.002

Guan, S. Y., Zhu, R., and Gao, Z. Y. (2008). The Influence of Geological Conditions on the Exploitation and Zoning Evaluation in Wuhan City. *Geotech. Investig.* 9, 5–10. CNKI:SUN:GCKC.0.2008-09-004.

He, H., He, J., Xiao, J., Zhou, Y., Liu, Y., and Li, C. (2020). 3D Geological Modeling and Engineering Properties of Shallow Superficial Deposits: A Case Study in Beijing, China. *Tunn. Undergr. Space Technol.* 100, 103390–103417. doi:10.1016/J.Tust.2020.103390

Hou, J. R. (1996). Present Situation of Geostatistical Development and Discussion on Some Problems. *Gold Geol.* 2 (1), 1–11.

Hou, J. R. (1997). Review and Prospect of Geostatistics(Spatial-Information Statistics) Developmant in China. *Geol. Prospect.* 33 (01), 53–58.

Hou, W., Yang, L., Deng, D., Ye, J., Clarke, K., Yang, Z., et al. (2016). Assessing Quality of Urban Underground Spaces by Coupling 3D Geological Models: the Case Study of Foshan City, South China. *Comput. Geosciences* 89, 1–11. doi:10.1016/J.Cageo.2015.07.016

Hu, X. L. (2007). *Research and Application of Sequentially Conditional Simulation Methods*. [Dissertation]. Chengdu: Chengdu University of Technology.

Li, F., Guo, S., Li, D., Li, X., Li, J., and Xie, S. (2020). A Multi-Criteria Spatial Approach for Mapping Urban Ecosystem Services Demand. *Ecol. Indic.* 112, 106119–106211. doi:10.1016/J.Ecolind.2020.106119

Li, P. Y., Han, H. D., Wang, D. H., and Wang, C. S. (2021). Current Situation and Development Trends of Suitability Evaluation of Urban Underground Space Resources. *Sediment. Geol. Tethyan Geol.* 41 (1), 121–128. doi:10.19826/J.Cnki.1009-3850.2020.11004

Liao, J. S., Peng, W. P., and Lin, B. H. (2006). Analysis and Partition Evaluation of Geological Factors Affecting Space Development and Utilization of Shallow Underground in Guangzhou City. *Chin. J. Rock Mech. Eng.* 25 (S2), 3357–3362. doi:10.3321/j.issn:1000-6915.2006.z2.003

Liu, K., Peng, J., and Peng, F. L. (2011). Evaluation Model for the Suitability of Underground Space Resources Exploitation and Utilization. *Chin. J. Undergr. Space Eng.* 7 (2), 219–231. doi:10.3969/J.issn.1673-0836.2011.02.003

Liu, Z. N., Song, Y. C., Meng, H. D., and Yu, X. Y. (2018). Application of Sequential Gaussian Simulation in Ore Grade Estimation. *Contributions Geol. Mineral Resour. Res.* 33 (1), 149–155.

Mao, S. Z., Hua, Q. W., Ying, D., Lin, L., Ping, P. S., and Ge, Z. (2020). Evaluation of Urban Underground Space Resources Using Negative List Method: Taking Xi'an City as an Example in China. *China Geol.* 3 (1), 124–136. doi:10.31035/cg2020006

Mielby, S., and Sandersen, P. B. E. (2017). Development of a 3D Geological/Hydrogeological Model Targeted at Sustainable Management of the Urban Water Cycle in Odense City, Denmark. *Procedia Eng.* 209, 75–82. doi:10.1016/J.Proeng.2017.11.132

Peng, J., Liu, K., Zheng, F. T., Li, X. J., and Peng, F. L. (2010). Evalution for the Suitability of Underground Space Exploitaion and Utilization Based on AHP.

Chin. J. Undergr. Space Eng. 6 (3), 688–694. doi:10.3969/J.issn.1673-0836.2010.04.006

Peng, J., and Peng, F.-L. (2018). A GIS-Based Evaluation Method of Underground Space Resources for Urban Spatial Planning: Part 2 Application. *Tunn. Undergr. Space Technol.* 77, 142–165. doi:10.1016/J.Tust.2018.01.00210.1016/j.tust.2018.03.013

Price, S. J., Terrington, R. L., Busby, J., Bricker, S., and Berry, T. (2018). 3D Ground-Use Optimisation for Sustainable Urban Development Planning: A Case-Study from Earls Court, London, UK. *Tunn. Undergr. Space Technol.* 81, 144–164. doi:10.1016/J.Tust.2018.06.025

Rahimi, H., Asghari, O., and Afshar, A. (2018). A Geostatistical Investigation of 3D Magnetic Inversion Results Using Multi-Gaussian Kriging and Sequential Gaussian Co-Simulation. *J. Appl. Geophys.* 154, 136–149. doi:10.1016/J.Jappgeo.2018.05.003

Tame, C., Cundy, A. B., Royse, K. R., Smith, M., and Moles, N. R. (2013). Three-Dimensional Geological Modelling of Anthropogenic Deposits at Small Urban Sites: A Case Study from Sheepcote Valley, Brighton, UK. *J. Environ. Manag.* 129, 628–634. doi:10.1016/J.Jenvman.2013.08.030

Tan, F., Wang, J., Jiao, Y. Y., and Ma, B. C. (2021). Current Situation and Development of Urban Underground Space Suitability Evaluation. *Earth Sci.* 46 (5), 1896–1908. doi:10.3799/Dqkx.2020.155

Wei, X. J., Fu, B., Deng, X. L., and Wang, Z. L. (2017). The Risk Evalution on Geological Hazards Assessment in Guang'an Urban Overall Plan Areas. *J. Chang. Inst.Tech. (Nat. Sci. Edi.)* 18 (2), 110–116. doi:10.3969/J.issn.1009-8984.2017.02.026

Wycisk, P., Hubert, T., Gossel, W., and Neumann, C. (2009). High-Resolution 3D Spatial Modelling of Complex Geological Structures for an Environmental Risk Assessment of Abundant Mining and Industrial Megasites. *Comput. Geosciences* 35 (1), 165–182. doi:10.1016/J.Cageo.2007.09.001

Xin, H. X., Ju, T. Z., and Lin, J. Y. (1997). The Ordinary Krig's Application to Mineral Calculation of Reserves. *Geol. Prospect.* 33 (4), 46–51.

Xiong, J. X., Ni, S. J., Zhang, C. J., Ding, J., and Wei, L. W. (2006). The Design and Implementation of the GIS Software for Risk Assessment of Urban Geo-Environments. *Sediment. Geol. Tethyan Geol.* 26 (2), 106–109. doi:10.3969/j.issn.1009-3850.2006.02.021

Yan-lin, S., Ai-ling, Z., You-bin, H., and Ke-yan, X. (2011). 3D Geological Modeling and its Application under Complex Geological Conditions. *Procedia Eng.* 12, 41–46. doi:10.1016/J.Proeng.2011.05.008

Yu, X. C., Deng, W. K., Xiao, K. Y., and Zou, W. (2013). Visualized Reserves Estimation Based on 3D Kriging Method. *Earth Sci. Front.* 20 (4), 320–331.

Zhang, M.-s., Wang, H. Q., Wang, H.-q., Dong, Y., Li, L., Sun, P.-p., et al. (2020). Evaluation of Urban Underground Space Resources Using a Negative List Method: Taking Xi'an City as an Example in China. *China Geol.* 3 (1), 124–136. doi:10.31035/Cg2020006

Zhang, Y., Dai, Y., Wang, Y., Huang, X., Xiao, Y., and Pei, Q. (2021a). Hydrochemistry, Quality and Potential Health Risk Appraisal of Nitrate Enriched Groundwater in the Nanchong Area, Southwestern China. *Sci. Total Environ.* 784, 147186. doi:10.1016/J.Scitotenv.2021.147186

Zhang, Y., He, Z., Tian, H., Huang, X., Zhang, Z., Liu, Y., et al. (2021b). Hydrochemistry Appraisal, Quality Assessment and Health Risk Evaluation of Shallow Groundwater in the Mianyang Area of Sichuan Basin, Southwestern China. *Environ. Earth Sci.* 80 (17), 576–592. doi:10.1007/S12665-021-09894-Y

Zhao, Y. F., Sun, Z. Y., and Chen, J. (2010). Analysis and Comparison in Arithmetic for Kriging Interpolation and Sequential Gaussian Conditional Simulation. *J. Geo-Information Sci.* 12 (6), 767–776. CNKI:SUN:DQXX.0.2010-06-006.

Zhou, D., Li, X., Wang, Q., Wang, R., Wang, T., Gu, Q., et al. (2019). GIS-based Urban Underground Space Resources Evaluation toward Three-Dimensional Land Planning: A Case Study in Nantong, China. *Tunn. Undergr. Space Technol.* 84, 1–10. doi:10.1016/J.Tust.2018.10.017

Zhou, F., Wang, B. D., He, J., Hao, M., Wang, P., and Dong, Y. X. (2020). Deep Ore Body Targeting Based on 3D Integrated Information. *Earth Sci.* 45 (08), 3028–3039. doi:10.3799/Dqkx.2020.143

Zhu, H., Huang, X., Li, X., Zhang, L., and Liu, X. (2016). Evaluation of Urban Underground Space Resources Using Digitalization Technologies. *Undergr. Space* 1 (2), 124–136. doi:10.1016/J.Undsp.2016.08.002

Conflict of Interest: The authors declare that the research was conducted in the absence of any commercial or financial relationships that could be construed as a potential conflict of interest.

The reviewer ZL declared a shared affiliation with the author BW to the handling editor at the time of review.

Publisher's Note: All claims expressed in this article are solely those of the authors and do not necessarily represent those of their affiliated organizations, or those of the publisher, the editors, and the reviewers. Any product that may be evaluated in this article, or claim that may be made by its manufacturer, is not guaranteed or endorsed by the publisher.

Copyright © 2022 Zhou, Li, Huang, Liang, Liu, Zhang, Wang and Hao. This is an open-access article distributed under the terms of the Creative Commons Attribution License (CC BY). The use, distribution or reproduction in other forums is permitted, provided the original author(s) and the copyright owner(s) are credited and that the original publication in this journal is cited, in accordance with accepted academic practice. No use, distribution or reproduction is permitted which does not comply with these terms.

frontiers | Frontiers in Earth Science

TYPE Original Research
PUBLISHED 18 July 2022
DOI 10.3389/feart.2022.902034

Check for updates

OPEN ACCESS

EDITED BY
Xiangjun Pei,
Chengdu University of Technology, China

REVIEWED BY
Sreekanth J,
Commonwealth Scientific and Industrial Research Organisation (CSIRO), Australia
Pingping Luo,
Chang'an University, China

*CORRESPONDENCE
Qichen Hao,
haoqichen_iheg@163.com

SPECIALTY SECTION
This article was submitted to Geohazards and Georisks, a section of the journal Frontiers in Earth Science

RECEIVED 22 March 2022
ACCEPTED 29 June 2022
PUBLISHED 18 July 2022

CITATION
Cui W, Hao Q, Xiao Y, Zhu Y, Li J, Yuanjing Zhang (2022), Combining river replenishment and restrictions on groundwater pumping to achieve groundwater balance in the Juma River Plain, North China Plain.
Front. Earth Sci. 10:902034.
doi: 10.3389/feart.2022.902034

COPYRIGHT
© 2022 Cui, Hao, Xiao, Zhu, Li and Yuanjing Zhang. This is an open-access article distributed under the terms of the Creative Commons Attribution License (CC BY). The use, distribution or reproduction in other forums is permitted, provided the original author(s) and the copyright owner(s) are credited and that the original publication in this journal is cited, in accordance with accepted academic practice. No use, distribution or reproduction is permitted which does not comply with these terms.

Combining river replenishment and restrictions on groundwater pumping to achieve groundwater balance in the Juma River Plain, North China Plain

Weizhe Cui[1,2,3], Qichen Hao[1,2,3]*, Yong Xiao[4], Yuchen Zhu[1,2,3], Jianfeng Li[1,2,3] and Yuanjing Zhang[1,2,3]

[1]Fujian Provincial Key Laboratory of Water Cycling and Eco-Geological Processes, Xiamen, China, [2]Institute of Hydrogeology and Environmental Geology, Chinese Academy of Geological Sciences, Shijiazhuang, China, [3]Key Laboratory of Groundwater Contamination and Remediation of Hebei Province and China Geological Survey, Shijiazhuang, China, [4]Faculty of Geosciences and Environmental Engineering, Southwest Jiaotong University, Chengdu, China

In recent years, to alleviate the decline in groundwater levels, extensive restrictions on groundwater pumping have been implemented in the North China Plain (NCP). In September 2018, a large-scale ecological water replenishment project was executed involving 22 rivers and lakes. How to adjust the layout of reduction on groundwater pumping within the context of ecological water replenishment is a key issue to be addressed in the study of groundwater level recovery in the NCP. This study adopted the Juma River Plain in Baoding city as a case study, established a numerical model of river replenishment of groundwater, predicted groundwater level changes over the next 15 years (2021–2035) and quantitatively calculated the impact of river replenishment on groundwater levels. To achieve the goal of an overall groundwater balance by 2035, a suitable groundwater pumping restriction scenario was defined based on the impact of river replenishment on groundwater levels. The results indicated that by 2035, the relative rise in groundwater levels attributed to river replenishment and restrictions on groundwater pumping could reach 3.51 and 2.28 m, respectively. River replenishment significantly impacts groundwater levels, especially those near the river. Under the current groundwater exploitation conditions, river replenishment could ensure groundwater level recovery near the river, which accounts for 15% of the total study area. The goal of an overall groundwater balance by 2035 could be achieved if restrictions on groundwater pumping were superimposed, with an average annual reduction of 56 million m^3. This study provides valuable insights into groundwater management across the NCP. The proposed methods are useful for the management of other depleted aquifers recharged via ecological water replenishment.

KEYWORDS

river replenishment, restrictions on groundwater pumping, groundwater balance, groundwater model, China

1 Introduction

Groundwater is an essential source of water for agricultural, industrial, and environmental uses and the drinking water supply due to its generally good quality and widespread occurrence (Cao et al., 2013). However, groundwater depletion has extensively occurred and become a global hotspot due to the unremitting and unreasonable overexploitation in many regions (Aeschbach-Hertig and Gleeson, 2012; Gleeson et al., 2012; Feng et al., 2013; Huang et al., 2015; Alin et al., 2017), such as North Africa (Shah et al., 2003), Northwest India (Rodell et al., 2018), the Middle East (Voss et al., 2013), and the North China Plain (NCP) (Xiao et al., 2022a; Xiao et al., 2022b). The NCP occurs among the most severe regions, with groundwater levels declining as fast as 1 m/a between 1974 and 2000 (Qiu, 2010). This region has begun to experience adverse water shortages, and groundwater overdraft has led to environmental problems such as groundwater drawdown cones, seawater intrusion, groundwater quality deterioration and subsidence, as the water demand has exceeded the natural renewable supply (Zheng et al., 2010; Nakayama, 2011; Zhu et al., 2013; Xiao et al., 2021).

The implementation of the South-to-North Water Diversion Project (SNWD), where water is diverted from the humid south to the arid north, has provided an opportunity for groundwater management in the NCP. To alleviate groundwater depletion, a groundwater extraction restriction policy has been adopted in SNWD water-receiving areas across the NCP since 2014, and groundwater withdrawal has been reduced via the adoption of water conservation in various fields, water source replacement, and adjustment of crop cultivation structures (Chen et al., 2021). By the end of 2018, the average annual groundwater overexploitation level in the NCP decreased to 3.19 km^3, a 33% reduction below 2011–2013 levels, and several issues including groundwater drawdown cones and subsidence were alleviated (Li et al., 2020). To restore river ecosystems and further increase the intensity of restrictions on groundwater pumping, the Hebei government initiated the adoption of ecological water replenishment in August 2018, which constitutes the largest ecological replenishment project in China. Three typical rivers in the NCP, the Hutuo River, Fuyang River and Juma River, are replenished by the SNWD and water diversion from the Yellow River, Luan River and local reservoirs (Chen et al., 2020). Based on groundwater level monitoring data, the average groundwater level recovery within 10 km on both sides of these rivers in February 2019 reached 1.62 m compared to pre-replenishment period levels (Chen et al., 2021). Several rivers and lakes were recharged in 2020, and river replenishment has become an important method to restore groundwater levels in the NCP.

Many scholars have conducted studies on groundwater level recovery in the NCP. Cao et al. (2013) applied a groundwater model to evaluate the impact of several alternatives, including restrictions on groundwater pumping, aquifer recharge management, water use efficiency enhancement, and brackish water use, on groundwater in the NCP and indicated that the combination of these strategies could be employed to recover groundwater storage by 50 km^3 over a 15-year period. Li et al. (2017) combined climate and water-diversion scenarios to predict groundwater levels in the Beijing–Tianjin–Hebei Plain and estimated that shallow groundwater levels could rise by a maximum value of 17 m over the next 40 years (2011–2050) when considering scenarios combining climate change and restrictions on groundwater pumping. Shu et al. (2012) integrated dynamic and distributed hydrological data to evaluate the spatiotemporal implications of various water use and management options in the NCP and concluded that deficit irrigation of winter wheat could reverse groundwater decline. Sun et al. (2021) adopted machine learning models to describe dynamic changes in streamflow and groundwater levels in response to ecological water replenishment of the Yongding River in the Beijing Plain and estimated that the river could recharge the aquifer by 170 million m^3.

In 2019, the Ministry of Water Resources of China and Hebei Province promulgated an action plan and implementation opinions for comprehensive management of groundwater overexploitation. It was clearly stated that the Beijing–Tianjin–Hebei region in the NCP is the focus of treatment, through river replenishment and restrictions on groundwater pumping, to achieve a provincial exploitation–replenishment balance by 2022, meaning that the total exploitation equals the total replenishment in the region, and to accomplish a complete exploitation–replenishment balance by 2035, that is, exploitation equals replenishment overall in the region (The Ministry of Water Resources of the People's Republic of China, 2019; The People's Government of Hebei Province, 2019). Previous studies on groundwater recovery in the NCP could help to achieve groundwater balance. However, these studies mainly focused on the impact on groundwater levels of water diversion (Liu et al., 2008; Zhang et al., 2019), climate change (Kang and Eltahir, 2018; Long et al., 2020), restrictions on extraction (Cao et al., 2013; Li and Ren, 2019) and crop water consumption (Sun et al., 2006; Li and Ren, 2019) but did not consider the impact of the implementation of the above river ecological replenishment project, especially on groundwater levels near the river. There are a few studies on the relationship between ecological replenishment and the groundwater regime in the NCP. However, these studies basically applied certain methods, including the genetic algorithm (Hao et al., 2018), water resource allocation (Yan et al., 2018) and machine learning (Sun et al., 2021), to propose an optimal river replenishment plan but did not elucidate in detail the impact of river replenishment on groundwater levels. In addition, previous studies based only on changes in the total groundwater storage and average groundwater level across the region compared the groundwater recovery between different simulated scenarios and

thus selected the optimal scenario facilitating a groundwater balance. Obviously, these studies could only help to achieve a provincial exploitation–replenishment balance, that is, these studies could contribute to the achievement of the groundwater balance goal by 2022 but could not ensure that a complete exploitation–replenishment balance will be achieved by 2035.

River replenishment and groundwater pumping restriction are currently the main measures to restore groundwater storage in the NCP. The implementation of river replenishment not only impacts the overall groundwater balance but also impacts groundwater level rise near the river. These impacts of river replenishment should be considered in the development of restriction policies on groundwater pumping to more effectively achieve groundwater level recovery. The groundwater numerical simulation method is clearly appropriate for the assessment of sustainable water use given the complexity and heterogeneity of aquifer systems and can assist in the formulation of groundwater regulation and storage management policies (Wolfgang et al., 2003; Hao et al., 2012). Several numerical models have been constructed for sustainable groundwater management in the NCP (Hu et al., 2010; Zhang and Li, 2014; Zhang et al., 2018). General groundwater models often have difficulty in precisely simulating local groundwater level changes near rivers with large groundwater level changes. In this study, we used local grid refinement to finely characterise groundwater level changes near the river, and Cui and Hao (2020) have successfully applied this method to numerical simulations with ecological water replenishment of rivers. This study was conducted in the Juma River Plain, which flows through the Juma River, one of three ecological replenishment rivers. A numerical groundwater model was applied to simulate and predict the impact of river replenishment on groundwater levels, and a groundwater pumping restriction scenario was subsequently established based on the impact of river replenishment to achieve the goal of an overall groundwater balance by 2035.

The novelty of this study is that a numerical model of river replenishment of groundwater was developed to analyze the impact of river replenishment on groundwater levels, and an appropriate groundwater pumping restriction plan was determined to achieve an overall groundwater balance by 2035. The objective of the study was to quantify the impact of river replenishment on groundwater levels and to propose an optimal groundwater pumping restriction scenario that could minimize the extraction restriction volume while meeting the goal of groundwater balance by 2035.

2 Study area and hydrogeological setting

The Juma River is the only perennial river in Hebei Province constantly flowing throughout the year, with a total length of 69 km and an average bed width ranging from 100 to 200 m (Yao and Lu, 2017). Due to many dam constructions upstream, the runoff volume decreased to an extremely low level. The Juma River Plain occurs in the piedmont plain of the Taihang Mountains, covering an area of approximately 3,300 km^2 and ranging in elevation from 15 to 85 m (Figure 1A). The climate in the Juma River Plain is a continental semiarid climate, with a mean annual temperature of 10.7°C and an annual average precipitation of approximately 517–581 mm (Ding et al., 2013). In addition, precipitation is unevenly distributed throughout the year, and rainfall from June to September accounts for 70%–80% of the total annual precipitation amount (Yu et al., 2012).

The stratigraphy in the study area mainly comprises unconsolidated Quaternary sediments where most of the groundwater occurs. The aquifer structure varies from a single aquifer comprising gravel particles and pebbles in the upper parts of the piedmont fan in the northwest to multiple aquifers composed of sand, silt and clay in the southeast. The groundwater system can be divided into four aquifer groups (I, II, III, and IV) based on the stratigraphy (Figure 1B). Aquifer groups I and II represent shallow aquifers, whereas groups III and IV represent deep aquifers.

Recharge primarily occurs through precipitation infiltration, lateral flow in the mountains and return flow from irrigation. Groundwater pumping is currently the main discharge mode from the aquifer system. The water table is relatively deep, and there essentially occurs no phreatic evaporation. Groundwater flows from northwest to southeast under natural conditions.

3 Methods

3.1 Groundwater flow model

A three-dimensional heterogeneous anisotropic transient flow model was developed comprising two aquifers: the top aquifer is a phreatic aquifer, and another aquifer is a confined aquifer. The phreatic aquifer comprised aquifer groups I and II, and the confined aquifer comprised aquifer groups III and IV.

The model domain was discretized with the quadtree refinement method in MODFLOW–USG, which achieves a high simulation precision in modeling river recharge to aquifers (Cui and Hao, 2020). The finest grid was 250 m × 250 m, and the cell size gradually increased to 500 m × 500 m away from both sides of the river. The simulation period was 20 years (2001–2020), and the prediction period was 15 years (2021–2035), with a stress period of 15 days. During each stress period, constant average hydrological conditions were assumed.

The mountain front in the northwest was defined as an inflow boundary because the region experiences significant water exchange with the outside region of the study area, and the flux rate from the northwest boundary was determined based on the profiling method of previous studies (Shao et al., 2013). The northern and southwestern boundaries were defined as no-flow

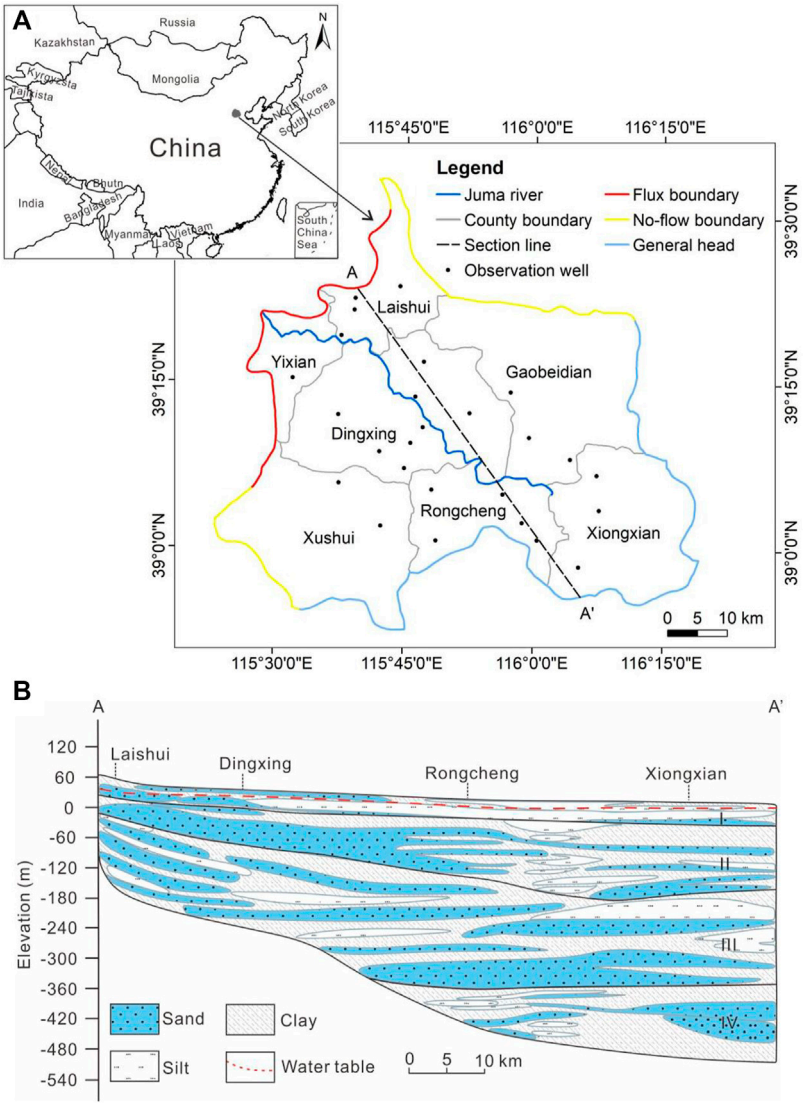


FIGURE 1
(A) Location and model boundaries of the study area; **(B)** hydrogeological section of the study area.

boundaries because the flow lines are generally parallel to these boundaries under present conditions (Figure 1A). The eastern and southern boundaries were treated as general head boundaries, and groundwater heads were obtained from measured data.

The main recharge source of groundwater in the study area includes rainfall infiltration, irrigation infiltration, and river replenishment, whereas the main discharge mode of groundwater is exploitation. The amount of river replenishment was provided by the Ministry of Water Resources of the People's Republic of China, and other recharge and discharge volumes of aquifers were collected from previous studies and investigations (Zhang and Che, 2017; Zhang et al., 2017). The amount of river replenishment is the average amount over the replenishment period (September 2018–December 2020) during the prediction period, and the annual replenishment volume reaches 101 million m^3. Due to the implementation of restriction policies on groundwater pumping, the amount of groundwater extracted in Hebei province has been reduced by 4.35 billion m^3 by 2021. Therefore, the exploitation amount during the projection period was set to the same amount as that in 2020. The values of the other source–sink items, such as rainfall and irrigation, are multiyear averages of the corresponding items over the simulation period.

The model was calibrated against data retrieved from 26 observation wells in the vicinity of the river (Figure 1A).

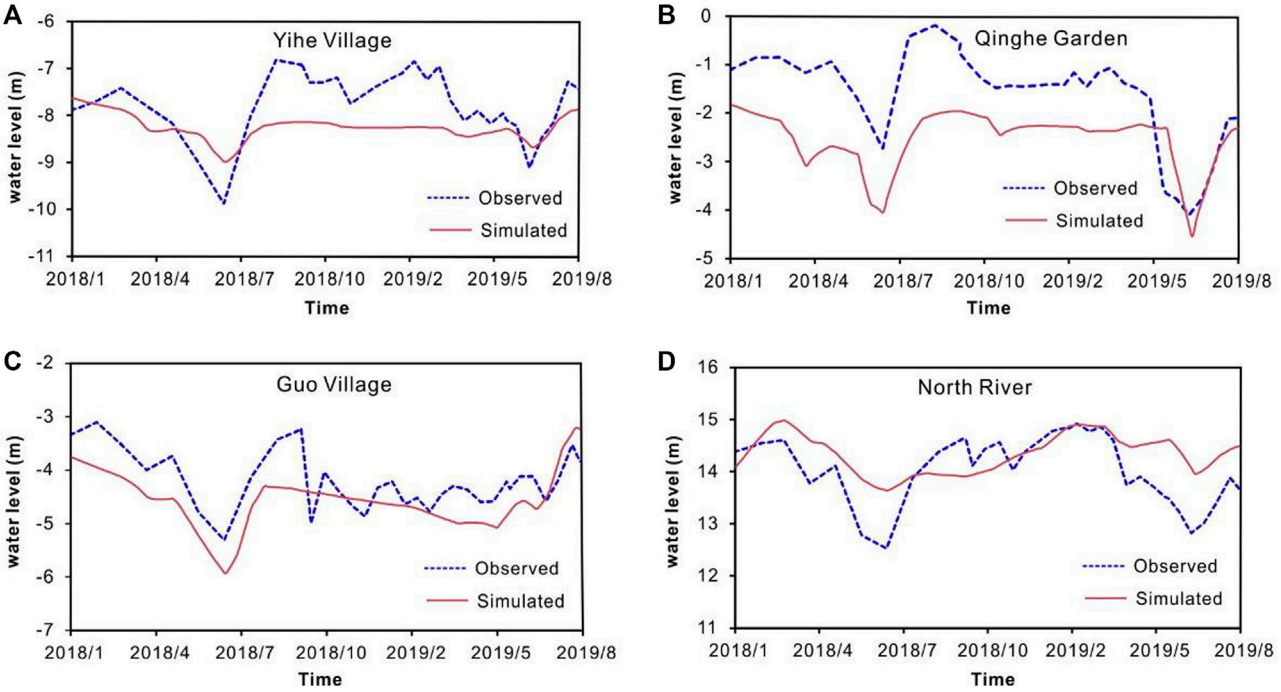


FIGURE 2
Comparison of the observed and simulated groundwater levels in observation wells. **(A)** Observation well in Yihe Village, **(B)** Observation well in Qinghe Garden, **(C)** Observation well in Guo Village, **(D)** Observation well in North River.

Among all the observation wells, a comparison of the simulated and observed water levels in six observation wells is shown in Figure 2. The results demonstrated that the model simulations suitably reflected the actual features of the groundwater regime. The initial aquifer parameter values, including hydraulic conductivity and storage parameters pertaining to groundwater flow, were zoned and assigned based on sediment features and results obtained from a previous investigation (Zhang et al., 2012). These parameters were then manually adjusted in the calibration process. The hydraulic conductivity values ranged from 2 to 130 m/d for the phreatic aquifer and 2–50 m/d for the confined aquifer.

3.2 Relative and absolute groundwater level changes

The relative groundwater level change (RGLC) refers to the difference between groundwater levels altered as a result of a change in certain conditions and groundwater levels under the original conditions. This quantity can be employed to indicate the extent to which changes in conditions affect groundwater levels. In this study, the RGLC with river and non–river replenishment, that is, the groundwater level with river replenishment minus that without river replenishment over the same period, was applied to represent the degree of the impact of river replenishment on groundwater levels. The parameters of two models describing river and non–river replenishment remained constant, including recharge and discharge items and hydrogeological parameters, except for the differences with and without river replenishment.

The absolute groundwater level change (AGLC) refers to the difference in groundwater levels at different times in the same model. This quantity can be employed to indicate the magnitude of groundwater level change over a given time interval. In this study, the AGLC was represented as the current water level minus the previous level, e.g., the AGLC between the end of 2034 and the end of 2035 is the groundwater level in December 2035 minus that in December 2034. The water level in 2035 increases overall if the AGLC values are greater than zero at every location in the study area. The method of the AGLC can therefore be applied to determine the overall state of groundwater balance within a given time interval.

3.3 Zoning for restriction on groundwater pumping

3.3.1 Restriction zone

Prior to the implementation of the ecological water replenishment project, the overall groundwater levels in the study area decreased at a rate of 0–1 m/a. After project

implementation, there was a considerable impact on groundwater levels near the river, with some rebound in groundwater levels in the vicinity of the river according to the obtained monitoring data. Considering that water levels recovered in certain areas near the river under the influence of river replenishment, it is only necessary to manage those areas where groundwater levels decreased to minimize the amount of groundwater pumping restriction. In this study, we characterised the achievement of overall groundwater balance by the fact that groundwater levels in each small district (the smallest district is a town in the study area) did not decline any further. In order to achieve the goal of overall groundwater balance in 2035, the AGLC values between 2034 and 2035 required to be greater than 0 in each town in the study area. Therefore, the areas where the AGLC value between 2034 and 2035 is less than zero were set as the groundwater pumping restriction zone, in which the extraction amount should be reduced to achieve the goal of overall groundwater balance in 2035.

The SNWD allows most of the urban areas in Hebei Province to use diverted water as a replacement of groundwater for industrial and domestic purposes, thereby reducing groundwater withdrawal. Given this situation, the urban areas in the study area were identified, and the groundwater pumping restriction volume could be concentrated more in these areas if necessary to ensure that groundwater restrictions in adjacent rural areas (town areas) remained within reasonable limits.

3.3.2 Restriction volume

The total groundwater pumping restriction volume can be preliminarily calculated with the equation of the relationship between the changes in groundwater level, area and specific yield.

$$Q = \sum_{i=1}^{n} (H_i S_i \mu_i) \quad (1)$$

Subscript i denotes the zone where the groundwater level declines, n is the number of zones where the groundwater level drops, H is the average value of the groundwater level decline, S is the area of the groundwater level decline, and μ is the specific yield.

Agricultural water use in the NCP accounts for 74.5%–76.6% of the groundwater extraction volume (Zhang et al., 2009), and restrictions on groundwater pumping could lead to a decrease in agricultural irrigation, which in turn could result in a reduction in crop yields. Wheat is the major crop in the NCP and is also a highly water-intensive crop, accounting for 70% of the total agricultural water use among all irrigated crops (Zhang et al., 2016). Given the impact of groundwater extraction restriction on crops, the groundwater pumping restriction scenario developed in this study was designed to ensure that the maximum reduction in crop yield did not exceed 10%. Sun et al. (2006) demonstrated that a 29.5% reduction in agricultural irrigation in the NCP was associated with a 19.5% reduction in the wheat yield. Based on this research, it was assumed that the reduction in wheat yield is linearly related to the reduction in irrigation within this interval. Notably, a 1% reduction in irrigation reduced the wheat yield by 0.66% when the reduction in the irrigation amount remained below 29.5%. It was also assumed that in rural (town) areas, all restrictions on groundwater pumping occurred in the agricultural sector, while other water uses, such as domestic water, experienced no restrictions, and all agricultural water was employed for wheat irrigation. Therefore, the degree of groundwater pumping restriction (the ratio of restriction to exploitation) in rural areas should be lower than 15% to ensure that the reduction in wheat yield remained below 10%. In addition, the replacement of irrigation equipment with water-saving equipment has been strongly promoted in town areas in Hebei Province, and the degree of groundwater pumping restriction could increase. In urban areas, diverted water can serve as a replacement of groundwater for the water supply as a result of SNWD development, therefore assuming that groundwater within these areas could be considered subject to unrestricted extraction reduction, that is, the maximum restriction amount could match the amount of groundwater pumping set in the model.

4 Results and discussion

4.1 Effect of river replenishment on groundwater levels

4.1.1 Flow field change

Because shallow aquifers are more sensitive to river replenishment than deep aquifers, only shallow water levels were analyzed. A comparison of the shallow groundwater flow fields with and without river replenishment in 2020 and 2035 is shown in Figure 3. In terms of the groundwater contours of flow field, river replenishment created water concentration areas along the river, resulting in a significant increase in groundwater levels near the river. In 2020, the impact of river replenishment was less extensive, causing only a rise in groundwater levels very close to the river, whereas the water levels (with and without river replenishment) overlapped in other areas away from the river. With the operation of the developed model, the morphological differences in groundwater contours between the two flow fields (with and without river replenishment) obviously increased. The water concentration areas along the river expanded, and the morphological differences gradually spread from the center of the river to both sides. By 2035, the morphological differences were manifested at the northern boundary, where groundwater levels with river replenishment were higher than those without river replenishment in most of the study area, and the impact of river replenishment on the overall groundwater levels increased.

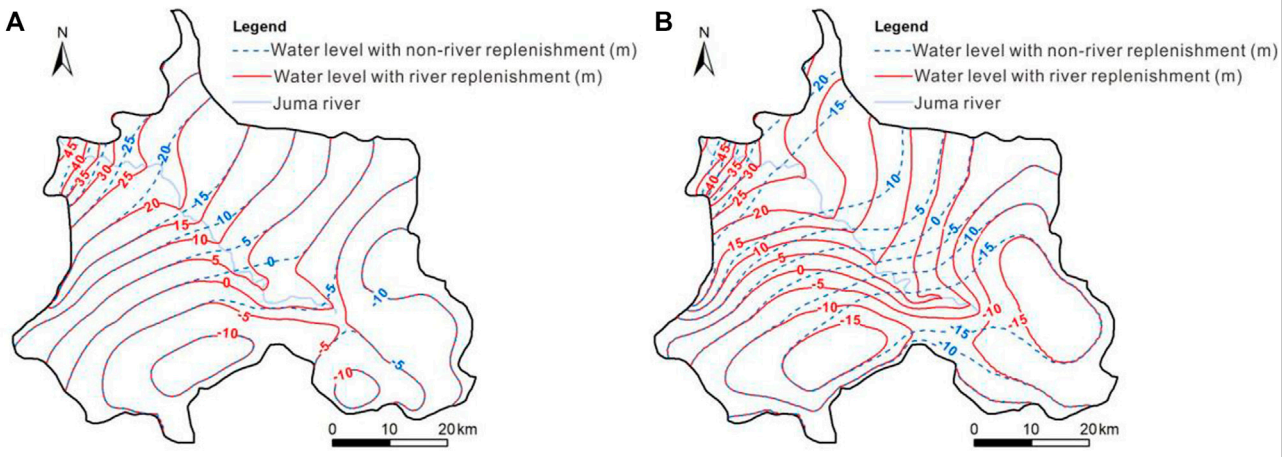


FIGURE 3
Comparison of the flow fields with and without river replenishment: **(A)** at the end of 2020 and **(B)** at the end of 2035.

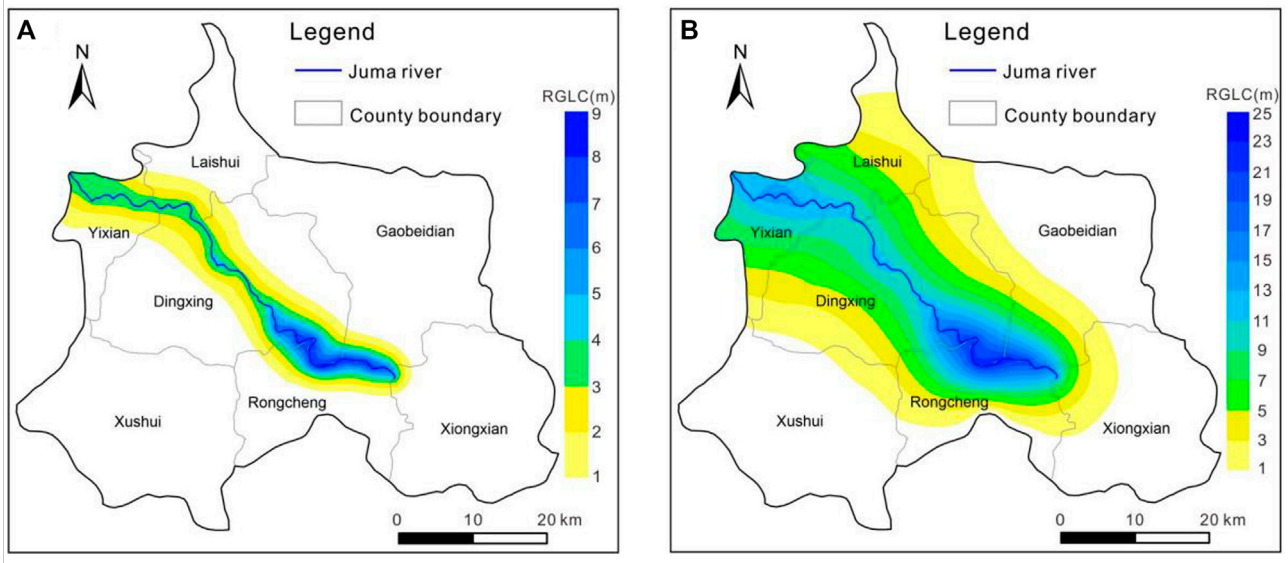


FIGURE 4
Comparison of the RGLC with and without river replenishment: **(A)** at the end of 2020 and **(B)** at the end of 2035.

4.1.2 RGLC and changes in the average groundwater level

The RGLC was calculated at the end of 2020 and at the end of 2035, and areas were identified where the RGLC value exceeded 1 m, as shown in Figure 4. In 2020, the maximum RGLC value was 8 m, and the area with a relative rise of more than 1 m reached 563.36 km^2. By 2035, the RGLC value could reach a maximum value of 23 m, and this value could exceed 1 m in an area of 1,722.68 km^2, which accounts for more than half the total study area (53%). In addition, Figure 4 shows that the lower reaches of the river were more affected by river replenishment, with a relatively greater increase in groundwater levels, whereas the effect decreased toward the upper reaches. This occurs because the lithology in the downstream area mostly includes medium and fine sandy, which is finer grained than the lithology in the upstream area and generates a relatively lower specific yield, thus causing groundwater levels to be more sensitive to river replenishment.

TABLE 1 Comparison of the average groundwater levels.

Time/year	Average water levels (no river replenishment) (m)	Average water levels (river replenishment) (m)	Relative rise (m)	Average annual relative rise (m)
2020	3.49	4.04	0.55	0.24
2035	−2.56	0.95	3.51	0.23

The average groundwater level visually reflects the total groundwater storage in the area. The impact of river replenishment on groundwater recovery was investigated by comparing changes in the average groundwater level with and without river replenishment during different periods. Table 1 provides changes in average groundwater level across the shallow aquifer with and without river replenishment in 2020 and 2035. Under the realistic simulation scenario, after more than 2 years of river replenishment (from September 2018 to December 2020), the average relative rise in groundwater level due to river replenishment was 0.55 m. Under the predicted scenario, all source and sink terms, such as the amount of river replenishment, extraction, and rainfall, remained constant every year, and the average relative rise in the water level due to river replenishment could reach 3.51 m over 15 years (from January 2021 to December 2035), with an average relative rise of 0.23 m per year.

At the prediction stage, the average groundwater levels decreased at a rate of 0.44 m/a assuming no further river replenishment after 2020, whereas the levels could decrease at a rate of 0.21 m/a within the context of river replenishment. This indicates that river replenishment decreased the rate of groundwater level decline, which is conducive to groundwater level recovery. However, the total groundwater storage could still decrease, even under consistent river replenishment, indicating that the magnitude of river replenishment attained under current projection conditions could not achieve complete groundwater recovery over the next 15 years. It was estimated that if the amount of river replenishment during the prediction period was doubled, the regional exploitation–replenishment balance could basically be achieved, that is, the total groundwater storage volume would no longer decrease. As such, only a provincial extraction–replenishment balance (the groundwater balance goal by 2022) could be achieved, not a complete extraction–replenishment balance (the groundwater balance goal by 2035). Therefore, reasonable groundwater pumping restrictions will be required to meet the goal of an overall groundwater balance by 2035.

4.2 Scenario and effect of groundwater pumping restriction

4.2.1 Restriction scenario

The AGLC between the end of 2035 and the end of 2034 under river replenishment conditions is shown in Figure 5, with districts where the value was less than zero identified as the groundwater pumping restriction zone.

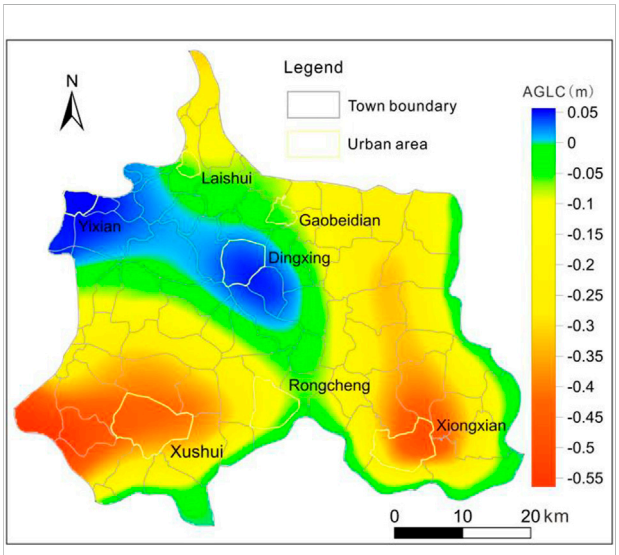


FIGURE 5
AGLC between the end of 2035 and the end of 2034.

Groundwater levels declined in most districts of the study area, whereas levels rose within a small area near the river. In these districts with rising groundwater levels, the increase in groundwater level due to river replenishment was greater than the decrease due to other source–sink items (mainly groundwater pumping). The area with the most significant area of water level decrease was is located in the west of Xushui, with a maximum decrease of 0.55 m. While the area with the greatest rise in groundwater levels was located in Dingxing, with a maximum rise of 0.05 m. The area with rising groundwater levels reached 484 km^2, accounting for approximately 15% of the total study area. Areas where groundwater levels rised as a result of river replenishment have achieved an overall groundwater balance and there is no need to reduce groundwater extraction in these areas. However, in districts with decreasing groundwater levels, the increase in groundwater levels due to river replenishment no longer offset the decrease due to source–sink items such as groundwater pumping. In these areas, that is, the restriction zone, groundwater extraction reduction is necessary if the goal of an overall groundwater balance by 2035 is to be reached.

The districts of the greatest groundwater level decline were concentrated in or near the urban areas of Xiongxian and Xushui,

with a maximum decrease of 0.55 m. The flow fields in Figure 3 also indicate that two groundwater depression cones were located approximately near these two areas. Therefore, more intensive groundwater pumping restrictions are required in the urban areas of Xiongxian and Xushui to restore groundwater levels. When setting the restriction volume, it is possible to allocate a larger volume to these two urban areas, considering the availability of water replacement within urban areas, to ensure that the restriction degree remains lower than 15% in other rural areas (town areas) by the time the groundwater balance goal of 2035 is reached. The groundwater pumping restriction volume was calculated according to the equation in section 3.2.2, with the restriction amount increasing by an equal proportion each year over the prediction period (2021–2035), that is, the amount of groundwater pumping was reduced by an equal proportion each year.

If the restriction volume calculated with the equation in section 3.2.2 was directly applied in the prediction model, the restrictions in the rural areas adjacent to the urban areas of Xushui and Xiongxian could exceed the maximum limit. Therefore, a larger restriction amount was allocated to these two urban areas, considering that urban areas could be supplied by diverted water as a replacement of groundwater to ensure that the restriction degree in the town areas remained lower than 15%. It was finally determined that when the minimum total volume of groundwater pumping restriction reached 0.84 km^3, that is, the average annual reduction volume reached 56 million m^3, the goal of an overall groundwater balance could be achieved by 2035.

However, if the effect of river replenishment was not considered, that is, no river replenishment of groundwater occurs in the prediction model (2021–2035), both the area and amount of restriction could increase. It was calculated that to achieve the goal of an overall groundwater balance by 2035 without river replenishment, groundwater extraction would have to be reduced across almost the entire study area, with a total volume of 1.22 km^3 and an average annual volume of 81 million m^3, which is 25 million m^3 greater than the volume under river replenishment conditions.

4.2.2 Restriction effect

The AGLC between December 2034 and December 2035 after the implementation of groundwater pumping restrictions is shown in Figure 6. The groundwater levels in the study area rose overall, but the rise was not significant. The greatest rise in groundwater levels was near the lower reaches of the river, with the largest rise reaching 0.15 m. While other areas away from the river showed rises of less than 0.1 m, with the smallest rise of 0.01 m, located within Xiongxian. This indicates that the groundwater levels in 2035 could no longer decline anywhere in the study area under this restriction scenario, which suggests that the groundwater balance goal by 2035 could be

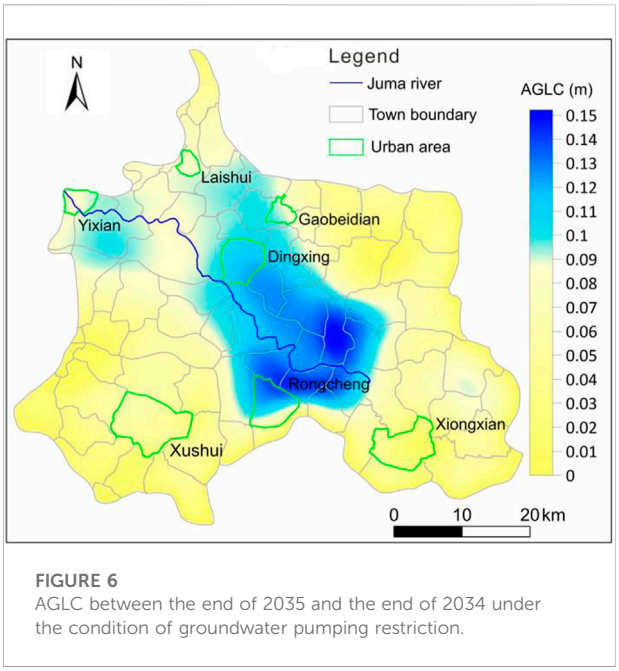


FIGURE 6
AGLC between the end of 2035 and the end of 2034 under the condition of groundwater pumping restriction.

achieved. The overall average groundwater level in 2035 reached 3.23 m when groundwater pumping restrictions were superimposed, which is 2.28 m greater than that without restriction during the same period.

The maximum annual degree of groundwater pumping restriction in the rural and urban areas of the study area is shown in Figure 7. In the urban areas, Xushui and Xiongxian exhibited the highest degree of restriction at 55% and 50%, respectively, while Dingxing and Yixian did not require restriction due to river replenishment, and the other three urban areas remained consistent with the original calculated values. In the rural (town) areas, the greatest restriction on groundwater extraction occurred near the urban area of Xushui, with a reduction of 13.4%, which is below the maximum restriction limit (15%). In addition, only three towns near the urban area of Xushui and one town near the urban area of Xiongxian exhibited a restriction degree higher than 10%, while that in the remaining areas occurred within 10%. These results indicate that under this groundwater pumping restriction scenario, extraction reduction slightly affected the crop yield, with the resulting yield reduction not exceeding a maximum value of 8.9%.

Overall, the two counties of Xushui and Rongcheng required the highest degree of groundwater pumping restriction, which in turn reflects the relatively serious groundwater overexploitation issue in both counties and the need for strict groundwater management. In addition to the influence of groundwater extraction in these two counties, another reason is that these counties are farther away from the river and thus less affected by river replenishment, requiring greater groundwater pumping reductions to achieve groundwater balance.

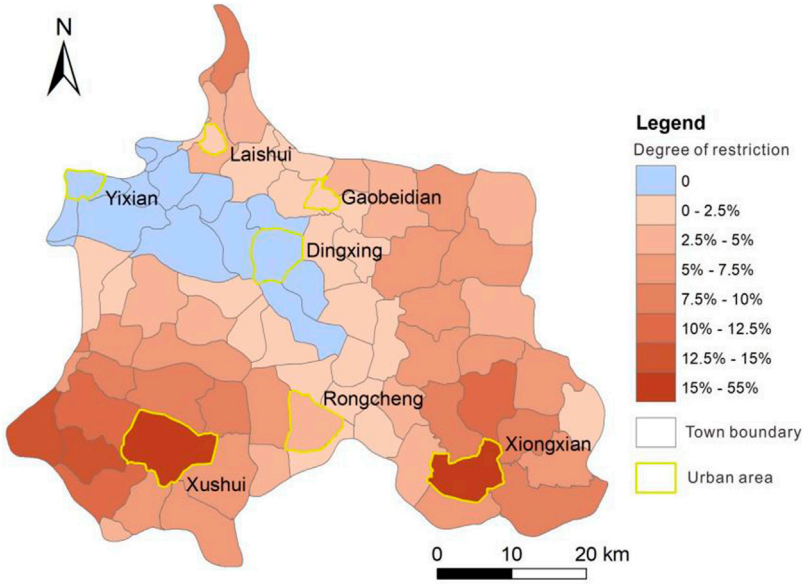


FIGURE 7
Distribution of the degree of groundwater pumping restriction.

Groundwater pumping restrictions not only facilitated the recovery of the groundwater levels but also facilitated the overall groundwater balance, meeting the government's groundwater management goal of 2035. The implementation of the SNWD plays a key role in restoring groundwater levels across the NCP by providing additional water supply sources, which in turn reduces groundwater exploitation. Many studies have predicted the impact of groundwater extraction reduction in the NCP or parts of the interior region. With a decrease of 6.0 km^3/a in groundwater pumping in the NCP, groundwater levels in piedmont areas, especially in Beijing, could notably recover by 2030, and the rate of groundwater level decrease could decline in the central and coastal plains by 2030 (Cao et al., 2013). In Beijing, the depletion of groundwater storage is decreasing at a rate of 2.8 km^3/a after reducing water use for agricultural purposes (Long et al., 2020). The shallow groundwater levels in the NCP could significantly increase due to climate change and groundwater pumping restriction, and the maximum increase in the absolute rise in groundwater levels could reach 6.71 m after 40 years, in which the relative rise in groundwater levels due to groundwater pumping restrictions could reach approximately 7.94 m (Li et al., 2017). In this study, the relative rise in shallow groundwater levels due to 15 consecutive years of restrictions was 2.28 m, which is generally consistent with the above research results and can provide a certain guiding significance for the development of groundwater pumping restriction policies in the future.

5 Conclusion

The impact of river replenishment on groundwater levels over the next 15 years was simulated and calculated with a numerical model and calculation of the RGLC to achieve the goal of groundwater balance by 2035, considering the policies of river replenishment and restrictions on groundwater pumping currently implemented and to be implemented in the long term. Then, based on the influence of river replenishment, other factors were comprehensively considered, including the impact of extraction reduction on crop yields in rural (town) areas and replacement of groundwater withdrawal with diverted water in urban areas, and a suitable groundwater pumping restriction scenario was proposed, combined with calculation of the AGLC. The objective was to achieve a complete exploitation–replenishment balance by 2035 while minimizing the volume of groundwater pumping reduction and thus minimize the impact on human production and livelihood.

River replenishment facilitates groundwater level recovery, particularly in the vicinity of the river, ensuring that groundwater levels in 15% of the total study area could be recovered without extraction reduction. However, under the current replenishment and extraction conditions, the groundwater level only gradually increased in specific areas near the river, while the overall average groundwater water level still decreased at a rate of 0.21 m/a. Therefore, extraction reduction is necessary to achieve the goal of an overall groundwater balance by 2035. Considering that the groundwater levels near the river already increased due to river replenishment, only in those areas with falling water levels should exploitation be reduced. It was determined that with an average

annual reduction in the groundwater pumping volume of 56 million m^3, a complete exploitation–replenishment balance could be achieved by 2035. The maximum annual degree of groundwater pumping restriction in town areas under this restriction plan was 13.4%, with a maximum reduction in crop yields of 8.9%.

In the study of sustainable groundwater management with ecological water replenishment and extraction restrictions, it is necessary to fully consider the impact of river replenishment on groundwater levels, and appropriate restrictions on groundwater pumping should subsequently be implemented in specific areas to accomplish more effective restriction. This study did not consider the impact of climate change on groundwater levels. The direct impact of climate change on rainfall and the indirect impact on other sources and sinks require further research to be integrated into the groundwater model.

Data availability statement

The original contributions presented in the study are included in the article/supplementary material, further inquiries can be directed to the corresponding author.

Author contributions

WC and QH designed the conceptualization, methodology, data curation, and original draft preparation. YX performed data curation and formal analysis. YZ was responsible for data curation and language. JL and YZ designed the methodology.

Funding

This study was financially sponsored by the Natural Science Foundation of China (Grant Nos. 41702282), and the China Geological Survey Project (Grant Nos. DD20160238 and DD20190303).

Conflict of interest

The authors declare that the research was conducted in the absence of any commercial or financial relationships that could be construed as a potential conflict of interest.

Publisher's note

All claims expressed in this article are solely those of the authors and do not necessarily represent those of their affiliated organizations, or those of the publisher, the editors and the reviewers. Any product that may be evaluated in this article, or claim that may be made by its manufacturer, is not guaranteed or endorsed by the publisher.

References

Aeschbach-Hertig, W., and Gleeson, T. (2012). Regional strategies for the accelerating global problem of groundwater depletion. *Nat. Geosci.* 5 (12), 853–861. doi:10.1038/ngeo1617

Alin, C. D., Wada, Y., Kastner, T., and Puma, M. J. (2017). Erratum: Corrigendum: Groundwater depletion embedded in international food trade. *Nature* 543 (7647), 366. doi:10.1038/nature24664

Cao, G., Zheng, C., Scanlon, B. R., Jie, L., and Li, W. (2013). Use of flow modeling to assess sustainability of groundwater resources in the North China Plain. *Water Resour. Res.* 49 (1), 159–175. doi:10.1029/2012WR011899

Chen, F., Ding, Y., Li, Y., Li, W., Tang, S., Yu, l., et al. (2020). Thinking of groundwater overdraft restoration in north plain China. *s. N. Water Transf. Water Sci. Technol.* 018 (002), 191–198. doi:10.13476/j.cnki.nsbdqk.2020.0042

Chen, F., Ding, Y., Tang, S., Ding, L., and Yang, Y. (2021). Practice and effect analysis of river-lake ecological water supplement and groundwater recharge in the North China region. *China Water Resour.* 7, 36–39.

Cui, W., and Hao, Q. (2020). Comparing Q-tree with nested grids for simulating managed river recharge of groundwater. *Water* 12 (12), 3516. doi:10.3390/w12123516

Ding, Z., Li, W., and Zhao, Y. (2013). Study on land use change and its driving forces in the Juma River Basin in recent 20 years. *Haihe Water Resour.* 5 (05), 27–29.

Feng, W., Zhong, M., Lemoine, J.-M. L., Biancale, R., Hsu, H.-T., Xia, J., et al. (2013). Evaluation of groundwater depletion in North China using the Gravity Recovery and Climate Experiment (GRACE) data and ground-based measurements. *Water Resour. Res.* 49 (4), 2110–2118. doi:10.1002/wrcr.20192

Gleeson, T., Wada, Y., Bierkens, M., and Beek, L. (2012). Water balance of global aquifers revealed by groundwater footprint. *Nature* 488 (7410), 197–200. doi:10.1038/nature11295

Hao, Q. C., Shao, J. L., Xie, Z. H., and Xing, G. Z. (2012). A Study of the artificial adjustment of groundwater storage of the Yongding River alluvial fan in Beijing. *Hydrogeol. Eng. Geol.* 39, 12–18. doi:10.1007/s11783-011-0280-z

Hao, Q., Shao, J., Cui, Y., Zhang, Q., and Huang, L. (2018). Optimization of groundwater artificial recharge systems using a genetic algorithm: A case study in beijing, China. *Hydrogeol. J.* 26, 1749–1761. doi:10.1007/s10040-018-1781-7

Hu, Y., Moiwo, J. P., Yang, Y., Han, S., and Yang, Y. (2010). Agricultural water-saving and sustainable groundwater management in shijiazhuang irrigation district, north China plain. *J. Hydrol. X.* 393 (3-4), 219–232. doi:10.1016/j.jhydrol.2010.08.017

Huang, Z., Pan, Y., Gong, H., Yeh, J. F., Li, X., Zhou, D., et al. (2015). Subregional-scale groundwater depletion detected by GRACE for both shallow and deep aquifers in North China Plain. *Geophys. Res. Lett.* 42 (6), 1791–1799. doi:10.1002/2014GL062498

Kang, S., and Eltahir, E. A. B. (2018). North China Plain threatened by deadly heatwaves due to climate change and irrigation. *Nat. Commun.* 9, 2894. doi:10.1038/s41467-018-05252-y

Li, P., and Ren, L. (2019). Evaluating the effects of limited irrigation on crop water productivity and reducing deep groundwater exploitation in the north China plain using an agro-hydrological model: I. Parameter sensitivity analysis, calibration and model validation. *J. Hydrol. X.* 574, 497–516. doi:10.1016/j.jhydrol.2019.04.053

Li, W., Wang, L., Yang, H., Deng, Y., Cao, W., and Liu, K. (2020). The groundwater overexploitation status and countermeasure suggestions of the North China Plain. *China Water Resour.* 13 (13), 26–30.

Li, X., Ye, S. Y., Wei, A. H., Zhou, P. P., and Wang, L. H. (2017). Modelling the response of shallow groundwater levels to combined climate and water-diversion scenarios in Beijing-Tianjin-Hebei Plain, China. *Hydrogeol. J.* 25, 1733–1744. doi:10.1007/s10040-017-1574-4

Liu, J., Zheng, C., Li, Z., and Lei, Y. (2008). Ground water sustainability: Methodology and application to the north China plain. *Ground Water* 46 (6), 897–909. doi:10.1111/j.1745-6584.2008.00486.x

Long, D., Yang, W., Scanlon, B. R., Zhao, J., Liu, D., Burek, P., et al. (2020). South-to-North Water Diversion stabilizing Beijing's groundwater levels. *Nat. Commun.* 11, 3665. doi:10.1038/s41467-020-17428-6

Nakayama, T. (2011). Simulation of complicated and diverse water system accompanied by human intervention in the North China Plain. *Hydrol. Process.* 25 (17), 2679–2693. doi:10.1002/hyp.8009

Qiu, J. (2010). China faces up to groundwater crisis. *Nature* 466 (7304), 308. doi:10.1038/466308a

Rodell, M., Famiglietti, J. S., Wiese, D. N., Reager, J. T., Beaudoing, H. K., Landerer, F. W., et al. (2018). Emerging trends in global freshwater availability. *Nature* 557 (7707), 651–659. doi:10.1038/s41586-018-0123-1

Shah, T., Roy, A. D., Qureshi, A. S., and Wang, J. (2003). Sustaining asia's groundwater boom: An overview of issues and evidence. *Nat. Resour. Forum* 27 (2), 130–141. doi:10.1111/1477-8947.00048

Shao, J., Li, L., Cui, Y., and Zhang, Z. (2013). Groundwater flow simulation and its application in groundwater resource evaluation in the north China plain, China. *Acta Geol. Sin. - Engl. Ed.* 87 (1), 243–253. doi:10.1111/1755-6724.12045

Shu, Y., Villholth, K. G., Jensen, K. H., Stisen, S., and Lei, Y. (2012). Integrated hydrological modeling of the North China Plain: Options for sustainable groundwater use in the alluvial plain of Mt. Taihang. *J. Hydrol. X.* 464–465 (5), 79–93. doi:10.1016/j.jhydrol.2012.06.048

Sun, H.-Y., Liu, C.-M., Zhang, X.-Y., Shen, Y.-J., and Zhang, Y.-Q. (2006). Effects of irrigation on water balance, yield and WUE of winter wheat in the North China Plain. *Agric. Water Manag.* 85, 211–218. doi:10.1016/j.agwat.2006.04.008

Sun, K., Hu, L., Guo, J., Yang, Z., Zhai, Y., Zhang, S., et al. (2021). Enhancing the understanding of hydrological responses induced by ecological water replenishment using improved machine learning models: A case study in Yongding River. *Sci. Total Environ.* 768, 145489. doi:10.1016/j.scitotenv.2021.145489

The Ministry of Water Resources of the People's Republic of China (2019). Groundwater overexploitation comprehensive management action plan [Online]. Available: http://szy.mwr.gov.cn/dtxx/201904/t20190429_1132485.html.[Accessed].

The People's Government of Hebei Province (2019). Groundwater overexploitation comprehensive management implementation of the views [Online]. Available: http://info.hebei.gov.cn//eportal/ui?pageId=6806152&articleKey=6862328&columnId=6807806 ([Accessed].

Voss, K. A., Famiglietti, J. S., Lo, M. H., Linage, C. D., Rodell, M., Swenson, S. C., et al. (2013). Groundwater depletion in the Middle East from GRACE with implications for transboundary water management in the Tigris-Euphrates-Western Iran region. *Water Resour. Res.* 49 (2), 904–914. doi:10.1002/wrcr.20078

Wolfgang, K., Peter, B., Tobias, S., and Philip, B. (2003). Sustainable groundwater management–problems and scientific tools. *Episodes* 26, 279–284. doi:10.18814/epiiugs/2003/v26i4/002

Xiao, Y., Hao, Q., Zhang, Y., Zhu, Y., Yin, S., Qin, L., et al. (2021). Investigating sources, driving forces and potential health risks of nitrate and fluoride in groundwater of a typical alluvial fan plain. *Sci. Total Environ.* 802, 149909. doi:10.1016/j.scitotenv.2021.149909

Xiao, Y., Liu, K., Hao, Q., Li, Y., Xiao, D., Zhang, Y., et al. (2022a). Occurrence, controlling factors and health hazards of fluoride-enriched groundwater in the lower flood plain of Yellow River, northern China. *Expo. Health*, 345–358. doi:10.1007/s12403-021-00452-2

Xiao, Y., Liu, K., Hao, Q., Xiao, D., Zhu, Y., Yin, S., et al. (2022b). Hydrogeochemical insights into the signatures, Genesis and sustainable perspective of nitrate enriched groundwater in the piedmont of Hutuo watershed, China. *Catena* 212, 106020. doi:10.1016/j.catena.2022.106020

Yan, Z., Zhou, Z., Sang, X., and Wang, H. (2018). Water replenishment for ecological flow with an improved water resources allocation model. *Sci. Total Environ.* 643, 1152–1165. doi:10.1016/j.scitotenv.2018.06.085

Yao, P., and Lu, G. (2017). Hydrochemical and isotopic characteristics of the Juma River and their implications. *Environ. Chem.* 36 (7), 1525–1536.

Yu, Y., Wang, Y., and Liu, Y. (2012). Analysis of "12.7" rainstorm flood in Juma River. *Haihe Water Resour.* 5 (05), 22–24.

Zhang, C., Duan, Q., Yeh, P., Pan, Y., Gong, H., Gong, W., et al. (2019). The effectiveness of the South-to-North Water diversion Middle route project on water delivery and groundwater recovery in north China plain. *Water Resour. Res.* 56, e2019WR026759. doi:10.1029/2019WR026759

Zhang, F., Cheng, W., and Ran, H. (2017). Variation of groundwater level and it's influencing factors analysis in plain areaof baoding city. *Water Resour. Power* 35 (8), 128–132.

Zhang, G., Fei, Y., Wang, H., Yan, M., and Liu, Z. (2009). Effects of grain increase and irrigation water saving on groundwater extraction in plain area of Hebei Province. *Geol. Bull. China* 28, 645–650.

Zhang, J., Wang, D., and Pan, S. (2012). Calculation of ecological water requirements based on groundwater model in baoding. *Earth Sci.* 37 (002), 370–374. doi:10.3799/dqkx.2012.044

Zhang, K., Zeng, S., Zhao, J., Wang, X., Zhou, J., Xu, H., et al. (2016). Effects of groundwater pressure extraction on wheat production in North China Plain. *J. Agr. Sci. Technol.* 18, 111–117.

Zhang, M., Hu, L., Yao, L., and Yin, W. (2018). Numerical studies on the influences of the South-to-North water transfer project on groundwater level changes in the Beijing Plain, China. *Hydrol. Process.* 32, 1858–1873. doi:10.1002/hyp.13125

Zhang, Y., and Che, Y. (2017). Analysis on the status quo and countermeasures of shallow groundwater overexploitation in Baoding Plain area. *Groundwater* 39 (03), 60–61.

Zhang, Y., and Li, G. M. (2014). Influence of south-to-north water diversion on major cones of depression in North China Plain. *Environ. Earth Sci.* 71 (9), 3845–3853. doi:10.1007/s12665-013-2771-7

Zheng, C., Jie, L., Cao, G., Kendy, E., and Jia, Y. (2010). Can China cope with its water crisis?-Perspectives from the north China plain. *Ground Water* 48 (3), 350–354. doi:10.1111/j.1745-6584.2010.00695_3.x

Zhu, L., Gong, H., Li, X., Li, Y., Su, X., Guo, G., et al. (2013). Comprehensive analysis and artificial intelligent simulation of land subsidence of Beijing, China. *Chin. Geogr. Sci.* 23 (2), 237–248. doi:10.1007/s11769-013-0589-6

frontiers | Frontiers in Earth Science

ORIGINAL RESEARCH
published: 18 July 2022
doi: 10.3389/feart.2022.941948

How do Geohazards Affect Household Consumption: Evidence From China

Luman Zhao[1] *and Boyi Zhu*[2]*

[1]School of Finance, Hebei University of Economics and Business, Shijiazhuang, China, [2]School of Economics, Renmin University of China, Beijing, China

Geohazards trigger well-documented adverse effects on human health and economic development. However, previous studies mostly focused on the impact of one specific geohazard on consumption and discussed the impact mechanism from a limited perspective. In this paper, we focus on the consequences of generalized geohazards on household consumption in China and investigate the mechanisms of the impact of geohazards on consumption from three perspectives by using the China Household Finance Survey 2017 microdata and National Bureau of Statistics provincial-level data. The study finds that, firstly, household consumption is significantly higher in areas with more geohazards and the effect is found to be long-term. This finding passes a series of robust tests. Secondly, heterogeneity analysis reveals that the consumption structure of families is changed by geohazards. Moreover, the frequency of geohazards affects the consumption of households at different income-level to different degrees. Thirdly, among three possible impact mechanisms, the main mechanism of the impact of geohazards on household consumption is through the increasing of individuals' impatience.

Keywords: geohazards, time preference, risk preference, income, household consumption

OPEN ACCESS

Edited by:
Yunhui Zhang,
Southwest Jiaotong University, China

Reviewed by:
Canlin Xu,
Guizhou University of Finance and Economics, China
Ying Zhou,
Guangdong University of Finance and Economics, China

***Correspondence:**
Boyi Zhu
2019000464@ruc.edu.cn

Specialty section:
This article was submitted to Geohazards and Georisks, a section of the journal Frontiers in Earth Science

Received: *12 May 2022*
Accepted: *24 June 2022*
Published: *18 July 2022*

Citation:
Zhao L and Zhu B (2022) How do Geohazards Affect Household Consumption: Evidence From China. Front. Earth Sci. 10:941948. doi: 10.3389/feart.2022.941948

INTRODUCTION

Scholars are actively researching the interconnection and interaction between geohazards and human society (Yao et al., 2022; Zhang et al., 2021a, 2021b), to reveal the socio-economic attributes of geological disasters more comprehensively. According to the findings from the literature, geohazards are disruptive and responsive to human health and economic development in many ways. For instance, human casualties (Salvati et al., 2018; Alam and Ray-Bennett, 2021; Li et al., 2021; Shinohara and Kume, 2022), direct damage to infrastructure or private property (Rosenbaum and Culshaw, 2003; Yang et al., 2022), the negative impact on household income (Mertens et al., 2016; Pham et al., 2021), the change of consumer behavior among groups with different level of income (Moniruzzaman, 2019; Yao et al., 2019) and lower life satisfaction (Sapkota, 2018; Berlemann and Eurich, 2021; Burrows et al., 2021).

In the field of consumption, there is no consistent academic conclusion on how the hazards impact consumer behavior. One perspective is examining the impact of disaster experiences on individual risk preferences. Some scholars, based on a precautionary savings motivation perspective, argued that personal experience of disasters led to increased risk aversion (Cameron and Shah, 2015; Bourdeau-Brien and Kryzanowski, 2020). These risk-averse consumers would consequently increase current savings and crowd out current consumption to prevent unexpected declines in future income and to smooth out future consumption. However, other scholars believed that hazards experience increased individual risk preference (Eckel et al., 2009; Page et al., 2014). The current consumption expenditure would not decrease significantly, but people who suffered a loss would be more likely to

take a risk. Others found that hazard experience has no significant impact on consumers' risk preference (Voors et al., 2012; Callen, 2015). Cameron and Shah (2015) randomly selected individuals in rural Indonesia to play standard risk games. They found that people who recently suffered from floods or earthquakes showed more risk aversion. Experiencing natural disasters would make people aware that they are now facing greater risks of future disasters. Similarly, Bourdeau-Brien and Kryzanowski (2020) used the monetary value of losses owing to natural disasters, that covered natural hazards such as thunderstorms, hurricanes, floods, wildfires, or tornados. Their results showed that natural disasters led to a statistically and economically significant increase in risk aversion at the local level. On the contrary, Eckel et al. (2009) investigated the risk preferences of evacuees shortly after Hurricane Katrina, evacuees at 1 year later and samples in Houston with similar demographic data. The results indicated that the first group of samples showed significant risk preferences compared with the other two groups. And Page et al. (2014) used the edge of the 2011 Australian flood as a natural experimental environment. They found homeowners who suffered floods and faced a huge loss of property value are 50% more likely to choose risky gambling. While Voors et al. (2012) found drought or excess rainfall and Callen (2015) found tsunamis had no significant effect on risk preferences.

The second perspective is testing whether disaster experience changes time preference. Some scholars believed that consumers would realize that life and the future is uncertain after experiencing the disaster and would prefer current utility (Cassar et al., 2017). In the intertemporal decision-making of savings and consumption, the current consumption utility was stronger than the future consumption utility for these consumers, so they were more inclined to the current consumption. Other scholars believed that consumers' time preference was prone to long-term after a natural disaster (Isoré and Szczerbowicz, 2017; Chantarat et al., 2019), leading to a decline in current consumption and an increase in savings. Cassar et al. (2017) conducted a series of experiments in rural Thailand and found that the 2004 tsunami led to significant long-term increases in risk aversion, prosocial behavior, and impatience. Conversely, Isoré and Szczerbowicz (2017) developed a New Keynesian model. The study found that the increase in disaster risk could produce recession and countercyclical risk premium, and agents became more patient in dealing with disaster risk shocks. Chantarat et al. (2019) used primary survey data to examine the effects of the 2011 mega-flood on Cambodian rice farmers' household preferences, subjective expectations, and behavior. They found that flood victims exhibited greater risk aversion and altruism, reduced impatience and trust in friends and local government.

The third idea is that disaster experience affects consumption by reducing income (Mottaleb et al., 2013; Mertens et al., 2016). Both those who worked as self-employed, such as farmers, and on a wage were more likely to suffer reduced income after the disaster. However, other scholars found that disaster experience had no significant impact on income but on financial hardship and risk aversion (Johar et al., 2022). Based on the above research, the mechanism of geohazards on household consumption is shown in **Figure 1**.

Academic research on the impact of geohazards on consumer behavior is currently limited by the availability of data, and there is still much room for development. Firstly, most of the relevant research objects are restricted to specific disasters. To go beyond that, this paper uses the generalized geohazards data in China, and the research conclusions are more universally applicable. Secondly, most of the relevant studies only focused on the impact based on one mechanism, while this paper comprehensively tests three mechanism channels of the impact of disaster experience on consumption and provides micro evidence from Chinese households' perspective. Thirdly, the empirical analysis of this paper uses Chinese household microdata, discusses and solves potential endogenous issues, and performs multidimensional robust tests and heterogeneity analysis to increase the reliability of the results. Besides the three theoretical and empirical aspects above, on a practical aspect, the outbreak of COVID-19 has been a huge shock to the global economy, and the findings of this paper could help predict the impact of this pandemic on households time preferences, risk preferences and consumption.

The remainder of this study is arranged as follows. The second section is the theoretical model, the third section is the econometrics model, data sources and descriptive statistics, the fourth section is the empirical tests, and the last is the conclusion section.

THEORETICAL MODEL

The existing consumption models have well-established the representations of time preference inconsistency, and this paper draws on the work of Phelps and Pollak (1968) and Krusell et al. (2002). However, there is a lack of authoritative expressions of changes in risk preferences. In order to find an analytical solution, this paper uses the common CARA function to describe the consumer utility function, that is $u_t = -\frac{1}{\theta}\exp(-\theta c_t)$, where θ is the absolute risk aversion factor.

Based on the research of Phelps and Pollak (1968) and Krusell et al. (2002), this paper sets the discount factor of consumers as $\{1, \beta\delta, \beta\delta^2 \ldots \beta\delta^t\}$. Then introducing the hyperbolic discounting model into the utility function:

$$U_t = u(c_t) + \beta \sum_{s=t+1}^{\infty} \delta^{s-t} u(c_{t+1}) \quad (1)$$

Among them, the long-term discount factor used between the future T period and T+1 period (long-term) is δ. The short-term discount factor between period 0 and period 1 (short term) is $\beta\delta$. β=1 represents the exponential discount function in which consumers have time consistency. β<1 represents short-term impatience of the consumer, lack of patience compared to the original plan and overspending relative to the original plan. β>1 means that consumers are more tolerant, more patient than the original plan, and spend less than the original plan.

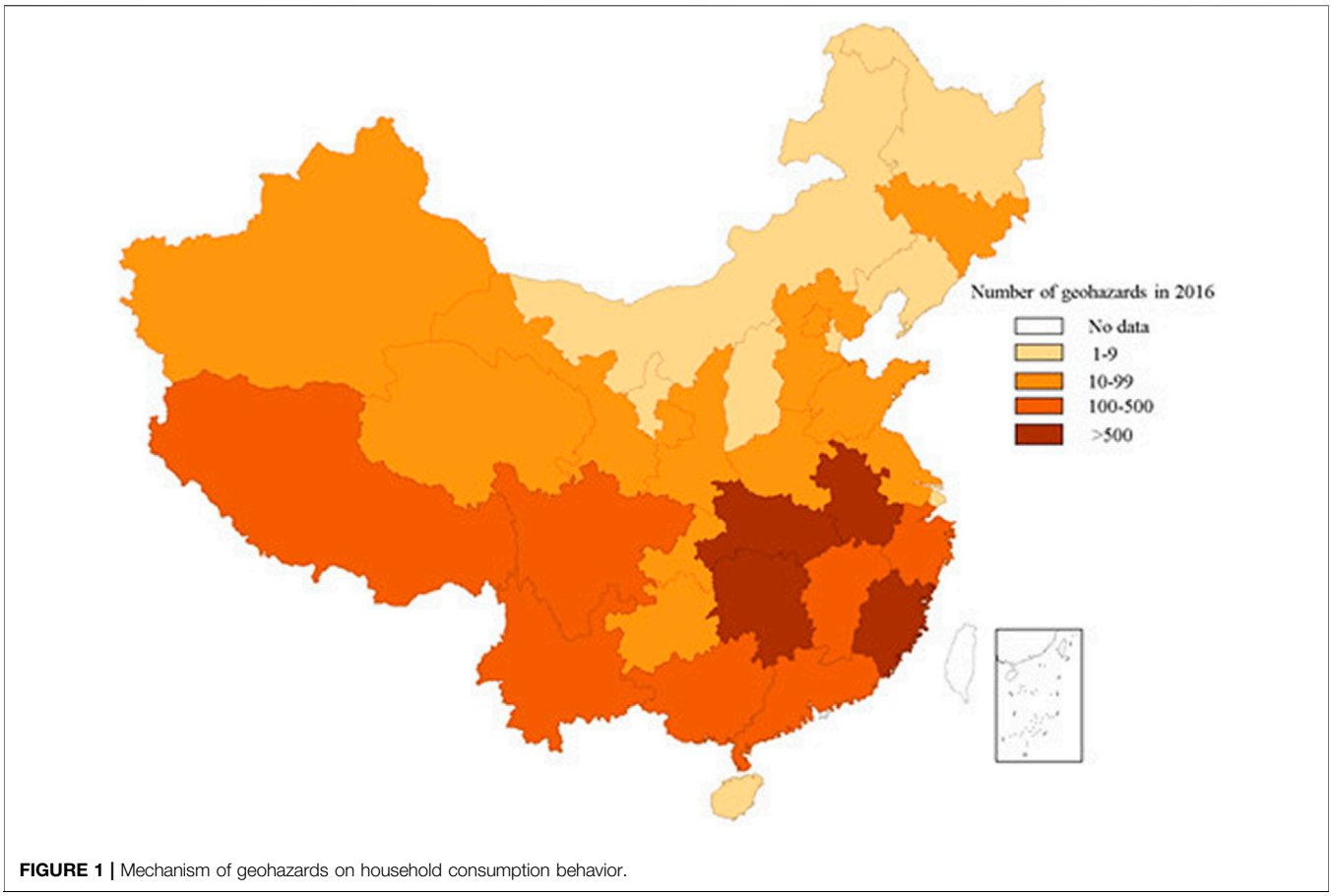


FIGURE 1 | Mechanism of geohazards on household consumption behavior.

Then the intertemporal decision-making of consumers can be expressed as the following dynamic programming problem:

$$\max_{c_t, c_{t+1}\ldots} \left(u_t + \beta E_t \sum_{s=t+1}^{\infty} \delta^{s-t} u_{t+1}\right) \tag{2}$$

$$\text{s.t.} \begin{array}{l} a_{t+1} = (1+r)a_t + y_t - c_t \\ y_{t+1} = y_t + \varepsilon_{t+1}^{y} \end{array}$$

where β is the short-term discount factor and δ is the long-term discount factor used to express time preference inconsistency. y_t is disposable income, a_t is household wealth, r is the interest rate, ε_{t+1}^{y} represents the income shock, obeys the normal distribution with the mean value of 0 and the variance of σ_y^2, and the instantaneous utility function of consumers is $u_t = -\frac{1}{\theta}\exp(-\theta c_t)$.

By establishing the Behrman equation, the optimal consumption is:

$$c_t = ra_t + y_t - \frac{\theta\sigma_y^2}{2r} - \frac{1}{r\theta}\ln\left[\delta(1+r\beta)\right] \tag{3}$$

This optimal consumption shows that the change in household income, time preference and uncertainty of future income affect household consumption, which is consistent with the possible mechanism of previous literature. The disposable income y_t and household wealth a_t, is positively correlated with consumer current spending c_t. The variance of expected future income σ_y^2, which means uncertainty of future income, is negatively correlated with the current consumption c_t. From the perspective of time preference, in contrast to no inconsistency in time preference that β=1, consumption increases when consumers are impatient that β<1, and decreases when β>1 consumers are more patient. The theoretical conclusion indicates the possible consequence of income, time preference and uncertainty on consumption. Empirical tests will further study the impact of geohazards on consumption through those variables.

ECONOMETRICS MODEL, DATA AND DESCRIPTIVE STATISTICS

Econometrics Model

Based on the above ideas, the following econometric model is constructed to test the impact of geohazards on residents' consumption.

$$c_{ij} = \beta_1 haz_{ij} + \beta_2 Z_i + \beta_3 X_j + \varepsilon_{ij} \tag{4}$$

Where c_{ij} is the consumption of household i in region j, Z_i represents other factors that may affect consumption,

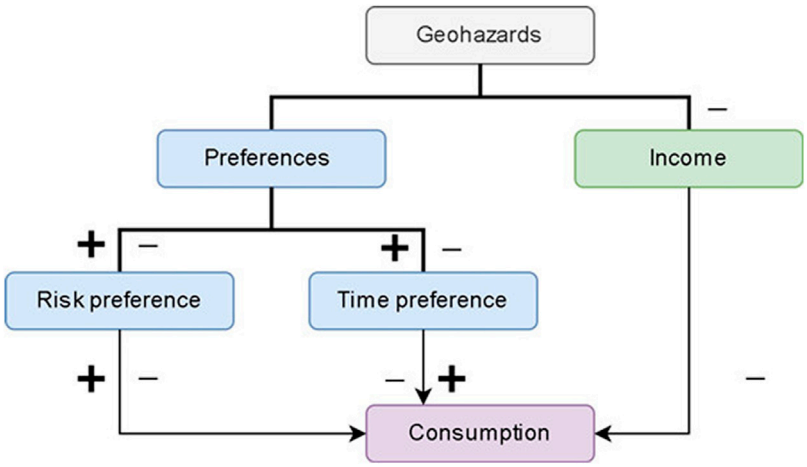


FIGURE 2 | Geographic dispersion of the number of geohazards.

including household head characteristics and household characteristics. X_j is the control variable at the macro level.

The data in this paper comes from the China Household Finance Survey 2017 and the China National Bureau of Statistics in 2016, respectively conducted by the Southwestern University of Finance and Economics in 2017 (CHFS 2017) and the Chinese government. The CHFS 2017 sample covers 29 provinces (autonomous regions and municipalities) in China except for Xinjiang, Tibet, Hong Kong, Macao and Taiwan. In 2017, China Household Finance Survey collected 40,011 valid samples. The questionnaire questions covered the interviewees' income, consumption, subjective preferences and other specific conditions of the participants in 2016, with national, provincial and sub-provincial city representation. The China National Bureau of Statistics provides provincial-level data.

Variable Selection and Descriptive Statistics

Household consumption variable includes total household consumption, categorized consumption expenditure and annual credit card spending. In testing the mechanism of the influence of geohazard experience on household consumption choice, the amount of annual credit card spending is selected as the measurement variable of household time preference for the reason that the credit card usage represents the household attitude between immediate utility and expected future utility (Meier and Sprenger, 2010; Gathergood, 2012).

As for the geohazards variable, the frequency of provincial geological hazards is used as the measurement variable of the degree of geological disasters in the region. The number of casualties of provincial geological disasters is used as the robust test. In the China National Bureau of Statistics, geohazards refer to sudden geological hazards such as landslides, avalanches, mudslides, ground subsidence and slow-varying geological hazards such as ground cracks, ground subsidence and seawater intrusion. **Figure 2** displays the geographic dispersion of frequency of geohazards.

Referring to the previous literature, control variables include household characteristics, household head characteristics, and macro control variables. Where household characteristics include annual household income, assets, whether the household lives in rural, whether the household owns houses, family size, and dependency ratio. The characteristics of a head of household include gender, age, square item of age, whether to pay medical insurance or endowment insurance, education level and marital status. Macro variables are provincial GDP, population and local fiscal general public expenditure.

In order to reduce the influence of extreme value on the results, this paper uses 99% quantile to deal with the extreme value of variables and takes the logarithm of non-dummy variables to reduce the influence of heteroscedasticity. Descriptive statistics of main variables are shown in **Table 1**.

EMPIRICAL RESULTS AND DISCUSSION

Analysis of Basic Results and Robust Tests

Table 2 displays the OLS basic results and a series of robust test results of the impact of geological hazard frequency on household consumption.

Table 2 regression 1) reports the effect of provincial geohazard frequency on total household consumption in 2016. The results show that when other conditions remain unchanged, a 1% increase in the frequency of geological disasters will promote the total consumption of households by 1.22%. This result is significant at the statistical level of 1%.

Take **Table 2** regression 1) as an example to explain the effect of control variables on consumption. Household assets and income have a significant positive impact on consumption, which is consistent with the conclusion of classical economic theory. The age of the household head has an inverted U-shaped relationship with consumption, with consumption showing an

TABLE 1 | The statistics description of main variables.

	Observations	Mean	Std. Dev	Min	Max
total consumption	40,011	65,337.565	83,908.3460	736.8	3,434,645
hazard freq	40,011	415.4377	930.7913	1	4,478
hazard casualties	40,011	18.9516	23.9163	0	84
total income	40,011	88,264.781	109,250.3346	-1,068	690,180
total asset	40,011	1,055,887.7	1,785,408.3507	1,580	10,220,302
age	39,992	55.1923	14.0989	24	86
family size	40,011	3.1657	1.5170	1	8
support rate	40,011	0.3320	0.3439	0	1
married	39,966	0.8528	0.3543	0	1
edugrp 2	39,958	0.2693	0.4436	0	1
edugrp 3	39,958	0.0847	0.2785	0	1
rural household	40,011	0.3182	0.4658	0	1
female	40,010	0.2067	0.4050	0	1
insurance pension	39,683	0.8208	0.3835	0	1
insurance medicine	39,678	0.9332	0.2497	0	1
own houses	39,972	0.9044	0.2940	0	1
gdp	40,011	31,807.8040	22,250.4533	2,258.200	82,163.2030
population	40,011	5,448.4684	3,072.8354	582	11,908
public expenditure	40,011	514.0853	273.3921	75.79	1,147.35
Rdls	40,011	0.8439	0.9548	0.0044	4.3263
the Han nationality	25,983	0.9358	0.2451	0	1

upward movement and then a downward trend as age increases. Family size has a significant positive effect on total household consumption. The proportion of family support has a negative inhibitory effect on family consumption. Married or cohabiting households spend significantly more compared to households in other marital status. The higher the education level of the head of household, the higher the family's expectation of future income. With the increase of expectation permanent income, household consumption will consequently increase significantly. There are differences in consumption between rural and urban families in China, which shows that the consumption of rural families is lower than that of urban families. Households headed by women consume more. If the head of household has medical insurance or endowment insurance, it will reduce the motivation for preventive savings and promote family consumption, but the role of endowment insurance in promoting family consumption is not significant. Households that own their own houses will have lower consumption. The more developed the economy of the province, the more government public expenditure, the higher the level of household total consumption, and the population of the province is negatively correlated with the total household consumption.

Further empirical tests reveal that the above results passed the robust tests based on the replacement of explanatory variables and the empirical tests to mitigate the endogenous problem of omitted variables, that is, the results of regression 2) to regression 5) in **Table 2**. Among them, regression 2) is a robust test based on the replacement of explanatory variables. Replacing the explanatory variable with the number of casualties due to geohazards, the results confirm that the deeper the area is affected by geohazards, the higher the level of total household consumption and the total household consumption level increases statistically significant at the 1% level. **Table 2** Regression 3) to regression 5) is to reduce the endogenous problem of missing variables. The impact on consumption in disaster areas may be uncertain due to the compensation effect of receiving government disaster relief funds based on the income level. In order to distinguish between the effects of receiving disaster relief funds and the degree of geological disaster on consumption, the dummy variable of whether the family received government disaster relief funds in that year was added to the regression (3). The results show that the promotion effect of disaster relief funds on consumption does not change the significance of the care variable coefficient of regional geohazards frequency on household consumption. Areas with different frequencies of geohazards may have different geographical environments or cultural backgrounds, and they may affect the consumption level. **Table 2** regression 4) uses the topographic relief degree of the province as the proxy variable of the geographical environment and **Table 2** regression 5) uses the Han nationality dummy as the proxy variable of the cultural differences. After adding those variables, the coefficient of the core explanatory variable remains robust.

Heterogeneity analysis

Tables 3, **4** analyze the heterogeneity of household consumption structure and different income groups.

Table 3 shows the heterogeneous impact of the frequency of geological disasters on eight types of consumption. According to the estimation results in **Table 3**, the frequency of geological disasters will significantly promote the consumption types of food, clothing, household equipment and services, transportation and communication. The type of consumption of housing, health care and education, culture and entertainment services are significantly suppressed, and the effect on other categories of consumption is not significant. Overall, the results of heterogeneity analysis support the conclusion of

TABLE 2 | Impact of geological hazard frequency on household consumption.

Variables	(1)	(2)	(3)	(4)	(5)
	ln_total_consumption	ln_total_consumption	ln_total_consumption	ln_total_consumption	ln_total_consumption
ln_hazard_freq	0.0122***	—	0.0121***	0.0112***	0.0166***
	(0.0018)	—	(0.0018)	(0.0018)	(0.0035)
ln_hazard_casualties	—	0.0281***	—	—	—
	—	(0.0020)	—	—	—
relief	—	—	0.1156**	—	—
	—	—	(0.0518)	—	—
Rdls	—	—	—	0.0101**	—
	—	—	—	(0.0042)	—
the Han nationality	—	—	—	—	0.0172
	—	—	—	—	(0.0237)
ln_total_income	0.0909***	0.0908***	0.0909***	0.0909***	0.0886***
	(0.0036)	(0.0036)	(0.0036)	(0.0036)	(0.0066)
ln_total_asset	0.1549***	0.1551***	0.1551***	0.1548***	0.1535***
	(0.0027)	(0.0027)	(0.0027)	(0.0027)	(0.0052)
age	-0.0210***	-0.0204***	-0.0211***	-0.0208***	-0.0199***
	(0.0018)	(0.0018)	(0.0018)	(0.0018)	(0.0041)
age_2	0.0001***	0.0001***	0.0001***	0.0001***	0.0001***
	(0.0000)	(0.0000)	(0.0000)	(0.0000)	(0.0000)
fami_size	0.1145***	0.1138***	0.1145***	0.1146***	0.1141***
	(0.0026)	(0.0025)	(0.0026)	(0.0026)	(0.0049)
support_r	-0.0470***	-0.0456***	-0.0471***	-0.0471***	-0.0488*
	(0.0129)	(0.0129)	(0.0129)	(0.0129)	(0.0251)
Married	0.1496***	0.1509***	0.1498***	0.1496***	0.1381***
	(0.0111)	(0.0111)	(0.0111)	(0.0111)	(0.0222)
edugrp_2	0.1543***	0.1556***	0.1544***	0.1550***	0.1451***
	(0.0078)	(0.0078)	(0.0078)	(0.0078)	(0.0148)
edugrp_3	0.2937***	0.2942***	0.2937***	0.2942***	0.2893***
	(0.0130)	(0.0129)	(0.0130)	(0.0129)	(0.0280)
Rural	-0.2930***	-0.2943***	-0.2937***	-0.2933***	-0.2994***
	(0.0084)	(0.0084)	(0.0084)	(0.0084)	(0.0153)
female	0.0569***	0.0563***	0.0570***	0.0564***	0.0483***
	(0.0086)	(0.0086)	(0.0086)	(0.0086)	(0.0169)
insur_pension	-0.0090	-0.0068	-0.0090	-0.0096	-0.0063
	(0.0094)	(0.0094)	(0.0094)	(0.0094)	(0.0186)
insur_med	0.0285**	0.0270*	0.0284**	0.0284**	0.0012
	(0.0140)	(0.0139)	(0.0140)	(0.0139)	(0.0287)
House	-0.3491***	-0.3478***	-0.3493***	-0.3492***	-0.2922***
	(0.0127)	(0.0127)	(0.0127)	(0.0127)	(0.0258)
ln_gdp_prov	0.1219***	0.1489***	0.1212***	0.1367***	0.1617***
	(0.0107)	(0.0108)	(0.0107)	(0.0122)	(0.0192)
ln_popu_prov	-0.3308***	-0.3114***	-0.3305***	-0.3280***	-0.2961***
	(0.0159)	(0.0160)	(0.0159)	(0.0159)	(0.0289)
ln_ public_prov	0.1770***	0.1185***	0.1779***	0.1606***	0.0657
	(0.0227)	(0.0229)	(0.0228)	(0.0237)	(0.0407)
Constant	8.7481***	8.6506***	8.7480***	8.6674***	8.6857***
	(0.0761)	(0.0759)	(0.0761)	(0.0831)	(0.1543)
Observations	39,342	39,342	39,342	39,342	10,976
R-squared	0.4606	0.4627	0.4607	0.4607	0.4514

*Standard error in parentheses; *, **, *** denote statistical significance levels at 10, 5, and 1%, respectively.*

baseline regression and suggest that geological hazards affect the structure of household consumption.

In order to explore whether the consumption of households at different income levels differs according to their wealth traits, **Table 4** reports the impact of the frequency of geohazards on household consumption at different income levels. Considering the differences in the level of economic development of each province, we classified the full sample households into four groups in descending order of per capita income within their respective provinces. The lowest 25% of households ranked in terms of per capita income are considered low-income households, households ranked 25–50% are regarded as lower-middle-income households, households ranked 50–75% are considered upper-middle-income households, and households with per capita income ranked the highest 25% are regarded as high-income households. The results of **Table 4** show that for families at different income levels, the impact of the frequency of geological disasters on their current consumption is different. The promotion effect of geological disaster frequency on the consumption of low-income and lower-middle-income households is higher than that of upper-middle-income and high-income groups, among which the

TABLE 3 | Heterogeneity of the frequency of geohazards in the category of consumption.

Variables	(1)	(2)	(3)	(4)
	ln_food_c	ln_clothing_c	ln_resident_c	ln_equipment_c
ln_hazard_freq	0.0335***	0.0288***	-0.0109***	0.0238***
	(0.0018)	(0.0063)	(0.0038)	(0.0043)
Control variables	Yes	Yes	yes	yes
Observations	39,342	39,342	39,342	39,342
R-squared	0.3825	0.3416	0.2404	0.2893
Variables	**(5)**	**(6)**	**(7)**	**(8)**
	ln_medical_c	**ln_travel_c**	**ln_educ_c**	**ln_other_c**
ln_hazard_freq	-0.0588***	0.0150***	-0.0424***	-0.0049
	(0.0094)	(0.0034)	(0.0099)	(0.0055)
Control variables	Yes	yes	Yes	yes
Observations	39,342	39,342	39,342	39,342
R-squared	0.0638	0.4120	0.3365	0.0277

*Standard error in parentheses; *, **, *** denote statistical significance levels at 10, 5, and 1%, respectively.*

TABLE 4 | The impact of frequency of geohazards on household consumption at different income levels.

Dependent variable: ln_wtotal_consump	(1)	(2)	(3)	(4)
	Lowest 25%	25–50%	50–75%	Top 25%
ln_hazard_freq	0.0153***	0.0197***	0.0121***	-0.0008
	(0.0036)	(0.0033)	(0.0032)	(0.0035)
Control variables	Yes	Yes	yes	yes
Observations	9,806	9,816	9,866	9,854
R-squared	0.4610	0.3908	0.3650	0.3540

*Standard error in parentheses; *, **, *** denote statistical significance levels at 10, 5, and 1%, respectively.*

TABLE 5 | Mechanism analysis and long-term impact test.

Variables	(1)	(2)	(3)	(4)
	ln_total_income	risk_aversion	ln_credit_c	ln_total_c
ln_hazard_freq	0.0082	-0.0036	0.0891***	0.0074***
	(0.0052)	(0.0042)	(0.0271)	(0.0027)
	—	—	—	0.0066**
	—	—	—	(0.0028)
Control variables	Yes	Yes	yes	yes
Observations	24,824	35,089	1,389	39,342
R-squared	0.2480	—	—	0.4607

*Standard error in parentheses; *, **, *** denote statistical significance levels at 10, 5, and 1%, respectively.*

promotion effect on the consumption of lower-middle-income households is the strongest. The promotion effect on the consumption of high-income families is not significant.

Mechanism Analysis

This paper discusses the impact mechanism of the frequency of geological disasters on household consumption from the perspective of income, risk preference and time preference, as well as discuss the long-term impact of the frequency of geological disasters on household consumption.

According to the conclusions of the theoretical model, household consumption is positively influenced by income. The frequency of geological disasters has an impact on income in two directions. On one hand, due to the occurrence of disasters, the possibility of income decline or unemployment increases (Berlemann and Eurich, 2021), causing a decrease in household income. On the other hand, the hazard relief funds issued by the government can make up for the decline in income. Post-disaster construction assistance and relief work can drive employment and investment to a certain extent in the affected areas, with a positive effect on the income of households. We need to test whether the frequency of geological disasters will affect the income level of affected families. The results of regression 1) in **Table 5** show that the frequency of geological hazards has no significant effect on household income level. This indicates that the change in income level is not a mechanism by which the frequency of geohazards affects household consumption.

According to the precautionary saving theory, the higher the degree of risk aversion of residents, the more inclined they are to increase current savings to smooth future consumption, leading to a reduction of current consumption. On the contrary, the lower the level of risk aversion in the household, the fewer savings are made for precautionary motives and the weaker inhibition effect on current consumption. Therefore, we test whether the frequency of geohazards affects consumption by changing affected residents' risk preferences. According to the CHFS questionnaire on the measurement of risk preference, that is, 'If you had two lottery tickets to choose from right now and if you choose the first one, you have a 100% chance of getting 4,000 yuan, if you choose the second one, you have a 50% chance of getting 10,000 yuan, and 50% chance of getting nothing, which one would you like to choose?' In this paper, the risk aversion dummy variable is set to one for respondents who choose the first lottery ticket, and the risk aversion dummy variable is set to 0 for a respondent who chooses the second lottery ticket. The results of regression 2) in **Table 5** show that the frequency of geohazards has no significant impact on household risk preference, indicating that the change of risk preference is not the mechanism of the frequency of geohazards affecting household consumption.

Time preference is an important factor influencing individuals' intertemporal decisions; individuals with long-term time preference have higher utility for future consumption and are more inclined to increase savings and decrease consumption in the current period. In contrast, individuals with short-term time preferences are more likely to increase current consumption and reduce savings. This paper tests whether the frequency of geological hazards changes the temporal preferences of affected residents. Credit card expenditure, which is closely related to time preference, is selected as the proxy variable of time preference. Since credit card expenditure can only be observed by using credit cards, the observed value of credit card consumption of households without credit cards is 0, resulting in truncated data, so Tobit regression is used. **Table 5** regression 3) shows that the frequency of geohazards has a significant positive effect on the amount of credit card spending. This suggests that the frequency of geohazards may be a mechanism for households to increase their consumption by changing individual time preferences to place more emphasis on the utility of current consumption, which in turn promotes household current consumption. Changing the time preference may be a mechanism for families to increase consumption after geological disasters experience.

Table 5 regression four adds the provincial geohazard frequency variable with a 5-years lag to test the long-term effect of geohazard frequency on household consumption. The regression results show that experiencing a geological disaster not only has an immediate and significant boosting effect on residents' consumption but also has a significant long-term boosting effect on their consumption.

CONCLUSION

Geological hazards have a significant impact on consumer behavior, but few previous studies have focused on the impact of generalized geohazards on consumption and conducted multi-perspective mechanism discussions. Moreover, the existing literature has not reached a consensus conclusion. To address this research gap, this paper examines how geohazards in China affect household consumption by using CHFS 2017 microdata and the National Bureau of Statistics provincial-level data. Based on the above theoretical model and empirical test results, the conclusions reached in this study are as follows:

Firstly, the level of household consumption is significantly higher in regions with more geohazards. The results remain robust after changing the explanatory variables, excluding the impact of government disaster relief funds and solving the endogenous problems that may be brought by different geographical environments or cultural backgrounds.

Secondly, a more detailed heterogeneity analysis reveals that geohazards affect the consumption structure of households, with significant increases in consumption categories such as food, clothing, household equipment supplies and services, transportation and communication consumption types. In addition, the frequency of geological hazards affects households' consumption at different income-level to different degrees, with a stronger consumption boost for low-income and lower-middle-income households. In addition, the empirical results also confirm that the frequency of geohazards has a significant increase impact on household consumption not only in the short term but also in the long term.

Thirdly, the empirical results show that the impact mechanism of the frequency of geohazards on household consumption mainly lies in changing the individual's time preference, making the individual prone to indulge in the present and increase the current consumption. While income and risk attitudes do not change significantly after geohazards and are not the influencing mechanisms.

DATA AVAILABILITY STATEMENT

The original contributions presented in the study are included in the article/Supplementary material, further inquiries can be directed to the corresponding author.

AUTHOR CONTRIBUTIONS

BZ contributed to conception and design of the study. LZ performed the statistical analysis and wrote the first draft of the manuscript. All authors contributed to manuscript revision, read, and approved the submitted version.

FUNDING

This study is supported by the 1. Research Center for Finance and Enterprise Innovation, Hebei University of Economics and Business; 2. Scientific Research and Development Program Fund of Hebei University of Economics and Business (2021ZD11).

REFERENCES

Alam, E., and Ray-Bennett, N. S. (2021). Disaster Risk Governance for District-Level Landslide Risk Management in Bangladesh. *Int. J. Disaster Risk Reduct.* 59, 102220. doi:10.1016/j.ijdrr.2021.102220

Berlemann, M., and Eurich, M. (2021). Natural Hazard Risk and Life Satisfaction - Empirical Evidence for Hurricanes. *Ecol. Econ.* 190, 107194. doi:10.1016/j.ecolecon.2021.107194

Bourdeau-Brien, M., and Kryzanowski, L. (2020). Natural Disasters and Risk Aversion. *J. Econ. Behav. Organ.* 177, 818–835. doi:10.1016/j.jebo.2020.07.007

Burrows, K., Desai, M. U., Pelupessy, D. C., and Bell, M. L. (2021). Mental Wellbeing Following Landslides and Residential Displacement in Indonesia. *SSM - Ment. Health* 1, 100016. doi:10.1016/j.ssmmh.2021.100016

Callen, M. (2015). Catastrophes and Time Preference: Evidence from the Indian Ocean Earthquake. *J. Econ. Behav. Organ.* 118, 199–214. doi:10.1016/j.jebo.2015.02.019

Cameron, L., and Shah, M. (2015). Risk-taking Behavior in the Wake of Natural Disasters. *J. Hum. Resour.* 50 (2), 484–515.

Cassar, A., Healy, A., and von Kessler, C. (2017). Trust, Risk, and Time Preferences after a Natural Disaster: Experimental Evidence from Thailand. *World Dev.* 94, 90–105. doi:10.1016/j.worlddev.2016.12.042

Chantarat, S., Oum, S., Samphantharak, K., and Sann, V. (2019). Natural Disasters, Preferences, and Behaviors: Evidence from the 2011 Mega Flood in Cambodia. *J. Asian Econ.* 63, 44–74. doi:10.1016/j.asieco.2019.05.001

Eckel, C. C., El-Gamal, M. A., and Wilson, R. K. (2009). Risk Loving after the Storm: A Bayesian-Network Study of Hurricane Katrina Evacuees. *J. Econ. Behav. Organ.* 69, 110–124. doi:10.1016/j.jebo.2007.08.012

Gathergood, J. (2012). Self-control, Financial Literacy and Consumer Over-indebtedness. *J. Econ. Psychol.* 33, 590–602. doi:10.1016/j.joep.2011.11.006

Isoré, M., and Szczerbowicz, U. (2017). Disaster Risk and Preference Shifts in a New Keynesian Model. *J. Econ. Dyn. Control* 79, 97–125. doi:10.1016/j.jedc.2017.04.001

Johar, M., Johnston, D. W., Shields, M. A., Siminski, P., and Stavrunova, O. (2022). The Economic Impacts of Direct Natural Disaster Exposure. *J. Econ. Behav. Organ.* 196, 26–39. doi:10.1016/j.jebo.2022.01.023

Krusell, P., Kuruşçu, B., and Smith, A. A. (2002). Time Orientation and Asset Prices. *J. Monetary Econ.* 49, 107–135. doi:10.1016/S0304-3932(01)00095-2

Li, X., Huang, X., and Zhang, Y. (2021). Spatio-temporal Analysis of Groundwater Chemistry, Quality and Potential Human Health Risks in the Pinggu Basin of North China Plain: Evidence from High-Resolution Monitoring Dataset of 2015-2017. *Sci. Total Environ.* 800, 149568. doi:10.1016/j.scitotenv.2021.149568

Meier, S., and Sprenger, C. (2010). Present-Biased Preferences and Credit Card Borrowing. *Am. Econ. J. Appl. Econ.* 2, 193–210. doi:10.1257/app.2.1.193

Mertens, K., Jacobs, L., Maes, J., Kabaseke, C., Maertens, M., Poesen, J., et al. (2016). The Direct Impact of Landslides on Household Income in Tropical Regions: A Case Study from the Rwenzori Mountains in Uganda. *Sci. Total Environ.* 550, 1032–1043. doi:10.1016/j.scitotenv.2016.01.171

Moniruzzaman, S. (2019). Income and Consumption Dynamics after Cyclone Aila: How Do the Rural Households Recover in Bangladesh? *Int. J. Disaster Risk Reduct.* 39, 101142. doi:10.1016/j.ijdrr.2019.101142

Mottaleb, K. A., Mohanty, S., Hoang, H. T. K., and Rejesus, R. M. (2013). The Effects of Natural Disasters on Farm Household Income and Expenditures: A Study on Rice Farmers in Bangladesh. *Agric. Syst.* 121, 43–52. doi:10.1016/j.agsy.2013.06.003

Page, L., Savage, D. A., and Torgler, B. (2014). Variation in Risk Seeking Behaviour Following Large Losses: A Natural Experiment. *Eur. Econ. Rev.* 71, 121–131. doi:10.1016/j.euroecorev.2014.04.009

Pham, N. T. T., Nong, D., and Garschagen, M. (2021). Natural Hazard's Effect and Farmers' Perception: Perspectives from Flash Floods and Landslides in Remotely Mountainous Regions of Vietnam. *Sci. Total Environ.* 759, 142656. doi:10.1016/j.scitotenv.2020.142656

Phelps, E. S., and Pollak, R. A. (1968). On Second-Best National Saving and Game-Equilibrium Growth. *Rev. Econ. Stud.* 35, 185–199. doi:10.2307/2296547

Rosenbaum, M. S., and Culshaw, M. G. (2003). Communicating the Risks Arising from Geohazards. *J. R. Stat. Soc. A* 166, 261–270. doi:10.1111/1467-985x.00275

Salvati, P., Petrucci, O., Rossi, M., Bianchi, C., Pasqua, A. A., and Guzzetti, F. (2018). Gender, Age and Circumstances Analysis of Flood and Landslide Fatalities in Italy. *Sci. Total Environ.* 610-611, 867–879. doi:10.1016/j.scitotenv.2017.08.064

Sapkota, J. B. (2018). *Human Well-Being after 2015 Nepal Earthquake: Micro-evidence from One of the Hardest Hit Rural Villages*. Munich, Germany: MPRA Paper.

Shinohara, Y., and Kume, T. (2022). Changes in the Factors Contributing to the Reduction of Landslide Fatalities between 1945 and 2019 in Japan. *Sci. Total Environ.* 827, 154392. doi:10.1016/j.scitotenv.2022.154392

Voors, M., Nillesen, E., Verwimp, P., Bulte, E., Lensink, R., and Van Soest, D. (2012). Violent Conflict and Behavior: A Field Experiment in Burundi. *Am. Econ. Rev.* 102 (2), 941–964.

Yang, H.-Q., Zhang, L., Gao, L., Phoon, K.-K., and Wei, X. (2022). On the Importance of Landslide Management: Insights from a 32-year Database of Landslide Consequences and Rainfall in Hong Kong. *Eng. Geol.* 299, 106578. doi:10.1016/j.enggeo.2022.106578

Yao, D., Xu, Y., and Zhang, P. (2019). How a Disaster Affects Household Saving: Evidence from China's 2008 Wenchuan Earthquake. *J. Asian Econ.* 64, 101133. doi:10.1016/j.asieco.2019.101133

Yao, R., Yan, Y., Wei, C., Luo, M., Xiao, Y., and Zhang, Y. (2022). Hydrochemical Characteristics and Groundwater Quality Assessment Using an Integrated Approach of the PCA, SOM, and Fuzzy C-Means Clustering: A Case Study in the Northern Sichuan Basin. *Front. Environ. Sci.* 10. doi:10.3389/fenvs.2022.907872

Zhang, Y., Dai, Y., Wang, Y., Huang, X., Xiao, Y., and Pei, Q. (2021a). Hydrochemistry, Quality and Potential Health Risk Appraisal of Nitrate Enriched Groundwater in the Nanchong Area, Southwestern China. *Sci. Total Environ.* 784, 147186. doi:10.1016/j.scitotenv.2021.147186

Zhang, Y., He, Z., Tian, H., Huang, X., Zhang, Z., Liu, Y., et al. (2021b). Hydrochemistry Appraisal, Quality Assessment and Health Risk Evaluation of Shallow Groundwater in the Mianyang Area of Sichuan Basin, Southwestern China. *Environ. Earth Sci.* 80, 576. doi:10.1007/s12665-021-09894-y

Conflict of Interest: The authors declare that the research was conducted in the absence of any commercial or financial relationships that could be construed as a potential conflict of interest.

Publisher's Note: All claims expressed in this article are solely those of the authors and do not necessarily represent those of their affiliated organizations, or those of the publisher, the editors and the reviewers. Any product that may be evaluated in this article, or claim that may be made by its manufacturer, is not guaranteed or endorsed by the publisher.

Copyright © 2022 Zhao and Zhu. This is an open-access article distributed under the terms of the Creative Commons Attribution License (CC BY). The use, distribution or reproduction in other forums is permitted, provided the original author(s) and the copyright owner(s) are credited and that the original publication in this journal is cited, in accordance with accepted academic practice. No use, distribution or reproduction is permitted which does not comply with these terms.

frontiers | Frontiers in Earth Science

ORIGINAL RESEARCH
published: 22 July 2022
doi: 10.3389/feart.2022.943700

Time-Varying Effect of Ductile Flexural Toppling Failure on Antidip Layered Rock Slope

Junchao Cai[1,2], *Da Zheng*[2,3]*, *Nengpan Ju*[2,3], *Jue Wang*[2,3], *Xin Zhou*[2,3] *and Da Li*[1]

[1]School of Civil Engineering, Henan University of Science and Technology, Luoyang, China, [2]State Key Laboratory of Geohazard Prevention and Geoenvironment Protection, Chengdu University of Technology, Chengdu, China, [3]College of Environment and Civil Engineering, Chengdu University of Technology, Chengdu, China

Ductile flexural toppling failure is a common form of toppling failure, and it is the product of long-term geological history and shows the characteristics of long-term deformation and progressive failure. The creep characteristics of rock mass have been seldom considered in the current research on toppling, especially interlayer creep of rock layers in the process of toppling. Based on the thought of deformation stability analysis, the flexural toppling failure was divided into the following four stages: start-up, rapid deformation, transient stability, and long-term creep stages. Combined with mechanical analysis, the developmental conditions of the start-up, transient stability, and long-term creep development stages are discussed respectively. Finally, several cases were selected to analyze the stage and the stability of the toppling deformation body, as well as to verify the rationality of the mechanical analysis condition. Study results show that the start-up conditions meet **Equation 2**, the rock layer inclination and slope angle is $0.5\pi - \varphi$ in the transient stability stage, and that angle is the infinite 0.5π in the long-term creep stage. Other external forces (such as water pressure) will intensify the development of ductile flexural toppling failure, so that the angle between the toppled bedding surface and the slope surface increases. It is of great significance to analyze the development stage of the ductile flexural toppling, comprehensively analyze and evaluate the stability of the ductile flexural toppling, reasonably develop and utilize its self-stability ability, and set up support measures.

Keywords: antidip layered rock slope, ductile flexural toppling, time-varying effect, shear creep, transient stable state

OPEN ACCESS

Edited by:
Yunhui Zhang,
Southwest Jiaotong University, China

Reviewed by:
Jiajun Peng,
Kyoto University, Japan
Bo Zhao,
Institute of Mountain Hazards and Environment (CAS), China
Pinglang Kou,
Chongqing University of Posts and Telecommunications, China

***Correspondence:**
Da Zheng
zhengda@cdut.cn

Specialty section:
This article was submitted to Geohazards and Georisks, a section of the journal Frontiers in Earth Science.

Received: *14 May 2022*
Accepted: *01 June 2022*
Published: *22 July 2022*

Citation:
Cai J, Zheng D, Ju N, Wang J, Zhou X and Li D (2022) Time-Varying Effect of Ductile Flexural Toppling Failure on Antidip Layered Rock Slope. Front. Earth Sci. 10:943700. doi: 10.3389/feart.2022.943700

HIGHLIGHTS

1. Based on the thought of deformation stability analysis, we divided flexural toppling failure into four stages.
2. The developmental conditions of the start-up, transient stability, and long-term creep development stages are discussed respectively using mechanical analysis.
3. Several cases were selected to verify the rationality of the developmental conditions.
4. This study is of great significance for comprehensively analyzing the development stage and evaluating the stability of the ductile flexural toppling.

INTRODUCTION

Toppling failure of antidip layered rock slope, as a typical slope failure, has been reported in an increasing number of situations with the construction of mines, highways, hydropower stations, and so on (Cruden and Hu 1994; Tamrakar et al., 2002; Huang 2007; Liu et al., 2016; Zhang et al., 2018; Cai et al., 2019; Ning et al., 2019; Zhu et al., 2020). Goodman (2013) summarized the developments in the research of toppling deformation and concluded that toppling generally occurs in foundations, tunnels, and underground chambers or on a small scale in any rocky landscape where frost, creep, or water forces are active.

According to the characteristics of deformation and scale of toppled slopes, the following two types of failure mechanisms associated with toppling were proposed by Nichol et al. (2002) and Huang and Li (2017): a ductile flexural toppling mechanism and a brittle toppling mechanism, as described by Goodman (2013). Brittle toppling is generally developed in hard layered rock mass, mainly characterized by "fold and break" of the rock plate, rigid rotational structural deformation, and small-scale instability in the shallow of a slope. Furthermore, ductile flexural toppling often occurs in a thin layer of soft rock mass over a long time and at a considerable depth, and the slope deformation is mainly characterized by "bent but not broken." The deformation essence is mainly the gravity creep deformation of rock strata in the long geological history, and its development depth can reach tens or even hundreds of meters.

Toppling failure has been found in many locations, and new topples continue to be discovered and observed (Wang et al., 1992; Huang 2007; Zhang et al., 2015; Xie et al., 2018; Xia et al., 2019; Tu et al., 2020; Zhao et al., 2021). In particular, in mountain and gorge regions, this type of toppling failure has a large toppling development depth more than 100 m and has been observed in several notable locations: the left bank slope of Jinping-I Hydropower Station (>200 m), the Yinshuigou deformable slope at Xiaowan Hydropower Station (>200 m), the slope of Miaowei Hydropower Station (>200 m), the right abutment slope of Huangdeng Hydropower Station (>150 m), the right bank slope of Wulonglong Hydropower Station (>130 m), and the left bank slope of Longtan Hydropower Station (>200 m). Such large-scale toppling will eventually and possibly develop into a giant landslide, posing threats to the project. Huang (2007), Huang (2008), and Huang and Li (2017) proposed the concept of three-stage development of surface regeneration, long-term time-dependent deformation, and progressive failure of high slope based on the above studies.

Previous studies on toppling failure mainly focus on the mechanical theory research based on the mechanics of brittle materials, stability analysis at a certain moment, or study on the deformation failure mechanism based on physical tests and numerical tests. Aydan and Kawamoto (1992), Adhikary et al. (1997), and Adhikary and Dyskin (2007) established the toppling mechanics model of cantilever beam by applying the limit equilibrium theory, assuming that the interlayer force is the concentrated force and considering the self-weight of rock strata, and they verified it through the physical test. Amini et al. (2009), Amini et al. (2012), Amini et al. (2017), Amini et al. (2018) combined the GB method with the method of Aydan to introduce a solution for the analysis of block flexure toppling failure, secondary toppling failure, and they proposed an efficient method for analysis of the toppling based on compatibility principles governing the behavior of a cantilever beams. Liu et al. (2009) proposed the transfer coefficient method to analyze the stability of the toppling deformation body, and they analyzed the stability or designed the support scheme by calculating the residual sliding force of the slope foot block.

The existing studies of toppling fracture depth concentrate on the first toppling depth, since the actual field phenomenon is the product of multi-toppling, and there are several toppling interfaces or discontinuities. After the first toppling, the shape of the progressive failure of the second or multiple toppling illustrates the characteristics of flexural toppling. The studies indicate that the flexural toppling has notably the characteristics of time-dependent deformation and progressive failure. The creep characteristics of rock mass are seldom considered in the current studies of toppling, especially interlayer creep of rock layers in the process of toppling. Xiao and Wang (1991) and Wang et al. (1992) studied the creep mechanism of bending toppling of the toppled slope on the left bank of Longtan Hydropower Station. Pang et al. (2016) introduced a rheological model to consider creep characteristics of rock mass in the analysis of toppling fracture depth. Whereas, the creep contribution rate of rock mass is seldom for the flexural toppling, which is mainly due to the interlaminar dislocation and shear creep. Therefore, based on the start-up condition of toppling, a method for the analysis of bending toppling stage considering interlaminar shear creep is proposed in this study. From the perspective of time-dependent deformation and progressive failure, the mechanical conditions and stage characteristics of slope morphology were analyzed, and they further studied the deformation characteristics under the action of external forces (water pressure). It is important to understand the relationship between the development stage and the development state of the deformed body. According to the thought of deformation stability, the creep model of interlayers can be better and actually used to analyze the development process of ductile flexural toppling deformation.

MECHANICAL CONDITIONS OF THE PROCESS OF DUCTILE FLEXURAL TOPPLING

The ductile flexural toppling is based on the following assumptions. 1) The toppling can occur when the bedding surface is steeper and the slope angle is larger. 2) The thickness of the rock layer is infinitesimal relative to the scale of the whole slope, which can be regarded as a thin slab with little stiffness. 3) The unbalanced force on thin rock slab drives the bending and toppling of rock slabs, and the weight of that is negligible relative to the value of the stress field. 4) The maximum principal stress appears in the slope surface approximately parallel to the slope surface.

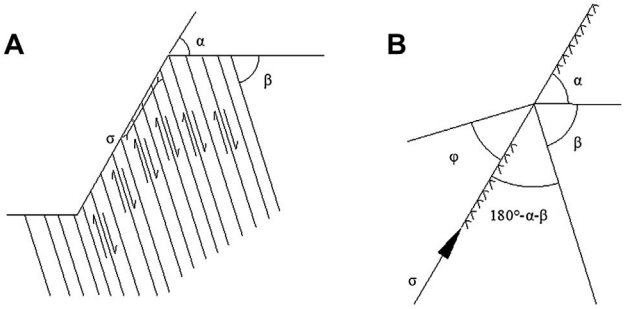


FIGURE 1 | Kinematic conditions for flexural slip preceding toppling: **(A)** directions of stress and slip directions in rock slope; **(B)** condition for interlayer slip.

The bending and toppling deformation of antidip layered rock mass can be divided into translational displacement and rotational displacement. This study only deals with the rotational displacement. Considering the complexity of stress change and adjustment in the process of bending toppling, the deformation state at instantaneous termination is only considered in the analysis. The process of bending toppling occurs as follow: the start-up, rapid deformation, transient stability, and long-term toppling creep stage. The mechanical conditions at each stage are briefly described in the following:

Start-Up Condition

Goodman and Bray (1976) believed that the occurrence of flexural toppling needs to meet the requirements of interlayer dislocation, and the bending tensile stress of rock slab exceeds its tensile strength. This approach ignored the cohesion between layers and only considered the relationship between the slope angle, the inclination angle of the rock slab, and the internal friction angle, and the kinematic conditions for the toppling of the rock slab were obtained (**Figure 1**):

$$(180 - \alpha - \beta) \le (90 - \varphi), \text{simplified to } \beta \ge (90 - \alpha) + \varphi, \quad (1)$$

where σ is parallel to the slope surface, β is the angle between the bedding plane and the horizontal plane, φ is the internal friction angle of the bedding plane, and α is the angle between the slope surface and the horizontal plane.

Due to the neglect of cohesion between layers, the calculation results are safer. Therefore, a comprehensive internal friction angle can be adopted to comprehensively analyze the start-up conditions of interlayer dislocation considering cohesion.

$$\beta \ge (90 - \alpha) + \varphi_e, \quad (2)$$

where φ_e is the comprehensive angle of internal friction.

Transient Stability

Based on the assumption of basic conditions, an element is selected from a part of a rock slab in the slope (**Figure 2**), plane a is the bedding surface, and plane b is the virtual surface. Assume that the internal friction angle of the bedding surface is φ, and cohesion is c, taking the center point O of the microelement zone as the rotation center point. The moment condition for the suspension of the rotation of the element is $M_r \ge M_t$, i. e,

$$0.5b \cdot a \cdot [\tau_r + (\tau_r + \Delta\tau)] \ge 0.5a \cdot b \cdot [\tau_t + (\tau_t + \Delta\tau)]. \quad (3)$$

Because of $\tau_r + (\tau_r + \Delta\tau) \le \sigma_r \cdot \tan\varphi + c + (\sigma_r + \Delta\sigma) \cdot \tan\varphi + c$ Then,

$$\tau_t \le \sigma_r \cdot \tan\varphi + c. \quad (4)$$

When the rotation is terminated, the stress reaches the equilibrium state and is in the transient stable state.

When the rotation of the rock slab terminates, the stress of the rock slab that reaches the equilibrium state and then it gets into the transient stable state. Thus,

$$\begin{aligned} &\tau_r = \tau_t \\ &\tau_r \le \sigma_r \cdot \tan\varphi + c. \end{aligned} \quad (5)$$

The toppling bending deformation of layered rock mass is mainly realized by the relative shear displacement between layers. The accumulated shear displacement and the rotation of rock slabs present the overall bending and the toppling deformation of slope.

Using the graphic method of the Coulomb–Mohr strength theory, the stress, corresponding to the shaded region in **Figure 3A**, does not satisfy the condition of transient stability. Assuming that V is the angle between the normal of the bedding surface and σ_1, the instability interval can be expressed as upper bound V_1 and lower bound V_2.

$$\sin\omega = \frac{\sigma_1 + \sigma_3 + 2c\ \tan\varphi}{\sigma_1 - \sigma_3} \cdot \sin\varphi$$

$$2V_1 = \omega + \varphi\ 2V_2 = \pi - \omega + \varphi, \text{then}$$

$$V_1 = 0.5\left[\varphi + \sin^{-1}\left(\frac{\sigma_1 + \sigma_3 + 2c\ \cot\varphi}{\sigma_1 - \sigma_3} \cdot \sin\varphi\right)\right], \quad (6)$$

$$V_2 = 0.5\left[\pi + \varphi - \sin^{-1}\left(\frac{\sigma_1 + \sigma_3 + 2c\ \cot\varphi}{\sigma_1 - \sigma_3} \cdot \sin\varphi\right)\right], \quad (7)$$

where $V \in [V_1, V_2]$, the rock slab will toppled and bended.

During the process of toppling, the angle V between the normal of bedding surface and σ_1 gradually increases, and the angle θ between the bedding surface and the slope surface decreases. The conditions for toppling can be expressed by V:

$$V = V_1 = 0.5\left[\varphi + \sin^{-1}\left(\frac{\sigma_1 + \sigma_3 + 2c\ \cot\varphi}{\sigma_1 - \sigma_3} \cdot \sin\varphi\right)\right]. \quad (8)$$

Assuming that the stress distribution in the slope is continuous, the ductile flexural toppling deformation shape is approximately continuous as well. Finite element method can be used to determine the slope stress distribution, and the experiments were used to determine the internal friction angle of the bedding surface. Then, the profile of flexural toppling shape can be calculated and ascertained. The stress field obtained at the slope surface is as follows: σ_1 is parallel to the slope surface, and σ_3 approaches 0:

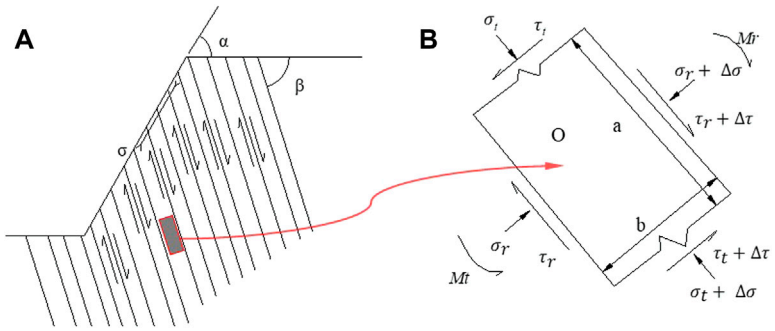


FIGURE 2 | Force system on elements of bending and toppling deformation slope: **(A)** toppling model; **(B)** elements.

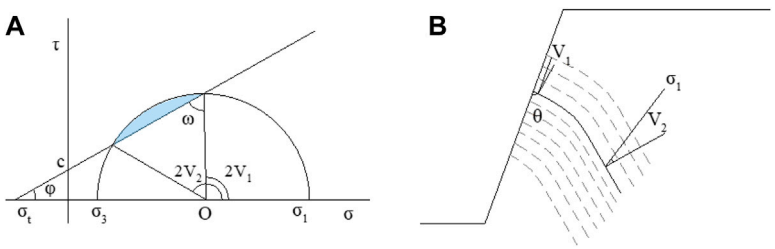


FIGURE 3 | Coulomb–Mohr diagram of the toppling condition of rock slab. **(A)** Coulomb–mohr diagram of toppling condition; **(B)** toppling form.

$$V_0 = 0.5\left[\varphi + sin^{-1}\left(\left(1 + 2c\frac{cot\,\varphi}{\sigma_1}\right) sin\,\varphi\right)\right]. \tag{9}$$

Assuming θ is the angle between bedding plane and slope surface, then

$$\theta = 0.5\pi - V_0 = 0.5\pi - 0.5\left[\varphi + sin^{-1}\left(\left(1 + 2c\frac{cot\,\varphi}{\sigma_1}\right) sin\,\varphi\right)\right]. \tag{10}$$

Considering weathering or other external forces, the bedding surface opens and separates, c tends to 0, and it is concluded that

$$V_0 = \varphi \quad \theta = 0.5\pi - \varphi. \tag{11}$$

To sum up, with respect to the antidip layered slope transformed by weathering or external forces, the angle θ at the slope surface is no more than $0.5\pi - \varphi$, toppling deformation will occur. For the slope of original rock mass, θ may be $<0.5\pi - \varphi$, and then **Equation 11** can be regarded as an intuitive criterion for whether the start-up occurrence of flexural toppling in antidip weathered rock mass.

Time-Varying on Interlaminar Shear Creep

The shear stress on the bedding surface meets $\tau_t = 0.5 \cdot (\sigma_1 - \sigma_3) \cdot sin\,2V$ at transient stability state, and the shear stress will cause rock slab shear creep along the bedding plane and further toppling. Interlaminar shear dislocation creep property was expressed by $\tau_r = \eta \cdot \dot{\varepsilon}$ reported by Sun and Zhang (1985); among them, the η and ε are for viscous coefficient and the shear strain of the bedding surface, respectively.

By combining the above two formulas, we can obtain:

$$\eta \cdot d\varepsilon = 0.5 \cdot (\sigma_1 - \sigma_3) \cdot sin\,2V \cdot dt\varepsilon. \tag{12}$$

When the toppled deformation occurs slightly, we can obtain **Equation 13** from **Figure 4**:

$$d\varepsilon = -dV, \tag{13}$$

where dV is the increment of toppled angle of bedding surface of rock slab,

$$\text{then, } dt = -\frac{\eta}{\sigma_1 - \sigma_3} \cdot \frac{d2V}{sin\,2V}. \tag{14}$$

We integrate both sides to get

$$\int_0^t dt = -\frac{\eta}{\sigma_1 - \sigma_3} \cdot \int_{V_1}^{V} \frac{d2V}{sin\,2V}, \tag{15}$$

$$\text{that is, } V = tan^{-1}\left(tan\,V_1 \cdot e^{-\frac{\sigma_1 - \sigma_3}{\eta}t}\right), \tag{16}$$

V_1 can be obtained from **Equation 6**. Then,

$$0 \le V \le V_1\; t \in [0, \infty), \tag{17}$$

where $t = 0$, $V = V_1$, $t \to \infty$, and $V \to 0_o$.

At the slope surface, the cohesion

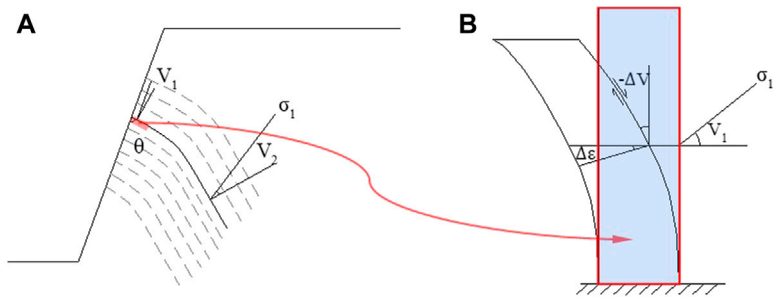


FIGURE 4 | Model for shear creep of bedding surface. **(A)** Toppling element of shear creep; **(B)** stress-strain state.

TABLE 1 | Some examples of toppling deformation and failure.

No.	Toppling Slopes	φ (°)	α (°)	β (°)	β_0 (°)	(90—α)+φ (°)	0.5π − φ (°)	θ (°)
1	Jiefanggou slope at Jinping Hydropower Station	24	45	45	80	34	66	90
2	Shuiwenzhan landslide at Jinping Hydropower Station	22	30	50	85	27	68	100
3	Toppling slope on Xiluodu Reservoir	17	39	60	80	27	73	81
4	Dam site slope on Miaowei Hydropower Station	25	45	42	82	33	65	93
5	Bank slope on Miaowei Hydropower Station	25	35	40	85	30	65	105
6	Bank slope on Laxiwa Hydropower Station	24	50	35	82	33	66	95
7	Left dam abutment slope on Jinshajiang Hydropower Station	24	50	42	83	31	66	88
8	Highway slope of southern mountainous area in Anhui Province	20	56	50	80	30	70	74
9	Toppling slope on Longtan Hydropower Station	19	40	32	60	49	71	108
10	Yinshuigou toppled body on Xiaowan Hydropower Station	21	40	40	80	30	69	100

Note: Internal friction angle φ (°); slope angle α (°); toppled slope angle β (°); un-toppling slope angle β_0 (°); start-up condition (90—α)+φ (°); transient stability condition 0.5π − φ (°); angle of bedding plane and slope surface θ (°).

$$c \cong 0, \sigma_3 \cong 0, then\ V = tan^{-1}\left(tan V_1 \cdot e^{-\frac{\sigma_1}{\eta}t}\right), \quad (18)$$

according to **Equation 18**:

$$0 \le V \le \varphi, 0.5\pi - \varphi \le \theta \le 0.5\pi\ t \in [0, \infty), \quad (19)$$

where $t = 0$, $0 \le V \le \varphi$, $0.5\pi - \varphi \le \theta \le 0.5\pi$; $t \to \infty$, $V \to 0$, $\theta \to 0.5\pi$.

When there is water, the water pressure will cause the rock slab to be further toppled and developed, according to the effective stress principle. Then, the angle V_1 between the major stress and the normal of the bedding surface becomes V_1':

$$V_1' = 0.5 \cdot \left[\varphi + sin^{-1}\left(\frac{\sigma_1 + \sigma_3 + 2c\ cot\ \varphi - 2\mu}{\sigma_1 - \sigma_3} \cdot\ sin\ \varphi\right)\right] \le V_1. \quad (20)$$

CASES VALIDATION AND DISCUSSION

Several typical toppling deformation cases were analyzed by using the mechanical model corresponding to the toppling deformation stage, and the following conclusions were obtained. The details information of typical toppled slopes are shown in **Table 1**.

Because case 1 has been toppled and destroyed, it must meet the requirements of $\beta \ge (90—\alpha) + \varphi$. With the relevant information of the formula substituted, it can be obtained that 45°≥ (90° -80°) +24°=34°. The current state the toppled slope is 45°≤ (90° -50°) +24°=64°, indicating that the start-up condition is not satisfied at this time. Judging by the transient stability condition, $\theta = 0.5\pi - \varphi$ =90°–24°=66°, and the angle between the bedding surface and the slope surface is 180°-45°–50°=85° > 66°, which indicates that the transient stability state has passed. Now the time effect of creep was still endured and has not reached the final state of long-term creep by using formula θ_∞=90°>85°.

Similarly, the toppled deformation states of other cases can be judged by the information from **Table 1**. As for case 9, the initial start-up condition is 40°≤ (90°–60°) +19°=49°, which does not meet the start-up condition formula. Judging from the transient stability condition, $\theta = 0.5\pi - \varphi$ =90°–19°=71°, the angle between the untoppled bedding surface and the slope surface is 180°-60°–40°=80°>71°, indicating that the initial state of the untoppled layers is in the creep stage. The angle of toppled bedding surface and the slope surface was 180°-32°–40°=108°>θ_∞=90°, which indicated that the state of the toppled slope exceeds the final

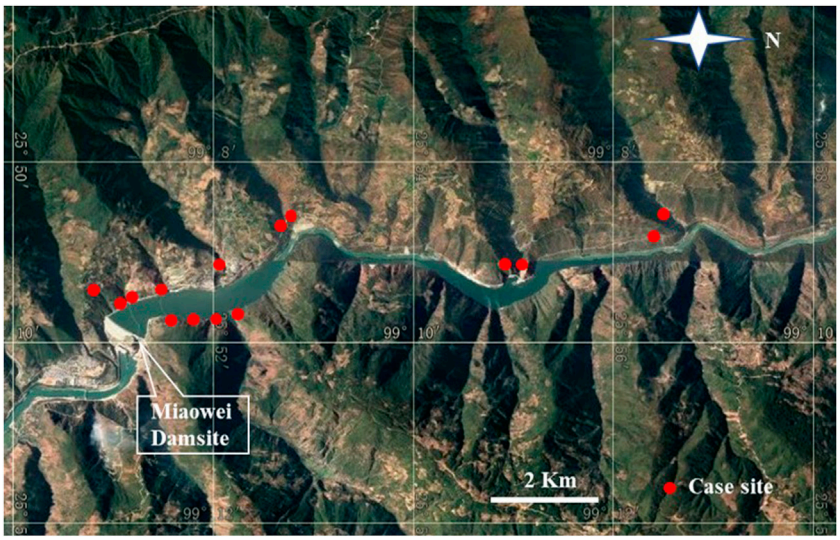


FIGURE 5 | Cases from bank slope on the Miaowei Hydropower Station.

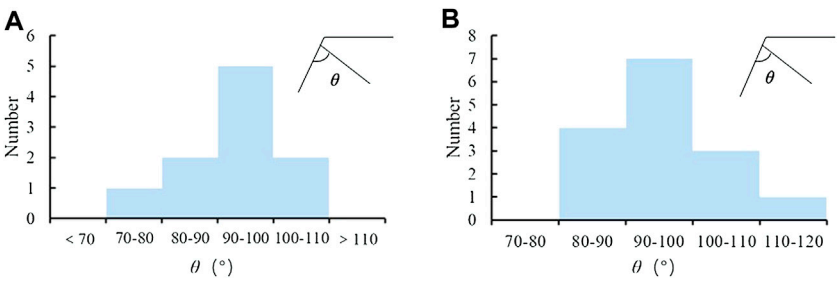


FIGURE 6 | Cases of flexural toppling deformation: **(A)** cases from typical example; **(B)** cases from bank slope on the Miaowei Hydropower Station.

time-varying state, and the toppled angle reaches 18° caused by the long-term cumulative creep and external forces. This example illustrates that interlaminar creep plays a significant role in ductile flexural toppling.

According to the analysis results of typical toppled slopes (**Figure 5**), the angle θ between the slope surface and bedding surface is summarized in **Figure 6A**. When the toppling deformation is stable, the angle θ is relatively close to 0.5π. This study investigated the toppling slopes near the Miaowei Hydropower Station, and the investigation results indicate that the angle θ between the toppling layers plane and slope surface is mostly about 0.5π (as shown in **Figure 6B**), when the toppling rock layer is stable. In some cases, the angle θ near the slope surface increased due to slope structure and other external forces. The similar results were reported by Wu (1997), who investigated the cutting slope along the Yangpingguan–Yanzibian section of the Baocheng railway, and found that several ductile flexural toppling slopes induced by rainfall occur in this region, and the angle θ was close to 90° or >90°. Those cases illustrate the water pressure stress intensified flexural toppling deformation.

CONCLUSION

Ductile flexural toppling is a product of long-term geological evolution history. Considering its progressive failure characteristics, the development process of ductile flexural toppling takes place as follows: the initial start-up stage, rapid development stage, transient stability stage and long-term toppling creep stage.

1) The start-up condition of ductile flexural toppling satisfies **Equation 2**, which ignores the cohesion between rock strata, and the calculated result is safer. Therefore, a comprehensive internal friction angle can be used to comprehensively analyze the start-up condition of interlayer dislocation with considering cohesion. Under the condition of transient stability, the angle of V_1 between the normal of bedding surface and σ_1 is determined by **Equation 6**, and θ between the bedding surface and the slope surface is determined by **Equation 10** at the final stage of the ductile flexural toppling, where the angle between the toppled bedding surface and the slope surface is $\theta = 0.5\pi - \varphi$.

2) Slip and shear creep occurs between the layers in the transient stability state, thus causing the whole bending and toppling creep deformation of deformation. The angle of V at any time can be determined by **Equation 16** and the angle of the slope surface determined by **Equation 18**. The final state of angle V, considering interlaminar shear creep, is perpendicular to σ_1. That is, the toppled bedding surface is perpendicular to the slope surface.
3) The water pressure can decrease the deformation and stability angle V of the transient stability state and aggravate the toppling of the rock slab. The angle θ of partial toppling deformation bodies between the bedding surface and the slope surface may be $>0.5\pi$ due to disturbances of other external forces. Various typical cases were statistically analyzed, and the mechanical conditions during the development of ductile flexural toppling deformation were comprehensively analyzed from the start-up stage, over the transient stage, to the long-term creep stage.

DATA AVAILABILITY STATEMENT

The original contributions presented in the study are included in the article/supplementary material. Further inquiries can be directed to the corresponding author.

AUTHOR CONTRIBUTIONS

JC, DZ, and NJ conceived and designed the paper. JC and DZ analyzed the mechanical model; NJ analyzed and interpreted the data; JC wrote the paper, DZ, JW, XZ, and DL revised the paper.

FUNDING

The study is financially supported by the National Key R&D Program of China (2018YFC1504905), the Opening Fund of State Key Laboratory of Geohazard Prevention and Geoenvironment Protection (Chengdu University of Technology, SKLGP 2022K004), and the National Natural Science Foundation of China (41907250,41772317). The Opening Fund of State Key Laboratory of Geohazard Prevention and Geoenvironment Protection (Chengdu University of Technology, SKLGP 2022K004) pays for open access publication fees.

ACKNOWLEDGMENTS

Special thanks go to the expertise comments from the reviewers and editors for improving the manuscript.

REFERENCES

Adhikary, D. P., Dyskin, A. V., Jewell, R. J., and Stewart, D. P. (1997). A Study of the Mechanism of Flexural Toppling Failure of Rock Slopes. *Rock Mech. Rock Engng* 30 (2), 75–93. doi:10.1007/BF01020126

Adhikary, D. P., and Dyskin, A. V. (2007). Modelling of Progressive and Instantaneous Failures of Foliated Rock Slopes. *Rock Mech. Rock Engng.* 40 (4), 349–362. doi:10.1007/s00603-006-0085-8

Amini, M., Ardestani, A., and Khosravi, M. H. (2017). Stability Analysis of Slide-Toe-Toppling Failure. *Eng. Geol.* 228, 82–96. doi:10.1016/j.enggeo.2017.07.008

Amini, M., Majdi, A., and Aydan, Ö. (2009). Stability Analysis and the Stabilisation of Flexural Toppling Failure. *Rock Mech. Rock Eng.* 42, 751–782. doi:10.1007/s00603-008-0020-2

Amini, M., Majdi, A., and Veshadi, M. A. (2012). Stability Analysis of Rock Slopes against Block-Flexure Toppling Failure. *Rock Mech. Rock Eng.* 45, 519–532. doi:10.1007/s00603-012-0220-7

Amini, M., Sarfaraz, H., and Esmaeili, K. (2018). Stability Analysis of Slopes with a Potential of Slide-Head-Toppling Failure. *Int. J. Rock Mech. Min. Sci.* 112, 108–121. doi:10.1016/j.ijrmms.2018.09.008

Aydan, O., and Kawamoto, T. (1992). The Stability of Slopes and Underground Openings against Flexural Toppling and Their Stabilisation. *Rock Mech. Rock Engng* 25 (3), 143–165. doi:10.1007/BF01019709

Cai, J.-C., Ju, N.-P., Huang, R.-Q., Zheng, D., Zhao, W.-H., Li, L.-Q., et al. (2019). Mechanism of Toppling and Deformation in Hard Rock Slope: a Case of Bank Slope of Hydropower Station, Qinghai Province, China. *J. Mt. Sci.* 16, 924–934. doi:10.1007/s11629-018-5096-x

Cruden, D. M., and Hu, X.-Q. (1994). Topples on Underdip Slopes in the Highwood Pass, Alberta, Canada. *Q. J. Eng. Geol. Hydrogeology* 27, 57–68. doi:10.1144/GSL.QJEGH.1994.027.P1.08

Goodman, R. E., and Bray, J. W. (1976). "Toppling of Rock Slopes," in *Rock Engineering for Foundations & Slopes* (Boulder, CO: ASCE), 201–234.

Goodman, R. E. (2013). "Toppling - - A Fundamental Failure Mode in Discontinuous Materials --- Description and Analysis," in *2013 Congress on Stability and Performance of Slopes and Embankments III, Geo-Congress 2013* (San Diego, United States: Geotechnical Special Publication. ASCE), 2348–2378. doi:10.1061/9780784412787.227

Huang, R. Q. (2008). Geodynamic Process and Stability Control of High Rock Slope Development. *Chin. J. Rock Mech. Eng.* 27 (08), 1525–1544. doi:10.3321/j.issn:1000-6915.2008.08.002

Huang, R. Q. (2007). Large-scale Landslides and Their Sliding Mechanisms in China since the 20th Century. *Chin. J. Rock Mech. Eng.* 26, 433–454. doi:10.3321/j.issn:1000-6915.2007.03.001

Huang, R. Q., and Li, Y. S. (2017). Yan M the Implication and Evaluation of Toppling Failure in Engineering Geology Practice. *J. Eng. Geol.* 25 (05), 1165–1181. doi:10.13544/j.cnki.jeg.2017.05.001

Liu, C. H., Jaksa, M. B., and Meyers, A. G. (2009). A Transfer Coefficient Method for Rock Slope Toppling. *Can. Geotech. J.* 46 (1), 1–9. doi:10.1139/t08-094

Liu, M., Liu, F.-Z., Huang, R.-Q., and Pei, X.-J. (2016). Deep-seated Large-Scale Toppling Failure in Metamorphic Rocks: a Case Study of the Erguxi Slope in Southwest China. *J. Mt. Sci.* 13, 2094–2110. doi:10.1007/s11629-015-3803-4

Nichol, S. L., Hungr, O., and Evans, S. G. (2002). Large-scale Brittle and Ductile Toppling of Rock Slopes. *Can. Geotech. J.* 39 (4), 773788–788. doi:10.1139/t02-027

Ning, Y., Zhang, G., Tang, H., Shen, W., and Shen, P. (2019). Process Analysis of Toppling Failure on Anti-dip Rock Slopes under Seismic Load in Southwest China. *Rock Mech. Rock Eng.* 52, 4439–4455. doi:10.1007/s00603-019-01855-z

Pang, B., Zheng, D., and Huang, P. (2016). Geological Model Analysis on the Depth of Toppling Deformation in the Anti-dip Rock Slopes. *Sci. Technol. Eng.* 16 (18), 129–134. 1671-1815(2016) 018-0129-06. doi:10.3969/j.issn.1671-1815.2016.18.023

Sun, G. Z., and Zhang, W. B. (1985). A Common Rock Structure-Board Crack Structure and its Mechanical Model. *J. Eng. Geol.* 28 (3), 275–282.

Tamrakar, N. K., Yokota, S., and Osaka, O. (2002). A Toppled Structure with Sliding in the Siwalik Hills, Midwestern Nepal. *Eng. Geol.* 64, 339–350. doi:10.1016/S0013-7952(01)00095-3

Tu, G., Deng, H., Shang, Q., Zhang, Y., and Luo, X. (2020). Deep-Seated Large-Scale Toppling Failure: A Case Study of the Lancang Slope in Southwest China. *Rock Mech. Rock Eng.* 53, 3417–3432. doi:10.1007/s00603-020-02132-0

Wang, S. J., Xiao, Y., and Du, Y. L. (1992). The Mechanism of Bending Creep of Bedded Rockmass in the Slope on the Left Bank of Longtan Dam Site in Hongshui River, Guangxi, China. *Chin. J. Geol.* S1, 342–352.

Wu, F. Q. (1997). Theoretical Analysis of Bending and Toppling Deformation in Slopes of Mica-Quartz Schist. *J. Eng. Geol.* 5 (04), 19–24.

Xia, M., Ren, G. M., Li, T. B., Cai, M., Yang, T. J., and Wan, Z. L. (2019). Complex Rock Slope Deformation at Laxiwa Hydropower Station, China: Background, Characterization, and Mechanism. *Bull. Eng. Geol. Environ.* 78, 3323–3336. doi:10.1007/s10064-018-1371-x

Xiao, Y., and Wang, S. J. (1991). Flexural Failure of Rockmass in Slopes. *Chin. J. Rock Mech. Eng.* 10 (04), 331–338.

Xie, L., Yan, E., Wang, J., Lu, G., and Yu, G. (2018). Study on Evolutionary Characteristics of Toppling Deformation of Reverse-Dip Layered Rock Slope Based on Surface Displacement Monitoring Data. *Environ. Earth Sci.* 77 (4), 156. doi:10.1007/s12665-018-7352-3

Zhang, G., Wang, F., Zhang, H., Tang, H., Li, X., and Zhong, Y. (2018). New Stability Calculation Method for Rock Slopes Subject to Flexural Toppling Failure. *Int. J. Rock Mech. Min. Sci.* 106, 319–328. doi:10.1016/j.ijrmms.2018.04.016

Zhang, Z., Liu, G., Wu, S., Tang, H., Wang, T., Li, G., et al. (2015). Rock Slope Deformation Mechanism in the Cihaxia Hydropower Station, Northwest China. *Bull. Eng. Geol. Environ.* 74 (3), 943–958. doi:10.1007/s10064-014-0672-y

Zhao, W., Zhang, C., and Ju, N. (2021). Identification and Zonation of Deep-Seated Toppling Deformation in a Metamorphic Rock Slope. *Bull. Eng. Geol. Environ.* 80, 1981–1997. doi:10.1007/s10064-020-02027-y

Zhu, C., He, M., Karakus, M., Cui, X., and Tao, Z. (2020). Investigating Toppling Failure Mechanism of Anti-dip Layered Slope Due to Excavation by Physical Modelling. *Rock Mech. Rock Eng.* 53 (11), 5029–5050. doi:10.1007/s00603-020-02207-y

Conflict of Interest: The authors declare that the research was conducted in the absence of any commercial or financial relationships that could be construed as a potential conflict of interest.

Publisher's Note: All claims expressed in this article are solely those of the authors and do not necessarily represent those of their affiliated organizations, or those of the publisher, the editors and the reviewers. Any product that may be evaluated in this article, or claim that may be made by its manufacturer, is not guaranteed or endorsed by the publisher.

Copyright © 2022 Cai, Zheng, Ju, Wang, Zhou and Li. This is an open-access article distributed under the terms of the Creative Commons Attribution License (CC BY). The use, distribution or reproduction in other forums is permitted, provided the original author(s) and the copyright owner(s) are credited and that the original publication in this journal is cited, in accordance with accepted academic practice. No use, distribution or reproduction is permitted which does not comply with these terms.

frontiers | Frontiers in Earth Science

TYPE Original Research
PUBLISHED 10 August 2022
DOI 10.3389/feart.2022.895884

Check for updates

OPEN ACCESS

EDITED BY
Xiaoyan Zhao,
Southwest Jiaotong University, China

REVIEWED BY
Zhao Liu,
Hebei GEO University, China
Yanyan Li,
Chinese Academy of Geological Sciences (CAGS), China

*CORRESPONDENCE
Mo Xu,
xm@cdut.edu.cn

SPECIALTY SECTION
This article was submitted to Geohazards and Georisks, a section of the journal Frontiers in Earth Science

RECEIVED 14 March 2022
ACCEPTED 11 July 2022
PUBLISHED 10 August 2022

CITATION
Zhang W, Xu M and Wu S (2022), Study on the genetic mechanism of high-temperature geothermal system and its engineering impact in the Woka graben, Tibet.
Front. Earth Sci. 10:895884.
doi: 10.3389/feart.2022.895884

COPYRIGHT
© 2022 Zhang, Xu and Wu. This is an open-access article distributed under the terms of the Creative Commons Attribution License (CC BY). The use, distribution or reproduction in other forums is permitted, provided the original author(s) and the copyright owner(s) are credited and that the original publication in this journal is cited, in accordance with accepted academic practice. No use, distribution or reproduction is permitted which does not comply with these terms.

Study on the genetic mechanism of high-temperature geothermal system and its engineering impact in the Woka graben, Tibet

Wen Zhang[1,2], Mo Xu[1]* and Sen Wu[3]

[1]Chengdu University of Technology, Chengdu, Sichuan, China, [2]Institute of Exploration Technology, Chinese Academy of Geological Sciences, Chengdu, Sichuan, China, [3]Sichuan Institute of Geological Engineering Investigation Group Co. Ltd., Chengdu, Sichuan, China

The geothermal resource has become the significant constitution of renewable and clean energies in the world. This study focuses on the genetic mechanism of a high-temperature geothermal system and its engineering impact in the Woka graben, southern Tibet, via hydrochemical and isotopic analyses. The hydrochemical types are mainly SO_4-Na type, SO_4-Cl-Na type, and HCO_3-SO_4-Na type. Geothermal water is characterized as medium to alkaline affinity with low total dissolved solids. D-O isotopes indicate that geothermal water is recharged by atmospheric precipitation at the elevation of 5193–5247 m. Na-K-Mg equilibrium diagram shows partial equilibrium or mixed water, and the proportion of cold water mixing is 73–83%. The temperature ranges of shallow and deep geothermal reservoirs are from 96.85°C to 119.57°C and from 120°C to 200°C, respectively. Geothermal water is heated by melting crust and controlled by deep faults. For major construction projects in the Woka graben, detailed investigation and demonstration should be conducted to avoid the geothermal water channel as much as possible, or to divert the geothermal water and reasonably arrange the construction sequence to overcome the problem.

KEYWORDS

formation mechanism, high-temperature geothermal system, hydrochemical characteristics, D-O-C isotopes, engineering influence

Introduction

Among the more than 3,000 hydrothermal activity areas identified in China, 677 are occurring in Tibet (Liao, 2018; Wang et al., 2018; Zhang and Hu, 2018). In addition, 342 geothermal manifestations are available for exploration, with the vast majority having a temperature of more than 80°C. Geothermal resource in Tibet is characterized by high-temperature, various types, and extensive distribution (Guo, 2012; Kong et al., 2014). The distribution of geothermal resources in Tibet is strictly controlled by active faults and is closely related to the regional geothermal heat flow background (Jiang et al., 2018; Tan et al., 2018). Taking the high-temperature vapor geothermal manifestations in southern Tibetan as an example, numerous active tectonic belts have developed in the N-S direction and consist of a series of uplift

zones and fracture zones along the Himalayan arc tectonic belt. Afterward, a series of Quaternary graben basins were formed, in which strong modern hydrothermal activity has developed, e.g., the Langjiu, Kawu, Yangbajing, and Gudui geothermal fields (Zhang et al., 2015; Wang et al., 2016).

The Cona–Woka rift valley belt is the easternmost side of the Tibetan rift valley belt near the north–south fracture belt, by the Woka, Qiongduojiang, and Cona grabens. The graben is enriched in geothermal resources, where the second largest geothermal manifestation (Gudui geothermal field) in Tibet is distributed. The Woka geothermal manifestation is located in the Woka graben in the northern section of the Cona–Woka rift valley. Along the Zengjiuqu River valley and slope, geothermal manifestation with a length of 3 km and temperature of 43°C–68.2°C is developed, belonging to the low- to medium-temperature geothermal system. Previous studies focused on the hydrochemical characteristics and genetic mechanism of geothermal waters in Tibet (Elenga et al., 2021; Li et al., 2021; Tian et al., 2021; Wang et al., 2021; Klemperer et al., 2022; Wang et al., 2022). However, the studies on the genesis mode of the Woka geothermal springs are lacking. The geothermal reservoir and heat source are still unclear, making it difficult to evaluate the prospecting potential. So far, the Woka geothermal springs have been utilized for the bathing function. Therefore, research on the genetic mechanism of the Woka geothermal system can provide scientific guidance for the assessment of geothermal resource potential in the Woka graben and other areas in southern Tibet.

In this study, the hydrogeochemical characteristics, reservoir temperature, and subsurface cold water mixing ratio of geothermal springs in the Woka geothermal system are comprehensively studied using hydrochemical and isotopic data. Afterward, the conceptual model of a medium- to high-temperature geothermal system in the Woka geothermal zone is established. At last, the engineering significance of the geothermal system is investigated.

Study area

The study area is located in Sangri Township and Lobsa Township, 40 km away from Sangri County, Tibet. The study area has an alpine valley landform, steep bank slope, terrain slope of 30°–50°, and a height difference of 1000–1500 m. The climate in the area belongs to the plateau temperate monsoon semihumid climate zone, with an annual average temperature of 6.4°C–8.2°C and annual average precipitation of 500–600 mm, mainly concentrated from May to September, accounting for more than 89% of the annual rainfall. Rainfall has the characteristics of large annual variation and concentrated rainfall periods.

The Woka graben basin is located in the Himalayas terrane (Zhang et al., 2019a, 2022; Cao et al., 2019). The geothermal water system in the Woka graben basin is composed of the many geothermal springs distributed along the Zengjiuqu River valley in Woka graben basin, with 22 existing geothermal springs and a total flow rate of more than 20 L/s (Table 1). According to the characteristics of the underground geothermal water outcropping and the current situation of development and utilization, it can be divided into Kanai, Woka, Cuoba, and Lobosha geothermal springs. The upper part is light yellow subsandy or gravelly subsandy soil, and the lower part is mixed-colored pebbles, drift stones, and muddy pebbles. The Cretaceous–Paleocene black mica diorite ($\eta\gamma\beta K_2$), granodiorite ($\gamma\delta K_1$), quartz diorite (δoK_1), *etc*. are distributed along the watershed; the Middle to Lower Jurassic Yerba Formation ($J_{1-2}y$) is exposed along the watershed, divided into three lithological sections: the first section is characterized by volcanic breccia and volcanic agglomerate; the second section is dominated by medium-acid andesite, andesite, rhyolite, and crystalline clastic tuff; and the third section is composed of sunken tuff, metamorphic sandstone, and siltstone. The geothermal geological background of the Woka graben is shown in Figure 1.

Woka basin is located in southern Tibet near the N-S development rift valley—the northern section of the Cuona—Woka rift valley, for regional extension and deformation, and the formation of the Quaternary activity is an obvious graben-type fracture basin (Cao et al., 2020; Cao et al., 2021). The total length of the rift basin is approximately 50 km, north of the Jinzhu township area, the southern end of the Luobusha chromite. Region-wise, the southern end of the Woka graben is bounded by the south-trending rebound fault zone, Yarlung Tsangpo River suture tectonic zone, and the north-trending Xela-Riduo-Palo fault in the northern section, which is interrupted by the near E-S trending development of the Mocun ductile fault and some pot faults.

The main boundary fault zone controlling the development of the Woka basin is the NNE-trending, west-trending, 50- to 60-km-long orthotropic fault on the eastern margin of the basin (Zhang et al., 2019b). In addition, there are ultra-low-resistance areas with a resistivity of less than 50 Ω m along the Zengjiuqu River valley based on several high-density physical profiles. Meanwhile, seismic activity is frequent within the Woka graben basin, and the results of fracture activity rate estimation indicate the vertical activity rate of this fault zone since MIS six ranges from 0.4 to 0.9 mm/a. Under the effect of long-term seismic activity, a network of tectonic fissures has been formed in the Woka graben basin that crosses east–west and north–south directions, providing storage space and runoff channels for the development of the underground geothermal water system in the Woka graben basin.

TABLE 1 Exposure characteristics of geothermal springs.

Name	Flow/L·s^{-1}	T/°C	TDS/mg L^{-1}	Location
Kanai geothermal spring	>1	53.3	744	Right bank of the Zengjiuqu I class terrace
Woka geothermal spring	>10	25–50.5	345–403	Right slope of Zengjiuqu
Cuoba geothermal spring	1.5	36.25	285.9	Right bank of the Zengjiuqu I class terrace
Luobusha geothermal spring	1.7	57.77	8642.95	Right bank of the Yarlung Tsangpo River
Amaka geothermal spring	3.86	35.7	404	Right bank of the Zengjiuqu I class terrace
Woka hekou spring	3	13.3	171	North bank of the Yajiang River
Zhumosha geothermal spring	—	55–75.5	—	Right bank of the Yarlung Tsangpo River

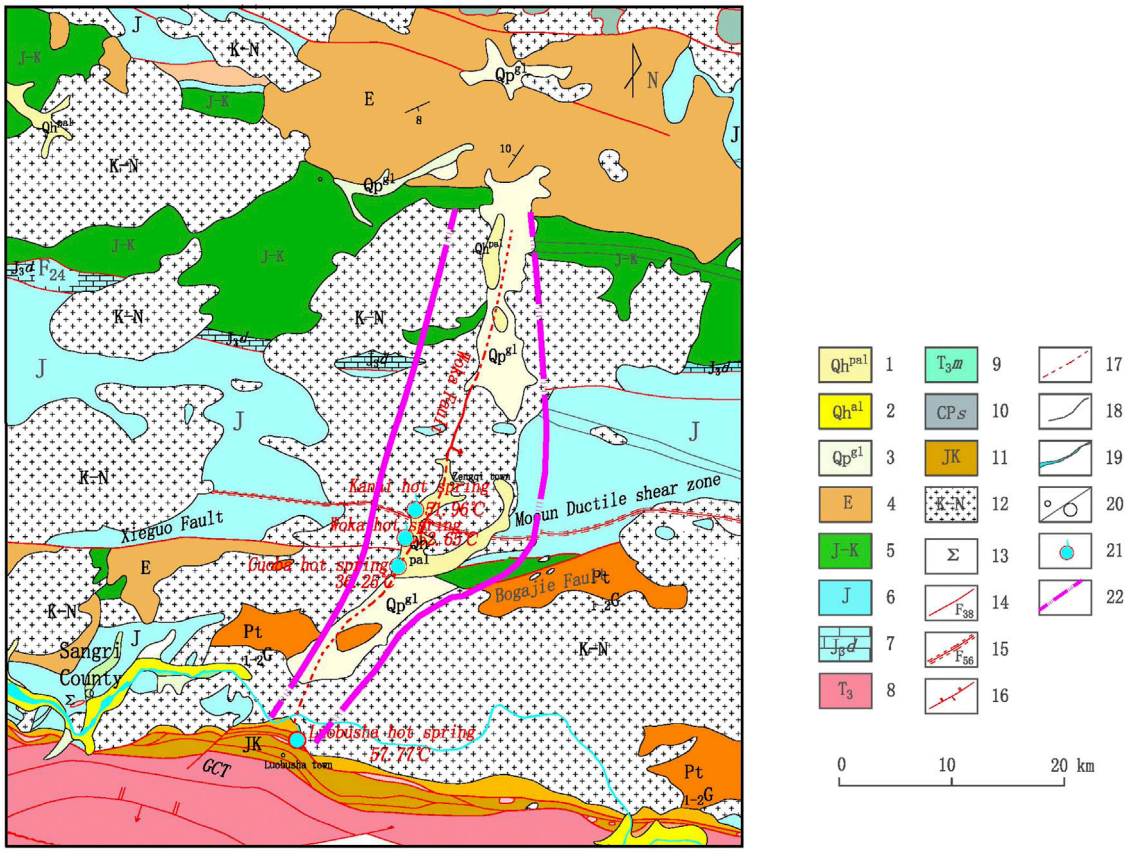


FIGURE 1
Geological background map of Oiga Graben basin. 1-Holocene alluvial deposits; 2-Holocene alluvium; 3-Pleistocene glacial deposits; 4-Paleogene volcanic rocks; 5-Late Jurassic Cretaceous and Cretaceous; 6-Sedimentary assemblage of Jurassic volcanic and continental clastic rocks; 7-Duodigou formation limestone; 8-Late Triassic Century; 9-Mailonggang formation; 10-Songduo group; 11-Jurassic-Cretaceous melange; 12-Cretaceous-Neogene intrusive rocks; 13-Ultrabasic block; 14-Fault and number; 15-Ductile shear zone and number; 16-Reverse fault; 17-Inferred fault; 18-Geological boundary; 19-River system; 20-Town/City; 21-Hot spring; 22-Range of fault graben basin.

Sampling and methodology

In this study, four geothermal water samples were collected in January 2020 for the experiments of hydrochemistry, δ^2H, $\delta^{18}O$, and $\delta^{13}C$. pH, total dissolved solids (TDS), and flow were measured in the field using a portable WTW device. The HCO_3^- content was *in situ* constraint by Gran titration. K^+, Na^+, Ca^{2+}, and Mg^{2+} were determined via inductively coupled plasma-optical emission spectrometry, and Cl^- and SO_4^{2-} were measured via ion chromatography (Dionex ICS-1100) in the State Key Laboratory

TABLE 2 Hydrochemical and D-O-C isotopic results of geothermal springs.

Parameter		Kanai geothermal spring	Woka geothermal spring	Cuoba geothermal spring	Luobusha geothermal spring
T/°C		51.96	52.65	36.25	57.77
pH		8.25	8.25	7.95	6.71
TDS/(mg/L)		440.51	398.43	285.90	8642.95
Cation/(mg/L)	K^+	1.90	1.97	1.48	343
	Na^+	111	106	63.9	1472
	Mg^{2+}	0.026	0.088	0.44	7.85
	Ca^{2+}	5.24	7.69	12.2	80.6
Anion/(mg/L)	HCO_3^-	31	43	37	214
	SO_4^{2-}	147	137	94.4	120
	Cl^-	42.5	52.7	31.8	4060
H_2SiO_3/(mg/L)		74.9	62.4	43.3	312
δ^2H/‰		−156.3	−154.8	−150.8	−129.5
$\delta^{18}O$/‰		−19.86	−19.71	−19.46	−11.96
d=δD-8δ^{18}O		2.58	2.88	4.88	−33.82
$\delta^{13}C$/‰		−6.1	−6.49	−5.41	−3.45
Hydrochemical type		SO_4-Na	Cl·SO_4-Na	HCO_3·SO_4-Na	Cl-Na

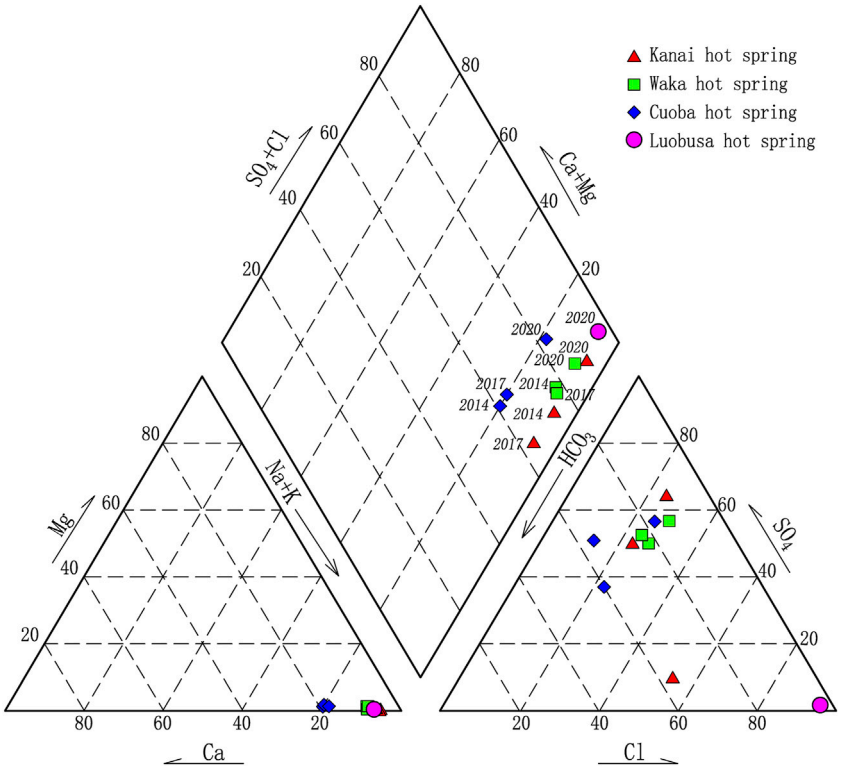


FIGURE 2
Piper diagram of geothermal waters.

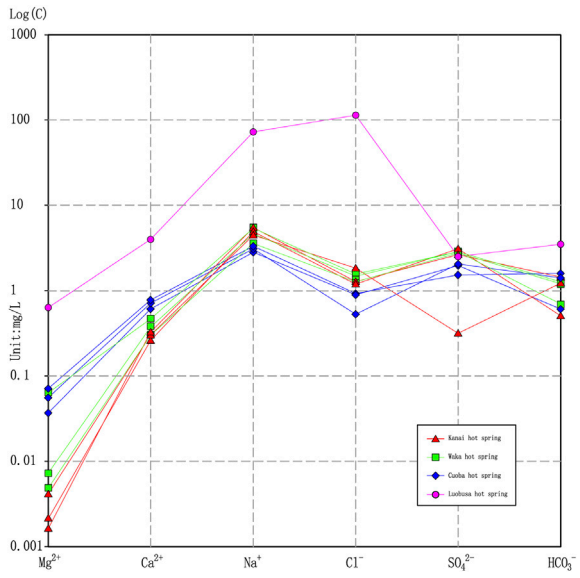


FIGURE 3
Schöeller diagram of geothermal waters.

of Geohazard Prevention and Geoenvironment Protection, Chengdu University of Technology. The charge balance was lower than ±10%. δD and $\delta^{18}O$ were analyzed using a mass spectrometer (MAT253), and $\delta^{13}C$ was measured via stable isotope ratio mass spectrometry (Delta Plus XP) at the Institute of Karst Geology, Chinese Academy of Geological Science.

Results and discussion

Water–rock interaction by hydrochemical characteristics

Table 2 shows that the water chemistry of geothermal water in the Woka geothermal area is dominated by Na^+, Ca^{2+}, and K^+ in cations and SO_4^{2-} and Cl^- in anions, followed by HCO_3^-. The pH values and total dissolved solid concentrations are 7.95–8.25 and 285.90–440.51 mg/L, respectively. Geothermal waters belong to medium–high alkaline water. The hydrochemistry types are mainly SO_4-Na type, Cl-SO_4-Na type, and HCO_3-SO_4-Na type.

The hydrochemical characteristics of geothermal water and bedrock fracture cold water in the fault rift basin are very different (Figure 2). The geothermal waters are enriched in H_2S but poor in CO_2. Their hydrochemical type is influenced by H_2S, and there are more complex hydrochemical types such as SO_4 type, SO_4-Cl type, and HCO_3-SO_4 type, consistent with the Riduo geothermal spring and Gudui geothermal field in the fault rift zone. The hydrochemical type of the Luobusa geothermal spring is different from that of geothermal waters in the Woka rift, indicating that they do not belong to the same geothermal system.

As shown in the Schoeller diagram (Figure 3), all ions in the geothermal water have regular variations, revealing that the source and formation pattern of geothermal water in the basin have similar characteristics. In addition, the geothermal waters have high SO_4^{2-} contents, consistent with the strong sulfur smell of the geothermal water outcrop, as typified by the Woka geothermal spring. The source of SO_4^{2-} in geothermal water is mainly from geothermal water dissolution filtration of sulfate rocks, and a small part is H_2S carried by deep fluids. Therefore, the higher SO_4^{2-} contents in the geothermal water of Woka mainly come from the strong dissolution filtration of volcanic clastic rocks such as andesitic and rhyolitic lava dominated by the Yeba Formation strata. The saturation indices of geothermal water calculated using Phreeqc software are mostly lower than zero. The results show that most minerals, except for chalcedony and quartz, are unsaturated (Table 3), reflecting the short runoff pathway and weak water–rock reaction.

Four geothermal water samples were taken for $\delta^{13}C$ analysis. The $\delta^{13}C$ values of geothermal spring water are −6.49‰ to −3.45‰: the $\delta^{13}C$ value of Kanai geothermal spring is −6.1‰, the $\delta^{13}C$ value of Woka geothermal spring is −6.49‰, the $\delta^{13}C$ value of Misbah geothermal spring is −5.41‰, and the $\delta^{13}C$ value of Lobsa geothermal spring is −3.45‰ (Figure 4). Previous studies showed that the $\delta^{13}C$ value of upper mantle material source is −8‰ to −4‰, the $\delta^{13}C$ value of carbonate metamorphic source is −2‰ to +2‰, and the $\delta^{13}C$ value of carbonate metamorphic source is −2‰ to +2‰. Therefore, it is presumed that mantle-sourced CO_2 from deep faults was involved in the formation of geothermal waters in the study area.

Recharge source implied by D-O isotopes

Four geothermal water samples were selected for the analysis of hydrogen and oxygen isotopes. The results show that the δ^2H values range from −150.8‰ to −156.3‰ and the $\delta^{18}O$ values range from −19.46‰ to −19.86‰. In Figure 5, all samples are distributed near the global atmospheric precipitation equation line, indicating that the source is recharged by atmospheric precipitation and less infiltration of snow-melting water. The deuterium excess parameter (d) is similar between the geothermal spring and the cold spring, indicating that there is no obvious oxygen drift in the geothermal water. The result reveals the characteristics of atmospheric precipitation recharge and shallow circulation in the geothermal water system of the Woka rift. The deuterium excess parameter d of the Luobusa geothermal spring is −33.82, which shows significant oxygen

TABLE 3 Saturation indices of geothermal springs.

Mineral phase	Chemical content	Kanai spring	Woka spring	Cuoba spring	Luobusha spring
Anhydrite	$CaSO_4$	−2.48	−2.34	−2.46	−1.93
Aragonite	$CaCO_3$	−0.90	−0.55	−0.85	−0.56
Calcite	$CaCO_3$	−0.77	−0.43	−0.71	−0.43
Chalcedony	SiO_2	0.33	0.25	0.28	0.94
Quartz	SiO_2	−0.42	−0.51	−0.53	0.20
Chrysotile	$Mg_3Si_2O_5(OH)_4$	−4.23	−2.71	−4.29	−4.64
Dolomite	$CaMg(CO_3)_2$	−3.39	−2.32	−2.43	−1.36
Gypsum	$CaSO_4{:}2H_2O$	−2.46	−2.32	−2.27	−1.96
Halite	NaCl	−6.91	−6.83	−7.03	−3.96
Sylvite	KCl	−8.34	−8.24	−8.50	−4.29
$O_2(g)$	O_2	−25.85	−25.66	−31.72	−30.40
$CO_2(g)$	CO_2	−3.68	−3.51	−3.34	−1.25

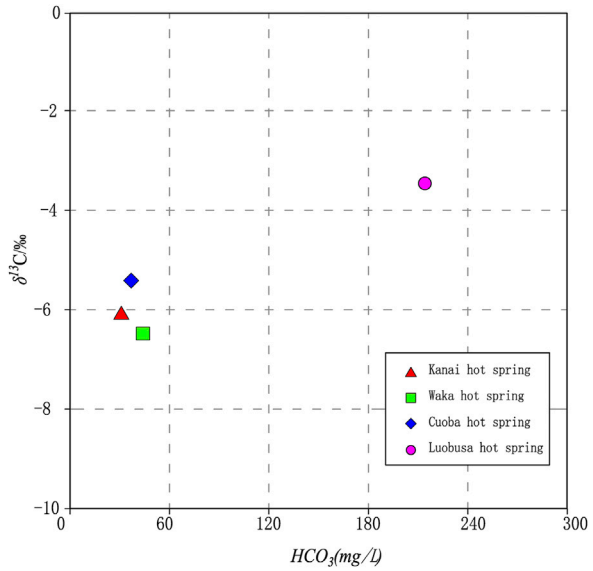


FIGURE 4
$\delta^{13}C$-HCO_3 plot of geothermal waters.

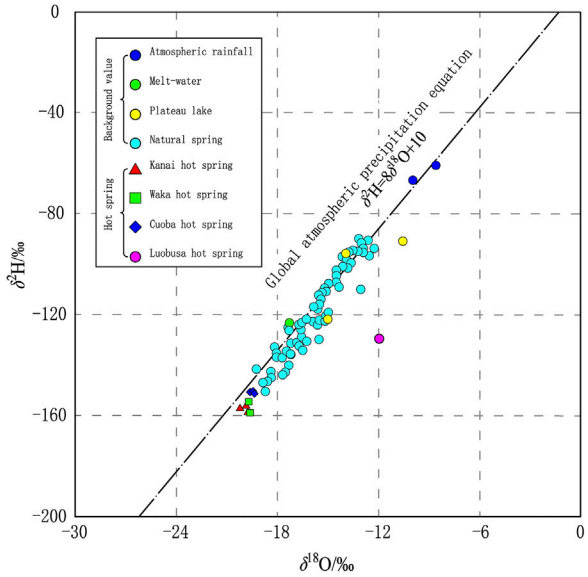


FIGURE 5
δ^2H-$\delta^{18}O$ plot of geothermal waters.

drift, further supporting that it belongs to a different geothermal system from the Woka graben, with deep circulation recharge characteristics.

The isotopic composition of atmospheric precipitation has an elevation effect, and the recharge elevation of geothermal springs can be calculated using $\delta^{18}O$ isotopic values based on this feature (Zhang et al., 2018). The calculation equation is as follows:

$$H = \frac{\delta_G - \delta_P}{K} \times 100 + h \quad (1)$$

where H is the elevation of the recharge area, m; h is the elevation of the sampling point, m; δ_G is the $\delta^{18}O$ value of the geothermal spring; δ_P is the $\delta^{18}O$ value of atmospheric precipitation; and K is the $\delta^{18}O$ elevation gradient of atmospheric precipitation (δ/100 m). The gradient value of $\delta^{18}O$ is determined as follows: four typical cold springs were selected along the Zengjiuqu from upstream to downstream, and the $\delta^{18}O$ was obtained by fitting the $\delta^{18}O$ to the outcrop elevation of the spring. The curve is $\delta^{18}O$ = −0.0037*H-

TABLE 4 Recharge elevation of geothermal springs.

No.	Name	Isotopic results		Exposure elevation/m	Recharge elevation/m
		$\delta^{18}O$/‰	$\delta^{2}H$/‰		
1	Kanai geothermal spring	−19.86	−156.3	3933	5247
2	Waka geothermal spring	−19.71	−154.8	3920	5193
3	Cuoba geothermal spring	−19.46	−150.8	3988	5193
4	Luobusa geothermal spring	−11.96	−129.5	3568	2746
5	Zhenbucuo lake	−15.00	−121.6	4643	—

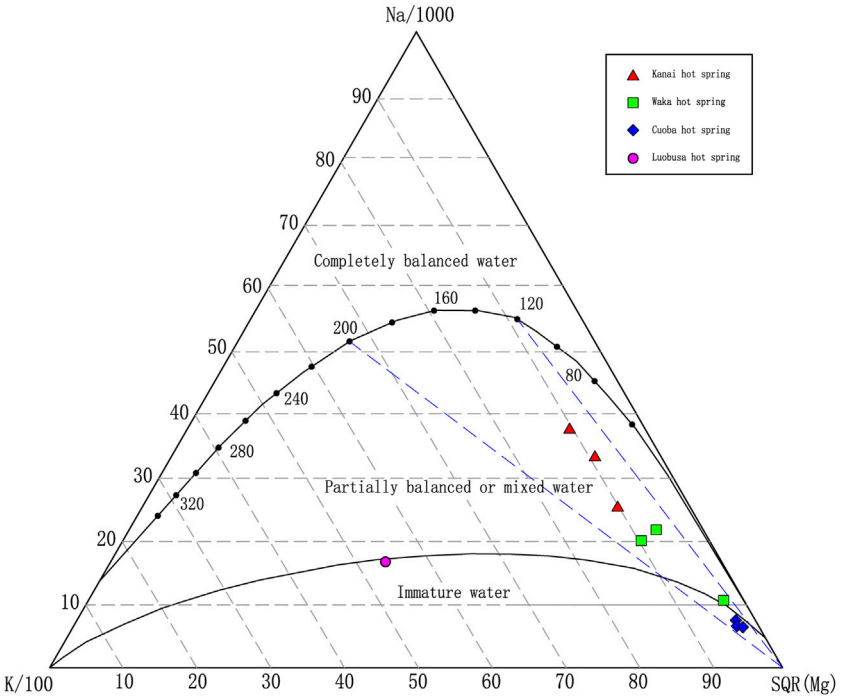


FIGURE 6
Na-K-Mg triangle diagram of geothermal waters.

107.98, R^2 = 0.9473, and the height gradient obtained from the fit is 0.37‰/100 m, which is in good agreement with the height gradient of 0.31‰/100 m in Tibetan area. The elevation reference value is determined as follows: The lake water is used as the elevation reference point, and its $\delta^{18}O$ = −15.0‰. The calculation results of the recharge elevation of each geothermal spring are shown in Table 4, and the results show that the recharge elevation of the geothermal water system in the Woka graben basin is 5193–5247 m, which is consistent with the elevation of the alpine basin where the regionally distributed snow mountains are located.

Reservoir temperature

The temperature of geothermal springs, as natural outcrops of geothermal water systems, is often low because of the mixing of shallow groundwater or surface water and cannot actually represent the temperature of the geothermal reservoir (Zhang, Xu, 2018; Li et al., 2020; Chang et al., 2021). Therefore, quantitative geochemical geothermometers such as SiO_2 and cation geothermometers are usually used to calculate the reservoir temperature (Fournier, 1977; Truesdell and Fournier, 1977; Fournier, 1979). As seen in Figure 6, the Kanai geothermal springs and the Woka geothermal springs all fall in the partially

TABLE 5 Relationship of water temperature, enthalpy, and SiO_2 concentration.

t/°C	S/4.1868J/g	ρc_{SiO2}/mg·L^{-1}
50	50.0	13.5
75	75.0	26.6
100	100.1	48.0
125	125.1	80.0
150	151.0	125.0
175	177.0	185.0
200	203.6	265.0
225	230.9	365.0
250	259.2	486.0
275	289.0	614.0
300	321.0	692.0

equilibrated zone or mixed water zone, and the Cuoba geothermal springs and the Luobosha geothermal springs fall in the immature water zone, indicating that the water–rock interaction in the geothermal water system of the Woka fault rift basin has not reached to complete equilibrium, or the geothermal water is mixed with a large proportion of cold water in a nonequilibrium state. Hence, the cation geothermometer has limitations in estimating the temperature of the reservoir. In this study, the SiO_2 geothermometer is selected for the calculation of the geothermal reservoir. The geothermal reservoir temperatures range from 95.22°C to 121.66°C (no steam loss) and 96.85°C–119.57°C (maximum steam loss), respectively, measured using the SiO_2 geothermometer. From the Na-K-Mg equilibrium diagram (Figure 6), it can be seen that the four outcrops of the Woka geothermal spring all fall between the 120°C and 200°C isotherms. In addition, the estimated reservoir temperatures based on the SiO_2 geothermometer are all lower than this range, indicating that the geothermal water in the basin is mixed by the shallow fractured cold water or surface water in the process of gushing out of the surface.

The above analysis shows that the geothermal springs in the Woka basin have the characteristics of mixing with shallow cold water, and a mixing model can be established to estimate the initial geothermal reservoir temperature in the deep position. The mixing model equation is as follows:

$$S_c X_1 + S_h (1 - X_1) = S_s \quad (2)$$

$$\rho c_{SiO2} X_2 + \rho h_{SiO2} X_2 (1 - X_2) = \rho S_{SiO2} \quad (3)$$

where S_c is the enthalpy of cold water (J/g); S_s is the final enthalpy of spring water (J/g, the enthalpy of saturated water below 100°C is equal to the number of the temperature of water in degree Celsius; above 100°C, the relationship between temperature and enthalpy of saturated water can be found in Table 5); S_h is the initial enthalpy of geothermal water (J/g); $\rho cSiO_2$ is the mass concentration of SiO_2 of cold water (mg/L); $\rho sSiO_2$ is the mass concentration of SiO_2 of spring water (mg/L); $\rho hSiO_2$ is the initial mass concentration of SiO_2 of geothermal water (mg/L); and X is the mixing ratio of cold water.

According to the above equation, the cold water temperature is taken as the local average annual temperature of 8.2°C in Woka, and the cold water SiO_2 content is taken as the average value of cold springs in the basin. The initial temperature of geothermal water is assumed to be equal to 75°C–300°C, and the corresponding enthalpy values can be found in Table 6. The temperature at the mouth of the spring and the SiO_2 content were based on the measured values. The enthalpy and the mass concentration of SiO_2 at each temperature are substituted into Eqs 1, 2, respectively, to find the X_1 and X_2 values at different temperatures and plot the curve of X and geothermal water temperature at different temperatures (Figure 6), and the intersection point of X_1 and X_2 curves is the calculated reservoir temperature value.

Figure 7 shows that the reservoir temperature of Kanai geothermal spring is 200°C, and the proportion of cold water mixing is 77%; the reservoir temperature of Woka geothermal spring is 175°C, and the proportion of cold water mixing is 73%; the reservoir temperature of Amaka geothermal spring is 175°C, and the proportion of cold water mixing is 83%; thus, it can be seen that the underground geothermal water system of Woka rift basin is a high-temperature geothermal water system, but it is strongly affected by the mixing of cold water on the surface. The estimated reservoir temperature based on the mixing model is basically consistent with the reservoir temperature range on the Na-K-Mg equilibrium diagram, which can reflect the reservoir temperature value of the subsurface geothermal water system in the Woka graben basin more realistically.

Genetic mechanism

Heat source

According to previous research on high-temperature geothermal systems in Tibet, the heat source of Tibetan geothermal heat is mostly the contribution of the local melt layer in the crust, which is characterized by high conductivity and low gravity anomalies (Zhang, Tan, 2015). The melt bodies are mostly arranged in a string of beads and form extensional faults and fracture zones with linear spreading characteristics on the surface. In addition, they gradually form a fault valley system characterized by a string of bead-like fracture basins in the later geological history, which often becomes the dominant site for underground geothermal water and nurtures many geothermal fields such as Nimu, Yangbajing, and Gulu. Combined with the hydrogeochemical characteristics of the geothermal springs exposed in the Woka graben, it is believed that there is a deep local melt in the Woka graben,

TABLE 6 Reservoir temperature of geothermal springs.

Spring name	T/°C	No steam loss	Max steam loss
		$t = \frac{1309}{5.19 - logSiO_2} - 273.15$	$t = \frac{1522}{5.75 - logSiO_2} - 273.15$
Kanai geothermal spring	51.96	121.66	119.57
Waka geothermal spring	52.65	112.44	111.70
Cuoba geothermal spring	36.25	95.22	96.85
Luobusa geothermal spring	57.77	212.41	194.32

which provides a good heat source condition for the underground geothermal water system in the Woka graben basin.

Transport channel

The interlocking fracture system in the Woka basin provides storage space and transport channels for the formation of geothermal water. From the point of view of the development of the geothermal water system, the intersection of fractures in different directions is the dominant part of geothermal water storage, transportation, enrichment, and even discharge and is the area with intensive geothermal water activity. The main heat control structure of the Woka geothermal area can be divided into the northern Regan–Songduo fault zone, the central Mocun fault zone, and the southern Yarlung–Zangbo River tectonic zone. They are distributed in the E-W direction and cut by the N-S direction Cuona–Woka fault. These tectonic intersections constitute the favorable location of the geothermal water system. In particular, the intersection of NS-oriented faults and EW-oriented faults is not only a channel for geothermal water recharging but also a space for geothermal water transportation and storage. Hence, it is the most active part of the geothermal water system, and the existence of a low-resistance zone has a resistivity of less than 100 Ω m, which is approximately 300 m wide, along the geothermal spring outcrop zone of the Zengjiuqu River Valley.

Recharging source

The analysis of hydrogeochemical characteristics shows that the geothermal springs in the study area are mainly recharged by atmospheric precipitation and snow-melting water. The geothermal water is affected by water–rock action and cold water mixing in the circulation process, showing different types of water chemistry. The geothermal springs in the area are mixed with cold water in varying proportions from 73 to 83%. The hydrogen and oxygen isotopic characteristics of the geothermal springs show that the geothermal springs in the area are recharged at elevations from 5193 to 5247 m.

Reservoir affinity

Based on the hydrogeochemical characteristics of the geothermal springs and their reservoir characteristics, the reservoirs in the area can be divided into two types: Quaternary pore and bedrock fracture.

Quaternary pore sediment reservoir

According to the results of physical prospecting, the thickness of the fourth series loose cover layer of Zengjiuqu in the Woka area is 50–150 m. In addition, its lithology is sand and gravel, with a dense sand layer or geothermal water colloid layer as a cover layer locally. In the process of recharge and runoff, the geothermal water gushes out along the buried Woka fault developed in the basement of the riverbed or the boundary faults on both sides of the Woka rift basin. Then, geothermal water enters into the pore space of the Quaternary loose sediments with good permeability along the valley of Zengjiuqu, forming a good Quaternary pore sediment reservoir.

The outcrop of geothermal water in this geothermal reservoir is mainly a warm water swamp. In addition, the outcrop along Zengjiuqu is wide. The closer distance to the surface water is, the more obvious the mixing effect is, and the temperature is lower. However, the borehole can reveal underground geothermal water with a higher temperature than the natural outcrop geothermal spring.

Bedrock fracture type reservoir

This reservoir is mainly distributed in the bedrock on both sides of Zengjiuqu, and its aquifer is composed of Cretaceous–Paleocene granite intrusive rocks, which are influenced by active faults, and the tectonic fissures are developed, with rich water reserve. The development of tectonic fissures is not only an advantageous channel for geothermal water transportation but also an excellent space for geothermal water storage. Most of the geothermal springs flow along the fissures in granite, which is the main reservoir of geothermal water in the area.

Conceptual model for geothermal system in the Woka graben

Because of the continuous and strong plate collision activities of the Eurasian plate, intensive and frequent structural deformation has been formed on the Tibetan Plateau. It creates a deep melt-type magma source area in

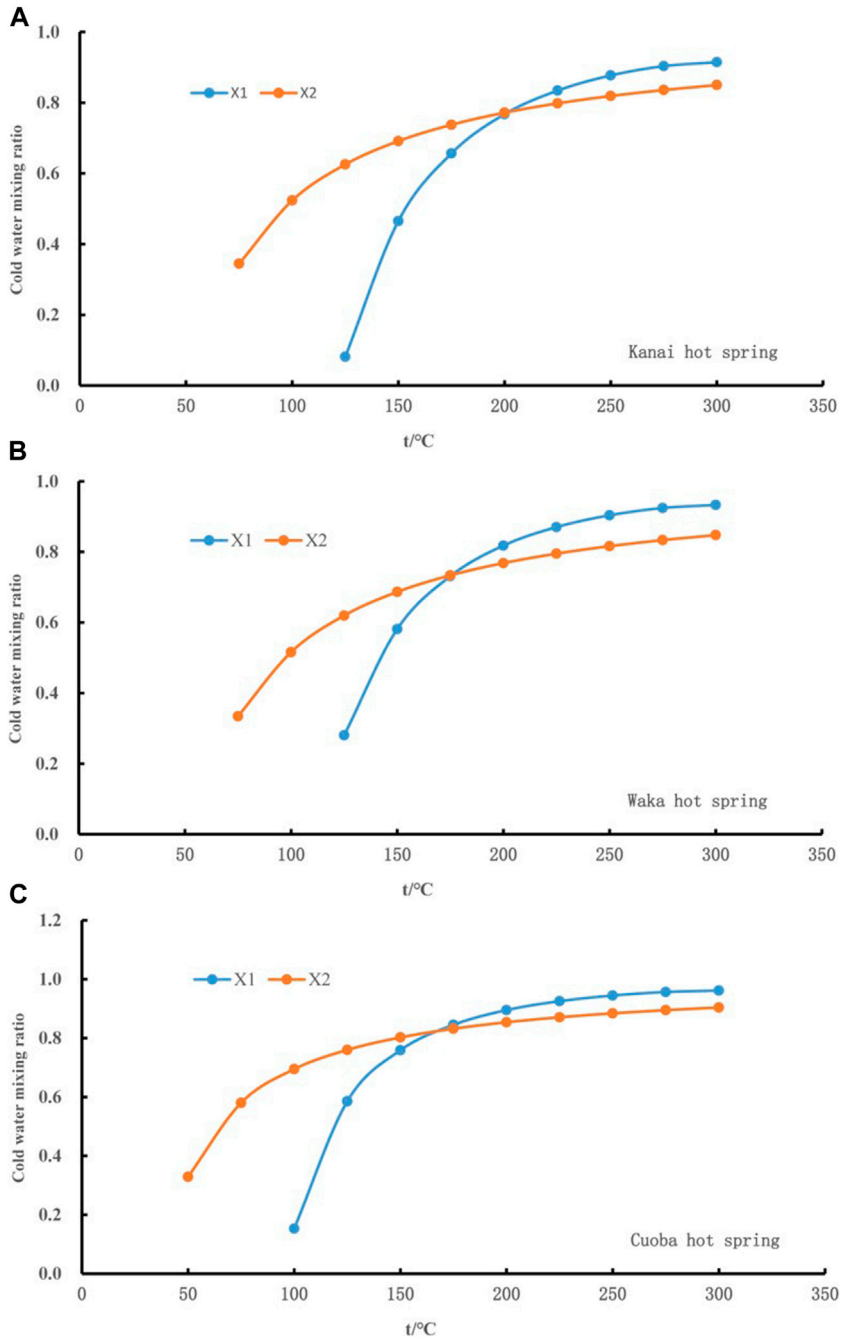


FIGURE 7
Relations between fraction of cold water and temperature in the mixing model.

the lower crust and a local low-velocity melt layer in the middle and forms shallow intrusive magma capsules and local banded melt bodies at different depths within a certain depth in the upper crust, providing the necessary heat source for the formation of the underground geothermal water system on the Tibetan Plateau. Therefore, the Tibetan Plateau geothermal resources are mostly uplifted mountain convection type. The conceptual model of the subsurface geothermal water system within the Woka graben basin was established by synthesizing the research results of many geothermal fields in the Tibetan region, such as Yangpaijing and Nimu-Naqu geothermal fields (Figure 8).

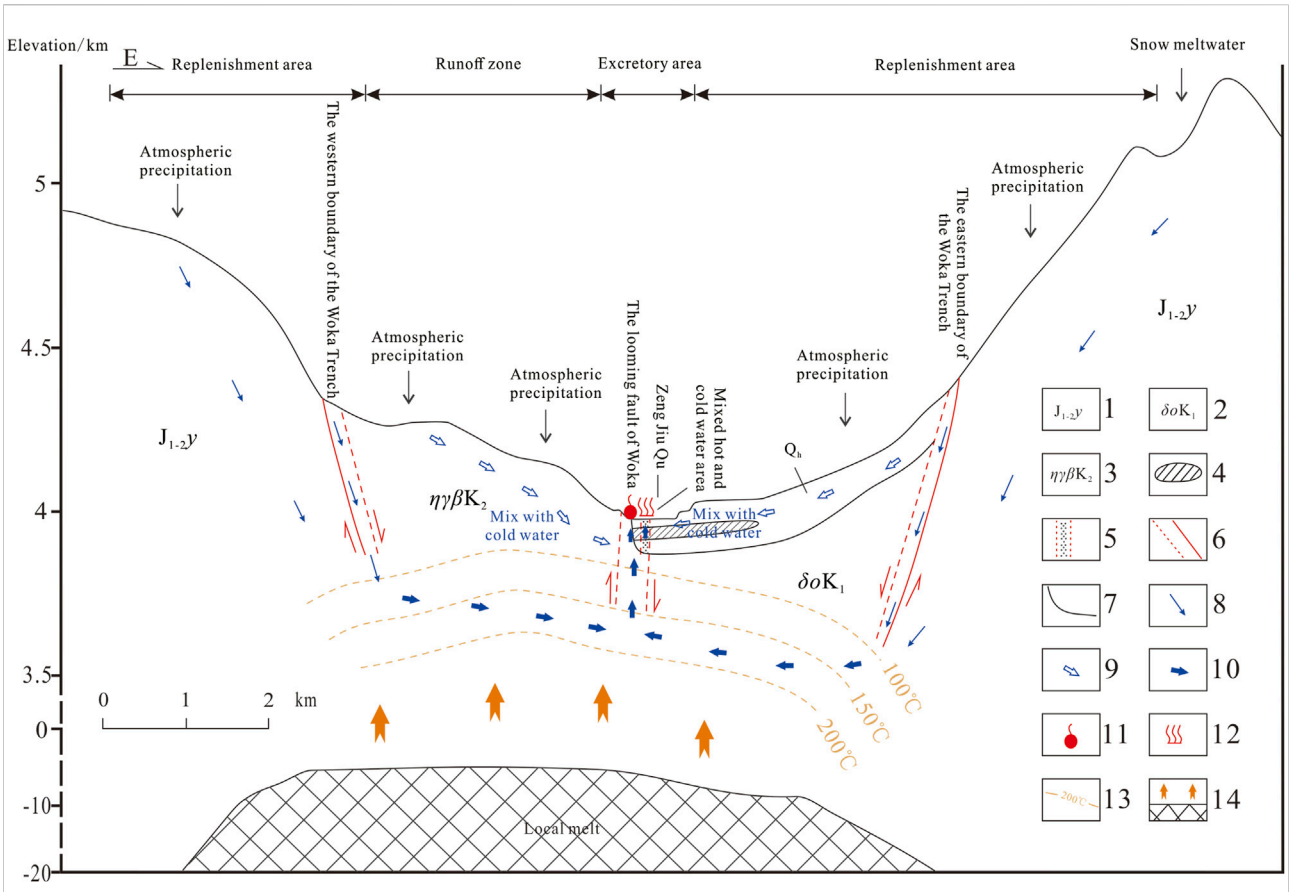


FIGURE 8
Genetic model of geothermal waters in the Woka Graben basin. 1-Middle to Lower Jurassic Yeba formation; 2-Lower Cretaceous quartz diorite; 3-Middle Cretaceous monzogranite;4-Tight sand cover; 5-Channel of Quaternary thermal reservoir; 6-Measured or inferred fault; 7-Geological boundary; 8-Cold water and transport direction; 9-Mixed cold water and its migration direction; 10-Geothermal water and flow direction; 11-Geothermal spring; 12-Warm water swamp; 13-Inferred temperature contour; 14-Heat source.

The atmospheric precipitation and alpine ice and snow melt water on both sides of the Woka graben basin are the main recharge sources of geothermal water, and the cold water receiving the recharge keeps seeping down along the fractures developed by the tectonic activity. In addition, cold water is heated by the local strip melt at a certain depth to provide a heat source and thus forms geothermal water involved with deep gas components. Then, geothermal water begins to flow upward, controlled by the fault-controlled bedrock fracture type reservoir. During the ascent of geothermal water along the river valley or the basin boundary fractures, its temperature decreases because of the mixing of the shallow cold water. In Zengjiuqu River valley, geothermal water enters into the pore aquifer of the fourth system loose rock type with good permeability along the bedrock fracture reservoir. In addition, the dense sand layer or geothermal water cementation layer is used as the cover layer, forming the Quaternary pore type shallow reservoir, which is mixed with the surface water during the rising of geothermal water and forms a warm water swamp along the riverbed.

The effect of high-temperature geothermal water on underground construction

The Woka graben is adjacent to Mochukongka Qu in the north and reaches the valley of Yarlung Tsangpo River in the south, which is an essential place for the Sichuan–Tibet railway line. Because of the construction of the Lhasa–Linzhi railway, many major projects such as hydropower and road construction are further planned in the area. According to the above analysis, the geological structure of Woka graben is complex, with active fracture development and strong hydrothermal activity, and its deep reservoir temperature can reach more than 120°C. Hence, it belongs to the high- and medium-temperature geothermal system. Engineering construction will be affected by the enrichment of geothermal resources.

As for the engineering thermal damage, the water temperature of the surface outcrop in the Woka rift valley is 36.25°C–57.77°C, and the calculated reservoir temperature is 97.86°C–125.56°C. The water temperature in the deep or good geothermal channels will be even higher. After the project exposure, there will be a large flow of high-temperature geothermal water caused by the surge water disaster; the sulfate content of geothermal water in the graben is 94.4–147 mg/L, and toxic and harmful gases such as H_2S will be escaped after the project exposure. Therefore, the construction of the project in the geothermal development area of the rift valley will pose a great threat to the safety of construction workers because of the high-temperature geothermal water and harmful gases, leading to a significant increase in project costs.

As for the corrosiveness of the project, the pH value of the geothermal water in the rift valley is 6.71–8.25, the HCO_3^- content is 31–214 mg/L, the Mg^{2+} content is 0.026–7.85 mg/L, and the SO_4^{2-} content is 94.4–147 mg/L, which is not corrosive to the project. However, the Cl^- ion content of the Luobusa geothermal spring is 4060 mg/L, which is more than 1000 mg/L. It is a corrosive hazard to the tunneling equipment as well as the tunneling facilities, which must be considered in tunnel construction. Therefore, for major construction projects in the Woka graben, a detailed investigation should be conducted to avoid the geothermal water channel or to divert the geothermal water and reasonably arrange the construction sequence to overcome the problem.

Conclusion

(1) The geothermal water system in the Woka graben belongs to the medium- to high-temperature geothermal system, and the geothermal heat shows a belt-like distribution along the Woka semiburied fracture. The geothermal water is medium alkaline water with a TDS concentration of 150.8–744 mg/L. The hydrochemical types are mainly SO_4-Na type, SO_4-Cl-Na type, and HCO_3-SO_4-Na type.

(2) The hydrogeochemical characteristics show that the Woka geothermal water system has the characteristics of atmospheric precipitation recharge and shallow circulating groundwater and is subject to the mixing effect of fracture diving or surface water. In addition, the geothermal water is in the range of partial equilibrium or mixed water and immature water on the Na-K-Mg equilibrium diagram.

(3) The reservoir temperatures range from 97.86°C to 125.56°C, estimated using a silica geothermometer. The geothermal water was subject to the mixing of shallow fissure cold water or surface water. By establishing the reservoir temperature mixing model, the initial reservoir temperature of geothermal water and the proportion of mixed cold water are determined. The temperature range of shallow and deep geothermal reservoirs is from 96.85°C to 119.57°C and from 120°C to 200°C, respectively, and the proportion of mixed cold water is 73–83%.

(4) Based on the isotope elevation effect characteristics, the recharge elevations of the geothermal water system in the Woka graben basin are from 5193 to 5247 m, mainly recharged by atmospheric rainfall and alpine snow-melting water, and the geothermal water comes from the release of mantle-sourced CO_2 from deep regional faults.

(5) Some geothermal waters possess high Cl^- concentrations, leading to the corrosiveness of the project. For major construction projects in the Woka graben, a detailed investigation should be conducted to avoid the geothermal water channel or to divert the geothermal water and reasonably arrange the construction sequence to overcome the problem.

Data availability statement

The original contributions presented in the study are included in the article/Supplementary Material; further inquiries can be directed to the corresponding author.

Author contributions

WZ: Investigation, data curation, and writing—original draft. SW: Data curation and methodology. MX: Writing—review and editing and conceptualization.

Conflict of interest

SW is employed by the Sichuan Institute of Geological Engineering Investigation Group Co., Ltd.

The remaining authors declare that the research was conducted in the absence of any commercial or financial relationships that could be construed as a potential conflict of interest. The reviewer YL declared a shared affiliation with the author WZ to the handling editor at the time of review.

Publisher's note

All claims expressed in this article are solely those of the authors and do not necessarily represent those of their affiliated organizations, or those of the publisher, the editors, and the reviewers. Any product that may be evaluated in this article, or claim that may be made by its manufacturer, is not guaranteed or endorsed by the publisher.

Supplementary material

The Supplementary Material for this article can be found online at: https://www.frontiersin.org/articles/10.3389/feart.2022.895884/full#supplementary-material

References

Cao, H-W., Li, G-M., Zhang, R-Q., Zhang, Y-H., Zhang, L-K., Dai, Z-W., et al. (2021). Genesis of the Cuonadong tin polymetallic deposit in the tethyan himalaya: evidence from geology, geochronology, fluid inclusions and multiple isotopes. *Gondwana Res.* 92, 72–101. doi:10.1016/j.gr.2020.12.020

Cao, H-W., Li, G-M., Zhang, Z., Zhang, L-K., Dong, S-L., Xia, X-B., et al. (2020). Miocene Sn polymetallic mineralization in the tethyan himalaya, southeastern tibet: a case study of the cuonadong deposit. *Ore Geol. Rev.* 119, 103403. doi:10.1016/j.oregeorev.2020.103403

Cao, H-W., Zhang, Y-H., Santosh, M., Li, G-M., Hollis, S. P., Zhang, L-K., et al. (2019). Petrogenesis and metallogenic implications of cretaceous magmatism in central lhasa, tibetan plateau: a case study from the lunggar Fe skarn deposit and perspective review. *Geol. J.* 54, 2323–2346. doi:10.1002/gj.3299

Chang, X-W., Xu, M., Jiang, L-W., Li, X., and Zhang, Y-H. (2021). Hydrogeochemical characteristics and formation of low-temperature geothermal waters in mangbang-longling area of western yunnan, China. *J. Chem.* 2021, 1–13. doi:10.1155/2021/5527354

Elenga, H. I., Tan, H., Su, J., and Yang, J. (2021). Origin of the enrichment of B and alkali metal elements in the geothermal water in the Tibetan Plateau: Evidence from B and Sr isotopes. *Geochemistry* 81, 125797. doi:10.1016/j.chemer.2021.125797

Fournier, R. (1977). Chemical geothermometers and mixing models for geothermal systems. *Geothermics* 5, 41–50. doi:10.1016/0375-6505(77)90007-4

Fournier, R. O. (1979). Geochemical and hydrologic considerations and the use of enthalpy-chloride diagrams in the prediction of underground conditions in hot-spring systems. *J. Volcanol. Geotherm. Res.* 5, 1–16. doi:10.1016/0377-0273(79)90029-5

Guo, Q. (2012). Hydrogeochemistry of high-temperature geothermal systems in China: a review. *Appl. Geochem.* 27, 1887–1898. doi:10.1016/j.apgeochem.2012.07.006

Jiang, Z., Xu, T., Owen, D. D. R., Jia, X., Feng, B., Zhang, Y., et al. (2018). Geothermal fluid circulation in the Guide Basin of the northeastern tibetan Pplateau: isotopic analysis and numerical modeling. *Geothermics* 71, 234–244. doi:10.1016/j.geothermics.2017.10.007

Klemperer, S. L., Zhao, P., Whyte, C. J., Darrah, T. H., Crossey, L. J., Karlstrom, K. E., et al. (2022). Limited underthrusting of India below Tibet: $^{(3)}$He/$^{(4)}$He analysis of thermal springs locates the mantle suture in continental collision. *Proc. Natl. Acad. Sci. U. S. A.* 119, e2113877119. doi:10.1073/pnas.2113877119

Kong, Y., Pang, Z., Shao, H., Hu, S., and Kolditz, O. (2014). Recent studies on hydrothermal systems in China: a review. *Geotherm. Energy* 2, 19. doi:10.1186/s40517-014-0019-8

Li, X., Huang, X., Liao, X., and Zhang, Y. (2020). Hydrogeochemical characteristics and conceptual model of the geothermal waters in the xianshuihe fault zone, southwestern china. *Int. J. Environ. Res. Public Health* 17, 500. doi:10.3390/ijerph17020500

Li, X., Qi, J., Yi, L., Xu, M., Zhang, X., Zhang, Q., et al. (2021). Hydrochemical characteristics and evolution of geothermal waters in the eastern himalayan syntaxis geothermal field, southern tibet. *Geothermics* 97, 102233. doi:10.1016/j.geothermics.2021.102233

Liao, Z. (2018). Hot springs in southwestern China. *Therm. Springs Geotherm. Energy Qinghai-Tibetan Plateau Surroundings* chapter 6, 79–163. doi:10.1007/978-981-10-3485-5_6

Tan, H., Su, J., Xu, P., Dong, T., and Elenga, H. I. (2018). Enrichment mechanism of Li, B and K in the geothermal water and associated deposits from the kawu area of the tibetan plateau: constraints from geochemical experimental data. *Appl. Geochem.* 93, 60–68. doi:10.1016/j.apgeochem.2018.04.001

Tian, J., Pang, Z., Liao, D., and Zhou, X. (2021). Fluid geochemistry and its implications on the role of deep faults in the genesis of high temperature systems in the eastern edge of the Qinghai Tibet Plateau. *Appl. Geochem.* 131, 105036. doi:10.1016/j.apgeochem.2021.105036

Truesdell, A., and Fournier, R. (1977). Procedure for estimating the temperature of a hot-water component in a mixed water by using a plot of dissolved silica versus enthalpy. *USGS J. Res.* 5, 49–52.

Wang, P., Chen, X., Shen, L., Wu, K., Huang, M., Xiao, Q., et al. (2016). Geochemical features of the geothermal fluids from the mapamyum non-volcanic geothermal system (Western Tibet, China). *J. Volcanol. Geotherm. Res.* 320, 29–39. doi:10.1016/j.jvolgeores.2016.04.002

Wang, Y., Gu, H., Li, D., Lyu, M., Lu, L., Zuo, Y., et al. (2021). Hydrochemical characteristics and Genesis analysis of geothermal fluid in the zhaxikang geothermal field in cuona county, southern tibet. *Environ. Earth Sci.* 80, 415. doi:10.1007/s12665-021-09577-8

Wang, Y., Li, L., Wen, H., and Hao, Y. (2022). Geochemical evidence for the nonexistence of supercritical geothermal fluids at the yangbajing geothermal field, southern tibet. *J. Hydrology* 604, 127243. doi:10.1016/j.jhydrol.2021.127243

Wang, Y., Zheng, C., and Ma, R. (2018). Review: safe and sustainable groundwater supply in China. *Hydrogeol. J.* 26, 1301–1324. doi:10.1007/s10040-018-1795-1

Zhang, W., Tan, H., Zhang, Y., Wei, H., and Dong, T. (2015). Boron geochemistry from some typical tibetan hydrothermal systems: origin and isotopic fractionation. *Appl. Geochem.* 63, 436–445. doi:10.1016/j.apgeochem.2015.10.006

Zhang, X., and Hu, Q. (2018). Development of geothermal resources in China: a review. *J. Earth Sci.* 29, 452–467. doi:10.1007/s12583-018-0838-9

Zhang, Y., Xu, M., Li, X., Qi, J., Zhang, Q., Guo, J., et al. (2018). Hydrochemical characteristics and multivariate statistical analysis of natural water system: a case study in kangding county, southwestern China. *Water* 10, 80. doi:10.3390/w10010080

Zhang, Y., Cao, H., Hollis, S., Tang, L., Xu, M., Jiang, J., et al. (2019a). Geochronology, geochemistry and Sr-Nd-Pb-Hf isotopes of the early paleogene gabbro and granite from central lhasa, southern tibet: petrogenesis and tectonic implications. *Int. Geol. Rev.* 61, 868–894. doi:10.1080/00206814.2018.1476187

Zhang, Y., Wang, Y., Wang, W., Liu, J., and Yuan, L. (2019b). Zircon U-Pb-Hf isotopes and mineral chemistry of early cretaceous granodiorite in the lunggar iron deposit in central Lhasa, Tibet Y, China. *J. Central South Univ.* 26, 3457–3469. doi:10.1007/s11771-019-4266-5

Zhang, Y., Yao, R., Wang, Y., Duo, J., and Cao, H. (2022). Zircon U-Pb and sericite Ar-Ar geochronology, geochemistry and S-Pb-Hf isotopes of the Zebuxia Pb-Zn deposit, Tibet, southwestern China. *Ore Geol. Rev.* 148, 104999. doi:10.1016/j.oregeorev.2022.104999

frontiers | Frontiers in Earth Science

TYPE Original Research
PUBLISHED 13 September 2022
DOI 10.3389/feart.2022.943383

Check for updates

OPEN ACCESS

EDITED BY
Yunhui Zhang,
Southwest Jiaotong University, China

REVIEWED BY
Cong Zhang,
Hohai University, China
Sun Wenjibin,
Guizhou University, China
Cheng Zeng,
The University of Newcastle, Australia
Shiyuan Huang,
Chongqing Jiaotong University, China

*CORRESPONDENCE
Meng Zhao,
zhaomeng@cdu.edu.cn

SPECIALTY SECTION
This article was submitted to Geohazards and Georisks, a section of the journal Frontiers in Earth Science

RECEIVED 13 May 2022
ACCEPTED 22 July 2022
PUBLISHED 13 September 2022

CITATION
Zhao M, Wu H-G, Guo W, Tan B-R, Hu C, Deng R and Chen L-Y (2022), Experimental study of the particle agglomeration on its mechanical properties of collapsible loess. *Front. Earth Sci.* 10:943383. doi: 10.3389/feart.2022.943383

COPYRIGHT
© 2022 Zhao, Wu, Guo, Tan, Hu, Deng and Chen. This is an open-access article distributed under the terms of the Creative Commons Attribution License (CC BY). The use, distribution or reproduction in other forums is permitted, provided the original author(s) and the copyright owner(s) are credited and that the original publication in this journal is cited, in accordance with accepted academic practice. No use, distribution or reproduction is permitted which does not comply with these terms.

Experimental study of the particle agglomeration on its mechanical properties of collapsible loess

Meng Zhao [1,2]*, Hong-Gang Wu [3], Wei Guo [2], Bo-Ren Tan [1], Cheng Hu [1], Rui Deng [1] and Li-Yi Chen [2]

[1]Sichuan Engineering Research Center for Mechanical Properties and Engineering Technology of Unsaturated Soils, Chengdu University, Chengdu, China, [2]State Key Laboratory of Geo-Hazard Prevention and Geo-Protection, Chengdu University of Technology, Chengdu, China, [3]China Northwest Research Institute Co., Ltd of CREC, Lanzhou, China

Loess, distributed all over the world, exhibits the behavior that is related to their formation history, mineralogy, and microstructure, which can cause serious geotechnical engineering problems. This paper presents the Baozhong railway is a key transportation channel for Guyuan city in Ningxia province of northwestern China. Based on field investigations treasure middle section of the railway in the study area, it is found that the more serious diseases subgrade settlement, local roads embankment platform dislocation occurs and lots of cracks were founded. For several years, with the train speed increasing, and due to the influence of widespread flood irrigation on the farmland, the subgrade experienced a degree of settlement. This settlement was not alleviated after three treatments, which seriously affected train safety. In order to analyze the reason for the railway line settlement, soil samples were collected from the collapsible loess subgrade. Consolidation test, particle size analysis test, X-ray diffraction test (XRD), and scanning electron microscopy test (SEM) were performed to investigate the mechanism of the subgrade disease. The results reveal that loess collected from severe differential settlements at locations has a highly compressible, and its clay content and agglomeration level was generally low. These results illustrated that the particle size of 20–50 microns has a direct effect on its mechanical properties of loess. This part of the particles has a cementation effect. It can effectively connect the large particles of the skeleton to form particle agglomerates and is an effective composition of loess clay minerals. Therefore, the loess structure was not stable due to its relatively low internal molecular attraction. When such saturated collapsible loess subgrade subjected to train vibration load, the soil might be liquefied, and its structure might be instable. If the drainage of the subgrade was not well designed, severe differential settlements would occur. The research is of great significance to clarify the relationship between loess particle composition, microstructure and its macromechanics, providing a vital reference for the engineering construction in the loess-dominated areas.

KEYWORDS

particle agglomeration, mechanical properties, existing railway line, collapsible loess, experimental study

1 Introduction

Loess is found all over the world, this soil exhibits behavior that is related to their formation history, mineralogy, and microstructure, which can cause serious geotechnical engineering problems (Zhao et al., 2020). In the loess area, many engineering diseases occurred due to its collapsibility behavior, such as widespread distribution of the ground cracks, deformation of urban buildings, landslides caused by rain or irrigation, subgrade settlement of highways and railways (Derbyshire, 2001; Delage et al., 2005; Sun et al., 2009). With the development of cities around the world, the demand for municipal, highway, railway is also growing. The constructional will have more problems associated with the collapsible behavior of the loess in this area.

Water shortage is common around world, especially in the northwest China (He et al., 2020; Zhang et al., 2021a, 2021b; Yao et al., 2022). A balance between a reasonable flow rate for irrigation and the effective loess collapse control is a challenge in this area. Loess collapse is a concern in China and other countries. Guyuan, an important city of the Belt and Road trade route, is a key city for rail transport, where loess is widely distributed. With the development of transportation such as the Baozhong railway, many subgrade diseases spread in the last 2 decades. The K329-K331 section of the Bao Zhong railway is situated in the Malian town of Guyuan City (Figure 1). Due to weather changes and irrigating activities, the ground water level in this area and the moisture content of the railway loess subgrade are not stable. Differential or uneven settlements may occur along the railway, when the saturated collapsible loess subgrade is subjected to dynamic loads induced by trains. Placing additional railway slag to re-level the low portions induced by the differential settlements was a routine maintenance work in this area. After many years of the maintenance activities, additional static railway slag loads became significant, and the potential of differential settlements might be more severe in this area (Zhao et al., 2019). In addition, the railway loads were increased significantly in last few decades. As a result, the differential settlement in this area has become a severe threat on the safety operation of the railway. Therefore, In order to treat the differential settlements in this area, the study on the collapsibility mechanism of loess under train load conditions and the uneven settlement of Baozhong Railway are extremely urgent for the development of railway transportation in Ningxia, China.

Many researches were completed on loess in China and other countries (Wen and Yan, 2014). Hu (2005), Lommler and Bandini (2015), Li et al. (2016) studied the mechanism of loess collapse and researches mainly focused on the particle composition, pore characterization, and porosity of loess. Silt with particle sizes between 0.05 and 0.01 mm was considered critical on the behavior of loess (Zhao and Lei, 2011; Jiang M. et al., 2014). The composition of loess determined its mechanical and chemical properties, especially quartz and feldspar, which consisted of the skeleton composition of soil (Zhang et al., 2018). Clay minerals are mainly, illite, chlorite, rock, water mica, etc. They wrapped in particulate matters around the soil to determine the water sensitivity (Sun, 2010; Muñoz-Castelblanco et al., 2012). The mineral compositions of loess encountered in different areas of China were almost the same. However, the content of the microcrystalline calcium carbonate showed an increasing trend from the southeast to the northwest. Using polarized light, microscopic and scanning electron microscopy, Susan (2017) found that the coarse calcium carbonate was important as a support skeleton, and the native microcrystalline calcium carbonate played a role in cementing soil particles. The size, shape, distribution and structure of pores directly affected the permeability, collapsibility and other related geotechnical engineering properties of loess Romero and Simms (2008). The mechanical properties of loess were closely related to their microstructure. Luo et al. (2018) and Assadi-Langroudi et al. (2018) mainly explored the microstructure of the loess with a polarizing microscope. Romero and Simms (2008) and Xie et al. (2018) had a more detailed view on description and classification of the microstructure of loess. They found that the microstructure characteristics of loess were directly related to the loess collapsibility, and the arrangement of soil particles also played an important role. Jiang MJ. et al. (2014) observed the loess in Xi'an area by polarizing mirror and scanning electron microscope, he founded that the coarse particles of Q_2 loess in Xi'an area was mainly less attached and dispersed. Ye et al. (2012), Zhuang et al. (2018) quantitatively studied the microstructure parameters and macroscopic characteristics of loess. They found that the macro-mechanical properties and the microstructure of loess were closely related. The research on collapsible loess in China and other countries were mainly focused on the experiments and analyses of the loess. Limited studies have been conducted to understand the mechanism of the loess collapses.

In this paper, from a mesoscopic-microscopic perspective, macroscopic and microscopic test methods are used to analyze the occurrence mechanism of subgrade disease in collapsible loess in serious diseased areas. The results of this study are of great significance for the prevention and control of loess subgrade collapse.

2 Engineering geological background

The study area was the K329~K331 section of Bao Zhong railway which is located at the Malian town of Guyuan city

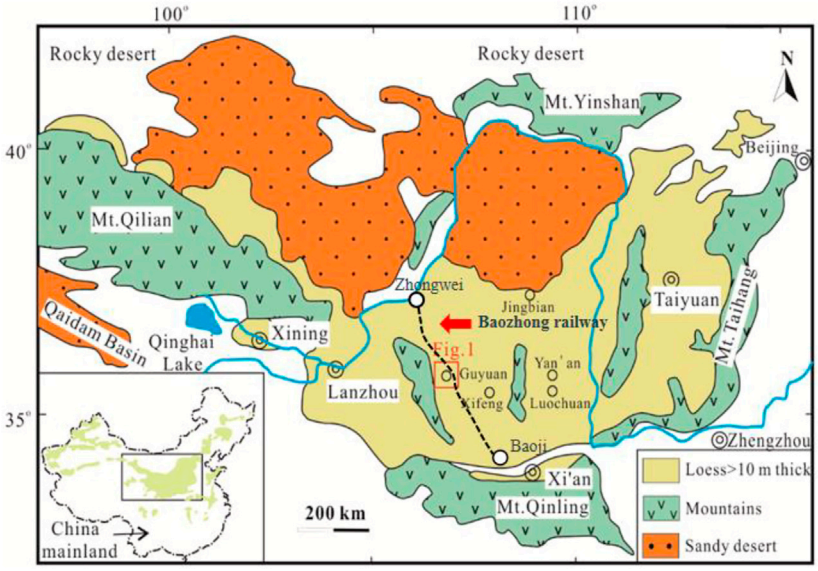


FIGURE 1
Shows Google earth map of the study area (Zhao et al., 2020).

(Figure 1), east of the Qingshui River. The starting point in the southeast was Baoji in Shaanxi Province, after passing through Pingliang City, Gansu Province, and the furthest end of the northwestern side was the town of Luobao in Zhongwei County, Ningxia Province (Zhao et al., 2020).

The location is at the Xiji Basin on the northwestern edge of the Loess Plateau in China, northeastern margin of Tibet Plateau (Yan et al., 2017; Zhang et al., 2022). The climate in the study area is characterized by a semi-arid and semi-humid continental climates with predominantly summer rainfall. About seventy percent of rainfall occurs within June to September. Due to water scarcity, large-scale farmland irrigation is required every spring and autumn for agricultural crops, which causes the rising of the groundwater level. A proliferation of loess disease had occurred along the railway line (Figure 2). Due to the influence of widespread flood irrigation on the farmland, the subgrade had a degree of settlement. The settlement had not been alleviated after three treatments. The "three treatment methods" are actually high-pressure jet grouting. High-pressure jet grouting is a method of treating ground with a high-pressure cement slurry sprayed from a horizontal nozzle through a drill pipe to form a jet stream, cutting the soil and mixing it with the soil. The lime soil water retaining wall for the foot of subgrade and grouting reinforcement for the hard shoulder were used at the three treatments. The lime soil water retaining wall for the foot of subgrade and grouting reinforcement for the hard shoulder were used at the three treatments (Zhao et al., 2020). Additionally, after many years of subgrade subsidence, the railway subgrade had produced uneven settlement, which leads to uneven tracks (Figure 2A), and worse: there were many cracks on both sides of the roadbed (Figures 2B,C). The longest extension of the crack was about 600 m long. The warning signs on both sides of the railway sink down with the maximum sinking level being 1.5 m. In addition, traffic safety is seriously threatened. For these reasons, the cause of the uneven settlement for the Baozhong railway subgrade loess is in urgent need of being addressed.

3 Sample preparation and methods

Three samples (Sample numbers 1, 2, and 3) were selected at Station K331 + 530, where significant roadbed diseases were observed (called the disease segment in this paper) (shown in Figure 3). For comparison, another three samples (Sample numbers 4, 5, and 6) were selected at Station K331 + 585, where no or limited roadbed diseases were observed (called the non-disease segment in this paper) (shown in Figure 3). These six samples were obtained at depths of 3 m, 6 and 9 m. The information of these six samples was shown in Table 1 below.

3.1 Test methods

Consolidation test, particle size analysis test, XRD diffraction test and SEM scanning electron microscopy test



FIGURE 2
Subgrade disease of Baozhong railway. **(A)** uneven track; **(B,C)** cracks on both sides of the subgrade.



FIGURE 3
Sampling on site.

were performed in this study. Detailed descriptions for these tests are as follows:

3.1.1 Consolidation tests

WG (WG-1C) single lever consolidation instrument was used in this study. The sample was prepared by a φ61.8 mm × 20 mm ring knife. The applied consolidation pressures were 50, 100 and 200 kpa.

3.1.2 Particle size analysis tests

The Mastersizer 2000 Laser Grain Size Analyzer was used in the grain size distribution tests. Firstly, the specimen was dried in a drying oven, pulverized, and passed through a 1 mm sieve. Secondly, a 15 g powder specimen was taken into the test chamber of the laser grain size analyzer. Finally, the percentage of the total volume of the soil grains of each grain size was ascertained by laser diffraction.

TABLE 1 The basic situation of the sample.

Sample number	Mileage number	Subgrade type	Sampling depth	Disease degree
1	K329 + 530	Disease segment	3	slight
2	K329 + 530	Disease segment	6	serious
3	K329 + 530	Disease segment	9	serious
4	K331 + 585	Non-disease segment	3	no
5	K331 + 585	Non-disease segment	6	slight
6	K331 + 585	Non-disease segment	9	slight

TABLE 2 Consolidation test parameters.

Sample number	Coefficient of consolidation	Coefficient of compressibility	Compression modulus
1	4.02	0.383	3.702
2	1.95	0.500	2.951
3	3.27	0.445	3.322
4	3.78	0.299	4.918
5	3.66	0.430	3.411
6	3.47	0.402	3.522

3.1.3 XRD diffraction tests

This test was conducted using a stoichiometric DMAX-3C diffractometer, in which CuKa and Ni were used to diffract ata diffraction angle range, between 5° and 60°. The obtained data was analyzed by a MID Jade software.

3.1.4 Scanning electron microscopy tests

The test samples were placed on Hitachi S-3000 N scanning electron microscope, and the photomicrographs were observed in a high vacuum mode. Photographs were taken with different magnification for each representative area of each sample.

4 Test results and discussion

4.1 Compressibility

The compressibility of the soil is generally determined by the compressive modulus, Es: Es ≤ 4 MPa is a highly compressible soil; 20 MPa≥Es ≥ 4 MPa is moderate compressible soil; and Es ≥ 20 MPa is lowly compressible soil. Consolidation test results were shown in Table 2.

The results revealed that samples 1, 2, and 3 in the disease segment, and Samples 5 and six in the non-disease segment were highly compressible soils. The compressive modulus of samples 2 and 3 was lower than that in samples 1, 5, and 6, indicating a relative high compressibility of these two samples. It is understood that the compressibility of a soil was directly related to its internal pores. The higher the compressibility, the larger the void ratio of a soil. It could be concluded that samples obtained in the disease segment were generally highly compressible with a relatively high void ratio. Therefore, relatively severe differential settlements were observed.

Relatively high compression index was achieved from Samples 5 and 6, which were obtained at the non-disease segment. However, the shallowest sample (Sample 4 at a depth of 3 m) at this non-disease segment did not show a high compression index. Therefore, it can be concluded that soils at a relatively shallow depth played a critical role on the subgrade performance. A better railway performance could be expected, where a stiff soil layer existed near the ground surface, even a relatively highly compressible soil lied underneath it. It is understood that the performance of the roadbed might be affected by the flood, irrigation activity and the dynamic loads induced by trains. The differential settlements might be related to the soil particles composition. The particle structure might be related to the porosity of soil.

4.2 Grain distribution

The grain size gradation curve and the particle distribution curve of the six test samples were plotted and shown in Figure 4.

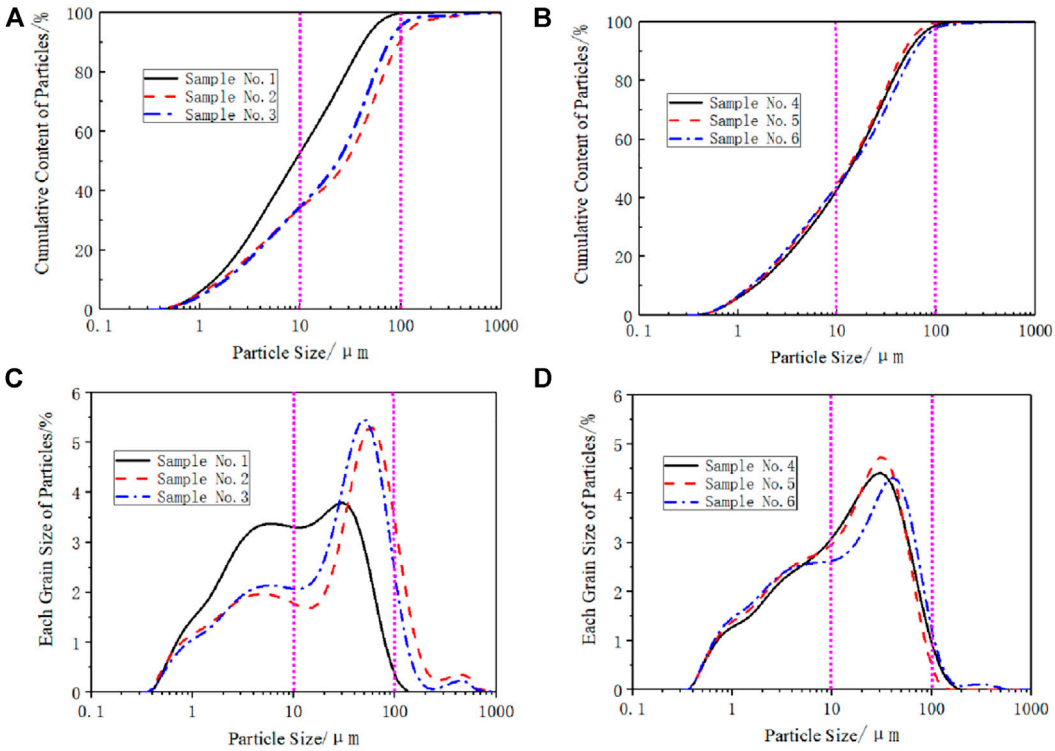


FIGURE 4
(A) Logarithmic curve of the particle size distribution on samples at disease segments, **(B)** Logarithmic curve of the particle size distribution on samples at non-disease segments, **(C)** Cumulative logarithmic curve of the particle size distribution on samples at disease segments, and **(D)** Cumulative logarithmic curve of the particle size distribution on samples at non-disease segments.

TABLE 3 Particle size analysis parameters.

Sample number	Nonuniformiy coefficient	Curvature coefficient	Clay content (%)	Silt content (%)	Sand content (%)
			< 0.002 mm	0.002 ~ 0.02 mm	0.02 ~ 2.0 mm
1	9.12	0.76	15.04	55.03	29.91
2	23.98	0.87	11.89	31.20	56.90
3	19.42	0.93	10.75	35.49	53.74
4	12.02	1.00	13.07	48.17	38.74
5	12.91	0.93	14.40	48.36	37.59
6	15.84	0.75	14.80	43.90	41.29

The particle size analysis data are summarized in Table 3 and Figure 4.

As shown in Figures 4A,B, the particle size distribution curves of Samples 2 and 3 in the disease segment appeared to be less smooth than those of Samples in the non-disease segment. As shown in Figures 4C,D compared to samples in the non-disease segment, the content of the small size particles (<50 μm) of Samples 2 and 3 in the disease segment were relatively low, but the big size particles (>100 μm) of them were relatively high. Therefore, it was considered that due to the low clay contents, the internal molecular attraction in Samples 2 and 3 might be relatively small, resulting in a relatively poor performance of a railway subgrade.

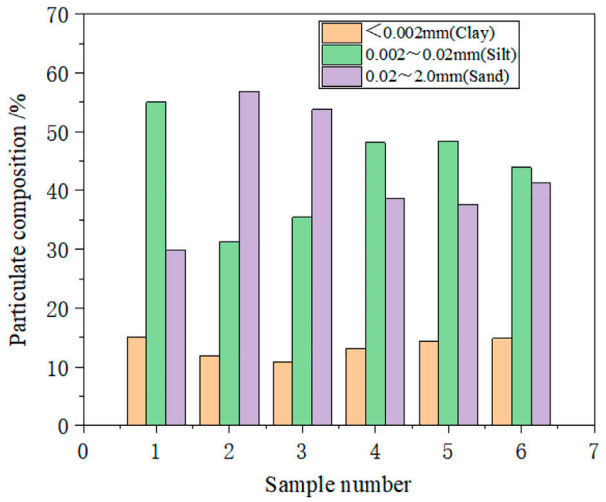


FIGURE 5
Particulate composition. A is illite, B is chlorite, C is quartz, D is plagioclase, E is potassium feldspar, F is calcite, and G is dolomite.

According to Table 3 and Figure 5, the results reveal that Samples 2 and 3 had relatively low clay contents and relatively high sand contents compared to other samples. From the soil structure perspective, the loess has a relatively high sensitivity to water. In samples 2 and 3, the clay content might be not enough to fill the voids between sand and silt, and the internal molecular attraction was small. This may be part of the reason that samples 2 and 3 showed high compressibility, and severe subgrade diseases were observed in this segment of the railway.

4.3 Mineral composition

XRD diffraction tests were carried out on all samples, and the results were shown in Figure 6. The results indicated that the samples in the diseased area were quite different from those in the non-disease area. Significant differences can be observed on Samples 3 and 3 compared to other samples.

Figure 6 showed that the maximum values was bascically the same for all samples. The maximum values of Samples 2 and 3 in the disease segment were relatively higher than others, the maximum values of Samples 1, 5, and 6 were similar, and the maximum value of Sample 4 was the lowest.

The maximum diffraction value (A + B + C) was the sum of illite, chlorite and quartz, respectively. This value reflected the degree of crystallization of the sample. Since the degree of crystallization of quartz was greater than that of illite and chlorite, a great maximum diffraction value indicated a relatively great quartz contain of a sample, based on results shown in Figure 6, compared to other samples, Samples 2 and 3 in the disease segment contained more quartz, but less calcite. The content of plagioclase, potassium feldspar, and dolomite in all samples were almost the same. This result indicated that the contents of illite, chlorite, quartz, and calcite might affect the subgrade performance.

Table 4 showed that Samples 2 and 3 contained more than 50% of quartz and only approximately 25% of cohesive particles, which were generally formed of chlorite and illite. This result was consistent with the results of particle analysis test, in which Samples 1, 2, and 3 in the disease segment contained relatively larger size particles compared to other samples. The quartz content of Samples in the non-disease segment was relatively low (<46%) but chlorite and illite based clay mineral contents were relatively high (between 35 and 42%). Therefore, it was considered that relatively high clay mineral content was likely to increase the destructive resistance of a soil and improve the performance of the railway subgrade.

4.4 Microstructure

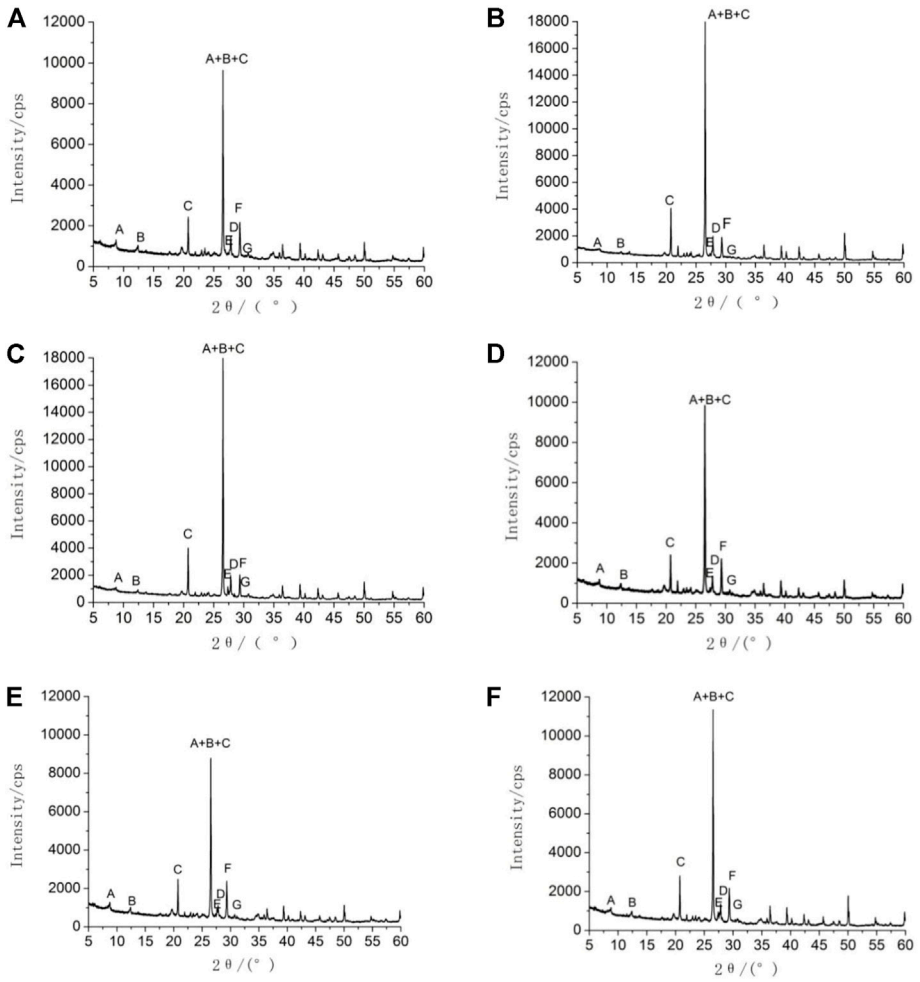
4.4.1 Micro qualitative analysis

In order to further study the mechanism of the disease loess subgrade soil, the scanning electron microscopy (SEM) was performed on Sample 2 in the disease segment. As a comparison, SEM was also performed on Sample 5 in the non-disease segment. Figure 7 and Figure 8 showed the details of the SEM results.

Figure 7 showed that the microstructure of sample 2 in the diseased area was dominated by the structure type of scaffolds with large pores and micro-cementation or weakly cemented, with low connection strength. The contact surface is very small, and the particles support each other, sometimes in point contact, and sometimes in edge and edge contact, forming relatively large interparticle pores. At the same time, due to the relatively high sand content, there are few clay cements between the particles, and the cements fill the pores between the particles sporadically, showing micro-cementation; the skeleton particles are mainly composed of single granular particles under the microscope. It has the characteristics of sand-like, the shape is relatively clear, and the particle size is relatively uniform.

Figure 8 showed that the microstructure of Sample 5 in the non-disease segment was strong and honeycomb. The skeleton particles in the microstructure are composed of agglomerates formed by the agglomeration of small particles, and there are certain large pores and small pores. The agglomerated particles are connected by cementing substances, and the graininess is not obvious. At the same time, the content of clay particles in the cement is the highest, and the particles are aggregated. The skeleton particles are embedded in the cement and do not contact each other. The connection strength is the highest.

From the above, it can be clearly seen that the loess samples in the diseased area and the non-disease area have detailed



A is illite, B is chlorite, C is quartz, D is plagioclase, E is potassium feldspar, F is calcite, and G is dolomite.

FIGURE 6
XRD diffraction patterns from samples in the disease segment (a、b、c) non-disease segment (d、e、f):**(A)** sample No. 1,**(B)**sample No.2, **(C)** sample No.3, **(D)** sample No. 4, **(E)** sample No.5, **(F)** sample No.6.

TABLE 4 Percentage of material composition derived from XRD diffraction.

Sample number	Illite (%)	Chlorite (%)	Quartz (%)	Potash feldspar (%)	Plagioclase (%)	Dolomite (%)	Calcite (%)
1	29	13	38	1	7	1	11
2	22	4	57	1	8	1	8
3	19	6	54	2	8	2	9
4	21	11	44	1	7	2	14
5	29	11	40	1	5	1	13
6	21	12	46	3	7	1	12

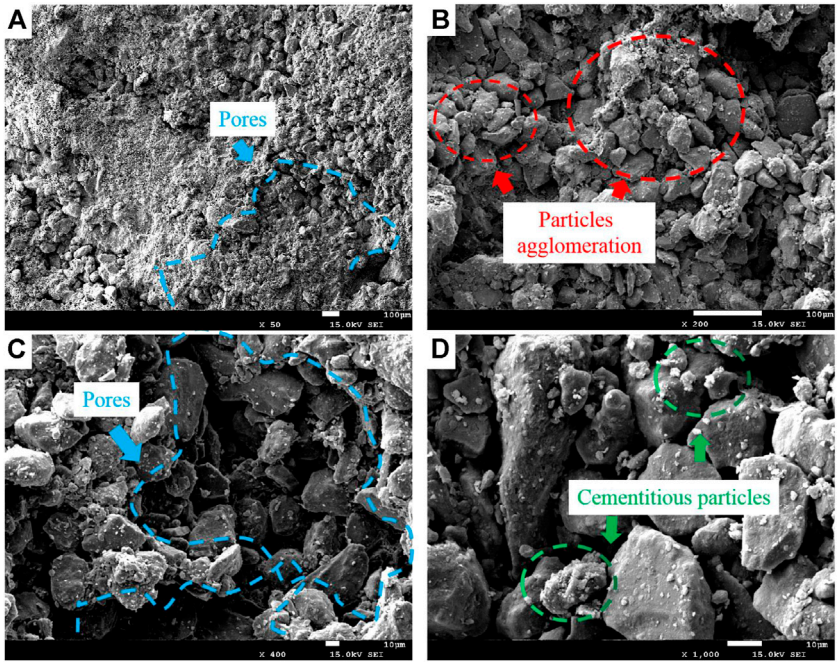


FIGURE 7
Electron microscopic scanning of the sample at disease segment:**(A)** Sample No.2–50 times, **(B)** sample No.2–200 times, **(C)** sample No.2–400 times,**(D)** sample No.2–1,000 times.

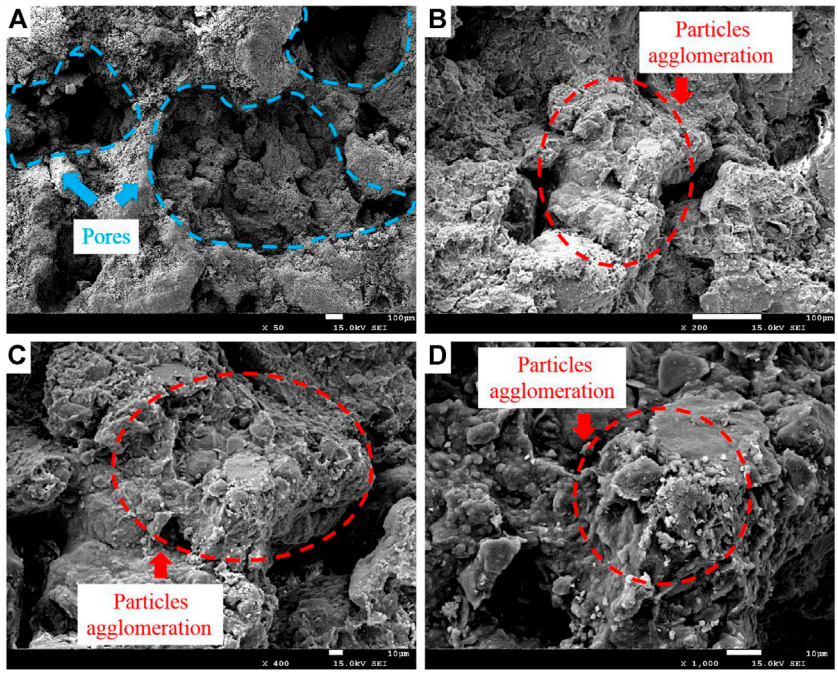


FIGURE 8
Electron microscopic scanning of the sample at non-disease segment:**(A)** Sample No.5–50 times, **(B)** sample No.5–200 times, **(C)** sample No.5–400 times, **(D)** sample No.5–1,000 times.

TABLE 5 Micro characteristic parameters.

Sample number	Entropy	Area ratio		Roundness	
		Particles	Porosity	Particles	Porosity
2	1.95	0.59	0.41	1.34	1.42
5	1.41	0.8	0.2	1.3	1.39
Sample Number	Distribution fractal dimension		Degree of orientation		Euler number
	Particles	Porosity	Euler number	Porosity	
2	0.22	0.54	0.97	0.95	0.31
5	0.21	0.7	0.97	1.01	0.52

microstructure differences. The non-disease area is the loess roadbed with good mechanical properties, and its loess microstructure was more blurred compared to samples in the disease segment. Flake like particles were mainly covered by dust grains. The pore sizes were generally between 10 and 50 μm. They were mainly uniformly distributed, generally irregular or elongated, and well connected. As shown in Figures 8C,D, clay size particles filled the majority of the relatively big pores in the Sample 5, which was obtained from the non-disease segment. Therefore, the internal molecular attraction of this sample should be better than that in the disease segment.

4.4.2 Micro quantitative analysis

The obtained relevant microcosmic characteristic parameters from Sample 2 in the disease segment and sample 5 in the non-disease segment were summarized in Table 5.

As shown in Table 5, the porosity of Sample 2 in the disease segment was 0.41, which was obviously more than that of Sample 5 in the non-disease segment. The fractal dimension of grain and pore distribution of Sample 2 in the disease segment was larger than that in the non-disease segment, indicating that the soil particles in the disease segment were more dispersed, and the internal molecular attraction was relatively low. The porosity of the degree of orientation of Sample 2 in the disease segment was 0.54, which was significantly lower than that in the non-disease segment. The pores were small and in a disordered manner, and their connectivity was poor, indicating that the soil might have a poor drainage. The Euler numbers of Sample 2 in the disease segment was smaller than that in the non-disease segment, implying that the internal molecular attraction of Sample 2 in the disease segment was poor.

5 Discussions

5.1 Quantitative analysis of the agglomerated clay

The form of the particle connection has direct point-contact、direct surface contact、 indirect point contact and indirect surface contact (Shao et al., 2018). The direct contact refers to the interface between particles with limited cohesion. The indirect contact is the interface between particles having a film which consists of clay and salt crystal. The point and surface contacts stand for particle interfaces with relatively small and large contact areas, respectively. Those contact forms a shown in Figure 9.

Clay particles with direct or indirect contact surfaces may form a group of soil particles. This is called clay “agglomeration” in this paper. SEM scanning electron microscopy images showed a relatively low content of clay films and sheets of Sample 2 at the disease segment, and thus, the level of clay “agglomeration” of this sample was relatively weak. The voids between soil particles of Sample 5 in the non disease segment were filled with clay films and sheets and the interfaces between soil particles were mainly surface contacts. Some soil particles in Sample 5 were completed wrapped with clay minerals. Therefore, the level of clay “agglomeration” of Sample 5 was strong. The clay “agglomeration” effects of the two Samples were shown in Figure 10.

As shown in Figures 10A,B, the soil clay mineral content and the clay “agglomeration” level of Sample 2 in the disease segment were relative low, resulting in a weak cohesion. The structures of such saturated soil might be liquefied and instable under dynamic loads. It could also be observed from Figures 10C,D that the clay “agglomeration” level of Sample 5 in the non-disease segment was relatively high. A strong connection between soil particles was formed, resulting in a strong cohesion between soil particles. A better performance was expected for such soil used as a railway subgrade.

5.2 Qualitative analysis of the agglomerated clay

The results of the particle size analysis tests and the XRD tests showed that the contents of clay minerals and quartz particles of the samples in disease segment and those in the non-disease segments were not the same, resulting in their different

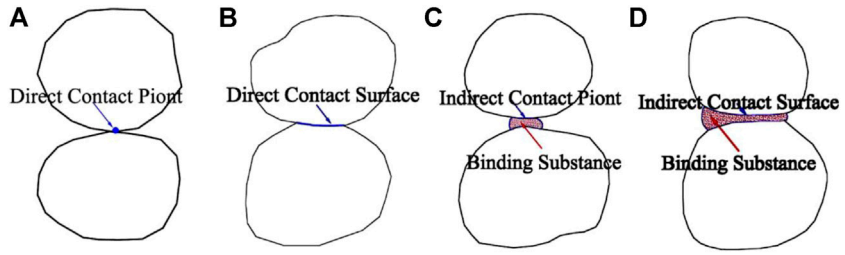


FIGURE 9
(A) Direct point contact, **(B)** direct surface contact, **(C)**, indirect point contact, **(D)** indirect surface contact.

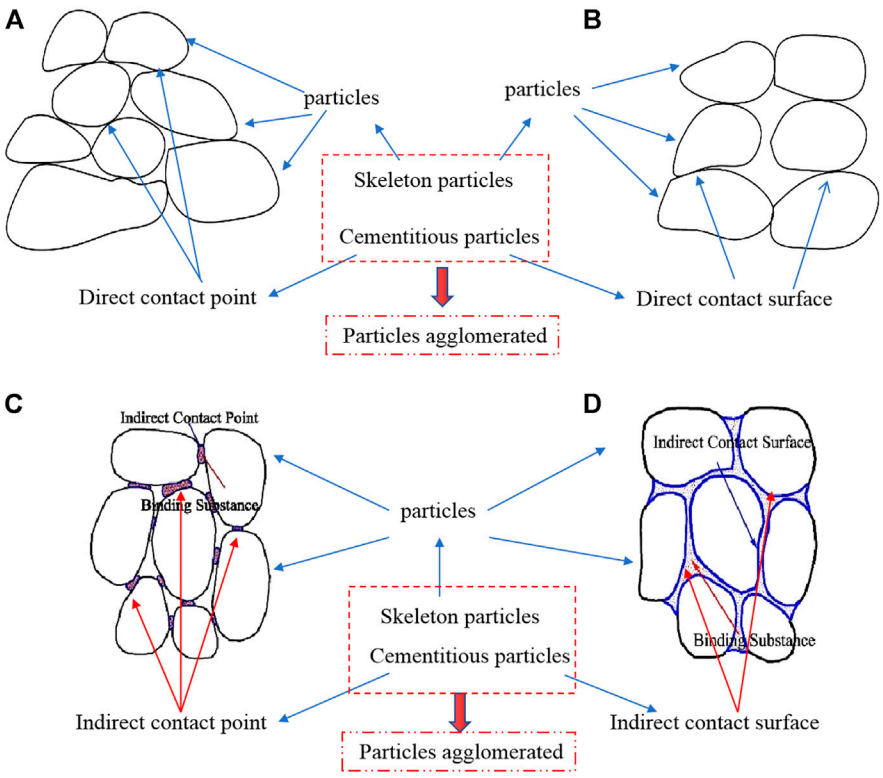


FIGURE 10
The clay agglomeration effects: **(A,B)** Sample 2 in disease segment, **(C,D)** Sample 5 in non-disease segment.

engineering behaviors. Both particle size analysis test and XRD tests had proved that the contents of clay particles of samples in the disease segment were lower than those in non-disease segment. It was considered that the clay minerals performed a function to fill t the void in soils, and increase the internal molecular attraction. The clay fines in combination with other soil particles in loess were agglomerated. Better performances might be expected for a loess subgrade with a relatively high content of "agglomerated" clay. In this paper, the "agglomerated" clay mineral content was defined as the difference between the clay mineral content obtained from the XRD Diffraction Test and the clay content from the particle size analysis test. The results were shown in Table 6.

Table 6 showed that the clay content of the highly compressible soil (Sample 2) in the disease segment was relatively low. Its agglomerated clay mineral content was

TABLE 6 Percentage of "agglomerated" clays in each sample.

Sample number	Clay mineral content (illite + chlorite) (%)	Clay content (%)	"Agglomerated" clay mineral content (%)
1	42	15.04	26.96
2	26	11.89	14.11
3	25	10.75	14.25
4	35	13.07	21.93
5	40	14.40	25.6
6	38	14.80	23.2

relatively low. Such level of "agglomerated" clay content could not form good attraction forces between particles. The soil (Sample 1, 4, 5, and 6) consisted of a relatively higher "agglomerated" clay mineral content and could provide relatively higher internal molecular attraction Their structure was relatively stable when they were saturated and subjected to dynamic loads.

6 Conclusion

1) The results of the consolidation tests showed that in the disease segment, Samples 2 and 3, which were obtained at depths of 6 and 9 m, respectively, were highly compressible. This is considered to be a reason of the differential settlements in this area. In the non-disease segment, Samples 5 and 6, which were obtained at depths of 6 and 9 m, respectively, were relatively highly compressible. However, Sample 4, which was obtained at a depth of 3 m, has a low compressibility. Therefore, differential settlement was not observed in this area.
2) The results of the particle size analysis tests, XRD tests and SEM tests showed that the content of the small size particles (clay) of Samples 2 and 3 in the disease segment was relatively low, and the particle size distribution of them was poorly graded, resulting in a relatively low internal molecular attraction. It was also found that Samples 2 and 3 in the disease segment contained more than 50% of quartz and only approximately 25% of cohesive particles. The quartz content of Samples in the non-disease segment was low (<46%), but chlorite and illite-based clay mineral contents were relatively high (between 35 and 42%). In addition, the results of scanning electron microscopy test illustrated that the pores of Sample 2 in the disease segment was relatively large and dispersed. The soil particles in the disease segment were disordered and the internal molecular attraction was relatively small. The pores were small and the connectivity was poor, indicating that the soil might have a relatively poor drainage.
3) The experiment results in this study showed that the clay content in the loess had significant effects on the engineering performance of the subgrade. Samples in the disease segment generally had relative low clay contents. Without enough clay particles to fill the voids in silt and fine sand, the "agglomeration" level of the soil was relatively low. When such saturated subgrade undertook dynamic loads induced by train, the soil might be liquefied and its structures became instable. If the drainage of the roadbed was not well designed, severe differential settlements might occur.

Data availability statement

The raw data supporting the conclusions of this article will be made available by the authors, without undue reservation.

Author contributions

MZ is mainly responsible for the overall planning of the thesis, H-GW and WG are responsible for on-site data processing, B-RT, CH, and RD are responsible for image processing, and Professor L-YC is responsible for the final draft of the thesis.

Funding

The research reported in this manuscript is funded by the Natural Science Foundation of China (Grants No. 41272331) and China railway academy Co.,ltd (Grant No. 2016-KJ001-Z001-03).

Conflict of interest

Author H-GW is employed by China Northwest Research Institute Co., Ltd.

The authors declare that the research was conducted in the absence of any business or financial relationships that could be construed as potential conflicts of interest.

Publisher's note

All claims expressed in this article are solely those of the authors and do not necessarily represent those of their affiliated organizations, or those of the publisher, the editors and the reviewers. Any product that may be evaluated in this article, or claim that may be made by its manufacturer, is not guaranteed or endorsed by the publisher.

References

Delage, P., Cui, Y-J., and Antoine, P. (2005). "Geotechnical problems related with loess deposits in northern France," in Proceedings of international con- ference on problematic soils.

Derbyshire, E. (2001). Geological hazards in loess terrain, with particular reference to the loess regions of China. *Earth. Sci. Rev.* 54 (1), 231–260. doi:10.1016/S0012-8252(01)00050-2

He, S., Li, P. Y., Wu, J. H., Elumalai, V., and Adimalla, N. (2020). Groundwater quality under land use/land cover changes: A temporal study from 2005 to 2015 in xi'an, northwest China. *Hum. Ecol. Risk Assess. Int. J.* 26 (10), 2771–2797. doi:10.1080/10807039.2019.1684186

Hu, F. (2005). Treatment of foundation of wet sinking loess. *City Bridge Flood* 1, 97–98.

Jiang, M., Zhang, F., Hu, H., Cui, Y., and Peng, J. (2014a). Structural characterization of natural loess and remolded loess under triaxial tests. *Eng. Geol.* 181, 249–260. doi:10.1016/j.enggeo.2014.07.021

Jiang, M. J., Li, T., Hu, H. J., and Thornton, C. (2014b). DEM analyses of one-dimensional compression and collapse behaviour of unsaturated structural loess. *Comput. Geotech.* 60, 47–60. doi:10.1016/j.compgeo.2014.04.002

Li, P., Vanapalli, S., and Li, T. (2016). Review of collapse triggering mechanism of collapsible soils due to wetting. *J. Rock Mech. Geotechnical Eng.* 8 (2), 256–274. doi:10.1016/j.jrmge.2015.12.002

Lommler, J. C., and Bandini, P. (2015). "Characterization of collapsible soils," in IFCEE, 1834–1841.

Luo, H., Wu, F., Chang, J., and Xu, J. (2018). Microstructural constraints on geotechnical properties of malan loess: A case studyfrom zhaojiaan landslide in Shaanxi province, China. *Eng. Geol.* 236, 60–69. doi:10.1016/j.enggeo.2017.11.002

Monroy, Z. L., and Ridley, A. (2010). Evolution ofmicrostructure in compacted London clay during wetting and loading. *Géotechnique* 60 (2), 105–119. doi:10.1680/geot.8.P.125

Muñoz-Castelblanco, J. A., Pereira, J. M., Delage, P., and Cui, Y. J. (2012). The water retention properties of a natural unsaturated loess from northern France. *Géotechnique* 62 (2), 95–106. doi:10.1680/geot.9.P.084

Romero, E., and Simms, P. H. (2008). Microstructure investigation in unsaturated soils: A review with special attention to contribution of mercury intrusion porosimetry and environmental scanning electron micros- copy. *Geotech. Geol. Eng. (Dordr).* 26 (6), 705–727. doi:10.1007/s10706-008-9204-5

Shao, X., Zhang, H., and Tan, Y. (2018). Collapse behavior and microstructural alteration of remolded loess under graded wetting tests. *Eng. Geol.* 233, 11–22. doi:10.1016/j.enggeo.2017.11.025

Sun, P., Peng, J-B., Chen, L-W., Yin, Y-P., and Wu, S-R. (2009). Weak tensile characteristics of loess in China — An important reason for ground fissures. *Eng. Geol.* 108 (1), 153–159. doi:10.1016/j.enggeo.2009.05.014

Sun, P. (2010). Reply to the discussion by ling xu on"weak tensile characteristics of loess in China — An important reason for ground fissure"by ping Sun, jian-bing peng, Li-Wei chen, Yue-ping yin and shu-ren Wu, [engineering geology 108 (2009) 153– 159]. *Eng. Geol.* 114 (1), 107. doi:10.1016/j.enggeo.2010.04.008

Susan, D. (2017). *A microstructural model for collapsing soils*. United Kingdom: Nottingham Trent University.

Wen, B-P., and Yan, Y-J. (2014). Influence of structure on shear characteristics of the unsaturated loess in Lanzhou, China. *Eng. Geol.* 168, 46–58. doi:10.1016/j.enggeo.2013.10.023

Xie, W-L., Li, P., Zhang, M-S., Cheng, T-E., and Wang, Y. (2018). Collapse behavior and microstructural evolution ofloess soils from the loess plateau of China. *J. Mt. Sci.* 15 (8), 1642–1657. doi:10.1007/s11629-018-5006-2

Yan, Y., Ma, L., and Sun, Y. B. (2017). Tectonic and climatic controls on provenance changes of fine-grained dust on the Chinese Loess Plateau since the late Oligocene. *Geochimica Cosmochimica Acta* 200 (1), 110–122. doi:10.1016/j.gca.2016.12.009

Yao, R. W., Yan, Y. T., Wei, C. L., Luo, M., Xiao, Y., and Zhang, Y. H. (2022). Hydrochemical characteristics and groundwater quality assessment using an integrated approach of the PCA, SOM and fuzzy c-means clustering: A case study in the northern sichuan basin. *Front. Environ. Sci.* 10. doi:10.3389/fenvs.2022.907872

Ye, W., Yang, G., Peng, J., Huang, Q., and Xu, Y. (2012). Test research on mechanism of freezing and thawing cycle resulting in loess slope spalling hazards in Luochuan. *Yanshilixue Yu Gongcheng Xuebao/Chinese J. Rock Mech. Eng.* 31 (1), 199–205.

Yuan, J. X. (2009). The analysis oftriggering factors of loess collapsibility. *J. West-China Explor. Eng.* 31, 31–34.

Zhang, Y. H., Dai, Y. S., Wang, Ying, Huang, X., Xiao, Y., and Pei, Q. M. (2021a). Hydrochemistry, quality and potential health risk appraisal of nitrate enriched groundwater in the Nanchong area, southwestern China. *Sci. Total Environ.* 784, 147186. doi:10.1016/j.scitotenv.2021.147186

Zhang, Y. H., He, Z. H., Tian, H. H., Huang, X., Zhang, Z. X., Liu, Y., et al. (2021b). Hydrochemistry appraisal, quality assessment and health risk evaluation of shallow groundwater in the Mianyang area of Sichuan Basin, southwestern China. *Environ. Earth Sci.* 80 (17), 576. doi:10.1007/s12665-021-09894-y

Zhang, Y. H., Yao, R. W., Wang, Y., Duo, J., and Cao, H. W. (2022). Zircon U–Pb and sericite Ar–Ar geochronology, geochemistry and S–Pb–Hf isotopes of the Zebuxia Pb–Zn deposit, Tibet, southwestern China. *Ore Geol. Rev.* 148, 104999. doi:10.1016/j.oregeorev.2022.104999

Zhang, Y., Hu, Z., Li, L., and Xue, Z. (2018). Improving the structure and mechanical properties of loess by acid solutions – An experimental study. *Eng. Geol.* 244, 132–145. doi:10.1016/j.enggeo.2018.07.023

Zhao, M., Chen, L. Y., Wang, S. Y., and Honggang, W. (2020). Experimental study of the microstructure of loess on its macroscopic geotechnical properties of the Baozhong railway subgrade in Ningxia, China. *Bull. Eng. Geol. Environ.* 79 (9), 4829–4840. doi:10.1007/s10064-020-01816-9

Zhao, M., Guo, W., Chen, L. Y., and Wang, S. y. (2019). Experiment on the frost resistance of modified phospho gypsum: A case used to improve Baozhong railway subgrade loess. *J. Mt. Sci.* 16 (12), 2920–2930. doi:10.1007/s11629-018-5014-2

Zhao, S., and Lei, Y. (2011). "The autonomous robot object recognition algorithm based on multi-feature fusion," in Paper presented at the 2011 interna- tional conference on electric information and control engineering. doi:10.1109/ICEICE.2011.5777691

Zhuang, J., Peng, J., Wang, G., Javed, I., Wang, Y., and Li, W. (2018). Distribution and characteristics of landslide in Loess Plateau: A case study in Shaanxi province. *Eng. Geol.* 236, 89–96. doi:10.1016/j.enggeo.2017.03.001

frontiers | Frontiers in Earth Science

TYPE Original Research
PUBLISHED 14 September 2022
DOI 10.3389/feart.2022.943075

Check for updates

OPEN ACCESS

EDITED BY
Filippo Catani,
University of Florence, Italy

REVIEWED BY
Jiajun Peng,
Kyoto University, Japan
Bo Zhao,
Institute of Mountain Hazards and Environment (CAS), China

*CORRESPONDENCE
Shengbin Wang,
wsb13897651096@126.com

SPECIALTY SECTION
This article was submitted to Geohazards and Georisks, a section of the journal Frontiers in Earth Science

RECEIVED 13 May 2022
ACCEPTED 28 July 2022
PUBLISHED 14 September 2022

CITATION
Xiao Y, Liu K, Zhang Y, Yang H, Wang S, Qi Z, Hao Q, Wang L, Luo Y and Yin S (2022), Numerical investigation of groundwater flow systems and their evolution due to climate change in the arid Golmud river watershed on the Tibetan Plateau.
Front. Earth Sci. 10:943075.
doi: 10.3389/feart.2022.943075

COPYRIGHT
© 2022 Xiao, Liu, Zhang, Yang, Wang, Qi, Hao, Wang, Luo and Yin. This is an open-access article distributed under the terms of the Creative Commons Attribution License (CC BY). The use, distribution or reproduction in other forums is permitted, provided the original author(s) and the copyright owner(s) are credited and that the original publication in this journal is cited, in accordance with accepted academic practice. No use, distribution or reproduction is permitted which does not comply with these terms.

Numerical investigation of groundwater flow systems and their evolution due to climate change in the arid Golmud river watershed on the Tibetan Plateau

Yong Xiao[1], Kui Liu[1], Yuqing Zhang[1], Hongjie Yang[1], Shengbin Wang[2,3]*, Zexue Qi[2,3], Qichen Hao[4], Liwei Wang[1], Yinfei Luo[5,6] and Shiyang Yin[7]

[1]Faculty of Geosciences and Environmental Engineering, Southwest Jiaotong University, Chengdu, China, [2]Bureau of Qinghai Environmental Geological Prospecting, Xi'ning, China, [3]Key Lab of Geo-environment of Qinghai Province, Xi'ning, China, [4]Institute of Hydrogeology and Environmental Geology, Chinese Academy of Geological Science, Shijiazhuang, China, [5]Center for Hydrogeology and Environmental Geology, China Geological Survey, Baoding, China, [6]School of Water Resources and Environment, China University of Geosciences (Beijing), Beijing, China, [7]School of Water Resources and Hydropower Engineering, North China Electric Power University, Beijing, China

Climate warming is the greatest future challenge to the hydrosphere and the human community, especially in arid and semiarid regions. This study took the Golmud river watershed on the Tibetan Plateau as an example to numerically identify the development of groundwater flow systems in a large arid sedimentary basin and explore what would the dramatic climate warming pose on groundwater flow system. The numerical results show that the Golmud river watershed has developed three hierarchical groundwater flow systems. River seepage is the predominant recharge for the groundwater systems inside the basin. The local groundwater flow system discharges some 82.69% of all groundwater in the basin, followed by the intermediate system with 14.26% and the regional system with 3.05%. The local system is mainly distributed in the shallow area of the alluvial-pluvial fan at the piedmont and provides the dominant water resource for human exploitation and oasis ecological usages. Climate warming would increase about 30.78% of the quantity of the recharge water to the groundwater system inside the basin *via* river seepage due to the increasing precipitation and increased glacier melt in the headwater region of the watershed. These waters would pose disturbances to all groundwater flow systems but to different degrees. The local flow system exhibits the largest response to the climate warming with more than 90% of increased water cycled in and discharged through it. The significant groundwater level rising leads to the trailing edge of the overflow belt at the piedmont moving ~5 km towards to the mountain pass, which would potentially pose a water disaster to the local region. The influences of climate warming on the intermediate and regional flow system are relatively limited. This study provides a preliminary understanding of the influences of climate warming on the groundwater flow systems in arid endorheic basins and is

essential for tackling future climate change challenges faced by arid and semiarid regions.

KEYWORDS

groundwater flow system, climate change, numerical modelling, arid watershed, Tibetan plateau

Introduction

Groundwater is a crucial constitutive part of the hydrosphere of our planet and accounts for approximately 97% of continental liquid freshwater resources (Hatch-Kuri and Carrillo-Rivera, 2021). It is essential for maintaining the eco-environment, irrigating agriculture, and for supporting the development of industry and human communities (Gu et al., 2018; Xiao et al., 2018; Adimalla, 2019; Li et al., 2019; Zhang et al., 2021a). It is estimated that 50% of agricultural production, 40% of industrial consumption, and 40% of domestic water consumption of the global population rely on groundwater resources (Dash et al., 2019; Xiao et al., 2021). In fact, groundwater is the only water supply for the daily consumption of about 2.5 billion people around the world (Díaz-Alcaide and Martínez-Santos, 2019; Xiao et al., 2022b). The intensive exploitation of groundwater resource has resulted in groundwater resource depletion, ecological degradation, and geohazards in many regions worldwide (Xu et al., 2015; Gu et al., 2017b; Antonellini et al., 2019; Li et al., 2019; Huang et al., 2020; Zhang et al., 2021b). It is a more significant factor in arid and semiarid regions where surface water is scarce (Moharir et al., 2019; Hao et al., 2020; Mookiah et al., 2021; Qu et al., 2021; Xiao et al., 2022c; Liu et al., 2022). Groundwater and its behaviors are a fundamental part of the scientific management of groundwater resource for implementing the sustainable development of human society and eco-environment systems.

In addition to anthropogenic disturbances, dramatic climate change is another factor that has posed and will continue to pose unprecedented challenges and threats to water safety and sustainability globally (Brolsma et al., 2010; Ghimire et al., 2021). The planet is suffering from rapid climate warming, and this is expected to continue for the foreseeable decades or centuries (Hemmerle and Bayer, 2020; David Raj et al., 2022; IPCC, 2022). Climate warming not only results in increased temperatures but also poses a series of related influences on earth system (Bussi et al., 2022; Gan et al., 2022). The hydrosphere is expected to be the main sphere that is directly and significantly affected by the global climate change (Kim et al., 2022; Rafiei-Sardooi et al., 2022). The warming climate will significantly change the status of the balance of water reservoirs on earth. It is widely known that the polar icecaps and glaciers on high plateaus and mountains are melting under the climate warming (Straneo and Heimbach, 2013; Kraaijenbrink et al., 2017). This is releasing a giant quantity of liquid water, increasing the amount of liquid water in water circulation and leading to geohazards like global sea level rising (Minea et al., 2022). Compared to the effects on sea level, the influence on continental water and its circulation are more significant and will present more complex challenges, especially for arid and semiarid regions that have relatively fragile eco-environments (Sarzaeim et al., 2017). Due to the scarcity of surface water, groundwater is the critical water that participates in water circulation and supports the natural ecosystems and human communities in arid and semiarid regions (Goderniaux et al., 2011; Xiao et al., 2022a). Thus, groundwater and its behaviors in arid and semiarid regions under climate change should be given special attentions.

The Tibetan plateau has been called the third pole of the earth, and it features the largest amount of water in glaciers anywhere on earth apart from the north and south poles (Qu et al., 2019). Although the Tibetan plateau is known as the water tower of Asia (Hao et al., 2021), the northern part of it is typically arid and semiarid (Gu et al., 2017a; Hao et al., 2018; Luo et al., 2021; Wang et al., 2022). The potential giant quantity of melted water from glaciers for the arid and semiarid regions can amplify the effects of climate warming for the continental hydrosphere (Ma Y. et al., 2017; Chen et al., 2021). Thus, a typical endorheic watershed in the arid northern Tibetan plateau was selected as the study area to obtain insights into the likely outcomes of climate warming for the hydrosphere, groundwater circulation, and behavior of the groundwater system.

The specific aims of this study are 1) modeling the status of groundwater at present climate conditions, 2) revealing the development of the hierarchical groundwater flow systems in an arid and semiarid large sedimentary basin, and 3) developing a preliminary understanding of groundwater behaviors and the evolution of groundwater flow systems in arid sedimentary basins due to climate warming. This study can provide scientific support for managing groundwater resources, coping with the water crisis and related geohazards posed by climate warming, and implementing the sustainable development of arid and semiarid regions in the future challengeable environment.

Study area

General setting of the Golmud river watershed

The Golmud river watershed is a typical endorheic watershed on the Tibetan Plateau. It is located at the south margin of the Qaidam basin, which is the largest basin on the Tibetan Plateau. This watershed is bounded by the Kunlun Mountains in the

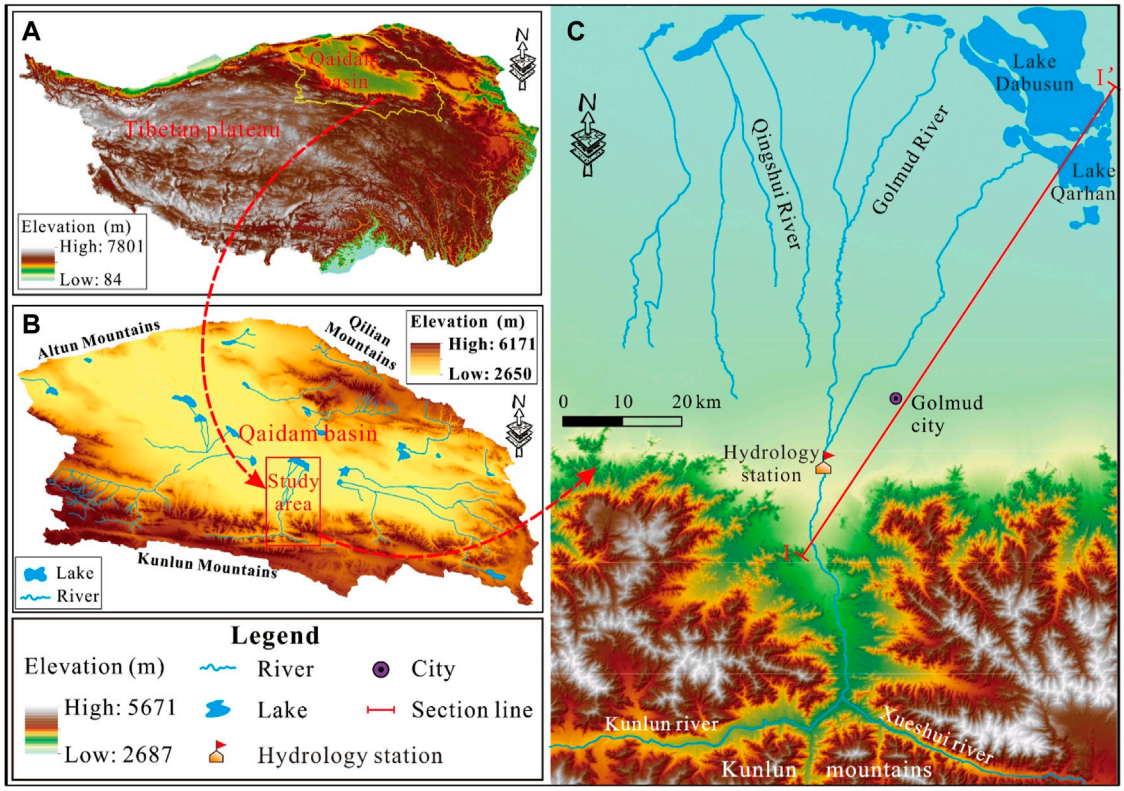


FIGURE 1
Location of **(A)** the Tibetan Plateau, **(B)** the Qaidam Basin, and **(C)** the Golmud river watershed.

south and Lake Dabusun in the north (Figure 1), and it extends between 36°59′43.60″ and 35°50′12.34″ latitude and from 94°16′13.86″ to 95°20′19.56″ longitude with a covering area of ~12180 km^2. The Golmud river, the second largest river in the basin, runs through this watershed and flows from the Kunlun Mountains to Lake Dabusun. This watershed is characterized by the dry continental climate of the plateau. The precipitation and evaporation are extremely variable in time and space. Annual precipitation can reach 200 mm in the mountainous area, but it is below 50 mm in the basin. Most of precipitation occurs in the rainy season (June to August), and accounts for more than 60% of the precipitation over the course of the year. Conversely, evaporation presents an increasing trend from south to the north and even exceeds 2600 mm per year in the basin. The high annual evaporation and low precipitation in the basin result in nearly no effective production of water resources for surface and ground water from local precipitation. The water resources of the watershed are mainly produced in the south and source from precipitation and snow/ice melt water in the mountainous area. The water resources in the basin are dominantly derived from river water and a part of underground lateral flow at mountain passes. River water flows into the basin, and almost all water seepages into the aquifers in the middle-upper part of the alluvial fan. Only in the flooding season, some river waters reach the lower part of the alluvial fan. As a result, the ecology in the basin is groundwater dependent. Due to the scarcity of precipitation and surface water, groundwater is also the main supplying water source for the various purposes of the human community. Thus, understanding groundwater and its behavior is significant for the sustainable development of this hyper arid region.

Geology and hydrogeology

The Qaidam basin is a closed basin, formed during the uplift of the Tibetan Plateau. The Golmud watershed is one of numerous endorheic watersheds in the basin (Figure 1). This watershed has an outcropping stratigraphy at an age from Proterozoic to Quaternary. The pre-Quaternary strata are dominantly located in the mountainous areas. Inside the basin, the strata are dominated by hundreds and thousands of meters of Quaternary deposits. There are four types of aquifer systems in the watershed, including the permafrost aquifer system, carbonate karst aquifer system, fractured aquifer system, and porous aquifer system (Hu and Jiao, 2015). With

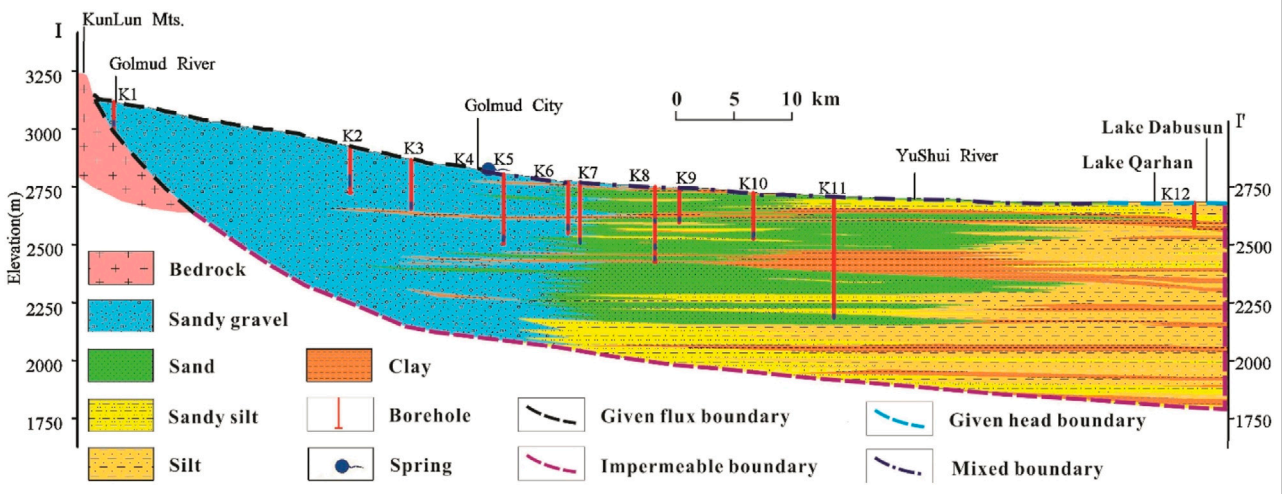


FIGURE 2
The hydrogeological profile along I-I'.

the exception of the porous aquifer system, the other three aquifer systems are only distributed in the mountainous area. A porous aquifer system occurs along the river valleys in the mountainous area and inside the basin. The lithologies of Quaternary deposits inside the basin are spatially variable, varying from pebble and gravel in the upper parts of the alluvial fan to coarse sand in the middle-lower alluvial fan and then to fine sand and clay in the middle-lower lying depression of the watershed. Regionally, there are three continuous clay layers distributed at the depths of 60, 290, and 450 m in the basin (Figure 2). As a result, the aquifer system in the basin has a variable structure and changes from a single thick phreatic structure to a multilayer one.

The Quaternary porous aquifer system in the basin mainly receives its recharge water from river seepage in the middle-upper areas of the alluvial fan. The lateral inflow at the mountain pass also contributes recharge water to the Quaternary aquifer systems in the basin to some degree. Groundwater flows from the upper area of the Golmud alluvial fan towards the basin center and experiences several transformations between groundwater and surface water. The groundwater level has great depths in the middle-upper areas of the alluvial fan, which can reach to hundreds of meters, but it gradually evolves to a much shallower depth along the groundwater flow path towards the basin center. Most of the groundwater level in the areas from the front of alluvial fan to the basin center has depths of less than 3 m, so significant evaporation occurs. All groundwater and surface water finally discharge into the salt Lake Dabusun, the terminal of the Golmud watershed, and is lost to evaporation. Due to the shortage of surface water in human-settled areas, the groundwater has been greatly exploited for supporting the development of human community in the watershed. Additionally, the ecology in the oasis and the lower areas of the watershed is dependent on the groundwater. Overall, the groundwater inside the basin is mainly recharged by river seepage in the middle-upper area of the alluvial fan and lateral inflow at the mountain pass and discharges through evaporation, human pumping, and plant usage.

Materials and methods

Development of the groundwater flow model

Conceptual model and numerical model methodology

Aquifers inside the basin can be generally divided into hydrogeological layers using three regional aquitards (Figure 2). The upper layer is distributed from the mountain pass to the low-lying depression (Lake Dabusun) of the basin, with lithologies, varying from high hydraulic permeability to relatively low hydraulic permeability. This layer is regarded as the upper aquifer, which is phreatic in the alluvial fan area and semi-confined in parts of the middle to lower areas of the watershed. It has great thickness in the alluvial fan but smaller thickness from the front of the alluvial fan northwards. The second layer is distributed from the front of the alluvial fan to the lower parts of the fine-soil plain. This layer is constrained by the regional continuous aquitards at the depths of 60 and 290 m. It is semiconfined at the front of the alluvial fan and confined in the lower stream area. Below the continuous clay layer, at a depth of 290 m, there are still two further regional aquifers, which are divided by a regional aquitard at a depth of 450 m and all

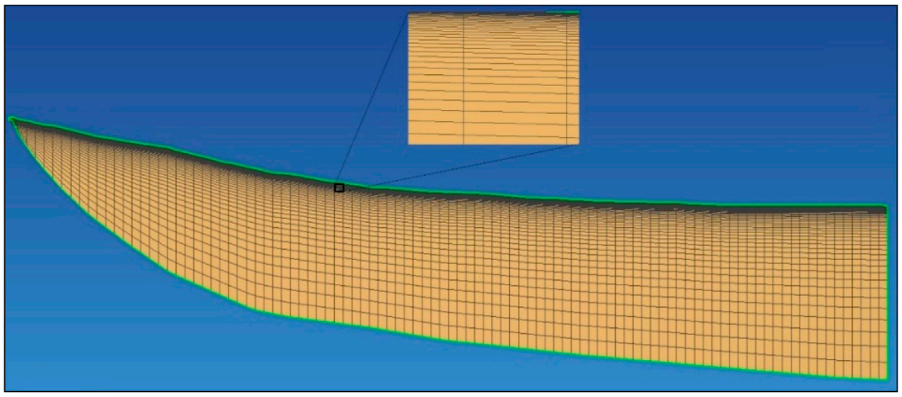


FIGURE 3
The model mesh of the simulation domain.

confined. The third aquifer has a relatively good hydraulic connectivity and great thickness. The fourth aquifer is intercalated with many layers of differing relative permeability in the fine soil plain and salt marsh plain, and as a result, the groundwater there flows very slowly.

To investigate the groundwater flow system in the basin and its behaviors due to climate change, a cross section parallel to the main groundwater flow direction in the watershed (I-I′ presented in Figure 1) is chosen as the geometry for the simulation of two-dimensional steady flow. This geometry ranges from the mountain pass to the terminal lake with a length of 100 km (Figure 2). To illustrate the strong evaporation effects on the groundwater level fluctuation in the fine soil plain and salt marsh plain, the geometry of the simulation is discretized vertically as irregular cells with the aid of the gradient mesh size method. The smallest cells have a thickness of 0.1 m and are located near the surface (Figure 3). The thickness of the cells gradually increases with increasing depth, reaching ~80 m at the deepest point. Horizontally, the geometry is discretized using the equal discretization method. The viscosity and density of the groundwater are assumed to have negligible spatial variatio. Thus, groundwater flows inside the basin can be considered to be driven by gravity, as described by the following equation:

$$\boldsymbol{\sigma}(\boldsymbol{h})\frac{\partial \boldsymbol{h}}{\partial \boldsymbol{t}} - \nabla[\boldsymbol{K}(\boldsymbol{h})\nabla(\boldsymbol{h}+\boldsymbol{z})] = \mathbf{q} \quad (1)$$

where $\sigma(h)$ is the specific storage, h represents the pressure head, z is the elevation, t signifies time, $K(h)$ denotes the unsaturated hydraulic conductivity, and q represents the source or sink. The two-dimensional groundwater flow simulations are established and solved using the TOUGH 2 program (Transport Of Unsaturated Groundwater and Heat).

Parametrization and boundary conditions

In the model domain, five predominant lithologies are found inside the basin, including sandy gravel/pebble, sand, silty soil, silty clay, and clay. The hydrogeological parameters of these lithologies are initially given in the model according to the borehole drilling records, pumping tests, and empirical values from similar studies (Gu et al., 2017a; Hao et al., 2018). The parameters are adjusted in the calibration and validation process, with the aid of hydraulic head observation data. There are two types of recharge for the groundwater, including river infiltration (seepage) and lateral inflow. The river infiltration mainly occurs at the piedmont (i.e., the alluvial fan area). The lateral inflow only exists at the boundary between the bedrock at the mountain pass and the sediments of the alluvial fan plain. These two groundwater recharges are set as the specified flow boundary and introduced by the WATE module of TOUGH2 in the model. The groundwater in the study area is mainly discharged via human pumping, evaporation, and springs. Human pumping is dominantly located in the alluvial fan plain, which is also set as a specified flow boundary and modelled using the WATE module. The evaporation and springs are defined as mixed boundary and simulated using the EVAP and DELV module of TOUGH2, respectively. The EVAP module is a new development module for evaporation calculation, which is based on the content of soil water (Hao et al., 2016). The lake boundary at the low-lying depression of the watershed is defined as the specific head boundary. The DELV module is similar to the Drain module of MODFLOW. The bottom boundary and the northern lateral boundary of the model geometry are generalized as impermeable boundaries (Figure 2), i.e., a zero flux boundary. The parameters of the aforementioned boundaries are given according to the field survey and measurement.

TABLE 1 Meteorological and hydrological scenarios for groundwater modelling.

Scenario	Years	Temperature /°C	Potential evaporation (%)	Precipitation (%)	Melt water (%)	River runoff flux (%)	River seepage quantity (%)
Scenario 1	2016	6.85	100	100	100	100	100
Scenario 2	2100	9.06	52	110.35	160	140.14	130.78

Scenario analysis

Scenario 1: Present status

Scenario 1 illustrates groundwater flow patterns under present climatic and pumping condition. The sources and sinks of the model are assigned according to the annual average seen in 2016. Potential evaporation is defined as 2600 mm, drawing on local meteorological data (Table 1). The seepage/infiltration of the river water is given based on hydrological station data and is set as 135.65 $m^3 \cdot d^{-1}$ along the profile. The lateral inflow of the bedrock from the mountainous area is estimated using Darcy's section method and is 0.04 $m^3 \cdot d^{-1}$ for the model geometry (Table 1). The pumping quantity is obtained according to the results of the regional hydrogeological survey and assigned as 20.65 $m^3 \cdot d^{-1}$ for the cross section domain.

Scenario 2: Climate warming

Scenario 2 presents the evolution of the groundwater flow system under the influence of global climate warming. Previous research indicates that the Qaidam basin has experienced significant warming over the past few decades, and it is estimated that this trend will continue (Kuang and Jiao, 2016). This warming will significantly influence the climatic and hydrological features of the watershed. The quantity of melting snow and ice water would increase. The same trend would occur for the annual precipitation in the watershed. As a result, the quantity of recharge water into the basin from the mountainous area would increase. However, evaporation would decrease along with the climate warming due to increased humidity. Overall, the influence of climate warming on water resources inside the basin would be *via* the recharge water quantity at the piedmont and through evaporation inside the basin.

It is estimated that about 40% of the total water at the mountain pass originates from the precipitation in the mountainous area, and the remainder is from the snow and ice melt water (Chen et al., 2014). The temperature of the Qaidam basin is expected to increase at a rate of 0.26°C/10 a (Table 1) (Nan et al., 2004). As a result, the precipitation and melt water will increase to approximately 110.35% (Hu et al., 2015) and 160% (Shi, 2001), respectively, by 2100, and the evaporation rate in 2100 would be 52% of the present rate (Table 1) (Ma R. et al., 2017). According a previous survey, the quantity of water seepage from the riverbed has no significant relationship to the river water runoff flux from the mountain pass to the hydrology station (Figure 1C) but relates to the one from the hydrology station north. The seepage water quantity of different parts of the Golmud river can be estimated using the empirical equation below:

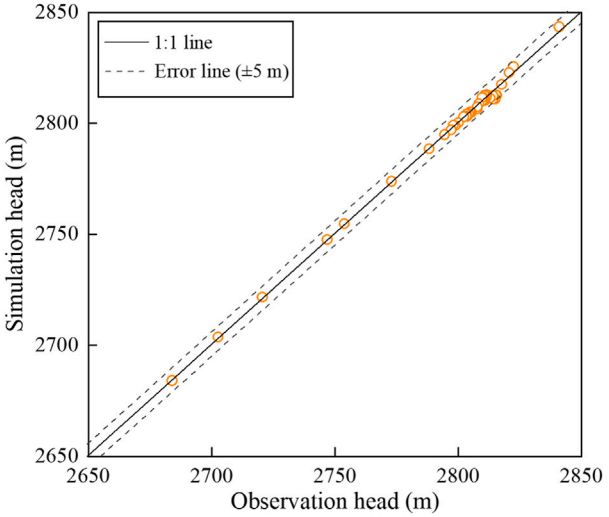


FIGURE 4
Comparison of observation head and simulation head.

$$\mathbf{Q_S = 0.05 \times Q_{ms} + 6.686} \quad (2)$$

$$\mathbf{Q_N = Q_{hs}} \ (\text{if } Q_{hs} \leq 10.2\ m^3 \cdot s^{-1}) \quad (3)$$

$$\mathbf{Q_N = 4.0286 \times [Q_{hs}]^{0.4}} \ (\text{if } Q_{hs} > 10.2\ m^3 \cdot s^{-1}) \quad (4)$$

where Q_S and Q_N represent the river seepage water quantity from the mountain pass to the hydrology station (Figure 1C) and from the hydrology station northward, respectively. Q_{ms} and Q_{hs} are the river water runoff flux at the mountain pass and the hydrology station, respectively.

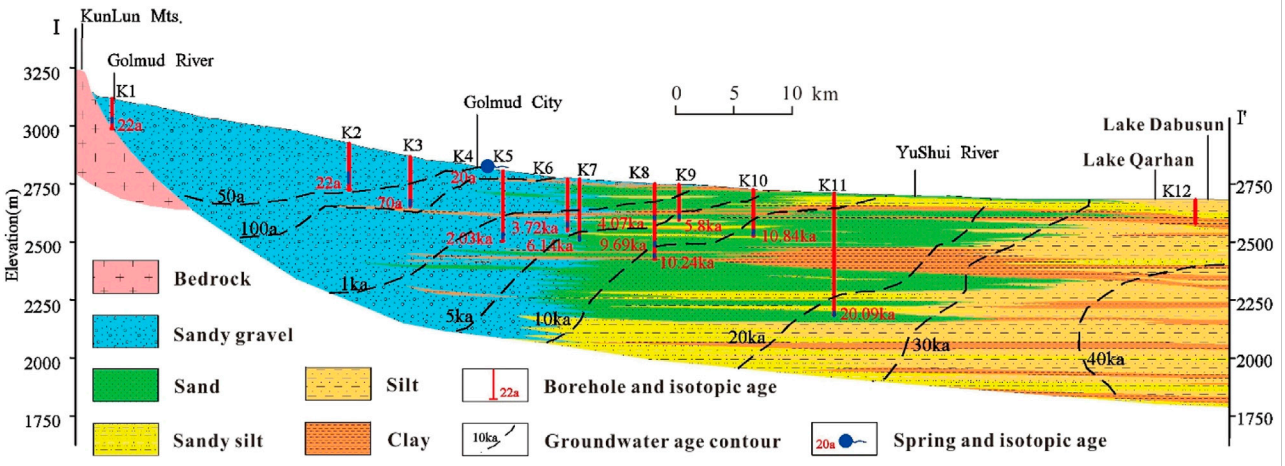


FIGURE 5
Comparison of isotopic age and hydraulic age of groundwater.

Results and discussion

Model calibration and validation

The model was calibrated to minimize the difference between the model simulation results and real hydrogeological conditions to an acceptable threshold. Hydraulic heads from 63 boreholes from the mountain pass to the terminal lake were observed in this process. Trial and error correction was employed to adjust the hydraulic parameters to reflect the real hydrogeological conditions of the watershed.

The comparison of the simulated hydraulic heads after parameter calibration and observed hydraulic heads is given in Figure 4. The deviation between the simulated and observed hydraulic heads varied in spatial terms, from a small one in the fine soil plain and salt marsh plain to a relatively large one in the alluvial fan (the piedmont area). The maximum deviation between the simulated hydraulic head and the observed hydraulic head was within 0.8 m in the fine soil plain and salt marsh plain and reached 4.8 m in the alluvial fan. Large seasonal hydraulic head fluctuation and a steep hydraulic gradient were the main causes of relatively large deviations for model results (Islam et al., 2017). The deviation for the simulated hydraulic heads in the middle- to lower-stream area (the fine soil plain and the salt marsh plain) is attributed to the lithological heterogeneity of the aquifers (Gu et al., 2017a). For the whole model cross section, the root mean square error (RMSE) of the simulated hydraulic head and the observed hydraulic head was only 1.57 m. Overall, the simulated results reflect the real regional hydrogeological conditions.

To further validate the calibrated model, the isotopic ages of the groundwater were introduced to compare the hydraulic age of the groundwater. Groundwater samples along the cross section were collected for radioactive isotope analysis (Figure 5). A total of 13 groundwater samples were obtained, including 4 from the phreatic aquifers in the alluvial fan and 9 from the deep aquifers of the fine soil plain and salt marsh plain. Isotopic ages of the groundwater were estimated using the tritium approach if the water had a tritium content greater than 1 TU (tritium unit) and obtained by the radiocarbon method if the tritium content was below 1 TU. Particle tracking was employed for calculating groundwater hydraulic age, contoured by linear interpolation (Gu et al., 2017a). As shown in Figure 5, the simulated hydraulic ages of groundwater are largely consistent with the isotopic ages of the groundwater. Thus, the calibrated model has superior performance in simulating the groundwater flow in the study area and can be used for exploring the flow pattern and behaviors of groundwater.

The calibrated hydrological parameters of the two-dimensional groundwater model are presented in Table 2. The horizontal permeabilities (K_h) of sand and sandy gravel/pebble are in the range of 13.7–56.3 $m{\cdot}d^{-1}$, with an anisotropy ratio (K_h/K_v) of 10. For the silty soil and silty clay, the horizontal permeabilities (K_h) were 0.62 $m{\cdot}d^{-1}$ and 0.13 $m{\cdot}d^{-1}$, respectively, with an anisotropy ratio (K_h/K_v) of 5. The clay had the horizontal permeability (K_h) of 0.001 and an anisotropy ratio (K_h/K_v) of 5. The porosity of sandy gravel/pebble, sand, and silty soil ranged from 0.35 to 0.50, and those of silty clay and clay were in the range of 0.60–0.65.

The present groundwater flow system

The groundwater flow pattern in the present climate and pumping condition is presented in Figure 6. The present study area is a typical Tóthian basin and features several hierarchical

TABLE 2 Hydrological parameters of the calibrated model.

Lithology	Porosity	Horizontal permeability K_h ($m \cdot d^{-1}$)	Anisotropy ratio K_h/K_v
Sandy gravel/pebble	0.35	56.3	10
Sand	0.40	13.7	10
Silty soil	0.50	0.62	5
Silty clay	0.60	0.13	5
Clay	0.65	0.001	5

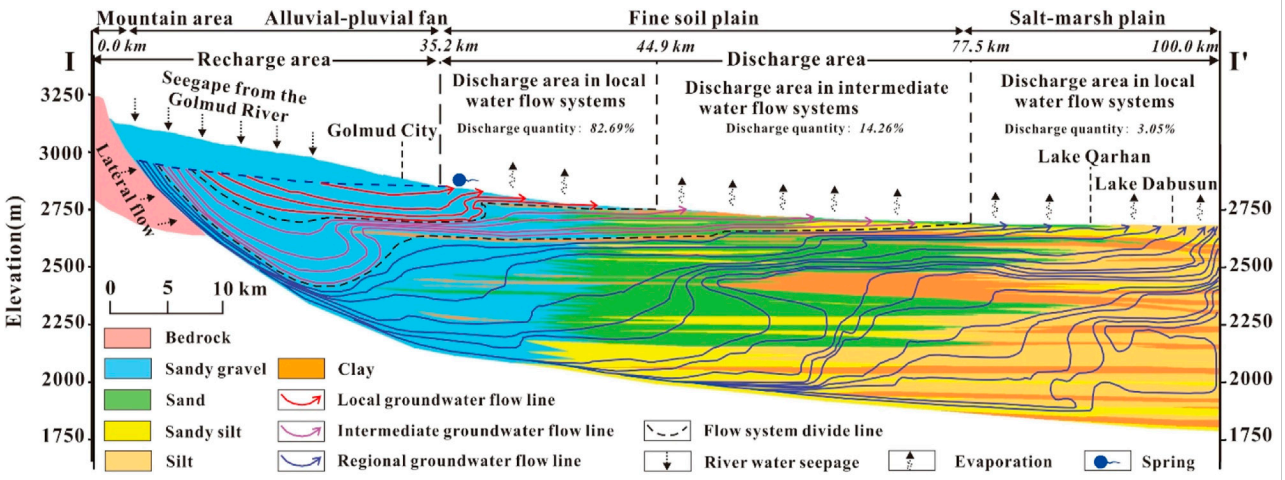


FIGURE 6
The present groundwater flow pattern of the Golmud watershed.

groundwater flow systems. Three hierarchical groundwater flow systems, including the local, intermediate, and regional system, have developed inside the basin. The flow patterns of groundwater are strictly governed by the distribution of lithology distribution along the profile. The groundwater flow lines present an upwardly convex shape when meeting poor permeable strata. This is significant at the front of the alluvial fan and in the middle area of the fine soil plain, where a lot of continuous clay exists.

The local groundwater flow system is distributed in the alluvial fan plain. The groundwater in this flow system obtains recharge water from the seepage of the Golmud river in the middle and upper parts of the alluvial fan. It generally discharges at the front of the alluvial fan, where the overflow area of the watershed is found. The cycled groundwaters in this flow system provide the predominant water source for domestic usage and industrial purposes. The shallow buried features of the groundwater level and the largely natural overflow quantity of this system at the lower area make the front of the alluvial fan plain being the oasis of the watershed and suitable for perch.

The intermediate groundwater flow system occurs below the local groundwater flow system and ranges from the upper part of the alluvial fan plain to the lower parts of the fine soil plain. This system receives recharge water from the seepage of the Golmud river in the upper part of the alluvial fan plain. The groundwater in this flow system moves northward and sinks into the aquifer in the upper and middle areas of the alluvial fan. However, due to the influence of continuous clay layers in the lower parts of the alluvial fan, groundwater presents an upward-flowing patterns there, and the flow paths are constrained by the two continuous clay layers. The largest cycle depth of the groundwater in this system reaches approximately 600 m at the middle to lower parts of the alluvial fan and adjacent to the continuous clay layers. All groundwaters in this system are discharged in the middle to lower parts of the fine soil plain through springs and evaporation. The groundwater in this system supports the ecology of the fine

TABLE 3 The discharge of various groundwater flow systems of the profile.

Groundwater flow system	Scenario 1		Scenario 2	
	Discharge water quantity/$m^3 \cdot d^{-1}$	Percentage/%	Discharge water quantity/$m^3 \cdot d^{-1}$	Percentage/%
Local system	112.16	82.69	152.40	85.91
Intermediate system	19.34	14.26	20.05	11.30
Regional system	4.14	3.05	4.95	2.79

soil plain and is significantly important for the environment maintenance of the watershed.

The regional groundwater flow system ranges from the mountain pass to the low-lying depression (Lake Dabusun) of the watershed and is distributed below the local groundwater flow system and the intermediate groundwater flow system. This groundwater flow system is mainly controlled by a continuous clay layer at a depth of 290 m regionally and is developed below it. The groundwater in this system is dominantly recharged by river seepage at the top of the alluvial fan and discharged as evaporation and salt lake water in the salt marsh plain. The flow paths of groundwater in this system are disorganized in middle to lower area of the watershed (i.e., the fine soil plain and the salt marsh plain). The distribution of clay layers has a great influence on the shape of groundwater flow paths.

The discharge water quantity of various groundwater flow systems at present were identified. The three hierarchical flow systems perform quite differently in terms of cycling and discharging water quantity in the basin (Table 3). Most groundwater in the basin is cycled and discharged through the local flow system and flows in the shallow parts of the watershed. This part of the groundwater accounts for more than 80% of the cycling groundwater in the watershed. The intermediate groundwater flow system accounts for the second-most amount of the cycling groundwater in the watershed but far less than the local groundwater flow system. In its cycling and discharging quantity, it accounts for approximately 14.26% of the water of the entire watershed. Although the regional groundwater flow system has the largest distribution area in the watershed, it features the lowest cycling and discharging water quantity, only 3% of the entire basin. This is ascribed to the relatively poor permeability of the aquifer regionally. Thus, the surface water in salt lakes in low-lying depression (Lake Qarhan and Lake Dabusun) is not dominantly recharged by the water cycle beneath the ground. It is supported and maintained by the flowing water of various spring-fed rivers of the watershed. It is also suggested that the rich salt minerals in the low-lying depression of the watershed are not simply brought and formed by the regional groundwater flow. The water of the ancient salt lakes migrating from the west to the center of the Qaidam basin over the course of geological history may form the predominant contribution of these rich salts of the low-lying depression of the Golmud watershed.

The evolution of groundwater flow system under climate warming

Climate warming has a significant influence on the groundwater system in the study area. The water balances of the modeled profile under the present climate scenario and the climate warming scenario are presented in Table 4. Compared to the present climate, climate warming would greatly increase the recharge water quantity from the mountainous area. River seepage, which is the dominant recharge water for aquifers inside the basin, has increased from 135.61 $m^3 \cdot d^{-1}$ to 177.35 $m^3 \cdot d^{-1}$ for this profile. Climate warming would cause the river seepage water quantity to increase 30.78% over its present quantity. Due to the limited water quantity from bedrock lateral inflow, climate warming would not significantly change the percentage of each recharge in the total recharged water. The increase in river seepage water quantity has had a significant influence on the discharges of groundwater system inside the basin, and the quantities of all natural discharges would increase under the climate warming scenario. The discharge quantity of the springs has the largest variation and would increase from 78.59 $m^3 \cdot d^{-1}$ to 120 $m^3 \cdot d^{-1}$ for the whole profile. The quantities of discharge water due to evaporation and outflow into the lake would also increase under the climate warming, but their changes are not significant.

The percentage of each discharge shows that the climate warming would not change the order of the recharge and discharge quantities inside the basin (Table 4). River seepage would still be the predominant means of recharge for groundwater systems in the basin and would account for 99.98% of the total recharge water quantity under climate warming scenario. The bedrock water quantity in lateral inflow is limited and only accounts for about 0.02%. For the discharge in the groundwater system, although the order of water quantities would not be changed by climate warming, the percentage of each discharge in the total discharge of the profile would be significantly changed. The percentage of

TABLE 4 Groundwater balance of the modeled domain.

		Scenario 1		Scenario 2	
		Water quantity/$m^3 \cdot d^{-1}$	Percentage/%	Water quantity/$m^3 \cdot d^{-1}$	Percentage/%
Recharge	River seepage	135.61	99.97	177.35	99.98
	Bedrock lateral inflow	0.04	0.03	0.04	0.02
	Total	135.65	100.00	177.39	100.00
Discharge	Spring	−78.59	57.94	−120.00	67.65
	Evaporation	−35.08	25.86	−35.10	19.79
	Pumping	−20.65	15.22	−20.65	11.64
	Outflow into the lake	−1.33	0.98	−1.65	0.93
	Total	−135.65	100.00	−177.39	100.00

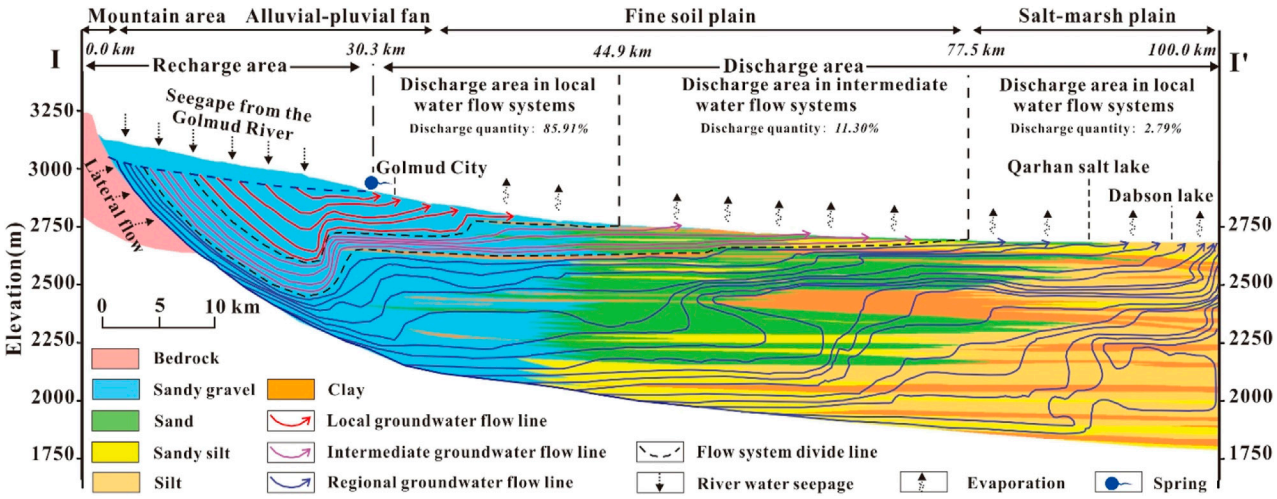


FIGURE 7
The groundwater flow pattern of the Golmud river watershed after climate warming.

spring discharge on the total discharge water quantity would greatly increase, from 57.94 to 67.65%. On the other hand, other natural discharge and human pumping would decrease in the percentage of the total discharge quantity. Evaporation discharge would decrease from 25.86 to 19.79% in percentage, and the human pumping would decrease from 15.22 to 11.64%. The percentage of outflow into the lake would have a small influence, only decreasing from 0.98 to 0.93%.

Climate warming would also significantly change the flow characteristics of groundwater along the profile (Figure 7). The groundwater level in the alluvial-pluvial fan would greatly increase as a result, and the trailing edge of the overflow belt would move about 5 km toward to the mountain pass. This would make most of the urban area of the city of Golmud into the overflow area of the groundwater, increasing the susceptibility of the region to water disasters. The hierarchical groundwater flow systems developed in the basin would also be disturbed by climate warming. Overall, the influences on the three flow systems would differ. Significant influences would only be observed in the local groundwater flow system. The largest cycle depth of groundwater in this system would increase from the 280 m of present climate (Scenario 1) to 360 m in the climate warming condition (Scenario 2). Climate warming would not have a significant influence on the intermediate groundwater flow system or the regional groundwater flow system, and the discharge water ranges of these two systems would experience nearly no change under climate warming.

The cycling water of all hierarchical groundwater flow systems would increase in quantity due to climate warming, but the degree of increase varies among the systems. The increase in cycling water in local groundwater is especially significant. The cycling water quantity of this system would increase from

112.16 $m^3 \cdot d^{-1}$ to 152.40 $m^3 \cdot d^{-1}$. Although the quantities of cycling water of the intermediate groundwater flow system and the regional groundwater flow system would increase due to climate warming, the increase would not be significant for these two systems. The cycling water quantities of these two systems would only increase from 19.34 $m^3 \cdot d^{-1}$ to 20.05 $m^3 \cdot d^{-1}$ and from 4.14 $m^3 \cdot d^{-1}$ to 4.95 $m^3 \cdot d^{-1}$, respectively. On a percentage basis, the quantity of cycling water in the local system would increase from 82.69 to 85.91% of the total cycling water of the profile, but in the intermediate and regional systems, it would decrease from 14.26 to 11.30% and from 3.05 to 2.79%.

Overall, the climate warming would increase groundwater recharge in the basin predominantly through the river seepage at the piedmont, and most of the additional water would discharge out of the groundwater system via springs. It should be noted that the discharge outflow into the lake would be relatively stable and not significantly disturbed by climate change. All hierarchical groundwater flow systems would respond to climate warming. Local groundwater shows the strongest response to the climate warming, ranked by the intermediate system. The regional groundwater flow system has the weakest response to climate change and may be negligible. The local groundwater flow system cycles and discharges most of the water added by climate warming. Thus, the local groundwater system developed at the piedmont should be examined with a view to reducing and eliminating potential water disasters posed by climate warming in this arid region.

Conclusion

Climate change is an unprecedented challenge facing the human community and will significantly influence the earth's hydrosphere. The present study examines a large sedimentary watershed in the arid northern Tibetan Plateau as an example to numerically investigate the development of groundwater flow systems in an arid basin and their behaviors under climate warming. The main findings are as follows:

The study area is a typical Tóthian basin and has developed three hierarchical groundwater flow systems, i.e. the local, intermediate, and regional systems, under present climate condition. The river seepage that occurs at the middle to upper part of the alluvial-pluvial plain is the predominant recharge water for all systems in the basin, and it accounts for more than 99% of the total water quantity. The distribution of groundwater flow systems is controlled by the sedimentary lithology inside the basin. The local system is distributed in the alluvial-pluvial plain with the shallowest buried features and largest quantity of cycling water. Approximately 82.69% of the cycled groundwater inside the basin is discharged through the local flow system and provides the dominant water resource for human exploitation and the oasis in the watershed. The intermediate system distributing below the local system has the largest cycled depth of ~600 m. The cycled water in this system accounts about 14.26% of the total groundwater quantity in the basin and is significantly important for the eco-environmental maintenance in the middle and lower watershed. The regional system is located below all the other flow systems and ranges from the mountain pass to the low-lying depression of the basin. The cycled water quantity in this system only accounts for ~3% and is not the dominant contribution of water and salt minerals for the basin center.

Climate warming would have a significant influence on groundwater systems in the basin. More water would be yielded in the headwater area, and the recharge water of the groundwater system in the basin would be greatly increased. By 2100, climate warming would increase the river seepage water quantity 130.78% of its present level. This giant recharge water quantity would cause a significant disturbance to the groundwater system. Most of the increased water would discharge out of the groundwater system through springs. Influences on other means of discharge would not be significant. Groundwater flow systems produce different responses to climate warming. The local system has the strongest response, followed by the intermediate system. The influence on the regional system is limited and negligible. Most of the increased water due to climate warming would cycle and discharge through the local system and result in a significant increase in groundwater level. This leads to the trailing edge of the overflow belt at the piedmont moving about 5 km toward the mountain pass, threatening a potential water disaster to the local regions. Climate warming would result in a slight increase in the cycled water quantity in the intermediate system but nearly no change for its discharge range. This study can provide scientific insights into the development of groundwater flow systems in a large arid sedimentary basin and their behaviors under climate warming, and is essential to address the water challenges induced by future climate warming in arid and semiarid regions.

Data availability statement

The original contributions presented in the study are included in the article/Supplementary material, and further inquiries can be directed to the corresponding author.

Author contributions

Conceptualization: YX, SW, and YL; methodology: YX, QH, KL, and YZ; formal analysis: YX, HY, SY, and LW; investigation: SW, ZQ, KL, and YL; data curation: SW, KL, ZQ, HY, and LW; software: YX, KL, YZ, and QH; writing—original draft: YX; writing—review and editing: QH; supervision: SW and SY.

Funding

This research was funded by the National Natural Science Foundation of China (grant number 42007183), the Natural Science Foundation of Sichuan Province (grant number 2022NSFSC1084), the Fundamental Research Funds for the Central Universities (grant number 2682021ZTPY063), the Key Lab of Geo-environment of Qinghai Province (grant number 2021KJ011, 2021KJ00102), and the Student Research Training Program of Southwest Jiaotong University (grant number 2022174).

Acknowledgments

The authors appreciate the editors and reviewers for their critical comments and suggestions which greatly helped us to improve the present manuscript.

Conflict of interest

The authors declare that the research was conducted in the absence of any commercial or financial relationships that could be construed as a potential conflict of interest.

Publisher's note

All claims expressed in this article are solely those of the authors and do not necessarily represent those of their affiliated organizations, or those of the publisher, the editors and the reviewers. Any product that may be evaluated in this article, or claim that may be made by its manufacturer, is not guaranteed or endorsed by the publisher.

References

Adimalla, N. (2019). Groundwater quality for drinking and irrigation purposes and potential health risks assessment: A case study from semi-arid region of South India. *Expo. Health* 11 (2), 109–123. doi:10.1007/s12403-018-0288-8

Antonellini, M., Giambastiani, B. M. S., Greggio, N., Bonzi, L., Calabrese, L., Luciani, P., et al. (2019). Processes governing natural land subsidence in the shallow coastal aquifer of the Ravenna coast, Italy. *CATENA* 172, 76–86. doi:10.1016/j.catena.2018.08.019

Brolsma, R. J., van Vliet, M. T. H., and Bierkens, M. F. P. (2010). Climate change impact on a groundwater-influenced hillslope ecosystem. *Water Resour. Res.* 46 (11), 8782. doi:10.1029/2009WR008782

Bussi, G., Whitehead, P. G., Nelson, R., Bryden, J., Jackson, C. R., Hughes, A. G., et al. (2022). Green infrastructure and climate change impacts on the flows and water quality of urban catchments: Salmons Brook and Pymmes Brook in north-east London. *Hydrology Res.* 53 (4), 638–656. doi:10.2166/nh.2022.013

Chen, J., Kuang, X., Lancia, M., Yao, Y., and Zheng, C. (2021). Analysis of the groundwater flow system in a high-altitude headwater region under rapid climate warming: Lhasa River Basin, Tibetan Plateau. *J. Hydrology Regional Stud.* 36, 100871. doi:10.1016/j.ejrh.2021.100871

Chen, Y., Zhi, L., Fan, Y., Wang, H., and Fang, G. (2014). Research progress on the impact of climate change on water resources in the arid region of Northwest China. *Acta Geogr. Sin.* 69 (9), 1295–1304. doi:10.11821/dlxb201409005

Dash, C. J., Sarangi, A., Singh, D. K., and Adhikary, P. P. (2019). Numerical simulation to assess potential groundwater recharge and net groundwater use in a semi-arid region. *Environ. Monit. Assess.* 191 (6), 371. doi:10.1007/s10661-019-7508-y

David Raj, A., Kumar, S., and Sooryamol, K. R. (2022). Modelling climate change impact on soil loss and erosion vulnerability in a watershed of Shiwalik Himalayas. *Catena* 214, 106279. doi:10.1016/j.catena.2022.106279

Díaz-Alcaide, S., and Martínez-Santos, P. (2019). Review: Advances in groundwater potential mapping. *Hydrogeol. J.* 27 (7), 2307–2324. doi:10.1007/s10040-019-02001-3

Gan, R., Li, D., Chen, C., Yang, F., and Ma, X. (2022). Impacts of climate change on extreme precipitation in the upstream of Chushandian Reservoir, China. *Hydrology Res.* 53 (3), 504–518. doi:10.2166/nh.2022.135

Ghimire, U., Shrestha, S., Neupane, S., Mohanasundaram, S., and Lorphensri, O. (2021). Climate and land-use change impacts on spatiotemporal variations in groundwater recharge: A case study of the bangkok area, Thailand. *Sci. Total Environ.* 792, 148370. doi:10.1016/j.scitotenv.2021.148370

Goderniaux, P., Brouyère, S., Blenkinsop, S., Burton, A., Fowler, H. J., Orban, P., et al. (2011). Modeling climate change impacts on groundwater resources using transient stochastic climatic scenarios. *Water Resour. Res.* 47 (12), 12516. doi:10.1029/2010WR010082

Gu, X., Shao, J., Cui, Y., and Hao, Q. (2017a). Calibration of two-dimensional variably saturated numerical model for groundwater flow in arid inland basin, China. *Curr. Sci.* 113 (3), 403–412. doi:10.18520/cs/v113/i03/403-412

Gu, X., Xiao, Y., Yin, S., Hao, Q., Liu, H., Hao, Z., et al. (2018). Hydrogeochemical characterization and quality assessment of groundwater in a long-term reclaimed water irrigation area, north China plain. *Water* 10 (9), 1209. doi:10.3390/w10091209

Gu, X., Xiao, Y., Yin, S., Shao, J., Pan, X., Niu, Y., et al. (2017b). Groundwater level response to hydrogeological factors in a semi-arid basin of Beijing, China. *J. Water Supply. Res. Tec.* 66 (4), 266–278. doi:10.2166/aqua.2017.093

Hao, Q., Lu, C., Zhu, Y., Xiao, Y., and Gu, X. (2018). Numerical investigation into the evolution of groundwater flow and solute transport in the eastern Qaidam basin since the last glacial period. *Geofluids* 2018 (1), 1–12. doi:10.1155/2018/9260604

Hao, Q., Shao, J., Cui, Y., and Zhang, Q. (2016). Development of a new method for efficiently calculating of evaporation from the phreatic aquifer in variably saturated flow modeling. *J. Groundw. Sci. Eng.* 4 (1), 26. doi:10.19637/j.cnki.2305-7068.2016.01.004

Hao, Q., Xiao, Y., Chen, K., Zhu, Y., and Li, J. (2020). Comprehensive understanding of groundwater geochemistry and suitability for sustainable drinking purposes in confined aquifers of the wuyi region, central north China plain. *Water* 12 (11), 3052. doi:10.3390/w12113052

Hao, S., Zhu, F., and Cui, Y. (2021). Land use and land cover change detection and spatial distribution on the Tibetan Plateau. *Sci. Rep.* 11 (1), 7531. doi:10.1038/s41598-021-87215-w

Hatch-Kuri, G., and Carrillo-Rivera, J. J. (2021). "Groundwater flow systems and their importance in the assessment of transboundary groundwater: The Mexico–U.S.A. Case," in *Intensified land and water use: A holistic perspective of local to regional integration*. Editor M. M. Alconada-Magliano (Cham: Springer International Publishing), 141.

Hemmerle, H., and Bayer, P. (2020). Climate change yields groundwater warming in bavaria, Germany. *Front. Earth Sci. (Lausanne).* 8, 575894. doi:10.3389/feart.2020.575894

Hu, L., and Jiao, J. J. (2015). Calibration of a large-scale groundwater flow model using GRACE data: A case study in the Qaidam basin, China. *Hydrogeol. J.* 23 (7), 1305–1317. doi:10.1007/s10040-015-1278-6

Hu, Q., Jiang, D., and Fan, G. (2015). Climate change projection on the Tibetan Plateau: Results of CMIP5 models. *Chin. J. Atmos. Sci.* 39 (2), 260.

Huang, F., Chunyu, X., Zhang, D., Chen, X., and Ochoa, C. G. (2020). A framework to assess the impact of ecological water conveyance on groundwater-dependent terrestrial ecosystems in arid inland river basins. *Sci. Total Environ.* 709, 136155. doi:10.1016/j.scitotenv.2019.136155

Islam, M. B., Firoz, A. B. M., Foglia, L., Marandi, A., Khan, A. R., Schüth, C., et al. (2017). A regional groundwater-flow model for sustainable groundwater-resource management in the south Asian megacity of Dhaka, Bangladesh. *Hydrogeol. J.* 25 (3), 617–637. doi:10.1007/s10040-016-1526-4

Kim, S. J., Asadzadeh, M., and Stadnyk, T. A. (2022). Climate change impact on water supply and hydropower generation potential in Northern Manitoba. *J. Hydrology Regional Stud.* 41, 101077. doi:10.1016/j.ejrh.2022.101077

Kraaijenbrink, P. D. A., Bierkens, M. F. P., Lutz, A. F., and Immerzeel, W. W. (2017). Impact of a global temperature rise of 1.5 degrees Celsius on Asia's glaciers. *Nature* 549 (7671), 257–260. doi:10.1038/nature23878

Kuang, X., and Jiao, J. J. (2016). Review on climate change on the Tibetan Plateau during the last half century. *J. Geophys. Res. Atmos.* 121 (8), 3979–4007. doi:10.1002/2015jd024728

Li, P., He, X., Li, Y., and Xiang, G. (2019). Occurrence and health implication of fluoride in groundwater of loess aquifer in the Chinese loess plateau: A case study of tongchuan, northwest China. *Expo. Health* 11 (2), 95–107. doi:10.1007/s12403-018-0278-x

Liu, J., Ma, Y., Gao, Z., Zhang, Y., Sun, Z., Sun, T., et al. (2022). Fluoride contamination, spatial variation, and health risk assessment of groundwater using GIS: A high-density survey sampling in weifang city, north China. *Environ. Sci. Pollut. Res.* 29 (23), 34302–34313. doi:10.1007/s11356-021-18443-w

Luo, Y., Xiao, Y., Hao, Q., Zhang, Y., Zhao, Z., Wang, S., et al. (2021). Groundwater geochemical signatures and implication for sustainable development in a typical endorheic watershed on Tibetan plateau. *Environ. Sci. Pollut. Res.* 28 (35), 48312–48329. doi:10.1007/s11356-021-14018-x

Ma, R., Huang, J., Tian, H., Cui, X., and Wang, D. (2017a). Characteristics of precipitation,evaporation and temperature at the Golmud River Catchment in recent 60 years. *Arid. Land Geogr.* 40 (5), 1005.

Ma, Y., Ma, W., Zhong, L., Hu, Z., Li, M., Zhu, Z., et al. (2017b). Monitoring and modeling the Tibetan plateau's climate system and its impact on east asia. *Sci. Rep.* 7 (1), 44574. doi:10.1038/srep44574

Minea, I., Boicu, D., Amihăiesei, V., and Iosub, M. (2022). Identification of seasonal and annual groundwater level trends in temperate climatic conditions. *Front. Environ. Sci.* 10, 852695. doi:10.3389/fenvs.2022.852695

Moharir, K., Pande, C., Singh, S. K., Choudhari, P., Kishan, R., and Jeyakumar, L. (2019). Spatial interpolation approach-based appraisal of groundwater quality of arid regions. *J. Water Supply Res. Technology-Aqua* 68 (6), 431–447. doi:10.2166/aqua.2019.026

Mookiah, M., Jha, S. K., and Biswas, A. (2021). Assessment of groundwater mass balance and zone budget in the semi-arid region: A case study of palar sub-basin, Tamil nadu, India. *J. Earth Syst. Sci.* 130 (4), 187. doi:10.1007/s12040-021-01691-2

Nan, Z., Li, S., and Cheng, G. (2004). Scenario prediction of permafrost change on the Qinghai-Tibet Plateau in the next 50 and 100 years. *Sci. China Ser. D Earth Sci.* 34 (6), 528–534. doi:10.1360/zd2004-34-6-528

Qu, B., Zhang, Y., Kang, S., and Sillanpää, M. (2019). Water quality in the Tibetan plateau: Major ions and trace elements in rivers of the "water tower of asia". *Sci. Total Environ.* 649, 571–581. doi:10.1016/j.scitotenv.2018.08.316

Qu, S., Shi, Z., Liang, X., Wang, G., and Jin, X. (2021). Origin and controlling factors of groundwater chemistry and quality in the Zhiluo aquifer system of northern Ordos Basin, China. *Environ. Earth Sci.* 80 (12), 439. doi:10.1007/s12665-021-09735-y

Rafiei-Sardooi, E., Azareh, A., Joorabian Shooshtari, S., and Parteli, E. J. R. (2022). Long-term assessment of land-use and climate change on water scarcity in an arid basin in Iran. *Ecol. Model.* 467, 109934. doi:10.1016/j.ecolmodel.2022.109934

Sarzaeim, P., Bozorg-Haddad, O., Fallah-Mehdipour, E., and Loáiciga, H. A. (2017). Climate change outlook for water resources management in a semiarid river basin: The effect of the environmental water demand. *Environ. Earth Sci.* 76 (14), 498. doi:10.1007/s12665-017-6834-z

Shi, Y. (2001). Estimation of the water resources affected by climatic warming and glacier shrinkage before 2050 in west China. *J. Glaciol. Geocryol.* 23 (4), 333.

IPCC (2022). "*Climate change 2022: Mitigation of climate change*", (Eds) P. R. Shukla, R. S. J. Skea, A. A. Khourdajie, R. v. Diemen, D. McCollum, M. Pathak, et al. (Cambridge, UK and New York, NY, USA: IPCC.

Straneo, F., and Heimbach, P. (2013). North Atlantic warming and the retreat of Greenland's outlet glaciers. *Nature* 504 (7478), 36–43. doi:10.1038/nature12854

Wang, S., Xie, Z., Wang, F., Zhang, Y., Wang, W., Liu, K., et al. (2022). Geochemical characteristics and quality appraisal of groundwater from huatugou of the Qaidam basin on the Tibetan plateau. *Front. Earth Sci. (Lausanne).* 10. doi:10.3389/feart.2022.874881

Xiao, Y., Hao, Q., Zhang, Y., Zhu, Y., Yin, S., Qin, L., et al. (2022a). Investigating sources, driving forces and potential health risks of nitrate and fluoride in groundwater of a typical alluvial fan plain. *Sci. Total Environ.* 802, 149909. doi:10.1016/j.scitotenv.2021.149909

Xiao, Y., Liu, K., Hao, Q., Li, Y., Xiao, D., and Zhang, Y. (2022b). Occurrence, controlling factors and health hazards of fluoride-enriched groundwater in the lower flood plain of Yellow River, Northern China. *Expo. Health* 14, 345–358. doi:10.1007/s12403-021-00452-2

Xiao, Y., Liu, K., Hao, Q., Xiao, D., Zhu, Y., Yin, S., et al. (2022c). Hydrogeochemical insights into the signatures, genesis and sustainable perspective of nitrate enriched groundwater in the piedmont of Hutuo watershed, China. *Catena* 212, 106020. doi:10.1016/j.catena.2022.106020

Xiao, Y., Liu, K., Yan, H., Zhou, B., Huang, X., Hao, Q., et al. (2021). Hydrogeochemical constraints on groundwater resource sustainable development in the arid Golmud alluvial fan plain on Tibetan plateau. *Environ. Earth Sci.* 80 (22), 750. doi:10.1007/s12665-021-10076-z

Xiao, Y., Shao, J., Frape, S., Cui, Y., Dang, X., Wang, S., et al. (2018). Groundwater origin, flow regime and geochemical evolution in arid endorheic watersheds: A case study from the Qaidam basin, northwestern China. *Hydrol. Earth Syst. Sci.* 22 (8), 4381–4400. doi:10.5194/hess-22-4381-2018

Xu, Y.-S., Yuan, Y., Shen, S.-L., Yin, Z.-Y., Wu, H.-N., and Ma, L. (2015). Investigation into subsidence hazards due to groundwater pumping from Aquifer II in Changzhou, China. *Nat. Hazards (Dordr).* 78 (1), 281–296. doi:10.1007/s11069-015-1714-x

Zhang, Y., Dai, Y., Wang, Y., Huang, X., Xiao, Y., and Pei, Q. (2021a). Hydrochemistry, quality and potential health risk appraisal of nitrate enriched groundwater in the Nanchong area, southwestern China. *Sci. Total Environ.* 784, 147186. doi:10.1016/j.scitotenv.2021.147186

Zhang, Y., He, Z., Tian, H., Huang, X., Zhang, Z., Liu, Y., et al. (2021b). Hydrochemistry appraisal, quality assessment and health risk evaluation of shallow groundwater in the Mianyang area of Sichuan Basin, southwestern China. *Environ. Earth Sci.* 80 (17), 576. doi:10.1007/s12665-021-09894-y

frontiers | Frontiers in Earth Science

TYPE Original Research
PUBLISHED 23 September 2022
DOI 10.3389/feart.2022.944549

Check for updates

OPEN ACCESS

EDITED BY
Yunhui Zhang,
Southwest Jiaotong University, China

REVIEWED BY
Huangsong Pan,
Southeast University, China
Zuosen Luo,
China Three Gorges University, China

*CORRESPONDENCE
Zuan Pei,
peizuan@cdut.edu.cn

SPECIALTY SECTION
This article was submitted to Geohazards and Georisks, a section of the journal Frontiers in Earth Science

RECEIVED 15 May 2022
ACCEPTED 31 August 2022
PUBLISHED 23 September 2022

CITATION
Yang H, Pei Z, He Z, Lei J and Xia X (2022), An empirical model for the travel distance prediction of deflection-type rock avalanches in the wenchuan earthquake area.
Front. Earth Sci. 10:944549.
doi: 10.3389/feart.2022.944549

COPYRIGHT
© 2022 Yang, Pei, He, Lei and Xia. This is an open-access article distributed under the terms of the Creative Commons Attribution License (CC BY). The use, distribution or reproduction in other forums is permitted, provided the original author(s) and the copyright owner(s) are credited and that the original publication in this journal is cited, in accordance with accepted academic practice. No use, distribution or reproduction is permitted which does not comply with these terms.

An empirical model for the travel distance prediction of deflection-type rock avalanches in the wenchuan earthquake area

Hailong Yang[1], Zuan Pei[1]*, Zhihao He[2], Jin Lei[1] and Xiaotian Xia[3]

[1]State Key Laboratory of Geohazard Prevention and Geoenvironment Protection, Chengdu University of Technology, Chengdu, China, [2]School of Emergency Management, Xihua University, Chengdu, China, [3]Northwest Bureau of China Metallurgical Geology Bureau, Xi'an, China

Travel distance is a significant indicator for evaluating the mobility of rock avalanches and is usually used to identify the approximate delineation of potentially endangered regions. The deflection-type rock avalanche is a typical laterally confined rock avalanche and is characterized by obvious changes in the travel path. In this study, we selected deflection-type rock avalanches that occurred in the Wenchuan earthquake area as the research object and statistically analyzed 54 rock avalanches collected from the literature. Multiple linear regression of the logarithm of the ratio of slope height to travel distance (h/L) versus the logarithm of other parameters was developed to obtain a best-fit empirical model for the travel distance prediction of deflection-type rock avalanches. The validity of the proposed empirical model was verified by the satisfactory agreement between observations and predictions. Moreover, the sensitivity of local topographic parameters on the mobility of deflection-type rock avalanches is also discussed using regression analysis.

KEYWORDS

rock avalanche, deflection-type, travel distance, empirical model, local topography

1 Introduction

Rock avalanches are extremely rapid mass flows following the fragmentation of large rockslides or rockfalls (Hungr et al., 2014; Knapp and Krautblater, 2020; Mitchell et al., 2020). In the recent 2 decades, numerous typical rock avalanches have struck the southwestern mountain area of China, such as Touzhai rock avalanches (Yang et al., 2017), Guanling landslide (Kang et al., 2017), Chenjiaba landslide (Huang et al., 2017), Jiweishan landslide (Ge et al., 2019), Zhongbao landslide (Chen et al., 2021), etc., Due to their extremely high mobility (Ge et al., 2020a; Lin et al., 2022), they can travel unexpectedly long distances along different topographies (Hsu 1975; Ge et al., 2019), which always cause huge destructiveness to local residents and property in mountainous regions (Mitchell et al., 2019; Liu et al., 2021a).

The term "Fahrböschung" was first proposed by Heim (1932) in Elm landslide survey, and was used to measure the mobility of rock avalanches. A previous study revealed the inverse

relationship between the Fahrböschung values and volumes of rock avalanches (Strom et al., 2019; Mitchell et al., 2020). Thus, large rock avalanches are considered more mobile (Liu et al., 2021a). The travel distance, also called the runout distance, is another significant consideration for evaluating the mobility of rock avalanches. Since the famous Elm landslide event in 1881, the rapid long-travel distance rock avalanche harvest attention to continuously increasing interest from the scientists (e.g., Hsu 1975; Hungr and Evans 2004), which motivates further study to better estimate the mobility of these events. Moreover, travel distance is usually used to identify the rough delineation of potentially endangered regions (Hattanji and Moriwaki 2009). Therefore, it also has significance in the risk assessment of rock avalanches.

Previous studies have revealed that the mobility of rock avalanches is strongly affected by the local topography (Ge et al., 2020b; Liu et al., 2021a). The local topography along the travel path of rock avalanches mainly includes three basic confinement types: laterally confined, unconfined and frontally confined (Strom et al., 2019), also called valley, open and blocked topography (Zhang and Yin 2013). Laterally confined rock avalanches often move down a narrow or broad valley due to the constraint of the valley slopes of lateral mountains (Liu et al., 2021a), and their travel path usually undergoes obvious changes. The deflection angle, also known as impact angle (Ge et al., 2020b), is defined as the acute angle between the initial motion direction of the rock avalanches and the valley extension direction in the horizontal plan (Figure 1), which is used to describe the change in the travel path (Fan et al., 2015). According to the size of the deflection angle, the laterally confined rock avalanches can be further divided into two types, that is, deflection-type and channelized rock avalanches. The Wenjia gully rock avalanches triggered by the Wenchuan earthquake are striking examples of deflection-type rock avalanches. It underwent multiple changes in its travel path (Tang et al., 2012; Kang et al., 2021) and caused more than 50 people to lose their lives (Zhang et al., 2013, 2016). However, the effects of various topographical parameters on the mobility of deflection-type rock avalanches are still unclear at present.

Although the Wenchuan earthquake was over 10 years ago, it provided enormous amount of unstable slope for the post-earthquake hazards, such as the rainfall-induced Sanxicun landslide (Gao et al., 2017) and Xinmo rock avalanches (Huang et al., 2019) that severely threaten dwellings and infrastructures (Ding and Hu 2014). Therefore, the post-earthquake effect is still significant (Fan et al., 2018). Rock avalanches are the most common type of geological disasters in this region. Accordingly, the construction of a prediction model for the travel distance of rock avalanches is meaningful for the risk assessment of rock avalanches in this region (Zhan et al., 2017). Generally, travel distance prediction for rock avalanches is a complicated issue due to the great diversity in travel path materials (Liu et al., 2021a) and geotechnical parameters of mass flows (Qiu et al., 2018). The empirical prediction model, which avoids the usage of uncertain and highly variable parameters, provides a practical method (Qiu et al., 2018). Therefore, it has been widely applied to preliminary assessments of the travel distance of rock avalanches (e.g., Guo et al., 2014; Zhan et al., 2017; Strom et al., 2019; Mitchell et al., 2020). In the present study, the deflection-type rock avalanche was selected as the research object. A multiple linear regression model of the logarithm of h/L versus the logarithm of other parameters was developed to obtain a best-fit empirical model for the travel distance prediction of deflection-type rock avalanches, which provides a useful tool for the preliminary prediction of the potential threat range of such rock avalanches in the Wenchuan earthquake area. In addition, the effects of local topography on the mobility of deflection-type rock avalanches are further discussed.

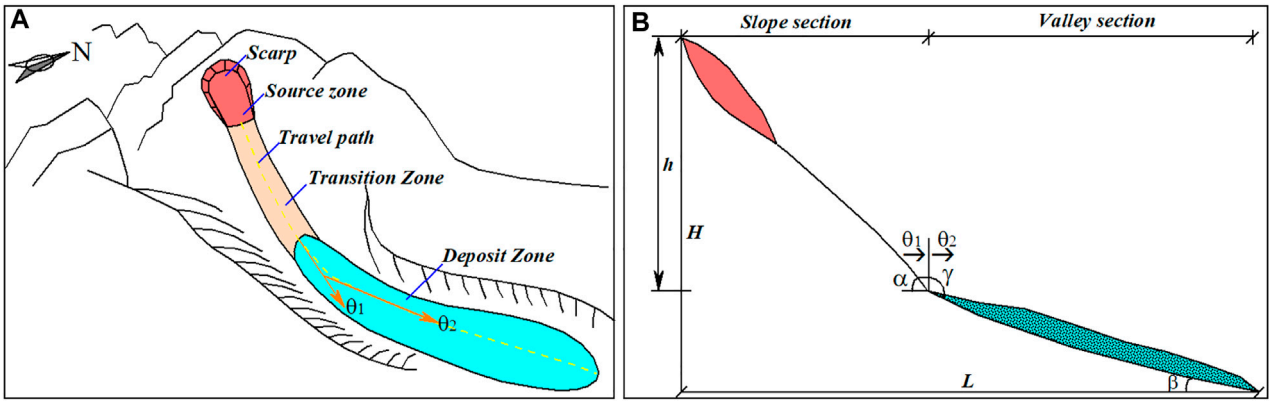


FIGURE 1
(A) Plane sketch of the deflected-type rock avalanches (θ_1 is refers to the initial motion direction of the rock avalanches, and θ_2 is refers to the valley extension direction); **(B)** Schematic diagram of local topography longitudinal section along the direction of motion path showing the main local topographic parameters of the deflection-type rock avalanches consist of the slope angle (α), channel angle (β), slope height (h), deflection angle (θ), slope transition angle (γ) and fall height (H).

2 Rock avalanche database

The Tibetan Plateau, located at the junction of Indian and Asian plates, has undergone long–term and complex tectonic activities since the late Mesozoic (Zhang et al., 2022). Longmen Shan Mountain (LMS) Orogenic Zone belongs to southeastern region of the Tibetan Plateau, and is one of the most intense areas in mainland China on crustal deformation characterized by frequent large earthquakes (Wang et al., 2014). Rock slides and collapses are the main types of earthquake disasters in LMS Orogenic Zone, and each strong earthquake usually causes massive rockslides and collapses in this region. For example, the tectonic uplift caused by the Wenchuan earthquake changed the slope gradient instantly (Li et al., 2014) and triggered more than 60,000 rock slides over an elliptical area of approximately 44,000 km^2 along the fault rupture zone (Liu et al., 2021b), which directly led to approximately 20,000 deaths.

The co-seismic landslides triggered by Wenchuan earthquake provides a rich database for landslide statistical analysis. Therefore, we compile three databases of rock avalanches in this study (see Tables 1, 2, 3). The collected data is associated with the Wenchuan earthquake area. As shown in Figure 2, the rock avalanches listed in the databases are distributed on the surface rupture zone with northeast-trending between the Sichuan Basin and the Tibetan Plateau. Database one consists of 22 rock avalanches collected from the literature (Table 1). It was used to validate the general applicability of the empirical model proposed in this paper in travel distance prediction. Database two consists of 54 deflected-type rock avalanches (Table 2). The volumes of these rock avalanches ranged from 2.6 to 1996 × 10^4 m^3, with travel distances between 0.13 and 2.40 km (Table 2). Deflected-type rock avalanches were used to develop an empirical model for travel distance prediction. In addition, as shown in Table 3, database three consisting of 10 deflected-type rock avalanches was applied to verify the validity of the presented model. The data in database three were collected based on remote sensing interpretation and field investigation on Subaohe river Basins, Beichuan county in the Wenchuan earthquake area (see inset of Figure 2).

TABLE 1 The database of laterally confined rock avalanches.

No	Landslide name	Landslide volume V (10^4m^3)	Slope angle α (°)	Channel angle β (°)	Fall height H (m)	Observed travel distance L observed (m)	Predicted travel distance L predicted (m)	Estimation errors
1	WenjiaGully	5,000	26	7	1,320	4,000	4,686	17.14(%)
2	HongshiGully	1,341	37	17	1,040	2,700	1999	25.95(%)
3	Xiaojiashan 1#	781	48	24	930	1,350	1,246	7.72(%)
4	NiumianGully	750	32	13	800	2,640	1887	28.51(%)
5	LiqiGully	536	37	12	650	1,500	1,434	4.39(%)
6	Caocaoping	534	31	17	580	1,340	1,247	6.93(%)
7	HuoshiGully	468	38	17	700	1,320	1,305	1.16(%)
8	Shibangou	450	34	9	650	1800	1705	5.29(%)
9	Xiejiadianzi	400	34	15	720	1,600	1,523	4.84(%)
10	DashuiGully	315	30	17	560	1,400	1,218	12.97(%)
11	Changping	284	37	16	500	1,200	972	19.04(%)
12	Xiaomuling	274	45	26	710	1,025	955	6.86(%)
13	Dawan	248	28	20	480	1,000	1,015	1.49(%)
14	Xiaojiashan 2#	239	44	20	650	1,135	1,000	11.87(%)
15	Shicouzi	192	30	26	640	1,200	1,141	4.92(%)
16	Changtan	164	33	25	1,050	1,650	1771	7.34(%)
17	Zhangzhengbo	92	29	15	320	800	741	7.42(%)
18	Dujiayan	86	33	17	400	880	804	8.63(%)
19	Madiping	86	27	31	395	740	687	7.13(%)
20	Yandiaowo	82	30	26	390	800	691	13.66(%)
21	ChuangziGully	82	35	15	295	670	604	9.85(%)
22	Waqianshan	56	24	18	250	620	598	3.59(%)

Note: The database collected from the literature of Zhan et al. (2017).

TABLE 2 Data of various parameters of deflected-type rock avalanches.

No	Landslide name	Landslide volume V (10^4m^3)	Slope height h (m)	Slope angle α (°)	Channel angle β (°)	Deflection angle θ (°)	Transition angle γ (°)	Fall height H (m)	Observed travel distance L observed (m)	Predicted travel distance L predicted (m)	Estimation errors
1	Anzi	2.6	57	33	31	52	178	107	171	157	8.19(%)
2	Daihuashan	2.8	38	32	31	48	179	78	130	122	6.35(%)
3	Majiahe	2.8	90	46	36	43	170	145	163	153	6.22(%)
4	Jiulong Gully 1#	2.9	81	29	28	65	179	137	251	246	1.80(%)
5	Laohuzui Gully 1#	3.3	154	37	27	43	167	221	335	363	13.11(%)
6	Siping	4	179	38	25	27	169	268	418	328	11.80(%)
7	Muguayuan	7.2	117	30	19	35	173	176	372	271	2.94(%)
8	Tianping Village	7.6	112	37	30	40	172	189	279	362	8.93(%)
9	Huangnigang	8.2	175	43	35	23	165	321	398	271	14.04(%)
10	Pianqiaozi	8.8	153	35	19	36	168	205	372	409	7.21(%)
11	Wujibao	9.3	112	32	17	71	178	153	315	529	4.03(%)
12	Zaojiaowan Gully 1#	13.1	217	42	30	64	172	335	441	376	5.99(%)
13	Jinxi Gully	14.6	138	49	40	30	162	297	312	455	4.52(%)
14	Jiulong Gully 2#	16.5	198	37	35	52	162	403	551	380	26.70(%)
15	Qilangmiao	19.5	113	31	23	20	172	201	400	937	30.02(%)
16	Chuangzi Gully 2#	20.1	203	39	21	37	171	274	435	828	15.79(%)
17	Yangjiayan	25.4	164	41	23	27	160	304	518	639	7.08(%)
18	Xiaowan	20.4	342	31	23	42	170	409	721	945	16.33(%)
19	Shanshulin	27.9	340	34	25	66	169	433	715	651	10.34(%)
20	Huangjiabacun	32	282	38	18	45	168	362	597	493	0.37(%)
21	Zaojiaowan Gully 2#	37.4	428	39	29	56	162	582	812	648	22.48(%)
22	Pingshang	38.2	215	31	20	44	161	300	590	650	6.92(%)
23	Yuzixi	40	212	40	28	56	177	342	495	931	25.32(%)
24	Huangbashi	44.7	275	47	23	62	179	414	579	542	7.39(%)
25	Liushuping	34.9	200	26	8	57	149	218	529	810	6.37(%)

(Continued on following page)

10.3389/feart.2022.944549

TABLE 2 (*Continued*) Data of various parameters of deflected-type rock avalanches.

No	Landslide name	Landslide volume V (10^4m^3)	Slope height h (m)	Slope angle α (°)	Channel angle β (°)	Deflection angle θ (°)	Transition angle γ (°)	Fall height H (m)	Observed travel distance L observed (m)	Predicted travel distance L predicted (m)	Estimation errors
26	Xingziping	52.6	284	41	22	37	172	396	608	749	14.05(%)
27	Laoshuzui Gully 2#	58.7	281	35	32	21	166	491	743	669	15.87(%)
28	Muhongping	85.7	171	28	21	47	170	403	931	957	25.38(%)
29	Laojiaozi Gully	65.6	139	27	26	85	161	259	505	693	14.61(%)
30	Daozaiqiao	67.3	399	40	9	70	174	464	865	494	26.92(%)
31	Weiziping	68.6	157	22	14	28	162	222	657	519	5.22(%)
32	Pujia Gully	71.8	239	35	21	50	155	413	795	881	7.31(%)
33	Fuyan Gully	51.9	385	38	28	40	171	530	763	718	3.80(%)
34	Zhangjiaping	74.7	286	39	20	50	154	379	605	699	1.96(%)
35	Zhaojiashan	78.4	94	22	16	30	157	223	676	876	31.66(%)
36	Chuangzi Gully 1#	90.9	178	34	16	60	175	261	548	1,280	8.97(%)
37	Longwan Village	102.1	268	32	29	55	168	489	830	462	42.99(%)
38	Zhuanwan	113.3	498	48	23	69	165	713	950	1,136	26.94(%)
39	Qinglong Village	118.9	133	20	11	37	163	194	692	1,053	26.51(%)
40	Linjiashan	120.6	258	32	6	80	167	285	686	1,089	23.76(%)
41	Changheba	120.9	354	41	18	30	167	439	665	1,396	28.58(%)
42	Maochongshan	130.6	392	37	22	33	162	566	938	1,351	18.28(%)
43	Pengjiashan	142.1	316	29	24	24	156	591	1,175	1818	25.82(%)
44	Baiguoshu	161.8	104	26	14	50	158	255	811	1,465	28.51(%)
45	Hongmagong	169.6	320	29	14	45	150	403	895	2039	15.05(%)
46	Fengyanzi	192.1	289	30	13	31	170	365	832	312	6.88(%)
47	Yinshan Gully	224.1	363	38	25	30	164	556	880	360	3.34(%)
48	Baishu Gully	280.4	331	39	22	43	171	622	1,147	264	15.44(%)
49	Dongxi Gully	350.6	360	28	15	55	156	471	1,086	492	15.11(%)
50	Mianjiaoping	629.2	461	38	20	64	173	660	1,142	659	29.24(%)
51	Haixin Gully	969.8	720	40	16	80	177	891	1,445	939	13.17(%)
52	Donghekou	1,500	560	35	5	27	165	700	2,400	1,097	16.92(%)
53	Woqian	1,602.3	375	30	8	75	163	575	2050	950	17.16(%)
54	Shuimo Gully	1996	578	34	16	50	162	754	2000	2,182	9.12(%)

Note: The database collected from the literature of Fan et al. (2015).

10.3389/feart.2022.944549

TABLE 3 Database of deflection-type rock avalanches used for applicability verification of the improved empirical model.

No.	Landslide name	Landslide volume V (10^4m^3)	Slope height h (m)	Slope angle α (°)	Channel angle β (°)	Deflection angle θ (°)	Observed travel distance L observed (m)	Predicted travel distance L predicted (m)	Estimation errors
1	Tianba	0.74	95	30	27	51	200	223	11.50(%)
2	Yangjiayan	18.60	119	35	23	25	574	334	41.81(%)
3	Shuicheping	4.44	74	28	23	14	354	242	31.64(%)
4	Liujiaping	1.26	49	28	20	45	148	131	11.49(%)
5	Huangjiashan	3.31	109	34	30	33	228	276	21.05(%)
6	Yinbashi	99.19	257	32	20	21	878	882	0.46(%)
7	Shaojiashan	1.49	212	35	28	13	368	432	17.39(%)
8	Tianping	8.87	91	30	24	28	381	290	23.88(%)
9	Chenshan	0.24	27	24	17	63	105	69	34.29(%)
10	Yuanxing	2.98	114	35	33	41	268	287	7.09(%)

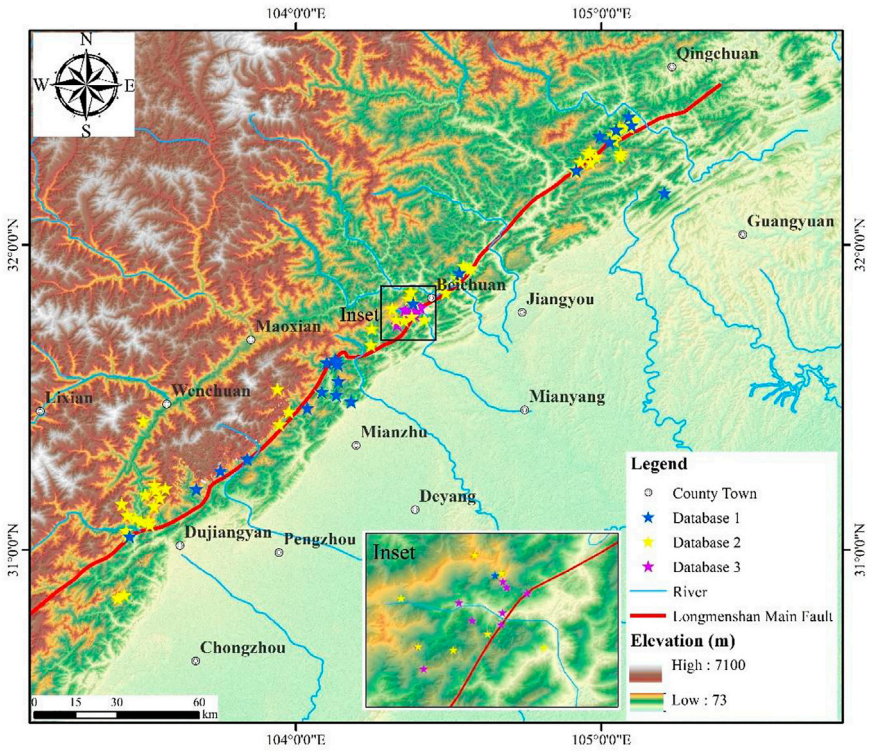


FIGURE 2
The locations of rock avalanches in the Wenchuan earthquake area collected in three databases.

3 Method

3.1 Relevant parameters

The local morphology of a deflection-type rock avalanche can be divided into two sections consisting of slope and valley sections (Figure 1A). The terms and notations of the deflection-type rock avalanches are shown in Figure 1B. The slope angle (denoted as α) refers to the average inclination from the slope toe to the top of the scarp (Qiu et al., 2018). The channel angle (denoted as β) refers to the average inclination of the sectional valley (Zhan et al., 2017). The topographic relief change between slope and valley is defined as the

slope transition angle (denoted as γ) (Guo et al., 2014). The fall height (denoted as H) is the vertical distance from the top of the scarp to the front end of the deposit (Basharat et al., 2015). The slope height (denoted as h) refers to the vertical distance from the top of the scarp to the slope toe. The symbol θ_1 is used to represent the initial motion direction of the rock avalanches, whereas the symbol θ_2 is used to represent the valley extension direction. The deflection angle (denoted as θ) is the acute angle between θ_1 and θ_2 (Fan et al., 2015). Therefore, the main local topographic parameters of the deflection-type rock avalanches consist of the slope angle (α), channel angle (β), slope height (h), deflection angle (θ), slope transition angle (γ) and fall height (H).

3.2 Empirical model

Empirical-statistical methods have been used as common tools to study the mobility of rock avalanches (Zhan et al., 2017). In reference to existed study (e.g., Heim 1932; Hsu 1975; Qiu et al., 2018; Zheng et al., 2018), although there are many empirical models available for travel distance prediction of rock avalanches, they can be summarized into just three categories, as shown in Eqs 1, 2, 3. However, Eqs 1, 2 only describe the simple statistical relationships between mobility parameters and landslide volume, while Eq. 3-1 proposed by Zheng et al. (2018) and Eq. 3-2 proposed in this paper have much more physical significance. Therefore, Eq. 3 was selected as the empirical model for travel distance prediction.

$$L(V) = \lambda_0 V^{\lambda_1}, \tag{1}$$

$$\frac{H}{L}(V) = \gamma_0 V^{\gamma_1}, \tag{2}$$

$$L(VH) = \eta_0 (VH)^{0.25}, \tag{3-1}$$

$$\frac{H}{L}(V) = \chi_0 \left(V^{1/3} H^{-1}\right)^{\chi_1}, \tag{3-2}$$

where the L is the indicator variable, H is the fall height, V is the landslide volume, and λ_0, λ_1, γ_0, γ_1, η_0, χ_0 and χ_1 are the corresponding regression coefficients.

The mobility of rock avalanches is affected by several influential factors (Guo et al., 2014). Hence, some scholars have aimed to introduce more quantifiable influential factors in empirical models to improve the prediction accuracy of travel distance (e.g., Finlay et al., 1999; Guo et al., 2014; Zhan et al., 2017; Qiu et al., 2018). The local topography is an important factor influencing the mobility of rock avalanches (Liu et al., 2021a). Therefore, after introducing the main topographic parameters in Eq. 3-1 and Eq. 3-2, the empirical model can be expressed as Eq. 4. The linear regression model on the logarithmic transform of the variables was conducted under the assumption of linear association, in which logarithmic transformation of the variables is equivalent to a power law consistent with the existing research (Mitchell et al., 2020).

$$\log L = \beta_0 + \beta_1 \log (VH)^{0.25} + \beta_2 \log C_1 + \beta_3 \log C_2 + \ldots + \beta_{n+1} \log C_n + \varepsilon, \tag{4-1}$$

$$\log\left(\frac{H}{L}\right) = \beta_0 + \beta_1 \log\left(V^{1/3} H^{-1}\right) + \beta_2 \log C_1 + \beta_3 \log C_2 + \ldots + \beta_{n+1} \log C_n + \varepsilon, \tag{4-2}$$

where log is the logarithm of 10, L is the travel distance, H is the fall height, V is the landslide volume, C_i (i = 1, 2, 3..., n + 1) are the indicator variables of topographical parameters, β_i (i = 1, 2, 3..., n + 1) are the regression coefficients and ε is the residual error, which is assumed to be normally distributed with zero mean (Mitchell et al., 2020).

As shown in Eqs 5, 6, the mean absolute percentage error, hereinafter referred to as $MAPE$ (Armstrong and Collopy 1992), and the Theil inequality coefficient, hereinafter referred to as TIC (Leuthold 1975), can be used to evaluate the prediction accuracy of the empirical model for the travel distance prediction of deflected-type rock avalanches.

$$MAPE = \frac{1}{\mathrm{n}} \sum_{1}^{n} \left| \frac{p_i - A_i}{A_i} \right|, \tag{5}$$

$$TIC = \frac{\sqrt{1/\mathrm{n} \sum_{1}^{n} (p_i - A_i)^2}}{\sqrt{1/\mathrm{n} \sum_{1}^{n} p_i^2} + \sqrt{1/\mathrm{n} \sum_{1}^{n} A_i^2}}, \tag{6}$$

where p_i and A_i refer to predictions and actual observations of travel distance, respectively. A smaller MAPE or TIC value indicates that the empirical models are more accurate in predicting the travel distance of rock avalanches (Qiu et al., 2018).

4 Results and validation

4.1 General applicability validation

The parameters of 22 rock avalanches listed in the test database one consist of landslide volume (V), fall height (H), slope angle (α) and channel angle (β). Therefore, the slope angle (α) and channel angle (β) were considered in Eq. 4. Based on the multivariate regression method, the best-fit regression equation for travel distance prediction was derived from the dataset of Table 1 (see Eq. 7).

$$L = e^{2.312} (\tan\alpha)^{-0.308} (\tan\beta)^{-0.817} (VH)^{0.25}, \tag{7-1}$$

$$\frac{H}{L} = e^{0.1247} (\tan\alpha)^{0.5211} (\tan\beta)^{0.4017} \left(V^{1/3} H^{-1}\right)^{-0.0184}. \tag{7-2}$$

The regression results show that correlation coefficients are 0.39 and 0.77 for Eq. 7-1 and Eq. 7-2. Meanwhile, the p value of Eq. 7-2 is 0.013 and is less than that of Eq. 7-1, which indicates that the

overall regression of Eq. 7-2 satisfies higher statistical significance level. In addition, the residual plots illustrate normality, constant variance and absence of trends in the residuals (Figure 3), which shows that the selection of Eq. 7-2 as empirical prediction model for travel distance is more reasonable. To further validate Eq. 7-2, we list the estimation errors ($|L_{predicted} - L_{observed}|/L_{observed} \times 100\%$) of 22 rock avalanches in Table 1. Most of the estimation errors are less than 10%, which indicates that the travel distance of most rock avalanches is predicted accurately. Therefore, the empirical model (Eq. 4-2) has good applicability in travel distance prediction for rock avalanches.

4.2 Travel distance prediction for the deflection-type rock avalanches

For the travel distance prediction of deflected-type rock avalanches, four characteristic parameters of local topography, including α, β, θ and γ, were considered in the empirical model (Eq. 4-2), and the best-fit multivariate regression model (Eq. 8) was obtained based on the regression analysis of the database of deflection-type rock avalanches, which is as follows:

$$\frac{H}{L} = e^{0.1839} (tan\,\alpha)^{0.6181} (tan\,\beta)^{0.2586} (tan\,\theta)^{0.0318} (sin\,\gamma)^{0.0063} (V^{1/3}H^{-1})^{-0.0480}. \quad (8)$$

The histogram of relative frequency (Figure 4A) shows that log(H/L) regression residuals approximately fit a normal distribution, which supports the normality assumption. The plot of residuals shows an absence of trends (Figure 4B), indicating the independence in residuals and its homogeneity of variance (Liu et al., 2021a). Moreover, the p value (0.0062) of the significance test of Eq. 8 is less than 0.05, indicating that the regression relationship is statistically significant at a 95% confidence level. The regression results indicate that the best-fit multivariate regression model (Eq. 8) has a high correlation coefficient (R^2=0.93) and a strong statistical significance level.

However, some uncertain parameters were included in the empirical model, resulting in limitations in its practical engineering application. For example, the fall height H is an uncertain parameter before the occurrence of rock avalanches. Some scholars have introduced the height of the source area (h') or slope height (h) to replace the fall height (H) in empirical models (e.g., Zhan et al., 2017; Fan et al., 2015). However, the slope height (h) has much more physical significance because it implies the preimpact potential energy of rock avalanches (Guo et al., 2014). In addition, the channel angle (β) is closely related to the slope angle (α) and slope transition angle (γ). Therefore, the slope height (h), landslide volume (V), slope angle (α), slope transition angle (γ) and deflection angle (θ) were considered in the improved empirical model (see Eq. 9). Eventually, the best-fit regression equation was derived from the dataset of Table 2, as shown in Eq. 9:

$$h/L = e\,0.1621\,(tan\,\alpha)^{0.6958} (\tan\theta)^{0.0727} (\sin\gamma)^{0.0865} (V^{1/3}h^{-1})^{-0.1206} \quad (9)$$

The adjusted coefficient of determination R^2 is relatively high, with a value of 0.7, which indicates a good correlation between h/L and the landslide volume, slope height and the three characteristic parameters of local topography. This high R^2 indicates the small scatter in the data points about the regression line. In addition, the histogram of relative frequency (Figure 5A) shows that the regression residuals of log h/L also follow an approximate normal distribution. Meanwhile, the plot of residuals (Figure 5B) demonstrates the independence in residuals and homogeneity of variance. The p value (0.036) of the significance test for Eq. 9 is less than 0.05,

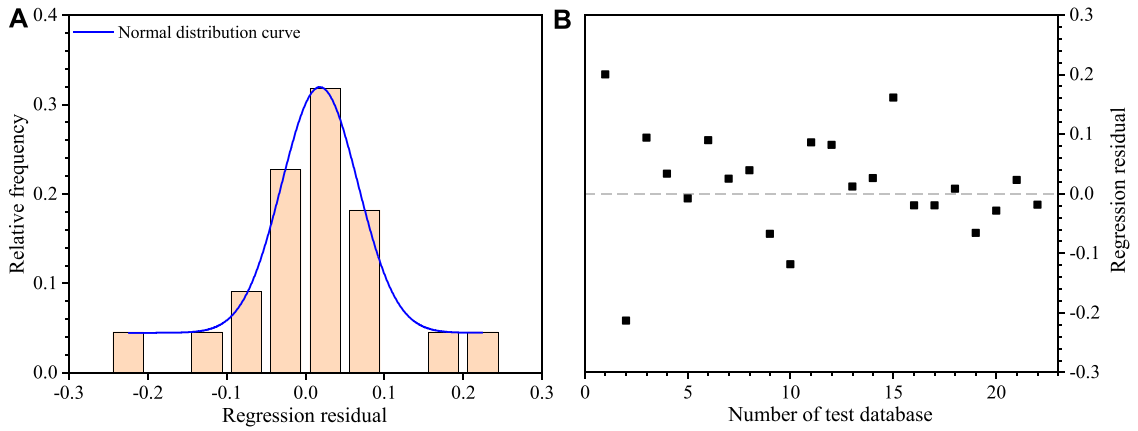


FIGURE 3
The regression analysis results of Eq. 7-2 based on the test database of 22 channelized rock avalanches: **(A)** Histogram of the relative frequency of the log(H/L) regression residuals. **(B)** Plot of regression residuals of log(H/L).

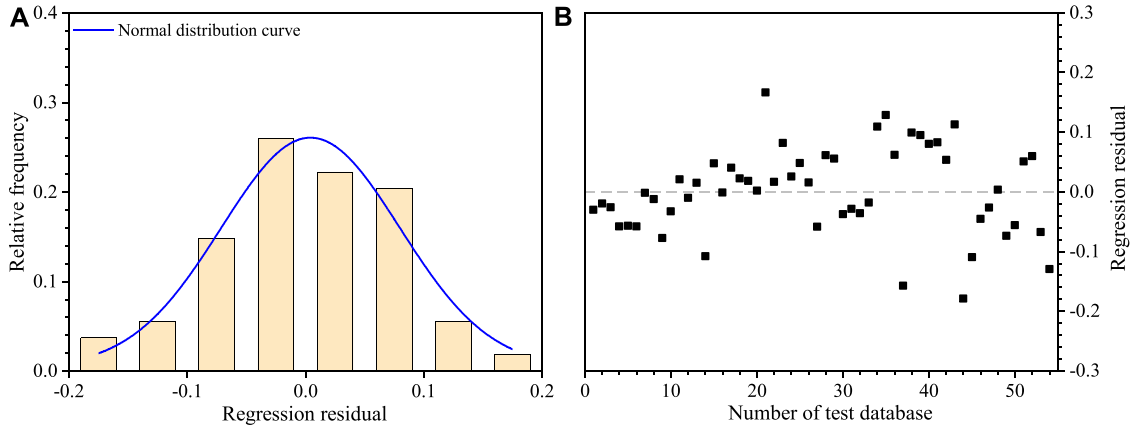


FIGURE 4
The regression analysis results of Eq. 8 based on the database of 54 deflected-type rock avalanches: **(A)** Histogram of the relative frequency of the log(H/L) regression residuals. **(B)** Plot of regression residuals of log(H/L).

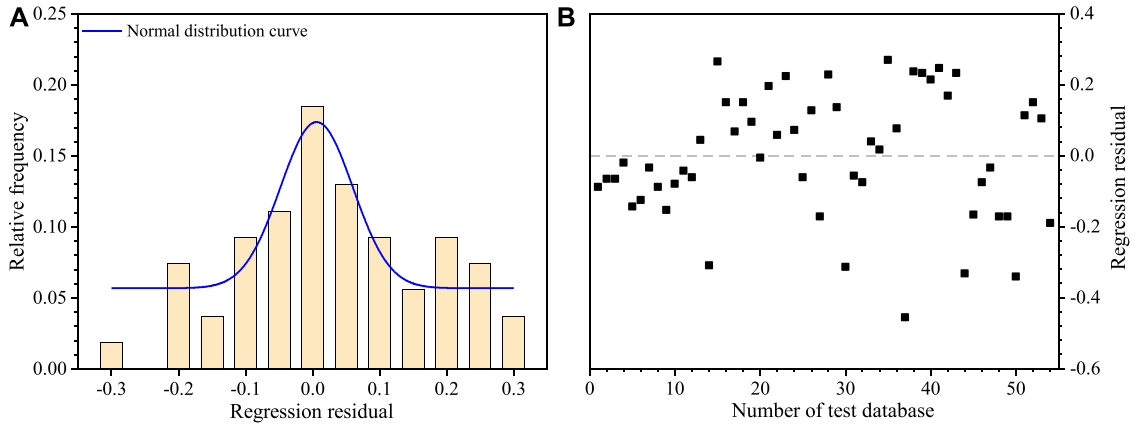


FIGURE 5
The regression analysis results of Eq. 9 based on the database of 54 deflected-type rock avalanches: **(A)** Histogram of the relative frequency of the log(h/L) regression residuals. **(B)** Plot of regression residuals of log(h/L).

indicating that this improved empirical model is also statistically significant at a 95% confidence level.

4.3 Applicability validation

The agreement between predictions and observations is usually used to evaluate the prediction accuracy of the empirical model (Qiu et al., 2018). Figure 6A compares the predicted travel distances estimated by Eq. 9 with the observed avalanches of 54 deflected-type rock avalanches. The predicted values of the samples are close to the observed values (Figure 6A). The estimation error results show that Eq. 9 has an average error of < 20% (Table 2). The self-verification results suggest that Eq. 9 is valid for most deflection-type rock avalanches (Figure 6A). The database of Table 3 is used to further discuss the validity of Eq. 9. The compared results between the observed and predicted travel distances of 10 deflected-type rock avalanches are depicted in Figure 6B. The analysis results of the estimation error show that the maximum error is 41.81%, the minimum error is 0.46% and the average error is approximately 20% (Table 3). Based on this, it can be determined that the improved empirical model (Eq. 9) achieves an acceptable prediction accuracy for the travel distance of deflected-type rock avalanches in the Wenchuan earthquake area.

5 Discussion

The H/L ratio is commonly used to study the mobility of rock avalanches in previous study (e.g., Qiu et al., 2018; Liu et al., 2021a).

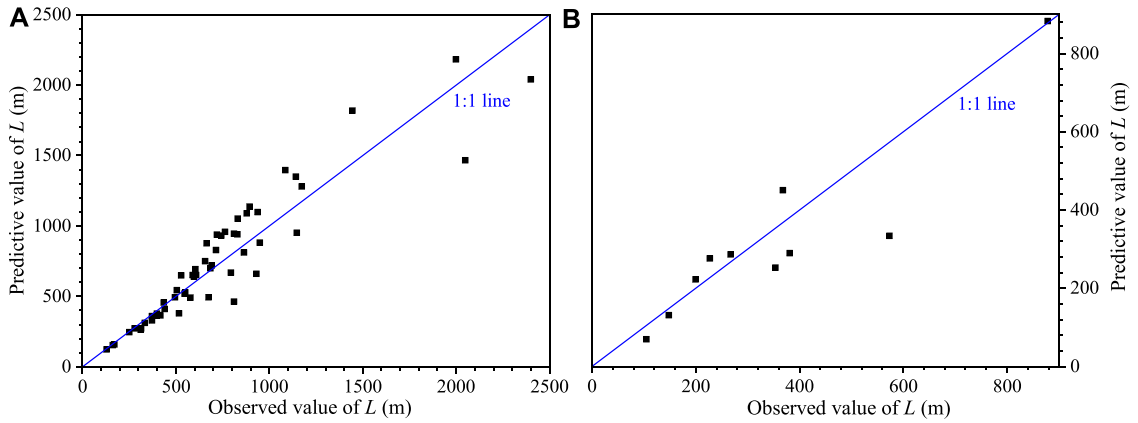


FIGURE 6
The comparison between the observed and predicted travel distances for Eq. 9: **(A)** Comparison results of 54 deflected-type rock avalanches; **(B)** comparison results of an independent validation dataset of 10 deflected-type rock avalanches.

Many studies have shown a negative correlation between the H/L ratio and the landslide volume, although the slope and intercept of its regressive relationship are varied (e.g., Hattanji and Moriwaki 2009; Qiu et al., 2018; Strom et al., 2019; Mitchell et al., 2020). In this study, we propose an alternative parameter, the h/L ratio, and the regression analysis results show that the h/L ratio decreases with an increasing landslide volume (V), suggesting the h/L ratio also can be used to evaluate the mobility of rock avalanches. Compared to H/L ratio, the h/L ratio is preferable as a measure of the travel distance prediction of rock avalanches due to the higher coefficient of determination of h. In addition, the simple linear regression of the logarithm of the h/L ratio plotted against the logarithm of $V^{1/3}/h$ also show a negative correlation, but the very low coefficient of determination R^2 (0.26) indicates that the simple linear regression is weak (Figure 7A). This finding may primarily be attributed to neglecting the effects of other influence factors, such as local topographic parameters, etc., As shown in Eq. 9, the multiple linear regression of the logarithm of h/L versus the logarithm of other parameters consisting of slope height (h), landslide volume (V), slope angle (α), deflection angle (θ) and slope transition angle (γ) has a high correlation coefficient (R^2=0.7) and strong statistical significance level. It can be concluded that the local topography plays an important role in the mobility of rock avalanches. Therefore, more consideration should be given to the influence of local topographic parameters in the empirical model for the travel distance prediction of deflection-type rock avalanches.

In previous study, the effects of local topography on rock avalanches' mobility have been constantly focus of attention by some authors who explored the variability in behaviour between the rock avalanches events of different local topography categories (e.g., Zhang and Yin, 2013; Liu et al., 2021a). However, the focus of this paper is the sensitivity analysis of different local topographic parameters to rock avalanches' mobility for a certain confinement type. Therefore, another three best-fit regression models, in which only two local topographic parameters are considered, were derived from the dataset of 54 deflected-type rock avalanches (Table 4). A comparison shows that the correlation coefficients for these three regression models are 0.52, 0.68, 0.67 respectively, which both lower than that of Eq. 9. This means that the travel distance predicted using three independent topographic variables performs better than the travel distance predicted using two independent variables. Additionally, MAPE and TIC values can directly reflect the effect of various topographic parameters on the mobility of deflected-type rock avalanches. The results show that the MAPE and TIC values calculated by Eq. 12 are the lowest, followed by the MAPE and TIC values calculated by Eq. 11. The MAPE and TIC values calculated by Eq. 10 are the highest. The results suggest that the prediction accuracy decreases in turn for Eqs 10–12. Hence, according to the MAPE and TIC values, it can be inferred that the order of sensitivity of the three independent topographic parameters on the mobility of deflected-type rock avalanches is as follows from large to small successively: $\alpha > \theta > \gamma$. This indicate that the slope angle (α) is predominant in the travel distance, which is reverse to the channelized rock avalanches. Previous study shows the slope angle (α) does not have a significant correlation with travel distance, whereas the channel angle (β) plays the dominating role in the travel distance of channelized rock avalanches (Zhan et al., 2017). Moreover, the sensitivity analysis results indicate that the mobility of deflected-type rock avalanches is also strongly dependent on the deflection angle (θ), which is different from channelized rock avalanches.

The positive correlation between travel distance and landslide volume of rock avalanches has been discussed in previous study (e.g., Budetta and De Riso 2004; Guo et al., 2014), and the predominant effects of landslide volume on mobility of rock avalanches was stressed. In this study, 54 deflected-type rock avalanches were divided into three categories, including large-scale ($V > 100 \times 10^4$ m^3), medium-scale ($10 \times 10^4 \leq V \leq 100 \times 10^4$ m^3) and

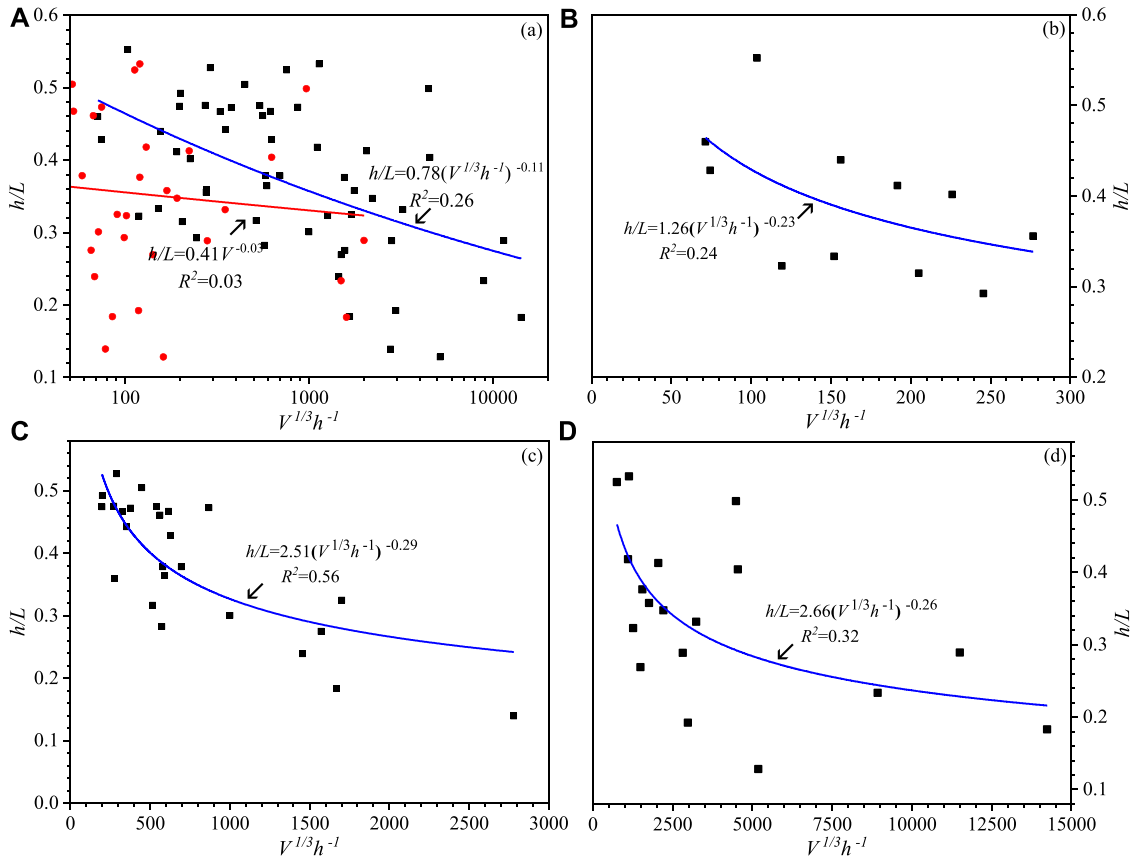


FIGURE 7
Simple linear regression of the logarithm of the h/L ratio predicted from the logarithm of $V^{1/3}/h$ or V without consideration of the local topography: **(A)** Regardless of the volume effect; **(B)** large-scale rock avalanches; **(C)** medium-scale rock avalanches; **(D)** small-scale rock avalanches.

TABLE 4 Comparison of the regression results for different empirical models using different independent topographic variables.

Equation	Intercept	Coefficients				R^2	*p*-value	Comments	MAPE (%)	TIC
		tanα	tanθ	sinγ	$V^{1/3}h^{-1}$					
Eq. 9	1.1760	0.6958	0.0727	0.0865	−0.1206	0.70	0.035	Good correlation	14.61	0.0194
Eq. 10	1.7153	—	0.0942	0.1905	−0.1902	0.52	0.05	Minor correlation	17.84	0.0281
Eq. 11	1.1026	0.7226	—	0.0777	−0.1104	0.68	0.038	Good correlation	16.57	0.0215
Eq. 12	0.8907	0.8361	0.0633	—	−0.0929	0.67	0.039	Good correlation	15.49	0.0196

small-scale (V <10 × 10^4 m^3) rock avalanches according to the landslide volume. The results show a lower significance level and correlation coefficients of the simple linear regressions of the logarithm of h/L versus the logarithm of $V^{1/3}/h$ for rock avalanches with different scales (Figures 7B–D). This indicate that the simple linear regressions between the logarithm of h/L ratio and logarithm of $V^{1/3}$/h is rather weak. However, the multiple linear regression models in which the local topographic parameters were considered (Eqs. 13–15) have higher significance levels and correlation coefficients (Table 5). The correlation coefficients in sequence from large to small corresponds to the regression models of small-, medium- and large-scale rock avalanches. In addition, the calculation results of MAPE and TIC show that the prediction accuracy from large to small corresponds to Eqs 13–15 (Table 5). This result suggests that the effect of local topography on the mobility of rock avalanches gradually decreases with increasing landslide scale. Therefore, we suggest that more quantifiable influential factors should be introduced in the empirical model to

TABLE 5 The multiple linear regression results for deflection-type rock avalanches with different landslide scales.

Equations	Volume scale	Intercept	Coefficients				R^2	*p*-value	Comments	MAPE (%)	TIC
			tanα	tanθ	sinγ	$V^{1/3}h^{-1}$					
Eq. 13	Small ($<10^4m^3$)	1.0314	0.7577	0.0717	0.0616	−0.1173	0.96	0.0025	Strong correlation	8.15	0.0550
Eq. 14	Medium (10^4–10^6m^3)	2.9871	0.3808	0.1011	0.0886	−0.2834	0.81	0.026	High correlation	13.59	0.0880
Eq. 15	Large ($\geq10^6m^3$)	2.9084	0.7796	0.0434	0.0854	−0.2241	0.71	0.045	Good correlation	20.72	0.1129

improve the prediction accuracy of large-scale deflection-type rock avalanches.

Empirical models as a practical tool to estimate travel distance can be introduced in the GIS operation platform, which can provide a preliminary delineation of potentially endangered regions of potential rock avalanche (Mergili et al., 2015). This puts forward higher requirements for the accuracy of the prediction models. Although we have verified the validity of the presented empirical model (see Eq. 9) for travel distance prediction of deflected-type rock avalanches triggered by earthquake, there are also some limitations or constraints. On the one hand, the effects of numerous factors, such as ground water, substrate material, stratum lithology, etc., on travel distance were not considered in empirical model. Previous studies have revealed that these factors have a significant impact on the mobility of rock avalanches (e.g., Corominas 1996; Sassa et al., 2004; Guo et al., 2014). For example, due to extensive distribution of groundwater (Zhang et al., 2021), it provides hydrological conditions for the seismic liquefaction of the base material on the movement path, which contributes to the long-distance movement of rock avalanches. Therefore, it deserves more attention that how to quantify these relevant influence factors and incorporate them into the empirical model for travel distance prediction in the future study. On the other hand, in this paper, our database is limited to 54 deflected-type rock avalanches with only seven quantifiable parameters, which might result in wide dispersion and a low coefficient of correlation in some empirical models. Therefore, the next phase of the research focus on a much larger rock avalanche database creation with more quantifiable influential factors, which is conducive to further improve the prediction accuracy of the empirical model.

6 Conclusion

In this study, a database consisting of 54 deflection-type rock avalanches triggered by the Wenchuan earthquake was compiled to obtain a best-fitting empirical model for travel distance prediction. The results indicated that the multiple linear regression of the logarithm of h/L versus the logarithm of other multivariable parameters consisting of slope height (h), landslide volume (V), slope angle (α), deflection angle (θ) and slope transition angle (γ) had a high correlation coefficient and strong statistical significance level. The validity of the proposed empirical model was verified by an independent validation database consisting of 10 deflected-type rock avalanches in the same area. One of the greatest advantages of this empirical model is that all parameters can be quantifiable and obtained before a landslide occurs; thus, this model might be practically applicable in the Wenchuan earthquake area. The results also suggested that the influence of the slope angle (α) on the mobility of rock avalanches was greater than that of the deflection angle (θ) and slope transition angle (γ). However, the influence of local topography on the mobility of large-scale rock avalanches was less than that of small- and medium-scale rock avalanches.

Data availability statement

The original contributions presented in the study are included in the article/Supplementary Material, further inquiries can be directed to the corresponding author.

Author contributions

ZP: Supervision; Project administration; Writing- reviewing and editing. HY: Methodology; Investigation; Writing-original draft preparation. ZH: Investigation; Data-gathering. JL: Investigation; Drafting. XX: Investigation; Data-gathering.

Acknowledgments

We sincerely thank anonymous reviewers for their constructive and valuable suggestions, which help improving this manuscript substantially.

Conflict of interest

The authors declare that the research was conducted in the absence of any commercial or financial relationships that could be construed as a potential conflict of interest.

Publisher's note

All claims expressed in this article are solely those of the authors and do not necessarily represent those of their affiliated organizations, or those of the publisher, the editors and the reviewers. Any product that may be evaluated in this article, or claim that may be made by its manufacturer, is not guaranteed or endorsed by the publisher.

References

Armstrong, J. S., and Collopy, F. (1992). Error measures for generalizing about forecasting methods: Empirical comparisons. *Int. J. Forecast* 8, 69–80. doi:10.1016/0169-2070(92)90008-W

Basharat, M., and Rohn, J. (2015). Effects of volume on travel distance of mass movements triggered by the 2005 Kashmir earthquake, in the Northeast Himalayas of Pakistan. *Nat. Hazards* 77, 273–292. doi:10.1007/s11069-015-1590-4

Budetta, P., and De, Riso. R. (2004). The mobility of some debris flows in pyroclastic deposits of the northwestern Campanian region (southern Italy). *Bull. Eng. Geol. Environ*. 63 (4), 293–302. doi:10.1007/s10064-004-0244-7

Chen, L. C., Yang, H. Q., Song, K. L., Huang, W., Ren, X. H., and Xu, H. (2021). Failure mechanisms and characteristics of the Zhongbao landslide at liujing village, wulong, China. *Landslides* 18, 1445–1457. doi:10.1007/s10346-020-01594-1

Corominas, J. (1996). The angle of reach as a mobility index for small and larger landslides. *Can. Geotech. J.* 33, 260–271. doi:10.1139/t96-005

Ding, M. T., and Hu, K. H. (2014). Susceptibility mapping of landslides in Beichuan County using cluster and MLC methods. *Nat. Hazards* 70, 755–776. doi:10.1007/s11069-013-0854-0

Fan, X. M., Hsein, J. C., Janusz, W., Huan, R. Q., Xu, Q., Gianvito, S., et al. (2018). What we have learned from the 2008 wenchuan earthquake and its aftermath: A decade of research and challenges. *Eng. Geol.* 241, 25–32. doi:10.1016/j.enggeo.2018.05.004

Fan, X. Y., Leng, X. Y., and Duan, X. D. (2015). Influence of terrain factor on movement distances of toe-type and turning-type landslides triggered by earthquake. *Chin. J. Rock Soil Mech*. 36, 1380–1388. doi:10.16285/j.rsm.2015.05.021

Finlay, P. J., Mostyn, G. R., and Fell, R. (1999). Landslide risk assessment: Prediction of travel distance. *Can. Geotech. J.* 36, 556–562. doi:10.1139/cgj-36-3-556

Gao, Y., Yin, Y. P., Li, B., Feng, Z., Wang, W. P., and Zhang, N., (2017). Characteristics and numerical runout modeling of the heavy rainfall-induced catastrophic landslide–debris flow at sanxicun, dujiangyan, china, following the wenchuan Ms 8.0 earthquake. *Landslides* 14 (4), 1361–1374. doi:10.1007/s10346-016-0793-4

Ge, Y. F., Tang, H. M., Eldin, M. A. M. Ez., Chen, H. Z., Zhong, P., and Zhang, L., (2019). Deposit characteristics of the Jiweishan rapid long-runout landslide based on field investigation and numerical modeling. *Bull. Eng. Geol. Environ.* 78 (6), 4383. doi:10.1007/s10064-018-1422-3

Ge, Y. F., Zhou, T., Tang, H. M., and Lin, Z. S. (2020a). Influence of the impact angle on the motion and deposition of granular flows. *Eng. Geol.* 275, 105746. doi:10.1016/j.enggeo.2020.105746

Ge, Y. F., Zhou, T., Tang, H. M., and Lin, Z. S. (2020b). Influence of the impact angle on the motion and deposition of granular flows. *Eng. Geol* 275, 105746. doi:10.1016/j.enggeo.2020.105746

Guo, D., Hamada, M., He, C., Wang, Y., and Zou, Y. (2014). An empirical model for landslide travel distance prediction in Wenchuan earthquake area. *Landslides* 11 (2), 281–291. doi:10.1007/s10346-013-0444-y

Hattanji, T., and Moriwaki, H. (2009). Morphometric analysis of relic landslides using detailed landslide distribution maps: Implications for forecasting travel distance of future landslides. *Geomorphology* 103 (3), 447–454. doi:10.1016/j.geomorph.2008.07.009

Heim, A. (1932). *Landslides and human lives*. Vancouver, BC, Canada: Bitech Publishers. 0-921095-06-6.

Hsu, K. J. (1975). Catastrophic debris streams (sturzstroms) generated by rockfalls. *Geol. Soc. Am. Bull.* 86, 1292–2140. doi:10.1130/0016-7606(1975)86<129:CDSSGB>2.0.1

Huang, D., Li, Y. Q., Song, Y. X., Xu, Q., and Pei, X. J. (2019). Insights into the catastrophic xinmo rock avalanche in maoxian county, China: Combined effects of historical earthquakes and landslide amplification. *Eng. Geol.* 258, 105158. doi:10.1016/j.enggeo.2019.105158

Huang, T., Ding, M. T., Tao, S., Tian, S. J., and Yang, J. T. (2017). Numerical simulation of a high-speed landslide in Chenjiaba, Beichuan, China. *J. Mt. Sci.* 14 (11), 2137–2149. doi:10.1007/s11629-017-4516-7

Hungr, O., and Evans, S. G. (2004). Entrainment of debris in rock avalanches: An analysis of a long run-out mechanism. *Geol. Soc. Am. Bull.* 116 (9–10), 1240–1252. doi:10.1130/B25362.1

Hungr, O., Leroueil, S., and Picarelli, L. (2014). The Varnes classification of landslide types, an update. *Landslides* 11, 167–194. doi:10.1007/s10346-013-0436-y

Kang, C., Ren, D. X., Gao, X. F., Han, C. T., and Wang, Y. X. (2021). Study of kinematic characteristics of a rock avalanche and subsequent erosion process due to a debris flow in Wenjia gully, Sichuan, China. *Nat. Hazards* 106, 937–964. doi:10.1007/s11069-021-04501-6

Kang, Y., Zhao, C. Y., Zhang, Q., Lu, Z., and Li, B. (2017). Application of InSAR techniques to an analysis of the guanling landslide. *Remote. Sens.* 9 (10), 1046. doi:10.3390/rs9101046

Knapp, S., and Krautblatter, M. (2020). Conceptual framework of energy dissipation during Disintegration in rock avalanches. *Front. Earth Sci.* 8, 263. doi:10.3389/feart.2020.00263

Leuthold, R. M. (1975). On the use of Theil's inequality coefficients. *Am. J. Agric. Econ.* 57, 344–346. doi:10.2307/1238512

Li, Y., Zhou, R. J., Zhao, G. H., Li, H. B., Su, D. C., and Ding, H. R., (2014). Tectonic uplift and landslides triggered by the wenchuan earthquake and constraints on orogenic growth: A case study from hongchun gully, longmen mountains, sichuan, China. *Quatern. Int.* 349 (28), 142–152. doi:10.1016/j.quaint.2014.05.005

Liu, H. W., Zhao, X. Y., and Xiao, D. (2021a2021). Effects of local topography on the mobility of rock avalanches: A statistical analysis based on 36 cases from south-western China. *Eng. Geol.* 294, 106351. doi:10.1016/j.enggeo.2021.10635

Liu, H. X., Qiu, T., and Xu, Q. (2021b). Dynamic acceleration response of a rock slope with a horizontal weak interlayer in shaking table tests. *PLoS ONE* 16 (4), e0250418. doi:10.1371/journal.pone.0250418

Mergili, M., Krenn, J., and Chu, H-J. (2015). r.randomwalk v1, a multi-functional conceptual tool for mass movement routing. *Geosci. Model Dev.* 8, 4027–4043. doi:10.5194/gmd-8-4027-2015

Mitchell, A., McDougall, S., Nolde, N., BrideauWhittall, M. A. J., and Aaron, J. B. (2020). Rock avalanche runout prediction using stochastic analysis of a regional dataset. *Landslides* 17, 777–792. doi:10.1007/s10346-019-01331-3

Qiu, H. J., Cui, P., Hu, S., Regmi, A. D., Wang, X. G., and Yang, D. D. (2018). Developing empirical relationships to predict loess slide travel distances: A case study on the loess plateau in China. *B. Eng. Geol. Environ.* 77, 1299–1309. doi:10.1007/s10064-018-1328-0

Sassa, K., Wang, G. H., Fukuoka, H., Wang, F. W., Ochiai, T., and Sugiyama, M. (2004). Landslide risk evaluation and hazard zoning for rapid and long-travel landslides in urban development areas. *Landslides* 1, 221–235. doi:10.1007/s10346-004-0028-y

Strom, A. L., Li, L., and Lan, H. (2019). Rock avalanche mobility: Optimal characterization and the effects of confinement. *Landslides* 16, 1437–1452. doi:10.1007/s10346-019-01181-z

Tang, C., van Asch, T. W. J., Chang, M., Chen, G. Q., Zhao, X. H., and Huang, X. C. (2012). Catastrophic debris flows on 13 august 2010 in the qingping area, southwestern China: The combined effects of a strong earthquake and subsequent rainstorms. *Geomorphol* 139–140, 559–576. doi:10.1016/j.geomorph.2011.12.021

Wang, H., Ran, Y. K., Li, Y. B., Gomez, F., and Chen, L. C. (2014). Southwest China is on the southeastern edge of the Tibetan Plateau and is characterised by complex geological structures. *Tectonophysics* 628, 206–217. doi:10.1016/j.tecto.2014.04.040

Yang, J. Q., Xu, Z. M., Zhang, R., Chen, J. P., Ren, Z., and Luo, R. Z., (2017). Formation and evolution of Emeishan basalt saprolite in vadose zones of Touzhai landslide source Rockmass. *J. Mt. Sci.* 14 (6), 1174–1184. doi:10.1007/s11629-016-4169-y

Zhan, W. W., Fan, X. M., Huang, R. Q., Pei, X. J., Xu, Q., and Li, W. L. (2017). Empirical prediction for travel distance of channelized rock avalanches in the Wenchuan earthquake area. *Nat. Hazards Earth Syst. Sci.* 17, 833–844. doi:10.5194/nhess-17-833-2017

Zhang, M., Yin, Y., and McSaveney, M. (2016). Dynamics of the 2008 earthquake-triggered wenjiagou creek rock avalanche, qingping, sichuan, China. *Eng. Geol.* 200, 75–87. doi:10.1016/j.enggeo.2015.12.008

Zhang, M., and Yin, Y. P. (2013). Dynamics, mobility-controlling factors and transport mechanisms of rapid long-runout rock avalanches in China. *Eng. Geol.* 167, 37–58. doi:10.1016/j.enggeo.2013.10.010

Zhang, Y. H., Dai, Y. S., Wang, Y., Huang, X., Xiao, Y., and Pei, Q. M. (2021). Hydrochemistry, quality and potential health risk appraisal of nitrate enriched groundwater in the Nanchong area, southwestern China. *Sci. Total Environ*. 784, 147186. doi:10.1016/j.scitotenv.2021.147186

Zhang, Y. H., Yao, R. W., Wang, Y., Duo, J., and Cao, H. W. (2022). Zircon U–Pb and sericite Ar–Ar geochronology, geochemistry and S–Pb–Hf isotopes of the Zebuxia Pb–Zn deposit, Tibet, southwestern China. *Ore Geol. Rev*. 148, 104999. doi:10.1016/j.oregeorev.2022.104999

Zheng, G., Xu, Q., and Peng, S. Q. (2018). Chute experiments of the long-runout distance of rock avalanche (in Chinese). *Rock Soil Mech*. 40 (12), 1–10. doi:10.16285/j.rsm.2018.1827

frontiers | Frontiers in Earth Science

TYPE Original Research
PUBLISHED 06 January 2023
DOI 10.3389/feart.2022.946301

Check for updates

OPEN ACCESS

EDITED BY
Xiangjun Pei,
Chengdu University of Technology, China

REVIEWED BY
Zhilu Chang,
Nanchang University, China
Zhice Fang,
China University of Geosciences Wuhan, China

*CORRESPONDENCE
Stephen G. Evans,
sgevans@uwaterloo.ca

SPECIALTY SECTION
This article was submitted to Geohazards and Georisks, a section of the journal Frontiers in Earth Science

RECEIVED 17 May 2022
ACCEPTED 23 August 2022
PUBLISHED 06 January 2023

CITATION
Han M, Evans SG, He K, Sun H and Ma Z (2023), The structure of a magnitude-frequency relation for debris flows conditioned by earthquake shock. *Front. Earth Sci.* 10:946301. doi: 10.3389/feart.2022.946301

COPYRIGHT
© 2023 Han, Evans, He, Sun and Ma. This is an open-access article distributed under the terms of the Creative Commons Attribution License (CC BY). The use, distribution or reproduction in other forums is permitted, provided the original author(s) and the copyright owner(s) are credited and that the original publication in this journal is cited, in accordance with accepted academic practice. No use, distribution or reproduction is permitted which does not comply with these terms.

The structure of a magnitude-frequency relation for debris flows conditioned by earthquake shock

Mei Han [1], Stephen G. Evans[2]*, Kun He[3], Hao Sun[4] and Zhigang Ma[5]

[1]Faculty of Mathematics, Southwest Jiaotong University, Chengdu, China, [2]Department of Earth and Environmental Sciences, University of Waterloo, Waterloo, ON, Canada, [3]Faculty of Geosciences and Environmental Engineering, Southwest Jiaotong University, Chengdu, China, [4]Key Laboratory of Mountain Hazards and Earth Surface Process, Institute of Mountain Hazards and Environment, Chinese Academy of Sciences, Chengdu, China, [5]Sichuan Institute of Land and Space Ecological Restoration and Geological Hazard Prevention, Chengdu, China

Debris flow is a major secondary geological process associated with the 2008 M7.9 Wenchuan Earthquake area, causing the loss of around 200 lives as well as extensive property damage. Based on data developed over the past 21 years (1998–2018) of continuous monitoring of debris flow events in Sichuan, the temporal and spatial aspects of debris flows have been analyzed, including magnitude and frequency. The 21-year study period is divided into three time-intervals: 1998–2007 (pre-earthquake), 2008–2013 (short-term post-earthquake), and 2014–2018 (long-term post-earthquake). Distribution maps are plotted to compare debris flow distribution density in the three periods and to visualize debris flow development throughout Sichuan Province from 1998 to 2018. Many large-scale debris flows occur in groups immediately following the earthquake (2008–2013). After 2014, the magnitude and frequency of debris flows begin to decrease and gradually returned near to the pre-earthquake level as the damaged landscape recovered. The effect of rainfall is investigated by analyzing a 21-year record of precipitation; Following the earthquake the threshold rainfall values for debris flow triggering decrease only to recover to pre-earthquake levels as the landscape heals. Magnitude-frequency (M-F) relations for debris flows of the three periods were developed, and the distribution can be well fitted by a power-law function. Finally, the work done by debris flow was defined by multiplying the magnitude by frequency. At the regional scale, the work peaks in the three time periods have been determined and it is found that the peaks corresponded with the larger debris flow sizes. The concept of offset is introduced to describe the shift of the work peak in relation to the probability peak and is termed the Wolman-Miller offset. It is concluded that with a greater offset in the short-term post-earthquake period, more work has been done by larger events and that the greater proportion of the volume being mobilized by larger events occurring more frequently is a key process in the landscape returning to a pre-earthquake (equilibrium) state. The recovery of an earthquake-damaged landscape represents a transient period of high hazard that should be considered in

any hazard assessment of earthquake-triggered landslides (in addition to co-seismic landslides).

KEYWORDS

debris flow, temporal and spatial distribution, 2008 wenchuan earthquake, magnitude-frequency relation, work peak, Wolman-Miller

Introduction

Debris flow, a major disaster-generating hazard in mountainous areas, is often triggered by heavy rains. It mobilizes poorly sorted rock and soil debris from hillslopes and stream channels which cause destructive mass movements that frequently result in both loss of life and damage to infrastructures (Jakob and Hungr, 2005; Dowling and Santi, 2014; Chang et al., 2017; Hu et al., 2019). Many studies focused on the mechanisms and behavior of debris flows (Iverson, 1997; Gregoretti, 2000; Brayshaw and Hassan 2009; Tang et al., 2011a; Yu et al., 2021). Of particular interest is the geomorphic response of landscapes to earthquake shaking, especially the occurrence and characteristics of post-seismic debris flows (Marc et al., 2015; Marc et al., 2016; Fan et al., 2019).

It is well known that the occurrence rate of rainfall-generated debris flows (and similar landslide types) increases over a number of years after a strong earthquake in mountainous area, marking a period of enhanced post-seismic landsliding (Lin et al., 2003; Fan et al., 2019; Cui et al., 2022). The rate then decreases (Fan et al., 2018a), finally reverting to near pre-earthquake levels (Hovius et al., 2011; Marc et al., 2015). It has also been established that, in the aftermath of a strong earthquake, the rainfall threshold for debris flows is reduced (Shieh et al., 2009; Yu et al., 2014; Guo et al., 2016a; Guo et al., 2016b; Fan et al., 2019). This reduction persists for a number of years before reverting back (increasing) to near pre-earthquake levels (Yu et al., 2014; Zhang and Zhang, 2017; Domènech et al., 2019). All the effects indicate a dramatic transient increase in the sensitivity of the landscape to rainfall which decreases in a relatively short time after a seismic shock due to the exhaustion of source materials. The exhaustion is caused by debris flow mobilisation and the healing of the landscape through re-vegetation (Lin et al., 2006; Li et al., 2016a; Domènech et al., 2019; Shen et al., 2020a; He et al., 2022).

However, still largely unknown are the effects of strong earthquakes on pre-earthquake debris flow magnitude frequency relations and how these change in the post-seismic period as the landscape reverts to a pre-earthquake state. Some questions that may be asked include 1) How does the size distribution of debris flows change during this process? 2) Does the contribution of debris flows of certain sizes to total debris volume mobilised change? 3) How do the frequencies of debris flow sizes change? 4) How long does the effect of earthquake-generated landscape damage persist? and 5) what are the implications of these changes for landscape evolution and the mass movement geomorphology of terrain subjected to earthquake shock? Marc et al. (2015) studied transient changes of landslide rates in epicentral areas of four major earthquakes and established (see Figure 3 in Marc et al., 2015) that the magnitude (measured by area)–frequency relation for landslides during the recovery phase of the post-seismic period is similar to the background (pre-earthquake period) of the four earthquakes studied suggesting a process of full recovery to pre-seismic levels. However, the resolution of their landslide data could not be used to investigate the M-F relation of landslides in the immediate post-seismic period. Thus, the limit of a landslide M-F relation resulting from earthquake-generated landscape damage is defined.

The M7.9 Wenchuan Earthquake on 12 May 2008 caused serious destruction owing to its high magnitude and long fracture zone (Yin, 2008; Huang and Meng, 2009; Cui et al., 2021). During and immediately after the Wenchuan Earthquake, the terrain surface was severely altered because of the generally high seismic intensity (IX degrees or more). Compared with other types of landslides, debris flows played a more significant role in earthquake-related geological disasters in Sichuan Province. Post-earthquake debris flows were caused by an acute increase of slumped material that blocked streams in debris flow gullies. This contributed to high-frequency and spatially grouped debris flows under significantly decreased critical rainfall values. For example, the first debris flow, the 72-Gully Debris Flow occurred in Beichuan County on 24 September 2008, 4 months after the Wenchuan Earthquake killed 42 people (Tang et al., 2011a). On 17 July 2009, a large-scale debris flows occurred in Dujiangyan County-level City (You et al., 2012). Moreover, a total of 85 debris flows were induced by heavy rainfall on 13 August 2010 in Qingping Town, Yinxiu Town, and Longchi Town (Tang et al., 2011b). In addition, debris flows occurred along the Dujiangyan-Wenchuan (Du-wen) Expressway and Dujiangyan County-level City in the seismic area on 10 July 2013 (Ge et al., 2015).

The Wenchuan Earthquake showed that a catastrophic seismic event can 1) produce a great deal of loose landslide deposits in stream channels and on slopes and 2) could also result in more active mass movement geo-hazard (such as landslides and debris flows) than pre-earthquake periods (Fan et al., 2018c; Liu et al., 2021a; He et al., 2021). Coseismic landslide deposits and shattered mountain slopes provided plentiful source materials for debris flow initiation, which also required a lower antecedent rainfall and a lower hourly rainfall intensity threshold to trigger debris flow after an earthquake (Zhou and Tang 2014).

Consequently, debris flows occurred more frequently in the region affected by earthquake shock. Furthermore, landslides triggered by earthquakes have a major influence on long-term slope erosion and sediment yield (Guo et al., 2021; Xiong et al., 2021), which can directly lead to long-term material supply to valley floors, and increase the magnitudes of debris flows for a post-earthquake period.

Since the earthquake, many scientists have explored the post-seismic effect on debris-flow occurrence, mainly involving characteristics, initiation and runout mechanisms (Zeng et al., 2014; Hu and Huang 2017; Shen et al., 2020b), triggering rainfall thresholds variation (van Asch et al., 2014; Chang et al., 2021), and long-term evolution of debris flow occurrence (Cui et al., 2014; Zhang et al., 2014). The volume of erodible materials produced by coseismic landslides in the Wenchuan Earthquake reached 5–15 km^3 and was deposited on slopes or in gullies of mountainous areas, which in turn provided abundant source materials for debris flow generation (Parker et al., 2011). Tang et al. (2011b) and Tang et al. (2012) studied the combined effects of strong earthquake and rainstorms on the 13 August 2010 debris flows in Qingping Town, and found that the deposit had a volume ranging from 5,760 m^3 to 3.1 Mm^3, showing the huge possibility for future debris flow activity.

In addition, post-seismic rainfall thresholds have also been widely studied since the Wenchuan event. The critical amount of accumulative precipitation and hourly rainfall intensity to initiate debris flow decreased after the Wenchuan Earthquake (Tang et al., 2009; Liu et al., 2021b). Yu et al. (2014) suggested that the rainfall triggering threshold is lower after the earthquake than that before the earthquake (cf. Marc et al., 2015). Zhang and Zhang (2017) revealed that the post-seismic rainfall thresholds for debris flow triggering decreased by 75% after the Wenchuan Earthquake. Despite the fact that there have been a large number of studies on the long-term changes in debris flow occurrence over time (Fan et al., 2018c; Xiong et al., 2021), the M-F relation for debris flow activity before and after the Wenchuan Earthquake are still poorly documented and largely understudied.

Debris-flow activity can be characterized by the magnitude and frequency of occurrence, and magnitude-frequency (M-F) characteristics are essential elements of the debris flow process in terms of hazard assessment (van Steijn, 1996; Hungr et al., 2008; Jakob and Friele, 2010). The M-F relation at a regional scale can be used to characterize debris-flow activity and indicate the evolutionary process of activity in a given drainage basin thus providing the basis for engineering design, land use planning, and the geomorphic analysis of landscape evolution (Guthrie ad Evans, 2007; Hungr et al., 2008; Mao et al., 2009; Stoffel, 2010). In several studies, M-F relation for debris flows in different areas over different time scales have been obtained using direct and indirect dating methods (Innes, 1983; Innes, 1985; Jakob et al., 2005; Stoffel and Beniston, 2006; Scheidl et al., 2008).

Wolman and Miller (1960) proposed a way to measure of relative effectiveness of geomorphic processes based on the work of varying frequencies and magnitudes, to establish which event of magnitude is the ultimate control landscape morphology. Analysis indicated that a majority of work is accomplished by events of moderate magnitude which recur relatively frequently rather than by rare events of unusual high magnitude. Guthrie and Evans (2007) defined the work of landslides as the product of probability and magnitude (measured by area). Then they applied it to the Clayoquot study area of coastal British Columbia (n=1109) and landslides triggered by the 1994 Northridge earthquake, California (n=11,036) to test the Wolman-Miller hypothesis with respect to landslides. After systematic analysis of these landslide datasets, Guthrie and Evans (2007) found that moderate-sized landslides performed the most work of transporting material on hillslopes (forming the work peak) as originally conceived by Wolman and Miller (1960) for rivers. Landslides that form the work peak are distinct from high-magnitude catastrophic landslides that are themselves formative and system resetting (Guthrie and Evans, 2007).

From an evolution perspective of debris flows after a strong earthquake, most previous studies mainly investigated the initiation conditions of debris flows. In order to determine the effect of the earthquake on debris-flow activity, the pre- and post-earthquake debris-flow occurrence in Sichuan Province was studied by field investigations and statistical analysis. A dataset of 2,572 debris flows derived from work by the Sichuan Institute of Land and Space Ecological Restoration and Geological Hazard Prevention was used to examine the relationships between the magnitude and frequency of debris flows in Sichuan Province in the period of 1998–2018, representing a total mobilized volume of 123.4 Mm^3. According to the database, the evolution of debris flow occurrence before and after the Wenchuan earthquake was illustrated and evaluated both in Sichuan Province as a whole, in the epicentral area itself, and in three sub-regions. At the same time, the work done by debris flow events in the Sichuan database was also analysed by evaluating the work peaks in three periods before and after the Wenchuan Earthquake. The concept of the Wolman-Miller Offset is introduced to describe the offset of the work peak in relation to the probability peak. The specific objectives of this study are thus to evaluate the effect of the M7.9 Wenchuan earthquake on the temporal and spatial patterns of occurrence, to determine the sensitivity of an earthquake damaged landscape through an investigation of rainfall-trigger thresholds, to explore their M-F relation, and to explore the geomorphic work done by debris flows and their contributions by magnitude to the total volume mobilized.

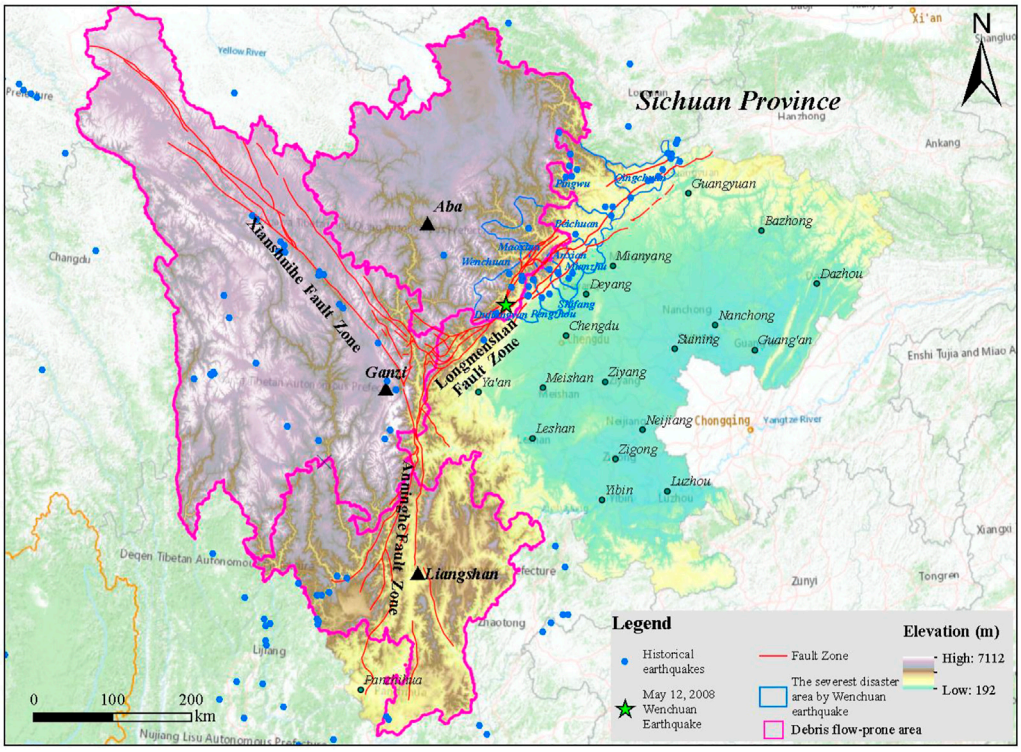


FIGURE 1
Location and tectonic map of the study area (Base map is from http://www.ngac.org.cn/).

Study area

The study area is located in Sichuan Province, southwest China (Figure 1), within the Longmen Shan Thrust Belt Region. The area is characterized by steep mountain terrain, strong tectonic motion due to the rapid convergence of the India Plate at rates of 5–5.5 cm/a (Tang and van Westen, 2018), and frequent strong earthquakes (Figure 1). The study area with the elevation ranging from 302 to 7,143 m has a high relative relief which provides the topographical conditions for the formation of debris flow and landslides. Three major faults (Longmenshan Fault, Anninghe Fault and Xianshuihe Fault) occur in the study area (Figure 1). The Longmenshan Fault is a thrust fault which runs along the base of the Longmen Mountains, with a average strike of approximately NE (Wang and Meng, 2009). Motion on this fault is responsible for the uplift of the mountains relative to the lowlands of the Sichuan Basin to the east. Representing the eastern boundary of the Qinghai-Tibet Plateau, it forms the border between the Bayan Kola Block in the Plateau and the South China block in the Eurasian Plate. Both the 2008 Wenchuan Earthquake and the 2013 Ya'an Earthquake were generated on the main structure of the Longmenshan Fault. The Anninghe Fault Zone is a highly active left-lateral strike-slip fault system with a length of about 200 km. The fault zone is located in the eastern margin area of the Tibetan Plateau, and is a portion of a larger fault system forming the eastern edge of the Sichuan-Yunnan Active Tectonic Block, which is recognized as a seismic gap having a high potential of earthquakes (Wen et al., 2008a). The Xianshuihe Fault is an important left-lateral strike-slip fault on the eastern margin of the Tibetan Plateau. Along the entire length of the fault, there have been seven major earthquakes higher than Ms 7.0 during the past 300 years (Wen et al., 2008b).

The climate in the study area varies from region to region. The river valley area of the Western Sichuan Plateau mainly includes the valleys of Ganzi Prefecture, Aba Prefecture and some areas in the northwest of Liangshan Prefecture, which are characterized by few rainstorms with average daily precipitation of 50 mm or more. The mountainous area around the Sichuan Basin has three rainstorm areas, including Qingyi River, Longmenshan and Dabashan Rainstorm Area, where the average annual rainfall is greater than 1200 mm. In these places, the rainfall is concentrated from June to September, a period accounting for about 70% of the annual rainfall.

Furthermore, in addition to an analysis of Province-wide debris flow occurrence, two regions were selected in the study area for detailed study. These are defined as the severest disaster area, by earthquake damage (and approximately corresponding

to the epicentral area) and the debris-flow prone region by pre-earthquake debris flow activity. The severest disaster area is identified based on field investigations and comprehensive assessment of disaster intensity, severity of the Wenchuan Earthquake and associated geo-hazard influences (see *Report on the Scope of Disaster Affected by Wenchuan Earthquake Disasters Assessment, 2008*). The severest disaster area includes Wenchuan County, Beichuan County, Mianzhu County-level City, Shifang County-level City, Qingchuan County, Maoxian County, Anxian County, Dujiangyan County-level City, Pingwu County, 202 and Pengzhou County-level City. In Figure 1, the severest disaster area affected by the earthquake is defined by the red line, with the epicenter indicated as a red star. Debris-flow prone regions before the earthquake cover Aba Prefecture, Ganzi Prefecture and Liangshan Prefecture (see yellow dots in Figure 1). From the study of the whole Sichuan Province and two sub-regions, the effect of earthquake on the debris flows was comprehensively.

Data sources and methodology

Data sources

Compared to pre-earthquake debris flows, those debris flows that occurred after the Wenchuan Earthquake in the earthquake-affected region show many particular characteristics including the fact that 1) the variety and quantity of material mobilized in debris flow events increased, 2) debris flows often occurred in spatial and temporal clusters and were of long duration, 3) the critical precipitation necessary to trigger debris flows was clearly reduced, and 4) the debris flows formed critical components of long complex post-seismic cascades of geo-hazards (Fan et al., 2019). A large number of collapses, landslides triggered by the Wenchuan Earthquake generated abundant loose source materials for debris flow. On July10th, 2013, several large-scale debris flow events occurred in groups and combined with many previous debris flow gullies (Figure 2A) along the Minjiang River and Du-Wen Highway (Xu 2010), which generally lasted 1.5–2.0 h, even as long as 3 h. Meanwhile, the critical rainfall condition for debris flow formation in some small watersheds reduced from a 50-years to a 20-years rainstorm return period, and the volume of mobilized material reached twice as much as the level of pre-earthquake period (Yu et al., 2011). For example, the area of Wayao and Taoguan Gully are 1.21 and 50.86 km^2 respectively, and the flow volume that rushed out from these two gullies on 10 July 2013 was 1.2×10^5 and 1.08×10^6 m^3 respectively (Figure 2B–E). In summary, the debris flow activity in Sichuan Province, especially in the Wenchuan Earthquake area, has changed significantly since 2008 (Figure 2).

The impact of Wenchuan Earthquake on the occurrence of debris flow events and the outbreak tendency of debris flow in Sichuan Province have been analyzed utilizing a 21-year dataset of debris flow occurrence. The dataset has been developed through 21-years of continuous monitoring and data collection, field investigations and field data analysis by the Sichuan Institute of Land and Space Ecological Restoration and Geological Hazard Prevention from 1st July 1998 to 26 September 2018. There were 2,572 debris flows occurred during the period 1998–2018 throughout Sichuan Province (Table 1). The database included information on occurrence time, location, and mobilized volume for each debris flow event. The volume was determined by on-site investigation by professional and technical staffs, aerial photography by UAV and comparison of satellite images. The volume range covers several orders of magnitude, from 5 m^3 to 4.0×10^6 m^3; the largest debris flow in the dataset occurred on 9th July 2013, in Mianzhu County level City of Deyang City (Yu et al., 2010). According to the dataset, 873 debris flows with magnitudes larger than $\times 1.0$ 10^4 m^3 (34% of total) occurred in the study area during the period 1998–2018.

Xiong et al. (2021) suggested that the transfer process of landslide sediment from hillslopes to channels in alpine basins was intense during the first 5 years after the Wenchuan earthquake; then, it gradually weakened without the influence of extreme rainfall. However, strong rainfall hit Wenchuan County again in 2013, which caused the number and area to increase significantly. Subsequently, both the number and area of landslides gradually decreased from 2013 to 2017.

For further analysis, three periods of debris flow activity were distinguished, which were the 10-years pre-earthquake period (1998–2007), the 6-years short-term (immediate) post-earthquake period (2008–2013), and the 5-years long-term post-earthquake period (2014–2018) respectively.

By extracting the annual and cumulative number as well as the volume versus time for the three periods of the 21-years debris flow record, the temporal aspects of debris flow occurrence were analyzed to determine the seismic effect on debris flow occurrence and characteristics. To evaluate the spatial aspects of debris flow occurrence, the number and volume of mobilized debris flow in the entire Sichuan Province and the severest disaster areas were analyzed. Furthermore, the data of debris flows in three debris flow-prone regions pre-earthquake including Ganzi Prefecture, Aba Prefecture and Liangshan Prefecture were analyzed to reveal the relation between the frequency of debris flow occurrence and distance from the epicenter. The relationship with annual precipitation in the study area was also studied.

Methodology

The relationship between magnitude (size) and frequency is an important indicator to be considered in assessing societal risk caused by landslides (Friele et al., 2008; Jakob and Friele, 2010).

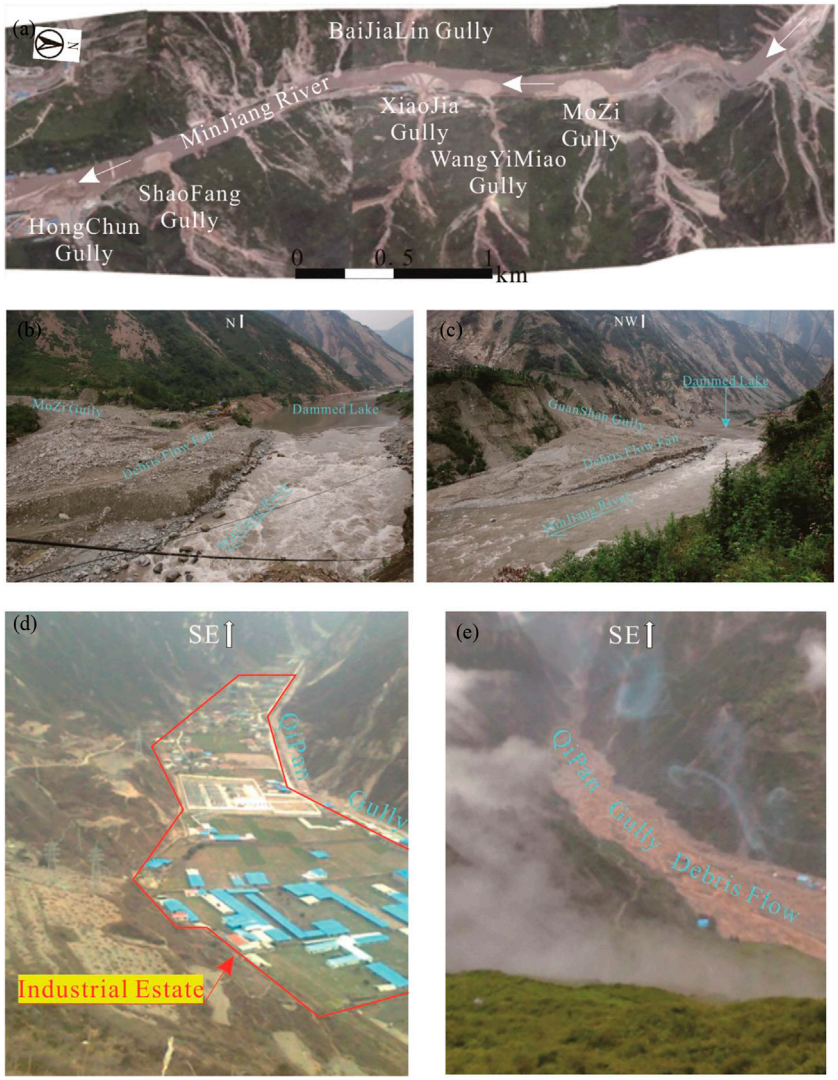


FIGURE 2
Typical debris flow events after Wenchuan earthquake. **(A)** Debris flows occurred in 9th to 12th July, 2013, along Du-Wen Highway in Wenchuan county (Aerial photo, taken by UAV on 21th July 2011). **(B,C)** Debris flow occurred in Mozi gully blocked Minjiang River. **(D,E)** Qipan gully outlet before and after debris flow occurred in 9th July 2013.

TABLE 1 Number and volume of debris flow events in Sichuan Province in the three time periods examined in this paper.

Debris flow	Period	Sichuan Province
Number	Pre-earthquake (1998–2007)	338
	Short-term post-earthquake (2008–2013)	1650
	Long-term post-earthquake (2014–2018)	584
Total volume ($\times 10^7 m^3$)	Pre-earthquake (1998–2007)	1.16
	Short-term post-earthquake (2008–2013)	9.52
	Long-term post-earthquake (2014–2018)	1.66

Dai and Lee (2001) have proposed a frequency-volume relation for rainfall-induced landslides. In order to better understand the effect of the Wenchuan Earthquake on debris flow occurrence, the structure of the magnitude-frequency (M-F) relation of debris flow events was examined in the period 1998–2018. In this study, magnitude is characterized by the debris flow volume. The percentage contribution to total volume mobilized in a given period is defined as:

$$M_j = \frac{V_j}{\sum_{j=1}^{n} V_j} \tag{1}$$

which satisfies that $\sum_{j=1}^{n} M_j = 1$, where n represents the number of debris flows in a given period, and V_j represents the volume of the jth debris flow in the period according to the time sequence.

Through (1), the cumulative percentage of debris flow in each magnitude bin was calculated, and then plotted for the three periods to show the contribution of debris flows at different magnitudes to the total volume mobilized. This enabled us to see which magnitude accounted for the largest proportion of total mobilized volume, and the influence of a strong earthquake on debris flow magnitude.

Then, the events are ranked in the order of decreasing magnitude. The incremental frequency of an event of rank i is determined as (Hungr et al., 2008):

$$f_i = \frac{1}{T_i} \tag{2}$$

where T_i is the length in years of the respective interval 1998–2007, 2008–2013, and 2014–2018. The M-F relation is constructed by accumulating the incremental frequencies from the largest magnitude downward (Hungr et al., 2008):

$$F_i = \sum f_i \tag{3}$$

In (3), F_i is the cumulative frequency of debris flow events of magnitude M_i or larger. Then it can be determined whether the distribution of debris flows occurring in the three periods can be well fitted by a power-law function:

$$y = a \times x^b \tag{4}$$

In (4), y is the cumulative debris flow frequency, x is the debris flow magnitude, and a and b are regression parameters of the power law relation. Furthermore, the coefficients can be compared to gain insight into the pattern of debris flow occurrence.

Moreover, the work done by debris flow events can be used to measure the relative importance of extreme or catastrophic events and more frequent events of smaller magnitude on geomorphic processes, as well as the quantity of material transported by debris flow. The work done by each debris flow event was obtained by multiplying the frequency of debris flow event of a given size by the magnitude of the same event in the study area during the three periods. The magnitude at which the maximum occurs provides a measure of the level at which the largest portion of the total work is accomplished (Wolman and Miller, 1960), the "work peak" of Guthrie and Evans (2007).

Meanwhile, a probability term defined to describe the likelihood of a debris flow occurring with a given volume in each period to study the effect of earthquake on the magnitude and frequency of debris flows in Sichuan Province in the period 1998–2018:

$$P_i = \frac{n_{x_i}}{\sum n_{xi}} \tag{5}$$

where n_{x_i} is the occurrence number of debris flow with a magnitude rank of x_i:

$$x_i = [lgV \times 10]/10 \tag{6}$$

where [·] represents a rounding function. Furthermore, a work peak index parameter is defined to study the interaction of magnitude (i.e., the debris flow volume) and earthquake effects:

$$Work\ peak = V \times P_i \tag{7}$$

By this method, the pulse of debris flows that occurred during 2008–2013 in the immediate aftermath of the earthquake was documented to see if a gradual return to a near steady state in the longer term post-seismic period occurred, and if an echo of the earthquake perturbation persists.

Temporal and spatial aspects of debris flow occurrence

Using the 21-year record of debris flows, the temporal and spatial aspects of debris flow occurrence were explored in Sichuan Province in the period 1998–2018 with respect to the annual number of debris flows, the annual debris flow volume mobilized, and the evolution of the spatial pattern of debris flow occurrence.

Temporal pattern of debris flow occurrence versus precipitation

Owing to the influence of the Wenchuan Earthquake, the source debris volume increased dramatically with changes in slope topography and stream channel conditions. The Sichuan database recorded the occurrence of 2,572 debris flows in the period 1998–2018. The annual number of debris flows during this time period is indicated in Figure 3A. Data (n =724; 28% of total) from the severest disaster areas is shown by the blue bars and curves in Figure 3A. In Figure 3A the peak occurs in 2012 for Sichuan Province and in 2013 for the severest disaster area.

With respect to the Sichuan dataset, in the short-term post-earthquake period (2008–2013), the number and mobilized volume of debris flow events that occurred in 2008 was not

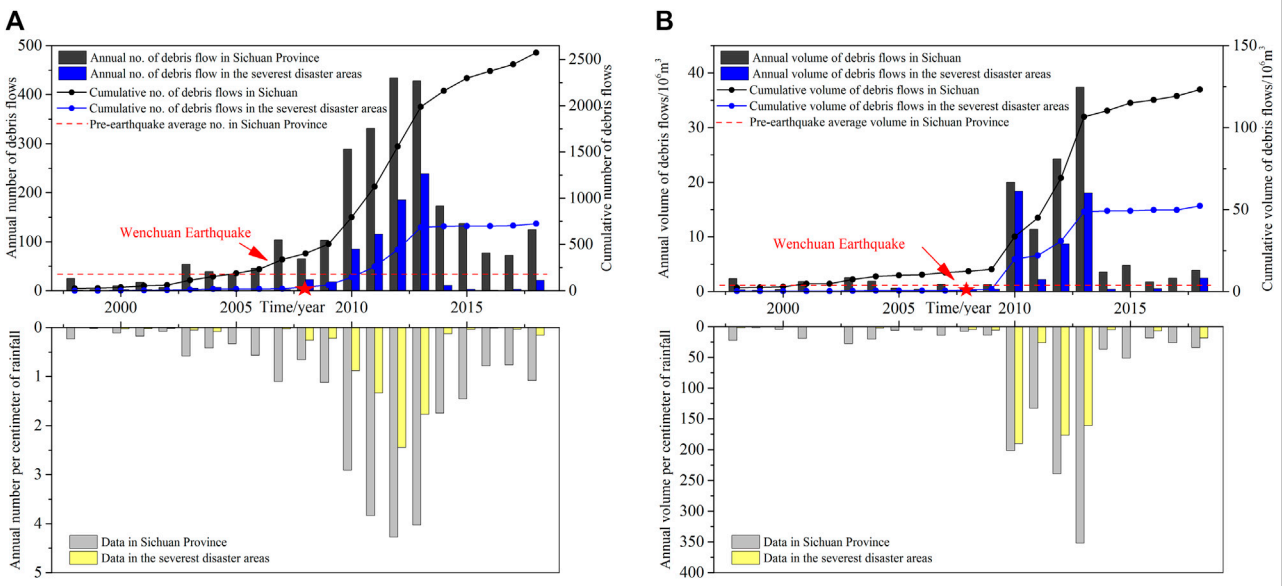


FIGURE 3
(A). Annual number and cumulative number of debris flow events in Sichuan Province (1998–2018; n=2,572) and the severest disaster areas (1998–2018; n=724). **(B)** Annual volume and cumulative volume mobilized by debris flows in Sichuan Province and the severest disaster area.

particularly high because the materials originating from coseismic landslide were simply deposited in debris gullies, and only materials in short and steep valleys were mobilized within a short time of the seismic shock.

338 debris flows had occurred (13.1% of total) prior to the 2008 Wenchuan Earthquake (pre-earthquake period 1998–2007). In this period the annual number of debris flows throughout Sichuan Province fluctuated steadily below 100; the annual average number of debris flows was 70 with a maximum of 198 in 2007 (Figure 3A). This was taken to represent a background annual frequency of debris flow occurrence for Sichuan. In the short-term aftermath of the 2008 Wenchuan earthquake (2008–2013), debris flows occurred frequently and massively during the 6-year short-term post-earthquake period (2008–2013). Debris flows reduced gradually in number, approaching the pre-earthquake level from 2014, while the impact of the earthquake decayed to a relatively low level in 2018.

With reference to the Sichuan Province total and regional data in Figure 3A, a lag time between the 2008 earthquake and the peak in the annual number of debris flows in 2012 was noted. This delayed (rather than immediate) response may reflect the delay in debris flow entering the long and complex chain of secondary processes caused by the earthquake and/or the lack of high-magnitude triggering rainfalls during the period of delay. On the basis of Figure 3B, the total volume of debris flows mobilized in the study period (1998–2018) was 123.4 Mm^3 in 2,572 events at an average of 4.8×10^4 m^3 per event. The average annual pre-earthquake (1998–2007) debris flow volume was 1.16 Mm^3 in 338 events and reached 15.9 Mm^3 in the short-term post-earthquake period (2008–2013; in 1650 events) with a maximum in 2013 of 37.4 Mm^3. From 2014 to 2018, the annual average volume decreased to 3.3 Mm^3 in 584 events, still somewhat larger than the pre-earthquake figure.

According to the above analysis, debris flow activity can be concluded to have essentially returned to pre-earthquake conditions by 2018, even though an echo of the earthquake remains owing to heavy rainfall, remaining source materials that were yet to be mobilized, and several other earthquakes that followed the 2008 Wenchuan Earthquake, such as the Ya'an Earthquake (M7.0) on 20 April 2013 (Pei and Huang, 2013) and the Kangding Earthquake (M6.3) on 2 November 2014 (Yi et al., 2015). Debris flow occurrences are anticipated to return to pre-earthquake values eventually but more time is required. From the above-mentioned figures, the debris flow frequency switches from low to high and then back to low, which illustrates the amplification effects of earthquake shock in 2008–2013 and subsequent weakening of the earthquake effect.

At the same time, the threshold of hydrological conditions leading to debris flow initiation decreased significantly; namely, the critical rainfall intensity necessary to trigger a debris flow decreased to that before earthquake (Cui et al., 2010; Zhou and Tang 2014; Li TT. et al., 2016; Guo et al., 2016c; Chang et al., 2021). After this initial decrease in the rainfall threshold, the threshold then increased as the supply of co-seismic source material became exhausted. For example, the triggering rainfall amount of Gaojiagou debris flow shows an increasing trend after the significant drop in 2008. The rainfall threshold of 4 debris flows occurring successively in Gaojiagou Gully was 155.5 mm in 2010, 163.1 mm in 2011, 173.7 mm in 2013 and 176.5 mm in 2016 (Fan et al., 2018b) due to the reduced source materials, the increased particle size and the restoration of vegetation.

From 1998 to 2007, the precipitation curves in Figure 3 fluctuate over a narrow range with an average of 0.4 debris flows per centimeter of rainfall. After the Wenchuan Earthquake (2008–2013), the annual number of debris flows per centimeter of rainfall increased and reached a maximum of 4.3 debris flows per centimeter of rainfall. While after 2013 (in the long-term post-earthquake phase, 2014–2018), the number of debris flows per centimeter of rainfall curves decreases sharply (Figure 3) to an average of 1.2 debris flows/cm close to but still above the pre-earthquake level. A similar pattern with the annual debris flow volume mobilized per centimeter of rainfall plot was found. In the pre-earthquake period, the average annual volume of debris flow per centimeter of rainfall is 12×10^3 m^3/cm. After the earthquake, it shows a dramatic increase to a peak of 350×10^3 m^3/cm and an average of 158×10^3 m^3/cm for the period. In the long-term post-earthquake period (2014–2018) the average annual volume per centimeter of rainfall decreases to 33×10^3 m^3/cm of rainfall, almost at pre-earthquake levels. Thus the annual number and volume of debris flow events per centimeter of rainfall in Sichuan Province present a similar temporal pattern to that of debris flow occurrence.

This analysis helps to verify the immediate post-earthquake debris flow characteristic that rainfall threshold values for triggering debris flows showed a dramatic decrease (i.e., for a given amount of rainfall more debris flows were triggered and a greater volume is mobilized). In the longer-term post-earthquake period, the annual number of debris flows and volume mobilized per centimeter of rainfall (Figure 3), whilst approaching pre-earthquake values, were still higher than those in 2008, which suggests that a period of time is still required for the debris flow system to recover to pre-earthquake rainfall threshold levels.

Spatial distribution of debris flow occurrence

As noted, the Sichuan database (n = 2,572) recorded the number and magnitude of debris flow events that occurred in 1998–2018; these are plotted as red dots in Figure 4, and the magnitude is expressed in terms of the dot size. Data (n = 724) selected from the database recorded the debris flow events in the most severe disaster areas, outlined in blue in Figure 4. The maps compare the debris flow distribution density in the three time-intervals, and visualize the debris flow development throughout Sichuan Province (Figure 4).

In these three maps, the red dots indicate the location and magnitude of debris flows in the Sichuan database. Before the earthquake (Figure 4B), some small-scale debris flows were distributed evenly in the alpine valley region and low mountains, while in the short-term post-earthquake period (Figure 4A), the number and volume of debris flows grew dramatically, and were concentrated in the vicinity of the Longmenshan Fault Zone. The main reason for this is that rocks on the fault zone are relatively broken and the slopes are prone to instability under heavy rainfall, providing the source materials for debris flow formation (Yang et al., 2018). In Figure 4C (long-term post-earthquake phase), the spatial distribution of debris flows is quite similar to that in the pre-earthquake map (Figure 4B) suggesting a return to pre-earthquake conditions.

To further clarify the characteristics of the number and magnitude of debris flows in the three periods, pre-earthquake was selected for analysis in three debris flow-prone regions, including Aba Prefecture, Ganzi Prefecture and Liangshan Prefecture, shown as yellow dots in Figure 4. The occurring number and volume of these debris flow events in these three regions are listed in Table 2 for the three time periods.

The number of debris flow events during the short-term post-earthquake period (2008–2013) in Aba Prefecture and Liangshan Prefecture increased to 7 and twice the number in the pre-earthquake period respectively. Whereas in the long-term post-earthquake period, this value decreased to twice and 1.5 times the number in the pre-earthquake period. The volume of debris flows occurring in these three regions presents a similar pattern in Aba Prefecture and Ganzi Prefecture. However, in Ganzi Prefecture, the number of debris flows during these three periods show only slight differences owing to its long distance from the Longmenshan Fault Zone. At the same time, the debris flow volume in Liangshan Prefecture did not fluctuate as noticeably over these three periods.

Debris flow magnitude and frequency

Magnitude and cumulative percentage of total volume mobilize

Fan et al. (2018b) showed that, after the Wenchuan earthquake, the landslide frequency increased by a large margin. Of the nearly 200,000 landslides triggered originally, many remobilized within a few years after the initial event by rainfall, which often caused catastrophic debris flows. At the same time, sufficient material supply and poor restoration of vegetation in the northern Wenchuan County led to longer-term debris flow activity in the earthquake disaster regions. This subsequently decreased within 10 years to the equivalent level of pre-earthquake debris flow activity. Xiong et al. (2022) found that landslide sediment showed a trend of substantial increase.

Debris flow volume is taken to represent debris flow magnitude and the contribution of different magnitudes of debris flow to total volume mobilized was examined in the three periods under consideration (Figure 5, Table 3). In the short-term post-earthquake period (2008–2013), the higher percentage of large-magnitude events contributed to a gentler

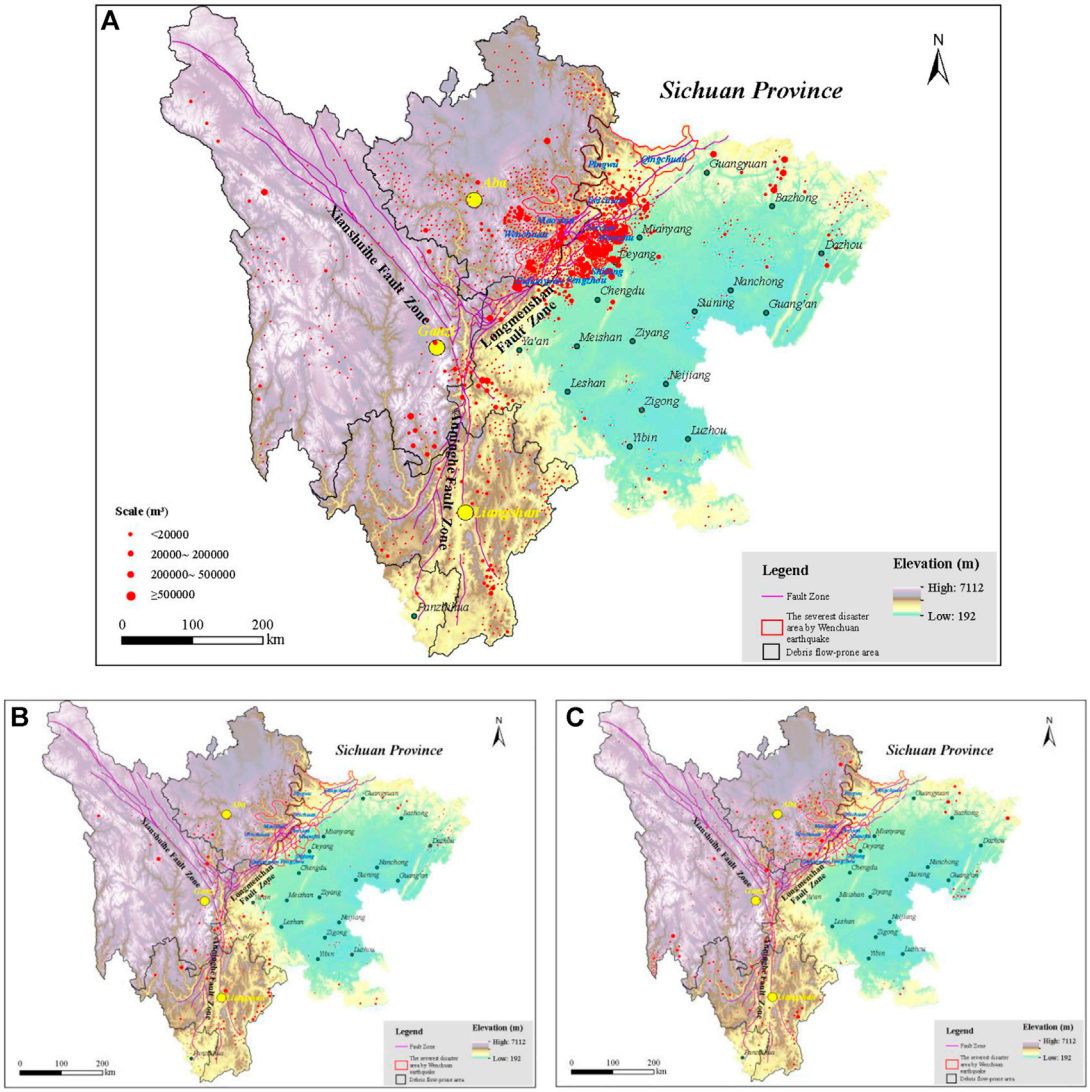


FIGURE 4
Maps showing distribution of debris flows (red dots, n=2,572) in Sichuan Province before and after the 2008 Wenchuan Earthquake: **(A)** short-term post-earthquake (2008–2013, n=1650); **(B)** pre- earthquake (1998–2007, n=338); **(C)** long-term post-earthquake (2014–2018, n=584).

TABLE 2 Number and volume of debris flow events in three pre-earthquake debris flow-prone regions in the three time periods.

Debris flow	Period	Aba	Ganzi	Liangshan
Number	Pre-earthquake (1998–2007)	84	49	86
	Short-term post-earthquake (2008–2013)	587	159	169
	Long-term post-earthquake (2014–2018)	172	204	113
Total volume ($\times 10^6 m^3$)	Pre-earthquake (1998–2007)	1.43	2.65	3.76
	Short-term post-earthquake (2008–2013)	21.63	5.38	1.98
	Long-term post-earthquake (2014–2018)	5.48	4.15	2.82

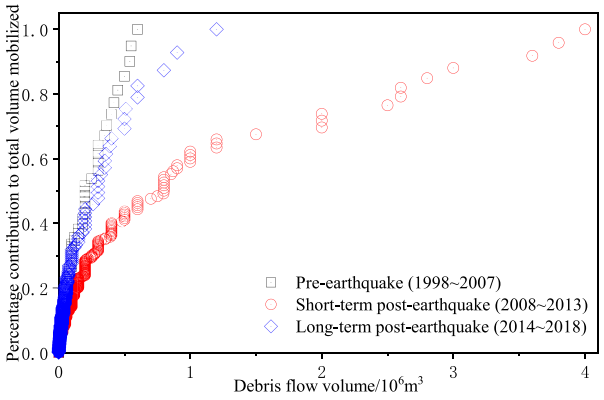


FIGURE 5
Relationship between percentage contribution to total volume mobilized and debris flow volume in the three periods of concern.

slope of the cumulative curve that differentiates it from the pre-earthquake and long-term post-earthquake curves (Figure 5). It can be seen that debris flow events with volume higher than 1 × 10^6 m^3 contributed about 40% of the entire volume mobilized during this period with the largest debris flow being 4 × 10^6 m^3 in volume. Moreover, the relatively flat slope in the period 2008–2013 (Figure 5) implies that the large-scale debris flows (>1 Mm^3) moved proportionately more materials in this period than in the other two periods.

Figure 5 also shows that the cumulative percentage contribution of the higher magnitudes in 2014–2018 is still a little greater than it was in the pre-earthquake period (1998–2007) and thus has not returned to pre-seismic levels. Specifically, debris flow events with magnitude lower than ×0.210^6 m^3 in 2014–2018 contributed to the total volume mobilized more or less at the pre-earthquake level. The events in the larger volume range (0.5–1.0 × 10^6 m^3) still contributed above pre-earthquake levels (Figure 5). Thus, the cumulative contribution of pre-earthquake debris flow events with specified magnitude to the total volume mobilized, is practically coincident with that in the longer-term post-earthquake period (2014–2018; Figure 5). In contrast, in the short-term post-earthquake period (2008–2013), the form of the curve shows a deviation from pre-earthquake and long-term post-earthquake conditions. In this period larger debris flows contributed a greater proportion of the total volume mobilized. This largely reflects the fact that the volume of the largest debris flow occurring between 2008 and 2013 was 4 × 10^6 m^3, substantially larger than the maximum of 6 × 10^5 and 1.2 × 10^5 m^3 in the other two periods (Figure 5).

Table 3 shows that, in 1998–2007, there were 318 debris flows with volumes lower than 2 × 10^5 m^3, so the data points in Figure 5 are concentrated in the first 41% of the total volume mobilized in the pre-earthquake period. 7 debris flows occurred with volumes between 4 × 10^5 and 6 × 10^5 m^3, which made up about 30% of the total volume in this period; 13 debris flows occurred with volume between 2 × 10^5 and 4 × 10^5 m^3, contributed 29% of the total volume mobilized (Figure 5). 100% of the material mobilized in this period were by debris flows ≤ 1 × 10^6 m^3 in volume.

In the short-term post-earthquake period (2008–2013), there were only 19 debris flow events with magnitude larger than ×1 10^6 m^3 (Table 3; Figure 5). But these events contributed 42% of the total volume mobilized. At the same time, 1,596 debris flows with volumes less than 4 × 10^5 m^3 contributed 36% of the total volume mobilized. Debris flows with volumes between 4 × 10^5 m^3 and 1 × 10^6 m^3 contributed the remaining 22% of the total volume mobilized in the period 2008–2013. 58% of the

TABLE 3 Volume and contributions to total debris flow volume mobilized during each of the three periods under examination.

Period	Magnitude (m^3)	Number	Cumulative volume (m^3)	Percentage of total volume mobilised
Pre-earthquake (1998–2007)	<2.0×10^5	318	4.80×10^6	41%
	[2.0×10^5, 4.0×10^5)	13	3.37×10^6	29%
	[4.0×10^5, 6.0×10^5)	7	3.46×10^6	30%
Short-term post-earthquake (2008–2013)	<2.0×10^5	1549	2.25×10^7	24%
	[2.0×10^5, 4.0×10^5)	47	1.16×10^7	12%
	[4.0×10^5, 6.0×10^5)	17	7.48×10^6	8%
	[6.0×10^5, 1.0×10^6)	18	1.36×10^7	14%
	[1.0×10^6, 4.0×10^6]	19	4.00×10^7	42%
Long-term post-earthquake (2014–2018)	<2.0×10^5	559	6.15×10^6	37%
	[2.0×10^5, 4.0×10^5)	16	4.43×10^6	27%
	[4.0×10^5, 6.0×10^5)	4	1.91×10^6	11%
	[6.0×10^5, 1.0×10^6)	4	2.90×10^6	18%
	[1.0×10^6, 4.0×10^6]	1	1.20×10^6	7%

material mobilized in this period were by debris flows ≤ 1 × 10^6 m^3 in volume.

At the bottom of Table 3, it can be seen that in the period of 2014–2018, there were 559 debris flows with magnitude less than ×2 10^5 m^3, which contributed 37% of the total volume mobilized in this period. 20 debris flows with volume between 2 × 10^5 m^3 and 6 × 10^5 m^3 contribute a total volume of 38%. 5 debris flows with volume larger than 6 × 10^6 m^3, made up the remaining 25% of the total volume mobilized during 2014–2018. 93% of the material mobilized in this period were contributed by debris flows ≤ 1 × 10^6 m^3 in volume.

From Figure 5 and Table 3, it can be seen that in the immediate post-earthquake period of 2008–2013, 19 debris flows occurred with magnitudes larger than ×1 10^6 m^3 occurred and contributed almost half (42%) of the total volume mobilized in this period. At the same time, the cumulative contribution plots of the other two periods (pre-earthquake and long-term post-earthquake) are similar, which indicate a lower contribution by large-scale debris flows (Table 3). The percentage contribution of small and medium-sized debris flows to the total volume mobilized during the long-term post-earthquake period appears to have recovered to the pre-earthquake level in a stepwise manner.

In the pre-earthquake period (1998–2007) 100% of the debris mobilized in 338 debris flows were contributed by debris flows ≤ 1Mm^3; 41% of the debris, mobilized were contributed by smaller debris flows ≤ 2 × 10^5 m^3. In the immediate post-earthquake period (2008–2013) 58% of the debris mobilized in 1,650 debris flows were contributed by debris flows ≤ 1 Mm^3; 24% of the debris mobilized were contributed by smaller debris flows ≤ 2 × 10^5 m^3. In the longer term post-earthquake period (2014–2018), 93% of the debris mobilized in 584 debris flows was by debris flows ≤ 1 Mm^3; 37% of the debris mobilized were contributed by smaller debris flows ≤ 2 × 10^5 m^3. Thus in the immediate post-earthquake period 1) larger debris flows contributed a greater proportion of the total volume mobilized than in pre-earthquake and long-term post-earthquake periods, and 2) smaller debris flows still contributed a significant proportion of the total volume mobilized by virtue of their increased frequency (Table 3).

Magnitude-Frequency (M-F) relation

The M-F relation of debris flow events in Sichuan Province from 1998 to 2018 is given for the three periods under examination in Figure 6. According to the figure, magnitude (M) is the volume of debris flow (in m^3) and frequency (F) is the annual frequency of M or greater (see Eq. 3). The shape of the plots is remarkably similar to the long-term post-earthquake curve plotting between the pre-earthquake and short-term post-earthquake curves (cf. Marc et al., 2015). The earthquake had a great impact on the frequency and severity of debris flow events (Figure 6). At a given frequency, the magnitude of debris flow in the short-term post-earthquake period (2008–2013) is substantially higher than the other two periods. Whereas for the same magnitude, the frequency in the second period (2008–2013), in the immediate aftermath of the earthquake, is the largest (Figure 6). The form of the three curves illustrates that with increasing magnitude, frequency decreases at a similar rate over the three periods. A decade after the earthquake, the frequency and magnitude of debris flows occurrence have more-or-less returned to the pre-earthquake level (Figure 6), indicating that the seismic effect has gradually dissipated.

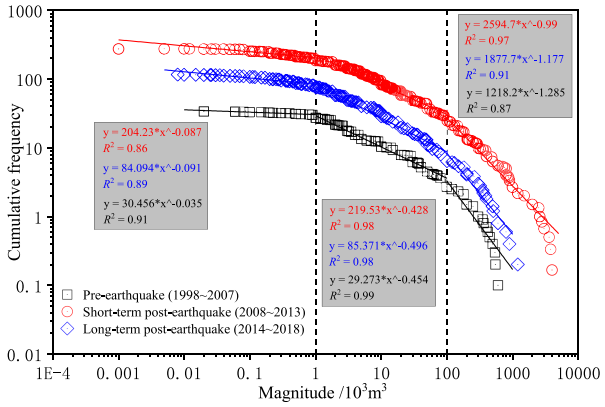


FIGURE 6
The M-F relation for debris flows in the whole Sichuan Province over the three periods under examination.

It is seen in Figure 6 that the similar shapes of the three M-F curves have similar inflection points to a rollover at around 1 × 10^3 and 100 × 10^3 m^3, respectively (see vertical dashed lines in Figure 6); the curve can thus be divided into 3 segments, which are <1 × 10^3 m^3, 1–100 × 10^3 m^3, and >100 × 10^3 m^3. The distribution of the three segments can be fitted by a power-law function (Eq. 4); regression parameters of the relation are listed in Table 4.

The segments of the M-F relation well satisfy a power law form with a goodness of fit (R^2) higher than 0.86 for each segment of each curve (Table 4). The value of Parameter a in Eq.4 during the long-term post-earthquake (2014–2018) is between the values of the pre- and short-term post-earthquake; at the same time, it increased rapidly when the debris flow magnitude increases from volume range of [1×10^3 m^3, 1×10^5 m^3] to the magnitude larger than 10^5 m^3. Therefore, the Parameter a in Eq. 4 shows the same pattern of change as the M-F curve (Table 4) over the three periods.

The exponent *b* also shows a low-high-low tendency in the three periods except when the debris flow magnitude is <10^3 m^3. The value of parameter b remains essentially the same with only slight fluctuation over the three periods with maximum

TABLE 4 Regression parameters of M-F relation for debris flow events in the three periods under examination (see Figure 6).

Period	Magnitude (volume of debris flow in m^3)	Number of debris flow events	a	b	R^2
Pre-earthquake (1998–2007)	$<1\times10^3$	38	30.46	−0.035	0.92
	$[1\times10^3, 1\times10^5]$	265	29.27	−0.453	0.99
	$>1\times10^5$	35	1218.2	−1.285	0.87
Short-term post-earthquake (2008–2013)	$<1\times10^3$	457	204.41	−0.087	0.86
	$[1\times10^3, 1\times10^5]$	1018	219.53	−0.428	0.98
	$>1\times10^5$	175	2,594.7	-0.99	0.97
Long-term post-earthquake (2014–2018)	$<1\times10^3$	181	84.09	−0.091	0.89
	$[1\times10^3, 1\times10^5]$	364	84.07	−0.483	0.98
	$>1\times10^5$	39	1877.7	−1.177	0.91

differences of −1.25 (between −0.035 and −1.285), −0.903 (between −0.087 and −0.99), and −1.086 (between −0.091 and −1.177), respectively. The exponent b increases with increasing magnitude of debris flow for each period as it approaches the upper limit of debris flow volume. The change in parameters a and b reveals the impact of earthquake on debris flow magnitude and frequency.

To verify the effect of the 2008 Wenchuan Earthquake on debris flow occurrences, the data (n=724) from the most severe disaster areas affected by the earthquake was also analyzed (Figure 7). The M-F relation of the debris flows in this area also well satisfied a power law distribution (Figure 7). For example, the exponent b changes little between the same segments in the three periods. Whereas the parameter a indicates a significant difference between them reflecting differences in frequency for a given magnitude. The constant a is 110.35 in 2008–2013 in the segment corresponding to the magnitude range from ×1 10^3 to 100 × 10^3 m^3, which is 73 times larger than it was in the pre-earthquake period (1.5048), and remains nearly 12 times larger than it was in 2014–2018 (9.372) (Figure 7).

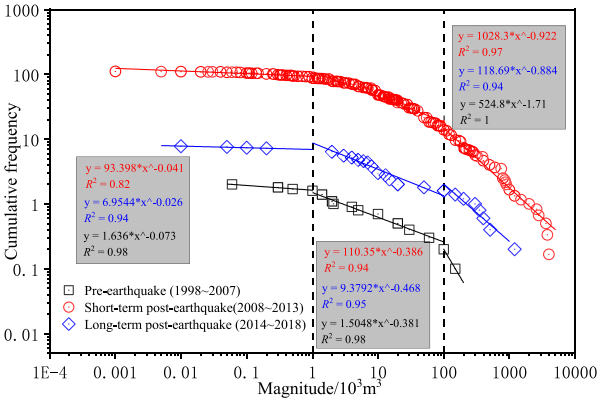


FIGURE 7
The M-F relation in the severe disaster areas over the three periods under examination.

Debris flow work

Work done by debris flow events

Following the concepts and methodology of Wolman and Miller (1960) and Guthrie and Evans (2007), the Sichuan debris flow record (n = 2,572; 1998–2018) was used to analyze the work done by debris flow events of different magnitudes. The work done by debris flow events of a given magnitude equals the probability of an event with that magnitude multiplied by the volume (our measure of magnitude) of the event. Units of work are a function of the magnitude and frequency, and work on each graph is scaled back linearly to enable visual comparison to the probability of occurrence. The important component of the work portion in Figure 8 is the magnitude at its peak rather than its actual metric, the so-called work peak (Guthrie and Evans 2007).

The probability distribution of debris flow volumes is shown in Figures 8A–C over the three periods under examination, in which the Y axis shows the probability of a debris flow event in a given magnitude class with the total value of 1. In all three phases (Figures 8A–C), the relatively high-probability debris flow events were associated with those of small- and moderate-volume, generally on the order of 10^3–10^4 m^3. In contrast, the work peak (see Eq. 7) is associated with the larger-scale debris flow events in the range >10^5 >10^6 m^3 (Figures 8A & C), and in the case of the short-term post-earthquake period the maximum debris flow magnitude (Figure 8B). This represents a violation of Wolman-Miller conditions, in which most work in a geomorphic system (corresponding to the work peak) is done by events of moderate magnitude, and is in contrast to the findings of Guthrie

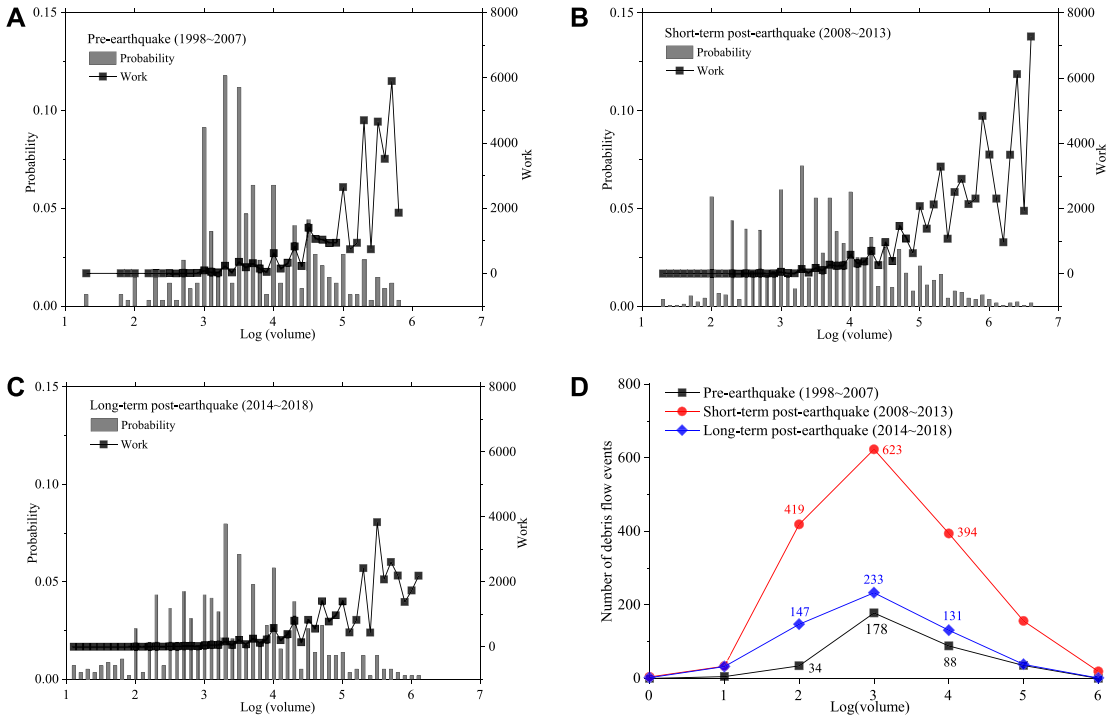


FIGURE 8
Probability and work in **(A)** 1998–2007, **(B)** 2008–2013, and **(C)** 2014–2018. **(D)** Number of debris flow events with different orders of magnitude in the three periods under study.

and Evans (2007) for debris flow systems in British Columbia. In Figure 8B, it was seen that in the period of 2008–2013, the work peak is displaced to the right and reached a maximum in excess of 10^6 m^3, whilst the high-probability debris flow events were concentrated in moderate events (<10^5 m^3). In the long-term post-earthquake period (2014–2018), the highest probability is distributed in moderate-size debris flow events and the work peak again occurs in association with the maximum debris flow magnitude (Figure 8C), similar to the pre-earthquake work profile in pattern (Figure 8A). The offset between the probability peak and the work peak in Figures 8A–C is noted and its significance is explored further.

The Wolman-Miller Offset

The offset between the probability peak and the work peak is termed here the "Wolman-Miller Offset" (see Figure 1 in Wolman and Miller, 1960). It is speculated that a large offset (e.g., Figure 8B for the immediate post-earthquake period) is representative of the mass movement response of a landscape in disequilibrium where the work peak is associated with larger events (in this case say >10^6 m^3). In the Wenchuan Earthquake, the Wolman-Miller Offset has decreased in the long-term post-earthquake period (2014–2018) for the work peak's migrating to the left of the probability peak as the landscape heals and returns to a background state. It is further suggested that a smaller W-M Offset is associated with a background state and represents the geomorphic signature of a particular landscape where still the most work is done by the largest debris flow events. It appears, even at background levels of debris flow activity, Wolman-Miller conditions, i.e., most work (corresponding to the work peak) done by events of moderate magnitude, do not prevail in the Sichuan landscape. Furthermore, it appears that larger events occurring more frequently are key elements of the process that returns a landscape to a steady state after a seismic shock. In this process, larger events mobilize a greater proportion of the total amount of material moved (see Figure 5). A further observation is that a large W-M offset (a highly displaced work peak) represents a transient high-hazard landscape in which large-scale debris flows occur more frequently. The limits, threshold behavior, and implications of the Wolman-Miller offset for landscape geomorphology and geohazard assessment are topics for future examination.

In terms of the size distribution of debris flows (Figure 8D), a debris flow event with a volume of 1 Mm^3 was not reported in the pre-earthquake period and only one was reported in the long-term post-earthquake period. In contrast 19 debris flow events of 1 Mm^3 in volume or greater occurred in the short-term post-seismic period (2008–2013). This demonstrates that the pulse of

large magnitude debris flows which occurred during 2008–2013 gradually decreased and returned to a steady state after 2013, although there remains an echo of earthquake impact in the long-term post-earthquake period (2013–2018). During this process it is significant that debris volume magnitude shows a similar distribution in all three periods.

Discussion

After a strong earthquake, most previous studies mainly investigated the initiation conditions of debris flows (Lin et al., 2003; Xu et al., 2012; Zhang and Zhang 2017). Conspicuous differences before and after the earthquakes were revealed in the triggering rainfall amount and intensity for debris flows, the area extent in which debris flows occurred, the frequency of debris flow and the source materials supply of debris flows. Cheng et al. (2005) suggested that debris flows induced by 2001 Toraji typhoon were primarily caused by rainstorm on inherently unstable slopes that had been loosened in the 1999 Chichi earthquake. Dong et al. (2009) proposed an equation between debris flow volume and catchment area. Chang et al. (2011) studied the sediment volume of debris flows after the 1999 Chichi earthquake, and proposed an empirical model for estimating the sediment volume in a debris flow, involving landslide area, catchment area, geological index, cumulative rainfall and rainfall duration as the input variables. Hovius et al. (2011) studied the prolonged seismically induced erosion of the ChiChi earthquake and found that erosion peaked at more than five times the background rate and returned progressively to pre-earthquake levels in about 6 years. However, the aforementioned studies rarely explored the M-F relation of debris flows in earthquake-affected areas. We extracted debris flow data after the 1999 Chichi earthquake from Chang et al. (2011) and built the M-F relation of those debris flows in the Chichi earthquake area (Figure 9).

According to the database, after the earthquake in 1999, many debris flows with an average magnitude greater than ×10 10^4 m^3 occurred due to the Toraji typhoon in 2001. Subsequently, Typhoon Mindulle in 2004, Haitang in 2005 and Kalmaegi in 2008 also triggered a great deal of debris flows, which had smaller magnitude than that of the 2001 events. Therefore, we identified two periods to construct the M-F relations, the 1999–2001 and 2002–2008 periods. Through the fitted curve in Figure 9, it can be noticed that the Chi-Chi earthquake has a time-delayed effect on the debris flow occurrence, and the M-F relation of the two periods also conforms to the power-law distribution. Comparing the fitting formulas, it can be observed that the impact of the effects of ChiChi earthquake and Wenchuan earthquake on the debris flow activity has similar charactersitics. In the Wenchuan earthquake, the constant a is 2,594.7 in 2008–2013, which is 6.2 times larger than that of the ChiChi earthquake of 417.62 in 1999–2001, indicating that the Wenchuan earthquake has a

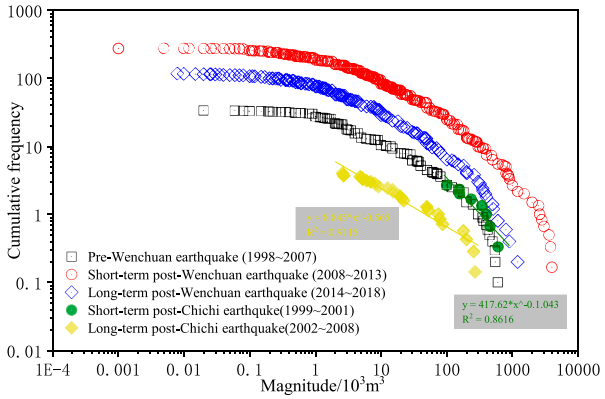


FIGURE 9
M-F relation contrasted in Wenchuan and Chichi earthquake.

greater impact on the magnitude and frequency of the debris flow in the strongly earthquake-affected period. From 2008 to 2013 after the Wenchuan earthquake, the magnitude of debris flow has been at a high level, especially after reaching the peak in 2013, and then gradually decreased. Debris flows continued to occur until 2018, and the curve was still above the pre-earthquake level. However, the ChiChi earthquake area only experienced large-magnitude debris flow in 2001, two years after the earthquake. The subsequent debris flows in 2002–2008 present a relatively small volume. This decay process took 10 years for the ChiChi earthquake. By contrast, it took longer for the Wenchuan earthquake to return the debris-flow activity to a pre-earthquake level. This result also shows that the post-seismic effect of the Wenchuan earthquake is greater and the debris flows are more active.

Xu et al. (2016) studied the 2008 Wenchuan and 2015 Gorkha earthquakes, which have comparable magnitudes of Mw 7.8 and 7.9, both occurred on the margins of the Tibetan Plateau, and both are characterized by high topography and steep slopes. However, the number, total area and volume of large landslides (≥10,000 m^2) triggered by the Wenchuan Earthquake were 12–16 times of those triggered by the Gorkha Earthquake. The significant difference between the two earthquakes lies in the dip of the seismogenic fault and the area of surface region directly above the rupture plane, which controls the manner of earthquake energy release and influences the deformation of the hanging wall bedrock. The Wenchuan Earthquake has a much steeper dip of the seismogenic fault and relatively small overlying surface area, which concentrated the surface energy and resulted in many large, intense landslides. This research indicates that local topography and PGA cannot explain the large difference in landsliding between the events, and the much different dip angle of their seismogenic faults is the primary reason.

In addition, the co-seismic landslides triggered by the Wenchuan Earthquake generated several km^3 of debris, which was deposited along the slopes and in low-order channels and became a large and distributed source of material for successive post-seismic debris flows (Parker et al., 2011). Terrain analysis after the Wenchuan Earthquake shows that a large volume of material was deposited on slopes; these slope deposits represented an increasing number of debris flow sources. The total number of slope collapses and landslides triggered by the Wenchuan Earthquake reached 30,000–50,000 (Huang and Li, 2009). These collapses and landslides created abundant loose source materials to be potentially mobilized in debris flow. For example, the area of slope collapse and landslides located along Du-wen Highway is as high as 6.97% of the Minjiang drainage basin area. The total volume of the loose materials is 2.13×10^8 m^3 (Liu et al., 2012), which covers 10–50% of the debris flow drainage area. The volume of loose materials per unit area is 1×10^6 m^3/km^2, which is seven times that in the pre-earthquake debris flow gullies (Cui et al., 2010).

Conclusion

The regional mass movement (debris flow) response to earthquake-generated landscape damage was quantified through the analysis of long-term (1998–2018) monitoring data on 2,572 debris flow events in Sichuan Province, China. This unique record of largely rainfall-generated debris flows represents a total mobilized volume of 123.4 Mm^3. For this analysis the debris flow record was divided into three time intervals: pre-earthquake (1998–2007), short-term post-earthquake (2008–2013), and long-term post-earthquake (2014–2018).

The geomorphic structure of the transient pulse of debris flow activity associated with the earthquake shock is characterized by a dramatic increase in the average annual number and volume of material mobilised by debris flows in 2010 after a lag of 2 years; this peak had decreased almost to pre-earthquake levels by 2018. The impact of the earthquake on rainfall thresholds for debris flow initiation was also examined and it was found that the landscape became hyper-sensitive to rainfall in the short-term post-earthquake period. This response reflects the availability of debris flow source materials in a damaged landscape that became exhausted in the longer-term post-earthquake period as well as being stabilized by re-vegetation.

The spatial distribution of debris flows in the immediate aftermath of the earthquake was clearly concentrated along the source fault becoming more diffused in the longer-term post-earthquake period. The contribution of different debris flow magnitudes to the total volume of material mobilised was investigated in the three periods under examination. We found that in the short-term post-earthquake period, 19 debris flow events greater than 1 Mm^3 contributed 42% of the volume mobilised; no debris flow of this magnitude was recorded before the earthquake and only one (volume > 1 Mm^3) was recorded in the long-term post-earthquake period. Thus, the debris flow hazard in the immediate post-earthquake period is characterised by more frequent, larger debris flows and represents a transient high-hazard landscape.

In terms of Magnitude-Frequency (M-F) relations, it was found that the three time periods yielded very similar shaped M-F curves, each one exhibited three segments consisting of low, medium, and high magnitudes. They were characterized by robust power law fits with very similar exponents in each segment of the M-F curve. It was hypothesised that the similarities in the form of the M-F relation reflect control at the landscape scale (e.g., topographic characteristics) conditioned by material properties, and environmental effects (e.g., vegetation and rainfall effects).

Finally, the work done by debris flow events in the Sichuan database was also analysed by evaluating the work peaks in the three periods. The concept of the Wolman-Miller Offset was introduced to describe the offset of the work peak in relation to the probability peak. It was concluded that with a greater W-M Offset in the immediate post-earthquake period, more work is done by larger events and the work peak corresponds to the maximum debris flow size (in violation of the Wolman-Miller precept). At the same time, the greater proportion of the volume being mobilised by larger events occurring more frequently is a key process in the landscape returning to a pre-earthquake (equilibrium) state.

Data availability statement

The original contributions presented in the study are included in the article/Supplementary Material; further inquiries can be directed to the corresponding author. Requests to access the datasets should be directed to MH at hanmei@home.swjtu.edu.cn.

Author contributions

MH: Methodology, Writing—original draft preparation, Data curation and processing. SE: Conceptualization, Writing—review and editing, English and text arrangement. KH: Structure, manuscript shaping. HS: Figure revision, Data analysis. ZM: data procurement.

Funding

This paper was funded by the National Science Fund for Young Scholars of China (Grant No. 41907225 to MH), State Key Laboratory of Geohazard Prevention and Geoenvironment Protection (China) Open Fund (Grant No. SKLGP2017K003 to

SE, SKLGP2018K011 to MH), Fundamental Research Funds for the Central Universities (Grant No. 2682021ZTPY100).

Conflict of interest

The authors declare that the research was conducted in the absence of any commercial or financial relationships that could be construed as a potential conflict of interest.

Publisher's note

All claims expressed in this article are solely those of the authors and do not necessarily represent those of their affiliated organizations, or those of the publisher, the editors and the reviewers. Any product that may be evaluated in this article, or claim that may be made by its manufacturer, is not guaranteed or endorsed by the publisher.

References

Brayshaw, D., and Hassan, M. A. (2009). Debris flow initiation and sediment recharge in gullies. *Geomorphology* 109 (3-4), 122–131. doi:10.1016/j.geomorph.2009.02.021

Chang, C. W., Lin, P. S., and Tsai, C. L. (2011). Estimation of sediment volume of debris flow caused by extreme rainfall in Taiwan. *Eng. Geol.* 123, 83–90. doi:10.1016/j.enggeo.2011.07.004

Chang, M., Tang, C., Van Asch, T. W., and Cai, F. (2017). Hazard assessment of debris flows in the Wenchuan earthquake-stricken area, SouthWest China. *Landslides* 14 (5), 1783–1792. doi:10.1007/s10346-017-0824-9

Chang, M., Dou, X., Hales, T. C., and Yu, B. (2021). Patterns of rainfall-threshold for debris-flow occurrence in the Wenchuan seismic region, Southwest China. *Bull. Eng. Geol. Environ.* 80 (3), 2117–2130. doi:10.1007/s10064-020-02080-7

Cheng, J. D., Huang, Y. C., Wu, H. L., Yeh, J. L., and Chang, C. H. (2005). Hydrometeorological and landuse attributes of debris flows and debris floods during typhoon Toraji, July 29–30, 2001 in central Taiwan. *J. Hydrology* 306 (1-4), 161–173. doi:10.1016/j.jhydrol.2004.09.007

Cui, P., Zhuang, J. Q., and Chen, X. C. (2010). Characteristics and countermeasures of debris flow in Wenchuan area after the earthquake. *J. Sichuan Univ. Eng. Sci. Ed.* 42 (5), 10–19. doi:10.1016/S1876-3804(11)60004-9

Cui, P., Guo, C. X., Zhou, J. W., Hao, M. H., and Xu, F. G. (2014). The mechanisms behind shallow failures in slopes comprised of landslide deposits. *Eng. Geol.* 180, 34–44. doi:10.1016/j.enggeo.2014.04.009

Cui, S., Pei, X., Jiang, Y., Wang, G., Fan, X., Yang, Q., et al. (2021). Liquefaction within a bedding fault: Understanding the initiation and movement of the Daguangbao landslide triggered by the 2008 Wenchuan Earthquake (Ms = 8.0). *Eng. Geol.* 295, 106455. doi:10.1016/j.enggeo.2021.106455

Cui, S., Wu, H., Pei, X., Yang, Q., Huang, R., and Guo, B. (2022). Characterizing the spatial distribution, frequency, geomorphological and geological controls on landslides triggered by the 1933 Mw 7.3 Diexi Earthquake, Sichuan, China. *Geomorphology* 403, 108177. doi:10.1016/j.geomorph.2022.108177

Dai, F. C., and Lee, C. F. (2001). Frequency-volume relation and prediction of rainfall-induced landslides. *Eng. Geol.* 59, 253–266. doi:10.1016/s0013-7952(00)00077-6

Domènech, G., Fan, X., Scaringi, G., van Asch, T. W. J., Xu, Q., Huang, R., et al. (2019). Modelling the role of material depletion, grain coarsening and revegetation in debris flow occurrences after the 2008 Wenchuan earthquake. *Eng. Geol.* 250, 34–44. doi:10.1016/j.enggeo.2019.01.010

Dong, J. J., Lee, C. T., Tung, Y. H., Liu, C. N., Lin, K. P., and Lee, J. F. (2009). The role of the sediment budget in understanding debris flow susceptibility. *Earth Surf. Process. Landf.* 34 (12), 1612–1624. doi:10.1002/esp.1850

Dowling, C. A., and Santi, P. M. (2014). Debris flows and their toll on human life: A global analysis of debris-flow fatalities from 1950 to 2011. *Nat. Hazards (Dordr).* 71, 203–227. doi:10.1007/s11069-013-0907-4

Fan, X., Domènech, G., Scaringi, G., Huang, R., Xu, Q., Hales, T. C., et al. (2018a). Spatio-temporal evolution of mass wasting after the 2008 Mw 7.9 Wenchuan Earthquake revealed by a detailed multi-temporal inventory. *Landslides* 15, 2325–2341. doi:10.1007/s10346-018-1054-5

Fan, X., Juang, C. H., Wasowski, J., Huang, R., Xu, Q., Scaringi, G., et al. (2018b). What we have learned from the 2008 Wenchuan Earthquake and its aftermath:A decade of research and challenges. *Eng. Geol.* 241, 25–32. doi:10.1016/j.enggeo.2018.05.004

Fan, R. L., Zhang, L. M., Wang, H. J., and Fan, X. (2018c). Evolution of debris flow activities in Gaojiagou Ravine during 2008–2016 after the Wenchuan earthquake. *Eng. Geol.* 235, 1–10. doi:10.1016/j.enggeo.2018.01.017

Fan, X., Scaringi, G., Korup, O., West, J. A., van Westen, C. J., Tanyas, H., et al. (2019). Earthquake-induced chains of geologic hazards: Patterns, mechanisms and impacts. *Rev. Geophys.* 57, 421–503. doi:10.1029/2018RG000626

Friele, P., Jakob, M., and Clague, J. J. (2008). Hazard and risk from large landslides from Mount Meager volcano, British Columbia, Canada. *Georisk Assess. Manag. Risk Eng. Syst. Geohazards* 2 (1), 48–64. doi:10.1080/17499510801958711

Ge, Y. G., Cui, P., Zhang, J. Q., Zeng, C., and Su, F. H. (2015). Catastrophic debris flows on July 10 th 2013 along the Min River in areas seriously-hit by the Wenchuan earthquake. *J. Mt. Sci.* 12 (1), 186–206. doi:10.1007/s11629-014-3100-7

Gregoretti, C. (2000). The initiation of debris flow at high slopes: Experimental results. *J. Hydraulic Res.* 38 (2), 83–88. doi:10.1080/00221680009498343

Guo, X., Cui, P., Li, Y., Ma, L., Ge, Y., and Mahoney, W. B. (2016a). Intensity–duration threshold of rainfall-triggered debris flows in the Wenchuan earthquake affected area, China. *Geomorphology* 253, 208–216. doi:10.1016/j.geomorph.2015.10.009

Guo, X., Cui, P., Li, Y., Zhang, J., Ma, L., and Mahoney, W. B. (2016b). Spatial features of debris flows and their rainfall thresholds in the Wenchuan earthquake-affected area. *Landslides* 13, 1215–1229. doi:10.1007/s10346-015-0608-z

Guo, X., Cui, P., Li, Y., Zou, Q., and Kong, Y. (2016c). The formation and development of debris flows in large watersheds after the 2008 Wenchuan Earthquake. *Landslides* 13, 25–37. doi:10.1007/s10346-014-0541-6

Guo, X., Li, Y., Chen, X., Zhang, J., and Sun, Y. (2021). Variation of debris flow/flood formation conditions at the watershed scale in the Wenchuan Earthquake area. *Landslides* 18, 2427–2443. doi:10.1007/s10346-021-01644-2

Guthrie, R. H., and Evans, S. G. (2007). Work, persistence, and formative events: The geomorphic impact of landslides. *Geomorphology* 88 (3-4), 266–275. doi:10.1016/j.geomorph.2006.11.010

He, K., Li, Y., Ma, G., Hu, X., Liu, B., Ma, Z., et al. (2021). Failure mode analysis of post-seismic rockfall in shattered mountains exemplified by detailed investigation and numerical modelling. *Landslides* 18 (1), 425–446. doi:10.1007/s10346-020-01532-1

He, K., Liu, B., Hu, X., Zhou, R., Xi, C., Ma, G., et al. (2022). Rapid characterization of landslide-debris flow chains of geologic hazards using multi-method investigation: Case study of the tiejiangwan LDC. *Rock Mech. Rock Eng.* 55, 5183–5208. doi:10.1007/s00603-022-02905-9

Hovius, N., Meunier, P., Lin, C. W., Chen, H., Chen, Y. G., Dadson, S., et al. (2011). Prolonged seismically induced erosion and the mass balance of a large earthquake. *Earth Planet. Sci. Lett.* 304 (3-4), 347–355. doi:10.1016/j.epsl.2011.02.005

Hu, T., and Huang, R. Q. (2017). A catastrophic debris flow in the wenchuan earthquake area, july 2013: Characteristics, formation, and risk reduction. *J. Mt. Sci.* 14 (1), 15–30. doi:10.1007/s11629-016-3965-8

Hu, X., Hu, K., Tang, J., You, Y., and Wu, C. (2019). Assessment of debris-flow potential dangers in the Jiuzhaigou Valley following the August 8, 2017, Jiuzhaigou earthquake, Western China. *Eng. Geol.* 256, 57–66. doi:10.1016/j.enggeo.2019.05.004

Huang, R. Q., and Li, W. L. (2009). Analysis of the geo-hazards triggered by the 12 may 2008 wenchuan earthquake, China. *Bull. Eng. Geol. Environ.* 68 (3), 363–371. doi:10.1007/s10064-009-0207-0

Hungr, O., McDougall, S., Wise, M., and Cullen, M. (2008). Magnitude–frequency relations of debris flows and debris avalanches in relation to slope relief. *Geomorphology* 96 (3), 355–365. doi:10.1016/j.geomorph.2007.03.020

Innes, J. L. (1983). Lichenometric dating of debris-flow deposits in the scottish highlandsflow deposits in the scottish highlands. *Earth Surf. Process. Landf.* 8, 579–588. doi:10.1002/esp.3290080609

Innes, J. L. (1985). Lichenometric dating of debris-flow deposits on alpine colluvial fans in Southwest Norwayflow deposits on alpine colluvial fans in Southwest Norway. *Earth Surf. Process. Landf.* 10 (5), 519–524. doi:10.1002/esp.3290100510

Iverson, R. M. (1997). The physics of debris flows. *Rev. Geophys.* 35 (3), 245–296. doi:10.1029/97rg00426

Jakob, M., Bovis, M., and Oden, M. (2005). The significance of channel recharge rates for estimating debris-flow magnitude and frequency. *Earth Surf. Process. Landf.* 30, 755–766. doi:10.1002/esp.1188

Jakob, M., and Friele, P. (2010). Frequency and magnitude of debris flows on cheekye river, British Columbia. *Geomorphology* 114, 382–395. doi:10.1016/j.geomorph.2009.08.013

M. Jakob and O. Hungr (Editors) (2005). *Debris-flow hazards and related phenomena* (Springer-Verlag), 739. doi:10.2113/gseegeosci.13.1.75

Li, L., Yao, X., Zhang, Y., Iqbal, J., Chen, J., and Zhou, N. (2016a). Surface recovery of landslides triggered by 2008 Ms 8.0 wenchuan earthquake (China): A case study in a typical mountainous watershed. *Landslides* 13 (4), 787–794. doi:10.1007/s10346-015-0594-1

Li, T. T., Huang, R. Q., and Pei, X. J. (2016b). Variability in rainfall threshold for debris flow after Wenchuan earthquake in Gaochuan River watershed, Southwest China. *Nat. Hazards (Dordr).* 82, 1967–1980. doi:10.1007/s11069-016-2280-6

Lin, C. W., Shieh, C. L., Yuan, B. D., Liu, S. H., and Lee, S. Y. (2003). Impact of chi-chi earthquake on the occurrence of landslides and debris flows: Example from the chenyulan river watershed, nantou, taiwan. *Eng. Geol.* 71, 49–61. doi:10.1016/s0013-7952(03)00125-x

Lin, W-T., Lin, C-Y., and Chou, W-C. (2006). Assessment of vegetation recovery and soil erosion at landslides caused by a catastrophic earthquake: A case study in central taiwan. *Ecol. Eng.* 28, 79–89. doi:10.1016/j.ecoleng.2006.04.005

Liu, J. F., You, Y., and Chen, X. C. (2012). Potential damages and identification of debris flow barrier lakes in the upper Minjiang River drainage. *Sci. Geogr. Sin.* 32 (7), 885–891. doi:10.13249/j.cnki.sgs.2012.07.885

Liu, B., He, K., Han, M., Hu, X., Wu, T., Wu, M., et al. (2021a). Dynamic process simulation of the Xiaogangjian rockslide occurred in shattered mountain based on 3DEC and DFN. *Comput. Geotechnics* 134, 104122. doi:10.1016/j.compgeo.2021.104122

Liu, B., Hu, X., Ma, G., He, K., Wu, M., and Liu, D. (2021b). Back calculation and hazard prediction of a debris flow in Wenchuan meizoseismal area, China. *Bull. Eng. Geol. Environ.* 80 (4), 3457–3474. doi:10.1007/s10064-021-02127-3

Mao, L., Cavalli, M., Comiti, F., Marchi, L., Lenzi, M. A., and Arattano, M. (2009). Sediment transfer processes in two Alpine catchments of contrasting morphological settings. *J. Hydrology* 364 (1-2), 88–98. doi:10.1016/j.jhydrol.2008.10.021

Marc, O., Hovius, N., Meunier, P., Uchida, T., and Hayashi, S. (2015). Transient changes of landslide rates after earthquakes. *Geology* 43 (10), 883–886. doi:10.1130/g36961.1

Marc, O., Hovius, N., Meunier, P., Gorum, T., and Uchida, T. (2016). A seismologically consistent expression for the total area and volume of earthquake-triggered landsliding. *J. Geophys. Res. Earth Surf.* 121, 640–663. doi:10.1002/2015jf003732

Parker, R. N., Densmore, A. L., Rosser, N. J., De Michele, M., Li, Y., Huang, R., et al. (2011). Mass wasting triggered by the 2008 Wenchuan earthquake is greater than orogenic growth. *Nat. Geosci.* 4 (7), 449–452. doi:10.1038/ngeo1154

Pei, X. J., and Huang, R. Q. (2013). Analysis of characteristics of geololical hazard by 4 ·20 Lushan Earthquake in Sichuan China. *J. Chengdu Univ. Technol. Sci. Technol. Ed.* 40 (3), 257–263. doi:10.3969/j.issn.1671-9727.2013.03.05

Scheidl, C., Rickenmann, D., and Chiari, M. (2008). The use of airborne LiDAR data for the analysis of debris flow events in Switzerland. *Nat. Hazards Earth Syst. Sci.* 8 (5), 1113–1127. doi:10.5194/nhess-8-1113-2008

Shen, P., Zhang, L. M., Fan, R. L., Zhu, H., and Zhang, S. (2020a). Declining geohazard activity with vegetation recovery during first ten years after the 2008 Wenchuan earthquake. *Geomorphology* 352, 106989. doi:10.1016/j.geomorph.2019.106989

Shen, W., Wang, D., He, S., and Li, T. (2020b). Numerical assessment of the impeding effect of check dams in the Hongchun debris flow gully, Sichuan Province, China. *Bull. Eng. Geol. Environ.* 79 (6), 2833–2845. doi:10.1007/s10064-020-01755-5

Shieh, C. L., Chen, Y. S., Tsai, Y. J., and Wu, J. H. (2009). Variability in rainfall threshold for debris flow after the Chi-Chi earthquake in central Taiwan, China. *Int. J. Sediment Res.* 24, 177–188. doi:10.1016/s1001-6279(09)60025-1

Stoffel, M., and Beniston, M. (2006). On the incidence of debris flows from the early little ice age to a future greenhouse climate: A case study from the Swiss alps. *Geophys. Res. Lett.* 33 (16), L16404. doi:10.1029/2006gl026805

Stoffel, M. (2010). Magnitude–frequency relations of debris flows - a case study based on field surveys and tree-ring records. *Geomorphology* 116 (1-2), 67–76. doi:10.1016/j.geomorph.2009.10.009

Tang, C., and van Westen, C. J. (2018). *Atlas of wenchuan-earthquake geohazards: Analysis of co-seismic and post-seismic geohazards in the area affected by the 2008 wenchuan earthquake*. Beijing: Science Press.

Tang, C., Zhu, J., Li, W. L., and Liang, J. T. (2009). Rainfall-triggered debris flows following the Wenchuan earthquake. *Bull. Eng. Geol. Environ.* 68 (2), 187–194. doi:10.1007/s10064-009-0201-6

Tang, C., Zhu, J., Qi, X., and Ding, J. (2011a). Landslides induced by the wenchuan earthquake and the subsequent strong rainfall event: A case study in the beichuan area of China. *Eng. Geol.* 122, 22–33. doi:10.1016/j.enggeo.2011.03.013

Tang, C., Zhu, J., Ding, J., Cui, X. F., Chen, L., and Zhang, J. S. (2011b). Catastrophic debris flows triggered by a 14 August 2010 rainfall at the epicenter of the Wenchuan earthquake. *Landslides* 8 (4), 485–497. doi:10.1007/s10346-011-0269-5

Tang, C., van Asch TwjChang, M., Chen, G. Q., Zhao, X. H., and Huang, X. C. (2012). Catastrophic debris flows on 13 August 2010 in the qingping area, southwestern China: The combined effects of a strong earthquake and subsequent rainstorms. *Geomorphology* 139, 559–576. doi:10.1016/j.geomorph.2011.12.021

van Asch, T. W. J., Tang, C., Alkema, D., Zhu, J., and Zhou, W. (2014). An integrated model to assess critical rainfall thresholds for run-out distances of debris flows. *Nat. Hazards (Dordr).* 70 (1), 299–311. doi:10.1007/s11069-013-0810-z

van Steijn, H. (1996). Debris-flow magnitude—frequency relations for mountainous regions of central and northwest Europe. *Geomorphology* 15 (3-4), 259–273. doi:10.1016/0169-555x(95)00074-f

Wang, E., and Meng, Q. (2009). Mesozoic and Cenozoic tectonic evolution of the Longmenshan fault belt. *Sci. China Ser. D-Earth. Sci.* 52, 579–592. doi:10.1007/s11430-009-0053-8

Wen, X., Fan, J., Yi, G., Deng, Y., and Long, F. (2008a). A seismic gap on the Anninghe fault in Western Sichuan, China. *Sci. China Ser. D-Earth. Sci.* 51 (10), 1375–1387. doi:10.1007/s11430-008-0114-4

Wen, X. Z., Ma, S. L., Xu, X. W., and He, Y. N. (2008b). Historical pattern and behavior of earthquake ruptures along the eastern boundary of the Sichuan-Yunnan faulted-block, Southwestern China. *Phys. Earth Planet. Interiors* 168, 16–36. doi:10.1016/j.pepi.2008.04.013

Wolman, M. G., and Miller, J. P. (1960). Magnitude and frequency of forcesin geomorphic processes. *J. Geol.* 68, 54–74. doi:10.1086/626637

Xiong, J., Tang, C., Chen, M., Gong, L., Li, N., Zhang, X., et al. (2021). Long-term changes in the landslide sediment supply capacity for debris flow occurrence in Wenchuan County, China. *Catena* 203, 105340. doi:10.1016/j.catena.2021.105340

Xiong, J., Tang, C., Gong, L. F., Chen, M., Li, N., Shi, Q. Y., et al. (2022). How landslide sediments are transferred out of an alpine basin: Evidence from the epicentre of the Wenchuan earthquake. *CATENA* 208, 105781. doi:10.1016/j.catena.2021.105781

Xu, Q. (2010). The 13 August 2010 catastrophic debris flows in sichuan province: Characteristic, genetic mechanism and suggestions. *J. Eng. Geol.* 18 (5), 596–608. doi:10.3724/SP.J.1231.2010.06586

Xu, Q., Zhang, S., Li, W. L., and van Asch Twj (2012). The 13 August 2010 catastrophic debris flows after the 2008 Wenchuan earthquake, China. *Nat. Hazards Earth Syst. Sci.* 12, 201–216. doi:10.5194/nhess-12-201-2012

Xu, C., Xu, X. W., Tian, Y. Y., Shen, L. L., Yao, Q., Huang, X. Q., et al. (2016). Two comparable earthquakes produced greatly different coseismic landslides: The 2015 Gorkha, Nepal and 2008 wenchuan, China events. *J. Earth Sci.* 27 (6), 1008–1015. doi:10.1007/s12583-016-0684-6

Yang, W., Qi, W., and Zhou, J. (2018). Decreased post-seismic landslides linked to vegetation recovery after the 2008 Wenchuan earthquake. *Ecol. Indic.* 89, 438–444. doi:10.1016/j.ecolind.2017.12.006

Yi, G. X., Long, F., Wen, X. Z., Liang, M. J., and Wang, S. W. (2015). Seismogenic structure of the M6.3 kangding earthquake sequence on 22 Nov.2014, southwestern China. *Chin. J. Geophysics-Chinese Ed.* 58 (4), 1205–1219. doi:10.6038/cjg20150410

Yin, Y. P. (2008). Researches on the geo-hazards triggered by Wenchuan earthquake, Sichuan. *J. Eng. Geol.* 16 (4), 433–444.

You, Y., Liu, J., Chen, X., and Pan, H. (2012). Debris flow formation conditions and optimal characteristics of drainage canal following Wenchuan earthquake. *Environ. Earth Sci.* 65 (4), 1005–1012. doi:10.1007/s12665-011-1024-x

Yu, B., Ma, Y., and Wu, Y. F. (2010). Investigation of severe debris flow hazards in wenjia gully of sichuan province after the wenchuan earthquake. *J. Eng. Geol.* 18 (6), 827–836. doi:10.3724/SP.J.1231.2010.06586

Yu, B., Ma, Y., and Zhang, J. N. (2011). The group debris flow hazards after the Wenchuan earthquake in Longchi, Dujiangyan, Sichuan province. *J. Mt. Sci.* 29 (6), 738–746. doi:10.1007/s12583-011-0163-z

Yu, B., Wu, Y., and Chu, S. (2014). Preliminary study of the effect of earthquakes on the rainfall threshold of debris flows. *Eng. Geol.* 182, 130–135. doi:10.1016/j.enggeo.2014.04.007

Yu, B., Yang, L., Chang, M., and van Asch, T. W. (2021). A new prediction model on debris flows caused by runoff mechanism. *Environ. Earth Sci.* 80 (1), 26–11. doi:10.1007/s12665-020-09336-1

Zeng, C., Cui, P., Ge, Y., Zhang, Y., Lei, Y., and Yan, Y. (2014). Characteristics and mechanism of buildings damaged by debris flows on 11 July, 2013 in Qipangou of Wenchuan, Sichuan. *J. Earth Sci. Environ.* 36 (2), 81–91. doi:10.3969/j.issn.1672-6561.2014.02.012

Zhang, L. M., Zhang, S., and Huang, R. Q. (2014). Multi-hazard scenarios and consequences in Beichuan, China: The first five years after the 2008 Wenchuan earthquake. *Eng. Geol.* 180, 4–20. doi:10.1016/j.enggeo.2014.03.020

Zhang, S., and Zhang, L. M. (2017). Impact of the 2008 Wenchuan earthquake in China on subsequent long-term debris flow activities in the epicentral area. *Geomorphology* 276, 86–103. doi:10.1016/j.geomorph.2016.10.009

Zhou, W., and Tang, C. (2014). Rainfall thresholds for debris flow initiation in the Wenchuan earthquake-stricken area, southwestern China. *Landslides* 11 (5), 877–887. doi:10.1007/s10346-013-0421-5

Frontiers in Earth Science

Investigates the processes operating within the major spheres of our planet

Advances our understanding across the earth sciences, providing a theoretical background for better use of our planet's resources and equipping us to face major environmental challenges.

Discover the latest Research Topics

See more →



Frontiers

Avenue du Tribunal-Fédéral 34
1005 Lausanne, Switzerland
frontiersin.org

Contact us

+41 (0)21 510 17 00
frontiersin.org/about/contact